THE
PHYSICAL REVIEW

A journal of experimental and theoretical physics established by E. L. Nichols in 1893

SECOND SERIES, VOL. 98, No. 5 JUNE 1, 1955

Direct Evaluation of Fractional Parentage Coefficients Using Young Operators: Normalization of Four-Particle Wave Functions

M. J. ENGLEFIELD
Mathematics Department, The University, Southampton, England
(Received February 28, 1955)

In a recent paper by Jahn, four-particle wave functions of specified symmetry were generated by using Young operators. When three of the angular momenta of the individual particles were the same, the functions were not normalized, an undetermined factor $N_{\alpha\beta}$ being introduced. Explicit expressions for this factor, in terms of the Hope χ function, are given.

1. $j_1^2 j_2$ CONFIGURATION

EQUATION (62D) of Jahn's paper[1] reads:

$$\begin{aligned}
&\Phi(\alpha,\beta|\,j_1^2 J_1, j_1 j_2 J_2, JM\,|\,\rho,\sigma)\\
&=N_{\alpha\beta}(f_\lambda/6)^{\frac{1}{2}}\delta_p(\alpha,\,2j_1-J_1)\\
&\times\Big\{\delta(\alpha,\rho)\delta(\beta,\sigma)\Phi(j_1^2 J_1, j_1 j_2 \sigma J_2, JM)\\
&+S(\lambda)\delta_p(\alpha,\sigma)\delta_p(\beta,\rho)(-1)^{J_1+J_2-J}\\
&\times\Phi(j_1 j_2 \rho J_2, j_1^2 J_1, JM)+2\theta_{\alpha\beta,\rho\sigma}{}^{[\lambda]}(P_{23})\\
&\times\sum_{J_3 J_4}\chi\begin{bmatrix} j_1 & j_1 & J_1\\ j_1 & j_2 & J_2\\ J_3 & J_4 & J\end{bmatrix}\Big[\delta_p(\rho,\,2j_1-J_3)\\
&\times\Phi(j_1^2 J_3, j_1 j_2 \sigma J_4, JM)+\delta_p(\sigma,\,2j_1-J_3)\\
&\times(-1)^{\alpha+\beta+J_3+J_4-J}\Phi(j_1 j_2 \rho J_4 j_1^2 J_3, JM)\Big]\Big\}. \qquad (1)
\end{aligned}$$

For this configuration, the following notation will be used:

$$\chi=\chi\begin{bmatrix} j_1 & j_1 & J_1\\ j_1 & j_2 & J_2\\ J_1 & J_2 & J\end{bmatrix}, \qquad (2)$$

$$\chi_\alpha=\chi\begin{bmatrix} j_1 & j_1 & J_1\\ j_1 & j_2 & J_2\\ J_3 & J_4 & J\end{bmatrix}+\alpha\delta(J_1,J_3)\delta(J_2,J_4), \qquad (3)$$

$$\begin{aligned}
\xi_\alpha{}^2&=\sum_{J_3,J_4}\delta_p(2j_1,J_3)\chi_\alpha{}^2,\\
\eta_\alpha{}^2&=\sum_{J_3,J_4}\delta_p(2j_1+1,\,J_3)\chi_\alpha{}^2.
\end{aligned} \qquad (4)$$

These symbols have the following properties[2]: If

$$\delta_p(2j_1,J_1)=0,\quad \xi_\alpha=\xi_0;\quad \text{if}\quad \delta_p(2j_1,J_1)=1,\quad \eta_\alpha=\eta_0, \qquad (5)$$

$$\xi_\alpha{}^2+\eta_\alpha{}^2=1+2\alpha\chi+\alpha^2, \qquad (6)$$

$$\xi_\alpha{}^2+\xi_{-\alpha}{}^2=2\xi_0{}^2+2\alpha^2\delta_p(2j_1,J_1), \qquad (7)$$

$$\eta_\alpha{}^2+\eta_{-\alpha}{}^2=2\eta_0{}^2+2\alpha^2\delta_p(2j_1+1,\,J_1), \qquad (8)$$

$$\xi_0{}^2=\tfrac{1}{2}(1+\chi), \qquad (9)$$

$$\eta_0{}^2=\tfrac{1}{2}(1-\chi). \qquad (10)$$

Consider now, as an example, the determination of $N_{11,22}$. From (1) and (3),

$$\begin{aligned}
&\Phi(11,22|\,j_1^2 J_1, j_1 j_2 J_2, JM\,|\,11,22)\\
&=N_{11,22}(1/\sqrt{3})\delta_p(2j_1,J_1)\\
&\times\{\Phi([j_1^2]J_1,[j_1 j_2]J_2,JM)\\
&+(-1)^{J_1+J_2-J}\Phi([j_1 j_2]J_2,[j_1^2]J_1,JM)\\
&-\sum_{J_3 J_4}\chi_0\delta_p(2j_1,J_3)\Phi([j_1^2]J_3,[j_1 j_2]J_4,JM)\\
&-\sum_{J_3 J_4}\chi_0\delta_p(2j_1,J_3)(-1)^{J_3+J_4-J}\\
&\qquad\times\Phi([j_1 j_2]J_4,[j_1^2]J_3,JM)\},
\end{aligned}$$

where the square brackets[3] denote a symmetric state of

[1] H. A. Jahn, Phys. Rev. **96**, 989 (1954). The symbols used in Eq. (1) are defined in this paper.

[2] These results are proved in an Appendix.

[3] This notation is due to H. A. Jahn.

two particles. If we use (3),

$$\Phi(11,22|\,j_1^2J_1,j_1j_2J_2,JM\,|\,11,22)$$
$$=-N_{11,22}(1/\sqrt{3})\delta_p(2j_1,J_1)$$
$$\times\sum_{J_3J_4}\chi_{-1}\delta_p(2j_1,J_3)\{\Phi([j_1^2]J_3,[j_1j_2]J_4,JM)$$
$$+(-1)^{J_3+J_4-J}\Phi([j_1j_2]J_4,[j_1^2]J_3,JM)\}.$$

By using (4), this state is normalized if $\frac{2}{3}\xi_{-1}^2N_{11,22}^2=1$. By using (5), (6), and (10), $N_{11,22}^2=(1-\chi)^{-1}$. Similarly,

$$\Phi(11,22|\,j_1^2J_1,j_1j_2J_2,JM\,|\,12,12)$$
$$=N_{11,22}(1/\sqrt{3})\delta_p(2j_1,J_1)\sqrt{3}\sum_{J_3J_4}\chi_0\delta_p(2j_1+1,J_3)$$
$$\times[\Phi(\{j_1^2\}J_3,\{j_1j_2\}J_4,JM)+(-1)^{J_3+J_4-J}$$
$$\times\Phi(\{j_1j_2\}J_4,\{j_1^2\}J_3,JM)],$$

where the curly brackets[3] indicate an antisymmetric state of two particles. This state is normalized if

$$2\eta_0^2N_{11,22}^2=1;\quad\text{using (10), } N_{11,22}^2=(1-\chi)^{-1}.$$

It is necessary to consider both these states in order to verify that $N_{11,22}$ is independent of ρ and σ.

Examining the other cases in a similar way, the following results may be obtained:

$$N_{11,11}^2=(1+2\chi)^{-1};\quad N_{12,34}^2=(1-2\chi)^{-1},\quad (11),\ (12)$$
$$N_{11,21}^2=N_{12,13}^2=1,\quad (13)$$
$$N_{11,12}^2=N_{12,11}^2=N_{12,12}^2=(1+\chi)^{-1},\quad (14)$$
$$N_{11,22}^2=N_{11,23}^2=N_{23,11}^2=(1-\chi)^{-1}.\quad (15)$$

2. j^4 CONFIGURATION

Equation (62E) of Jahn's paper[1] may be simplified to read

$$\Phi(\alpha,\beta|\,j^2J_1,j^2J_2,JM\,|\,\rho,\sigma)$$
$$=N_{\alpha\beta}(f_\lambda/6)^{\frac{1}{2}}\delta_p(\alpha,2j-J_1)\delta_p(\beta,2j-J_2)$$
$$\times\Big[\delta(\alpha,\rho)\delta(\beta,\sigma)\Phi(j^2J_1,j^2J_2,JM)$$
$$+S(\lambda)\delta_p(\alpha,\sigma)\delta_p(\beta,\rho)(-1)^{J_1+J_2-J}\Phi(j^2J_2,j^2J_1,JM)$$
$$+4\theta_{\alpha\beta,\rho\sigma}{}^{[\lambda]}(P_{23})\sum_{J_3J_4}\chi\begin{bmatrix}j&j&J_1\\j&j&J_2\\J_3&J_4&J\end{bmatrix}\delta_p(\rho,2j-J_3)$$
$$\times\delta_p(\sigma,2j-J_4)\Phi(j^2J_3,j^2J_4,JM)\Big].\quad (16)$$

For the evaluation of the constant $N_{\alpha\beta}$, it is convenient to define

$$\chi=\chi\begin{bmatrix}j&j&J_1\\j&j&J_2\\J_1&J_2&J\end{bmatrix},\quad (17)$$

$$\chi_{\alpha\beta}=\chi\begin{bmatrix}j&j&J_1\\j&j&J_2\\J_3&J_4&J\end{bmatrix}+\alpha\delta(J_1,J_3)\delta(J_2,J_4)$$
$$+(-1)^J\beta\delta(J_1,J_4)\delta(J_2,J_3),\quad (18)$$

$$\xi_{\alpha\beta}^2=\sum_{J_3J_4}\delta_p(2j,J_3)\delta_p(2j,J_4)\cdot\chi_{\alpha\beta}^2,\quad (19a)$$

$$\eta_{\alpha\beta}^2=\sum_{J_3J_4}\delta_p(2j+1,J_3)\delta_p(2j+1,J_4)\cdot\chi_{\alpha\beta}^2,\quad (19b)$$

$$\zeta_{\alpha\beta}^2=\sum_{J_3J_4}\delta_p(2j,J_3)\delta_p(2j+1,J_4)\cdot\chi_{\alpha\beta}^2,\quad (19c)$$

$$\xi_{00}=\xi,\quad \eta_{00}=\eta,\quad \zeta_{00}=\zeta.\quad (20)$$

These symbols have the following properties[2]:

$$\xi^2+\eta^2+2\zeta^2=1,\quad (21)$$

$$\sum_{J_3J_4}\delta_p(2j+1,J_3)\delta_p(2j,J_4)\chi_{\beta\alpha}{}^2=\zeta_{\alpha\beta}{}^2,\quad (22)$$

$$\xi_{\alpha\beta}{}^2=\xi^2+\delta_p(J_1,J_2)\delta_p(2j,J_1)$$
$$\times[\alpha^2+\beta^2+2(\alpha+\beta)\chi+2(-1)^J\alpha\beta\delta(J_1,J_2)],\quad (23a)$$

$$\eta_{\alpha\beta}{}^2=\eta^2+\delta_p(J_1,J_2)\delta_p(2j+1,J_1)$$
$$\times[\alpha^2+\beta^2+2(\alpha+\beta)\chi+2(-1)^J\alpha\beta\delta(J_1,J_2)],\quad (23b)$$

$$\zeta_{\alpha\beta}{}^2=\zeta^2+\delta_p(J_1,J_2+1)[\delta_p(2j,J_1)$$
$$\times\{\alpha^2+2\alpha\chi\}+\delta_p(2j,J_2)\{\beta^2+2\beta\chi\}].\quad (23c)$$

If $J_1\neq J_2$,

$$\xi^2=\tfrac{1}{4}+\tfrac{1}{2}\chi,\quad \eta^2=\tfrac{1}{4}-\tfrac{1}{2}\chi,\quad \zeta^2=\tfrac{1}{4}.\quad (24)$$

If $J_1=J_2$, J even,

$$\xi^2=\tfrac{1}{2}+\tfrac{1}{2}\chi,\quad \eta^2=\tfrac{1}{2}-\tfrac{1}{2}\chi,\quad \zeta^2=0.\quad (25)$$

If $J_1=J_2$, J odd,

$$\xi^2=\eta^2=0,\quad \zeta^2=\tfrac{1}{2}.\quad (26)$$

By using these results, the $N_{\alpha\beta}$ of (16) is found to be:
If $J_1\neq J_2$,

$$N_{11,11}^2=(1+4\chi)^{-1},\quad (27)$$
$$N_{12,34}^2=(1-4\chi)^{-1},\quad (28)$$
$$N_{11,21}^2=N_{12,13}^2=1,\quad (29)$$
$$N_{11,12}^2=N_{12,11}^2=N_{12,12}^2=(1+2\chi)^{-1},\quad (30)$$
$$N_{11,22}^2=N_{11,23}^2=N_{23,11}^2=(1-2\chi)^{-1}.\quad (31)$$

If $J_1=J_2$, J even:

$$N_{11,11}^2=\tfrac{1}{2}(1+2\chi)^{-1},\quad (32)$$
$$N_{12,34}^2=\tfrac{1}{2}(1-2\chi)^{-1},\quad (33)$$
$$N_{11,22}^2=\tfrac{1}{2}(1-\chi)^{-1},\quad (34)$$
$$N_{12,12}^2=\tfrac{1}{2}(1+\chi)^{-1},\quad (35)$$
$$N_{11,21}^2=N_{11,12}^2=N_{12,11}^2=N_{11,23}^2$$
$$=N_{23,11}^2=N_{12,13}^2=0.\quad (36)$$

If $J_1=J_2$, J odd:

$$N_{11,21}^2=N_{12,13}^2=\tfrac{1}{2},\quad (37)$$

and for all other values of α and β,

$$N_{\alpha\beta}=0. \tag{38}$$

Equations (36) and (38) mean that the wave functions generated vanish identically, e.g.,

$$\Phi(11,21\,|\,j^2J_1,j^2J_1,JM\,|\,\rho\sigma)=0$$

when J is even.

3. ORTHOGONALITY OF STATES AND THEIR CLASSIFICATION

By varying the values of α, β, J_1, and J_2 in Eqs. (1) and (16), different sets of states may be obtained, but they are not necessarily orthogonal. For example, if in Eq. (1) $(\alpha,\beta)=(\rho,\sigma)=(11,11)$, $j_1=1$, $j_2=2$, and $J=1$, then there are four possible pairs of values for J_1 and J_2. These give rise to four linearly dependent states: the rank of the matrix of fractional parentage coefficients is only two, showing that the p^3d configuration has two totally symmetric P-states.[4] When the p^3d states of symmetry-type [31] are obtained, however, the correct number of orthogonal states are derived by taking $(\alpha,\beta)=(11,21)$, and all allowed values of J_1 and J_2. In this case, states with the same J may be classified according to the values of J_1 and J_2 in the generating function Φ_0.

In the general case of the $j_1{}^3j_2$ configuration, it seems clear that a complete, orthogonal set of coefficients could be obtained by using states $\Phi(j_1{}^3[\lambda]J_1,j_2,JM)$ as generating functions. The application of the permutations would then require the $\langle j_1{}^3\,|\,j_1{}^2,j_1\rangle$ coefficients.

The application of these results to numerical cases has been made using the standard (P_{12},P_{34})-diagonal Young Yamanouchi representation[5]; this involves replacing the label (23,11) by (12,31), and changing sign whenever the substitution is made. The $\langle 4\,|\,2,2\rangle$ fractional parentage coefficients for a complete, orthogonal set of states have been obtained in the cases $j_1=1$, $j_2=2$ (p^3d), j^4 with $j=1$ (p^4), and $j=\frac{3}{2}$.

In conclusion, the author would like to thank Professor H. A. Jahn for a patient explanation of the Young operator method, and also the Department of Scientific and Industrial Research for a maintenance grant.

4. APPENDIX

Equations (5)–(8) and (21)–(23) are obvious from the definitions. Equations (9) and (10) are obtained as follows: Let $\Phi_0=\Phi(j_1(1)j_1(2)J_1,j_1(3)j_2(4)J_2,JM)$, where the numbers in brackets are the particle numbers. Then

$$\Phi_0=\sum_{J_3J_4}\chi_0\Phi(j_1(1)j_1(3)J_3,j_1(2)j_2(4)J_4,JM); \tag{39}$$

$$\Phi_0=\sum_{J_3J_4}\delta_p(2j_1,J_3)\chi_0\Phi([j_1(1)j_1(3)J_3],j_1(2)j_2(4)J_4,JM)$$
$$+\sum_{J_3J_4}\delta_p(2j_1+1,J_3)\chi_0$$
$$\times\Phi(\{j_1(1)j_1(3)J_3\},j_1(2)j_2(4)J_4,JM), \tag{40}$$

where square and curly brackets are used as before. Using this expansion, it is easily seen that

$$\bar{\Phi}_0P_{13}\Phi_0=\xi_0{}^2-\eta_0{}^2. \tag{41}$$

But

$$\bar{\Phi}_0P_{13}\Phi_0=\bar{\Phi}_0P_{12}P_{23}P_{12}\Phi_0=\bar{\Phi}_0P_{12}P_{23}(-1)^{2j_1-J_1}\Phi_0$$
$$=\bar{\Phi}_0P_{12}(-1)^{2j_1-J_1}\sum_{J_3J_4}\chi_0$$
$$\times\Phi(j_1(1)j_1(2)J_3,j_1(3)j_2(4)J_4,JM)$$
$$=\sum_{J_3J_4}(-1)^{J_1+J_3}\chi_0\bar{\Phi}_0$$
$$\times\Phi(j_1(1)j_1(2)J_3,j_1(3)j_2(4)J_4,JM)$$
$$=\chi. \tag{42}$$

Comparing (41) and (42),

$$\chi=\xi_0{}^2-\eta_0{}^2, \tag{43}$$

which is also true if $j_1=j_2$. But from (6), $\xi_0{}^2+\eta_0{}^2=1$. Equations (9) and (10) follow immediately.

Equations (24)–(26) are obtained by a similar method:

$$\bar{\Phi}(j(1)j(2)J_1,j(3)j(4)J_2,JM)$$
$$\times\Phi(j(1)j(2)J_2,j(3)j(4)J_1,JM)=\delta(J_1,J_2).$$

The left-hand side of this equation may be expanded as a sum over χ functions as in (39); this sum may be split up according to the symmetry of the first and last pairs of particles as in (40). This gives

$$\xi^2+\eta^2-2\zeta^2=(-1)^J\delta(J_1,J_2). \tag{44}$$

When $j_1=j_2=j$, the analysis leading to (43) gives

$$\chi=\xi^2-\eta^2. \tag{45}$$

Equations (24) and (25) are obtained from (21), (44), and (45). The symmetry relations[6] of the χ function show that $\chi\begin{bmatrix}j & j & J_1\\ j & j & J_1\\ J_1 & J_1 & J\end{bmatrix}=0$ if J is odd; this leads to (26).

[4] This is, of course, more easily deduced by other methods.

[5] Elliott, Hope, and Jahn, Trans. Roy. Soc. (London) **A246**, 241 (1953).

[6] H. A. Jahn and J. Hope, Phys. Rev. **93**, 318 (1954).

Inelastic Collision Cross Sections at 1.0-, 4.0-, and 4.5-Mev Neutron Energies*

J. R. Beyster, R. L. Henkel, R. A. Nobles, and J. M. Kister
University of California, Los Alamos Scientific Laboratory, Los Alamos, New Mexico
(Received January 26, 1955)

Inelastic cross sections have been obtained from measurements of sphere transmission for incident neutron energies of 1.0, 4.0, and 4.5 Mev. Cross sections were measured for Al, Fe, Cu, Zn, Ag, Cd, Sn, Au, Pb, and Bi at the three neutron energies. In addition, the carbon inelastic cross section was measured at 1.0 Mev, the Be, C, Ti, Ni, Zr, and W cross sections were measured at 4.0 Mev, and the Ti, Ni, Zr, and W were measured at 4.5. The cross sections were determined at about ten energy thresholds of the neutron detector to obtain information about the energy spectra of inelastic neutrons. The experimental techniques and the method of evaluating the measurements are discussed. The results of this investigation are compared with other determinations of inelastic cross sections.

I. INTRODUCTION

THE measurement of inelastic collision cross sections for neutron energies in the Mev region has long been a difficult problem. A need for these cross sections arises in the study of neutron behavior in the core and shielding of nuclear reactors. Moreover, cross sections of this type are important for testing the validity of current nuclear models. From theoretical considerations on a specific model, the cross section for formation of the compound nucleus can be calculated.[1] The inelastic collision cross section is an experimental measure of this cross section if compound elastic scattering is negligible.

The cross sections to be discussed here were obtained from sphere transmission experiments. This method has been used extensively in the past.[2,3] Part of the experimental results of this work have been published previously.[4] In this paper the experimental procedures, numerical analysis, and all of the experimental results will be presented.

II. METHOD OF ANALYSIS

The sphere method of measuring inelastic collision cross sections has been discussed in detail elsewhere,[5,6] and only a brief description and justification of the analytical procedures will be given here. The inelastic collision cross section is the sum of the cross sections for all processes except elastic scattering. The experimental arrangement for measuring sphere transmission is shown schematically in Fig. 1. The sphere transmission in a constant neutron flux is the ratio of the counting rate with the sphere surrounding the detector to the counting rate with the sphere removed. To interpret this quantity in terms of the inelastic collision cross section the neutron source is considered to be at the sphere center in Fig. 1, with the detector outside the sphere at the original source position. The validity of this interchange of source and detector (reciprocity theorem) has been demonstrated elsewhere.[5] The neutron multiple scattering analysis for spherical geometries proposed by Bethe[5,6] is applied to specify the relationship between inelastic cross section and transmission. In this report, only neutrons which have no inelastic scatterings are considered. Two quantities P_n and $\bar{P}_n$ ($n=0, 1, 2, 3, 4, \cdots$) are now defined. P_n is the average probability that a neutron will escape from the spherical shell without another collision after having had n elastic collisions. $\bar{P}_n$ is the average probability that a neutron will escape and be detected after having had n elastic collisions, divided by the probability of detection per source neutron when no sphere is present. Thus the transmission of a spherical shell is as follows:

$$T=\bar{P}_0+(1-P_0)\frac{\sigma_{el}}{\sigma_t}\bar{P}_1+(1-P_0)(1-P_1)\left(\frac{\sigma_{el}}{\sigma_t}\right)^2\bar{P}_2+\cdots, \quad (1)$$

where σ_{el} is the total elastic cross section and σ_t the total cross section. If N_0 is the number of atoms per cubic centimeter in the shell and r_1 and r_2 the inner and outer shell radii, respectively,

$$P_0=\bar{P}_0=e^{-N_0\sigma_t(r_2-r_1)}. \quad (2)$$

The general P_n is given by

$$P_n=\int_0^{\pi}\int_{r_1}^{r_2}N_n(r)dr\phi_n(\theta)d\omega\varepsilon^{-N_0\sigma Y}\Big/\int_{r_1}^{r_2}N_n(r)dr, \quad (3)$$

* Work performed under the auspices of the U. S. Atomic Energy Commission.

[1] Feshbach, Porter, and Weisskopf, Phys. Rev. **96**, 448 (1954).

[2] Amaldi, Bocciarelli, Cacciapuoti, and Trabacchi, Nuovo cimento **3**, 203 (1946); C. H. Collie and J. H. E. Griffiths, Proc. Roy. Soc. (London) **A155**, 434 (1936); Szilard, Bernstein, Feld, and Ashkin, Phys. Rev. **73**, 1307 (1948); Gittings, Barschall, and Everhard, Phys. Rev. **75**, 1610 (1949); Phillips, Davis, and Graves, Phys. Rev. **88**, 600 (1952).

[3] R. E. Carter and J. R. Beyster, Phys. Rev. **90**, 389 (1953).

[4] Beyster, Henkel, and Nobles, Phys. Rev. **97**, 563 (1955).

[5] H. A. Bethe, Report of Second Conference on Medium Energy Nuclear Physics at the University of Pittsburgh, 1953 (unpublished); H. A. Bethe, Los Alamos Report La-1428, 1952 (unpublished).

[6] Bethe, Beyster, and Carter, Los Alamos Report LA-1429 (unpublished).

where σ is the cross section which determines whether the neutron makes another collision in the distance Y. The quantity $N_n(r)dr$ is the number of nth elastic collisions between r and $r+dr$. $\phi_n(\theta)d\omega$ is the probability normalized to unity of scattering elastically into solid angle $d\omega$ at angle θ on the nth elastic collision. Y is the distance through material a neutron must travel at polar angle θ from position r to escape from the sphere. $\bar{P}_n$ is given by

$$\bar{P}_n=\frac{\int_0^{\pi}\int_{r_1}^{r_2} N_n(r)dr\phi_n(\theta)d\omega\dfrac{W(\alpha)}{\cos\alpha}\varepsilon^{-N_0\sigma Y}}{\int_{r_1}^{r_2} N_n(r)dr}. \quad (4)$$

The $\cos\alpha$ occurs in this expression because of a geometrical effect which depends on the relative magnitudes of the sphere radius and the source to detector distance.[5] The $W(\alpha)$ occurs because of the intensity and energy variation of the neutron source with angle.[6] The determination of $W(\alpha)$ is discussed in Sec. III. The angle α in Fig. 1 is related to the independent variables in the above integral by the expression

$$\sin\alpha=(r/b)\sin\theta. \quad (5)$$

At this point three simplifying assumptions are made:

(1) The first assumption is that transport cross sections may be used to describe the second and later collisions in the shell (i.e., $\sigma=\sigma_{tr}$). The transport cross section is defined by

$$\sigma_{tr}=\sigma_{in}+\sigma_{el}\int_0^{\pi}2\pi\sin\theta\phi_1(\theta)(1-\cos\theta)d\theta,$$

where the right side of the equation is the sum of the inelastic collision cross section and the elastic transport cross section. P_1 and $\bar{P}_1$ may be calculated numerically now since $N_1(r)$ is $N_0\sigma_{el}\exp[-N_0\sigma_t(r-r_1)]$, $\phi_1(r)$ is proportional to the differential cross section for elastic scattering, and $W(\alpha)$ is available from experiment.

(2) The second assumption is that no significant errors will be made in computing P_n or $\bar{P}_n$ $(n>1)$ if the asymptotic normal mode collision distribution for the shell $[N_m(r)dr]$ is used. The escape probabilities calculated for Eqs. (3) and (4) by using the normal mode distribution are called P_m and $\bar{P}_m$, respectively. This assumption is justifiable for two reasons[6]: (a) The average escape probabilities do not depend markedly on the radial collision distribution, $N_n(r)dr$, used in the Eqs. (3) or (4). (b) The radial collision distributions converge quite rapidly with increasing n to the limiting distribution which is the normal mode. This approximation is most realistic for n large, but it gives reliable results even for P_2 and $\bar{P}_2$. In the calculations for this report a slightly more accurate approximation to $N_2(r)dr$ than $N_m(r)dr$ is actually used.[6]

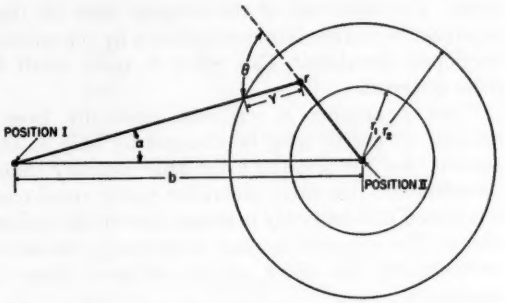

FIG. 1. Neutron source at Position I and neutron detector at Position II for the experimental measurements. These positions were reversed for the analysis of the measured transmissions.

(3) The third assumption made in the evaluation is that the quantities $\phi_2(\theta), \ldots\phi_n(\theta)$ are independent of θ, or that neutrons which have made second- or higher-order elastic transport collisions in the shell have their directions randomly oriented in space. All of the quantities needed to calculate P_2, $\bar{P}_2$, P_m, and $\bar{P}_m$ are now available. Based on these considerations, Eq. (1) becomes

$$T=\varepsilon^{-N_0\sigma_t(r_2-r_1)}+(1-\varepsilon^{-N_0\sigma_t(r_2-r_1)})\frac{\sigma_{el}}{\sigma_t}\left[\bar{P}_1+(1-P_1)\frac{\sigma_{et}}{\sigma_{tr}}\bar{P}_2+\frac{(1-P_1)(1-P_2)\sigma_{et}^2\bar{P}_m}{\sigma_{tr}(\sigma_{in}+\sigma_{et}P_m)}\right]. \quad (6)$$

The quantities σ_{et} and σ_{in} are the elastic transport and inelastic cross sections, respectively. Knowing three parameters [plus such auxiliary information as r_2, r_1, b, and $W(\alpha)$], one is able now to calculate the right side of Eq. (6). These parameters are the total neutron cross section σ_t, the shape of the elastic scattering angular distribution $\phi_1(\theta)d\omega$, and the inelastic collision cross section σ_{in}. A parametric study has shown that Eq. (6) is quite sensitive to the inelastic collision cross section for reasonably thin shells but not sensitive to the other parameters.[6] Therefore one obtains the first two parameters from other sources of information and uses the observed sphere transmission to determine the inelastic cross section.

Equation (6) may be evaluated completely in a few seconds by a high-speed computing machine. It might therefore seem worthwhile to go a step further and to compute exactly the radial and angular distributions of neutrons that make second collisions or, for that matter, to treat all collisions exactly, using the Monte Carlo method. Many test cases[6] have shown that this approximation [Eq. (6)] gives results in complete agreement with those obtained by the Monte Carlo method. In fact, for many problems it is not necessary to use a transmission equation as involved as Eq. (6),[6] and the necessity of machine computing is thus eliminated.

Formulas previously presented assume a point de-

tector. The finite size of the detector used for these experiments is taken into consideration by the methods developed elsewhere.[6] This effect is quite small for these detectors.

When a neutron is scattered elastically from a nucleus, its energy may be changed by only a small amount, but the sensitivity for detection may change considerably. This effect occurs for proton recoil counters biased to detect only neutrons close to the incident energy. The apparent increase in inelastic cross section produced by this effect can be estimated from the expression

$$\Delta\sigma=\sigma_{el}[1-S(\bar{E})]. \quad (7)$$

$\bar{E}$ is the average neutron energy after an elastic collision and $S(\bar{E})$ is the relative sensitivity for detecting this average energy neutron. To consider this effect as exactly as possible, the energy of a neutron while making elastic collisions in the shell is followed by the Monte Carlo method. On escaping from the shell, this neutron is placed in one of 46 energy groups. Each group is assigned an experimentally measured relative detection sensitivity. The observed shell transmission can now be corrected for this effect. If p_i is the relative probability of being in energy group i after escape and s_i is the relative detection sensitivity in this group, then

$$T_{obs}=T_{true}\sum_{i=1}^{46} p_i s_i. \quad (8)$$

It is necessary to process about 5000 neutrons to make this correction accurately in extreme cases.

To evaluate measured transmissions, the Bethe methods and the Monte Carlo method were combined and coded for the Los Alamos MANIAC computer. Inelastic collision cross sections are obtained as follows: For the input parameters T, σ_i, $\phi_1(\theta)$, r_1, r_2, etc., the computer calculates an apparent inelastic cross section by successive iterations using Eq. (6) plus a detector size correction term. It subtracts $\Delta\sigma$ [Eq. (7)] from this cross section to obtain an estimate of the true inelastic collision cross section. This cross section, the total cross section, and the angular distribution for elastic scattering are introduced into the Monte Carlo problem. After the Monte Carlo analysis is completed, to remove the effect of losses of energy on elastic collisions, T_{true} [from Eq. (8)] is set equal to the right side of Eq. (6) with the addition of a detector size term. The inelastic collision cross section is determined from successive iterations in this modified equation. The entire problem for one element at one neutron energy with ten transmissions (measured at ten energy thresholds of the neutron detector) requires about an hour of computing time on the Los Alamos MANIAC.

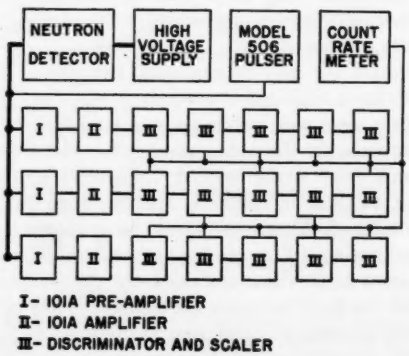

FIG. 2. Electronic arrangement used for the measurement of sphere transmission.

III. EXPERIMENTAL PROCEDURES

A. General

The geometry for all of the sphere transmission experiments is shown in Fig. 1. A $T(p,n)He^3$ neutron source was used. The total spread in neutron energies from the tritium target was about 160 kev at 1 Mev and 70 kev at 4.0 and 4.5 Mev. The analyzed proton beam from the Los Alamos large electrostatic generator passed through an aluminum foil 0.0001 in. thick into a tritium gas target 6 cm long. The sphere and neutron detector were placed in the forward direction at about 30 in. from the source. A long counter[7] was positioned at 120° from the forward direction and about 2 meters from the target. This counter and a precision current integrator were used independently for monitoring.

The neutron detectors were of the biased proton recoil type. Electronic-amplifying and pulse-height discrimination circuits had to be very stable because of the high biases (energy thresholds) used in the experiments. At these biases a fraction of a percent drift in the gain could change the counting rate several percent. Three carefully chosen amplifiers and preamplifiers were placed in parallel as indicated in Fig. 2. Pulses from these circuits were fed into a system of 15 discriminators and scalers. Ten energy thresholds were used; the remaining scaling circuits were placed in parallel on the selected biases. Scalers with the same bias used different amplifiers so that gain fluctuations in any counting channel could be detected while data were being taken. To check over-all gain stability directly, a signal from a precision pulser was applied at the preamplifier input and a counting-rate meter measured the output counting rate after the pulse-height discrimination stage in a scaler. When the pulse-height discrimination was adjusted so that a certain height of pulse applied at the preamplifiers would just trigger a discriminator, then a subsequent gain change in an amplifier or a change in the pulse-height discrimination level in the scaler could be easily detected. It was possible to detect and compensate for changes in gain or discrimination level of less than 0.05 percent. All of

[7] A. O. Hanson and J. L. McKibben, Phys. Rev. 72, 673 (1947).

the amplifiers and scalers used 115-volt ac from regulated power supplies. Temperature control was maintained to about ±1°C on the amplifiers, preamplifiers, and seven of the scalers. These scalers were used on the most critical high biases. Gain drifts of less than 0.2 percent occurred in a normal day's operation.

Routine data taking consisted of measuring the sphere transmissions at least twice for a consistency check. Runs were arranged symmetrically (i.e., sphere off, sphere on, sphere off, sphere on, sphere off) to minimize any electronic gain or neutron yield drifts. The statistical error of a transmission measurement was about 0.4 percent at the higher biases, introducing usually less than 3 percent uncertainty in the final inelastic cross section.

B. 1-Mev Neutron Measurements

In the 1-Mev measurements the proton recoil proportional counter shown in Fig. 3 was used. The envelope of this counter was $\frac{1}{32}$-in. thick brass and the collecting

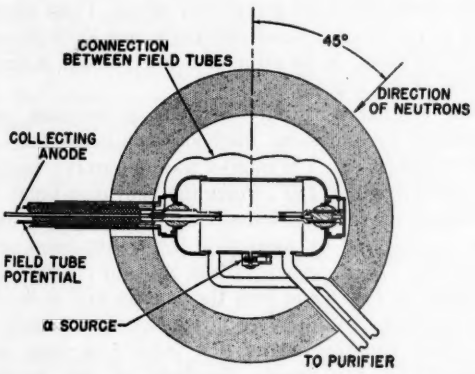

FIG. 3. Gas proportional counter for 1-Mev neutron measurements shown in position inside a sphere.

anode was a stainless steel wire 0.001 in. in diameter. At each end of the counter, field tubes[8] surrounded the central wire so that the counting volume would be precisely determined. The gas filling was 20 percent methane and 80 percent krypton at a pressure of 100 psi. The gas was purified with magnesium ribbon at a temperature of about 160°C.

The characteristics of this detector of importance for the sphere experiment were investigated. The sensitivity of the detector to gamma rays was measured with known source strengths of Cs^{137} and ThC″. This investigation showed that gamma rays from inelastic scattering in the sphere would not be detected significantly (less than 1 gamma-ray count per 1000 neutron counts). An asymmetric counter was undesirable since it would preferentially detect neutrons scattered into it from certain regions of the sphere. The angular

[8] A. L. Cockroft and S. C. Curran, Rev. Sci. Instr. 22, 37 (1951).

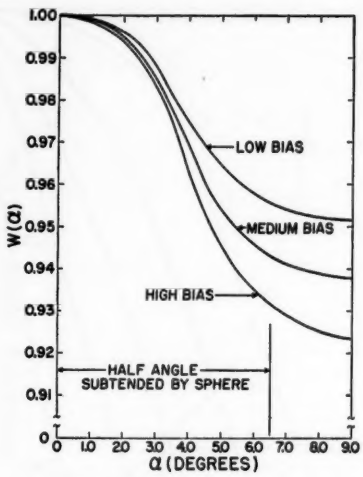

FIG. 4. Intensity *versus* angle for 1-Mev neutrons from $T(p,n)He^3$ neutron source.

asymmetry of the counter was investigated by rotating the counter, keeping its center at a fixed distance from the neutron source. When the gas multiplication was adjusted to be less than about five, the maximum asymmetry was less than 10 percent. To minimize the possible error due to this asymmetry, the counter was positioned as shown in Fig. 3. Counting losses were investigated by reducing the intensity of the neutron source by a factor of about ten and counting a correspondingly longer time, with no apparent change in the total counts recorded. The effect of room-scattered background neutrons was studied by measuring sphere transmissions, using a shadow cone to shield the direct neutrons from the counter. The magnitude of this background was less than 2 percent at the lowest bias and became negligible at the highest bias. Since sphere transmissions measured with the background flux were very nearly the same as those observed for the direct source neutrons, the effect was ignored.

The quantity $W(\alpha)$, used in Sec. II, was measured with the proportional counter at several angles smaller than 8° from the direction of the proton beam. Measurements were made at angles in both the horizontal and vertical planes. The counting rate relative to that at $\alpha=0.0°$ was then plotted for each angle (α) and for each bias of the detector. Three of the measured curves of $W(\alpha)$ are shown in Fig. 4. The relative sensitivity of the detector to neutron energy $S(E)$ for the Monte Carlo calculations was measured by reducing the neutron energy in several steps of about 100 kev. The counting rate at each energy, divided by the rate at 1 Mev and adjusted for target yield changes with energy, is $S(E)$. The relative $T(p,n)He^3$ yields were measured with a long counter placed in the forward direction and agreed with the unpublished measurements of Jarvis *et al.* at this laboratory. Five of the

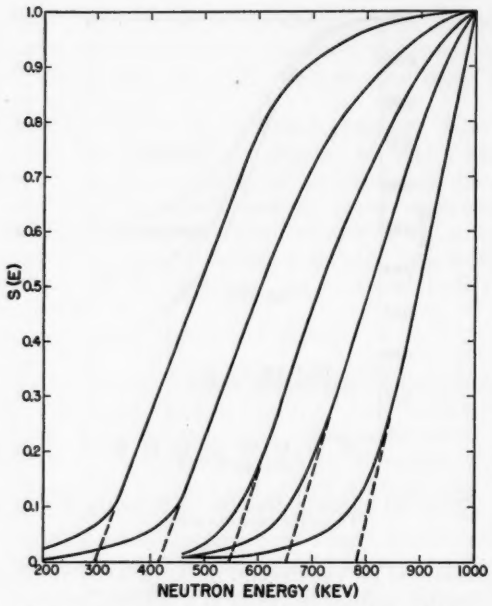

FIG. 5. Sensitivity *versus* neutron energy for biased gas proportional counter.

curves of $S(E)$ measured for this detector are given in Fig. 5.

C. 4.0- and 4.5-Mev Neutron Measurements

The recoil scintillation detector used in this experiment was similar to the counters designed and built by Bonner and co-workers[9] to minimize gamma-ray sensitivity. The counter is shown in Fig. 6. Nine 0.100-inch diameter spheres were machined from a plastic phosphor, Pilot Chemicals Scintillator B. Each sphere was placed in a close-fitting hole ground into a quartz disk. These holes were located in three layers so that light from one phosphor emitted in the direction of the photomultiplier would not traverse another phosphor sphere. Optical contact between quartz and scintillator was obtained with Dow Corning 200 oil. The pulse-height distribution for monoenergetic 4.5-Mev neutrons in this detector, was not much different from that obtained from one plastic sphere. This indicated that there was nearly the same light-collecting efficiency from the various phosphor locations in the quartz assembly. At least 0.4 in. of clear quartz separated spheres in the assembly, eliminating the possibility of electrons with energy less than 5 Mev traversing any two spheres. It was possible, however, for an electron with an energy of about 800 kev to lose all of its energy in one phosphor sphere. The resulting pulse height would be equivalent to the maximum produced by a neutron of about 2.5 Mev. The gamma-ray sensitivity of the detector was measured for the various biases with sources of Cs^{137} and ThC″ of known activity. For the worst situation (2.4-Mev threshold), gamma rays produced by inelastic neutron scattering in the sphere produced less than 0.5 percent of the counts with the sphere on.

The background from the electrostatic generator and target assembly was investigated by filling the target with helium. For the lowest-energy threshold this background was about 1 percent. Sphere transmissions of this background were then measured and indicated that an error less than 0.3 percent in transmission might arise if no correction were made for this background. The effect of room-scattered background was again studied with sphere transmissions measured behind shadow cones. The magnitude of this background was also about 1 percent; neglecting it would cause an error less than 0.3 percent in transmission. A nuclear emulsion was exposed to the 4.0-Mev neutron source by L. Rosen of this laboratory, and showed that almost all of the neutrons above 2.5 Mev were in a single peak. The few percent that were not in this peak were in a continuous background spectrum. The measured transmissions at the low biases were not corrected for the above background and gamma-ray effects. These effects tend to cancel each other and neglecting them should result, at most, in an error of a few percent in cross section at the lowest bias.

The angular sensitivity of detector response was examined by the same methods mentioned for the 1-Mev experiment. The counter was uniformly sensitive at angles less than 150°, where the light pipe began to attenuate the neutron beam. Counter asymmetry was also investigated by measuring the transmission of a very thick ($2\frac{1}{2}$ in.) sphere of lead with the counter axis as shown in Fig. 6 and with the counter axis at 90° to this position. No difference in transmission outside of statistical counting errors (0.4 percent or less) was observed at any energy threshold of the neutron detector.

The effect of a magnetic material on the magnetically shielded Dumont photomultiplier was checked by replacing the neutron-sensitive detector with a NaI crystal at the end of the light pipe and placing a Cs^{137} gamma-ray source near this crystal. The crystal and source were then surrounded by an iron sphere and the position and shape of the photoelectric peak examined. No changes were observed.

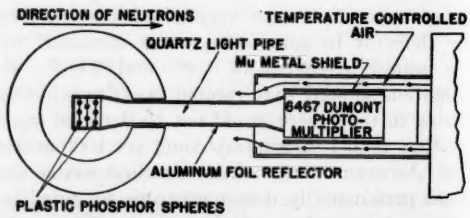

FIG. 6. Scintillation detector for 4.0- and 4.5-Mev neutron measurements shown in position inside a sphere.

[9] McCrary, Taylor, and Bonner, Phys. Rev. **94**, 808(A) (1954).

To investigate the over-all effect of temperature on the light output of the crystal and on the photomultiplier tube gain, the detector shown in Fig. 6 was placed in an oven. These studies indicated that the over-all gain of this system changed by about 0.5 percent per degree centigrade change in temperature. This was a serious difficulty at the higher biases. Therefore the temperature controlled air system shown in Fig. 6 was installed.

Since the gain of the Dumont 6467 photomultiplier was very sensitive to tube high voltage, a precision potentiometer arrangement was used for monitoring and adjusting this voltage.

The quantities $W(\alpha)$ and $S(E)$ were measured by the methods discussed in the 1-Mev experimental section, Sec. III B.

IV. RESULTS AT 1 MEV

Inelastic cross sections measured at several energy thresholds of the neutron detector are given in Table I. The over-all rms errors in the 750-kev measurements are given. Smaller uncertainties are obtained at lower biases. The inelastic collision cross section for each element is also given in Table I. The best determination of this quantity is the measured inelastic cross section for the lowest-energy threshold at which a negligible number of inelastic neutrons are detected. The selection of this threshold is influenced by the available information on the energy levels of the target nuclei,[10] and by the observed variations of inelastic cross section with energy threshold.

The uncertainties included in the determination of experimental error are: (1) the statistical uncertainty in the measurement of sphere transmission, (2) uncertainties in the measurements of $W(\alpha)$ and $S(E)$, (3) uncertainties in the parameters used in the multiple scattering analysis (σ_t and the angular distribution for elastic scattering), and (4) the uncertainty in the correction for loss of energy on elastic collisions. The total cross section and angular distribution parameters were obtained from 1-Mev elastic scattering angular distribution measurements.[11,12] The fourth effect contributed most of the uncertainty in the cross sections given in Table I. By comparing the cross sections given in Fig. 7, it can be seen that the correction due to this effect is very large. If this correction had been made using the approximate method [Eq. (7)] instead of the Monte Carlo method, an additional uncertainty of as much as 10 percent would have occurred in the inelastic cross sections for the 750-kev bias.

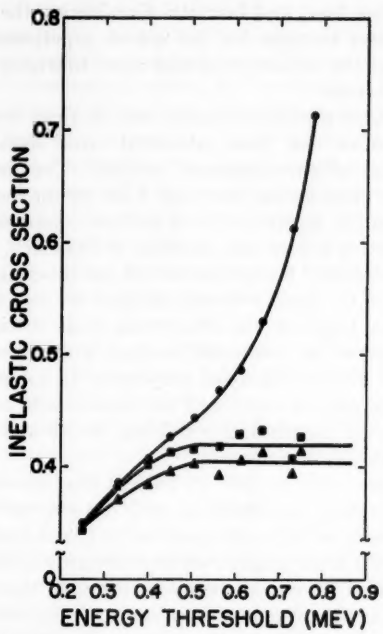

FIG. 7. Measured inelastic cross sections for iron at 1-Mev neutron energy. The circular points represent the cross sections before correcting for loss of energy in elastic collisions. The squares show cross sections calculated from the thin shell transmissions after correcting for loss of energy in elastic collisions. The triangles represent cross sections calculated from the thick iron shell transmissions after the energy loss correction.

TABLE I. Inelastic cross sections for 1-Mev neutrons (barns).

Element	Inelastic collision cross section	Energy threshold (kev) 750	650	550	450	350	250
C	0.0 ±0.04	−0.09±0.14	−0.06	−0.03	−0.02	−0.01	0.00
Al	−0.01±0.03	0.04±0.08	0.04	0.03	0.01	0.00	−0.01
Fe	0.41±0.03	0.41±0.04	0.41	0.41	0.40	0.38	0.35
Cu	0.21±0.04	0.21±0.05	0.21	0.21	0.20	0.18	0.15
Zn	0.10±0.06	0.10±0.06	0.10	0.10	0.10	0.09	0.07
Ag	1.80±0.20	1.61±0.16	1.50	1.34	1.12	0.85	0.56
Cd	1.04±0.08	0.99±0.06	0.99	0.96	0.89	0.74	0.45
Sn	0.06±0.05	0.07±0.05	0.07	0.07	0.06	0.04	0.00
Au	1.80±0.25	1.63±0.10	1.46	1.26	1.05	0.79	0.54
Pb	0.21±0.03	0.23±0.04	0.23	0.22	0.21	0.19	0.16
Bi	0.12±0.03	0.12±0.04	0.12	0.12	0.12	0.12	0.12

Cross sections were measured as a function of energy threshold using two sphere thicknesses for iron and copper. Although the shell thicknesses differed by a factor of two, the calculated cross sections are the same within experimental errors, as shown for iron in Fig. 7.

The inelastic collision cross sections in Table I were compared with those given in reference 11 for elastic scattering angular distribution experiments. The uncertainties in the cross sections determined from those experiments were between five and ten times as large as the uncertainties given in Table I. The two methods agree however within quoted errors. Kiehn and Goodman[13] have reported cross sections at 1 Mev for exciting gamma rays by inelastic neutron scattering in alumi-

[10] Hollander, Perlman, and Seaborg, Revs. Modern Phys. **25**, 469 (1953); Way, Fuller, King, McGinnis, and Hankins, *Nuclear Data Cards* (National Research Council, Washington, D. C., 1955).

[11] M. Walt and H. H. Barschall, Phys. Rev. **93**, 1062 (1954).

[12] The angular distribution of elastic scattering (ϕ_1) for aluminum at 1-Mev neutron energy was obtained from recent unpublished measurements by Walton, Allen, and Taschek.

[13] R. M. Kiehn and C. Goodman, Phys. Rev. **95**, 989 (1954).

num, iron, lead, and bismuth. Considering the spread in neutron energies for the sphere experiments, the results of the two investigations agree to within experimental errors.

Measured inelastic collision cross sections should be equal to or less than calculated cross sections for formation of the compound nucleus. The measured inelastic cross sections in Table I are for the most part less than the theoretical cross sections computed using the complex square-well potential of Feshbach, Porter, and Weisskopf.[1] Exceptions to this are silver and gold, for which the measured cross sections are two to three times as large as the theoretical cross sections for formation of the compound nucleus. Possible explanations of this are discussed elsewhere.[1] It appears that rounding off the corners of the square-well potential used in the calculations will bring theory and experiment into better agreement.[14]

Inelastic cross sections in Table I were measured at several energy thresholds to test the over-all experimental method in known cases and to gain a qualitative idea of the neutron spectrum from inelastic collisions in other cases. Threshold energy is defined as that energy at which the straight-line portion of the sensitivity curve extrapolates to zero sensitivity (see Fig. 5). Ideally, the difference between the total inelastic collision cross section for neutrons of energy E_0 and the cross section obtained for an energy threshold E_T is the cross section for inelastic processes resulting in excitation of levels in the target nucleus below energy E_0-E_T. This is only qualitatively true here, however, since the proportional counter does not have an ideal sensitivity response.

The threshold data in Table I may be used to obtain cross sections for exciting *known* energy levels below 1 Mev by inelastic neutron scattering. The uncertainties in the derived cross sections are large, however, primarily for two reasons: (1) In many cases small cross section changes have to be interpreted and these changes are uncertain to 30 percent or more. (2) The multiple scattering of the inelastic neutrons in the sphere must in general be considered. Thus knowledge of the inelastic collision cross sections and elastic scattering angular distributions at energies less than 1 Mev is required. This information must be estimated at present and is quite uncertain.

The cross sections measured for each element at the various thresholds will next be considered.

Carbon, as expected, has zero inelastic cross section within the experimental uncertainty at the thresholds indicated in Table I.

Aluminum appears to have a very small inelastic cross section at 1 Mev, in agreement with the findings of Kiehn and Goodman.[13]

Iron has nearly the same cross section at all biases. However, slightly lower cross sections were measured at the lowest biases. This effect is somewhat larger than experimental error and may be due to several causes. One such cause is that the neutrons produced in inelastic scattering processes in the iron sphere may count with low sensitivity at these biases. Therefore the cross sections measured for the higher energy thresholds are the best measure of the iron inelastic cross section.

Copper has a small inelastic cross section at 1 Mev as might be expected, since the lowest energy level reported in either stable isotope is at 0.96 Mev.[10]

Zinc has a very small inelastic collision cross section at 1-Mev neutron energy. There are energy levels, however, below 1 Mev in Zn^{67} (a 4 percent abundant isotope)[10] which could be excited by inelastic neutron scattering.

Silver has two stable isotopes, Ag^{107} and Ag^{109}. The assignment of cross sections for exciting the known levels in these isotopes is somewhat ambiguous. This interpretation of the cross-section variations with threshold is based on four levels, with energies of 0.09, 0.31, 0.41, and 0.94 Mev. A consistent assignment of cross sections for exciting these states is 0.21, 0.45, 0.45, and 0.69 barn per silver atom, respectively. The 0.69-barn cross section is probably the most accurately determined quantity, and it is uncertain to about 0.30 barn.

Cadmium has several stable isotopes and many excited states below 1 Mev. There is, however, no indication from the present experiment of very much inelastic scattering to levels below about 350 kev. Furthermore, the observed variation of inelastic cross section with energy threshold is explained if one assumes that about 90 percent of the inelastic events excite a level at about 0.60 Mev in the target nucleus.

Tin also has many stable isotopes. One gamma ray with energy less than 1 Mev has been observed to accompany neutron inelastic scattering.[10] The cross sections in Table I, however, indicate that very little inelastic scattering takes place to excited states with energy less than 1 Mev in the tin nucleus.

Gold has excited states reported at 0.077, 0.268,

TABLE II. Inelastic cross sections at 4.0-Mev neutron energy (barns).

Element	Inelastic collision cross section	Energy threshold (Mev) 3.4	3.2	3.00	2.80	2.60	2.40	Results of reference 16
Be	0.62±0.03[a]	0.62±0.05	0.62	0.62	0.62	0.62	0.62	0.60±0.10
C	0.04±0.04[a]	0.04±0.08	0.04	0.03	0.04	0.04	0.04	0.08±0.10
Al	0.75±0.04	0.75±0.05	0.75	0.75	0.74	0.71	0.68	0.70±0.20
Ti	1.28±0.07	1.28±0.09	1.28	1.25	1.20	1.15	1.09	1.2 ±0.20
Fe	1.42±0.05	1.42±0.07	1.42	1.41	1.36	1.30	1.22	1.5 ±0.20
Ni	1.35±0.10	1.35±0.09	1.35	1.35	1.35	1.34	1.32	
Cu	1.60±0.05	1.60±0.07	1.60	1.60	1.58	1.53	1.47	
Zn	1.69±0.06[a]	1.69±0.06	1.69	1.68	1.63	1.56	1.46	1.7 ±0.20
Zr	1.56±0.05	1.56±0.07	1.56	1.56	1.56	1.54	1.50	1.8 ±0.20
Ag	2.05±0.10	2.05±0.10	2.05	2.03	1.99	1.93	1.87	
Cd	2.06±0.10	2.05±0.10	2.03	2.02	2.01	1.96	1.86	2.10±0.20
Sn	2.09±0.07	2.09±0.10	2.09	2.09	2.08	2.03	1.96	2.10±0.20
W	2.60±0.20	2.58±0.20	2.55	2.50	2.42	2.36	2.28	2.40±0.30
Au	2.75±0.15	2.75±0.12	2.75	2.72	2.67	2.62	2.57	2.7 ±0.30
Pb	1.86±0.10	1.84±0.08	1.84	1.81	1.76	1.72	1.67	1.9 ±0.30
Bi	1.98±0.09	1.98±0.10	1.98	1.98	1.97	1.92	1.85	2.2 ±0.30

[a] The neutron energy used in these experiments was 4.07 Mev.

[14] C. E. Porter (private communication).

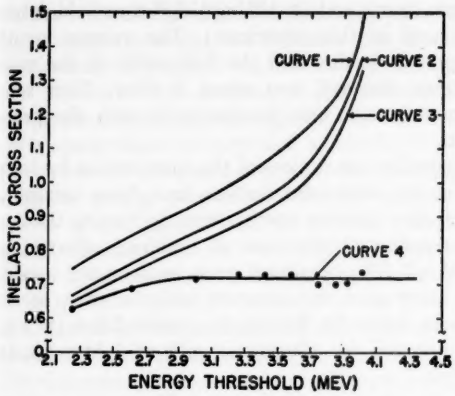

FIG. 8. Aluminum inelastic cross section at 4.5-Mev neutron energy. Curve 1 shows the cross section obtained from the exponential relationship {i.e., $T=\exp[-N_0\sigma_{in}(r_2-r_1)]$}. Curve 2 shows the cross section obtained after correcting for multiple neutron scattering in the shell. Curve 3 shows the cross section computed with corrections for multiple scattering and source intensity variation with angle. Curve 4 is drawn through the cross sections for the ten energy thresholds of the detector, and is computed with all of the corrections, namely, those of Curve 3 and the correction for loss of energy in elastic collisions.

0.279, 0.409,[10] and 0.545 Mev.[15] The general decrease in the cross section with threshold energy indicates that there is inelastic scattering to both low- and high-energy levels. A possible method of explaining these variations is to assign a 0.9-barn cross section to the excitation of the 545-kev level and 0.22, 0.45, and 0.23 barn, respectively, with the excitation of the 0.077-Mev level, the 0.268 and 0.279 levels taken together, and the 0.409 level. The uncertainty of each of these numbers is about 0.30 barn.

Lead has a measured inelastic cross section which varies slightly with energy threshold. This effect may be caused by inelastic collisions which excite the 0.55- and 0.89-Mev levels in Pb^{207} with a cross section of about 0.1 barn per lead atom.

Bismuth has a single stable isotope with its first excited state at 904 kev. No variation of inelastic cross section with energy threshold is indicated in Table I. One would expect the detection at low bias of the neutrons from inelastic scattering to produce a change in cross section of about 0.006 barn. The existence of this small change in cross section is very difficult to establish by the experimental methods employed here.

V. RESULTS AT 4.0 AND 4.5 MEV

Inelastic cross sections obtained at various energy thresholds of the detector for 4.0- and 4.5-Mev neutrons are given in Tables II and III, respectively. Experimental errors are placed on the data taken at a threshold of 85 percent of the incident neutron energy. The inelastic collision cross section for each element is also given in the tables. This value is obtained from the measurement of inelastic cross section for the lowest energy threshold at which a negligible number of inelastic neutrons are detected. This threshold is chosen on the basis of information presently available on the energy levels in the target nucleus[10] and on the basis of the observed behavior of the inelastic cross section with energy threshold. The sources of experimental error at 4.0 and 4.5 Mev are the same as those listed for the 1-Mev measurements. Total cross sections and elastic scattering angular distributions used in the numerical analysis are those measured recently at 4.1 Mev.[16] The importance of various corrections applied to the data can be seen in Fig. 8. These results are based on the transmission measurements of an 8-in. diameter aluminum sphere at 4.5-Mev neutron energy. Figure 8 shows that even at this neutron energy the most important correction is that for loss of energy in elastic collisions. This is true also for heavy elements such as lead at 4.5-Mev neutron energy, for which a 12-percent correction must be made at the 3.8-Mev energy threshold.

The cross sections given in Table III at 4.5-Mev neutron energy for iron, copper, tin, cadmium, lead, and bismuth are based on transmission measurements for two shells differing by a factor of two in thickness. In all cases the two measurements agree to within the counting errors, suggesting that corrections are being made properly.

The energy thresholds of the neutron detector indicated in Tables II and III are obtained as at 1 Mev by extrapolating the sensitivity *versus* energy curves. Observed variations of cross sections as a function of threshold can only be considered a qualitative guide to which states of the target nucleus are being excited by inelastic events. Qualitatively then, one may say that 4.0- and 4.5-Mev neutrons will not excite low-lying levels in the target nucleus with high probability. In several cases it is possible to estimate the cross section for exciting known low-lying levels by inelastic scattering. The cross section changes observed at the various

TABLE III. Inelastic cross sections at 4.5-Mev neutron energy (barns).

Element	Inelastic collision cross sections	Energy threshold (Mev) 3.80	3.60	3.38	3.15	2.93	2.70	2.48	Results of reference 3
Al	0.72±0.04	0.72±0.06	0.72	0.72	0.72	0.72	0.70	0.67	0.82
Ti	1.18±0.07	1.18±0.09	1.18	1.18	1.16	1.13	1.10	1.04	
Fe	1.33±0.05	1.34±0.07	1.34	1.34	1.32	1.28	1.23	1.16	1.20
Ni	1.50±0.06	1.50±0.09	1.50	1.50	1.50	1.49	1.44	1.38	1.34
Cu	1.60±0.05	1.60±0.06	1.60	1.60	1.60	1.58	1.53	1.46	1.45
Zn	1.81±0.10	1.81±0.09	1.81	1.77	1.72	1.66	1.60	1.54	
Zr	1.59±0.07	1.59±0.09	1.59	1.59	1.58	1.58	1.56	1.52	1.64
Ag	2.02±0.10	2.02±0.11	2.02	2.02	2.01	1.97	1.92	1.84	2.01
Cd	2.12±0.12	2.12±0.11	2.11	2.10	2.07	2.05	1.99	1.92	2.11
Sn	2.18±0.06	2.18±0.10	2.18	2.18	2.17	2.13	2.09	2.02	2.05
W	2.60±0.20	2.56±0.20	2.56	2.56	2.56	2.52	2.45	2.38	2.68
Au	2.70±0.15	2.69±0.13	2.69	2.69	2.69	2.67	2.63	2.58	2.62
Pb	2.02±0.14	2.02±0.16	2.02	2.02	2.02	2.00	1.97	1.93	2.19
Bi	2.19±0.08	2.19±0.10	2.19	2.19	2.19	2.17	2.14	2.09	2.32

[15] W. I. Goldburg and R. M. Williamson, Phys. Rev. **95**, 767 (1954).

[16] M. Walt and J. R. Beyster, Phys. Rev. **98**, 677 (1955).

energy thresholds of the detector are interpreted as in the 1-Mev analysis. In certain cases below it will be necessary to combine the cross sections for exciting two states because of a lack of sufficient energy resolution in the neutron detector. To increase the statistical accuracy of the calculation, the cross section for exciting a particular level is computed for both 4.0- and 4.5-Mev neutrons and the value given below is the average of these two numbers. The cross section for exciting the 0.84-Mev level, plus that for exciting the 1.02-Mev level in Al^{27}, is 0.19 ± 0.12 barn. The 840-kev level in Fe^{56} is excited with a cross section of 0.50 ± 0.20 barn by inelastic neutron scattering. The sum of the cross sections for exciting the 0.96-Mev level in Cu^{63} and the 1.12-Mev level in Cu^{65} is 0.49 ± 0.20 barn per copper atom. The 0.90-Mev level in Bi^{209} is excited with a cross section of 0.28 ± 0.15 barn by inelastic neutron scattering.

The 4.0-Mev cross sections are compared in Table II with those obtained from reference 16. The agreement between measurements done by the two methods is very good. In Table III the cross sections measured at 4.5 Mev are compared with those obtained from another sphere transmission experiment.[3] A fission neutron source and an $Al^{27}(n,p)Mg^{27}$ threshold detector were used in this experiment. The average neutron energy was 6 Mev and the half-width of the energy spectrum detected was about 3 Mev. This set of measurements is also in agreement with the present results.

Theoretical predictions of the cross section for formation of the compound nucleus have been carried out for 4.0-Mev neutron energy recently,[16] using the complex square-well potential of Feshbach, Porter, and Weisskopf. The calculated cross sections are considerably lower than the observed inelastic cross sections given in Table II. This is the same difficulty which was observed for silver and gold at 1-Mev neutron energy.

ACKNOWLEDGMENTS

The authors gratefully acknowledge the considerable assistance of L. P. Grant and C. W. Johnstone with the electronic problems encountered in the experiments. We are also very much indebted to E. D. Cashwell and C. J. Everett for setting up the entire numerical computing problem for the Los Alamos MANIAC computer.

PHYSICAL REVIEW VOLUME 98, NUMBER 5 JUNE 1, 1955

Spin, Quadrupole Moment, and Mass of Selenium-75*

L. C. Aamodt† and P. C. Fletcher
Columbia University, New York, New York

(Received January 27, 1955)

The microwave spectrum of $OCSe^{75}$ has been observed and from it the spin, quadrupole moment, and mass of Se^{75} were measured. Frequencies of the six observed lines of the $J=2\rightarrow3$ rotational transition give a nuclear spin of 5/2, a quadrupole coupling constant $eqQ=946.0$ Mc/sec, and a rotational constant $B_0=4081.926$ Mc/sec. From these and other known properties of the OCSe molecule, one obtains the quadrupole moment of Se^{75} as $Q=1.1\times10^{-24}$ cm$^2\pm20$ percent, and the mass ratio $(M_{Se^{75}}-M_{Se^{76}})/(M_{Se^{75}}-M_{Se^{80}})=0.199566\pm0.000030$. The odd-even mass difference for Se^{75} is 1.5 ± 0.2 mMU. The observed spin disagrees with that expected from the shell model which predicts a spin of 1/2 or 9/2. Three possible nuclear configurations which agree with the observed spin and also indicate a positive quadrupole moment are $[p_{1/2}(g_{9/2})^2]_{5/2}$, $(g_{9/2})^3_{5/2}$, and $(f_{5/2})^5_{5/2}$. Magnetic moment measurements are needed to clearly distinguish between configurations. The sample material was obtained by bombarding arsenic with deuterons. Approximately 1½ micrograms of sample material were produced but only 0.07 microgram could be used in each spectroscopic run because of difficulties in synthesizing OCSe.

INTRODUCTION

THE stable selenium isotopes Se^{74}, Se^{76}, Se^{77}, Se^{80}, and Se^{82} have sufficient natural abundance to make them available for microwave spectroscopy. Their nuclear properties have been determined or in the case of the even-even nuclei, confirmed by previous investigators.[1–3] Of the radioactive isotopes, Se^{79}, with a half-life of 6.5×10^4 years, has had its nuclear properties determined by Hardy *et al.*[4] Another selenium isotope which is amenable to microwave spectroscopy, because of a sufficiently long half-life (128 days[5]), is Se^{75}. Since this atom cannot be obtained with sufficient specific activity from pile bombardment to make measurements by microwave techniques possible, the sample material was produced by cyclotron bombardment. This is the first case where cyclotron bombard-

* Work supported by the U. S. Atomic Energy Commission.
† Now at Brigham Young University, Provo, Utah.
[1] Strandberg, Wentink, and Hill, Phys. Rev. **75**, 827 (1949).
[2] Geschwind, Minden, and Townes, Phys. Rev. **78**, 174 (1950).
[3] W. Low, thesis, Columbia University, 1950 (unpublished).
[4] W. A. Hardy *et al.*, Phys. Rev. **92**, 1532 (1953).
[5] Cork, Rutledge, Branyan, Stoddard, and Le Blanc, Phys. Rev. **79**, 889 (1950).

ment has been used as a source of sample material for microwave spectroscopy, and indicates that a number of additional radioactive nuclei can be studied by similar methods. The amount of Se^{75} obtained was small (approximately 1½ micrograms) and required the use of a spectrometer of very high sensitivity.[6]

The spectrum measured indicates the following regarding the nuclear properties of the Se^{75} nucleus: (1) The spin of the nucleus is 5/2; (2) the quadrupole coupling constant for Se^{75} in OCSe is 946.0±0.4 Mc/sec; (3) it possesses an electrical quadrupole moment of 1.1×10^{-24} cm²±20 percent; (4) the mass ratio $M_{Se^{75}}/M_{Se^{76}}$ is 0.98686±0.00001; and (5) the odd-even mass difference is 1.5±0.2 mMU.

The observed spin does not agree with the individual particle model following the Mayer[7] and Jensen[8] scheme. This model predicts a spin of 1/2 or 9/2. Three possible nuclear configurations agree with the observed spin and also indicate a positive quadrupole moment. These are $[p_{1/2}(g_{9/2})^2]_{5/2}$, $(g_{9/2})^3_{5/2}$, and $(f_{5/2})^5_{5/2}$. Parity considerations appear to favor the second configuration. On the other hand the large positive quadrupole moment that was observed agrees better with the estimate of the quadrupole moment for the first configuration rather than the second. Magnetic moment measurements should resolve the ambiguity.

PREPARATION OF THE TARGET

Se^{75} may be produced by two processes: $Se^{74}(n,\gamma)Se^{75}$ and $As^{75}(d,2n)Se^{75}$. In the first process the stable selenium cannot be chemically separated from the Se^{75} so that only a low specific activity can be obtained. Samples available from pile bombardment using this process have specific activities of 1300 mC/g.[9] This corresponds to 0.009 percent abundance. This is not sufficient abundance for microwave spectroscopy; for example, the spectrometer used required an abundance of the order of 0.1 percent to measure the lines observed.

The second process allowed easy chemical separation of the arsenic but it had certain disadvantages. Various factors make arsenic a very unfavorable target material. Arsenic sublimes, having a vapor pressure of 1 mm at 372°C. In addition it oxidizes forming AsO_2 which also sublimes. Experimentally, the heat of bombardment readily evaporated the target surface, even with the best possible cooling of the target holder, unless good thermal conductivity was obtained throughout the target volume. This made it desirable to have a target of solid arsenic. Several methods or producing such a target were attempted. Arsenic which was plated electrolytically proved to be too flaky and porous. Melting the arsenic proved difficult because of its high vapor pressure, 36 atmospheres, at its melting point of 814°C. A bomb was constructed to melt the arsenic but a satisfactory surface upon which to melt it was not readily obtainable. The arsenic was found to alloy with gold and iron and react with platinum. A quartz container was not satisfactory because the arsenic solidified in small spherical balls on the quartz surface. However, it was found possible to press arsenic powder under high pressure into wafers having a density of 90 percent of that of solid arsenic. These wafers had sufficient thermal conductivity to withstand the heat of bombardment.

Chemical considerations dictated a small target volume. The dimensions of the cyclotron beam and the depth of penetration determined the minimum cross-sectional area and the minimum thickness, respectively, and required a thin wafer-like target. For mechanical strength the wafers had to be considerably thicker than the minimum set by the penetration and could not be formed with as large a cross-sectional area as desired, therefore making it necessary to use several wafers in each target. The wafers were ½ mm thick and were originally pressed in a circular shape and trimmed to size with a razor blade. The pressure used in pressing wafers was 85 tons per square inch.

In order to assure a good thermal contact with the target holder, which was made of copper, the arsenic wafers were heated, tinned with pure tin using ammonium chloride as a flux, and soldered into the target holder. The target holder was a water-cooled block with dimensions 6 inches by 1 inch by 1 inch. The target was placed in a shallow rectangular cavity cut into one of the sides of the copper block and covered with a one-mil aluminum foil which prevented the loss of any evaporated arsenic.

BOMBARDMENT DETAILS AND IDENTIFICATION OF THE Se^{75}

Since the cross section of the $As^{75}(d,2n)Se^{75}$ reaction was not known initially and estimates obtained varied quite widely, several preliminary bombardments were made to determine the yield. The earliest targets were badly evaporated but gave sufficient information to determine the approximate bombardment time for the later perfected targets. The final bombardment used a maximum cyclotron current of 75 microamperes and 500 microampere hours of bombardment. The bombardments were made in the Brookhaven cyclotron which has a 22-Mev deuteron beam.

The Se^{75} was identified by measuring the lines grouped around the 124-kev and the 269-kev lines[5] in its decay spectrum. The measurements were sufficiently quantitative to indicate the yield for monitoring purposes although no attempt was made to resolve the individual lines of the spectrum. The measurements were made with a sodium iodide scintillation counter. The yield measured for the bombardment conditions listed above was 1½ micrograms. This indicated an average cross section of the order of 2.7 barns (assuming

[6] W. A. Hardy and G. Silvey, Phys. Rev. **95**, 385 (1954).
[7] Maria Goeppert Mayer, Phys. Rev. **78**, 16 (1950).
[8] Haxel, Jensen, and Suess, Phys. Rev. **75**, 1766 (1949).
[9] *Radioactive Isotope Bulletin* (Isotope Division, U. S. Atomic Energy Commission, Washington, D. C., 1955).

a 50-mg/cm² range). Additional confirmation of the identity of the Se^{75} was made by observing that the radioactivity followed the expected position of the selenium during chemical manipulations.

CHEMISTRY

After bombardment the target was freed from the target holder by heating the target holder on an electric hotplate. In addition to $1\frac{1}{2}$ micrograms of Se^{75} it consisted of 7 grams of arsenic, 1 gram of tin, and traces of copper and aluminum. (The selenium was probably in the form of As_2Se_3 or $AsSe_5$.) The target material was then dissolved in aqua regia; 50 micrograms of normal selenium carrier added; and the Se^{75} reduced to elemental selenium by adding the reducing agent hydrazine hydrochloride. At this point the selenium was precipitated and the arsenic and other solubles were filtered out. After rinsing, the selenium was combined with a large excess of CO and heated at 500°C for 15 minutes. This produced the molecule OCSe—carbonyl selenide—which was the molecule used in the absorption cell.

(1) Partial Molecular Synthesis

The $1\frac{1}{2}$ micrograms of Se^{75} obtained from cyclotron bombardment could not all be synthesized into the carbonyl selenide molecule at the same time. Each time the Se was heated with CO and the OCSe removed, only about 10 to 15 percent of the Se atoms were found to have formed carbonyl selenide molecules. This process could be repeated several times but the presence of diluting gases prevented the combining of these separate yields. The partial synthesis was determined by measuring the ratio of the radioactivity in the OCSe sample material to the radioactivity remaining in the reaction vessel. In order to rule out the possibility that some of the activity in the reaction vessel was coming from extraneous sources, the intensity of the decay spectrum of Se^{75} was measured in both the reaction vessel and in the molecular sample material by using the sodium iodide scintillation counter. These measurements agreed well with those originally made using a proportional counter. This partial synthesis reduced the total amount of Se^{75} available for spectroscopy to about 0.2 micrograms per run.

(2) Dilution of the Sample

At least two foreign gases, OCS and CO_2, were present in the sample material. The OCS was due to sulfur that was present in the target material or in the reagents used. Sulfur follows the same chemistry as selenium, and forms OCS rather than OCSe. The carbon dioxide may have entered as an impurity in the carbon monoxide, or it may have been formed by the carbon monoxide reacting with oxygen that was either present in the reaction vessel or that entered as an impurity in the carbon monoxide. The presence of these gases reduced the intensity of the $OCSe^{75}$ absorption lines by not allowing all of the sample material to be put into the absorption cell. Only about 0.07 micrograms of Se^{75} could be put into the cell per run.

The OCS was minimized by reducing the sulfur content in the target material and reagents used. The CO_2 was minimized by a method of fractional distillation (which will be described under spectroscopic procedure) and purification of the carbon monoxide.

Since the ratio of arsenic and tin to Se^{75} was large (approximately 4.6×10^6 and 6×10^5 respectively) sulfur impurities in either of these materials in even small percentages were troublesome. To test the amount of sulfur present in the aresnic and tin, a "blank" chemical run was made using 7 grams of arsenic, 1 gram of tin, and 50 micrograms of ordinary selenium. Since the sulfur in the arsenic formed OCS and the selenium formed OCSe, the amount of sulfur present was measured by observing the relative intensities of the carbonyl selenide and carbonyl sulfide absorption lines with the microwave spectrometer. The amount of sulfur present in commercially available chemically pure arsenic was found to vary considerably from lot to lot. A source was finally found that contained less than 10 micrograms of sulfur in 7 grams of arsenic. This proved satisfactory. Purification of the arsenic by electrolysis was not successful since the physical form of the purified arsenic was such that it was impossible to press it into suitable wafers for the target. The tin proved to contain a negligible amount of sulfur.

Carbon dioxide was difficult to remove because its vapor pressure was approximately the same as that of carbonyl selenide. To insure a dilution of less than 50 percent (equal amount of diluting gas and OCSe) the CO used had to contain less than 0.0004 percent CO_2. Since the gas available was only 99.97 percent pure, it was necessary to purify it. The purification process consisted of sealing off a volume of CO and heating it to 500°C. The oxygen in the CO reacted to give CO_2, and this gas along with the CO_2 originally present was removed by freezing it out with liquid nitrogen. Purification by this method gave good results; it allowed the effective sensitivity to be increased by a factor of two in later runs.

SPECTROSCOPIC PROCEDURE

(1) Admittance of the Sample into the Absorption Cell

The large dilution of the carbonyl selenide made it desirable to preferentially admit it to the absorption cell. The method of fractional distillation used was the following. A carbon disulfide bath was prepared by using a liquid nitrogen cold finger. The first portion of the diluted sample was admitted to the absorption cell while the spectrometer was adjusted to observe the $J=2\rightarrow3$ rotational transition of the $OCSe^{74}$ molecule. This line was used as a monitoring line. The sample

material was admitted until this absorption line first began to appear. Then the material that had entered the absorption cell (the material consisting mainly of CO_2) was discarded; the carbon disulfide bath was then replaced by a dry ice-acetone bath, and the remainder of the sample admitted.

Definite improvement resulted from this procedure. During the manipulations the radioactivity always moved in a manner consistent with the carbonyl selenide, and the radioactivity in the absorption cell agreed semiquantitatively with the carbonyl selenide spectral intensities.

(2) Molecular Dissociation

Each molecular synthesis produced sufficient sample material to fill the absorption cell only once, and each cyclotron bombardment enough material to allow about four good molecular syntheses. This made it desirable to keep the sample material in the spectrometer for long periods of time to facilitate measurements with the minimum of sample preparation.

Carbonyl selenide is unstable at room temperature. At dry ice temperature, which was the temperature at which the spectrometer was operated, dissociation was inhibited sufficiently to allow 12-hour runs to be made before noticeable decrease in intensity occurred. (Other factors in addition to molecular dissociation were partially responsible for this decrease in intensity.) To preserve the sample material for this length of time it was necessary to keep the temperature below $-60°C$ at all times. Any increase in temperature immediately decreased the line intensity, and also increased the amount of radioactivity left in the absorption cell after the sample material had been removed. This gave a semiquantitative means of monitoring the amount of molecular dissociation in the absorption cell.

(3) Sensitivity Tests and Requirements

The spectrometer sensitivity was tested by observing the $F=3/2\rightarrow1/2$ quadrupole component of the $J=2\rightarrow3$ rotational transition of OCS^{33}. This absorption line has an intensity (absorption coefficient) of 7.2×10^{-9} cm^{-1} at room temperature. The spectrometer was adjusted until this line was observed 20 to 30 times noise (at room temperature) giving an ultimate sensitivity (detectable absorption coefficient) of approximately 3 or 4×10^{-10} cm^{-1}. Based on the signal-to-noise ratio of this test line, the absorption coefficient of the observed $OCSe^{75}$ lines ranged from 3×10^{-9} cm^{-1} for the $F=9/2\rightarrow11/2$ transition to 6×10^{-10} cm^{-1} for the $F=3/2\rightarrow3/2$ transition. These values agree well with those estimated from the data on the nuclear bombardment, molecular synthesis, and dilution in the absorption cell.

ENERGY LEVELS

The Hamiltonian for a molecule with a single nucleus possessing an electrical quadrupole moment may be written as $H=H_0+H_Q$, where H_0 is the Hamiltonian for the rotating-vibrating molecule and H_Q consists of the additional energy terms due to the interaction between the molecular electric field and the nuclear quadrupole moment. Since no vibrational transition is involved and since the rotational-vibrational interactions are small, the Hamiltonian H_0 may be considered to be H_R, the pure rotational component of the Hamiltonian. Thus we may write $H=H_R+H_Q$.

The most convenient representation is the $IJFM$ representation which $\mathbf{F}=\mathbf{I}+\mathbf{J}$ and M is the component of $\mathbf{F}$ along a space fixed axis. In this representation the quadrupole energy matrix is diagonal in F and M but not in J. The first-order energies are given by the expression (for a linear molecule)[10]:

$$(IJFM|H_Q|IJF'M') = -eqQ\frac{\frac{3}{4}C(C+1)-I(I+1)J(J+1)}{2I(2I-1)(2J-1)(2J+3)},$$

where $C=F(F+1)-I(I+1)-J(J+1)$, e=electronic charge, Q=quadrupole moment of the nucleus, $q=\partial^2V/\partial z^2$, at the nucleus with the quadrupole moment. Here V is the electrostatic potential due to all charges outside the nucleus, and z is the coordinate along the molecular axis.

The large quadrupole coupling in the $OCSe^{75}$ molecule made it necessary to correct the first-order energies by second-order perturbation theory involving different rotational levels. Since the second-order corrections were small, however, the identification of the nuclear spin could be made by using first-order theory. The main lines in the characteristic quadrupole hyperfine patterns for spins of 3/2, 5/2, 7/2, 9/2, and 11/2 and

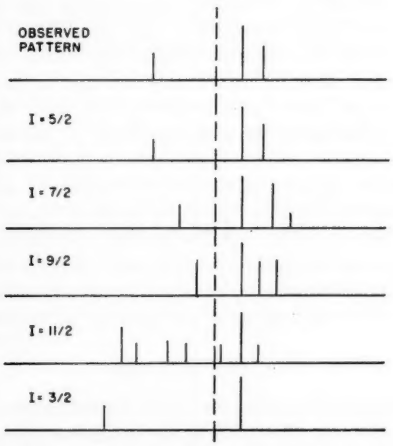

FIG. 1. The comparison of the main lines in the quadrupole hyperfine patterns for various spins ($J=2\rightarrow3$ transition). The dashed line indicates the frequency of the $J=2\rightarrow3$ rotational transition, assuming no quadrupole coupling coefficients have been adjusted so that the major components of the various patterns fall in line.

[10] J. Bardeen and C. H. Townes, Phys. Rev. 73, 627 (1948).

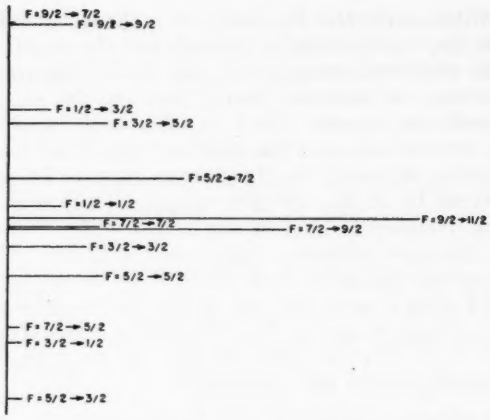

FIG. 2. Quadrupole hyperfine pattern for $J=2\rightarrow3$ transition, $I=5/2$.

for $J=2\rightarrow3$ are shown in Fig. 1. The observed lines are shown for comparison. The complete quadrupole pattern for a spin of 5/2 is shown in Fig. 2.

OBSERVED LINES OF $OCSe^{75}$

Six lines were observed and their frequencies measured. Table I lists these lines with their identification. In Fig. 1 the three strongest observed lines are shown along with the various theoretical patterns. It can easily be seen to agree with the pattern for a spin of 5/2 and to disagree with the others. The theoretical frequencies are listed in column three of Table I. These were computed using the values of eqQ and ν_0 indicated. These frequencies agree within experimental error with the observed values.

Determination of relative intensities of the observed lines was difficult because of unresolved Stark components. Even so, there is general agreement between theory and observation as can be seen in columns four and five of Table I. Column five lists the theoretical relative intensities with the intensity of the strongest line set equal to one. Column four was obtained by listing the signal-to-noise ratio of each line and then dividing by the signal-to-noise ratio of the strongest line. These calculations disregarded unresolved Stark components and also the fact that slightly different operating conditions existed in the different measurements. Even so, agreement is seen to be qualitatively good.

STARK PATTERN

Additional confirmation of the identification of individual lines in the quadrupole hyperfine pattern was made by observing their line shapes. These line shapes were altered by unresolved Stark components. If the dipole moment of the carbonyl selenide molecule had been larger, the separate Stark components could have been individually observed and used for identification. The dipole moment was small enough however, to make it impossible to completely resolve them with the modulating voltages available. A theoretical calculation was made of the Stark pattern for each of the lines in the quadrupole hyperfine pattern for a spin of 5/2. Then, by assuming a reasonable line width, a composite line was drawn including the line and its Stark components. (The Stark components were plotted negatively since in the spectrometer the phase detector inverts the Stark components.) The resulting lines are shown in Fig. 3 (for the three strongest lines in the pattern). As can be seen, the agreement between the observed and theoretical patterns is very good.

NUCLEAR CONSTANTS

The spin of Se^{75} and the quadrupole coupling constant in the $OCSe^{75}$ molecule were determined by the frequency separations of the components of the quadrupole hyperfine pattern. (These are listed in Table I.) The quadrupole coupling constant doesn't allow the quadrupole moment to be calculated directly. The value of q must first be estimated. Even without doing this, however, the ratio of quadrupole moments for two selenium isotopes may be obtained from the experimental data. The value of q is approximately the same for all of the selenium isotopes; consequently a ratio of quadrupole coupling constants represents the ratio of quadrupole moments. Considering the molecule $OCSe^{79}$ which has a quadrupole coupling constant[4] of 752.09 $\pm$0.05 Mc/sec, we find the ratio $Q_{Se^{75}}/Q_{Se^{79}}$ to be 1.25783$\pm$0.00062. An estimate of q has been made by Bird and Townes[11] for the molecule OCS, by using the methods of Townes and Dailey.[12] By using this value of q, and assuming that the molecules of OCS and OCSe have similar bonding structures, which is a reasonable assumption, the quadrupole moment of Se^{75} becomes 1.1×10^{-24} cm$^2\pm$20 percent.

The frequency of the rotational transition (assuming no hyperfine structure) allows a determination of the molecular B_0 value for the $OCSe^{75}$ molecule as 4081.925

TABLE I. Comparison of the observed frequencies and relative intensities of the $OCSe^{75}$ electric quadrupole hyperfine pattern with the corresponding theoretical values (for the $J=2\rightarrow3$ rotational transition and for $I=5/2$).

Line F'	Line F''	Observed frequency (Mc/sec)	Theoretical frequency[a] (Mc/sec)	Relative intensities Observed	Relative intensities Theoretical
9/2	11/2	24480.45±0.05	24480.407	1.0	1.000
7/2	9/2	24471.31±0.05	24471.354	0.6±0.1	0.678
5/2	7/2	24517.93±0.05	24517.935	0.5±0.1	0.430
3/2	5/2	24565.87±0.03	24565.871	0.2±0.05	0.240
5/2	5/2	24429.58±0.05	24429.600	0.2±0.05	0.230
3/2	3/2	24455.21±0.05	24455.226	0.2±0.05	0.190

[a] The theoretical frequencies were computed by using $eqQ=946$ Mc/sec and $\nu_0=24491.553$ Mc/sec. Second-order corrections were included. (ν_0 is the frequency of the $J=2\rightarrow3$ rotational transition, assuming no hyperfine pattern.)

[11] G. Bird and C. H. Townes, Phys. Rev. **94**, 1203 (1954).
[12] C. H. Townes and B. P. Dailey, J. Chem. Phys. **17**, 796 (1949).

± 0.002 Mc/sec. From this, following Geschwind, Minden, and Townes,[2] one obtains the ratio of mass differences $(M_{Se^{75}}-M_{Se^{76}})/(M_{Se^{75}}-M_{Se^{80}})=0.199566 \pm 0.000030$ and an odd-even mass difference for Se^{75} of 1.5 ± 0.2 mMU.

DISCUSSION

According to the nuclear shell model proposed by Mayer[7] and by Haxel, Jensen, and Suess,[8] the nuclear spin is determined by the last added odd nucleon, the other nucleons pairing off to give zero spin and zero magnetic moment. Levels in the fourth shell are supposed to occur in the order $p_{3/2}$, $f_{5/2}$, $p_{1/2}$, and $g_{9/2}$, which would make the last odd neutron in the $_{34}Se^{75}{}_{41}$ nucleus (which has 13 particles in this shell), in the $g_{9/2}$ state. According to the nuclear shell model the spin of the nucleus should then be 9/2. Pairing energy however, might favor the situation where two neutrons pair in the $g_{9/2}$ state, leaving the odd neutron in the $p_{1/2}$ state and giving the nucleus a spin of 1/2. Neither of these spins agrees with the experimentally observed spin of 5/2, and the Se^{75} nucleus can be considered to be another definite exception to the individual-particle nuclear shell model. Other exceptions[13-15] are Na^{23}, Mn^{55}, Se^{79}, Eu^{153}, and Yb^{173}. These other exceptions however, all show a spin one less than that which would be predicted by shell theory while Se^{75} differs by 2 from the two spins that might be expected, 9/2 or 1/2.

If one still uses the individual-particle model, but assumes that the nuclear configuration involves the coupling of several neutrons in the fourth shell, several possible configurations suggest themselves. The three most plausible configurations are the following $[(p_{1/2})(g_{9/2})^2]_{5/2}$, $(g_{9/2})^3{}_{5/2}$, and $(f_{5/2})^5{}_{5/2}$ (the remaining neutrons pairing off to give zero spin). Each of these configurations is possible, i.e., they do not violate the Pauli exclusion principle, and they all predict a positive quadrupole moment in agreement with experiment.

In order to distinguish between configurations, several criteria can be used. The exceptionally large positive quadrupole moment agrees with the estimate of quadrupole moment for the first configuration rather than the second, while parity considerations[14] on the other hand seem to favor the second over the first. This ambiguity can be probably resolved by a measurement of the magnetic moment. It is interesting to note that Townes and Moszkowski[15] have pointed out that all exceptions to the individual-particle shell model have large positive quadrupole moments.

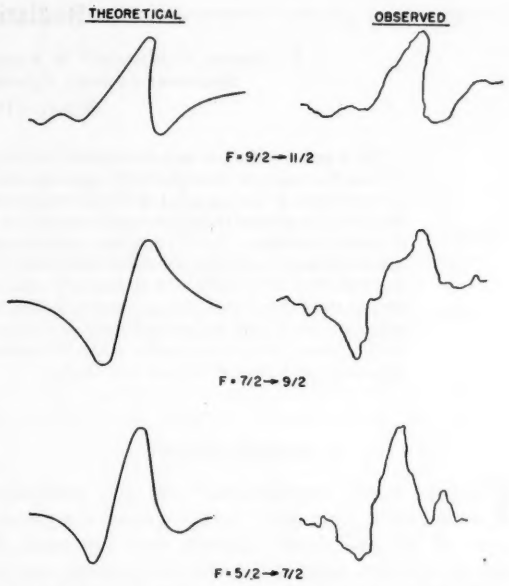

FIG. 3. Comparison of the theoretical and observed line shapes of the three main lines in the quadrupole hyperfine patterns of $OCSe^{75}$ ($J=2\rightarrow 3$ transition).

To make magnetic moment measurements, considerably more sample material must be available than that used in the present measurements. The spectral lines involving large F values are the most intense lines, and these in turn possess too many Zeeman components to make them practical for magnetic moment measurements. In this experiment lines involving low values of F were barely observable and an increase in abundance by a factor of five or ten would be necessary to make magnetic moment measurements feasible. The estimated magnetic moments for the three configurations are as follows: $[(p_{1/2})(g_{9/2})^2]_{5/2}$, -0.212; $(g_{9/2})^3{}_{5/2}$, -1.06; and $(f_{5/2})^5{}_{5/2}$, 0.546. The units are nuclear magnetons. As can be seen, a magnetic moment measurement could clearly distinguish between these three configurations.

[13] J. M. Blatt and V. F. Weisskoff, *Theoretical Nuclear Physics* (John Wiley and Sons, Inc., New York, 1952), p. 770.
[14] J. P. Welker (private communication).
[15] S. A. Moszkowski and C. H. Townes, Phys. Rev. **93**, 306 (1954).

Radiations of I^{126}†

L. KOERTS, P. MACKLIN,* B. FARRELLY, R. VAN LIESHOUT,‡ AND C. S. WU
Department of Physics, Columbia University, New York, New York

(Received December 28, 1954)

The β and γ radiations and the electron capture process of I^{126} have been thoroughly investigated. The β^- branch consists of three groups of maximum energies 1.25, 0.865, and 0.385 Mev. The relative intensities of these three β^- groups are 1:3.1:0.63 respectively. The shape of the highest energy β^- group identifies the ground to ground transition to be a unique first forbidden one ($\Delta I=2$, yes). The spectrum of the middle β^- group as measured by the magnetic coincidence spectrometer has an allowed shape. The number of β^+ disintegrations is only 2.8 percent of that of the β^- disintegration. Two groups of maximum energies 1.11 and 0.46 Mev were found with an intensity ratio of 3.5:1. The shape of the β^+ spectrum of the ground to ground transition is also the unique first forbidden type. The correlations among the various γ lines and x-line and their relative intensities are determined by a selective coincidence scintillation spectrometer. In conclusion, the spin and parity of the I^{126} ground state is definitely 2^- and its decay scheme is in general agreement with that of Perlman and Welker.

I. INTRODUCTION

IN two recent investigations[1,2] on I^{126}, conflicting assignments were given to the spin of the ground state of I^{126} and decay schemes were proposed. In general practice, some of the arguments which may be used in determining the spin are based on the classification of the *ft* values and the ratio of *K*-capture to positron emission. These values are in rather good agreement in both the above-mentioned investigations and both values strongly indicate 2^- for the ground state of I^{126}. Nevertheless, on the basis of evidence obtained from the shape of the β^- spectrum, Marty, Langevin, and Hubert were forced to give up the favored assignment of 2^- in preference to 1^+ for the ground state of I^{126}. The questions remain, whether there are some real discrepancies between the distribution of the β^- spectrum and the designation of the spin and parity of the states, and which of the two possible spin assignments is correct.

Early in 1951, the β^- spectrum of I^{126} was investigated with the solenoidal magnetic spectrometer and the coincidence magnetic spectrometer of this laboratory. The results were briefly reported at the International Nuclear Physics Conference in Chicago[3] (September 1951) and also indirectly quoted in a letter to the editor[4] by Stevenson and Deutsch. It was found that the β^- spectrum of I^{126} for the ground to ground transition has an end point of 1.25 Mev and exhibits the unique forbidden shape associated with $\Delta I=2$ (yes). The β^- spectrum to the first excited state as shown by the coincidence spectrometer, yields a linear Kurie plot from 865 kev to ~350 kev. This was supported by the Kurie plot obtained by subtracting the uniquely shaped high-energy component from the composite spectrum. Therefore, it must be concluded that the spin and parity of the ground state of I^{126} are 2^-.

Recently we extended our investigation to the β^+ spectrum of I^{126}. Because of the larger energy difference between the ground to ground transition and ground to the first excited state transition, the unique forbidden shape of the high-energy β^+ component should show up to a greater advantage. This expectation was borne out by the results.

In addition, we reinvestigated the x and gamma radiations with our coincidence scintillation spectrometer. Since our calibration methods in intensity measurements differed from those of Perlman and Welker, it is interesting to compare the results obtained by these two different methods.

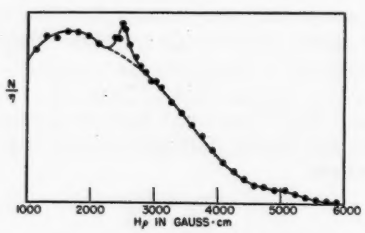

FIG. 1. Momentum distribution of composite electron spectrum of I^{126}.

2. SOURCE PREPARATION

The first I^{126} source used in 1951 was generously offered to us by Dr. M. Deutsch. It was prepared by activating the separated Te^{126} isotope by $(d,2n)$ reaction in the M.I.T. cyclotron. This source was the best one used because of its high specific activity. Its thickness was less than 200 $\mu g/cm^2$.

The subsequent I^{126} sources were prepared by the Szilard-Chalmers method after activating KIO_3 by fast neutrons from the M.I.T. or Brookhaven cyclotron.

† This work partially supported by the U. S. Atomic Energy Commission.

* Now at Miami University, Oxford, Ohio.
‡ On leave from the Institute for Nuclear Research, Amsterdam, The Netherlands.

[1] Marty, Langevin, and Hubert, J. phys. radium **14**, 663 (1953).
[2] M. L. Perlman and J. P. Welker, Phys. Rev. **95**, 133 (1954).
[3] C. S. Wu, Proceedings of the International Nuclear Physics Conference in Chicago (unpublished).
[4] D. T. Stevens and M. Deutsch, Phys. Rev. **84**, 1071 (1951).

In order to reduce the exchange rate between "I⁻" and "I" in the KIO_3, the KIO_3 was kept in dry ice during bombardment and during transportation. Because of the presence of "I⁻" in KIO_3 as impurity, no additional "I⁻" tracer was required. The iodine was first extracted into the carbon tetrachloride layer and then purified by cyclic reduction with dilute sulfite solution followed by oxidation back to the organic fraction. Finally, the purified iodine in the carbon tetrachloride fraction was shaken together with 10 cc of distilled water containing about 5 mg Zn dust. The ZnI_2 thus formed was then filtrated. Unfortunately, ZnI_2 is hydroscopic and therefore unsuitable for use as a β^- source. This necessitated the conversion of ZnI_2 to the more stable KI. In order to accomplish this the solution was passed through a cation exchange resin column (Dowex-59, *K*-form).

The β source was prepared by evaporating a drop of KI in a vacuum desiccator. As a precautionary measure against the escape of I_2 during the investigation a thin layer of collodion (6 $\mu g/cm^2$) was used to cover all the β^- sources.

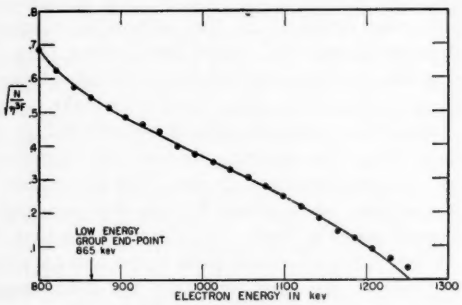

FIG. 2. Uncorrected electron Kurie plot.

3. INVESTIGATION OF THE β^- SPECTRUM

(a) Total β^- Spectrum

(1) *Kurie Plot Analysis*

The β^- spectrum of I^{126} was investigated in both the solenoidal magnetic spectrometer and the coincidence magnetic spectrometer. The total spectrum is composite (Fig. 1). The corresponding Kurie plot (Fig. 2) shows that the spectrum of the high-energy component deviates from a straight line. For a complex spectrum the deviation of a unique first forbidden spectrum from an allowed one can be judged only through the very short upper energy segment because of the presence of the lower energy group. Special attention must then be paid to those points near the upper energy limit and suitable resolution corrections must be applied. It can be seen from the figure that the uncorrected Kurie plot has a slight curvature concave towards the energy axis. However, when the unique correction factor[5]

[5] Rose, Perry, and Dismuke, Oak Ridge National Laboratory ORNL-1459, 1953 (unpublished).

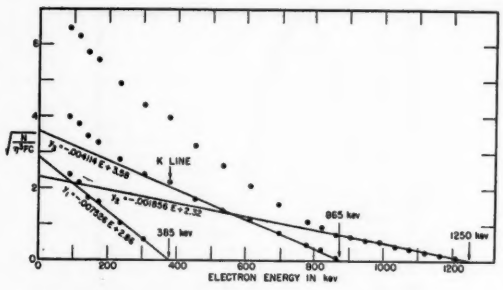

FIG. 3. Kurie analysis of the composite electron spectrum; high-energy component corrected for α shape.

$[(1/12)K^2L_0+\frac{3}{4}L_1]$ is applied, the Kurie plot is straightened out (Fig. 3), thereby giving the energy limit of the highest energy group as 1.25±0.01 Mev. The corrected Kurie plot starts to deviate from a linear plot in the region of 800–900 kev. When the unique forbidden spectrum with upper energy limit of 1.25 Mev is subtracted from the total spectrum, a second Kurie plot (Fig. 3) is obtained which gives an energy limit of 865 kev for the second β^- group. This is in accord with the expected value calculated from the maximum energy of the highest β-ray group (1.25 Mev), and the energy of the coincident gamma ray of 386 kev. This second Kurie plot starts to deviate around 400 kev and once again utilizing the subtraction method, one obtains the third β group with an upper energy of 385 kev. This is in accord with the second gamma-ray line (480 kev) observed in the β^- branch.

(2) *Branch Ratio Analysis*

The area of the total β spectrum may be analyzed into several groups, corresponding to different transitions, by means of the Kurie plot analysis. The β spectrum of the highest-energy group exhibits a unique forbidden shape. It is important for the analysis that one takes this into consideration. The remainder of the total area after the subtraction of the highest energy group is the sum of the other two β-ray groups. Since the Kurie plot of the second group, as obtained from the graphical analysis and also from the coincidence spectrometer investigation, indicates a linear plot, one may again resolve the area under the curve into the second and third groups. The branching ratio of these three groups thus obtained are 21.1:65.7:13.2 for the 1.25, 0.865, and 0.385 Mev groups (Fig. 4). The ratio of the intensity of the 1.25-Mev β spectrum to that of the 0.865-Mev β spectrum is 0.32, which is lower than the value 0.38 quoted by Marty and her co-workers. The reason for this disagreement is that no unique forbidden correction factor was applied to the ground to ground β transition in Marty's analysis.[1] The quoted branching ratio of the 0.385-Mev β transition may be a little bit higher than its true value because of the distortion which results from the scattering of the

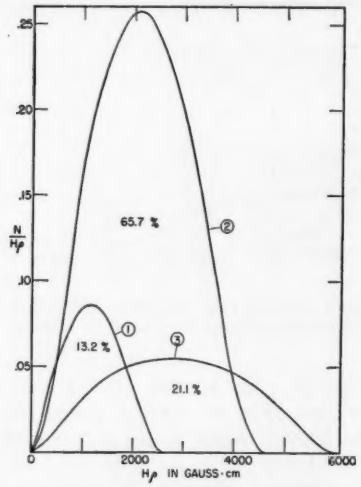

FIG. 4. Resolved electron momentum distribution, showing intensities of the three groups.

electrons of higher energies. However, the end-point energy of the third group is correct and the intensity is in good agreement with the ratio derived from the measurement of gamma-ray intensities. (See Table I.)

(3) *K-Conversion Coefficient and $K/(L+M)$ Ratio of the 386-kev Line*

The only internal conversion line with any measurable amount of intensity is that of the 386-kev gamma ray. The energy of the K-conversion line is 351.7 ± 2.0 kev and since the K-binding energy of Xe is 34.55 kev this gives the energy of the gamma ray as 386 ± 2 kev. The $K/(L+M)$ ratio calculated by comparing the area under the peaks is 6.7 ± 1.0. The value of α_K is obtained by taking the ratio of the area of the K line to the area of the total β spectrum multiplied by the factor.

$$\frac{I_{\beta1}+I_{\beta2}+I_{\beta3}}{I_{\beta2}+I_{\beta3}[I_{\gamma480}/(I_{\gamma480}+I_{\gamma860})]}.$$

This yields a value of $(\alpha_K)_{386}=1.7\times10^{-2}$. The theoretical values of α_K/α_L and α_K for electric quadrupole radiation are 6 ± 1 and 1.7×10^{-2} respectively for a 386-kev transition in Xe. The agreement with our experimental results is excellent.

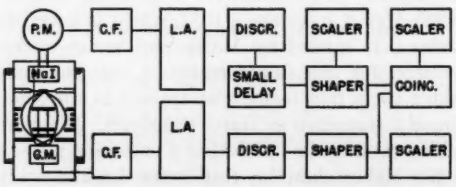

FIG. 5. Schematic diagram of coincidence solenoidal spectrometer.

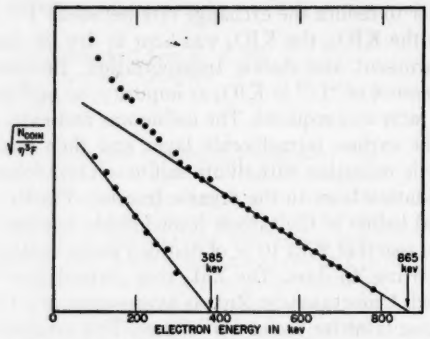

FIG. 6. Kurie analysis of electron spectrum in coincidence with gamma radiation, showing the linearity of the Kurie plots.

(b) β^--γ Coincidence Spectrum

When dealing with a composite β spectrum the β^--γ coincidence technique is far more reliable for determining the upper energy limit and the spectrum shape of the β transition to the excited states than the conventional graphical analysis. A NaI scintillation detector was installed in the solenoidal magnetic spectrometer about 1 in. behind the β source (Fig. 5). The scintillation flashes are piped out through a tapered Lucite light pipe, 40 in. long, in order to make certain that the electron-multiplier tube is not affected by the magnetic field. The resolving time of the coincidence system is approximately 0.25 μsec. The Kurie plot of the β spectrum as obtained by the β-γ coincidence technique is given in Fig. 6. This clearly shows that the high-energy group has an allowed shape and an upper energy limit of 865 kev, and that the lower energy group has an upper energy limit of 385 kev. The results from the coincidence technique confirm the results derived from the analysis of the composite spectrum.

(c) Composite Spectrum of β^+

The β^+ spectrum of I^{126} was also investigated in the solenoidal magnetic spectrometer. Since the positron intensity is only 2 to 3 percent of that of the negatrons, the counting rate is rather low and consequently a long

TABLE I. Relative intensity.

Radiation (kev)	By single-channel analyzer	By coincidence spectrometer	By the analysis of the Kurie plot of the composite β spectrum
γ_1 0.386	100	100	100
γ_2 0.480	15[a]	16[b]	14
0.510	7[c]		
γ_3 0.650	97	97	
γ_4 0.740	12	11	
γ_5 0.866	2.5		
γ_6 1.420	<1.5		

[a] Obtained by subtracting the annihilation radiation from the composite peak at ~490 kev.
[b] The contribution due to Compton electrons of the 511- and 650-kev lines in the 380-kev peak is corrected.
[c] Estimated from the β^+/β^- ratio.

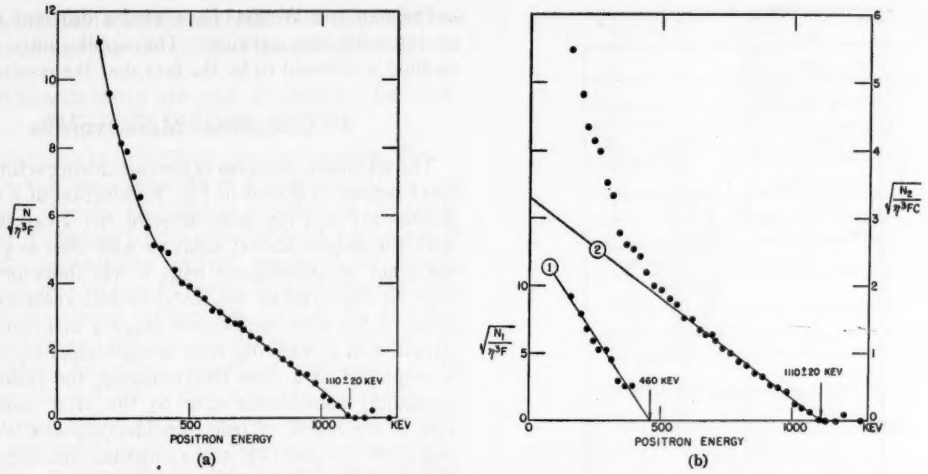

FIG. 7. (a) Uncorrected positron Kurie plot. (b) Kurie analysis of composite I^{126} positron spectrum, with high-energy component corrected for α shape.

counting time is required. The composite Kurie plot is given in Fig. 7(a). The upper energy group definitely shows a deviation from the allowed shape. The high-energy end of the Kurie plot of an allowed spectrum is always slightly curving above the extended straight line because of the finite resolution effect. In this case, it is obviously different from the allowed shape. When it is corrected by the unique first forbidden correction factor, a linear Kurie plot results and the upper energy limit is only 1.11±0.02 Mev [Fig. 7(b)]. This value is much lower than the value given by Marty, Langevin, and Hubert.[1]

The second β^+ group obtained from the graphical analysis gives an upper energy limit of 460 kev (Fig. 7).

The branching ratio of these two β^+ transitions was determined from a comparison of the areas under each of the distributions as calculated from the resolved Kurie plots. These ratios are 22.3 percent and 77.7 percent for the low- and high-energy groups, respectively.

The ratio of the β^+ to β^- is also obtained by comparing the areas under corresponding distribution curves. It is 2.8±0.1 percent.

4. GAMMA-RAY SPECTRUM

(a) Single Spectrum Analysis

The gamma-ray spectrum was studied with a single-channel pulse-height analyzer and with the gamma–gamma and x-ray–gamma coincidence scintillation spectrometer. Both were calibrated for energy and for over-all efficiency.

The single-channel scintillation spectrometer employed a 1 in.×1 in. NaI(Tl) crystal and a Dumont K 1186 photomultiplier tube together with an AIC-500 single-channel analyzer. The energy calibration was performed at ten well-known energies with RaD, Tl^{204}, In^{114}, Se^{75}, Au^{198}, Na^{22}, Bi^{207}, and Cs^{137}. The resolution is 9 percent for the 661-kev line. The gamma-ray spectrum of I^{126} is given in Fig. 9(a).

To determine the relative over-all efficiency as a function of energy, Bi^{207}, Na^{22}, In^{114}, and Se^{75} were employed for calibration. Peak heights of lines with known intensity ratios were compared and the various efficiency ratios obtained in this way were fitted to a smooth curve on a log-log plot of efficiency *versus* energy.[6] An additional check was made by using I^{131}, which has lines with known intensities at 364, 637, and 722 kev close to the main lines of I^{126}.

The intensity of the 386-kev line was normalized to 100. On this scale the intensities for the other single and composite peaks in Fig. 9(a) are given in Table I, with an accuracy of about 10 percent. The intensity of the 1.4-Mev line was exceedingly low and it is possible to give only an upper limit.[7]

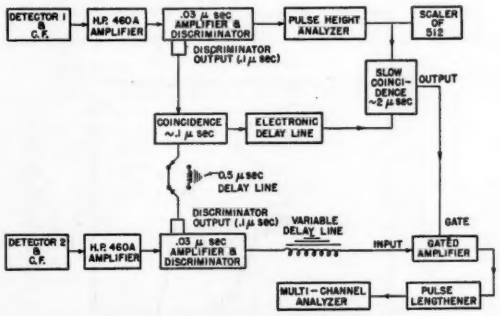

FIG. 8. Block diagram of the selective coincidence scintillation spectrometer.

[6] Åström, Wapstra, Thulin, and Bergström, Arkiv Fysik **7**, 247 (1954).

[7] The particular source to detector distance used in obtaining this spectrum eliminates the possibility of any contribution by summation pulses other than a negligible amount.

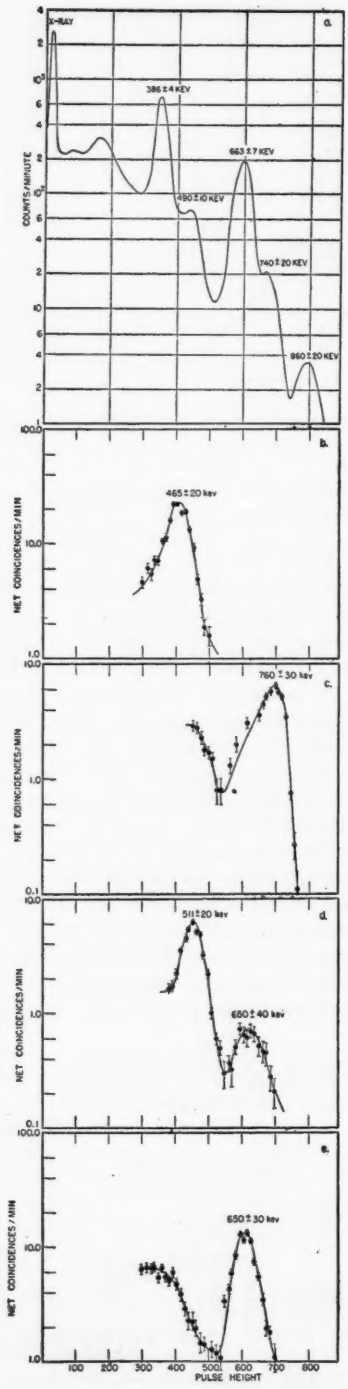

FIG. 9. Scintillation spectrum of I^{126}, showing (a) the total gamma-ray spectrum; (b) the gamma radiation in coincidence with the 385-kev gamma rays, (c) with the 650-kev gamma rays, (d) with the annihilation radiation, and (e) with the Te x-rays.

Perlman and Welker[2] have used a different method of intensity measurement. The applicability of our method is attested to by the fact that the results agree.

(b) Coincidence Measurements

The schematic diagram of the coincidence scintillation spectrometer is shown in Fig. 8. Selection of a definite gamma ray or x-ray from detector No. 1 can be made with the single-channel analyzer and then any β or γ spectrum in coincidence with it via detector No. 2 may be displayed on the multichannel analyzer. Since prior to the slow-coincidence stage a fast-coincidence circuit with a resolving time of approximately 0.1 μsec is employed as a time discriminator, the ratio of the accidental coincidence rate to the true coincidence rate in the region of true coincidence peaks is usually negligible. In practice, the accidental coincidence rate is directly determined by throwing the $\frac{1}{2}$-μsec delay line into the branch of the No. 2 detector of the fast coincidence circuit. Figure 9 exhibits the gamma-ray spectrum from the single-channel analyzer and the spectra of those radiations in coincidence with the 386-kev γ line, the 650-kev γ line, the annihilation radiation, and the Te x-rays. The spectra are plotted one above the other on the same energy scale in order to facilitate interpretation. Unfortunately, a high bias limitation in the design of our multichannel analyzer prevented us from extending the coincidence spectrum to the very low-energy region.

The determination of the relative intensities of gamma rays in coincidence required a knowledge of the over-all efficiencies of detector No. 2 as a function of energy. Assume a radioactive substance emits two gamma rays in cascade; then, the rate of detecting coincidences between γ_a in detector No. 1 and γ_b in detector No. 2 is given by

$$N_{\text{coin}} = N_0 \epsilon_{1a} \epsilon_{2b},$$

where N_0 is the number of disintegrations per unit time, ϵ_{1a} is the over-all efficiency of detecting γ_a (in the photopeak) of detector No. 1 and ϵ_{2b} is the over-all efficiency of detecting γ_b (in the photopeak) of detector No. 2. Since the product $N_0\epsilon_{1a}$ is precisely the counting rate (in the photopeak) of γ_a (after being corrected for the Compton contribution from gamma rays of higher energy), then it follows that the ratio

$$\frac{N_{\text{coin}}}{N_0 \epsilon_{1a}} = \left(\frac{N_{\text{coin}}}{N_{\text{single}}} \right)_{\text{monitor set at } \gamma_a} = \epsilon_{2b}.$$

Using available sources of Na^{22}, In^{114}, and Co^{60}, we obtained the value of ϵ_{2b} at energies of 0.511, 0.722, 1.17 and 1.28 Mev. By drawing a smooth line through the points a very useful calibration curve is obtained. The relative intensities of gamma rays of I^{126} determined in this way are listed in Table I and agree well with

those determined from the analysis of the single-channel γ spectrum and the branching of the different β groups.

5. DETERMINATION OF THE INTENSITY OF THE ELECTRON CAPTURE PROCESS

I^{126} also decays to Te^{126} by electron capture. The Te x-rays which were detected in a proportional counter were very intense. To evaluate the ratio of the probability of K-capture to the probability of β emission we used the comparison method employed by Marty, Langevin, and Hubert.[1] This method utilized the closeness of the energy between the Te and Ba K x-rays and the 650- and 661-kev gamma rays in I^{126} and Cs^{137} respectively. Since the conversion coefficient of the 661-kev line in Cs^{137} is known rather accurately, the comparison method yields the intensity ratio between the Te x-ray and the 650-kev gamma ray. The relative intensities of the 650-kev line to other gamma lines can be determined by scintillation spectrometer analysis. This enables one to derive the ratio of the probabilities of electron capture to total β^- emission as well as the ratio of K-capture to positron emission for the various states.

A proportional counter 12.5 cm in diameter filled with 3 atmos of krypton was used for the measurement of the Te and Ba K x-rays. The ratio of the height of the escape peaks to that of the main peak is practically identical in this counter for each of these two x-rays. This simplifies the calculation. The relative net efficiency of detection of Ba and Te x-rays was calculated from the coefficient of the photoelectric effect in krypton, the dimensions of the counter, the pressure of the gas, and the absorption by the Be window. This efficiency was calculated to be 1:1.1. The relative intensities of the 650- and 661-kev gamma rays were measured under identical conditions by the NaI scintillation spectrometer. The sources used were the same as those employed in the proportional counter determinations. The results are

$$I_{\text{Ba } K \text{ x-ray}}/I_{\text{Te } K \text{ x-ray}}=0.645,$$

and

$$I_{661 \text{ kev}}/I_{650 \text{ kev}}=9.33.$$

If we now adopt the K-conversion coefficient of the 661-kev line of Cs^{137} as 0.097 and the K-fluorescence yields[8] of Ba and Te as 0.900 and 0.872 respectively, then we find that

$$I_{K\text{-capt. in } I^{126}}/I_{650 \text{ kev}}=1.46.$$

This is in fair agreement with the values given by Perlman. The x-ray intensity of I^{126} was measured for a period of several half-lives. Any contribution from possible contamination due to I^{125}, produced in $(n,3n)$ reactions, was negligible. The above ratio is converted to

$$I_{K\text{-capt. in } I^{126}}/\beta^-$$

[8] Broyles, Thomas, and Haynes, Phys. Rev. 89, 715 (1953).

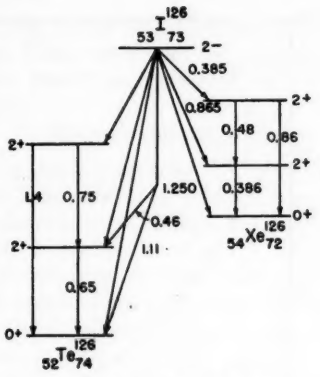

FIG. 10. Decay scheme of I^{126}.

by applying the following relationship:

$$1.46\times\frac{I_{650}}{I_{386}}\times\frac{\beta_2+\beta_3[I_{\gamma,480}/(I_{\gamma,480}+I_{\gamma,860})]}{\beta_1+\beta_2+\beta_3}=1.11.$$

If one uses the value of 1.12 for the ratio[9] of total capture to K-capture then

$$(K+L)\text{-capture}/\beta^-=1.24\pm0.10.$$

The ratios of K-capture to positron emission for the different states are

$$(K\text{-capture}/\beta^+)_{\text{ground}}=20.2\pm2.0,$$

and

$$(K\text{-capture}/\beta^+)_{650 \text{ state}}=95\pm10.$$

DISCUSSION

The main features of the decay of I^{126} are represented in Fig. 10. The decay scheme is in agreement with the one proposed by Perlman and Welker.[2] The intensities of the various radiations observed are collected in Table II.

TABLE II. Branching ratios.

Radiation	(kev)	Abundance (percent)	log ft	log fu
β_1^-	385±5	5.82±0.30	7.34	
β_2^-	865±5	29.0 ±1.5	7.90	
β_3^-	1250±10	9.31±0.45	9.12	8.75
β_1^+	460±15	0.28±0.02	7.16	
β_2^+	1110±20	0.96±0.05	8.41	8.00
EC_1	(730)	4.0 ±0.5	7.55	
EC_2	(1480)	28.7 ±2.8	7.35	
EC_3	(2130)	22.0 ±2.0	8.00	8.14
γ_1	386±2	33.6 ±1.6		
γ_2	480±10	5.0 ±0.4		
γ_3	650±10	33.0 ±2.6		
γ_4	750±20	3.6 ±0.4		
γ_5	860±20	0.84±0.09		
γ_6	(1420)	<0.50		

[9] Calculated from the formula of M. E. Rose and J. L. Jackson, Phys. Rev. 76, 1540 (1949).

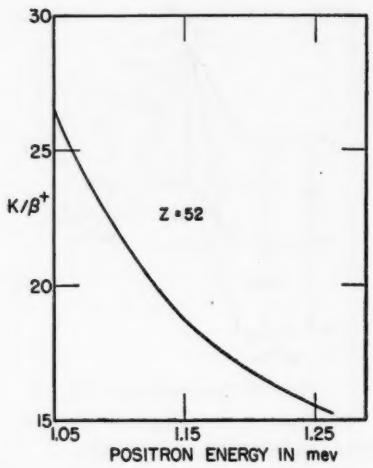

FIG. 11. Ratio of K-capture to positron emission as a function of the maximum energy of the positrons for $Z=52$ and $\Delta I=2$ (yes).

The relative intensities of the three negatron groups have been determined from a Kurie analysis of the total negatron spectrum. The high-energy group exhibits the α shape. It is felt that the intensity of the lowest energy group may be somewhat high due to scattering, etc., but that the value given is correct to within 10 percent. The relative intensities of γ_1 and γ_2 found from the gamma–gamma coincidence experiment (Table I) agree with those derived from the negatron spectrum within the error limits.

The relative intensities of the two positron branches have also been determined from a Kurie analysis in which the higher energy group has been corrected for an α shape (Table II). Here again it is felt that the intensity of the lower energy group is somewhat high but is accurate to within 10 percent.

The ratio of K x-rays to γ_3 as determined by the technique described in Sec. 5 is known with great accuracy because the corrections necessary are well known for the proportional counter. The correction of 12 percent for L-capture seems reasonable, although this value strictly applies to allowed transitions only.

The intensity ratio of γ_1 to γ_3 has been calculated from the single spectrum (Table I) using crystal efficiencies which are known only to about 10 percent. However, it may be pointed out that there are now three independent determinations of this ratio which agree very well. Therefore, we have chosen the mean value of these results as the basis for our calculations:

$$I_{\gamma 3}/I_{\gamma 1}=0.98\pm0.04.$$

The branching ratio of K-capture to the three states in Te^{126} can be calculated from the data on the relative intensities of γ_3 and γ_6 from the single spectrum (Table I), and those of γ_3 and γ_4 from the coincidence experiment.

All groups of relative intensities can subsequently be converted to absolute branching ratios and these are shown in Table II, together with the ft-values of the various transitions.

Although in the calculations no use has been made of the intensities of γ_4 or the intensity of the composite γ_2 and annihilation radiation peak obtained in the single gamma-ray spectrum (Table I), it is still interesting to note that these values check very nicely with those calculated from Table II. The branching ratio of the two positron spectra is substantiated by the results obtained from the coincidence measurements and annihilation radiation (Table I).

CONCLUSION

The ground-state spin of I^{126}, which has been the subject of some disagreement, is definitely established as 2^- by the shape of the 1.11-Mev β^+ spectrum[10] and the 1.25-Mev β^- spectrum. The end point of the β spectrum to the first excited state obtained by subtracting the uniquely shaped high-energy component from the composite spectrum is in agreement with other data in contrast to Marty's analytic results. The value of the K-capture to positron emission ratio as measured for the transition to the ground state of Te^{126} is 20.2 ± 2.0, while the theoretical ratio calculated for a unique 1st forbidden transition using the formulas given by Nataf and Bouchez[11] and displayed in Fig. 11 is 21.9 for $(E^+)_{max}=1.11$, while the theoretical value for an allowed or an l-forbidden transition is 4.5 and 3.5 respectively. Again this agreement strongly favors a unique first forbidden transition.

All β transitions to the four excited states are of the type $2^-\rightarrow2^+$ and the ft-values are compatible with the mean value[12] of $\log ft=7.5\pm0.5$. The ratio of K-capture to positron emission to the first excited state in Te^{126} is 95 ± 10 and the theoretical value for an allowed transition is 152 ± 13 for $(E^+)_{max}=0.46\pm0.02$. However, it is not certain that these two values should agree, since more than one nuclear matrix element is involved.

The only possibility of obtaining a negative parity for the I^{126} ground state lies in assigning an $h_{11/2}$ state to the 73rd neutron. Of the two plausible assignments[13] $d_{5/2}$ or $g_{7/2}$ for the 53rd proton, only the latter can give a spin of 2; for the same reason all other possibilities are ruled out. Although this spin assignment disagrees with the original one proposed by Nordheim,[14] it does agree with his alternate suggestion and with Nordheim's rule.

[10] It may be pointed out that a linear extrapolation of the Kurie plot from the lower energy region in Fig. 7 leads to an end-point energy of 1.20 Mev, in close agreement with the value given by Marty *et al.*, see reference 1.
[11] R. Nataf and R. Bouchez, J. phys. et radium **13**, 190 (1952).
[12] R. W. King and D. C. Peaslee, Phys. Rev. **94**, 1284 (1954).
[13] P. F. A. Klinkenberg, Revs. Modern Phys. **24**, 63 (1952).
[14] L. W. Nordheim, Revs. Modern Phys. **23**, 322 (1951).

The same situation seems to apply to the ground state of other odd-odd nuclides in this mass region. I^{124} and Sb^{122} exhibit an α-shape ground state spectrum. There is some indication that both I^{134} and I^{136} have a 2^- ground state. If the spin of Sb^{124} is 3^- as proposed, this again points to an $h_{11/2}$ state for the 73rd neutron while the proton may be in the $d_{5/2}$ state. The disintegration schemes of both I^{130} and I^{132} seem to require an odd-parity ground state.

Moreover, the even-even isotopes of Te and Xe in this mass region seem to possess at least a second 2^+ state at an excitation energy slightly larger than twice that of the first excited 2^+ state. This situation now has been found in Te^{122}, Te^{124}, Te^{126}, Xe^{126}, and Xe^{136}.

Nothing can be concluded about the occurrence of a 4^+ state in the energy region considered in Te^{126} and Xe^{126}, since these would not be populated to any considerable extent as estimated by the *ft*-value consideration.

ACKNOWLEDGMENTS

We wish to thank Professor J. M. Miller of the Department of Chemistry for his constant interest and advice on the chemical preparation of the source. The help given by Dr. R. H. Herber of M.I.T. and Dr. C. P. Baker of Brookhaven National Laboratory on the fast-neutron bombardments is deeply appreciated. We are particularly indebted to Miss N. Benczer for her invaluable aid in analyzing the β^- spectrum data. One of the authors (R.v.L.) wishes to thank the Netherlands Organization for Pure Research (Z.W.O.) for a grant.

PHYSICAL REVIEW VOLUME 98, NUMBER 5 JUNE 1, 1955

Pair Spectrometer Measurements of the Radiations from Excited States of Light Nuceli*

R. D. Bent, T. W. Bonner, and R. F. Sippel
The Rice Institute, Houston, Texas

(Received January 14, 1955)

A magnetic-lens pair spectrometer has been used to study the radiations produced by the bombardment of certain light nuclei with protons and deuterons from a Van de Graaff accelerator. Gamma rays from the bombardment of F^{19} with 3.7-Mev protons were observed at 6.10±0.04 and 6.99±0.04 Mev. At 4.7-Mev bombarding energy, no lines were observed between 7.5 and 11.0 Mev with an intensity as great as 10 percent of that of the 6.99-Mev line. Gamma rays from the bombardment of C^{13} with 2.0-Mev deuterons were observed at 3.42±0.03, 3.71±0.05, 3.94±0.06, 4.48±0.04, 4.96±0.03, 5.12±0.04, 5.74±0.03, 6.14 ±0.03, 6.53±0.05, and 6.72±0.03 Mev. At 4.0-Mev bombarding energy, lines were observed at 6.14±0.03, 6.53±0.04, 6.72±0.03, 7.09±0.03, and 7.34±0.04 Mev. Gamma rays from the bombardment of C^{12} with 4.0-Mev deuterons were observed at 3.76±0.02 and 3.86±0.02 Mev. No lines were observed between 3.86 and 5.8 Mev with an intensity as great as 10 percent of that of the 3.86-Mev line. All the energies of γ rays given above are uncorrected for Doppler shifts which in some cases are as large as 40 kev. A search was made for nuclear pairs which might originate from the proton bombardment of B^{11}. No pairs were observed at 4.0-Mev bombarding energy in the energy range between 6.5 and 9.5 Mev. A search was also made for nuclear pairs which might result from the $Li^7(d,n)Be^8$ reaction. No pairs were observed in the energy range between 5.0 and 8.5 Mev.

I. INTRODUCTION

MEASUREMENTS of γ-ray energies greater than about 3 Mev can best be made by utilizing the pair production process since the probability for the production of pairs increases, whereas the Compton and photoelectric cross sections decrease, with increasing γ-ray energy. The work of Bame and Baggett,[1] Siegbahn and Johansson,[2] and Alburger[3] showed that the magnetic lens pair spectrometer was well suited for making such measurements and indicated that with further refinements this technique would be useful for studying complicated γ-ray spectra. The resolution of these earlier spectrometers was limited by low counting rates resulting from small solid angles and by large background effects due to accidental coincidences and real coincidences of scattered electrons, γ rays, and neutrons. It was apparent that in order to improve the resolution of these earlier instruments it would be necessary to improve the transmission to resolution ratio of the spectrometer and the resolving time and energy discrimination of the coincidence circuit.

The work of DuMond[4] indicated that the transmission to resolution ratio of the spectrometer used by Bame and Baggett[1] could be increased if a ring focus was employed and the average acceptance angle was increased to approximately 45°. To accomplish this the spectrometer was shortened and a small coil was added in the center of the spectrometer to create a fairly uniform field. Photographic techniques were used to locate the ring focus. The Geiger counters used by Bame and Baggett were replaced by scintillation detectors and the spectrometer was used in this form by Bent, Bonner, and Sippel.[5] Experiments were then

* Supported by the U. S. Atomic Energy Commission.
[1] S. J. Bame and L. M. Baggett, Phys. Rev. **79**, 415(A) (1950); Phys. Rev. **84**, 891 (1951).
[2] K. Siegbahn and S. Johansson, Rev. Sci. Instr. **21**, 442 (1950).
[3] D. E. Alburger, Rev. Sci. Instr. **23**, 671 (1952).
[4] J. W. M. DuMond, Rev. Sci. Instr. **20**, 160 (1949).
[5] Bent, Bonner, and Sippel, Phys. Rev. **91**, 472(A) (1953).

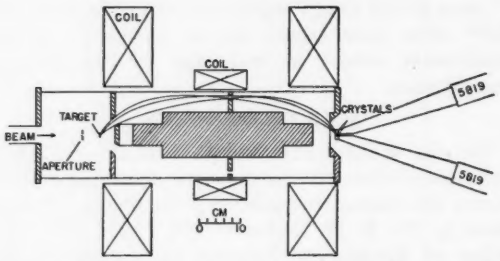

FIG. 1. Diagram of the pair spectrometer. The proton or deuteron beam from the Rice Institute 6-Mev Van de Graaff accelerator strikes the target after passing through a defining aperature 3 mm in diameter. The positron-electron pairs come to a focus outside of the vacuum chamber and are counted in coincidence with scintillation detectors.

performed to investigate an intermediate-image focusing principle similar to that used by Slätis and Siegbahn,[6] and Daniel and Bothe,[7] which resulted in the reduction of the aberration of the instrument and in the elimination of an unexplained "ghost image" which appeared with the ring focus spectrometer. The resolving time of the coincidence circuit was reduced to 2 millimicroseconds by using a coincidence detection system consisting of stilbene crystals, R.C.A. 5819 phototubes, and a fast coincidence circuit of the type described by Fischer and Marshall.[8]

With this improved spectrometer and coincidence detection system it became feasible to observe the γ spectra from a number of reactions in light nuclei with 2.5 percent energy resolution. The Rice Institute 6-Mev Van de Graaff accelerator was used to study a number of reactions at higher bombarding energies than previously.

II. APPARATUS

A. Spectrometer

A drawing of the spectrometer used in this work is shown in Fig. 1. The two large focusing coils are those which were used by Bame and Baggett in an earlier spectrometer.[1] They contain about 150 turns each of $\frac{3}{8}$-inch copper tubing which are cooled by water flowing through them. The small coil in the center contains 626 turns of solid $\frac{3}{32}$-inch copper wire. The vacuum chamber of the spectrometer is an 8-inch o.d. brass tube with $\frac{1}{8}$-inch wall. The acceptance baffles and intermediate ring baffle are made of aluminum $\frac{3}{8}$ inch thick and the central cylinder which shields the detectors from direct radiation from the source is made of lead. The inside of the brass tube and the outside of the central lead cylinder are lined with polyethylene to reduce the scattering of electrons. There are no iron parts in the spectrometer. The beam from the vertical 6-Mev Rice Institute Van de Graaff is bent through 90° by an analyzing magnet and enters the spectrometer horizontally. It then passes through a hole 3 mm in diameter in a tantalum sheet which is placed about 4 cm in front of the target. The electron pairs focused by the spectrometer pass through 10 mils of aluminum at the other end of the spectrometer and are detected outside of the vacuum chamber. The current supply and regulating equipment have been described by Bame and Baggett.[1] The center coil, in series with a variable resistor, is connected in parallel with the large coils so that the ratio between the current in the large coils and the current in the small center coil can be varied within limits. The whole spectrometer is surrounded by two Helmholtz coils which are used to cancel the component of the earths magnetic field which is perpendicular to the axis of the spectrometer. The optimum field gradient and the positions of the acceptance and intermediate ring baffles were determined by techniques similar to those described by Slätis and Siegbahn.[6] The dimensions of the spectrometer are as follows: Distance from center of first large coil to center of second large coil=43.8 cm. Distance from target to center of first large coil=6.7 cm. Distance from plane half-way between two large coils to intermediate ring baffle=2.5 cm. Distance from crystals to center of second large coil=5.5 cm. Distance from target to detectors=56 cm. Outer radius of intermediate ring baffle=9.0 cm. Average acceptance angle=41°.

The optimum field gradient was obtained when the current in the center coil was 1/39 times the current in the large coils and opposite in direction to the current in the large coils. The magnitude of axial component of the magnetic field on the axis of the spectrometer at the center of the spectrometer was then 0.45 times its value at the center of one of the large coils. With a source 3 mm in diameter, an intermediate ring baffle 6 mm wide and an acceptance solid angle equal to 9 percent of the total sphere, the best resolution obtained with the Cs^{137} internal conversion line was 2.7 percent. 2.0 percent resolution was obtained with an acceptance solid angle equal to 4 percent of the total sphere and an intermediate ring baffle 3 mm wide. Improvements in transmission and resolution may result from better alignment. So far it has not been possible to make the resolution for positive and negative electrons quite optimum at the same time. The paths of positrons are simulated with a Cs source by changing the direction of the current in the coils. With this arrangement 33 kilowatts of power are needed to focus 4.2-Mev electrons, which corresponds to a γ-ray energy of 9.4 Mev. Measurements of higher γ-ray energies with this input power are planned by changing the geometry of the coils. Changes in the field shape resulting from two additional coils are expected to result in improved transmission and resolution.

The dc generator available for the spectrograph could not be used at a power level above 33 kw except for short periods of time. Thus with the preceding arrangements the experiments were limited to a study of

[6] H. Slätis and K. Siegbahn, Arkiv Fysik **1**, 339 (1949).
[7] H. Daniel and W. Bothe, Z. Naturforsch. **9a**, 402 (1954).
[8] J. Fischer and J. Marshall, Rev. Sci. Instr. **23**, 417 (1952).

γ radiation with energies less than 9.4 Mev. In order to be able to look for γ rays with energies greater than 9.4 Mev the center coil of the spectrometer was connected so that the current in this coil was in the same direction as the current in the two large coils, the intermediate image baffles and the acceptance baffles were removed, and a ring baffle 1.8 cm wide was placed 4.1 cm from the exit foil of the spectrometer. The correct position and size of the ring baffles were determined by photographic techniques. The resolution of the O^{16} nuclear pair line with this spectrometer arrangement was 3.6 percent.

B. Coincidence Detection System

The requirements of the coincidence detection system are that it have a short time resolution in order that the accidental coincidence rate be small, and that it have some energy discrimination to make possible the reduction of true coincidences due to scattered electrons, γ rays, neutrons, and annihilation radiation.

Stilbene crystals $\frac{3}{4}$ inch in diameter and of differing thicknesses were used for detection. The crystal thickness was chosen so that the electrons focused by the spectrometer would lose most of their energy in the crystals. The crystals were connected to photomultiplier tubes with lucite rods which were 12 inches long and the photomultipliers were magnetically shielded. Negative pulses from the photomultipliers were fed to the grids of 6*AG7s*, cutting the tubes off. Positive pulses were taken from the plates of the 6*AG7s* and fed to a 6*BN*6 coincidence circuit of the type described by Fischer and Marshall.[8] The pulses were clipped at the input of the coincidence circuit with shorted stubs. The time resolution of this type of coincidence circuit is about equal to the width of the pulses which are fed into it. With 10-inch clipping stubs the resolving time (half-width at the half-height of a delay curve) was 2×10^{-9} seconds. Most of the data were taken, however, with a resolving time of 10^{-8} seconds. The output of the coincidence circuit goes to an amplifier then to a pulse-height discriminator and a scalar. Since the output pulse size of the coincidence circuit is a rapidly varying function of the input pulse sizes, the pulse-height discriminator could be used to prevent the counting of true coincidences due to pulses in the crystals which were smaller than the pulses due to the pairs focused by the spectrometer.

III. PROCEDURE

In most of the experiments internal pairs produced in the product nuclei of the reactions were observed. The probability of this process is low, but all these pairs from a certain excited state have the same energy except for Doppler broadening. If external pairs produced in a heavy radiator are used, an extra spread in the pair energy results from the radiator thickness. For an energy resolution for γ radiation of about 5 percent or greater, the use of an external radiator to produce pairs gives a higher intensity than is obtained with internal pairs. When higher resolution is wanted, the internal pairs will give more intensity.

The use of an external radiator is also useful in reactions where high-intensity β emitters are formed in the target. In cases of this type, the chance coincidences of the β particles may be prohibitive, requiring the use of an absorber of low atomic number to stop the β rays and then a heavy radiator as a source of external pairs.

Three types of background tend to obscure weak γ-ray peaks. The accidental coincidence rate is measured by inserting a long piece of cable in one side of the coincidence circuit. A second type of background results from single high-energy electrons producing pulses in both crystals. This background is minimized by placing a tungsten sheet, 1.5 mm thick, between the two crystals, and by biasing to exclude annihilation photons. A third background is due to the scattering of high-energy γ rays and neutrons from the walls and coils of the spectrometer and can be minimized by using small crystals for detection, biased to accept the largest pulses. An approximate determination of this effect is obtained by measuring the coincidence rate with zero current in the spectrometer coils.

In order to count the coincidences due to the positron-electron pairs and to exclude as many background pulses as possible, the crystal thickness was generally chosen so that the pairs would lose nearly all of their energy in the crystals. If the crystals are thick enough to stop the electrons focused by the spectrometer, the pulse size varies with the energy of these electrons, and hence the discriminator must be varied to give constant detection efficiency for γ radiation of different energies. In order to avoid this complication, thinner crystals can be used where background effects are small. The pulse size then is about the same for all electrons which pass through the crystals. Usually crystals $\frac{1}{4}$ inch thick were used for γ-ray energies between 3 and 7 Mev, crystals $\frac{3}{8}$ inch thick were used for the region between 7 and 9 Mev, and crystals $\frac{1}{2}$ inch thick were used between 9 and 11 Mev.

Geiger and scintillation counters were used to monitor the γ radiation from the target. Also, the total beam striking the target was measured with a microammeter so that approximate γ-ray yields could be calculated. The efficiency of the pair spectrometer for detecting γ rays of different energies was determined by comparing the pair yields obtained with this spectrometer from the $C^{13}+D$, and $B^{10}+D$ reactions with the absolute γ-ray yields given for these reactions by Baggett and Bame,[9] Thomas and Lauritsen,[10] and Terrell and Phillips.[11] Because of uncertainties in background corrections and in detection efficiencies, and since the multipole order of the radiation is in general

[9] L. M. Baggett and S. J. Bame, Phys. Rev. 84, 154 (1951).
[10] R. G. Thomas and T. Lauritsen, Phys. Rev. 88, 969 (1952).
[11] J. Terrell and G. C. Phillips, Phys. Rev. 83, 703 (1951).

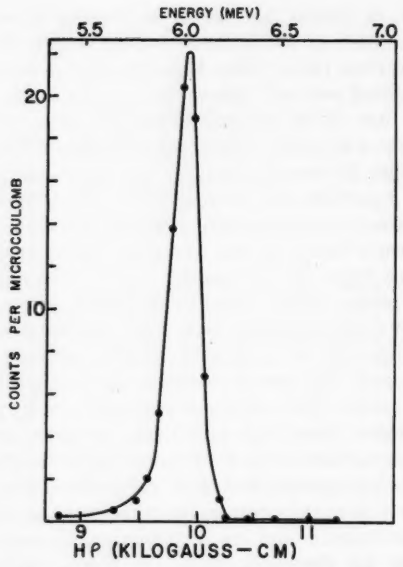

FIG. 2. The 6.05-Mev nuclear pair line from the bombardment of a 3.98-mg/cm² CaF_2 target with 2.0-Mev protons. Spectrometer resolution: 2.5 percent.

not known, the relative γ-ray yields for some of the weak lines are only accurate to within a factor of 2 and the absolute values to within a factor of 3 or 4.

The 6.055±0.015 Mev nuclear pair line from O^{16*} was used for energy calibration of the instrument in terms of the current. The γ-ray energies were determined from the values of the current at the positions of the peaks. The errors of the γ-ray energies include errors in picking the position of the O^{16} pair peak, in the knowledge of the energy of the O^{16} pair-emitting state, in the determination of target thicknesses, and in picking the positions of the peaks from the spectra. Most of the error is due to uncertainties in picking the peak positions from the spectra.

The positions and shapes of the pair lines obtained are affected by the motion of the radiating nucleus if

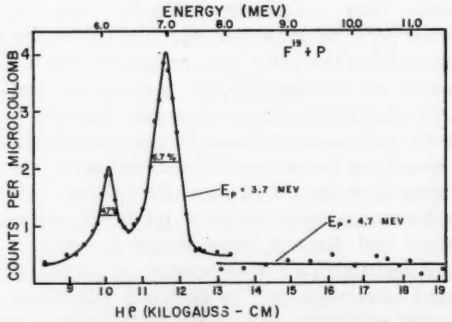

FIG. 3. The external pair spectrum from the bombardment of a thick CaF_2 target with 3.7- and 4.7-Mev protons. A 61-mg/cm² lead converter was separated from the target by 3 mm of aluminum. Spectrometer resolution: 4.0 percent.

the excited nucleus radiates before coming to rest in the target material (see Thomas and Lauritsen[10]). Corrections have been listed only for the maximum possible Doppler shift due to the center-of-mass motion, and an additional error has been added to the Doppler-corrected γ-ray energies to allow for the possible effects of the angular distribution of the radiating nuclei which in most cases is unknown.

IV. RESULTS AND DISCUSSION

A. $F^{19}+H^1$

Because of the large intensity of the nuclear pairs emitted from the first excited state of O^{16}, the $F^{19}(p,\alpha\pi)O^{16}$ reaction has been used extensively both for testing the performance of the pair spectrometer and for energy calibration. The target was 3.98 mg/cm² of CaF_2 evaporated onto a 11.8-mg/cm² copper foil. The nuclear pair line observed at 2.0-Mev bombarding energy with 2.5 percent resolution is shown in Fig. 2.

The γ radiations from the reaction $F^{19}(p,\alpha)O^{16*}$ were observed with an external radiator. Such an arrangement was needed to prevent the strong nuclear pair line from obscuring the γ rays. The thick CaF_2 target was backed by 3 mm of aluminum and a lead converter which had a mass of 61 mg/cm². The results obtained at 3.7- and 4.7-Mev bombarding energy are shown in Fig. 3, uncorrected for background effects. The energies of the two lines were calculated assuming that each external pair peak was shifted down by an amount equal to the most probable energy lost by a single electron in passing through the 61-mg/cm² lead converter. This shift was calculated to be 0.12 Mev. The energies of the γ rays and the cross sections for their production are given in Table I. No lines were seen between 7.5 and 11.0 Mev with an intensity greater than 10 percent of that of the 6.99-Mev peak.

TABLE I. Energies and yields of the γ rays from the bombardment of a thick CaF_2 target with 3.7-Mev protons.

Uncorrected energy (Mev)	Doppler-corrected energy (Mev)	Yield (γ/proton) $\times 10^3$	Total cross section[a] (mb)	Assignment (Mev)	Reference
6.10±0.04	6.08±0.05	1.3	2.7	O^{16}(6.14)	14
6.99±0.04	6.97±0.05	1.8	3.7	O^{16}(6.91) (7.12) unresolved	14

[a] Average value, E_p=0 to 3.7 Mev.

DISCUSSION

These results are in agreement with those obtained in several other measurements of the γ rays resulting from the $F^{19}(p,\alpha)O^{16*}$ reaction[3,12,13] except that in

[12] R. L. Walker and B. D. McDaniel, Phys. Rev. 74, 315 (1948).
[13] Rasmussen, Hornyak, Lauritsen, and Lauritsen, Phys. Rev. 77, 617 (1950).

previous measurements the 6.1-Mev line was always more intense than the 7.0-Mev peak. It was shown by Walker and McDaniel[12] that the 7.0-Mev radiation became more intense relative to the 6.1-Mev line as the bombarding energy was increased from 0.45 to 1.15 Mev. Table II gives the ratio of the intensities of these two peaks at different bombarding energies.

The 6.10±0.04 Mev γ-ray energy is less than the 6.14-Mev energy of the O^{16*} as determined from measurements of particle groups.[14] If the maximum Doppler shift of 0.02 Mev is subtracted from the γ-ray measurement, the disagreement is made worse. This is an indication that the 6.10-Mev γ ray is emitted after the radiating nucleus loses most of its velocity in the target material (i.e., after $\sim 10^{-13}$ second). Radiation from this 3^- level in O^{16} to the 0^+ ground state is expected to be relatively slow ($\sim 10^{-10}$ second).

There are several possible explanations for the absence of γ rays with energies greater than 7 Mev in addition to the possibility that they may have been too weak to be observed. If the states in O^{16} in this region have even parity and even angular momentum or odd parity and odd angular momentum they would break up into $C^{12}+\alpha$ much faster than they could emit γ radiation. Also, if the states have high angular momenta ($\gtrsim 2$), then transitions to the 6.1-, 6.9- or 7.1-Mev states would be expected to be more probable than transitions to the ground state.

TABLE II. Ratio of the intensities of the 7.0- and 6.1-Mev γ rays from the $F^{19}+p$ reaction at different bombarding energies. Data 0.45 to 1.15 Mev from Walker and McDaniel, 3.7-Mev data present experiment.

Bombarding energy (Mev)	Intensity of 7.0-Mev γ rays / Intensity of 6.1-Mev γ ray
0.45	0.043
0.70	0.17
1.15	0.38
3.7	1.4

B. $C^{13}+H^2$

A 48 percent C^{13} target was made by cracking methyl iodide onto a hot strip of tungsten. Flakes of carbon approximately 4 mg/cm² thick were then removed from the tungsten strip and mounted onto a 9.2-mg/cm² copper foil. The internal pair spectrum obtained at 2.0-Mev bombarding energy is shown in Fig. 4. A zero-current background which was about 50 percent of the lowest points and an accidental-coincidence rate which was about 10 percent of the lowest points has been subtracted from the original data. The high-energy region of the spectrum observed at 4.0-Mev bombarding energy is shown in Fig. 5, uncorrected for background effects. At 4.0-Mev bombarding energy, additional data were taken up to a γ energy of 8.6 Mev, but no lines were observed between 7.5 and 8.6 Mev with an intensity as great as 5 percent of that of the 6.1-Mev line. The resolution of all well-resolved lines in Figs. 4 and 5 is 2.5 percent. The γ-ray energies and yields are given in Table III.

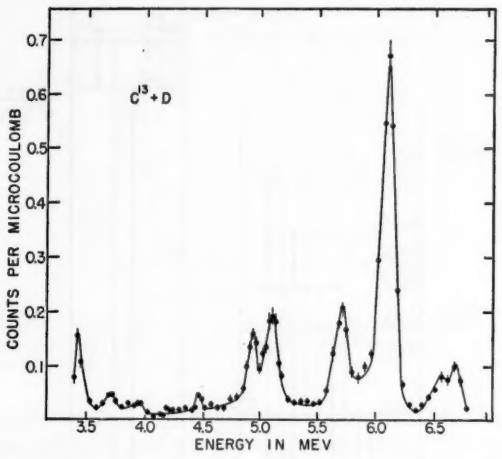

FIG. 4. The internal pair spectrum from the bombardment of a 4-mg/cm² carbon target (48 percent C^{13}) with 2.0-Mev deuterons. Spectrometer resolution: 2.5 percent.

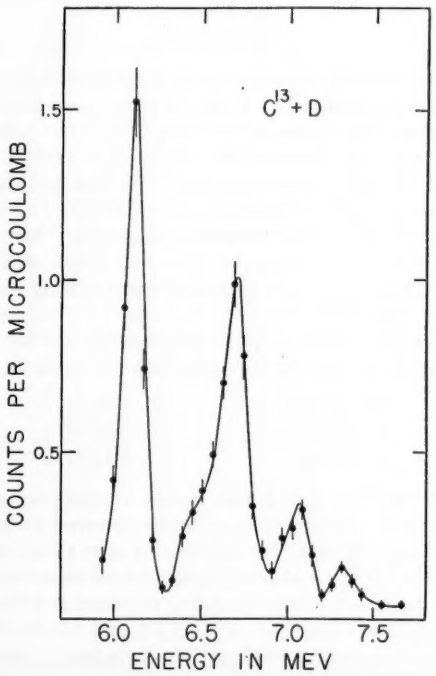

FIG. 5. The internal pair spectrum from the bombardment of a 4-mg/cm², 48 percent C^{13} target with 4.0-Mev deuterons. Spectrometer resolution: 2.5 percent.

[14] F. Ajzenberg and T. Lauritsen, Revs. Modern Phys. 24, 321 (1952).

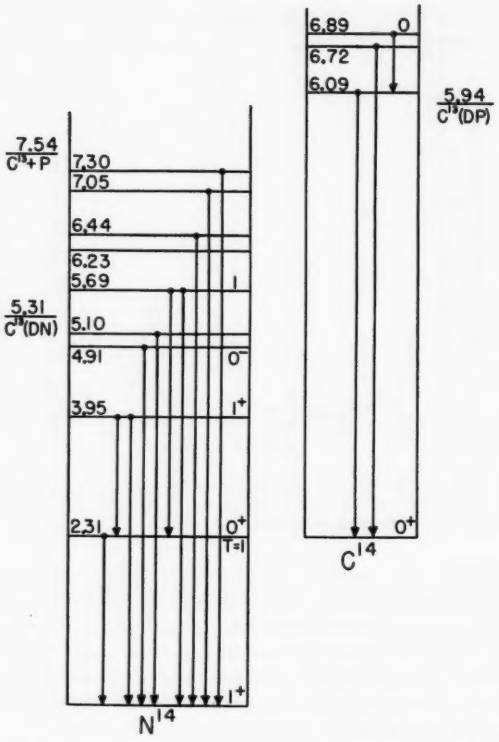

FIG. 6. Energy levels of N^{14} and C^{14} and the γ rays from $C^{13}+H^2$.

DISCUSSION

Gamma rays from the deuteron bombardment of C^{13} have been reported at 3.05, 3.40, 5.04, and 6.10 Mev by Baggett and Bame,[9] at 3.08, 3.39, 5.05, 5.69, and 6.11 Mev by Thomas and Lauritsen,[10] and at 3.91, 4.93, 5.13, 5.73, 6.12, 6.45, and 6.73 Mev by Mackin, Mims, and Mills.[15] The 3.71-, 4.48-, 7.09-, and 7.34-Mev γ rays have not been previously observed. There is no indication of a strong 4.1-Mev line which would be expected if there was a nuclear pair-emitting state in C^{14} at this energy.[10]

When C^{13} is bombarded with deuterons the following reactions, which could account for the γ rays, occur.

$$C^{13}(d,n)N^{14} \qquad Q=5.31 \text{ Mev},$$
$$C^{13}(d,p)C^{14} \qquad Q=5.94 \text{ Mev},$$
$$C^{13}(d,\alpha)B^{11} \qquad Q=5.16 \text{ Mev}.$$

The 6.14- and 6.72-Mev γ rays are assigned to C^{14} since they correspond to recently observed levels[16] in C^{14}. The 7.34-Mev line is probably due to an excited state in N^{14} since no proton groups were observed from the (d,p) reaction corresponding to a level in C^{14} at this energy. The 7.09-, 6.53-, 5.74-, 5.12-, and 4.96-Mev lines are all assigned to N^{14} since they correspond to ground-state transitions from known states in N^{14}. The 3.42-Mev line is probably due to a transition between the 5.69- and 2.31-Mev states in N^{14}. The 3.71- and 3.94-Mev lines are probably from excited states in C^{13}, resulting from the $C^{12}(d,p)C^{13}$ reaction; both the intensities and energies are consistent with this assignment. The 3.94-Mev γ ray could also be from N^{14}. A definite assignment for the 4.48-Mev line cannot be made. The energy agrees well with the 4.46-Mev state in B^{11}, however, the intensity of the line is greater than would be expected in view of the failure of Thomas and Lauritsen[10] to detect a 2.14-Mev γ ray from the $C^{13}(d,\alpha)B^{11*}$ reaction. It seems unlikely that a 4.46-Mev state in N^{14} would have escaped detection by Bockelman, Browne, Buechner, and Sperduto,[17] or by Benenson.[18] It may be that this line is due to a ground-state transition from a 4.46-Mev state in C^{14} since apparently no experiment has been performed which would eliminate this possibility. The line could also be due to a transition from a state at 6.77 Mev in N^{14} to the 2.31-Mev state.

At 7.0-Mev bombarding energy, the proton group corresponding to the level in C^{14} at 6.9 Mev has been observed with an intensity about equal to the intensity of the group leaving C^{14} in the 6.72-Mev state.[16] The fact that no 6.9-Mev γ ray was observed with an intensity greater than 10 percent of the intensity of the 6.7-Mev γ ray indicates that the 6.9-Mev level probably cascades to the 6.1-Mev level.

TABLE III. Energies and yields of the γ rays from the bombardment of a 4-mg/cm² 48 percent C^{13} target with 2.0- and 4.0-Mev deuterons.

Uncorrected energy (Mev)	Doppler-corrected energy (Mev)	Yield (γ/deut) $\times 10^6$	Total cross section (mb)	Assignment (Mev)	Reference
E_d=2.0 Mev			[a]		
6.73±0.03	6.70±0.04	0.38	4.1	C^{14}(6.72)	16
6.52±0.05	6.49±0.06	0.31	3.3	N^{14}(6.43)	18
6.14±0.03	6.11±0.04	2.3	25	C^{14}(6.09)	16
5.74±0.03	5.72±0.04	0.84	9.1	N^{14}(5.69)	19
5.12±0.04	5.10±0.05	1.0	11	N^{14}(5.10)	17
4.96±0.03	4.94±0.04	0.90	9.7	N^{14}(4.91)	17
4.48±0.04	4.46±0.05	0.32	3.5	B^{11}(4.46), C^{14}, or N^{14}(Cascade)	14
3.94±0.06	3.92±0.07	0.31	3.3	C^{13}(3.86) or N^{14}(3.95)	16 17
3.71±0.05	3.69±0.06	0.49	5.3	C^{13}(3.68)	16
3.42±0.03	3.41±0.04	1.8	19	N^{14}(Cascade 5.69→2.31)	
E_d=4.0 Mev			[b]		
7.34±0.04	7.30±0.05	0.29	3.1	N^{14}(7.50?)	18
7.09±0.03	7.05±0.04	0.76	8.2	N^{14}(7.00)	18
6.72±0.03	6.68±0.04	2.4	26	C^{14}(6.72)	16
6.53±0.04	6.49±0.05	0.9	9.7	N^{14}(6.43)	18
6.14±0.03	6.10±0.04	4.8	52	C^{14}(6.09)	16

[a] Average value, E_d=1.0 to 2.0 Mev.
[b] Average value, E_d=3.4 to 4.0 Mev.

[15] Mackin, Mims, and Mills, Phys. Rev. **93**, 950(A) (1954).
[16] Sperduto, Buechner, Bockelman, and Browne, Phys. Rev. **96**, 1316 (1954).
[17] Bockelman, Browne, Buechner, and Sperduto, Phys. Rev. **92**, 665 (1953).
[18] R. E. Benenson, Phys. Rev. **90**, 420 (1953).

By comparing the γ-ray energies with the energies that would be expected from other experiments, it should be possible to tell whether or not Doppler shifts occur. Because of the experimental errors it is not possible to say anything definite about this. However, it is noted that, except for the 6.72-Mev line, the Doppler-corrected energies are in better agreement with other experiments than are the uncorrected values.

Energy level diagrams of N^{14} and C^{14} showing the γ rays from $C^{13}+D$ are shown in Fig. 6. The energies of the 2.31, 3.95, 4.91, and 5.10-Mev levels have been accurately measured by Bockelman, Browne, Buechner, and Sperduto from the inelastic scattering of protons and deuterons on N^{14}.[17] The energy of the 5.69-Mev level has been accurately measured by Cook, Marion, and Bonner[19] from a neutron threshold measurement. The energies of the 6.23- and 6.44-Mev states are due to Benenson.[18] The 7.05- and 7.30-Mev values are from the present γ-ray measurements. Spin and parity assignments are given which are consistent with the present γ-ray measurements and with measurements of the γ rays from the $C^{13}(p,\gamma)N^{14}$ reaction,[20–22] together with the neutron angular distributions of Benenson.[18] The 1.64- and 2.31-Mev γ rays were not observed in the present work but have been reported by Thomas and Lauritsen.[10] The energy levels of C^{14} have been accurately determined by the magnetic analysis of the proton groups from the $C^{13}(d,p)C^{14}$ reaction.[16] The cascade transition between the 6.89- and 6.09-Mev levels is inferred from the present experiment from the absence of 6.89-Mev γ radiation; recently a 0.811-Mev γ ray has been observed by Mackin and Mills,[23] which confirms this conclusion. An angular momentum of zero is assigned to the 6.89-Mev level to account for the absence of the ground state transition from this level.

C. $C^{12}+H^2$

A 57.8 mg/cm² graphite target was bombarded with 4.0-Mev deuterons and the internal pair spectrum was observed with 2.5 percent resolution. The results shown in Fig. 7 have been corrected for a zero-current background which was about 10 percent of the 3.86-Mev peak and for a chance coincidence rate which was about 5 percent of the 3.86-Mev peak. The slow rise in the counting rate above 5 Mev is probably an increase in background due to the fact that the discriminator bias accepting the pulses from the coincidence circuit was not increased rapidly enough as the pulse size increased. The spectrum shows two peaks corresponding to γ rays with energies of 3.76 ± 0.02 and 3.86 ± 0.02 Mev, uncorrected for Doppler effects. No lines were observed between 3.9 and 5.8 Mev with an intensity as great as 10 percent of that of the 3.86-Mev γ ray. The results are summarized in Table IV.

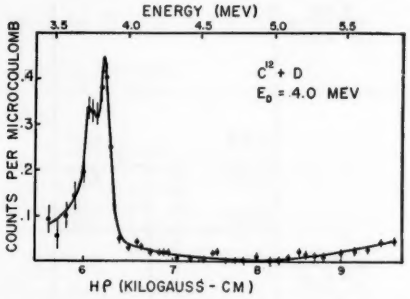

FIG. 7. The internal pair spectrum from the bombardment of a 57.8-mg/cm² carbon target with 4.0-Mev deuterons. Spectrometer resolution: 2.5 percent.

TABLE IV. Energies and yields of the γ rays from the bombardment of a thick graphite target with 4.0-Mev deuterons.

Uncorrected energy (Mev)	Doppler-corrected energy (Mev)	Yield (γ/deut) $\times10^8$	Total cross section[a] (mb)	Assignment (Mev)	Reference
3.76 ± 0.02	3.74 ± 0.03	3.5	4.0	$C^{13}(3.68)$	16
3.86 ± 0.02	3.84 ± 0.03	4.0	4.5	$C^{13}(3.85)$	16

[a] Average value, $E_d=0$ to 4.0 Mev.

DISCUSSION

The 3.76- and 3.86-Mev γ-ray lines are assigned to C^{13} since it is energetically impossible to get γ rays of this energy from the (d,n) and (d,α) reactions. The energies of these levels have been reported by Sperduto *et al.*[16] to be 3.684 ± 0.01 and 3.855 ± 0.01 Mev. The γ-ray energy of 3.74 Mev disagrees with the 3.683-Mev energy of C^{13*} by more than the estimated experimental error; however, no other interpretation of this γ ray has been suggested.

It has been reported by Rotblat[24] and Sperduto *et al.*[16] that at ~8-Mev bombarding energy the proton group leaving C^{13} in the 3.68-Mev state is much weaker than the proton group leaving C^{13} in the 3.86-Mev state. The fact that the γ rays corresponding to transitions to the ground state from the 3.68- and 3.86-Mev states are of about equal intensity suggests that a cascade transition takes place between the 3.86-Mev level and the 3.68-Mev level. This interpretation is in agreement with other measurements of the γ rays from the $C^{12}(d,p)C^{13*}$ reaction[25] and with measurements of the γ rays from the $B^{10}(\alpha,p)C^{13*}$ reaction.[26,27] An energy level diagram summarizing the results is shown in Fig. 8.

[19] Cook, Bonner, and Marion, Phys. Rev. **95**, 639(A) (1954); and private communication.
[20] Woodbury, Day, and Tollestrup, Phys. Rev. **92**, 1199 (1953).
[21] Hicks, Husain, Sanders, and Beghian, Phys. Rev. **90**, 163 (1953).
[22] Hird, Whitehead, Butler, and Collie, Phys. Rev. **96**, 702 (1954).
[23] R. J. Mackin and W. R. Mills (private communication).
[24] J. Rotblat, Phys. Rev. **83**, 1271 (1951).
[25] R. J. Mackin, Jr., Phys. Rev. **92**, 529(A) (1953).
[26] Shire, Wormald, Lindsay-Jones, Lunden, and Stanley, Phil. Mag. **44**, 1197 (1953).
[27] A. G. Stanley, Phil. Mag. **45**, 430 (1954).

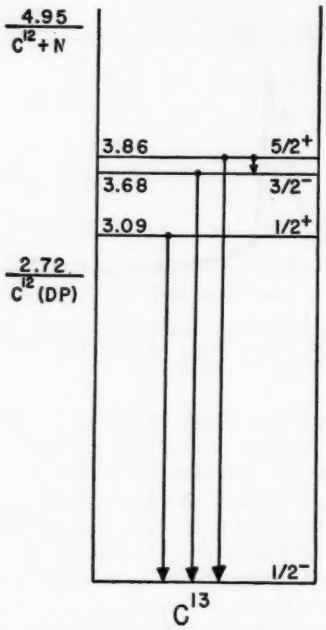

FIG. 8. Energy levels and decay scheme of C^{13}.

D. $B^{11}+H^1$ and Li^7+H^2

Phillips, Cowie, and Heydenburg[28] observed a soft radiation when B^{11} was bombarded with 7.9-Mev protons, which they suggested might be due to nuclear pairs from an odd-parity zero-angular-momentum level at about 7 Mev in Be^8. Other investigations[29–32] suggest that this soft radiation may have been due to a level in C^{12} of zero spin and even parity. The purpose of this experiment was to look for possible nuclear pairs from excited states in C^{12} and Be^8.

In order to have the greatest intensity in these experiments, they were carried out with the acceptance baffles, shown in Fig. 1, completely removed and with an intermediate-image ring baffle 2.7 cm wide. With this geometry the resolution of the Cs^{137} internal conversion line was 13 percent and the intensity of the line was 2.5 times greater than with the geometry shown in Fig. 1. The resolution of the O^{16} nuclear pair line was 5.5 percent and the intensity of this line was 10 times greater than that obtained with 2.5 percent resolution.

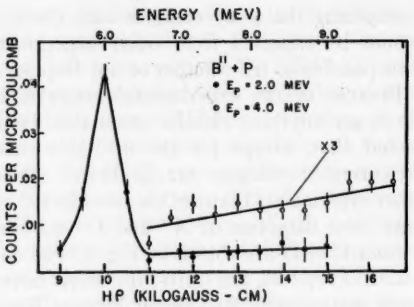

FIG. 9. The internal pair spectrum from the bombardment of a 19-mg/cm² natural boron target with 2.0- and 4.0-Mev protons. The 6.0-Mev peak is attributed to fluorine contamination. Spectrometer resolution: 5.5 percent.

The internal pair spectrum resulting from the bombardment of a 19-mg/cm² natural boron target at 2.0 and 4.0 Mev is shown in Fig. 9, uncorrected for background effects. The counts between 7 and 9 Mev were mostly due to the zero-current background. The chance rate was about 3 percent of this background.

DISCUSSION

The curve shows a peak at 6.04 Mev which is presumably due to fluorine contamination either in the boron or in the glyptal used to stick the thick powdered boron to the copper foil. This conclusion follows since the energy is the same, and the intensity of the line is 2700 times weaker than the intensity of the line resulting from the proton bombardment of a thick CaF_2 target with 2.0-Mev protons. An upper limit for the total cross section (average value, $E_p=1.7$ to 4.0 Mev) for the production of nuclear pairs in the energy range between 6.5 and 9.5 Mev is 3×10^{-5} mb.

A search was also made for nuclear pairs which might result from the $Li^7(d,n)Be^{8*}$ reaction by bombarding lithium targets with 330-kev deuterons. This low bombarding energy was used to minimize the amount of Li^8 produced in comparison to the amount of Be^8. No pairs were observed in the energy range between 5.0 and 8.5 Mev. An upper limit for the total cross section (average value, $E_d=0$ to 330 kev) is 2×10^{-5} mb.

[28] Phillips, Cowie, and Heydenburg, Phys. Rev. **83**, 1049 (1951).
[29] G. Harries and W. T. Davies, Proc. Phys. Soc. (London) **A65**, 564 (1952).
[30] Beghian, Halban, Husain, and Sanders, Phys. Rev. **90**, 1129 (1953).
[31] Dunbar, Pixley, Wenzel, and Whaling, Phys. Rev. **92**, 649 (1953).
[32] G. Harries, Proc. Phys. Soc. (London) **A67**, 153 (1954).

Electric Excitation of Certain Medium-Weight Nuclei by Protons*

HANS MARK, CLYDE MCCLELLAND, AND CLARK GOODMAN
Department of Physics and Laboratory for Nuclear Science, Massachusetts Institute of Technology, Cambridge, Massachusetts
(Received February 24, 1955)

Electric excitation has been used to study energy levels in sixteen elements ranging from scandium to iodine. Seventeen γ rays have been observed. Electric quadrupole transition probabilities for the energy levels corresponding to these γ rays have been calculated from the measured electric-excitation cross sections. The results are substantially larger than those expected from transitions of single particles but are significantly and uniformly lower than those calculated from the energies of the levels by using the hypothesis of rotational excitation. Similar observations have been made previously for a series of heavy nuclei. It is suggested that this effect results from either a nonuniform distribution of charge and mass in the nucleus or from a breakdown of the assumption that the collective motion can be represented as an irrotational flow.

I. INTRODUCTION

THE usefulness of electric excitation for studying nuclear structure has been demonstrated effectively in recent months.[1–3] Measurements of electric-excitation cross sections have been used to determine electric multipole transition probabilities for many nuclear energy levels, and in some cases it has been possible to clarify uncertainties in energy level assignments by performing electric excitation experiments with enriched isotopes.[2,3] Since the cross section for electric excitation of a nuclear energy level is proportional to its electric multipole transition probability, this method of excitation is particularly useful for studying those levels with large transition probabilities (that is, short half-lives). The "collective" model of nuclear structure[4] predicts the existence of nuclear energy levels which have large electric quadrupole transition probabilities. Since most of the energy levels reported in this work have transition probabilities that are appreciably larger than those expected from transitions of single particles, our results serve as a qualitative confirmation of the validity of the collective model in this region of the periodic table.

II. EXPERIMENTAL METHODS

The experimental methods used are simple. A target of the material under investigation is bombarded by monoenergetic protons from the MIT-Rockefeller electrostatic generator. The energy of the protons is determined, using the $Li^7(p,n)$ threshold at 1881.4 kev[5] as a calibration point. The existence of nuclear excitations were detected by measuring the γ rays emitted from the target during bombardment. A NaI(Tl) single-crystal scintillation spectrometer was used to measure both the energy and the intensity of the γ rays emitted. This unit consisted of a 2 in.$\times$2 in. Harshaw Chemical Company "canned" NaI(Tl) crystal bonded optically with a thin film of clear Nujol oil to the face of a DuMont 6292 photomultiplier tube. The pulses from this unit were fed through a wide-band amplifier (Model 100) and a single-channel pulse-height analyzer (AIC Model 510). The energy standards used for calibrating the unit fall into two categories; radioactive sources and γ rays from various targets bombarded with protons. The radioactive sources were: Cs^{137}, 661 kev;[6] Na^{22}, 511 kev; and Co^{57}, 123 kev.[7] The γ rays at 303 and 137 kev[8] from electric excitation of Ta^{181} and the x-rays of Ta at 57 kev and Pb at 75 kev[9] were also used. Energies quoted are accurate within about 8 percent. The intensity of a γ ray (and hence the cross section for production) was determined either by comparing the yield to a calibrated source placed at the target position or by using the extensive calculations of Maeder, Muller, and Wintersteiger[10] to determine the efficiency of the detector. All counting rates were monitored by a beam current integrator which was calibrated by a standard battery. The proton current was known within 5 percent.

The axis of the crystal was mounted perpendicular to the direction of the proton beam, and the front face was about 5 cm from the target for all measurements. This geometry was necessary in order to shield the unit from the collimating apertures of the machine. An inch of lead was sufficient to reduce the background from this source to a very low level.

Several types of targets were used. The thick targets consisted either of metal sheets or of metallic and metallic-oxide powders that were compressed into a small depression in a lead or tin backing disk. The thin targets were obtained by evaporating the material

* This work has been supported in part by the joint program of the Office of Naval Research and the U. S. Atomic Energy Commission.

[1] T. Huus and A. Lunden, Phil. Mag. **45**, 966 (1954).
[2] G. M. Temmer and N. P. Heydenburg, Phys. Rev. **95**, 861 (1954).
[3] McClelland, Mark, and Goodman, Phys. Rev. **93**, 904 (1954).
[4] A. Bohr and B. Mottelson, Kgl. Danske Videnskab. Selskab, Mat.-fys. Medd. **27**, No. 16 (1953).
[5] Jones, Douglas, McEllistrem, and Richards, Phys. Rev. **94**, 947 (1954).
[6] Muller, Hoyt, Klein, and DuMond, Phys. Rev. **88**, 775 (1952).
[7] D. E. Alburger and M. A. Grace, Proc. Phys. Soc. (London) **A67**, 280 (1954).
[8] T. Huus and J. Bjerregard, Phys. Rev. **92**, 1579 (1954).
[9] A. H. Compton and S. K. Allison, *X-Rays in Theory and Experiment* (D. van Nostrand Company, Inc., New York, 1935).
[10] Maeder, Muller, and Wintersteiger, Helv. Phys. Acta **27**, 3 (1954).

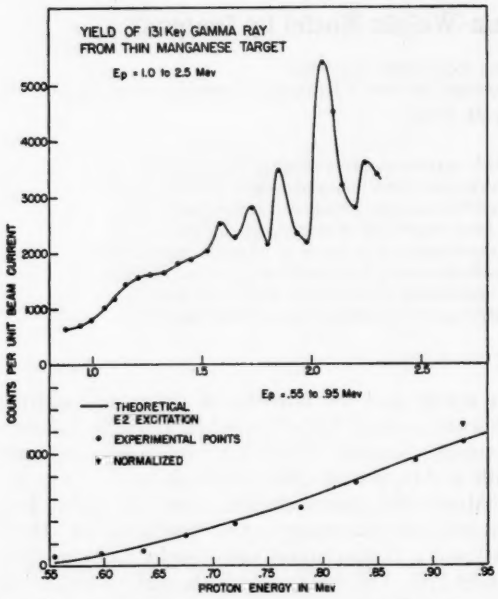

FIG. 1. The yield of the 131-kev γ ray from a thin manganese target as a function of proton energy. In the region below 1 Mev, the excitation curve agrees well with the expected electric quadrupole excitation function, while above 1 Mev the strong resonance structure indicates that the γ ray is produced by a process involving formation of a compound nucleus.

either on a tin or a lead backing. For thin-target cross-section measurements, the thickness was determined by measuring the stopping power using the "sandwich" target technique of Madsen *et al.*[11] and then calculating the number of atoms per square centimeter from published data.[12]

Impurities in the target materials often yield γ rays which interfere with the measurements. A common impurity in many materials is sodium which gives rise to a strong γ ray at 439 kev[13] from $Na(p,p'\gamma)$. Aluminum, fluorine, and oxygen are also troublesome sources of γ rays in the energy region of interest. In most cases, cleaning the surface of metallic targets and extensive leaching with hot distilled water of the powdered metals before preparing the targets eliminated the worst effects. Impurity effects will be discussed in greater detail in the section dealing with each element separately.

Characteristic x-rays and proton bremsstrahlung are important background effects whenever protons are used as bombarding particles in electric-excitation experiments.[14] In the region of the periodic table under consideration, the energy of the x-rays is so small that they are effectively absorbed by 0.04 inch of cadmium placed between the target and the crystal. Proton bremsstrahlung, which is the subject of a forthcoming paper, is not so easily eliminated. The effect makes it difficult to observe weak γ rays below 150 kev and also contributes to the error in determining energies of intense lines.

Once it has been determined that a given γ ray originates in the element being bombarded, it must be ascertained whether the γ ray is the result of an electric-excitation process or of a process involving penetration of the Coulomb barrier. For heavy nuclei ($Z>60$), the Coulomb barrier is so large that for 4.0-Mev protons there is no appreciable penetration. For lighter elements, this is not the case and a measurement of the yield of the γ ray as a function of proton energy must be made to determine the process from which it originates. Figure 1 shows the yield of the 131-kev γ ray from a thin manganese (Mn^{55}) target. Below 1 Mev, the curve agrees well with the calculated electric quadrupole excitation function, indicating that electric excitation is the dominant process in this region. The strong resonance structure in the yield above 1 Mev shows that the energy level is formed mainly by compound nucleus inelastic scattering of protons. The yields of the 315- and 418-kev γ rays from thick and thin silver targets are shown in Fig. 2. In this case, because of the relatively large value of the nuclear charge, barrier penetration is not very important. Both yield curves agree reasonably well with the theoretical

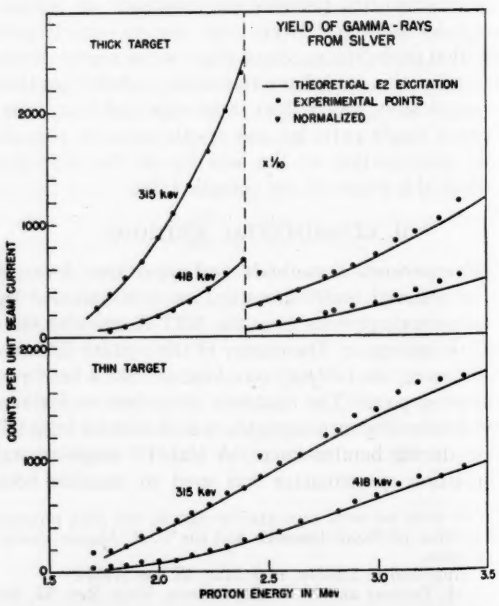

FIG. 2. The yield of the 315- and 418-kev γ rays from thick and thin silver targets. The curves for both γ rays agree well with the theoretical electric quadrupole excitation function. The thick target used in these measurements was about 80 kev thick to 2-Mev protons.

[11] C. B. Madsen and P. Venkateswarlu, Phys. Rev. **74**, 648 (1948).
[12] S. K. Allison and S. D. Warshaw, Revs. Modern Phys. **25**, 779 (1953).
[13] Donahue, Jones, McEllistrem, and Richards, Phys. Rev. **89**, 824 (1953).
[14] C. Zupančič and T. Huus, Phys. Rev. **94**, 205 (1954).

electric quadrupole excitation function over the whole energy range. It should be pointed out that a measurement of the excitation curve is not a particularly sensitive method for determining the multipole order of a given γ ray. It is important to rule out all other processes of excitation of the level, because it is only legitimate to calculate the transition probability from the cross section if electric excitation is the primary cause of formation.

III. EXPERIMENTAL RESULTS

Sixteen elements (scandium, vanadium, chromium' manganese, cobalt, zirconium, niobium, molybdenum, palladium, silver, cadmium, indium, tin, antimony, tellurium, iodine) were bombarded. Seven of these elements (scandium, cobalt, zirconium, niobium, tin, antimony, tellurium) showed no γ rays which could be attributed to electric excitation with reasonable certainty when bombarded with protons up to 2.75 Mev. The other elements studied showed γ rays ranging in energy from 131 to 610 kev. In three cases (chromium, palladium, cadmium), samples of enriched isotopes were bombarded in order to determine isotopic assignments of observed γ rays.

Vanadium.—Targets made of spectroscopically pure (Massey Ltd.) V_2O_5 were bombarded with 1.5-Mev protons. A γ ray was observed at 325 kev, which probably arises from a level at about this energy in 99 percent abundant V^{51}, observed previously by Kurie and Ter-Pogossian[15] and Temmer and Heydenburg.[16] Since compound nucleus formation is probably the dominant process in the excitation of this level at 1.5 Mev, it is not possible to calculate the transition probability from the cross section. This γ ray could not be observed at bombarding energies less than 1.3 Mev.

Chromium.—Targets made of Cr_2O_3 were bombarded with protons between 1.0 and 1.8 Mev. No γ rays attributable to electric excitation were observed from the natural Cr_2O_3 target. A weak γ ray at 155 kev is observed when 90.06 percent enriched $Cr_2{}^{53}O_3$ targets are bombarded with 1.3-Mev protons. The reaction $Cr^{53}(p,n\gamma)Mn^{53}$ may be ruled out as the source of this γ ray, since the threshold for this reaction is greater than 1.4 Mev.[17] It is possible that this γ ray originates in Cr^{53}, but it is difficult to confirm this assignment. The yield of the γ ray as a function of proton energy does not agree too well with the characteristic electric-excitation yield curve, but this is expected since compound nucleus formation certainly contributes to the formation of this level. The assignment of this line must therefore be considered doubtful.

Manganese.—The energy-level structure of Mn^{55} has been studied previously by inelastic scattering of protons[18] and electric excitation with α particles.[16] Both methods reveal the existence of an excited level at roughly 130 kev. The yield of this γ ray from thin Mn^{55} targets has been studied as a function of proton energy (see Fig. 1). The measured yield begins to get larger than the one predicted by electric excitation above 1 Mev, since compound nucleus formation begins to be appreciable in this region.[19]

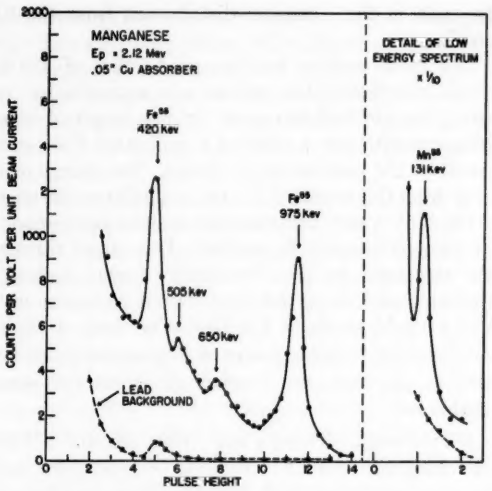

FIG. 3. The pulse-height spectrum obtained from a thin manganese target bombarded with 2.12-Mev protons. The peak at 131 kev is due to de-excitation of the level in Mn^{55} following inelastic proton scattering. The two peaks at 420 and 975 kev probably come from γ rays following the reaction $Mn^{55}(p,n\gamma)Fe^{55}$. Possible origins of the 505- and 650-kev peaks are discussed in the text. The small peak at 440 kev in the background curve is due to a sodium impurity in the lead backing on which the manganese was evaporated. A 0.05-inch copper absorber was used to attenuate the lead x-rays.

The pulse-height spectrum produced by γ rays from a thin manganese target during bombardment with 2.12-Mev protons is shown in Fig. 3. Peaks corresponding to γ rays having energies of 131, 420, 505, 650, and 975 kev are observed. The 420- and 975-kev γ rays probably come from the $Mn^{55}(p,n\gamma)Fe^{55}$ reaction and are due to the first two excited levels[20] in Fe^{55}. The 975-kev γ ray could also come from an excited level in Mn^{55} at approximately 1 Mev reported by Housman *et al.*[18] The origin of the 505- and 650-kev lines is not quite clear. Housman *et al.*,[18] and Temmer and Heydenburg[16] do not report any levels in Mn^{55} at these energies; hence, it is unlikely that they arise from inelastic proton scattering. It is possible that the weak line at 505 kev represents the cascade transition between the 975- and 420-kev level in Fe^{55}, although its energy is somewhat too low. The 650-kev line could be due to

[15] F. N. D. Kurie and M. Ter-Pogossian, Phys. Rev. **74**, 677 (1948).
[16] G. M. Temmer and N. P. Heydenburg, Phys. Rev. **96**, 426 (1954).
[17] McClelland, Goodman, and Stelson, Phys. Rev. **86**, 631 (1952).
[18] Housman, Allen, Arthur, Bender, and McDole, Phys. Rev. **88**, 1296 (1952).
[19] M. Shapiro, Phys. Rev. **90**, 171 (1953).
[20] P. H. Stelson and W. M. Preston, Phys. Rev. **82**, 655 (1951).

the peak in the Compton distribution from the 975-kev line.

The cross section for the production of 131-kev γ rays with 0.940-Mev protons was measured by comparing the yield of this γ ray from a target of known thickness with the γ yield of a calibrated Co^{57} source placed at the position of the target. The energy of the γ ray from this source (123 kev) is similar to the energy of the Mn^{55} γ ray, and therefore a direct comparison of the two photopeaks is justified. The target thickness was measured by the "sandwich" target method of Madsen *et al.*,[11] using the sharp double resonance in the $Al(p,\gamma)$ yield at about 1.4 Mev. The data of Chilton *et al.*[21] on the stopping power of copper and nickel were used to calculate the number of atoms per square centimeter.

Molybdenum.—Three γ rays (199, 440, and 525 kev) are observed when a powdered molybdenum metal target is bombarded with 2.46-Mev protons. The γ ray at 199 kev has been observed previously by Temmer and Heydenburg[22] and is probably due to electric excitation of a level at about this energy in Mo^{95} which has also been observed[23] in the positron decay of Tc^{95}. The origin of the 440- and 525-kev γ rays is not clear. It is probable that the 440-kev line is due to a sodium impurity in the target. The 525-kev line has been observed by Temmer and Heydenburg[24] using 6-Mev α particles. The isotopic assignment of this line is in doubt.

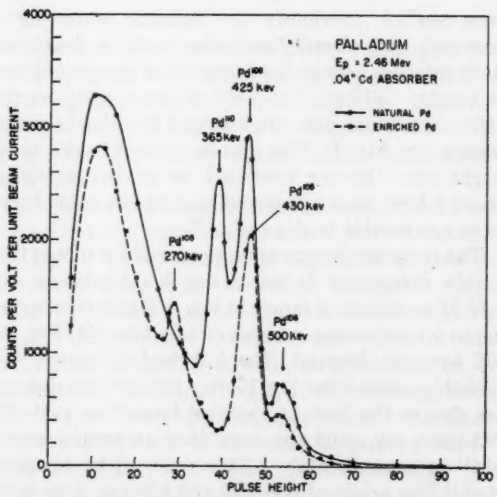

FIG. 4. The pulse-height spectra obtained when natural Pd and enriched Pd^{105} targets are bombarded with 2.46-Mev protons. The principal isotopes present in the enriched Pd^{105} target are Pd^{105}, 78.19 percent, and Pd^{106}, 16.04 percent. The peak at 425 kev from the natural Pd target is a composite line caused by γ rays of nearly equal energies in Pd^{105} and Pd^{108}. A 0.04-inch Cd absorber was used to attenuate the palladium x-rays. The broad low-energy pulse distribution is due to proton bremsstrahlung.

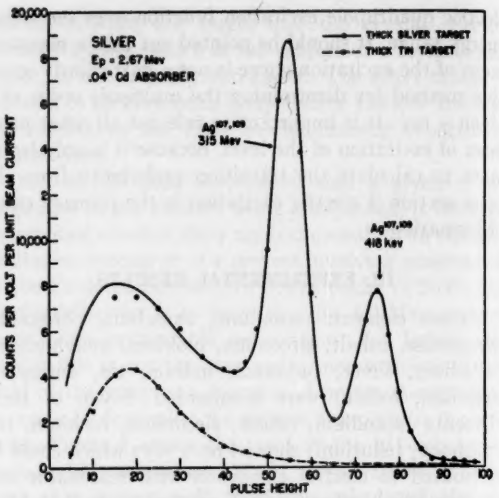

FIG. 5. The pulse-height spectrum obtained from a thick silver metal target bombarded with 2.75-Mev protons. The peaks at 315 and 418 kev are composite lines caused by γ rays of nearly equal energies from both silver isotopes. A pulse-height spectrum obtained from a thick tin target under similar conditions is shown to demonstrate the background effects caused by proton bremsstrahlung. The characteristic x-rays of both materials are almost entirely absorbed by a 0.04-inch cadmium sheet placed between the crystal and the target.

Palladium.—The pulse-height spectrum produced by γ rays from powdered Pd and enriched Pd^{105} targets during bombardment with 2.46-Mev protons is shown in Fig. 4. Peaks corresponding to γ rays having energies of 365, 425, and 500 kev from natural Pd and 270, 430, and 500 kev from enriched Pd^{105} are observed. The 270-kev line is caused by electric excitation of Pd^{105} and probably corresponds to the known level at 282 kev in this isotope which is observed[25] in the K-capture decay of Ag^{105}. The line at 500 kev is due to electric excitation of 27.1 percent abundant Pd^{106} and can also be identified with a known level in this isotope at 505 kev which is observed[25] in the K-capture decay of Ag^{106}. The 500-kev γ ray is also observed from the enriched Pd^{105} sample with about 0.6 the intensity of the γ ray from the natural Pd, since the enriched sample contains 16.04 percent Pd^{106}. The 425- and 430-kev γ rays are more difficult to assign to the proper isotopes. The most probable interpretation is that the 430-kev γ ray seen in the enriched Pd^{105} comes from electric excitation of a level in Pd^{105} at this energy,[25] while the 425-kev γ ray seen in natural Pd is a composite line caused partially by excitation of the 430-kev level in 22.6 percent abundant Pd^{105} and of a known level at about this energy in 26.7 percent abundant Pd^{108} which is

[21] Chilton, Cooper, and Harris, Phys. Rev. **91**, 495 (1953).
[22] G. M. Temmer and N. P. Heydenburg, Phys. Rev. **93**, 351 (1953).
[23] Huber, Medicus, Preiswerk, and Steffen, Phys. Rev. **73**, 1211 (1948).
[24] G. M. Temmer and N. P. Heydenburg (private communication).
[25] Deutsch, Roberts, and Elliott, Phys. Rev. **61**, 389 (1942).

observed[26] in the K-capture decay of Ag^{108}. The 365-kev line in natural Pd is due to electric excitation of a level in 13.5 percent abundant Pd^{110} which has been identified by Temmer and Heydenburg.[24]

Silver.—The γ rays (315 and 418 kev) emitted when thick silver metal targets are bombarded with 2.75-Mev protons are shown in Fig. 5. These energy levels have been studied extensively by Huus and Lunden[1] and Temmer and Heydenburg.[2] The lines shown are due to the superposition of γ rays of nearly equal energies coming from both isotopes. The cross section for the production of these γ-rays was measured using both thick-target yield data and thin-target methods described for manganese. The reasonable agreement between the results is good evidence that the techniques used in obtaining the cross section from the thick-target yield are probably valid. The large absolute error in these measurements, which is due primarily to the estimation of the detector efficiency, does not alter this conclusion, since the same corrections were applied to both thick- and thin-target yields.

Cadmium.—The pulse-height spectra produced when targets of CdO, enriched $Cd^{111}O$, and enriched $Cd^{113}O$ are bombarded with 2.46-Mev protons are shown in Fig. 6. The γ ray at 330 kev is due to electric excitation of a level in Cd^{111} at about this energy which is observed[27] in the β^- decay of Ag^{111}. The line at 610 kev which appears in the enriched sample and also in the natural target is due to electric excitation of a level in Cd^{112}. The 290-kev peak is caused by electric excitation of a level in Cd^{113} and the line at 545 kev which appears in the enriched $Cd^{113}O$ sample and also in natural CdO is due to electric excitation of Cd^{114}. This γ ray corresponds to a known level in Cd^{114} at 548 kev which is observed[28] in the K-capture decay of In^{114}. It is improbable that the 420- and 500-kev γ rays observed from all three targets arise from electric excitation of any Cd isotope. They are probably the result of bombardment of oxygen with protons, since they appear with roughly equal intensities from all targets. (The reaction $O^{16}(p,\gamma)F^{17}$ could give rise to 500-kev γ rays coming from cascade between the 4.35- and 3.86-Mev levels in the decay of F^{17}.)

Indium.—A 500-kev γ ray is observed when a thick indium metal target is bombarded with protons. This γ ray has been observed by Temmer and Heydenburg[22] and probably arises from a known level in In^{115} at this energy.[29]

Iodine.—A fairly intense 212-kev γ ray is observed when compressed PbI targets are bombarded with 2.0-Mev protons. This line has been observed previously by Temmer and Heydenburg[22] and also by inelastic scattering of neutrons from iodine.[30] The PbI targets were quite difficult to work with, since PbI sublimes readily at low temperatures. The cross section for the production of this γ ray could therefore not be measured. It was not possible to observe the 60-kev level in this nucleus[22] because of the strong interference from characteristic lead and iodine K-series x-rays.

The cross sections obtained for the production of all the above-mentioned γ rays are listed in Table I. The absolute errors in the cross sections are due to the following causes: 1. error in estimating detector efficiency; 2. error caused by possible anisotropy of emitted γ rays; 3. error in estimating stopping powers of the various materials; 4. errors in graphical subtractions of bremsstrahlung background; 5. error in calibrating activity of standard source; 6. error in calibration of beam current integrator. The most accurate measurement is the cross section for the 131-kev γ ray in Mn^{55}, since this result does not include a calculation of the detector efficiency. The other measurements, except for the γ ray in iodine, are considered reliable to within a factor of 2.

IV. INTERPRETATION

The reduced transition probability, $B(E2)$, for the levels can now be calculated from the observed cross

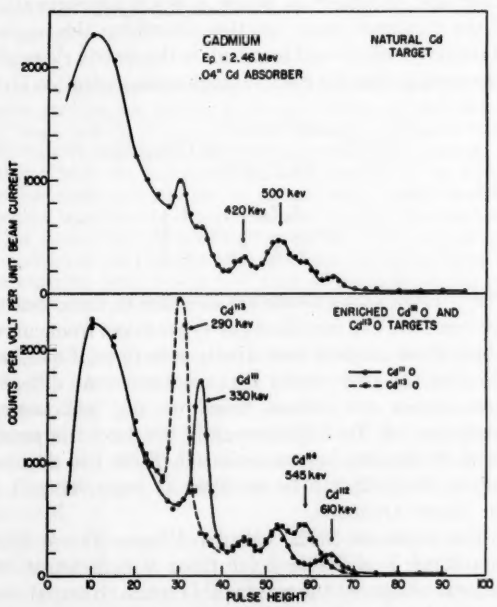

FIG. 6. The pulse-height spectra obtained when natural CdO, enriched $Cd^{111}O$, and enriched $Cd^{113}O$ targets are bombarded with 2.46-Mev protons. The principal isotopes present in the $Cd^{111}O$ target are Cd^{111}, 64.5 percent and Cd^{113}, 26.9 percent and the principal isotopes present in the Cd^{113} target are Cd^{113}, 54.1 percent and Cd^{114}, 37.9 percent. The peaks at 420 and 500 kev that appear in all three spectra are probably the result of some process following the bombardment of oxygen with protons. The broad low-energy pulse distribution is due to proton bremsstrahlung.

[26] Perlman, Bernstein, and Schwartz, Phys. Rev. **92**, 1236 (1953).
[27] S. Johansson, Phys. Rev. **79**, 896 (1950).
[28] F. Boehm and P. Preiswerk, Helv. Phys. Acta **22**, 331 (1949).
[29] Cork, Rutledge, Stoddard, Branyan, and LeBlanc, Phys. Rev. **79**, 938 (1950).
[30] R. M. Kiehn and C. Goodman, Phys. Rev. **95**, 989 (1954).

TABLE I. Summary of results. Column 3 lists the proton energy at which the cross-section measurement for each level was made. In column 6, the spin change of the transition is shown for those cases in which it is known or can be reasonably inferred from the collective model. Column 7 shows the value of $B(E2)$ for the excitation of the levels obtained from the measured cross sections shown in columns 4 and 5 and from the measured energies shown in column 2.

Nuclide	Measured excitation energy (kev)	Proton energy (Mev)	σ(thin) millibarns	σ(thick) millibarns	$I_0 \rightarrow I$	$B(E2)$ in $\text{cm}^4 \times 10^{-49}$ from $\sigma(E2)$	from ΔE
V^{51}	325	1.50	...	0.1	7/2→?	...	...
Cr^{53}	155(?)	1.50	...	0.12	7/2→?	0.15	...
Mn^{55}	131	0.94	0.29±0.11	...	5/2→?	0.87	...
Mo^{95}	199	2.46	...	0.043	5/2→?	0.57	...
Pd^{105}	270	2.46	...	0.02[a]	5/2→?	0.084	...
	430	2.75		0.10[a]	5/2→?	0.57	...
Pd^{106}	500	2.75	...	0.080	0→2	1.8	49
Pd^{108}	425	2.75	...	0.15[b]	0→2	2.1	58
Pd^{110}	365	2.75	...	0.10	0→2	2.6	67
$Ag^{107,109}$	315	2.75	0.27[b]	0.24[b]	1/2→3/2	0.79	18
	418	2.75	0.20[b]	0.19[b]	1/2→5/2	0.86	27
Cd^{111}	330	2.75	...	0.010	1/2→3/2	0.27	...
Cd^{112}	610	2.75	...	0.028	0→2	1.3	43
Cd^{113}	290	2.75	...	0.020	1/2→3/2	0.58	...
Cd^{114}	545	2.75	...	0.050	0→2	1.4	48
In^{115}	500	3.00	...	0.010	9/2→?	0.58	...
I^{127}	212	2.00	...	...	5/2→?	...	...

[a] Enriched isotope target.
[b] Composite line.

sections. All excitations are assumed to be electric quadrupole. The formula used is one proposed by Alder and Winther[31] in which a WKB approximation of the Coulomb wave function describing the motion of the projectile is used to calculate the matrix elements. The cross section for electric quadrupole excitation is:

$$\sigma(E2)=\frac{2\pi^2}{25}\frac{m_1 v_f^2}{Z_2^2 e^2 \hbar^2}B(E2)g_{E2}(\xi), \tag{1}$$

and

$$\xi=\frac{Z_1 Z_2 e^2}{\hbar}\left[\frac{1}{v_f}-\frac{1}{v_i}\right]. \tag{2}$$

The notations used above are identical to those used in reference 31. The functions $g_{E2}(\xi)$ are taken from curves which these authors have kindly sent to us. Equations (1) and (2) give results that are somewhat different from earlier calculations based on the semiclassical treatment of Ter-Martirosyan.[32] We have purposely listed all measured cross sections in Table I so that our values of $B(E2)$ can be modified as improvements in the theory are made.

The values of $B(E2)$ calculated from (1) are listed in column 7 of Table I for those γ rays where the isotopic assignment is reasonably certain. Internal conversion has been ignored, since none of the conversion coefficients for any of the levels studied are greater[33] than 0.1. The possible cascade decay of any of the observed levels has also been ignored in the calculation of $B(E2)$.

[31] K. Alder and A. Winther, Phys. Rev. **96**, 237 (1954).
[32] K. A. Ter-Martirosyan, J. Exptl. Theoret. Phys. (U.S.S.R.) **22**, 284 (1952).
[33] M. E. Rose (private communication).

The "collective" model[4] predicts the existence of "rotational" energy levels that have three unique properties:

1. They possess reduced $E2$ transition probabilities, $B(E2)$, which are larger by at least an order of magnitude than those calculated for transitions of single particles from one orbit to another.
2. They exhibit an energy spectrum very similar to that of a rigid rotator.
3. The energy of the first excited level and its reduced $E2$ transition probability depend upon the same parameter; the ground-state deformation of the nucleus.

Condition 3 implies a unique relationship between $B(E2)$ and the energy of the first rotational level. Following Bohr[34]:

$$B(E2)=\frac{\hbar^2 R_0^2 Z^2}{mA}K(I,I_0)\frac{1}{\Delta E}, \tag{3}$$

where R_0 is the nuclear radius, Z the nuclear charge, A the number of nucleons, m the mass of a nucleon, and ΔE the energy of the level. $K(I,I_0)$ is a numerical factor which depends upon the spins of the ground and first excited levels, I_0 and I. The last column in Table I shows the values of $B(E2)$ calculated from (3) by using the experimental energies ΔE.

The striking difference between the values of $B(E2)$ obtained from these two sources is a phenomenon that has already been observed in a series of heavy nuclei[35] and has also been deduced from a comparison of nuclear deformations obtained from electric quadrupole moments and isotope shift data and nuclear moments of inertia.[36] It has been suggested that this effect results either from a nonuniform distribution of charge and mass in the nucleus or from a breakdown of the hypothesis that the collective motion can be represented as an irrotational flow.

Several other comments may be made regarding the results shown in Table I. Since the reduced transition probability depends on the nuclear deformation, it is possible to calculate $B(E2)$ from the electric quadrupole moment of the nucleus. The only nuclide in Table I for which the quadrupole moment is known,[37] and for which the cross section has been measured, is In^{115}. The value of $B(E2)$ calculated from this quadrupole moment is 0.4×10^{-49} cm^4, which is in reasonable agreement with the value obtained from the electric excitation cross section shown in column 7 of Table I.

In two cases, Pd^{105} and the silver isotopes, it was possible to excite two levels in the same isotope. It is of interest therefore to compare the properties of the observed levels with the theoretical predictions of the

[34] A. Bohr, Dissertation on *Rotational States of Atomic Nuclei* (Ejnar Munksgaard, Copenhagen, 1954).
[35] McClelland, Mark, and Goodman, Phys. Rev. **97**, 1191 (1955).
[36] K. W. Ford, Phys. Rev. **95**, 1250 (1954).
[37] J. E. Mack, Revs. Modern Phys. **22**, 64 (1950).

collective model. In the case of the silver isotopes, both Ag^{107} and Ag^{109} have a ground-state spin of 1/2 and therefore do not exhibit a regular rotational spectrum.[4] However, the rotational (strong coupling) model does predict that the ratio of $B(E2)$ for the 315-kev transition to that of the 418-kev transition should be 0.66. This value is considerably smaller than the one obtained from the experimental cross-section measurement and is possibly a reflection of the fact that the transition probabilities obtained from the γ-ray measurement are distorted by possible cascade decay of the 418-kev level. The nuclide Pd^{105}, with a ground-state spin of 5/2, should exhibit a regular rotational spectrum if the collective model applies rigorously to this nucleus. If the first rotational level of Pd^{105} is at 270 kev, then the second level should be at about 617 kev, which is almost 200 kev higher than the observed energy of 430 kev. The values $B(E2)$ for these two levels are also inconsistent with those which would be expected if the rotational model were strictly valid for Pd^{105}. It is possible that the 430-kev level is actually the first rotational level in this isotope. The level at 270 kev would then not be strongly excited, and the peak that appears at this energy in Fig. 4 could arise from the cascade decay of the 430-kev level. A peak at 160 kev, which should accompany such a decay, would be hidden by the bremsstrahlung background.

The authors wish to express their thanks to Dr. C. P. Keim of the Oak Ridge National Laboratory for his aid in procuring the enriched isotopes and to Dr. Caspar Borkowski, also of Oak Ridge, for calibrating the Co^{57} source. We are also indebted to Dr. G. M. Temmer and Dr. N. P. Heydenburg for sending us some of their results prior to publication, and to Professor V. F. Weisskopf and Professor S. D. Drell for many useful discussions.

PHYSICAL REVIEW VOLUME 98, NUMBER 5 JUNE 1, 1955

Radionuclides Al^{24}, P^{28}, Cl^{32}, and Sc^{40}*

NEEL W. GLASS† AND J. REGINALD RICHARDSON
Physics Department, University of California, Los Angeles, California
(Received January 18, 1955)

Three new short-lived positron emitters, P^{28}, Cl^{32}, and Sc,[40] of the nuclear series $Z=2n+1$, $A=4n$ have been produced by p-n reactions using 20-Mev protons from the UCLA 41-in. FM cyclotron. Al^{24} has also been investigated. Al^{24} has a half-life of 2.10 ±0.04 sec and five gamma rays from 1.39 Mev to 7.12 Mev. 2-Mev alpha particles are emitted in a small fraction of the decays. P^{28} has a half-life of 0.280 ±0.010 sec, threshold of 15.6±0.5 Mev, eight gamma rays from 1.79 Mev to 7.59 Mev, and positrons of maximum energy 10.6±0.4 Mev. No heavy particles were detected in the decay. Cl^{32} has a half-life of 0.306±0.004 sec, threshold of 14.3±0.5 Mev, four gamma rays from 2.21 Mev to 4.77 Mev, and positrons of maximum energy 9.5±0.4 Mev. 2–3 Mev alpha particles are emitted in a small fraction of the decays. Sc^{40} has a half-life of 0.22±0.03 sec, threshold of 15.9±1.0 Mev, a 3.75±0.04 Mev gamma ray, and maximum positron energy of 9.0±0.4 Mev. No heavy particles were detected in the decay. Possible decay schemes can be set up which involve favored positron transitions to calculated analog levels in the daughters in the cases of Al^{24}, P^{28}, and Cl^{32}. In the P^{28} decay, the positron component to the 1.78-Mev level in Si^{28} has the same ft value as the negatron decay to this level from Al^{28}, thus indicating the similarity of the nuclear wave functions of P^{28} and Al^{28}.

I. INTRODUCTION

IN 1950 Alvarez[1] reported the discovery of the delayed alpha-particle emitters B^8, N^{12}, and Na^{20}, all members of the nuclear series $Z=2n+1$, $A=4n$. These nuclides are positron emitters which decay, at least partially, to an excited state of the daughter which in turn breaks up into an alpha particle and a residual nucleus. The lifetime of the excited state is extremely short compared to the lifetime of the parent, hence the apparent lifetime of the alpha activity is that of the parent. Alvarez also searched for F^{16}, the member between N^{12} and Na^{20}, but concluded that it was proton-unstable. Birge[2] subsequently reported the discovery of Al^{24}, the next member of the series. Al^{24} was produced by the $Mg^{24}(p,n)Al^{24}$ reaction and was detected by means of a heavy-particle activity. Both delayed alpha particles and delayed protons are energetically possible in the Al^{24} decay and it was not determined which occurred.

Mass estimates of possible additional members of the series, P^{28}, Cl^{32}, and Sc^{40}, placed them on the borderline of proton instability. A search for these nuclides and an investigation of their properties, and a further investigation of Al^{24}, has been carried out in this laboratory. The nuclides were produced by p-n reactions using 20-Mev protons generated in the UCLA 41-inch frequency-modulated cyclotron. Some earlier results of this investigation have been published.[3]

* Work supported by joint program of Office of Naval Research and U. S. Atomic Energy Commission. Part of a thesis submitted by N. W. Glass to the Graduate Division, University of California, Los Angeles, California, in partial fulfillment of requirements for the Ph.D. degree in Physics.
† Now at University of California, Los Alamos Scientific Laboratory, Los Alamos, New Mexico.
[1] L. W. Alvarez, Phys. Rev. 80, 519 (1950).
[2] A. C. Birge, Phys. Rev. 85, 753(A) (1952).
[3] Glass, Jensen, and Richardson, Phys. Rev. 90, 320 (1953); N. W. Glass and J. R. Richardson, Phys. Rev. 93, 942 (1954).

II. APPARATUS AND METHOD

Since the activities were expected to have short half-lives, a sample carrier in a pneumatic tube was used to transport the sample from the bombarding position in the internal beam of the cyclotron to the exterior where measurements were made. A schematic sketch of the tube and carrier is shown in Fig. 1. The balsa sample carrier fits into a $\frac{1}{2}$ in.$\times\frac{1}{2}$ in. square tube. The carrier is moved from bombarding to counting position, and vice versa, by atmospheric or higher pressure on one side, and low pressure provided by a vacuum cleaner system on the other. The delayed valve is closed by an interval timer just before the carrier reaches the end of its travel, and it is cushioned to a stop by compressing the residual air between itself and the needle valve. The sample is then held in counting position by the positive pressure on the rear of the carrier. The machinery was cycled automatically by a master sequence timer, which also gated the cyclotron beam and the detectors. The transit time of the carrier was of the order of one-tenth second.

A. Gamma-Ray Measurements

The activities reported on in this paper were all first detected in this laboratory by means of the relatively high-energy gamma radiation associated with their decay. The gamma rays were detected and measured with a $\frac{7}{8}$ in.$\times\frac{7}{8}$ in. cylindrical NaI(Tl) crystal in conjunction with a RCA 5819 photomultiplier. The pulses were fed through a preamplifier to a linear amplifier containing a delay line clipper compensated to provide a flat top pulse. The pulses were then displayed on a high stability oscilloscope and the resulting pulse-height distribution was photographed. The oscilloscope was designed and built by Dr. H. K. Ticho of the UCLA Physics Department Staff.

Different exposures and gain settings were used to accentuate the different areas of the pulse-height distributions. For an average case with full gain on the scope face, about 100 000 pulses were required. With continuous cycling of the samples, longer-lived components built up large lower-energy backgrounds, hence, for the lower-lying gamma rays, it was necessary to wait between bombardments for a sufficiently long time to prevent this buildup. The possible appearance of peaks in the longer-lived background activities was checked by making exposures for various lengths of time after the activity of interest had decayed. Densitometer traces of the film density distributions were made, and positions of the peaks were determined from the traces. Many measurements of each spectrum were taken to check the consistency of the energy measurements, and the consistency of appearance of some of the less easily distinguished peaks.

The calibration of the energy scale was always made on the same film as the pulse-height distribution being measured. Sources of Na^{22} and Na^{24} provided calibration points corresponding to photopeaks at 0.51, 1.28, 1.37, and 2.75 Mev, and a RaD-Be source furnished the pair peak of the 4.44-Mev gamma ray from C^{12}. The pair peak of the 7.639-Mev gamma ray from neutron capture in iron[4] found in the normal cyclotron background provided a high-energy calibration point.

Gamma-ray intensities were estimated from differential discriminator runs over the spectra. The areas under the peaks of each gamma ray were estimated after subtraction of the Compton distribution of higher-energy gamma rays, and the intensities were then determined from the absorption coefficients for the various absorption processes in NaI.

B. Positron Energy Measurements

Since the estimated positron energies were in the vicinity of 10 Mev, it seemed that information at least on the high-energy end point could be gotten by direct measurements with a scintillation crystal even in the presence of the high-energy gamma rays. This proved to be true except for the case of Al^{24}.

Since there are very few high-energy beta sources suitable for calibration purposes, a $\frac{7}{8}$ in.$\times\frac{7}{8}$ in. cylindrical NaI crystal was used for the positron measurements, and gamma-ray peaks used for calibration. The positrons entered the crystal through a collimating

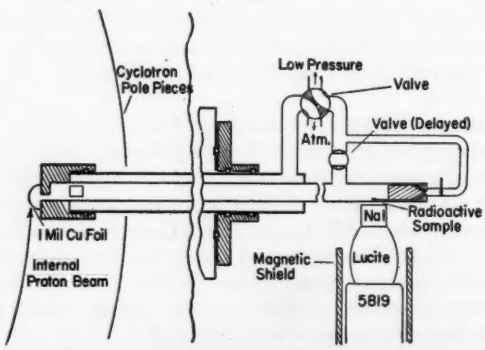

FIG. 1. Schematic of the pneumatic tube and sample carrier. Closing the delayed valve causes the sample carrier to be cushioned to a stop at the end of its travel.

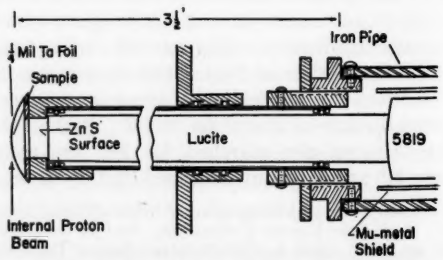

FIG. 2. Probe for measurement of heavy particle emissions.

[4] B. B. Kinsey and G. A Bartholomew, Phys. Rev. 89, 375 (1953).

TABLE I. Experimental data on Al^{24}, P^{28}, Cl^{32}, and Sc^{40}. The alpha particles emitted in the decay of Al^{24} and Cl^{32} occur to the order of one per several thousand disintegrations.

	p-n threshold (Mev)	Half-life (sec)	Alpha particles (Mev)	Mass value (aMU)	Gamma rays Energy (Mev)	Gamma rays Estimated intensity	Positrons Energy (Mev)	Positrons Logft	Branching ratio
Al^{24}	15.4±0.3[a]	2.10 ±0.04	~2	24.0076 ±0.0003	1.39±0.03 2.73±0.06 4.22±0.10 5.35±0.10 7.12±0.10	40% 32% 15% 6% 7%	~8½	···	Weak
P^{28}	15.6±0.5	0.280±0.010	···	28.0006 ±0.0004	1.79±0.02 (2.6 ±0.2) 4.44±0.05 (4.93±0.08) 6.14±0.10 6.70±0.12 7.04±0.10 7.59±0.15	75% 10% 10% 5%	10.6±0.4	4.9±0.1	0.47±0.15
Cl^{32}	14.3±0.5	0.306±0.004	2–3	31.9960 ±0.0004	2.21±0.03 2.77±0.08 or 3.79 4.27±0.08 4.77±0.04	70% 10% 7% 14%	9.5±0.4 ~7½	4.6±0.1 ···	0.48±0.15 ···
Sc^{40}	15.9±1.0	0.22 ±0.03	···	39.9901 ±0.0004	3.75±0.04	···	9.0±0.4	4.1	100% assumed

[a] See reference 2.

hole in a ⅜-in. brass disk. The positron spectra were measured with a single channel discriminator with a two volt window and with the end point of the spectrum corresponding to about 100 volts. A separate counter and channel were used to monitor the source intensities. In all cases except that of Al^{24} the gamma contribution, determined by covering the collimating hole, was small compared with the positron contribution, hence the error introduced by subtraction of the gamma contribution was small. The capture of 0.51-Mev quanta from the annihilation of the positrons in the crystal produces a tail at the high end of the spectrum. A correction was applied for this effect and also for the effect of resolution on the end point. Check runs were made on the positron spectrum of Cl^{34}. The end point of the Cl^{34} high-energy component was measured as 4.40±0.2 Mev. This is in good agreement with the reported value of 4.50±0.03 Mev.[5] The deviation from a straight line on the Kurie plot was consistent with the presence of the 28 percent branch with 2.58-Mev end point.

C. Half-Life and Threshold Measurements

The half-lives of the activities were measured by means of a Sanborn Twin-Viso Recorder. The output of a decimal scaler was fed to the galvanometer coil of the recorder pen. At every tenth, hundredth or thousandth count, depending on the scale factor used, a pip was marked on the recorder tape. The tape speed was calibrated timewise by means of a one second marker provided with the Sanborn unit.

Threshold measurements were made by moving the probe assembly in to smaller cyclotron radii by small increments until the activity under scrutiny no longer appeared. Comparison was made with the threshold of Al^{24} measured by Birge[2] for the absolute energy calibration. The slope of a previously determined proton energy *vs* radius curve was then used to determine the energy threshold.

D. Heavy-Particle Search

Heavy-particle emission was reported[2] in the decay of Al^{24} and is energetically possible in the P^{28}, Cl^{32}, and Sc^{40} activities; hence a search was made for such emissions. Since negative results were gotten by viewing the bombarded sample in the pneumatic tube by a ZnS phosphor, a more sensitive arrangement in respect to counting rates and minimum particle energy was used. This consisted of a long Lucite light pipe with RCA type 33–*Z*–16*A* ZnS phosphor on the end which viewed the sample inside the cyclotron as shown in Fig. 2. A thin film of the sample to be bombarded was coated on the inside of the 0.25-mil tantalum foil. The phosphor was kept about an inch away from the target so that the cyclotron magnetic fields prevented the large number of positrons emitted from the target from reaching the phosphor and Lucite. This spacing also reduced the number of protons scattered into the phosphor which excited long-lived components in the luminescent decay of the phosphor.

Measurements were made by simply gating the cyclotron on and off and visually observing the resulting decay pulses on an oscilloscope. Unmistakable large pulses consistent with the respective half-lives were observed in the decay of Al^{24} and Cl^{32}. Threshold

[5] D. Green and J. R. Richardson, Phys. Rev. 96, 858(A) (1954).

checks were also made and the activities disappeared below the respective thresholds. The number of pulses observed was about 4–8 per bombardment for Al^{24} and $\frac{1}{2}$ to 1 per bombardment for Cl^{32}. A rough pulse-height calibration was obtained by bombarding Bi powder in the probe and observing the maximum pulse height of the 4.86-Mev alpha particles from Po^{209}. The Al^{24} particles appeared to be ~2 Mev and the Cl^{32} particles 2–3 Mev. Since both alpha particle and proton emission are energetically possible in these activities, an absorption check was made to determine which occurred. Aluminum foil absorbers of 0.15 mg/cm², 0.60 mg/cm², and 1.7 mg/cm² were in turn placed between the target and phosphor. For both Al^{24} and Cl^{32} the results were consistent with a 2–3 Mev alpha particle range in aluminum but clearly not with the proton range.

III. EXPERIMENTAL RESULTS

A. Aluminum-24

Al^{24} was produced by the $Mg^{24}(p,n)Al^{24}$ reaction by using a Mg foil of thickness about 5 mils as the target. The half-life was measured as 2.10±0.04 seconds in agreement, within experimental error, with that reported by Birge.[2] The gamma-ray spectrum was found to be quite complex, with five gamma rays identified with certainty as listed in Table I. The 1.39-Mev and 2.73-Mev gamma rays were calibrated with respect to the 1.37- and 2.75-Mev gamma rays from Na^{24}, and there is no doubt that they arise from the same level transitions in Mg^{24} as the Na^{24} gammas.

An attempt was made to measure the positron energy of Al^{24}, but the high-energy positron branch is of fairly weak intensity and not a great deal higher in energy than the high-energy gamma ray. About all that can be said is that there appears to be a fairly low intensity positron branch with end point of around 8½ Mev.

Delayed alpha particles of energy ~2 Mev with a branching ratio of the order of one in several thousand disintegrations were observed.

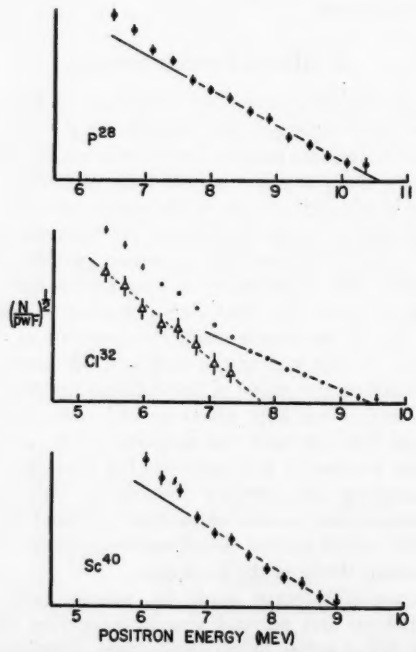

FIG. 3. Kurie plots of the high-energy positrons from P^{28}, Cl^{32}, and Sc^{40}. The Cl^{32} plot shows a first subtraction indicating a positron component to the region of 7½ Mev.

B. Phosphorus-28

P^{28} was produced by the $Si^{28}(p,n)P^{28}$ reaction. Silicon metal targets were used for the gamma ray measurements and powered silicon metal mixed with polystyrene binder pressed between ¼-mil Ta foil for the positron measurements. No contributions from the Ta or polystyrene were observed in the energy regions measured. The gamma-ray spectrum was found to be very complex. Since some of the peaks are not easily distinguishable, many runs were made to check the consistency of appearance of these peaks. Table I lists the measured gamma-ray energies and other data. The gamma ray of energy 4.93 Mev is not completely certain, since its pair peak falls on the position of a small peak arising from the pair energy plus a single annihilation quantum capture of the more intense 4.44-Mev gamma ray. However, this peak appears to be quite consistently more intense than would be expected from annihilation capture effect. Weak peaks in the vicinity of 2.6 Mev appeared on some of the spectra. Because of the complexity of the spectrum, there is a distinct possibility of other weak gamma rays existing in the decay.

Figure 3 shows a Kurie plot of the corrected P^{28} positron spectrum. The end point from three such runs is 10.6±0.4 Mev. The consistency from run to run was better than the quoted error would indicate but since a long extrapolation from the calibration points is necessary, the quoted error is felt to be a safer limit. In the three runs, the plots deviate from a straight line in the region of 7½ Mev.

The *ft* value of the high-energy component is found from the slope of the Kurie plot, normalized by determining the total number of counts in the entire positron distribution compared with the counts in the monitor channel. The total number of counts was determined from an analysis of the decay of all the activities present as they appeared on the pen recorder tape. In this manner the *ft* value of the 10.6 Mev component is found to be $(8\pm2)\times10^4$ sec or $\log ft = 4.9\pm0.1$. No heavy-particle activity was detected. If present, it is less than an estimated one out of 30 000 disintegrations, or less than ¾ Mev in energy.

C. Chlorine-32

Cl^{32} was produced by the $S^{32}(p,n)Cl^{32}$ reaction. Sulfur powder wrapped in $\frac{1}{4}$-mil Ta foil was used for gamma-ray measurements. Positron sources were made by pressing sulfur powder mixed with polystyrene binder between $\frac{1}{4}$-mil Ta foil. Four gamma rays are identified in the spectrum as listed in Table I. It is not certain whether the peak at 2.77 Mev is a pair peak or a photoelectric peak, but it is probably a pair peak corresponding to a gamma ray of 3.79 Mev.

Figure 4 shows a Kurie plot of the corrected Cl^{32} positron spectrum. A fairly reasonable first subtraction can be made as shown which indicates a component in the region of $7\frac{1}{2}$ Mev. The logft value of the high-energy component is 4.6 ± 0.1, corresponding to a 0.48 ± 0.15 branching ratio.

Alpha particles of 2–3-Mev energy were detected in the Cl^{32} decay. These occurred to the order of one out of several thousand disintegrations.

D. Scandium-40

Sc^{40} was produced by the $Ca^{40}(p,n)Sc^{40}$ reaction by using calcium pounded into a thin sheet as the target material. The measurements on Sc^{40} were more difficult than those of the other activities since the competing activities were of shorter half-life and of higher energy, and the activity itself was weak. The experimental data are given in Table I. Only one gamma ray of energy 3.75 ± 0.04 Mev was identified in the spectrum. There are numerous weak peaks which also appear in the background spectra. Hence, the possibility of weak peaks in the Sc^{40} decay occurring and falling near peaks in the background cannot be eliminated. However, if such peaks do occur, they are weak compared to the 3.75-Mev gamma.

Figure 3 shows a Kurie plot of the Sc^{40} positron distribution. No heavy-particle activity was detected.

IV. DISCUSSION OF RESULTS

From the comparison of measured threshold values and maximum positron energies, it is evident that none of the positron emissions goes to the ground state. The differences between maximum positron energies available and those measured correspond to positions of known levels in the daughter nuclei, and to gamma rays associated with decay of the nuclei. The occurrence of gamma rays corresponding to the energies of the first excited states of the daughter nuclei in the cases of Al^{24}, P^{28}, and Cl^{32}, and to the second in that of Sc^{40}, is confirmation of the correct assignment of the activities. The masses of P^{28}, Cl^{32}, and Sc^{40} are found from a weighted mean of the positron-gamma ray and threshold energies, using the mass values of Li^6 and Johnson.[7] These masses would indicate that P^{28}, Cl^{32}, and Sc^{40} are proton-stable by 2.5 Mev, 1.0 Mev, and 0.5 Mev respectively.

A. Analog Levels and Isobaric Spin

The charge multiplet theory,[8] which results from the assumption of charge-independent nuclear forces and the treatment of the Coulomb energy as a small perturbation, predicts that the energy levels of the members for which $T_z=(N-Z)/2=\pm1$ of an isobaric triad will have corresponding, or "analog," levels in each other and in the member for which $T_z=0$. N and Z are the numbers of neutrons and protons, respectively, which make up the nucleus. The levels in $T_z=0$ not having analogs in $T_z=+1$ and $T_z=-1$ are considered to belong to a state of total isobaric spin $T=0$, or an isobaric spin singlet state. Those having analogs belong to a state of $T\geqq1$, constituting an isobaric triplet or higher multiplet. Thus, with the difference in Coulomb energy and the neutron proton mass difference taken into account, the ground states of the $T_z=+1$ and $T_z=-1$ members of the triad should have the same energy, and the $T_z=0$ member should have an analog state corresponding to these ground states. Actually, the levels in $T_z=+1$ and $T_z=-1$ should have analog levels in each other if p-p forces are equal to the n-n forces. However, the existence of the analog levels in the $T_z=0$ member requires the complete charge independence of nuclear forces.

Since each of the nuclides reported in this paper is the $T_z=-1$ member of an isobaric triad and decays by positron emission to the $T_z=0$ member, it is possible to see whether some aspects of the decay are consistent with the predictions of the charge multiplet theory. In each case, the properties of the $T_z=+1$ member are quite well known. Thus, some further evidence regarding the charge independence of nuclear forces might be available. The isobaric triads $C^{10}-B^{10}-Be^{10}$ and $O^{14}-N^{14}-C^{14}$ have been studied[9] and the results shown to be consistent with the theory. The triads under consideration here are heavier and the charge effect considerably greater, hence the theory might not be expected to hold so well.

TABLE II. Values of r_0 calculated from energy differences of $T_z=-1$ and $+1$ members of $A=4n$ triads, and resulting position of analog levels in $T_z=0$ members.

T_z			$r_0\times10^{13}$ (cm)	Analog level in $T_z=0$ (Mev)
−1	0	+1		
Al^{24}	Mg^{24}	Na^{24}	1.38 ± 0.04	9.5
P^{28}	Si^{28}	Al^{28}	1.43 ± 0.05	9.0
Cl^{32}	S^{32}	P^{32}	1.33 ± 0.04	7.1
Sc^{40}	Ca^{40}	K^{40}	1.38 ± 0.05	7.5

[6] C. W. Li, Phys. Rev. **88**, 1038 (1952).
[7] W. H. Johnson, Jr., Phys. Rev. **88**, 1213 (1952).
[8] J. M. Blatt and V. F. Weisskopf, *Theoretical Nuclear Physics* (John Wiley and Sons, Inc., New York, 1952), p. 254.
[9] Sherr, Muether, and White, Phys. Rev. **75**, 282 (1949); R. Sherr and J. B. Gerhart, Phys. Rev. **91**, 909 (1953).

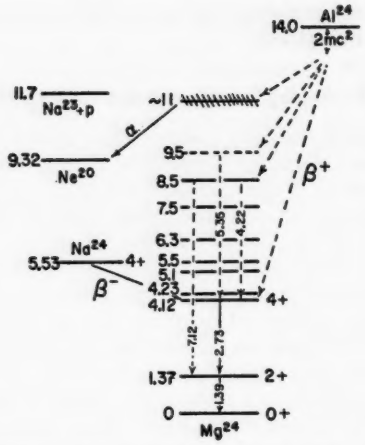

FIG. 4. Known Mg^{24} energy levels and possible Al^{24} decay scheme. The dotted line at 9.5 Mev is the calculated position of the analog level corresponding to the ground states of Na^{24} and Al^{24}.

Assuming that the Coulomb energy of a nucleus is given by $\frac{1}{2}Z(Z-1)(6/5)(e^2/r_0A^{\frac{1}{3}})$, r_0 can be calculated from the ground state energy differences of the $T_z=+1$ and $T_z=-1$ members of the triads, and the position of the analog level in the $T_z=0$ member determined. Table II lists these calculated values. The calculated r_0's are in quite reasonable agreement with the values from the mirror nuclei in this mass region.[10] In Si^{28} there is a measured level at 9.16 Mev[11] which could correspond to this analog level. In the other three cases, these regions have not been completely surveyed.

A test for the similarity of the wave functions of the ground states of the $T_z=+1$ and -1 members of a triad can be gotten from the comparison of the ft values for the beta decay to the same level of the $T_z=0$ member. As it turns out, the $A=28$ triad is the only one for which a quantitative comparison can be made. In the P^{28} decay the high-energy positron component goes to the same excited level of Si^{28} as does the negatron emission from Al^{28}. The logft value of this P^{28} component is measured as 4.9 ± 0.1. This is in good agreement with the value of log$ft=4.92$ found in the Al^{28} negatron decay.[12]

Assuming the equality of the ft values to the same state gives results consistent with those found in the other three cases. In the Al^{24} decay, the Na^{24} value[13] of log$ft=6.11$ would give about a 10 percent branch to the 4.14-Mev level of Mg^{24}. This is consistent with the observed results. In the Cl^{32} decay, no positron branch to the S^{32} ground state is observed, which is consistent with the P^{32} logft value of 7.90.[13] The same thing is true of the Sc^{40} decay.

[10] E.g., D. C. Peaslee, Phys. Rev. **95**, 171 (1954); P. Stahelin, Phys. Rev. **92**, 1016 (1953).
[11] R. A. Peck, Phys. Rev. **76**, 1279 (1949).
[12] H. T. Motz and D. E. Alburger, Phys. Rev. **86**, 165 (1952).
[13] A. M. Feingold, Revs. Modern Phys. **23**, 10 (1951).

Hence the energies of the ground states of the $T_z=-1$ nuclei reported in this paper are quite well accounted for by the charge effect, and the positron decay is consistent with the negatron decay of the $T_z=+1$ member of each triad. Thus, according to this picture, the ground state of the $T_z=-1$ member in each case should have the same spin and parity as the corresponding $T_z=+1$ member. If the analog state exists in the $T_z=0$ member, it should also have this same spin and parity.

B. Possible Decay Schemes

Although the decay schemes cannot be uniquely determined from the data reported here, it is interesting to note that decay schemes can be set up which are consistent with the known energy levels of the daughter nuclei, with the assumed presence of analog levels at the calculated positions, and with the estimated intensities of the positron and gamma-ray branches.

Aluminum-24.—Possible transitions which account for the positron and gamma ray activity are shown by the dotted lines in Fig. 4. From this scheme, a level at 9.49 Mev would be required which is very close to the calculated analog level. The gamma-ray intensities would indicate a logft of 3.8 to this level which is consistent with the expected favored transition. An alpha-particle emission ratio of 1/5000 gives a log$ft=5.5$ to a level around 11 Mev which indicates an allowed positron transition to that level.

Phosphorus-28.—In this decay there are measured[11] energy levels which could correspond to every gamma ray, as shown in Fig. 5. However, the 1.79-Mev gamma ray appears more intense than would be expected from the positron branching ratio to this level, so that other gamma rays are probably in cascade with the 1.79-Mev gamma. A positron transition to an analog level

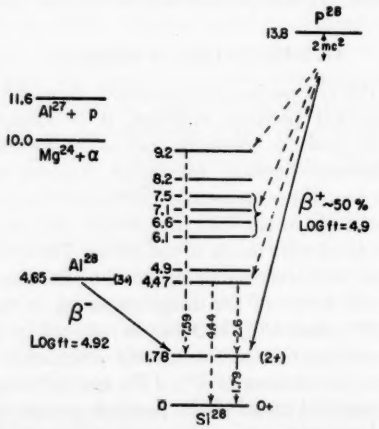

FIG. 5. Known Si^{28} energy levels and possible P^{28} decay scheme. The level at 9.2 Mev may correspond to the analog of the ground states of Al^{28} and P^{28}. The equality of the ft values for the β^- and β^+ components to the 1.78-Mev level indicates the similarity of the P^{28} and Al^{28} wave functions.

around 9 Mev giving rise to the 7.59 Mev or 7.04-Mev gamma ray in cascade with the 1.79-Mev level would require a logft of 3.4–3.7 which would indicate a favored transition, if it occurs. The deviation from linearity of the P^{28} positron plot is consistent with a branch to the 4.47-Mev level from which the 4.44-Mev gamma probably arises. Casson[14] has reported work which also indicates a 2.7-Mev gamma from this level in cascade with the 1.8-Mev level.

Chlorine-32.—Figure 6 shows the measured[15] energy levels and calculated analog level position for S^{32}. The intensity of the 2.21-Mev gamma ray appears somewhat greater than would be expected from the positron branch to this level, indicating possible cascade gammas through this level. The sum of energies of the 2.21 Mev and 4.77 Mev gammas is 6.98 Mev as compared with 7.1 Mev for the calculated energy of the analog level. If the 4.77 Mev dòes arise from a 7-Mev level, then the necessary positron branch to this level would have a logft of 3.6, indicating a favored transition. An alpha-particle energy of 2–3 Mev and branching ratio of 1/5000 gives a logft of about 4.9–5.5 for positron emission to a level at 9–10 Mev. This indicates an allowed transition to a level in this region.

Scandium-40.—Harvey[16] reports a level at 3.8 Mev in Ca^{40}, and Braams *et al.*[17] report levels at 3.35, 3.74, 3.90, and 4.49 Mev. The 3.75-Mev gamma ray probably arises from the 9.0-Mev positrons to the 3.74-Mev level. No strong lines appear which would indicate a transition to an analog level in the region of 7.5 Mev. Unfortunately, the appearance of several gamma-ray peaks in the longer-lived background leaves the possibility of one or more additional weak peaks appearing in the Sc^{40} decay.

CONCLUSION

During the course of this work and subsequent to the publication[3] of initial results on Al^{24}, P^{28}, and Cl^{32}, it was learned[18] that workers at McGill University, Montreal, had independently discovered the P^{28} and Cl^{32} activities and had made gamma-ray measurements on these and Al^{24}. Their results (half-lives, thresholds, and gamma rays) were in quite good agreement with those reported here. They listed several more gamma rays than we have been able to identify with certainty in P^{28}, and ascribe the 2.77-Mev peak in Cl^{32} to a 3.79-Mev gamma ray.

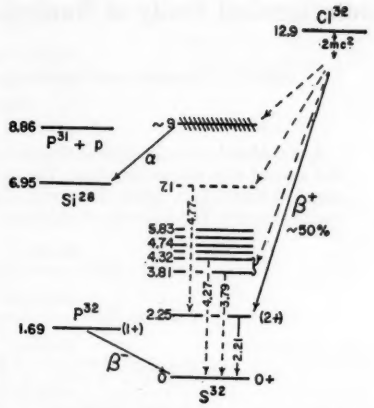

FIG. 6. Known S^{32} energy levels and possible Cl^{32} decay scheme. The dotted line at 7.1 Mev shows position of the calculated analog level corresponding to the ground states of P^{32} and Cl^{32}.

In conclusion, then, three new activities belonging to the nuclear series $Z=2n+1$, $A=4n$ have been discovered and further measurements made on a fourth. From the results reported herein, it is seen that these results appear to be consistent with those of the charge multiplet theory. In the case of P^{28}, comparison of the positron decay to the first excited state of Si^{28} with the negatron decay of Al^{28} gives additional evidence for the charge symmetry of nuclear forces.

We wish to express our appreciation for the help and interest of many present and former members of the Cyclotron Laboratory, particularly Professor Byron T. Wright, Dr. Louis K. Jensen, Dr. Harry E. Handler, Mr. Steve Plunkett, and Mr. Bowman C. Collins. Special thanks are also due by one of us (N.W.G.) to Professor R. Sherr of Princeton University for some very interesting discussions.

[14] Harvey Casson, Phys. Rev. **89**, 809 (1953).
[15] Arthur, Allen, Bender, Hausman, and McDole, Phys. Rev. **88**, 1291 (1952).
[16] J. A. Harvey, Phys. Rev. **88**, 162 (1952).
[17] Braams, Bockelman, Browne, and Buechner, Phys. Rev. **91**, 474 (1953).
[18] Breckon, Henrikson, Martin, and Foster, Can. J. Phys. **32**, 223 (1954).

Radiochemical Study of Neutron-Deficient Chains in the Noble Metal Region*

W. G. SMITH AND J. M. HOLLANDER
Radiation Laboratory and Department of Chemistry, University of California, Berkeley, California

(Received February 23, 1955)

A radiochemical study of some neutron-deficient nuclides in the noble metal region has been undertaken, and several new chains identified. The method used to establish genetic relationships was that of timed chemical separations, where the parent activities are initially produced by cyclotron or linear accelerator bombardments. The following chains have been identified:

$$A=191\text{: } Hg^{191} \xrightarrow{55\text{ min}} Au^{191} \xrightarrow{3.0\text{ hr}} Pt^{191} \xrightarrow{3.0\text{ day}} Ir^{191},$$

$$A=189\text{: } Hg^{189} \xrightarrow{\sim 20\text{ min}} Au^{189} \xrightarrow{42\text{ min}} Pt^{189} \xrightarrow{10.5\text{ hr}} Ir^{189} \xrightarrow{11\text{ day(?)}} Os^{189},$$

$$A=188\text{: } Pt^{188} \xrightarrow{10.0\text{ day}} Ir^{188} \xrightarrow{41\text{ hr}} Os^{188},$$

$$A=187\text{: } Au^{187} \xrightarrow{\sim 15\text{ min}} Pt^{187} \xrightarrow{2.5\text{ hr}} Ir^{187} \xrightarrow{14\text{ hr}} Os^{187}.$$

INTRODUCTION

RECENT energy level studies[1–3] of odd-mass nuclei in the region $A=191$ through $A=197$ have shown that interesting regularities exist in the movement of proton and neutron energy levels as pairs of nucleons of the other kind are added. In this laboratory several isotopes of platinum and gold with mass number less than 191 had been observed in the course of other work, but a systematic radiochemical study of this region had not been pursued. Because of recent interest, however, it seemed worthwhile to search for and identify new neutron deficient chains in gold and platinum with $A \leq 191$ which might be susceptible to spectroscopic investigation. In this paper we report on the synthesis and identification of the following chains:

$$Hg^{191} \rightarrow Au^{191} \rightarrow Pt^{191} \rightarrow Ir^{191}$$

$$Hg^{189} \rightarrow Au^{189} \rightarrow Pt^{189} \rightarrow Ir^{189} \rightarrow Os^{189}$$

$$Pt^{188} \rightarrow Ir^{188} \rightarrow Os^{188}$$

$$Au^{187} \rightarrow Pt^{187} \rightarrow Ir^{187} \rightarrow Os^{187}.$$

EXPERIMENTAL METHOD

In the work reported here, targets of element Z were bombarded in general with protons from the 184-inch cyclotron to produce isotopes of element $(Z+1)$ by the (p,xn) reactions. The proton energy was varied between 50 and 130 Mev, to bring in various values of x. Some excitation function experiments were also performed with the 32-Mev proton beam of the Berkeley linear accelerator, and a few proton and heavy ion bombardments were made in the 60-inch cyclotron.

The Geiger counter decay curves of the primary $(Z+1)$ chemical fractions were in general so complex that their resolution was difficult at best and often unsuccessful. Consequently, half-lives and genetic chain relationships were often determined by means of the chemical "milking" technique introduced by Neumann and Perlman[4] and Karraker and Templeton.[5] In this method, chemical separations of daughter activities from the purified $(Z+1)$ fractions are made at a sequence of equal time intervals, the interval corresponding approximately to the expected half-life of the parent.

The number of atoms of a daughter substance present at a time t after purification of its parent is given by the formula

$$N_2=\frac{\lambda_1}{\lambda_2-\lambda_1}N_1^0(e^{-\lambda_1 t}-e^{-\lambda_2 t}).$$

The activity of the daughter is then

$$A_2=C_2\lambda_2 N_2=\frac{C_2\lambda_2\lambda_1}{\lambda_2-\lambda_1}N_1^0(e^{-\lambda_1 t}-e^{-\lambda_2 t}),$$

where C_2 is the counting efficiency of the daughter. Since the time interval between successive chemical separations is held constant, the exponential terms become a constant factor, and A_2 is proportional to the disintegration rate $(\lambda_1 N_1^0)$ of the parent at the beginning of each growth period. Thus, if one plots the logarithm of the initial activity of each daughter fraction against the time of separation, the slope of the line will correspond to the half-life of the parent.

Although the primary emphasis in this work has been on the radiochemical analysis, examination of the gamma-ray spectra of some of these neutron-deficient nuclides has also been made with a NaI(Tl) scintillation

* This work was performed under the auspices of the U. S. Atomic Energy Commission.

[1] de-Shalit, Huber, and Schneider, Helv. Phys. Acta **25**, 279 (1952).

[2] Gillon, Gopalakrishnan, de-Shalit, and Mihelich, Phys. Rev. **93**, 124 (1954).

[3] J. W. Mihelich and A. de-Shalit, Phys. Rev. **93**, 135 (1954).

[4] H. Neumann and I. Perlman, Phys. Rev. **78**, 191 (1950).

[5] D. G. Karraker and D. H. Templeton, Phys. Rev. **80**, 646 (1950).

spectrometer coupled to a 50-channel differential analyzer. These gamma-ray data are far from definitive, but they have been helpful in the identification of the various nuclides encountered, both new and old. Some of these data will be quoted here when they appear to provide relevant information.

RADIOCHEMICAL RESULTS

Figure 1 is a segment of an isotopic chart in the noble metal region showing the activities identified in the present study. The half-lives of previously reported activities are also given in parentheses.

The following is a summary of the experimental results given by mass number.

$A=191$. Genetics

Following a 120-Mev proton irradiation of gold metal, a pure mercury fraction was prepared by a procedure involving removal of the gold into amyl acetate and precipitation of mercury metal with $SnCl_2$. The decay curve of the mercury fraction itself was complex, with at least five components. Therefore, a series of seven timed gold separations was made from this fraction at intervals of eight minutes, by amyl acetate extraction. These gold "milkings" showed the

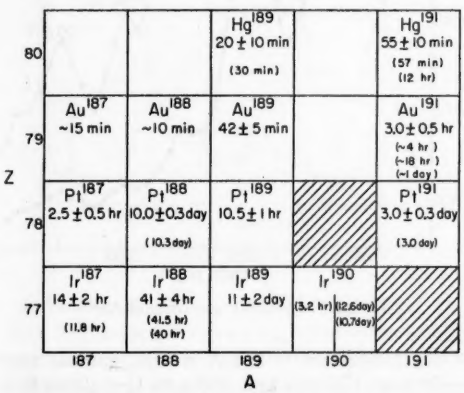

FIG. 1. Segment of an isotopic chart in the noble-element region (half-lives in parentheses are previously reported values).

activities and genetic relationships illustrated in Table I and Fig. 2.

The 40-minute gold activity is Au^{189}, and will be discussed under that mass number. The 3-hour and 3-day activities descend from the same mercury ancestor, whose half-life is ~50 minutes. Further chemical experiments with this gold "milking" fraction have identified the 3-hour activity as an isotope of gold and the 3-day activity as platinum, hence probably the daughter of the 3-hour gold. Since Pt^{191} is a fairly well known 3.0-day activity,[6,7] this chain can be assigned to

[6] G. Wilkinson, Phys. Rev. 75, 1019 (1949).
[7] Swan, Portnoy, and Hill, Phys. Rev. 90, 257 (1953).

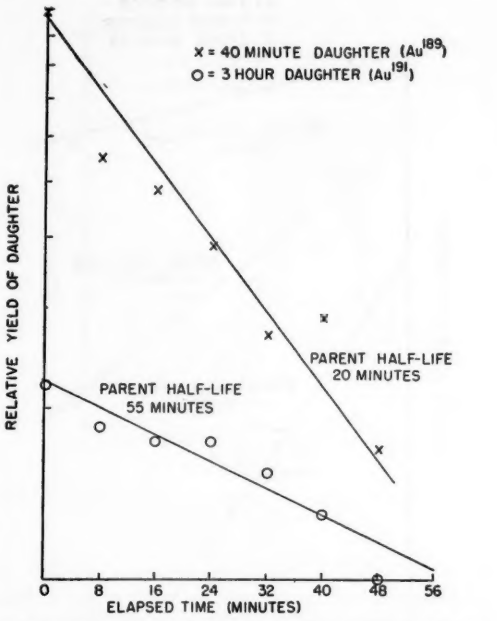

FIG. 2. Radiochemical yield of daughter activities as a function of time. Gold separated from parent mercury fraction at 8-minute intervals. (Bombardment: gold+120-Mev protons.)

mass 191.

$$Hg^{191} \xrightarrow{55\text{ min}} Au^{191} \xrightarrow{3\text{ hr}} Pt^{191} \xrightarrow{3.0\text{ days}} Ir^{191}.$$

These results are in agreement with the recent work of Gillon *et al.*,[2] who found in their study of conversion lines from 60-Mev proton bombardments of gold:

$$Hg^{191} \xrightarrow{57\text{ min}} Au^{191} \xrightarrow{\sim 4\text{ hr}} Pt^{191} \xrightarrow{3\text{ days}} Ir^{191}.$$

The genetic relationship between the 3-hour Au^{191} and 3.0-day Pt^{191} was also established independently in two other ways:

(a) Platinum was irradiated with 130-Mev protons, and a pure gold fraction prepared. Seven timed platinum separations were made at 30-minute intervals, with the results shown in Table II and Fig. 3.

This experiment indicates a half-life of 2.5±0.5 hours for Au^{191}. The other activities will be discussed under the appropriate mass numbers.

TABLE I. Genetic relationships. Gold separated from parent mercury fraction at 8-minute intervals. (Bombardment: gold +120-Mev protons.)

Activity	Half-life of Hg parent (or ancestor)	Assignment
40±10 min	20±10 min	Au^{189}
3.0±0.5 hr	55±10 min	Au^{191}
15 hr (weak)	>50 min	Au^{193}
3 day (weak)	~50 min	Pt^{191}

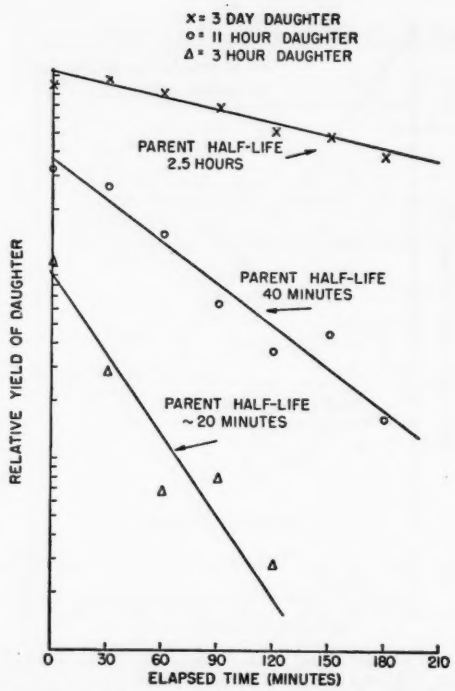
X = 3 DAY DAUGHTER
o = 11 HOUR DAUGHTER
Δ = 3 HOUR DAUGHTER
PARENT HALF-LIFE 2.5 HOURS
PARENT HALF-LIFE 40 MINUTES
PARENT HALF-LIFE ~20 MINUTES
RELATIVE YIELD OF DAUGHTER
0 30 60 90 120 150 180 210
ELAPSED TIME (MINUTES)

FIG. 3. Radiochemical yield of daughter activities as a function of time. Platinum separated from parent gold fraction at 30-minute intervals. (Bombardment: platinum+130-Mev protons.)

(b) Gold was irradiated with 120-Mev protons, and a pure mercury fraction separated. This was allowed to stand for about two hours, after which a gold separation was made from it. Five "milkings" of platinum were then made from this gold fraction at 3-hour intervals. The platinum milkings contained largely 3.0-day Pt^{191}, and the yields indicated a half-life of 3.0±0.5 hours for its gold parent.

Moon and Thompson[8] have reported an 18-hour Au^{191} descending from a 12-hour Hg^{191}. We have no evidence concerning the mercury isotope reported by these workers, but we can say that if such a Au^{191} isomer exists, it is not the parent of 3-day Pt^{191} within the limits of detection of the chemical genetic experiments reported here. A small amount of a 17-hour gold activity *was* observed in one of the gold fractions milked from mercury, but its gamma spectrum was shown to be identical (at 8 percent resolution in a scintillation spectrometer) to that of 17-hour Au^{193} and hence it is most likely Au^{193}.

TABLE II. Genetic relationships. Platinum separated from parent gold fraction at 30-minute intervals. (Bombardment: platinum+130-Mev protons.)

Pt activity	$T_{\frac{1}{2}}$ of gold parent	Assignment
3 day	2.5±0.5 hr	Pt^{191}
11±1 hr	40±10 min	Pt^{189}
3±0.5 hr	15−20 min	Pt^{187}

[8] J. H. Moon and A. L. Thompson (private communication, October 1952).

$A = 191$. Gamma-Ray Spectra

The gamma spectrum of 3-hour Au^{191} was examined in the scintillation spectrometer with a sample which contained mostly that isotope; one of the spectra is shown in Fig. 4. Gamma rays were seen at 140±20 kev, 300±10 kev, 390±20 kev, 475±20 kev, and 600±20 kev, with intensities (corrected for counting efficiency) relative to the K x-rays of 0.1, 0.6, 0.05, 0.04, and 0.1, respectively. Because of the high intensity of the x-rays at ~60 kev, we cannot say anything about gamma radiation softer than ~100 kev.

In the course of several "milking" experiments, samples containing essentially pure 3-day Pt^{191} were obtained. Scintillation spectra taken with these samples showed, in addition to the K x-rays, gamma rays at 125±10 kev, 175±10 kev, 265±10 kev, 355±10 kev, 405±10 kev, 445±20 kev, and 530±10 kev. One of these scintillation spectra is reproduced in Fig. 5. The relative intensities of the 265, 355, 405, 445, and 530 kev gamma rays as determined from the areas under their photopeaks are 0.2, 1.00, 0.8, 0.2, and 1.7, respectively. The abundances of the 125- and 175-kev gamma-ray photopeaks were measured as 0.5 and 0.4 relative to that of the 345-kev gamma ray; however, the background under these peaks is rising sharply and there must also be some contribution from backscattered radiation, so these relative abundances are only estimates.

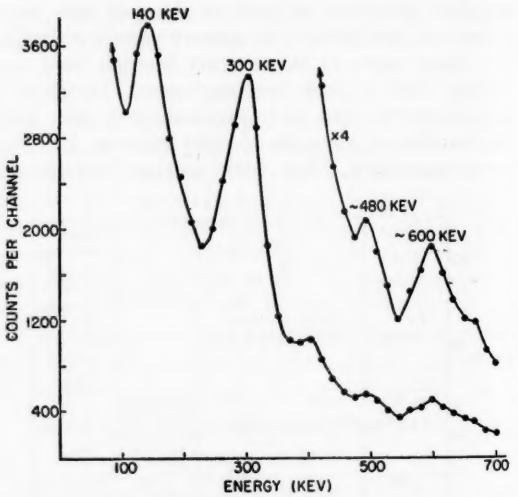

FIG. 4. Gamma-ray spectrum of Au^{191}.

Swan, Portnoy, and Hill[7] have examined the conversion line spectrum of Pt^{191} and have reported gamma rays at 62, 82, 94, 125, 129, 171, 178, 267, 350, 359, 408, 455, and 537 kev. The present scintillation meas-

urements would of course not resolve the 125–129, 171–178, 350–359 pairs, but otherwise are in agreement with the results of Swan *et al.*, above 100 kev. (We could not examine the gamma-ray spectrum below 100 kev because of the overwhelming area of the K x-ray peak.)

$A=189$. Genetics

An ~12-hour activity in platinum was first observed in 1950 by Thompson and Rasmussen[9] from 50-Mev proton bombardments of iridium, but a mass assignment was not made at that time. With the aid of J. O. Rasmussen, this activity has now been assigned to Pt^{189} by means of proton excitation function experiments in which its yield from iridium is compared with that of 3.0-day Pt^{191} produced from the $(p,3n)$ reaction on Ir^{193}. The excitation experiments were done in the Berkeley 32-Mev proton linear accelerator with a set of stacked iridium and aluminum foils as targets and absorbers. Figure 6 shows the resulting yield curves,

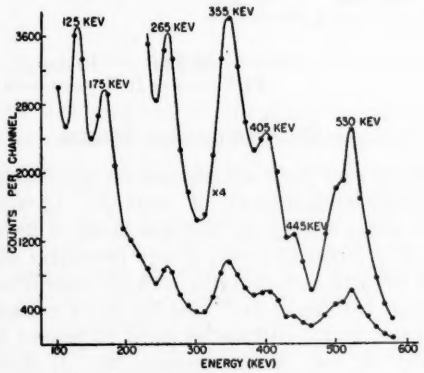

FIG. 5. Gamma-ray spectrum of Pt^{191}.

which exhibit similar maxima at ~28 Mev. On the basis of its production from a $(p,3n)$ reaction in iridium, the new activity can be only Pt^{189} or an isomer of Pt^{191}. The following is evidence against its assignment to Pt^{191m}: (a) we have bombarded iridium with 12-Mev protons in the 60-inch cyclotron, and observe in the platinum fraction the known 3-day Pt^{191} and 4-day Pt^{193m} which are produced from the (p,n) reaction. The 10-hour activity is not found. This is consistent with its assignment to Pt^{189}, because a $(p,3n)$ reaction is energetically not possible at this proton energy. (Anticipating the discussion of gamma-ray studies of the mass 189 chain, we also observed in this 12-Mev bombardment that the gamma spectrum of the platinum fraction was identical to the known spectrum of Pt^{191}, and had none of the gamma rays associated with the 10-hour platinum.) (b) Wilkinson, in his study of platinum isotopes produced by 18-Mev deuteron bombardments of iridium,[6] observed no platinum activity

[9] S. G. Thompson and J. O. Rasmussen (unpublished).

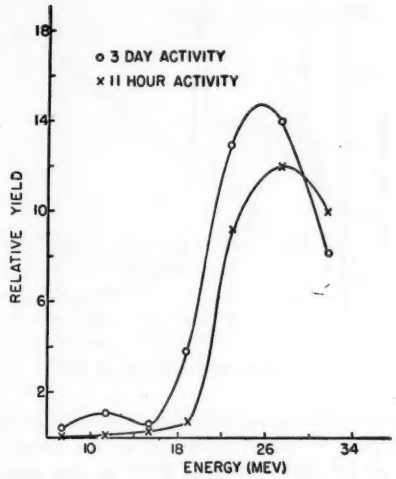

FIG. 6. Excitation curves for the production of 3-day Pt^{191} and 10-hour Pt^{189}.

with half-life shorter than that of 3-day Pt^{191}. He should not have been able to detect Pt^{189} because at 18 Mev the yield of the $(d,4n)$ reaction is quite small.

It is also noted from Fig. 6 that the yield curve for the 3-day component shows two maxima. The small peak at approximately 10 Mev indicates the production of 3-day Pt^{191} from the $Ir^{191}(p,n)$ reaction and of 4-day Pt^{193m} from the $Ir^{193}(p,n)$ reaction, while the tenfold larger peak at approximately 28 Mev corresponds to the $Ir^{193}(p,3n)Pt^{191}$ reaction. The 11-hour component shows no peak at approximately 10 Mev as might be expected if it were Pt^{191m}, but it seems to be produced only from the $(p,3n)$ reaction.

Because of these considerations we assign this activity to Pt^{189}. Our best value for its half-life is 10.5 ± 1 hours.

In the decay curves of the platinum fractions from these 32-Mev proton bombardments of iridium, an 11 ± 1-day activity also appears in addition to and in comparable yield to 10.5-hour Pt^{189} and 3.0-day Pt^{191}. A similar activity was seen in the decay curves of the iridium fractions (in addition to 75-day Ir^{192}). Attempts were made to establish the parentage of this 11-day activity by the timed separation procedure described above, but these were not successful because of lack of reproducibility of the iridium-platinum "milkings." Accordingly, platinum-iridium separations were performed on the initial platinum fractions after the "complete" decay of activities shorter than approximately 10 days, and it was found that an approximately 11-day activity appeared in both the platinum and the iridium fractions. The gamma-ray spectra of these activities were studied with the scintillation spectrometer, and were found to be different from each other (dispelling the fear of grossly incomplete chemical separation). The 11-day platinum activity is undoubtedly Pt^{188}; evidence for this will be discussed under $A=188$. That the 11-day iridium activity does

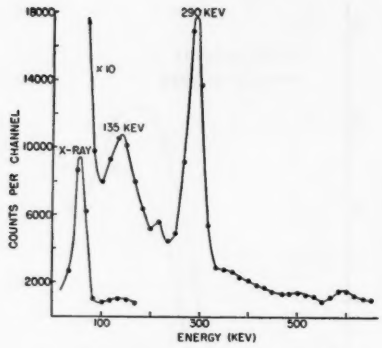

FIG. 7. Gamma-ray spectrum of Au^{189}.

not belong to the mass 188 chain was substantiated by showing that it is still produced at the lower proton energy of 25 Mev, whereas Pt^{188} is not seen. This energy should be below the threshold for the $(p,4n)$ reaction.

There remain three choices for the assignment of this activity: Ir^{191m}, Ir^{189}, or Ir^{190} arising from iridium impurity in the original platinum fractions. The first choice, Ir^{191m}, may probably be ruled out by the recent discovery of 6-second Ir^{191m} by Mihelich *et al.*[10] and by Naumann and Gerhart,[11] and also by the fact that we have searched for this activity following 12-Mev proton bombardments of iridium, with negative results.

Our data indicate that the 11-day iridium is Ir^{189}. However, Ir^{190} has also been reported[12,13] as an 11 to 13 day activity; in some of our milkings of iridium from platinum in which the 11-day iridium is observed, there is also seen a small amount of Ir^{192} which must have entered the original platinum fraction as an impurity. Because Ir^{190} would be present in the same way we cannot exclude the possibility that the 11-day iridium which we observe may be Ir^{190}. However, in the following discussion on the gamma spectra we shall refer to this isotope as Ir^{189}.

Once Pt^{189} has been identified it becomes easier to recognize its Au^{189} parent. This isotope has been produced in several different ways:

(a) Bombardments of tantalum ($Z=73$) with high-energy carbon ions in the 60-inch cyclotron produced activities in the gold fraction of half-lives 10 ± 5 minutes, 42 ± 5 minutes (predominant), $\sim$11 hour, and $\sim$10 day (weak). The yields were very low in these experiments because of inadequate beam currents, but timed platinum separations from the gold fraction indicated that the 11-hour platinum (189) is the daughter of an approximately 35-minute gold parent activity.

(b) Platinum metal was irradiated with 130-Mev protons, and a gold chemical fraction isolated. Timed milkings of platinum from this fraction (done in separate experiments at intervals of 10 minutes and 30 minutes, respectively) verified that 11-hour Pt^{189} has a gold parent of 40 ± 10-minute half-life. The yield curves from these milking experiments are shown in Figs. 3 and 14.

These experiments demonstrate that Au^{189} has a half-life of 42 ± 5 minutes.

In the experiment discussed under $A=191$ (the results of which are given in Table I and Fig. 2), it was seen that the 40-minute gold activity grew from an approximately 20-minute mercury parent. The experiments cited here which establish the 42-minute gold as Au^{189} therefore also set the half-life of Hg^{189} as approximately 20 minutes. This Hg^{189} half-life, however, is the result of only one experiment, so a considerable uncertainty is attached to this value.

The mass 189 chain, insofar as we have studied it, can be written as:

$$Hg^{189} \xrightarrow{\sim 20\text{ min}} Au^{189} \xrightarrow{42\text{ min}}$$

$$Pt^{189} \xrightarrow{10.5\text{ hr}} Ir^{189} \xrightarrow{10\text{ day}(?)} Os^{189}.$$

$A=189$. Gamma-Ray Spectra

A fairly pure Au^{189} sample was obtained from the carbon-ion bombardment of tantalum. Gamma-ray spectra taken during the first few hours of its decay show, in addition to x-rays, a very prominent gamma ray at 290 ± 10 kev, decaying with the approximately 40-minute half-life of Au^{189} (see Fig. 7). A gamma ray is also seen at 135 ± 10 kev in about 10 percent of the intensity of the 290-kev gamma ray. High-energy radiations (>800 kev) may also be present.

The Pt^{189} gamma-ray spectrum indicates a fairly certain photon at 140 ± 10 kev, with probable gamma radiation at $\sim$550 kev, slightly greater than 550 kev, and at $\sim$700 kev.

Bombardments of iridium with 32-Mev protons produce in the platinum fraction active isotopes of masses

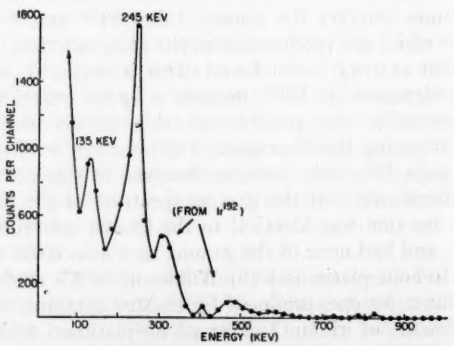

FIG. 8. Gamma-ray spectrum of Ir^{189}.

[10] Mihelich, McKeown, and Goldhaber, Phys. Rev. **96**, 1450 (1954).
[11] R. A. Naumann and J. B. Gerhart, Phys. Rev. **96**, 1452 (1954).
[12] L. J. Goodman and M. L. Pool, Phys. Rev. **71**, 288 (1947).
[13] T. C. Chu, Phys. Rev. **79**, 582 (1950).

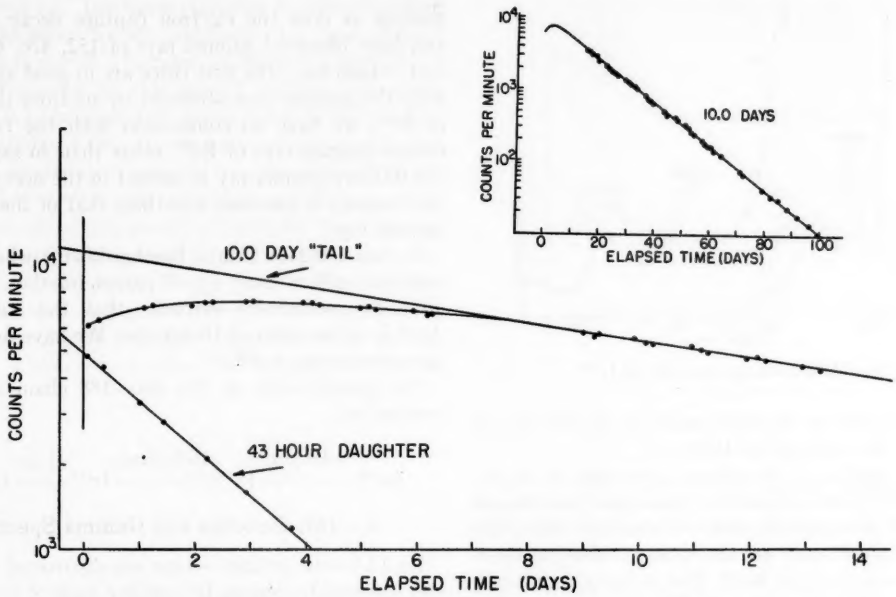

FIG. 9. Growth and decay curve for Pt^{188}, as daughter Ir^{188} grows into equilibrium with parent.

193, 191, 189, and 188. If one allows this fraction to decay for several weeks and then removes iridium from it, good samples of Ir^{189} and Ir^{188} are obtained, because Pt^{191} and Pt^{193m} have no active iridium daughters. The 11-day Ir^{189} can be distinguished from 41-hour Ir^{188} by virtue of their very different half-lives. We have obtained in this way the spectrum of Ir^{189} (see Fig. 8), which shows a strong gamma ray at 245±10 kev, and perhaps a weak gamma ray at approximately 135 kev (although this may be backscattered 245-kev radiation). No other radiations than x-rays were seen which could be attributed to Ir^{189}.

$A=188$. Genetics and Gamma Spectra

Naumann[14] has reported the synthesis of a new neutron-deficient isotope of platinum, Pt^{188}, with a half-life of 10.3 days. Although the present work was aimed primarily toward the study of new odd-particle chains, it was of interest to examine the 188 chain because of the possibility of confusion of this 10-day Pt^{188} with the 10-day Ir^{189} reported here. (It has already been mentioned under $A=189$ that a 10-day activity had been observed in both the platinum and the iridium fractions from 30- to 50-Mev proton bombardments of iridium.)

We have studied the Pt^{188}-Ir^{188} pair in the following way: a proton bombardment of iridium metal was made at 32 Mev, and a platinum fraction chemically separated. This fraction was allowed to stand for about a month, at which time an iridium-platinum separation was performed. This second platinum fraction exhibited an initial growth, and then decayed with a 10.0±0.3 day half-life. Analysis of the growth curve[15] plus direct decay data yields a daughter half-life of 41±4 hours. This curve is shown in Fig. 9.

Our evidence for the assignment of the 10-day activity to Pt^{188}, in agreement with Naumann, is the following:

(a) We have observed this 10-day platinum in bombardments of iridium with 32-Mev protons, which is consistent with its production from the reaction $Ir^{191}(p,4n)Pt^{188}$.

(b) The daughter iridium activity has been assigned

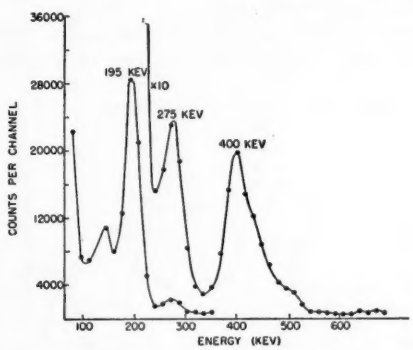

FIG. 10. Gamma-ray spectrum of Pt^{188}.

[14] R. A. Naumann, Phys. Rev. **96**, 90 (1954).

[15] The total amount of activity at time t can be expressed as $A=\sum_i a_i e^{-\lambda_i t}$, where the a_i's can be either positive or negative. To resolve this growth and decay curve, the "tail" was extrapolated back to the time of purification of the parent and subtracted from the observed curve. The series of negative differences, when plotted, gives the half-life of the daughter.

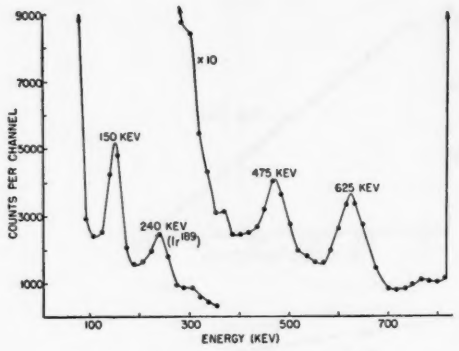

FIG. 11. Gamma-ray spectrum of Ir^{188}.

by Chu[13] to Ir^{188} on the basis of its production by an $(\alpha,3n)$ reaction on enriched Re^{187}.

(c) Our studies of the gamma spectrum of the 41-hour iridium (described below) show that the energies of the first two excited states in osmium which are populated by its decay are the same as those produced from the beta decay of Re^{188}. This is fairly convincing evidence for its assignment to Ir^{188}.

The gamma spectra of Pt^{188}, Ir^{188}, and of the Pt^{188}-Ir^{188} equilibrium mixture are shown in Figs. 10, 11, and 12, respectively. Gamma rays are seen in Pt^{188} at 195 ± 10 kev, 275 ± 15 kev, and there is a broad peak at approximately 400 kev which may represent two unresolved gamma rays. The measured relative abundances are 1.0, 0.1, and 0.3, respectively. As the Ir^{188} grows into the sample, gamma rays appear at 150 ± 10 kev, 475 ± 10 kev, and 625 ± 15 kev. The relative intensities were measured directly in the second iridium fraction which contains Ir^{188} plus a small fraction of Ir^{189} activity. From the pure Ir^{188} spectrum (Fig. 11) we obtain relative intensities 0.9, 0.6, and 1.0 for the three gamma rays, respectively. There also seems to be harder gamma radiation in low intensity.

Richmond, Grant, and Rose[16] have studied the beta decay of Re^{188} (which leads to the same daughter

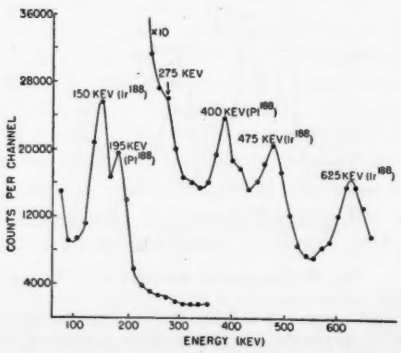

FIG. 12. Gamma-ray spectrum of Pt^{188} in equilibrium with Ir^{188}.

[16] Richmond, Grant, and Rose, Proc. Phys. Soc. (London) A65, 484 (1952).

nucleus as does the electron capture decay of Ir^{188}) and have observed gamma rays of 152, 476, 638, 933, and ~1300 kev. The first three are in good agreement with the gamma rays observed by us from the decay of Ir^{188}; we have no comparison with the two high-energy gamma rays of Re^{188} other than to say that if the 933-kev gamma ray is present in the decay of Ir^{188} its intensity is less than one-third that of the 625-kev gamma ray.

In two 130-Mev proton bombardments where platinum was milked from a gold parent fraction, we have obtained preliminary evidence that the half-life of Au^{188} is of the order of 10 minutes. We have no further data concerning Au^{188}.

Our genetic data on the mass-188 chain are summarized as:

$$Au^{188} \xrightarrow{\sim 10\text{ min}} Pt^{188} \xrightarrow{10.0\text{ days}} Ir^{188} \xrightarrow{41\text{ hr}} Os^{188}.$$

$A=187$. Genetics and Gamma Spectra

An 11.8-hour iridium isotope was discovered by Chu[13] and assigned by him to Ir^{187} on the basis of its production from an $(\alpha,2n)$ reaction upon Re^{185}. The shape of the excitation curve which he presents [as $(\alpha,2n)$ plus small contribution from $(\alpha,4n)$] is not convincing, however, especially in view of the fact that others have been unable to detect an $(\alpha,4n)$ reaction with 38-Mev alpha particles in the 60-inch cyclotron. Although our genetic data neither prove nor disprove this mass assignment, but only establish the gold and platinum activities which are isobaric with the 12-hour iridium, we shall here specify this reference activity as Ir^{187}. It will be seen, however, that our gamma-ray data tend to support this assignment.

TABLE III. Genetic relationships. Platinum separated from parent gold fractions at 7- and 10-minute intervals. (Bombardments: platinum+130-Mev protons.)

Activity	Half-life of gold parent or ancestor	Assignment
Experiment A—five milkings at 7-minute intervals		
2.5±0.5 hr	~13 minutes	Pt^{187}
12 ±2 hr	~14 minutes	Ir^{187}
Experiment B—eight milkings at 10-minute intervals		
3 ±0.5 hr	~17 minutes	Pt^{187}
12 ±2 hr	~12 minutes (plus ~40 minutes)	Ir^{187} (plus Pt^{189})

We have identified Pt^{187} in the following way: iridium metal was bombarded with 120-Mev protons and a pure platinum fraction chemically separated. (Its decay curve was complex, with components of $2\frac{1}{2}$ hours, ~10 hours, ~2.2 days, and ~10 days.) After allowing this platinum fraction to stand for one day, iridium was separated from it. This first iridium milking contained largely 14 ± 1 hour (Ir^{187}) and 43 ± 4 hour (Ir^{188}) activities, with a ratio (in counts per minute) of

Ir^{187}/Ir^{188} of 6.5. The same platinum fraction was then allowed to stand for an additional day, and iridium was again removed. The ratio (in counts per minute) of Ir^{187}/Ir^{188} present in this second milking was much lower, ~0.2. Because Ir^{188} grows from a "long"-lived parent (10-day Pt^{188}), its actual yield during the two intervals of growth is roughly constant and hence the ratio of Ir^{187}/Ir^{188} in the two milkings gives some idea of the half-life of the parent of Ir^{187}. By the factor of approximately 32 decrease in Ir^{187} in 24 hours, one would say that the half-life of its parent is approximately 5 hours. A possible error would arise from a small amount of 10-hour Pt^{189} impurity in the iridium milkings, which would cause the half-life of Pt^{187} to

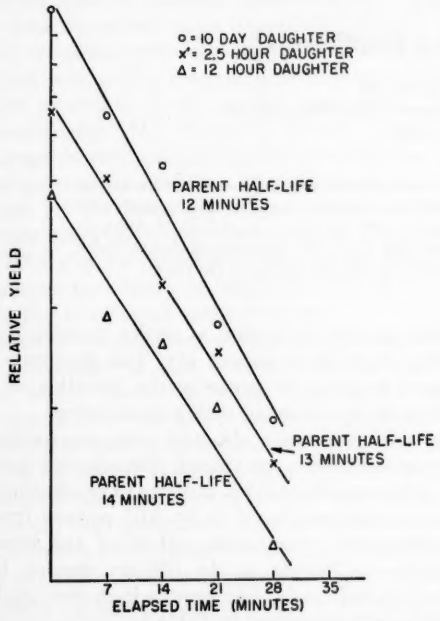

FIG. 13. Radiochemical yield of daughter activities as a function of time. Platinum separated from parent gold fraction at 7-minute intervals. (Bombardment: platinum+130-Mev protons.)

appear too long. The experiment, then, indicates that the half-life of Pt^{187} is ≤ 5 hours, and probably is the 2.5-hour platinum seen in the original platinum fraction.

Several other genetic experiments were done to identify the mass 187 chain. On two occasions, platinum metal was irradiated with 130-Mev protons, and pure gold fractions prepared. As was expected, the gold fraction decay curves were complex, with at least five components. Therefore, timed platinum milkings were made in each experiment by aqueous extraction of the platinum from the gold, which was in an amyl acetate solution. The results of these milkings are given in Table III, and some of the yield curves are shown in Figs. 13 and 14.

Our genetic data on the mass-187 chain are summarized as:

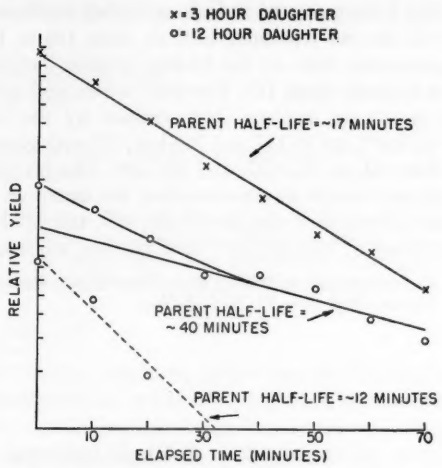

FIG. 14. Radiochemical yield of daughter activities as a function of time. Platinum separated from parent gold fraction at 10-minute intervals. (Bombardment: platinum+130-Mev protons.)

$$Au^{187} \xrightarrow{\sim 15\ \text{min}} Pt^{187} \xrightarrow{2.5\ \text{hr}} Ir^{187} \xrightarrow{14\ \text{hr}} Os^{187}.$$

The only reasonably good gamma-ray data at mass 187 were obtained with 14-hour Ir^{187}. Three gamma rays are seen, at 135±10 kev, 300±10 kev, and 435±15 kev, with relative intensities respectively 1.0/1.1/0.8. Weak gamma rays are also seen at ~500 kev and at ~625 kev, but these may belong in part to Ir^{188}. This spectrum is shown in Fig. 15.

One further remark may be made about the assignment of this chain to mass-187. In two bombardments of iridium with 32-Mev protons where fast chemistry was done, the 2.5-hour platinum activity has not been observed, whereas Pt^{188}, Pt^{189}, and heavier platinum isotopes are all found. We interpret this as evidence that this isotope has a mass lighter than 188, since it is produced from high-energy proton bombardments of iridium. Yet it could not be lighter than 186, or Chu[13]

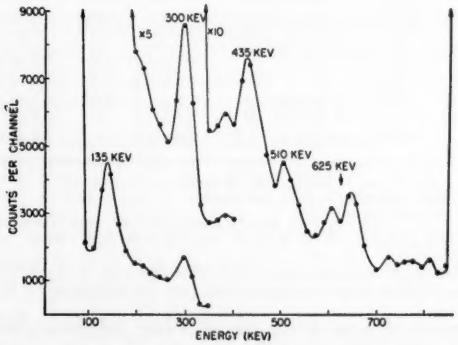

FIG. 15. Gamma-ray spectrum of Ir^{187}.

could not have produced it from an $(\alpha,3n)$ reaction on Re^{185}. Of the two remaining choices, mass 186 or 187, our gamma-ray data on the 14-hour iridium daughter lead us to prefer mass 187. The first two excited states of the even-even nucleus Os^{186}, defined by the beta decay of Re^{186}, are at 137 and 764 kev,[17,18] with gamma rays observed at 137, 627, and 764 kev. The principal gamma rays which we observe from the decay of the 14-hour iridium, however, are at 135, 300, and 435 kev. These do not fit into the Os^{186} level pattern, whereas in the case of mass 188, the gamma-ray energies which we observe from the decay of Ir^{188} agree quite well with those found[16] from the beta decay of Re^{188}.

We would like to express our appreciation to Professor J. O. Rasmussen and to Dr. M. I. Kalkstein for their extensive assistance during the course of this study, and also to Professor G. T. Seaborg, Professor D. H. Templeton, and Professor I. Perlman for their helpful comments. The cooperation of the staffs and crew members of the 184-inch cyclotron, linear accelerator, and 60-inch cyclotron is also gratefully acknowledged.

[17] F. R. Metzger and R. D. Hill, Phys. Rev. **82**, 646 (1951).
[18] L. Koerts, Phys. Rev. **95**, 1358 (1954).

PHYSICAL REVIEW VOLUME 98, NUMBER 5 JUNE 1, 1955

K-Shell Internal Conversion Coefficients*

R. C. Rohr† and R. D. Birkhoff
Department of Physics, The University of Tennessee, Knoxville, Tennessee
(Received January 28, 1955)

Internal conversion coefficients for the *K*-shells of several medium-energy gamma emitters have been measured with a solenoidal beta spectrometer and a 30 mg/cm² lead radiator. Isotopes investigated, with gamma energies and conversion coefficients $\times 10^3$, are as follows: Nb^{95}, 722 kev, 1.6±0.8; Cd^{110}, 657 kev, 2.2±0.8; Te^{122}, 570 kev, 6.6±1.7; La^{140}, 541 kev, 5.6±1.9; Ce^{140}, 489, 5.3±2.0. These values lead to multipolarity assignments of *E*2 or *M*1 for the first three, *E*2 for the La^{140}, and *E*1 or *E*2 for the Ce^{140}.

SEVERAL medium-energy gamma rays have been investigated and the *K*-shell internal conversion coefficients have been obtained. In addition, the ratios of some $K/(L+M)$ coefficients have been determined. The instrument used was a solenoidal type beta spectrometer previously described.[1] Sources were made in the form of a ring placed coaxially with the slits and set back from the point-source position by a distance equal to the radius of the ring. Gamma rays leaving the source at an angle of 45°±1° with the axis and converging on the point slit produced photoelectrons in the lead radiator at this position which were then accepted by the slit system at angles between 0 and 90° with the incident gamma ray. This geometry was employed in order to minimize the variation of the efficiency of the convertor with gamma energy.

The coefficients were obtained from measurements of internal conversion spectra and photoelectron spectra using a 30 mg/cm² lead foil radiator. The efficiency of the convertors was found to be 0.03 percent from a comparison with the known values of the internal conversion coefficients of the 662-kev gamma from barium-137 and the 412-kev gamma from mercury 198. The data are summarized in Table I.

In several cases other measurements have been made but in most cases these have been obtained with different methods and geometries. In all cases the limits of experimental error overlap.

The 754-kev gamma ray reported by Mittelman[2] as due to zirconium-95 was observed in the photoelectron spectrum but was not observed in the internal conversion spectrum. The reason for this is believed to be partially the fact that the line is weak and only weakly converted and partially that it was not resolved from the 764-kev line of niobium-95.

A comparison has been made with theoretical calculations of the internal conversion coefficients[3] and a determination of the multipolarity of the radiation has been obtained. All results are summarized in Table I.

TABLE I. Multipolarity of radiation from several nuclear transitions as determined from internal conversion ratios.

Isotope	γ-ray energy (kev)	$K/(L+M)$ This research	$K/(L+M)$ Previous research	$\alpha_K \times 10^3$ This research	$\alpha_K \times 10^3$ Previous research	Multipolarity
Nb 95	722	···	···	1.6±0.8	1.4[a]	*E*2 or *M*1
Cd 110	657	···	···	2.2±0.8	2.5[b]	*E*2 or *M*1
Te 122	570	2.3±0.4	[c]	6.6±1.7	4.9[d]	*E*2 or *M*1
La 140	541	5.2±0.5	6[e]	5.6±1.9	[c]	*E*2
Ce 140	489	4.2±1.4	3.7[e]	5.3±2.0	[e]	*E*1 or *E*2

[a] P. S. Mittleman, Phys. Rev. **99**, 94 (1954).
[b] K. Siegbahn, Phys. Rev. **77**, 233 (1950).
[c] No previous measurement.
[d] M. J. Glaubman and F. R. Metzger, Phys. Rev. **87**, 2039 (1952).
[e] R. E. Maerker and R. D. Birkhoff, Phys. Rev. **89**, 1159 (1953).

* This paper is based on a thesis submitted by R. C. Rohr in partial fulfillment of the requirements for the degree of Ph.D. in physics.
† Present address: Knolls Atomic Power Laboratory, Schenectady, New York.
[1] R. D. Birkhoff and F. Kalil, Phys. Rev. **91**, 505 (1953).
[2] P. S. Mittelman, Phys. Rev. **94**, 99 (1954).
[3] Rose, Goertzel, Spinrad, Haar, and Strong, Phys. Rev. **83**, 79 (1951).

Radiation Width Variations in the Slow-Neutron Resonances of Europium and Indium†

H. H. LANDON AND V. L. SAILOR
Brookhaven National Laboratory, Upton, New York
(Received February 8, 1955)

The parameters of the lowest-energy resonances in europium and indium have been determined from total cross section measurements using the Brookhaven crystal spectrometer. The data have been analyzed for variations in the radiation width parameter Γ_γ from resonance to resonance. The method of analysis used to take account of Doppler effect in the observed cross section is discussed. The radiation width in the 0.327-ev resonance in Eu is 70±10 mv, which is definitely smaller than that for the 0.461-ev and 1.056-ev resonances which are respectively 93±3 mv and 94±3 mv. The widths of the 1.456-ev and 3.85-ev resonances in In are 72±2 mv and 81±4 mv respectively. The remaining one-level parameters for each resonance are also presented.

INTRODUCTION

SLOW neutron radiative capture studies have long been recognized as an important technique in the study of nuclear structure. Capture of a neutron into a nucleus results in a compound nucleus excited in the region of virtual states, on the average for $A>100$, approximately 7 Mev above the ground state. For slow neutrons the predominant mode of decay of these states is by gamma-ray emission. Analysis of the total cross section for the Breit-Wigner parameters of resonance capture yields directly a measure of the lifetime of the virtual states for de-excitation by gamma emission, a parameter for which theoretical estimates can be made according to assumed nuclear models.[1]

In recent years, great advances have resulted from the availability of high neutron flux and consequent good energy resolution. Large numbers[2] of neutron resonances have been isolated over a considerable range of energy in nuclei from most of the periodic table. The general features of resonance parameters are beginning to become clear. Hughes and Harvey[3] have summarized the most recent generalizations that can be made about the radiation width parameter Γ_γ. To within the accuracy available for their compilation (approximately 20 percent), Γ_γ appears to show with a few exceptions a uniform slow decrease with mass number but little variation from resonance to resonance in a single isotope and no dependence upon the spin of the target nucleus or level spacing in the compound nucleus.

It has been the program of the BNL crystal spectrometer group, however, to improve the accuracy with which these parameters are known in a limited energy region. Particular emphasis has been placed upon isotopes for which level spacings are sufficiently small to yield results for more than one resonance.

More than two years ago, one of us (VLS) observed that the first two levels in $In^{115}(n,\gamma)In^{116}$ showed rather large differences in the ratio of ground state to isomeric state activity produced upon irradiation with monoenergetic neutrons at each of the respective levels. The gamma-ray multiplicity upon capture in this isotope is known[4] to be approximately 3.3. These measurements imply that the mode of de-excitation of each virtual state is rather considerably different. This fact may be reflected in different partial widths for decay from the parent state, these partial widths adding to give variations in the total radiation width. Differences of this kind are not predicted by present theory in regions where the statistical model is expected to apply.[5]

Interest in proper statistical factors which obtain in both partial and total widths has recently arisen.[6] Precision measurements of total widths as a function of total angular momentum are involved in comparisons with theory. Such questions, however, cannot be fully answered on the basis of total-width measurements, alone; the very difficult partial-width measurements for individual transitions are also necessary.

When this work was undertaken, sufficiently good resolution was not available to permit the analysis of the In^{116} resonances to the precision desired here, even though a great deal of work has been reported previously.[7] Consequently, it was decided to study europium, the element with the closest spacing known at the time. In the course of activation studies to assign the known resonances[8] isotopically, Wood observed[9] that the same type of variations of isomeric state activities as occur in In^{116} are present when activations are made at selected resonances. A relative population ratio, R, for each level can be defined as the fraction of the compound nuclei which decay to the isomeric state relative to the fraction

† Research performed under contract with the U. S. Atomic Energy Commission.

[1] J. M. Blatt and V. F. Weisskopf, *Theoretical Nuclear Physics* (John Wiley and Sons, Inc., New York, 1952), Chap. XII.

[2] See *Neutron Cross Sections*, Atomic Energy Commission Report AECU-2040 (Office of Technical Services, Department of Commerce, Washington, D. C., 1952) for a compilation of the voluminous data available.

[3] D. J. Hughes and J. A. Harvey, Nature 173, 942 (1954).

[4] C. O. Muehlhause, Phys. Rev. 79, 278 (1950).

[5] Reference 1, p. 648.

[6] D. J. Hughes, Phys. Rev. 94, 740 (1954).

[7] C. P. Baker and R. F. Bacher, Phys. Rev. 59, 332 (1941); Bacher, Baker, and McDaniel, Phys. Rev. 69, 443 (1945); B. D. McDaniel, Phys. Rev. 70, 832 (1946); W. W. Havens, Jr., and J. Rainwater, Phys. Rev. 70, 154 (1946); Havens, Wu, Rainwater, and Meaker, Phys. Rev. 71, 165 (1947); Borst, Ulrich, Osborne, and Hasbrouch, Phys. Rev. 70, 557 (1946); V. L. Sailor and L. B. Borst, Phys. Rev. 87, 161 (1952).

[8] Sailor, Landon, and Foote, Phys. Rev. 93, 1292 (1954).

[9] R. E. Wood, Phys. Rev. 95, 453 (1954).

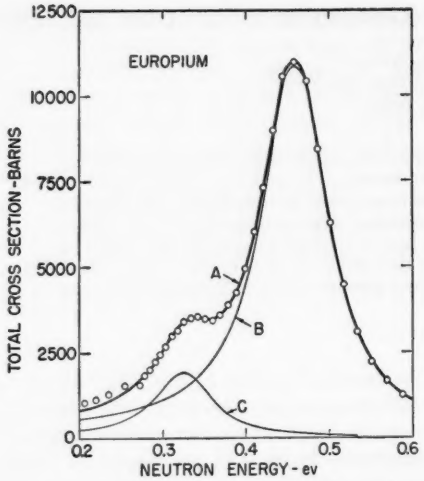

FIG. 1. Total cross section measured for the 0.327-ev and 0.461-ev resonances in europium. Curve *A* is the experimental curve, while curves *B* and *C* are calculated from parameters of the text.

from one arbitrary level. Wood's results were consistent with there being two different values of R in the negative energy level and first three virtual levels of Eu^{152}. We decided then to re-examine our measurements and analysis of the first two positive energy levels and to rerun with greater accuracy the third level.

MEASUREMENTS

The details of total cross-section measurements with the BNL crystal spectrometer have been published[10]

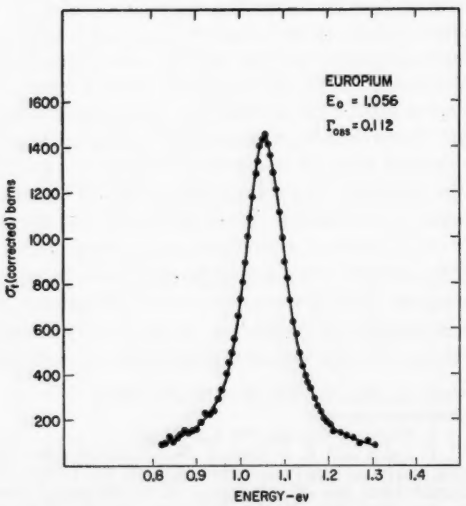

FIG. 2. Total cross section measured for the 1.056-ev resonance in europium, corrected for the presence of other resonances up to 4 ev.

[10] L. B. Borst and V. L. Sailor, Rev. Sci. Instr. 24, 141 (1953).

previously. The europium samples were the same as used in reference 8 and detailed description of sample preparation and purity can be found there. The total cross section as measured for europium is shown in Fig. 1 of reference 8. The neutron monochromators used were NaCl (240) and Be ($12\bar{3}1$). The region between 0.3- and 0.4-ev neutron energy was examined, using both crystals to give a region of overlapping energy scale. The energy resolution of the spectrometer during the europium runs was such as to make resolution corrections negligible for the 0.327- and 0.461-ev resonances and approximately 40 barns at the peak of the 1.056-ev resonance. A detailed plot of the data for the first and second resonances is shown in Fig. 1, using a linear ordinate scale, since this type of plot is needed in the analysis section. Similarly, the third resonance is shown in Fig. 2. Single points near the peak of each resonance were run with considerably higher counting statistics than other points, but, in most cases, the statistical inaccuracy of each point is less than the size of the plotted points.

Sample preparation for indium was carried out according to standard procedures. Six high-purity samples actually were run at the large 1.456-ev resonance. Each of these was in foil form except for the two thinnest used in the region of the peak of the resonance. These were deuterated indium nitrate dissolved in D_2O. Four foils were run at the weaker 3.85-ev resonance. In all cases, the sample thickness is known to 1 percent or better. The resulting data are shown plotted in Figs. 3 and 4. These data represent averages over at least three runs, with the points at the peak of the resonances being particularly significant statistically. The resolution of the instrument was very significantly improved just prior to running these data. Details of the improvement will be published shortly, but it has been achieved by a greatly improved collimator design utilizing a series of narrow, closely spaced slits in place of a single slit. The figure of merit for resolution, expressed in angular measure is approximately 1.6 minutes of arc or, in units used for velocity selectors, 0.17 μsec/m. The resolution correction is negligible at the 1.456-ev resonance, being approximately 0.3 percent in cross section. A resolution correction of 25 barns or approximately 3 percent in cross section is necessary at the peak of the 3.85-ev resonance.

ANALYSIS

The analysis of measured total cross-section data for resonance parameters to the precision required for this study necessitates careful consideration of the role of Doppler effect. Bethe and Placzek[11] have modified a simplified, one-level Breit-Wigner equation for the case where the target atoms can be treated as free, having velocities distributed according to a Maxwellian distribution. A direct experimental test of this treatment has

[11] H. A. Bethe and G. Placzek, Phys. Rev. 51, 462 (1937); H. A. Bethe, Revs. Modern Phys. 9, 140 (1937).

been previously reported.[12] The effective cross section for neutrons of energy E near the resonance energy E_0 is

$$\sigma(t,E)=\sigma_0[E_0/E]^{\frac{1}{2}}\psi(t,x),$$

where

$$\psi(t,x)=\tfrac{1}{2}t^{-\frac{1}{2}}\pi^{-\frac{1}{2}}\int_{-\infty}^{\infty}\frac{\exp[-\frac{1}{4}t^{-1}(x-y)^2]}{1+y^2}dy \qquad (1)$$

and

$$x\equiv(E-E_0)/\tfrac{1}{2}\Gamma,\quad y\equiv(E'-E_0)/\tfrac{1}{2}\Gamma,\quad t^{\frac{1}{2}}\equiv\Delta/\Gamma.$$

The so-called Doppler width of the resonance is $\Delta=2(E_0kTm/M)^{\frac{1}{2}}$, where m is the neutron mass, M the mass of the resonant isotope, and kT the "atom temperature" in energy units. $\psi(t,x)$ has been evaluated numerically[13] over a region of t and x which obtains for

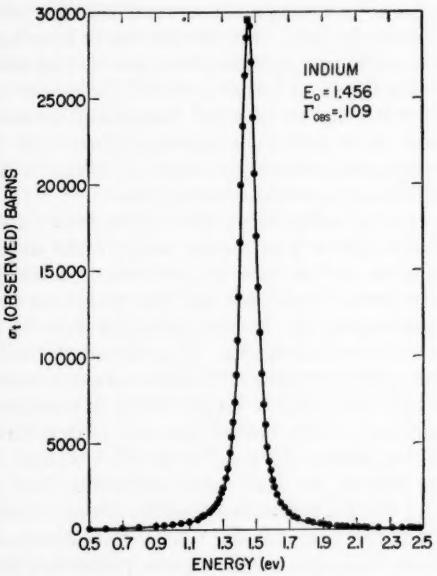

FIG. 3. Total cross section measured for the 1.456-ev resonance in indium. The point noted by ■ is point of especially high statistical accuracy.

most cases of physical interest in the energy region considered here. A plot of the function is shown in Fig. 5 for typical values of t used in these data. It is immediately evident that a shape analysis which is based on an unmodified Breit-Wigner equation is only possible in regions of large x where $\psi(t,x)$ approaches the Breit-Wigner form $1/(1+x^2)$. A point-by-point shape analysis using an analytic form for ψ is not, at present, possible in the region of the center of a resonance. Consequently, a form of area analysis was developed which, combined with a shape-type analysis applied to the maximum and half-maximum points, permits an accurate evaluation of

[12] H. H. Landon, Phys. Rev. **94**, 1215 (1954).

[13] For a tabulation of $\psi(t,x)$ see M. E. Rose *et al.*, Brookhaven National Laboratory Report BNL-257 (T-40) (unpublished); also Rose, Miranker, Leak, Rosenthal, and Hendrickson, Westinghouse Atomic Power Division Report SR-506 (unpublished).

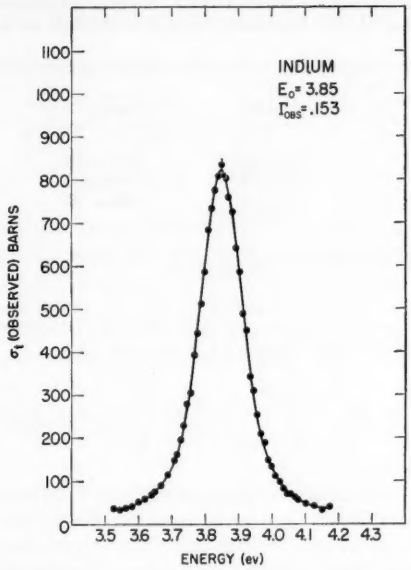

FIG. 4. Total cross section measured for the 3.85-ev resonance in indium. The point noted by ■ is point of especially high statistical accuracy.

the individual parameters σ_0 and Γ. From these, Γ_γ can be obtained with only a negligible error caused by uncertainty in g, the statistical factor resulting from spin.

The area method evolves from the fact that, if one neglects the $1/v$ part of the cross section,

$$\int_{-\infty}^{\infty}\sigma(E)dE=\frac{\Gamma}{2}\int_{-\infty}^{\infty}\sigma_0\psi(t,x)dx=\pi\sigma_0\frac{\Gamma}{2}.$$

Since $\psi(t,x)\to 1/(1+x^2)$ in the wings of the resonance, this integration can be made between definite limits. As can be seen in Fig. 5, for the cases dealt with here, one need integrate only to values of $x\simeq 5$ to preserve approximate equality. Once explicit limits are speci-

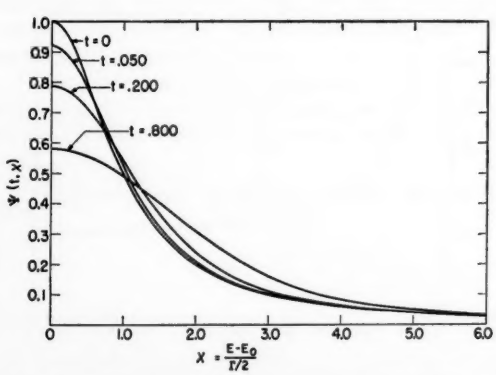

FIG. 5. Numerically evaluated $\psi(t,x)$ *versus* x for values of t typical of those obtaining in this investigation.

TABLE I. Resonance parameters for elemental europium resonances. $(\sigma_0\Gamma^2)_w$ is the value obtained from a "wing fit." Γ_γ is calculated, assuming $g=\frac{1}{2}$. The population ratio, R, is the ratio on a relative scale of isomeric state to ground-state activity following neutron capture.

Energy ev	$\sigma_0\Gamma$ barns-ev	σ_0 barns	Γ mv	Γ_γ mv	$\sigma_0\Gamma^2$ barns-ev^2	$(\sigma_0\Gamma^2)_w$ barns-ev^2	R
-6×10^{-4} [a]			67[a]	67[a]			0.24±0.03[b]
0.327	130±20	1840±150	70±10	70±10			0.19±0.02[b]
0.461	1065±15	11 500±300	93± 3	93± 3	99±5	102	0.11±0.03[b]
1.056	154± 3	1640± 30	94± 3	94± 3			0.08±0.03[b]

[a] N. Holt, see reference 14.
[b] R. E. Wood, Phys. Rev. 95, 453 (1954).

fied, the evaluation of $\int_{x_1}^{x_2}\psi(t,x)dx$ can be carried out numerically, thus yielding a correction to

$$\int_{E_1}^{E_2}\sigma(E)dE=\frac{\Gamma}{2}\int_{x_1}^{x_2}\frac{1}{1+x^2}dx=\sigma_0\frac{\Gamma}{2}[\tan^{-1}x_2+\tan^{-1}x_1],$$

which, in all cases, was 1 percent or less. For the energy regions involved, neglect of asymmetries in the resonances due to scattering interference or $1/v$ terms was negligible. This analysis yields, then, the product $\sigma_0\Gamma$ but requires an initial choice of Γ to specify x. It is, however, insensitive to that choice.

Since we are observing directly by experiment the ψ function, we can use the maximum and half maximum points to yield an independent choice of σ_0 and Γ. A plot of Γ_{obs}/Δ *versus* Δ/Γ obtained directly from the ψ tables is shown in Fig. 6. A measurement of the width at half-maximum, Γ_{obs}, and calculation of Δ gives directly a choice of Γ. The accuracy of this determination depends on the region of the curve involved, but for $\Delta/\Gamma<1$, which is an extreme choice for these studies, accuracy to a few percent is possible. This choice of Γ, used in the above area method, can also be used to obtain σ_0 from the measured peak cross section, σ_{max}^{obs}, since $\sigma_{max}^{obs}/\psi(t,0)=\sigma_0$. Dividing the $\sigma_0\Gamma$ obtained from the area by this σ_0 yields a Γ which can be compared with the choice originally made. A reiteration of the scheme can then be carried out if necessary.

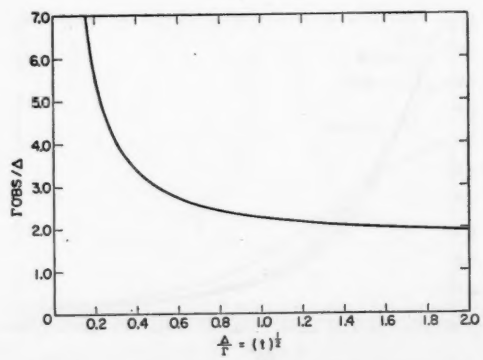

FIG. 6. Γ_{obs}/Δ *versus* Δ/Γ as obtained directly from table of numerically evaluated $\psi(t,x)$.

The method of analysis outlined previously has numerous practical advantages when applied to properly chosen resonances. Since the operations are performed on cross section, resolution corrections must be kept small, but there is the advantage that several carefully chosen samples can be used. This permits one to keep experimental sample transmissions, from which cross sections are obtained, within narrow specified limits, thus minimizing errors due to improper background determination and beam order contamination corrections. Also, good statistical accuracy for cross section can be maintained without excessive counting times.

As a further independent check of the results, a shape analysis of the data in the far wings of the strongest resonance in each element was performed. A discussion of the important features of this type of analysis is to be published shortly. It involves fitting the data by least squares to a Breit-Wigner equation which includes scattering and scattering interference as well as capture. Since the cross section in the wings is sensitive essentially only to the combination $\sigma_0\Gamma^2$ of parameters, it is just this product which can be reliably obtained. Only limited regions of data were sufficiently free from Doppler effect and contributions of nearby resonances to permit this analysis. The nearby resonances can be taken into account with adequate precision but any Doppler broadening will tend to raise the resulting $\sigma_0\Gamma^2$. The results are taken, therefore, as an upper limit to the probable choice of parameters.

RESULTS

The parameters which result from the europium analysis are shown in Table I. Included in this table are the results[14] recently obtained at JENER, Kjeller, Norway, for the negative energy resonance. The analysis of each resonance was carried out after a suitable correction for the presence of all other resonances up to 4 ev. The analysis of the weak first resonance is particularly difficult because of the proximity of the strong second resonance. The previously reported[8] shape analysis of these resonances was of considerable assistance in the initial steps of this analysis. The area method was extended to include both resonances and the integration between definite limits carried out by measuring graphi-

[14] N. Holt, Bull. Am. Phys. Soc. 30, No. 1, 23 (1955).

cally the area with a planimeter. The area resulting from integration under the large resonance alone was then obtained using the shape of the resonance on the high energy side as the first approximation to its true shape. Subtraction of the resulting areas gives an initial set of parameters for the weak resonance. A consequent readjustment and reiteration was then possible. The errors in the determination of the parameters for the weak resonance are, however, considerably greater than for the strong resonance. The results of a wing fit to a portion of the data on the high energy side of the strong resonance is also listed. It can be seen that the agreement is good to approximately 3 percent, with the wing fit being somewhat larger, as expected.

The results for the third resonance are seen to yield a Γ_γ which is within 1 percent of that from the second. It should be noted that the value of the population ratio, R, for these two resonances is the same within experimental error. The results from the first resonance are less precise, but it should be observed that Γ_γ appears definitely to be lower than for the second and third resonances. It is also significant that the resulting Γ_γ for the negative energy resonance is in agreement with this value, particularly since R for these two resonances also appears to be the same.

The results for the two indium resonances are shown in Table II. In this case, it is only possible to say that the total radiation widths, Γ_γ, for each resonance are different. It should be pointed out that these widths are considerably smaller than previously suspected.[7] The importance of Doppler effect is particularly evident here, as can be seen by noting the difference between the observed width Γ_{obs} and the true width, Γ. The agreement with the wing fit results is not as good in this case. This is undoubtedly due to remaining Doppler effect, which is actually present to 4 percent for a value of $x=6$. A final check, however, can be made using the thermal absorption cross section, $\sigma_{th}=191\pm5$ barns, as reported by Pomerance.[15] The thermal absorption cross section calculated using the parameters of Table II is 197 barns.

The estimation of errors in the quoted parameters has been made, taking into consideration not only errors of measurement but also internal consistency of independent determinations. It is felt that the differences in quoted Γ_γ are real, since the quoted errors are absolute errors and would be of the same type in each measurement, therefore making observed differences between parameters significant.

[15] H. Pomerance, Phys. Rev. 83, 641 (1951).

TABLE II. Resonance parameters for elemental indium. $(\sigma_0\Gamma^2)_w$ is the value obtained from a "wing fit." Γ_γ is calculated, assuming $g=\frac{1}{2}$.

Energy ev	$\sigma_0\Gamma$ barns-ev	σ_0 barns	Γ mv	Γ_γ mv	$\sigma_0\Gamma^2$ barns-ev^2	$(\sigma_0\Gamma^2)_w$ barns-ev^2
1.456	2880±50	38 500±1000	75±2	72±2	216	221
3.85	103± 4	1270± 40	81±4	81±4		

CONCLUSIONS

Since the radiation widths in europium fall in two groups and the population ratios of the resonances of the same width are the same, the resonances appear to be of two distinct types. The obvious inference is that they belong to the two different spin states which are possible. A proof of this inference by means of the required scattering measurements would be very difficult at the present time because of the small Γ_n's associated with these resonances. Work in this field is rapidly progressing, however, and results in this case may not be impossible in the near future.

If the spin states are different, it appears that there is a "spin memory" associated with the gamma-ray cascade process to the isomeric and ground states; i.e., depending upon in which spin state the compound nucleus is formed, decay to the lowest states is sufficiently dissimilar to populate the final states differently. It may, perhaps, be significant that the ratio of radiation widths is greater in the case of the lower spin target nucleus.

It is not possible, at the present time, to say what the origin of such an effect can be because of the lack of a suitable model. Weisskopf has made calculations of the transition probability between two nuclear states based on the independent particle model.[1] He has extended these calculations to estimates of absolute total widths for the case of neutron capture, using a statistical model of level structure. [See Eq. (7.23), reference 1.] Any dependence of level spacing upon spin in this equation should cancel if the dependence is of the type one might expect in a statistical model. If the configurations involved in the initial states are complex such that $E1$ radiation can predominate,[16] then any differences arising through the statistical factors associated with this equation[6] should also be small.

These studies are being continued with emphasis being placed on the lower-spin target nuclei; in particular, on adjacent even-even and even-odd isotopes of a single element.

[16] B. B. Kinsey and G. A. Bartholomew, Phys. Rev. 93, 1260 (1954).

Model for Asymmetric Fission*

R. D. HILL
Physics Department, University of Illinois, Urbana, Illinois
(Received December 8, 1954)

On the basis of shell effects, asymmetric fission is attributed to symmetrical division except for a non-fissionable core. Distributions of fission-fragment yields, *vs* fragment charges and masses, are obtained from simple statistical considerations of the division.

THE mechanism of asymmetric fission, as distinct from that of fissionability, does not appear as yet to have been clearly explained. As is well known, the customary analysis[1] leads to the conclusion that the two fission fragments should be of approximately equal mass. In order to resolve this disagreement with experimental facts it has been suggested on several occasions[2] that the binding energies of the fission fragments are affected by nuclear shell-structure effects and the most favorable division is an asymmetrical one.[3]† Hill and Wheeler,[4] however, consider that neither energy release nor shell-structure effects constitute an explanation of asymmetric fission. Another explanation[5] of asymmetrical fission based on the variation of barrier penetration with fission fragment mass has also been considered by Hill and Wheeler as untenable.

In the following note, we have looked into the possibility that there are still shell-structure effects but that their influence on fission might be more direct than simply affecting binding energies. We have assumed that even in the deformed nucleus the shells persist and preserve a degree of independence from each other. The act of fission is looked upon, once the critical deformation of the nuclear surface has been reached, as a symmetrical severing of the individual shells except for a core of inner shells. This core does not necessarily have to be the same group of inner shells in all fissions, but may vary somewhat according to the energy available in the fission process. The final stage of fission occurs when the core moves with one half of the nucleons of the outer shells.[6]

As, according to the present model, fission starts out symmetrically and continues symmetrically up to the point at which the core is reached, it would seem to remove the criticism raised by Hill and Wheeler that it is hard to see how a nucleus would know in the transition stage the potential shell structure of the not-yet-formed products.

An interesting aspect of the fission problem, if one is to accept the assumption of independence of the shells, is the threshold energy required for fissioning of intermediate shell-cores within the nucleus. If we employ the relationship derived by Hill and Wheeler[4] for the maximum energy of deformation, we obtain for the fission threshold of $_{20}Ca^{40}$ a value of 167 Mev. It is significant that this energy is greater than the observed U^{235} symmetrical fission energy of ~150 Mev and is identical with the observed maximum energy from asymmetrical fission.[6a] The value of the fission threshold energy for $_{20}Ca^{40}$ should be compared with those for neighboring larger closed shells, such as $_{28}Ni^{56}$ and the hypothetical $_{50}Sn^{100}$, for which the calculated values are 120 and 35 Mev, respectively.‡ It seems plausible, therefore, that fission takes place beyond the $Z=N=50$ shell and up to the $Z=N=20$ core.

MASS DISTRIBUTION OF FRAGMENTS

We assume that the fissioning nucleus of $_{92}U^{235}$ is not a uniform liquid droplet but rather a series of neutron and proton shells conforming[7] to the j-subshells of the spin-orbit coupling model.[8]

One might expect on the basis of a literal interpretation of the shell model, that if the nucleons were confined to subshells in accordance with Pauli's principle, then

* Assisted by the joint program of the Office of Naval Research and the U. S. Atomic Energy Commission.

[1] N. Bohr and J. A. Wheeler, Phys. Rev. **56**, 426 (1939).

[2] M. G. Mayer, Phys. Rev. **74**, 235 (1948); G. C. Wick, Phys. Rev. **76**, 181 (1949); K. H. Kingdon, Phys. Rev. **76**, 136 (1949); G. Gamow and C. L. Critchfield, *Theory of the Atomic Nucleus* (Oxford University Press, London, 1949); L. Meitner, Nature **165**, 561 (1950); T. D. Newton, Phys. Rev. **87**, 187 (1952); P. Fong, Phys. Rev. **89**, 332 (1953).

[3] After this paper was written, the author's attention was directed to a discussion by D. Curie of asymmetric fission based on a nuclear model of a core of 50 protons and 82 neutrons, together with a corona of the remaining nucleons [D. Curie, Compt. rend. **235**, 1286 (1952); **237**, 1401 (1953)].

† *Note added in proof.*—A model of asymmetric fission rather similar to the one being presently discussed, but not based on shell-structure ideas, was given by P. F. Gast in 1947 [Phys. Rev. **72**, 1265 (1947)]. The author is indebted to the editor for drawing attention to this note.

[4] D. L. Hill and J. A. Wheeler, Phys. Rev. **89**, 1102 (1953).

[5] S. Frankel, J. Phys. (U.S.S.R.) **10**, 533 (1946); E. Bagge, Z. Naturforsch. **2a**, 565 (1947).

[6] A name for this model which has been suggested to us is "peach" model.

[6a] D. C. Brunton and G. L. Hanna, Can. J. of Research **28A**, 190 (1950); R. B. Leachman, Phys. Rev. **87**, 444 (1952).

‡ *Note added in proof.*—These fission threshold energies, evaluated for "free surface" nuclei, are clearly maximum values. The observed fission energy is similarly a maximum value as it refers to the completely separated fragments. Both values are undoubtedly modified in a deformed and incompletely fissioned nucleus.

[7] See, however, the arguments of level order in a deformed nucleus; reference 4.

[8] M. G. Mayer, Phys. Rev. **75**, 1969 (1949); Haxel, Jensen, and Suess, Phys. Rev. **75**, 1766 (1949); P. F. A. Klinkenberg, Revs. Modern Phys. **24**, 63 (1952).

the nucleons in a particular subshell would not be permitted to move randomly throughout the whole shell. Rather, it is plausible that only those nucleons which at the instant of fissioning are within the region of the neck are allowed to distribute statistically between the two fragments.

If the partition width is of the order of a nucleon diameter, it is readily estimated that the fraction of statistically-uncertain nucleons in a subshell is $\sim\Delta R/R$, where ΔR is of the order of a nucleon radius and R is of the order of the shell radius. This fraction is therefore of the order of $N^{-\frac{1}{2}}$, where N is the total number of nucleons enclosed within a particular j-subshell.

Estimates of the numbers of neutrons and protons in the various subshells of $_{92}U^{235}$ are given in Table I.[9] The neutrons and protons are treated independently and the total number of neutrons distributed between the two fragments is assumed to be 142, two neutrons being assumed lost in the fission process.

In the calculation it is assumed that, with the exception of the statistically uncertain nucleons, the subshells tend to divide equally. The statistical probability of r uncertain nucleons of a particular subshell which choose to go with one fragment and of $(n-r)$ uncertain nucleons which choose to go with the other fragment is assumed to be $\binom{n}{r}$. By continuing the division of the subshells down to the innermost $_{20}Ca^{40}$ core, it can readily be shown that the probabilities P_N and P_P of obtaining N neutrons in one fragment out of 29 uncertain neutrons, and P protons in one fragment out of 19 uncertain protons, respectively, are those given in Table II.

TABLE I. Numbers of neutrons and protons in the j subshells of $_{92}U^{235}$, and estimates of the numbers of statistically-uncertain neutrons and protons in fission.

Nuclear subshell	Numbers of neutrons	Uncertain neutrons	Numbers of protons	Uncertain protons
$7i$ 11/2	6	1		
$6g$ 9/2	10	2		
$7i$ 13/2	14	3		
$4p$ 1/2	2	0		
$4p$ 3/2	4	1		
$5f$ 5/2	6	1		
$6h$ 9/2	10	2	10	2
$5f$ 7/2	8	2		
$3s$ 1/2	2	0	2	0
$4d$ 3/2	4	1	4	1
$6h$ 11/2	12	3	12	3
$5g$ 7/2	8	2	8	2
$4d$ 5/2	6	2	6	2
$5g$ 9/2	10	3	10	3
$3p$ 1/2	2	0	2	0
$4f$ 5/2	6	2	6	2
$3p$ 3/2	4	1	4	1
$4f$ 7/2	8	3	8	3
20–20 core	20		20	

[9] The levels are probably not in the order given by a spherical nuclear shell model. However, the numbers of uncertain nucleons from one level to another are small and much the same no matter what levels are involved. Moreover, the distributions are not very susceptible to the order in which the numbers are taken.

TABLE II. Probability distributions of obtaining numbers of neutrons and protons out of statistically uncertain neutrons and protons in fission.

Neutron distribution N	Neutron distribution $P_N \times 2^{29}$	Proton distribution P	Proton distribution $P_P \times 2^{19}$
0 or 29	1	0 or 19	1
1 or 28	29	1 or 18	19
2 or 27	406	2 or 17	171
3 or 26	3654	3 or 16	969
4 or 25	23 751	4 or 15	3876
5 or 24	118 755	5 or 14	11 628
6 or 23	475 020	6 or 13	27 132
7 or 22	1 560 780	7 or 12	50 388
8 or 21	4 292 145	8 or 11	75 582
9 or 20	10 015 005	9 or 10	92 378
10 or 19	20 030 010		
11 or 18	34 597 290		
12 or 17	51 895 935		
13 or 16	67 863 915		
14 or 15	77 558 760		

The probability, P_A, of obtaining a fragment of particular mass value A will then be obtained by summing over all possible ways of obtaining a constant value of a particular $(P+N)$ sum. The mass values A_1 and A_2 of the two fragments will be given by

$$A_1=(20+26.5+P)+(20+46.5+N)=113+(P+N),$$
$$A_2=(26.5+19-P)+(46.5+29-N)=121-(P+N).$$

The calculated values of P_A are shown plotted as full circles in Fig. 1, where the heavy curve represents the experimental distribution[10] for the slow-neutron fission of U^{235}. The points have been normalized to the experimental curve at the maximum yields.

If we compare the calculated points with the experimental curve, two features are in evidence. Firstly, the calculated peaks occur at approximately the correct mass values and secondly, the gross fall-off in yield fits the experimental curve closely. The calculated widths of the yield curves, however, do not agree with experiment. Nevertheless, an adequate fit between calculation and experiment can be achieved by adding to the calculated full circle points a similar set of yield curves displaced slightly from the calculated ones. The second set of curves is indicated in Fig. 1 by the triangle points which have been obtained simply by subtracting the full circle points from the experimental curve. It is significant that the peaks of the subsidiary yield curves are approximately 56 mass numbers apart and also have rather closely the same form as the initially calculated curves. It would seem plausible that the subsidiary curves arise from symmetrical division of the $_{92}U^{235}$ nuclei only to the $_{28}Ni^{56}$ core.

The small, though significant, fission yield observed in the symmetrical trough of the yield curve cannot evidently be attributed to an overlapping of the fission yields of the $_{20}Ca^{40}$-core type. Although accurate subtraction of the calculated points from the experimental

[10] Plutonium Project Report, Revs. Modern Phys. **18**, 513 (1946).

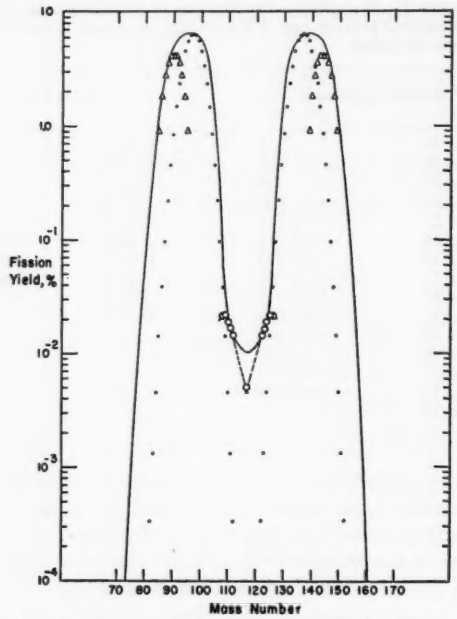

FIG. 1. U^{235} slow-neutron fission yields *vs* mass number. The full curve represents the smoothed experimental data. The full points represent the calculated probabilities, P_A, for the $_{20}Ca^{40}$-core type of fission. Triangle points are the differences between the curve and full points and probably represent the $_{28}Ni^{56}$-core type of fissions. Similarly the open-circle points and dotted curve probably represent the $_8O^{16}$-core type of fissions.

curve cannot be made along the steep sides of the trough, approximate subtractions near the base are shown by open circle points in Fig. 1. It seems possible that these subsidiary curves, which are of the order of 16 mass numbers apart, might be attributed to symmetrical fission processes occurring to the $_8O^{16}$ core. According to the analysis indicated in Fig. 1, this would occur at thermal neutron excitation energies, only to the extent of a few tenths of a percent of the normal fissions. At higher energies of excitation and deformation, it would seem feasible that the fraction of $_8O^{16}$-core type of fissions might increase, especially at the expense of the $_{28}Ni^{56}$-core type of fissions. Some evidence in support of these changes in the form of the fission yield curve appears to exist in experiments with higher energies of excitation.[11,12]

CHARGE DISTRIBUTION OF FRAGMENTS

The distribution of protons which might be apportioned between the two fragments is already available in Table II. Unfortunately, to date, it does not appear to have been experimentally feasible to obtain accurate data on the direct yields of particular Z-fragments. However, some notion of the distribution may be obtained from the known yields of radioactive chains and the probable decay lengths of these chains.

According to Glendenin, Coryell, and Edwards[13] and Pappas,[14] the most probable chain length of the U^{235} fragments is approximately three charge units. In Fig. 2, the experimental yields[10] of the chains from slow-neutron fission of $_{92}U^{235}$ are plotted *vs* the atomic numbers which are three units removed from the stable end-products of the chains. (In order to improve the continuity of available data, both light and heavy fragments have been superimposed on the same plot.)

If the Z-distributions for different chains are the same, and it will be shown later that this is very likely the case, then the points of Fig. 2 should represent approximately the Z-yield curve of the directly-produced fragments. The full curve of Fig. 2 represents the calculated distribution obtained from the values of P_P of Table II. This curve has been normalized and moved laterally a small amount to fit the experimental points at the peak. The calculated peaks actually occur at $Z=36$ and $Z=56$, if one assumes only 20–20 core type of

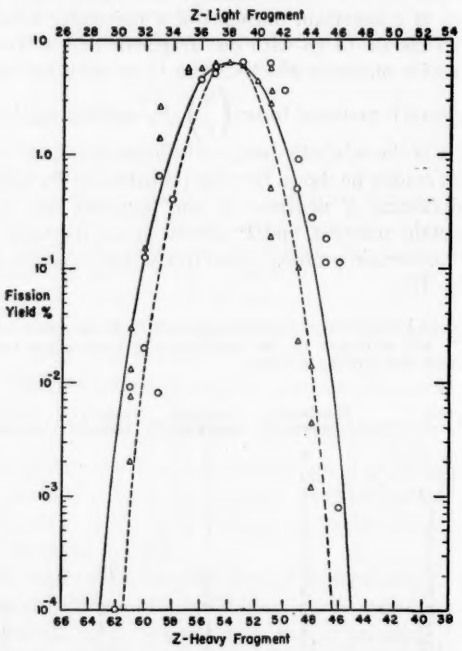

FIG. 2. U^{235} slow-neutron fission yields *vs* atomic number. The full curve represents the calculated probability distribution, P_P, for direct production of fragments of atomic number Z. The open circle points refer to experimental yields of light fragments (upper Z-scale). The triangle points refer to experimental yields of heavy fragments (lower Z-scale). The dotted curve represents the probability distribution, P_Z, for fragments of a particular atomic mass chain.

[11] R. W. Spence, Brookhaven National Laboratory Report, No. C-9, 1949 (unpublished).
[12] R. A. Schmitt and N. Sugarman, Phys. Rev. 89, 1155 (1953).
[13] Glendenin, Coryell, and Edwards in *Radiochemical Studies: The Fission Products* (McGraw-Hill Book Company, Inc., New York, 1951), Paper No. 52, National Nuclear Energy Series, Plutonium Project Record, Vol. 9, Div. IV.
[14] A. C. Pappas, Massachusetts Institute of Technology Technical Report No. 63, 1953 (unpublished).

fission. The experimental peaks occur at approximately $Z=38$ and $Z=54$. Apart from this small shift, the agreement of the calculated curve with experiment is excellent.[15]

In obtaining the probability distribution of fission fragments of mass value A, the probability distributions of fission fragments of atomic charge Z for a particular value of A were also necessarily obtained. In Fig. 3, these distributions P_Z are shown plotted *vs* atomic charge Z for various values of the atomic mass A. Only those values of A, between 126 and 136 for the heavy fragment and between 98 and 108 for the light fragment, have here been considered as largely representative of the 20–20 core type of fission for which the calculations were carried out. All curves of Fig. 3 are seen to be of the same form and width, which is somewhat narrower than the direct-Z distribution already considered. For comparison, the Z-distribution curve for constant A is shown by the dotted curve in Fig. 2. It should be pointed out that the calculated Z-distribution for constant A is still wider than the distribution experimentally evaluated by Pappas.[14]

The calculated yields of particular Z-fragments as fractions of the total chain yields of fragments of the same A, can now be compared with the fractional yields determined from experiment.[14] For nuclides which would appear to result largely from the 20–20 core type of fission, the above comparison is made in Table III. The fission-fragment yield, P_Z, is obtained for a particular Z from a curve of a particular A in Fig. 3. The total chain yield, P_A, is obtained from the same curve

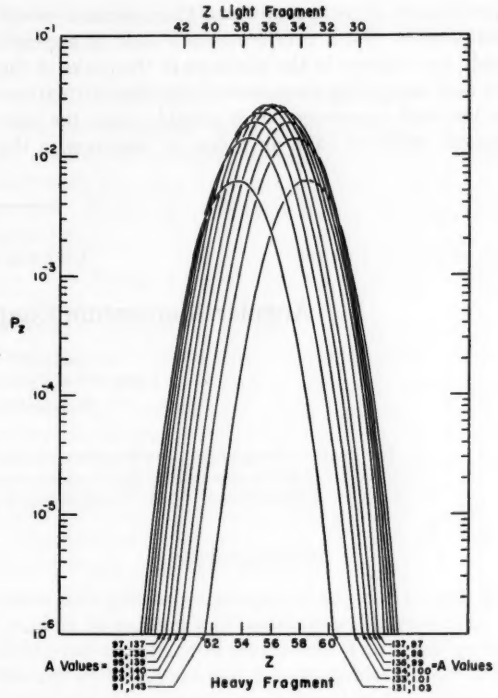

FIG. 3. Calculated probability distributions, P_Z, of fragments of atomic numbers Z, as a function of Z, for various atomic mass values A of particular radioactive chains.

by summing the yields for all Z. From Table III, it is seen that there is reasonable agreement between calculated and experimental fractional yields.

Another point of contact between calculation and experiment can be made by comparing the most probable chain lengths for constant values of A. For the A values applicable to the present calculations, the most probable values of the charges, Z_P, of the fragments can be obtained immediately from Fig. 3. The values of Z_A, the charges of the end-products of the chains, have been taken from the report by Pappas.[14] The calculated lengths of the chains, Z_A-Z_P, are then given in Table IV. It is seen that for the light fragment of the listed A-values, the chain length is approximately one unit, and for the heavy fragment of the listed A-values, the chain length is approximately six to seven units. Experimentally, both of these lengths are believed to be

TABLE III. Comparison of calculated and experimental values of the fractional chain yield of a particular Z-fragment.

Nuclide	A	Z	Fractional yield (expt.)	P_A (calc.)	P_Z (calc.)	Fractional yield (calc.)
Nb^{96}	96	41	9×10^{-5} 4×10^{-3}	1.1×10^{-1}	1.6×10^{-4}	$1.45\times10^{-}$
Te^{131}	131	52	4×10^{-1}	2.6×10^{-2}	4.0×10^{-3}	1.54×10^{-1}
Te^{133}	133	52	3.6×10^{-1}	5.95×10^{-2}	5.0×10^{-3}	0.84×10^{-1}
I^{134}	134	53	1.6×10^{-1}	7.93×10^{-2}	1.1×10^{-2}	1.4×10^{-1}
Xe^{135}	135	54	5×10^{-2}	9.73×10^{-2}	1.8×10^{-2}	1.85×10^{-1}
Cs^{136}	136	55	1.5×10^{-2} 9×10^{-4}	1.1×10^{-1}	2.4×10^{-2}	2.2×10^{-1}
La^{140}	140	57	$<3\times10^{-2}$	7.93×10^{-2}	1.8×10^{-2}	2.2×10^{-1}

[15] It should be pointed out however that no account has been taken of the rather smaller possibility of 28–28 core type of fission affecting the Z-distribution. The agreement of the proton distributions with experiment would seem to indicate that the proton shells are generally split right down to the $_{20}Ca^{40}$ core. In view of the alternative $_{28}Ni^{68}$ mode of fission, already indicated from the mass distribution analysis, it would thus seem admissible that the proton and neutron shells down to $_{20}Ca^{40}$ are not necessarily fissioned to the same extent, and that the width of the A-distribution curve could be taken up by an indefiniteness in the splitting of only the neutron shells.

TABLE IV. Probable chain lengths in U^{235} fission.

Heavy fragment	A	131	133	135	137	139	141	143
	Z_P	53.5	54.5	55.5	56.0	57.0	57.5	58.5
	Z_A	54	55	56	56.5	57.5	58.5	60
	(Z_A-Z_P)	0.5	0.5	0.5	0.5	0.5	1.0	1.5
Light fragment	A	91	93	95	97	99	101	103
	Z_P	33.5	34.5	35.0	36.0	36.5	37.5	38.5
	Z_A	40	41	42	43	44	44	45
	(Z_A-Z_P)	6.5	6.5	7.0	7.0	7.5	6.5	6.5

approximately three to four units. Thus, again, it would seem possible that a complementary shift of approximately two charges in the positions of the peaks of the light and heavy fragments would bring the calculations into line with experiment. It is possible, since the light fragment tends to have an excess of neutrons in the division, that some allowance for neutron-proton interactions might be able to account for this shift.

It is a pleasure to acknowledge the valuable discussions on these problems with R. B. Duffield. Thanks are also due A. T. Nordsieck and J. Weneser for criticism of the manuscript.

PHYSICAL REVIEW VOLUME 98, NUMBER 5 JUNE 1, 1955

Angular Momentum Coupling in Deuteron Reactions*

T. AUERBACH† AND J. B. FRENCH
University of Rochester, Rochester, New York
(Received February 9, 1955)

Information about nuclear coupling schemes which can be derived from relative cross sections in deuteron stripping and pickup reactions in light nuclei is considered. In a few cases, experimental results are applied to give a determination of the intermediate-coupling parameter.

1. INTRODUCTION

IN recent years, the intermediate-coupling shell model has received the attention of a number of authors.[1] Energy levels of p shell nuclei in particular have been studied in intermediate coupling because they are not consistent with either of the extreme coupling schemes. The most striking cases are given in the very complete and useful survey paper of Inglis[1] where approximate level schemes are given as a function of the intermediate-coupling parameter which measures the relative effective strengths of the spin-orbit and central parts of the interaction.

Our present purpose is to consider certain deuteron stripping and pickup reactions using intermediate coupling wave functions. By considering the ratio of the cross sections of a d-p reaction leading to different states of the same final nucleus one can also deduce the value of the intermediate-coupling parameter and thus obtain an independent check on the validity of the model.

We should remark that the present work was stimulated by an investigation of Christy[2] on angular momentum coupling in a certain class of resonant nuclear reactions. Christy's work confined itself to the two extreme coupling schemes and did not require the construction of explicit nuclear wave functions. These become essential, however, if we wish to depart from the extreme cases. When one does this one encounters, among others, the difficulty that the compound state is almost always quite highly excited and thus may not be a good candidate for description by a shell model. Deuteron reactions do not have this difficulty, for we may restrict ourselves to low-lying states. There is also the important fact that the essential features of these reactions are well understood and adequately described by Butler's theory.[3]

An analysis similar to ours has already been published by Lane.[1] Lane has in fact emphasized the desirability of using intermediate-coupling wave functions for many purposes beyond the elementary one of calculating level schemes. In his first-cited paper, magnetic dipole moments and transition strengths and reduced widths for nucleon emission are considered and applied with success to the low-lying states of C^{13} and N^{13}. In the present work (which was done independently of Lane) we consider stripping and pick-up reactions involving nuclei with $A=6, 7, 13, 14$.

2. DEUTERON REACTION CROSS SECTIONS

We first write the d-p cross section using the "Born approximation" theory[4] which is equivalent to, but simpler in formulation, than the original theory of Butler. Corrections such as the Coulomb effect and the interaction between proton and nucleus are neglected because of the large uncertainties in the shell model treatment of nuclear spectroscopy. The details of the Born approximation are well-known and we do not give them; we consider in detail only the overlap integral between the initial and final systems since it is from this (or rather a ratio of two of them) that we shall gain information concerning the intermediate coupling parameter. This integral can be related to a

* Supported in part by the U. S. Atomic Energy Commission.
† Now at the Brookhaven National Laboratory, Upton, New York.
[1] D. R. Inglis, Revs. Modern Phys. **25**, 390 (1953); Phys. Rev. **87**, 915 (1952); N. Zeldes, Phys. Rev. **90**, 416 (1953); G. E. Tauber and T. Y. Wu, Phys. Rev. **93**, 295 (1954); **94**, 1307 (1954); A. M. Lane, Proc. Phys. Soc. (London) **A66**, 977 (1953); Phys. Rev. **92**, 839 (1953); R. Schulten, Z. Naturforsch. **8**, 759 (1953); R. Schulten and R. A. Ferrell, Phys. Rev. **94**, 739 (1954).
[2] R. F. Christy, Phys. Rev. **89**, 839 (1953).
[3] S. T. Butler, Proc. Roy. Soc. (London) **A208**, 559 (1951).
[4] P. B. Daitch and J. B. French, Phys. Rev. **87**, 900 (1952); Bhatia, Huang, Huby, and Newns, Phil. Mag. **43**, 485 (1952).

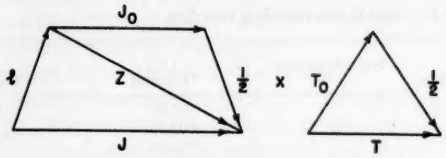

FIG. 1. Vector-coupling diagram for $\psi(zJ_0JT_0T)$.

"reduced width" of the final state (see Lane[1]) but we prefer not to adopt this point of view.

Consider

$$A[J_0,T_0,M_{T_0}]+\text{nucleon}[l,m]\rightarrow(A+1)[J,T,M_T], \quad (1)$$

which symbolically describes a stripping reaction. A and $A+1$ are atomic numbers, J_0 and J are nuclear angular momenta, T_0, T, M_{T_0}, and M_T refer to nuclear isotopic spins, and l, m refer to the orbital angular momentum and isotopic spin of the captured nucleon. By vector-coupling the initial nuclear wave function to that for the nucleon, we may form the wave function $\psi(zJ_0JT_0T)$ which has specified channel spin z. To simplify the notation, the dependence of ψ on space and spin coordinates will not be shown explicitly except where needed. The angular momenta, spins, and isotopic spins in $\psi(zJ_0JT_0T)$ are coupled according to the vector diagram in Fig. 1.

We now find in the cross section the factor $\sum_z|\langle\psi(JT)\psi(zJ_0JT_0T)\rangle|^2$. If we describe the nuclear wave functions in terms of the configurations l^{n-1}, l^n the integral occurring here may be factored into two parts. If we take only the first part involving the radial integrations (which is independent of z) we find (except of course for the isotopic spin vector coupling factor $[C^{T_0\frac{1}{2}T}(M_{T_0}m)]^2$) simply the single-particle model stripping cross section which of course is entirely independent of the nuclear structure. Consideration of the second factor multiplies the cross section by $n\sum_z\beta_z^2$, where we have

$$\beta_z=\int\psi(JT;\xi)\psi(zJ_0JT_0T;\xi)d\xi. \quad (2)$$

In (2), we understand by ξ the angular spin and isotopic spin coordinates only.

It is clear that β_z will in general depend on the details of the shell-model wave functions and in particular on the intermediate-coupling parameter $\zeta=$Inglis' a/K.[1] Moreover, if we consider the ratio $d\sigma/d\sigma^*$ for a deuteron reaction leading to two different states of the final nucleus (with preferably the same l value) then the kinematic factors entering in the cross section may be largely eliminated and the cross-section ratio expressed in terms of the "stripping ratio" $R(\zeta)=(\sum_z\beta_z^2)/(\sum_z\beta_z^{*2})$. The details of this are given in the Appendix. Broadly speaking, we expect this to be a reasonable procedure if the angular distributions are well described by Butler's theory[3] and if the outgoing velocities for the two levels are not too different. (Both of these criteria may be satisfied if the incident beam energy is high enough.)

3. NUCLEAR WAVE FUNCTIONS

To find the nuclear wave functions appearing in (2), we perform a standard intermediate-coupling calculation using LS wave functions as a basis. For the two-particle interaction we take Rosenfeld's saturation potential,[5]

$$H_1=\sum_{i<j}V(r_{ij})(0.1+0.23\boldsymbol{\sigma}_i\cdot\boldsymbol{\sigma}_j)\boldsymbol{\tau}_i\cdot\boldsymbol{\tau}_j. \quad (3)$$

A general expression, in terms of the L and K of Feenberg and Phillips,[6] for the matrix elements of H_1 for p-shell nuclei (and in this paper we consider only p-shell cases) has been first given by Racah.[7] In order to have consistency in phase relations with other results which we need, we use the equivalent result as given by Elliott, Hope, and Jahn.[8] For numerical work we take $L/K=6$ as suggested by Hummel and Inglis.[9]

The spin-orbit dependence is accounted for by a single-particle spin-orbit force:

$$H_2=\sum_i a(r_i)\mathbf{s}_i\cdot\mathbf{l}_i. \quad (4)$$

The matrix elements of H_2 may be readily derived in terms of p-shell fractional parentage coefficients which have been completely tabulated by Jahn and Van Wieringen.[10] Except for a sign the result is as given in Eq. (32) of the first cited paper by Lane.[1]

The procedure now is to evaluate and diagonalize the Hamiltonian matrix H for a specified J and T. We do this as a function of the coupling parameter $\zeta=a/K$, and then find for the eigenfunction

$$\psi(JT)=\sum_{\alpha LS}K(\alpha LSJT;\zeta)\psi(\alpha LSJT), \quad (5)$$

where $\alpha\equiv$partition describing the space symmetry of the corresponding basis vector and the constants K emerge from the diagonalization. In terms of these constants, we have

$$\beta_z(\zeta)=\sum_{\substack{\alpha_0L_0S_0\\ \alpha LS}}(-1)^{1+L_0+L}K(\alpha LSJT;\zeta)\times K(\alpha_0L_0S_0J_0T_0;\zeta)U(L_0S_0z\tfrac{1}{2};J_0S)\times U(L_0S|J;zL)\langle\alpha LST|\alpha_0L_0S_0T_0\rangle, \quad (6)$$

where U is a normalized Racah coefficient[11] and $\langle\alpha LST|\alpha_0L_0S_0T_0\rangle$ a coefficient of fractional parentage.

[5] L. Rosenfeld, *Nuclear Forces* (North-Holland Publishing Company, Amsterdam, 1948).
[6] E. Feenberg and M. Phillips, Phys. Rev. **51**, 597 (1937).
[7] G. Racah, Helv. Phys. Acta **23**, Suppl. 3, 229 (1950).
[8] Elliott, Hope, and Jahn, Trans. Roy. Soc. (London) **A246**, 241 (1953).
[9] H. H. Hummel and D. R. Inglis, Phys. Rev. **77**, 736 (1950).
[10] H. A. Jahn and H. Van Wieringen, Proc. Roy. Soc. (London) **A209**, 502 (1951).
[11] L. C. Biedenharn, "Tables of the Racah Coefficients," Oak Ridge National Laboratory Report ORNL-1098, 1952 (unpublished); Simon, Van der Sluis, and Biedenharn, Oak Ridge National Laboratory Report ORNL-1679, 1954 (unpublished).

TABLE I. The low-lying p^n-states of $A=6$, 7, 13, 14 nuclei in intermediate coupling.

Nucleus	State of excitation (Mev)	Wave functions: Intermediate coupling	*LS* limit	*jj* limit
Li^6	Ground	$^3S_1[2]$ $^3D_1[2]$ $^1P_1[11]$	$^3S_1[2]$	$p_{3/2}^2$
Li^6	2.19	$^3D_3[2]$	$^3D_3[2]$	$p_{3/2}^2$
Li^6	3.57	$^1S_0[2]$ $^1P_0[11]$	$^1S_0[2]$	$p_{3/2}^2$
Li^6	4.52	$^3D_2[2]$	$^3D_2[2]$	$p_{3/2}^2$
Li^7, (Be^7)	Ground	$^2P_{3/2}[3]$ $^2P_{3/2}[21]$ $^4P_{3/2}[21]$ $^2D_{3/2}[21]$ $^4D_{3/2}[21]$	$^2P_{3/2}[3]$	$p_{3/2}^3$
Li^7, (Be^7)	0.48	$^2P_{1/2}[3]$ $^2P_{1/2}[21]$ $^4P_{1/2}[21]$ $^4D_{1/2}[21]$ $^2S_{1/2}[111]$	$^2P_{1/2}[3]$	$p_{3/2}^3$
Li^7, (Be^7)	4.62	$^2F_{7/2}[3]$ $^4D_{7/2}[21]$	$^2F_{7/2}[3]$	$p_{3/2}^3$
Li^7, (Be^7)	7.47	$^2F_{5/2}[3]$ $^4P_{5/2}[21]$ $^2D_{5/2}[21]$ $^4D_{5/2}[21]$	$^2F_{5/2}[3]$	$p_{3/2}^3$
C^{13}, (N^{13})	Ground	$^2P_{1/2}[441]$ $^2P_{1/2}[422]$ $^4P_{1/2}[422]$ $^4D_{1/2}[422]$ $^2S_{1/2}[333]$	$^2P_{1/2}[441]$	$p_{3/2}^3$ $p_{1/2}$
C^{13}, (N^{13})	3.68	$^2P_{3/2}[441]$ $^2P_{3/2}[422]$ $^4P_{3/2}[422]$ $^2D_{3/2}[422]$ $^4D_{3/2}[422]$	$^2P_{3/2}[441]$	$p_{3/2}^3$ $p_{1/2}$
C^{13}, (N^{13})	?	$^2F_{5/2}[441]$ $^4P_{5/2}[422]$ $^2D_{5/2}[422]$ $^4D_{5/2}[422]$	$^2F_{5/2}[441]$	$p_{3/2}^3$ $p_{1/2}$
C^{14}	Ground	$^1S_0[442]$ $^3P_0[433]$	$^1S_0[442]$	$p_{3/2}^3$ $p_{1/2}$
C^{14}	6	$^1D_2[442]$ $^3P_2[433]$	$^1D_2[442]$	$p_{3/2}^3$ $p_{1/2}$
N^{14}	Ground	$^3S_1[442]$ $^3D_1[442]$ $^1P_1[433]$	$^3S_1[442]$	$p_{3/2}^3$ $p_{1/2}$
N^{14}	2.31	$^1S_0[442]$ $^3P_0[433]$	$^1S_0[442]$	$p_{3/2}^3$ $p_{1/2}$
N^{14}	3.95	$^3S_1[442]$ $^3D_1[442]$ $^1P_1[433]$	$^3D_1[442]$	$p_{3/2}^3$ $p_{1/2}$

The states for which this procedure has been carried out are listed in Table I. The correlation between wave functions and levels is made on the basis of Inglis' review article[1] and the survey paper by Ajzenberg and Lauritsen.[12] The third column lists, in spectroscopic notation, $^{2T+1,2S+1}L^{[\alpha]}$, the *LS* wave functions which enter in each case. The last two columns list the states to which the intermediate coupling functions go in the two coupling schemes.

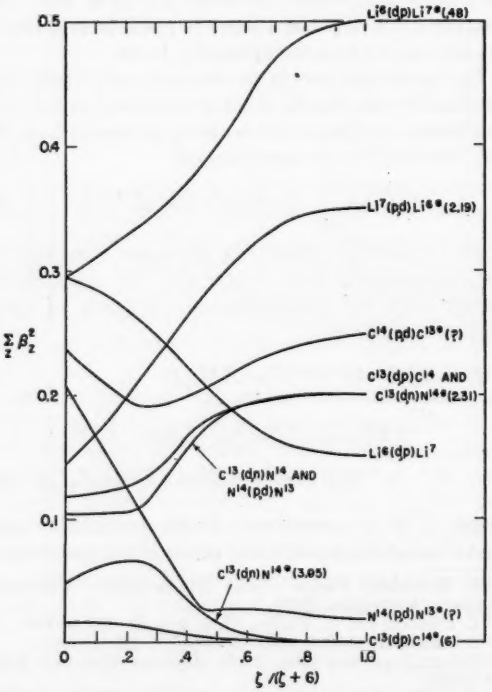

FIG. 2. Variation of $\Sigma_z \beta_z^2$ as a function of the intermediate-coupling parameter ζ. Numbers in parentheses indicate excitation energies.

[12] F. Ajzenberg and T. Lauritsen, Revs. Modern Phys. 24, 321 (1952).

We omit here the numerical details of the calculation. They are contained in an unpublished report.[13]

4. COMPARISON WITH EXPERIMENT

We are now enabled to deduce the coupling parameter in two ways. The first is by comparison of the predicted level schemes with the observed ones. The procedure here is equivalent to that of Inglis,[1] minor differences being that we use a slightly different interparticle potential and derive the transition curves by exact diagonalization rather than by the approximate procedure often used by Inglis. The results are not significantly different from those of Inglis and we do not reproduce the curves here. Specifically we find as the optimum value $\zeta=1.4$, 1.1, 4.4 for $A=6$, 7, 14, respectively. For $A=13$, only one odd-parity excited state has been identified below 10 Mev and hence, following Inglis, we arbitrarily take $\zeta=5$ and with this value predict a $5/2^-$ level near 5.3 Mev.

The second determination of ζ comes from deuteron reactions. In Fig. 2 we plot against $\zeta/(\zeta+6)$ the quantity $\sum_z \beta_z^2$ and in Fig. 3 the "stripping ratio" $R(\zeta)$ for a variety of reactions.

We now discuss briefly a few pertinent experiments. In each case the comparison is made by first fitting Butler curves to the angular distribution and then using the best value of r_0 thus found to calculate the F_l factor of the Appendix. We are then enabled to compute $R(\zeta)$ from experiment and a comparison with the curves of Fig. 3 gives us the value of ζ. We are of course free to take different ζ values for the two nuclei entering in a reaction, but it is perhaps to be expected that the values should be about the same for neighboring nuclei and we shall in fact make this assumption.

(a) $Li^7(p,d)Li^6$, Li^{*6}

In this experiment, by Standing,[14] the proton energy is 17.5 Mev and the first two states of Li^6 are observed.

[13] T. Auerbach and J. B. French, Atomic Energy Commission Report NYO-3711, 1954 (unpublished).

[14] K. G. Standing (private communication).

The best value of r_0 is given by Standing as 5.5×10^{-13}. The peaks occur near $\theta=18°$ and the cross-section ratio at this angle is $d\sigma/d\sigma^*=2.0\pm0.2$.

We find $R(\zeta)=0.65(d\sigma/d\sigma^*)=1.3\pm0.1$.

From Fig. 3 we have $1.4\leqslant\zeta\leqslant2.1$, where of course the quoted "error" corresponds simply to the transcription of the experimental error and does not include any error assignments for parameters which have been chosen, or for more fundamental defects in the entire theory.

The value of ζ found here is in excellent agreement with the value $\zeta=1.4$ found from the level scheme.

(b) $Li^6(d,p)Li^7$, Li^{*7}

Two experiments are available: Holt and Marsham[15] use an incident energy of 8 Mev; Whaling and Bonner[16] measure the same reaction at several energies, the highest being 1.4 Mev which, from our point of view, is still quite low. In each case the first two states are observed.

The data of Holt and Marsham are fitted with $r_0=4.9\times10^{-13}$ cm. We compare at $\theta=25°$. There we find $R(\zeta)=0.52(d\sigma/d\sigma^*)=0.68\pm0.5$.

This corresponds (by Fig. 3) to $2.3\leqslant\zeta\leqslant3.5$. The data of Whaling and Bonner lead to about the same value. The value of ζ is considerably larger than that given by the level scheme. However, as discussed in detail by Inglis,[1] the picture of almost pure LS coupling in this nucleus which is implied by a very small ζ is incompatible with the relatively large observed ratio between the ^2F and ^2P splitting. We assume that the 4.62-Mev level has $J=7/2^-$. It is true that this situation is not at all improved by increasing ζ, but we may expect that it could be if we were to use a more adequate model and interaction.

The difference between the ζ values of (a) and (b) could perhaps be reconciled by taking different values for the two nuclei but at the moment this seems an unnecessary refinement.

(c) $C^{13}(d,p)C^{14}$, C^{*14}

The experiment with 4-Mev deuterons by Benenson[17] indicates that the ground-state reactions at 10° and 25° are about 3 percent and 40 percent as intense as the first excited state. This is in disagreement with the theory (assuming the excited state to be 2^+) which gives $R(\zeta)\geqslant7$, and hence $d\sigma/d\sigma^*>0.2$ and >0.5 for the two angles. It has since become clear[18] that in the region 6–7 Mev of excitation in C^{14} there are three levels. The 6.1-Mev level observed by Benenson corresponds presumably to $l=0$, thus giving a rather better fit than $l=1$ to his data and explaining the relatively large cross section. It is possible that the 6.72-Mev level is the 2^+ level predicted by the theory.

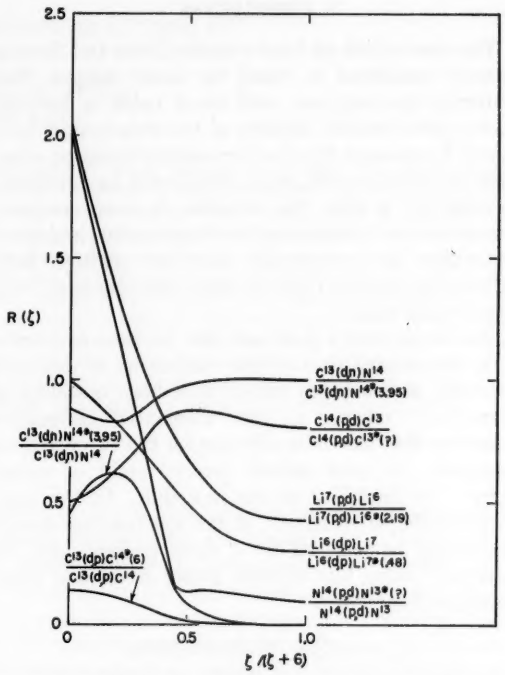

FIG. 3. Variation of the stripping ratio $R(\zeta)$ as a function of ζ. Numbers in parentheses indicate excitation energies.

(d) $C^{13}(d,n)N_{14}{}^*$, $N_{14}{}^{**}$

This experiment with 4-Mev deuterons is also due to Benenson.[17] The accuracy is unfortunately not very satisfactory for our purposes and at best we can determine the coupling parameter only very roughly. We do not consider the ground state reaction because it gives a quite poor fit to an $l=1$ curve. (The ground state reaction is known from the work of Bromley[19] and also of Standing[20] to have $l=1$.)

Taking $r_0=4.8\times10^{-13}$ cm and $\theta\sim20°$, we find $R(\zeta)=4.0d\sigma/d\sigma^*$; and estimating the cross-section ratio from Benenson's paper, we decide that $\zeta=3.7\pm1.5$. This range of values is consistent with the value $\zeta=4.4$ from the level scheme.

We note, incidentally, that the Q values here are quite small as is also the deuteron energy. Both these effects make the kinematical corrections quite large (the factor arising from the deuteron Fourier transform alone provides almost a factor 2 in the ratio). One may well doubt whether our understanding of the dynamics of a deuteron reaction is sufficient to make such large corrections trustworthy.

[15] J. R. Holt and T. N. Marsham, Proc. Phys. Soc. (London) A66, 1032 (1953).
[16] W. Whaling and T. W. Bonner, Phys. Rev. 79, 258 (1950).
[17] R. E. Benenson, Phys. Rev. 90, 420 (1953).
[18] A. Sperduto, Massachusetts Institute of Technology Progress Report, May, 1954 (unpublished).
[19] D. A. Bromley, Phys. Rev. 88, 565 (1952).
[20] K. G. Standing, Phys. Rev. 94, 731 (1954).

5. CONCLUSION

The cases which we have examined here and the one already considered in detail by Lane[1] suggest that deuteron reactions may well be of value in learning about quite detailed features of the structure of light nuclei. To examine this, further results for several other cases involving p-shell nuclei will shortly be published. Beyond the p shell the situation is more complex; one encounters a large number of parameters and quite incomplete data concerning spins and parities. Still, information derived from deuteron reactions may be of considerable value.

We should finally point out that we have adopted a quite elementary view of the mechanism of deuteron reactions, and for that reason have been unwilling to place much reliance on the "kinematic" corrections whenever they are quite different for the two reactions compared. A more refined theory would of course extend the flexibility of the procedure. In the same way the simple treatment of the spectroscopy should eventually be replaced by a more realistic one, for example, taking into account tensor forces and interconfiguration mixing.

6. ACKNOWLEDGMENTS

Finally, we wish to thank Dr. D. A. Bromley and Dr. R. E. Benenson for valuable discussions concerning the experiments and Dr. K. G. Standing for information concerning his work with Li^7. We have benefited from a discussion with Dr. D. R. Inglis. S. P. Pandya, B. J. Raz, and Mrs. M. Halbert have been helpful in many ways.

APPENDIX

For the stripping reaction of Eq. (1), the "Born approximation" theory gives

$$\frac{d\sigma}{d\Omega}=C\frac{2J+1}{2J_0+1}\frac{k}{k_D}\frac{1}{(\alpha^2+\kappa^2)^2(\gamma^2+\kappa^2)^2}\times F_l^2(q,r_0,l)\{[C^{T_0\frac{1}{2}T}(MT_0m)]^2\sum_s\beta_s^2\},$$

where C is an immaterial constant. We have used the Hulthén wave function for the deuteron defined by α and $\gamma\simeq 7\alpha$, $\mathbf{k}$ and $\mathbf{k}_D$ are the nucleon and deuteron momenta in the c.m. system,

$$\mathbf{q}=\mathbf{k}_D-\frac{A}{A+1}\mathbf{k},\quad \boldsymbol{\kappa}=\tfrac{1}{2}\mathbf{k}_D-\mathbf{k},\quad \hbar^2\gamma^2=\left(\frac{2A}{A+1}\right)MB,$$

where B is the binding energy of the captured nucleon and

$$F_l=-\hbar^2\frac{A+1}{2AM}R_l(r_0)r_0^2\left\{\frac{\partial j_l(qr)}{\partial r}-\frac{j_l(qr)}{h_l^{(1)}(ilr)}\frac{\partial}{\partial r}h_l^{(1)}(ilr)\right\}_{r_0}.$$

Here $R_l(r_0)$ is the captured nucleon amplitude at the nuclear radius and we make the approximation that this is independent of the state of excitation.

To calculate the kinematic factors for both stripping and pickup reactions it is convenient to introduce the following quantities: Let $Q=Q$-value in c.m. system *for a stripping reaction*, $E_0=$deuteron kinetic energy in system with A at rest, $E_1=$nucleon kinetic energy in system with $(A+1)$ at rest, and $\theta=$c.m. angle ($\mathbf{k}\cdot\mathbf{k}_0=kk_D\cos\theta$). For a stripping reaction we will be given (Q,E_0), for a pickup reaction (Q,E_1). We have $(A+1)E_1-AE_0=(A+2)Q$. Then, measuring energies in Mev and wave numbers in units of 10^{13} cm^{-1}, we have

$$q=0.22\left(\frac{A}{A+2}\right)[2E_0+E_1-2(2E_0E_1)^{\frac{1}{2}}\cos\theta]^{\frac{1}{2}},$$

$$\kappa^2=0.0242Q+\frac{A+1}{2A}q^2,\quad l=0.22\left[\frac{A}{A+1}(Q+2.22)\right]^{\frac{1}{2}}.$$

We have now for the stripping reaction of Eq. (1):

$$\frac{d\sigma}{d\sigma^*}=\frac{2J+1}{2J^*+1}\left(\frac{E_1}{E_1^*}\right)^{\frac{1}{2}}\left(\frac{C^{T_0\frac{1}{2}T}(MT_0m)}{C^{T_0\frac{1}{2}T^*}(MT_0m^*)}\right)^2\times\left[\frac{(\alpha^2+\kappa^{*2})(\gamma^2+\kappa^{*2})}{(\alpha^2+\kappa^2)(\gamma^2+\kappa^2)}\right]^2\left(\frac{F_l}{F_l^*}\right)^2R(\zeta),$$

and for the inverse defined also by Eq. (1):

$$\frac{d\sigma}{d\sigma^*}=\left(\frac{E_0}{E_0^*}\right)^{\frac{1}{2}}\left(\frac{C^{T_0\frac{1}{2}T}(MT_0m)}{C^{T_0^*\frac{1}{2}T}(MT_0^*m^*)}\right)^2\times\left[\frac{(\alpha^2+\kappa^{*2})(\gamma^2+\kappa^{*2})}{(\alpha^2+\kappa^2)(\gamma^2+\kappa^2)}\right]^2\left(\frac{F_l}{F_l^*}\right)^2R(\zeta).$$

Electric Monopole Transitions in C^{12} and O^{16}†

L. I. SCHIFF
Stanford University, Stanford, California

(Received February 9, 1955)

The matrix elements for the electric monopole ($0^+ \rightarrow 0^+$) transitions between the ground and 7.68-Mev state in C^{12} and between the ground and 6.06-Mev state in O^{16} may be estimated from inelastic electron scattering and from the pair emission lifetime, respectively. The two are equal to each other within the rather large error of the electron scattering determination, and are given by $(\sum_P r_P^2)_{f0} \cong 3.8 \times 10^{-26}$ cm^2, where 0 and f represent initial and final states of the nucleus, and r_P is the radial distance of a proton from the center of the nucleus. Calculations based on the alpha-particle model and on an elastic-fluid model yield three to five times this experimental value. Therefore, a calculation was made in the case of C^{12}, based on the jj-coupling independent-particle model, according to which two nucleons undergo transitions between the $p_{\frac{1}{2}}$ shell and the $p_{\frac{3}{2}}$ shell. The matrix element vanishes if there are no internucleon forces. Pair forces are included to first order, and the sum over configurations is performed exactly by means of a Green's function. For simplicity it is assumed that the independent-particle potential is an infinitely deep square well, and that the pair interaction has zero range. Even assuming that the pair interaction has its free-space triplet magnitude, the calculated matrix element is only about one-sixth the experimental value. It is concluded, therefore, that a model that is more collective than the independent-particle model with pair interactions, and less collective than the alpha-particle or elastic-fluid models, is required to account for the experimental results.

I. EXPERIMENTAL SITUATION

THE half-life for emission of electron-positron pairs from the 6.06-Mev state in O^{16} has been measured by Devons, Goldring, and Lindsey[1] to be $(5.0 \pm 0.5) \times 10^{-11}$ sec. According to the theory of Oppenheimer and Schwinger and of Dalitz,[2] this provides a value of 3.8×10^{-26} cm^2 for the matrix element (M.E.) of the electric monopole operator $\sum_P r_P^2$ between initial and final 0^+ states, where r_P is the radial distance of a proton from the center of the nucleus.

The energy of the 7.68-Mev state in C^{12} has been measured accurately by Dunbar, Pixley, Wenzel, and Whaling.[3] Its angular momentum and parity are not as definitely known as for the 6.06-Mev state in O^{16}, although it is most probably also a 0^+ state. Harries[4] has observed pairs of approximately the correct energy. Bell and Jordan[5] have observed 7.4-Mev gamma rays, but attribute these to neutron capture in an iron shield. Beghian, Halban, Husain, and Sanders[6] have observed 3.16-Mev gamma rays that would correspond to a transition from the 7.68-Mev state to the 4.43-Mev (2^+) state, and do not find any gamma rays of about 7.5-Mev energy. These cascade gamma rays are also observed by Uebergang,[7] and an angular correlation study by Seed[8] indicates that the transitions correspond to $0^+ \rightarrow 2^+ \rightarrow 0^+$. We assume, therefore, that the 7.68-Mev state is actually a 0^+ state.

Differential cross sections for elastic and inelastic scattering of 190-Mev electrons from carbon have been measured by Fregeau and Hofstadter.[9] As indicated in an earlier paper,[10] the ratio of the 7.68-Mev excitation cross section to the elastic cross section can be used to determine the electric monopole matrix element, since the Born approximation is valid for such a light nucleus. For primary electron energies that are large in comparison with the excitation energy, the square root of this cross-section ratio is approximately equal to

$$\left| \frac{(\sum_P [j_0(qr_P) - 1])_{f0}}{(\sum_P j_0(qr_P))_{00}} \right| \underset{q \rightarrow 0}{\longrightarrow} \frac{q^2}{6Z} (\sum_P r_P^2)_{f0}, \qquad (1)$$

where 0 and f refer to the ground and excited states of the nucleus of atomic number Z, $\hbar q$ is the momentum transfer from electron to nucleus, and j_0 is a spherical Bessel function. Thus a plot of the square root of the cross-section ratio against q^2 gives M.E. in terms of the slope at the origin. The experiments cover a range of q^2 from about 0.5 to 1.5 in units of 10^{26} cm^{-2}, so that the extrapolation in to $q=0$ requires some guesswork. A rough value for the initial slope can nevertheless be obtained in this way, and corresponds to about the same value M.E. $= 3.8 \times 10^{-26}$ cm^2 as is found in the case of O^{16}. A determination of M.E. can also be made from the absolute value of the inelastic cross section as a function of angle. While not as reliable, it is in agreement with the above value.

II. COLLECTIVE MODELS[11]

In the alpha-particle model, we assume that C^{12} consists of three alpha particles with equilibrium positions at the corners of an equilateral triangle, and that O^{16} consists of four alpha particles with equilibrium

† Supported in part by the Office of Scientific Research, Air Research and Development Command.

[1] Devons, Goldring, and Lindsey, Proc. Phys. Soc. (London) A67, 134 (1954).

[2] J. R. Oppenheimer and J. Schwinger, Phys. Rev. 56, 1066 (1939); R. H. Dalitz, Proc. Roy. Soc. (London) A206, 521 (1951).

[3] Dunbar, Pixley, Wenzel, and Whaling, Phys. Rev. 92, 649 (1953).

[4] G. Harries, Proc. Phys. Soc. (London) A67, 153 (1954).

[5] P. R. Bell and W. H. Jordan, Phys. Rev. 79, 392 (1950).

[6] Beghian, Halban, Husain, and Sanders, Phys. Rev. 90, 1129 (1953).

[7] R. G. Uebergang, Australian J. Phys. 7, 279 (1954).

[8] J. Seed, Phil. Mag. 46, 100 (1955).

[9] J. H. Fregeau and R. Hofstadter, Bull. Am. Phys. Soc. 30, No. 1, 45 (1955); and private communication.

[10] L. I. Schiff, Phys. Rev. 96, 765 (1954).

[11] Calculations similar to those reported in this section have been made by R. H. Dalitz (private communication); see also reference 1, and Devons, Hereward, and Lindsey, Nature 164, 586 (1949).

positions at the corners of a regular tetrahedron. Dennison[12] has achieved some success in accounting for the excited states of O^{16} with this model. In each case, the first excited 0^+ state corresponds to single excitation of the "breathing" mode, in which the alpha particles oscillate radially and in phase; the restoring force is fixed in terms of the excitation energy. The matrix element is

$$\text{M.E.}=2^{\frac{1}{2}}[ZR_\alpha\hbar/(AM\Delta)^{\frac{1}{2}}], \tag{2}$$

where M is the nucleon mass, A is the atomic weight, $\Delta\equiv E_f-E_0$ is the excitation energy, and R_α is the equilibrium distance of the center-of-mass of each alpha particle from the center of the nucleus. If we assume that R_α is smaller than the nuclear radius $R=1.3\times10^{-13}A^{\frac{1}{3}}$ cm by 1.0×10^{-13} cm, we obtain M.E.$(C^{12})=11\times10^{-26}$ cm^2, M.E.$(O^{16})=17\times10^{-16}$ cm^2. In both cases, the amplitude of oscillation is small enough for the model to be reasonable. However, as pointed out by Inglis,[13] the period of oscillation is close enough to the periods associated with the motions of the constituent nucleons in each alpha particle so that the adiabatic approximation implied in the use of the alpha-particle model is not well justified.

In the elastic-fluid model, we assume that the nucleus consists of a sphere of elastic fluid of radius R that has uniform charge and mass density. The first excited 0^+ state then corresponds to single excitation of the lowest radial mode of oscillation, in which the change in density of the fluid at radial distance r is proportional to $j_0(\pi r/R)$; again, the compressibility is fixed in terms of the excitation energy. When account is taken of the oscillation of the nuclear surface, the matrix element is found to be

$$\text{M.E.}=(3^{\frac{1}{2}}6/\pi^2)[ZR\hbar/(AM\Delta)^{\frac{1}{2}}]. \tag{3}$$

With the above expression for R, Eq. (3) gives M.E.$(C^{12})=13\times10^{-26}$ cm^2, M.E.$(O^{16})=19\times10^{-26}$ cm^2. The elastic stiffness of the fluid that is required to give agreement with the observed excitation energies is about one-seventh of that deduced from other considerations.[14]

It is not surprising that these two collective models yield such similar results. The fact that both give too large a matrix element by a factor of three to five suggests that the independent-particle model is worth investigating, since only a small number of protons are expected to take part in the transition on the basis of this model.

III. INDEPENDENT-PARTICLE MODEL FOR C^{12}

On the basis of the jj-coupling independent-particle model, the ground state of C^{12} has the $p_{\frac{3}{2}}$ shell filled with four neutrons and four protons. It is expected that the lowest excited states arise when a small number of nucleons are promoted from the $p_{\frac{3}{2}}$ shell to the $p_{\frac{1}{2}}$ shell, or possibly to the $d_{\frac{5}{2}}$ or $s_{\frac{1}{2}}$ shell. In none of these cases can an excited 0^+ state be produced by promoting a single nucleon. If however two nucleons are promoted, a 0^+ state can be obtained.[15] We assume that the 7.68-Mev state has six nucleons or two holes in the $p_{\frac{3}{2}}$ shell and two nucleons in the $p_{\frac{1}{2}}$ shell, so that it necessarily has even parity. We further assume that this state has total isotopic spin $T=0$, since the ground states of the neighboring isobars lie considerably higher. The pair of holes can be coupled together such that their total angular momentum J is 3, 2, 1, or 0; then $T=0$ for odd values of J and $T=1$ for even values of J. The pair of nucleons can similarly be coupled together such that (T,J) is equal to (1,0) or (0,1). Thus a state with $T=0$ and $J=0$ can be produced by combining the substates (1,0) and (1,0), or by combining the substates (0,1) and (0,1). According to Redlich,[16] the effect of the interaction between pairs of nucleons is generally to decrease the energy of the states of highest space symmetry with respect to the others. In the situation under consideration here, the (1,0) substate of two $p_{\frac{1}{2}}$ nucleons has a slightly higher energy than the (0,1) substate, by 0 to 0.73 Mev depending on the interaction assumed; on the other hand the (1,0) substate of two $p_{\frac{3}{2}}$ nucleons or holes has a lower energy than the (0,1) substate, by 1.19 to 1.56 Mev.[16] We therefore assume that the 7.68-Mev state results from combination of the $(T,J)=(1,0)$ substates of the two $p_{\frac{1}{2}}$ nucleons and the two $p_{\frac{3}{2}}$ holes.

The matrix element of an operator like the electric monopole operator

$$\Omega=\sum_{P=1}^{Z} r_P^2=\sum_{i=1}^{A}\tfrac{1}{2}(1+\tau_i)r_i^2=\sum_{i=1}^{A}\Omega_1(i), \tag{4}$$

which is a sum of single-particle terms, vanishes between pure independent-particle states that differ in the configurations of more than one nucleon. The effect of the interaction between pairs of nucleons is to mix in other nucleon configurations so that the initial and final perturbed independent-particle states have components that differ in the configuration of only one nucleon. The calculation is carried through only to first order in the pair interaction. On the other hand, all admixed states are included, this being accomplished by means of a Green's function. In principle, any forms can be assumed for the independent-particle potential and for the pair interaction. The complications are such, however, that for simplicity the independent-particle potential is assumed in this paper to be an infinitely deep square

[12] D. M. Dennison, Phys. Rev. **96**, 378 (1954); see also Peterson, Fowler, and Lauritsen, Phys. Rev. **96**, 1250 (1954).

[13] D. R. Inglis (private communication); see also Revs. Modern Phys. **25**, 390 (1953), Sec. 10.

[14] E. Feenberg, Revs. Modern Phys. **19**, 239 (1947).

[15] The idea that the matrix element might be small because more than one nucleon is excited to form the upper state, was suggested independently by D. H. Wilkinson (private communication); see also A. M. Lane and D. H. Wilkinson, Phys. Rev. **97**, 1199 (1955).

[16] M. G. Redlich (private communication); see also thesis, Princeton University, 1954 (unpublished); and Phys. Rev. **95**, 448 (1954).

well, and the pair interaction to be of zero range (δ function).

IV. DETAILS OF THE CALCULATION

The Hamiltonian for the nucleus is assumed to have the form

$$H=H_0+H',$$

$$H_0=\sum_{i=1}^{A} H_1(i), \quad H'=\sum_{i>j}^{A} H_p'(i,j), \tag{5}$$

where H_0 represents the independent-particle potential including the spin-orbit interaction, and H' represents the interaction between pairs of nucleons. The unperturbed energy eigenfunctions u_k form a complete orthonormal set:

$$H_0u_k=E_ku_k, \quad \int \bar{u}_k u_l d\tau=\delta_{kl}. \tag{6}$$

The first-order perturbed wave functions are

$$\psi_n\cong u_n+\sum_{k\neq n}(E_n-E_k)^{-1}u_kH'_{kn},$$

$$H'_{kn}\equiv\int \bar{u}_kH'u_nd\tau. \tag{7}$$

We wish to calculate the matrix element of the electric monopole operator Ω given by Eq. (4), between perturbed initial and final states ψ_0 and ψ_f given by Eq. (7). The result through first order in H' is

$$\int\bar{\psi}_f\Omega\psi_0d\tau=\Omega_{f0}+\sum_{k\neq f}(E_f-E_k)^{-1}H'_{fk}\Omega_{k0}+\sum_{k\neq 0}(E_0-E_k)^{-1}\Omega_{fk}H'_{k0}, \tag{8}$$

$$\Omega_{kn}\equiv\int\bar{u}_k\Omega u_nd\tau.$$

Since the initial and final states differ in the configurations of two nucleons and Ω is a sum of single-nucleon terms, we have that the zero-order part of (8), Ω_{f0}, is zero. Because of this, the restrictions on the sums over k in the first-order parts of (8) can be dropped; then since H' and Ω are Hermitian, we can put

$$\int\bar{\psi}_f\Omega\psi_0d\tau=-S_{f0}-\bar{S}_{0f},$$

$$S_{f0}\equiv\sum_k(E_k-E_f)^{-1}H'_{fk}\Omega_{k0}, \tag{9}$$

$$\bar{S}_{0f}\equiv\sum_k(E_k-E_0)^{-1}\Omega_{fk}H'_{k0}.$$

The unperturbed energy eigenfunctions are antisymmetrized products of single-particle functions, each of which is the product of a radial function and a spin-angle-isotopic spin (s-a-i) function. The operator Ω is a sum of terms $\Omega_1(i)$, each of which can alter only the radial coordinate of one particle, so that the state k must have the same distribution of s-a-i functions as the state 0. Now the state f differs from 0, and hence also from k, in the s-a-i functions of two particles. The terms in the summand of S_{f0} can then be divided into two classes, those in which the nucleon that appears as the argument of Ω_1 is one of the two which appear as arguments of H_p', and those in which it is not. In both classes of terms, it is apparent that the two nucleons in H_p' are those that change their s-a-i functions. Then in the second class, the nucleon in Ω_1 must not change its state at all (neither radial nor s-a-i part), so that the states k and 0 are identical. The second-class part of S_{f0} is thus equal to

$$(E_0-E_f)^{-1}H'_{f0}\Omega'_{00}, \tag{10}$$

where the prime on Ω'_{00} indicates that the summation in (4) is carried only over the nucleons that do not change their state. In similar fashion, the second-class part of $\bar{S}_{0f}$ is equal to

$$(E_f-E_0)^{-1}\Omega'_{ff}H'_{f0}. \tag{11}$$

Since the single-particle states involved in Ω'_{00} and Ω'_{ff} are the same, Eqs. (10) and (11) are equal in magnitude and opposite in sign, and hence cancel when added in Eq. (9). Thus only the first-class parts of S_{f0} and $\bar{S}_{0f}$ need be considered in what follows.

A typical term in the summand of the first-class part of S_{f0} is

$$\sum_\kappa\int\int\bar{v}_c(1)\bar{v}_d(2)H_p'(1,2)v_\kappa(1)v_b(2)d\tau_1d\tau_2\times(\epsilon_\kappa+\epsilon_b-\epsilon_c-\epsilon_d)^{-1}\times\int\int\bar{v}_\kappa(1')v_b(2')\Omega_1(1')v_a(1')v_b(2')d\tau_1'd\tau_2', \tag{12}$$

where the v's and ϵ's are unperturbed single-particle eigenfunctions and eigenvalues. None of the other particles in the nucleus changes its state as the nucleus goes from 0 to k to f, so that the integrations over the coordinates of these $A-2$ nucleons give unity. The integration over $2'$ also gives unity, as does the s-a-i part of the integration over $1'$. We write each of the v's as the product of an s-a-i part I and a radial part R; for example, $v_a(1)=I_a(1)R_a(r_1)$, $v_\kappa(1)=I_a(1)R_\kappa(r_1)$. Then, Eq. (12) can be written in the form

$$\int\int\bar{v}_c(1)\bar{v}_d(2)H_p'(1,2)w_a(1)v_b(2)d\tau_1d\tau_2,$$

$$w_a(1)=\tfrac{1}{2}(1+\tau_1)I_a(1)Q_{a\epsilon}(r_1), \quad \epsilon\equiv\epsilon_c+\epsilon_d-\epsilon_b, \tag{13}$$

$$Q_{a\epsilon}(r)\equiv\sum_\kappa(\epsilon_\kappa-\epsilon)^{-1}R_\kappa(r)\int_0^\infty\bar{R}_\kappa(r')R_a(r')r'^4dr'.$$

The summation in the last of Eqs. (13) over all radial states κ that have the same s-a-i part I_a, can be evalu-

ated in terms of a Green's function:

$$\sum_\kappa(\epsilon_\kappa-\epsilon)^{-1}R_\kappa(r)\bar{R}_\kappa(r')=G_{a\epsilon}(r,r'),$$
$$-(\hbar^2/2M)[r^{-2}(d/dr)(r^2d/dr)-l(l+1)/r^2]G_{a\epsilon}(r,r')$$
$$+[V_a(r)-\epsilon]G_{a\epsilon}(r,r')=r^{-2}\delta(r-r'); \quad (14)$$

here, M is the nucleon mass, l is the orbital quantum number and $V_a(r)$ is the total (including spin-orbit) potential associated with the s-a-i state I_a. The calculation thus consists of (1) finding the Green's function (14) associated with the potential $V_a(r)$, (2) evaluating the radial integral in (13) for $Q_{a\epsilon}(r)$:

$$Q_{a\epsilon}(r)=\int_0^\infty G_{a\epsilon}(r,r')R_a(r')r'^4dr', \quad (15)$$

(3) evaluating the integrals in the first of Eqs. (13), and (4) combining terms (12) into S_{f0}.

In order to simplify steps (1) and (2), we assume that $V_a(r)$ is a finite constant for $0\leqq r<R$ and positively infinite for $r>R$, and in order to simplify step (3), we assume that the pair interaction has zero range:

$$H_p'(1,2)=C\delta(\mathbf{r}_1-\mathbf{r}_2). \quad (16)$$

Step (4) is independent of the assumptions made concerning the forms of $V_a(r)$ and $H_p'(1,2)$, and involves instead the combinations of single-particle s-a-i states that are used to build up the initial and final states.

The Green's function for the infinitely deep square well potential is

$$G_{a\epsilon}(r,r')=-(2M\alpha/\hbar^2)\{[j_l(\alpha r_<)n_l(\alpha r_>)]$$
$$-[j_l(\alpha r)j_l(\alpha r')n_l(\alpha R)/j_l(\alpha R)]\}, \quad (17)$$
$$\hbar^2\alpha^2/2M=\epsilon-V_a,$$

where $r_<$ and $r_>$ are the lesser and greater, respectively, of r, r', and j_l and n_l are the spherical Bessel functions that are regular and irregular, respectively, at the origin. The second square bracket term in (17) is needed to make $G_{a\epsilon}$ vanish at $r=R$, as is required by the infinite potential step. The normalized radial function for the state a is

$$R_a(r)=Bj_l(\alpha_0 r), \quad j_l(\alpha_0 R)=0,$$
$$\hbar^2\alpha_0^2/2M=\epsilon_a-V_a, \quad B^2\int_0^R j_l^2(\alpha_0 r)r^2dr=1. \quad (18)$$

Substitution of Eqs. (17) and (18) into (15) gives

$$Q_{a\epsilon}(r)=-(2M\alpha B/\hbar^2)\Big\{n_l(\alpha r)\int_0^r j_l(\alpha r')j_l(\alpha_0 r')r'^4dr'$$
$$+j_l(\alpha r)\int_r^R n_l(\alpha r')j_l(\alpha_0 r')r'^4dr'$$
$$-[j_l(\alpha r)n_l(\alpha R)/j_l(\alpha R)]$$
$$\times\int_0^R j_l(\alpha r')j_l(\alpha_0 r')r'^4dr'\Big\}. \quad (19)$$

In the case of C^{12} under consideration here, the radial functions for states a, b, c, d are all of the form (18) with $l=1$. The initial states a and b have $j=\frac{3}{2}$, and the final states c and d have $j=\frac{1}{2}$. Both pairs of states have the same value of α_0, since this is determined by the boundary condition at $r=R$. Thus, $\epsilon_a-V_a=\epsilon_c-V_c$; also, $\epsilon_c-\epsilon_a$ is equal to half the excitation energy $\Delta=7.68$ Mev. With our assumption that the excited state is built up as the (0,0) combination of $(T,J)=(1,0)$ substates of two $p_{\frac{1}{2}}$ nucleons and two $p_{\frac{1}{2}}$ holes, it can be shown after some calculation that steps (3) and (4) lead to the following expression for the first-class part of S_{f0}[17]:

$$-[7(\tfrac{3}{2})^{\frac{1}{2}}M\alpha CB^4/15\pi\hbar^2]\int_0^R j_1^3(\alpha r)F(r)r^2dr, \quad (20)$$

where $F(r)$ is the curly bracket of Eq. (19) with $l=1$. The first-class part of $\bar{S}_{0f}$ is given by Eq. (20) with α replaced throughout by α', where

$$\hbar^2\alpha'^2/2M=\epsilon'-V_c, \quad \epsilon'\equiv\epsilon_a+\epsilon_b-\epsilon_d. \quad (21)$$

From Eqs. (17), (18), and (21), it follows that

$$\alpha^2=\alpha_0^2+(2M\Delta/\hbar^2), \quad \alpha'^2=\alpha_0^2-(2M\Delta/\hbar^2). \quad (22)$$

In principle, all of the radial integrations implied in Eq. (20) can be performed analytically. In practice, it is desirable to calculate $F(r)$ analytically, and then to carry through the final integration over r numerically. This procedure suffers from the draw back that α, α', and α_0 are close together in magnitude: $\Delta=7.68$ Mev, and $\hbar^2\alpha_0^2/2M=46.5$ Mev for $R=3\times10^{-13}$ cm. This means that $F(r)$ is large because of the appearance of $j_1(\alpha R)$ in the denominator of the last term, since $j_1(\alpha_0 R)=0$. Moreover, since $j_1(\alpha R)$ is negative and $j_1(\alpha' R)$ is positive, the large contributions from S_{f0} and $\bar{S}_{0f}$ nearly cancel, so that the numerical work must be done with great accuracy. It is therefore desirable to expand Eq. (20) as a Taylor series in α about the point α_0, treat $\bar{S}_{0f}$ in the same way, and keep the leading term in the sum. It is easily shown that the error in this procedure is of relative order $(2M\Delta/\hbar^2\alpha_0^2)^2=0.027$, and a numerical check of the value quoted below shows that the error is actually less than one percent. The resulting expression for the sum of the first-class parts of S_{f0} and $\bar{S}_{0f}$ is the same as Eq. (20) with α replaced by α_0 and $F(r)$ replaced by

$$-(6\alpha_0^7r^2)^{-1}\{\sin x[(3\beta^2+5)-(2\beta^2+5)x^2+2x^4]$$
$$-x\cos x[(3\beta^2+5)-5x^2]\}, \quad (23)$$
$$x\equiv\alpha_0 r, \quad \beta\equiv\alpha_0 R.$$

In deriving Eq. (23), use has been made of the fact that $\tan\beta=\beta$, which is a consequence of $j_1(\beta)=0$. The matrix

[17] It is convenient to make use of some relations given by E. U. Condon and G. H. Shortley, *The Theory of Atomic Spectra* (Cambridge University Press, London, 1935), Chap. 6, Sec. 5 and Chap. 12, Sec. 1; individual nucleon quantum numbers j, m, τ may be substituted for the individual electron quantum numbers l, m_l, m_s used by Condon and Shortley.

element of Ω is the negative of the sum of the first-class parts of S_{J0} and $\bar{S}_{0J}$, and so is equal to

$$\text{M.E.}=[7(\tfrac{3}{2})^{\frac{1}{2}}MCR(B^2R^3)^2/90\pi\hbar^2\beta^7] \times\int_0^\beta j_1{}^3(x)\{\ \}dx, \quad (24)$$

where { } denotes the curly bracket in Eq. (23).

V. NUMERICAL RESULT AND DISCUSSION

The x integral in Eq. (24) can be evaluated analytically, but is much easier to do numerically; it is equal to -1.98. From Eq. (18), the normalization constant B is given by $B^2R^3=6\beta/\sin 2\beta$. Substitution of $\beta=4.493$ gives finally

$$\text{M.E.}=-1.58\times10^{22}CR\ \text{cm}^2,$$

where R is measured in cm and C in Mev-cm^3. If now we set $|\text{M.E.}|=3.8\times10^{-26}$ cm^2, as in Sec. I, and $R=3.0\times10^{-13}$ cm, we obtain $C=8.0\times10^{-36}$ Mev-cm^3. This is about six times as large as the volume integral of the triplet neutron-proton interaction, when it is assumed to be of Gaussian form.[18] Conversely, even if C were chosen to correspond to the free-space neutron-proton interaction, in which case the first-order perturbation theory used here would not be reliable, M.E. would have only about one-sixth the experimental value.

This result, together with those of Sec. II, suggests that a model that is more collective than the independent-particle model with pair interactions and less collective than the alpha-particle or elastic-fluid models, is required to account for the experimental observations. The suggestion of Christy and Fowler,[19] that low-lying excited states in the p shell nuclei arise from excitation of four nucleons, may be promising in this connection.

The writer is indebted to Dr. D. R. Yennie and Dr. M. G. Redlich for stimulating conversations, and to Professor R. Hofstadter for discussion of the experimental situation.

[18] J. M. Blatt and J. D. Jackson, Phys. Rev. **76**, 18 (1949); other forms for the interaction have roughly similar volume integrals.

[19] R. F. Christy and W. A. Fowler, Phys. Rev. **96**, 851(A) (1954), and private communication from W. A. Fowler. With the Hamiltonian (5) and this model for the excited state, it would be necessary to go at least to second order in H' in order for the matrix element not to vanish; it would probably then be desirable for the calculation to stress the collective rather than the perturbation aspects of the situation.

PHYSICAL REVIEW VOLUME 98, NUMBER 5 JUNE 1, 1955

Nuclear Moments of Nb^{93}, La^{139}, Os^{187}, and Hg^{201}

KIYOSHI MURAKAWA
Institute of Science and Technology, Komaba-machi, Meguro-ku, Tokyo, Japan
(Received February 18, 1955)

The effective charge Z^* for a d-electron was studied by means of a hyperfine structure (hfs) investigation; the screening correction $(Z-Z^*)$ was found to range from 15 to about 19 for the charge number Z ranging from 27 to 78. Investigation of the hfs of the spectra of Nb I and La I yielded the result that $Q(Nb^{93})=(-0.2\pm0.1)\times10^{-24}$ cm^2 and $Q(La^{139})=(+0.6\pm0.2)\times10^{-24}$ cm^2, respectively, in which the polarization correction (due to Sternheimer) is taken into account. In the hfs of the spectrum of Os I the components due to the rarer odd isotope Os^{187} were detected and it was found that Os^{187} has a spin 1/2 and a magnetic moment most probably equal to $+0.12$ nm (possible range being from $+0.16$ nm to $+0.09$ nm). The quadrupole moment of Hg^{201} was calculated from the hfs of $6s6p\ ^1P_1$ and $6s6p\ ^3P_2$ of the spectrum of Hg I, taking the configuration interaction into account, and $Q(Hg^{201})=(+0.45\pm0.04)\times10^{-24}$ cm^2 was obtained.

I. SCREENING CORRECTION FOR A d-ELECTRON

IN the hyperfine structure (hfs) formulas for both the interval factor (A) and the quadrupole coupling constant (B) of a configuration containing d-electrons, the effective charge $Z_d{}^*$ for a d-electron frequently enters. It is usual to put $Z_d{}^*=Z-\sigma_d$, where σ_d is the screening correction for a d-electron. Casimir[1] assumed that $\sigma_d=10$, and this value has been adopted by many investigators. However, as far as the author is aware, this has no sound experimental basis. In order to fill this gap, an experimental investigation of the hfs of several atomic spectra was undertaken. A liquid-air-cooled hollow-cathode discharge tube described previously[2] was used, and a Fabry-Pérot etalon was used to resolve the hfs.

We begin with the analysis of the configuration $4d^3$ of Nb I.[3] Nb is known to consist of only one isotope Nb^{93} with spin 9/2.[4] The hfs was previously measured by Meeks and Fisher,[5] using a water-cooled hollow

[1] H. Casimir, Verhandel. Teylers Tweede Genootschap, Haarlem (1936), p. 11.

[2] K. Murakawa, J. Phys. Soc. (Japan) **9**, 391 (1954).

[3] The notation of the level symbol of the spectrum of Nb I was taken from W. F. Meggers and B. F. Scribner, J. Research Natl. Bur. Standards **14**, 629 (1935).

[4] J. E. Mack, Revs. Modern Phys. **22**, 64 (1950). P. F. A. Klinkenberg, Revs. Modern Phys. **24**, 63 (1952). K. Murakawa and T. Kamei, Rept. Inst. Sci. Technol. Univ. Tokyo **7**, 219 (1953).

[5] W. W. Meeks and R. A. Fisher, Phys. Rev. **72**, 451 (1947).

TABLE I. Hfs of Nb I.

$4d^35s^2$	A (cm^{-1}) K.M.[a]	A (cm^{-1}) M and F[b]	$4d^45s$	A (cm^{-1}) K.M.[a]	A (cm^{-1}) M and F[b]
$^4F_{9/2}$	0.0109	0.005	$^6D_{9/2}$	0.0250	0.021
$^4F_{7/2}$	0.0101	0.004	$^6D_{7/2}$	0.0249	0.022
$^4F_{5/2}$	0.0129	0.013	$^6D_{5/2}$	0.0255	0.024
$^4F_{3/2}$	0.02190	0.021	$^6D_{3/2}$	0.02863	0.028
			$^6D_{1/2}$	0.06264	0.060

[a] Our value.
[b] Value given in reference 5.

cathode. In the present work using an improved technique, more accurate results were obtained, as shown in Table I. The $4d^3$ configuration of Nb I is of fairly good LS coupling, so the values of $A(^4F)$ can be described by the formulas[6]:

$$\begin{aligned} A(d^3\,{}^4F_{9/2}) &= (8a_d'+a_d''+8a_d''')/9, \\ A(d^3\,{}^4F_{7/2}) &= (281a_d'+34a_d''+128a_d''')/315, \\ A(d^3\,{}^4F_{5/2}) &= (712a_d'+163a_d''-424a_d''')/875, \\ A(d^3\,{}^4F_{3/2}) &= (59a_d'+66a_d''-368a_d''')/125, \\ a_d' &= a(d_{5/2}), \quad a'' = a(d_{3/2}), \quad a''' = a(d_{5/2,\,3/2}). \end{aligned} \tag{1}$$

Of the levels arising from the configuration $4d^45s$ of Nb I, only ^6D and ^4D are available to the author and it is impossible to calculate accurate percentage of mixing[7] of $4d^35s^2\,{}^4F$ and $4d^4(_4{}^3F)5s\,{}^4F$. However, a calculation based on the interpolation between neighboring elements shows that within the accuracy of about six percent the mixing of $4d^4(_4{}^3F)5s\,{}^4F$ will not influence $A(4d^3\,{}^4F)$. The values of $A(4d^3\,{}^4F)$ listed in Table I can be fitted fairly well into the aforementioned formulas by choosing $a(d_{5/2})=0.0234$ cm^{-1}. Putting this and $\zeta_d=450$ and $\mu/I=1.3701$ in the well-known formula (the notations are the same as reference 1)

$$a(d_l)=\frac{8}{5}\frac{\zeta_d}{Z_d^*}\frac{F_2''}{H_2}\frac{1}{1836}\frac{\mu}{I}, \tag{2}$$

TABLE II. Screening correction for d-electrons.

Spectrum	Z	$a(d_{3/2})$	Z_d^*	σ_d	Data
Co^{59} I	27	0.0382	11.8	15.2	a
Nb^{93} I	41	0.0234 0.0222	23.5	17.5	
La^{139} I	57	0.00696	39.7	17.3	b
Lu^{175} I	71	0.01120	51.0	20.0	c
Pt^{195} I	78	0.0744	60.3	17.7	d

[a] See reference 8.
[b] See references 9 and 10, and some unpublished data of the present author.
[c] See reference 11. Gollnow found $a^{175}(6s)=0.320$ cm^{-1} in the spectrum of Lu II. Putting this and F (relativity correction) $=1.465$, $1-\delta$ (nuclear finite volume correction) $=0.917$, $(d\nu^*/dn)/\nu^{*3}=0.125$, $I=7/2$ in the modified Goudsmit-Fermi-Segrè formula, we get $\mu=2.77\pm0.3$ nm instead of Gollnow's $\mu=2.6\pm0.5$ nm. The new value of μ was used in deriving the value of Z_d^*.
[d] See reference 12.

[6] When the relativity correction is neglected, these formulas go over to those that are calculated by the formulas given by S. Goudsmit [Phys. Rev. **37**, 663 (1931)] and by R. E. Trees [Phys. Rev. **92**, 308 (1953)].
[7] The lower index attached to ^3F is the seniority number defined by G. Racah, Phys. Rev. **63**, 367 (1943).

we get $Z_d^*=23.0$. Since $Z(\mathrm{Nb})=41$, we obtain $\sigma_d=18.0$.

Similarly from the configuration $4d^35s\,{}^6D$ (Table I), we get $a(d_{3/2})=0.0222$ cm^{-1}, $a(5s)=0.217$ cm^{-1} [Meeks and Fisher[5] obtained $a(5s)=0.155$ cm^{-1}]. Putting this $a(d_{3/2})$ and $\zeta_d=450$ cm^{-1} in the formula (2), we get $Z_d^*=24.1$ and therefore $\sigma_d=16.9$. The mean of the two values of σ_d obtained from the $4d^3$ and $4d^45s$ configurations is $\sigma_d=17.5$.

In an analogous way we can derive the values of σ_d for other arc spectra, using spectroscopic data given in the literature[8–12] and the values of μ[4]. They are listed in Table II. In the practical use for the present work, Table II was represented by a graph plotting σ_d *versus* Z.

II. QUADRUPOLE MOMENT OF Nb^{93}

The hfs of Nb I that are suited for deriving the value of Q are shown in Figs. 1 and 2. From these measurements we get the constants: $A=0.02190$, $B=0.0021\times10^{-3}$ cm^{-1} for $4d^35s^2\,{}^4F_{3/2}$, and $A=0.02864$, $B=-0.0036\times10^{-3}$ cm^{-1} for $4d^45s\,{}^6D_{3/2}$. Two lines lie close to λ4195, and the measurement is therefore difficult, so the accuracy of $B(4d^45s\,{}^6D_{3/2})$ is inferior to $B(4d^35s^2\,{}^4F_{3/2})$. For the former level we can use the formula derived by Schmidt[13]:

$$(d^3\,{}^4F_{3/2}{}^{3/2}|\omega|d^3\,{}^4F_{3/2}{}^{3/2}) = (13R_2'+14R_2''-12S_2)8/875, \tag{3}$$

in which we have put $\omega=3\cos^2\theta-1$ for brevity. Putting $R_2'\doteqdot S_2=1.00_5$, $R_2''=1.03$ in (3) and then putting the value of B and $Z_d^*=23.5$, $\zeta_d=450$ in modified Casimir's formula

$$Q=-BZ^*HI(2I-1)J(2J-1)(1+\Delta)1.988\times10^{-21}/[\zeta\langle\textstyle\sum\omega\rangle_{Nr}], \tag{4}$$

we get $Q=-0.20\times10^{-24}$ cm^2 from the level $4d^35s^2\,{}^4F_{3/2}$. In the formula (4), Δ is the polarization correction due to Sternheimer,[14] and we have assumed $\Delta_d=0.196$ for Nb.

Similarly for the level $4d^45s\,{}^6D_{3/2}$ the formula

$$(d^4s\,{}^6D_{3/2}{}^{3/2}|\omega|d^4s\,{}^6D_{3/2}{}^{3/2}) = -(2/175)\times[(3128/175)R_2'+(29/25)R_2''+(1044/175)S_2] \tag{5}$$

was derived and $Q=-0.15\times10^{-24}$ cm^2 was obtained.

The value of Q derived from $4d^3\,{}^4F_{3/2}$ is more trustworthy, and taking the possible effect of the configuration interaction as well as the experimental error into account, we might consider

$$Q(\mathrm{Nb}^{93})=(-0.20\pm0.10)\times10^{-24}\ \mathrm{cm}^2$$

as the final value. Cotts and Knight[15] have observed

[8] E. Rasmussen, Z. Physik **102**, 229 (1936).
[9] O. E. Anderson, Phys. Rev. **46**, 473 (1934).
[10] M. F. Crawford, Phys. Rev. **47**, 768 (1935).
[11] H. Gollnow, Z. Physik **103**, 443 (1936).
[12] T. Schmidt, Z. Physik **101**, 486 (1936).
[13] T. Schmidt, Z. Physik **121**, 63 (1943).
[14] R. Sternheimer, Phys. Rev. **84**, 244 (1951); **86**, 316 (1952).
[15] R. M. Cotts and W. D. Knight, Phys. Rev. **93**, 940 (1954).

nuclear resonance of Nb^{93} in $KNbO_3$ and found definite evidence of the existence of a quadrupole moment[16] in Nb^{93}.

III. QUADRUPOLE MOMENT OF La^{139}

In a previous work[17] the hfs of the line La I λ5106 $[5d^26s\,{}^4F_{3/2}-5d^2(^3F)6p\,{}^4D_{1/2}]$ was studied. In the present work this line and other lines involving the same final level were studied, and $A=-0.01615$ cm^{-1}, $B=0.0062\times10^{-3}$ cm^{-1} were obtained for the level $5d^26s\,{}^4F_{3/2}$. This value of B is somewhat smaller than that of the previous work. Putting $Z_d^*=39.7$ (instead of $57-10=47$ of the previous work) and $(d^2s\,{}^4F_{3/2}'|\omega|d^2s\,{}^4F_{3/2}')=-0.1352$ (calculated in reference 2) and $\Delta_d=0.164$, $\zeta_d=420$ (instead of Crawford's[10] 400), $H_2=1.01$ in the formula (4), we get

$$Q(\mathrm{La}^{139})=(0.6\pm0.2)\times10^{-24}\ \mathrm{cm}^2.$$

This is more accurate than the previous value.[17]

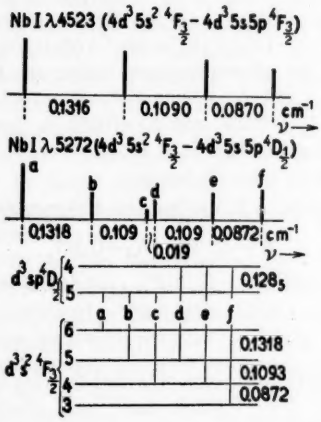

FIG. 1. Hfs of Nb I, λ4523 and λ5272.

IV. NUCLEAR SPIN OF Os^{187}

Osmium is known[18] to consist of seven isotopes: 184 (0.018), 186 (1.59), 187 (1.64), 188 (13.3), 189 (16.1), 190 (26.4), and 192 (41.0). The abundance in percent is in parentheses. The isotope 184 is too weak to be detected in hfs patterns, but 187 could be detected in the line Os I λ4447 as shown in Fig. 3.[19] Since another strong line lies close, the measurement of the positions of 187 and 186 in λ4447 was difficult and has no great accuracy. The component 187 was found to be relatively sharp, so $\mu(Os^{187})$ must be small. The hfs of λ4260 which had been studied in detail previously[20] was again studied, and indeed a component α due to Os^{187} was detected (see Fig. 3). Assuming the intensity of the 186-component to be 15.9, the intensity of α was measured to be 8.9 ± 0.9. This can be interpreted only by the assumption that Os^{187} has a spin 1/2 and that $\mu(Os^{187})$ is positive. The hfs of Os I λ4420 and λ4135 were then examined, and it was found that they support the above-mentioned assumption for Os^{187}.

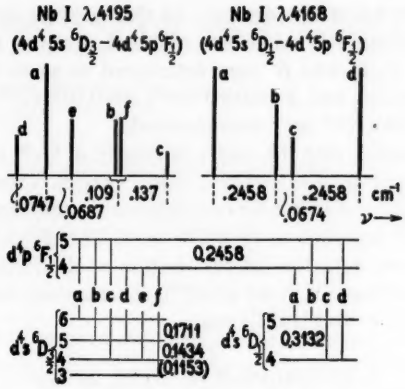

FIG. 2. Hfs of Nb I, λ4195 and λ4168.

The value of $\mu(Os^{187})$ can be determined relative to $\mu(Os^{189})=+0.65065$ nm that has been determined by Loeliger and Sarles[21] by the nuclear induction method.

Let A, B and A', B' denote the interval factor and quadrupole coupling constant of the initial and the final level of λ4260, respectively, for the isotope Os^{189} with spin 3/2.[20] Since the $5d^66s^2$ configuration of Os I is of jj coupling, we can put $A(5d^66s^2\,{}^5D_4')=a(d_{5/2})=0.008$ cm^{-1}, in which we have assumed that $Z_d^*=76-19=57$. The wave function for the initial level was first expressed as a linear combination of jj-coupling wave functions and then transformed into a linear combination of LS-coupling wave functions, and electrostatic interaction with other configurations was

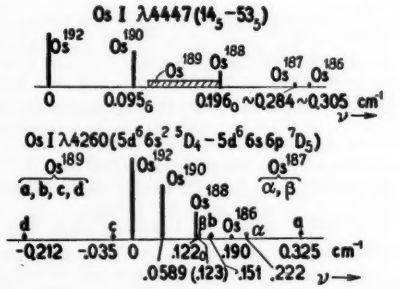

FIG. 3. Hfs of Os I, λ4447 and λ4260.

[16] Just before submitting the present paper, we received the short note of D. R. Speck and F. A. Jenkins, Bull. Am. Phys. Soc. 29, No. 8, 34 (1954). They measured the hfs of the level $4d^25s^2\,{}^4F_{3/2}$ of Nb I and obtained $Q(Nb^{93})=(-0.4\pm0.3)\times10^{-24}$ cm^2.

[17] K. Murakawa and T. Kamei, Phys. Rev. 92, 325 (1953). See also reference 2.

[18] O. Nier, Phys. Rev. 52, 885 (1937).

[19] The classification of the Os I spectrum was given by W. Albertson, Phys. Rev. 45, 304 (1934).

[20] K. Murakawa and S. Suwa, Phys. Rev. 87, 1048 (1952).

[21] H. R. Loeliger and L. R. Sarles, Phys. Rev. 95, 291 (1954).

roughly taken into account. In this way the approximate relation $B' \approx 3.0B$ was obtained. Keeping this in mind, A, B, and B' were determined so as to fit the observation, and $A=0.0383$ cm^{-1}, $B=0.10\times10^{-13}$ cm^{-1}, $B'=0.34\times10^{-3}$ cm^{-1} were obtained.[22]

Assuming that the center of gravity of Os^{187} is such that the ratio $(Os^{186}-Os^{187})/(Os^{187}-Os^{188})$ is the same for λ4447 and λ4260, we can estimate the total splitting of Os^{187} in λ4260 to be 0.099 cm^{-1}. This gives, when compared with the interval factors of the initial and final levels of Os^{189} and $\mu(Os^{189})$, the magnetic moment of Os^{187} as $+0.12\{^{+0.04}_{-0.03}\}$ nm.

V. QUADRUPOLE MOMENT OF Hg^{201}

As a continuation of the study of the hfs of the spectrum of mercury by means of a high-frequency electrodeless discharge tube[23] which is better than a hollow cathode, the hfs of the lines Hg I λ5790 ($6p\,^1P_1-6d\,^1D_2$) and λ4916 ($6p\,^1P_1-8s\,^1S_0$) was studied, and data concerning $6p\,^1P_1$ that are more accurate than before[24] were obtained: the splitting of Hg^{201} ($I=3/2$) in $6p\,^1P_1$ was found to be $F_{5/2}-F_{3/2}=0.124_2$ cm^{-1}, $F_{3/2}-F_{1/2}=0.042_8$ cm^{-1} and that of Hg^{199} ($I=1/2$) $F_{3/2}-F_{1/2}=-0.179_9$ cm^{-1}, from which we get $A=0.0443$ cm^{-1}, $B=1.32_2\times10^{-3}$ cm^{-1} for $6p\,^1P_1(Hg^{201})$. The wave function of $6s6p\,^1P_1$ can be obtained by the procedure published by Hume and Crawford[25] in treating the analogous spectrum of Pb III. In the case of Hg I, the mixing of the configuration $5d^96s^26p$ is essential. Expressing the wave function in the present case as a linear combination of LS-coupling wave functions, we have

$$6s6p\,^1P_1' = K_1\,^3P_1(6s6p)+K_2\,^1P_1(6s6p) +K_3\,^1P_1(6s7p)+K_4\,^1P_1(5d^9\,6s^26p), \quad (6)$$

$$K_1=-0.158, \quad K_2=0.883, \quad K_3=0.286, \quad K_4=0.336,$$

where the prime denotes that the wave function is actually of intermediate coupling and also perturbed. The quadrupole moment of Hg^{201} can be calculated by the equation:

$$Q=-BI(2I-1)J(2J-1)1.988 \times10^{-21}\Big/\Big[\frac{\zeta_{6p}}{Z_p^*H_1(1+\Delta_p)}\Big\{K_1^2(sp\,^1P_1|\omega|sp\,^1P_1) +K_2^2(sp\,^3P_1|\omega|sp\,^3P_1)+2K_1K_2(sp\,^1P_1|\omega|sp\,^3P_1)\Big\} +\frac{\zeta_{7p}}{Z_p^*H_1(1+\Delta_p)}K_3^2(sp\,^1P_1|\omega|sp\,^1P_1) +K_4^2\Big\{\frac{\zeta_{6p}}{Z_p^*H_1(1+\Delta_p)}(dp\,^1P_1|\omega|dp\,^1P_1)_p -\frac{\zeta_{5d}}{Z_d^*H_2(1+\Delta_d)}(dp\,^1P_1|\omega|dp\,^1P_1)_d\Big\}\Big], \quad (7)$$

where $(dp\,^1P_1|\omega|dp\,^1P_1)_l$ means the angular part (including R', R'' and S) of $(dp\,^1P_1|\omega/r^3|dp\,^1P_1)$ contributed by the l-electron. The matrix elements of ω are $(sp\,^3P_1|\omega|sp^3P_1)=(-R'+4S)/15$, $(sp\,^1P_1|\omega|sp\,^1P_1) =-(2/15)(R'+2S)$, $(sp\,^3P_1|\omega|sp\,^1P_1)=(2^{1/2}/15)\times(R'-S)$, and $(dp\,^1P_1|\omega/r^3|dp)\,^1P_1=-(1/75)(R'+2S)\times\langle1/r_p^3\rangle_{Hg}-(1/125)(12R_2'+7R_2''+6S_2)\langle1/r_d^3\rangle_{Hg}$.

Putting the aforementioned value of B and $\zeta_{5p}=4300$, $\zeta_{7p}=460$, $\zeta_{5d}=6150$, $Z_p^*=80-4=76$, $Z_d^*=80-20=60$, $\Delta_p=0.019$, and $\Delta_d=0.085$ in Eqs. (6), (7), and (4), we get $Q(Hg^{201})=0.42\times10^{-24}$ cm^2.

Similarly for $6s6p\,^3P_2$ we get

$$6s6p\,^3P_2' = K_1\,^3P_2(6s6p)+K_2\,^3P_2(5d^96p), \quad (8)$$

$$K_1=0.958, \quad K_2=0.287,$$

$$(sp\,^3P_2|\omega|sp\,^3P_2)=-(2/5)R', \quad (dp\,^3P_2|\omega/r^3|dp\,^3P_2) =(-1/125)(36R_2'+R_2''-12S_2)\langle1/r_d^3\rangle_{Hg} +(1/25)(3R'-4S)\langle1/r_p^3\rangle_{Hg}. \quad (9)$$

The constants that were obtained for this level previously[24] are $A=-0.1119_0$ cm^{-1} and $B=0.278\times10^{-3}$ cm^{-1} for Hg^{201}. Putting (8) and (9) in an expression similar to (7) and then in (4), we get $Q(Hg^{201})=0.46\times10^{-24}$ cm^2.

Because of the insufficient number of equations for determining the composition of $6s6p\,^1P_1$ the mixing of $6s8p\,^1P_1$ was tentatively neglected. Inclusion of this will slightly increase the value of Q obtained from $6s6p\,^1P_1$. We might thus consider

$$Q(Hg^{201})=(0.45\pm0.04)\times10^{-24} \text{ cm}^2$$

as the best value available at present. Schüler and Schmidt[26] obtained 0.5×10^{-24} cm^2, without taking configuration interaction into account, and Dehmelt, Robinson, and Gordy[27] obtained 0.6×10^{-24} cm^2 by a nuclear quadrupole resonance experiment.

[22] Since the final level is of jj-coupling, we have $(d^4\,^5D_4'|\omega|d^4\,^5D_4') =(16/35)R_2'$. Putting $B=0.34\times10^{-3}$ cm^{-1}, $\Delta_d=0.10$, $\zeta_d=2700$, $R_2'=1.05$ and $H_2=1.02_3$ in the formula (4), and reversing the sign, we get $Q(Os^{189})=(2.7\pm1.3)\times10^{-24}$ cm^2. The uncertainty comes mainly from the fact that the splitting of the final level cannot be deduced from the observed hfs by a purely empirical method.

[23] K. Murakawa, Phys. Rev. **93**, 1232 (1954).

[24] K. Murakawa, Phys. Rev. **78**, 480 (1950). K. Murakawa and S. Suwa, J. Phys. Soc. (Japan) **5**, 429 (1950).

[25] J. N. P. Hume and M. F. Crawford, Phys. Rev. **84**, 486 (1951).

[26] H. Schüler and T. Schmidt, Z. Physik **98**, 239 (1935).

[27] Dehmelt, Robinson, and Gordy, Phys. Rev. **93**, 480 (1954).

Energy Levels in B^9 and Be^7 from the Reactions $C^{12}(p,\alpha)B^9$ and $B^{10}(p,\alpha)Be^7$†

J. B. REYNOLDS
Palmer Physical Laboratory, Princeton University, Princeton, New Jersey
(Received February 10, 1955)

The energy levels of Be^7 and B^9 have been studied by observation of the alpha-particle spectra resulting from the reactions $B^{10}(p,\alpha)Be^7$ and $C^{12}(p,\alpha)B^9$. Alpha groups were observed corresponding to the ground state of B^9 and an excited state at 2.39±0.08 Mev. Groups were observed corresponding to Be^7 being left in the ground state and excited states of the following energies: 0.49±0.10 Mev, 4.72±0.08 Mev, 6.27±0.10 Mev, 7.21±0.10 Mev, 14.6±0.3 Mev.

I. INTRODUCTION

A STUDY of the energy levels of Be^7 and B^9 has been made by observation of the alpha-particle spectra resulting from the reactions $B^{10}(p,\alpha)Be^7$ and $C^{12}(p,\alpha)B^9$. The (p,α) reaction is often particularly suitable for such studies since in many cases in the light nuclei it is possible to reach final states which are accessible otherwise only by the (p,n) reaction. Although the photographic plate technique for neutron spectroscopy has been most successful, it is still more convenient to deal with reactions in which charged particles are involved if possible. The disadvantage of the (p,α) reaction for such studies is that with a few (notable) exceptions the Q's for such reactions in the light elements are quite highly negative. 18-Mev protons from the Princeton synchrocyclotron, however, are sufficiently energetic to produce the (p,α) reaction in any element.[1]

The alpha-particle spectrometer employed in the experiment is an obvious extension of the differential-range ion chamber of Rutherford *et al.*[2] and seems to have occurred to several workers[3] nearly simultaneously. Its main advantages are good resolution (for a range-measuring device), extreme stability, and lack of sensitivity to any particles except alpha and He^3 particles.

II. EXPERIMENTAL ARRANGEMENT

The scattering chamber in which the experiment was performed has been described by Likely and Franzen.[4] The collimated proton beam passed through the target foil and was collected in a Faraday cup. Total charge collected by the cup during a run was measured and used to normalize data with respect to the incident beam intensity. Alpha particles ejected from the target foil as a result of proton bombardment were received by the detecting apparatus which could be placed at any of 5 ports spaced 30° apart on the scattering chamber. A detailed view of the detection apparatus is shown in Fig. 1. The detector consisted of an air absorption chamber (of known length), in which the air pressure could be varied, followed by a series of three proportional counters. Pulses from counters No. 1 and No. 2 were in coincidence with one another and in anticoincidence with those from counter No. 3; i.e., only those alphas were counted which traversed the absorption chamber and counters No. 1 and No. 2, but not No. 3. The relative counting rate *vs* pressure in the absorption chamber gives a differential range curve. A "monochromatic" α group (e.g., Po α's) entering the detector results in maximum counting rate when the absorption chamber pressure is such as to make the α's stop in a small region between chambers No. 2 and No. 3. The "line" obtained by plotting counting rate *vs* pressure for such a group is approximately Gaussian in shape and has a full width at half-maximum of ~100 kev.

Figure 2 shows the spectrum obtained from a ThC+C′ source. The peak width (full width at half-maximum) is ~100 kev for the 6.05-Mev group (this peak is actually due to two groups, which has the effect of broadening the peak) and ~140 kev for the 8.78-Mev group. The range of an α group whose energy is to be measured consists of two parts: (1) the known distance traveled in the absorption chamber in air of known pressure, temperature, and humidity and (2) that part of the particle range accounted for by the two mica windows and counters No. 1 and No. 2 which particles also have to traverse. Part (2) is a constant of the apparatus[5] and can be determined by measuring the range of an α group of known energy; e.g., assume the energy of the ThC group (Fig. 2) to be 6.05 Mev and hence to have a range[6] of 4.72 cm. Of this the absorption chamber accounts for (27.7 cm Hg/76.0 cm Hg)×6.87 cm×0.958=2.39 cm, leaving 2.33 cm as residual range accounted for by foils and counters. 27.7-cm Hg is the pressure at which the peak occurs, 6.87 cm is the ab-

† This work was supported by the U. S. Atomic Energy Commission and the Higgins Scientific Trust Fund.

[1] The (p,d) reaction also can sometimes be used to reach the same final states as are accessible to (p,n) reactions, but for these also the Q is usually highly negative.

[2] Rutherford, Ward, and Wynn-Williams, Proc. Roy. Soc. (London) **A129**, 211 (1930).

[3] E.g., J. R. Holt and T. N. Marsham, Proc. Roy. Soc. (London) **A66**, 249 (1953); also used such a scheme in their study of (d,p) reactions.

[4] J. G. Likely and W. Franzen, Phys. Rev. **87**, 666 (1952).

[5] Constant except for the fact that the equivalent of the first mica window varies slightly with the incident α energy. This correction is usually negligible but can be easily made if necessary.

[6] The range-energy curves of H. A. Bethe, Revs. Modern Phys. **22**, 217 (1950), and H. A. Bethe, U. S. Atomic Energy Commission Report BNL-T-7 (unpublished), were used to compute α energies in this work.

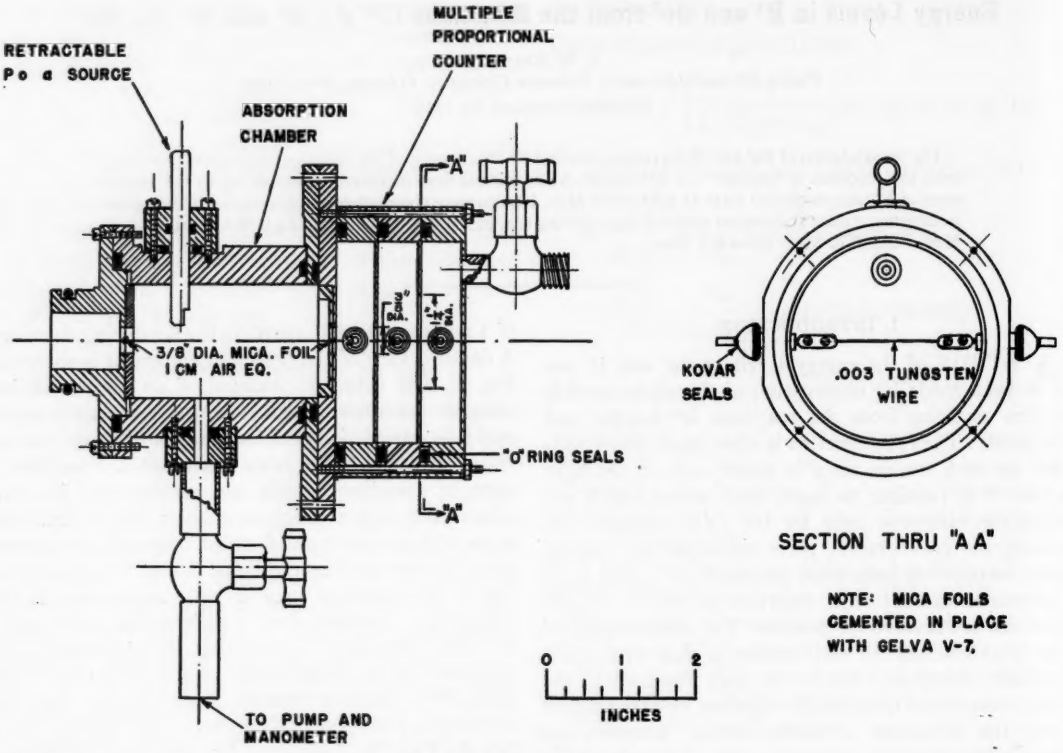

FIG. 1. The alpha-particle detector.

sorption chamber length, and 0.958 is a factor which converts from air at 24.5°C and 40 percent humidity (conditions under which the data were taken) to dry air at 15°C (the conditions for which Bethe's curves were drawn). Using this value for the residual stopping power, one obtains $R=2.33+6.87\times(71.4/76.0)\times 0.958 = 8.50$ cm as the range of the ThC′ α group. This corresponds to an α energy of 8.76 Mev as opposed to the accepted value of 8.78 Mev.

The constructional details of the counters are shown in Fig. 1. The counters were filled to ~5 cm Hg with a 2 percent CO_2 in argon mixture. The circuitry was of standard design; Model 100 amplifiers set at about full gain were used for the α pulses which were then fed to integral discriminators, the outputs of which went to a conventional coincidence-anticoincidence circuit. The counters were operated with ~750 v on the central wires and gave ~50 v pulses from the model 100 amplifiers.

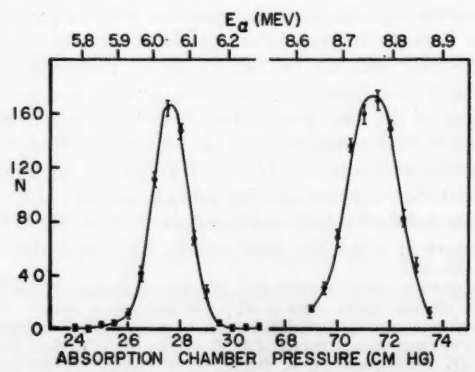

FIG. 2. Alpha-particle spectrum from a ThC+C′ source. N is the anticoincidence counting rate in arbitrary units.

Variation of setting of the discriminator associated with counter No. 3 by as much as 20 percent did not appreciably shift the position of an α peak. Drifts in discriminator settings amounted to less than 1–2 percent over intervals long compared to the time required to take a spectrum. In practice, discriminator No. 2 was set to take pulses well above noise but well below the α pulse height due to ~5-Mev α's traversing counter No. 2. Discriminator No. 3 was set one-half as high as No. 2. Discriminator No. 1 was slightly below the maximum value it could have without reducing the height of an α peak. With this setting, the apparatus was insensitive to any particles except He^3 and He^4.

The energy of the incident proton beam was measured by determining the range in aluminum of protons scattered out of the incident beam at 90° by a thin polythene foil. The accurate proton range-energy results

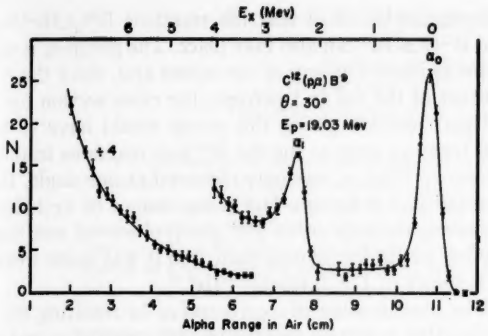

FIG. 3. Spectrum of alpha particles observed at 30° as a result of the bombardment of C^{12} with 19 Mev protons. N is the relative anticoincidence rate per unit of integrated beam current. E_x is the excitation energy of the final B^9 nucleus for the given alpha range.

of Bichsel and Mozley[7] were used in determining proton energies.

The line widths of α groups resulting from proton bombardment (Fig. 3 and following) are approximately 300 kev. Contributing factors to this are mainly cyclotron beam energy spread, target foil thickness, and finite angle subtended by the detector.

The absorption chamber was not operated at pressures greater than atmospheric. Alpha groups whose range was greater than the length of the absorption chamber were studied by inserting aluminum foils of appropriate thickness into the alpha-particle path. The spectra of Figs. 3–7 are plotted as a function of alpha range in air, the total amount of material traversed by the alphas having been converted to an equivalent amount of air at 76 cm Hg and 15°C. Absorption chamber pressure was read on a mercury manometer which was calibrated by use of a cathetometer.

III. RESULTS FOR $C^{12}(p,\alpha)B^9$

This reaction was observed using targets of 0.5 mg/cm² polythene foil and also with targets of (~0.2 mg/cm²) lampblack on a platinum backing.

Figures 3 and 4 are typical of the alpha spectra obtained from the reaction. Data were also taken at 60° and 120° with similar results. Alpha groups resulting in B^9 being left in its ground state (α_0) and an excited state (α_1) are seen at all angles. The ratio of the number of α's in α_1 to the number in α_0 appears to be about the same at 30°, 90°, and 120° and somewhat lower at 60°.

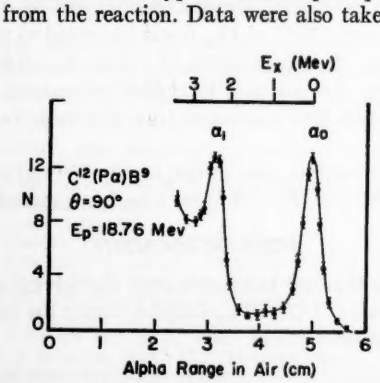

FIG. 4. $C^{12}(p,\alpha)B^9$ alpha spectrum at 60° in the laboratory system.

[7] H. Bichsel and R. F. Mozley, Phys. Rev. 94, 764(A) (1954).

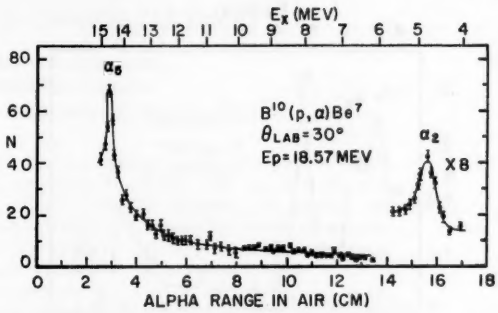

FIG. 5. $B^{10}(p,\alpha)Be^7$ alpha spectrum at 30° in the laboratory system.

The group α_0 appears not to have a strong variation in differential cross section as a function of angle. The average differential cross section for α_0 for the five angles observed ($E_p \sim 18$ Mev) is 3 ± 1 mb/sterad.

Previous information on the B^9 ground state has been obtained by the $Be^9(p,n)$ and $B^{10}(\gamma,n)$ reactions.[8] Using the mass values assigned by Li *et al.*,[9] one obtains for the Q of the $C^{12}(p,\alpha)B^9$ (ground state) reaction a value of -7.56 ± 0.03 Mev. The average of two determinations at $0=60°$ and one at 90° in the present experiment gave $Q=-7.58\pm0.1$ Mev. The Q difference, ΔQ, for (p,α) reactions leading to the B^9 ground state and the observed excited state was found to be 2.39 ±0.08 Mev. This may be compared with the value obtained by Ajzenberg and Buechner[10] who, by studying neutron groups from the reaction $B^9(p,n)B^9$, obtain the value 2.37 ± 0.04 for ΔQ.

No evidence was found for other α-particle groups. The minimum α energy detected was ~3 Mev. At 30°

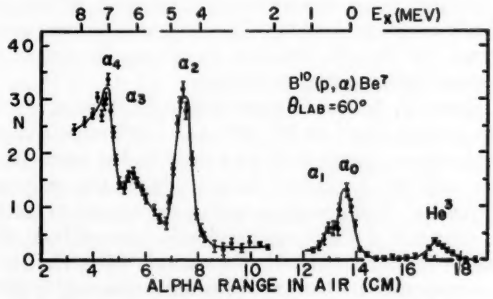

FIG. 6. $B^{10}(p,\alpha)Be^7$ alpha spectrum at 60°.

[8] F. Ajzenberg and T. Lauritsen, Revs. Modern Phys. 24, 321 (1952).

[9] Li, Whaling, Fowler, and Lauritsen, Phys. Rev. 83, 512 (1951).

[10] F. Ajzenberg and W. W. Buechner, Phys. Rev. 91, 674 (1953).

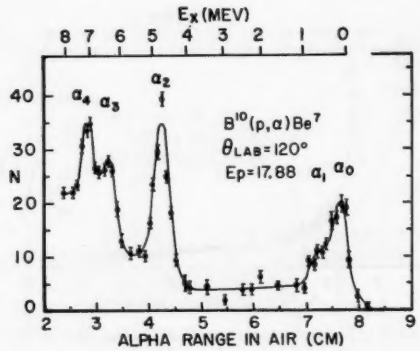

FIG. 7. $B^{10}(p,\alpha)Be^7$ alpha spectrum at 120°.

in the laboratory, this α energy would correspond to the B^9 nucleus being excited by about 7.9 Mev. The mirror image of the reported 6.8-Mev level[7] in Be^9 was not observed.

The two levels in B^9 discussed here have also been studied by the writer[11] by the reaction $B^{10}(p,d)B^9$. An analysis of the deuteron angular distributions indicates negative parity and spin $>\frac{1}{2}$ for both states.

The groups α_0 and α_1 are superimposed on a continuous alpha-particle background, the origin of which is not certain. Its most likely source is from the reaction $C^{12}(p,p')C^{12*}$ followed by $C^{12*}\rightarrow 3\alpha$. The Q for this reaction is -7.27 Mev as opposed to -7.56 Mev for the $C^{12}(p,\alpha)B^9$ (ground state) reaction. This is consistent with the fact that the alpha continuum appears to start somewhere under the α_0 peak. The high-energy part of this continuum cannot arise from B^9(ground)$\rightarrow p+2\alpha$ for which the Q is 281 kev or from Be^8(ground)$\rightarrow 2\alpha$ for which $Q=90$ kev. It is, of course, possible that the continuum comes from decay of excited states of either B^9 or Be^8.

IV. EXPERIMENTAL RESULTS: $B^{10}(p,\alpha)Be^7$

The B^{10} target consisted of a thin ($\sim$0.2 mg/cm^2) evaporated layer of enriched (97 percent) B^{10} on an 0.2-mil platinum backing. The evaporation was performed by Dr. W. Franzen to whom the writer is indebted for supplying the target.

Figures 5, 6, and 7 show the alpha spectra for θ (lab system) equal to 30°, 60°, and 120°, respectively. The group α_2 corresponds to a level in Be^7 previously seen only by Thomson[12] in a study of the reaction $Li^7(p,n)Be^7$. The groups α_3 and α_4 correspond to levels the existence of which was previously inferred from the observation of resonances in the reaction[7] $Li^6(p,He^4)He^3$. α_5 corresponds to a level not previously observed in Be^7.

[11] J. B. Reynolds and K. G. Standing, Phys. Rev. **95**, 639 (1954).
[12] D. M. Thomson, Phys. Rev. **88**, 954 (1952).

It should be noted that the reactions $B^{10}(p,He^3)Be^8$ and $B^{11}(p,\alpha)Be^8$ can also take place. The group α_5 is ten times as intense as any of the others and, since the B^{11} content of the foil is 3 percent, the cross section for a $B^{11}(p,\alpha)$ reaction giving this group would have to be 300 times as large as for the $B^{10}(p,\alpha)$ reactions leading to $\alpha_0-\alpha_4$. Since α_5 was only observed at one angle, the possibility of it being a He^3 group cannot be excluded. However, the only other He^3 group observed was that leaving Be^8 in the ground state and it was quite weak. It is shown in Fig. 6 labeled "He^3."

The identification of α_0, α_1, and α_2 as resulting from $B^{10}(p,\alpha)Be^7$ is certain and the identification of α_4 and α_5 as resulting from the same reaction is quite certain. Table I summarizes the energy level diagram of Be^7 as determined by the experiment.

The Q for the reaction giving α_0 has been accurately measured[7] and was taken to be 1.15 Mev. The excitation energies of Table I were calculated by assuming this value for the ground state Q; e.g., the Q for the reaction leading to α_0 was *measured* to be 1.07 Mev. An exception to this was α_1, for which the excitation energy was calculated relative to the measured ground state Q.

TABLE I. Experimentally determined excitation energy in Be^7 for observed alpha-particle groups.

Group	Excitation energy, E_x (Mev)
0	0.08±0.10
1	0.49±0.10
2	4.72±0.08
3	6.27±0.10
4	7.21±0.10
5	14.6 ±0.3

In all cases except α_5, the experimental uncertainty in a single determination of E_x was estimated to be ±0.15 Mev. This represents uncertainty in determining beam energy, angle of observation, and range of alpha particles. To obtain the values shown in Table I, various independent determinations of E_x were averaged, the error being correspondingly reduced.

The group "He^3" of Fig. 6 was identified as such by comparing its experimental Q value of -0.60 Mev [assuming the reaction $B^{10}(p,He^3)Be^8$(ground)] with that of 0.53 Mev calculated from the mass values of Li *et al.*

The differential cross section for the $B^{10}(p,\alpha)$ reaction leading to α_3 is ($E_p\sim$18 Mev) 1.6±1 mb/sterad.

ACKNOWLEDGMENT

It is a pleasure to acknowledge the advice and encouragement of Dr. P. C. Gugelot during the course of the experiment.

K and *L* X-Ray Intensities in Cesium-131 Decay*

RICHARD W. FINK† AND BEROL L. ROBINSON‡
University of Arkansas, Fayetteville, Arkansas

(Received January 3, 1955; revised manuscript received March 3, 1955)

A measurement of the relative intensities of the K and L x-rays following electron-capture in Cs^{131} is reported. The result may be expressed $[L_I/K+L_{II,III}/K+n]\bar{\omega}_L=0.106\pm0.008$, where L_i/K is the ratio of L_i-shell capture to K-shell capture, n is the probability of an L-ionization following a K-vacancy, and $\bar{\omega}_L$ is the mean L-fluorescence yield of xenon. Upon combining this with recent theoretical results on electron-capture, the mean value of the L-fluorescence yield of xenon is found to be $0.10_3\pm0.01$. This value is suggested as a normalization point for the relative photographic values of $\bar{\omega}_L$ in the region $Z=54$.

In order to explain the observed anomalies in inner bremsstrahlung spectra of electron-capture on the basis of p-electron capture, one must conclude that L_{II}-capture is considerably more radiative than L_I-capture, and, furthermore, that the probability of radiative capture increases more strongly with Z for L_{II}-capture than for L_I-capture.

Traces of 6.2-day Cs^{132} and 13.6-day Cs^{136} were found in the first cesium fraction from pile-irradiated barium nitrate, presumably induced by (n,p) reactions.

INTRODUCTION

MARSHAK,[1] Rose and Jackson,[2] and Brysk and Rose[3] have computed theoretical values of the L_I/K-capture ratio as a function of atomic number and disintegration energy. From the curves of Brysk and Rose, the value of this ratio is computed to be 0.14 for Cs^{131}.

Saraf[4] has found an anomaly in the shape of the inner bremsstrahlung spectrum of Cs^{131} (which we have confirmed independently[5]); similar anomalies have been reported[6-8] in other electron capturers. Glauber and Martin[9] have suggested that the observed shape can be explained by taking into account the capture of electrons of nonzero angular momentum. This indicates that capture of L_{II} and L_{III} electrons might make a significant contribution to the inner bremsstrahlung.

The electron-capture of Cs^{131} is an allowed transition since $\log ft=5.3$ and the shell model predicts a $d_{5/2}\rightarrow d_{3/2}$ ($\Delta I=1$, no) transition.[4] In an attempt to investigate the relative contribution of p-electron capture, it seemed of interest to measure the ratio of the intensities of K and L x-rays following electron capture in Cs^{131}.

EXPERIMENTAL METHOD

A source was prepared by chemical separation of cesium from 44 grams of barium nitrate irradiated for 28 days in the Oak Ridge reactor. After precipitation of $BaCl_2\cdot H_2O$ from evaporation with (5:1) HCl-diethyl ether mixture, the supernatant cesium fraction was scavenged extensively with barium chloride precipitations, followed by lanthanum hydroxide, ferric hydroxide, and silver chloride scavengings. Separation from other alkali metals was accomplished by precipitation as the silicotungstate. Scintillation spectrometer studies of the final cesium fraction detected no trace of the intense gamma rays of Ba^{131}, indicating a decontamination factor from barium of better than 10^6. Traces of 6.2-day Cs^{132} and 13.6-day Cs^{136} were identified by scintillation spectrometry; these isotopes presumably are formed by (n,p) reactions in barium. Saraf[4] also observed Cs^{132} produced in this way. The traces of these isotopes have negligible effect on measurements reported here.

The L and K x-ray intensities were measured using an x-ray proportional counter filled with 2.1 atmos argon—0.2 atmos methane mixture. The counter was constructed of brass with an aluminum liner to eliminate fluorescent radiation from the brass. The side window was a 164 mg/cm² disk of Brush beryllium. The x-ray path length in the counter was about 10 cm. A potential of 3850 volts was applied to the 0.004-inch diameter stainless steel wire, and the amplified output was fed through a single-channel pulse analyzer into a recording ratemeter or scaler. A typical spectrum is shown in Fig. 1. The observed ratio of x-ray intensities, (N_L/N_K), was obtained by graphical integration using a planimeter. This ratio is $0.33_4\pm0.01$, representing an average of many determinations. The same value was also determined by the method of integral-bias counting, giving an independent check on the result. The intensity ratio may be expressed by Eq. (1)

$$\left(\frac{N_L}{N_K}\right)=\left[\frac{L_I+L_{II,III}+nK}{K}\right]\times\left(\frac{\bar{\omega}_L}{\omega_K}\right)\left(\frac{T_L}{T_K}\right)_W\left(\frac{T_L}{T_K}\right)_A\left(\frac{\xi_L}{\xi_K}\right)\left(\frac{S_L}{S_K}\right), \quad (1)$$

where K is the probability that a disintegration will

* Supported in part by the U. S. Atomic Energy Commission.
† Department of Chemistry.
‡ Department of Physics.
[1] R. E. Marshak, Phys. Rev. **61**, 431 (1942).
[2] M. E. Rose and J. L. Jackson, Phys. Rev. **76**, 1540 (1949).
[3] H. Brysk and M. E. Rose, Oak Ridge National Laboratory Report ORNL-1830, January 13, 1955 (unpublished).
[4] B. Saraf, Phys. Rev. **94**, 642 (1954).
[5] B. L. Robinson and R. W. Fink, *Annual Progress Report*, University of Arkansas, March 15, 1954 (unpublished).
[6] B. Saraf, Phys. Rev. **95**, 97 (1954).
[7] L. Madansky and F. Rasetti, Phys. Rev. **94**, 407 (1954).
[8] T. Lindqvist and C. S. Wu, Phys. Rev. **98**, 231(A)*(1955).
[9] R. J. Glauber and P. C. Martin, Phys. Rev. **95**, 572 (1954).

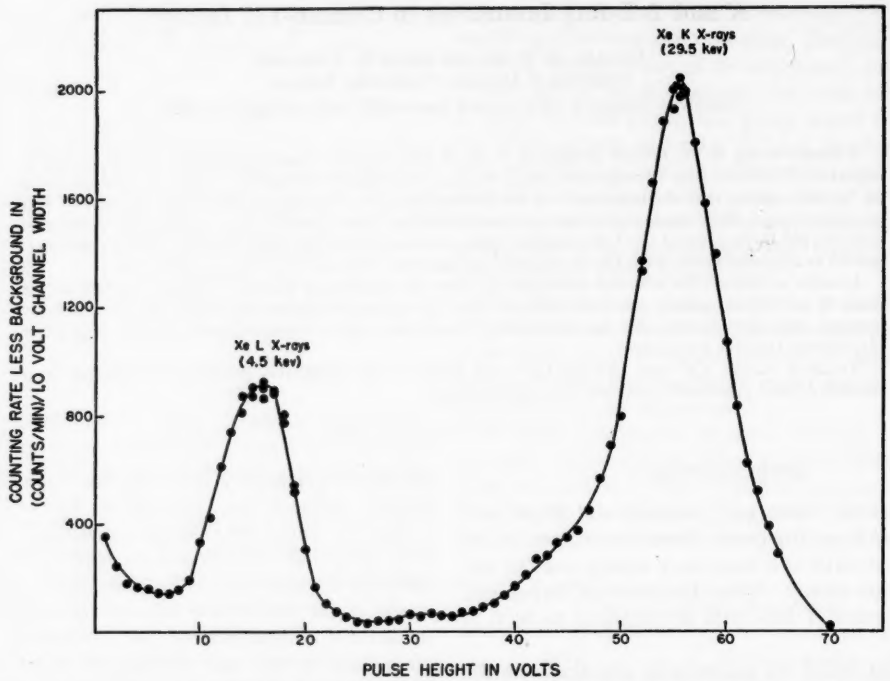

FIG. 1. Pulse-height spectrum of 9.8-day Cs^{131} in x-ray proportional counter filled with 2.1 atmos argon and 0.2 atmos methane. The points are those determined using a scaler and are corrected for background. The ratio of areas, (N_L/N_K), is $0.33_4 \pm 0.01$ by graphical integration. Integral-bias counting agrees exactly with this ratio within the above error limits.

occur by capture of an electron from the K-shell; $L_{\rm I}$, $L_{\rm II}$, and $L_{\rm III}$ are the probabilities of capture from the respective L-shells; n is the probability that a K-shell vacancy is filled by an L-electron; ω_K is the K x-ray fluorescence yield of xenon, taken as 0.87 ± 0.03 from the curve of Broyles, Thomas, and Haynes[10]; $\bar{\omega}_L$ is the mean L-fluorescence yield of xenon, which is discussed below; $(T_L/T_K)_W$ is the relative window transmission of xenon L and K x-rays, evaluated as 0.279 ± 0.006; $(T_L/T_K)_A$ is the relative air transmission which turns out to be very close to unity; (ξ_L/ξ_K) is the ratio of the gas counting efficiencies of xenon L and K x-rays in argon, which is 9.9 ± 0.5, computed from mass absorption coefficients from Allen[11]; and (S_L/S_K) is the correction for the self-absorption and self-scattering of x-rays in the source, taken as unity in the first approximation.

TABLE I. Xe L-shell ionization probabilities following K-shell ionizations.

Shell	Radiative transition	Auger transition	Total
$L_{\rm I}$	0.00	0.07	0.07
$L_{\rm II}$	0.23_5	0.04_5	0.28
$L_{\rm III}$	0.47	0.06_5	0.53
$L_{\rm total}$	0.70	0.18	$0.88 = n$

[10] Broyles, Thomas, and Haynes, Phys. Rev. 89, 715 (1953).
[11] S. J. M. Allen, tables in *Handbook of Chemistry and Physics* (Chemical Rubber Publishing Company, Cleveland, 1952), thirty-fourth edition.

Equation (1) may be rearranged and evaluated to give the quantity

$$[L_{\rm I}/K + L_{\rm II,III}/K + n]\bar{\omega}_L = 0.106 \pm 0.008, \quad (2)$$

which is our experimental result.

INTERPRETATION AND DISCUSSION

1. Ratio of $L_{\rm I}$ to K Capture

Brysk and Rose[8] have shown that for an allowed transition

$$L_{\rm I}/K = g_{L{\rm I}}^2 q_{L{\rm I}}^2 / g_K^2 q_K^2, \quad (3)$$

where $g_{L{\rm I}}$, g_K are screened relativistic Coulomb wave functions evaluated at the nuclear surface, and $q_{L{\rm I}}$, q_K are the neutrino energies associated with $L_{\rm I}$ and K capture, respectively. For Cs^{131}, q_K is 320 ± 10 kev from inner bremsstrahlung measurements.[4,5] From the relativistic wave-function ratios of Rose and Jackson[2] and from the graphs of Brysk and Rose, the value of $L_{\rm I}/K$ is found to be 0.14.

2. Ratio of $L_{\rm II}$ and $L_{\rm III}$ to K Capture

Brysk and Rose have shown that $L_{\rm III}$ capture always is negligible for allowed and first-forbidden ($\Delta I = 0, 1$)

transitions because the neutrino is forced into a higher angular momentum state. From their curves one finds that $L_{II}/L_I=0.027$ in the case of Cs^{131} and thus $L_{II}/K=0.004$.

3. *L*-Ionization Following *K*-Ionization

The probability that a *K*-shell vacancy is filled by an *L*-electron can be calculated from x-ray and Auger line intensities. The values of n have been interpolated from Burhop[12] and Massey and Burhop,[13] and are given in Table I. Since the *K*-fluorescence yield of xenon is large, the greatest contributions to n arise from radiative transitions, the intensities of which are well known.[13] The contribution of Auger transitions has been taken from the relative intensities of Auger lines at higher Z.[14] Coster-Krönig transitions, in which *L*-vacancies are shifted from one subshell to another, do not occur for $50<Z<75$.

4. *L*-Fluorescence Yield of Xenon

Experimental determinations of $\bar{\omega}_L$ have been made by Auger and by Bower, using cloud-chamber techniques, and by Lay, using a photographic method.[12] Their values are summarized in Table II, and are too large to be consistent with the work reported here. Using the values for L_I/K, L_{II}/K, L_{III}/K, and n deduced in the aforementioned, we find that $\bar{\omega}_L=0.10_3\pm0.01$ for xenon.

CONCLUSION

Combining the theoretical values of Brysk and Rose[3] for *L*-capture with our experimental x-ray intensity ratio, we have determined the mean *L*-fluorescence yield of xenon:

$$\bar{\omega}_L=0.10_3\pm0.01.$$

Lay's values,[15] obtained by making photographic comparisons between the intensities of incident and fluorescent x-ray beams for $40<Z<92$, are considered to be internally consistent; our absolute value might serve as a normalization point, at least in the region of $Z=54$.

If the observed inner bremsstrahlung anomaly[4–8] is attributed to radiative capture of *p*-electrons,[9] then a comparison of the intensity of the anomalous radiation with the theoretical probability of L_{II}-capture leads to to the conclusion that L_{II}-capture must be considerably more radiative than L_I-capture. Comparing the spectrum[7] of Fe^{55} with that[4,5] of Cs^{131}, one further concludes that the probability of radiative capture increases more strongly with Z for L_{II}-capture than for L_I-capture.

TABLE II. *L*-fluorescence yields of xenon.

$\bar{\omega}_L$	Investigator	Remarks
0.25	Auger[a]	Using Xe-filled cloud chamber
0.21	Bower[b]	Using Xe-filled cloud chamber
(0.13)	Lay[c]	Photographic comparison of incident to fluorescent beams (as interpolated by present authors).
0.03	Present authors	Calculated according to the method of Kinsey[d] (see Appendix).
$0.10_3\pm0.01$	Present authors	From present experiment.

[a] P. Auger, J. phys. radium **6**, 205 (1925).
[b] J. C. Bower, Proc. Roy. Soc. (London) **A157**, 662 (1936).
[c] H. Lay, Z. Physik **91**, 533 (1934).
[d] See reference 16.

ACKNOWLEDGMENTS

We are indebted to Professor H. M. Schwartz for helpful discussions.

APPENDIX

Calculation of $\bar{\omega}_L$ for Xenon

Following the method of Kinsey,[16] the fluorescence yield of the *L* levels of xenon have been computed separately on the basis of radiation widths obtained by interpolation from the work of Massey and Burhop,[13] and the existing information on the widths of *L*-levels. The method depends on the fact that (if Coster-Krönig transitions are absent)

$$\omega=\Gamma_{rad}/\Gamma_{total}, \tag{4}$$

where ω is the fluorescence yield of a given level, Γ_{rad} is the level width for radiation, and Γ_{total} is the total level width.

The total widths can be measured by studying the shapes of the absorption edges of the *L* levels. Green's[17] values for barium and iodine, and Sandström's[18] values for tellurium and antimony are shown in Table III, along with our assumed values for xenon. Sandström shows that widths vary only slowly with Z. The radiation widths of the *L* levels, obtained by interpolating between values of Massey and Burhop for anti-

TABLE III. *L*-level widths in the region of xenon and partial *L*-fluorescence yields.

	Γ_{total}(ev)						
Level	Sb[a]	Te[a]	I[b]	Ba[b]	Xe[c]	Γ_{rad}(ev)[d]	ω
L_I	5.6	4.9			5.2	0.09	0.017
L_{II}	4.7	4.6			4.7	0.12	0.025
L_{III}	4.1	4.7	2.6±0.1	≤4.06	4.2 2.8	0.10	0.023 0.036
						Weighted mean	$\bar{\omega}_L=0.03\pm0.01$

[a] See reference 18.
[b] See reference 17.
[c] Assumed by present authors.
[d] Interpolated from reference 13.

[12] E. H. S. Burhop, *The Auger Effect* (Cambridge University Press, Cambridge, 1954), p. 50 ff.
[13] H. W. S. Massey and E. H. S. Burhop, Proc. Cambridge Phil. Soc. **32**, 461 (1936).
[14] See reference 12, page 61.
[15] H. Lay, Z. Physik **91**, 533 (1934).
[16] B. B. Kinsey, Can. J. Research **A26**, 404 (1948).
[17] E. H. Green, Phys. Rev. **55**, 1072 (1939).
[18] A. E. Sandström, Phil. Mag. **22**, 497 (1936).

mony and gold, are also shown in Table III. Values of the separate L-fluorescence yields are shown in the last column of Table III. From these values and the values of n in the last column of Table I, we compute a weighted mean fluorescence yield for xenon, $\bar{\omega}_L=0.03$.

Fluorescence yields calculated in this manner by Kinsey for high Z are in general somewhat lower than values found experimentally. For xenon the value is considerably lower and is inconsistent with the present experiment.

PHYSICAL REVIEW VOLUME 98, NUMBER 5 JUNE 1, 1955

Photoneutron Cross Sections in Mg^{24}, Mg^{25}, Zr^{90}, Zr^{91}†

ROBERT NATHANS* AND PAUL F. YERGIN
University of Pennsylvania, Philadelphia, Pennsylvania
(Received February 25, 1955)

The variation of $\sigma(\gamma,n)$ with E_γ from threshold to 24 Mev has been measured by detecting neutrons produced from betatron bremsstrahlung irradiation of separated isotope samples in oxide form. Despite the large threshold differences (9.3 Mev for the Mg isotopes and 5.0 Mev for the Zr isotopes) the peaks of the giant dipole resonances are very close for each pair of adjacent isotopes: Mg^{24}, 19.5 Mev; Mg^{25}, 20.3 Mev; Zr^{90}, 16.4 Mev; Zr^{91}, 16.3 Mev. The half-widths of the Zr resonances are unusually small, 4.1 and 5.4 Mev, compared to 8 Mev for nearby nuclei observed previously. This is apparently a "magic number" effect.

INTRODUCTION

PREVIOUS measurements in this laboratory[1] have indicated that the giant dipole resonances in (γ,n) processes occur at a photon energy which depends only on the mass number of the nuclide. The energy (E_m) at which the maximum cross section occurs varies slowly from about 13.5 Mev for $A=200$ to about 22.5 Mev for $A\leq 20$. Measurements elsewhere[2] have generally been in accord with this observation, but deviations from the smooth variation have been reported. It has been suggested[3] that the apparent smooth variation of E_m with A is accidental and that E_m is instead closely related to the (γ,n) threshold energy, E_{th}, so that E_m-E_{th} is approximately constant. Since E_{th} does in general decrease slowly with increasing A, this is not in absolute contradiction to our observations.

A second interesting feature of the giant resonances which was observed here previously[1] is that the width of the resonance varies slowly from about 7 Mev for $A=238$ to 10 Mev for $A=31$. (Below $A=31$ the widths for the 5 elements we have measured so far are much smaller, 3 to 7 Mev.) However, the nuclides with 28, 52, 82, and 126 neutrons have widths from 2 to 4 Mev less than the smooth variation noted for other nuclides. Except for $N=52$ these are "magic" neutron number nuclides, and $N=52$ is only two units away from the magic number 50.

In making a careful study of the variation of E_m with A or with E_{th}, the neutron detection method is to be preferred over the method of residual activity because the apparatus is identical for all target materials, and problems of half-lives, decay schemes, and decay energies differing for the various nuclides used do not enter. (It is also necessary to use only data from a single laboratory in making a critical evaluation, because of the known difficulties in comparing photonuclear cross sections measured in different laboratories.[4]) There is however the limitation that one is restricted to measurements on isotopes of not much less than 100 percent abundance. It is thus possible that observed variations of E_m with A might be of a special nature, related to the properties of the relatively small number of nuclides which can be studied in their naturally occurring abundances. This limitation can be overcome by using separated isotopes, which are now rather extensively available from the Oak Ridge National Laboratory.

A critical test of the dependence of E_m on E_{th} or on A can be made by measuring the (γ,n) cross section *vs* energy curve for two adjacent isotopes which have very different E_{th} values. On the hypothesis that the mass number is the determining factor, E_m will be the same for the two isotopes. On the hypothesis that E_{th} is the determining factor, the difference in the E_m values for the two isotopes should be comparable to the difference in the E_{th} values.

One of the most extreme cases available for examination is the isotopic pair Mg^{24}-Mg^{25}. The natural abun-

† Supported in part by the U. S. Air Research and Development Command and the joint program of the Office of Naval Research and the U. S. Atomic Energy Commission.
* Present address: Pennsylvania State University, University Park, Pennsylvania.
[1] R. Nathans and J. Halpern, Phys. Rev. **93**, 437 (1954).
[2] See Montalbetti, Katz, and Goldemberg, Phys. Rev. **91**, 659 (1953) for a summary of much data on this and other features of (γ,n) cross sections.
[3] L. Katz and A. S. Penfold, Phys. Rev. **81**, 815 (1951); Katz, Baker, Haslam, and Douglas, Phys. Rev. **82**, 271 (1951).
[4] J. Goldemberg and L. Katz, Can. J. Phys. **32**, 49 (1954), discuss the degree of agreement among various laboratories engaged in this work.

dances and (γ,n) thresholds are given in Table I. The difference in the E_{th} values is 9.3 Mev. Katz *et al.*[5] have reported measurement of the $Mg(\gamma,n)$ cross section, of the natural element, by neutron detection, and of the $Mg^{24}(\gamma,n)Mg^{23}$ cross section by residual activity. They have used these results to estimate the $Mg^{25}(\gamma,n)$ and $Mg^{26}(\gamma,n)$ cross sections, but a direct measurement is necessary if the results are to be used for a quantitative check of the hypotheses.

It is also desirable to investigate a case with a larger value of A, since the parameters of the giant resonance are believed to behave more regularly for A values above 40. A favorable case for study is the isotopic pair Zr^{90}-Zr^{91}, the natural abundances and (γ,n) thresholds of which are given in Table I. The difference in the E_{th} values is 5 Mev. These isotopes are also favorable for studying the "magic number" effect on the widths of the giant resonances, since Zr^{90} has 50 neutrons.

EXPERIMENT

The neutron detector consisted of four BF_3 counters embedded in a large (2 ft×2 ft×3 ft) paraffin block,

TABLE I. (γ,n) thresholds and natural abundances of isotopes investigated.

Nuclide	Natural abundance (percent)	$E_{th}(\gamma,n)$ (Mev)
Mg^{24}	78.60	16.6
Mg^{25}	10.11	7.3
Zr^{90}	51.46	12.2
Zr^{91}	11.23	7.2

with shielding from external neutrons. This is the same apparatus used in previous measurements, and has been described in detail.[6] The only modification for the present work was in the sample holder. This consisted of an aluminum tube 0.645 in. in diameter and $1\frac{7}{16}$ in. long with 0.011 in. thick walls, supported in the center of the hole through the paraffin house by a light aluminum ring. The samples, which were powdered oxides, were held in the tube by polyethylene end caps 0.0015 in. thick. These end caps, being flexible, bowed out somewhat in the middle, and for Zr^{91} it was necessary to take a check point on the yield curve using flat aluminum end caps, in order to determine the mass of the sample in the beam during the main run. The correction in this case was about 15 percent. For the other samples it was negligible. The Mg^{25} sample was compressed into a solid pill $\frac{5}{16}$ in. in diameter and was held by the taut polyethylene end caps so that it was entirely in the gamma-ray beam from the betatron, which had a diameter of 0.95 cm at the sample.

The isotopic compositions of the samples are shown in Table II. The contribution of the oxygen content of the samples was subtracted from the measured yields using the oxygen yield measured here previously.[7] The contribution of the Mg^{24} in the Mg^{25} sample was subtracted, using the present Mg^{24} measurements. Similarly the Zr^{90} contribution to the Zr^{91} sample was subtracted. In addition, the contribution of a 1.1 percent Hf impurity in the Zr^{91} sample was subtracted on the assumption that the (unknown) Hf yield is the same as that measured for Ta.[1] The conversion of the net yield curves into cross-section curves was done by the usual "total spectrum" method, using the Schiff thin-target bremsstrahlung spectrum modified by the absorbing materials in the beam.

TABLE II. Isotopic compositions (atomic percent) of the 4 samples used. The mass numbers refer to the magnesium and zirconium isotopes.

Mass No.	Abundance	Abundance
	A	*B*
24	99.59	5.87
25	0.30	92.33
26	0.11	1.80
	C	*D*
90	98.66	12.3
91	0.77	75.1
92	0.34	10.5
94	0.18	1.9
96	0.04	0.2

The total number of counts recorded for each sample is shown in Table III. The background varied from about 15 percent in Mg^{25} to about 1.5 percent in Zr^{90}, and about 20 000 counts were recorded each of the three times the background was measured, once for the zirconium isotopes and once each for the magnesium isotopes. The oxygen contribution varied from 25 percent of the total yield at maximum energy in Mg^{24} to 1.8 percent in Zr^{91}.

RESULTS

The parameters of the "giant resonance" cross section curves are given in Table IV for the four isotopes we have measured. There is a discussion of the sources and magnitudes of the errors in these quantities in reference 1, which is applicable to the present work. It

TABLE III. The total number of counts recorded in measuring the yield curves of the four samples, the mass of the samples within the γ-ray beam, and the area densities of the sample in the direction of the γ-ray beam.

	Sample	Counts	Sample in γ-ray beam Grams	Grams/cm²
A	$Mg^{24}O$	280 000	2.610	2.394
B	$Mg^{25}O$	186 000	0.870	1.759
C	$Zr^{90}O_2$	687 000	1.606	2.253
D	$Zr^{91}O_2$	309 000	0.446	0.626

[5] Katz, Haslam, Goldemberg, and Taylor, Can. J. Phys. **32**, 580 (1954).

[6] Halpern, Mann, and Nathans, Rev. Sci. Instr. **23**, 678 (1952).

[7] Ferguson, Halpern, Nathans, and Yergin, Phys. Rev. **95**, 776 (1954).

TABLE IV. Parameters of the (γ,n) cross-section curves measured. E_m is the energy at which the maximum cross section, σ_m, occurs. Γ is the full width of the curve between the two points at $\frac{1}{2}\sigma_m$. Column 6 gives the value predicted for E_m from an empirical relationship (see reference 1).

1 Nuclide	2 E_m (Mev)	3 Γ (Mev)	4 σ_m (mb)	5 $\int\sigma dE$ (Mev-b)	6 $38.5A^{-0.19}$
Mg^{24}	19.5	7–8	8.4	0.055	21.1
Mg^{25}	20.3	5.0	16.5	0.096	20.9
Zr^{90}	16.0	4.1	185	0.89	16.4
Zr^{91}	16.2	5.4	200	1.27	16.3
Errors	±1.0	±1.0	±15%	±15%	

should be noted, however, that the errors quoted in Table IV are estimates of the absolute errors in the quantities, and the *relative* magnitudes for two isotopes of the same element are probably much better known. For example, the quoted errors on the half-widths would permit the possibility that the two zirconium isotopes have the same widths. The data actually show unambiguously that the Zr^{90} curve is narrower than that of Zr^{91}. Individual comments for each of the isotopes follow.

Magnesium-24

The (γ,n) cross section measured for Mg^{24} is shown in Fig. 1. The agreement with the result of Katz *et al.*[8]

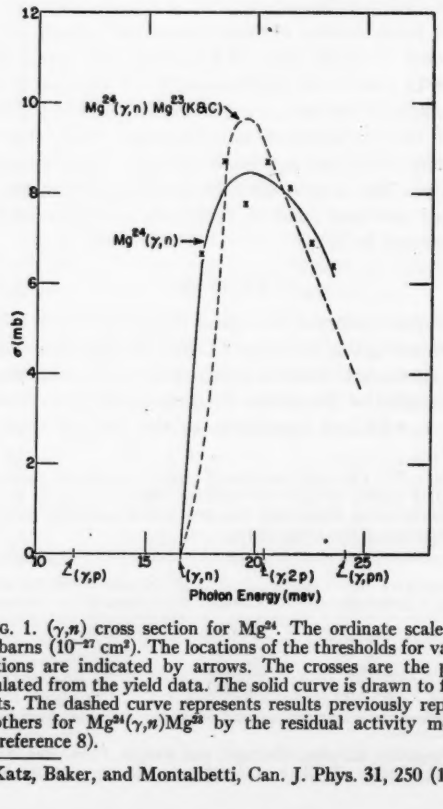

FIG. 1. (γ,n) cross section for Mg^{24}. The ordinate scale is in millibarns (10^{-27} cm²). The locations of the thresholds for various reactions are indicated by arrows. The crosses are the points calculated from the yield data. The solid curve is drawn to fit the points. The dashed curve represents results previously reported by others for $Mg^{24}(\gamma,n)Mg^{23}$ by the residual activity method (see reference 8).

[8] Katz, Baker, and Montalbetti, Can. J. Phys. **31**, 250 (1953).

for $Mg^{24}(\gamma,n)Mg^{23}$ by residual activity is as good as is to be expected.

Magnesium-25

The (γ,n) cross section measured for Mg^{25} is shown in Fig. 2. It is apparent that the peak of the cross section curve occurs at about the same place as that of Mg^{24}, despite the enormous (9.3-Mev) threshold difference. This is in disagreement with the estimate by Katz *et al.*[5] of the $Mg^{25}(\gamma,n)$ cross section. It would seem that the error in that estimate arose from the assumption that the entire giant resonance in the natural element is due to Mg^{24}, when in fact our results

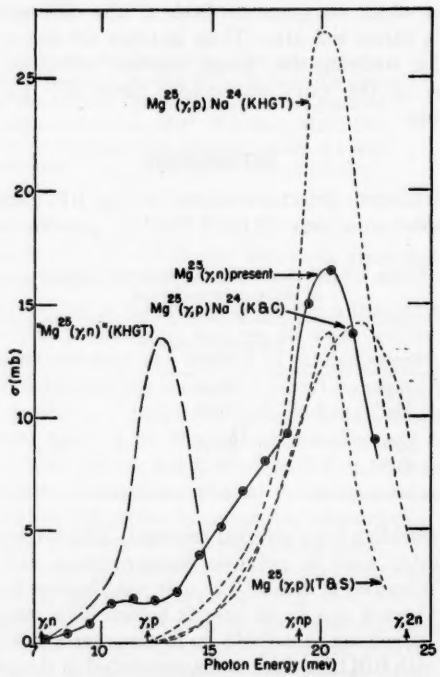

FIG. 2. (γ,n) cross section for Mg^{25}. The ordinate scale is in millibarns (10^{-27} cm²). The locations of the thresholds for various reactions are indicated by arrows. The circles are the points calculated from the yield data. The solid curve is drawn to fit the points. The three dotted curves are the previously reported $Mg^{25}(\gamma,p)Na^{24}$ cross sections (see references 5, 9, and 10). The dashed curve is the estimate of the $Mg^{25}(\gamma,n)$ cross section made previously by subtracting the $Mg^{24}(\gamma,n)$ of reference 8 from the measured cross section for natural Mg (see reference 5).

show that Mg^{25} contributes in this region twice as much as its abundance would suggest, relative to Mg^{24}; and also from the assumption that the Mg^{24} and Mg^{25} yields are the same far above the thresholds, while our measurements give a 22-Mev yield for Mg^{25} which is almost three times that of Mg^{24}. For comparison with our results the $Mg^{25}(\gamma,p)$ cross sections measured by others[5,9,10] are shown in Fig. 2. As has been generally

[9] L. Katz and A. G. W. Cameron, Phys. Rev. **84**, 1115 (1951).
[10] E. Toms and W. E. Stephens, Phys. Rev. **82**, 709 (1951).

observed, the (γ,n) and (γ,p) curves are quite similar in shape and location. Our $Mg^{25}(\gamma,n)$ results are for a net sample of 98.1 percent Mg^{25} and 1.9 percent Mg^{26}.

Zirconium-90

The $Zr^{90}(\gamma,n)$ cross section is shown in Fig. 3. For comparison the measurement of Katz *et al.*[8] for $Zr^{90}(\gamma,n)Zr^{89*}$ is also shown. Making allowance for the usual failure of agreement on shape among different laboratories, it is observed that the peak cross sections agree fairly well, indicating that most of the (γ,n) events in Zr^{90} lead to the isomeric state of Zr^{89}, and few if any to the ground state. For energies near threshold this has been observed previously.[11]

Zirconium-91

The $Zr^{91}(\gamma,n)$ cross section is shown in Fig. 3. Its resemblance to that of Zr^{90} is remarkable. The location and height of the peak are in excellent agreement. However, the width is definitely greater. The low energy "shelf" is typical of what has been seen in the light elements like N, O, and F which have narrow resonances well above their thresholds. This shelf is not observed when the resonance is broad or close to the threshold. The results represent a sample of 85.6 percent Zr^{91}, 12.0 percent Zr^{92}, 2.2 percent Z^{94} and 0.2 percent Zr^{96}.

DISCUSSION

E_m

The lack of dependence of the location of the giant resonance peak on the (γ,n) threshold is clearly shown by the Zr^{90}-Zr^{91} results, and also by the Mg^{24}-Mg^{25} results. The Zr isotopes are presumably more typical of the intermediate and heavy nuclides, and so verify the A-dependence of the peak location for this region. The second and sixth columns of Table IV compare the observed peak locations with those calculated from the empirical formula, $E_m = 38.5A^{-0.19}$, derived from previous observations.[1] The agreement is excellent. One expects marked deviations from the systematic behavior for light elements, and the shapes of the Mg^{24} and Mg^{25} curves are accordingly radically different. Despite this the peaks are within 1 Mev of each other. This, as well as the closeness with which all the E_m values we have so far observed fall on a smooth curve suggest that the location of the peak of the resonance is almost completely independent of anything except the mass number A. It has been pointed out that on rather fundamental grounds there ought to be a close connection between the location of the peak and the mean kinetic energy of nucleons in the nucleus. This latter quantity is presumably determined mostly by the mass number, via the nuclear radius.

[11] P. Axel and J. D. Fox, Phys. Rev. 95, 613(A) (1954).

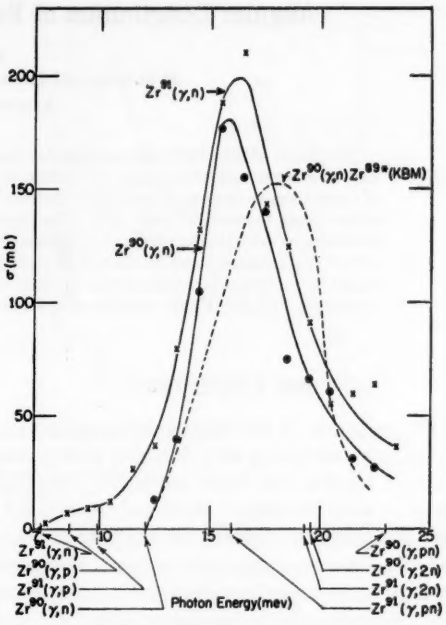

FIG. 3. (γ,n) cross sections for Zr^{90} and Zr^{91}. The ordinate scale is in millibarns (10^{-27} cm^2). The points shown are those calculated from the yield data. The solid curves are drawn to fit the points. The dashed curve is the cross section reported (see reference 8) for the production of the isomeric state of Zr^{89} by photon bombardment of natural Zr. The locations of the thresholds for various reactions in the two isotopes are indicated by the arrows.

Half-Widths

The half-widths of the cross-section curves for the Zr isotopes are substantially less than for most other medium and heavy elements.[1] The Zr^{90} curve is the narrowest of the 16 elements above a mass number of 30 that we have so far measured. The isotopes Zr^{90}, Zr^{91}, and Nb^{93} form a progression of neutron numbers, 50, 51, and 52. The corresponding half-widths are 4.1, 5.4, and 6.8 Mev. This strongly suggests a sharp "dip" in the half-widths at magic neutron numbers.

The estimate of Katz *et al.* regarding the $Mg^{25}(\gamma,n)$ cross section being incorrect, there is now no indication that the inversion of the usual order of the thresholds for (γ,p) and (γ,n) in this isotope produces any anomaly in the location of the corresponding resonance peaks. The agreement of the locations and shapes of the $Mg^{25}(\gamma,n)$ and $Mg^{25}(\gamma,p)$ peaks is excellent.

ACKNOWLEDGMENTS

We acknowledge the encouragement and support of Dr. J. Halpern, the assistance of Dr. B. Fabricand in making the measurements, and the help of the staff of the betatron laboratory in operating the betatron.

Angular Distribution of Fast Neutrons Scattered from Lead*

W. J. RHEIN†
Department of Physics, University of Texas, Austin, Texas
(Received January 14, 1955)

The elastic differential cross sections for the scattering of 1.0-, 3.7-, 5.0-, and 15.0-Mev neutrons from lead have been measured, using a minimum of experimental variables in order to investigate the behavior of these cross sections as a function of neutron energy. The scatterers were ring-shaped, permitting a scattering range between 10° and 150°. The neutrons were counted with ZnS—plastic scintillators. It was necessary to subtract the effects of inelastically scattered neutrons from the experimental results in order to arrive at the elastic cross sections. The results show the expected prominent variation in the width and height of the forward scattering peak and indicate that the number and direction of the secondary maxima of scattering are a prominent function of neutron energy.

THE EXPERIMENT

THE variation of the differential cross section for neutron scattering as a function of the mass of the target nucleus has been extensively studied by Whitehead and Snowdon,[1] Walt and Barschall,[2] and others. We sought to investigate the behavior of this cross section as a function of the energy of the neutrons, using natural lead for the target and keeping constant as many experimental factors as possible.

Neutrons of energy 1.0±0.03, 3.7±0.28, 5.0±0.22, and 15.0±0.8 Mev were generated by bombarding various targets with the beam from the 4-Mev electrostatic accelerator of the University of Texas and were scattered from lead rings. The experimental arrangements are indicated in Fig. 1. They are similar to those of Whitehead and Snowdon.[1]

The thickness of the scatterers was in each case less than the mean free path of neutrons in lead. The neutrons were detected with a scintillator made of zinc sulfide suspended in clear plastic material and mounted on a RCA-5819 photomultiplier.[3] The axis of the scattering ring, the axis of the detector, and the beam from the accelerator lay along the same straight line. The scatterer was located 50 cm from the neutron source. The scattering angle was varied by moving the detector along the axial line. A cone of paraffin or iron, centered on this line, shielded the detector from the direct neutron beam. It was so designed that it attenuated 98 percent of the neutron beam. The neutron output from the generator was monitored with a scintillation counter of the same type as the detector.

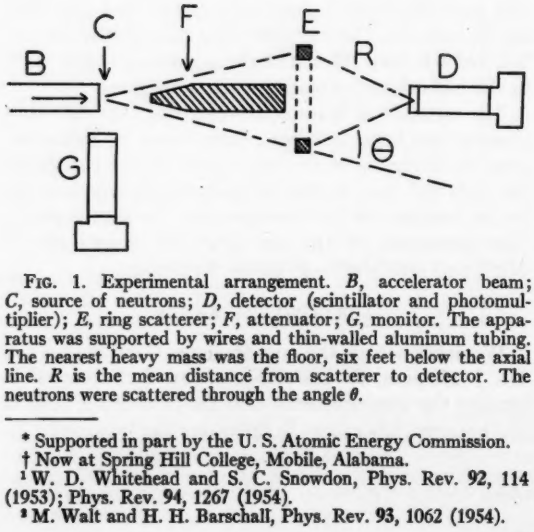

FIG. 1. Experimental arrangement. *B*, accelerator beam; *C*, source of neutrons; *D*, detector (scintillator and photomultiplier); *E*, ring scatterer; *F*, attenuator; *G*, monitor. The apparatus was supported by wires and thin-walled aluminum tubing. The nearest heavy mass was the floor, six feet below the axial line. *R* is the mean distance from scatterer to detector. The neutrons were scattered through the angle θ.

TABLE I. The first column gives the energy of the scattered neutrons. The second column shows the integral of the experimental curves. The next two columns show the total and inelastic cross sections. The last shows an estimate of the percentage of the measured integral cross section that was due to inelastic scattering.

E_n Mev	I barns	σ_t barns[a]	σ_{in} barns[b]	Percent inelastic
1.0	5.5	5.8	0.3	0
3.7	6.5	7.7	1.7	8
5.0	6.4	7.3	2.4	23
15.0	3.9	5.6	2.6	23

[a] See reference 4.
[b] Private communication from Taylor, Lönsjö, and Bonner of the Rice Institute. These inelastic cross sections were measured by the method of spheres.

To discuss the procedure for obtaining absolute differential cross sections from the counting rate, it is convenient to use the following symbols: R is the mean distance from the scatterer to the detector, N_s is the counts due to the scattered neutrons, N_i is the counts due to the direct beam when the detector is placed at the position of the scatterer, ϵ is the angular sensitivity of the detector relative to the sensitivity in the direction of the axis, σ_t is the total cross section of the target material for neutrons, A is the area of the scattering ring as seen from the neutron source, n is the nuclear density of the scatterer, and a is the mean thickness of the scatterer.

It can be shown that the absolute differential cross

* Supported in part by the U. S. Atomic Energy Commission.
† Now at Spring Hill College, Mobile, Alabama.
[1] W. D. Whitehead and S. C. Snowdon, Phys. Rev. **92**, 114 (1953); Phys. Rev. **94**, 1267 (1954).
[2] M. Walt and H. H. Barschall, Phys. Rev. **93**, 1062 (1954).
[3] W. F. Hornyak, Rev. Sci. Instr. **23**, 264 (1952). Dr. Hornyak kindly furnished the scintillators used in the present experiment.

section can be calculated from

$$\sigma(\theta)=N_s R^2\sigma_t/N_t\epsilon A[1-\exp(-n\sigma_t a)].$$

This formula is similar to the one given by Walt and Barschall[2] after taking our differing experimental geometry into consideration.

The following procedure was employed for each scattering angle and for each energy of the neutrons. (1) For a given monitor count and with the scatterer and attenuator in place, the counts from the neutron detector were recorded. (2) Step 1 was repeated with the scattering ring removed, but with other circumstances identical. The difference between the counts in steps 1 and 2 gave N_s. The above two steps were repeated twice or more. (3) The detector was placed in the position that had been occupied by the left side of the ring, and the counts from the direct beam were taken for the given monitor count. (4) Step 3 was repeated on the right side. The average of steps 4 and 5 gave N_t.

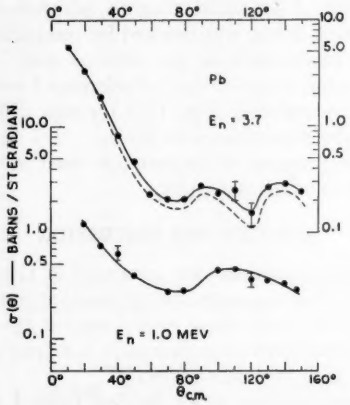

FIG. 2. Differential scattering cross sections of natural lead to neutrons of energy 1.0 and 3.7 Mev. The circles are experimental points and the broken line curve is the probable elastic differential cross section.

The values for σ_t were obtained from AECU-2040[4] and are listed in Table I. The other quantities needed to calculate $\sigma(\theta)$ were obtained by straightforward and familiar methods.

THE RESULTS

The differential cross sections for the scattering of fast neutrons from lead as measured by the above method are shown in Figs. 2 and 3. The errors shown on the curves are probable statistical errors only. The total error amounted to about 15 percent.

The angular resolution of the counter was about ±10°. To find the effect of double scattering we determined eight points for the 3.7- and 5.0-Mev curves using scatterers 1 in. thick, and repeated the points using scatterers ½ in. thick. There were no significant differences between the results from the thick and thin scatterers. We concluded that the correction for double scattering fell within our error.

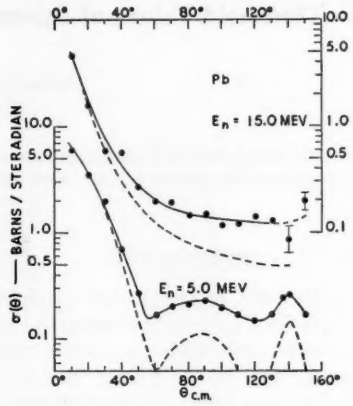

FIG. 3. Differential scattering cross section of natural lead to neutrons of energy 5.0 and 15.0 Mev. The circles are experimental results and the broken line curve is the probable elastic differential cross section.

The counter did not completely discriminate against inelastically scattered neutrons. Column 5 of Table I shows an estimate of what percentage of the integral measured cross section was due to inelastic scattering. This was calculated from the formula:

$$\%\ \text{inelastic}=\left(\frac{I-\sigma_{el}}{I}\right)\times 100.$$

Here $I=\int\sigma(\theta)d\Omega$ and is the integral of our curves over 4π steradians. It is shown in column 2 of the table. The integral elastic cross section, σ_{el}, is given by the difference between the total and inelastic cross sections, $\sigma_t-\sigma_{in}$.

The dashed curves of Figs. 1 and 2 show the results of subtracting the effect of inelastic scattering from our curves. We have assumed that inelastic scattering is isotropic. Hence the dashed curves should be nearer to the elastic differential cross sections than the solid curves.

Our results for 1.0 and 3.7 Mev agree well with those given in references 1 and 2. There may be fine structure in the curve for 15-Mev neutrons which we did not observe because of insufficient resolution of our counter.

Besides the prominent variation of the width and height of the forward scattering peak as a function of energy, our results show that the number and direction of the secondary maxima are a prominent function of energy, and that when the neutron wavelength changes by only a small fraction of itself there is little or no change in the number and direction of these maxima.

The assistance of the personnel of the Nuclear Physics Laboratory of the University of Texas is gratefully acknowledged.

[4] *Neutron Cross Sections*, Atomic Energy Commission Report AECU-2040 (Technical Information Division, Department of Commerce, Washington, D. C., 1952).

Threshold Values of Internal Conversion Coefficients for the *K*-Shell

B. I. SPINRAD
Argonne National Laboratory, Lemont, Illinois
(Received February 28, 1955)

Corrected relativistic calculations for the internal conversion coefficients of *K*-shell electrons at threshold energies of the gamma rays are presented. A comparison is made with nonrelativistic formulas.

INTRODUCTION

CALCULATIONS of the *K*-shell internal conversion coefficients for threshold values of the gamma-ray energy in an unperturbed central Coulomb field were previously reported in a very brief communication.[1] Since that time, results of low-energy experiments which have been brought to the author's attention have indicated that these results were in error. In addition, it was pointed out[2] that these old calculations were in disagreement with results obtained from the Dancoff-Morrison[3,4] and Drell[5] formulations, even in the limit of low Z where these should be exact.

As a result of these indications, the previous work was rechecked, with the consequence that errors in formulation were discovered. Consequently, the whole problem was reformulated and the formulation checked by using two independent derivations. The problem was then programmed for computation on AVIDAC[6]; the programming was checked by comparing intermediate results with previously computed numbers, by using library routines wherever possible, and by multiple scrutiny of program and code. Numerical results were checked by running the problem several times on AVIDAC during periods of reliable operation.

It must be emphasized that the computations here are, as described previously, of interest as mathematical limits to the function which correctly describes internal conversion in the absence of screening. For example, the threshold energies used are the values computed for the unscreened single-electron atom, rather than the *K*-shell cutoff energies which are significantly different for large Z. The validity of various simplified methods for taking screening into account must ultimately depend on experiment. Since internal conversion coefficients generally show a more rapid variation with energy than with Z, however, it seems reasonable to expect that the correlation of conversion coefficient with gamma-ray energy at threshold (k in the tables) will be somewhat better than a correlation with Z.

FORMULATION

The computations were formulated in two ways. In the first method, the general formulas for conversion coefficients given by Rose, Goertzel *et al.*,[7] were reduced to the limit as p, the momentum of the outgoing electron, approaches zero. In the second method, the wave functions of the outgoing electron[8] were reduced to the zero-momentum limit before substitution into the radial integrals of reference 7. Essentially, then, the computation of the radial integrals, which is the major mathematical labor, was checked by comparing results of direct substitution of the reduced wave functions into Eqs. (13c–f) and (17b,c) of reference 7 with results obtained by reducing Eqs. (21) through (29) of that paper to the zero-momentum limit.

The presentation of the formulas used in computation is made in the Appendix.

RESULTS AND DISCUSSION

The results obtained are presented in tabular form in Table I. The concentration of points at low Z is due to a desire to check these results against the Dancoff-Morrison and Drell formulations in the limit as $Z \rightarrow 0$. At $Z=0$, their formulas are exact.

The computations which yielded Table I were performed to seven significant-figure precision. Table I has been rounded off to give six significant figures, although there is a possibility that successive truncation errors in the complicated arithmetical computations may have penetrated to the fifth figure in some cases.

The comparison formulas used were obtained from them by substituting into the general equations given in references 3 and 5 the gamma-ray energy at threshold, as a function of Z. The equations so obtained were then rearranged as series in ascending powers of Z, and the first term was retained. Identical results were obtained by finding the limiting form of the exact calculations given in the Appendix for $Z \rightarrow 0$.

A comparison of the ratios of the results obtained in Table I to the results obtained from the approximate equations (11a) and (11c) is made in graphical form in Figs. 1 and 2 for electric and magnetic conversion, respectively. The smoothness of the ratios, as seen in Figs. 1 and 2, indicates that interpolation to intermediate Z can be conveniently performed on these

[1] B. I. Spinrad and L. B. Keller, Phys. Rev. **84**, 1056 (1951).
[2] Church, Herbst, and Monahan, Argonne National Laboratory Quarterly Report ANL-5174, February, 1954, pp. 69–71 (unpublished).
[3] S. Dancoff and P. Morrison, Phys. Rev. **55**, 122 (1939).
[4] M. Hebb and G. Uhlenbeck, Physics **5**, 605 (1938).
[5] S. D. Drell, Phys. Rev. **75**, 132 (1949).
[6] AVIDAC is the automatically sequenced, electronic, digital computing machine now in service at Argonne National Laboratory. A report on its design and programming is in preparation.
[7] Rose, Goertzel, Spinrad, Harr, and Strong, Phys. Rev. **83**, 79 (1951).
[8] M. E. Rose, Phys. Rev. **51**, 484 (1937).

TABLE I. Threshold values of K-shell internal conversion coefficients.[a]

A. Electric multipoles

k (mc^2 units)	Z	α_1	α_2	α_3	α_4	α_5
0.00002663	1	1.89502(7)	3.07795(11)	1.97352(15)	7.13197(18)	1.68289(22)
0.00010652	2	1.18428(6)	4.80813(9)	7.70579(12)	6.96062(15)	4.10543(18)
0.00023967	3	2.33888(5)	4.21917(8)	3.00427(11)	1.20572(14)	3.15963(16)
0.00066582	5	3.02954(4)	1.96577(7)	5.03385(9)	7.26570(11)	6.84786(13)
0.00170609	8	4.61655(3)	1.16770(6)	1.16510(8)	6.55299(9)	2.40686(11)
0.0026664	10	1.88861(3)	3.05138(5)	1.94397(7)	6.98183(8)	1.63762(10)
0.0107085	20	1.16835(2)	4.64159(3)	7.24914(4)	6.38675(5)	3.67723(6)
0.024259	30	2.26901(1)	3.88934(2)	2.61155(3)	9.90373(3)	2.45728(4)
0.043553	40	7.01220(0)	6.45825(1)	2.32648(2)	4.74275(2)	6.33931(2)
0.068947	50	2.78769(0)	1.53738(1)	3.33305(1)	4.10686(1)	3.33417(1)
0.100957	60	1.29709(0)	4.52694(0)	6.33805(0)	5.10154(0)	2.74308(0)
0.140322	70	6.71873(−1)	1.52266(0)	1.46042(0)	8.31641(−1)	3.27786(−1)
0.188113	80	3.76149(−1)	5.63962(−1)	4.05247(−1)	1.85118(−1)	6.11577(−2)
0.233459	88	2.46902(−1)	2.77935(−1)	1.78623(−1)	7.58180(−2)	2.27476(−2)
0.286423	96	1.67115(−1)	1.61666(−1)	1.04270(−1)	4.12401(−2)	1.06695(−2)

B. Magnetic multipoles

k (mc^2 units)	Z	β_1	β_2	β_3	β_4	β_5
0.00002663	1	1.83974(4)	1.24191(9)	2.22055(13)	1.80155(17)	8.30293(20)
0.00010652	2	4.60131(3)	7.76405(7)	3.47011(11)	7.03761(14)	8.10789(17)
0.00023967	3	2.04643(3)	1.53426(7)	3.04697(10)	2.74585(13)	1.40571(16)
0.00066582	5	7.38356(2)	1.99116(6)	1.42254(9)	4.61222(11)	8.49547(13)
0.00170609	8	2.89989(2)	3.04848(5)	8.49251(7)	1.07395(10)	7.71655(11)
0.0026664	10	1.86527(2)	1.25253(5)	2.22953(7)	1.80190(9)	8.27558(10)
0.0107085	20	4.86496(1)	8.03482(3)	3.52677(5)	7.04250(6)	8.00028(7)
0.024259	30	2.32537(1)	1.65881(3)	3.16119(4)	2.75014(5)	1.36366(6)
0.043553	40	1.45535(1)	5.59317(2)	5.79573(3)	2.75595(4)	7.49006(4)
0.068947	50	1.07857(1)	2.49430(2)	1.58022(3)	4.62831(3)	7.77724(3)
0.100957	60	9.11391(0)	1.34218(2)	5.56398(2)	1.07733(3)	1.20284(3)
0.140322	70	8.69887(0)	8.32455(1)	2.34933(2)	3.14107(2)	2.43774(2)
0.188113	80	9.49930(0)	5.81850(1)	1.14045(2)	1.08016(2)	5.99073(1)
0.233459	88	1.15504(1)	4.73879(1)	6.95823(1)	5.04608(1)	2.16247(1)
0.286423	96	1.65777(1)	4.16743(1)	4.54694(1)	2.52489(1)	8.38363(0)

[a] The numbers in the parentheses are the powers of 10 by which the corresponding numbers are to be multiplied.

ratios; and their smooth approach to unity for low Z values is a further check on the correctness of the computations.

ACKNOWLEDGMENTS

The author would like to acknowledge his indebtedness to Dr. G. David Jackson of the Radiation Laboratory, McGill University, for his stimulating discussion on this problem; Dr. Joseph Cook of the Mathematics and Computing Section, Physics Division, Argonne National Laboratory, for his assistance in checking formulation; Mrs. Ruth Freshour of that Section for the programming of the problem for AVIDAC; Miss Mildred Schlapkohl of the Reactor Engineering Division, Argonne National Laboratory, for miscellaneous computation; and finally, Mrs. Lorraine B. Keller, co-author of reference 1, whose work was extensively used in checking the present problem.

APPENDIX

The following formulas were used in the computation. These are presented as they were used in programming the problem, so that extensive rearrangement of terms and redisignation of symbols will be noted on comparison with reference 7

$$\gamma=[1-(\alpha Z)^2]^{\frac{1}{2}}=1-k, \tag{1}$$

where k is gamma-ray energy at threshold, in m_0c^2 units.

$$N^2=2\pi\alpha(1+\gamma)^{1+\gamma}2\gamma/(\alpha Z)^2\Gamma(2\gamma+1), \tag{2}$$

$$\gamma_J'=[(J+\tfrac{1}{2})^2-(\alpha Z)^2]^{\frac{1}{2}}, \tag{3}$$

$$D_J^2=(2\gamma+2)^{\gamma_J'}[\Gamma(\gamma_J'+\gamma)/\Gamma(2\gamma_J'+1)]^2, \tag{4}$$

$$x=-1-\gamma-i\alpha Z, \tag{5}$$

$$F_{J,0}=F(\gamma_J'+\gamma;\,2\gamma_J'+1;\,x), \tag{6a}$$

$$G_{J,0}=2\gamma_J'F(\gamma_J'+\gamma;\,2\gamma_J';\,x), \tag{6b}$$

when F is the confluent hypergeometric function.

$$F_{J,\nu}=\{[\alpha Z+i(1+\gamma)]/2\alpha Z\nu(\gamma_J'+\gamma-\nu)(\gamma_J'-\gamma+\nu)\}\times[G_{J,\nu-1}-(\gamma_J'+\gamma-\nu+x)F_{J,\nu-1}], \tag{7a}$$

$$G_{J,\nu}=\{[\alpha Z+i(1+\gamma)]/2\alpha Z\nu(\gamma_J'+\gamma-\nu)\}\times[G_{J,\nu-1}-xF_{J,\nu-1}], \tag{7b}$$

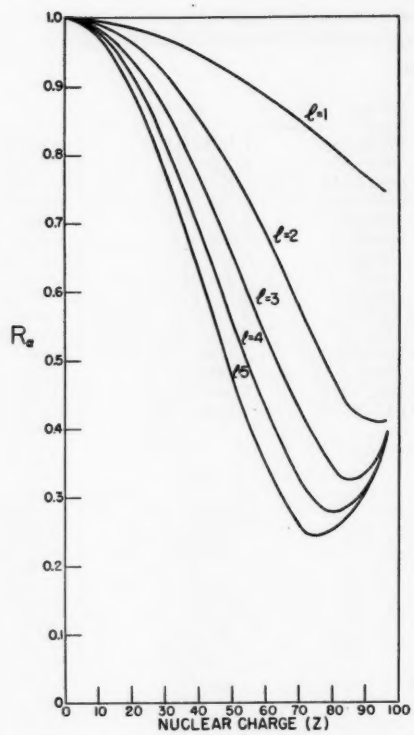

FIG. 1. Ratio ($R\alpha$) of "exact" electric internal conversion coefficients at threshold to low-Z limiting form.

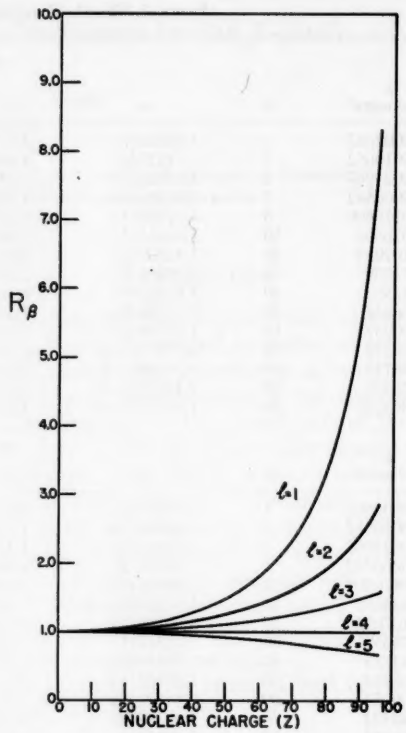

FIG. 2. Ratio ($R\beta$) of "exact" magnetic internal conversion coefficients at threshold to low-Z limiting form.

$$\begin{pmatrix} F^{I,J} \\ G^{I,J} \end{pmatrix} = \sum_{\nu=0}^{I} \frac{(I+\nu)!}{(I-\nu)!} \begin{pmatrix} F_{J,\nu} \\ G_{J,\nu} \end{pmatrix}, \tag{8}$$

$$W_1{}^J = \left(\frac{J-\tfrac{1}{2}}{2J}\right)(1+\gamma)D_J{}^2 |(\tfrac{3}{2}+J-\gamma-\gamma_J{}')F^{J-\frac{1}{2},J} + G^{J-\frac{1}{2},J} + [2i\alpha Z/(1+\gamma)] \times [(\gamma_J{}'-J-\tfrac{1}{2})F^{J-\frac{1}{2},J} - G^{J-\frac{1}{2},J}]|^2, \tag{9a}$$

$$W_2{}^J = \frac{(J+\tfrac{1}{2})^2}{(J+\tfrac{3}{2})(2J+2)}(1+\gamma)D_J{}^2 |(\tfrac{1}{2}-J-\gamma-\gamma_J{}') \times F^{J+\frac{1}{2},J} + G^{J+\frac{1}{2},J} + [i\alpha Z/(1+\gamma)][G^{J-\frac{1}{2},J}/(J+\tfrac{1}{2}) + \{2\gamma+1+(1+\gamma-\gamma_J{}')/(J+\tfrac{1}{2})\}F^{J-\frac{1}{2},J}|^2, \tag{9b}$$

$$W_3{}^J = \left(\frac{J-\tfrac{1}{2}}{2J}\right)\frac{(\alpha Z)^2}{(1+\gamma)}D_J{}^2 \times |(\gamma_J{}'-\gamma+J+\tfrac{1}{2})F^{J-\frac{1}{2},J} - G^{J-\frac{1}{2},J}|^2, \tag{9c}$$

$$W_4{}^J = \left(\frac{J+\tfrac{3}{2}}{2J+2}\right)\frac{(\alpha Z)^2}{(1+\gamma)}D_J{}^2 \times |(\gamma-\gamma_J{}'+J+\tfrac{3}{2})F^{J+\frac{1}{2},J} + G^{J+\frac{1}{2},J}|^2. \tag{9d}$$

In all the foregoing equations, J assumes half odd-integral values.

$$\alpha_l = N^2(W_1{}^{l+\frac{1}{2}} + W_2{}^{l-\frac{1}{2}}), \tag{10a}$$

$$\beta_l = N^2(W_3{}^{l+\frac{1}{2}} + W_4{}^{l-\frac{1}{2}}). \tag{10b}$$

As $Z \to 0$, these equations approach the limiting form of the Dancoff-Morrison and Drell equations at threshold:

$$\alpha_l \doteq 16\pi\alpha[l/(l+1)](l!)^{-2}(2/\alpha Z)^{2l+2}B_l{}^2, \tag{11a}$$

where

$$B_l = 1/(2l+1)F(2; 2l+2; -2), \tag{11b}$$

$$\beta_l \doteq 16\pi\alpha[(l+1)/(2l+1)] \times [(l-1)!]^{-2}(2/\alpha Z)^{2l}C_l{}^2, \tag{11c}$$

where

$$C_l{}^2 = 1 + l^{-1}(l+1)^{-3}B_{l+1}{}^2. \tag{11d}$$

Search for the Reaction $T(d,\gamma)He^5$†

GEORGE A. SAWYER AND LOUIS C. BURKHARDT
University of California, Los Alamos Scientific Laboratory, Los Alamos, New Mexico
(Received December 20, 1954)

An attempt was made to detect the reaction $T(d,\gamma)He^5$, using a Cockcroft-Walton accelerator. A tritium-zirconium target was bombarded with 160-kev deuterons. A NaI scintillation counter was used to search for 16-Mev gamma rays from the $T(d,\gamma)He^5$ reaction. No 16-Mev gamma-rays were detected. It was concluded that the cross section was less than 0.5 millibarn at 160 kev.

INTRODUCTION

IT has been reported by a group at the University of Minnesota[1] that the cross section for the $He^3(d,\gamma)Li^5$ reaction is 0.05 mb at a bombarding energy of 450 kev. Since this cross section was surprisingly large it seemed important to search for the mirror reaction $T(d,\gamma)He^5$.

APPARATUS

Tritium-zirconium targets were bombarded by the analyzed deuteron beam from a Cockcroft-Walton accelerator. A bombarding energy of 160 kev was used throughout the experiment. Two NaI scintillation counters were used. One, having a 3-in. diameter, 3-in. long NaI crystal was used to detect gamma rays. The other, having a $\frac{1}{2}$-in. diameter, 1-mm thick crystal was used to monitor alpha particles from the $T(d,n)He^4$ reaction. The gamma counter pulses were amplified and fed into a 12-channel pulse-height analyzer which recorded the spectrum of the gamma rays detected. The alpha counter pulses were amplified, and recorded by a scaler.

A shadow bar was placed between the target and the gamma counter to remove neutrons selectively. The shadow bar was of beryllium, 3-in. in diameter and 10-in. long, and had a transmission for 14-Mev neutrons of 5 percent and a transmission for 16-Mev gamma rays of 52 percent. Longer shadow bars produced little improvement in the ratio of neutron to gamma ray transmission because neutrons scattered around the shadow bar into the gamma counter became a predominant effect for long shadow bars. Figure 1 shows the apparatus schematically.

RESULTS

The pulse-height distribution of the counts recorded by the gamma counter when the tritium target was bombarded with the shadow bar in place is shown as the solid line in Fig. 2, and the dashed line shows the pulse-height distribution obtained from the $Li^7(p,\gamma)Be^8$ reaction. This reaction produces a 17-Mev gamma ray and thus provides a convenient means for determining the pulse-height distribution expected for the 16-Mev gamma-ray from the $T(d,\gamma)He^5$ reaction. It is clear that the pulse-height distribution shown as the solid line of Fig. 2 does not have the shape expected for 16-Mev rays.

It was not known whether the counts recorded by the gamma counter with the shadow bar in place, as shown in Fig. 2, were caused primarily by neutrons or gamma rays. Therefore, a lead absorption curve was taken in each channel of the pulse-height analyzer to identify the radiation counted by the gamma counter. The experimental absorption curve obtained is shown as the solid line in Fig. 3. This absorption curve is for the channel of the pulse-height analyzer which would contain the peak of a 16-Mev gamma-ray line. A calculated absorption curve for 16-Mev gamma rays and an experimental absorption curve for 14-Mev neutrons are also shown. The neutron absorption curve was taken by removing the shadow bar and repeating the lead absorption curve. With the shadow bar out, the neutron intensity at the counter was so large that it was clearly the dominant radiation. The absorption curve indicated that the radiation from the tritium target consisted of both neutrons and gamma rays. A good fit to the experimental curve was obtained by assuming that 68 percent of the counts were caused by 14-Mev neutrons and 32 percent were caused by 16-Mev gamma rays. The calculated curve for 68 percent neutrons, 32 percent gamma rays is shown as a dashed line just below the experimental curve. Although the experimental curve shown in Fig. 3 is for a single channel of the pulse-height analyzer, substantially the same ratio of neutrons to gamma rays was obtained in

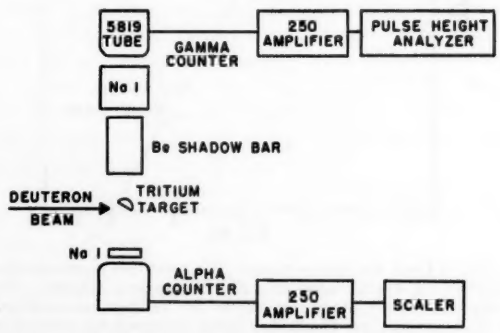

FIG. 1. Schematic diagram of the apparatus.

† Work done under the auspices of the U. S. Atomic Energy Commission.

[1] Blair, Hintz, and Van Patter, Phys. Rev. 96, 1023 (1954).

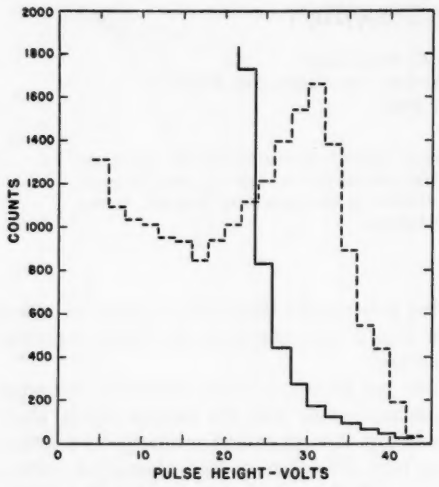

FIG. 2. Pulse-height distribution. The solid curve represents the radiation counted by the gamma counter with the shadow bar in place. The dashed curve represents the distribution from the $Li^7(p,\gamma)Be^8$ reaction.

all except the very highest energy channels where the ratio of neutrons to gamma rays decreased. It was concluded that about $\frac{1}{3}$ of the counts in the gamma counter were due to gamma rays. The pulse height spectrum of the gamma-ray component was derived from the absorption curves in all channels of the analyzer. The gamma-ray distribution (shown as the dashed curve in Fig. 4) has the same general shape as the total distribution shown in Fig. 2 and does not correspond to the 16-Mev gamma ray. It is probable that the gamma rays observed arise largely from inelastic neutron scattering processes.

In order to set an upper limit on the cross section, the pulse-height distribution to be expected from the $T(d,\gamma)He^5$ reaction if one assumes a cross section 10^{-4} of that for the $T(d,n)He^4$ reaction, was computed and is shown as the shaded area at the bottom of Fig. 4. The shape of the distribution was obtained from the shape of the $Li^7(p,\gamma)Be^8$ calibration shown in Fig. 2. The amplitude of the distribution was derived from the counting rate in the alpha counter which, when corrected for counter solid angle, gave the number of $T(d,n)He^4$ reactions occurring per gamma ray counted by the gamma counter. The efficiency of the gamma counter was calculated to be 66 percent for 16-Mev gamma rays and this was the efficiency used in deriving the expected yield of gamma rays.

It was concluded that the ratio between the cross sections must be greater than 10^4 and, therefore, that the cross section for the reaction $T(d,\gamma)He^5$ was less than 0.5 mb at 160 kev.

A rough estimate was made of the cross section to be expected for the reaction $T(d,\gamma)He^5$. It was pointed out by Thomas[2] that because the reduced charges for the reactions $T(d,\gamma)He^5$ and $He^3(d,\gamma)Li^5$ are the same, one might expect the radiation width, Γ_γ, for the two reactions to be the same. By using $\Gamma_\gamma = 11$ ev deduced

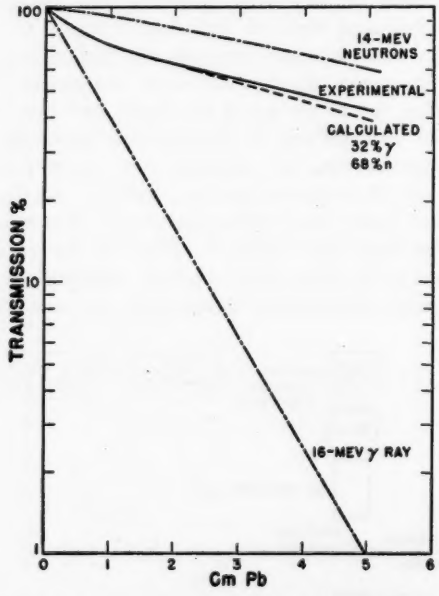

FIG. 3. Lead absorption curves. The solid line represents the experimental curve obtained with the gamma counter. The broken curves are absorption curves for 14-Mev neutrons and 16-Mev gamma rays. The dashed curve represents the absorption curve for 32 percent 16-Mev gamma rays and 68 percent 14-Mev neutrons.

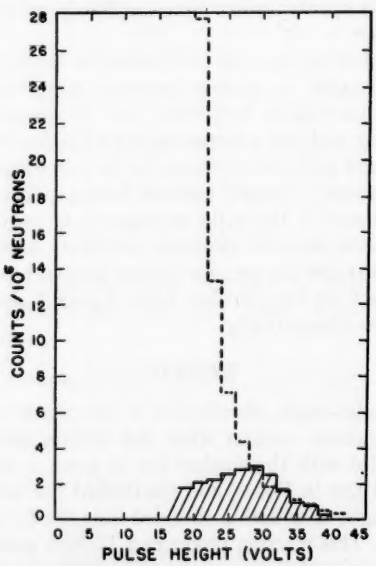

FIG. 4. Pulse-height distribution. The dashed curve is for the gamma-ray component of the radiation detected. The shaded area at the bottom is the distribution expected from the gamma rays from the $T(d,\gamma)He^5$ reaction if its cross section is 10^{-4} of the $T(d,n)He^4$ cross section.

[2] R. G. Thomas (private communication).

by Blair, Hintz, and Van Patter[1] for $He^3(d,\gamma)Li^5$, and $\Gamma_n=66$ kev deduced by Argo *et al.*[3] for $T(d,n)He^4$, it was estimated that the ratio of the cross sections $T(d,n)He^4$ and $T(d,\gamma)He^5$ should be 6×10^3. This is approximately the lower limit on the ratio set by our measurement.

[3] Argo, Agnew, Taschek, Hemmindinger, and Leland, Phys. Rev. 87, 612 (1952).

PHYSICAL REVIEW VOLUME 98, NUMBER 5 JUNE 1, 1955

Gamma Rays in the Decay of Na^{25}†

JOHN E. IWERSEN* AND W. S. KOSKI
Department of Chemistry, The Johns Hopkins University, Baltimore, Maryland
(Received December 6, 1955)

Studies of the gamma-ray spectrum of Na^{25} with a scintillation spectrometer showed that gammas with energies of 0.98, 0.59, 0.41, and possibly 0.46 Mev were associated with the decay. The first three gamma rays are compatible with existing energy levels in Mg^{25}.

THE half-life[1–3] and beta rays[4] of Na^{25} have been measured by several investigators, but published material on the gamma rays of this isotope is very meager. Recently, we have had occasion to make some measurements on the gamma rays associated with Na^{25} and the following is a report of our results.

The Na^{25} was prepared by irradiating magnesium with fast neutrons produced by bombarding lithium with 2–3 Mev deuterons from an electrostatic generator. The half-life of the Na^{25} was determined by following the decay for five half-lives with a scintillation counter consisting of a sodium iodide-thallium activated crystal coupled to a Dumont 6292 photomultiplier tube. An Atomic Instrument Company model 204-C amplifier and model 1030A scaler were used to amplify and scale the counts. An average of four such curves gave a half-life of 60 ± 2 sec which is in agreement with published results.

The gamma-ray energies were measured by photographing pulses displayed on a Tektronix 514-AD oscilloscope. A block of pure magnesium was irradiated with neutrons and then placed near the crystal. The exposure time was for two Na^{25} half-lives. This gave sufficient intensity to yield good photographs of the spectrum. The spectrometer was calibrated with the 0.66-Mev line of Cs^{137} and the 1.12-Mev line of Sc^{46}. Previous measurements indicated no deviation from linearity, within our limits of error, for this spectrometer from 87 kev to 4.46 Mev. Gamma rays with energies of 0.98, 0.59, 0.46, and 0.41 Mev were observed. The error in these energies is estimated to be ±0.01 Mev. The last two closely spaced lines appeared as a one broad line in some pictures, but several photographs showed a distinct doublet, in which case the peaks would be shifted toward each other. At our resolution, this shift could amount to 0.01–0.02 Mev; in which case, the second and fourth gamma-ray energies add to give the first. This observation is in agreement with the energy level scheme of Mg^{25} given by Endt and Kluyver,[5] where levels are reported at 0.98 and 0.58 Mev. Two β transitions corresponding to maximum energies of 2.7 and 3.7 ± 0.3 Mev have been proposed.[4] These observations are also compatible with the gamma rays observed in this study. In order to get an estimate of the half-lives of the individual gamma rays, the appropriate energy region was bracketed with a single-channel pulse height analyzer and the decay was followed for 4–5 half-lives. In all cases, the results were compatible to within the reported experimental error with a half-life of 60 seconds. The gamma ray corresponding to 0.46 Mev does not seem to agree with any levels reported in Mg^{25}. In testing the possibility that it represented branching from the 0.58-Mev level to ground, we carefully searched for a line in the region around 100–120 kev but found nothing. This gamma ray may involve a higher level as yet unknown or may simply be due to an impurity; however, if an impurity is responsible, the half-life of the contamination would have to be fairly close to that of Na^{25}.

One of the authors (J.E.I.) wishes to acknowledge a grant-in-aid from the Hynson, Westcott, and Dunning Research Fund.

† Work done under the auspices of the U. S. Atomic Energy Commission.

* Abstracted in part from a thesis submitted by John E. Iwersen in partial fulfillment of the requirements for the degree of Doctor of Philosophy, The Johns Hopkins University, Baltimore, Maryland.

[1] Huber, Lienhard, Scherrer, and Wäffler, Helv. Phys. Acta 17, 139 (1944).

[2] W. Riezler, Physik. Z. 45, 191 (1944).

[3] G. C. Baldwin and G. S. Klaiber, Phys. Rev. 70, 259 (1946).

[4] E. Bleuler and W. Zünti, Helv. Phys. Acta 20, 195 (1947).

[5] P. M. Endt and J. C. Kluyver, Revs. Modern Phys. 26, 95 (1954).

Properties of Excited States of Pd and Cd Nuclei by Coulomb Excitation

G. M. TEMMER AND N. P. HEYDENBURG
Department of Terrestrial Magnetism, Carnegie Institution of Washington, Washington, D. C.
(Received February 14, 1955)

We have Coulomb-excited the first-excited (2^+) states of most even-even nuclei of Pd and Cd using enriched targets. Three of these states were previously unknown (Pd^{108}, Pd^{110}, and Cd^{116}). We also observed excited states in Pd^{105}, Cd^{111}, and Cd^{113}, the latter yielding a new level at 290 kev. Transition probabilities (lifetimes) for these transitions have been determined and show definite systematic trends.

WE have observed Coulomb excitation of most nuclei of Pd and Cd, using our 6-Mev He^{++} beam[1] and targets enriched in the various isotopes.[2] Because of the $E2$ character of the excitation process, we excite only 2^+ states in the even-even nuclei; a measurement of the energy and yield of gamma radiation emitted from these states amounts therefore to a determination of spin, parity, energy, and transition probability (lifetime) of first-excited states of even-even nuclei. In view of the systematic behavior of the position, spin, and parity of these states,[3,4] it is of interest to obtain information concerning the systematics of their lifetimes as well; no such information for nuclei around $A=100$ is presently available because the lifetimes are beyond the range accessible to fast-coincidence studies (see below).

For the odd-A nuclei the spin assignments are not as definite and the positions of the levels reached are not necessarily equal to the gamma-ray energies observed. For the odd Cd nuclei ($I_0=\frac{1}{2}^+$) the excited states must have $I=3/2^+$ or $5/2^+$; a wider range of possibilities exists for the states excited in Pd^{105}($I_0=5/2^+$).

The gamma-ray yields from thick targets of Pd and CdO were measured with a $1\frac{3}{4}$ in.$\times$2 in. NaI(Tl) crystal in our standard arrangement.[5] The He^{++} beam was produced by using a gas stripper similar to the one described by Bittner,[6] but installed some 30 inches below the rf ion source in the accelerating tube. The He^+ ions are stripped of their second electron after having reached about 300 kev, and receive twice the voltage of the remainder of the electrostatic generator. At the present time our knowledge of the energy of the He^{++} beam is somewhat approximate (6.00$\pm$0.050 Mev). Up to 0.12 microampere of He^{++} beam has been available. The absolute efficiency of the crystal for the 411-kev gamma radiation from Au^{198} had been determined previously[7]; correction for effective photopeak efficiency at slightly different energies was made adapting the results of some Swiss workers.[8] The enriched CdO yields were converted to equivalent Cd yields by determining the ratio experimentally. (Observed CdO yields had to be multiplied by 1.35.) The thick-target yields were converted to cross sections making some simplifying assumptions suggested by Huus.[9] The cross sections in turn were reduced to transition probabilities $B(E2)$ using the improved theory of Alder and Winther.[10] The justification for the last step rests on empirical[11] and theoretical[10,12] evidence concerning the correctness of the semiclassical treatment of the Coulomb excitation process.*

We shall now discuss the excited levels in some detail.

Palladium.—Figure 1 shows the pulse-height spectra obtained from the even-even isotopes of Pd (with the exception of Pd^{102}, whose enrichment was insufficient). Previously established first-excited states were confirmed with respect to position, spin, and parity in Pd^{104} (550 kev) and Pd^{106} (510 kev); new 2^+ states were found in Pd^{108} (424 kev) and Pd^{110} (370 kev). The latter state is not accessible by other means. The systematic trend in position of these states is very apparent. The heights of the peaks in the pulse-height distributions reflect many factors in addition to transition probability, such as Coulomb excitability, thick-target yield dependence on level energy, and crystal efficiency. When these factors are taken into account, some of the trend remains, as can be seen from Table I. Two lines are observed in Pd^{105} (266 and 433 kev); transition probabilities were computed assuming that these energies correspond to levels at those energies, and that their sole decay occurs via the observed gamma ray.

[1] Some preliminary results on these and other medium-heavy nuclei, using natural targets, were presented at the Glasgow International Conference on Nuclear Physics, July 13–17, 1954, and can be found in the Proceedings (Pergamon Press Ltd., London, 1955).
[2] Obtained on loan from Brookhaven National Laboratory through the kindness of G. Scharff-Goldhaber.
[3] G. Scharff-Goldhaber, Phys. Rev. **90**, 587 (1953).
[4] P. Stähelin and P. Preiswerk, Nuovo cimento **10**, 1219 (1953).
[5] N. P. Heydenburg and G. M. Temmer, Phys. Rev. **94**, 1252 (1954).
[6] J. W. Bittner, Rev. Sci. Instr. **25**, 1058 (1954).
[7] N. P. Heydenburg and G. M. Temmer, Phys. Rev. **95**, 861 (1954).
[8] Maeder, Müller, and Wintersteiger, Helv. Phys. Acta **27**, No. 1, 3 (1954).
[9] See also a forthcoming review article on Coulomb excitation in Revs. Modern Phys. by Alder, Bohr, Huus, Mottelson, Winther, and Zupančič.
[10] K. Alder and A. Winther, Phys. Rev. **96**, 237 (1954).
[11] G. M. Temmer and N. P. Heydenburg, Phys. Rev. **96**, 426 (1954).
[12] G. Breit and P. B. Daitch, Phys. Rev. **96**, 1447 (1954); L. C. Biedenharn and C. M. Class, Phys. Rev. **98**, 691 (1955).

* *Note added in proof.*—We recently examined the thick-target excitation function, from 2.75- to 7.00-Mev alpha energy, for the 370-kev transition in Pd^{110}, and found it to be in very good accord with the $E2$ theory.

These assumptions are completely justified in the case of the even-even nuclei. Internal conversion correction has been neglected in view of the smallness of the conversion coefficients.

Cadmium.—Figure 2 shows the pulse-height spectra obtained from the even-even isotopes of Cd (with the exception of Cd^{106} and Cd^{108}, whose enrichment was insufficient). Previously established first-excited 2^+ states were confirmed in Cd^{110} (654 kev), Cd^{112} (620 kev), and Cd^{114} (550 kev); a new 2^+ state was found in Cd^{116} (508 kev), the latter again not accessible by other means. The persistent peak at 342 kev is due to the presence of oxygen and results from the $O^{18}(\alpha,n\gamma)Ne^{21}$ reaction, as pointed out previously.[11] Once again, the systematic trend of the level positions stands out. In the odd-A isotopes, the known 340-kev level ($I=3/2^+$) was excited in Cd^{111}; this level is known to decay predominantly to the ground state,[13] and the transition probability was computed accordingly. An interesting situation exists in Cd^{113}, whose one neighboring isobar, In^{113}, is stable, whereas the other neighbor, Ag^{113}, decays without gamma-ray emission. We have found a gamma ray of 290 kev in Cd^{113} and have shown it to be the first excited state of that nucleus by its excitation function. The absence (?) of gamma radiation in the decay of Ag^{113} would favor a $5/2^+$ spin assignment for that level. The latter cannot be the 5-year isomer of Cd^{113} because of the multipolarity of the transition. We find some slight evidence for another state at 550 kev. A state in that vicinity has been reported from a study of the $Cd^{112}(d,p)Cd^{113}$ Q-values.[14] If we see this same state, it too cannot be the isomeric level. A summary of the results on Cd can be found in Table I.

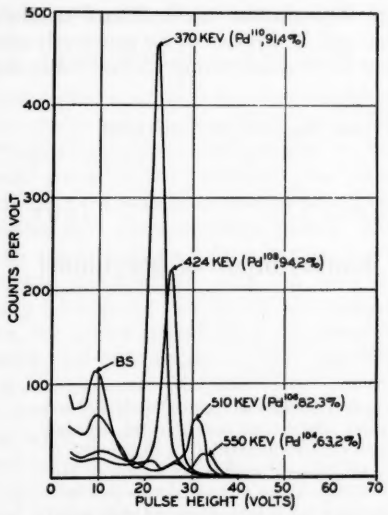

FIG. 1. Pulse-height spectra obtained for gamma rays from enriched even-even Pd isotopes under 6-Mev alpha-particle bombardment. $1\frac{3}{4}$ in.×2 in. NaI crystal. Gamma-ray energies, responsible isotopes and target enrichments are indicated over each peak. Peak *BS* is due to backscattered gamma rays.

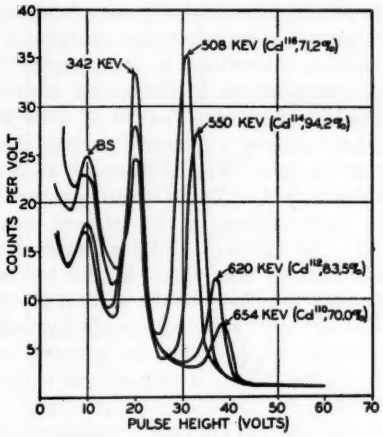

FIG. 2. Pulse-height spectra obtained for gamma rays from enriched even-even Cd isotopes under 6-Mev alpha-particle bombardment. $1\frac{3}{4}$ in.×2 in. NaI crystal. Gamma-ray energies, responsible isotopes and target enrichments are indicated over each peak. Peak *BS* is due to backscattered gamma rays. Peak at 342 kev, always present in oxide targets, is due to $O^{18}(\alpha,n\gamma)Ne^{21}$ reaction. Excess at that position in Cd^{110} target is due to 18.6 percent Cd^{111} component. To compare peak heights of these CdO targets with metallic Pd targets in Fig. 1, they must be raised by 35 percent (see text).

The accuracy in the energy determinations of the gamma rays is about ±1 percent. The over-all uncertainty in the final values of the transition probabilities is estimated at ±30 percent in *absolute* value; the relative values for the series of Pd and Cd isotopes are less uncertain (±15 percent).

As was mentioned above, a definite trend in the size of the even-even transition probabilities can be dis-

TABLE I. Properties of excited states of Pd and Cd nuclei Coulomb-excited with 6-Mev alpha particles. I_0 and I^* are ground-state and excited-state spins and parities, respectively; $B(E2)$ is the reduced transition probability; Q_0 is the intrinsic quadrupole moment derived from $B(E2)$. $B(E2)$ refers to the *upward* transition.

Nucleus	I_0	I^*	E_γ(kev)	$B(E2)$ (10^{-48} cm^4)	Q_0(10^{-24} cm^2)
$_{46}Pd^{104}$	0^+	2^+	550	0.61	2.5
Pd^{105}	$5/2^+$	?$^+$	266	0.013	···
		?$^+$	433	0.18	2.0[a]
Pd^{106}	0^+	2^+	510	0.73	2.7
Pd^{108}	0^+	2^+	424[b]	0.80	2.8
Pd^{110}	0^+	2^+	370[b]	0.94	3.1
$_{48}Cd^{110}$	0^+	2^+	654	0.66	2.6
Cd^{111}	$1/2^+$	$3/2^+$	340	0.16	2.0
Cd^{112}	0^+	2^+	620	0.70	2.6
Cd^{113}	$1/2^+$	$(5/2^+)$	290[b]	0.080	1.2
		?$^+$	(550)	0.14[c]	···
Cd^{114}	0^+	2^+	550	0.73	2.7
Cd^{116}	0^+	2^+	508[b]	0.76	2.8

[a] Computed by assuming $I^*=7/2^+$.
[b] Level previously unknown.
[c] Represents upper limit.

[13] C. L. McGinnis, Phys. Rev. **81**, 734 (1951).

[14] N. S. Wall, Phys. Rev. **96**, 664 (1954).

cerned, increasing monotonically with increasing neutron number, while the excitation energies of the 2^+ states decrease. According to the simplest "strong coupling" approximation in the unified description of the nucleus,[15,16] which identifies the 2^+ state with the first rotational state of a deformed nucleus, this is just as expected: in both Pd and Cd we are moving away from the closed shell at $N=50$ toward greater deformation, i.e., larger values of the intrinsic quadrupole moment Q_0. The nuclei of $_{48}$Cd are presumably somewhat less deformed than those of $_{46}$Pd because their proton number lies closer to the shell at $Z=50$. Now the *position* of the 2^+ state is *inversely* proportional to $Q_0^2(E_{2^+}=6\hbar^2/2\mathcal{I}; \mathcal{I}\sim Q_0^2)$, while the (upward) *transition probability* to the 2^+ state is proportional to $Q_0^2[B(E2)=5/16\pi(e^2Q_0^2)]$.[15,16] The values of Q_0 obtained from the transition probabilities are listed in the last column of Table I. The values are quite comparable to those we found previously for the odd-Z nuclei $_{45}$Rh^{103}, $_{47}$Ag^{107}, and $_{47}$Ag^{109},[7] as well as to the spectroscopically measured Q_0 in $_{49}$In^{115}. It is just such continuity of nuclear properties which seems to support the unified model. The values of Q_0 as derived from the moments of inertia (level positions) follow the same trend but turn out to be about three times larger, a tendency which has been previously noted.[15,17] All transition probabilities are about twenty times greater than would be predicted on the basis of a single-particle transition.

Since all these nuclei have spins of either 0 or $\frac{1}{2}$ (except Pd^{105}), their intrinsic quadrupole moments are not accessible to conventional measurement. The equivalent lifetimes for the transitions we observe here range between 2 and 7×10^{-11} second.

We have obtained additional results in even-even nuclei of Ti, Fe, Zn, Ge, Se, Ru, and Mo, to be published at a later date.

ACKNOWLEDGMENTS

We are very grateful to G. Scharff-Goldhaber, P. Colsmann, and M. McKeown for generously arranging the loan of the enriched isotopes which made this work possible.

[15] A. Bohr and B. R. Mottelson, Kgl. Danske Videnskab. Selskab, Mat.-fys. Medd. **27**, No. 16 (1953).
[16] A. Bohr, "Rotational states of atomic nuclei," dissertation, Copenhagen, 1954 (unpublished).
[17] K. W. Ford, Phys. Rev. **95**, 1250 (1954).

PHYSICAL REVIEW VOLUME 98, NUMBER 5 JUNE 1, 1955

Gamma Rays from the Low-Energy Proton Bombardment of Beryllium†

R. R. Carlson and E. B. Nelson
State University of Iowa, Iowa City, Iowa
(Received February 7, 1955)

The gamma radiation produced in the $Be^9(p,\gamma)B^{10}$ reaction at proton energies of approximately 300 kev was investigated with scintillation spectrometers. A three-crystal scintillation spectrometer detected 6.7±0.15, 6.0±0.1, 5.1±0.1, and 4.7±0.15-Mev gamma rays with relative intensities (±25 percent) of 0.15, 0.40, 1.00 and 0.45, respectively. A thick target yield of $(1.2\pm0.3)\times10^{-10}$ gamma per proton at 315-kev proton energy was measured for gamma radiation of 5.1-Mev energy. These gamma rays are produced in transitions to the ground-state and low-lying levels in B^{10} and their relative intensities and yield imply spin 1^- for the level at 6.89 Mev. A limited single-crystal spectrometer detected 0.41±0.02, 0.72±0.02, 1.03±0.03, and 1.43±0.03-Mev gamma rays corresponding to transitions between the low-lying levels in B^{10}. The angular correlation of the 0.72- and 1.03-Mev gamma rays was found to be consistent with a spin of 1^+ or 2^+ for the first excited state of B^{10}.

INTRODUCTION

THE energy levels of the B^{10} nucleus have been studied in a number of nuclear reactions. The results are summarized in the review article by Ajzenberg and Lauritsen.[1] Briefly, low-lying levels at 0.72, 1.74, 2.15, and 3.58 Mev are very well established, having been deduced from inelastic scattering experiments with protons and deuterons (with the exception of the 1.74-Mev state in the case of deuterons). Also, the first level has been seen in the reaction $C^{12}(d,\alpha)B^{10}$; the first and second, in the beta decay of C^{10}; the first, second, and third, in the reaction $Li^7(\alpha,n)B^{10}$. A level at 4.78 Mev has appeared in the inelastic proton scattering work. The above-mentioned levels and levels at 5.11, 5.17, 5.37, 5.58, 5.72, 5.93, 6.12, 6.38, 6.58, and 6.77 Mev appear in work on the neutron groups from $Be^9(d,n)B^{10}$. Further levels resulting from proton capture resonances in Be^9 show up at 6.89, 7.03, 7.19, 7.48, and 7.56 Mev.

The ground-state spin of B^{10} is known[2] to be 3 and the parity even.[3] Sherr and Gerhart[4] present various arguments to show that the first, second, third, and fourth excited states have spins and parities of 1^+, 0^+,

† Supported in part by the U. S. Atomic Energy Commission.
[1] F. Ajzenberg and T. Lauritsen, Revs. Modern Phys. **24**, 321 (1952). See also forthcoming supplement in the Reviews of Modern Physics. We wish to thank Professor Lauritsen for a preprint of the supplement.
[2] Gordy, Ring, and Burg, Phys. Rev. **78**, 512 (1950).
[3] F. Ajzenberg, Phys. Rev. **88**, 298 (1952).
[4] R. Sherr and J. B. Gerhart, Phys. Rev. **91**, 909 (1953).

1^+, and 2^+, respectively. The parity assignments come from the work of Ajzenberg[3] on the reaction $Be^9(d,n)B^{10}$. The spin assignments are made on the basis of a comparison of the theoretical and observed intensities of gamma ray transitions between the low-lying levels of B^{10} formed in the reaction $Be^9(d,n)B^{10}$ and in the beta decay of C^{10}. Spin-0 assignment for the second excited state is strengthened by the fact that this state does not appear in the inelastic deuteron scattering making it the spin-0 analog of the ground states of Be^{10} and C^{10}. Arguments for the spin and isotopic spin of the levels at 5.11 and 5.17 Mev have also been made.[5]

We have studied the gamma-ray decay of the 6.89-Mev level in B^{10}. Various high-energy gamma rays have been resolved and their relative intensities measured. From the nature of the decay and the yield, the spin and parity of this level may be deduced. Low-energy gamma rays presumably following these high-energy gamma rays have also been studied.

HIGH-ENERGY GAMMA RAYS

Gamma rays of a few Mev in energy can be measured quite accurately with sodium iodide crystal detectors, but for higher energies a single gamma ray gives rise to several peaks in the photomultiplier pulse-height distribution or the peak is excessively broadened. Since the gamma rays resulting from proton capture by beryllium are as high as 6 Mev in energy, we used a three-crystal spectrometer. This has been described previously.[6] Briefly, it consisted of three NaI crystals in a row, the center crystal being 2 in. long by $1\frac{1}{2}$ in. in diameter and the two side crystals being 1 in. long by $1\frac{1}{2}$ in. in diameter. The pulses from the center detector were analyzed by a 10-channel pulse-height analyzer when a triple coincidence between the three detectors occurred. By this means, pulses from the center detector are measured when a pair has been produced in the center crystal and both annihilation quanta escape.

The physical layout and electronic circuitry used were the same as previously reported.[6] The improvement in resolution with the 6.13-Mev gamma ray from $F^{19}(p,\alpha\gamma)O^{16}$ is shown in Fig. 3 of this previous report. A single peak of 7 percent width at half-maximum and a peak-to-valley ratio of 13 to 1 are obtained. The resolution is not as good at lower energies, being 9 percent with the 4.43-Mev gamma ray from $B^{11}(p,\gamma)C^{12}$. It is also poorer at higher energies, being 11 percent with the 11.67-Mev gamma ray from this same reaction. The reasons for this have been discussed previously.

The spectrometer was calibrated with the 6.13-Mev and 4.43-Mev gamma rays mentioned above. In addition, the requirement of triple coincidence was relaxed and three points on the calibration curve resulting from the 2.62-Mev gamma ray from ThC″ were obtained. The calibration curve was linear within the accuracy of the measurement which was two percent at 6 Mev.

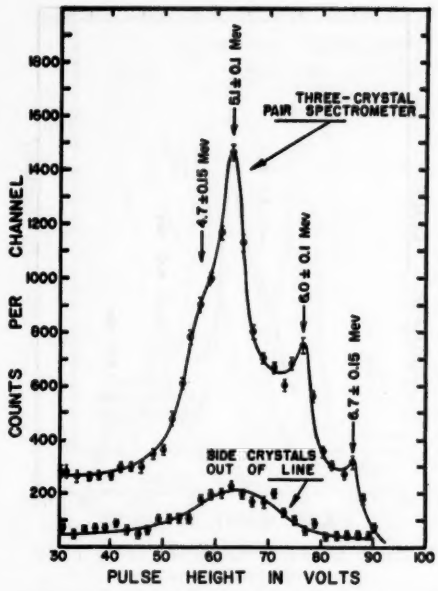

FIG. 1. Spectrum of high-energy capture gamma rays from a thick beryllium target bombarded with 315-kev protons, measured with a three-crystal pair spectrometer.

Gamma rays from proton capture in beryllium were obtained by bombarding a 2 mm thick metallic beryllium target with 100 microamperes of 315±5 kev protons from the State University of Iowa Cockcroft-Walton accelerator. The beam was analyzed and its energy determined by a 90° deflection magnet. The magnet was calibrated using the $B^{11}(p,\gamma)C^{12}$ resonance at 163 kev and the $F^{19}(p,\alpha\gamma)O^{16}$ resonance at 340 kev bombarding energy.

A spectrum of high-energy gamma rays obtained with the three-crystal spectrometer is shown in Fig. 1. The stability of the entire system was checked repeatedly throughout the six hours required to obtain the above spectrum. This was done by increasing the signal level four-fold by an input attenuator preceding the amplifier and measuring the photopeak of the Cs^{137} (663-kev) gamma ray. Shifts were less than 2 percent during any of the runs. Pulse heights during any run were normalized to a standard value by means of the stability checks with the Cs^{137} source.

In Fig. 1, four gamma rays may be seen: 6.7±0.15, 6.0±0.1, 5.1±0.1, and 4.7±0.15 Mev. The last is not completely resolved from the 5.1-Mev gamma ray but its existence is definitely established by the shape of the spectrum. A single gamma ray, such as the 6.13-Mev gamma ray from $F^{19}(p,\alpha\gamma)O^{16}$, produces a single symmetrical peak with a low valley on the low-energy side. On this basis, one must ascribe the asymmetry observed to a 4.7±0.15-Mev gamma ray.

[5] G. A. Jones and D. H. Wilkinson, Phys. Rev. **90**, 722 (1953).
[6] Carlson, Geer, and Nelson, Phys. Rev. **94**, 1311 (1954).

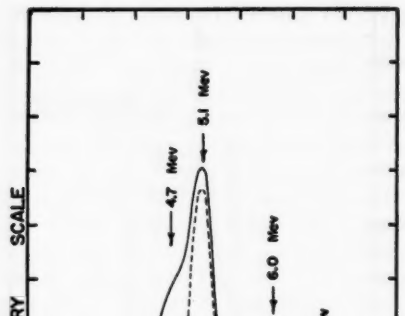

FIG. 2. Analysis of the spectrum of Fig. 1 into constituent gamma rays.

From the known shape of a peak due to a single gamma ray and from the known variation in this shape for different gamma-ray energies, the spectrum was decomposed into its constituent parts. Before this can be done, one must subtract the contribution of true triple coincidences resulting from the detection of other than annihilation quanta in the side detectors. To measure this, the side detectors were moved out of line with the center detector but kept the same distance from the target so that their counting rate was unchanged. The result is shown in Fig. 1, where it was assumed that the angular correlation of any cascades is isotropic. Accidental triple coincidences were measured by delaying the pulses from one side detector and were found to be negligible. If one now takes the difference of the two curves in Fig. 1 and analyzes it into peaks coming from the four gamma rays listed previously, one obtains the curves shown in Fig. 2. Taking into account the change in the pair-production cross section and the resolution, these peak heights give an estimate of the relative intensity of these gamma rays. With an error of ± 25 percent the result is 0.15, 0.40, 1.00, and 0.45 for the 6.7-, 6.0-, 5.1-, and 4.7-Mev gamma rays, respectively.

The spectrum of high-energy gamma rays was also studied at bombarding energies of 280 ± 5 kev and 365 ± 5 kev. The aforementioned four gamma rays were found with the same relative intensities within 25 percent as at a bombarding energy of 315 kev. The intensity at the lower energy was 0.55 ± 0.05 that at 315 kev; at the higher energy it was 2.2 ± 0.2 that at 315 kev. Two other thick targets with beryllium from different sources were also used and gave the same results at a bombarding energy of 315 ± 5 kev.

The absolute yield of 5.1-Mev gamma rays was obtained by comparing the counting rate in the peak due to this gamma ray with that in the peak due to the 6.13-Mev gamma ray from the 340 kev proton bombardment of a thick calcium fluoride target. The yield of the latter is known to be 1.74×10^{-8} gamma per proton.[7] The only changes were in the target and bombarding voltage. The peak counting rate due to the 5.1-Mev gamma ray must be obtained from the spectrum in the same manner as in the determination of relative intensities. Corrections for a slight change in resolution and pair production cross section must then be applied to the ratio of the observed counting rates to reduce it to a ratio of intensities. The result is 1.2×10^{-10} gamma of energy 5.1 Mev per proton at 315-kev bombardment of thick beryllium with an error of ± 25 percent.

Single-crystal pulse-height distributions from the high-energy gamma rays were measured at 0° and 90° to the beam direction by using the center detector of the three-crystal spectrometer. The target consisted of a piece of 2-mm thick beryllium metal mounted at 45° to the beam direction in the center of a pillbox shaped chamber. The detector viewed the back of the target at either angle from a distance of 3 in. The results are shown in Fig. 3. The peaks result from the superposition of the two peaks from each of the 4.7-, 5.1- and 6.0-Mev gamma rays. Such pulse-height distributions were ob-

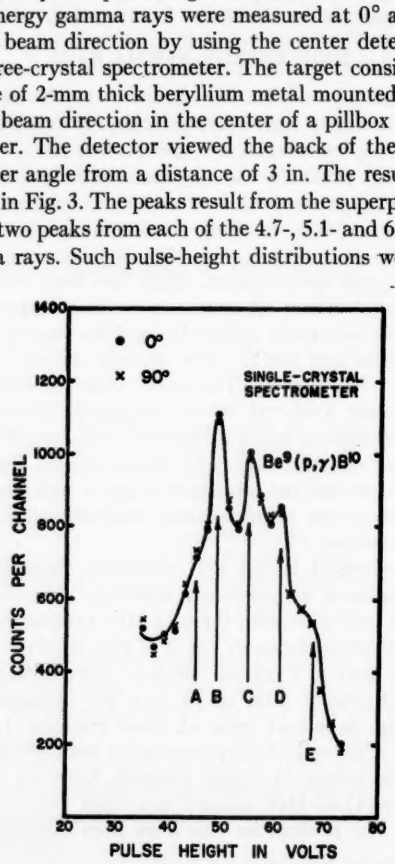

FIG. 3. Spectrum of high-energy gamma rays from a thick beryllium target bombarded with 315-kev protons measured with a single-crystal spectrometer at 0° and 90° to the beam direction. The irregularity at *A* is caused by gamma rays of 4.7 Mev; at *B*, 4.7 and 5.1 Mev; at *C*, 5.1 Mev; at *D*, 6.0 Mev; at *E*, 6.0 and 6.7 Mev.

[7] Chao, Tollestrup, Fowler, and Lauritsen, Phys. Rev. **79**, 108 (1950).

served for the single 6.13-Mev gamma ray from the $F^{19}(p,\alpha\gamma)O^{16}$ reaction. With the poor resolution of a single-crystal spectrometer, the 6.7-Mev ground-state transition was not observed. Pulses caused by 4.7-Mev gamma rays which lose 3.7 Mev in the crystal appear at *A*. The peaks at *B* and *C* are caused by 5.1-Mev gamma rays which lose 4.1 and 4.6 Mev in the crystal, respectively, with some contribution to the peak at *B* coming from 4.7-Mev gamma rays which lose 4.2 Mev in the crystal. The peaks at *D* and *E* are caused by 6.0-Mev gamma rays which lose 5.0 and 5.5 Mev in the crystal, respectively. Some contributions to the peak at *E* may come from 6.7-Mev gamma rays which lose 5.7 Mev in the crystal. From the *C* and *D* peaks one can say that there is less than 15 percent anisotropy of the 6.0-Mev gamma ray relative to the 5.1-Mev gamma ray. Jacobs, Malmberg, and Wahl[8] used Geiger counters to measure the angular distribution of the total gamma radiation from a thick target bombarded with 340-kev protons and found the radiation to be isotropic within 10 percent.

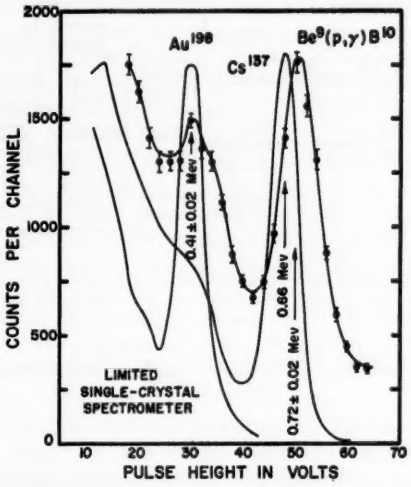

FIG. 5. Spectrum of low-energy capture gamma rays from a thick beryllium target bombarded with 315-kev protons, measured with a single-crystal spectrometer limited at 1 Mev.

LOW-ENERGY GAMMA RAYS

The spectrum of low-energy gamma rays was studied with a limited single crystal spectrometer of the same type previously described.[6] Briefly, this consisted of a sodium iodide crystal detector with a 2 in. long by $1\frac{1}{2}$-in. diameter crystal followed by a RCA 5819 photomultiplier and a pulse limiter set to limit all pulses corresponding to gamma-ray energies greater than 2 Mev to the same height. This enables one to expand the gain of the amplifier following the limiter without danger of overloading. The amplifier output was then analyzed by a 10-channel pulse-height analyzer.

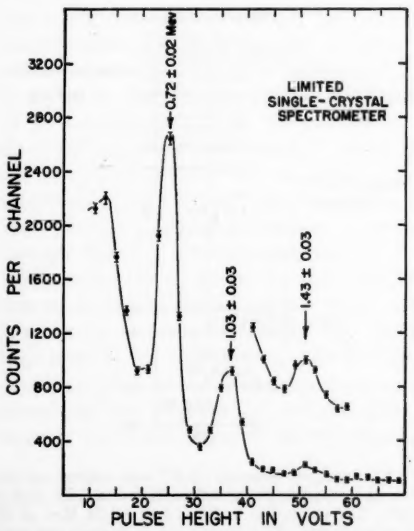

FIG. 4. Spectrum of low-energy capture gamma rays from a thick beryllium target bombarded with 315-kev protons, measured with a single-crystal spectrometer limited at 2 Mev.

The spectrometer was calibrated by using the 663-kev gamma ray from Cs^{137}, the 1.17-Mev and 1.33-Mev gamma rays from Co^{60}, and the 1.60-Mev energy loss from the 2.62-Mev gamma ray of ThC″. Over the range of pulse heights of interest the calibration was linear to within the accuracy of measurement which was 1 percent at 1.6 Mev. The spectrum obtained at a bombarding energy of 315 kev is shown in Fig. 4. Three gamma rays are observed: 0.72 ± 0.02, 1.03 ± 0.03, and 1.43 ± 0.03 Mev. The observed peak heights above background of the 1.03- and 1.43-Mev gamma rays relative to that of the 0.72-Mev gamma ray are 0.27 ± 0.03 and 0.05 ± 0.01, respectively. Any peak due to the total absorption of a 1.74-Mev gamma ray in the crystal is less than 0.01 the height of that due to the total absorption of the 0.72-Mev gamma ray. The spectrum was taken at bombarding energies of 255, 385, 440, and 495 kev as well as 315 kev. No change in the relative intensities of the gamma rays was observed.

The limiting was changed to take place at 1 Mev and the spectrometer calibrated by using the 0.41-Mev gamma ray from Au^{198}, the annihilation radiation from Na^{22}, and the 0.66-Mev gamma ray from Cs^{137}. Gamma radiation of energy 0.41 ± 0.02 Mev from the proton bombardment of beryllium at 315 kev was found with an intensity of a few percent of the 0.72-Mev radiation. A more accurate estimate is difficult because the peak is superimposed on the Compton distribution of the 0.72-Mev gamma ray. The peak is definitely caused by a 0.41-Mev gamma ray and not the Compton distribution of the 0.72-Mev gamma ray, for the 0.66-Mev gamma ray from Cs^{137} was found to have no such peak in its Compton distribution. The results are shown in Fig. 5.

[8] Jacobs, Malmberg, and Wahl, Phys. Rev. **73**, 1130 (1948).

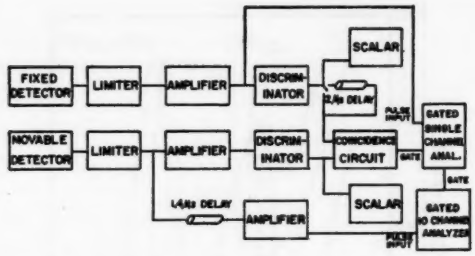

FIG. 6. Block diagram of the electronic circuits for the measurement of the angular correlation of the 1.03- and 0.72-Mev gamma rays.

ANGULAR CORRELATION OF LOW-ENERGY GAMMA RAYS

The angular correlation of the 1.03- and 0.72-Mev gamma rays was investigated with the same thick target and chamber used for the angular distribution measurements. A calcium fluoride target could be substituted for the beryllium target and the known[1] isotropy of the 6.13-Mev gamma radiation used to check the centering of the beam. Two NaI crystal detectors, limited at 2 Mev, were used. A 1-in. long by $1\frac{1}{2}$-in. diameter crystal was used on a fixed detector which viewed the front of the target from a distance of 3 in. at 90° to the beam direction. A 2-in. long by $1\frac{1}{2}$ in.-diameter crystal was used on a movable detector which viewed the back of the target from a distance of $2\frac{1}{2}$ in. at either 0° or 90° to the beam direction. Beam currents of 20 microamperes were used. The bombarding energy was 315 kev.

A block diagram of the circuit is shown in Fig. 6. Pulses from the limiter were amplified by Atomic Instrument Company Model 204B amplifiers (which include the discriminators shown) and coincidences detected by an Atomic Instrument Company Model 502, 0.5-microsecond resolving time, coincidence circuit. A 2-microsecond delay could be interposed in the fixed detector channel to check for accidental coincidences, which were negligible. An Atomic Instrument Company Model 502 anticoincidence circuit was used as a gated single-channel pulse-height analyzer to select pulses from the fixed detector corresponding to the 0.72-Mev gamma ray total absorption peak. Pulses from the movable detector were amplified after a 1.4-microsecond delay and analyzed by a 10-channel pulse-height analyzer. This was gated by the time coincidence of a pulse in the movable detector channel and a pulse in the fixed detector channel having a height corresponding to the total absorption peak of the 0.72-Mev gamma ray. The 10-channel analyzer was set on the pulse heights corresponding to the total absorption peak of the 1.03-Mev gamma ray. All gains and discriminator settings were checked throughout the run and no appreciable shifts were found.

About a thousand coincidence counts were accumulated with the movable detector at 0° to the beam and also at 90° to the beam. The counts were accumulated alternately in many short runs over a period of twenty hours. The coincidence spectrum shows a peak of the same shape as that of the 1.03-Mev gamma ray in Fig. 4. The anisotropy observed is:

$$[W(180°)/W(90°)]-1=-0.12\pm0.04,$$

where $W(\theta)$ is the coincidence rate with the angle θ between the detectors. This value is in agreement with the value of -0.10 ± 0.05 found by Shafroth and Hanna[9] using the $Be^9(d,n)B^{10*}(\gamma,\gamma)B^{10}$ reaction.

DISCUSSION

The level at 6.89-Mev excitation in B^{10} is quite broad.[10] For this reason, s-wave proton capture in Be^9 has been assumed for this level.[1] This is certainly consistent with the observed relative angular isotropy. Two possible spins for the level, 1^- and 2^-, result. The latter is ruled out because ground-state transitions would be more probable than transitions to the excited states. Transitions to the ground state are known[11] to predominate overwhelmingly for the 7.48-Mev level which has spin 2^-. In Fig. 7, the known energy levels of B^{10} have been shown with the observed high-energy gamma rays indicated as transitions to the ground and low-lying excited states. The relative intensities of the high- and low-energy gamma rays are in agreement with the mode of decay indicated. The ground-state transitions may be ascribed to the influence of the 7.48-Mev level. This is possible despite the apparent constancy of the relative intensities of the high-energy gamma rays over an 85-kev range in bombarding energy because of the

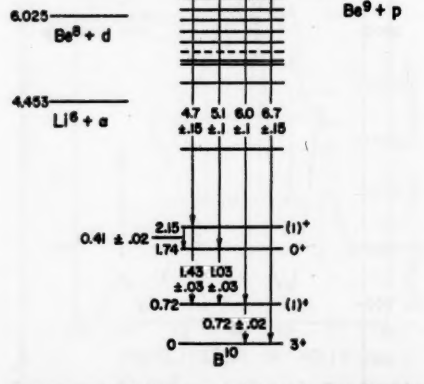

FIG. 7. Energy level diagram of B^{10} and related nuclear configurations with energies on the left in Mev and spins and parities on the right. The excitation in B^{10} is 6.87 ± 0.04 Mev at 315-kev proton bombardment. The transitions indicated are consistent with the measured gamma-ray energies.

[9] S. M. Shafroth and S. S. Hanna, Phys. Rev. **95**, 86 (1954).
[10] S. E. Hunt, Phys. Rev. **87**, 902 (1952).
[11] W. F. Hornyak and T. Coor, Phys. Rev. **92**, 675 (1953).

175-kev breadth of the resonance and the large dependence of the cross section on penetrability in this energy range.

The yield of the 5.1-Mev gamma rays from a thick target is equal to the integral of σ/ϵ, where σ is the cross section for emission of these gamma rays and ϵ is the energy loss per atom per cm^2 for protons in beryllium. The latter is known[12] over the energy range where there is any appreciable contribution to the integral. The yield is calculated from

$$Y=\sigma_r\int_0^E\left(\frac{\sigma}{\sigma_r}\right)\frac{dE}{\epsilon},$$

where σ_r is the cross section at resonance. Hunt's[10] thin-target yield curve gives the variation of σ/σ_r with energy for the 336-kev resonance. The cross section for emission of 5.1-Mev gamma rays is $(1.2\pm0.4)\times10^{-29}$ cm^2 at resonance. Extrapolating the values given by Hornyak[11] for the 993-kev resonance down to 336 kev, one finds the cross section for emission of gamma rays to the ground state to be about 10 percent of the aforementioned cross section.

Assuming that single-level Breit-Wigner resonance theory is applicable to the 336-kev resonance, the resonance cross section is equal to $4\pi\lambda^2\omega\Gamma_\gamma\Gamma_p/\Gamma^2$, where $2\pi\lambda$ is the de Broglie wavelength of the proton in the center of mass system, Γ_γ is the partial width for gamma emission, Γ_p is the partial width for proton emission, Γ is the total width of the level, and ω is the statistical weight factor equal in this case to $\frac{3}{8}$. From the measured values[13] of the $Be^9(p,d)Be^8$ and $Be^9(p,\alpha)Li^6$ cross sections, one can estimate the proton width of the level at 6.89 Mev in B^{10} to be either about 20 kev or about 155 kev. Using the expression given by Thomas[14] for the reduced width, one finds the large value to be unacceptable. The partial width for emission of 5.1-Mev gamma rays from the 6.89-Mev level in B^{10} is then 5 ev. This is to be compared with the prediction of the Weisskopf radiation lifetime formula[15] which gives a width of 58 ev for a 5.1-Mev $E1$ transition.

The isotopic spin selection rule calling for a large inhibition of electric dipole transitions between levels with isotopic spin 0 in self-conjugate nuclei[16] is apparently violated in the decay of the 6.89-Mev state to the lower states of B^{10}. The transitions to the 0.72- and 2.15-Mev levels are overwhelmingly $E1$; that to the 1.74-Mev level is $E1$. The state at 6.89 Mev probably has isotopic spin 0 since the nearest levels corresponding to those of Be^{10} are at about 5.2 and 7.6 Mev in B^{10}. The isotopic spin assignment is strengthened by the observation that the $Be^9(p,d)Be^8$ and $Be^9(p,\alpha)Li^6$ reactions both require isotopic spin 0 for the compound state of B^{10}. The 1.74-Mev state in B^{10} has isotopic spin 1 and the 0.72 and 2.15 Mev states in B^{10} have[17] isotopic spin 0. Consequently, one would expect a large inhibition of the transitions to the 0.72- and 2.15-Mev states relative to those to the 1.74-Mev state. Actually, all three are of comparable intensity. A similar case occurs at the 993-kev resonance for which the ground-state transition shows much less inhibition than would be expected on the basis of the isotopic-spin selection rules.[11]

The 1.03-Mev gamma rays and some of the 0.72-Mev gamma rays observed above presumably come from the cascade decay of the 1.74-Mev level in B^{10}. Since this level has spin 0, there is no memory of how it was formed to affect its subsequent decay. The correlation of the cascade radiation reduces, therefore, to a simple double-correlation problem.[18] Effects of the environment of B^{10} on the correlation are expected to be small because, first of all, it is located in a metal[19] and secondly, recent measurements[20] of the lifetime of the first excited state of B^{10} give a value of about 7×10^{-10} second which is rather short for extranuclear influences to have any effect.[19]

The measured anisotropy of -0.12 ± 0.04 is to be compared with that predicted for the various possible spins of the first excited state of B^{10}. The only possible values are 1^+ and 2^+. A spin of 0^+ would rule out the 1.03-Mev transition besides giving isotropy for the correlation and spins higher than 2 would favor a 1.74-Mev transition over a cascade. The spin 1^+ requires the first transition to be $M1$ and the second is predominantly $E2$. The $M3$ and $E4$ components are usually retarded by large factors. Assuming $M1-E2$ decay the predicted anisotropy is -0.10, in agreement with the measured value. The spin 2^+ requires the first transition to be $E2$ but the second may be a mixture of $M1$ and $E2$. The higher multipole components are probably retarded by large factors. The predicted anisotropy is $-(0.10+1.1\delta)$, when δ^2 is the ratio of $E2$ to $M1$ in the mixture and the possibility of higher multipole components is discarded. For any value of δ^2 less than 0.25 percent, this is in agreement with the value found within the accuracy of measurement. Since the radiation lifetime formulas[15] predict a value for δ^2 here of about 0.015 percent, all one can say is that the observed correlation is consistent with either spin 1^+ or spin 2^+ for the first excited state of B^{10}.

We are indebted to Dr. D. H. Wilkinson for a fruitful discussion of this work.

[12] S. D. Warshaw, Phys. Rev. **76**, 1759 (1949).
[13] Thomas, Rubin, Fowler, and Lauritsen, Phys. Rev. **75**, 1612 (1949).
[14] R. G. Thomas, Phys. Rev. **88**, 1109 (1952).
[15] V. F. Weisskopf, Phys. Rev. **83**, 1073 (1951).
[16] L. A. Radicati, Phys. Rev. **87**, 521 (1952).
[17] Bockelman, Browne, Buechner, and Sperduto, Phys. Rev. **92**, 665 (1953).
[18] L. C. Biedenharn and M. E. Rose, Revs. Modern Phys. **25**, 729 (1953).
[19] H. Frauenfelder, Ann. Rev. Nuclear Sci. **2**, 129 (1953).
[20] J. Thirion and V. L. Telegdi, Phys. Rev. **92**, 1253 (1953).

Nuclear Magnetic Moments of Cl^{36}, Rh^{103}, and W^{183}†‡

P. B. Sogo and C. D. Jeffries
Department of Physics, University of California, Berkeley, California

(Received January 24, 1955)

The nuclear magnetic resonance of Cl^{36} in HCl solution has been observed by nuclear induction, and the magnetic moment is found to be $\mu(Cl^{36})=+1.2838\pm0.0002$ nm. Calculations on a jj coupling model yield $\mu(Cl^{36})=+1.16$ nm. The magnetic resonances of Rh^{103} and W^{183} have been observed in powdered metallic samples. The magnetic moments are found to be $\mu(Rh^{103})=-0.08790\pm0.00007$ nm, and $\mu(W^{183})=+0.115\pm0.001$ nm, where in each case a calculated correction for the Knight shift due to the conduction electrons has been applied.

USING a nuclear induction spectrometer of high sensitivity, we have observed the nuclear magnetic resonance of Cl^{36} contained in a 250-microcurie sample in 4 normal HCl solution. The resonance occurs at a frequency of 4.88 Mc/sec in a field of 10 000 gauss and has a signal-to-noise ratio of approximately 6. By observing the polarity of the resonance signal relative to that of Cl^{35} in the same sample, we have established that the magnetic moment of Cl^{36} is positive. In the same magnetic field the frequency of the Cl^{36} resonance relative to that of D in a sample of D_2O containing 1-molar Mn^{++} ions has been observed to be

$$\nu(Cl^{36})/\nu(D)=0.74873\pm0.00003. \quad (1)$$

Using the value of the spin $I(Cl^{36})=2$ as first measured by Townes and Aamodt[1] and also by Johnson, Gordy, and Livingston,[2] we thus find for the magnetic moment of Cl^{36}:

$$\mu(Cl^{36})=+1.2838\pm0.0002 \text{ nm}, \quad (2)$$

without diamagnetic correction. In this calculation we have used the known ratio $\mu(D)/\mu(H)=0.307015$[3] and have taken the proton magnetic moment to be $\mu(H)=2.7925$.[4] Since Cl^{36} is one of the relatively few odd-odd nuclei for which nuclear moment data are available, it is of particular interest to compare our results with the predictions of the Mayer-Jensen nuclear shell model. Cl^{36} contains 19 neutrons as does S^{35}. The odd neutron in S^{35} is in a $d_{\frac{3}{2}}$ state and the nuclear g factor as calculated from the measured value of the magnetic moment is $g_n=0.66$. Cl^{36} contains 17 protons as do Cl^{35} and Cl^{37}. The odd proton is in a $d_{\frac{3}{2}}$ state in the stable chlorine isotopes and the average value of the nuclear g factor as calculated from the observed moments is $g_p=0.50$. If one assumes that in Cl^{36} these odd-neutron and odd-proton states are jj coupled to give a resultant spin of $I=2$, the resultant magnetic moment is readily calculated to be $\mu(Cl^{36})=1.16$ nm, in good agreement with our measured value.

From optical hfs for Rh^{103}, Kuhn and Woodgate[5] have reported that $I=\frac{1}{2}, \mu=-0.11$ nm, and hfs splitting in the atomic ground state $=0.023$ cm^{-1}. In a finely powdered sample of 11 grams of metallic Rh, we have observed the nuclear magnetic resonance of Rh^{103} at a frequency of 1.34 Mc/sec in a field of 10 000 gauss; the signal-to-noise ratio is approximately 30 at room temperature. By comparing the polarity of this signal to that of the deuteron, we have verified that the magnetic moment is negative. The resonance frequency of Rh^{103} in metal to that of D in D_2O containing 1-molar Mn^{++} ions is found to be

$$\nu(Rh^{103})/\nu(D)=0.205574\pm0.000007. \quad (3)$$

Attempts to observe the resonance in ionic solutions have been unsuccessful, probably because of the lower nuclear concentrations available and the formation of paramagnetic complexes. Knight[6] has found that nuclear magnetic resonance frequencies are shifted in metals due to the Pauli paramagnetism of the conduction electrons. In order to obtain a reliable value for the magnetic moment of Rh^{103}, we have estimated the Knight shift in the following way. As shown by Townes, Herring, and Knight,[7] the fractional additional field at the nucleus due to the electrons may be written

$$\frac{\Delta H}{H}=\chi_p M\frac{Ihc\Delta\nu}{(2I+1)\mu_\beta\mu_0}\frac{\langle|\psi_k(0)|^2\rangle_{Av}}{|\psi_a(0)|^2},$$

where χ_p = Pauli susceptibility/gram, $\Delta\nu$ = atomic hyperfine splitting, $\langle|\psi_k(0)|^2\rangle_{Av}$ = square of metallic wave function at the nucleus averaged over the electrons at the top of the Fermi surface, $\psi_a(0)$ = atomic wave function at the nucleus, M = mass of one atom, I = nuclear spin, μ_0 = nuclear magneton μ_β = Bohr magneton. Of these quantities, all are either measured or readily calculable except the expression involving the wave functions. However, for Ag, which is structurally similar to Rh, the Knight shift has been measured,[8] and this

† This work has been supported in part by The Research Corporation and the U. S. Atomic Energy Commission.

‡ Presented at the 1954 Berkeley meeting of the American Physical Society [Bull. Am. Phys. Soc. **29**, No. 8, 17 (1954)] and at the 1955 Washington meeting [Bull. Am. Phys. Soc. **30**, No. 3, 13 (1955)].

[1] C. H. Townes and L. C. Aamodt, Phys. Rev. **76**, 691 (1949).
[2] Johnson, Gordy, and Livingston, Phys. Rev. **83**, 1249 (1951).
[3] J. E. Mack, Revs. Modern Phys. **22**, 64 (1950).
[4] F. Bloch and C. D. Jeffries, Phys. Rev. **80**, 305 (1950).
[5] H. Kuhn and G. K. Woodgate, Nature **166**, 906 (1950); Proc. Phys. Soc. (London) **A64**, 1090 (1950).
[6] W. D. Knight, Phys. Rev. **76**, 1259 (1949).
[7] Townes, Herring, and Knight, Phys. Rev. **77**, 852 (1950).
[8] Brun, Oeser, Staub, and Telschow, Phys. Rev. **93**, 172 (1954); P. B. Sogo and C. D. Jeffries, Phys. Rev. **93**, 174 (1954).

affords an approximate determination of the wave function ratio. The result for Ag^{109} is $\langle|\psi_k(0)|^2\rangle_{Av}/|\psi_a(0)|^2 = 0.66$. Taking this value as appropriate also for Rh, we find for the Knight shift $\Delta H/H = 0.0022$. Applying this correction to the magnetic moment of Rh^{103} as calculated from (3), we find

$$\mu(Rh^{103}) = -0.08790 \pm 0.00007 \text{ nm}, \quad (4)$$

without diamagnetic correction.

The spin of W^{183} has been determined to be $\frac{1}{2}$ by Grace and More,[9] Kopfermann and Meyers,[10] and Fowles[11] from optical hfs; the magnetic moment has been reported to be +0.080 nm by Vreeland and Murakawa.[12] We have observed the magnetic resonance of W^{183} in 14 grams of the powdered metal at a frequency of 1.79 Mc/sec in 10 000 gauss with a signal-to-noise ratio of about 10 at room temperature. We have verified that the magnetic moment is positive. The ratio of the W^{183} resonance frequency in the metal to that of D in D_2O containing 1-molar Mn^{++} ions is found to be

$$\nu(W^{183})/\nu(D) = 0.27395 \pm 0.00003. \quad (5)$$

Chemical difficulties in obtaining sufficiently concentrated ionic solutions with paramagnetic catalysts have to date prevented observation of the resonance in any other compounds besides the metal. In order to obtain a reliable value for the magnetic moment of W^{183}, we have made an attempt to estimate the Knight shift, as was outlined above for Rh^{103}. However the atomic hfs splitting in the ground state has not been measured for W; also, the metallic/atomic wave function ratio cannot be conveniently estimated from an analogous known case as was possible for Rh. If one estimates the hfs splitting from that of Ta, which is known, and furthermore if one assumes a wave function ratio of unity, the resulting Knight shift can be estimated to be about 1.5 percent. Applying this correction to the magnetic moment of W^{183} as determined from (5), one obtains

$$\mu(W^{183}) = +0.115 \pm 0.001 \text{ nm}. \quad (6)$$

Informative discussions with W. D. Knight are gratefully acknowledged.

Since the completion of the work reported we have learned that Aamodt and Fletcher[13] have independently measured the magnetic moment of Cl^{36} by microwave spectroscopy. Their result, $\mu(Cl^{36}) = +1.32 \pm 0.08$ nm, is in agreement with our value quoted above.

[9] N. S. Grace and K. R. More, Phys. Rev. **45**, 166 (1934).
[10] H. Kopfermann and D. Meyers, Z. Physik **124**, 685 (1948).
[11] G. R. Fowles, Phys. Rev. **78**, 744 (1950).
[12] J. A. Vreeland and K. Murakawa, Phys. Rev. **83**, 229 (1951).
[13] P. C. Fletcher and L. C. Aamodt, Bull. Am. Phys. Soc. **30**, No. 3, 13 (1955); L. C. Aamodt and P. C. Fletcher, Phys. Rev. **98**, 1317 (1955).

PHYSICAL REVIEW VOLUME 98, NUMBER 5 JUNE 1, 1955

Magnetic Moment and Mass of Chlorine-36*

L. C. Aamodt,† and P. C. Fletcher
Columbia University, New York, New York

(Received February 24, 1955)

The magnetic moment of the Cl^{36} nucleus was measured by observing the Zeeman splitting of the $F=2\rightarrow2$ line in the electric quadrupole hyperfine pattern of the molecule CH_3Cl^{36} ($J=0\rightarrow1$, $K=0$ transitions). It was found to be 1.32 ± 0.08 nuclear magnetons. The magnitude of the magnetic moment was measured by using a rectangularly cross-sectioned absorption cell with plane polarized microwave radiation, and observing the $\Delta M=\pm1$ transitions. The sign of the magnetic moment was measured by using a circularly cross-sectioned absorption cell with circularly polarized microwave radiation. This allowed the $\Delta M=1$ and the $\Delta M=-1$ transitions to be observed separately. The magnetic field was calibrated by observing the Zeeman splitting of the spectrum of CH_3Cl^{35}. This value of magnetic moment indicates a nuclear configuration $(d_{\frac{3}{2}})_N(d_{\frac{3}{2}})_P$.

Measurements of the quadrupole spectrum without the Zeeman perturbation gave the following additional information: the spin of Cl^{36} was confirmed to be 2, the mass difference ratio $[m(Cl^{36})-m(Cl^{35})]/[m(Cl^{37})-m(Cl^{36})]$ was found to be 1.00168 ± 0.04 percent, the molecular rotational constant of the CH_3Cl^{36} molecule was found to be 13187.604 ± 0.015 Mc/sec, and its quadrupole coupling constant to be -15.83 ± 0.20 Mc/sec.

INTRODUCTION

THE $_{17}Cl^{36}{}_{19}$ nucleus is one of the interesting group of β-active nuclei with an odd number of both protons and neutrons. Townes and Aamodt[1] have previously determined the spin of this nucleus to be 2 and its quadrupole moment to be small and negative. This information was insufficient to allow any predictions concerning nuclear configurations of the Cl^{36} nucleus. Determination of the magnetic moment gives enough information to distinguish between possible configurations. Such a determination was the primary object of the present experiment.

The magnitude of the magnetic moment was measured

* This work was done under the auspices of the U. S. Atomic Energy Commission, and was supported in part jointly by the Signal Corps, the Office of Naval Research, and the Air Research and Development Command.
† Now at Brigham Young University, Provo, Utah.
[1] C. H. Townes and L. C. Aamodt, Phys. Rev. **76**, 691 (1949).

by observing the $\Delta M=\pm 1$ Zeeman splittings of the $F=2\rightarrow 2$ line in the quadrupole hyperfine pattern of the $J=0\rightarrow 1$ rotational transition of the molecule CH_3Cl^{36}. The sign of the magnetic moment was determined by observing the $\Delta M=\pm 1$ and the $\Delta M=-1$ Zeeman transitions separately.

EXPERIMENTAL APPARATUS

The spectrometer used in these measurements was a conventional Stark spectrometer using an adaptation of Pound's ac stabilizing circuit[2] to allow the microwave frequency source to be swept at a very slow rate. The purpose of the slow sweep was to allow the absorption line signal to be transmitted without distortion through circuits having an exceptionally long time constant. The long time constant was used to narrow the noise band width and improve sensitivity. Another variation from the usual spectrometer was the short absorption cells used. These cells have several advantages which will be mentioned later.

The microwave source was a 2K50 reflex klystron. It fed microwave energy directly into the stabilizing circuit with a small portion of the power coupled into the absorption cell. The signal received at the detecting crystal was amplified, first, by a tuned-plate tuned-grid three-stage amplifier, and then by a regenerative narrow-band amplifier. The output band width of the narrow-band amplifier was adjustable down to 50 cycles per second. This small band width was necessary to avoid saturation of the phase detector which followed. The microwave frequency was measured by beating the microwave power with the harmonics of a crystal oscillator whose frequency was compared with that of *WWV*.

The magnitude of the magnetic moment was measured by using an 18-inch long rectangular *K*-band wave guide (with a Stark septum) as an absorption cell. The total volume of the absorption cell, including input leads and thermocouple gauge, was 40 cc. The thermocouple gauge accounted for approximately one-fourth of this volume. With the small amount of sample material available, this small volume allowed the cell to be filled several more times than would have been possible with absorption cells of longer lengths. The sign of the magnetic moment was measured using a 36-inch long circular-cylindrical wave guide as an absorption cell. The Stark septum consisted of a circular-cylindrical rod along the axis of the cell.

These short cells reduced some of the effects caused by power reflections in the microwave system. In a Stark spectrometer the process of Stark modulation reduces, but does not completely eliminate, the effects of power fluctuations. The short cells decreased the rate at which these power fluctuations occurred (with respect to variations in frequency).

The Zeeman field for the rectangular guide was provided by permanent magnets. The field covered an area of 18 inches by $2\frac{3}{4}$ inches with a gap of $\frac{5}{8}$ inch. It was produced by using six magnetron magnets (horn type) and connecting all of the corresponding poles of the six magnets with rectangular pole pieces of the dimensions mentioned above. The average field was 2166 gauss. Because six separate magnetic sources were used in the assembly there was some inhomogeniety. The minimum field differed from the maximum field by 6 percent. This variation broadened the spectral lines slightly. The measurement of g_J was made with smaller pole pieces and a field of 3186 gauss.

The magnet assembly and circular wave guide used in the measurement of the sign of the magnetic moment will be described in detail in a later paper. Briefly it consisted of a solenoid with the circular wave-guide absorption cell along the solenoid axis. Circular polarization of the microwave radiation was obtained by squeezing a short section of the circular wave guide immediately preceding the absorption cell into a slightly elliptical shape (making it a quarter-wave section). At the[3] receiving end of the absorption cell the unwanted component of the circularly polarized radiation was removed by an attenuator.

The slow-sweep microwave source utilized Pound's ac stabilizing circuit[2] with the balanced bridge arrangement of Zafferano.[4] The slow sweep was produced by tuning the reference cavity slowly with a clock motor. The sweep speeds used varied from 50 kc/min to 1 Mc/min. The slow tuning of the klystron allowed the use of filter time constants at the output of the phase detector as large as one minute without excessive distortion of the line shape. This corresponds to an output band width of the order of 0.02 cycle per second. Since the noise power was proportional to band width under the conditions of operation, this small band width resulted in considerable reduction of noise with consequent increased in sensitivity. For sweep speeds as slow as those used, some form of klystron frequency stabilization was required; otherwise the klystron would have drifted back and forth over the absorption line and thus averaged it out and obscured it.

PREPARATION OF THE SAMPLE

The sample material was obtained in form of a 2 normal solution of HCl enriched in Cl^{36} at the Oak Ridge National Laboratory. The abundance of Cl^{36} in the sample material was 1.6 percent. The synthesis into methyl chloride was as follows: 0.25 millimole of HCl was precipitated with $AgNO_3$ in a 5-ml centrifuge tube. The AgCl precipitate was centrifuged, washed, and dried. The dried AgCl was wrapped in aluminum foil and heated *in vacuo* until reaction occurred. The $AlCl_3$ produced was sublimed into another vessel to which an

[2] R. V. Pound, Rev. Sci. Inst. 17, 490 (1946).

[3] F. Coester, Phys. Rev. 77, 454 (1950).

[4] Tuller, Galloway, and Zaffarano, Technical Report No. 53, Nov. 20, 1947, Research Laboratory of Electronics, Massachusetts Institute of Technology (unpublished).

TABLE I. The H_Q+H_M matrix for $J=1$, $K=0$, and $I=2$. $E_1=-0.175eqQ$, $E_2=0.175eqQ$, $E_3=-0.05eqQ$; $A=\frac{3}{8}\alpha+\delta$, $B=\frac{5}{8}\alpha+\delta$, $C=\frac{3}{8}\alpha+\delta$; $\alpha=\mu_N H(g_I-g_J)$, $\delta=\mu_N H g_J$.

		$M'=3$	2		1			0			−1			−2		−3
M	F	$F'=3$	3	2	3	2	1	3	2	1	3	2	1	3	2	3
3	3	E_3-3A														
	3		E_3-2A	$\frac{1}{2}\sqrt{2}\alpha$												
2	2		$\frac{1}{2}\sqrt{2}\alpha$	E_2-2B												
	3				E_3-A	$(4\sqrt{5}/15)\alpha$										
1	2				$(4\sqrt{5}/15)\alpha$	E_2-B	$(3/2\sqrt{5})\alpha$									
	1					$(3/2\sqrt{5})\alpha$	E_1-C									
	3							E_3	$(\sqrt{\frac{1}{2}})\alpha$							
0	2							$(\sqrt{\frac{1}{2}})\alpha$	E_2	$(\sqrt{\frac{1}{2}})\alpha$						
	1								$(\sqrt{\frac{1}{2}})\alpha$	E_1						
	3										E_3+A	$(4\sqrt{5}/15)\alpha$				
−1	2										$(4\sqrt{5}/15)\alpha$	E_2+B	$(3/2\sqrt{5})\alpha$			
	1											$(3/2\sqrt{5})\alpha$	E_1+C			
	3													E_3+2A	$\frac{1}{2}\sqrt{2}\alpha$	
−2	2													$\frac{1}{2}\sqrt{2}\alpha$	E_2+2B	
−3	3															E_3+3A

excess of CH_3OH was added. The vessel was then opened to air and allowed to stand one hour after which the excess CH_3OH was pumped off leaving a glossy deposit of the complex $CH_3O\cdot AlCl_2$. The complex was decomposed at 140°C and the volatile products (CH_3Cl and HCl) were collected in a trap cooled by liquid nitrogen. The HCl was removed by distillation over KOH.

ENERGY LEVELS AND SPECTRUM

The Cl^{36} nucleus has a spin of 2 and an electric quadrupole moment of -0.017×10^{-24} cm².[1] Without Zeeman effects the rotational transition is perturbed by the quadrupole interaction giving a quadrupole hyperfine pattern. For the rotational transition used, ($J=0\rightarrow1$, $K=0$), the resulting pattern consisted of three lines. The small quadrupole coupling (−15.8 Mc/sec) of the Cl^{36} nucleus in the CH_3Cl molecule made the separation between lines small, the distance between the outer two lines being only about 5.5 Mc/sec. This resulted in several experimental difficulties when the spectrum was split by a Zeeman field.

The Hamiltonian for the molecule may be written $H=H_R+H_Q+H_M$, where H_R represents the part of the Hamiltonian due to rotation of the molecule; H_Q and H_M are due to quadrupole and Zeeman effects respectively. The last two terms of the Hamiltonian are small compared with the rotational term and produce only a small perturbation of the rotational energy levels. However, since experimental conditions required that these last two terms be approximately equal, neither could be considered as a perturbation on the other. This produced an intermediate coupling situation and required the solution of a secular equation. In solving these equations it proved most convenient to express the H_Q+H_M energy matrix in the $IJKFM_F$ representation. In this representation $\mathbf{F}=\mathbf{I}+\mathbf{J}$, and M_F is the component of $\mathbf{F}$ along the axis of quantization.

While the quadrupole matrix is diagonal in K, F, and M_F, it has off-diagonal elements in J. The quadrupole coupling constant is small enough, however, so that these terms shift the energy levels less than 150 cycles and may be neglected. The diagonal quadrupole matrix elements are given by the relationship (for $K=0$)

$$(IJKFM_F|H_Q|IJKFM_F) = -eqQ\frac{\frac{3}{4}C(C+1)-I(I+1)J(J+1)}{2I(2I+1)(2J-1)(2J+3)},$$

where $C=F(F+1)-I(I+1)-J(J+1)$, e=electronic charge, Q=quadrupole moment of the Cl^{36} nucleus, and q=the second derivitive of the electric field of the molecule (at the Cl^{36} nucleus) with respect to the coordinate along the molecular axis.

Since the interaction between the magnetic moment of the hydrogen nuclei and the magnetic field merely gives a constant energy term, it may be neglected. The Zeeman Hamiltonian may then be written (in operator form) $H_M=-\mu_N g_J(\mathbf{H}\cdot\mathbf{J})-\mu_N g_I(\mathbf{H}\cdot\mathbf{I})$,[3] where μ_N is the nuclear magneton, g_I the nuclear g factor (for the Cl^{36} nucleus), g_J the rotational g factor, and $\mathbf{H}$ the external magnetic field. By using angular momentum relationships given by Condon and Shortley,[5] the Zeeman matrix elements are easily calculated. The values obtained (for $J=1$) are indicated in Table I where they are included in the H_Q+H_M matrix shown there. (The matrix for $J=0$ is diagonal and has elements proportional to the quantum number M_F.)

The solution of the secular equations obtained from

[5] E. U. Condon and G. H. Shortley, *The Theory of Atomic Spectra* (Cambridge University Press, London, 1935), Chap. 3.

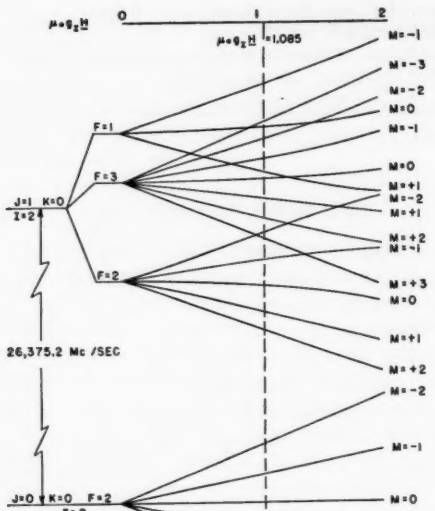

FIG. 1. The Zeeman energy levels for the CH_3Cl^{36} molecule plotted as a function of the parameter $\mu_N g_I H$.

the H_Q+H_M matrix gives the energy levels shown in Fig. 1. These have been plotted by using the product $\mu_N g_I H$ as a parameter and under the assumption that $g_J=0$. This assumption is in agreement with observation within experimental error. The dotted line indicates the value of the parameter under experimental conditions.

For plane polarized radiation in a rectangular wave guide two different sets of Zeeman transitions are possible. These depend upon the relative orientation of the external magnetic field **H** and the microwave electric field vector **E**. For the case where **E** and **H** are parallel, the selection rules are $\Delta F=0, \pm 1$; $\Delta M=0$; while for **E** and **H** perpendicular (crossed fields), the rules are $\Delta F=0, \pm 1$; $\Delta M=\pm 1$. When g_I and g_J are both unknown, and are of comparable magnitude, these two spectra supply sufficient information to evaluate both of these quantities. An ambiguity in sign remains, however, because of symmetries in the spectral pattern. In order to remove this symmetry circularly polarized microwave radiation must be used allowing the observation of the $\Delta M=1$ or the $\Delta M=-1$ transition separately.

In the case where the value of g_J is known, and only the value of g_I need be determined, the two spectra ($\Delta M=0$ and $\Delta M=\pm 1$) overdetermine g_I. For the molecule CH_3Cl^{36} this proved to be the case. In evaluating g_I, the crossed-field spectrum ($\Delta M=\pm 1$) gave g_I to much greater accuracy than did the parallel-field spectrum. Therefore the parallel-field spectrum was used merely to provide a qualitative check. Figure 2 shows the position of the lines in the crossed-field Zeeman spectrum as a function of the parameter $\mu_N g_I H$ (again under the assumption $g_J=0$). The dashed line indicates the value of the parameter under experimental conditions.

That the sign of g_I is ambiguous because of the symmetry of the $\Delta M=\pm 1$ spectrum, can be seen by noting the symmetry of the H_Q+H_M energy matrix. If one assumes the experimental condition $g_J=0$, it will be noted that changing the sign of g_I, (i.e., changing the signs of A, B, C, and α), merely interchanges the M and $-M$ energy levels. (This is true since the off-diagonal terms always appear squared in the secular equations, and therefore their sign is of no importance.) The consequence of this is that the $\Delta M=1$ and the $\Delta M=-1$ transitions are also interchanged. Since both transitions

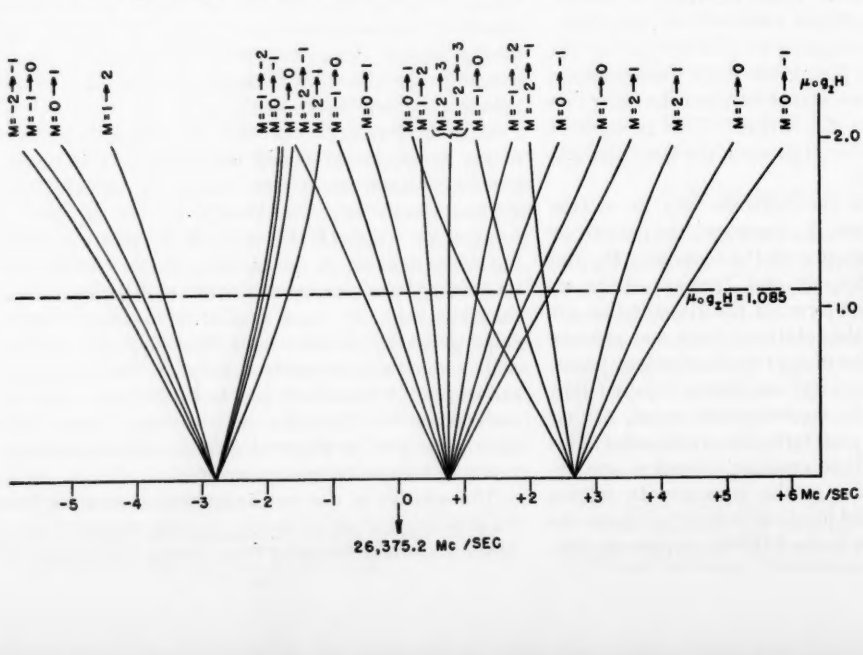

FIG. 2. The frequency position of the lines in the Zeeman (crossed-fields) spectrum of the CH_3Cl^{36} molecule plotted as a function of the parameter $\mu_N g_I H$.

are present, however, the spectrum itself is not altered. Thus, either sign of g_I gives the same spectrum and consequently the sign of g_I is ambiguous. It can be seen that the symmetry is such that measurements involving the $\Delta M=0$ transitions cannot be used to resolve this ambiguity; however, the use of circularly polarized radiation, where the $\Delta M=1$ and the $\Delta M=-1$ transitions are observed separately, yields a spectrum dependent on the sign of g_I.

The Zeeman perturbation mixes the quadrupole energy levels having different F values but the same M_F values, since with this perturbation M_F is still a good quantum number although F is not. The amount of mixing depends upon the strength of the Zeeman field (and consequently upon the value of the parameter $\mu_N g_I H$). This mixture affects the intensity of the spectral lines and makes these intensities also a function of this parameter. For the experimentally determined value of $\mu_N g_I H$, the calculated intensity (and position) of the lines in the observed spectrum are indicated in Fig. 3. Experimentally the individual lines were too close together to be resolved. The envelope in Fig. 3 shows how the lines should theoretically appear if they had a half-width of 300 kc/sec.

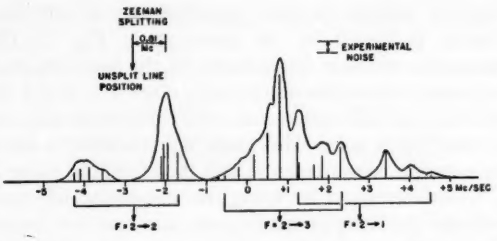

FIG. 3. The Zeeman (crossed-fields) spectrum of the CH_3Cl^{36} molecule ($J=0\rightarrow1$ rotational transition). The envelope assumes a half-width of approximately 300 kc/sec.

SPECTRUM WITHOUT ZEEMAN EFFECTS

The three frequencies at which the various curves in Fig. 2 converge, indicate the relative position of the lines in the quadrupole hyperfine pattern of the CH_3Cl^{36} molecule ($J=0\rightarrow1$, $K=0$ transitions). The observed frequencies of these three lines are listed in Table II and agree within experimental error with those computed using the constants indicated there. This agreement confirms the nuclear spin assignment of two for the Cl^{36} nucleus.

The value of B_0 given in Table II along with the corresponding rotational B_0 values for the molecules CH_3Cl^{35} and CH_3Cl^{37} allows the determination of the mass difference ratio $(m^{36}-m^{35})/(m^{37}-m^{36})$. The relationship involved, and the value obtained, are as follows:

$$\frac{m^{36}-m^{35}}{m^{37}-m^{36}}=\frac{M^{35}}{M^{37}}\frac{B_0{}^{37}}{B_0{}^{35}}\frac{B_0{}^{35}-B_0{}^{36}}{B_0{}^{36}-B_0{}^{37}}=1.00168\pm0.0004,$$

where m is the nuclear mass, M the molecular mass, and B_0 the rotational constant. The superscript indicates the isotope of chlorine which is involved. In this calculation the rotational constants for CH_3Cl^{35} and CH_3Cl^{37} that were used were those obtained by White[6] [$B_0(CH_3Cl^{35})=13\,292.840\pm0.008$ Mc/sec and $B_0(CH_3Cl^{37})=13\,088.136\pm0.002$ Mc/sec]. If the value of $m(Cl^{35})/m(Cl^{37})$ (0.945978±0.000003) given by Honig, Stitch, and Mandel[7] is used, the mass ratio $m(Cl^{36})/m(Cl^{37})$ is found to be 0.973012±0.00002.

[6] R. L. White (private communication).
[7] Honig, Stitch, and Mandel, Phys. Rev. **92**, 901 (1953).

The quadrupole coupling constant of the CH_3Cl^{35} molecule has been determined as -74.770 ± 0.015 Mc/sec,[8] making the ratio $eqQ(CH_3Cl^{36})/eqQ(CH_3Cl^{35})=0.2117\pm0.0027$. Since the value of q is essentially the same for both molecules, this ratio is also the ratio of the quadrupole moments of the two chlorine isotopes. This gives the value of the quadrupole moment of the Cl^{36} nucleus as -0.017×10^{-24} cm^2. The uncertainties in the determination of the quadrupole moment are primarily due to shielding effects.[9] It will be noted that the value of eqQ, and consequently the quadrupole moment, agree with those given by Gilbert[10] and by Johnson, Gordy and Livingston,[11] but are of somewhat higher precision.

ZEEMAN MEASUREMENTS

Figure 3 indicates that the $F=2\rightarrow3$ and the $F=2\rightarrow1$ lines in the quadrupole hyperfine pattern of the CH_3Cl^{36} molecule are separated by such a small amount (2 Mc/sec) that their Zeeman components overlap considerably even for relatively weak fields. This made it impossible to use them for measuring purposes and left only the $F=2\rightarrow2$ line as a feasible line to work with.

The $F=2\rightarrow2$ line has eight Zeeman components grouping themselves into two separate groups as indicated in Fig. 2. The individual lines within each group could not be resolved. (The experimental half-widths were of the order of 300 kc/sec.) Because of this, the

TABLE II. Comparison of the observed and calculated frequencies of the absorption lines in the quadrupole hyperfine pattern of CH_3Cl^{36} ($J=0\rightarrow1$).

Transition F'	Transition F''	Frequencies (Mc/sec) Observed	Theoretical
2	1	26377.96±0.025	26377.977
2	2	26372.42±0.025	26372.437
2	3	26376.03±0.035	26375.999

$B_0=13187.604\pm0.015$ Mc/sec
$eqQ=-15.83\pm0.20$ Mc/sec
$I=2$
$m(Cl^{36})/m(Cl^{37})=0.973012\pm0.000017$

[8] Geshwind, Gunther-Mohr, and Townes, Phys. Rev. **81**, 288 (1951).
[9] R. Sternheimer, Phys. Rev. **84**, 244 (1951).
[10] D. A. Gilbert, Phys. Rev. **85**, 716 (1952).
[11] Johnson, Gordy, and Livingston, Phys. Rev. **83**, 1249 (1951).

observed Zeeman pattern appeared as the two components indicated by the envelope in Fig. 3. The theoretical decrease in intensity of the low-frequency component of this line was actually observed; in fact the decrease was sufficient to make this component only two or three times noise. This made it impossible to use it for accurate measurements; and therefore, the value of g_I was determined by using the frequency difference between the unsplit quadrupole line and its largest observed Zeeman component.

The experimental accuracy was severely limited by the small separation between quadrupole components, since in order to obtain high accuracy the ratio of Zeeman splitting to the uncertainty in line position must be large. Large Zeeman fields could not be used, since at these fields Zeeman components from the $F=2\rightarrow3$ line began to overlap the $F=2\rightarrow2$ Zeeman components. A magnetic field of 2166 gauss gave close to optimum conditions. In this field the widening of the Zeeman component gave an uncertainty of 20 kc/sec in line position while the line itself was moved only 0.81 ± 0.02 Mc/sec from the unsplit position. Another alternative would have been to use the strong-field case but magnetic fields of the required magnitude were not available.

The method of evaluating the nuclear g factor of the Cl^{36} nucleus was simplified by being able to determine the rotational g factor of the CH_3Cl^{36} molecule independently. This was possible since the rotational g factors of the CH_3Cl^{36} and CH_3Cl^{35} molecules differ only by the ratio of their rotational frequencies; and this difference is small enough to be neglected. Hence, the Zeeman spectrum of the CH_3Cl^{35} molecule was used to evaluate g_J. The value of g_J was determined to be 0.00 ± 0.05 by measuring the Zeeman splitting of the $F=\frac{3}{2}\rightarrow\frac{1}{2}$ transition in the quadrupole hyperfine structure of CH_3Cl^{35}. The error in g_I caused by the uncertainty in g_J was of the order of 1.5 percent. The small value of g_J confirmed a previous observation of Jen.[12]

The value of g_I was obtained by the following procedure: Since the value of g_J was found to be zero within experimental error, preliminary calculations were made by setting $g_J=0$ in the $H_Q\pm H_M$ matrix. This made the secular equations, and consequently the frequencies and intensities of the individual Zeeman components, functions of the parameter $\mu_N g_I H$ only. Since the experimental Zeeman component of the $F=2\rightarrow2$ line consisted of four separate components (Fig. 3), and since all four of these components were within the experimental halfwidth, it was assumed that the peak of the observed line coincided with the center of intensity of these four components. The frequency of this center of intensity was determined theoretically, as a function of $\mu_N g_I H$, and this expression set equal to the frequency of the peak of the observed line. This allowed the value of $\mu_N g_I H$ to be obtained.

[12] C. K. Jen, Phys. Rev. 74, 1396 (1948).

Using the experimental value of $\mu_N g_I H$, g_I could then have been obtained by measuring the magnetic field. However, since the field was rather inhomogeneous, a determination of its effective value by direct measurement would not have been easy. To avoid this difficulty, the field was calibrated by using the nuclear g value[13] of Cl^{35}. Thus, the Zeeman splitting of the $F=\frac{3}{2}\rightarrow\frac{1}{2}$ line in the CH_3Cl^{35} quadrupole spectrum was measured, (using the same magnetic field as before), and the value of $\mu_N g_I H$ determined for this molecule. In this case, since the quadrupole moment of Cl^{35} is considerably larger than that of Cl^{36}, the quadrupole lines were separated sufficiently to allow the use of first-order theory.

The ratio of the two quantities, $(\mu_N g_I H)_{Cl^{36}}$ and $(\mu_N g_I H)_{Cl^{35}}$, gave the ratio of the g factors (since the other terms were common to both expressions). The result obtained was the following:

$$|g_I(Cl^{36}/g_I(Cl^{35})|=1.20\pm0.07.$$

By using the value of the magnetic moment of Cl^{35} given by Ramsey[13] (i.e., $\mu=0.82191\pm22$), and taking into account the relative spins of Cl^{35} and Cl^{36}, the absolute magnitude of the magnetic moment of the Cl^{36} nucleus was found to be 1.32 ± 0.08 nuclear magnetons.

The sign of the magnetic moment was determined by observing the $\Delta M=1$ and $\Delta M=-1$ transitions separately rather than simultaneously as in the magnitude determination. This was accomplished by using the circular wave guide and elliptical quarter-wave section previously described. The CH_3Cl^{35} spectrum and the CH_3Cl^{36} spectrum were both observed and the $\Delta M=1$ and $\Delta M=-1$ transitions in both spectra were correlated. The sign of the nuclear g factor of the Cl^{36} nucleus was then determined from the known sign of the Cl^{35} nuclear g factor. The Cl^{36} magnetic moment was found to be positive.

DISCUSSION

In the $j-j$ coupling nuclear shell model, using an oscillator potential, the fifteenth to twentieth nucleons occupy the third shell and are either in the $s_{\frac{1}{2}}$ or $d_{\frac{3}{2}}$ state. This model, as proposed by Mayer[14] and Jensen,[15] is based on the assumption of independent particles, and therefore, the aforementioned is assumed to hold for neutrons and protons independently. In the Cl^{36} nucleus, which has 19 neutrons and 17 protons, 5 neutrons and 3 protons are in this shell, the other nucleons forming closed shells.

The usual assumption in the case of even-odd nuclei (in regard to the particles with the odd number) is that all of these particles, except the last added one, pair off to give zero spin and nuclear moments. This leaves the last particle to determine the properties of the nucleus. A reasonable assumption in the case of odd-odd nuclei is that this pairing process occurs for the neutrons and

[13] N. F. Ramsey, *Nuclear Moments* (John Wiley and Sons, Inc., New York, 1953), p. 80.
[14] M. G. Mayer, Phys. Rev. 78, 16 (1950).
[15] Haxel, Jensen, and Suess, Phys. Rev. 75, 1766 (1949).

TABLE III. The magnetic moment of possible nuclear configurations involving one $s_{\frac{1}{2}}$ state and one $d_{\frac{3}{2}}$ state and giving a spin 2.

Configuration	Calculated magnetic moment (nuclear magnetons)
$(d_{3/2})_N(d_{3/2})_P$	0.846
$(s_{1/2})_N(d_{3/2})_P$	−1.794
$(d_{3/2})_N(s_{1/2})_P$	3.944
	μ(observed) = 1.32±0.08

TABLE IV. The magnetic moment of possible nuclear configurations involving more than two nucleons and giving a spin 2.

Configuration	Calculated magnetic moment (nuclear magnetons)
$(s_{1/2})_N[(s_{1/2})(d_{3/2^2})_2]_{3/2P}$	−3.498
$(s_{1/2})_N[(s_{1/2})(d_{3/2^2})_2]_{5/2P}$	4.034
$(d_{3/2})_N[(s_{1/2})(d_{3/2^2})_2]_{3/2P}$	−0.256
$(d_{3/2})_N[(s_{1/2})(d_{3/2^2})_2]_{5/2P}$	2.294
	μ(observed) = 1.32±0.08

protons independently, and then the last added odd neutron and last added odd proton couple together to determine the nuclear properties.

If this were true, and if the states in the third shell filled in the order expected, then the configuration of the Cl^{36} nucleus would be $(d_{\frac{3}{2}})_N(d_{\frac{3}{2}})_P$, where N and P indicate the neutron and proton configurations, respectively. In this case, since the spin of Cl^{36} is known to be two, the spins of the odd proton and neutron would neither be parallel nor antiparallel.

The possibility exists, however, that the odd nucleon is in an s state, allowing three other possible configurations. Furthermore, none of these configurations may be correct, and the configuration may actually involve a more complex coupling.

Of the four configurations involving all possible combinations of the two states, $s_{\frac{1}{2}}$ and $d_{\frac{3}{2}}$, the configuration $(s_{\frac{1}{2}})_N(s_{\frac{1}{2}})_P$ is ruled out from spin considerations. The other three configurations are possible, however. The magnetic moments calculated for these three configurations appear in Table III. It can be seen that the observed magnetic moment favors the first configuration.

That the nuclear magnetic moment is not due to the coupling of more than two nucleons in the third shell is illustrated by Table IV. In this table the four possible coupling schemes are shown that involve more than two nucleons and give the proper nuclear spin. It can be seen that none of the calculated moments are close to the observed value.

The quadrupole moment of Cl^{36} is not inconsistent with the configuration $(d_{\frac{3}{2}})_N(d_{\frac{3}{2}})_P$, which would have a quadrupole moment of zero if it were pure. The measured quadrupole moment is in fact quite small, being only $\frac{1}{5}$ that of Cl^{35}.

ACKNOWLEDGMENTS

The authors wish to thank Dr. C. H. Townes for his suggestion of this project and his direction of it. We are also grateful to the staff of the Columbia Radiation Laboratory, especially to Mr. Dechert and the machine shop personnel for their assistance in constructing the apparatus used.

Positron Emission from Np^{234}†

R. J. Prestwood, H. L. Smith, C. I. Browne, and D. C. Hoffman
Los Alamos Scientific Laboratory, University of California, Los Alamos, New Mexico
(Received January 31, 1955)

An investigation of Np^{234} with a trochoidal analyzer revealed the presence of positrons having an end-point energy of approximately 0.8 Mev. The ratio of positron emission to electron capture was found to be $(4.6\pm1.0)\times10^{-4}$.

A URANIUM–235 target was bombarded with 21-Mev deuterons in the Argonne National Laboratory 60-in. cyclotron. The neptunium fraction was chemically isolated, and the decay followed with scintillation, internal and external beta proportional and 4π counters. The 4.4-day activity[1,2] of Np^{234} [1,2] was detected as well as the 22-hour activity of Np^{236}.

The gamma and electron spectra of Np^{234} were examined (before and after decay of most of the Np^{236}) with NaI(Tl) and trans-stilbene crystals in conjunction with a 10-channel analyzer and coincidence circuit. Numerous gamma rays decaying with a 4.4 day half-life and presumably belonging to Np^{234} were found. Further purification of the Np sample resulted in no visible change in the gamma spectra. A detailed report of these studies will be published later after the decay of the electromagnetic radiations has been further verified and corrections for any contribution from Np^{235} have been made.

The Np^{234} was also investigated on our trochoidal analyzer[3] which makes use of a semicircular fringing magnetic field to separate positrons from negatrons. Four inches of lead are interposed between the detector (a methane proportional counter) and the sample which are ten inches apart. One can count either negatrons or positrons depending on the field orientation. When counting positrons the discrimination against both negatrons and gamma rays is exceedingly good. A sample of Sr^{90}-Y^{90} containing approximately 1.8×10^7 disintegrations per minute gives only 6 counts per minute above the normal background of 10.5 counts per minute. A sample of 1.2-Mev gamma rays emitting 1.2×10^6 dis/min gives no detectable counts above the normal background. The efficiency of counting positrons using the external probe is 5 ± 1 percent. An Np^{234} sample of 2.6×10^7 dis/min (determined from coincidence and internal beta measurements) gave 600 positron counts per minute above background which corresponds to a branching ratio of $(4.6\pm1.0)\times10^{-4}$. A total background of 14.9 counts per minute was obtained by absorbing out the negatrons and positrons. An aluminum absorption curve was run on the positrons and the half-thickness compared directly with the half-thickness obtained on the same instrument for Na^{22} ($\beta^+=0.54$ Mev). The Np^{234} positron was found to have an end-point energy of approximately 0.8 Mev, which sets a lower limit of 1.8 on the disintegration energy of the nuclide. The decay of the positron was followed for several days and gave a half-life of (4.4 ± 0.1) days which is in excellent agreement with the published value.[2]

This is believed to be the first observation of the emission of positrons by a nuclide of atomic number higher than 80.[4]

The authors wish to thank the members of the cyclotron group of the Argonne National Laboratory for their cooperation in providing the bombardment. We are indebted to Dr. R. W. Spence for his continued interest and advice.

† This work was done under the auspices of the U. S. Atomic Energy Commission.

[1] James, Florin, Hopkins, and Ghiorso, *The Transuranium Elements: Research Papers* (McGraw-Hill Book Company, Inc., New York, 1949), Paper No. 22.8, National Nuclear Energy Series, Plutonium Project Record, Vol. 14B, Div. IV.

[2] Hyde, Studier, and Ghiorso, *The Transuranium Elements: Research Papers* (McGraw-Hill Book Company, Inc., New York, 1949), Paper No. 22.8, p. 1622, National Nuclear Energy Series, Plutonium Project Record, Vol. 14B, Div. IV.

[3] R. J. Prestwood and H. C. Eberline (to be published).

[4] R. W. Fink and E. O. Wiig, J. Am. Chem. Soc. **74**, 2457 (1952).

Nuclear Pairs from the 3.4-Mev State in Ca^{40}†

R. D. Bent, T. W. Bonner, and J. H. McCrary
The Rice Institute, Houston, Texas

(Received February 14, 1955)

A thick calcium metal target was bombarded with 4.84-Mev protons and a search was made with a magnetic lens pair spectrometer for pairs from the 3.35-Mev state of Ca^{40}. A peak was observed in the spectrometer at an energy of 3.46±0.1 Mev. In a second experiment with a 1 mm Al absorber between the calcium target and a 2-mil lead converter, no external pair peak was observed, indicating that the pairs coming from the target were nuclear pairs and not internally converted gamma-ray pairs. The existence of pairs and the absence of gamma radiation establish the angular momentum of the first excited state of Ca^{40} as zero.

INTRODUCTION

SINCE the discovery of the nuclear pairs from the $F^{19}(p,\alpha\pi)O^{16}$ reaction,[1] a number of searches have been made for other nuclear pair emitting nuclei. In analogy to the $F^{19}(p,\alpha)$ reaction, Phillips, Cowie, and Heydenburg[2] looked for nuclear pairs from the proton bombardment of Li, Be, normal boron, enriched B^{10}, C, Na, Al, P, and Ag. They observed a soft radiation when B^{11} was bombarded with 7.9-Mev protons which they suggested might be due to nuclear pairs from an odd-parity zero-angular-momentum level at about 7 Mev in Be^8. Other investigations[3] suggested that this soft radiation may have been due to a level in C^{12} of zero spin and even parity. Searches have been made by Bent, Bonner, and Sippel[4] for nuclear pairs from excited states of Be^8 and C^{12} by means of the $Li^7(d,n)Be^8$, $B^{11}(p,\alpha)Be^8$, $B^{11}(p,\gamma)C^{12}$, $B^{11}(d,n)C^{12}$, and $N^{14}(d,\alpha)C^{12}$ reactions, which yielded negative results. At the present time the existence of a nuclear pair emitting state in Be^8 or C^{12} is not clearly established.

Scharff-Goldhaber[5] has pointed out that the first excited states of doubly magic nuclei should be 0^+ and not 2^+. However, the only case of this type besides O^{16} which has been studied is Pb^{208} and it has a first excited state which is 3^-.[6] Ca^{40} is doubly magic with a first excited state at 3.35±0.01 Mev and a ground state with zero angular momentum and even parity.[7] If the spin of the 3.35-Mev state is zero, then a single gamma transition between this state and the ground state is forbidden, and the state should decay by nuclear pair emission.[8] The purpose of the present experiment was to look for possible nuclear pairs from the first excited state of Ca^{40}. The magnetic lens pair spectrometer used for the present measurements has been described in an earlier paper.[4] In order to have a high intensity, the intermediate-image arrangement giving 5.5 percent resolution was used.

RESULTS

A target was prepared by pounding a piece of calcium metal to a thickness of 13 mils. This target, with no other backing, was first bombarded with a beam of 4.84-Mev protons and a search was made for pairs originating in the target itself. The results obtained, uncorrected for background effects, are shown by the solid dots in Fig. 1. Next the experiment was repeated with the addition of a 1-mm aluminum absorber and a 2-mil lead converter. The aluminum absorber was placed between the calcium target and the lead converter. The thickness of the lead converter was chosen so that the yield of external pairs produced in the converter would be about equal to the yield of internal

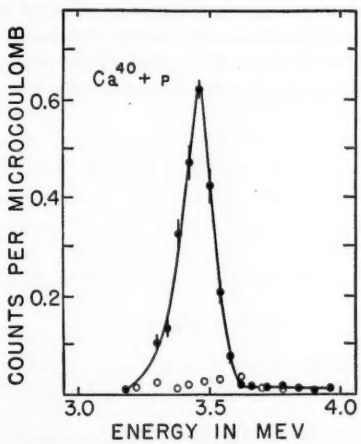

FIG. 1. The 3.46±0.1 Mev nuclear pair line from the bombardment of a metallic calcium target with 4.84-Mev protons. The solid dots correspond to data obtained with a bare calcium target. The open circles were obtained when a search was made for external pairs formed in a lead converter 2 mils thick which was separated from the target by 1 mm of aluminum absorber.

† Supported in part by the U. S. Atomic Energy Commission.

[1] W. A. Fowler and C. C. Lauritsen, Phys. Rev. **56**, 840 (1939).

[2] Phillips, Cowie, and Heydenburg, Phys. Rev. **83**, 1049 (1951).

[3] G. Harries and W. T. Davies, Proc. Phys. Soc. (London) **A65**, 564 (1952); Beghian, Halban, Husain, and Sanders, Phys. Rev. **90**, 1129 (1953); Dunbar, Pixley, Wenzel, and Whaling, Phys. Rev. **92**, 649 (1953); G. Harries, Proc. Phys. Soc. (London) **A67**, 153 (1954).

[4] Bent, Bonner, and Sippel, Phys. Rev. **98**, 1237 (1955), and private communication.

[5] G. Scharff-Goldhaber, Phys. Rev. **90**, 587 (1953).

[6] Elliott, Graham, Walker, and Wolfson, Phys. Rev. **93**, 356 (1954).

[7] P. M. Endt and J. C. Kluyver, Revs. Modern Phys. **26**, 95 (1954).

[8] J. R. Oppenheimer and J. Schwinger, Phys. Rev. **56**, 1066 (1939); R. Thomas, Phys. Rev. **58**, 714 (1940).

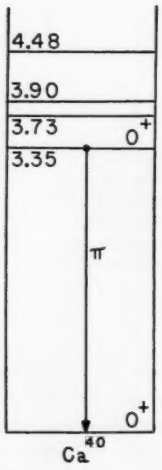

FIG. 2. Energy levels of Ca^{40} showing pair emission (π) from the 3.35-Mev state.

pairs if the 3.35-Mev state were a gamma-emitting state. The results obtained with the absorber and converter in position are shown by the open circles in Fig. 1, and indicate no gamma-ray peak. In order to make sure that the target had not deteriorated between the internal and external pair runs, the absorber and radiator were then removed from the back of the target and the experiment was repeated; the results were the same as those originally obtained, showing a pronounced peak at 3.4 Mev. The absence of an external pair line shows that no 3.4-Mev gamma-radiation is present and that the pairs which are observed are of nuclear origin. The calcium target was then replaced by a 3.98-mg/cm^2 CaF_2 target and the 6.05-Mev nuclear pair line from the reaction $F^{19}(p,\alpha\pi)O^{16}$ was observed for energy calibration.

The energy of the Ca^{40} nuclear pair emitting state was calculated to be 3.46 ± 0.1 Mev. Most of the error is due to uncertainties in picking the peak position from Fig. 1, and in the knowledge of the energy loss of the electron pairs in the calcium target. The yield at the peak of the line was 0.6 coincidence per microcoulomb, which is about 600 times weaker than the yield of the 6.05-Mev nuclear pair line from the bombardment of the 3.98-mg/cm^2 CaF_2 target with 2.0 Mev protons. The average value of the cross section for the formation of Ca^{40} in the 3.4-Mev state from the threshold at $E_p=3.43$ to 4.84 Mev is 0.003 millibarn.

DISCUSSION

The fact that the 3.35-Mev state decays with the emission of nuclear pairs and not by gamma emission establishes the angular momentum of this state as zero. An energy level diagram for Ca^{40} is given in Fig. 2. Table I summarizes the reported cases of 0^+ to 0^+ transitions.

TABLE I. Summary of reported cases of 0^+ to 0^+ transitions.

Nucleus	Number of protons	Number of neutrons	Transition energy (Mev)	Lifetime (sec)	References
O^{16}	8	8	6.05	7×10^{-11}	a
Ca^{40}	20	20	3.35		
Ge^{72}	32	40	0.7	3×10^{-7}	b
Po^{214}(RaC′)	84	130	1.4	2.5×10^{-11}	c

[a] Rasmussen, Hornyak, Lauritsen, and Lauritsen, Phys. Rev. **77**, 617 (1940); Devons, Hereward, and Lindsey, Nature **164**, 586 (1949); G. C. Phillips and N. P. Heydenburg, Phys. Rev. **83**, 184 (1951).
[b] S. K. Haynes, Phys. Rev. **74**, 423 (1948); Bowe, Goldhaber, Hill, Meyerhof, and Sala, Phys. Rev. **73**, 1219 (1948); McGowan, DeBenedetti, and Francis, Phys. Rev. **75**, 1761 (1949).
[c] C. D. Ellis and G. H. Aston, Proc. Roy. Soc. (London) **A129**, 180 (1930); R. H. Fowler, Proc. Roy. Soc. (London) **A129**, 1 (1930); D. E. Alburger and Arne Hedgran, Arkiv Fysik **7**, 423 (1954).

transitions which, except for the case of Po^{214}, are first excited states. The 0^+ excited states of Ge^{72} and Po^{214} have been observed to decay by internal conversion.

An explanation of the 0^+ first excited state of O^{16} on the basis of an α-particle model of the nucleus has been given by Dennison.[9] Shell model interpretations of exceptions to the general rule that even-even nuclei have 2^+ first excited states have been given by Scharff-Goldhaber.[5]

[9] D. M. Dennison, Phys. Rev. **96**, 378 (1954).

U^{235} Thermal Neutron Fission Yields at Masses 90 and 91*

GEORGE W. REED
Argonne National Laboratory, Lemont, Illinois
(Received December 6, 1954)

Thermal neutron fission yields in U^{235} have been determined for Sr^{90} and for Y^{91}. The fission yield at Sr^{90} is 4.02 percent based on a half-life of 20 years. The yield for Y^{91}, 5.35 percent, agrees within experimental error with that previously reported for Sr^{91}. The apparent low yield at mass 90 is discussed.

I. INTRODUCTION

STRONTIUM-90 is one of the longer-lived fission products and one of the most important in terms of biological hazards. No accurate determination of its yield in fission has been reported. Interest in masses 90 and 91 arises from what appears to be an anomaly in the yield-mass curve reported by Glendenin *et al.*[1] and by Reed and Turkevich.[2] Instead of rising smoothly from mass 89 to about mass 95, as originally reported by the Plutonium Project workers,[3] the yield-mass curve appears to flatten in the mass region 89 to 92 and then rises again. Some of the fission yields in this mass region are given in Sec. IV.

The chains discussed here are:

Mass 90:

$$\mathrm{Kr} \xrightarrow{33\text{-sec}} \mathrm{Rb} \xrightarrow{2.7\text{-min}} \mathit{Sr} \xrightarrow{19.9\text{-yr}} \mathit{Y} \xrightarrow{65\text{-hr}} \mathrm{Zr}\ (\text{stable}).$$

Mass 91:

$$\mathrm{Kr} \xrightarrow{10\text{-sec}} \mathrm{Rb} \xrightarrow[14\text{-min}]{1.7\text{-min}} \mathrm{Sr} \xrightarrow{9.7\text{-hr}} \mathit{Y} \xrightarrow{57\text{-day}} \mathrm{Zr}\ (\text{stable}).$$

The yields of the italicized nuclides in the thermal neutron fission of U^{235} were determined. The yield of Sr^{90} was measured through its yttrium daughter; that of Y^{91} was measured directly. The current status of the fission yields at masses 90 and 91 and information pertinent to determining the yields, half-lives in particular, are given below.

Early studies by Nottorf[4] and by Glendenin and Coryell[5] of fission-produced Sr^{90} lead to estimates of the half-life of from 23 to 30 years. Direct decay[4] over a period of about 1.5 yr and fission-yield[5] measurements were used. A yield of 5.2 percent, in thermal neutron fission of U^{235}, was assumed from the smooth mass yield curve as a basis for calculating the half-life. More recently, Powers and Voight[6] followed samples of fission strontium for seven years and reported a half-life of 19.9 yr. This has been generally accepted as the more accurate value and has been used in this work in calculating the fission yield. The half-life of Y^{90} was observed to be 65 hr in the work reported here. This is in agreement with the original determination by Nottorf[4] and also with the recently reported value of Chetham-Strode and Kinderman.[7] The cumulative fission yield at Y^{91} has been reported to be 5.9 percent[8] based on a 57-day half-life. This half-life was also observed in this work.

Although interest was primarily in the cumulative or total chain yields at masses 90 and 91, some experiments were designed to permit detection of any abnormally large primary yields at Y^{90} and Y^{91}. The primary or independent yield of a nuclide is defined as the fraction of fissions that result in the direct formation of that nuclide. The primary fission yield of Y^{90}, in particular, was of interest because of the low yield of mass 90 at strontium. This point is discussed in Secs. III and IV.

Relative fission yields were determined as described in the General Procedure given below. Since such a method involves comparing the activity of a nuclide of unknown yield with the activity of one with a known yield, many of the errors inherent in the procedure, beta assay especially, partially cancel. The only other source of serious error is in the half-lives used in the calculations. As pointed out above, the half-life best fitting our decay data was used in all cases except that of Sr^{90} where the 19.9-yr value was used. Outside of reservations resulting from the half-lives used, it is felt that the error in the fission yields is no greater than 5 percent.

II. EXPERIMENTAL

Uranyl nitrate was irradiated with thermal neutrons at the Argonne CP-3′ pile. The uranium salt was dis-

* This work is presented in more detail in U. S. Atomic Energy Commission Unclassified Report ANL-5306, March, 1954 (unpublished).

[1] Glendenin, Steinberg, Inghram, and Hess, Phys. Rev. **84**, 860 (1951). The fission yield for mass 90 reported in Fig. 1 of their paper was erroneously inserted. (Private communication from L. E. Glendenin and E. P. Steinberg.)

[2] G. Reed and A. Turkevich, Phys. Rev. **92**, 1473 (1953).

[3] *Radiochemical Studies: The Fission Products* (McGraw-Hill Book Company, Inc., New York, 1951), National Nuclear Energy Series, Plutonium Project Record, Vol. 9, Div. IV, Appendix B. (Hereafter referred to as NNES.)

[4] R. W. Nottorf, Paper No. 77, NNES, Vol. 9, Div. IV.

[5] L. E. Glendenin and C. D. Coryell, Paper No. 78, NNES, Vol. 9, Div. IV.

[6] R. I. Powers and A. F. Voight, Phys. Rev. **79**, 175 (1950). Dr. Voigt has been kind enough to recheck the half-life, now over a nine-year period, and he reports a value of 20±1 yr.

[7] A. Chetham-Strode and E. Kinderman, Phys. Rev. **93**, 1029 (1954).

[8] Ballou, Novey, Engelkemeir, Brady, and Seiler, Paper No. 75, NNES (see reference 3), Vol. 9, Div. IV.

solved in dilute acid. Suitable carriers were added to aliquots of the solution and the fission products were separated radiochemically as indicated below. The radiochemical yield was determined and the samples were mounted on $\frac{1}{16}$-in. aluminum cards, covered with rubber hydrochloride, and then counted on the top shelf of an end-window Geiger counting setup.[2] Samples usually weighed from 10 to 30 mg. The activities were corrected for chemical yield, decay, absorption, and fraction of saturation and were compared with the activities of Sr^{89} and Mo^{99} samples from the same solution. The absolute fission yields of these nuclides have been previously reported as 4.78 and 5.98 percent.[2] Absorption and decay curves were used to check the radiochemical purity of the samples. At least two samples were separated in each determination and their decay was followed through more than three half-lives. Except in the experiments to detect independently formed Y^{90} and Y^{91}, the specific activities (cpm/mg) of duplicate samples agreed to within 1 to 2 percent.

Six irradiations were carried out. Three of these were used in the determination of Sr^{90}. In the others, the yields of Y^{91} and Y^{90} were measured. Sr^{89} was determined in all of the irradiations and Mo^{99} in one of them.

Sr^{90} was measured by isolation and counting of its 65-hr Y^{90} daughter which emits a beta ray of about 2.2 Mev. It was assumed that the scattering correction in the counting arrangement used would be the same as that for Sr^{89}.[9] Y^{91} was separated from the fission product solution after the 9.7-hr strontium parent had decayed. Since its beta-ray energy (1.54 Mev) and spectrum are similar to those of Sr^{89}, the samples were directly comparable. Limits to the yields of independently formed Y^{90} and Y^{91} were determined from samples separated immediately after the end of irradiations which were carried out in the pneumatic tube at the pile. The time of separation (15–18 min) was such as to reduce substantially the contribution to the observed activities from radioactive decay of the parent nuclides.

Radiochemical Separations

Strontium separations[10] were performed 1 month, 3 months, and 1.5 yr after the end of the irradiations so that the only strontium activities present were 53-day Sr^{89} and 19.9-yr Sr^{90}. A separation of the 65-hr Y^{90} daughter was performed by the addition of yttrium carrier and suitable chemistry after sufficient time elapsed for growth.

In order to determine the yields of yttrium nuclides directly, separation of yttrium from rare-earth fission products must be achieved. Two types of separations were used. Yttrium was eluted with 9*M* HCl from a column of Dowex-50 resin,[11] 200–400 mesh, 4 percent cross-linked. Preliminary experiments with tracer yttrium (effective $Z=65.5$) and europium ($Z=63$) indicated a decontamination factor of about 10^4. The second method involved solvent extraction of yttrium into tributyl phosphate-Gulf solvent BT solutions from conc. HNO_3.[12] In some experiments, both separations were carried out, in others ion exchange only. Yttrium was finally precipitated and weighed as the oxalate.

III. RESULTS

The ratios of the saturation activities of Sr^{90} to those of Sr^{89} and Mo^{99} are given in Table I, columns 3 and 4, respectively. The first column gives the experiment number and the number of separations (milkings) of yttrium from the various sets of separated strontium samples. In the second column the time lapse from the end of the irradiation until the Sr^{90} was separated is given. A fission yield of 4.02 ± 0.11 percent was calculated for Sr^{90} by using 4.78 percent for the yield of Sr^{89} and 5.98 percent for Mo^{99}, and a half-life of 19.9 yr for Sr^{90}. Each ratio in the table was weighted equally and the error quoted is the mean deviation.

The saturation activity of 57-day Y^{91} compared with that of Sr^{89} is given in Table II. The average ratio of 1.12 ± 0.04 leads to a fission yield of 5.35 ± 0.21 percent. Since independent formation at Y^{91} is small (see below), the best value for the yield at mass 91 might be taken as the average of 5.35 and 5.07, the Sr^{91} yield,[2] or 5.21 percent.

Since the fission yield of Sr^{90} appeared to be about 25 percent too low relative to yields of neighboring masses, it seemed that a possible explanation lay in an appreciable independent formation of Y^{90}. If independently

TABLE I. Saturation activity ratios in the Sr^{90} yield determination.

Experiment	Decay time from end of irradiation	Sr^{90}/Sr^{89}	Sr^{90}/Mo^{99}
1. Det'n. 1, milking 1	1.5 yr	0.843	
Det'n. 1, milking 2		0.801	
Det'n. 2, milking 1		0.809	
2. Det'n. 1, milking 1	3 months	0.876	0.687
Det'n. 1, milking 2		0.870	0.682
3. Det'n. 1, milking 1	1 month	0.820	

[9] Scattering by the sample and from the backing has been shown to be about constant for beta emitters of 1 Mev or greater for the counting conditions used. See, for instance, Engelkemeir, Seiler, Steinberg, and Winsberg, Papers No. 4 and 5, NNES (see reference 3), Vol. 9, Div. IV; and also reference 2, p. 1478.

[10] L. E. Glendenin, Paper No. 236, NNES (see reference 3), Vol. 9, Div. IV.

[11] Diamond, Street, and Seaborg, U. S. Atomic Energy Commission Report AECD-3517, 1953 (unpublished).

[12] TBP (tributyl phosphate), separations of the rare earths have been described in detail by Peppard *et al.*, J. Phys. Chem. **57**, 294 (1953). C. W. Stanley [Los Alamos Scientific Laboratory Report, LA-1566 (unpublished)] reports that adequate decontamination from europium and samarium may be accomplished by extraction of yttrium from 10 parts of conc. HNO_3 into 1 part of 60 percent TBP and 40 percent Gulf solvent BT. The organic phase is washed twice with 10 ml of conc. HNO_3 and the yttrium re-extracted into H_2O. Two such cycles were suggested.

It was found in this work that it is necessary to take precautions against carrying Np^{239} through the extractions as well as through the column. Np(IV) and (VI) extract well into TBP and Np(IV) elutes very close to yttrium in the column. Hence, oxidation followed by YF_3 precipitation was introduced to eliminate the Np^{239}.

formed Y^{90} were produced in 1 percent fission yield (about 25 percent of the chain yield), then several thousand counts per minute of 65-hr Y^{90} beta activity should be observed in the samples separated soon after the end of the irradiation. Actually, very little activity attributable to Y^{90} was observed after the decay of 11-hr Y^{93} and after correction for the 57-day Y^{91} activity. An upper limit of 3.2×10^{-2} was estimated as the percent of mass chain 90 formed independently as Y^{90}. This corresponds to an independent fission yield of <0.0013 percent[13] if one takes the Sr^{90} yield, 4.02 percent, as the chain yield. Hence, independently formed Y^{90} is not the explanation for the low yield of mass 90 determined at Sr^{90}.

From the amount of 57-day Y^{91} activity in samples separated soon after the end of the short irradiations, a generous upper limit of 0.9 was set as the percent of mass chain 91 formed independently at yttrium. This corresponds to an independent fission yield of less than 0.05 percent.

TABLE II. Ratio of Y^{91} to Sr^{89} saturation activities.

Experiment	Y^{91}/Sr^{89}
4	1.17
5	1.13
6	1.07
	Average 1.12
	Mean deviation 0.04

IV. DISCUSSION

Fission yields in the mass region 89 to 91 are summarized in Table III. The yields for Sr^{89} and Sr^{91}, in italics, are those reported earlier;[2] the others were determined in this work. The precision of the latter data is expressed in terms of the mean deviation.

TABLE III. Fission yields in the mass region 89 to 91.

Mass	Species measured	Fission yield (%)
89	Sr	*4.78±0.07*
90	Sr	4.02±0.11
90	Y (indep.)	<0.0013
91	Sr	*5.07±0.11*
91	Y (total)	5.35±0.21
91	Y (indep.)	<0.05

The most significant feature of the above data is the low yield at mass 90. Since independent formation beyond the measured nuclide cannot explain this observation, then either fine structure must be present in this mass region or the half-life used in the calculations must be incorrect. In order to raise the fission yield to about 5 percent so that the yield-mass curve is smooth, a half-life of around 25 yr for Sr^{90} is necessary. In fact, the half-life may actually be about 30 yr as observed in recent preliminary experiments carried out by the author. These measurements were made by determining the number of Sr^{90} disintegrations in a solution containing a known number of Sr^{90} atoms. The latter number was measured mass-spectrometrically. Such a half-life value would lead to a spike at mass 90 in the yield-mass curve. Future work on the half-life of Sr^{90} should resolve this question.[14,15]

This work was performed under the auspices of the U. S. Atomic Energy Commission.

[13] Another determination of this yield has come to our attention since the completion of this work. W. J. Whitehouse in his paper on *Nuclear Fission* which appeared in *Progress in Nuclear Physics* (Pergamon Press Ltd., London, 1952), Vol. 2, p. 143; quotes G. B. Cook who reports a yield of $<2.8\times10^{-3}$ percent.

[14] This region is also being investigated in this laboratory as part of a program to determine the entire U^{235} yield-mass curve mass-spectrometrically. (Private communication from Flynn, Glendenin, Hayden, and Steinberg.)

[15] Since this manuscript was prepared private communications concerning the half-life of Sr^{90} have been received from two groups of workers. Flynn, Glendenin, and Steinberg of this laboratory have determined the half-life to be 28.4 yr. H. G. Thode of McMaster University quotes a half-life of 27.7 yr on the basis of work by R. H. Tomlinson and D. R. Wiles, and also a fission yield of Sr^{90} of 5.4 percent based on the work of R. H. Tomlinson and J. A. Petruska.

Production of Charged Pions in $N-P$ Collisions*†

GAURANG B. YODH‡
Institute for Nuclear Studies, University of Chicago, Chicago, Illinois
(Received January 27, 1955)

The differential cross section and energy spectra for the production of $\pi^{\pm}$ mesons by the 400-Mev neutron beam of the Chicago synchrocyclotron on liquid hydrogen has been measured at 90° and 65° in the laboratory, using photographic emulsions as detectors. At 65° (corresponding to 90° in the center-of-mass system), roughly equal numbers of positive and negative pions were observed, while at 90° the ratio of positive to negative pions was found to be 2.01 ± 0.24. The laboratory integrated cross sections $(d\sigma_{Ni}/d\Omega)_{Ni}$, in cm²/sterad, are: for π^+ at 90° $(2.296\pm0.363)\times10^{-29}$, for $T>14$ Mev; for π^- at 90°, $(1.56\pm0.357)\times10^{-29}$, for $T>14$ Mev; for π^+ at 65°, $(1.22\pm0.30)\times10^{-29}$, for $T>41$ Mev; and for π^- at 65°, $(1.31\pm0.63)\times10^{-29}$. These experimental cross sections are the result of production due to neutrons of all energies above the threshold for pion production in the neutron beam.

A phenomenological analysis is made for the reaction $N+P\rightarrow\pi^{\pm}$ under the hypothesis of charge independence and the energy and angular distributions of the pions at a single neutron energy are deduced from the experimental cross sections. The total cross section for π^+ or π^- production, at neutron energy 409 Mev, is determined to be

$$\sigma(\pi^+)=\sigma(\pi^-)=0.16\pm0.04 \text{ millibarn},$$

and the differential cross section for the same neutron energy is calculated to be

$$(d\sigma/d\omega)^{\pm}=(1.07\pm0.39)\mp(1.38\pm0.78)\cos\theta+(0.57\pm1.14)\cos^2\theta\times10^{-29} \text{ cm}^2/\text{sterad}.$$

I. INTRODUCTION

ONE of the most significant developments that has been made following the construction of high-energy machines is the artificial production of pions. A considerable effort has been devoted to the study of fundamental processes of pion production in nucleon-nucleon collisions, of which the following are amenable to direct measurement:

$$P+P\rightarrow\pi^++D, \quad (1)$$

$$P+P\rightarrow\pi^++P+N, \quad (2)$$

$$P+P\rightarrow\pi^0+P+P, \quad (3)$$

$$N+P\rightarrow\pi^0+D, \quad (4)$$

$$N+P\rightarrow\pi^0+P+N, \quad (5)$$

$$N+P\rightarrow\pi^-+P+P, \quad (6)$$

$$N+P\rightarrow\pi^++N+N. \quad (7)$$

The processes that have not been most studied are (1) and (2), the production of positive pions in proton-proton collisions. The cross section, angular distribution, and energy spectrum were measured at three angles at 345 Mev by Cartwright, Richman, Whitehead, and Wilcox[1] at Berkeley. Since then the excitation function has been studied by Schulz[2] and Passman, Bloch, and Havens,[3] and careful measurements of reaction (1) have been carried out recently by Crawford and Stevenson[4] at 320 and 345 Mev, by Sutton *et al.*[5] at 430 Mev, and by Rosenfeld[6] at 440 Mev. The production of neutral pions in proton-proton collisions has been studied at only two energies: rather crude measurements of the total cross section have been made at 345 Mev by Mather and Martinelli,[7] and at 430 Mev by Marshall *et al.*[8]

With the availability of the high-energy neutron beam of the University of Chicago synchrocyclotron, a number of experiments were undertaken to study the production of pions in neutron-proton collisions. Hildebrand[9] has studied the production of neutral pions with deuteron formation and also the branching ratio between the reactions (4) and (5). Recently, Schluter[10] has measured the production of neutral pions in neutron-proton collisions using a diffusion cloud chamber, and has also obtained an excitation function for reactions (4) and (5).

The object of the experiment reported in this paper was to measure the production of charged pions in neutron-proton collisions. The energy spectrum and the differential cross sections at 90° and 65° in the laboratory system were measured for both negative and positive pions. Measurements of the same process are being made by Wright and Schluter[11] using a hydrogen diffusion cloud chamber.

These experiments are interesting for the study of pion-nucleon interaction. Pion-production process can be subjected to a phenomenological analysis under

* Supported by the joint program of the Office of Naval Research and the U. S. Atomic Energy Commission.
† Presented in partial fulfillment of the requirements for the degree of Doctor of Philosophy.
‡ Now at Stanford University, Stanford, California.
[1] Cartwright, Richman, Whitehead, and Wilcox, Phys. Rev. **91**, 677 (1953).
[2] A. G. Schulz, University of California Radiation Laboratory Report No. 1756 (unpublished).
[3] Passman, Bloch, and Havens, Phys. Rev. **88**, 1247 (1952).
[4] F. S. Crawford and M. L. Stevenson, Phys. Rev. **97**, 1305 (1955).
[5] Fields, Fox, Kane, Stallwood, and Sutton, Phys. Rev. **95**, 638(A) (1954).
[6] A. H. Rosenfeld, Phys. Rev. **96**, 130 (1954).
[7] J. W. Mather and E. A. Martinelli, Phys. Rev. **92**, 780 (1953).
[8] Marshall, Marshall, Nedzel, and Warshaw, Phys. Rev. **88**, 632 (1952).
[9] R. H. Hildebrand, Phys. Rev. **89**, 1090 (1952); and the results on bound-to-unbound ratio (to be published).
[10] R. A. Schluter, Phys. Rev. **96**, 734 (1954).
[11] S. C. Wright and R. A. Schluter, Phys. Rev. **95**, 639(A) (1954).

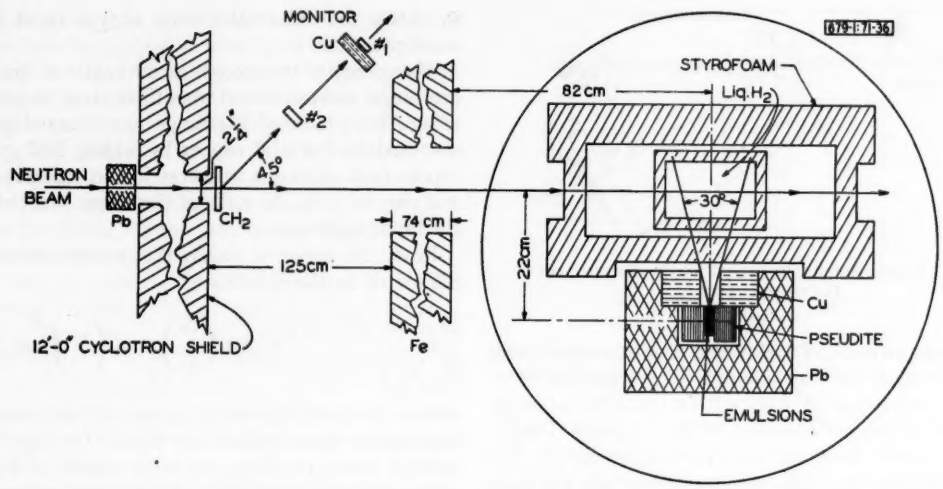

FIG. 1. General arrangement. The emulsion detector geometry for the first run at $\Theta=90\pm15$ is shown in the inset.

charge-independence hypothesis, such as carried out by Brueckner and Watson,[12] and also by Van Hove.[13] They show that it should be possible to describe all these reactions in terms of three fundamental matrix elements. The isotopic spin of the initial state can be zero only in reactions (4) to (7); hence the matrix element for the transition from this state can occur only in these reactions. One of the motivations for the present experiment was to obtain a measure of this matrix element. In addition, it will be of interest to see experimentally how well the charge-independence hypothesis describes the facts.

II. EXPERIMENTAL

This paper is a report of an experiment in which the production of $\pi^{\pm}$ mesons by 400-Mev neutrons interacting with liquid hydrogen was measured using photographic emulsions to detect the mesons.

A. General Arrangement

The 400-Mev neutron beam of the Chicago synchrocyclotron was used in this experiment. This neutron beam is produced by the circulating proton beam of the cyclotron by striking a Be target 2 in. long in the beam direction and 1 in. high. The neutrons selected were those emitted in the forward direction and defined by collimators placed at two ends of the neutron channel through the shielding wall of the cyclotron. The collimation produced a $2\frac{1}{2}$-in. diameter neutron beam at the center of the hydrogen target. Two inches of lead were placed in the path of the beam before the collimation in order to remove electron and gamma-ray contamination of the beam. The general layout is shown in Fig. 1.

The neutron beam was monitored by having it pass through a 1-cm thick polyethylene target, the recoil protons from which were counted by a telescope of two counters (Fig. 1).

Eight feet from the monitor target, neutrons struck a liquid-hydrogen target. An extra 3-ft thick iron shield protected the detectors from neutrons scattered from the end of the collimator or the monitor target. Positive and negative pions produced at 90° and 65° in the laboratory system struck a stack of nuclear emulsions placed at about 22 cm from the center of the hydrogen target. They were brought to rest in the emulsion and the density of track endings was measured as a function of pion range in the emulsion. Negative pions were identified by observing stars at the end of the track, and positive pions from $\pi^{+}\rightarrow\mu^{+}$ decay. The total number of pions leaving the hydrogen at a given angle, and their energy distribution, were obtained from the density of endings.

B. Neutron Beam

1. *Energy Spectrum.*—The neutron beam from a Be target is not monoergic; hence it was necessary to make a measurement of the neutron energy spectrum, which was obtained from a range measurement of the recoil protons from liquid hydrogen.

The neutron beam, collimated to $1\frac{1}{2}$-in. diameter, struck a liquid-hydrogen target.[14] The target used was $3\frac{3}{4}$ in. in diameter with a 5-mil stainless-steel wall, having an outside container with walls of 15-mil duraluminum. The range spectrum of recoil protons from the liquid hydrogen at 20° and 30° was measured by means of a telescope of four counters (see Fig. 2). The solid angle was defined by counter 2 which was placed 50 in. from the center of the hydrogen target,

[12] K. M. Watson and K. A. Brueckner, Phys. Rev. 83, 1 (1951).
[13] Van Hove, Marshak, and Pais, Phys. Rev. 88, 1211 (1952).
[14] The target used here was designed and built by Dr. M. Glicksman and is described in his paper, Phys. Rev. 94, 1335 (1954).

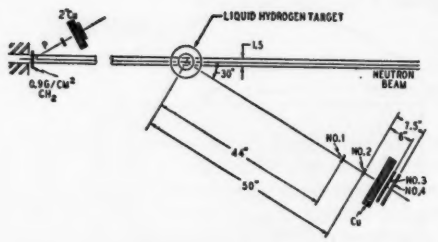

FIG. 2. Experimental arrangement for the measurement of the neutron spectrum.

subtending an angle of 0.04 radian. For this experiment, the neutron beam was monitored by counting recoil protons, emitted at 30° from a 0.9 g/cm² CH_2 target by means of a counter telescope of two counters. Double coincidences of these counters are denoted by M. The beam intensity was also monitored by two auxiliary monitors: (1) a BF_3 counter, which counted slow neutrons in the experimental area, and (2) a thermocouple which measured the heat dissipated in the neutron-producing target.

The quadruple coincidences Q of counters 1, 2, 3, and 4 per monitor count M were recorded for various thicknesses of copper absorbers placed between counters 2 and 3. The absorbers were placed as close to counter 3 as possible to minimize the corrections for multiple and diffraction scattering. The ratio Q/M as a function of x, the thickness of Cu, gives the range curve for the recoil protons. The two range curves for 20.25° and 30° are plotted in Fig. 3. These curves were differentiated to obtain the differential range curves dv/dx for the recoil protons.

The energy of the protons at the center of the hydrogen target was calculated from their range in copper by using Aron's tables.[15] The range was obtained from the observed thickness of copper by adding 2.62 g/cm² of copper equivalent due to energy loss in counters 1, 2, 3, and part of 4, in the walls of the target and in half of the liquid hydrogen.

From the curve of dv/dx, the neutron spectrum is calculated by the equation:

$$\frac{dv}{dx}=\frac{dn}{dT_N}\frac{dT_N}{dT_P}\frac{dT_P}{dx}N_H\Delta\Omega_l\left(\frac{d\sigma}{d\Omega}\right)_P\exp\left(-\int_0^x\sigma_{Cu}Ndx\right),$$

where x is the thickness of copper in g/cm²; dn/dT_N is the number of neutrons in the beam, of energy T_N, per monitor count, per Mev; N_H is the number of hydrogen atoms per cm² in the beam; $\Delta\Omega_l$ is the laboratory solid angle; $(d\sigma/d\Omega)_P$ is the differential cross section for producing recoil protons at Θ in the laboratory for neutrons of energy T_N; and $\exp(-\int_0^x\sigma_{Cu}Ndx)$ is the loss of protons due to absorption in thickness x of copper (N is the number of copper atoms per gram). This exponential was calculated using the values of σ_{Cu} (absorption) measured by Kirschbaum.[16] The multiple and diffraction scattering losses of protons were negligible in the geometry used. The laboratory cross section for producing a recoil proton at an angle Θ is given by

$$\left(\frac{d\sigma}{d\Omega}\right)_P=\left[\frac{d\sigma(\phi)}{d\omega}\right]_n\cdot\frac{d\omega}{d\Omega},$$

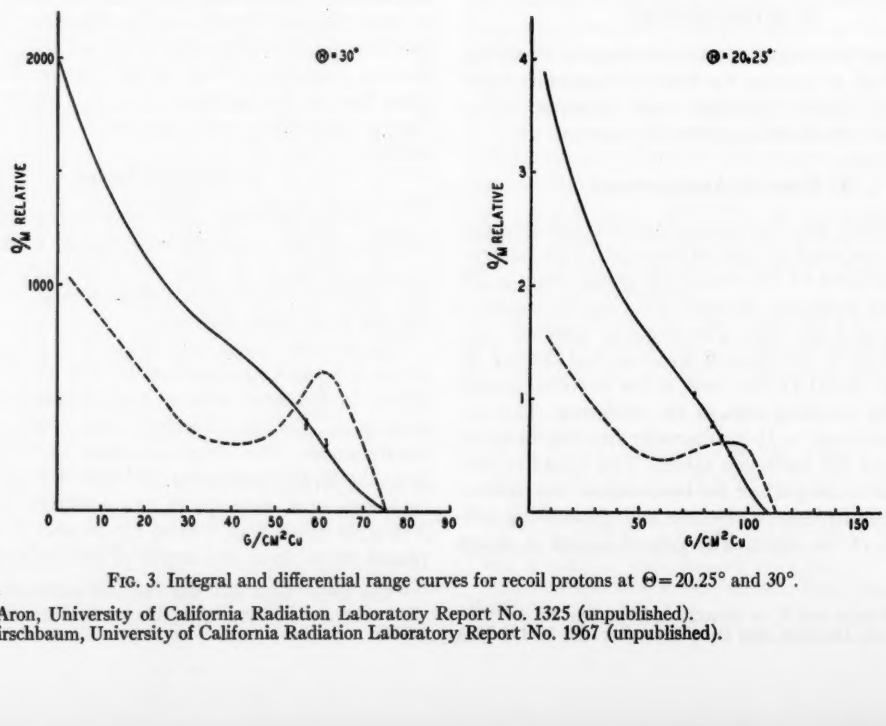

FIG. 3. Integral and differential range curves for recoil protons at $\Theta=20.25°$ and 30°.

[15] W. A. Aron, University of California Radiation Laboratory Report No. 1325 (unpublished).
[16] A. J. Kirschbaum, University of California Radiation Laboratory Report No. 1967 (unpublished).

where $[d\sigma(\phi)/d\omega]_n$ is the differential $N-P$ scattering cross section for giving a recoil proton at Θ in the laboratory or a neutron at the corresponding center-of-mass angle ϕ, and $d\omega/d\Omega$ is the center-of-mass laboratory solid angle transformation. Measured values[17–20] for the cross section $(d\sigma(\phi)/d\omega)_n$ are plotted against the neutron energy T_N in Fig. 4 and a smooth curve drawn through them for obtaining $(d\sigma/d\omega)_n$ at all neutron energies. In calculating the neutron spectrum the errors in the measurement of $(d\sigma/d\omega)_n$ were not included.

The neutron spectra dn/dT_n calculated from the measurements at $\Theta=20.25°$ and 30° are plotted in Fig. 5, and they agree well, within statistical errors. The spectrum shows a sharp high-energy peak with a 10 percent full width at half-maximum. In Fig. 6 is plotted the neutron spectrum $g(t_0)$ normalized to unity for the area from $T_N=280$ Mev to maximum possible neutron energy $T_{N\text{maximum}}=440$ Mev. The abscissa is the maximum meson energy t_0 in the center-of-mass system corresponding to a neutron energy T_N. This energy t_0 is slightly different for π^+- and π^--mesons but for the energy resolution of the experiment the same mean value is assumed for both. This function $g(t_0)$ was analytically approximated by a straight line and a parabola as shown in Fig. 6.

The analytical expressions are given by

$$g_{\mathrm{I}}(t_0)=(0.125t_0+9.65)\times10^{-3},\quad 0<t_0<29\text{ Mev},$$
$$g_{\mathrm{II}}(t_0)=[25.4-0.0772(45-t_0)^2]\times10^{-3},\quad 27<t_0<63\text{ Mev},\qquad(8)$$

where

$$\int_0^{t_0(\text{maximum})} g(t_0)dt_0=1.$$

These functions, when multiplied by the total number of neutrons incident on the hydrogen, give the number of neutrons per unit meson energy in the center-of-mass system.

2. *Neutron Monitor.*—The neutron flux was measured by counting the recoil protons from a 1-cm thick polyethylene target placed in the neutron beam 8 ft ahead of the liquid-hydrogen target (see Fig. 1). The recoil protons were counted by means of a telescope of two counters, with 19.79 g/cm² copper absorber in front of counter 2 which made the telescope sensitive to recoil protons from neutrons of energy greater than 280 Mev only. (This arrangement is shown in Fig. 7.) The counter voltages were set to be in the middle of the plateau curves of double coincidences against counter voltages. The telescope was at 45°±3° to the neutron beam.

[17] Hadley, Kelly, Leith, Segrè, Wiegand, and York, Phys. Rev. **75**, 351 (1949).
[18] Kelly, Leith, Segrè, and Wiegand, Phys. Rev. **79**, 96 (1950); **83**, 923 (1951).
[19] Brueckner, Hartsough, Hayward, and Powell, Phys. Rev. **75**, 555 (1949).
[20] J. de Pangher, Phys. Rev. **92**, 1084 (1953).

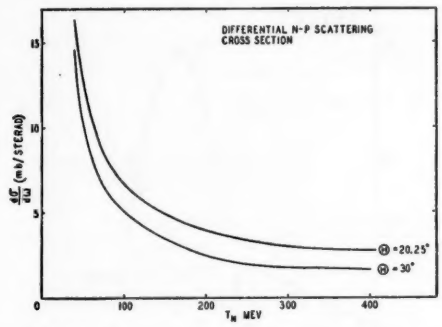

FIG. 4. Differential cross section in the center-of-mass system for scattering a proton at $\Theta=20.25°$ and 30° in $N-P$ collisions.

The number of recoil protons coming from the H_2 in CH_2 were determined by measuring the difference CH_2-C, using a carbon target having the same number of C atoms per cm² as the polyethylene target. The measurement of the ratio $(CH_2-C)/CH_2$ was done at three different times during the experiment and was found not to vary outside statistics. Its value was

$$(CH_2-C)/CH_2=R=0.383\pm0.0146.$$

Thus the number of protons from H_2 are the total number of counts from CH_2 multiplied by R.

To calculate the number of neutrons incident on the H_2, it is necessary to estimate the efficiency of the proton telescope. The counters were nearly 100 percent efficient, and the efficiency of the proton telescope was estimated to be 80 percent, mainly as a result of the loss of protons in the copper and the first counter by absorp-

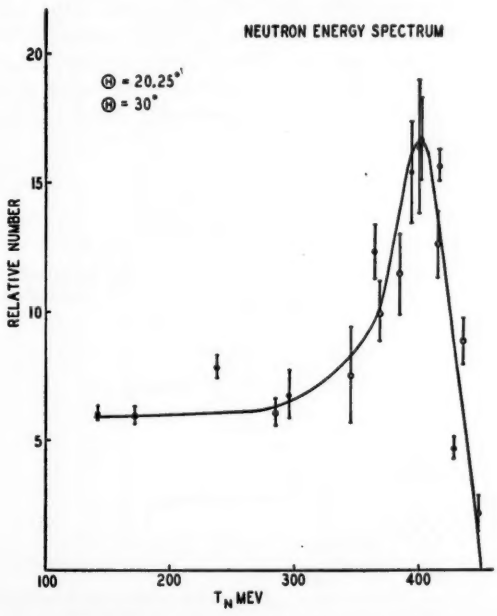

FIG. 5. Energy spectrum of the neutron beam.

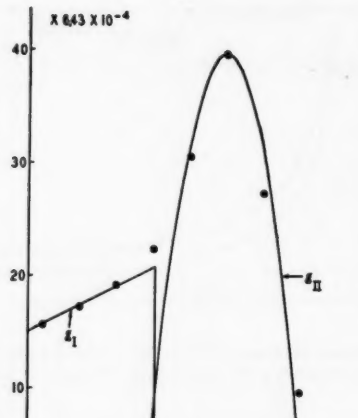

FIG. 6. Neutron energy spectrum as a function of the maximum pion energy in the center-of-mass system.

tion. The number of neutrons incident on the hydrogen are then calculated from

$$N_n = \frac{1}{N_H \Delta\Omega (d\omega/d\Omega)(d\sigma/d\omega)_n} \frac{\nu_p R}{\epsilon},$$

where ν_p is the total number of counts from hydrogen; ϵ is the efficiency of the telescope ($\epsilon=0.80$); N_H is the number of hydrogen atoms per cm² in CH_2 target ($N_H=7.924\times10^{22}$); $\Delta\Omega$ is the solid angle subtended by counter 2 ($\Delta\Omega=2.5\times10^{-3}$ sterad); $d\omega/d\Omega$ is the solid angle transformation from the laboratory system to the center-of-mass system ($d\omega/d\Omega=2.81$); and $(d\sigma/d\omega)_n$ is the $N-P$ differential cross section for producing recoil protons at $\Theta=45°$ in the laboratory: $(d\sigma/d\omega)_n=1.58 \pm 0.047$ mb/sterad.

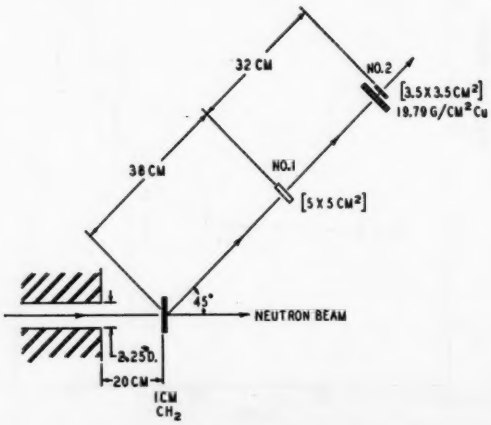

FIG. 7. Monitor geometry.

The differential cross section $(d\sigma/d\omega)_n$ was calculated at 400-Mev neutron energy using the measured value of the total $N-P$ cross section by Nedzel[21] and the angular distribution by Hartzler and Siegel.[22] The Berkeley value[19] was used at 280 Mev. The error in the knowledge of $(d\sigma/d\omega)_n$ is 3 percent. For the two exposures made, the total number of neutrons incident on the target for the effect and the background runs are given in Table I.

C. Hydrogen Target

A double-walled Styrofoam target, based on an original design by Marshall,[23] was used (Fig. 8). The outside container had 3-in. thick walls except where the beam passed through, where it was 1½ in. thick. It was also thinned down to 2 in. where the pions emerged at 65° to the beam. The inside container had 1-in. thick walls, and it was 8 in. long, 4 in. wide and 6 in. deep. Both containers were lined by 2-mil aluminum foil. The linings distributed the cold over the Styrofoam evenly to prevent thermal strains. The cold hydrogen vapor circulates around the inner container and then goes out of the hole at the bottom through an oil trap and gas meter to the exit. The level of the hydrogen was observed by measuring the level of a Styrofoam float C, noting the height of the balsa-wood stick in the Pyrex tube F. Liquid hydrogen is transferred through E. The two ends of the target were aligned with respect to the beam to within 1 mm.

The target had three important features to make it suitable for this experiment: (1) The hydrogen container was made long enough in the direction of the beam so that the walls through which the neutron beam passed were not directly visible by the detector. (2) The thicknesses of the Styrofoam walls in the beam were reduced so as to minimize the production of mesons from the walls. (3) The low density of Styrofoam makes the energy loss of pions passing through them small so that the energy threshold of the detector can be lower than otherwise.

D. Emulsion Detector

The detector consisted of a stack of stripped Ilford G-special emulsions, 1800 microns thick, placed at 22 cm from the center of the target at 90° and 65° to the neutron beam (Fig. 9). The pellicles (emulsions stripped from glass backing) were embedded in a holder of

TABLE I. Total number of neutrons incident on the target.

Target	Run A in units of 10^{11}	Run B in units of 10^{11}
With hydrogen	1.508±0.050	5.706±0.196
Without hydrogen	1.109±0.036	1.199±0.041

[21] V. A. Nedzel, Phys. Rev. **91**, 440 (1953).
[22] A. J. Hartzler and R. T. Siegel, Phys. Rev. **95**, 185 (1954).
[23] L. Marshall (to be published).

material, "pseudite,"[24] which has the same density, stopping power, and radiation length as that of the emulsion. The size of the emulsions at each angle was determined by the requirement that the maximum-energy pion at that angle would come to rest in the emulsion. The pellicles were 1.5 in. long for the 90° stack and 4 in. for the 65° stack.

The G-special emulsions are most suited for this type of experiment because they are insensitive to electrons, and they have higher sensitivity than C-2 emulsions, high enough to make the meson tracks sufficiently heavy and the variation in grain density near the end of the track rapid enough to produce very distinctive pion endings. Further, there is a marked change in grain density between the pion track at its end and the emitted muon track. This makes identification of $\pi^+ \rightarrow \mu^+$ decay immediate. Pellicles 1800 microns thick were used for the following reasons: (1) to be able to identify each π^+ ending by following the muon to its end, which was achieved by scanning only the middle third of the emulsion; (2) to halve the time of development and to permit more uniform development than for plates of equal thickness; (3) to avoid the presence of material different from emulsion in the detector stack.

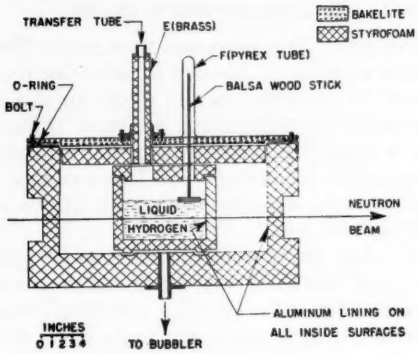

FIG. 8. Styrofoam liquid-hydrogen target.

The angular acceptance at each angle was determined by means of copper or lead collimators (Fig. 9). The angular spread was $\pm 15°$ for $\Theta = 90°$ for the first run and $\pm 5°$ and $\pm 3°$ for $\Theta = 90°$ and 65°, respectively, for the second run. A lead collimator with 1 cm of tungsten in the front edge was used on the upstream side of the 65° stack because the high densities of these materials could make the angular definition sharper by stopping high-energy particles in a small thickness.

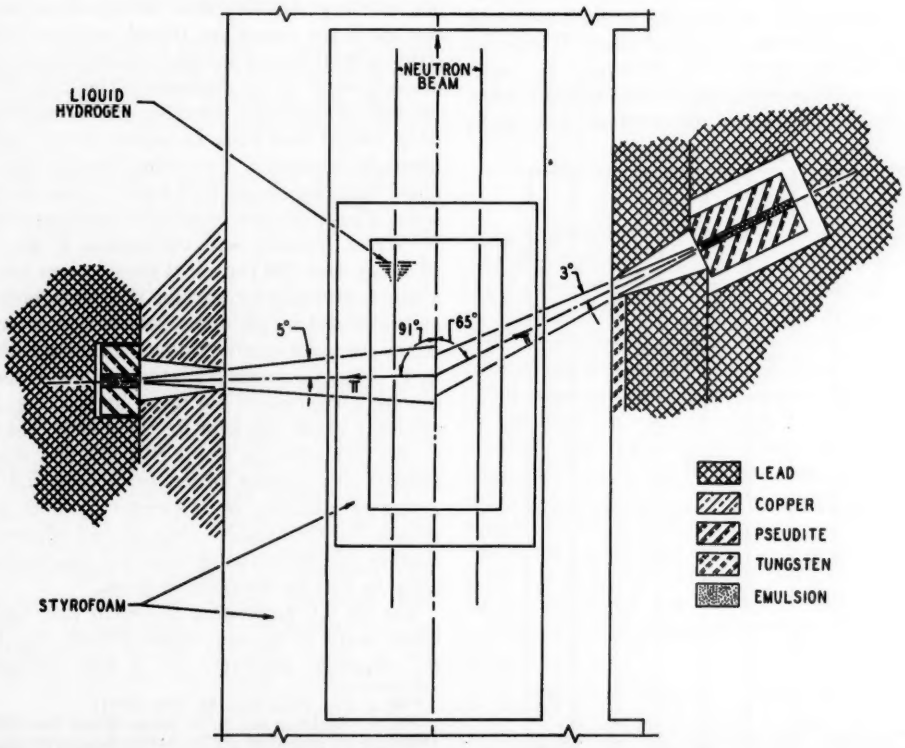

FIG. 9. The 91° and 65° geometries used in the second run.

[24] Pseudite is a machinable, molded mixture of fine Cu, Sn, and Lucite powders, 150 mesh or smaller. Each cc contains 1.28 g Cu, 1.94 g Sn, and 0.71 g Lucite, and has a total density of 3.93±2 percent. See Rosenfeld, reference 6.

E. Exposure and Scanning

1. *Exposure.*—Two exposures were made. The first was made at 90°±15° in order to determine the magnitude of the cross section and to get an idea of the background. The background, measured without hydrogen in target, was very low and permitted improving the angular resolution three-fold. This was done in the second exposure. Exposures were made at two angles: 91°±5° and 65°±3°.

At 91° there are no recoil protons from the hydrogen due to $N-P$ scattering, permitting one to scan all the way to the edge of the emulsion obtaining lowest possible threshold for the pions. For angles larger than 90°, the energy of the pions becomes too low to measure the pion spectrum adequately.

At 65° there is sufficient difference between the ranges of the maximum-energy recoil protons due to $N-P$ scattering and that of the pions to make scanning for pions beyond the proton range possible. The energy threshold of detection determined by the range of the maximum-energy recoil proton was 41 Mev. For smaller angles the number of recoil protons and neutrons becomes very large and their energy becomes high so that the plate would become impossible to scan because of too many extraneous events. Furthermore, the center-of-mass angle corresponding go the laboratory angle 65° is close to 90° so that the constant term a in the angular distribution $(a+b\cos\theta+c\cos^2\theta)$ can be determined directly (see Sec. VI, below).

The length of the second exposure was adjusted so as to obtain the same density of pion endings at 90° as in the first exposure. At both angles exposures were made with and without liquid hydrogen in the target, care being taken to have only hydrogen gas in the target during the background exposure.

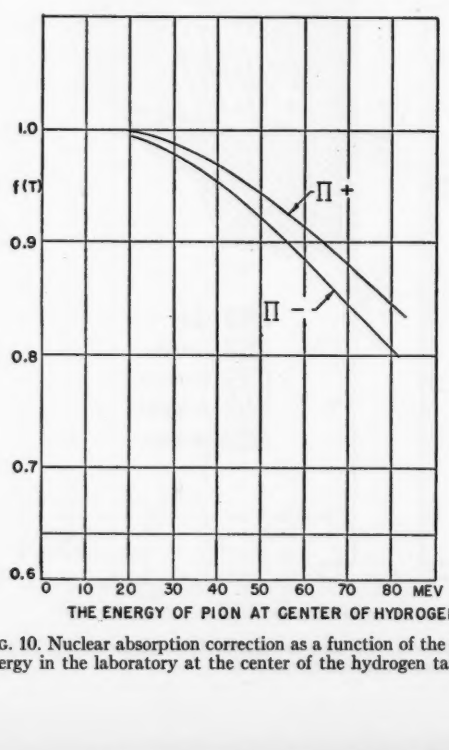

FIG. 10. Nuclear absorption correction as a function of the pion energy in the laboratory at the center of the hydrogen target.

2. *Scanning.*—The method of observation was to scan the emulsion using 22×oil objectives (also 12.5×oil objectives for the background plates) in strips starting from the threshold of detection, along the direction of pion incidence up to about 5 mm beyond the range of the maximum-possible-energy pion. For each strip only the middle 600 microns of the emulsion were scanned. Both pion and muon endings in this layer were recorded. This insured that whenever a $\pi^+\rightarrow\mu^+$ decay was found it was possible to follow the muon to the end of its range, 597±28 microns,[25] and thus identify the event unambiguously. For negative pions all π^- stars with one or more prongs were recorded. The number of no-pronged negative-pion endings were calculated by using the value[26] 1.36 for the ratio of the total number of negative-pion endings to the number of pion endings with stars having one or more prongs.

The advantage of scanning the middle 600 microns of a pellicle 1800-microns thick is that it permits a truly objective test of scanning efficiency.[27] If a $\pi^+\rightarrow\mu^+$ decay is found in this 600-micron layer, there is about 50 percent probability that the associated muon will also end in the same layer, though not necessarily in the strip currently being scanned, because the range of the muon is equal to the thickness of the layer. Therefore, one-half of the pions found by direct scanning in this layer should lead back to muons in the same layer. Similarly, one-half of the muons found in this layer by direct scanning should lead back to pions in the same layer. Thus pions are found in two independent ways: By direct scanning and via muons. If the scanning efficiency were 100 percent it should never happen that a pion is seen only by tracking the corresponding muon and is missed in the direct search. The scanning efficiency for pions found by direct scanning is then given by $1-(N_m/N_t)$, where N_m is the number of pions missed by direct observation but found by tracking. A similar efficiency check was kept for the muons. For example, in the first exposure about 50 pions and muons were tracked. The number missed was 3 pions and 3 muons, giving an efficiency of 94 percent for both pions and muons. For the negative pions no such efficiency test is possible and the scanning efficiency was assumed to be equal to that for the positive pions.

For the 90° experiment the event rate was about 1 event every 10 minutes under 22×oil objective. The 65° exposure, however, had a high background of

[25] W. F. Fry, Phys. Rev. **83**, 1268 (1951).

[26] F. L. Adelman and S. B. Jones, Phys. Rev. **75**, 1468(A) (1949); A. H. Rosenfeld and W. F. Fry (private communication); W. Dudziak, University of California Radiation Laboratory Report UCRL-5641, 1954 (unpublished).

[27] The scanning efficiency test was designed by A. H. Rosenfeld, see reference 6.

proton tracks and stars due to neutrons entering the emulsion, and made scanning much more difficult, reducing the event rate to 1 event every 1½ hours under the same magnification. It was possible to scan the background plates eight times faster than the effect plates. The optimum division of scanning time between effect and background plates required that equal time be spent scanning each of them for best statistics.

A certain fraction of the pions, positive and negative, were not observed in scanning either because they were absorbed by nuclei of the emulsion or suffered large-angle scattering. In the first case they disappear suddenly, and in the latter case they appear coming from the wrong direction. Figure 10 shows curves for the fraction of pions of energy T removed as a result of nuclear absorption and scattering as a function of the energy of the pion at the center of the hydrogen target. They are based on data on nuclear-absorption cross section of pions in emulsion at various energies.[28] Hence, from the observed density of pion track endings as a function of range in emulsion, pion range spectra were determined at two angles. The energy spectra of the pions were obtained by calculating what energy pion, starting at the center of hydorgen, ends at a given range in the emulsion.

F. Energy Resolution

The energy of a pion is determined from its range. This energy is not uniquely determined because of energy spreads due to: (1) straggling, (2) multiple scattering, and (3) variation in energy loss due to size of the beam.

The energy spread due to straggling of the range has a Gaussian distribution. The standard deviation of the straggling distribution has been calculated by using the formula:[29]

$$\frac{[\langle(R-\bar{R})^2\rangle_{Av}]^{\frac{1}{2}}}{\bar{R}}=\left(\frac{200m_e}{\mu}\right)^{\frac{1}{2}}f\left(\frac{E}{\mu c^2}\right),$$

where μ is the meson mass; the function f is taken from Rossi.[29] The energy spread due to multiple scattering does not have a Gaussian distribution; however, we have approximated the distribution by a Gaussian with 5-percent standard deviation. The spreading of the energy due to the size of the beam occurs because pions produced at different positions in the hydrogen suffer different energy losses in traversing the hydrogen. This energy spread is distributed almost uniformly. The three distributions were folded into each other and the width corresponding to the half-area point of the resultant distribution was calculated. Table II gives the energy spreads for different pion energies at the two angles of the experiment.

TABLE II. Energy resolution. Energy spreads are half-widths the laboratory system.

Laboratory angle	Pion energy in c.m. system (Mev)	Pion energy in lab. system (Mev)	Energy spread in Mev due to: Beam size	Multiple scattering	Straggling	Total spread (Mev)
	30	14.5	4.37	0.1	0.08	2.30
	40	23.5	3.00	1.1	0.60	1.55
	50	32.5	2.41	2.0	0.90	1.75
90°	60	41.5	2.10	2.5	2.00	2.00
	30	31.7	2.63	0.40	0.30	1.65
	40	42.0	2.32	1.50	1.00	2.10
65°	50	57.1	2.01	3.00	2.00	2.65
	60	70.0	1.83	4.80	3.00	3.85

III. CALCULATION OF THE LABORATORY CROSS SECTION

The energy spectra for π^+ and π^- mesons were observed at laboratory angles 90° and 65°. The pion spectra are the result of production due to neutrons of all energies above the threshold of pion production. First, these observations are reduced in terms of experimental cross sections for the particular neutron beam used in this experiment. An effort is then made (see Secs. V, VI, and VII) to reduce these experimental cross sections to center-of-mass cross sections for a single neutron energy.

Each element dv' of the active volume of the target produces

$$\nu_n\rho_H dv'\frac{A}{r^2}\frac{d^2\sigma_{Av}}{d\Omega dT}$$

pions of energy T into a solid angle A/r^2 at an angle Θ (see Fig. 11). Here $A\cdot\Delta R$= the volume of emulsion scanned for pions of energy T and $T+\Delta T$ which end in the emulsion between range R and $R+\Delta R$. $1/r^2(T,x',y',z')$= distance of the element dv' of the target from the point where a pion of energy T stops in the emulsion. ν_n= number of neutrons/cm² incident on the target. ρ_H= effective density of liquid hydrogen =0.0705 g/cc. $d^2\sigma_{Av}/d\Omega dT$= cross section for pion production at an angle Θ to the neutron beam, averaged over the neutron spectrum. The density dn/dT of pion tracks of energy T observed in the emulsion will be this number multiplied by: (1) the scanning efficiency ϵ, (2) the probability of decay in flight $\eta(T)$, and (3) the probability of loss due to nuclear absorption in emulsion $f(T)$; and integrated over the active volume of the target:

$$\frac{dn}{dT}=\nu_n\rho_H\epsilon\eta(T)f(T)\int_{\text{target}}dv'\frac{A}{r^2}\cdot\frac{d^2\sigma_{Av}}{d\Omega dT}. \quad (9)$$

The integral has been approximated by replacing $1/r^2$ and $d^2\sigma_{Av}/d\Omega dT$ by suitable averages over the target,

[28] G. Bernardini and F. Levy, Phys. Rev. **84**, 610 (1951); Bernardini, Booth, and Lederman, Phys. Rev. **83**, 1075 (1951); Hugh Bradner and Bayard Rankin, Phys. Rev. **87**, 547 (1952); D. H. Stork, Bull. Am. Phys. Soc. **27**, No. 6, 16 (1952).

[29] B. Rossi, *High-Energy Particles* (Prentice-Hall, Inc., New York, 1952), p. 37.

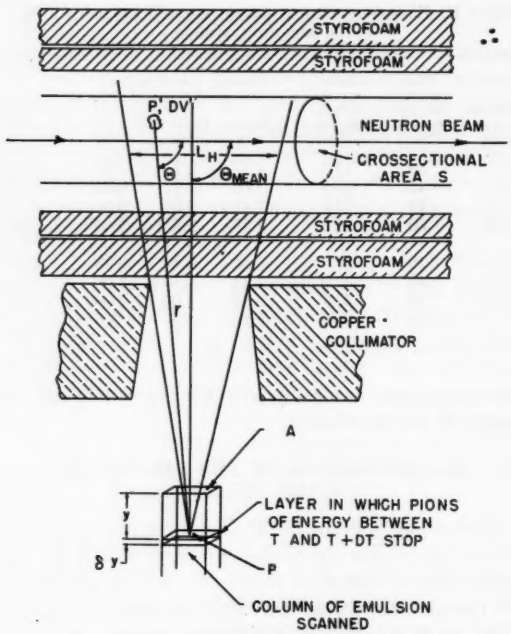

FIG. 11. Figure explaining the calculation of the laboratory cross section.

and the volume of the target by the cross section of the beam S times the active length $l_H(T)$ of the hydrogen. The active length of the hydrogen $l_H(T)$, is a function of T because the length of hydrogen seen through the collimator depends on the position of the pion ending. Then the density of endings, dn/dT, is given by:

$$\frac{dn}{dT}=N_n\rho_H A\epsilon\eta(T)f(T)\left(\frac{1}{r^2}\right)_{Av}\left(\frac{d^2\sigma_{Av}}{d\Omega dT}\right)_{Av}, \quad (10)$$

where $N_N=\nu_n\cdot S$, (the total number of neutrons incident on the target), $(1/r^2)_{Av}$ is the average of the inverse square distance over the target, and

$$\left(\frac{d^2\sigma_{Av}}{d\Omega dT}\right)_{Av}=\frac{1}{\Delta\Theta}\int_{\Theta_{min}}^{\Theta_{max}}\int_{T_N(\text{threshold})}^{T_N\max}\frac{d^2\sigma}{d\Omega dT}g(T_N)dT_N d\Theta, \quad (11)$$

where the average is carried out over the angular acceptance of the detector $\Delta\Theta$ and over the neutron energy spectrum $g(T_N)$.

IV. EXPERIMENTAL RESULTS

A. Measurement at 90°

The results of the two runs are collected in Table III. In columns 2 and 3 are given the number of pions, corrected for background, observed in the energy band listed in column 1. The active length of hydrogen determined by the geometry of the experimental arrangement is given in column 4. Columns 5, 6, and 7 give the corrections for decay in flight, and nuclear absorption in the emulsion, respectively. The calculated average of the inverse square distance is given in column 8. The experimental cross sections as determined from Eq. (11) are given in columns 9 and 10.

A total of 325 positive- and negative-pion endings were measured. No pions were observed beyond the kinematic limit for pion production from hydrogen.

The differential cross sections for $\pi^{\pm}$ production, integrated from the threshold of the detector to the kinematic limit, are:

$$\left(\frac{d\sigma}{d\Omega}\right)_{90^\circ}^{+}=[2.296\pm0.363]\times10^{-30}\ \text{cm}^2/\text{sterad}, \quad T>14\ \text{Mev},$$

$$\left(\frac{d\sigma}{d\Omega}\right)_{90^\circ}^{-}=[1.156\pm0.327]\times10^{-30}\ \text{cm}^2/\text{sterad}. \quad T>14\ \text{Mev}.$$

The laboratory energy spectra for $\pi^{\pm}$, calculated by using both runs, are plotted in Fig. 12(a).

A marked predominance of π^+ over π^- mesons is found at this angle. The ratio π^+/π^- is (2.01 ± 0.24). This indicates an asymmetry in the angular distribution of positive and negative pions with a preferential production of π^+ mesons at center-of-mass angles larger than 90°. This would mean, according to charge symmetry, that there should be an excess of π^- over π^+ mesons at center-of-mass angles less than 90°. Such an excess was found by Wright and Schluter[11] in their study of π^- production in $N-P$ collisions.

B. Measurement at 65°

At this angle, scanning was difficult and slow for two reasons: (1) There was a large flux of extraneous events, such as neutron stars and stray proton tracks; (2) the length of strip required to be scanned was longer than at 90° because the pion spectrum extends to higher energies. Hence only a crude measurement of the cross section was made.

The total number of pion endings found with hydrogen in the target was 22 π^+ and 50 π^- mesons. However, 2.1 π^+ and 28.6 π^- of these were due to background as determined from the run without hydrogen in the target, giving a net of 19.9 ± 1.45 π^+ and 21.4 ± 5.35 π^- from hydrogen alone. The total differential cross sections, obtained by integrating Eq. (10) from the threshold of detection to the kinematic limit, are:

$$\left(\frac{d\sigma}{d\Omega}\right)_{65^\circ}^{+}=(1.22\pm0.30)\times10^{-30}\ \text{cm}^2/\text{sterad}, \quad T>41\ \text{Mev},$$

$$\left(\frac{d\sigma}{d\Omega}\right)_{65^\circ}^{-}=(1.31\pm0.63)\times10^{-30}\ \text{cm}^2/\text{sterad}, \quad T>41\ \text{Mev}.$$

TABLE III. Differential cross sections for $\pi^{\pm}$ production at $\Theta=90°$.

Pion energy at center of hydrogen T_π^c(Mev)	No. of pions in energy band corrected for background π^+	π^-	Active length of liquid hydrogen, $l_H(T)$ (cm)	Correction for decay in flight $\eta(T)$	Correction for absorption in emulsion, $f(T)$ π^+	π^-	Effective $(1/r^2)$ (cm^{-2})	Average lab. cross section [(cm^2/sterad Mev) $\times 10^{-31}$] π^+	π^-
Run I. $N_n=(1.51\pm0.02)\times10^{11}$; $\epsilon=0.94$; $A=0.336$ cm^2; $\Theta=90°\pm15°$.									
14–20	43±6.7	18±7.0	11.6	0.946	0.999	0.999	0.002295	1.43 ±0.22	0.597±0.232
20–26	45±6.85	23±5.0	11.2	0.952	0.995	0.992	0.002217	1.60 ±0.24	0.818±0.178
26–32	22±4.69	18±4.69	10.65	0.956	0.988	0.982	0.002215	0.828±0.176	0.677±0.176
32–38	15±3.87	3±3.0	10.15	0.959	0.979	0.969	0.002030	0.651±0.168	0.13 ±0.130
38–44	6±2.44	1±1.73	9.7	0.961	0.967	0.953	0.001935	0.289±0.118	0.048±0.084
	131	63							
Run II. $N_n=(5.706\pm0.196)\times10^{11}$; $\epsilon=0.93$; $A=0.182$ cm^2; $\Theta=91°\pm5°$.									
14–20	31±5.5	12.6 ±4.6	4.71	0.946	0.999	0.999	0.001995	1.41 ±0.25	0.571±0.209
20–26	24±4.9	11.28±5.3	4.55	0.952	0.995	0.992	0.001930	1.164±0.24	0.547±0.257
26–32	19±4.35	7.64±4.0	4.35	0.956	0.988	0.982	0.001850	1.01 ±0.231	0.406±0.212
32–38	8±2.82	7.64±4.1	4.14	0.959	0.979	0.982	0.001780	0.468±0.166	0.447±0.239
38–44	4.3±2.56	5.82±3.3	3.94	0.961	0.967	0.953	0.001705	0.277±0.165	0.375±0.212
	86.3	44.98							
	217	108							

The pion spectra obtained at 65° are less reliably determined than those obtained at 90°. The histogram of the events observed at 65° is plotted in Fig. 13. The total number of π^- mesons quoted in figure have been corrected for no-prong stars.

According to the hypothesis of charge symmetry the π^+ and π^- cross sections should be equal at 90° in the center-of-mass system. The angle 65° in the laboratory corresponds to approximately 106° in the center-of-mass; therefore at 65° the number of π^+ and π^- mesons should be very nearly equal. The experimental results are consistent with this requirement of charge symmetry.

V. ANALYSIS OF DATA

The experimental cross sections can be reduced to center-of-mass cross sections for a single neutron energy provided the energy distribution of the neutron beam is known and provided the energy spectrum and angular distribution of the reaction are known. Before discussing the energy spectrum and angular distribution of the reaction, we shall make the following approximations and simplify the calculation.

(1) Because of the finite resolution $\Delta\Theta$ of the detector, to each pion energy T considered in the laboratory system there corresponds a range of energies Δt and a range of angles $\Delta\theta$ in the center-of-mass system, for a given neutron energy. The center-of-mass cross section $d^2\sigma/d\omega dt$ varies with θ and t. The angular spread $\Delta\Theta$ is small enough so that, in calculating the center-of-mass cross section for a given angle Θ in the laboratory, we may neglect the variation in $d^2\sigma(\theta,t)/d\omega dt$ with the center-of-mass angle θ and approximate the cross section $d^2\sigma(\theta,t)/d\omega dt$ by its value at the mean angle $\bar{\theta}$ calculated at the energy t in the center of mass corresponding to the angle Θ. Thus

$$\left(\frac{d^2\sigma(\theta,t)}{d\omega dt}\right)_{\Theta}\cong\frac{d^2\sigma(\bar{\theta},t(\Theta))}{d\omega dt}.$$

Then the differential cross section for production of pions in the laboratory system is given in terms of the center-of-mass cross section by

$$\left(\frac{d^2\sigma}{d\Omega dT}\right)_{T,\Theta}\cong\frac{d^2\sigma(\bar{\theta},t)}{d\omega dt}J\left(\frac{\omega,t}{\Omega,T}\right),$$

where $J(\omega,t/\Omega,T)$ is the Jacobian of the transformation from the center-of-mass system to the laboratory system.

(2) The second approximation is made by neglecting the variation with neutron energy of the center-of-mass energy t for a given pion energy T in the laboratory. This is a good approximation as long as $t>10$ Mev, as is the case for the present experiment. Hence $J(\omega,t/\Omega,T)=P/p$ (where P is the given momentum of the pion in the laboratory system and p is the corresponding momentum in the center-of-mass system) can be calculated at a mean neutron energy T_N^* and used for all neutron energies.

The double integral (11) for obtaining the experimental cross section is then reduced to

$$\left(\frac{d^2\sigma_{\bar{N}}}{d\Omega dT}\right)_{\bar{N}}\cong\frac{1}{\Delta\Theta}\int\frac{P}{p}d\Theta\int\frac{d^2\sigma}{d\omega dt}(\bar{\theta},t,T_N)g(T_N)dT_N, \tag{12}$$

where in the integration over the neutron spectrum $\bar{\theta}$ and t are treated as constant. The average center-of-mass cross section is calculated from Eq. (12) approximately, replacing the average of P/p over Θ by the

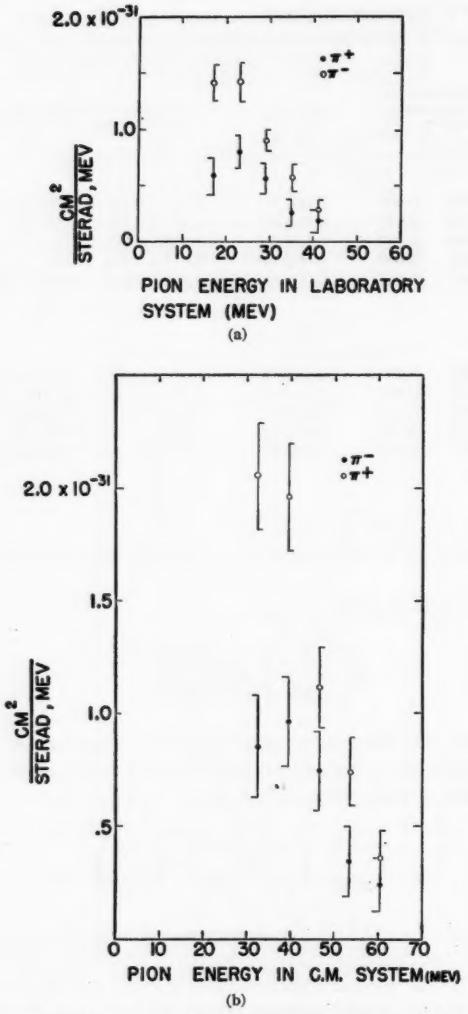

FIG. 12. (a) Average laboratory differential cross section for positive and negative pion production at 90°, due to neutrons of all energies in the beam. (b) Average center-of-mass differential cross section for positive and negative pion production at $\Theta=90°$, due to neutrons of all energies in the beam.

value of P/p at the mean angle $\bar{\theta}$.

$$\frac{d^2\sigma_{Av}}{d\omega dt}(\bar{\theta},t)\cong\left(\frac{p}{P}\right)_{\bar{\theta}}\left(\frac{d^2\sigma_{Av}}{d\Omega dT}\right)_{Av}.$$

The calculated average center-of-mass spectrum for

$$\Theta=90°(\bar{\theta}=128°)$$

is given in Fig. 12(b).

The integration over the neutron spectrum can be carried out only if the energy spectrum and the angular distribution of the cross section $d^2\sigma/d\omega dt$ is assumed. Hence we shall now discuss the nature of the energy spectrum and the angular distribution of the reaction under study.

VI. PHENOMENOLOGICAL ANALYSIS OF THE REACTION $N+P\rightarrow\pi^{\pm}$

The conservation of isotopic spin imposes severe restrictions on the production of pions in nucleon-nucleon collisions. All production processes can be described in terms of three independent reactions whose cross sections we denote by σ_{01}, σ_{11}, and σ_{10}.[30] The first subscript refers to the isotopic spin of the initial state and the second to that of the final state of the two outgoing nucleons. If the matrix elements of these three reactions are denoted by M_{01}, M_{11}, and M_{10}, then the differential cross sections for the reactions[13]

$$N+P\rightarrow\pi^-+P+P,\quad N+P\rightarrow\pi^+++N+N$$

are given by

$$\begin{aligned}\frac{d\sigma}{d\omega}(n+p\rightarrow\pi^-)&=\frac{2\pi}{\hbar}\{\tfrac{1}{2}|M_{11}+M_{01}|^2\}\frac{dN}{dW},\\ \frac{d\sigma}{d\omega}(n+p\rightarrow\pi^+)&=\frac{2\pi}{\hbar}\{\tfrac{1}{2}|M_{11}-M_{01}|^2\}\frac{dN}{dW},\end{aligned}\tag{13}$$

where dN/dW is the density of final states and the total cross sections are given by

$$\sigma(n+p\rightarrow\pi^-)=\sigma(n+p\rightarrow\pi^+)=\tfrac{1}{2}(\sigma_{01}+\sigma_{11}).\tag{14}$$

We may consider the phenomenon of pion production to take place at a characteristic distance R from the center of the collision, where $R\sim\hbar/\mu c$. At the energies of the experiment, $p_\pi\hbar/\mu c<1$ and $p^*\hbar/\mu c<1$, where p_π is the pion momentum and p^* is the relative momentum of the nucleons in the center-of-mass system. Hence it is reasonable to limit the discussion to the production of pions and nucleons into angular momentum states with $l=0$ or 1 only.

With this limitation the allowed transitions for the reaction are determined under conservation of angular momentum and parity. The allowed transitions are given in Table IV, whose construction is the following. Consider first the σ_{01} reaction, in which the final nucleons have $T=1$; therefore if the final nucleons are in an S state, it must be a singlet state. If the pion is emitted in a p state, then the final state is $({}^1S_0,p)_{T,J}$ in which the total isotopic spin $T=0$ and the total angular momentum $J=1$. Such a state can come from two initial states of the $N-P$ system, ${}^3S_1$ and ${}^3D_1$, both of which have even parity. This is shown in row (1) of the σ_{01} reaction column.

The transition of the σ_{11} reaction written in the same row is ${}^3P_0\rightarrow({}^1S_0,s)_{1,0}$ which can interfere with the transition of the σ_{01} reaction just described. For those reactions in which only one of the matrix elements is involved, no asymmetry in the pion angular distribution can arise. In the present experiment, only the pion is

[30] A. H. Rosenfeld, Phys. Rev. 96, 139 (1954).

observed so that, in obtaining the angular distribution of the pion, one has to integrate over the final nucleon states. Under these conditions, asymmetry in the pion angular distribution can arise due to interference between transitions of σ_{01} and σ_{11} reactions only if the spin functions of the initial states are the same and the final nucleon states are nonorthogonal. Table IV is arranged so as to list the reactions which can interfere to give asymmetry in the pion angular distribution in the same row.

In order to calculate the energy spectra and angular distributions for σ_{01} and σ_{11} reactions, it is necessary to discuss the relative importance of the transitions given in Table IV.

We first note that the meson, being a pseudoscalar particle, tends to be produced mainly in p states. Secondly, the production process is affected by two types of forces, (1) meson-nucleon force and (2) nucleon-nucleon force.

The cross section for production is proportional to the square modulus of the final nucleon wave function in a region of $\hbar/\mu c$ near the origin: $|\psi_f(r\sim\hbar/\mu c)|^2$. This is large if the nucleons are emitted in S-states where the nuclear forces enhance the wave function at the origin. Hence nucleon-nucleon forces favor the emission of nucleons in S-states rather than in P-states.

The meson-nucleon force is such that the interaction between a pion and a nucleon is greatly enhanced if they are in a state of isotopic spin $\frac{3}{2}$ and angular momentum $\frac{3}{2}$.[31] Therefore, transitions are enhanced if they

TABLE IV. Allowed transitions for the reaction $N+P\rightarrow\pi^{\pm}+2$ (nucleons).[a]

	Initial state	σ_{01} Parity	Final state ψ_f	Initial state	σ_{11} Parity	Final state ψ_f
(A)	Final nucleons in $^1S_0$ State					
1.	$^3S_1$	+	$(^1S_0,p)_{0,1}$	$^3P_0$	−	$(^1S_0,s)_{1,0}$
	$^3D_1$	+	$(^1S_0,p)_{0,1}$			
(B)	Final nucleons in $^3P_{2,1,0}$					
2.	$^1P_1$	−	$(^3P_0,p)_{0,1}$	$^1S_0$	+	$(^3P_0,s)_{1,0}$
3.				$^3P_1$	−	$(^3P_0,p)_{1,1}$
4.	$^1P_1$	−	$(^3P_1,p)_{0,1}$			
5.	$^3D_1$	+	$(^3P_1,s)_{0,1}$	$^3P_0$	−	$(^3P_1,p)_{1,0}$
				$^3P_1$	−	$(^3P_1,p)_{1,1}$
				$^3P_2$	−	$(^3P_1,p)_{1,2}$
				$^3F_2$	−	$(^3P_1,p)_{1,2}$
6.	$^1P_1$	−	$(^3P_2,p)_{0,1}$	$^1D_2$	+	$(^3P_2,s)_{1,2}$
7.	$^3D_2$	+	$(^3P_2,s)_{0,2}$	$^3P_1$	−	$(^3P_2,p)_{1,1}$
				$^3P_2$	−	$(^3P_2,p)_{1,2}$
				$^3F_2$	−	$(^3P_2,p)_{1,2}$
				$^3F_3$	−	$(^3P_2,p)_{1,3}$

[a] $\psi_{\text{final state}}=(\psi_{\text{nucleons}},\phi_{\text{meson}})_{T,J}$; ψ_{nucleons} is the state of final nucleons, S or P; ϕ_{meson} is the meson state, s or p; T is the total isotopic spin of ψ_{final}; and J is the total angular momentum of ψ_{final}.

[31] The study of pion-proton scattering shows the importance of $(\frac{3}{2},\frac{3}{2})$ state. See Anderson, Fermi, Martin, and Nagle, Phys. Rev. 91, 155 (1953).

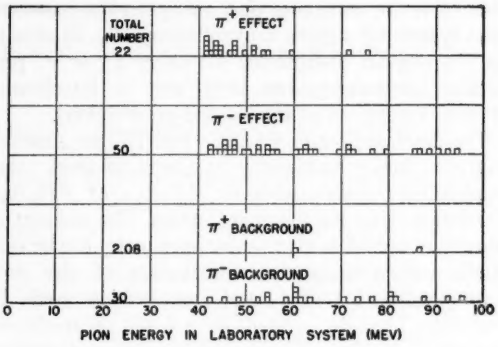

FIG. 13. Histogram of the events at 65°. In the column headed "total number," the value 30 should read 28.6.

can lead to a $(\frac{3}{2},\frac{3}{2})$ state for the pion and one of the nucleons. If the total isotopic spin of the final state has to be zero, as is the case for the σ_{01} reaction, there can be no $(\frac{3}{2},\frac{3}{2})$ enhancement. Thus enhancement due to pion-nucleon force can occur only for the σ_{11} reaction.

For the σ_{01} reaction, where no enhancement due to pion-nucleon force is possible, the most dominant transitions are assumed to be those leading to an (S,p) final state. These transitions are:

$$\left.\begin{matrix}{}^3S_1\\ {}^3D_1\end{matrix}\right\}\rightarrow(^1S_0,p)_{0,1}.$$

For the σ_{11} reaction, production into a (S,p) state is forbidden by angular momentum and parity conservation. The state (S,s) is allowed but can have no $(\frac{3}{2},\frac{3}{2})$ enhancement as the total angular momentum has to be zero. For (P,p) states enhancement due to pion-nucleon force can occur. Some information for the behavior of the σ_{11} reaction can be obtained from the study of the process $P+P\rightarrow\pi^0+P+P$. The two measurements of π^0 production at 345 Mev[7] and 430 Mev[8] seem to require a rapid energy dependence of the cross section and they are consistent with η_0^6 to η_0^8 variation of the cross section, where η_0 is the maximum pion momentum in the center-of-mass system, for a given neutron energy. Such an energy dependence can only arise from both the meson and nucleon both being emitted in P-states (see discussion below). Therefore it is assumed that transitions leading to (P,p) states are dominant for the σ_{11} reaction.

A. Angular Distributions

Since we consider only mesons produced in s- and p-states, the differential cross sections for the pure reactions σ_{01} and σ_{11} are, in general,

$$(d^2\sigma/d\omega dt)_{01}=A_{01}(t,t_0)+C_{01}(t,t_0)\cos^2\theta, \quad (15a)$$

$$(d^2\sigma/d\omega dt)_{11}=A_{11}(t,t_0)+C_{11}(t,t_0)\cos^2\theta, \quad (15b)$$

where t_0 is the maximum pion energy in the center-of-mass system for a given neutron energy T_N. In obtaining the angular distribution for either π^+ or π^- production, asymmetry can arise due to interference between transitions of the σ_{01} and σ_{11} reactions.

The dominant states $(^1S_0,p)_{0,1}$ and $(^3P_t,p)_{1,J}$ cannot interfere; hence asymmetry has to arise from other nondominant states, such as $(^1S_0,s)_{1,0}$ or $(^3P_1,s)_{0,1}$, interfering with the dominant states. The amount of admixture needed to give sizable asymmetry can be very small; consequently the contribution of the nondominant states to the total cross section would be negligible. Thus the constant term A and the coefficient C of the $\cos^2\theta$ term will be little affected by the presence of these interfering states. The constant term A and the coefficient C of the $\cos^2\theta$ term in the differential cross section for the π^+ or π^- angular distribution will therefor be proportional to each other; e.g.,

$$C_{01}=k_{01}A_{01}.$$

Hence we may write for the differential cross section for the production of negative pions:

$$2(d^2\sigma/d\omega dt)^-=\{1+k_{01}\cos^2\theta\}A_{01}(t,t_0)+(1+k_{11}\cos^2\theta)A_{11}(t,t_0)+B(t,t_0)\cos\theta. \quad (16a)$$

The asymmetry is given by the $\cos\theta$ term.

The coefficient of the $\cos\theta$ term has a different energy spectrum from both A_{01} and A_{11}. By charge symmetry, the corresponding equation for π^+ production is

$$2(d^2\sigma/d\omega dt)^+=(1+k_{01}\cos^2\theta)A_{01}(t,t_0)+(1+k_{11}\cos^2\theta)A_{11}(t,t_0)-B(t,t_0)\cos\theta. \quad (16b)$$

B. Energy Spectra

Let us define the pion energy spectra due to the dominant transitions of the reactions σ_{01} and σ_{11} as f_u and f_v respectively; then

$$A_{01}=h_{01}f_u(t,t_0); \quad A_{11}=h_{11}f_v(t,t_0), \quad (17a)$$

where h_{01} and h_{11} are constants.

Let us define the energy spectrum $B(t,t_0)$ by f_w; then

$$B(t,t_0)=k_wf_w(t,t_0), \quad (17b)$$

where k_w is a constant.

The final states assumed for the dominant transitions are $(^1S_0,p)_{0,1}$ for σ_{01} and $(^3P_t,p)_{1,J}$ for σ_{11} reactions, respectively. In calculating the energy spectra, the effects of final-state interactions have to be taken into account. There are two types of interactions which have to be considered: the meson-nucleon and the nucleon-nucleon interactions, respectively.

The meson-nucleon force is taken into account qualitatively in determining what states are dominant, and quantitatively in calculating the energy dependence of the cross section using the known variation of phase shift with energy. The distortion of the wave function from a plane wave due to the meson-nucleon force is not calculated in detail, but it is assumed that at the energies of the experiment this correction is energy-independent.

The nucleon-nucleon force is well known for the $^1S_0$ state, and it is taken into account in calculating the energy spectra following the method of phonomenological analysis given by Watson and others.[30,32] The pion spectrum, for a given neutron energy, for transitions leading to an $(^1S_0,p)_{0,1}$ state is given by[30]:

$$f_u(t,t_0)=\Lambda_u\frac{\eta^3(t_0-t)^{\frac{1}{2}}}{|B|+t_0-t}; \quad \Lambda_u=\frac{8}{3\pi}\left(\frac{2}{\mu}\right)^{\frac{1}{2}}; \quad (18)$$

where μ is the pion mass, $|B|$ is the binding energy of the nucleons in $^1S_0$ state and t_0 the maximum pion energy; η is the pion momentum in μc units; and t is the pion energy in the center-of-mass system. The constant Λ_u is so determined that in the nonrelativistic limit the integral of $f_u(t,t_0)$ from zero to the maximum energy t_0 is given by

$$\int_0^{t_0}f_u(t,t_0)dt\simeq\eta_0^4(1+\cdots),$$

where η_0 is the maximum pion momentum in μc units in the center-of-mass system. The numerator of (18) is the product of η^2/γ from the square of the matrix element for the production of a p-state pion and $\eta(t_0-t)^{\frac{1}{2}}\gamma$ which is the phase space available to the three final particles, where γ is the total pion energy in μc^2 units. The nucleon-nucleon force introduces the denominator[32] $(|B|+t_0-t)$.

For transitions leading to (P,p) states the effect of nuclear force is neglected, and therefore the denominator is absent. As the nucleons are emitted in P states the relative momentum of the nucleons appears in the matrix element. The resulting pion spectrum is

$$f_v(t,t_0)=\Lambda_v\eta^3(t_0-t)^{3/2}; \quad \Lambda_v=\frac{64}{3\pi}\left(\frac{4}{\mu}\right)^{5/2}, \quad (19)$$

where Λ_v is determined in the same way as for the previous spectrum, i.e., by requiring that

$$\int_0^{t_0}f_v(t,t_0)dt\cong\eta_0^8(1+\cdots)$$

in the nonrelativistic limit.

The asymmetry can arise from interactions between two nondominant states, e.g., $(^3P_0,p)_{0,1}$ with $(^3P_0,s)_{1,0}$, or between a dominant state and a nondominant state, e.g., $(^1S_0,p)_{0,1}$ with $(^1S_0,s)_{1,0}$. We shall neglect the contribution from the interaction between the two nondominant states. Then $B(t,t_0)$ is made up of two types

[32] K. M. Watson, Phys. Rev. 88, 1163 (1952); and Aitken, Mahmoud, Henley, Ruderman, and Watson, Phys. Rev. 93, 1349 (1954).

of terms: (1) a term due to interference of an (S,p) state of σ_{01} with an (S,s) state of σ_{11} reaction, and (2) a term due to interference of a (P,p) state of reaction σ_{11} with a (P,p) state of σ_{01} reaction. Following phenomenological analysis similar to that used for the pure isotopic spin reactions, we obtain the energy spectra for the coefficient of the $\cos\theta$ term. The energy spectrum for the term of type (1) is

$$f_{w1}=\Lambda_{w1}\frac{\eta^2(t_0-t)^{\frac{1}{2}}}{|B|+t_0+t};\quad \Lambda_{w1}=\frac{3}{\sqrt{8}}\frac{1}{\sqrt{\mu}} \tag{20}$$

and that for the term of type (2) is

$$f_{w2}=\Lambda_{w2}\eta^2(t_0-t)^{3/2};\quad \Lambda_{w2}=\frac{35}{\sqrt{2}}\frac{1}{\mu^{5/2}}. \tag{21}$$

Therefore coefficient $B(t,t_0)$ is given by

$$B(t,t_0)=kf_w(t,t_0)=k_{w1}f_{w1}+k_{w2}f_{w2},$$

where k_{w1} and k_{w2} are constants.

The total cross section is best analyzed in terms of the sum of positive- and negative-pion cross sections, where the interference term does not appear. From Eqs. (16a) and (16b), we get

$$(d^2\sigma/d\omega dt)^+ + (d^2\sigma/d\omega dt)^- = (a_1+b_1\cos^2\theta)f_u(t,t_0) + (a_2+b_2\cos^2\theta)f_v(t,t_0), \tag{22}$$

where $a_1=h_{01}$, $b_1=h_{01}k_{01}$, $a_2=h_{11}$, $b_2=h_{11}k_{11}$. Integrating over the pion energy spectrum, we get the differential cross section for $(\pi^+ + \pi^-)$ to be:

$$(d\sigma/d\omega)^+ + (d\sigma/d\omega)^- = (a_1+b_1\cos^2\theta)\left[4Z^2\left(1-\frac{Z}{4(2+Z)}\right)\left(1+\frac{Z}{2}\right)^2\right] + (a_2+b_2\cos^2\theta)[16Z^4(1+3Z/8)], \tag{23}$$

where $Z=t_0/\mu c^2$.

The asymmetry is directly measured by the difference of the positive- and negative-pion cross sections. From Eqs. (16a) and (16b), we get

$$(d^2\sigma/d\omega dt)^+ - (d^2\sigma/d\omega dt)^- = -B(t,t_0)\cos\theta = -[k_{w1}f_{w1}+k_{w2}f_{w2}]\cos\theta. \tag{24}$$

By integrating over the pion energy, the magnitude of the interference term at any angle is obtained to be

$$(d\sigma/d\omega)^+ - (d\sigma/d\omega)^- = -\{k_{w1}[2\sqrt{2}Z^{3/2}(1+\tfrac{2}{3}Z_0 - \tfrac{3}{8}\pi(2+Z_0)\sqrt{b})]+k_{w2}[8\sqrt{2}Z^{7/2}(1+2Z/9)]\}\cos\theta, \tag{25}$$

where $Z=t_0/\mu c^2$; $b=|B|/t_0$.

At nonrelativistic energies these differential cross sections become

$$(d\sigma/d\omega)^+ + (d\sigma/d\omega)^- \cong (a_1+b_1\cos^2\theta)\eta_0^4 + (a_2+b_2\cos^2\theta)\eta_0^8, \tag{23a}$$

$$(d\sigma/d\omega)^+ - (d\sigma/d\omega)^- \cong -(k_{w1}\eta_0^3+k_{w2}\eta_0^7)\cos\theta, \tag{25a}$$

where η_0 is the maximum momentum of the pion in the center-of-mass system in μc units for a given neutron energy.

VII. CALCULATION OF CENTER-OF-MASS CROSS SECTIONS AT A SINGLE NEUTRON ENERGY

A. Total Cross Section

The experimental cross sections for the sum of positive and negative pions at any angle are now expressed in terms of the center-of-mass cross section. The integration over the neutron spectrum and the average over the angular acceptance in Eq. (12) is then carried out. By using Eq. (22), Eq. (12) becomes:

$$[(d^2\sigma/d\Omega dT)^+ + (d^2\sigma/d\Omega dT)^-]_{Av} = \frac{1}{\Delta\Theta}\int_{\Theta_{\min}}^{\Theta_{\max}}\frac{P}{p}d\Theta\int_0^{t_{0\max}}\{(a_1+b_1\cos^2\tilde{\theta})f_u + (a_2+b_2\cos^2\tilde{\theta})f_v\}g(t_0)dt_0.$$

The effective pion spectra $u(t)$ and $v(t)$ in the center-of-mass system are defined by

$$u(t)=\int_0^{t_{0\max}} f_u(t,t_0)g(t_0)dt_0,$$

$$v(t)=\int_0^{t_{0\max}} f_v(t,t_0)g(t_0)dt_0.$$

The experimental cross section is then given by

$$[(d^2\sigma_{Av}/d\Omega dT)^+ + (d^2\sigma_{Av}/d\Omega dT)^-]_\Theta = a_1\alpha_1(T,\Theta) + b_1\beta_1(T,\Theta) + a_2\alpha_2(T,\Theta) + b_2\beta_2(T,\Theta), \tag{26}$$

where α_1, β_1, α_2, and β_2 are the effective pion spectra transformed to the laboratory system and averaged over the angular acceptance, after being multiplied by the appropriate weighting factor of unity or $\cos^2\theta$. They are given by

$$\alpha_1(T,\Theta)=\frac{1}{\Delta\Theta}\int_{\Theta_{\min}}^{\Theta_{\max}}d\Theta\frac{P}{p}u(t),$$

$$\alpha_2(T,\Theta)=\frac{1}{\Delta\Theta}\int_{\Theta_{\min}}^{\Theta_{\max}}d\Theta\frac{P}{p}v(t),$$

$$\beta_1(T,\Theta)=\frac{1}{\Delta\Theta}\int_{\Theta_{\min}}^{\Theta_{\max}}d\Theta\frac{P}{p}\cos^2\tilde{\theta}u(t),$$

$$\beta_2(T,\Theta)=\frac{1}{\Delta\Theta}\int_{\Theta_{\min}}^{\Theta_{\max}}d\Theta\frac{P}{p}\cos^2\tilde{\theta}v(t).$$

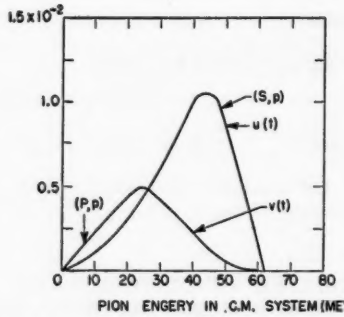

FIG. 14. Effective pion spectra $u(t)$ and $v(t)$ in the center-of-mass system.

The effective pion spectra in the center-of-mass system, $u(t)$ and $v(t)$ for the $(S,\frac{1}{2})$ and the $(P,\frac{1}{2})$ states respectively are shown in Fig. 14. The laboratory functions α_1, β_1, α_2, and β_2 calculated at the two angles of the experiment, 90° and 65°, are shown in Figs. 15 and 16. They are calculated for pion energies greater than the threshold of the detector.

The coefficients a_1, b_1, a_2, b_2 can be determined from the experimental spectrum for $(\pi^+ + \pi^-)$ at 90° alone. However, the functions α_1, β_1 and α_2, β_2 are sufficiently similar in shape to make it impossible to evaluate a_1 b_1 or a_2 and b_2 separately from the 90° data alone. Moreover it is a good approximation to take functions α_1, β_1 and α_2, β_2 to be proportional to each other, i.e.,

$$\beta_1 = l_1\alpha_1, \quad \beta_2 = l_2\alpha \quad \text{for } \Theta = 90°,$$

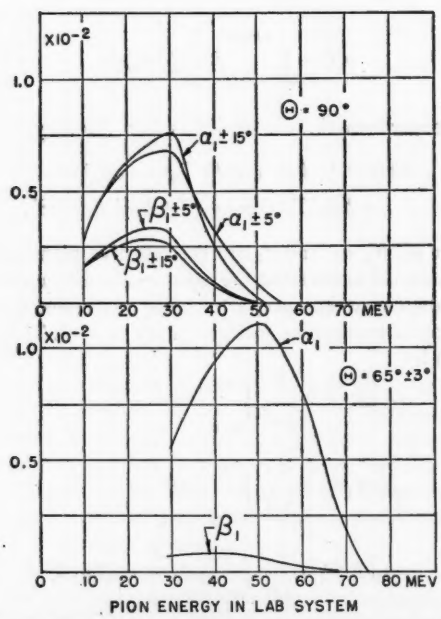

FIG. 15. Effective pion spectra for the two runs transformed to the laboratory system and averaged over the angular acceptance, for the $(S,\frac{1}{2})$ final states.

where l_1 and l_2 are constants, whose value is equal to the average of $\cos^2\theta$; then the 90° cross section can be written as:

$$[(d^2\sigma_{Av}/d\Omega dT)^+ + (d^2\sigma_{Av}/d\Omega dT)^-]_{90°} = C_1\alpha_1(T,90°) + C_2\alpha_2(T,90°), \quad (27)$$

where $C_1 = a_1 + l_1b_1$, $C_2 = a_2 + l_2b_2$; $l_1 = l_2 = \langle\cos^2\theta\rangle_{Av} = 0.36$.

The mean 90° spectrum for the sum of positive and negative pions was fitted, using a least-squares method, by the function previously given. In the analysis the results of the two runs were combined and the density of events

$$(dn/dT)^+ + (dn/dT)^-$$

was expressed in terms of the functions α_1 and α_2 calculated for the different geometries of the two runs. Thus the combined density of events is given by

$$\left(\frac{dn}{dT}\right)^+ + \left(\frac{dn}{dT}\right)^- = C_1\left\{\frac{\alpha_{11}}{G_1} + \frac{\alpha_{12}}{G_2}\right\} + C_2\left\{\frac{\alpha_{21}}{G_1} + \frac{\alpha_{22}}{G_2}\right\},$$

where the factor G is obtained from Eq. (10) as

$$G = N_n\rho_H\epsilon\eta f l_H(1/r^2)_{Av},$$

and G_1, α_{11}, α_{12}, and G_2, α_{21}, α_{22} are the values of G, α_1, and α_2 calculated for the two runs respectively. Table V gives the pertinent data for the least-squares analysis. In estimating the error in dn/dT, the errors in determining the length of hydrogen and in the number of neutrons incident are taken into account.

The values of the coefficients determined are:

$$C_1 = (1.57 \pm 0.35) \times 10^{-29} \text{ cm}^2/\text{sterad},$$
$$C_2 = (4.87 \pm 2.05) \times 10^{-29} \text{ cm}^2/\text{sterad}.$$

The correlation coefficient $\langle\Delta C_1 \Delta C_2\rangle_{Av}$ is equal to 0.305×10^{-58}. The weighted least-square sum

$$M = \sum(\Delta_i/X_i)^2,$$

where Δ_i are the deviation of the calculated value from the experimental value and X_i are the experimental errors in the ith measurement, was found to be 1.15. As the degrees of freedom for fitting are 3 this indicates a good fit to the data.

The smallness of the contribution of the $\cos^2\theta$ term at 65° is evident from the comparison of areas under the β_1, β_2 curves and α_1, α_2 curves in Figs. 15(b) and 16(b). Hence neglecting the β_1 and β_2 terms we may write the 65° cross section as:

$$[(d^2\sigma_{Av}/d\Omega dT)^+ + (d^2\sigma_{Av}/d\Omega dT)^-]_{65°} = a_1\alpha_1(T,65°) + a_2\alpha_2(T,65°).$$

A most probable fit of this function to the events observed was made using the method of maximum likelihood and the best values for coefficients a_1 and a_2 were

TABLE V. Density of $(\pi^+ + \pi^-)$ events at 90° in the laboratory system, and values of functions $\{(\alpha_{11}/G_1)+(\alpha_{12}/G_2)\}$ and $\{(\alpha_{21}/G_1)+(\alpha_{22}/G_2)\}$ used to calculate the coefficients C_1 and C_2.

Pion energy at center of hydrogen (Mev)	Total number of $(\pi^+ + \pi^-)$ mesons in energy band for both runs corrected for background	G_1 (In units of 10^{-28} cm² per sterad)	G_2	α_{11}/G_1	α_{12}/G_2 (In units of 10^{29} per Mev)	α_{21}/G_1	α_{22}/G_2
14–20	104.6 ±12.0	1.99	2.72	2.65	2.0	1.215	0.890
20–26	102.3 ±12.3	2.14	2.91	2.95	2.23	0.874	0.584
26–32	65.6 ± 9.5	2.26	3.19	2.92	2.26	0.451	0.256
32–38	33.64± 6.6	2.61	3.51	1.85	1.21	0.160	0.0855
38–44	16.12± 5.05	2.90	3.87	0.912	0.512	0.0231	0

found to be

$$a_1=(0.134\pm0.36)\times10^{-29}\ \text{cm}^2/\text{sterad},$$
$$a_2=(7.08\pm2.58)\times10^{-29}\ \text{cm}^2/\text{sterad}.$$

The correlation coefficient $\langle\Delta a_1\Delta a_2\rangle_{Av}$ is equal to -0.58×10^{-58}. Combining these with the values of C_1 and C_2 determined above, we obtain the values for the coefficients of the $\cos^2\theta$ term to be

$$b_1=(3.99\pm1.37)\times10^{-29}\ \text{cm}^2/\text{sterad},$$
$$b_2=(-6.14\pm9.1)\times10^{-29}\ \text{cm}^2/\text{sterad}.$$

The correlation coefficient $\langle\Delta b_1\Delta b_2\rangle_{Av}$ is equal to -8.04×10^{-58}.

The center-of-mass differential cross section for the production of $(\pi^+ + \pi^-)$ mesons at a single neutron energy $T_N(t_0)$ is given by

$$(d^2\sigma/d\omega dT)^+ + (d^2\sigma/d\omega dT)^- = \{(0.134\pm0.36)+(3.99\pm1.37)\cos^2\theta\}f_u + \{(7.08\pm2.58)+(-6.41\pm9.1)\cos^2\theta\}f_v \times10^{-29}\ \text{cm}^2/\text{sterad Mev}.$$

The total cross section for the production of $(\pi^+ + \pi^-)$ mesons is obtained by integrating over the energy and the angle of the pion:

$$\sigma(\pi^+ + \pi^-)=4\pi\left\{(1.46\pm0.56)\int_0^{t_0}f_u dt + (5.04\pm3.96)\int_0^{t_0}f_v dt\right\}\times10^{-29}\ \text{cm}^2.$$

This is evaluated at a neutron energy for which the result is least sensitive to the exact shape of the energy spectra and excitation functions. At $T_N=409$ Mev, the pure-isotopic-spin-reaction cross sections are calculated to be:

$$\sigma_{01}=(0.134\pm0.051)\ \text{mb},\quad \sigma_{11}=(0.183\pm0.143)\ \text{mb}.$$

Hence the total cross section is

$$\sigma(\pi^+ + \pi^-)=\sigma_{01}+\sigma_{11}=(0.317\pm0.147)\ \text{mb}. \quad (28)$$

From the experimental cross section at $\Theta=90°$ coefficients C_1 and C_2 have been calculated, and the differential cross section at the corresponding center-of-mass angle is

$$\left[\left(\frac{d\sigma}{d\omega}\right)^+ + \left(\frac{d\sigma}{d\omega}\right)^-\right]_{\Theta=90°} = (a_1+b_1\langle\cos^2\theta\rangle_{Av})\int_0^{t_0}f_u dt + (a_2+b_2\langle\cos^2\theta\rangle_{Av})\int_0^{t_0}f_v dt,$$

where θ is such that $\langle\cos^2\theta\rangle_{Av}=0.36$ or almost equal to $\frac{1}{3}$. Hence the total cross section can be obtained directly from their differential cross section by

$$\sigma(\pi^+ + \pi^-)=4\pi[(d\sigma/d\omega)^+ + (d\sigma/d\omega)^-]_{90°};$$

at $T_N=409$ Mev this is

$$\sigma(\pi^+ + \pi^-)=(0.321\pm0.082)\ \text{mb}. \quad (29)$$

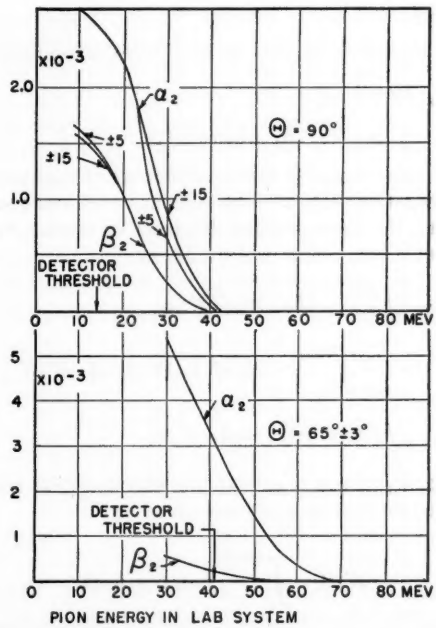

FIG. 16. Effective pion spectra for the two runs transformed to the laboratory system and averaged over the angular acceptance for the (P,ϕ) final states.

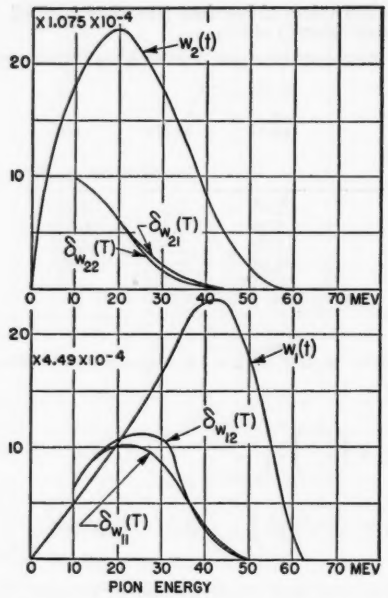

FIG. 17. Effective pion spectra in the center-of-mass system and transformed to the laboratory system for two types of interference terms.

This more accurate value is in agreement with that fetermined using the complete angular distribution obtained from both the 90° and 65° data [Eq. (28)].

Using Eq. (14) the total cross section for π^+ or π^- production is

$$\sigma(\pi^+)=\sigma(\pi^-)=\tfrac{1}{2}\sigma(\pi^++\pi^-)=(0.16\pm0.04)\text{ millibarn}$$

at $T_N=409$ Mev.

B. Asymmetry

By using Eq. (24) for the difference of the positive- and negative-pion cross sections in the center-of-mass system, the corresponding difference in the laboratory system is obtained from Eq. (12) as:

$$[(d^2\sigma_{Av}/d\Omega dT)^+-(d^2\sigma_{Av}/d\Omega dT)^-]_\Theta$$
$$=\frac{1}{\Delta\Theta}\int_{\Theta_{\min}}^{\Theta_{\max}}\frac{P}{p}\cos\theta d[k_{w1}W_1(t)+k_{w2}W_2(t)]$$
$$=k_{w1}\delta w_1(T,\Theta)+k_{w2}\delta w_2(T,\Theta), \qquad (30)$$

where $W_1(t)$ and $W_2(t)$ are the effective pion spectra in the center-of-mass system, given by

$$W_1(t)=\int_0^{t_0\max} f_{w1}(t,t_0)g(t_0)dt_0;$$

$$W_2(t)=\int_0^{t_0\max} f_{w2}(t,t_0)g(t_0)dt_0,$$

and the corresponding laboratory functions are given by

$$\delta w_1(T,\Theta)=\frac{1}{\Delta\Theta}\int_{\Theta_{\min}}^{\Theta_{\max}}\frac{P}{p}\cos\tilde{\theta}w_1(t)d\Theta,$$

$$\delta w_2(T,\Theta)=\frac{1}{\Delta\Theta}\int_{\Theta_{\min}}^{\Theta_{\max}}\frac{P}{p}\cos\tilde{\theta}w_2(t)d\Theta.$$

All these four functions w_1, w_2, δw_1, and δw_2 are shown in Fig. 17 calculated for $\Theta=90°$ for the two runs.

The mean 90° spectrum for the difference of π^+ and π^- mesons was fitted, by using a least-squares method, with the function given in Eq. (30). Here again in analyzing the data, the results of the two runs were combined and the total density of $(\pi^+-\pi^-)$ events was expressed in terms of the functions δw_1 and δw_2 by the equation

$$\frac{dn^+}{dT}-\frac{dn^-}{dT}=k_{w1}\left\{\frac{\delta w_{11}}{G_1}+\frac{\delta w_{12}}{G_2}\right\}+k_{w2}\left\{\frac{\delta w_{21}}{G_1}+\frac{\delta w_{22}}{G_2}\right\},$$

where G is the same factor as defined in the analysis of the sum of $(\pi^++\pi^-)$ events, G_1, δw_{11}, δw_{12} and G_2, δw_{21}, δw_{22} are the values of G, δw_1, and δw_2 calculated for the geometries of the two runs respectively. The data required for the least-squares analysis of the difference spectrum are given in Table VI. The values of the coefficients k_{w1} and k_{w2} are determined to be:

$$k_{w1}=(0.72\pm0.54)\times10^{-29}\text{ cm}^2/\text{sterad},$$
$$k_{w2}=(6.98\pm4.77)\times10^{-29}\text{ cm}^2/\text{sterad}.$$

The correlation coefficient $\langle\Delta k_{w1}\Delta k_{w2}\rangle_{Av}$ is equal to $-2.28\ 10^{-58}$. The weighted least-squares sum $M=\sum(\Delta_i/X_i)^2$ is 0.02 and the degrees of freedom one.

The coefficient of the $\cos\theta$ term is given by

$$B(t,t_0)=\{(0.72\pm0.54)f_{w1}+(6.98\pm4.77)f_{w2}\}$$
$$\times10^{-29}\text{ cm}^2/\text{sterad Mev}.$$

The coefficient integrated over the pion energy, for the neutron energy $T_N=409$ Mev, is

$$\int_0^{t_0}B(t,t_0)dt=(2.763\pm1.59)\times10^{-29}\text{ cm}^2/\text{sterad}.$$

Therefore the differential cross section for charged pion production in neutron-proton collisions at a single neutron energy $T_N(t_0)$ is determined to be:

$$(d^2\sigma/d\omega dt)^\pm$$
$$=\{[(0.067\pm0.18)f_u+(3.54\pm1.29)f_v]$$
$$+[(2.0\pm0.69)f_u+(-3.07\pm4.5)f_v]\cos^2\theta$$
$$\mp[(0.36\pm0.27)f_{w1}+(3.49\pm2.39)f_{w2}]\cos\theta\}$$
$$\times10^{-29}\text{ cm}^2/\text{sterad Mev}.$$

The differential cross section, integrated over pion energy, for a single neutron energy $T_N=409$ Mev, is

calculated to be

$$(d\sigma/d\omega)^{\pm}=\{(1.07\pm0.39)\mp(1.38\pm0.78)\cos\theta + (0.57\pm1.40)\cos^2\theta\}\times10^{-29}\ \text{cm}^2/\text{sterad}.$$

VIII. CONCLUSIONS

The differential cross sections and energy spectra for the production of charged pions in neutron-proton collisions have been measured at two laboratory angles, $\Theta=90°$ and 65°. The number of positive and negative pions at 65° (corresponds to 90° in the center-of-mass system) are roughly equal, while at 90° the ratio of positive to negative pions is 2.01 ± 0.24.

The total cross section for π^+ or π^- production at the neutron energy $T_N=409$ Mev is determined to be

$$\sigma(\pi^+)=\sigma(\pi^-)=(0.16\pm0.04)\ \text{mb}.$$

Because of the experimental low-energy cutoff for the pions, $\frac{2}{3}$ at most of the total pion energy spectrum at each angle was observed. Further, the pions observed were produced by neutrons of all energies from threshold for pion production to the maximum energy in the neutron beam. Hence, in orer to calculate the cross section at a single neutron energy, it was necessary to assume reasonable energy spectra and excitation functions for the reaction. This was done in a phenomenological way under the hypothesis of charge independence. From the experimental results, the contributions from these various assumed spectra were determined and the above total cross section calculated at a single neutron energy. The cross section is quoted at a neutron energy for which the result is least sensitive to the exact shape for the energy spectra and the excitation functions assumed. This is possible because the neutron beam has a sharp high-energy peak in its spectrum.

The angular distribution in the center-of-mass system at neutron energy $T_N(t_0)=409$ Mev was determined to be:

$$(d\sigma/d\omega)^{\pm}=\{(1.07\pm0.39)\mp(1.38\pm0.78)\cos\theta + (0.57\pm1.4)\cos^2\theta\}\times10^{-29}\ \text{cm}^2/\text{sterad}.$$

TABLE VI. Density of $(\pi^+-\pi^-)$ events at 90° in the laboratory system, and values of functions $(\delta\omega_{11}/G_1)+(\delta\omega_{12}/G_2)$ and $(\delta\omega_{21}/G_1)+(\delta\omega_{22}/G_2)$ used to calculate the coefficients $k\omega_1$ and $k\omega_2$.

Pion energy at center of hydrogen (Mev)	Total number of $(\pi^+-\pi^-)$ mesons in energy band for both runs corrected for background	G_1 (In units of 10^{-33} cm² per sterad)	G_2	$\left[\frac{\delta\omega_{11}}{G_1}+\frac{\delta\omega_{12}}{G_2}\right]$ (In units of 10^{29} per Mev)	$\left[\frac{\delta\omega_{21}}{G_1}+\frac{\delta\omega_{22}}{G_2}\right]$ (In units of 10^{29} per Mev)
14.0–21.5	55.2 ±12.5	2.015	2.750	3.807	0.6582
21.5–31.5	44.1 ±13.1	2.26	3.085	3.471	0.2621
31.5–50.0	15.05± 8.25	2.92	3.89	0.7748	0.0300

In determining the coefficient of the $\cos\theta$ term there is a large uncertainty not shown by the error quoted, which is due to the lack of knowledge of the number of states contributing.

The cross sections for the pure isotopic spin reactions σ_{01} and σ_{11} are calculated to be:

$$\sigma_{01}=(0.131\pm0.051)\ \text{mb},\quad \sigma_{11}=(0.183\pm0.143)\ \text{mb},$$

$$\text{at } T_N=409\ \text{Mev}.$$

It is seen that at the energy of the experiment the magnitude of the σ_{11} cross section is comparable to the σ_{01} cross section. The value for the σ_{11} cross section can be compared to the value estimated by Rosenfeld[30] from the measurement of the cross section of π^0 production in proton-proton collisions at 345 and 430 Mev. The estimated value of 0.1 mb is consistent with (0.183 ± 0.143) mb determined in this experiment.

IX. ACKNOWLEDGMENTS

It is indeed a great pleasure to acknowledge the excellent guidance of Professor H. L. Anderson throughout this research. I wish to thank Dr. Roger H. Hildebrand for his interest in the problem and for his active help throughout the course of the experiment. I also thank Dr. Arthur Rosenfeld and Dr. Frank Solmitz for many stimulating discussions and useful suggestions. Thanks are due to Tadao Fujii and Joseph Fainberg, for their help in conducting the experiment and assembling the equipment; to the cyclotron staff for their excellent cooperation during the experiment; and to the scanners J. T. Lach and Meera Backus.

Solar Flare and Magnetic Storm Effects in Cosmic-Ray Intensity near the Geomagnetic N Pole

JOHN W. GRAHAM AND SCOTT E. FORBUSH
Department of Terrestrial Magnetism, Carnegie Institution of Washington, Washington, D. C.

(Received January 20, 1955)

During the solar flare of July 25, 1946 an increase of 14 percent in hourly mean values of cosmic-ray ionization was observed at Thule, Greenland (geomagnetic latitude 88°N) at sea level, under 11 cm Pb. The increase and its gradual diminution toward normal during the 24 hours after the flare was statistically indistinguishable from results at Godhavn, Greenland (geomagnetic latitude 80°N). The subsequent decrease during the magnetic storm, which began 27 hours after the flare, was also in agreement at Thule and Godhavn. If the increase were due to charged particles from the sun, these observations at Thule emphasize the fact that the trajectories involved are markedly affected by factors other than the earth's magnetic dipole.

DURING the past decade or so, four large increases in cosmic-ray intensity began[1] within an hour or less after the onset of a solar flare. These increases were ascribed[2] to charged particles arriving from the sun. Efforts to answer the question of how such particles might accelerate, escape through the sun's magnetic field, and reach the earth were only partially successful.[3] The expected geographical distribution of "impact zones" for these cosmic-ray increases has been calculated by Schlüter[4] and Firor[5] for particles coming from the sun with no solar magnetic field. While the calculated impact zones are compatible with the meager observations[5] between geomagnetic latitudes from 60°S to 60°N, the calculations[4,5] indicate that no increase should be observed at geomagnetic latitudes greater than about 60°N or S. As the authors[4,5] point out, this conclusion is at variance with the fact that increases of cosmic-ray intensity were observed at Godhavn, geomagnetic latitude 80°N, during each of four flares and that an increase occurred at resolute,[6] geomagnetic latitude 83°N during the flare of November 19, 1946.

The increase of cosmic-ray ionization during the solar flare of July 25, 1946, was observed by one of us (J.W.G.), very near the geomagnetic N pole, while serving as technical observer for the Applied Physics Laboratory, The Johns Hopkins University, on the Navy's arctic operation Nanook. We are grateful to the Applied Physics Laboratory for making available to us

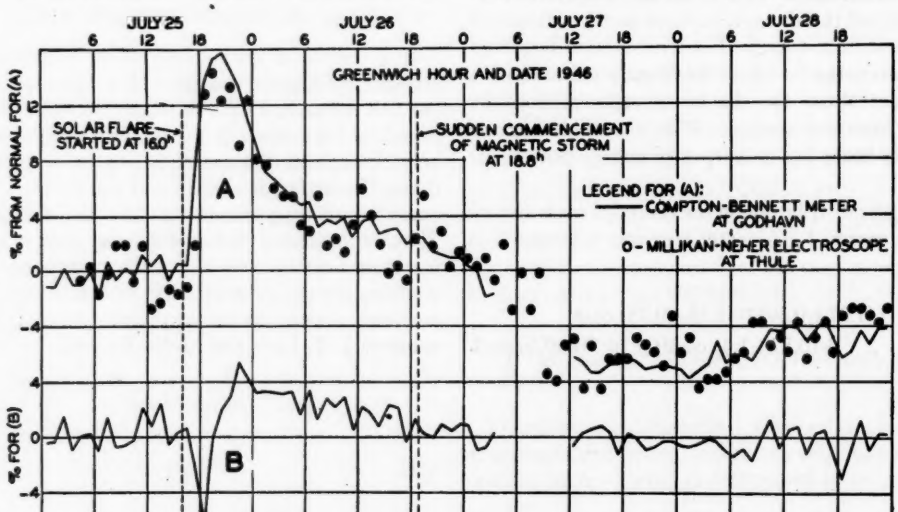
JULY 25
JULY 26
JULY 27
JULY 28
6 12 18 0 6 12 18 0 6 12 18 0 6 12 18
GREENWICH HOUR AND DATE 1946
% FROM NORMAL FOR (A)
SOLAR FLARE STARTED AT 16.0h
SUDDEN COMMENCEMENT OF MAGNETIC STORM AT 18.8h
A
LEGEND FOR (A):
COMPTON-BENNETT METER AT GODHAVN
O - MILLIKAN-NEHER ELECTROSCOPE AT THULE
% FOR (B)
B

FIG. 1. (A) Hourly means of cosmic-ray ionization at Thule and at Godhavn, Greenland. (B) Hourly means at Godhavn less hourly means at Cheltenham.

[1] Forbush, Stinchcomb, and Schein, Phys. Rev. **79**, 501 (1950).
[2] S. E. Forbush, Phys. Rev. **70**, 771 (1946).
[3] Forbush, Gill, and Vallarta, Revs. Modern Phys. **21**, 44 (1949).
[4] A. Schlüter, Z. Naturforsch. **6a**, 613 (1951).
[5] John Firor, Phys. Rev. **94**, 1017 (1954).
[6] D. C. Rose, Can. J. Phys. **29**, 227 (1951).

the Millikan-Neher records and a recently declassified report (by J.W.G.) describing the cosmic-ray effects at Thule. The results (shown by the open circles) in Fig. 1 were obtained aboard ship at Thule, Greenland, geomagnetic latitude 88°N, with a Carnegie Institution of Washington Millikan-Neher electroscope shielded by 11 cm Pb.

Since the range in barometric pressure at Thule was less than 4 mm Hg over the period covered in Fig. 1, corrections to the observed ionization were neglected. The agreement between hourly values at Thule and those at Godhavn where the applied barometric corrections were also nearly constant, is best indicated by the fact that the standard deviation of differences between hourly values in Fig. 1(A) is only 2.0 percent which is about what is expected from these two meters running at the same location.

The increase at Thulé on July 25, 1946 emphasizes the fact that if the increase were due to charged particles from the sun, then the arrival of such particles so near the geomagnetic pole requires explanation. The effect may possibly be explained if the particles from the sun are deflected in magnetic fields carried away from the sun in highly conducting clouds, although such effects would also likely alter the position of impact zones as computed by Schlüter[4] and Firor.[5] While the cosmic-ray increase, at Godhavn, on July 25 is similar to that at Cheltenham[1] (geomagnetic latitude 50°N), curve B of Fig. 1 for the differences in hourly values shows deviations between 18 hr July 25 and 12 hr July 26, that are statistically significant in view of the quiet barometric conditions at both stations.

Figure 1(A) shows that the decrease in cosmic-ray intensity during the magnetic storm beginning July 26, was the same at Thule as at Godhavn, where it was similar to the world-wide decrease at other stations.[1]

It is interesting to note that for about 72 hours after the onset of the solar flare, no radio signals from WWV at 5, 10, and 15 Mc/sec could be received at Thule, although on frequencies from 15 to 80 kc/sec, signal reception was unusually good from all parts of the world.

PHYSICAL REVIEW VOLUME 98, NUMBER 5 JUNE 1, 1955

Diffusion Cloud-Chamber Study of Very Slow Mesons.* I. Internal Pair Formation

C. P. SARGENT,† R. CORNELIUS,‡ M. RINEHART, L. M. LEDERMAN, AND K. ROGERS
Department of Physics, Columbia University, New York, New York

(Received January 10, 1955)

A beam of negative pi and mu mesons was moderated to very low energies and allowed to enter a hydrogen-filled 20-atmosphere continuously sensitive cloud chamber. The various phenomena were observed and classified. A detailed study was made of the internal pair formation of mesonic gamma rays produced in the pion-hydrogen reactions. The conversion coefficient for the reaction $\pi^0 \rightarrow \gamma + e^+ + e^-$ was found to be 0.0053 ± 0.0009; for the reaction $\pi^- + p \rightarrow n + e^+ + e^-$ the coefficient is 0.0062 ± 0.0013. Distributions in angle and energy were obtained from thirty-five of the forty-seven observed cases.

A. INTRODUCTION

THE development of the continuously sensitive high-pressure cloud chamber as a practical instrument of research[1] has opened new areas of investigation in particle physics. When accompanied by a precisely known, homogeneous magnetic field and suitable optics, it constitutes a powerful tool for precise measurements as well as for observations of rare processes. In this paper we describe the application of such an instrument to the observation of pi and mu mesons which are moderated and come to rest in the 19.4 atmosphere pressure of hydrogen gas that constitutes the chamber filling.

Earlier experiments[2] in this domain have consisted of a pair spectrometer study of high-energy gamma rays associated with π^- mesons stopping in high-pressure hydrogen gas. A broad peak in the spectrum was observed, centered about 70 Mev and attributed to the reaction:

$$\pi^- + p \rightarrow \pi^0 + n; \quad \pi^0 \rightarrow 2\gamma. \tag{1}$$

This assignment was confirmed by the counter detection of coincidences between the π^0 gamma rays.[3] Additional information was obtained from a study of the angular correlation of the two gamma rays.[4] The spectrum also yielded a sharper peak at about 130 Mev which was interpreted as the radiative capture reaction:

$$\pi^- + p \rightarrow n + \gamma. \tag{2}$$

* This research was supported in part by the joint program of the Office of Naval Research and the U. S. Atomic Energy Commission.

† Now at Laboratory for Nuclear Science, Massachusetts Institute of Technology, Cambridge, Massachusetts.

‡ Richard C. Cornelius, an Atomic Energy Commission predoctoral fellow, was principal designer of the diffusion cloud chamber before his untimely death in New York City, in July, 1952.

[1] R. P. Shutt, Rev. Sci. Instr. 22, 730 (1951).

[2] Panofsky, Aamodt, and Hadley, Phys. Rev. 81, 565 (1951).

[3] J. Steinberger and A. Sachs, Phys. Rev. 82, 973 (1951).

[4] W. Chinowsky and J. Steinberger, Phys. Rev. 95, 1561 (1954)

The ratio of the rates of (1) and (2) was found to be 0.94 ± 0.20.

The present experiment is one of a series which will study the behavior of very slow mesons in gases. The primary objective of this first run was the observation of the internal pair production of the γ rays of reactions (1) and (2). The same series of photographs contain about 850 negative mu meson endings with associated decay electrons. The spectrum of these decay electrons will constitute Part II of this series.

B. APPARATUS AND TECHNIQUE

1. Cloud Chamber and Magnet

Recently the Brookhaven diffusion chamber group has described a chamber and its operation with the Nevis cyclotron.[5] The Columbia chamber resembles the Brookhaven chamber in design and operation characteristics.

The chamber was filled with hydrogen to a pressure of 19.4 atmospheres. Since the experiment required a rather heavy ion load, it was necessary to maintain a 8°C/cm temperature gradient over the sensitive layer. This was accomplished by supplying 400 watts to the chamber wall at a point 1.4 inches above the top of the sensitive layer. The top plate with its associated vapor source was kept at +12°C. Temperatures were measured by thermistors set in the chamber wall.

The magnet is made of Helmholtz coils mounted in a soft iron shell. The shell, when saturated, adds 30 percent to the field without destroying the uniformity of the field. A Leeds and Northrup recording potentiometer operating across a shunt in series with the magnet recorded the magnet current. Marks were also made on this record when the cyclotron was pulsed. The recording system was calibrated dynamically against a proton resonance fluxmeter.

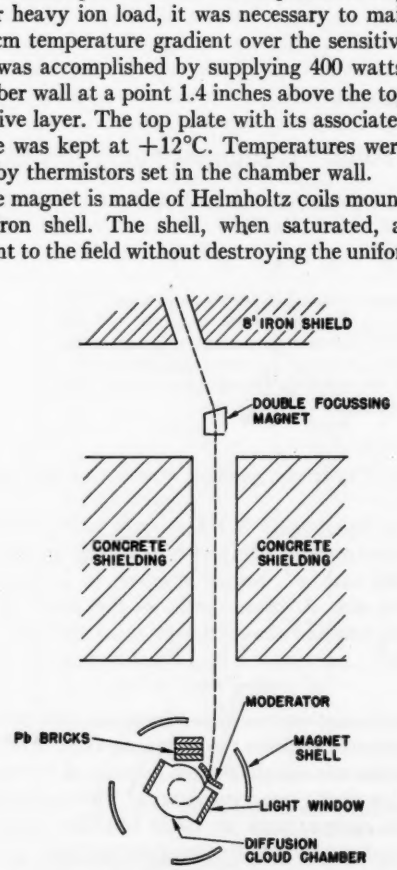

FIG. 1. Diffusion cloud-chamber exposure geometry at the Nevis cyclotron.

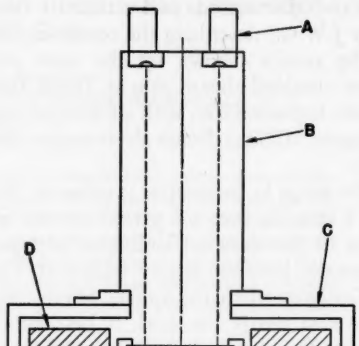

FIG. 2. Cross section of diffusion cloud chamber illustrating the optics and magnetic field. *A* are cameras; *B* is a light tight camera support; *C* is mild steel casing 2 in. thick; *D* hollow copper windings; *E* is black glass fiduciary plane.

2. Operation with the Cyclotron

The position of the cloud chamber relative to the 85-Mev π^- beam is shown in Fig. 1. A representative trajectory of a meson which stops in the chamber is also indicated. The beam is slowed in copper and in the chamber walls and is allowed to enter only the west side of the chamber, for the most part via the wall of a light portal. This mode of entrance in combination with the momentum resolving power of the cloud chamber magnet is useful in obtaining a large ratio of the number of slow mesons to the total number of mesons entering the main volume of the chamber. This arrangement resulted in an average of one meson stopping in the gas per three photographs.

In this series of pictures, the relatively low stopping power of the chamber gas made necessary the use of a very large flux of particles. These were obtained by double magnetic focusing of the meson beam (Fig. 1) and by the use of 4 to 8 cyclotron bursts. The resulting large background, consisting of electrons and neutron recoils, as well as heavily ionizing slow mesons, represents a large ion-load from which it is necessary to give the chamber time to recover. This dictated the choice of ten seconds as the photographic repetition rate.

[5] Fowler, Fowler, Shutt, Thorndyke, and Whittemore, Phys. Rev. 91, 135 (1953).

3. Measurement Procedure

One of the largest sources of error in conventional cloud chamber measurements is the turbulent distortions of tracks produced by the gas motion in the expansion. The absence of such motion in the diffusion chamber allows the possibility of considerably increased precision in angle and momentum measurements. The present arrangement capitalizes on this feature by providing in addition (1) a homogeneous magnetic field to minimize difficult corrections due to variations in H and to the existence of a horizontal component of H, and (2) long focal-length objectives to minimize corrections due to the finite object-to-lens distance (conical reprojection).

The cloud chamber was photographed on Eastman Linograph Ortho film by two Ektar 75 mm lenses operating at $f/8$. The camera axes were vertical and the lens centers 25.4 cm apart and 133.5 cm above the black glass (Fig. 2).

Each camera axis intersected the black glass in a fiduciary mark. Three additional marks were inscribed on the glass and all were visible in the photographs. In reprojection, no attempt was made to reconstruct events in space by superposition of the images from each of the two photographs. The two pictures were reprojected separately on an Eastman Recordak (rear surface) Screen.

The details of the calculation of true momentum and space angle from the measurements made on the reprojected images are more relevant to Part II and will be given there. The general technique is similar to that already described.[6]

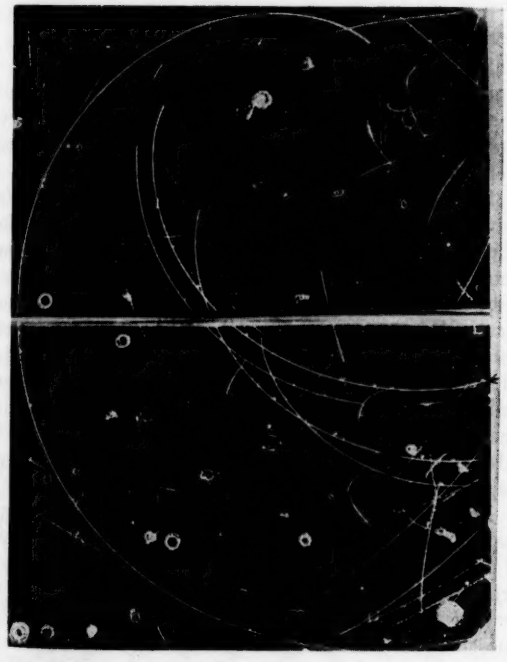

FIG. 3. Photograph of stopping mesons. Five stops are observed here. The horizontal sweeping plate does not intercept the particle trajectories. The arrow designates a track 15 cm long.

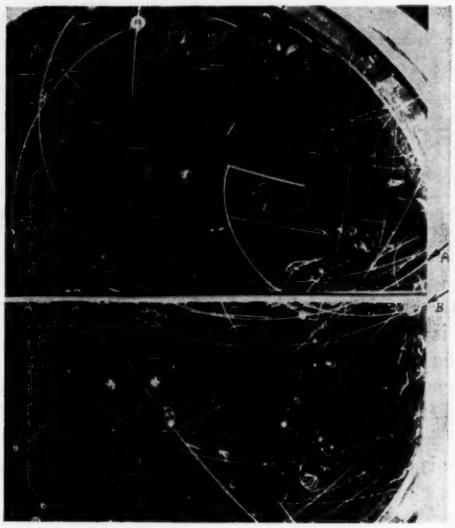

FIG. 4. *A* is a stopping pion. *B* is a stopping muon. The muon produces a one-prong star and recoil.

C. EXPERIMENTAL RESULTS

1. Classification of Phenomena

The incident flux consists principally of negative π and μ mesons with minor contamination of electrons and protons. A length S, of greater than 4 cm, of a track stopping in the gas, allows positive identification as a meson, based on ionization density, curvature, and rate of change of curvature. Furthermore the π^-/μ^- mass ratio is sufficiently large and multiple scattering in the hydrogen sufficiently small that when $s=15$ cm, residual range *vs* momentum measurements distinguish between stopping π and μ mesons with an uncertainty of about 10^{-3}. Such uncertainty decreases rapidly as s increases. At a range of 10 cm the momentum of a pion is 20 percent greater than the momentum of a muon. Figure 3 shows five stopping pions. The track marked with an arrow has a length s of 15 cm. Figure 4 contrasts π and μ mesons. It also contains an example of μ-meson-induced star, presumably due to interaction with an impurity in the hydrogen.

Table I lists events observed, classified according to the nature of the charged particles associated with the stopping meson. Table II also indicates the distribution of the mesons in S. Not included in Table I are 13 pair events which were found in the course of another experiment on low-energy pions.

It is estimated that the efficiency of the scanning in locating stopped mesons is 96 percent. Ordinarily in scanning, a stopped meson is closely examined for

[6] J. O. Kessler and L. M. Lederman, Phys. Rev. 94, 689 (1954).

TABLE I. Classification of events.

Run No.	No. of photographs	π Stops: No prongs $S>4$ cm[a]	π Stops: Star[b] $S>1$ cm	π Stops: Electron-positron pair $S>1$ cm	μ Stops: Electron $S>1$ cm	μ Stops: No track[c] $S>15$ cm	μ Stops: Star[c] $S>15$ cm	Totals[d]
1	7800	1896	48	15	376	25	11	448
2	6560	2009	50	17	434	39	4	520

[a] These are events in which the pion comes to rest, no associated tracks being observed at the end of the track. See Fig. 3.
[b] These are events in which one or more protons are associated with the end of the track. The length criterion does not assure identification as a pion.
[c] The 15-cm length criterion assures positive identification as a mu meson.
[d] The total number of μ stops has been extended by using Table II.

lightly ionizing particles associated with it; no correction is made for this scanning inefficiency.

The finite thickness of the sensitive layer and the presence in it of occasional insensitive regions introduce another form of inefficiency in the detection of charged particles associated with slow mesons. For example there is only a 50 percent probability of detection of a particle produced by a meson which stops exactly at the top or bottom of the sensitive layer. The slow mesons are uniformly distributed in height throughout the layer. If we require that 4 mm of an associated track be visible, we compute that a 10 percent inefficiency results from the finite (5.5 cm) depth of the sensitive region. This is probably a rather good estimate in the case of pairs associated with pions, but is too large for $\mu-e$ decay electrons. Shorter and fainter tracks are considered to be electrons resulting from μ-meson decay.

2. Mesonic Pair Production

The theoretical discussion of the internal pair production process is given in the accompanying paper by Kroll and Wada.[7]

Daniels, Davies, Hulvey, and Perkins[8] have observed correlated pairs of minimum-ionizing particles originating very near stars induced in emulsions by cosmic-ray mesons. The pairs seemed to satisfy the requirements of Dalitz' theory and were used to measure the mean life of the π^0 meson. Lord, Fainberg, Haskin, Schein, and Glasser[9,10] have detected seven similar pairs emerging from pion stars in emulsions. The pions were of known energy and were produced by the Chicago cyclotron. Lindenfeld *et al.*,[11] using counter techniques have observed coincidences between gamma rays and electrons associated with negative mesons stopped in liquid hydrogen. Assuming the theoretical angular correlation and energy distribution they find, for the conversion coefficient, $2\rho_0=0.0145_{-0.0045}{}^{+0.008}$. Anand[12] made use of this mode of decay to determine the lifetime of the π^0 meson. He also found a conversion coefficient of 0.013 ± 0.004.

When bound π^- mesons interact with protons, pairs should also be produced in appreciable number via $\pi^-+p\rightarrow n+e^++e^-$. One might expect the rate, ρ_γ, relative to the rate of $\pi^-+p\rightarrow n+\gamma$ (the radiative absorption process) to be at least of order ρ_0. Assuming $\rho_\gamma=\rho_0=\rho$, Lindenfeld *et al.* have found $\rho=0.0080\pm0.0019$. To obtain this result, the value 0.94 ± 0.20 measured by Panofsky, Aamodt, and Hadley for the ratio of the rate of mesonic absorption to the rate of radiative absorption was used.

TABLE II. Distribution in length.

Fraction of stopping mesons with S greater than	4	15	24 cm
π^-	0.92	0.57	0.40
μ^-	0.90	0.50	0.25

3. Experimental Results

It is assumed that the pairs observed to be associated with stopping pions are pairs of electrons. Schein, Fainberg, Haskin, and Glasser have been able to set an upper limit of 10 electron masses on the mass of one of the pair particles which they have detected. That they are electrons is consistent with the ionization and momentum observed in the cloud chamber.

In the rest system of the neutral pion, 70 Mev/c gamma rays are emitted from the reaction: $\pi^0\rightarrow\gamma+\gamma$. In the laboratory reference system the neutral pions are moving with velocity $\beta=0.202$, presumably oriented at random. The gamma-ray momentum spectrum is then flat between an upper limit of 83 Mev/c and a lower limit of 55 Mev/c. The $\pi^0\rightarrow\gamma+e^++e^-$ pairs are sufficiently well correlated that the total momentum of the pairs have this same spectrum to an excellent approximation. If the rest energy of the negative pion is 139 Mev, the total momentum distribution of the radiative capture pairs is essentially a line spectrum at 129 Mev/c.

Data on the measured total energy of each of the pairs are presented in Fig. 5. Not listed in this figure are 2 pairs produced by π^0's made in flight and 3 pairs for which no measurements were possible. Frequently only one of the pair of tracks is long enough to be well measured; in these cases it is possible only to set a lower limit on the total momentum. That limit is such that the

[7] N. M. Kroll and W. Wada, following paper [Phys. Rev. **98**, 1355 (1955)].
[8] Daniels, Davies, Hulvey, and Perkins, Phil. Mag. **43**, 753 (1952).
[9] Lord, Fainberg, Haskin, and Schein, Phys. Rev. **87**, 538 (1952).
[10] Schein, Fainberg, Haskin, and Glasser, Phys. Rev. **91**, 973 (1953).
[11] Lindenfeld, Sachs, and Steinberger, Phys. Rev. **89**, 531 (1953).
[12] B. Anand, Proc. Roy. Soc. (London) **A220**, 183 (1953).

probability that the pair's momentum is less than the limit is not more than a few percent. Each pair is kinematically consistent with production either by π^0 decay or else by internal conversion of radiative capture gamma rays. Figure 5 is used to assign to each pair a probability, Q, that it is a radiative capture pair on the assumption that only the two processes contribute to the pair production rate. This probability is indicated in the figure. Pairs 1–25 are used to measure the angular correlation and momentum distribution of the electrons from $\pi^0\to\gamma+e^+e^-$; pairs 26–35 serve a similar function for $\pi^-+p\to n+e^+e^-$. In pairs 36–42, momentum determinations were sufficient to establish the lower limit; however, either both individual momenta or the angle were not resolved. The absolute conversion coefficients are evaluated from only those pairs presented in Table I, thirty of which have pions with $S>4$ cm.

Process $\pi^0\to\gamma+e^+e^-$.—4105 mesons with visible range S greater than 4 cm have been observed to stop with no associated charged particles. This number includes the 3905 mesons of Table I plus 200 mesons photographed during a preliminary run made in November, 1952. No pairs were found in the preliminary pictures. To obtain ρ_0, the number 4105 must be corrected for the 10±4 percent electron detection inefficienty which results from the finite thickness of the sensitive layer and the presence of gaps in the layer. The 4105 events also include 30 prongless π stars, and 64 μ mesons for which $S<15$ cm. Using the probabilities Q, in Fig. 5, we find 18.5 of the pairs of Table I are π^0 pairs for which $S>4$ cm. Then $2\rho_0=18.5/3600x_0$; x_0 is the fraction of mesons leading to mesonic rather than radiative absorption and is found from R, the ratio of the rate of mesonic to the rate of radiative absorption. $R=0.94\pm0.20$. Values of $2\rho_0$ for $R=0.80$, 0.94, and 1.10 are recorded in Table III.

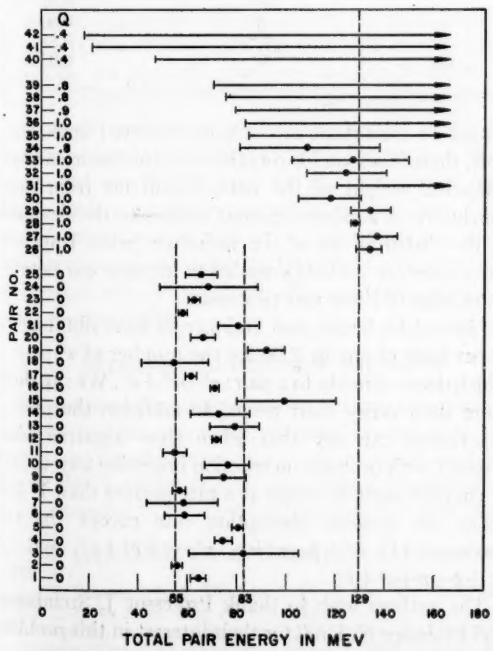

FIG. 5. Spectrum of total pair energies.

TABLE III. Values of $2\rho_0$ and ρ_γ for various values of R. $2\rho_0$ = (Rate of $\pi^0\to\gamma+e^+e^-$)/(Rate of $\pi^0\to\gamma+\gamma$); ρ_γ = (Rate of $\pi^-+p\to n+e^+e^-$)/(Rate of $\pi^-+p\to n+\gamma$); R = (Rate of $\pi^-+p\to n+\pi^0$)/(Rate of $\pi^-+p\to n+\gamma$) = 0.94±0.20.[a] Errors quoted for $2\rho_0$ and ρ_γ are statistical probable errors.

	$R=0.80$	$R=0.94$	$R=1.10$
$2\rho_0$	0.0116±0.0019	0.0106±0.0017	0.0099±0.0016
ρ_γ	0.0058±0.0012	0.0062±0.0013	0.0067±0.0014

[a] See reference 1.

TABLE IV. Angular correlation and momentum distribution of the electrons from $\pi^0\to\gamma+e^+e^-$. The momentum distribution parameter is $y=|p_+-p_-|/p_t$, where p_t is the total pair momentum.

Pair No.	θ	y	Pair No.	θ	y
1	15°	0.05	14	3°	0.24
2	1°	0.47	15	7.5°	0.13
3	5°	0.25	16	32°	0.96
4	43°	0.78	17	6.5°	0.60
5	15°	0.38	18	2°	0.37
6	38°	0	19	55°	0
7	13°	0.68	20	6°	0.10
8	1°	0.01	21	11°	0.24
9	58°	0.47	22	0°	0.60
10	11°	0.65	23	35°	0.76
11	8°	0.23	24	8.3°	0.55
12	89°	0.88	25	18°	0.26
13	31°	0.64			

Table IV presents the momentum partition parameter, $y=|p_+-p_-|/p_t$, where p_t is the total pair momentum, and the angular correlation data on the measurable π^0 pairs. Distribution in correlation angle fits a $d\theta/\theta$ curve with a median correlation angle of 11°. For purposes of comparison with theory, the effects of transformation from neutral pion rest system to laboratory system are well beyond experimental resolution. A detailed comparison with theory is made in the accompanying paper.[7] It is interesting to note that the π^0 pairs observed by Anand[12] are very strongly peaked toward small values of y (equal partition). He finds for the 5 equal intervals between $y=0$ and $y=1$, the numbers 17, 6, 3, 1, 0. Pair No. 4 is shown in Fig. 6. For this pair the correlation angle $\theta=43°$ and the distribution parameter $y=0.78$.

Process $\pi^-+p\to n+e^+e^-$.—Included in Table I are 11.5 pairs, for which $S>4$ cm, from $\pi^-+p\to n+e^+e^-$. $\rho_\gamma=11.5/3600x$; x is the fraction of stopping pions which lead to radiative absorption. Values of ρ_γ for $R=0.80$, 0.94, and 1.10 are listed in Table III.

Table V presents momentum distribution and angular correlation data on all the radiative pairs which are favorable for measurement. In evaluating these data one must consider both the poor statistics and an essentially kinematic correlation between the distribution parame-

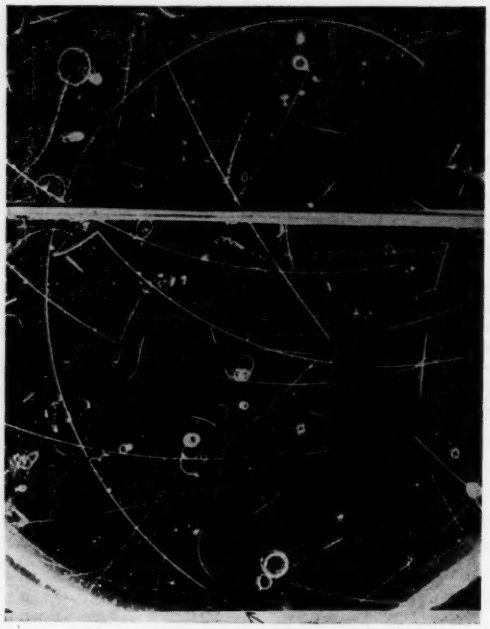

FIG. 6. π^0 pair No. 4. The angle between electrons is 43°, the distribution parameter $y=0.78$. The photograph also shows a typical $\pi-\mu-e$ decay.

ter y and θ such that unequal distribution of momentum between positron and electron tends to favor large θ. Comparison with theory is made in Figs. 1, 2, and 3 of the paper by Kroll and Wada.[7]

4. Rest Mass of the Negative Pion

Pair No. 28 has been previously reported.[13] The unusually long electron tracks and very small dip angle allow very precise determination of the pair energy and momentum. These are sufficient to determine the rest mass energy of the π^- meson. The reported value of 137.3 ± 0.9 Mev must be modified by two factors. A small systematic error in reprojection geometry since discovered changes this to 137.6 Mev. Also, no correction had been made for inner bremsstrahlung. Chang and Falkoff[14] have calculated the energy spectrum radiated by a relativistic electron produced in nuclear β decay. Since the effect is essentially classical, due to the sudden acceleration of electric charge the result should be independent of the production mechanism, especially in the important region of low photon momenta. For only one observed event no absolute correction can be made. The most precise measurements of the π^- mass made at Berkeley[15] yield $M_{\pi^-}=139.2\pm0.2$. The discrepancy is 1.6 Mev or 1.1 percent of the rest mass. However, the probability of a combined inner bremsstrahlung radiation loss of more than 1.6 Mev is 10 percent. Thus, the rest mass energy obtained in this way is quite consistent with other direct determinations of the mass of the π^- meson.

5. Conclusions

A sufficient number of pairs have been observed to provide convincing experimental verification of the existence of the reactions $\pi^0\rightarrow\gamma+e^++e^-$ and $\pi^-+p\rightarrow n+e^++e^-$. The internal conversion coefficients have been measured to be roughly equal. The angular distribution in the π^0 pairs, and the distribution in the parameter $x^2\approx 4p_+p_-\sin^2(\theta/2)$ are in reasonable agreement with the theory. However the momentum partition tends to favor equal distributions. A much more extreme disagreement in the same direction is observed by Anand.[12] An experimental bias against unequally distributed pairs is conceivable in the emulsion work, since these are correlated with large angles between electrons. This bias cannot be important in the work reported here. However, there is reason for confidence in the theory and the statistical weight of the data is still far from being conclusive. A similar comment applies to the deviation in the distributions of the radiative pairs. Improved techniques are probably needed to increase our detailed knowledge of these rare processes.

TABLE V. Angular correlation and momentum distribution of the electrons from $\pi^-+p\rightarrow n+e^++e^-$. $y=|p_+-p_-|/p_t$.

No.	θ	y
1	23°	0.93
2	80°	0.79
3	62°	0.90
4	11°	0.97
5	3°	0.70
6	3.5°	0.22
7	55°	0.57
8	2°	0.50
9	31°	0.81
10	0°	0.03

Lindenfeld, Sachs, and Steinberger have obtained an upper limit of one in 2000 for the number of π^0 mesons which decay directly to a pair: $\pi^0\rightarrow e^++e^-$. We can do no more than verify their result. In addition the present experiment can say that when slow negative pions interact with protons, no reaction involving any variety of charged particle occurs at a rate greater than 1/2000 times the mesonic absorption rate except the two processes (1) $\pi^-+p\rightarrow\pi^0+n$, $\pi^0\rightarrow\gamma+e^++e^-$, and (2) $\pi^-+p\rightarrow n+e^++e^-$.

The authors wish to thank Professor J. Steinberger and Professor N. Kroll for their interest in this problem.

[13] Cornelius, Sargent, Rinehart, Lederman, and Rogers, Phys. Rev. 92, 1583 (1953).
[14] C. S. W. Chang and D. L. Falkoff, Phys. Rev. 76, 365 (1949).
[15] Smith, Birnbaum, and Barkas, Phys. Rev. 91, 765 (1953). See also: Stearns, Stearns, DeBenedetti, and Leipuner, Phys. Rev. 95, 1353 (1954).

Internal Pair Production Associated with the Emission of High-Energy Gamma Rays

NORMAN M. KROLL, *Columbia University, New York, New York*

AND

WALTER WADA, *Naval Research Laboratories, Washington, D. C.*

(Received January 10, 1955)

The theory of inner pair production associated with the radiative capture of π^- mesons and with the decay of the π^0 meson is discussed. Appropriate distribution functions are derived and compared with recently obtained experimental results. The weak dependence of the theoretical predictions upon the details of meson theory is emphasized. The possible utility of the double conversion process, in which the π^0 meson decays into two electron-positron pairs, for the determination of the π^0 parity is also discussed.

A. INTRODUCTION

THE process of inner pair production (i.e., the emission of an electron positron pair by an excited system in place of a γ ray) has been extensively studied in connection with the decay of excited nuclei, and the dependence of what will be referred to as the conversion coefficient on the multipolarity of the γ ray has had some utility in the classification of transitions. It has been pointed out that as the energy of the transitions exceeds the necessary threshold energy by amounts large compared to mc^2 the dependence of the process on the multipolarity of the γ ray decreases, and, in fact, the conversion coefficient becomes essentially independent of the source of the γ ray in the high-energy limit.[1-3] Radiative processes accompanying the annihilation of a π meson are good examples of this situation. These have been studied experimentally in connection with π^0 decay and the radiative capture of π^- mesons.[4,5]

The main purpose of this note is to compare the predictions of the theory with the available experimental results on the mesonic processes mentioned above. In view of the present unsatisfactory state of meson theory the weak dependence of the theoretical predictions upon this theory is of importance. We shall therefore in Sec. 1 briefly rederive expressions for the conversion coefficient and appropriate distribution functions in a manner which makes this weak dependence manifest. In subsequent sections specific formulas for the processes of interest will be obtained and compared with the experimental results.

1. INTERNAL CONVERSION FORMULA

The internal conversion process may be described as follows. A given reaction produces, instead of a real photon, a virtual photon, which subsequently produces an electron positron pair. If the photon momentum is large compared to mc, then for pairs emitted with small transverse momentum the energy of the intermediate state containing the photon is nearly the same as that of the final state. This mode of production is highly favored by the associated small energy denominator and as a consequence the emitted pairs do tend to have small transverse momentum. It is the predominance of "nearly real" photons in the process which tends to dissociate the conversion of the photon from its emission.

Consider a physical system of zero total momentum which undergoes a transformation from a state A to a state B of energy difference E_{AB}, recoiling with momentum k. If the transition takes place by virtue of photon emission, then a current $J_\mu(k_\mu)$ may be associated with the process. [$k_\mu=(\mathbf{k},k_0)$ with $k_0=-(M^2+k^2)^{\frac{1}{2}}+M+E_{AB}$ where M is the mass of the recoil system.] The photon is then generated by the interaction energy $(1/c)J_\mu A_\mu$, yielding the matrix element for emission of a photon of polarization λ:

$$M_\gamma=(1/c)J_\mu(k)\epsilon_\mu{}^\lambda(\hbar c/2k)^{\frac{1}{2}}, \tag{1}$$

from which one obtains the transition probability

$$W_\gamma=\frac{k}{8\pi^2\hbar c^4}\frac{2(E+M)^2}{(E+M)^2+M^2}\int(J_{(1)}{}^2+J_{(2)}{}^2)d\Omega, \tag{2}$$

where $J_{(\lambda)}=J_\mu\epsilon_\mu{}^\lambda$.

The transition probability for emission of a pair by the same current with electron momentum $p_{1\mu}$ and positron momentum $p_{2\mu}$ is given by

$$W_{\text{pair}}=\frac{\alpha}{\pi^2}\frac{1}{8\pi^2\hbar c^4}\int J_\mu(k')J_\nu(k')\left(\frac{1}{k_\mu{}'^2}\right)^2 \times\sum_{\text{spins}}(\bar\psi(p_1)\gamma_\mu\psi(-p_2))(\bar\psi(-p_2)\gamma_\nu\psi(p_1)) \times d\mathbf{p}_1d\mathbf{p}_2\delta(p_{10}+p_{20}-k_0'), \tag{3}$$

with $k_\mu'=p_{1\mu}+p_{2\mu}$ and $k_0'=(M^2+k'^2)^{\frac{1}{2}}-M+E_{AB}$. Now letting $\mathbf{p}_1=\mathbf{q}+\frac{1}{2}(1+\lambda)\mathbf{k}'$, $\mathbf{p}_2=-\mathbf{q}+\frac{1}{2}(1-\lambda)\mathbf{k}'$, with $\mathbf{q}\cdot\mathbf{k}'=0$, and taking Ω for the angular variables associated with k and ϕ the azimuthal angle of q, we transform the differential elements $d\mathbf{p}_1d\mathbf{p}_2$ to $(\frac{1}{2}qk'dqd\lambda d\phi)(k'^2dk'd\Omega)$. The δ function may now conveniently be

[1] J. R. Oppenheimer and L. Nedelsky, Phys. Rev. **44**, 948 (1933).
[2] M. E. Rose and G. E. Uhlenbeck, Phys. Rev. **48**, 211 (1935).
[3] M. E. Rose, Phys. Rev. **76**, 678 (1939).
[4] Lindenfeld, Sachs, and Steinberger, Phys. Rev. **89**, 531 (1953).
[5] Sargent, Cornelius, Rinehart, Lederman, and Rogers, preceding paper [Phys. Rev. **98**, 1349 (1955)].

eliminated by integrating over q, the factor qdq becoming $p_{10}p_{20}/k_0'$. Now writing

$$\sum_{\text{spins}}(\bar{\psi}(p_1)\gamma_\mu\psi(-p_2))(\bar{\psi}(p_2)\gamma_\nu\psi(p_1))$$
$$=\frac{1}{4p_{10}p_{20}}\mathrm{Tr}(-i\gamma\cdot p_1+m)\gamma_\mu(i\gamma\cdot p_2+m)\gamma_\nu=\frac{1}{p_{10}p_{20}}T_{\mu\nu},$$

Eq. (3) becomes

$$W_{\text{pair}}=\frac{\alpha}{2\pi^2}\frac{1}{8\pi^2\hbar c^4}\int J_\mu(k')J_\nu(k')\left(\frac{1}{k_\mu'^2}\right)^2 \times T_{\mu\nu}\frac{k'^3dk'}{k_0'}d\lambda d\phi d\Omega. \quad (4)$$

The conservation laws yield

$$q^2=-\tfrac{1}{4}k_\mu'^2(1-\lambda^2k'^2/k_0'^2)-m^2.$$

The requirement that q^2 be positive now determines the domain of λ and k'. It is convenient at this point to resolve $J_\mu(k)$ into transverse and longitudinal components. Thus we write

$$J_\mu=(\mathbf{J};J_0)=(J_{(1)}\boldsymbol{\varepsilon}_1+J_{(2)}\boldsymbol{\varepsilon}_2+J_{(3)}\mathbf{k}'/k';\ J_{(3)}k'/k_0'),$$

since $k_\mu J_\mu=0$. Taking $\boldsymbol{\varepsilon}_1$ as the polar axis for ϕ, Eq. (4) becomes

$$W_{\text{pair}}=\frac{\alpha}{2\pi^2}\frac{1}{8\pi^2\hbar c^4}\int\frac{k'^3}{k_0'(k_\mu'^2)^2}\{J_{(1)}^2[-\tfrac{1}{2}k_\mu'^2 \times(\sin^2\phi+\lambda^2\cos^2\phi k'^2/k_0'^2)+2m^2\cos^2\phi]$$
$$+J_{(2)}^2[-\tfrac{1}{2}k_\mu'^2(\cos^2\phi+\lambda^2\sin^2\phi k'^2/k_0'^2)+2m^2\sin^2\phi]$$
$$+\mathrm{Re}[J_{(1)}J_{(2)}k_\mu'^2(1-\lambda^2k'^2/k_0'^2)\sin\phi\cos\phi]$$
$$+\mathrm{Re}[J_{(3)}\lambda qk'(J_{(1)}\cos\phi+J_{(2)}\sin\phi)k_\mu'^2/k_0'^2]$$
$$+J_{(3)}^2(k_0'^2-\lambda^2k'^2)(k_\mu'^2)^2/2k_0'^4\}dk'd\lambda d\phi d\Omega. \quad (5)$$

The integrand in (5) is then the distribution function in the variables k', λ, ϕ, and Ω. The angular correlations described by (5) are not generally accessible to observation due to a lack of knowledge of the direction of J_μ, although an exception to this remark will be noted in connection with the decay of the π_0 meson.[6] Integrating over angles yields

$$W_{\text{pair}}=\frac{\alpha}{2\pi}\frac{1}{8\pi^2\hbar c^4}\int\frac{k'^3dk'd\lambda}{k_0'}\left\{\left[\frac{k_0'^2+\lambda^2k'^2}{2k_0'^2(-k_\mu'^2)}+\frac{2m^2}{(k_\mu'^2)^2}\right] \times\int(J_{(1)}^2+J_{(2)}^2)d\Omega+\frac{k_0'^2-\lambda^2k'^2}{2k_0'^4}\int J_{(3)}^2d\Omega\right\} \quad (6)$$

[6] Some applications of these correlations in connection with nuclear transitions have been pointed out by G. Goldring, Proc. Phys. Soc. (London) A66, 391 (1953).

from which we obtain, for the conversion coefficient,

$$\rho=\frac{\alpha}{2\pi}\frac{2(E+M)^2}{(E+M)^2+M^2}\int\frac{k'^3dk'd\lambda}{k_0'k}\left\{\left[\frac{k_0'^2+\lambda^2k'^2}{2k_0'^2(-k_\mu'^2)}+\frac{2m^2}{(k_\mu'^2)^2}\right]R_T(k')+\frac{k_0'^2-\lambda^2k'^2}{2k_0'^4}R_L(k')\right\} \quad (7)$$

with

$$R_T=\frac{\int(J_{(1)}^2(k')+J_{(2)}^2(k'))d\Omega}{\int(J_{(1)}^2(k)+J_{(2)}^2(k))d\Omega};$$

$$R_L=\frac{\int J_{(3)}^2(k')d\Omega}{\int(J_{(1)}^2(k)+J_{(2)}^2(k))d\Omega}.$$

For the discussion of distribution functions it is somewhat more convenient to use $x^2=-k_\mu'^2$ instead of k' and $y=\lambda k/k_0$ instead of λ as variables,[7] in which case ρ is given by

$$\rho=\frac{\alpha}{4\pi}\int_{2m}^{E}dx\int_{-\eta}^{\eta}dy\left(\frac{k'}{k}\right)\frac{(E+M)^2+M^2-x^2}{(E+M)^2+M^2} \times\left\{\left[\frac{1+y^2}{x}+\frac{4m^2}{x^3}\right]R_T(x)+(1-y^2)\frac{4(E+M)^2x}{(2EM+E^2+x^2)^2}R_L(x)\right\}, \quad (8)$$

with

$$(k'/k)^2=\frac{(2EM+E^2)^2-2x^2(2M^2+2EM+E^2)+x^4}{(2EM+E^2)^2},$$
$$\eta=[1-(2m/x)^2]^{\frac{1}{2}}.$$

The y integration can also be performed without specifying R_T and R_L, to yield

$$\rho=\frac{2\alpha}{3\pi}\int_{2m}^{E}dx\left(\frac{k'}{k}\right)\frac{(E+M)^2+M^2-x^2}{(E+M)^2+M^2}\left(1-\frac{4m^2}{x^2}\right)^{\frac{1}{2}} \times\left(1+\frac{2m^2}{x^2}\right)\left[\frac{R_T}{x}+\frac{2(E+M)^2x}{(2EM+E^2+x^2)^2}R_L\right]. \quad (9)$$

It is clear that the coefficient of R_T is strongly peaked at small values of x, and always exceeds that of $R_L(x)$. Therefore, unless R_L is much greater than unity, the transverse conversion coefficient (i.e., the contribution

[7] Note that $y=(p_{01}-p_{02})/|\mathbf{p}_1+\mathbf{p}_2|$ is essentially a measure of the energy partition, while x may be thought of as the "rest mass" of the virtual photon. The smallness of x compared to k corresponds to the predominance of nearly real intermediate photons as discussed at the beginning of this section.

from R_T) is much larger than the longitudinal conversion coefficient. Furthermore, the strong peaking at small values of x means that a good estimate of ρ_T can be obtained by setting $R_T(x)=R_T(0)=1$. One finds in this way that

$$\rho_T=2\alpha/3\pi[\ln(2E/m)-11/6-g(E/M)], \quad (10)$$

with $g(E/M)\approx(5/24)(E/M)^2$ for small (E/M) and increasing to $\ln 2-\frac{1}{4}$ for $E/M=\infty$. The predominance of small values of x is reflected in the appearance of the logarithm in (10), and (10) is a good approximation whenever the logarithm is dominant. Clearly ρ_T is also very insensitive to the ratio E/M. Some idea of the sensitivity to variation in R_T can be had by noting that the replacement of R_T by k'/k instead of unity has the effect of changing the fraction $-11/6$ to $-(\ln 2+4/3)$.

In view of the weak dependence of ρ_T on the form of R_T, it is also worthwhile to obtain an approximate universal function for the distribution in y by replacing R_T by unity in (8) and integrating over x first. This yields

$$\rho_T=\frac{\alpha}{4\pi}\int_{-(1-4m^2/E^2)^{\frac{1}{2}}}^{(1-4m^2/E^2)^{\frac{1}{2}}}dy\left\{(1+y^2)\left[\ln\frac{E(1-y^2)^{\frac{1}{2}}}{m}-\left(1-\frac{4m^2}{E^2(1-y^2)}\right)^{\frac{1}{2}}+\ln\tfrac{1}{2}\left[1+\left(1-\frac{4m^2}{E^2(1-y^2)}\right)^{\frac{1}{2}}\right]\right]+\tfrac{1}{2}\left(1-\frac{4m^2}{E^2}-y^2\right)\right\} \quad (11)$$

for $E/M=0$. For $E/m\cong 270$ the distribution function is rather flat, with a relative minimum at $y=0$, a maximum at $y=\pm 0.88$, and falling to zero at the limits. The ratio of the maximum to the relative minimum is 1.3.

2. APPLICATION TO PHOTOMESONIC PROCESSES

(a) Reaction $\pi^-+p\rightarrow n+e^++e^-$

We now apply the theory described in Sec. 1 to the conversion of the γ ray emitted in the radiative capture of a π^- meson by a proton. The weak dependence of the conversion process on $R_T(x)$ and $R_L(x)$ has been emphasized in the preceding section. It is possible, however, to obtain approximate forms for these quantities from meson theory. Indeed the Kroll-Ruderman theorem[8] on photomeson production shows that the expressions for R_T and R_L obtained from the second order perturbation theory are valid to terms of order μ/M, where μ is the meson mass, even when all orders of perturbation theory are taken into account. The results from second order perturbation theory are simply $R_T=1$ and $R_L=2\mu^4/(2\mu^2-x^2)^2$, evaluated for $\mu/M=0$. Thus the results for ρ_T obtained in the preceding section may be applied unchanged. For ρ_L one

[8] N. Kroll and M. Ruderman, Phys. Rev. 93, 233 (1954).

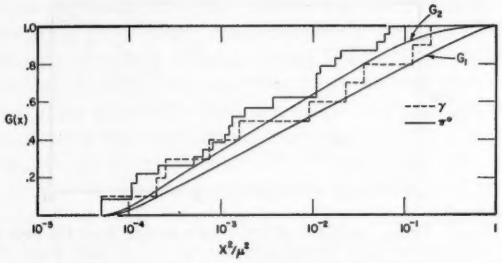

FIG. 1. Distribution in x for the inner pairs arising from the process $\pi^-+p\rightarrow n+e^++e^-$ (designated by γ - - - and G_1) and from the process $\pi^0\rightarrow\gamma+e^++e^-$ (designated by π_0 —— and G_2). The variable x is defined by $x^2=(p_1+p_2)_\mu(p_1+p_2)_\mu$. The functions $G_1(x)$ and $G_2(x)$ are, according to theory, the fractional number of events for which x is smaller than the value appearing in the argument. The step curves are the corresponding experimental results.

finds, again taking $\mu/M=0$,

$$\rho_L=\frac{2\alpha}{3\pi}\int_{2m}^{E}dx\left(1-\frac{x^2}{\mu^2}\right)^{\frac{1}{2}}\left(1-\frac{4m^2}{x^2}\right)^{\frac{1}{2}}\times\left(1+\frac{2m^2}{x^2}\right)\frac{x\mu^2}{(2\mu^2-x^2)^2}$$

$$\cong\frac{2\alpha}{3\pi}\int_0^{\mu}dx\left(1-\frac{x^2}{\mu^2}\right)^{\frac{1}{2}}\frac{x\mu^2}{(2\mu^2-x^2)}=\frac{\alpha}{6\pi}\left(\frac{\pi}{2}-1\right)$$

$$=\frac{\alpha}{8\pi}\left(\frac{\pi}{2}-1\right)\int_{-1}^{1}(1-y^2)dy. \quad (12)$$

Numerically, $\rho_T=0.00693$, $\rho_L=0.00022$,[9] and one notes that ρ_L is indeed much smaller than ρ_T. The result for ρ is thus in agreement with the value 0.0062 ± 0.0013 obtained by Sargent *et al.*[5]

The distribution functions in x and y can be conveniently compared with the few experimental events by comparing the integral of the distribution function with the cumulative number of events. Thus, in Fig. 1,

$$G(x)=\int_{2m}^{x}g(x')dx'\Big/\int_{2m}^{E}g(x')dx'$$

is compared with the fraction of the observed events for which x is less than the specified value. Similarly, in Fig. 2,

$$H(y)=\int_0^{y}h(y')dy'\Big/\int_0^{(1-4m^2/E^2)^{\frac{1}{2}}}h(y')dy'$$

is compared with the fraction of the observed events for which $|y|$ is less than the specified value.[10] Both dis-

[9] These results are in agreement with those reported by W. Wada, Phys. Rev. 95, 618(A) (1953), but in disagreement with that of W. Thirring, Proc. Roy. Irish Acad. A54, 205 (1951). In this latter work an expression for the current operator matrix element is used which fails to satisfy the conservation law.

[10] $g(x)$ and $h(y)$ are the integrands in Eqs. (9) and (11) respectively, modified to include the effects R_L.

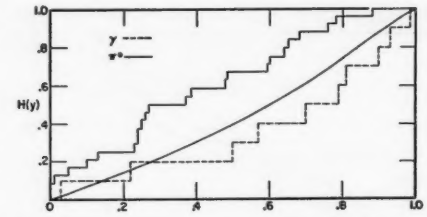

FIG. 2. Energy partition of inner pairs arising from the process $\pi^-+p\rightarrow n+e^++e^-$ (designated by γ----) and from the process $\pi^0\rightarrow\gamma+e^++e^-$ (designated by π^0——). The variable y is defined by $y=(p_{01}-p_{02})/|\mathbf{p}_1+\mathbf{p}_2|$. The function $H(y)$ is, according to theory, the fractional number of events for which $|y|$ is smaller than the value appearing in the argument. The step curves are the corresponding experimental results.

tributions are in satisfactory agreement with the experimental results.

For completeness we note the result obtained for scalar mesons. The Kroll-Ruderman theorem applies also in this case provided one includes the anomalous moments phenomenologically. One finds that ρ_T is given essentially by (9) while for ρ_L one obtains

$$=(2\alpha/3\pi)(2M/\mu)^2(5/4-3\pi/8)(g_p+g_n)^{-2},$$

where g_p and g_n are gyromagnetic ratios for the proton and neutron respectively in nuclear magnetons. One notes that the large enhancement of ρ_L arising from the factor $(2M/\mu)^2$ is compensated by the factor $(g_p+g_n)^2$ in the denominator. Consequently ρ_L is small compared to ρ_T for scalar mesons also, and ρ is thus only weakly dependent upon the parity of the captured meson.

(b) Reaction $\pi^0\rightarrow\gamma+e^++e^-$

The theory may also be applied to the conversion of the γ rays emitted in the decay of a neutral meson. We consider first the case in which only one of the γ rays is converted. In this case the recoiling system is, of course, the other photon, so that $M=0$. Furthermore, R_L vanishes for both scalar and pseudoscalar mesons. The form of R_T which one obtains from the lowest order of perturbation theory is, again for both scalar and pseudoscalar mesons, $(k'/k)f(x/2M)$ with $f(0)=1$ and varying only a small amount from this value over the available range of its argument. The factor k'/k is a

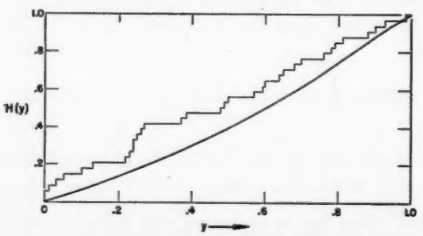

FIG. 3. Energy partition for the two processes considered together. The experimental results represented in Fig. 2, for the two processes $\pi^-+P\rightarrow n+e^++e^-$ and $\pi^0\rightarrow\gamma+e^++e^-$ are combined. The step curve gives the fractional number of events of either type for which $|y|$ is less than the value appearing in the argument.

consequence of gauge invariance, relativistic invariance and the form of the photon emission matrix elements while the behavior of $f(x/2M)$ can be attributed to the fact that x is always small compared to the energy of the intermediate states. (These always involve the presence of a nucleon-antinucleon pair.) It is therefore reasonable to take $R_T=k'/k$ (in spite of the inadequacy of perturbation theory) and thus obtain

$$\rho=\frac{4\alpha}{3\pi}\int_{2m}^{\mu}\left(1-\frac{x^2}{\mu^2}\right)^3\left(1-\frac{4m^2}{x^2}\right)^{\frac{1}{2}}\left(1+\frac{2m^2}{x^2}\right)\frac{dx}{x}$$

$$=\frac{\alpha}{2\pi}\int_0^{(1-4m^2/\mu^2)^{\frac{1}{2}}}dy\left\{(1+y^2)\left[\ln\frac{\mu^2(1-y^2)}{4m^2}-\frac{11}{6}\right.\right.$$

$$+3\left(\frac{4m^2}{\mu^2(1-y^2)}\right)-\frac{3}{2}\left(\frac{4m^2}{\mu^2(1-y^2)}\right)^2$$

$$\left.\left.+\frac{1}{3}\left(\frac{4m^2}{\mu^2(1-y^2)}\right)^3\right]+1-\frac{4m^2}{\mu^2}-y^2\right\}$$

$$=\frac{2\alpha}{3\pi}\left(\ln\frac{\mu^2}{m^2}-\frac{7}{2}\right)=0.0118. \quad (13)$$

In obtaining (13), (8) has been doubled to take into account the fact that either photon can convert.[11]

In Figs. 1 and 2 the distributions in x and y are compared to the experimental results in a manner similar to that used for the pairs associated with radiative capture. The theoretical distributions in y are so similar for the two situations that a single plot serves for both. In view of the fact that the π^0 meson is not at rest when it decays, it is worth noting that x is an invariant and therefore independent of the motion of the π^0. The variable y is essentially independent of the motion of the π^0 as long as both pair particles are highly relativistic and the angle between them is small. Since this is the case for virtually all of the pairs, no correction has been made. One notes that the x distribution is in good agreement with the theory. The y distribution, on the other hand, appears to be in some disagreement in a manner suggesting a marked preference for equipartition.[12] Considerably more data would be required, however, to establish a real contradiction. In view of the fact that the theoretical y distribution functions are essentially identical for the capture and the decay pairs it is worth noting that the combined distributions are in better agreement with the theory (Fig. 3).

(c) Reaction $\pi^0\rightarrow 2e^++2e^-$

The case in which both γ rays are internally converted, while a very rare process, may be of interest in connection with the determination of the parity of the

[11] This result has been obtained previously by R. H. Dalitz, Proc. Phys. Soc. (London) **A64**, 667 (1951).

[12] A much stronger effect of the same kind has been observed by A. M. Anand, Proc. Roy. Soc. (London) **A220**, 183 (1953).

π^0. This comes about as a result of the angular correlations described in Eq. (5). It has been pointed out that the polarizations of the two photons emitted in the decay of the π^0 are perpendicular or parallel as the π^0 is pseudoscalar or scalar.[13] According to (5), there is a strong correlation between the plane determined by the propagation and polarization vectors of the photon and the plane of the pair into which it converts. Thus the two pairs should tend to lie in perpendicular planes or the same plane accordingly as the meson is pseudoscalar or scalar.

Using the same form for the meson decay matrix element as was used in the derivation of (13), and neglecting exchange, one finds for the transverse conversion coefficient

$$\rho_T=\frac{1}{\pi}\left(\frac{\alpha}{4\pi}\right)^2\int_{2m}^{\mu-2m}dx_1\int_{2m}^{\mu-x_1}dx_2\int_{-\eta_1}^{\eta_1}dy_1\int_{-\eta_2}^{\eta_2}dy_2$$
$$\int_0^{2\pi}d\phi\left(1-\frac{2(x_1^2+x_2^2)}{\mu^2}+\frac{(x_1^2-x_2^2)^2}{\mu^4}\right)^{\frac{1}{2}}$$
$$\times\left\{\left[\frac{1}{x_1x_2}+\left(\frac{y_1^2}{x_1}+\frac{4m^2}{x_1^3}\right)\left(\frac{y_2^2}{x_2}+\frac{4m^2}{x_2^3}\right)\right]\sin^2\phi\right.$$
$$\left.+\left[\frac{y_1^2+y_2^2}{x_1x_2}+\frac{4m^2}{x_2x_1^3}+\frac{4m^2}{x_1x_2^3}\right]\cos^2\phi\right\} \quad (14)$$

for a pseudoscalar π^0, the $\sin^2\phi$ and $\cos^2\phi$ factors being interchanged for the scalar case. From the form of (14) it is apparent that the process can be regarded as resulting from nearly independent conversions of the two γ rays. Cross terms involving the longitudinal conversion of one photon and the transverse conversion of the other vanish for both the scalar and pseudoscalar case, while the longitudinal conversion of both photons contributes a negligible amount in the scalar case and vanishes in the pseudoscalar case. For any individual case of two pair decay there are two sets of values for the variables, x_1, y_1, x_2, y_2 corresponding to the two possible pairings of the electrons with the positrons. The neglect of exchange corresponds to the neglect of interference between the amplitudes arising from the two possible pairings. For the great majority of cases, the product x_1x_2 will be much smaller for one pairing than for the other, a fact which makes the exchange effect negligible. In comparing (14) with experiment, the pairing which yields the smaller value should be used.

The correlation function for the planes of the two pairs may be obtained by integrating ρ_T over the variables $x_1\cdots y_2$, yielding

$$\rho_T=\frac{1}{\pi}\rho_T\int_0^{2\pi}(0.59\sin^2\phi+0.41\cos^2\phi)d\phi$$

for the pseudoscalar case, with $\sin^2\phi$ and $\cos^2\phi$ interchanged for the scalar case. The numerical value of ρ_T is 3.47×10^{-5} so that only one out of 29 000 π^0's decay into two pairs. In spite of this small value, the process does offer some possibility of yielding information on the parity of the π^0.

[13] C. N. Yang, Phys. Rev. 77, 292 (1950), and 722 (1950).

Scattering of High-Energy Electrons by Nuclei*

A. E. GLASSGOLD†
Department of Physics and Laboratory for Nuclear Science and Engineering, Massachusetts Institute of Technology, Cambridge, Massachusetts

(Received February 7, 1955)

Calculations of elastic scattering of electrons have been carried out for simple, spherically symmetric charge distributions. The atomic numbers considered are $Z=13$, 29, 50, 74, and 79, and the electron energy varies from 15 to 90 Mev. The results for the homogeneous and shell distributions indicate that shape independence exists for energies such that $kR_h \lesssim 1.5$, where R_h is the radius of the homogeneous model and k is the electron wave number. This is a consequence of requiring that these two densities have the same mean square radius or second moment. The assumption that the scattering at higher energies depends on higher even moments has also been investigated. The scattering was calculated as a function of the fourth moment at an energy just above the shape independent region. Equating the second and fourth moments of two charge densities results in identical scattering for scattering angles up to 120°, but beyond this point the scattering differs by about 10 percent. An analysis of the existing experiments below 100 Mev indicates that the mean square radius of the nuclear charge density is given by a homogeneous distribution of radius $R_h=r_0A^{\frac{1}{3}}\times10^{-13}$ cm., with $r_0=1.2$ to within 10 percent.

I. INTRODUCTION

RECENT experiments on elastic scattering of electrons by atomic nuclei have yielded important information about the nuclear charge distribution. The results obtained by Lyman, Hanson, and Scott[1] with 15.7-Mev electrons have been analyzed by Bitter and Feshbach[2] to indicate a radius for the nuclear charge distribution given by $r_0=1.1$ in the usual rule,

$$R=r_0A^{\frac{1}{3}}\times10^{-13}\text{ cm}. \quad (1)$$

Agreement with this value of r_0, which is about 20 percent smaller than the one formerly quoted, has been obtained in other electron scattering experiments by Pidd, Hammer, and Raka[3] with 33- and 43-Mev electrons and by Hofstadter's group at Stanford for energies from 84 to 183 Mev.[4,5] There is also much additional evidence[2,6] for a smaller radius, as in the measurements by Fitch and Rainwater[7] of the energy levels of μ-mesonic atoms. In this paper exact numerical calculations of the elastic scattering of electrons are performed for energies from 15 to 90 Mev and the atomic numbers $Z=13$, 29, 50, 74, and 79. Some mention will also be made of the possibility of interpreting the experiments in terms of the moments of the nuclear charge density.

As a simple first approximation the nucleus is considered to be a spherically symmetric, static charge density inside a sphere of radius R. The interaction between the electron and the nucleus is simply the electrostatic potential between a point charge $-e$ and a charge Ze distributed over a finite region. Consequently, one is dealing with the diffraction of an electron of reduced wavelength λ by a charge distribution of linear dimension R. An essential parameter is the ratio of these two lengths,

$$R/\lambda=kR,$$

where k is the electron wave number. For long wavelengths ($kR\ll1$) the nucleus may be treated as a point charge, but when the wavelength becomes the same order of magnitude as the radius ($kR\gtrsim1$) significant deviations from point scattering will be obtained. In the latter case the electron's energy is much greater than the rest energy. For a heavy nucleus such as gold $kR=1$ corresponds to roughly 30 Mev.

The interpretation of electron scattering experiments depends on exact solutions of the Dirac equation. Such solutions have already been given by Elton[8] and Acheson[9] for energies where only one partial wave is modified by the finite nuclear size. Calculations at much higher energies have subsequently been reported by Yennie, Ravenhall, and Wilson[10,11] and Brenner, Brown, and Elton.[12] Unfortunately the Born approximation and analogous perturbation expressions for the phase shifts are too crude except for the lightest nuclei. The failure of the Born approximation is well known for the case of point Coulomb scattering from the exact calculation by Bartlett and Watson[13] for $Z=80$ and from the higher Born approximations derived by McKinley and Feshbach.[14] For finite nuclei and an energy low enough so that the familiar oscillatory behavior of the Born approximation cross section is not

* This work was supported in part by the Office of Naval Research and the U. S. Atomic Energy Commission.

† Now at Oak Ridge National Laboratory, Oak Ridge, Tennessee.

[1] Lyman, Hanson, and Scott, Phys. Rev. **84**, 626 (1951).
[2] F. Bitter and H. Feshbach, Phys. Rev. **92**, 837 (1953).
[3] Pidd, Hammer, and Raka, Phys. Rev. **92**, 436 (1953).
[4] Hofstadter, Fechter, and McIntyre, Phys. Rev. **92**, 978 (1953).
[5] Hofstadter, Hahn, Knudsen, and McIntyre, Phys. Rev. **95**, 512 (1954).
[6] L. N. Cooper and E. M. Henley, Phys. Rev. **92**, 801 (1953).
[7] V. L. Fitch and J. Rainwater, Phys. Rev. **92**, 789 (1953).
[8] L. R. B. Elton, Proc. Phys. Soc. (London) **A63**, 1115 (1950).
[9] L. K. Acheson, Phys. Rev. **82**, 488 (1951).
[10] Yennie, Ravenhall, and Wilson, Phys. Rev. **95**, 500 (1954).
[11] D. G. Ravenhall and D. R. Yennie, Phys. Rev. **96**, 239 (1954).
[12] Brenner, Brown, and Elton, Phil. Mag. **45**, 524 (1954).
[13] J. H. Bartlett and R. E. Watson, Proc. Am. Acad. Arts Sci. **74**, 53 (1940).
[14] W. A. McKinley, Jr., and H. Feshbach, Phys. Rev. **74**, 1759 (1948).

present, Elton has compared the Born approximation with his exact calculation of the ratio of the scattering to that for a point nucleus. In this case the Born approximation gives ratios which are roughly 50 percent too large for scattering angles beyond 60°. At higher energies it has been found[10,12] that the Born approximation can be misleading in that the actual cross section decreases quite smoothly with angle as compared to the pronounced maxima and minima of the Born approximation.

Approximate methods, however, can be helpful as guides for more precise calculations. Indeed, the effect of the finite nuclear size on electron scattering was first discussed by Guth[15] and Rose[16] with the Born approximation. Another example is Feshbach's explanation of the *shape independence* of electron scattering for low energies. Acheson[9] had previously carried out exact calculations for two simple charge distributions: (1) the *homogeneous* charge distribution, in which the nuclear charge is uniformly distributed throughout the interior of a sphere of radius R_h; (2) the *shell* charge distribution, in which the nuclear charge is uniformly distributed over the surface of a sphere of radius R_s. Acheson noticed that, for the entire range of his calculation, the shell and homogeneous phase shifts were the same if the shell radius R_s was about $\frac{3}{4}R_h$. Using a variational principle for the phase shift, Feshbach[17] showed that this equivalence applied more generally to any two charge densities, $\rho_1(r)$ and $\rho_2(r)$, whose mean square radii or second moments were equal:

$$\int d^3r\, r^2\rho_1(r)=\int d^3r\, r^2\rho_2(r). \tag{2}$$

For the shell and homogeneous distributions this leads to the relation,

$$R_s/R_h=(3/5)^{\frac{1}{2}}=0.775, \tag{3}$$

which agrees very closely with Acheson's exact calculations. Feshbach's restriction of this result to long wavelengths ($kR\ll 1$) can be discarded, however, since Acheson's work shows that shape independence holds at least up to $kR_h=1$. In fact, Elton[18] and Bodmer[19] have extended Feshbach's proof up to 35 or 40 Mev by applying perturbation methods directly to the Dirac radial equations.

The value of a general principle such as shape independence is that it provides a direct connection between the scattering and some essential characteristic of the nuclear charge distribution, in this case the second moment. This is especially useful in view of the difficulty of exact numerical solutions. If the general dependence of the scattering on the charge distribution is not known, special forms for the charge density must be assumed until one is found which agrees with experiment. However, this procedure may not be unique. Charge densities which are rather dissimilar in radial dependence may yet produce the same scattering, as was found for the shell and homogeneous distributions at low energies. What is needed, perhaps, is a standard set of parameters or properties of the nuclear charge density, which would apply equally well to all possible charge densities. If all these parameters were specified, the nuclear charge density would be uniquely determined as far as electron scattering was concerned. Otherwise, if only a few were known, any charge distribution which had these properties would be acceptable.

In Sec. IV we shall give some qualitative arguments for describing the scattering in terms of the even moments of the nuclear charge density. For a charge density $\rho(r)$ with a finite cutoff R, these are defined as

$$I^{(n)}=4\pi\int_0^R dr\, r^{n+2}\rho(r), \quad (n=0, 2, 4, \cdots). \tag{4}$$

According to the results quoted previously,[9,17–19] the scattering at low energies can be described in terms of the first two even moments, the total charge, and the mean square radius. A test of the moment interpretation at an energy just above the range of shape independence will be made in Sec. V. This involves exact calculations for charge densities slightly more complicated than the shell and homogeneous densities. The energy is such that only one additional moment, the fourth, should be effective. However, a brief summary of the calculational procedure will be first given in Sec. II. Section III will be devoted to calculations for the shell and homogeneous distributions for a wide variety of atomic numbers and energies to determine the range of shape independence. After the discussion of the effect of higher moments in Secs. IV and V, the experimental situation below 100 Mev will then be reviewed in Sec. VI.

II. PHASE SHIFT DESCRIPTION OF ELECTRON SCATTERING

The scattering theory for the Dirac equation has been given by Mott,[20] and his notation is followed here. The wave function is expanded in partial waves characterized by the total angular momentum and parity quantum numbers j and κ. Actually, Mott uses the orbital angular momentum quantum number l, so that for a given j, there are two values of l, $j+\frac{1}{2}$ for $\kappa=+(j+\frac{1}{2})$ states and $j-\frac{1}{2}$ for $\kappa=-(j+\frac{1}{2})$ states. If the rest mass is neglected, the phase shifts for these two states are identical[17,21] and the value of l for the

[15] E. Guth, Akad. Wiss. Wien. Math.-naturw. Kl. Anz. **71**, 299 (1934).
[16] M. E. Rose, Phys. Rev. **73**, 279 (1948).
[17] H. Feshbach, Phys. Rev. **84**, 1206 (1951).
[18] L. R. B. Elton, Proc. Phys. Soc. (London) **A66**, 806 (1953).
[19] A. R. Bodmer, Proc. Phys. Soc. (London) **A66**, 1041 (1953).
[20] N. F. Mott and H. S. W. Massey, *Theory of Atomic Collisions* (Oxford University Press, London, 1949).
[21] L. K. Acheson, Ph.D. thesis, Massachusetts Institute of Technology, 1950 (unpublished).

$\kappa<0$ states is sufficient for purposes of notation,

$$j=l+\tfrac{1}{2}, \quad (l=0, 1, 2, \cdots).$$

The error in the cross section from neglect of the rest mass[12,21] is of order $(Z\alpha/k)^2$, where α is the fine structure constant and k is the energy in units of mc^2.[22] For these calculations the error is always less than 1 percent.

The effect of the finite extension of the nuclear charge is described in terms of the difference δ_l between the total phase shift η_l and the point Coulomb phase shift η_l^+

$$\delta_l=\eta_l-\eta_l^+. \tag{5}$$

These phase shifts are defined by the asymptotic form of the Dirac radial functions

$$\begin{aligned} f_l &\xrightarrow[kr\to\infty]{} k^{\frac{1}{2}}\sin(kr+Z\alpha\ln 2kr-\tfrac{1}{2}l\pi+\eta_l^+ +\delta_l), \\ g_l &\xrightarrow[kr\to\infty]{} -k^{\frac{1}{2}}\cos(kr+Z\alpha\ln 2kr-\tfrac{1}{2}l\pi+\eta_l^+ +\delta_l) \end{aligned} \tag{6}$$

and the requirement that f_l and g_l vanish for $r=0$. The radial functions satisfy a pair of coupled linear first-order differential equations,

$$\begin{aligned} \left(\frac{d}{dr}-\frac{l+1}{r}\right)f_l &= -(k-V)g_l, \\ \left(\frac{d}{dr}+\frac{l+1}{r}\right)g_l &= (k-V)f_l. \end{aligned} \tag{7}$$

The evaluation of the δ_l for the charge densities considered here follows closely the method used by Elton.[8] These charge densities all have a finite cut-off radius R, so that for $r\geq R$ the potential is Coulombic. In this region the radial functions are a linear combination of regular and irregular Coulomb functions,[23]

$$\begin{pmatrix} f_l \\ g_l \end{pmatrix} = A_l^+\begin{pmatrix} f_l^+ \\ g_l^+ \end{pmatrix} + A_l^-\begin{pmatrix} f_l^- \\ g_l^- \end{pmatrix} \quad (r\geq R). \tag{8}$$

The regular (f_l^+, g_l^+) and irregular (f_l^-, g_l^-) Coulomb functions are solutions of Eq. (7) with $V=-Z\alpha/r$, and have the indicial behavior $r^{\rho_{l+1}}$ and $r^{-\rho_{l+1}}$, respectively, with $\rho_{l+1}=[(l+1)^2-Z^2\alpha^2]^{\frac{1}{2}}$. The asymptotic forms of these functions are given by Eq. (6) with $\delta_l=0$, and η_l^+ replaced by η_l^- for the irregular functions. Closed expressions for the Coulomb phase shifts have been derived by Mott.[20] By substituting the asymptotic form of each of the functions in Eq. (8), Elton obtained the following expression for the phase shift difference:

$$\tan\delta_l=\frac{\sin(\eta_l^- -\eta_l^+)}{(A_l^+/A_l^-)+\cos(\eta_l^- -\eta_l^+)}. \tag{9}$$

The ratio A_l^+/A_l^- is then evaluated from Eq. (8) at $r=R$:

$$\frac{A_l^+}{A_l^-}=-\left.\frac{f_l^- -(f_l/g_l)g_l^-}{f_l^+ -(f_l/g_l)g_l^+}\right|_{r=R}. \tag{10}$$

In Eqs. (9) and (10), the ratio f_l/g_l of the interior solutions is the only quantity, other than the radius R, which depends on the nuclear charge density. All of the others are point charge solutions. These have been collected in another report[24] which gives the methods of calculation and tables of the quantities themselves. In particular, the radial functions are evaluated from the series solutions $u_l^\pm$ and $v_l^\pm$ about the origin,

$$\begin{pmatrix} f_l^\pm \\ g_l^\pm \end{pmatrix} = B_l(kr)^{\pm\rho_{l+1}}\begin{pmatrix} u_l^\pm \\ v_l^\pm \end{pmatrix}. \tag{11}$$

With the normalization constant B_l chosen to give the asymptotic forms in Eq. (6), the expression for A_l^+/A_l^- in Eq. (10) becomes

$$\begin{aligned} \frac{A_l^+}{A_l^-} = -(2kR)^{-2\rho_{l+1}}\left|\frac{\Gamma(-\rho_{l+1}+1+iZ\alpha)}{\Gamma(\rho_{l+1}+1+iZ\alpha)}\right|\frac{\Gamma(2\rho_{l+1}+1)}{\Gamma(-2\rho_{l+1}+1)} \\ \times\left[\frac{l+1-\rho_{l+1}}{l+1+\rho_{l+1}}\right]^{\frac{1}{2}}\left[\frac{u_l^- -(f_l/g_l)v_l^-}{u_l^+ -(f_l/g_l)v_l^+}\right]_{r=R}. \end{aligned} \tag{12}$$

Finally, Acheson has shown that, for energies much greater than the rest energy, the scattering cross section may be written as

$$k^2\sigma(\theta)=|G^c+G'|^2\sec^2(\theta/2). \tag{13}$$

The function $G^c(Z\alpha,\theta)$ is the amplitude for scattering by a point charge tabulated by Feshbach,[25] and $G'(Z\alpha,kR;\theta)$ is the change in the scattering amplitude due to the finite size of the nucleus,

$$\begin{aligned} G'=\frac{1}{2i}\sum_{l=0}(l+1)\exp(2i\eta_l^+)(e^{2i\delta_l}-1) \\ \times[P_l(\cos\theta)+P_{l+1}(\cos\theta)]. \end{aligned} \tag{14}$$

The reason for the decomposition in Eq. (13) of the scattering amplitude is that the convergence of the series for G' is much better than that for the Mott series for G^c or (G^c+G'). The difficulties with the latter are associated with the long range of the Coulomb potential. The number of terms in Eq. (14) is only about $(kR+1)$. It is easier to do the difficult job of obtaining G^c just once and to evaluate G' for specific charge densities. On the other hand, there may be strong destructive interference between the two amplitudes. Then both G^c and G' have to be known to several more significant figures than is required for their sum.

[22] From this point, relativistic units are used in which $\hbar=m=c=1$.

[23] The plus and minus signs refer to regular and irregular, respectively.

[24] A. E. Glassgold and E. W. Mack, Massachusetts Institute of Technology Laboratory for Nuclear Science and Engineering, Technical Report No. 65, August 31, 1954 (unpublished).

[25] H. Feshbach, Phys. Rev. 88, 295 (1952).

For this reason, Yennie, Ravenhall, and Wilson[10] have devised a new method for evaluating the point Coulomb scattering amplitude G^c which is more simple and more accurate than previous ones.[13,25] Their results for $Z=13$, 29, and 79 have been used here[26] and their method has been applied to the additional cases of $Z=50$ and $Z=74$.

III. SHELL AND HOMOGENEOUS CHARGE DISTRIBUTIONS

In order to determine the range of validity of shape independence, it is sufficient to compare the simple-shell and homogeneous-charge densities used by Elton and Acheson. This is a safe comparison because the shell distribution deviates so much more widely from the homogeneous distribution than some more physically reasonable model. The shell distribution is used, of course, because of its simple radial functions.

The potentials for the shell and homogeneous distributions are square and oscillator wells, respectively:

$$V_s=-Z\alpha/R_s, \qquad (r\leq R_s); \quad (15a)$$

$$V_h=-\tfrac{1}{2}(Z\alpha/R_h)(3-r^2/R_h^2), \quad (r\leq R_h). \quad (15b)$$

The solutions of Eq. (7) for the shell distribution are

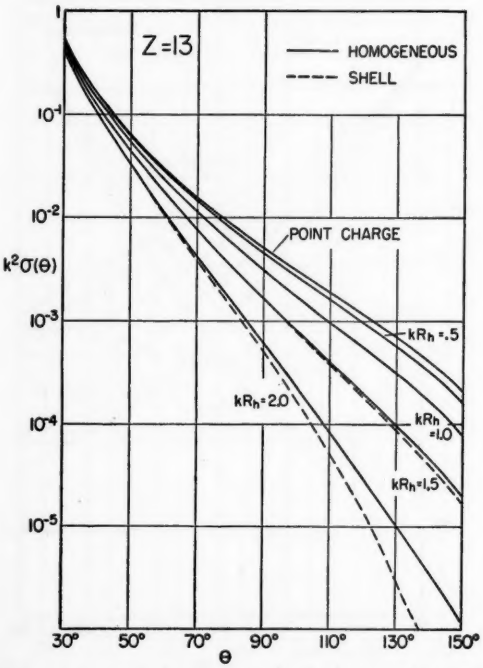

FIG. 1. Angular distributions, $k^2\sigma(\theta)$, of electrons scattered by aluminum for the homogeneous and shell distributions as a function of kR_h. The mean square radii of the two densities are equal ($kR_s=0.775kR_h$). For $kR_h=0.5$ and 1.0 the models are indistinguishable on this plot. For $kR_h=1.5$ and 2.0 the dash curves are for the shell, the solid curves for the homogeneous distribution. With $r_0=1.2$, $kR_h=1.0$ corresponds to an energy of 55 Mev.

[26] The author would like to thank Dr. D. R. Yennie for permission to use these results before publication.

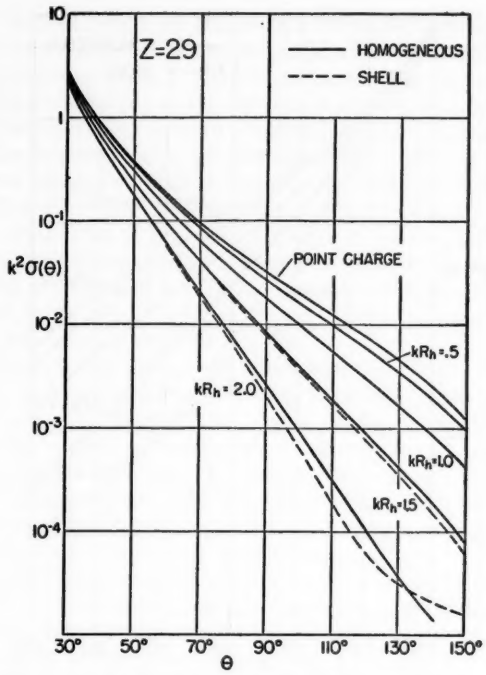

FIG. 2. Angular distributions, $k^2\sigma(\theta)$, of electrons scattered by copper for the homogeneous and shell distributions as a function of kR_h. The mean square radii of the two densities are equal ($kR_s=0.775kR_h$). For $kR_h=0.5$ and 1.0 the models are indistinguishable on this plot. For $kR_h=1.5$ and 2.0 the dash curves are for the shell, the solid curves for the homogeneous distribution. With $r_0=1.2$, $kR_h=1.0$ corresponds to an energy of 41 Mev.

spherical Bessel functions of argument $(kR_s+Z\alpha)$:

$$f_l(R)=j_l(kR_s+Z\alpha), \quad g_l(R)=j_{l+1}(kR_s+Z\alpha). \quad (16)$$

In this case $(k-V)$ is a constant and the differential equations may be identified as the recurrence relations for the spherical Bessel functions.[27] For the homogeneous distribution, series solutions about the origin are perhaps the easiest way of evaluating f_l/g_l:

$$f_l=r^{l+1}\sum_{n=0} a_n^{(l)}r^n \quad g_l=r^{l+1}\sum_{n=1} b_n^{(l)}r^n. \quad (17)$$

The series coefficients are obtained from the coupled recurrence relations

$$\begin{aligned} na_n^{(l)}&=-[1+\tfrac{3}{2}Z\alpha/kR_h]b_{n-1}^{(l)} \\ &\quad +[\tfrac{1}{2}Z\alpha/(kR_h)^3]b_{n-3}^{(l)}, \\ (n+2l+2)b_n^{(l)}&=[1+\tfrac{3}{2}Z\alpha/kR_h]a_{n-1}^{(l)} \\ &\quad -[\tfrac{1}{2}Z\alpha/(kR_h)^3]a_{n-3}^{(l)}. \end{aligned} \quad (18)$$

Once the ratios f_l/g_l are evaluated, the analysis of the preceding section is complete. The angular distributions $k^2\sigma(\theta)$ calculated in this way are given in Figs. 1, 2, 3, 4, and 5 for the atomic numbers $Z=13$,

[27] P. M. Morse and H. Feshbach, *Methods of Theoretical Physics* (John Wiley and Sons, Inc., New York, 1953).

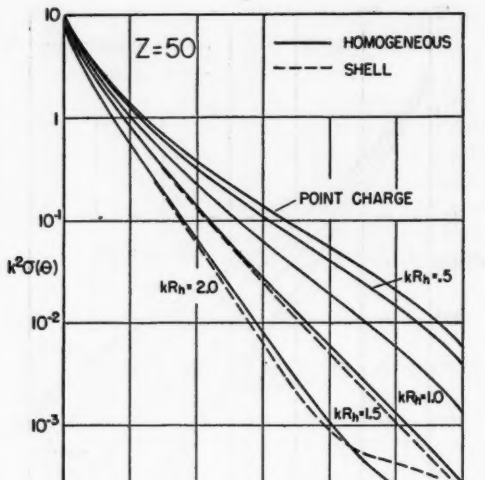

FIG. 3. Angular distributions, $k^2\sigma(\theta)$, of electrons scattered by tin for the homogeneous and shell distributions as a function of kR_h. The mean square radii of the two densities are equal ($kR_s=0.775kR_h$). For $kR_h=0.5$ and 1.0 the models are indistinguishable on this plot. For $kR_h=1.5$ and 2.0 the dash curves are for the shell, the solid curves for the homogeneous distribution. With $r_0=1.2$, $kR_h=1.0$ corresponds to an energy of 33 Mev.

29, 50, 74, and 79. The radii of the two charge densities have been adjusted according to Eq. (3) so that their second moments are equal. The solid curves in these figures are for the homogeneous distribution for $kR_h=0.5$, 1.0, 1.5, and 2.0. The corresponding angular distributions for the shell distribution with $kR_s=0.775\times(kR_h)=0.3875$, 0.775, 1.1625, and 1.55 are presented as dash curves only if they can be distinguished from those for the homogeneous distribution. Thus the cross sections for the shell and homogeneous distributions for $kR_h=0.5$ and 1.0 are indistinguishable on this plot, corresponding to tabular differences of a few percent. For $kR_h=1.5$ there appear small differences near 90° which increase to 10 or 15 percent at 150°. As kR_h becomes larger, the differences between the angular distributions at a given angle continue to increase. If the cross section can be measured with better than 10 percent accuracy beyond 90°, then it should be possible to distinguish between charge densities for $kR_h\gtrsim1.5$. In terms of the electron's energy, the upper limit for shape independence is thus roughly 85, 65, 50, and 45 Mev for the atomic numbers $Z=13$, 29, 50, and 79, respectively.[28] This result has been verified by calculations with other charge densities, such as those discussed in Sec. V. Potentials depending on the fourth power of r have also been considered.

Elton[18] and Bodmer[19] have used perturbation methods to show that shape independence of electron scattering holds outside the long wavelength region. The upper limit obtained by them is only slightly smaller than found here ($kR_h=1.5$) from exact calculations. Elton, for example, derived the following exact equation for the difference in the lth phase shift for the two potentials V_1 and V_2:

$$\sin[\eta_l^{(1)}-\eta_l^{(2)}]=-\frac{1}{k}\int_0^\infty dr(V_1-V_2)\times[f_l^{(1)}f_l^{(2)}+g_l^{(1)}g_l^{(2)}]. \quad (19)$$

Similar expressions have also been obtained by Parzen,[29] Rose,[30] and Elton.[31] If the phase shifts and radial functions are known for some (unperturbed) potential V_1, then a simple approximation for the other phase shift is obtained from Eq. (19) by using the same radial functions for V_2:

$$\sin[\eta_l^{(1)}-\eta_l^{(2)}]\simeq-\frac{1}{k}\int_0^\infty dr(V_1-V_2)[f_l^{(1)2}+g_l^{(1)2}]. \quad (20)$$

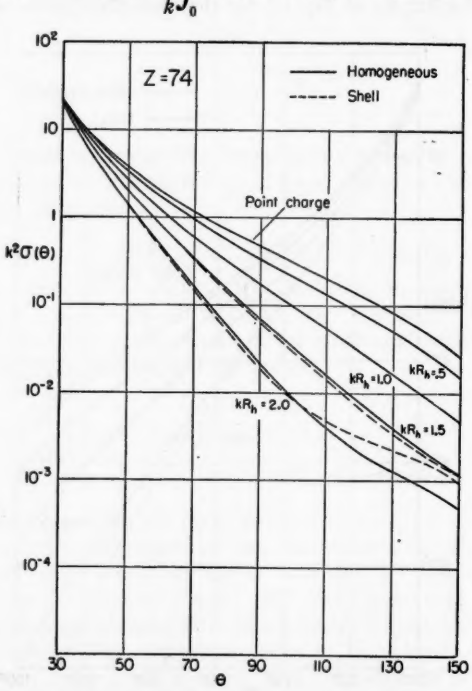

FIG. 4. Angular distributions, $k^2\sigma(\theta)$, of electrons scattered by tungsten for the homogeneous and shell distributions as a function of kR_h. The mean square radii of the two densities are equal ($kR_s=0.775kR_h$). For $kR_h=0.5$ and 1.0 the models are indistinguishable on this plot. For $kR_h=1.5$ and 2.0 the dash curves are for the shell, the solid curves for the homogeneous distribution. With $r_0=1.2$, $kR_h=1.0$ corresponds to an energy of 29 Mev.

[28] With $r_0=1.2$, $kR_h=1$ corresponds to electron energies of 55, 41, 33, 29, and 28 Mev for $Z=13$, 29, 50, 74, and 79, respectively.

[29] G. Parzen, Phys. Rev. **80**, 261 (1950).
[30] M. E. Rose, Phys. Rev. **82**, 389 (1951).
[31] L. R. B. Elton, Proc. Phys. Soc. (London) **A65**, 481 (1952).

We have used this method to compute homogeneous phase shifts from shell and Coulomb phase shifts. A comparison with exactly calculated phase shifts shows this approximation to be in error by about 50 percent. Better results would be expected for cases where the perturbed and unperturbed charge densities are not so different. This has been borne out by recent calculations of Trammel.[32]

IV. INTERPRETATION OF THE SCATTERING IN TERMS OF MOMENTS

To obtain the scattering for a particular charge density the phase shift differences δ_l have to be evaluated by the methods presented in Sec. II. The phase shift differences themselves are not really convenient for describing the nuclear charge density, however, because a clear connection is lacking between individual δ_l and specific properties of $\rho(r)$. Moreover, the number of phase shift differences needed for an exact calculation is usually larger than the number of parameters obtained from the observed scattering. Thus, for $kR_h=1$, δ_0 and δ_1 must be evaluated although the scattering determines only the mean square radius. At higher energies Ravenhall and Yennie[11] find that for $kR_h=4$, where six phase-shift differences are used, only one additional parameter can be obtained from the experimental data, a "surface distance." This surface distance is defined as the distance in which the charge density decreases from its essentially constant interior value to zero. Finally, the particular form of $\rho(r)$ which gives agreement with experiment may contain more information than the observed scattering implies. This is certainly so at low energies ($kR_h<1.5$) where only the mean square radius is essential. Similarly, in the work of Ravenhall and Yennie from 84 to 183 Mev for gold, it has been found that the scattering is insensitive to details inside the surface region.

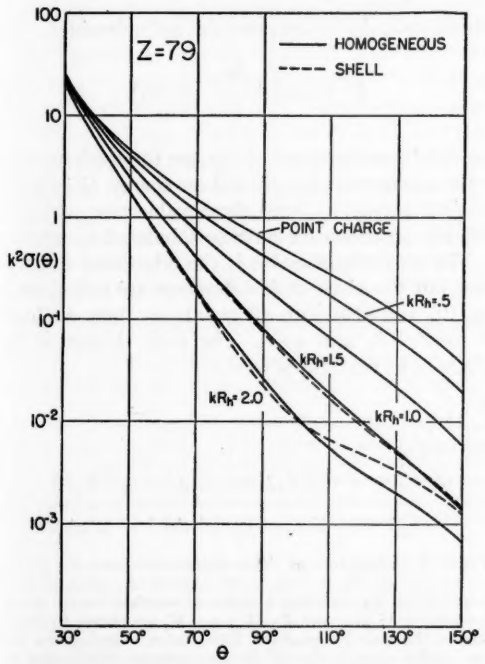

FIG. 5. Angular distributions, $k^2\sigma(\theta)$, of electrons scattered by gold for the homogeneous and shell distributions as a function of kR_h. The mean square radii of the two densities are equal ($kR_s=0.775kR_h$). For $kR_h=0.5$ and 1.0 the models are indistinguishable on this plot. For $kR_h=1.5$ and 2.0 the dash curves are for the shell, the solid curves for the homogeneous distribution. With $r_0=1.2$, $kR_h=1.0$ corresponds to an energy of 28 Mev.

[32] G. T. Trammel, Oak Ridge National Laboratory Semiannual Progress Report No. 1798, September 10, 1954 (unpublished).

Because the amount of information which can be obtained from electron scattering is limited, it would be useful to describe the nuclear charge density in terms of some minimum set of parameters. At low energies we have used the first two even moments of the charge density, the total charge and the mean square radius. For all Z and $kR_h \gtrsim 1.5$, charge densities with equal zeroth and second moments are indistinguishable. It may be possible to describe the differences which occur at higher energies in terms of the higher even moments defined in Eq. (4). This is suggested by the long wavelength limit of Eq. (20) for δ_l after two integrations by parts:

$$\sin\delta_l \propto 4\pi \int_0^R dr r^{2l+4}\rho(r). \tag{21}$$

Setting $l=0$ leads to Feshbach's result in Eq. (2). Certainly charge densities which are functions of only even powers of r can be characterized by the even moments. Thus, just above the shape independent region, the fourth moment should also be important. If this assumption is correct, charge densities, whose first three moments ($I^{(0)}$, $I^{(2)}$, $I^{(4)}$) are equal, must give the same scattering in this energy range ($kR_h \gtrsim 1.5$). To test this condition, we shall introduce in the next section charge densities with variable fourth moments. Their second moments will be set equal to that for the homogeneous distribution,

$$I^{(2)}=4\pi\int_0^R dr r^4\rho(r)=\tfrac{3}{5}ZeR_h^2, \tag{22a}$$

and their fourth moments will be expressed in units of the homogeneous fourth moment,

$$I^{(4)}=4\pi\int_0^R dr r^6\rho(r)=\lambda[(3/7)ZeR_h^4]. \tag{22b}$$

V. DOUBLE SHELL AND η CHARGE DISTRIBUTIONS

The first charge density considered is a simple combination of the shell and homogeneous charge densities which will be referred to as the "η distribution." A shell of charge ηZe and radius R_η encloses a region of constant charge density. The η distribution is not

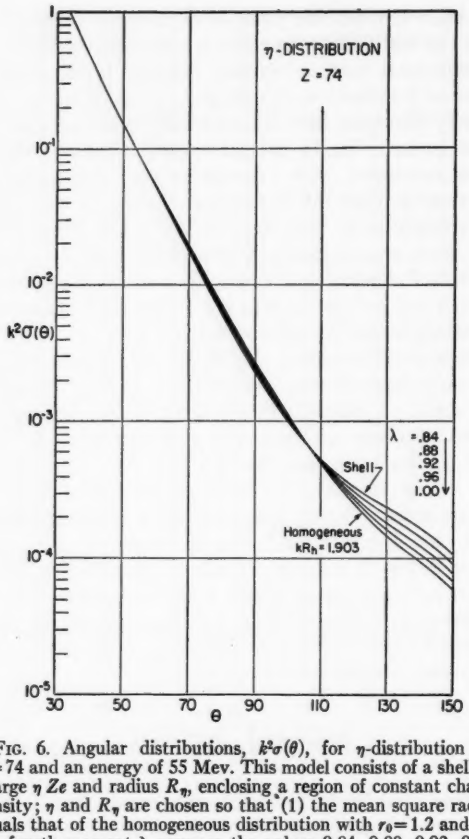

FIG. 6. Angular distributions, $k^2\sigma(\theta)$, for η-distribution for $Z=74$ and an energy of 55 Mev. This model consists of a shell, of charge ηZe and radius R_η, enclosing a region of constant charge density; η and R_η are chosen so that (1) the mean square radius equals that of the homogeneous distribution with $r_0=1.2$ and (2) the fourth moment λ assumes the values 0.84, 0.88, 0.92, 0.96, and 1.00. These parameters are listed in Table I.

completely unreasonable, for in a primitive way it represents the concentration of protons near the nuclear surface suggested by Feenberg.[33] Placing the shell at the edge, makes the potential parabolic as in the case of the homogeneous distribution in Eq. (15b),

$$V_\eta=-\tfrac{1}{2}Z\alpha[(3-\eta)-(1-\eta)r^2/R_\eta^2]/R_\eta. \quad (23)$$

The radial functions are obtained by the same series method used for the homogeneous distribution; the series coefficients in Eq. (17) are now found from the recurrence formulas

$$\begin{aligned} na_n^{(l)}&=-[1+3Z\alpha/2kR_\eta]b_{n-1}^{(l)} \\ &\quad+[Z\alpha/2(kR_\eta)^3]b_{n-3}^{(l)}, \\ (n+2l+2)b_n^{(l)}&=[1+3Z\alpha/2kR_\eta]a_{n-1}^{(l)} \\ &\quad-[Z\alpha/2(kR_\eta)^3]a_{n-3}^{(l)}. \end{aligned} \quad (24)$$

Table I lists the values of η considered and Fig. 6 gives the calculated angular distributions for $Z=74$ and an energy corresponding to $kR_h=1.90258$. If the radius of the equivalent homogeneous charge density is given by Eq. (1) with $r_0=1.2$, then the energy is 55 Mev. The angular distributions in Fig. 6 differ only slightly up to 108° where they intersect. Beyond this, appreciable differences occur. The extreme curves are for the shell ($\eta=1, \lambda=0.84$) and homogeneous ($\eta=0, \lambda=1.00$) distributions. Equal changes in the fourth moment ($\Delta\lambda=0.04$) result in nearly equal reductions (about 15 percent) in the large-angle scattering. The scattering for angles less than 108° is characteristic of the mean square radius.

The other charge distribution considered is the "double-shell," which consists of two concentric shells of charge Z_1e and Z_2e, and of radii r_1 and r_2, respectively ($r_1\leq r_2$). The potential inside the inner shell is a constant,

$$k-V_{ss}=k+\frac{Z_1\alpha}{r_1}+\frac{Z_2\alpha}{r_2}, \quad (r<r_1), \quad (25a)$$

so that the radial solutions are spherical Bessel functions. Between the shells, there is a $1/r$ term from the Coulomb potential of the inner shell:

$$k-V_{ss}=k+\frac{Z_1\alpha}{r}+\frac{Z_2\alpha}{r_2}, \quad (r_1<r<r_2). \quad (25b)$$

Outside both shells, the potential is Coulombic:

$$k-V_{ss}=k+\frac{Z\alpha}{r}, \quad (r>r_2). \quad (25c)$$

The radial functions for $r_1<r<r_2$ are Coulomb functions for the atomic number Z_1 and an energy $(k+Z_2\alpha/r_2)$. We shall choose Z_1 from those values for which the Coulomb functions are already tabulated in reference 24. The only complication is the additional matching point, but the phase shift differences are still given by Eqs. (9) and (10) with all quantities there evaluated for $Z=Z_1+Z_2$ and $r=r_2$. The only change is that $(f_l/g_l)_{r=r_2}$ in Eq. (10) is now

$$\left(\frac{f_l}{g_l}\right)_{r=r_2}=\frac{-(t_2/t_1)^{2\rho l+1(Z_1)}C_l(Z_1,t_1)u_l^+(Z_1,t_2)+u_l^-(Z_1,t_2)}{-(t_2/t_1)^{2\rho l+1(Z_1)}C_l(Z_1,t_1)v_l^+(Z_1,t_2)+v_l^-(Z_1,t_2)}, \quad (26)$$

TABLE I. Parameters of the η distribution used to calculate the scattering in Fig. 6. This model consists of a shell, of charge ηZe and radius R_η, enclosing a region of constant charge density. The energy is 55 Mev and $Z=74$; η and R_η are chosen to give the values of the fourth moment λ listed below, keeping the mean square radius equal to that of the homogeneous distribution with $r_0=1.2$.

η	R/R_h	λ
1.000	0.775	0.84
0.795	0.808	0.88
0.592	0.847	0.92
0.375	0.894	0.96
0.000	1.000	1.00

[33] E. Feenberg, Phys. Rev. 59, 593 (1940).

with

$$C_l(Z_1,t_1)=\frac{u_l^-(Z_1,t_1)-(j_l/j_{l+1})_{v1}v_l^-(Z_1,t_1)}{u_l^+(Z_1,t_1)-(j_l/j_{l+1})_{v1}v_l^+(Z_1,t_1)},$$

where $t_1=kr_1+Z_2\alpha(r_1/r_2)$, $y_1=t_1+Z_1\alpha$, $t_2=kr_2+Z_2\alpha$. With $Z_1=50$, and $Z=74$, r_1 and r_2 are chosen so that Eq. (22) is satisfied and the fourth moment ranges from $\lambda=0.84$ to $\lambda=1.16$ in steps of 0.04. The various parameters associated with this model are summarized in Table II and the scattering is plotted in Fig. 7 for an energy corresponding to $kR_h=1.90258$. The general variation of the large-angle scattering is the same as for the η distribution although the change from one curve to the next is not quite as regular. The average decrease in the large-angle scattering is about 10 percent for an increase in λ of 0.04. The corresponding change for the η distribution is about 15 percent. The angular distributions intersect at 110°, quite close to the intersection angle of 108° in Fig. 6.

The calculations for the η and double-shell densities agree fairly well as regards the general shape of the angular distributions and the rate of change of the large-angle scattering with the fourth moment. There is disagreement, however, in one crucial point. The angular distributions for the same fourth moment produce identical scattering only out to 120°. Beyond this there are differences as large as 7 percent, 5 percent, 10 percent, and 11 percent for fourth moments $\lambda=0.88$, 0.92, 0.96, and 1.00.[34] The validity of a description of electron scattering in terms of even moments is thus no greater than 10 percent for these calculations. This corresponds to an uncertainty in the fourth moment of about 4 percent. Only if the fourth moment of the nuclear charge density differs from that for the homogeneous distribution by much more than 4 percent can the moment interpretation be used.

VI. EXPERIMENTAL RESULTS BELOW 100 MEV

In Fig. 8 the scattering observed by Lyman, Hanson, and Scott[1] for 15.7-Mev electrons is compared with calculations for the homogeneous charge distribution, which are labeled by the value of r_0 in Eq. (1). The experimental points for a particular element do not match any one curve so that estimates of r_0 must be made at each angle and then an average taken. For aluminum the finite size effect is very small and the only angles yielding reasonable values are 120° and 150°, for which $r_0=1.2$. The 30° measurement for copper is significantly low; the other points give an average value of $r_0=1.20$. For silver, calculations of the ratio of the actual scattering for $Z=50$ have been used by normalizing the theoretical and experimental values at 30°. A correction has to be made, of course, for the fact that, for the same kR_h, σ/σ_c decreases more rapidly with angle for $Z=50$ than for $Z=47$. The radius for silver is then $r_0=1.13$. Finally the result for gold is $r_0=1.29$. All of these estimates involve an uncertainty of roughly 10 percent due to the standard errors in the data. Thus these determinations are not sufficiently precise to detect any variation with atomic number of the value of r_0 needed in Eq. (1). The average radius for the four elements considered is $r_0=1.2$ to within 10

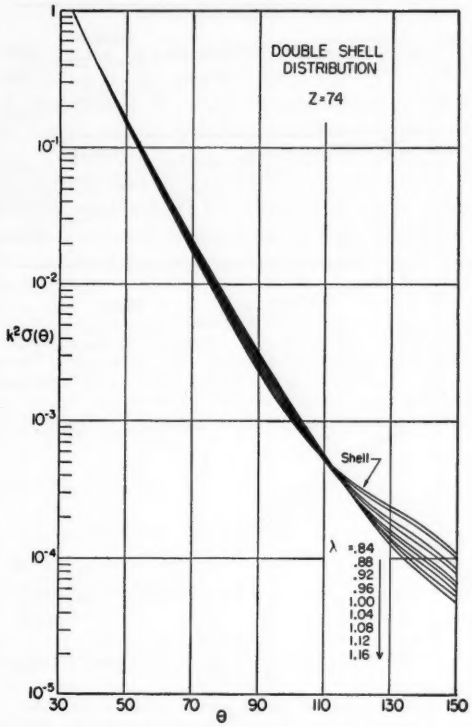

FIG. 7. Angular distributions, $k^2\sigma(\theta)$, for the double shell distribution for $Z=74$ and an energy of 55 Mev. This model consists of two concentric shells of charge Z_1e and Z_2e and radii r_1 and r_2. In this case $Z_1=50$ and $Z_1+Z_2=74$; r_1 and r_2 are chosen so that (1) the mean square radius equals that of the homogeneous distribution with $r_0=1.2$, and (2) the fourth moment λ ranges from 0.84 to 1.16 in steps of 0.04. These parameters are listed in Table II.

TABLE II. Parameters of the double shell density used to calculate the scattering in Fig. 7. This model consists of two concentric shells of charge Z_1e and Z_2e and radius r_1 and r_2. The energy is 55 Mev, and $Z=Z_1+Z_2=74$ with $Z_1=50$; r_1 and r_2 are chosen to give the values of the fourth moment λ listed below, keeping the mean square radius equal to that of the homogeneous distribution with $r_0=1.2$.

r_1/r_2	r_2/R_h	λ
1.000	0.775	0.84
0.803	0.888	0.88
0.738	0.931	0.92
0.691	0.963	0.96
0.654	0.989	1.00
0.623	1.011	1.04
0.596	1.031	1.08
0.576	1.049	1.12
0.550	1.065	1.16

[34] No comparison can be made for $\lambda=0.84$ because both models reduce to the simple shell in this case, or for $\lambda>1.00$ because the fourth moment of the η distribution is less than or equal to one.

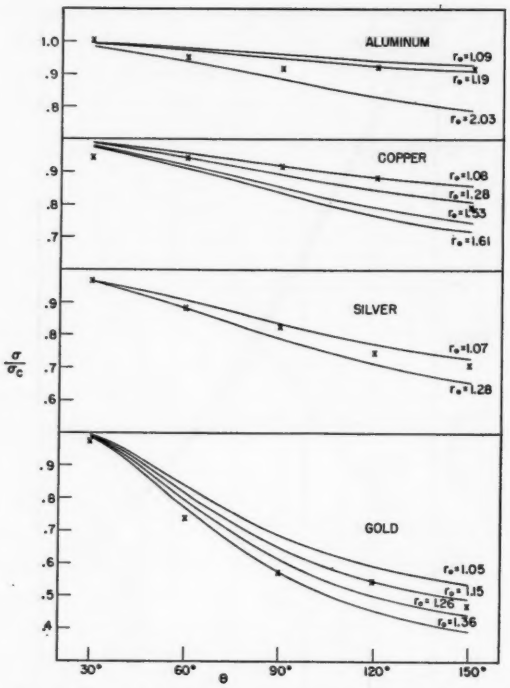

FIG. 8. Comparison of the experimental data at 15.7 Mev with curves for the homogeneous distribution, labeled by the corresponding value of r_0. Neglecting observations which cannot be fit by any reasonable choice of r_0, the average radius for each element is given by r_0=1.2, 1.20, 1.13, and 1.29, for Z=13, 29, 50, and 79, respectively. The over-all average is 1.2 with an uncertainty of about 10 percent.

percent, which is somewhat higher than the previous analysis of Bitter and Feshbach.[2]

The experimental values in Fig. 8 are absolute measurements and include an increment of from 5 to 9 percent from the Schwinger formula for radiative corrections.[35] Without these corrections all of the 30° measurements and some of the 60° measurements are too low for any reasonable choice of the radius. Best agreement is expected, however, for just these cases for which the deviations from point scattering are small. One conclusion is that the radiative corrections are not negligible at these energies. If the measurements are not considered as absolute, however, comparison with theory can still be made by normalization of the calculated and observed cross sections *without radiative corrections* at 30°. The average r_0 obtained in this way is very close to 1.2, the value obtained with the radiative corrections. The Schwinger formula is valid only for very small Z, since it is the Born approximation to the radiative corrections for a point charge. A more accurate examination of the radiative corrections, including the effect of the finite nuclear size, is thus essential. Without it, the 5 or 10 percent corrections of the Schwinger formula represent a limit on the reliability of conclusions from electron scattering.[36]

Some other experiments below 100 Mev are the work of Pidd's group at Michigan. The very precise determination by Pidd, Hammer, and Raka[3] of $\sigma(60°)/\sigma(90°)=7.77\pm0.08$ for $Z=50$ at 34 Mev gives $r_0=1.22\pm0.01$. From relative measurements at 33 and 43 Mev they concluded that the radius of the tungsten nucleus is given by Eq. (1) with $r_0=1.0\pm0.1$. This value is too small, partly because the single-phase-shift analysis[9] is inadequate for tungsten at these energies. Pidd and Hammer[37] have recently obtained new angular distributions (66.25° to 114.5°) for tungsten at 31, 40, and 60 Mev. These are relative measurements with a standard error of about 5 percent. A comparison with the scattering from the homogeneous distribution can be made by normalizing the observed and calculated values at the smallest angle for which measurements were made. No radiative corrections have been included. The values of r_0 determined at each energy are $r_0=1.01$, 1.22, and 1.18 at 31, 40, and 60 Mev, respectively. The uncertainty in this analysis is about 10 percent.

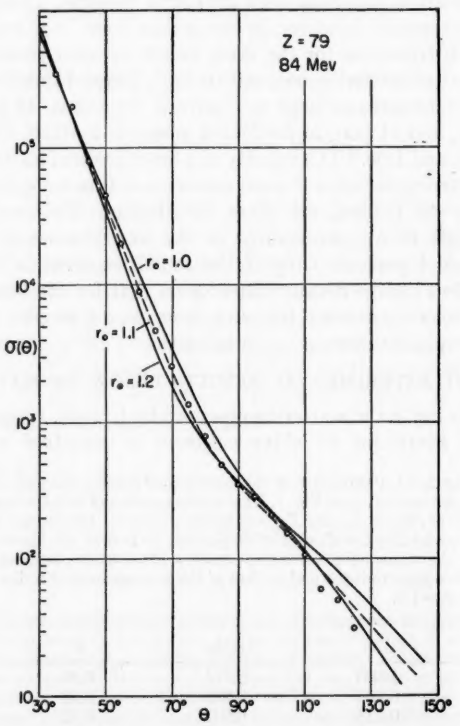

FIG. 9. Comparison of experimental data at 84 Mev for gold with calculations for the homogeneous distribution, labeled by the corresponding value of r_0. The curve for $r_0=1.1$ gives the best agreement with the measurements out to 110°.

[35] J. Schwinger, Phys. Rev. **76**, 790 (1949).

[36] R. Hofstadter (reference 4) has pointed out that, for relative measurements at much higher energies, the Schwinger correction is negligible because it changes so slowly with angle compared to the observed cross section.

[37] R. W. Pidd and C. L. Hammer (private communication).

In Fig. 9 we have compared the 84-Mev data for gold obtained at Stanford[5] with calculations for the homogeneous distribution. Here the curves are normalized to the cross section at 35°. For angles less than 110°, good agreement is obtained for a radius given by $r_0=1.10$. The deviation of the three points beyond 110° may be indicative of a fourth moment slightly larger than that for a constant charge density.

In conclusion, the present experimental data for energies below 100 Mev indicate that the mean square radius of the nuclear charge distribution is given by a uniform charge density with $r_0=1.2$. The spread in the experimental data and the uncertainty in the radiative corrections make this determination uncertain by about 10 percent.‡

‡ *Note added in proof.*—Recently the problem of the radiative corrections has received further study by H. Mitter and P. Urban, Acta Phys. Austriaca 8, 356 (1954); R. Newton, Phys. Rev. 97, 1162 (1955); H. Suura, Phys. Rev. 98, 278(A) (1955). Suura's result for the one-photon radiative corrections to high-energy electron scattering is that the leading term (for large momentum transfer and good resolution) of the fractional decrease is given by the Schwinger correction to *all* orders of the Born approximation in the nuclear field.

ACKNOWLEDGMENTS

The author would like to thank Professor A. O. Hanson for helpful comments on the 15.7-Mev data, and Professor R. W. Pidd for permission to quote his new results prior to publication. The assistance of the Joint Computing Group of M.I.T. is gratefully acknowledged, and in particular the skillful work of Mrs. Evelyn Mack. It is a pleasure to thank Professor Herman Feshbach for suggesting and guiding this work. His continued interest and encouragement is greatly appreciated.

PHYSICAL REVIEW VOLUME 98, NUMBER 5 JUNE 1, 1955

Nuclear Cross Sections for 1.4-Bev Neutrons*

T. Coor,† D. A. Hill,‡ W. F. Hornyak,§ L. W. Smith, and G. Snow||
Brookhaven National Laboratory, Upton, New York

(Received January 11, 1955)

Transmission measurements in good and poor geometry have been performed at the Brookhaven Cosmotron to measure the total and absorption cross sections of several nuclei for neutrons in the Bev energy range. The neutrons are produced by bombarding a Be target with 2.2-Bev protons. The neutron detector requires the incident particle to pass an anticoincidence counter and produce in an aluminum radiator a charged particle that will traverse a fourfold scintillation telescope containing 6 in. of lead. Contribution of neutrons below 800 Mev are believed small. The angular distribution of neutrons from the target is sharply peaked forward with a half-width of 6°.

The integral angular distributions of diffraction scattered neutrons from C, Cu, and Pb are measured by varying the detector geometry. The angular half-width of these distributions indicates a mean effective neutron energy of 1.4±0.2 Bev.

The total cross sections σ_H and $\sigma_D-\sigma_H$ are measured by attenuation differences in good geometry of CH_2-C and D_2O-H_2O, with the result: $\sigma_H=42.4\pm1.8$ mb, $\sigma_D-\sigma_H=42.2\pm1.8$ mb.

The cross sections of eight elements from Be to U are measured in good and poor geometry, and the following values of the total and absorption cross sections are deduced (in units of millibarns):

	Be	C	Al	Cu	Sn	Pb	Bi	U
σ_{total}	310	380	700	1390	2200	3210	3280	3640
$\sigma_{absorption}$	190	200	410	670	1160	1730	1790	1890

Experimental errors are about 3 percent in σ_{total} and 5 percent in $\sigma_{absorption}$.

An interpretation of these cross sections is given in terms of optical model parameters for two extreme nuclear density distributions: uniform (radius R) and Gaussian $[\rho=\rho_0\exp-(r/a)^2]$. The absorption cross-section data are well fitted with $R=1.28A^{\frac{1}{3}}$ or $a=0.32+0.62A^{\frac{1}{3}}$ in units of 10^{-13} cm. A nuclear density distribution intermediate between uniform and Gaussian will make the present results consistent with the recent electromagnetic radii.

I. INTRODUCTION

THERE has been, in the last few years, a considerable amount of work[1–10] done on the measurement of neutron-nuclei cross sections in the energy range 40–400 Mev. The emphasis has been mainly on transmission measurements in good geometry to measure total cross sections, although in some cases inelastic

* Work performed under contract with the U. S. Atomic Energy Commission.

† Now at Forrestal Research Center, Princeton, New Jersey.

‡ The subject matter of this paper is part of a dissertation presented to the Massachusetts Institute of Technology in partial fulfillment of the degree of Doctor of Philosophy by D. A. Hill. Now at General Electric Laboratory, Schenectady, New York.

§ On leave to the Physics Department, Princeton University, Princeton, New Jersey.

|| On leave to the Physics Department, University of Wisconsin, Madison, Wisconsin.

[1] Cook, McMillan, Peterson, and Sewell, Phys. Rev. **75**, 7 (1949).

[2] Taylor, Pickavance, Cassels, and Randle, Phil. Mag. **42**, 20, 328, 751 (1951).

[3] R. Hildebrand and C. E. Leith, Phys. Rev. **80**, 842 (1950).

[4] R. Hildebrand, University of California Radiation Laboratory Report UCRL-1159, March, 1951 (unpublished).

[5] Bratenahl, Fernbach, Hildebrand, Leith, and Meyer, Phys. Rev. **77**, 597 (1950).

[6] J. DeJuren and N. Knable, Phys. Rev. **77**, 606 (1950).

[7] J. DeJuren, Phys. Rev. **80**, 27 (1950).

[8] Fox, Leith, Wouters, and MacKenzie, Phys. Rev. **80**, 23 (1950).

[9] W. P. Ball, University of California Radiation Laboratory Report UCRL-1938, August 1952 (unpublished).

[10] V. A. Nedzel, Phys. Rev. **94**, 174 (1954).

and differential cross sections have also been measured. Much of the previous data has been summarized by Rossi,[11] Hildebrand,[12] and recently by Nedzel.[10] It has been shown[1] that neutron-nuclei cross sections exhibit a considerable transparency in this energy range. It is possible with the aid of suitable models of the nucleus to extract information from these data bearing on the size and gross structure of the nucleus. In addition, the neutron-proton and neutron-deuteron cross sections are of particular interest since any theory of nuclear forces must be able to explain these elementary interactions and their dependence on energy.

The interpretation of neutron-nuclei cross sections has to date been confined to extremely simplified models. For example, at the lower energies the analysis of Feshbach, Porter, and Weisskopf[13] pictures the nucleus as characterized by an average complex (absorptive +scattering) potential. A partial wave analysis using this potential has had considerable success in explaining the trend of the total and absorption cross sections at lower energies. At higher energies, however, a partial wave analysis becomes unwieldy. Fernbach, Serber, and Taylor[14] introduced the "optical model" by making the classical approximation that at high energies the wave normals (particle trajectories) are only slightly deflected in passing through nuclear matter. In this model the nucleus is described as having some radial density distribution, an absorption constant K, and a refractive index $(k+k_1)/k$ (where k_1 is the increment in the propagation constant within nuclear matter). This model has been shown to be equivalent to a partial wave analysis using the WKB approximation and is expected to become more valid as the energy increases.

Charged particles such as protons may also be used as a probe for exploring the nucleus, however, with the disadvantage that the observed effects are due to a combination of Coulomb and nuclear interactions.[15,16] (The scattering experiments using electrons, of Hofstadter *et al.*,[17] involve only Coulomb effects and give information as to the *charge* distribution within the nucleus.) The use of neutrons, on the other hand, increase the experimental difficulties because of the low efficiency and poor energy resolution of practical neutron detectors.

The present experiments were performed with neutrons having an average energy, weighted by the detector efficiency, of 1.4 Bev. At this energy essentially all of the diffraction scattering is contained within a cone of less than 6° half-angle even for the light nuclei. Hence it becomes relatively easy to measure in addition to the total cross section, the absorption cross section in "poor" geometry. It is also possible to measure the cross sections at intermediate points, which determine the integral angular distribution of diffraction scattering. Interpreted in the light of the optical model, using an assumed nuclear density distribution and the measured free nucleon-nucleon cross section, such experimental data yield values of the mean neutron energy, the nuclear radius, and the change of the incident neutron propagation constant within nuclear matter.

II. EXPERIMENTAL APPARATUS AND ANALYSIS OF THE BEAM

(a) Neutron Source

The Brookhaven Cosmotron[18] provides an internal beam of approximately 10^{10} protons per pulse with 2.2-Bev energy. By slowly turning off the radio-frequency voltage at the end of the acceleration cycle, the protons are made to hit an internal target over an interval of 30 milliseconds. The acceleration cycle is repeated every 5 seconds. In this experiment, a 6-in. beryllium target was used in order to maximize the number of high-energy neutrons coming from the target. The neutrons that emerge at 1° to the direction of the incident proton beam, the most forward unobstructed angle, are collimated by a 1 or 2 inch diameter hole extending through 8 feet of shielding concrete and 2 feet of lead. A plan view of the Cosmotron is shown in Fig. 1.

(b) Neutron Detector

Neutrons were detected by requiring that they traverse an anticoincidence counter A and produce in a 2 in. aluminum radiator, charged particles which penetrate a fourfold scintillation counter telescope containing 6 in. of lead. The fourth counter subtends an angle of $\pm 4.3°$ at the center of the radiator. The telescope is illustrated in Fig. 2.

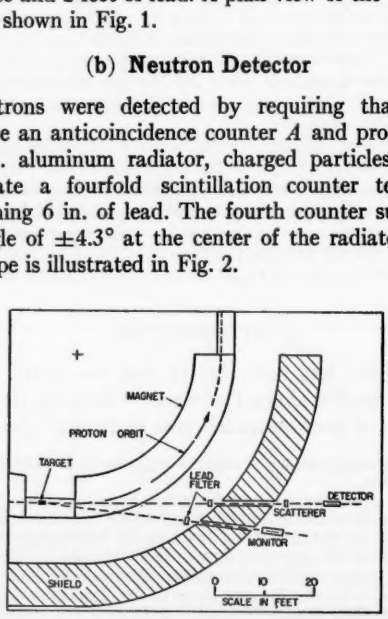

FIG. 1. Plan view of the NE quadrant of the Cosmotron, showing experimental arrangement.

[11] B. Rossi, *High-Energy Particles* (Prentice-Hall Inc., New York, 1952).
[12] Hildebrand, Hicks, and Harker, University of California Radiation Report UCRL-1305, 1951 (unpublished).
[13] Feshbach, Porter, and Weisskopf, Phys. Rev. **96**, 448 (1954).
[14] Fernbach, Serber, and Taylor, Phys. Rev. **75**, 1352 (1949).
[15] F. Chen, thesis, Harvard University, 1954 (unpublished); Chen, Leavitt, and Shapiro (to be published).
[16] J. M. Cassels and J. D. Lawson, Proc. Phys. Soc. (London) **A67**, 125 (1954).
[17] Hofstadter, Fechter, and McIntyre, Phys. Rev. **92**, 978 (1953).
[18] Cosmotron Staff, Rev. Sci. Instr. **24**, 723 (1953).

Both energetic protons and mesons are produced in the aluminum. A proton needs an energy of 400 Mev to traverse this telescope. Hence, 400 Mev is the absolute energy threshold for neutron detection, corresponding to an elastic charge exchange scattering of a neutron and a proton in the aluminum radiator. A charged meson needs 240 Mev to traverse 6 in. of lead, but this requires an incident neutron of at least 540 Mev.

Several preliminary measurements were made on the response of the telescope to different radiators and different thicknesses of lead absorber. Aluminum was chosen since it gave the largest counting rate per unit length of material. The thickness of lead absorber was chosen as a compromise between a high-energy threshold and a high detection efficiency. For lead absorbers thicker than a few inches the counting rate decreases exponentially with an absorption length corresponding approximately to the geometric absorption cross section. This fact suggests that only a small fraction of the neutron detected have energies less than ~800 Mev. A substantial increase in the threshold energy would have resulted in a prohibitive loss in counting rate, e.g., a 1-Bev proton has a range in lead of more than three absorption lengths. Some bias in favor of the detection of higher energy neutrons is obtained from the smallness of the angle subtended by the last counter with respect to the aluminum radiator.

The plastic scintillators are compression molded from polystyrene activated with terphenyl and a trace of diphenylhexatriene. The electronic circuitry is of standard design. The photomultiplier tubes are selected 1P21's which operate without breakdown at anode potentials up to 2000 volts. Each output signal is limited to about 2 volts with a biased crystal diode to prevent overloading, and is led through 100 feet of cable to a wide band, distributed amplifier (Hewlett-Packard Model 460 B). The fourfold coincidence signal with anticoincidence from A is formed in circuit of the type described by Garwin,[19] is amplified, and then enters a fast discriminator circuit using an EFP 60 secondary emission tube. The output pulses drive a fast scale of eight followed by a one microsecond scale of sixty-four and register. The integral bias curve obtained with this circuit shows a very satisfactory plateau for fourfold coincidences and an anticoincidence counter

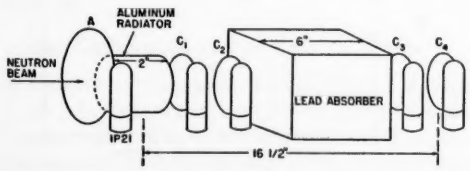

FIG. 2. Neutron detector. Coincident counters C_1-C_4 are plastic scintillators 2½-in. in diameter and ½-in. thick. Anticoincidence counter A is plastic scintillator 4 in. in diameter and ½ in. thick.

[19] R. Garwin, Rev. Sci. Instr. 24, 618 (1953).

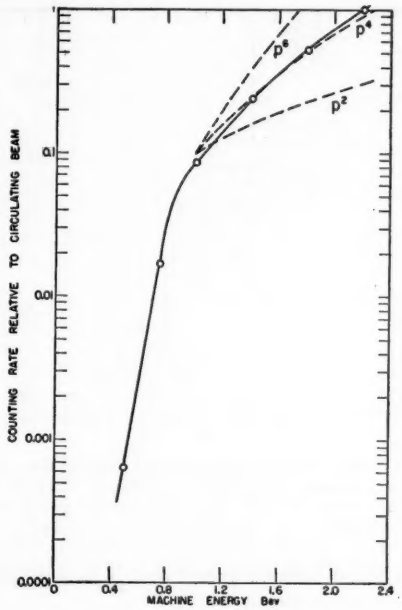

FIG. 3. Energy excitation function of the standard neutron detector. The ratio of the neutron detector counting rate to the proton circulating beam current is shown *vs* the incident proton energy. The neutrons emerge from a 6-in. Be target at 1° to the incident proton direction. Above 1 Bev the excitation function is proportional to p^4, where p is the incident proton momentum.

efficiency of greater than 0.99. The circuit is gated on only during the time that the beam strikes the target.

The measured resolving time of the coincidence circuit is about 8×10^{-9} second (half-width at half-maximum response) and is determined by the decay time of the scintillator; improvement by pulse clipping has not been necessary. The amplifier and discriminator following the coincidence circuit have a measured recovery time of 8×10^{-8} second; the counting speed is limited by the scale of eight which has a recovery time of 2×10^{-7} second. With typical beam intensities, we obtain 10 to 20 counts in a 30-millisecond interval. The expected counting losses based on this average rate are negligible; however, the peak counting rates in this interval may be many times larger due to "bunching" of the internal proton beam. Bunching is observed corresponding to the 1-kc synchroton oscillations; whether this also occurs with the higher frequency of betatron oscillations is not known at present.

A monitor of the beam intensity is provided by a threefold counter telescope placed outside the shield in a beam which emerges at 3° to the forward direction. The telescope contains 1½ inches of lead and is placed behind a 10-inch Lucite radiator. The counting rate is roughly 200 per pulse and is attributed mainly to neutron conversion in the Lucite since the counting rate with the Lucite removed is several times smaller. The construction and circuitry for the monitor is similar

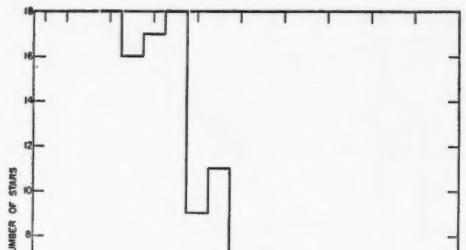

FIG. 4. Prong number distribution of neutron stars produced by forward neutrons from Be bombarded by 2.2-Bev protons. N_h is the number of gray plus black prongs (some minimum prongs included).

to that of the detector except that it does not have an anticoincidence counter.

To get some idea about the dependence of the neutron detection efficiency on energy, the ratio of the detector counting rate to the circulating proton beam current was measured as a function of machine energy, as shown in Fig. 3. (The proton beam current was monitored by measuring the voltage induced on a pair of pickup electrodes through which the beam passed.) This steeply rising function of energy represents the product of two probabilities: first, the probability that a proton striking the beryllium target will produce an energetic neutron in the forward direction and second, the probability that this neutron will produce in the aluminum radiator an energetic charged secondary in the forward direction. If recoil protons, both inelastic and elastic, cause most of the counts in the neutron telescope the first and second probabilities are quite similar. Hence, the p^4 dependence from 1 to 2 Bev, as shown in Fig. 3, suggests a neutron detection efficiency proportional to p^2. The fact that the counting rate falls off much more rapidly below 0.9 Bev suggests that the effective threshold of this neutron detector is substantially higher than the absolute threshold of 0.4 Bev. One simple explanation of the p^2 energy dependence is that the half-angle of the forward cone of recoil protons, both elastic and inelastic, decreases with energy proportional to $1/p$, so that the fractional probability for a proton to traverse a fixed solid angle in the forward direction increases approximately as p^2.

(c) Neutron Flux and Angular Distribution

A crude estimate of the neutron flux was obtained by exposing Ilford G5 emulsions in the collimated neutron beam at the position of the detector. Area scanning led to the star prong number distribution shown in Fig. 4. The mean free path for the production of events with $N_h \geq 9$ by 2.2-Bev protons has been measured[20] to be 190 cm of Ilford G5 emulsion. For neutrons, we adopt this mean free path for star production with $N_h \geq 8$, and hence obtain a flux of neutrons that can make 8-prong stars of about 10^3 neutrons per cm^2 per pulse. The average energy released among the slow secondaries in an 8-prong event is ~550 Mev. This energy is not very different from the energy threshold of the telescope. A comparison of this deduced flux with the observed counting rate in the telescope detector implies a detection efficiency of about 0.1 percent.

The angular distribution of energetic neutrons produced in the beryllium target was measured by moving the detector around to various ports in the shielding which view the target. Figure 5 shows the results obtained at two accelerated proton energies after correcting the observed counting rates for the varying thickness of obstruction in the neutron path (up to 28 percent correction) and the slightly different distances from the target to the detector (up to 9 percent correction). The distribution is strongly peaked in the forward direction. At 2.2 Bev, the half-width at half-maximum is 6.5°. The distribution is similar to that observed at Berkeley[21] with 340-Mev protons on a beryllium target if the angle scale is reduced with a factor of 3.5. This factor is just equal to the ratio of

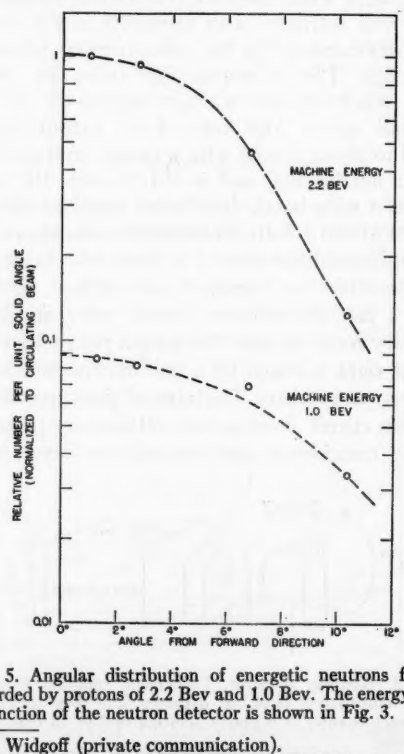
MACHINE ENERGY 2.2 BEV
MACHINE ENERGY 1.0 BEV
RELATIVE NUMBER PER UNIT SOLID ANGLE TO CIRCULATING BEAM (NORMALIZED)
ANGLE FROM FORWARD DIRECTION

FIG. 5. Angular distribution of energetic neutrons from Be bombarded by protons of 2.2 Bev and 1.0 Bev. The energy excitation function of the neutron detector is shown in Fig. 3.

[20] M. Widgoff (private communication).
[21] J. DeJuren, University of California Radiation Laboratory Report UCRL-773 (unpublished).

the incident proton momenta (lab system), and hence agrees with the previous explanation of the energy excitation function of the detector.

(d) Production of Penetrating Charged Secondaries by Neutrons

For comparison, the angular distribution of penetrating charged secondaries produced in beryllium, aluminum, and lead was measured with the arrangement shown in Fig. 6. The difference in counting rate with the sample in and out was measured for several angles up to 20°. Figure 7 presents the observed angular distributions from beryllium, aluminum, and lead. The angular resolution, as determined by the half-angle subtended by the last counter C_4 at the converter, is 4.2°. The angular distribution is again peaked forward and sensibly the same for these three elements. The relative yield per nucleus varies approximately as $A^{\frac{1}{3}}$, which suggests that mainly the nucleons around the perimeter of the nucleus contribute to the process giving rise to the penetrating charged particles. The measurements described above would be in error if an

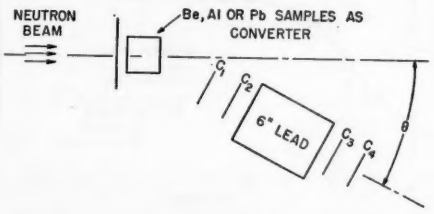

FIG. 6. Telescope arrangement for the measurement of the angular distribution of energetic charged secondaries produced by incident neutrons in beryllium, aluminum, and lead.

appreciable number of incoming neutrons interact not in the sample but in the 6-in. lead absorber giving rise to charged particles going forward to trip counters 3 and 4 and charged particles going backward to trip counters 1 and 2. This effect was estimated by putting the fourfold telescope in the beam and moving counters 1 and 2 out of the beam so that a single particle going forward from the converter cannot traverse 1, 2, 3, and 4, but a single backward-going particle from the lead can traverse 1 and 2. The contributions from events of this type constitute at most 6 percent of the observed counting rate.

(e) Collimation of the Neutron Beam

The forward neutron beam was collimated by either a 1-in. or 2-in. hole extending through 8 ft of shielding concrete and 2 ft of lead. The effectiveness of collimation for the 1-in. hole can be seen in Fig. 8 which shows the detector counting rate *versus* lateral displacement at a distance of 12 ft from the collimator. The measured dependence agrees with that expected from the overlap of a 1 in. diameter beam with a 2½-in. diameter detector. With the detector aligned in the beam, the counting

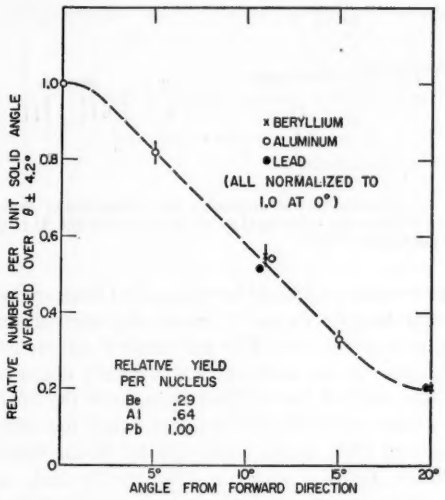

FIG. 7. Angular distribution of energetic charged secondaries produced by neutrons in beryllium, aluminum, and lead. The angular resolution is ±4.2°. The relative yield per nucleus varies approximately as $A^{\frac{1}{3}}$.

rate decreases by (3.5±2 percent) as the detector is moved from 3 feet to 12 feet from the collimator.

III. EXPERIMENTAL PROCEDURE AND RESULTS

(a) Hydrogen and Deuterium Total Cross Sections

Using the 2-in. diameter collimated neutron beam described in the last section, the total n-p cross section was determined by measuring the difference in the attenuation in good geometry of polyethylene $(CH_2)_n$, and carbon. The samples used were of high purity and were chosen to contain the same number of grams per cm² of carbon. The difference $\sigma_D - \sigma_H$ was measured in the same way with samples of heavy water (D_2O) and

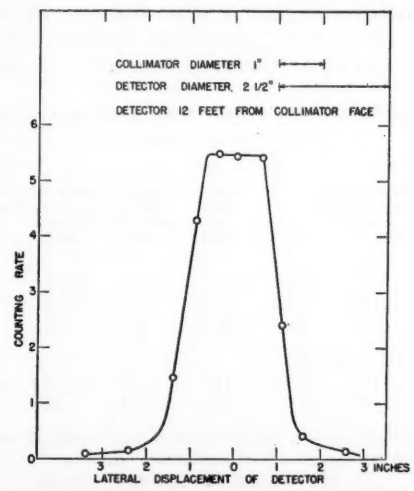

FIG. 8. Neutron beam profile for the 1-in. diameter collimator.

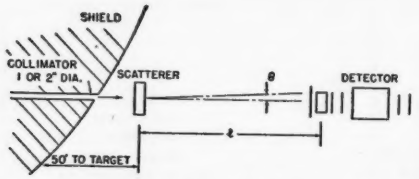

FIG. 9. experimental arrangement for transmission measurements. θ is the angle subtended at the scatterer by the Al radiator in the neutron detector.

ordinary water contained in thin walled brass cylinders of equal length. Figure 9 shows the disposition of scatterer and detector. The half-angle θ subtended by the detector at the scatterer was normally about 0.7°; the divergence of the incident beam is of the order of 0.2°. Data was collected by alternating the samples after about 5000 counts were recorded in the detector. The beam monitor was run concurrently and, in all cases, only the ratio of detector to monitor counts was used. One day's run comprised about 100 000 counts taken in this way.

The experimental arrangement was varied in the second *n-p* run by doubling the thickness of carbon and polyethylene used. In the third *n-p* run, the collimated beam was reduced to 1-in. diameter. The geometry was varied slightly in the second D_2O-H_2O run by increasing the angle subtended by the detector to 1.6°. Table I summarizes the results of five runs and gives the weighted average value with the estimated error. The mean effective neutron energy for this experiment is taken to be 1.4±0.2 Bev. This result is calculated from the half-width of the observed angular distribution of diffraction-scattered neutrons from C, Cu, and Pb and is discussed in more detail in the next section.

(b) Cross Sections of Heavier Elements

Measurements of the absorption cross sections and the total cross sections of eight elements, Be, C, Al, Cu, Sn, Pb, Bi, and U, were made. The integral angular distributions of the elastically scattered neutrons from C, Cu, and Pb were also determined. The thickness of each sample was chosen to be about one half an absorption length. This choice is a compromise between minimizing the multiple scattering effects and maximizing the statistical accuracy of the cross-section measurement.

The experimental arrangement is shown in Fig. 9. The neutron beam was collimated to a 1-in. diameter. The detector was displaced horizontally and vertically until the maximum counting rate was obtained and then held fixed. Data was collected by changing the scatterer or the geometry after about 2500 counts were recorded. Following every three or four such runs, 2500 counts were taken with the scatterer removed. For the three elements, C, Cu, and Pb, transmission measurements were made with the scatterer placed at distances ranging from 6 in. to 30 ft from the detector. In this way the half-angle, θ, subtended by the detector at the scatterer was varied from 12° to 0.2°. The values of these measured transmissions, as a function of θ are shown in Figs. 10, 11, and 12. The transmission measured in "good" geometry ($\theta=0.2°$ to 0.5°) determines the total nuclear cross section, σ_T. As θ increases, more and more of the very small-angle, elastically diffracted neutrons impinge on the detector and hence do not contribute in first approximation to the attenuation of the neutron beam. For $\theta \geq 6°$ the measured transmission remains constant, which indicates that what is being measured is just the absorption cross section, σ_a. This possibility of measuring the nuclear absorption cross section directly is one of the unique advantages of measuring nuclear cross sections with very high-energy neutrons. To obtain more accurate values for σ_a, the measured transmission must be corrected for the dependence of the telescope efficiency on incident neutron angle. This correction is shown on Figs. 10–12 and is discussed in detail in Sec. III(c). The shape of the transmission curves in the intermediate angular region can

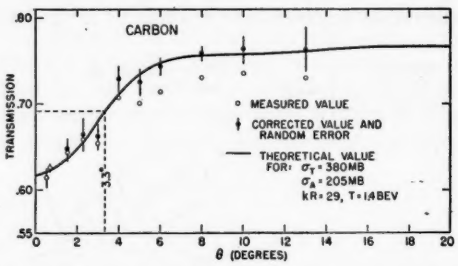

FIG. 10. Neutron transmission for carbon as a function of the angle, θ, subtended by the detector at the scatterer. Carbon sample thickness = 25.47 g/cm². The measured transmissions and the values of the transmissions corrected for the variation of neutron detection efficiency with incident neutron angle are shown. (A detailed discussion of these corrections are given in Appendices A and B.) The solid curve corresponds to a uniform-sphere diffraction scattering cross section for neutrons of 1.4 Bev, as described in Sec. IV.

TABLE I. Summary of CH_2-C and D_2O-H_2O results.

Run	Thickness of carbon (H_2O) in mean free paths	θ	Measured σ (mb)	Background correction (mb)	Observed standard deviation (mb)	Expected standard deviation (statistics only) (mb)
I CH_2-C difference						
7–24	0.56	0.66°	45.6	+0.2	±3.6	±3.3
7–30	1.02	0.68°	41.0	0.2	1.8	1.8
2–5	0.56	0.66°	47.3	0.5	6.3	3.5
II D_2O-H_2O difference						
7–25	1.09	0.67°	44.7	+0.2	±2.2	±2.2
7–29	1.09	1.5°	39.7	0.2	2.0	2.0

III Weighted averages including estimate of systematic error
Total cross sections for 1.4±0.2 Bev neutrons:
$\sigma_H = 42.4 \pm 1.8$ mb, $\sigma_D - \sigma_H = 42.2 \pm 1.8$ mb.

be used to determine the average energy of the incident neutrons, as shown in Sec. IV.

The same experimental arrangement was used to measure the attenuation of the other five elements Be, Al, Sn, Bi, and U. These were done in good geometry (0.21°–0.55°) and bad geometry (6°–10°) only. The experimental results at typical good- and bad-geometry angles, $\theta=0.55°$ and $\theta=6°$, respectively, are listed in Table II.

(c) Corrections and Errors

There are two instrumental effects which introduce an important systematic error in the poor-geometry measurements and for which a correction to the data has been made:

Directionality of the Detector

The arrangement of the detector is such that the efficiency of detection is dependent on the angle which the incident neutron makes with the axis of the detector. In general, the scattered neutrons which enter the detector in a diverging cone are counted with reduced efficiency relative to the unattenuated neutrons which enter parallel to the axis. The dependence of the detection efficiency on angle was measured directly by observing the counting rate as the detector is inclined at various angles to the collimated beam, the radiator remaining fixed in the beam. The result is the angular distribution of penetrating secondaries produced in aluminum (shown in Fig. 8). This shows, for example, that the detection efficiency falls off to half-maximum for neutrons entering the detector at an angle of 11° to the axis. The correction to the observed transmission at a given half-angle, is computed by averaging the measured relative efficiency with an approximate diffraction scattering angular distribution over the angular interval $0°-\theta$. Then that portion of the observed transmission which is due to scattered particles, i.e., $[T(\theta)-T(0)]$, is increased, so as to compensate for this calculated reduced efficiency. The correction is largest for the light elements: it amounts to 13 percent of σ_a in carbon, 3 percent of σ_a in lead.

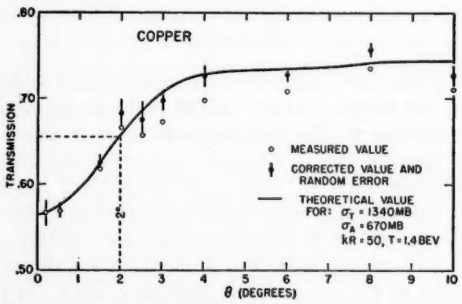

FIG. 11. Neutron transmission *vs* θ for copper (43.40 g/cm²). See caption of Fig. 10.

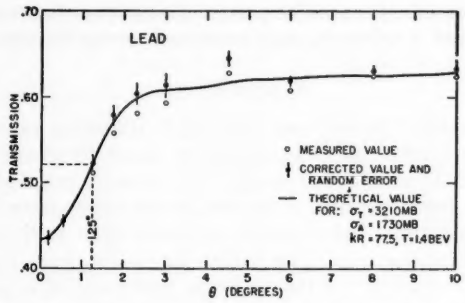

FIG. 12. Neutron transmission *vs* θ for lead (89.78 g/cm²). See caption of Fig. 10.

In good geometry the correction becomes negligible and hence does not affect σ_T. Appendix A discusses the calculation in more detail.

Finite Beam Size

In this experiment, the diameter of the collimated beam (1 in.) is not negligibly small compared to the aperture of the detector (2½ in.). Therefore, account must be taken of the fact that the probability g, that a particle scattered through an angle ξ shall enter the detector, depends upon ξ, upon the half-angle of collection θ, and upon the distance ρ from the axis at which the scattering occurs. Under the simplifying assumption that the detector efficiency is independent of angle and uniform over the 2½-in. aperture, the detector probability, g, is suitably averaged over an approximate angular distribution and over the cross section of the incident beam. Then a compensating correction is made to relate the observed transmission to the idealized case of a collimated beam of zero width. The correction to the transmission amounts at most to 6 percent of the contribution to the measured transmission from diffraction scattered particles, i.e., $T(\theta)-T(0)$. This maximum correction occurs in the region where T *vs* θ is rapidly rising. The correction is the same for all elements at corresponding points of the diffraction pattern and vanishes in both good and bad geometry limits in all cases. Details of the calculation are given in Appendix B.

TABLE II. Observed and corrected transmissions (T and T', respectively) at $\theta=0.53°$ and 6°, and the corresponding corrected cross sections.[a]

Element	Sample thickness (g/cm²)	$\theta=0.55°$ T	T'	σ(mb)	$\theta=6°$ T	T'	σ(mb)
Be	18.80	0.681	0.681	306	0.755	0.776	202
C	25.47	0.614	0.614	382	0.712	0.743	234
Al	41.20	0.532	0.533	685	0.643	0.666	446
Cu	43.40	0.569	0.570	1370	0.708	0.728	770
Sn	62.62	0.512	0.512	2110	0.660	0.673	1240
Pb	89.78	0.453	0.455	3020	0.608	0.618	1850
Bi	87.18	0.459	0.460	3090	0.614	0.622	1890
U	72.57	0.529	0.531	3430	0.681	0.691	2010

[a] Error in T' varies from 1.2 to 2.1 percent. Error in $\sigma(6°)$ varies from 2.6 to 6.4 percent. Error in $\sigma(0.55°)$ varies from 1.7 to 4.2 percent.

Several other possible sources of errors have been considered of which the most important are the following:

Random Errors

In the CH_2-C and D_2O-H_2O difference experiments, each day's run consists of about 10 groups of 5000 counts for each sample. The observed rms deviation from the mean of the ten groups ranges from 1.0 to 1.8 times the deviation expected from statistical fluctuations only. The excess fluctuation may arise from instability of the electronic equipment or it may reflect the variable operating conditions of the Cosmotron.

For the transmission measurements on the elements Be, C, $\cdots$U, all the data obtained over a six-month period were analyzed for fluctuations from the mean value. The observed rms deviations are, on the average, about 1.6 times the expected deviation due to statistics only.

Rate Effects

Chance coincidences and dead-time effects in the coincidence or scaling circuits can cause a systematic error in the transmission. An experimental estimate of the chance coincidence rate was made by delaying the signal from one counter by 2.5×10^{-8} second or about three times the resolving time. This accidental rate was 0.8 percent of the normal counting rate. This would suggest an error in the measured transmission of less than 0.3 percent. Counting losses due to dead time in the anticoincidence counter or the discriminator and scaling circuits are estimated to be negligible. In the normal course of operation, data were taken with beam intensities that varied by factors as large as 10. Analysis of the measured values of transmission shows fluctuations in excess of statistics but these fluctuations do not appear to be correlated with beam intensity. Effects of the order of 1 percent or less cannot be excluded.

Charged Particles

The presence of charged particles in the neutron beam caused the observed counting rate to increase 50 percent when the anticoincidence counter was disconnected. (The ratio of charged particles to neutrons in the beam was of the order of 0.1 percent. Their contribution to this counting rate is large because of the poor efficiency for detecting neutrons, $\sim$0.1 percent.) The measured efficiency of the anticoincidence counter is 0.99 or greater. Therefore, the maximum effect due to charged particles is about 0.5 percent of the measured transmission. The maximum effect is realized in the good-geometry measurements on the heavy elements; in this case the charged particles are almost completely removed from the detected beam because of Coulomb scattering. In the poor geometry measurements, the effect is probably negligible since the absorption cross section for the charged particles if they are protons or pions, is presumably not much different than that for neutrons.

Background

When the neutron beam was attenuated with a column of lead 3 in. wide and 52 in. thick a residual background counting rate of about 0.4 percent of the unattenuated beam was observed. The effect of this is to make the observed transmissions systematically too large by about 0.2 percent.

Gamma Rays

The number of gamma rays detected in the neutron telescope is believed to be negligible. On the average, it would require a gamma ray of 50 Bev to produce a shower capable of penetrating 6 in. of lead (27 radiation lengths). Furthermore, a $1\frac{1}{2}$-in. lead filter (6.7 radiation lengths) was placed in the beam between the target and the collimator (see Fig. 1). It was shown with the use of a gamma-ray detector that this lead filter substantially removed the gamma rays from the beam.

Secondaries

A priori, one might expect that secondary neutrons from the sample scatterer would make an appreciable contribution to the counting rate in poor geometry. Furthermore, this contribution is intrinsically difficult to measure directly. There are two indirect pieces of data that strongly suggest that the secondary neutrons make a very small contribution to the counting rate. The first is that a plateau is observed for the transmission of Pb, Cu and, less strikingly, for C, in poor geometries ($\theta=6°$ to $10°$). If the neutral secondaries made a significant contribution one would expect a rise in the transmission as θ increased. The second point is that the measured number of *charged* secondaries energetic enough to penetrate 6 in. of Pb is very small. Using the very rough calibration of the incident neutron flux described in Sec. II(c), and the measured number of charged secondaries from Be, Al, and Pb, described in Sec. II(d), one can deduce a cross section, $\sigma_S(8°)$, for the production, within an angle of 8°, of charged secondaries capable of penetrating 6 in. Pb. The values of $\sigma_S(8°)$ are 6.5, 14, and 22 mb for Be, Al, and Pb, respectively. These cross sections have a relative accuracy of about ±5 percent, and an absolute accuracy of about a factor of two. These cross sections are only 3.4, 3.4, and 1.2 percent of the measured absorption cross sections of Be, Al, and Pb, respectively. Hence if one assumes that the number of energetic secondary neutrons are comparable to the number of energetic secondary charged particles, their contribution to the measured cross section in poor geometry is small. This assumption is certainly a conservative one for interactions in which one or two mesons are made. In such cases, the number of secondary neutrons will be considerably smaller than the number of secondary charged particles (protons

TABLE III. Summary of measured nuclear cross sections and the derived optical model parameters for a uniform nuclear density.[a]

	Measured quantities				Derived for $\bar{\sigma}=43$		Derived for $\bar{\sigma}=30$	
	σ_a	σ_T	σ_d	σ_T/σ_a	K	R	K	R
Be	187±12	308±13	121± 18	1.65±0.13	0.41	2.83±0.21	0.15	3.50
C	201±13	378±10	177± 16	1.88±0.12	0.58	2.76±0.14	0.26	3.20
Al	414±23	703±18	289± 29	1.70±0.10	0.47	3.89±0.15	0.25	4.26
Cu	674±34	1388±39	714± 52	2.06±0.12	0.60	4.77±0.14	0.38	4.95
Sn	1158±63	2202±62	1044± 88	1.90±0.12	0.50	6.23±0.18	0.32	6.40
Pb	1727±45	3209±55	1482± 71	1.86±0.06	0.49	7.55±0.11	0.33	7.68
Bi	1793±55	3275±62	1482± 83	1.83±0.07	0.47	7.71±0.13	0.31	7.85
U	1887±98	3640±91	1753±134	1.93±0.11	0.50	7.89±0.22	0.33	8.01

[a] All cross sections are in units of 10^{-27} cm². R is in units of 10^{-13} cm. K is in units of 10^{13} cm^{-1}.

plus mesons). A further reduction of the secondary neutron contribution relative to the measured number of charged secondaries will be made by the anticoincidence counter in the neutron telescope, since any secondary neutron accompanied by a charged particle will not be counted. It should be noted here that the number of energetic charged secondaries does not form an upper bound to those neutrons that are scattered inelastically but coherently, e.g., neutrons that leave the target nucleus in a low-energy excited state. However, such coherent inelastic cross sections are probably quite small compared to the total absorption cross section.

"Scattering in"

The CH_2-C and D_2O-H_2O difference experiments were done in good geometry using a collimated beam 2 in. in diameter. Because the incident beam diverges slightly, a small portion if it (an estimated 7 percent) misses the detector unless scattered through the appropriate angle upon traversing the scatterer. However, due to the very small solid angle subtended by the detector, this effect contributes less than 0.5 percent to the observed counting rate for a typical carbon sample and is thus negligible.

In the transmission measurements of Be through U, a 1-in. collimated beam was used so that the entire unattenuated beam strikes the detector. Hence there is no scattering in effect.

Finite Scatterer Thickness

In the poor geometry measurements, the thickness, l, of the scattering sample is an appreciable fraction ($\sim\frac{1}{2}$) of the distance, l, from the center of the sample to the detector. Therefore, the half-angle θ, for collection is poorly defined. To correct the observed values of transmission to the idealized case of zero scatterer thickness and perfectly defined geometry, an approximate diffraction angular distribution is suitably averaged over the thickness, t, of the scatterer. The magnitude of this correction to the observed transmission is less than 0.6 percent in all cases and has been neglected. The effect is small for two reasons: (1) the integral angular distribution in bad geometry is a slowly varying function of θ; and (2) since the distance l is measured from the center of the sample, the correction is second order in (t/l).

Sample Dimensions and Impurities

The samples of polyethylene were molded from high purity commercial powder. The samples chosen are free from air bubbles and the measured density is 0.922±0.001 g/cm³. The carbon samples are blocks of reactor-grade graphite of extreme purity. The thickness in grams per cm² was measured to within ±0.5 percent. This uncertainty can introduce an error of at most 0.25 percent of the carbon cross section or ±0.9 mb.

The matched samples of heavy water—ordinary water are believed to contain negligible impurities and the thicknesses are known to 0.5 percent. The corresponding uncertainty in the "*n-n*" cross section is ±1.0 mb.

The samples of the eight elements, Be—U, were carefully weighed and measured so that the thickness in grams/cm² is known to within 0.5 percent. The effect of possible impurities is believed to be negligible in all cases.

Summary and Treatment of Error

In the measurement of the hydrogen and deuterium cross sections the dominant error arises from the random fluctuations. The standard deviations in the cross sections are listed in Table I. A minor correction is made for background.

The errors in measuring the transmissions of the elements Be—U consist of:

(a) An error due to random fluctuation which is taken is taken as 1.6 times the expected standard deviation due to statistics only.

(b) An uncertainty of 1 percent to include the effects of background, charged particles, and possible rate effects.

(c) An uncertainty in the correction for directionality of the telescope. This uncertainty is difficult to estimate. It is taken, somewhat arbitrarily, as ±20 percent of the correction itself. The contributions from (a), (b), and (c) are combined as random errors. The resultant errors in cross section are listed in Table III.

It should be noted that the uncertainties in the absorption cross sections do *not* include the possible effect of:

(d) Detection of neutral secondaries from inelastic processes. The estimates previously given in this section are probably upper limits to this effect.

(e) Uncertainties in the theoretical angular distributions that are used in Sec. IV(a) to interpret the measured cross sections.

IV. OPTICAL MODEL ANALYSIS OF THE NUCLEAR CROSS SECTIONS

The present experiment yields three quantities for each nucleus: the total nuclear cross section σ_T, the absorption cross section σ_a, and a measure of the width of the diffraction scattering. According to the optical model approximation, σ_a is a function of the nuclear radius R, and the absorption constant K; while σ_T and the shape of the diffraction curve are functions of R, K, and k_1, the increment in the wave number inside the nucleus. In addition, σ_a, σ_T, and the diffraction pattern, depend on the assumed nuclear density distribution (which may contain more than one radial parameter), and on the wave number k, of the incident neutrons. Furthermore, it has been recently shown[22–24] that a nuclear spin-orbit potential is present, which influences the diffraction part of the total cross section in the 200- to 400-Mev region.

It is clear that all of the pertinent parameters cannot be independently deduced from the three measured quantities. Since the incident neutrons are not monoenergetic, no information can be obtained about the nuclear density distribution. Rather, the width of the diffraction curve, is used to determine the effective mean neutron energy as detected by the counter telescope. Substituting the measured values of the free nucleon-nucleon cross sections into the definition of K, σ_a becomes a function of R only. Hence the value of σ_a will determine the nuclear radius parameter for an assumed nuclear density distribution.

(a) Uniform Density Model

The uniform density model has the virtue of simplicity, although it is certainly no more than a first approximation. The pertinent formulas as given by Fernbach, Serber, and Taylor,[14] for a sphere of radius R, are:

$$\sigma_a=2\pi\int_0^R(1-u^2)rdr=\pi R^2\left\{1-\frac{(1-2KR)e^{-2KR}}{2K^2R^2}\right\}, \quad (1)$$

$$\sigma_T=\sigma_a+\sigma_d=\sigma_a+2\pi\int_0^R|(1-u)|^2rdr, \quad (2)$$

where σ_d is the total diffraction scattering, and u is the transmitted wave amplitude at impact parameter r.

$$u=\exp\{-(K+ik_1)(R^2-r^2)^{\frac{1}{2}}\}. \quad (3)$$

The quantities K and k_1 can be expressed in terms of the average nucleon-nucleon cross section, $\bar{\sigma}$, and the nucleon-nucleon forward scattering amplitude, $f(0)$:

$$K=\frac{A\bar{\sigma}}{(4/3)\pi R^3} \quad \text{or} \quad KR=\frac{A\bar{\sigma}}{(4/3)\pi R^2}, \quad (4)$$

$$k_1=(2\pi\rho/k)\,\mathrm{Re}\,f(0), \quad (5)$$

where ρ is the nuclear density. The elastic differential scattering cross section is given by

$$\frac{d\sigma_d}{d\Omega}=k^2\left|\int_0^R(1-u)J_0(kr\sin\theta)rdr\right|^2. \quad (6)$$

For $KR>1$, $d\sigma_d/d\Omega$ is very similar in angular distribution to the diffraction scattering from a cylinder, namely

$$\frac{d\sigma_d}{d\Omega}\sim\left[\frac{J_1(kR\sin\theta)}{\sin\theta}\right]^2. \quad (7)$$

Finally we shall define the partially integrated differential cross section normalized to unity:

$$F(\theta)=\frac{1}{\sigma_d}\int_0^\theta\frac{d\sigma_d}{d\Omega}d\Omega. \quad (8)$$

$F(\theta)$ is quite insensitive to the values of KR and k_1/K. Its functional form depends almost exclusively on the parameter kR. Detailed numerical computations of $F(\theta)$ for a fixed R and for various values of k corresponding to energies from 1 to 2.2 Bev show that the values of $F(\theta)$ in the range 0.1 to 0.6 are independent of the spectrum of k values of the incident neutrons, and depend only on the average value of k, $\langle k\rangle$. In the Bev energy range, a linear average of k is equivalent to a linear average of energy. It can be shown that the following relationship is valid, independent of k_1 and K:

$$\langle k\rangle R\theta_{\frac{1}{2}}=1.7, \quad (9)$$

where $F(\theta_{\frac{1}{2}})=0.5$ defines $\theta_{\frac{1}{2}}$. The transmission measured at a given subtended angle θ determines a cross section $\sigma(\theta)$ given by

$$\sigma(\theta)=\sigma_a+[1-F(\theta)]\sigma_d. \quad (10)$$

If T_1 and T_2 denote the limiting transmissions in good and bad geometry [$F(\theta)=0$ and 1, respectively], then $\theta_{\frac{1}{2}}$ is determined by $T(\theta_{\frac{1}{2}})=(T_1T_2)^{\frac{1}{2}}$. Near T_1 and T_2, $F(\theta)$ is insensitive to the value of $\langle k\rangle R$. The angles $\theta=\theta_{\frac{1}{2}}$ are shown in Figs. 10, 11, and 12 for C, Cu, and Pb. By using the values of R deduced from σ_a for each element, $\langle k\rangle$ is deduced from Eq. (9). The results from the three experimental curves are consistent with the single value $\langle k\rangle=(10.2\pm1.4)\times10^{13}$ cm^{-1}. This corresponds to a mean effective neutron energy of 1.4 ± 0.2

[22] Oxley, Cartwright, and Rouvina, Phys. Rev. **93**, 806 (1954).
[23] Chamberlain, Segrè, Tripp, Wiegand, and Ypsilantis, Phys. Rev. **93**, 1430 (1954).
[24] Marshall, Marshall, and de Carvalho, Phys. Rev. **93**, 1431 (1954).

Bev. The solid curves shown in Figs. 10, 11, and 12 are theoretical curves obtained from Eq. (8) using this value of $\langle k \rangle$, as well as the measured values of σ_T and σ_a. Specifically, the curves are calculated for $KR=3$ and $k_1/K=0$.

The integral angular distribution of Eq. (8) describes single-diffraction scattering only. Multiple-diffraction scattering will introduce small changes in Eq. (10) as described in Appendix C. These corrections vanish at both small and large values of θ. They are only important in the intermediate angular region, that is, where $d\sigma_d/d\Omega$ has maximum curvature, e.g., 1.5° to 4° for Pb. This is the same region where the corrections for the directionality of the telescope and the effects of uncertainty in $\langle kR \rangle$ are largest. Hence this intermediate angular region is subject to considerable uncertainty, and is, therefore, not used in determining the values of σ_a and σ_d.

To determine σ_a and σ_d, Eq. (10) is averaged over the transmissions in good geometry (0.2° to 0.7°) and in poor geometry (6°–10°). The values of σ_a, σ_T, and σ_d for the eight elements Be−U are listed in the first three columns of Table III.

To determine the radius R from σ_a, we assume that $\bar{\sigma}$, the average nucleon-nucleon cross section for bound nucleons, is equal to the average n-p and n-n cross section for free nucleons. Equation (1) is then used to determine R from the experimental values of σ_a. Table III gives the values of K and R for $\bar{\sigma}=43$ mb, and also for a smaller value, $\bar{\sigma}=30$ mb. The values of R obtained for the heavy elements are quite insensitive to the variation in $\bar{\sigma}$, since the uniform sphere is fairly opaque, i.e., R is essentially equal to $[\sigma_a/\pi]^{\frac{1}{2}}$. The values of R are plotted *vs* $A^{\frac{1}{3}}$ in Fig. 13. For $\bar{\sigma}=43$ mb, the least

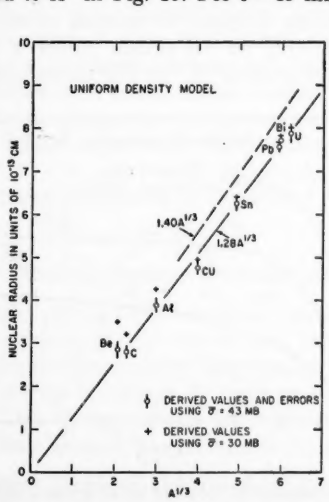

FIG. 13. Nuclear radius *vs* $A^{\frac{1}{3}}$ for the uniform density model, using two different values for $\bar{\sigma}$, the average nucleon-nucleon cross section in nuclear matter. The best straight line through the points and through the origin for $\sigma=43$ mb yields $R=(1.28\pm0.015)A^{\frac{1}{3}}\times10^{-13}$ cm. For comparison the curve $1.40A^{\frac{1}{3}}$ is shown.

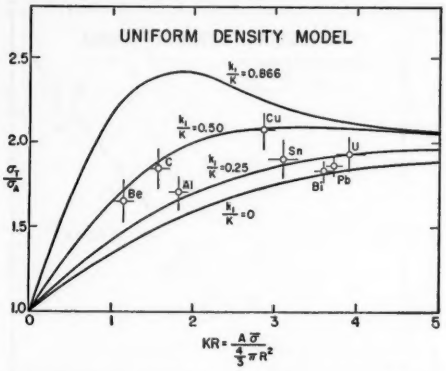

FIG. 14. Experimental points of σ_T/σ_a *versus* KR and the corresponding theoretical curves for various values of k_1/K using the uniform density model. R, K, and k_1 are the optical model parameters for a uniform sphere.

squares fit through the origin yields $R=(1.28\pm0.015)A^{\frac{1}{3}}\times10^{-13}$ cm. Having determined R and KR, the quantity (σ_T/σ_a), as determined by Eq. (2), is a function of k_1/K. In Fig. 14, theoretical curves of σ_T/σ_a *vs* KR are plotted for various values of k_1/K, together with the experimental values tabulated in Table III. The uncertainties are large, but it appears that the measured values are consistent with a single value of $k_1/K=0.3\pm0.1$ for all eight nuclei.

The uniform density interpretation is reasonably consistent in that (i) the nuclear density is constant for all the nuclei except possibly for beryllium, and (ii) a constant value of (k_1/K) crudely fits the data for all the nuclei. The significance of the derived values of R, k_1 and K is discussed in Sec. V.

(b) Gaussian Density Model

A similar analysis is carried through again by using the optical model but assuming a Gaussian density distribution. This distribution is chosen as an easily calculable extreme example of a smeared-out density distribution, and there are arguments based on the shell model which suggest that it may be a realistic one.[25] A normalized density of nucleons as given in Eq. (11) is assumed and the radius parameter, a, for each nucleus is then to be determined.

$$\rho(r)=\frac{A}{(a\sqrt{\pi})^3}\exp[-(r/a)^2]. \tag{11}$$

The path length t (in mean free paths) for impact parameter r is again Gaussian:

$$t(r)=2\int_0^\infty \rho([r^2+s^2]^{\frac{1}{2}})ds=(t_0)\exp[-(r/a)^2], \tag{12}$$

[25] M. Born and L. M. Yang, Proc. Phys. Soc. (London) **A64**, 632 (1951).

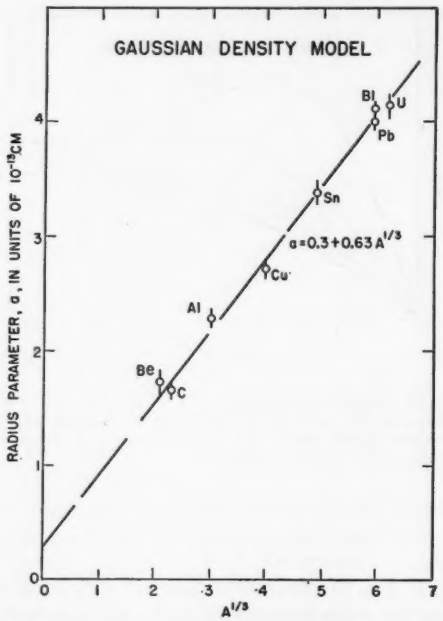

FIG. 15. Nuclear radius parameter a *versus* $A^{\frac{1}{3}}$ for the Gaussian density model, i.e., $\rho=\rho_0\exp[-(r/a)^2]$. The best straight line through the points is shown. The radii were determined from Eq. (13a) using $\bar{\sigma}=43$ mb.

where $t_0=A\bar{\sigma}/\pi a^2$. σ_a becomes

$$\sigma_a=2\pi\int_0^\infty rdr(1-e^{-t}),$$
$$\sigma_a=\pi a^2\{\gamma+\ln t_0-\mathrm{Ei}(-t_0)\}=\pi a^2 G(t_0), \tag{13}$$

where γ is Euler's constant (0.5772) and $\mathrm{Ei}(-t_0)$ is the exponential integral,

$$\mathrm{Ei}(-t_0)=\int_\infty^{t_0}(e^{-t}/t)dt.$$

To derive the values of the radius parameter a, Eq. (13) is rewritten in the form

$$\frac{\sigma_a}{A\bar{\sigma}}=\frac{1}{t_0}G(t_0). \tag{13a}$$

For an assumed $\bar{\sigma}$, this equation is solved graphically for t_0, which then yields the value of a. The results calculated on the assumption that $\bar{\sigma}=43$ mb are plotted in Fig. 15. The best fit yields $a=0.3+0.63A^{\frac{1}{3}}$.

To obtain a useful express for σ_T/σ_a as a function of t_0 and k_1/K, we consider:

$$\sigma_T(t_0,k_1/K)=2\pi\int_0^\infty rdr\{|1-u|^2+1-u^2\},$$
$$\sigma_T=4\pi\int_0^\infty rdr\{1-e^{-t/2}\}$$
$$+4\pi\int_0^\infty rdr[1-\cos(k_1 t/K)]e^{-t/2}, \tag{14}$$

where the first integral is $\sigma_T(t_0,0)$ and is recognized as:

$$\sigma_T(t_0,0)=2\pi a^2 G(t_0/2). \tag{15}$$

The second integral which contains the dependence on k_1/K is given to a good approximation, for $t_0\geq 5$ and $k_1/K\geq 0.6$, by:

$$4\pi\int_0^\infty rdr[1-\cos(k_1 t/K)]e^{-t/2}$$
$$=2\pi a^2\int_0^{t_0}\frac{dt}{t}[1-\cos(k_1 t/K)]e^{-t/2}$$
$$\cong\pi a^2\{\ln[1+4(k_1/K)^2]+2\,\mathrm{Ei}(-t_0/2)\}, \tag{16}$$

and for $k_1 t_0/K<1$ by:

$$\cong 4\pi a^2(k_1/K)^2\{1-(1+\tfrac{1}{2}t_0)e^{-t_0/2}\}.$$

With these results, σ_T/σ_a is plotted as a function of t_0 for $k_1/K=0$, 0.6 and 1.0 in Fig. 16. A value of $k_1/K=0.6\pm0.2$ fits the results for all eight nuclei. It is clear that to the accuracy of this experiment the Gaussian density model and the uniform density model fit the data equally well.

V. DISCUSSION AND CONCLUSIONS

(a) Neutron Energy Considerations

The fact that a broad energy spectrum must be employed in this experiment is probably not as serious an objection to the method as it might appear at first sight, since the expectation is that the cross sections of interest are not strongly energy-dependent in the energy range from about 1 to 2.2 Bev. (This appears to be borne out by recent results for the total p-p and p-d cross sections.)[26]

To determine whether the estimate of mean energy depends critically on the nuclear model, a numerical calculation was made of the diffraction angular dis-

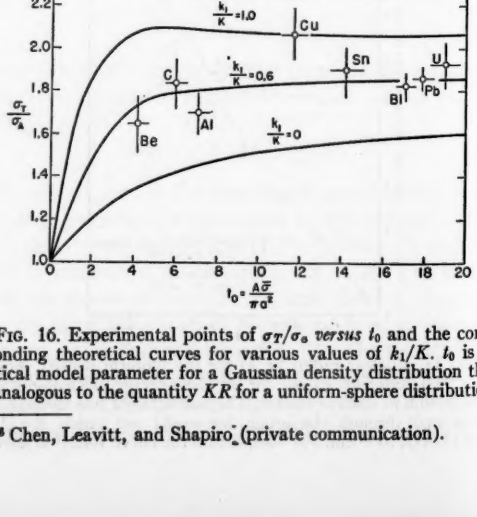

FIG. 16. Experimental points of σ_T/σ_a *versus* t_0 and the corresponding theoretical curves for various values of k_1/K. t_0 is an optical model parameter for a Gaussian density distribution that is analogous to the quantity KR for a uniform-sphere distribution.

[26] Chen, Leavitt, and Shapiro (private communication).

tribution expected for a Gaussian density model. The Gaussian model calculation for lead, using the radius parameter $a=4.0\times10^{-13}$ cm, derived in Sec. IV, yields an angular distribution for the first lobe of the diffraction pattern almost indistinguishable from the uniform model calculation. The second lobe is also present but reduced to about one-third the value for the uniform model. The important point is that the angular half-width of the diffraction pattern for lead is practically the same for Gaussian and uniform density models fitted to the same absorption cross section. Therefore, the mean energy estimate of 1.4±0.2 Bev is insensitive to the choice of nuclear model.

A study has been made by the Brookhaven Cloud Chamber Group[27] of energetic three-pronged events produced in a hydrogen-filled chamber in the forward neutron beam. Of some 150 events observed, about 100 are of the type $n+p\rightarrow n+p+\pi^+ +\pi^-$; the remaining events are $n+p\rightarrow p+p+\pi^-$ and $n+p\rightarrow p+p+\pi^- +\pi^0$. The mean primary energy for these three types of events is observed to be 1.7 Bev. A significant comparison of this mean value with the value 1.4 Bev from the present experiment is not possible, since neither the energy dependence of the meson production process nor the energy response of the neutron detector is known. However, it is certainly plausible that the three-prong events, being mainly two-meson production events, weight the higher energies more on the average than does the neutron telescope detector. There appears to be a suppression of one-meson n-p production events of the type $pp\pi^-$, which can be understood if the mesons are made predominantly in $T=\frac{3}{2}$ states.[28] There is no experimental evidence for any peaking of the neutron energy spectrum near 2.2 Bev, corresponding to elastic charge exchange scattering.

The fairly low mean neutron energy of 1.4 Bev for neutrons emerging at 1° to the incident proton beam implies that most of the neutrons arise from strongly inelastic events, such as two-meson production events. This conclusion agrees with the experiments of Lindenbaum and Yuan,[29] which show that the mesons emerging at 32° to the direction of the incident 2.2-Bev protons predominantly arise in two-meson production processes.

(b) Nucleon-Nucleon Cross Sections

A comparison of the 1.4-Bev hydrogen and deuterium total cross sections (42 mb and 85 mb, respectively) with previous measurements at lower energies is shown in Fig. 17. A large increase in the total cross sections is apparent. This figure includes an indication of the total p-p cross sections,[30] including the recent Brookhaven measurements[31] from 0.4 to 1.5 Bev which show in detail how the cross section changes with energy. The p-p cross section at 1.4 Bev is about 48 mb. Charge symmetry of nuclear forces implies an equal n-n total cross section. On the other hand, our measured $[(n,d)-(n,p)]$ cross section at 1.4 Bev is 42 mb. This discrepancy suggests that even at these high energies one cannot treat the deuteron total cross section as a simple sum of the neutron and proton total cross sections. This effect is further confirmed by the fact that the $[(p,d)-(p,p)]$ total cross section[31] is again smaller than the (n,p) total cross section at 1.4 Bev by 8±2 mb. Of course, these comparisons would be more precise if the neutron beam were monoenergetic, but the essential flatness of the p-p cross section from 0.8 to 2 Bev makes these discrepancies appear to be significant. A similar effect is indicated by a comparison of the (π^+,p) and $[(\pi^-,d)-(\pi^-,p)]$ total cross sections in the 1-Bev region,[32] and at 170 Mev.[33] On the other hand, there is no evidence for a difference between the (n,d) and the $(n,p)+(p,p)$ total cross sections at 410 Mev.[10]

A theoretical interpretation of the (n,d) cross section is a formidable problem. A simple addition of the elementary free nucleon cross sections may fail for many reasons, such as: (1) coherent elastic scattering from the two nucleons causing interference effects, (2) effects of the Pauli principle in excluding some final states, (3) shielding of one nucleon by the other and (4) three-body interactions. Gluckstern and Bethe[34] and Chew[35] have written several papers on the problem

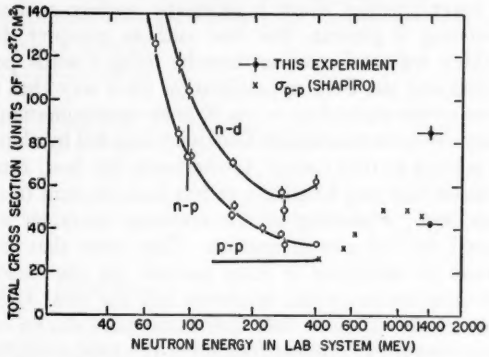

FIG. 17. Total n-p and n-d cross sections. The previously published data (see references 1–12) are indicated with open circles. An indication of the p-p total cross sections (see reference 30) is given, including the recent Brookhaven results (see reference 31).

[27] Fowler, Shutt, Thorndike, and Whittemore, Phys. Rev. **95**, 1026 (1954).
[28] D. C. Peaslee, Phys. Rev. **94**, 1085 (1954); **95**, 1580 (1954).
[29] S. J. Lindenbaum and L. C. L. Yuan, Phys. Rev. **95**, 638 (1954).
[30] The total p-p cross section from 150 to 400 Mev is consistent with a constant value about 25 mb. For example, see the work of H. de Carvalho, Phys. Rev. **96**, 398 (1954). Chamberlain, Pettengill, Segrè, and Wiegand, Phys. Rev. **93**, 1424 (1954); Marshall, Marshall, and Nedzel, Phys. Rev. **85**, 416 (1952); and Sutton, Fields, Fox, Kane, Mott, and Stallwood, Phys. Rev. **97**, 783 (1955).
[31] Shapiro, Leavitt, and Chen, Phys. Rev. **95**, 663 (1954).
[32] Cool, Madansky, and Piccioni, Phys. Rev. **93**, 637 (1954).
[33] Ashkin, Blaser, Feiner, Gorman, and Stern, Phys. Rev. **96**, 1104 (1954).
[34] R. L. Gluckstern and H. A. Bethe, Phys. Rev. **81**, 761 (1951).
[35] G. Chew, Phys. Rev. **74**, 809 (1948); **80**, 196 (1950); **84**, 710 (1951).

at lower energies where only elastic nucleon-nucleon scattering is present. The first authors interpret the 90-Mev *n-d* total cross sections by using a static potential and the Born approximation (in a way that is more or less equivalent to the impulse approximation). They conclude that simple additivity may fail by about 20 percent at that energy; furthermore, the (*n-d*) total cross section may be greater or less than the sum (*n-n*) plus (*n-p*), depending on the exchange character assumed for the *n-n* interaction. They note that the failure of additivity is more marked for the elastic *n-d* cross section which is almost half the total at 90 Mev. They estimate that the elastic part should remain roughly a constant fraction of the total at higher energies. At 1.4 Bev one might expect similar considerations to hold for the elastic parts of the *n-p* and *n-n* cross sections, since they involve small momentum transfers. On the other hand, the meson-production parts of the cross sections are probably more nearly additive, since they involve much larger momentum transfers.

It is this last point, that is, the presence of an inelastic nucleon-nucleon interaction (meson production involving large momentum transfer), that makes the identification of the $\bar{\sigma}$ of the optical model with the average "free" nucleon-nucleon cross section seem reasonable at 1.4 Bev. If it is true that only the elastic part of the nucleon-nucleon cross section is influenced appreciably by the Pauli principle acting inside a nucleus, then the percentage difference between $\bar{\sigma}$ and the free cross sections will be reduced in the ratio of the nucleon-nucleon elastic to total cross sections.

(c) Optical Model Parameters K and k_1

The analysis of Sec. IV in terms of the uniform density model leads to the following average values of the optical model parameters:

$$K=0.49\times10^{13}\ \text{cm}^{-1},$$
$$k_1=(0.15\pm0.05)\times10^{13}\ \text{cm}^{-1}. \tag{17}$$

Both of these values are considerably higher than those used to fit the data in the 300-Mev region according to the analysis of Taylor.[36] The increase in K reflects the increased nucleon-nucleon cross section and an increased nuclear density. No new information is contained in the parameter K since it is completely determined by the assumed value of $\bar{\sigma}$ and the deduced value for the nuclear radius. For the light elements, K is a sensitive function of the value assumed for $\bar{\sigma}$.

The constant k_1 does yield some additional information, since it is related to the real part of the average nucleon-nucleon forward scattering amplitude as given by Eq. (18).

$$k_1=(2\pi\rho/k)\ \text{Re}f(0), \tag{18}$$

where ρ is the nucleon density. The value of k_1 given in Eq. (17) corresponds to $\text{Re}f(0)=(2.1\pm0.7)\times10^{-13}$ cm. This implies a minimum value for the forward elastic neutron-nucleon cross section of the order of 44_{-24}^{+34} mb/steradian. This high value implies that the elastic nucleon-nucleon scattering is strongly peaked in the forward direction. For the Gaussian model the same calculation gives a value twice as large for $\text{Re}f(0)$. It has been customary in the lower-energy regions to relate the constant k_1 to an average nuclear potential. At these energies it is questionable whether an "average nuclear potential" has significance. In any case, applying the relativistic relation

$$k_1=\bar{V}/\hbar c\beta, \tag{19}$$

leads to an average potential $\bar{V}=26\pm9$ Mev.

(d) Nuclear Radii

The data of this experiment can be fitted to a good approximation with a uniform density model having radii given by $R=r_0A^{\frac{1}{3}}$ with $r_0=1.28$ in units of 10^{-13} cm.[37]

While the literature on neutron-nuclei cross sections above 40 Mev is extensive, the emphasis has been largely on transmission experiments in good geometry to measure total cross sections. In several cases, inelastic cross sections have been measured in bad geometry and, in a few cases, differential scattering experiments have been done. For comparison, we cite some of the uniform density radii obtained from these investigations.

Cook *et al.*[1] give the value $r_0=1.37$ from an analysis of the 14- and 25-Mev neutron data; Fernbach, Serber, and Taylor[14] find that the 90-Mev neutron data can be consistently fitted with the same value. Taylor[36] has interpreted the 50- and 150-Mev neutron data as well as Nedzel's 400-Mev data[10] to yield values of r_0 from 1.37 for lead to 1.54 for carbon.

Our method of analysis, using the absorption cross sections measured by Ball[9] at 300 Mev and assuming $\bar{\sigma}=27$ mb, yields $r_0=1.31$ for lead and 1.52 for carbon. Gatha and Riddell[38] have used the 340-Mev proton data of Richardson *et al.*[39] to obtain $r_0=1.25$. The recent work of Chen[15] with 860-Mev protons leads to the value $r_0=1.25$. The radii reduced from our data are believed to be consistent with most of the previous nuclear experiments. The apparent inconsistencies, particularly for the radii of light nuclei, are probably not outside the sum of the experimental errors and the uncertainties in the theoretical interpretations.

It is of interest to compare the nuclear proton distribution radii found from electromagnetic interactions with the nuclear radii found here. Since the various

[36] T. Taylor, Phys. Rev. **92**, 831 (1953).

[37] A least squares fit of the nuclear radii, assuming the relation $R=b+r_0A^{\frac{1}{3}}$ gives $R=0.16+1.31A^{\frac{1}{3}}$. For $b\neq0$, the coefficient r_0 deviates from the value 1.28, which holds for $b=0$, as $r_0=1.28+0.21b$.

[38] K. M. Gatha and R. J. Riddell, Phys. Rev. **86**, 1035 (1952).

[39] Richardson, Ball, Leith, and Mayer, Phys. Rev. **83**, 859 (1951).

measurements involve different radial averages the assumed shape of the density function can play an important role in such a comparison. For example, the analysis of Hill and Ford[40] of the μ-mesonic x-ray data of Fitch and Rainwater[41] yields, for lead, a uniform density model radius $R=6.95$ (corresponding to $r_0=1.17$) while for a Gaussian model, the radial parameter $a=4.62$ results. The results for lead in the present experiment are $R=7.55$ (uniform model) and $a=4.0$ (Gaussian model). Hence for the uniform model one obtains a smaller "electromagnetic" radius than the "neutron absorption" radius, while for the Gaussian model the *situation is reversed.* This is a consequence of the fact that the μ-mesonic x-ray data yields a parameter approximately proportional to $\langle r^{0.5}\rangle$ for heavy elements,[40] while the neutron absorption data yields a parameter that weights the tail of the density distribution much more heavily. On the other hand, the high-energy electron scattering data of Hofstadter *et al.*,[17] as interpreted by Ravenhall and Yennie,[42] show that a smoothed uniform density function, which lies in between the extreme uniform and Gaussian functions, is required. Fitting such a density function to our neutron absorption data for the heavy elements, R. Williams, in the following paper, finds radial parameters that agree quite well with the electron scattering parameters. Apparently a comparison of these two sets of data does not necessitate a nuclear radius that is 10–20 percent larger than the electromagnetic radius for a smoothed-out nuclear density function.

Comparison with Cosmic-Ray Results

The cosmic-ray data on the absorption of the high-energy nucleonic component provides information on the absorption cross sections for much higher energies than those used in this experiment. Table IV presents some of the cosmic-ray data for comparison with our results. There seems good evidence that the absorption length decreases with increasing primary energy.[11] In particular, λ_a becomes shorter than the value of λ_{geom} given by the present data. This result cannot be understood in terms of a uniform-density model but might be explained by a "long-tailed" density distribution if the nucleon-nucleon cross sections increase with energy. Williams has given such an explanation in a succeeding paper as well as a more critical survey of the subject.

The authors wish to express their appreciation to Professor R. Williams for several stimulating discussions, to the several members of the counter groups at the Cosmotron for the loan of special absorbers and for their helpful and sympathetic discussions, and to the members of the operating crew and staff of the Cosmotron for their unstinting cooperation in all phases of this work. We also wish to thank Mildred Widgoff and F. F. Chen, C. Leavitt, and A. M. Shapiro for making available their results prior to publication.

[40] D. L. Hill and K. W. Ford, Phys. Rev. **94**, 1617 (1954).
[41] V. L. Fitch and J. Rainwater, Phys. Rev. **92**, 789 (1953).
[42] D. G. Ravenhall and D. R. Yennie, Phys. Rev. **96**, 239 (1954).

TABLE IV. Comparison with cosmic-ray data.

1. Present experiment

	Carbon	Lead
λ_a	99±5 g/cm²	199±5 g/cm²
λ_{geom}	(83±8)	(191±6)

2. Values of λ_a from cosmic-ray data on absorption of N-rays

	Carbon	Lead	Multiplicity of detected event
Walker[a]		180±10	$N=4$, 5 penetrating 230 g/cm²
		147±10	$N>7$, 230 g/cm²
Walker, Walker and Greisen[b]			
charged primaries	82±8	157±12	$N>7$, penetrating
neutral primaries	80±7	164±15	230 g/cm² Pb
Boehmer and Bridge[c]			
neutral primaries	110	220	$N\geq 2$
Sitte[d]			$N\geq 3$ penetrating
charged primaries		196±13	100 g/cm² Pb
		162±10	200 g/cm² Pb

[a] W. D. Walker, Phys. Rev. **77**, 686 (1950).
[b] Walker, Walker, and Greisen, Phys. Rev. **80**, 546 (1950).
[c] H. W. Boehmer and H. S. Bridge, Phys. Rev. **82**, 306 (1951); Rossi, reference 11.
[d] K. Sitte, Phys. Rev. **78**, 714 (1950).

APPENDIX A

Directionality Correction

The correction for the variation of detection efficiency with angle is calculated from the idealized model of the detector shown in Fig. 18. Consider a uniform parallel beam of circular cross section (radius P) incident on a thin scatterer.

A typical particle incident on the scatterer at A (a distance ρ from the axis) is scattered through the space angle θ (and azimuthal angle β) and strikes the radiator at B giving rise to a distribution of charged secondaries in the forward direction with axial symmetry about the line AB. The probability that one of these secondaries shall discharge the last counter then depends only on the angle φ between AB and BC, where C is the center of the last counter. Summing the contributions to the observed counting rate from all elements of the beam

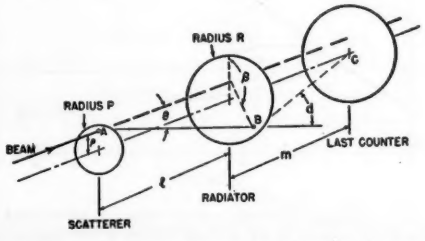

FIG. 18. Geometrical model used to calculate the correction factor C_1, due to the variation of detector response with incident neutron angle.

cross section and all scattering angles up to ξ leads to the expression:

$$C_{in}(\xi)=n_0\epsilon^{-t/\lambda T}\frac{2}{P^2}\int_0^P \rho d\rho g(\rho/m) + n_0 S\frac{2}{P^2}\int_0^P \rho d\rho \int_0^\xi \psi(\theta)\bar{g}(\varphi)d\theta, \quad \text{(A-1)}$$

$$C_{out}=n_0\frac{2}{P^2}\int_0^P \rho d\rho g(\rho/m), \quad \text{(A-2)}$$

where $C_{in}(\xi)$ = counting rate with scatterer in and detector subtending nominal half-angle ξ, $\xi=R/l$ for small angles, C_{out} = counting rate with scatterer out, $g(\varphi)$ = probability of detection of neutron entering radiator at some point B at angle φ to the line BC, n_0 = flux of neutrons incident on scatterer, S = probability that a neutron is scattered and emerges from the scatterer, and $\psi(\theta)$ = normalized angular distribution of scattered particles, i.e., $\int_0^\pi \psi(\theta)d\theta=1$. For small angles:

$$\varphi^2=\left(1+\frac{l}{m}\right)^2\theta^2+\left(\frac{\rho}{m}\right)^2+2\frac{\rho}{m}\left(1+\frac{l}{m}\right)\theta\cos\beta, \quad \text{(A-3)}$$

and $\bar{g}$ is the average of g over all values of β. In short, Eq. (A-1) represents an average of the efficiency g over (a) the angular distribution ψ, (b) the azimuth angle β, and (c) the cross section of the incident beam. It is expected to be valid only in the poor geometry limit since it contains the assumption that essentially all of the scattered particles strike the radiator. Only in this limit, is it proper to average g over all values of β and use the nominal angle ξ for the upper limit of the average (a) over the angular distribution. To be exact, this upper limit depends also on ρ and β but has a mean value of ξ. In the poor geometry limit the average (a) is insensitive to the upper limit.

The observed transmission T can now be written as:

$$T(\xi)=C_{in}/C_{out}=\epsilon^{-t/\lambda T} + S\int\rho d\rho\int\psi\bar{g}d\theta \Big/ \int\rho d\rho g. \quad \text{(A-4)}$$

The function g is expanded in even powers of φ according to Eq. (A-5). Then by using relation (A-3), the average over β is easily taken:

$$g(\varphi)=g_0(1-a\varphi^2+b\varphi^4+\cdots). \quad \text{(A-5)}$$

After the integration over ρ and rearrangement [noting that $T(0)=\epsilon^{-t/\lambda T}$], Eq. (A-4) becomes:

$$S\int_0^\xi \psi d\theta=[T(\xi)-T(0)]C_1=[T(\xi)-T(0)]\times\left\{1-\frac{(1+R/m\xi)^2[a-2b(P/m)^2]\langle\theta^2\rangle_\xi-b(1+R/m\xi)^4\langle\theta^4\rangle_\xi}{1-\frac{1}{2}a(P/m)^2+\frac{1}{3}b(P/m)^4}\right\}^{-1}, \quad \text{(A-6)}$$

in which

$$\langle\theta^2\rangle_\xi=\int_0^\xi\theta^2\psi d\theta \Big/ \int_0^\xi\psi d\theta, \text{ etc.} \quad \text{(A-7)}$$

This expresses the "true" integral angular distribution $S\int_0^\xi\psi d\theta$ in terms of the observed transmissions $T(\xi)-T(0)$, with a correction factor depending on the moments of the distribution, the angle ξ, and the constants a, b which enter in the function g. The function g was determined empirically by observing the relative counting rate as the detector is rotated, relative to the collimated beam, with the radiator remaining fixed in the beam. The result is the angular distribution of penetrating charged secondaries from aluminum as shown in Fig. 7. The distribution is very well fitted for angles up to 15° by a polynomial of the form (A-5) with the constants: $a=6.42\times10^{-3}$, $b=1.70\times10^{-5}$ (for φ in degrees).

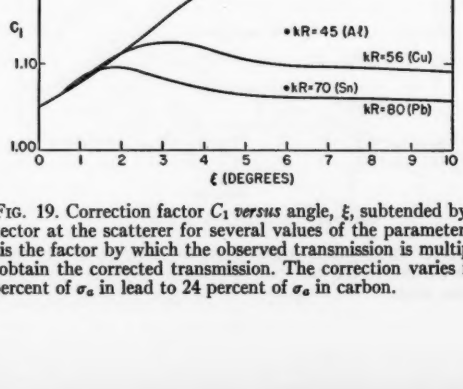

FIG. 19. Correction factor C_1 *versus* angle, ξ, subtended by the detector at the scatterer for several values of the parameter kR. C_1 is the factor by which the observed transmission is multiplied to obtain the corrected transmission. The correction varies from 6 percent of σ_a in lead to 24 percent of σ_a in carbon.

To evaluate the moments, $\langle\theta^2\rangle_\xi$ and $\langle\theta^4\rangle_\xi$, which enter the correction term, an approximate angular distribution is taken of the form:

$$\psi_1=(\theta/\eta)\exp(-\theta^2/2\eta^2), \quad 0\le\theta\le3\eta \quad \text{(A-8a)}$$

$$\psi_2=0.44(\eta/\theta)^2, \quad \theta>3\eta \quad \text{(A-8b)}$$

$$\eta=86.0/kR \text{ (in degrees)}. \quad \text{(A-8c)}$$

For all elements, ψ_1 is a good approximation to the first lobe of the diffraction pattern predicted by the optical model if the angle η at which the maximum occurs, is chosen according to (A-8c). The quantity ψ_2 approximates the "tail" of the pattern with the maxima and minima smoothed out; the normalization constant is chosen so that about 87 percent of the scattering is included in the first lobe. With this choice of ψ_1 and ψ_2, the moments are calculated. Inserting these in Eq. (A-7), one obtains the factor, C_1, by which the observed value of $T(\xi)-T(0)$ must be multiplied. Figure 19 displays C_1 *versus* ξ for several values of the parameter

kR. The value of C_1 in the good geometry limit, $\xi \to 0$, is gotten by comparing the average efficiency for detecting the scattered particles, which are in this case parallel to the axis and uniform over the $2\frac{1}{2}$-in. aperture, with the efficiency for the unattenuated beam, which is parallel and uniform over a 1-in. diameter circle.

$$\lim_{\xi\to 0} C_1 = \int_0^P \rho d\rho g \Big/ \int_0^R \rho d\rho g = 1.05. \qquad \text{(A-9)}$$

The absolute correction to the observed transmission vanishes in this limit since $T(\xi)-T(0)$ goes to zero.

It is noted that the effect on the correction of averaging over finite beam size is negligible; that is, if $P \to 0$ in Eq. (A-6) the correction is practically unchanged. In other words, the correction in poor geometry is necessary primarily because of the *divergence* of the scattered particles which are collected.

When the detector was modified by replacing the third and fourth counters with 4-in. and 6-in. diameter counters, the angular distribution, g, was remeasured and found to be about 30 percent broader than that for the narrow-angle telescope. The magnitude of the correction (that is, C_1-1) was recomputed and is about 30 percent smaller for the modified telescope.

APPENDIX B

Finite Beam Size Correction

Because of the diameter of the beam (1 in.) is not negligible compared to the aperture of the detector ($2\frac{1}{2}$ in.) the angle subtended by the detector is not well defined. To relate the observed transmission to the ideal case of zero beam width a correction is made using the simplified model of Fig. 20. Consider a uniform parallel beam of circular cross section incident on the scatterer. The probability, h, that a particle scattered at A shall enter the detector is a function of ρ, θ, R, and l. Picturing this scattering in the plane of the detector, it is seen that $h=\beta_1/\pi$, where β_1 is defined, as shown, by $l\theta/R$ and ρ/R. To make this correction it is assumed that the detection efficiency is uniform and independent of θ, since these effects were treated independently in Appendix A.

Using the notation of Appendix A, the observed counting rates can be expressed as:

$$C_{\text{in}}(\xi) = n_0 e^{-t/\lambda T} + n_0 S \frac{2}{P^2}\int_0^P \rho d\rho \int_0^\pi \psi(\theta) h\left(\frac{\rho}{R}, \frac{l\theta}{R}\right) d\theta, \qquad \text{(B-1)}$$

$$C_{\text{out}} = n_0.$$

Hence

$$T(\xi)-T(0) = S\frac{2}{P^2}\int \rho d\rho \int \psi(\theta) h\left(\frac{\rho}{R}, \frac{\theta}{\xi}\right) d\theta, \qquad \text{(B-2)}$$

where $\xi = R/l$. Solving the triangle of Fig. 20 for β_1,

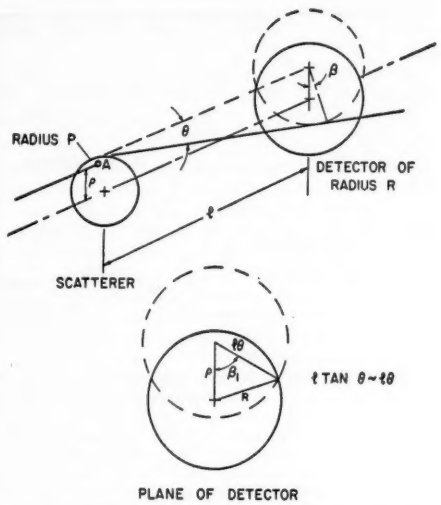

FIG. 20. Geometrical model used to calculate the correction factor C_2, due to the finite size of the incident neutron beam.

we obtain

$$\tan^2\left(\frac{\beta_1}{2}\right) = \frac{(1-\theta/\xi+\rho/R)(1+\theta/\xi-\rho/R)}{(1+\theta/\xi+\rho/R)(-1+\theta/\xi+\rho/R)},$$

$$h=\beta_1/\pi, \qquad \text{(B-3)}$$

from which h was calculated for several values of ρ/R. The function h is well approximated by straight line segments according to:

$$h = \begin{cases} 1, & (\theta/\xi) < (1-\rho/R) \\ \frac{1}{2} - \frac{1}{2\pi}\frac{\rho}{R} - \frac{1}{\pi}\frac{R}{\rho}\left(\frac{\theta}{\xi}-1\right), & \\ & [1-(\rho/R)] \le (\theta/\xi) \le 1+(\rho/R) \\ 0, & (\theta/\xi) > 1+(\rho/R). \end{cases} \qquad \text{(B-4)}$$

The integral of Eq. (B-2) is then rewritten as

$$S\left(\frac{2}{P^2}\right)\int_0^P \rho d\rho \left\{ \int_0^\xi \psi d\theta - \underbrace{\int_{\xi-(\rho/l)}^{\xi} \psi d\theta}_{\text{I}} + \underbrace{\int_{\xi-(\rho/l)}^{\xi+(\rho/l)} \psi h d\theta}_{\text{II}} \right\}.$$

To evaluate I and II, $\psi(\theta)$ is expanded in Taylor series about $\theta=\xi$. The approximation of (B-4) is used for $h(\rho/R,\theta/\xi)$ and the integration performed. Rearranging (B-2) and using the results of integration, we have

$$S\int_0^\xi \psi d\theta = [T(\xi)-T(0)]\left\{1 + A \Big/ \int_0^\xi \psi d\theta\right\}^{-1} = [T(\xi)-T(0)]\times C_2, \qquad \text{(B-5)}$$

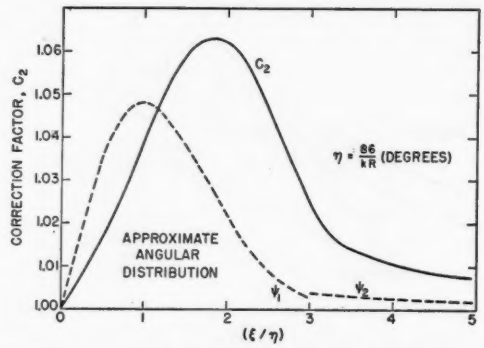

FIG. 21. Correction factor C_2 *versus* the ratio ξ/η. ξ is the angle subtended by the detector at the scatterer and $\eta=86/kR$, is the parameter used in the functions ψ_1 and ψ_2, defined by Eqs. (A-8a) and (A-8b), which approximate a diffraction pattern with the maxima and minima smoothed out. The functions ψ_1 and ψ_2, used to calculate corrections C_1 and C_2 are given by the dotted curves above.

with

$$A(\xi)=\sum_{n\ \text{even}}\frac{-2}{\pi(n+4)}\left(\frac{P}{R}\right)^{n+2}\frac{\xi^{n+1}\psi^{(n)}}{(n+1)!}$$
$$+\sum_{n\ \text{odd}}\left\{\frac{-4(n+1)}{\pi}+2(n+1)\right\}\left(\frac{P}{R}\right)^{n+1}\times\frac{\xi^{n+1}\psi^{(n)}}{(n+3)!},$$

where $\psi^{(n)}$ is the nth derivative of ψ evaluated at ξ. This expresses the true integral angular distribution in terms of the observed value $T(\xi)-T(0)$ and a correction factor C_2 which depends upon ψ and its derivatives at ξ. Assuming the approximate angular distributions of Appendix A and inserting the value $(P/R)=0.4$, it is found that the series for $A(\xi)$ converges rapidly with significant contributions only from terms in ψ and ψ'. To the extent that the *shape* of the angular distribution is the same for each element, the same correction C_2 applies for each element at corresponding points in the diffraction pattern. The quantity C_2 is plotted as a function of θ/η in Fig. 21; the scale factor η is given by $\eta=(86.0)/kR$ degrees according to (A-8c). The approximate angular distribution of Eqs. (A-8a) and (A-8b) is also included in the figure.

APPENDIX C

Multiple Scattering Considerations

As described in Sec. IV, the cross sections for the eight elements, Be through U, were fitted with the angular distribution for single scattering, that is, we set

$$N(\theta)=N_0e^{-l(\sigma_T-F_1\sigma_d)}$$
$$=N_0e^{-l\sigma_T}\left\{1+\sum_{n=1}^{\infty}\frac{1}{n!}(l\sigma_d)^nF_1{}^n\right\}, \quad \text{(C-1)}$$

where $N(\theta)$ = number of particles emerging from sample within a cone of half-angle θ, N_0 = number of incident particles, l = number of nuclei per unit area, and $F_1(\theta)\equiv F(\theta)$ = fraction of single diffraction scattered particles contained in a cone of half-angle θ, as defined in Eq. (8). More accurately one should write

$$N(\theta)=N_0e^{-l\sigma_T}\left\{1+\sum_{n=1}^{\infty}\frac{1}{n!}(l\sigma_d)^nF_n(\theta)\right\}, \quad \text{(C-2)}$$

where $F_n(\theta)$ = fraction of n-fold scattered particles contained in a cone of half-angle θ. Using a Gaussian approximation to $F_1(\theta)$, it follows that $F_n(\theta)$ is equal to $F_1(\theta/\sqrt{n})$ in the small angle approximation. Combining Eqs. (C-1) and (C-2), the cross section $\sigma(\theta)$ measured at an angle θ can be expressed as

$$\sigma(\theta)=\sigma_a+(1-F_1)\sigma_d$$
$$-\sigma_de^{-l\sigma_dF_1}\sum_{n=2}^{\infty}\frac{1}{n!}(l\sigma_d)^{n-1}(F_n-F_1{}^n). \quad \text{(C-3)}$$

The first two terms on the right-hand side form the single scattering approximation to $\sigma(\theta)$, used to fit the data. The third term is the correction due to multiple-diffraction scattering effects. The correction term vanishes both in good- and bad-geometry limits, and, for very thin scatterers it vanishes at all angles. Using the Gaussian, small-angle approximation to $F_n(\theta)$ the corrections to the cross sections are about $\frac{1}{2}$ percent for the scatterer thicknesses and geometries of this experiment.

High-Energy Cross Sections. I. The Size of the Nucleus*

ROBERT W. WILLIAMS
Physics Department and Laboratory for Nuclear Science, Massachusetts Institute of Technology, Cambridge, Massachusetts

(Received January 11, 1955)

An analysis is made of the recently available measurements of the absorption (reaction) cross sections of nuclei for 1.4-Bev neutrons. The nature of the approximations involved in interpreting such data is discussed, and it is pointed out that these measurements are more directly related to the nuclear density distribution than are the lower-energy measurements. If it is assumed that the density drops off smoothly to zero at the edge of the nucleus, in accord with electron scattering results, it is found that the size of the nucleus determined from these nuclear experiments is in good agreement with the size determined from electromagnetic experiments. This fact indicates that the spatial distribution of the protons is probably equal to that of the neutrons, and cannot be smaller by as much as 1×10^{-13} cm, even for heavy nuclei.

A simple formula is given for the nuclear density distribution; the radius of the *uniform* (square-well) density distribution which yields the same $\langle r^2\rangle_{Av}$ is $r_0=1.19A^{\frac{1}{3}}\times10^{-13}$ cm; the corresponding square-well radius for nuclear interactions is larger, and depends on the type and energy of observation. Some results are presented of a method for treating the effect of the finite range of interaction of the neutrons.

INTRODUCTION

RECENT results of electromagnetic measurements of nuclear size[1] make it evident that nuclear matter is considerably more dense than neutron and other purely nuclear measurements[2,3] had indicated. This has been suggested[1,4,5] to be a consequence of the fact that the nuclear density must fall to zero gradually rather than abruptly at the edge of the nucleus, and that the nuclear forces have finite range; recently it has also been suggested[6] that the proton distribution may be more highly concentrated than the neutron distribution.

Little quantitative work has followed these suggestions, perhaps because of the complexity of medium-energy nuclear physics. At very high energies the situation becomes simpler because the semiclassical picture of independent nucleons in the nucleus is more nearly valid, and because the experiments yield nonelastic cross sections directly. In the preceding paper,[7] Coor, Hill, Hornyak, Smith, and Snow show that the cross sections measured at Brookhaven in the 1.4-Bev neutron beam lead, with the standard analysis, to a nuclear radius which is smaller than the radius deduced from the lower energy nuclear measurements. In other words the Brookhaven results nearly agree with the electromagnetic radii, without taking into account the tapering of the nuclear density distribution or the finite range of interaction of the neutrons. In the present note we consider these two effects in order to relate the high-energy nonelastic cross sections measured at Brookhaven to the actual nucleon density distribution. By assuming a density distribution in accord with electron scattering results we find that the nuclear *size* as measured by high-energy neutron scattering agrees with the electromagnetic determinations.

In a subsequent note[8] we consider the implications of the cross sections which have been measured with cosmic rays at ultrahigh energies.

ANALYSIS

The Brookhaven group has described in the preceding paper their measurements of the attenuation of the 1.4-Bev neutron beam as a function of detector solid angle. These measurements enable them to ascertain the nonelastic part of the cross section as well as the total cross section. The nonelastic cross section, which we shall call the reaction cross section[9] σ_r, is simply related to the elementary nucleon-nucleon total cross section $\bar{\sigma}$, and the average density of nucleons at radius r, $\rho(r)$, under the conditions that: (a) the mass number of the nucleus be not too small (we formulate this more quantitatively below); and (b) the nucleons scatter or absorb the neutron wave independently of each other. For the independence condition to hold strictly it is necessary that both the neutron wavelength λ and the range of nucleon-nucleon interactions be smaller than the average internucleon spacing.

If the latter condition were fulfilled, one would feel more confident in treating each nucleon as uninfluenced by the others, but in fact the range of nuclear forces is about equal to the internucleon spacing in the central region of the nucleus. However, the average internucleon distance increases near the edge of the nucleus, and it turns out that this is the important region for

* This work was supported in part by the joint program of the Office of Naval Research and the U. S. Atomic Energy Commission.

[1] F. Bitter and H. Feshbach, Phys. Rev. **92**, 837 (1953); V. L. Fitch and J. Rainwater, Phys. Rev. **92**, 789 (1953); Hofstadter, Hahn, Knudsen, and McIntyre, Phys. Rev. **95**, 500 (1954).

[2] J. M. Blatt and V. F. Weisskopf, *Theoretical Nuclear Physics* (John Wiley and Sons, Inc., New York, 1952), p. 15.

[3] T. B. Taylor, Phys. Rev. **92**, 831 (1953).

[4] R. R. Wilson, Phys. Rev. **88**, 350 (1952).

[5] L. N. Cooper and E. M. Henley, Phys. Rev. **92**, 801 (1953).

[6] M. H. Johnson and E. Teller, Phys. Rev. **93**, 357 (1954).

[7] Coor, Hill, Hornyak, Smith, and Snow, preceding paper [Phys. Rev. **98**, 1369 (1955)].

[8] R. W. Williams, following paper [Phys. Rev. **98**, 1393 (1955)].

[9] This follows the usage of Blatt and Weisskopf, reference 2. In the Brookhaven paper and in reference 10 it is called the absorption cross section, and in cosmic-ray usage either the inelastic or collision cross section.

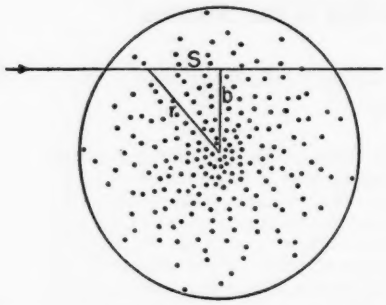

FIG. 1. The path of a neutron through the nucleus is designated by the coordinate s; the impact parameter is b. The dots are intended to illustrate the density of nuclear matter.

the calculation, at least for medium and heavy nuclei. We therefore assume that any nonadditive effects due to the failure of this condition will be small.

Following Fernbach, Serber, and Taylor,[10] we calculate σ_r by a semiclassical impact parameter method. As the neutron wave passes through the nucleus it will be attenuated exponentially[11] with an absorption coefficient $K(r)=\rho(r)\bar{\sigma}$. The size and shape of the nucleus are expressed by the density distribution $\rho(r)$, which approaches zero rapidly (usually exponentially) for large r. The total attenuation is obtained from an integral over s, the coordinate along the neutron trajectory (Fig. 1), and the cross section is then the probability of interaction integrated over the impact parameter b. Noting that $r^2=b^2+s^2$, we have:

$$\sigma_r=\int_0^\infty\left\{1-\exp\left[-\int_{-\infty}^{\infty}K((b^2+s^2)^{\frac{1}{2}})ds\right]\right\}2\pi bdb. \quad (1)$$

The Brookhaven measurements have several advantages for a determination of nuclear size. They yield σ_r directly, whereas at lower energies one must rely mainly on *total* cross sections, which involve a large amount of diffraction scattering and therefore require the full apparatus of the optical model[12] and the introduction of another unknown parameter, the index of refraction.[13] At 1.4 Bev, $\lambda\!\!\!^{-}=0.09\times10^{-13}$ cm, so the condition that $\lambda\!\!\!^{-}$ be small is well satisfied (the mean nucleon-nucleon separation is $\sim1.8\times10^{-13}$ cm). Finally, the effective cross section $\bar{\sigma}$ for elementary collisions inside the nucleus should approach more closely to the average free nucleon-nucleon total cross section σ_{nucleon}. We are therefore able to fix $\bar{\sigma}$ rather than leaving it a free parameter to be determined from the fit of the data, as is done in the lower-energy analysis.[3] If the nucleons were truly independent we would have $\bar{\sigma}=\sigma_{\text{nucleon}}$, but as Serber has pointed out[14] the binding of the nucleons will inhibit many small-momentum-transfer collisions, so that in fact $\bar{\sigma}<\sigma_{\text{nucleon}}$. The only calculations of $\bar{\sigma}$ known to the writer are those of Goldberger[15] for 90-Mev neutrons and Bernardini, Booth, and Lindenbaum,[16] for 400-Mev protons. In both cases an approximate treatment gave $\bar{\sigma}\sim\frac{2}{3}\sigma_{\text{nucleon}}$. Despite this discouragingly large effect we shall assume $\bar{\sigma}=\sigma_{np}$,[17] measured as 43 mb by the Brookhaven group. This may be partially justified by the consideration that at this energy meson production is likely to account for over half the cross section,[18] and that the average energy transfer in the remaining "elastic" collisions probably increases. One must expect, however, that the elastic part of the nucleon-nucleon cross section becomes more forward at energies where meson production is copious; preliminary results on (pp) scattering at 1 Bev confirm this.[19] The sensitivity of our results to error in $\bar{\sigma}$ is discussed below.

As the Brookhaven group points out,[7] the neutron cross sections above are not adequate to determine the *form* of the nuclear density distribution $\rho(r)$; the data are compatible with any reasonable form. We therefore adopt a *shape* of the density distribution which conforms well with the information from electromagnetic experiments, leaving the scale factor to be determined by the neutron cross sections. The relevant facts are: (1) the high-energy electron scattering data are most compatible with a proton density in gold and lead which is uniform in the central region and drops off smoothly at the edge,[20] the distance for falling from 90 percent to 10 percent being $\Delta r_{10-90}\approx(2.0\text{–}2.4)\times10^{-13}$ cm; (2) several different experiments define a "size" of the proton distribution, the exact meaning of which depends, for each experiment, on the distribution shape. Following Ford and Hill,[21] we give for each of these the equivalent square-well radius—the radius obtained from analysis of the experiment when a uniform density distribution is assumed. (Note that if the true distribution is nonuniform, not all experiments will give the same equivalent square-well radius.) Writing $r_0A^{\frac{1}{3}}$ for the square-well radius, we find (in units of 10^{-13} cm)

[10] Fernbach, Serber, and Taylor, Phys. Rev. **75**, 1352 (1949). For short-range, inelastic interactions our condition on $\lambda\!\!\!^{-}$ serves to justify the use of an impact parameter. More stringent conditions are required for elastic scattering [N. Bohr, Kgl. Danske Videnskab. Selskab, Mat.-fys. Medd. **18**, No. 8 (1948); E. J. Williams, Revs. Modern Phys. **17**, 217 (1945)].

[11] See, for example, L. L. Foldy, Phys. Rev. **67**, 107 (1945); M. Lax, Revs. Modern Phys. **23**, 287 (1951). This absorption coefficient is proportional to the imaginary part of the optical model potential.

[12] K. M. Watson, Phys. Rev. **89**, 575 (1953); N. C. Francis and K. M. Watson, Phys. Rev. **92**, 291 (1953); N. C. Francis and K. M. Watson, Am. J. Phys. **21**, 659 (1953).

[13] Actually the complete optical model has been used by Coor *et al.*, in determining corrections to the measured σ_r, and determining the mean energy of the neutron beam.

[14] R. Serber, Phys. Rev. **72**, 1114 (1947).

[15] M. L. Goldberger, Phys. Rev. **74**, 1268 (1948).

[16] Bernardini, Booth, and Lindenbaum, Phys. Rev. **88**, 1017 (1952).

[17] σ_{pp} seems to be higher, about 48 mb (Shapiro, Leavitt, and Chen, Phys. Rev. **95**, 663(A) (1954).

[18] Fowler, Shutt, Thorndike, and Whittemore, Phys. Rev. **95**, 1026 (1954).

[19] Smith, McReynolds, and Snow, Phys. Rev. **97**, 1378 (1955).

[20] R. Hofstadter (private communication); D. G. Ravenhall and D. R. Yennie, Phys. Rev. **96**, 239 (1954).

[21] K. W. Ford and D. L. Hill, Phys. Rev. **94**, 1630 (1954); D. L. Hill and K. W. Ford, Phys. Rev. **94**, 1617 (1954).

$r_0=1.17$ from μ-mesonic x-ray experiments,[22] 1.20 from high-energy electron scattering,[20] and 1.22 from the semiempirical mass equation.[23] The first two experiments also indicate that r_0 is quite constant as one proceeds toward lighter elements, at least down to $Z=22$ and probably much lower.[24]

The constancy of r_0 permits us to assume (though it does not prove) that all nuclei have a similar form and the same central density ρ_0; that is, for any nucleus that both Δr_{10-90} and the appropriate radius parameter R are proportional to $A^{\frac{1}{3}}$. While this assumption is surely unrealistic for the lightest nuclei, it may be true for the heavier nuclei.[25] (In what follows we shall put most weight on the data for heavy nuclei, which in any case yield the most reliable neutron cross sections.) Guided by the high-energy electron scattering results, we now choose a specific form for the nuclear density distribution, determine the radius parameter R from

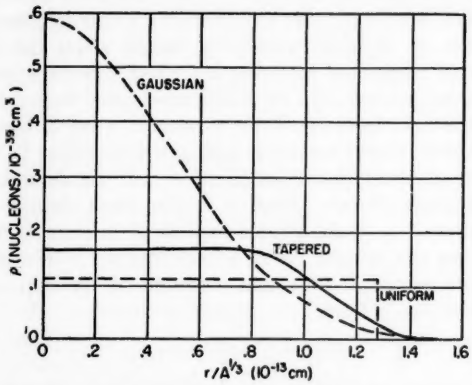

FIG. 2. Tapered nuclear density distribution function plotted against a universal radius $r/A^{\frac{1}{3}}$. Gaussian and uniform distributions, fitted to the same high-energy neutron data, are shown for comparison.

the Brookhaven neutron data, and show that the resulting nuclear size and shape agree with the electromagnetic data. The form chosen[26] (which we shall call the tapered density distribution) has a constant central region attached to a smoothly-dropping polynomial:

$$\begin{aligned} &\rho(r)=\rho_0 && r\leqslant R,\\ &\rho(r)=\rho_0(2r^3/R^3-9r^2/R^2+12r/R-4) && R\leqslant r\leqslant 2R, \quad (2)\\ &\rho(r)=0 && r\geqslant 2R. \end{aligned}$$

It is illustrated in Fig. 2 where the uniform and Gaussian forms are also shown. The "radius" as defined by Ravenhall and Yennie,[20] $\int_0^\infty \rho(r)dr/\rho(0)\equiv c$, is $c=1.5R$, and $\Delta r_{10-90}=0.6R$.

The density distribution is thus of the form:

$$\rho(r)=\rho_0 f(r/R). \quad (3)$$

The radius parameter R for any nucleus is given by $R=aA^{\frac{1}{3}}$, where a is a constant to be determined, and the central density ρ_0 is given by $\rho_0=1/(a^3v)$, where v is the volume-normalization constant characteristic of f; in particular, $v\equiv\int_0^\infty f(x)4\pi x^2dx=24\pi/5$ for the tapered distribution. For a specified $f(r/R)$, Eq. (1) now reduces to the form $\sigma_r=\pi R^2O(l_0/R)$, where the opacity, O, is a function only of the mean free path at the center of the nucleus, $l_0\equiv K_0^{-1}=(\rho_0\bar{\sigma})^{-1}$, divided by R.

Figure 3 shows on a log-log plot the results of a numerical calculation of O *versus* $(K_0R)^{-1}$ for the tapered model. Since $(K_0R)^{-1}=va^2/\bar{\sigma}A^{\frac{1}{3}}$, and $O=\sigma_r/\pi a^2A^{\frac{2}{3}}$, for a given model the measurements of σ_r should determine a, the only unknown quantity, from the best fit to the opacity curve. The Brookhaven data[7] are fitted to the curve of Fig. 3 with most weight being assigned to the heavy elements; the value of the size parameter which results is $a=0.736\times10^{-13}$ cm. A similar analysis for the uniform-density model yields $a=1.28\times10^{-13}$ cm $(=r_0)$, and for the Gaussian $(\rho=\rho_0\exp(-r^2/R^2))$, $a=0.675\times10^{-13}$ cm.

The nuclear size determined in this way agrees with the electromagnetic experiments if one adopts the tapered model, but does not agree for the uniform or Gaussian models. To see this we can calculate the

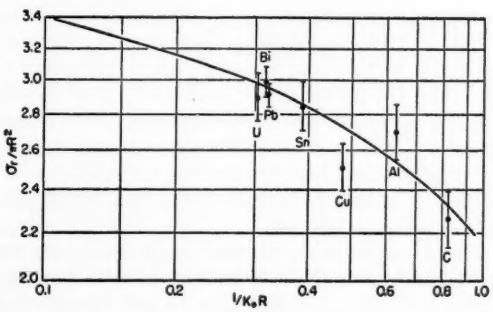

FIG. 3. Opacity, $\sigma_r/\pi R^2=\sigma_r/\pi a^2A^{\frac{2}{3}}$ as a function of $(K_0R)^{-1}=4.8\pi a^2/\bar{\sigma}A^{\frac{1}{3}}$, the mean free path at the center of the nucleus divided by R, for the tapered model. Experimental points are the Brookhaven measurements plotted with $\sigma=43$ mb, $a=0.736\times10^{-13}$ cm.

[22] V. L. Fitch (private communication). Two small corrections have been applied to the published results (reference 1), reflecting the effects of the new meson mass and of vacuum polarization, but these essentially cancel each other.

[23] A. E. S. Green, Phys. Rev. **95**, 1006 (1954).

[24] Our selection of data has excluded medium-energy electron scattering which has been quoted (reference 1) as indicating an r_0 of 1.1. A new analysis indicates that it should be nearer 1.2 [A. E. Glassgold (private communication)]. We have also omitted the evidence from energy differences of pairs of mirror nuclei, which indicates an r_0 somewhat larger than 1.20 for light nuclei [B. Jancovici, Phys. Rev. **95**, 389 (1954); B. C. Carlson and I. Talmi, Phys. Rev. **96**, 436 (1954); see, however, D. C. Peaslee, Phys. Rev. **94**, 717 (1954)]. The density distribution in light nuclei has also been considered by Gatha, Shah, and Patel, Proc. Phys. Soc. (London) **A67**, 773 (1954).

[25] For a discussion of some of the causes of nonuniformity of the nuclear density distribution, see D. L. Hill and K. W. Ford, Phys. Rev. **94**, 1617 (1954).

[26] The use of a polynomial to achieve this type of profile was suggested by Dr. W. Aron and Dr. J. MacIntosh; for this problem it is far easier to handle than a function involving exponentials. Possibly a simple linear drop-off would have served as well, but the finite-range-of-interaction transformation discussed below would change it into a curve of this form anyway.

TABLE I. Properties of the three models fitted to the high-energy neutron cross sections. Distances are in 10^{-13} cm.

	Uniform density	Gaussian	Tapered [Eq. (2)]
Radius parameter a	1.28	0.675	0.736
Central density, ρ_0, in nucleons per 10^{-39} cm^3	0.114	0.585	0.166
Mean distance between nucleons, $\rho_0^{-\frac{1}{3}}$	2.06	1.20	1.82
Mean free path in nuclear matter at center of nucleus $(\rho_0\bar{\sigma})^{-1}$	2.04	0.40	1.40
Equivalent square well, r_0, for μ-mesonic x-rays (*Observed:* 1.17), and for semi-empirical Coulomb energy (*Observed:* 1.22)	1.28	0.99	1.18
Equivalent square well, r_0, for high-energy electron scattering (*Observed:* 1.20)	1.28	1.07	1.19
Thickness of taper for 10%–90% change in density for Pb nucleus (*Observed:* from electron scattering, 2.0 to 2.4)	0	5.0	2.6

electromagnetic results to be expected from the neutron-determined nuclear size, for the three models, and compare these expected values with the observations. Ford and Hill[21] give an extensive series of calculations of the electromagnetic effects predicted by proton density distributions of various shapes, quoting their results in terms of the previously defined equivalent square-well radius, $r_0A^{\frac{1}{3}}$. For medium-energy electron scattering this is simply a measure of the second moment, $r_0A^{\frac{1}{3}}=(5/3)^{\frac{1}{2}}\langle r^2\rangle^{\frac{1}{2}}{}_{\text{Av}}$; other experiments are related to the charge distribution in a more complicated way. In Table I we have assembled our high-energy neutron determinations of nuclear size, and compared the corresponding electromagnetic predictions with experiment. It is clear that the Gaussian nucleus so determined is too *small*, the uniform density nucleus somewhat too *large*, and the tapered nucleus [Eq. (2)] a remarkably good fit (of course the approximate fit of the tapered model to the Δr_{10-90} of the electron scattering data was forced; the values are listed for convenience).

The illustration of Fig. 2 shows the three distributions in their true proportions.

The closest fit to our tapered model among the Ford and Hill families appears to be their Family II, $n=10$;[21] among the three possibilities for Au and Pb considered by Ravenhall and Yennie,[20] the closest to our curve is their $K=1.85$, $c=6.51$.

EFFECT OF THE FINITE RANGE OF NUCLEON-NUCLEON INTERACTION

In the analysis above we have identified the effective nuclear density as seen by high-energy neutrons with the true proton density as measured electrically. This cannot be correct, since it implies that our method of calculation applies to the mean density of point nucleons, whereas in fact each nucleon's influence extends over a region of radial extent at least 1×10^{-13} cm. To see the effect of this in a simple case, consider the integral of Eq. (1) for the uniform-density model: no contribution to the cross section occurs beyond $b=R$. However, we may legitimately ask what really happens to a neutron of impact parameter $b=R+0.5\times10^{-13}$ cm, say (since $\lambda\!\!\!^{-}=0.09\times10^{-13}$ cm such a difference in trajectories is well-defined), and we see that even though the mean position of the nucleons does not extend beyond R, their influence must extend farther, and there may be an interaction. This effect is often spoken of in terms of "size of the bombarding particle," but of course it is a property of the interaction of the two nucleons. Within the present framework of nuclear theory there is no reliable way to treat such problems from a fundamental standpoint. We suggest here a simple treatment, based on physical plausibility, which yields the expected result that the effect is far less important for a tapered nucleus than for a uniform-density nucleus.

We have assumed that the neutron wave in homogeneous nuclear matter is attenuated according to the multiple scattering approximation, with an absorption coefficient $K=\rho\bar{\sigma}$, where ρ is the mean density of nucleons; to make a more explicit picture we ascribe to the ith nucleon, at $\mathbf{r}_i$, a contribution to K which is proportional to $\bar{\sigma}$ but depends on $|\mathbf{r}-\mathbf{r}_i|$, say $\bar{\sigma}F(|\mathbf{r}-\mathbf{r}_i|)$. Thus:

$$K(\mathbf{r})=\textstyle\sum_i \bar{\sigma}F(|\mathbf{r}-\mathbf{r}_i|). \tag{4}$$

Passing to an average over positions of the nucleons:

$$K(\mathbf{r})=\int \bar{\sigma}F(|\mathbf{r}-\mathbf{r}'|)\rho(\mathbf{r}')d^3\mathbf{r}'. \tag{5}$$

The function F must be normalized according to $\int F(x)d^3x=1$. Then we recover the simple formula for K when (a) ρ is a constant or (b) F has a delta-function form.[27] In effect the operation of Eq. (5) "folds" the density with a resolution function for the finite range of influence of a nucleon. The effective density $\rho_e\equiv K(\mathbf{r})/\bar{\sigma}$ retains the property $\int\rho_e d^3\mathbf{r}=A$.

Watson's[12] formal theory of the optical model starts with an exact equation for the many-body problem in

[27] It might be expected that Eq. (1) would recover the nucleon-nucleon cross section, $\bar{\sigma}$, for $A=1$, but this proves to be true only if the nucleon's position is averaged over a large volume. Inspection of Eq. (1) shows that one would have to replace $\rho(r)$ not by a δ-function but by a smeared-out distribution which extended to a distance R such that $\pi R^2/\bar{\sigma}\gg1$. The difficulty can be traced to the essentially statistical nature of the exponential law of extinction. This law results either from a classical gas-kinetic argument or from the theory of multiple scattering of waves; in both cases the scatterers are assumed to occupy a large volume. This is the origin of the restriction on our analysis to A "not too small." In terms of the nuclear radius R and the "size of a nucleon" [the extent of the nucleon interaction function $F(r)$], say S, the condition on A can be restated as $R^2/S^2\gg1$.

terms of an assumed two-body interaction and therefore should contain the finite-range effect; however, he eventually expresses the optical model potential in terms of elementary scattering amplitudes, so that the details of the elementary interaction do not enter explicitly, and the finite-range effect is not present after some practical approximations are made. If one assumes only two-body forces, it is possible[28] to relate the optical model potential formally to a sum over the elementary two-body interaction "potentials" in the many-body problem, each potential depending on the coordinates of a nucleon. Since K is proportional to the imaginary part of the optical model potential, this relation could presumably be used as the starting point for a justification of the form of Eq. (4), but this has not been carried through.

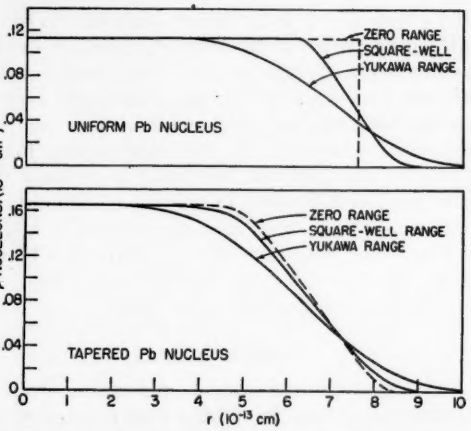

FIG. 4. Results of applying Eq. (5) for the finite-range-of-interaction correction to two nuclear density distributions: Uniform (upper curves) and tapered (lower curves). The effective density is shown for a square-well range-of-interaction of extent $\hbar/\mu c$ and a Yukawa range proportional to $r^{-1}\exp(-r\mu c/\hbar)$.

There is little to guide the choice of a form for F, except that it should bear some relation to the space dependence of the high-energy nucleon-nucleon interaction. We have calculated ρ_e with two simple forms for F, both expressed in terms of $\lambda\!\!\!^{-}_{\pi}=\hbar/\mu c=1.4\times10^{-13}$ cm:

$$\text{Square well: } F=\frac{1}{(4/3)\pi\lambda\!\!\!^{-}_{\pi}{}^{3}} \quad r<\lambda\!\!\!^{-}_{\pi} \qquad (6a)$$

$$=0 \quad r>\lambda\!\!\!^{-}_{\pi}.$$

$$\text{Yukawa: } F=\frac{1}{4\pi\lambda\!\!\!^{-}_{\pi}{}^{2}r}\exp(-r/\lambda\!\!\!^{-}_{\pi}). \qquad (6b)$$

Figure 4 shows the results of evaluating Eq. (5) with the two forms of Eq. (6), for two models of the Pb nucleus: uniform density and tapered density. The uniform-density model is rounded off considerably by the square-well range-of-interaction function, and drastically by the Yukawa function; the tapered model is scarcely changed at all by the square-well function, and changed moderately by the Yukawa function. Table II gives the tapering distances Δr_{10-90}, for the various cases. (The integral of Eq. (5) is three-dimensional, and was evaluated, for the tapered model, by approximate numerical methods.)

Since the Yukawa function appreciably smears out the effective density of the model that fits the electron scattering (tapered density) we have recomputed the opacity [Eq. (2)] from the new effective density curve, and determined the nuclear size parameter from a fit to the Brookhaven data, as before. This yields a nuclear radius 15 percent smaller: $a=0.640\times10^{-13}$ cm, r_0 for electron scattering $=1.03\times10^{-13}$ cm. Thus even the heaviest nuclei come out too small if we use the Yukawa function; in lighter nuclei the decrease would be more severe.

We are therefore faced with the rather unexpected result that the nuclear radius determined by neutron cross sections is *smaller* than the electromagnetic radius, when the neutron's interaction range is assumed to be as long-tailed as a Yukawa function with characteristic length $\lambda\!\!\!^{-}_{\pi}$. The nature of the static potential corresponding to pseudoscalar meson theory is not completely known, but it is certainly more complicated than a single Yukawa function, and contains some important short-range parts.[29] At energies high enough to involve meson production nothing is known, but it seems likely that shorter distances are involved, since the nucleons are no longer slow compared to the (virtual) mesons. We therefore assume that the square-well range results are more nearly correct, and that the curves of Fig. 4 justify our neglect of the finite-range effect in using the tapered nucleus.

Rossi and Safford[30] have considered the finite-range correction from a different point of view, using a classical hard-sphere interaction in analogy with the kinetic theory of gases. Their treatment, which is not mathematically identical to ours, gives a somewhat larger effect than our square-well case.

TABLE II. Δr_{10-90} for Pb, in 10^{-13} cm. The distance Δr_{10-90} for the effective density $K/\bar{\sigma}$ to drop from 90 percent to 10 percent of its central value is given for two models of the true nuclear density in Pb, for two assumptions concerning the spatial dependence of the range of interaction of a nucleon, Eq. (6).

	Zero range	Square-well range	Yukawa range
Uniform density	0	1.7	3.8
Tapered density	2.6	3.1	4.4

[28] These remarks owe much to a very helpful discussion with Professor S. D. Drell, and a brief but enlightening conversation with Professor K. M. Watson.

[29] K. A. Brueckner and K. M. Watson, Phys. Rev. 92, 1023 (1953).

[30] Quoted in B. Rossi, *High-Energy Particles* (Prentice-Hall, Inc., New York, 1952), p. 359.

DISCUSSION

The least-known quantity entering into the aforementioned determination of nuclear size is the effective elementary cross section $\bar{\sigma}$, which might well be less than σ_{np}, the value we have used. Even heavy-nucleus cross sections will depend on $\bar{\sigma}$ for any tapered model—the outer edge of the nucleus is always somewhat transparent—and one must investigate the sensitivity of r_0 to the value of $\bar{\sigma}$. From the opacity curve for the tapered model it turns out (for heavy nuclei) that $d(\ln r_0)/d(\ln\bar{\sigma})=-0.1$. Since $\bar{\sigma}$ is unlikely to be decreased by more than 20 percent, the value given in Table I for r_0 is probably not more than 2 percent too low on this account.

Only two measurements are known to the writer which seem directly comparable with the Brookhaven work. Shapiro, Leavitt, and Chen[31] have measured reaction cross sections of various nuclei at Brookhaven with 860-Mev protons; their results, interpreted with a uniform-density nuclear model, yield $r_0=1.25\times10^{-13}$ cm. Eisenberg[32] determined the reaction cross section in Pb of primary cosmic-ray heavy nuclei ($Z\geqslant6$) with a median energy of two or three Bev per nucleon. Using a uniform-density model he found $r_0=1.3\times10^{-13}$ cm. Both are in good agreement with the uniform-density value $r_0=1.28\times10^{-13}$ cm from the neutron work used here.

At lower energies neutron reaction cross-section measurements present great experimental difficulties. (An analysis of recent Berkeley results will be found in the preceding paper.[7]) The reaction cross sections of *complex* charged particles are more straightforward experimentally, but difficult to interpret.[33]

As is well known, neutron *total* scattering, in the low- and medium-energy region, can be interpreted in terms of the scattering by a complex potential (the optical model), usually assumed to be a square well. For this case the radius of the *potential*, r_0', is distinctly larger than the radius we have found for the nuclear density distribution, even assuming the latter to be uniform. For example, Taylor[3] finds from an analysis of all available data from 50 Mev to 400 Mev a value of $r_0'=1.37\times10^{-13}$ for Pb, and larger values for lighter nuclei, up to 1.50×10^{-13} cm for Al. The analysis in the Mev range[34] yields $r_0'=1.45\times10^{-13}$ cm; low-energy elastic scattering of charged particles give similar results.[35]

Although no extensive calculations are yet available, it already appears unlikely that agreement will be achieved solely by the use of a realistic shape of potential well. Heckrotte[36] has analyzed the 90-Mev data with a cut-off parabolic well and finds an $\langle r^2\rangle_{Av}$ no smaller than that given by the square-well analysis. Woods and Saxon[37] have fitted the angular distribution of elastically scattered 20-Mev protons with a tapered well somewhat similar in shape to the one used in the present paper, but it turns out to be about 25 percent larger in radius.

In our view this contrast between low-energy and high-energy results suggests a real difference in the effective range of nucleon-nucleon interaction in the two cases. The high-energy experiments may be interpreted quite directly in terms of nuclear density distributions, while the low-energy interpretation must involve more detailed consideration of the range of nuclear forces.

Johnson and Teller[6] have suggested that in heavy nuclei the neutron cloud has a larger extension than the proton cloud, by perhaps 1×10^{-13} cm. We find that the Brookhaven reaction cross-section measurements yield a nuclear size in agreement with the electromagnetic determination of the *proton*-distribution size, both experiments referring primarily to heavy nuclei. A rough estimate shows that the radius determined from the Brookhaven cross sections would be essentially the neutron-cloud radius. If the effect discussed by Johnson and Teller were present, we should have found an r_0 about 15 percent larger than the one actually observed. A reasonable limit of error on the increase of r_0 would be 5 percent, indicating that any difference between proton and neutron radii[38] should be not more than one-third as great as the proposed effect.

SUMMARY

Measurement of the reaction cross section—the noncoherent part of the total cross section—of very high-energy neutrons on nuclei is shown to be the most easily interpreted nuclear method of obtaining the true size of the nucleus (the spatial extension of nuclear matter); in particular, it is more straightforward, and involves the use of fewer unknown parameters, than the coherent scattering from an equivalent complex potential. The availability of reaction cross-section measurements, from the Brookhaven Cosmotron, combined with recent evidence for the shape of the nuclear matter distribution, has allowed the determination of the true nuclear size; such a determination proves to be in excellent agreement with the results of electromagnetic experiments on the nuclear charge distribution. There is no evidence for an excess of neutrons beyond the proton distribution.

The nuclear density distribution which fits the two sets of data is $\rho=\rho_0$, $r\leqslant R$; $\rho=\rho_0(2r^3/R^3-9r^2/R^2+12r/R-4)$, $R\leqslant r\leqslant2R$; $R=0.736A^{\frac{1}{3}}\times10^{-13}$ cm; $\rho_0=0.166\times10^{39}$ nucleons cm^{-3}. This distribution has an "electromagnetic" radius (the size of the square well with the same $\langle r^2\rangle_{Av}$) of $1.19A^{\frac{1}{3}}\times10^{-13}$ cm.

[31] Shapiro, Leavitt, and Chen (to be published).
[32] Y. Eisenberg, Phys. Rev. **96**, 1378 (1954).
[33] Millburn, Birnbaum, Crandall, and Schecter, Phys. Rev. **95**, 1268 (1954); contains references and results concerning previous inelastic cross-section measurements.
[34] Feshbach, Porter, and Weisskopf, Phys. Rev. **96**, 448 (1954); R. K. Adair, Phys. Rev. **94**, 737 (1954).
[35] J. S. Blair, Phys. Rev. **95**, 1218 (1954).
[36] W. Heckrotte, Phys. Rev. **95**, 1279 (1954).
[37] R. D. Woods and D. S. Saxon, Phys. Rev. **95**, 577 (1954).
[38] A decrease of proton density at the center of the nucleus—the so-called wine bottle shape—would not be noticeable in neutron cross-section experiments, which are insensitive to the central region of the nucleus.

High-Energy Cross Sections. II. Nucleon-Nucleon Cross Section at Cosmic-Ray Energies*

ROBERT W. WILLIAMS
Physics Department and Laboratory for Nuclear Science, Massachusetts Institute of Technology, Cambridge, Massachusetts

(Received January 11, 1955)

Cosmic-ray measurements are capable of yielding reliable results for the cross section of a nucleus for proton or neutron collisions involving a not too small energy transfer. This cross section should therefore be less than, or at most equal to, the true nonelastic cross section (reaction cross section). Results of recent cosmic-ray work are assembled and compared with the reaction cross sections measured at 1.4 Bev with the Brookhaven Cosmotron; it is found that the cosmic-ray cross sections are significantly *larger*, even for Pb. Assuming a nonuniform distribution of the density of nuclear matter, one can explain this surprising effect as the result of an increase in the elementary nucleon-nucleon cross section with energy. It is shown that the elementary cross section (the average of σ_{pp} and σ_{np}) must be $(120_{-20}^{+30})\times10^{-27}$ cm² in the neighborhood of 30 Bev.

INTRODUCTION

ALTHOUGH secondary cosmic radiation is an inconveniently heterogeneous beam to use as a source of high-energy particles for quantitative cross section work, a number of experimenters have refined the technique of one particular type of cosmic-ray measurement to the point where it is relatively straightforward and accurate. In the experiments we discuss, the quantity measured is the nonelastic or "reaction" cross section (usually called the collision cross section in cosmic-ray work) and the results should therefore be directly comparable with the Brookhaven reaction cross sections discussed in the preceding paper.[1] A systematic difference exists, however, and in a surprising direction: the cosmic-ray cross sections are *too large*. The experimental procedure for the cosmic-ray measurements is discussed in the Appendix, where it is pointed out that the only known important systematic error would make the cross sections *too small*.

ANALYSIS

In Table I the data of various experimenters[2–8] are collected, "best" values selected as discussed in the Appendix, and the results compared with the Brookhaven cross sections. It is seen that the light elements show the largest effect, but even lead—the most reliable of the cosmic-ray determinations—has a cross section at cosmic-ray energies ~24 percent higher than its value at 1.4 Bev. In Table II some additional measurements on Pb are collected; these show (with rather low statistical precision) an even higher cross section at the highest average energies selected. Since lead is already 96 percent opaque (in the usual optical-model sense) to the 1.4-Bev neutrons of the Brookhaven experiment,[2] an increase in opacity is not enough to account for the effect. We are rescued from this dilemma by observing that a realistic nuclear density distribution, such as that used in the preceding paper[1] (hereafter called I), has appreciable transparency even for heavy elements, because the outer region of the nucleus has a low density and therefore a small absorption coefficient. The observed increase in cross section with energy is caused by an increase in the effective nucleon-nucleon cross section $\bar{\sigma}$. From the calculated opacity curve and the nuclear size determination described in I, one can determine the ratio of $\bar{\sigma}$ at about 30 Bev to $\bar{\sigma}$ at 1.4 Bev. Since $\bar{\sigma}$ should be approximately the average of σ_{np} and σ_{nn}, we have the possibility of determining the elementary nucleon-nucleon cross section, σ_{nucleon}, in a new energy region.

The approximations involved in the high-energy semiclassical calculation of the reaction cross section, σ_r, are discussed in I. The basic assumption of the model is that the nucleons may be treated as though they were independent; this assumption should be best for the outer, low-density region of the nucleus, which is just the region involved in the increase of opacity with $\bar{\sigma}$. Thus the general scheme of calculation is fairly reliable, and the principal uncertainty is the *shape* of the effective nuclear density distribution; we have only an approximate knowledge of the true distribution, and, as we have shown, this distribution is altered (though not greatly) by the effect of the finite range of interaction. We have therefore computed the opacity curve for five different shapes of the effective density, as follows:

(1) uniform
$$\begin{cases}\rho_u=\rho_0, & r<R\\ \rho_u=0, & r>R;\end{cases}$$

(2) Gaussian $\rho_g=\rho_0\exp(-r^2/R^2)$;

(3) tapered
$$\begin{cases}\rho_t=\rho_0, & r\leqslant R\\ \rho_t=\rho_0(2r^3/R^3-9r^2/R^2+12r/R-4), & R\leqslant r\leqslant 2R\\ \rho_t=0, & r\geqslant 2R;\end{cases}$$

* This work was supported in part by the joint program of the Office of Naval Research and the U. S. Atomic Energy Commission.

[1] R. W. Williams, preceding paper [(Phys. Rev. 98, 1387 (1955)].
[2] Coor, Hill, Hornyak, Smith, and Snow, this issue [Phys. Rev. 98, 1369 (1955)].
[3] Walker, Walker, and Greisen, Phys. Rev. 80, 546 (1950).
[4] W. D. Walker, Phys. Rev. 77, 686 (1950).
[5] H. W. Boehmer and H. S. Bridge, Phys. Rev. 85, 863 (1952).
[6] Walker, Duller, and Sorrels, Phys. Rev. 86, 865 (1952).
[7] K. Sitte, Phys. Rev. 77, 714 (1950).
[8] R. R. Brown, Phys. Rev. 87, 999 (1952).

TABLE I. Reaction cross sections of nuclei for high-energy protons (σ_p) and neutrons (σ_n) in the cosmic-ray beam, in barns (reported in original sources as collision mean free paths). Errors quoted are standard deviations, and are obtained from the errors given in the original sources. We have assigned a larger error to the weighted means, in consideration of some possible systematic effects. The 1.4-Bev Brookhaven data are included for comparison; the 1.4-Bev values for S and Fe were obtained by interpolation.

Experiment	C σ_p	C σ_n	S σ_p	Fe σ_p	Pb σ_p	Pb σ_n
Walker *et al.*[a]	0.244±0.024	0.250±0.023			2.19±0.17	2.10±0.19
Walker[b] (average)					2.18±0.11	
Boehmer and Bridge[c] (average)		0.240±0.017				
Walker, Duller, and Sorrels[d]	0.262±0.028					
Sitte[e]					2.12±0.13	
Brown[f]	0.307±0.035		0.70±0.10	0.81±0.12		
Corrected mean values	0.256±0.015		0.68±0.10	0.79±0.12	2.15±0.10	
Brookhaven[g] 1.4-Bev neutrons	0.201±0.013		(0.44)	(0.67)	1.73±0.04	

[a] See reference 3. [b] See reference 4. [c] See reference 5. [d] See reference 6. [e] See reference 7. [f] See reference 8. [g] See reference 2.

(4) modified tapered

$$\rho_m=\int \rho_i(r')\frac{\exp(-|\mathbf{r}-\mathbf{r}'|\mu c/\hbar)}{4\pi(\mu c/\hbar)^2|\mathbf{r}-\mathbf{r}'|}d^3r';$$

(5) step

$$\begin{cases}\rho_s=\rho_0, & r<\frac{2}{3}R\\ \rho_s=\rho_0/5, & \frac{2}{3}R<r<R\\ \rho_s=0, & r>R.\end{cases}$$

The tapered density model (3) was shown in I to be the best[9] description of nuclear matter in medium and heavy nuclei; (4) is the extreme modification of this distribution, for a Yukawa type of interaction range, and is illustrated in Fig. 4 of I.

Opacity curves for the uniform, Gaussian, and tapered distributions are shown on a logarithmic plot in Fig. 1. The step-distribution curve lies between uniform and tapered; the modified-tapered curve lies between tapered and Gaussian; both have been omitted for the sake of clarity of the drawing.

The question now may be asked: by how much must the elementary cross section $\bar{\sigma}$ be increased in order that the opacities $\sigma_r/\pi R^2$ corresponding to Table I will fit the curve? Increasing $\bar{\sigma}$ decreases the mean free path in nuclear matter and moves the points to the left.

TABLE II. Some results of cross-section measurements on Pb, showing a trend toward still larger cross sections as the multiplicity of the detected event and therefore, loosely, the energy of the bombarding particle is increased. Cross section in barns, for protons only.

Experiment	Cross section Multiplicity Low	Medium	High
Walker[a]	1.9±0.1	2.3±0.1	2.3±0.15
Froehlich and Sitte[b]	2.1±0.1	2.3±0.15	2.6±0.2

[a] See reference 4. [b] See reference 24.

[9] According to the high-energy electron scattering, the best fit is obtained by a density which drops off slightly more sharply, but it is clear from Fig. 4 of I that the finite nuclear force range will cause the effective density distribution to be a little smoother.

A reasonable fit (see below) to the opacity curve for the tapered nucleus requires $\bar{\sigma}$ to be nearly three times the value at 1.4 Bev, or ~120 mb (1 mb=10^{-27} cm^2). The cosmic-ray points are plotted for this value in Fig. 1. For comparison, the points are dotted in at the positions they would have if $\bar{\sigma}$ were 43 mb, the Brookhaven value.[10] It is clear that even the Gaussian distribution, which was shown in I to be much too radically nonuniform, would demand an increase in $\bar{\sigma}$ of at least a factor of two. The uniform model, as we have already pointed out, cannot fit the cosmic-ray cross sections for any value of $\bar{\sigma}$ and this proves to be true also for the step model.[11]

One sees from Fig. 1 that a small rise in observed cross section, σ_r, corresponds to a large change in $\bar{\sigma}$; the reason is, of course, that most of the nucleons are located in the region of the nucleus that is already black, and the entire change must be due to those which are on the surface of the nucleus. We therefore must expect that the value of $\bar{\sigma}$ determined in this way has a large fractional error due solely to the statistical uncertainty in σ_r. Fitting the points by eye, one can see that they are consistent with a wide range of $\bar{\sigma}$, up to values so high as to be in definite conflict with the direct measurement of Walker, Duller, and Sorrels.[12] One must therefore conclude that the correct value of $\bar{\sigma}$ must not be far above the smallest acceptable value found in this analysis. In Table III we give this smallest value, for the "best" nuclear density distribution (3) and for the two which are more extremely nonuniform, (2) and (4). We arbitrarily set 10 percent probability

[10] Strictly, the ratio ($\bar{\sigma}$ at 30 Bev)/($\bar{\sigma}$ at 1.4 Bev) is all that is determined; in I it is argued that $\bar{\sigma}$ at 1.4 Bev is unlikely to be as much as 20 percent lower than the true total nucleon-nucleon cross section, so that the values of $\bar{\sigma}$ given in Table III should not be much affected by this uncertainty.

[11] Of course, the effective density cannot actually be represented by a square well; as pointed out in I, the finite-range-of-interaction effect will always result in some rounding off.

[12] Walker, Duller, and Sorrels, reference 6. This seems to be the only direct measurement of CH_2-C difference which is in a comparable energy range. They report $\sigma_{pp}=54\pm18$ mb, but our analysis raises this to 80 mb (see Discussion).

as defining "smallest acceptable"—i.e., in each case, if the true value of $\bar{\sigma}$ were smaller than that in the table, the probability of obtaining the experimentally observed cross sections[13] for Pb, Fe, and S would be less than 10 percent (calculated from the chi-squared of the experimental points). For the tapered distribution, 5 percent and 30 percent limits are also shown.

From Table III, recalling that the evidence discussed in I favors the tapered distribution, we conclude that the lower limit for $\bar{\sigma}$ is about 100 mb; a value as large as 150 mb seems almost certain to have shown up in the CH_2-C experiments; we therefore take the most likely value as 120 mb, with limits of 100 mb to 150 mb. This is the nucleon-nucleon cross section, averaged over (np), (pp), and (nn) collisions, and over energy in the 15 Bev–50 Bev region. The median energy (discussed in the Appendix) is 30 Bev. In Fig. 2 the variation of the σ_{np} and σ_{pp} with energy is illustrated on a logarithmic energy scale from 0.05 to 30 Bev.

DISCUSSION

Our indirect determination of σ_{nucleon} in the 20–50 Bev region shows it continuing the rise which starts in the 1-Bev region. From the attenuation of high-energy cosmic-ray protons in paraffin, Walker *et al.*[12] find by difference a (pp) cross section of 54 mb; however, they use for the carbon subtraction the cross section of Brown, which is 20 percent larger than our "best" cross section (Table I), and which would be quite far off the curve of Fig. 1. Using the carbon cross section of Table I, we find from Walker's paraffin data $\sigma_{pp}=80$ mb. This is still below our lower limit of ~100 mb. A possible explanation is offered in the Appendix, where an effect is pointed out which causes low-density materials (such as paraffin) to yield too small a cross section. Other cosmic-ray experiments using CH_2-C or D_2O-H_2O difference have been reported.[14] They indicate smaller cross sections but in general they refer to lower energies, in the few Bev region (see Appendix). The advantages of the present scheme are two: (1) the "difference" in our case is between one direct cosmic-ray measurement and a high-precision machine measurement, rather than between two cosmic-ray measurements; (2) the number of almost-free nucleons in a metal (on the periphery of the nuclei) per cubic centimeter is actually much greater than the density of H in CH_2.

Present knowledge of the nature of nucleons does not lead to any firm expectation for the behavior of the cross section at very high energies. One would be surprised if it greatly exceeded $\pi\times$(low-energy range of nuclear forces)^2, which is 200 mb for a range of 2.5×10^{-13} cm; this is in the same region as the figure obtained by attributing a "size" of $\hbar/\mu c$ (where μ is the pion mass) to each nucleon, $\pi(2\hbar/\mu c)^2=250$ mb. The figure we obtain, 120 mb, is still well within the reasonable region, although there is some suggestion (Table II) that the cross section may still be rising at ~50 Bev.

Fermi, in formulating his statistical theory of high-energy processes,[15] chose $R=\hbar/\mu c=1.4\times10^{-13}$ cm for the radius of the excited volume, and thus $\pi R^2=63$ mb for the cross section for meson production.[16] The angular

TABLE III. Illustrating the effect of statistics, and of the choice of nuclear density models, on the nucleon-nucleon cross section inferred from the rise in reaction cross sections. For each model, the "10 percent probability" cross section is given. This means that there is only 10 percent probability for the cross section to be less than the value quoted. In addition, 5 percent probability and 30 percent probability values are given for the preferred model (tapered density). "Best" value is ~120 mb (see text).

Model	Gaussian	Modified tapered	Tapered		
Probability limit	10%	10%	5%	10%	30%
Nucleon-nucleon cross section, in millibarns	86	103	108	116	160

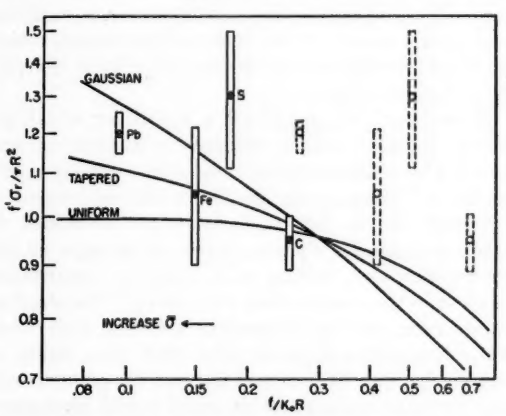

FIG. 1. Opacity, $\sigma_T/\pi R^2$, as a function of $(K_0R)^{-1}$, the mean free path in nuclear matter divided by R, for the uniform density model, on a log-log plot. The corresponding abscissas and ordinates for the tapered and Gaussian models (for which "R" has a different meaning) are multiplied by the appropriate scale factors f and f' so that all three curves refer to the same set of experimental points. The cosmic-ray data of Table I are plotted for $\bar{\sigma}=120$ mb. For comparison, they are also dashed in at the position they would occupy if $\bar{\sigma}=43$ mb, the (np) cross section at 1.4 Bev.

[13] The data on carbon are not included in this analysis because the opacity curves are probably incorrect for such a light nucleus.

[14] R. H. Rediker, Phys. Rev. **95**, 526 (1954); Froman, Kenny, and Regener, Phys. Rev. **91**, 707 (1953); E. Todd, thesis, University of Colorado, 1954 (unpublished).

[15] E. Fermi, Phys. Rev. **81**, 683 (1951).

[16] The question of whether the true total cross section should be larger than this because of possible diffraction scattering is irrelevant, since low-momentum-transfer events do not contribute to the cross section measured by the cosmic-ray techniques. The wave-diffraction picture is not very meaningful, anyway, since at these energies the nucleon must be considered to be a complex particle. It carries a meson cloud whose dimensions are much greater than the wavelength $\lambda\!\!\!^{-}$ of its center of mass. Any diffraction-like process would involve a momentum transfer of the same order of magnitude as the momentum of the virtual mesons. It is not clear without further study that this would correspond to elastic scattering of the particle as a whole.

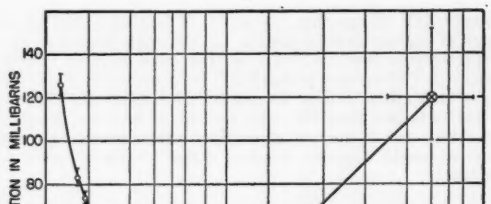

FIG. 2. Energy variation of the nucleon-nucleon total cross section. The low-energy (np) and (pp) cross sections come from various synchro-cyclotron and cosmotron experiments; the point at 30 Bev is the cosmic-ray value inferred in this paper. The flags on the high-energy point have the sense of reasonable limits rather than statistical standard deviations. The continuous curve is included only for convenience.

distribution of mesons is independent of R, in this theory, and the multiplicity varies only as $R^{\frac{1}{4}}$, so that a slow variation of R with energy would not worsen the comparison with experiment. However, it would be somewhat counter to the spirit of the model, which envisions the interaction taking place in a sharply-defined region of space.

Heisenberg[17] has suggested a model for ultrahigh-energy collisions which envisions a nucleon as surrounded by a diffuse meson cloud whose density tapers off like a Yukawa potential. The minimum amount of "overlap" of the two nucleons which is needed to produce mesons is then expected to decrease as the energy increases, leading to a (roughly) logarithmic increase in the cross section with energy The absolute values estimated by Heisenberg are very high—over 300 mb at the energy we deal with here, rising to about a barn at 10^{12} ev—and Cocconi has pointed out[18] that the latter value probably conflicts with photoplate observations. However, the general picture of a diffuse interaction region is supported by the rise in cross section which we have observed.[19]

The character of nucleon-nucleon interactions evidently changes as the energy is raised from 1 or 2 Bev to 20 or 30 Bev. At the lower energy, the various cosmotron results[20] may be summarized by the statement that each nucleon tends to emit "its own" meson; angular effects are therefore quite pronounced.[21] At the higher energy we have seen that the cross section is larger by about a factor of three; moreover, meson production has been found to be rather isotropic[22] (in the c.m. system). Both facts suggest that the strength of the interaction between the two nucleons increases strongly as the energy increases.

[17] W. Heisenberg, *Kosmiche Strahlung* (Springer-Verlag, Berlin, 1953), p. 148.
[18] G. Cocconi, Phys. Rev. **93**, 1107 (1954).
[19] Evidence from the diffraction scattering of pions on protons also seems to support this picture [Eisberg, Fowler, Lea, Shephard, Shutt, Thorndike, and Whittemore, Phys. Rev. **97**, 797 (1955)].
[20] Fowler, Shutt, Thorndike, and Whittemore, Phys. Rev. **95**, 1026 (1954).
[21] A scheme of this sort (but for high energies) is discussed by W. Kraushaar and L. Marks, Phys. Rev. **93**, 326 (1954).

ACKNOWLEDGMENTS

Most of the work of this and the preceding paper was done at Princeton University, where the author enjoyed the hospitality of the Physics Department and Cosmic-Ray Laboratory. He has been stimulated by conversations with several physicists, particularly S. B. Treiman, A. S. Wightman, M. L. Goldberger, and S. D. Drell. The author wishes also to acknowledge his debt to W. D. Walker, who suggested the interpretation of cosmic-ray results used here, and to record with pleasure his fruitful association with the Brookhaven physicists —T. Coor, D. A. Hill, W. Hornyak, L. Smith, G. Snow, and particularly E. O. Salant.

APPENDIX

The cross sections used in this note were all measured by similar methods, which we describe in general terms: the strongly-interacting high-energy component of cosmic rays in the atmosphere—at mountain altitudes about equal numbers of protons and neutrons, with a few percent of pions which we neglect—is detected by demanding an interaction in which several penetrating charged particles are produced (these prove to be mainly pions). Figure 3 shows a schematic cross section of such a detector; C and D are sets of Geiger-Mueller counters immersed in Pb and so arranged that at least two (for example) must be discharged in each tray. The detector will generally have excellent discrimination against mesons and electrons, a rather diffuse but adjustable energy threshold E_{th}, and poor directional properties. If one now defines a beam of protons by an additional set of counters such as A, and attempts to measure the attenuation of the beam as absorber Σ is inserted, he finds only about one-half the expected attenuation. The reason, of course, is that the number-energy spectrum of the protons falls so slowly—as $E^{-1.3}$—that there are many protons of energy well above E_{th}, and these may not be removed by a collision in the absorber because the collision products can still cause the detector to register a count. This difficulty is overcome[23] by inserting a densely-packed set of counters B between the absorber and the detector, and registering a count only if exactly one counter in B is discharged. Thus high-energy interactions in the absorber will nearly always discharge more than one counter in B; they are treated as "absorptions" even though their products may cause counts in C and D. The counting-rate decrease with absorber thickness therefore yields the cross section.

If a high-energy proton transfers only a small amount of energy to a nucleus so that the secondaries do not reach tray B, the method breaks down and the measured cross section is less than the true reaction cross section. Measurements by Walker *et al.*[6] have shown that this happens only a few percent of the time if the absorber is not too thick; Froehlich and Sitte[24] have also investigated this effect, with similar conclusions.

[22] N. Duller and W. D. Walker, Phys. Rev. **93**, 215 (1954).
[23] A detailed discussion of this technique is given by B. Rossi, *High-Energy Particles* (Prentiss-Hall, Inc., New York, 1952), pp. 500 ff.
[24] F. Froehlich and K. Sitte, Phys. Rev. **97**, 151 (1955).

This is the principal systematic error, expected to be a few percent; since it causes the measured cross section to be *less* than the true value, and our arguments are based on the fact that the measured cross section is already *larger* than the Brookhaven value, this error does not concern us further. There are, however, minor corrections in the opposite direction, which in some cases have apparently not been made by the experimenters: the thickness correction for the average path length in absorber (the incident intensity decreases as $\sim\cos^7\theta$); ionization loss in the absorber; spurious effect of knock-on electrons in the absorber (the latter two apply to protons only—modification of the apparatus to use neutrons is fairly obvious). In making the weighted averages of Table I, therefore, we have *decreased* the reported cross sections (by about 2 percent as it turns out) in those cases where we were able to estimate some needed corrections.

The neutron measurements (and some proton measurements) are done without the beam-defining tray, *A* (Fig. 3); since ~30 percent of the beam comes in at angles >30°, this means the absorber must be quite wide, as shown by the dotted lines. Thus for an absorber composed of low-density materials such as paraffin or water, which have a mean free path of two feet, the added absorber will intercept many protons and neutrons which previously missed the detector; the secondaries of some of these will cause spurious counts [ray (*c*) in Fig. 3]. This may account in part for the low values obtained for σ_{np} by difference measurements. One should also remark that the mean energy used in difference experiments is deliberately chosen to be low, so that a high counting rate is obtained; the median energy of the work of reference 14 is probably only a few Bev. At such low energies, the elimination of collisions in the absorber is inefficient, and the cross section (which means only the meson-production part of the total cross section) is not large.

The energy of the protons selected is estimated from the observed counting rate, using a calculated area-solid angle-efficiency product and assuming a known proton spectrum. We have done this very roughly, assuming the efficiency rises linearly from E_{th} to a saturation value of about ½. The proton spectrum for an atmospheric depth of 694 g cm^{-2} was compounded from several results,[25] and may be expressed, in the pertinent energy range, as $N(>E)=4\times10^{-5}(10/E)^{1.3}$ cm^{-2} sterad^{-1} sec^{-1}, E in Bev. Our results for average energies of initiating particles are in general agreement with those of Walsh and Piccioni,[26] who used a quite independent method (based on the latitude effect); their detector had a relatively low E_{th}.

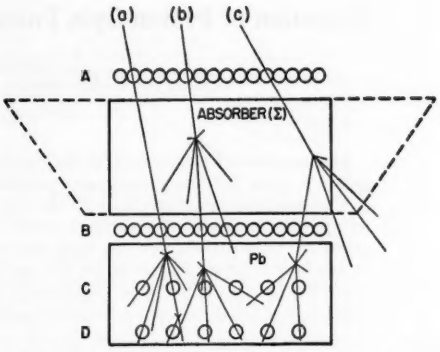

FIG. 3. Schematic diagram (sectional elevation) of the type of apparatus used to measure reaction cross sections in the cosmic-ray beam. Typically the dimensions might be 2 ft×2 ft×2 ft. *A*, *B*, *C*, and *D* are groups of Geiger-Mueller tubes. (a) A proton passes through the absorber and registers a normal count. (b) A proton interacts in the absorber; no count is registered because two counters in group *B* are discharged. (c) A proton which would not have registered a count with absorber absent registers a spurious count when absorber is added.

For each experiment we have made an estimate, in this way, of the median energy (which is in a sense the energy of the average event); this ranges from 15–20 Bev for Walker *et al.*[3] to 50–60 Bev for Brown[8]; we therefore use an intermediate value, 30 Bev, as "the" energy, with the remark that appreciable contributions to the flux come from a wide band centered on 30 Bev.

[25] H. S. Bridge and R. H. Rediker, Phys. Rev. **88**, 206 (1952) (contains other references); W. D. Walker (private communication).

[26] T. G. Walsh and O. Piccioni, Phys. Rev. **80**, 619 (1950).

Direction of Proton Spin Polarization Produced by Elastic Scattering*

L. MARSHALL AND J. MARSHALL
Institute for Nuclear Studies, The University of Chicago, Chicago, Illinois
(Received February 25, 1955)

A measurement has been made of the direction of spin polarization produced by elastic scattering of high-energy protons. 435-Mev protons were polarized by scattering elastically from beryllium to the right at 14° after which they were slowed to 0–20 Mev and scattered again elastically from helium. From the measured energies and angles of the scattered protons as recorded in photographic emulsions, together with the calculated polarizations resulting from interferences among the levels of the doublet P state involved in proton-helium elastic scattering, we find that the polarization of the proton beam is directed down. This result has been predicted by an hypothesis which extrapolates to high energies the effect of the spin-orbit coupling postulated for the nuclear shell model.

BEAMS of high-energy protons with spin polarization are produced by scattering unpolarized protons from nuclei.[1,2] If the protons are scattered elastically the polarization is considerably larger than if the scattering occurs by inelastic processes.[3,4] A theoretical interpretation has been suggested by Fermi and others,[5] which demonstrates that the polarization of the elastically scattered beam may be accounted for as a consequence of the spin-orbit coupling postulated in the nuclear shell model of Mayer and Jensen. This hypothesis gives correctly the magnitude of the observed polarization, and in addition predicts the direction of the polarization. In particular, if the scattering is to the right at small angles, this hypothesis requires the predominant spin direction to be downward.

The objective of the present experiment[6] was to measure the direction of the polarization. The measurement depended on knowledge of the polarization resulting from interference of the energy levels involved in the elastic scattering of protons on helium in the energy region 1–15 Mev. From the cross-section data for this reaction, Critchfield and Dodder[7] have evaluated the phase shifts. In fact two representations of the data were found, for both of which the ^2P phase shifts were positive (attractive potential). In one solution the ^2P levels were inverted and in the other solution they were normal. Interference among the states of the doublet produces a polarization of the scattered protons. Heusinkveld and Freier[8] observed the second scattering asymmetry resulting from this polarization, and by its magnitude at a given energy were able to conclude that the P state is an inverted doublet.

In principle, this information allows one to determine the spin direction of a beam of polarized protons by a similar experiment.

In the present investigation a 435-Mev polarized proton beam was produced in the cyclotron by scattering the 450-Mev maximum energy circulating protons elastically at 14° from an internal beryllium target, to the right and in the horizontal plane. The absolute value of the polarization of the emergent proton beam was found to be 53 ± 2 percent by measuring in the usual way the asymmetry of elastic scattering from beryllium at the same angle, i.e., 14°, and in the horizontal plane. Subsequently the protons were slowed down by passing through a thickness of copper corresponding to their mean range after which they were expected still to be polarized.[9] The protons, now of various low energies, mainly in the region from 0 to 20 Mev, were then collimated carefully. Next they entered a scattering chamber filled with helium at atmospheric pressure (see Fig. 1). Nuclear emulsions (Ilford $E1$) were placed to right and left in the scattering chamber in such a way that protons scattered by the collimating system could not reach them and in such a way that protons scattered in the horizontal plane by helium and at $\pm90°$ to the beam entered the emulsion in a direction normal to the surface.

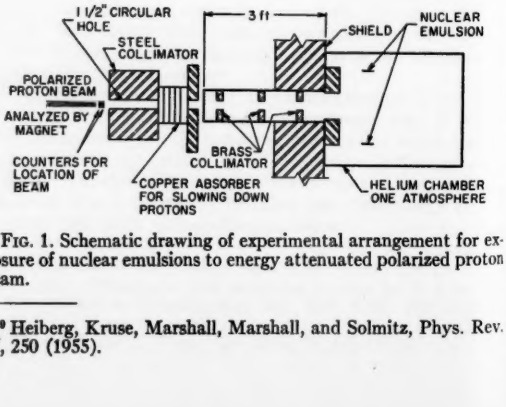

FIG. 1. Schematic drawing of experimental arrangement for exposure of nuclear emulsions to energy attenuated polarized proton beam.

* Research supported by a joint program of the Office of Naval Research and the U. S. Atomic Energy Commission.

[1] Oxley, Cartwright, Rouvina, Baskir, Klein, Ring, and Skillman, Phys. Rev. 91, 419 (1953).

[2] Chamberlain, Segrè, Tripp, Wiegand, and Ypsilantis, Phys. Rev. 93, 1430 (1954).

[3] Marshall, Marshall, and de Carvalho, Phys. Rev. 93, 1431 (1954).

[4] de Carvalho, Marshall, and Marshall, Phys. Rev. 96, 1081 (1954).

[5] E. Fermi, Nuovo cimento 11, 407 (1954); W. Heckrotte and J. V. Lepore, Phys. Rev. 95, 1109 (1954); B. J. Malenka, Phys. Rev. 95, 522 (1954); Snow, Sternheimer, and Yang, Phys. Rev. 95, 1073 (1954).

[6] L. Marshall and J. Marshall, Nature 174, 1184 (1954).

[7] C. L. Critchfield and D. C. Dodder, Phys. Rev. 76, 602 (1949).

[8] M. Heusinkveld and G. Freier, Phys. Rev. 85, 80 (1952).

[9] Heiberg, Kruse, Marshall, Marshall, and Solmitz, Phys. Rev. 97, 250 (1955).

There were approximately 30 000 high-energy protons arriving per second at the copper attenuator. The flux however was reduced approximately 1:30 by scattering during energy degradation and subsequent collimation. The frequency of occurrence of events in the plates is found to be in rough agreement with the estimated slow proton flux and with the elastic scattering cross section of helium.

Only those events were accepted for measurement in which the proton entered the emulsion within 45° of the normal to the surface of the emulsion, (i.e., for scattering to the left $-45°\leqslant\theta\leqslant-135°$, $135°\leqslant\phi\leqslant225°$, and for scattering to the right $45°\leqslant\theta\leqslant135°$, $-45°\leqslant\phi\leqslant45°$).

From the direction in which a scattered proton enters the emulsion and from its energy as determined by its range in the emulsion, one computes the energy of the proton before scattering.

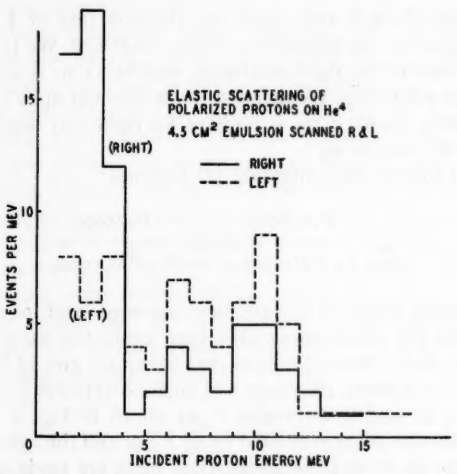

FIG. 2. Number of polarized protons per Mev incident energy observed to be scattered by helium to left and to right between $\theta=45°$ and $\theta=135°$ laboratory angle shown plotted *versus* energy of incident proton.

At present approximately 150 events have been found. In Fig. 2 the number of events per Mev energy interval is plotted against the incident energy computed for the scattered proton.

For comparison purposes we have calculated the helium cross sections for a proton beam polarized with spin down, for scattering to right and to left, as a function of energy and angle using the presently available phase shifts.[7,10,11] The differential cross sections have been integrated over the solid angle of acceptance and corrected for an incident polarization of 60 percent. The resultant cross sections, plotted in Fig. 3, show right scattering stronger than left scattering near 3 Mev, and

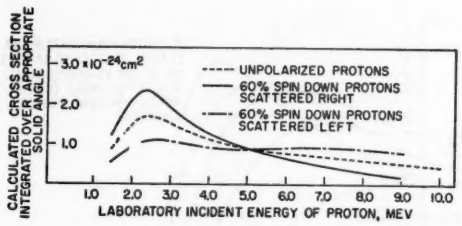
CALCULATED CROSS SECTION INTEGRATED OVER APPROPRIATE SOLID ANGLE
3.0 × 10⁻²⁴ cm²
UNPOLARIZED PROTONS
60% SPIN DOWN PROTONS SCATTERED RIGHT
60% SPIN DOWN PROTONS SCATTERED LEFT
LABORATORY INCIDENT ENERGY OF PROTON, MEV

FIG. 3. Helium elastic scattering cross sections for protons *versus* proton energy, calculated from phase shifts, and integrated over solid angle in which scattering events were accepted. The cross section for unpolarized protons scattered either to left or right is shown, and also the cross sections for protons 60 percent polarized with spin down, scattered to left and to right. For the case of protons 60 percent polarized with spin up, the designations on the two latter curves are interchanged.

at 7–11 Mev right scattering weaker than left scattering. If on the other hand, the incident beam were assumed polarized with spin up, the cross sections in Fig. 3 for scattering to the left and right would be interchanged.

The data in Fig. 2 show a behavior similar to the curves of Fig. 3, indicating that the proton beam incident on the helium is polarized with spin down.

For each scattered proton, three pieces of information have been measured: θ_i'=angle from incident beam direction to final trajectory, ϕ_i=azimuthal angle of final trajectory about beam direction, and E_i'=energy of scattered proton. From θ_i' and E_i', the incident energy E_i is readily calculated. The cross section for scattering may now be written using the barycentral angle θ_i:

$$\sigma_i(\theta_i\phi_iE_iP)=g_i(\theta_iE_i)\{1+PP_i(\theta_iE_i)\cos\phi_i\}. \quad (1)$$

In this expression, P_i is the polarization which will exist in a scattered beam if a previously unpolarized beam of energy E_i is scattered at angle θ_i. The variation of P_i with θ_i for various values of E_i has been calculated from the low-energy scattering data[11] and the results are shown plotted in Fig. 4. Likewise, the quantity $g_i(\theta_iE_i)$ is readily calculable from the low-energy scattering data. P, whose sign and magnitude we wish to calculate from the present data, is the polarization of the beam of protons incident on the helium.

It follows that P can be estimated from measured values of $\sigma_i(\theta_i\phi_iE_i)$. One hopes that the experimental estimates of P will be distributed about the true value, P^*, according to a Gaussian error function with an acceptable width. It is relevant to examine the proton-helium scattering data for the validity of this condition, and if it is valid, for an experimental value of P.[12]

The relative probability per incident proton to obtain the ith event of characteristics $(\theta_i\phi_iE_i)$ is $n\sigma_i(\theta_i\phi_iE_i)$ where n is the number of atoms of He/cm². Suppose Q_N is the probability per incident proton to have found N

[10] D. C. Dodder and J. L. Gammel, Phys. Rev. **88**, 520 (1952).
[11] Kreger, Jentschke, and Kruger, Phys. Rev. **93**, 837 (1954). See graph of phase shifts *vs* energy.

[12] Maximum likelihood method of analysis. See, for example, M. G. Kendall, *Advanced Theory of Statistics* (C. Griffen and Company, Ltd., London, 1948), fourth edition.

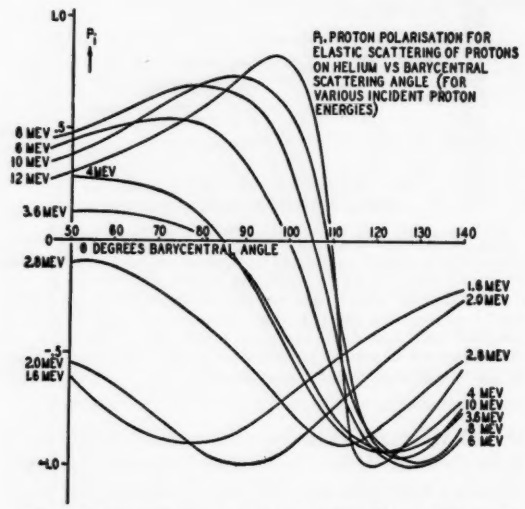

FIG. 4. Polarization P_i produced in scattered beam when protons of energy E are elastically scattered at angle θ from helium. Values of P_i have been calculated from the phase shifts and are shown plotted *versus* θ for various values of E.

events. Then

$$Q_N \cong n^N \sigma_1(\theta_1\phi_1 E_1 P)\sigma_2(\theta_2\phi_2 E_2 P)\cdots\sigma_N(\theta_N\phi_N E_N P),$$

$$\ln Q_N = \text{const} + \sum_{i=1}^{N} \ln\sigma_i(\theta_i\phi_i E_i P).$$

Expand $\ln\sigma_i(\theta_i\phi_i E_i P)$ in a Taylor's series about P^*,

$$\ln\sigma_i(P) = \ln\sigma_i(P^*) + (P-P^*)\left(\frac{\partial \ln\sigma_i}{\partial P}\right)_{P^*} + \frac{1}{2!}(P-P^*)^2\left(\frac{\partial^2 \ln\sigma_i}{\partial P^2}\right)_{P^*} + \cdots,$$

and sum over N events, letting $P-P^*=\Delta P$:

$$\ln Q_N - \text{const} = \sum_i \ln\sigma_i = \sum_i \ln\sigma_i(P^*) + (\Delta P)\sum_i\left(\frac{\partial \ln\sigma_i}{\partial P}\right)_{P^*} + \frac{(\Delta P)^2}{2!}\sum_i\left(\frac{\partial^2 \ln\sigma_i}{\partial P^2}\right)_{P^*} + \cdots.$$

The first term has no dependence on P. If the second term should be zero and in addition if the fourth, fifth, and higher terms should be small, then Q_N would have the P dependence:

$$\ln Q_N = \text{const}' + \frac{(\Delta P)^2}{2!}\sum_i\left(\frac{\partial^2 \ln\sigma_i}{\partial P^2}\right)_{P^*} + \text{small terms}, \tag{2}$$

$$Q_N \simeq \text{const}'' \exp\left[-\tfrac{1}{2}(\Delta P)^2\sum_i\left(-\frac{\partial^2 \ln\sigma_i}{\partial P^2}\right)_{P^*}\right],$$

which dependence approximates the desired Gaussian distribution of the experimentally determined values of P.

Accordingly, the first requirement is to have the coefficient of ΔP in the Taylor's expansion equal to zero. We set

$$\sum_i\left(\frac{\partial \ln\sigma_i}{\partial P}\right)_{P^*} = 0 = \sum_{\text{Right}}\left(\frac{\partial \ln\sigma_i}{\partial P}\right)_{P^*} + \sum_{\text{Left}}\left(\frac{\partial \ln\sigma_i}{\partial P}\right)_{P^*}. \tag{3}$$

For convenience we measure ϕ_i from the normals to the right hand or left hand photographic emulsions, so that ϕ_i is always less than 90°. The scattering cross section is[12]

$$\sigma_i = g_i(\theta_i E_i)\{1 + PP_i(\theta_i E_i)\mathbf{n}_1\cdot\mathbf{n}_2\},$$

where $\mathbf{P}=\mathbf{n}_1 P$ and where $\mathbf{n}_2$, the direction of $\mathbf{P}_i$, is defined by the relation $\mathbf{k}_{\text{scat}}\times\mathbf{k}_{\text{inc}} = \mathbf{n}_2 k^2 \sin\theta$. We take θ as positive for right scattering, and hence $\mathbf{n}_2$ is up for right scattering. We define $\mathbf{n}_1$ to be directed up. Consequently $\cos\phi = \mathbf{n}_1\cdot\mathbf{n}_2$ is positive for right and negative for left scattering.

It follows that condition (3) becomes:

$$\sum_{\text{Right}}\frac{P_i\cos\phi_i}{1+PP_i\cos\phi_i} = \sum_{\text{Left}}\frac{P_i\cos\phi_i}{1-PP_i\cos\phi_i}. \tag{4}$$

Various values of P have been assumed, and for each value the above sums have been evaluated using the data from 136 scattering events between 1 and 12 Mev. For each event, the range and angles determine E_i, and then E_i and θ_i determine P_i as shown in Fig. 4. The ratios above are evaluated using P_i, ϕ_i and the assumed value of P; and the appropriate sums are made separately for events to the left and to the right. These are shown plotted in Fig. 5. One sees that condition (2) is satisfied for $P=-37$ percent, the negative sign meaning average incident spin down.

Next we evaluate the probable error, i.e., the width of the Gaussian. According to Eqs. (1) and (2) the standard deviation is given by

$$\frac{1}{\sigma^2} = \sum\left(-\frac{\partial^2 \ln\sigma_i}{\partial P_i}\right)_{P^*} = \sum_{\text{Right}}\left\{\frac{P_i\cos\phi_i}{1+PP_i\cos\phi_i}\right\}^2 + \sum_{\text{Left}}\left\{\frac{P_i\cos\phi_i}{1-PP_i\cos\phi_i}\right\}^2.$$

Evaluation of these sums for $P^*=-0.37$ gives the result

$$1/\sigma^2 = 57.4 \quad \text{or} \quad \sqrt{2}\sigma = 0.19,$$

from which it follows that $P^*=-0.37\pm0.19$, provided that the higher moments in the Taylor's expansion

[12] See, for example, J. V. Lepore, Phys. Rev. 79, 137 (1950).

about P^* are sufficiently small that the dependence on ΔP is close to Gaussian. Accordingly, some of the higher moments have been evaluated; we obtain

$$\sum \ln\sigma_i(P)=\text{const}-\left(\frac{\Delta P}{0.19}\right)^2-\frac{(\Delta P)^3}{3}\{27.6\}$$

$$-\frac{(\Delta P)^4}{4}\{48.7\}-\cdots,$$

or

$$Q_N\simeq\text{const}''\exp\left\{-\left(\frac{\Delta P}{0.19}\right)^2[1-9.2(\Delta P)^3]\right.$$

$$\left.\times[1-12.2(\Delta P)^4][\cdots]\right\}.$$

One sees that the dependence of Q_N on ΔP is indeed close to Gaussian. For example, at $\Delta P=0.19$, a purely Gaussian dependence would give $Q_N=C''\epsilon^{-1}$ whereas the above relation gives $Q_N\simeq C''\epsilon^{-1}(0.945)$, (0.984), $(\cdots)$ which is a sufficiently good approximation.

On the basis of the foregoing figures, one would compute the probability that the incident beam has negative polarization to be greater than 99 percent. In truth, however, this probability should be somewhat smaller, as a result of experimental uncertainties in the constants of the proton-helium system. For example, the values of P_i in Fig. 4 depend on phase shifts computed from proton-helium scattering data and whose values may in consequence change somewhat (resulting in corresponding changes in P_i) when more scattering data is available.

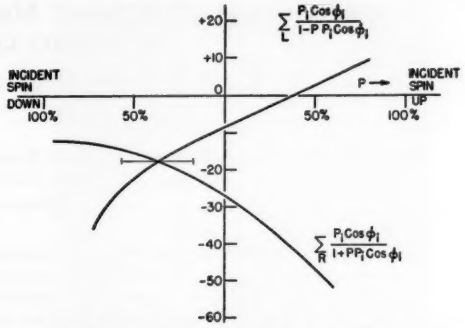

FIG. 5. Maximum likelihood method of analysis of data; first derivative of probability (i.e., probability to have observed the given events) plotted for right and left scattering against various assumed values of incident polarization P. The sums for right and left scattering are equal at $P=-37$ percent ± 18 percent, indicating incident proton spin down in agreement with the spin-orbit coupling hypothesis.

We now return to a consideration of the first scattering which produced the polarized beam. The first scattering, in the cyclotron, was to the right, for which, for an attractive potential, **L** is directed downward.

But the conclusion allowed by the foregoing evidence is that the average spin of the right scattered beam is downward, i.e., parallel to **L**. Then the elastic scattering is stronger at small angles for spin parallel to **L**, in agreement with the proposal[5] that the polarization is due to the spin orbit coupling effective in nuclear shell structure.

We are grateful to Robert March for aid in plate scanning and to Dr. Frank Solmitz for helpful calculations.

Association of a "Unipolar" Magnetic Region on the Sun with Changes of Primary Cosmic-Ray Intensity*

J. A. SIMPSON, *Institute for Nuclear Studies, University of Chicago, Chicago, Illinois*

AND

H. W. BABCOCK AND H. D. BABCOCK, *Mount Wilson and Palomar Observatories, Carnegie Institution of Washington and California Institute of Technology, Pasadena, California*

(Received January 17, 1955)

A new instrument for observing weak magnetic fields on the photosphere of the sun has recently revealed the presence of an unusual area on the solar surface which may be called a "unipolar" magnetic (UM) region because the field is of one sign and no magnetic flux has been found returning to the sun. A region of this type was observed at central solar meridian on seven consecutive solar rotations in 1953. In the present paper it is shown that there is a striking association of this UM region with (1) times of maximum primary cosmic ray intensity as measured by neutron detectors and an ionization chamber, and with (2) the recurring geomagnetic storms—the geomagnetic disturbances being most pronounced ~3–4 days after both the central meridian passage of the UM region and the time of maximum cosmic-ray intensity.

I. INTRODUCTION

IT has long been an outstanding problem to identify the solar phenomenon which produces the recurring 27-day geomagnetic storms. A hypothetical solar region capable of producing these magnetic storms was called a solar "M" region by Bartels.[1] Recently, on the basis of one observed sequence, it has been tentatively suggested that the solar "M" regions may be identified with unusual newly-observed magnetic-field regions on the sun.[2] It has also been shown that the 27-day maxima in cosmic-ray intensity are followed within 2–3 days by increased geomagnetic disturbances, often reaching the magnitude of geomagnetic storms. Although the evidence is incomplete, we wish to present a preliminary report showing that on seven consecutive rotations of the sun in 1953 there was a striking association of a peculiar solar magnetic field region with cosmic-ray intensity changes as well as with a series of recurring geomagnetic storms.

II. MAPPING OF MAGNETIC FIELDS ON THE SUN

A new instrument for observing weak magnetic fields on the photosphere of the sun was devised and put into use at Pasadena, California, late in 1952.[3] It utilizes the longitudinal Zeeman effect, wherein a spectral line (usually $\lambda 5250.216$ of iron) is split by the solar field into two overlapping, but oppositely polarized, components; thus, the measurement is of $H\cos\gamma$, the component of the field in the line of sight. The principal features of the instrument are:

1. A new plane grating is used in the 75-foot underground Littrow spectrograph. It has a dispersion (fifth order) of 11 mm/A and a resolving power of 6×10^5.

2. In the focal plane of the spectrograph two slits of a photoelectric detector are placed at the positions of steepest slope of the line profile. A photomultiplier is used at each slit, and the separate outputs are connected to a circuit (difference amplifier) that responds only to a difference in their output. An alternating potential is applied to a quarter wave analyzer to present alternately (120 cycle/sec) at the slits the two components which have been divided by the solar field.

3. A 40-cm diameter image of the sun is automatically scanned by the slit of 15-mm length. The effect of the magnetic field is shown by vertical fluctuations of a cathode-ray beam on the screen of a cathode ray tube (C.R.T.). A second, horizontal beam line is drawn as a fiducial mark. About 22 equally spaced traces across the disk are made in succession and recorded conformally by a camera focussed on the C.R.T. screen. Compensation is provided for the Doppler shift of the spectrum due to solar rotation. From these recordings the intensity, polarity and distribution of the magnetic fields on the sun may be determined.

The rms noise level is 0.1 gauss and a deflection equal to the vertical interval between two fiducial lines is about 1 gauss.

The apparatus is linear up to ~5 gauss and quasi-logarithmic above this range.

Approximately 80 minutes are required for a complete scanning of the sun. A complete map is shown in Fig. 1. The rotation axis is vertical and the east limb is on the right. The results of 450 magnetograms accumulated in two years of observing have recently been summarized.[2]

The records, in the form of magnetic maps, show the location, polarity and intensity of widespread weak fields apart from sun spots. A study of the recordings leaves the over-all impression that the magnetic pattern of the sun is one of remarkable detail, usually comprising a number of strong, localized multipolar fields along with other areas of magnetic fields, some extensive

* The cosmic-ray measurements reported herein were supported in part by the Office of Scientific Research, Air Research and Development Command, U. S. Air Force.

[1] J. Bartels, Terrestrial Magnetism and Atm. Elec. 37, 48 (1932).

[2] H. W. Babcock and H. D. Babcock, Astrophys. J 121, 349 (1955).

[3] H. W. Babcock, Astrophys. J. 118, 387 (1953).

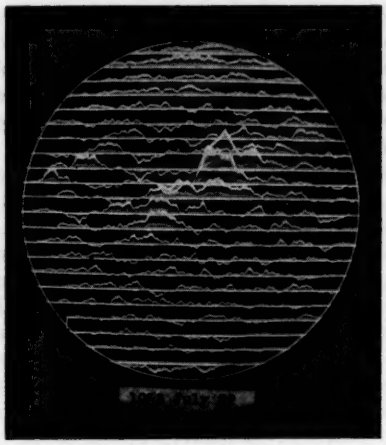

FIG. 1. The presence of a weak magnetic field predominantly of one sign is shown for July 22, 1953 by this conformal map of the solar disk. The magnitude of the magnetic field is given by vertical fluctuations (positive upward) of a cathode ray beam on a C.R. tube. A second horizontal beam line is drawn as a fiducial mark. The rms noise level is 0.1 gauss and a deflection equal to the vertical distance between two fiducial lines is about 1 gauss. The sense of solar rotation is from right to left.

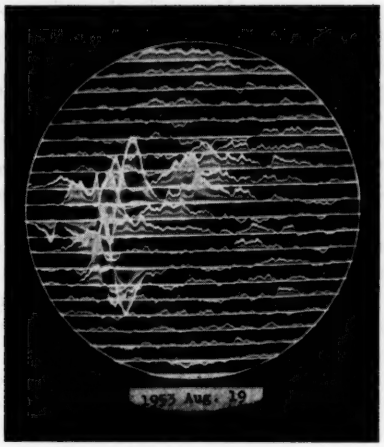

FIG. 2. The conformal mapping of the solar disk for August 19, 1953. See Fig. 1 for details. On this date the UM region had an area of more than 0.15 of the solar disk, an intensity of ~1 gauss, a positive polarity and a flux of 1×10^{21} maxwells. Two bipolar magnetic field regions are shown to the left of the UM region. In both Figs. 1 and 2, the North Pole is shown vertically upward.

and some local, identified by weaker fields ranging down to the limit of observation. There are considerable changes from day to day, and there is some evidence for appreciable fluctuations in detail, of the order of one gauss, in intervals of 30 minutes.

The numerous magnetic regions of the sun at low latitudes are more or less localized and are transient, with areas ranging up to a fraction of a hemisphere, intensities up to several gauss, and lifetimes up to several months.

Most of the prominent magnetic areas may be classed as bipolar magnetic (BM) regions; sunspots, when they occur, are within BM regions; if the field-intensity is greater than about 2 gauss they show a close identification with bright calcium flocculi or *plages* on spectro-heliograms. The archlike patterns of bright coronal radiations are located above the stronger BM regions; this, together with evidence from eclipse photographs, suggests that the vertical extent of the BM fields is at least as great as their surface extent. The magnetic polarities of the preceding (westerly) and following parts of BM regions in the northern and southern hemispheres obey the laws of polarity found by Hale for sunspots. These magnetic fields share the rotation of the sun. The records usually suggest at least approximate equality of positive and negative magnetic flux in the preceding and following parts of the BM regions. There is a great range in the total flux of different BM regions; a "typical" region (1953$H\phi$) had a flux of about 1×10^{21} maxwells.

III. "UNIPOLAR" MAGNETIC FIELDS

Of special interest here are a few special areas on the solar surface at low latitudes which may be classed as "unipolar" magnetic (UM) regions, because the deflections are predominantly of one sign, and it is not at all obvious where the emergent magnetic flux returns to the sun. UM regions have not been related to obvious features on spectroheliograms or to the preliminary records of the coronograph observers at Climax, Colorado. The most prominent low-latitude UM region had, near central meridian passage on August 19, 1953 (Fig. 2), an area of about 0.15 of the solar disk, an intensity of about one gauss, a positive polarity, and a flux of 1×10^{21} maxwells. It was observed first at the central meridian passage date of April 6, 1953 and was detected, on successive rotations of the sun, at central meridian on May 3, May 30, June 27, July 23, August 20, and September 15. By October 13, the region was faint and, later, when observations could be made, no positive identification of the region was possible.

The UM region tends to become elongated with time. No observation was made which would indicate whether or not the UM region was present at central meridian one rotation or more prior to the observation of April 6, 1953. Thus, the existence of the region is known over 7 consecutive rotations as well as the apparent disintegration of the region after October, 1953. In the following sections we shall discuss these UM regions in relation to changes of cosmic ray intensity and the mechanism for producing recurrent magnetic storms at the earth.

IV. CHANGES OF COSMIC RADIATION INTENSITY

Twenty-seven-day changes of cosmic-ray intensity have been extensively studied in recent years by secondary-neutron intensity observations deep within the atmosphere. These neutron measurements were

shown to represent changes in the primary-particle flux outside the atmosphere of the earth, especially the changes in intensity near the low-energy end of the primary-particle spectrum.[4] The methods for measuring these neutron intensity changes with a lead and paraffin pile, and the way in which the observations are related to changes in the primary-particle spectrum, have been described earlier in this journal. We shall report here on the observations of the 27-day recurrences in 1953 and consider their phase relationship to the unipolar, solar magnetic fields.

The daily mean neutron intensity (corrected for barometric pressure variations) was measured at Chicago, Illinois ($\lambda=52°$, near sea level) and Climax, Colorado ($\lambda=48°$, 11 500 feet). We now know that the average amplitude of the 27-day recurring intensity variation has been declining rapidly over the period 1950–1954 and that this decline is associated with the general level of solar activity.[5] Solar activity approached a minimum in 1954 and the amplitude of the 27-day variations to be reported here for 1953 are small, i.e., ~1 percent. Hence, we have taken the three-day running average of the mean daily intensity.

The (synodic) recurrence interval of 27-days for an observer located on the earth corresponds to a true solar rotation of ~25 days. The rotation period of the sun is a function of solar latitude; hence, the observed period on the earth represents the rotation period of solar latitudes not far from the solar equator. The question to consider here is what relationship, if any, do these cosmic-ray intensity variations have with respect to the unipolar magnetic fields found within ~20° of the solar equator?

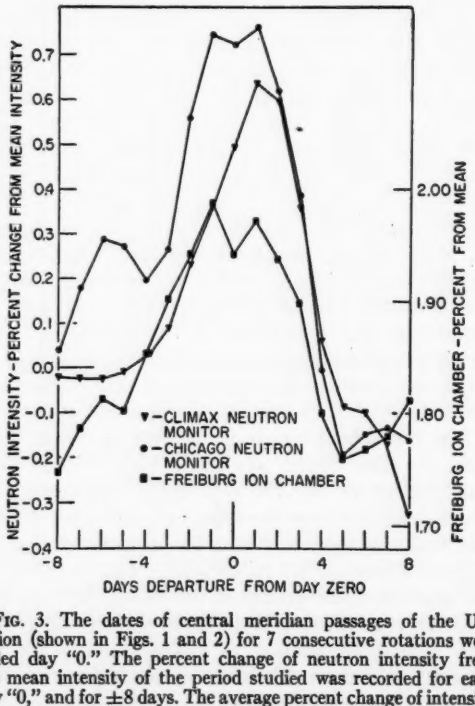

FIG. 3. The dates of central meridian passages of the UM region (shown in Figs. 1 and 2) for 7 consecutive rotations were called day "0." The percent change of neutron intensity from the mean intensity of the period studied was recorded for each day "0," and for ±8 days. The average percent change of intensity for the 7 rotations is shown. Each rotation produced a similar peak of cosmic-ray intensity. A similar process was followed for the Freiburg ionization chamber data (reference 6).

To explore the time-phase relationship between these two phenomena we designate each central meridian passage of the "unipolar" magnetic region as day "0" and record the cosmic-ray intensity on these days, and for $-n$ to $+n$ days for each day "0." The data for the seven consecutive meridian passages of the solar region are added with the results shown in Fig. 3. The maximum of cosmic-ray intensity appears to be centered close to the time of central meridian passage of the solar region although the range of individual cosmic-ray intensity maxima is somewhat greater than ±1 day. Each of the seven individual maxima which combine to produce the curves in Fig. 3 has approximately the same amplitude. The results are shown, independently, for the neutron detectors at $\lambda=48°$ and $\lambda=52°$. To demonstrate that this 27-day recurrence extends out to particle energies the order of 40 Bev, with much smaller amplitude, we have also shown the data for the shielded ion chamber of Sittkus at Freiburg, Germany.[6] Thus, we see that the best defined feature of the 27-day recurring intensity variation, namely, the time of maximum intensity, is clearly observed in time coincidence with the central meridian passage of the "unipolar" region.

To assist in deciding whether this coincidence is accidental or real we examined time intervals preceding and following the period investigated in Fig. 3. A maximum in cosmic-ray intensity was found on March 10, 1953, corresponding to one solar rotation preceding the first magnetograph observation of the UM region. However, for the three months prior to March 10 there are no cosmic-ray intensity maxima on day "0." There are no corresponding solar data for the rotations prior to April 6.

A similar investigation of the three solar rotations beyond September, 1953 (after which the UM region became diffuse and declined to background intensity) also showed that a cosmic-ray intensity maximum no longer existed at day "0."

From these observations we conclude that the first coincidence of UM region and cosmic-ray intensity maximum is uncertain within one solar rotation and that the decline in importance of the UM region coincides with the disappearance of the cosmic-ray intensity maximum at day "0" following the September, 1953 observations.

[4] J. A. Simpson, Phys. Rev. 94, 426 (1954). See also H. Elliott, Proceedings of the Bagnères Conference, Sessions on Time Variations, 1953 (unpublished), p. 14.

[5] P. Meyer and J. Simpson, Phys. Rev. 96, 1085 (1954).

[6] The ionization intensity is published quarterly by A. Sittkus in the "Sonnen-Zirkular" of the Fraunhofer Institute, Freiburg-in-Baden, Germany.

An examination of the entire period December, 1952 through February, 1954 reveals that the only well-defined cosmic-ray intensity maxima are those in the 27-day recurrence beginning March 10, 1953 and ending with September 15, 1953.

V. RECURRING GEOMAGNETIC STORMS

Recent investigations not only indicate that the 27-day neutron intensity maxima are followed within 2–3 days by the onset of geomagnetic disturbances, but they also show that the cosmic ray intensity variations are not produced by these magnetic disturbances.[4] There is evidence to support the view that both these phenomena have a common extra-terrestrial origin in an unknown mechanism within interplanetary space; this mechanism being generated by a special kind of solar region. The question then arises: could the recently observed UM regions satisfy the requirements for this special kind of solar region?

The magnitude of disturbances in the external terrestrial field may be represented on an approximately log scale by an index, K_p, prepared from a world-wide distribution of magnetic field observations. Large values of K_p represent geomagnetic storms. We already know that the cosmic ray intensity maxima for 27-day variations are related to K_p, consequently, we see that the unipolar regions are related in phase to the recurring values of large K_p. For example, calling the central meridian passages of UM regions day "0" we plot the values of K_p for day "0" and all days $-n$ to $+n$ for the 7 consecutive rotations. Figure 4 shows that the maximum geomagnetic disturbances occur approximately 4 days after day "0."

This recurring sequence of geomagnetic disturbances has three noteworthy features:

1. It represents, without doubt, the most outstanding sequence of recurrences in the period April–September, 1953 leading to magnetic storms. There are other geomagnetic disturbances within this period, but they do not develop into recurring geomagnetic storms.

2. For at least three of these recurrent storms there were sudden commencements.

3. Recurring geomagnetic storms, which apparently arise from the same solar longitude as those in the April–September, 1953 sequence, were observed as early as 1950.

The remarkable associations with unipolar magnetic regions indicated in Figs. 3 and 4 lead to the tentative suggestion that these UM regions are the source or starting point for the development of a large-scale phenomenon within the solar system; this phenomenon being capable of producing both the observed changes in cosmic-ray intensity and the recurring geomagnetic storms. From this point of view, the UM regions would correspond to the hypothetical and long-sought-for "M" regions invoked by Bartels and others to explain the recurring geomagnetic storms. In the following section we shall consider briefly the arguments for, and the difficulties with this hypothesis.

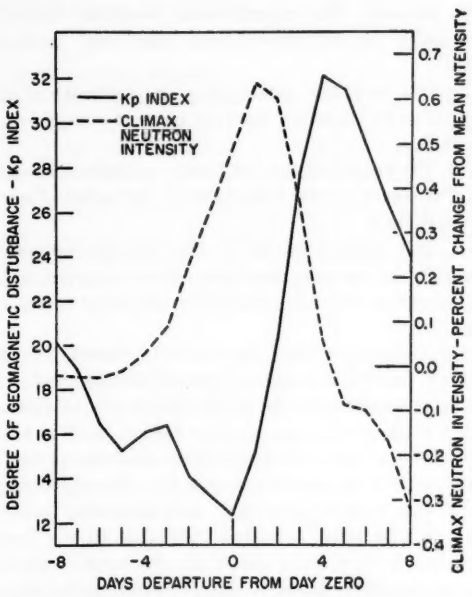

FIG. 4. The index K_p, representing the logarithm of amplitude in worldwide geomagnetic disturbances is shown for 7 consecutive rotations of the solar UM region with the times of central meridian passage designated as day "0."

VI. CONCLUSIONS

First, a word of caution: we wish to emphasize that additional observations over a long time interval will be required before any associations with the UM regions can be shown to be unique. For example, we have not demonstrated that UM type regions exist for every 27-day recurring cosmic-ray intensity maximum. For the present, therefore, we proceed on the tentative assumption that the relationships in Figs. 3 and 4 hold in general and inquire into the physical meaning of these relations.

We start with the association of the 27-day changes of primary cosmic-ray intensity and the solar UM regions. There are two ways in which the primary intensity could be changed:

1. There may be a modulation mechanism which either changes the momentum distribution of the pre-existent primary particle distribution (i.e., electromagnetic field acceleration) or changes the fraction of particles which reach the earth (i.e., a scattering of particles by large gas clouds or turbulent magnetic fields).

2. An injection and acceleration of new particles could conceivably take place in the region of the unipolar field; for particles of very much lower energy than cosmic rays a mechanism has been suggested recently.[2]

At present, the experimental evidence favors a modulation of the pre-existent cosmic-ray intensity, since:

(a) The radiation undergoing the intensity change appears to be isotropic, even for particle energies up to 20–40 Bev.

(b) The amplitude of the 27-day variations in earlier years involved a large fraction of the total observed intensity, and

(c) The general shape of the number-momentum spectrum for primary particles remains approximately unchanged as the cosmic-radiation intensity varies with time.

If the aforementioned conclusion is correct, then it is unlikely that the influence of the modulating mechanism could be restricted to the small volume of space located in the vicinity of a special solar region, such as a UM region, since the solid angle subtended—even by the entire sun—is too small to account for the magnitude of the 27-day variations as they were measured in earlier years of high solar activity. This leads to the further assumption that there exists an extensive, long-lived volume in interplanetary space extending far beyond the earth's orbit with its origin in the UM region. A stream of neutral ions, coronal streamers or outgoing turbulent magnetic fields might fill such a volume in space so as to provide the modulating mechanism for changing the primary particle intensity observed at the earth and subsequently induce severe disturbances in the earth's external magnetic field. Since the material or fields leaving the sun probably require 1–2 days to reach the earth, the relationships of the three phenomena in Figs. 3 and 4 are consistent with these general views.

In the past, special forms of neutral ion beams have been proposed by Chapman and Ferraro, Alfvèn and others to account for the magnetic storms. A more recent proposal by Morrison[7] assumes turbulent magnetic fields in the form of an outgoing "beam" which acts as a scatterer for cosmic-ray particles and, therefore, temporarily reduces the primary cosmic-ray intensity within the beam. However, detailed attempts to work out any of these mechanisms have so far not been satisfactory.

Most of our questions remain unanswered. The magnetic lines of force from the observed "unipolar" region presumably return somewhere on the sun. It is not yet clear whether the returning lines of force are distributed over a very large portion of the solar surface or whether there is a diffuse, related region remote from the observed "unipolar" region since we measure only the field component along the line of sight. The field distribution, the fluctuations in field intensity, and the decay time-constant of this kind of solar region will require study.

So-called "M" region phenomena are more pronounced in the declining years of the solar magnetic cycle, and it is unfortunate that these observations only begin near the time of solar minimum. There may be great difficulty in detecting these low-intensity, large-area magnetic field regions during the rapid rise in solar activity, even if they occur in this part of the magnetic cycle.

VII. ACKNOWLEDGMENTS

We wish to express our thanks to Dr. R. P. Kane, Mr. James Ayers, and Mr. Seymour Sudman for the preparation of the cosmic-ray neutron data.

[7] P. Morrison, Proceedings of Duke University Cosmic Rav Conferences, V-24, 1954 (unpublished).

$\Lambda^0-\theta^0$ Production in π^--P Collisions at 1 Bev

W. D. WALKER
Department of Physics, University of Wisconsin, Madison, Wisconsin
(Received February 14, 1955)

Two examples of $\Lambda^0-\theta^0$ production have been found in the collision of 1.0-Bev π^- mesons with protons. Data on these two cases are given. The two cases are qualitatively similar, yet there are quantitative differences in terms of the angles of production of the θ^0 and Λ^0 particles. One case is internally consistent with the production of a Λ^0 and θ^0 directly. The other case, in which the Λ^0 and θ^0 particles seem slightly noncoplanar with the incoming π^- meson, is not internally consistent with the direct production of a Λ^0 and θ^0. It is likely that either the θ^0 or the Λ^0 or both θ^0 and Λ^0 are the products of decay of heavier parents. It is also possible that a light particle (γ or ν) may be produced simultaneously with the θ^0 and Λ^0. If one supposes that the Λ^0 is the product of decay of a heavier parent then the Q of such a parent, were it to decay into a proton and π^- meson, is calculated to be 117 ± 30 Mev. This Q value is close to that of the charged hyperons. A short-lived neutral hyperon of this mass has been predicted by Gell-Mann.

IN the last two years a considerable advance has been made in the understanding of the mechanism for the production of hyperons and θ particles. This illumination has been largely due to the work of the Brookhaven cloud-chamber group with their hydrogen diffusion chamber.[1] They have found 3 cases in which Λ^0 particles have been produced in π^--P collisions at 1.4 Bev. In one of these cases a particle which could be a θ^0 is also observed to decay. The only anomalous feature about these events was that the mass deduced by energy and momentum conservation for the K^0 particle seemed to be higher than the mass of the θ^0 particle as measured by Thompson and his collaborators.[2] After these events were found at Brookhaven, Thompson *et al.*[3] found an event in which a Λ^0 and θ^0 particle were produced in what seemed to be a π^--P collision of about 1.5 Bev. In this case both the θ^0 and Λ^0 were well identified. The present note deals with two new examples of $\theta^0-\Lambda^0$ production in π^--P collisions. It is possible that the Λ^0 is the product of decay of a heavier hyperon in one of the examples. The Σ^0 particle postulated by Gell-Mann and Pais fits the data very well.[4,5] These examples were found in pictures taken at Brookhaven with the same hydrogen diffusion chamber used previously. The author is much indebted to the Brookhaven cloud-chamber group for taking these pictures for him with their apparatus.

The nominal energy of the π^- beam in this experiment is 1.11-Bev total energy. This energy has been checked by finding elastic π^--P scatterings in which the energy of the proton is low and readily measurable. The primary energy is then deduced from the energy of the proton. In this way the spurious effects due to possible turbulence and optical distortion in the system are minimized. In nine cases measured this way the momenta of the beam particles are close to the nominal value.[6]

The two examples are shown in Figs. 1 and 2. The further V particle decays near the edge of the chamber after going about 6 cm from the point at which the π^- meson vanishes. Both of the tracks appear to have greater than minimum ionization even though the tracks would be expected to appear heavier because of their position in the chamber. In particular, the negative member of the pair must have ionization greater than minimum because the track is thicker than a minimum track. The momentum of this track can be roughly estimated and seems to be lower than 100 Mev/c. The track is probably due to a π^- meson. The V closer to the end of the π^- track decays into particles of nearly minimum ionization. The positive member of this pair is fairly flat in the chamber and the measured momentum of this particle is 153 ± 8 Mev/c. This particle must be a π meson or lighter. The negative particle runs into the bottom of the chamber and is short and distorted. These two V's are qualitatively consistent with being a Λ^0 and θ^0 respectively. The two particles are nearly coplanar with the incoming track. The tracks are in an unfortunate part of the chamber in that there is some optical distortion which produces some apparent noncoplanarity with the incident π^-. However, after correcting for the optical effects, there still remains a noncoplanarity of about 10° in azimuth, between the particles. The primary track is short but measurements indicate a momentum between 1.05 and 1.3 Bev/c.

The second event is very similar to the first one. There are two V particles decaying that are associated with the disappearance of a π^-. One of the V particles decays into two lightly ionizing particles, and the longer-lived one into two tracks with greater than minimum ionization. These two V particles also have properties consistent with those of the θ^0 and Λ^0 respectively. Unfortunately the θ^0-like particle travels only

[1] Fowler, Shutt, Thorndike, and Whittemore, Phys. Rev. **91**, 1287 (1953); and **93**, 861 (1954).
[2] Thompson, Buskirk, Etter, Karzmark, and Rediker, Phys. Rev. **90**, 1122 (1953).
[3] Thompson, Burwell, Huggett, and Karzmark, Phys. Rev. **95**, 1576 (1954).
[4] M. Gell-Mann, Phys. Rev. **92**, 833 (1953).
[5] M. Gell-Mann and A. Pais, Proceedings of the Glasgow conference.
[6] The values of the incoming momentum in Bev/c obtained in this fashion are as follows: 1.05 ± 0.04, 1.07 ± 0.06, 1.11 ± 0.08, 1.11 ± 0.02, 1.08 ± 0.05, 1.04 ± 0.05, 1.13 ± 0.10, 1.11 ± 0.06, 0.985 ± 0.05.

TABLE I. Experimental data on $\Lambda^0-\theta^0$ production, with the momenta and Q's deduced from momentum conservation.

Case	Momentum deduced from cons. of momentum P_θ Bev/c	P_Λ Bev/c	Direction of θ^0 and Λ^0 with respect to the direction of the π^- θ_Λ	θ_θ	Opening angles of the decay products with respect to the direction of the Λ^0 and θ^0 $\varphi_{P\Lambda}$	$\varphi_{\pi\Lambda}$	$\varphi_{+\theta}$	$\varphi_{-\theta}$	Q's deduced from momentum and opening angle Q_Λ in Mev	Q_θ in Mev
I	0.396±0.015	0.745∓0.010	11° ±1.5°	21°±2°	$6°_{-1°}{}^{+3°}$	64°±2°	$77°_{-3°}{}^{+5°}$	20°±3°	$37_{-5}{}^{+10}$	200±15
II	0.488±0.015	0.767∓0.010	22.5°±1°	37°±3°	6.5°±1°	66°±1°	27°±2°	49°±2°	43±5	195±20

2.5 mm before decaying, which makes accurate angle or coplanarity measurements difficult. The primary track in this case is somewhat longer than in the first case and the measured momenta is 1.10±0.04 Bev/c. Unfortunately, none of the momenta of the secondary particles are measurable.

The analysis of these two events is done as follows. The incoming π^- is assumed to have momentum 1.1 Bev/c. The reaction is assumed to have only two products. Then, from conservation of momentum, the momenta of the two products can be deduced. If one knows the momentum of the parent particle and the angles of its decay products relative to its line of flight, the Q of decay may be deduced if the identities of the decay products are assumed. Unfortunately the angle of the π^- meson from the first θ-like particle is not well determined because of distortion; however, in this case the momentum and angle of the π^+ meson are well determined so that the Q may be deduced.

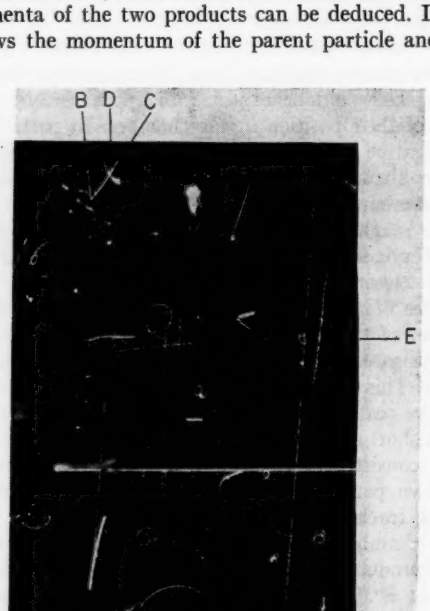

FIG. 1. $\Lambda^0-\theta^0$ production in a π^-P collision. Track A is the incoming π^- meson which disappears in flight. Direct measurements on this track give a momentum between 1.05 and 1.3 Bev/c. The adjacent π^- meson which crosses the chamber has a momentum of 1.14±0.10 Bev/c. Tracks B and C are the decay products of a Λ^0. Track C is short but momentum measurements give a momentum of less than 100 Mev/c and a negative sign. Tracks D and E are the π^- and π^+ mesons from the decay of the θ^0. Measurements on the π^+ meson give 153±8 Mev/c for the momentum.

The data concerning the angles of emission and the Q values deduced from the opening angles are given in Table I. In both cases it will be seen that the Q values of the V's agree fairly well with the values of 37±1 Mev[2,7] for the Λ^0 and 214 Mev for the θ^0.[2] Consequently it seems reasonable to conclude that the particles are the same as those found in cosmic radiation. There are, however, qualitative differences between the two events. In event I both the Λ^0 and θ^0 come out at a smaller angle than in the corresponding particles in event II. This would seem to indicate an energy much nearer threshold. As nearly as one can tell, however, the energies of the primaries are the same in both cases. In fact, if one assumes the accepted Q values for the Λ^0's and θ^0's, the momenta of these particles may be deduced, and then, by adding the longitudinal component of momenta of these particles, one finds an incoming momentum of 1.150±0.050 Bev/c for Case I and 1.090±0.050 Bev/c for Case II. In order to make these two cases consistent, the momentum of the incoming π^- in Case I would have to be lowered below 950 Mev/c.[8] On the basis of (1) the measurements on the primary and adjacent tracks in Case I, (2) the checks given by the momenta of the secondaries, and (3) the primary spectrum measurements, it seems very unlikely that the momentum of the incoming track was below 1 Bev/c.

Checks on the internal consistency of the two cases can be made in the following ways. First, the momentum of the Λ^0 particle is deduced from the opening angles of its products with respect to the line of flight by assuming the accepted Q value. Then, by using the conservation of momentum, the momentum of the

[7] Van Lint, Trilling, Leighton, and Anderson, Phys. Rev. 95, 295 (1954).

[8] One should probably expect that the momenta of the beam particles from the cosmotron will change slightly from pulse to pulse of the cosmotron. With this in mind the longest beam tracks in the picture in which event I occurred were measured. The results of the momentum measurements are, in Bev/c: 1.14±0.10, 1.07±0.05, 1.04±0.04, 1.07±0.02, 1.14±0.06. The errors are assigned on the basis of the consistency of the two views. Corrections for optical or chamber distortions are made on the basis of nearby no-field tracks.

TABLE II. Momenta of the Λ's and θ's as deduced from opening angles and the Q's of the θ's as deduced from momentum and energy of the Λ^0's. In this table the uncertainties in the momenta of the θ^0 and Λ^0 are deduced from the uncertainties in the opening angle measurements. The uncertainties in the P_Λ produce the uncertainties in the calculated values of P_θ and E_θ in the manner shown, i.e., a + change in P_Λ produces a − change in P_θ.

	Momenta and energy deduced from opening angles				Momentum and energy and Q of θ^0 deduced from momenta and energy of Λ^0		
	P_θ in Bev/c	E_θ in Bev	P_θ in Bev/c	E_θ in Bev	P_{θ^0} in Bev/c	E_θ in Bev/c	Q_θ in Mev
I	0.745±0.04	1.343±0.020	0.440±0.02	0.660±0.013	0.395∓0.035	0.707∓0.02	309±3
II	0.710±0.04	1.324±0.020	0.537±0.02	0.728±0.015	0.523∓0.025	0.726∓0.02	226±6
A[a]	0.610±0.04	1.273±0.02			0.988∓0.031	1.177∓0.02	362±10
B[a]	0.745±0.04	1.343±0.020			0.923∓0.03	1.107∓0.02	318±10

[a] Fowler *et al.*, reference 1. Note that in Case B a π^0 cannot have been produced in conjunction with a θ^0. In Case A a hypothetical π^0 meson would have to be closely correlated in angle and velocity with the θ^0. It seems unlikely that π^0's are produced in either case.

second particle is deduced. Finally, by using the conservation of energy, the energy, mass, and Q of the θ^0 are deduced. In Case II the Q of the θ^0, deduced in this way, is close to Thompson's value.[2] In Case I, however, the Q value deduced for the θ^0 is 309 Mev. This state of affairs is rather reminiscent of the cases found by the Brookhaven group in the 1.4-Bev π^- meson beam.[1] The results of these calculations together with those on the Brookhaven cases A and B of Fowler *et al.*[1] are given in Table II. Cases A and B are interesting in that the deduced mass of a possible K^0 in these cases is rather insensitive to the assumed beam energy and momentum of the Λ^0 particle.[9]

One might suppose that such a particle, which according to Table II seems to have a mass of 1200 to 1300 electron masses, would rapidly decay into a θ^0 particle and another neutral particle. If such a particle had a mass of more than 1240 electron masses, then it would be energetically impossible to produce them in conjunction with a Λ^0 particle in a $\pi^- - P$ collision at 1.1 Bev. If the mass of such a K^0 particle were in the neighborhood of 1200 electron masses and emitted a γ ray or neutrino then the average momentum of such a light particle in the laboratory would be about 140 Mev/c. This particle should be detectable by momentum balance alone, but it doesn't seem to be. It is also possible that both Λ^0 and θ^0 are decay products or that γ's or ν's are produced simultaneously with the θ^0 and Λ^0.

It seems slightly more reasonable to assume that it is the Λ^0 rather than the θ^0 that is the decay product. A particle which decays into a Λ^0 particle has been

TABLE III. Calculation of the Q value of the Λ^0 from the momenta and energy of the θ^0. In this table the uncertainties are calculated from the uncertainties in the measurement of P_{θ^0} from the opening angles. Because of the errors in the measurement of the angle of production of the θ^0 and uncertainties in the beam energy, the Q value in Case II is consistent with the accepted value for the Λ^0 particle.

Case	P_Λ in Bev/c	E_Λ in Bev	Q in Mev
I	0.707±0.017	1.39 ±0.013	117±3
II	0.745±0.010	1.322±0.015	14_{-5}^{+10}

[9] After the present manuscript was started, the author received a preprint from the Brookhaven group giving their most recent results. The author wishes to thank Dr. Fowler, Dr. Shutt, Dr. Thorndike, and Dr. Whittemore for the preprint. They have also reconsidered these first cases A and B and found them to be consistent with the production of a Σ^0 and θ^0. By using a calculation similar to the one given above, that is, assuming that momentum is balanced by a θ^0, one then finds an energy missing from the reaction of the order of 70 Mev. This missing energy is assumed to be associated with the decay of the Σ^0, and in this way the Q of the Σ^0 may be bracketed between 70 and 140 Mev.

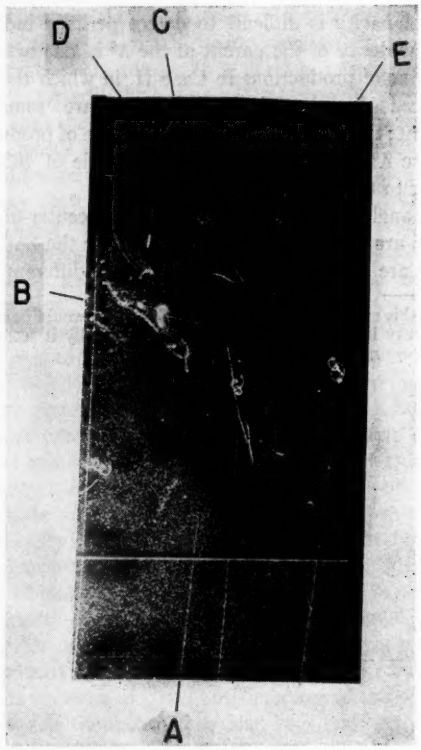

FIG. 2. The second example of $\Lambda^0 - \theta^0$ production in a $\pi^- - P$ collision. Track A is that of the primary pion. Its measured momentum is 1.10±0.04 Bev/c. It vanishes in flight and 2.5 mm from its point of disappearance the decay of a neutral meson into two lightly ionizing tracks, B and C, can be seen. A few centimeters further, a neutral hyperon may be seen to decay. The long track E, seems to have about two times minimum ionization as does track D. Track E was probably produced by a proton and D by the π^- meson from the Λ^0 decay.

proposed by Gell-Mann and Pais.[4,5] This is the neutral counterpart of the Σ^+ and Σ^-. To check this possibility, the measured momentum and energy of the θ^0 in the two cases are used to calculate mass and Q of the heavy hyperon (see Table III). The Q deduced in Case II seems consistent with that of the Λ^0; the Q deduced for Case I is 117 Mev,[10] which is the same as the Q observed for the charged Σ's. This number is, of course, subject to experimental uncertainty. The value of the Q is relatively insensitive to errors in the momentum of the θ^0. The change in Q for a 50-Mev change in the incoming energy is 30 Mev. The probable uncertainty in Q is the order of ± 30 Mev. The estimated unbalance of momentum for the products in Case I is (50_{-30}^{+30}) Mev/c and the energy that has vanished from the reaction is 47 ± 25 Mev. This result is consistent with the third particle being a single γ ray or neutrino.

The orientation of the planes of decay of the θ^0 and Λ^0 particles in Case I are rather similar to those observed by the Brookhaven group. The θ^0 decays perpendicular to the plane of production and the Λ^0 in the plane of production ($\Delta\varphi = 20°$). The fact that the noncoplanarity is difficult to detect perhaps indicates that the decay of the parent of the Λ^0 is also nearly in the plane of production. In Case II, in which the Λ^0 is produced directly, the orientations are somewhat different; the θ^0 decays nearly in the plane of production and the Λ^0 plane of decay is at an angle of 40° with respect to the plane of production.

The angles of production in the $\pi^- - P$ center-of-mass system are at 82° for the Λ^0 and 114° for the Σ^0. These angles are close to 90° which is rather different from the observations at 1.4 Bev in which the Λ^0's seem to go backward in the center-of-mass system. Observations of the momentum of isolated Λ^0's produced at 1 Bev seem at least to indicate that the backward direction is not preferred at this energy. It is interesting to note that the angular distribution of the Λ^0's at both energies closely parallels the distribution of the nucleons emerging from collisions in which π meson production takes place.[11]

The author wishes to express his gratitude to R. P. Shutt for his generosity in making this experiment possible. He is, of course, indebted to Dr. Fowler, Dr. Thorndike, Dr. Shutt, and Dr. Whittemore in instructing him in the use of their apparatus and taking the cloud chamber pictures. He wishes to thank Dr. G. B. Collins for making his stay at Brookhaven possible. The author has had the benefit of many interesting and informative conversations with his colleagues, Professor Fry, Professor Sachs, and Professor Takeda. The author also acknowledges some critical comments by Professor R. W. Thompson. This work was initiated while the author was at the University of Rochester and was supported by U. S. Atomic Energy Commission contract there. The work was greatly aided by a grant in aid from the Wisconsin Alumni Research Foundation. The author wishes to thank C. Kaufman, L. Watson, and J. S. Williams for their aid in scanning the pictures.

[10] In this case the Q of the Σ^0 means the Q it would have were it to decay into a π^- meson and proton. Actually it seems that $\Sigma^0 \to \Lambda^0 + \gamma$ or $\nu + 80$ Mev.

[11] Unpublished data of W. D. Walker. These examples were found among fifty $\pi^- - P$ collisions at 1.0 Bev. It is interesting to speculate further on possible parallels of meson production and hyperon production. If one uses the isotopic spin assignments of Gell-Mann (reference 4) then $\Lambda^0 + \theta^0$ can be produced only in an $I = \frac{1}{2}$ state and $\Sigma^0 + \theta^0$ in either $I = \frac{3}{2}$ or $\frac{1}{2}$. At 1 Bev the $\pi^- - P$ cross section is much larger in the $I = \frac{1}{2}$ than in the $I = \frac{3}{2}$ state and at 1.4 Bev the $\frac{1}{2}$ and $\frac{3}{2}$ state cross sections are about equal. If a real parallel between hyperon and meson production exists, one would expect relatively less Σ^0 than direct Λ^0 production at 1.0 Bev than at 1.4 Bev.

Measurement of the Čerenkov Radiation from Positive and Negative Pi Mesons*

J. R. WINCKLER, E. N. MITCHELL, K. A. ANDERSON, AND L. PETERSON
University of Minnesota, Minneapolis, Minnesota

(Received February 16, 1955)

Čerenkov light pulses from individual π^+ and π^- mesons from the Chicago cyclotron have been measured by using photomultipliers and Lucite radiators. An analysis of the pulse-height distributions has been made for comparing the velocity dependence of the radiation with the predictions of classical theory. Theory and experiment are in substantial agreement. However, saturation was found to set in at a somewhat lower energy than theory predicts for an end-window type tube (Dumont type 6363). A search was made for a difference in the photoeffect produced by positive and negative particles radiating Čerenkov light. The effect was found to be less than about 3 percent, the limit of resolution being determined by magnetic effects on photomultiplier gain.

I. INTRODUCTION

A THEORETICAL treatment of Čerenkov radiation proceeds by the straightforward application of Maxwell's equations to a charge moving in a dielectric. The problem, treated originally by Frank and Tamm,[1] is now found in textbooks on electromagnetic theory and quantum mechanics.[2] Experiments have shown very close agreement with the predictions of theory on the angle of emission of the radiation.[3] Classical theory also predicts the radiation intensity as a function of the refractive index and velocity of the moving charge. This aspect of the theory is more difficult to test experimentally because of the problems associated with quantitative light intensity measurements at very low level.

Interest in the present measurements arose because Čerenkov counters have proven to be very useful tools in research on the primary cosmic radiation. The advantages include:

(a) Preferential response to fast particles: Below a certain cut-off velocity (e.g., $\beta=0.75$ for water) no radiation is emitted. This property discriminates against secondary effects, such as evaporation stars, which cause trouble in ionization-type measurements of primary cosmic rays.

(b) Like ionization effects (but for a different reason) the radiation intensity is proportional to Z^2, the atomic charge of the particle or nucleus, provided β is constant. This effect has been used to study protons and α particles in the primary cosmic radiation.[4,5]

(c) The correlation of direction of emission of the radiation with the direction of motion of the charged particle enables one to sense the direction of motion of particles of light velocity, and is a useful tool in measurements of cosmic-ray albedo.[6-8]

(d) Over a certain range of velocities (e.g., for water $0.75<\beta<1$) Čerenkov counters may be used as velocity spectrometers. Because of the low light intensity and limitations of present phototubes, the velocity analysis can be made in a statistical sense only.[9]

(e) Identification of the mass of the charged particle may be made in certain energy regions by auxiliary knowledge of its range. If a particle passes through the detector without a detectable Čerenkov signal, an upper limit may be set on its velocity from the relation $\beta n=1$, where $n=$ the refractive index. If the range, or the minimum range through the equipment is known, one may then bracket, or at least place a lower limit on the mass value.[6]

(f) Čerenkov counters may easily be adapted to balloon or rocket equipment for very high altitude observations.

An excellent summary of many uses of Čerenkov counters is contained in a paper by Marshall.[10]

One object of the present investigation was to examine under controlled conditions several Čerenkov detectors used in high-altitude measurements. In one of these measurements[9] the detector was to be used as a velocity spectrometer. It was therefore important to investigate (d) above, i.e., to determine how closely the velocity response of the counter matched the dependence predicted by classical theory. Measurements of slow protons and alpha particles in another experiment[7] could be improved by a more exact knowledge of the behavior of the Čerenkov counter near velocity cutoff. Thirdly, it was desired to investigate the response of Čerenkov detectors to the polarity of charge of the moving particle. It is known that the photoelectric effect is sensitive to the angle of incidence of the electric radiation vector, because the amount of absorbed radiation depends on this angle. It was thought possible that the orientation of the electric

* This research supported in part by the joint program of the U. S. Atomic Energy Commission and the Office of Naval Research.

[1] I. Frank and I. Tamm, Compt. rend. **14**, 109 (1937).

[2] See, for example, L. I. Schiff, *Quantum Mechanics* (McGraw-Hill Book Company, Inc., New York, 1949), p. 261, and J. M. Jauch and K. M. Watson, Phys. Rev. **75**, 1249 (1949).

[3] R. L. Mather, Phys. Rev. **84**, 181 (1951).

[4] N. Horwitz, thesis, Minnesota, 1954 (unpublished); also Phys. Rev. **96**, 834(A) (1954). W. R. Weber, thesis, State University of Iowa, 1955 (unpublished).

[5] J. Linsley, Phys. Rev. **96**, 829(A) (1954).

[6] J. R. Winckler and K. Anderson, Phys. Rev. **93**, 596 (1954).

[7] K. A. Anderson, Phys. Rev. **96**, 829(A) (1954).

[8] L. Mezzetti and J. W. Keuffel, Phys. Rev. **95**, 858 (1954).

[9] E. N. Mitchell, Bull. Am. Phys. Soc. **30**, No. 1, 24 (1955).

[10] John Marshall, Ann. Revs. Nuclear Sci. **4**, 141-56 (1954).

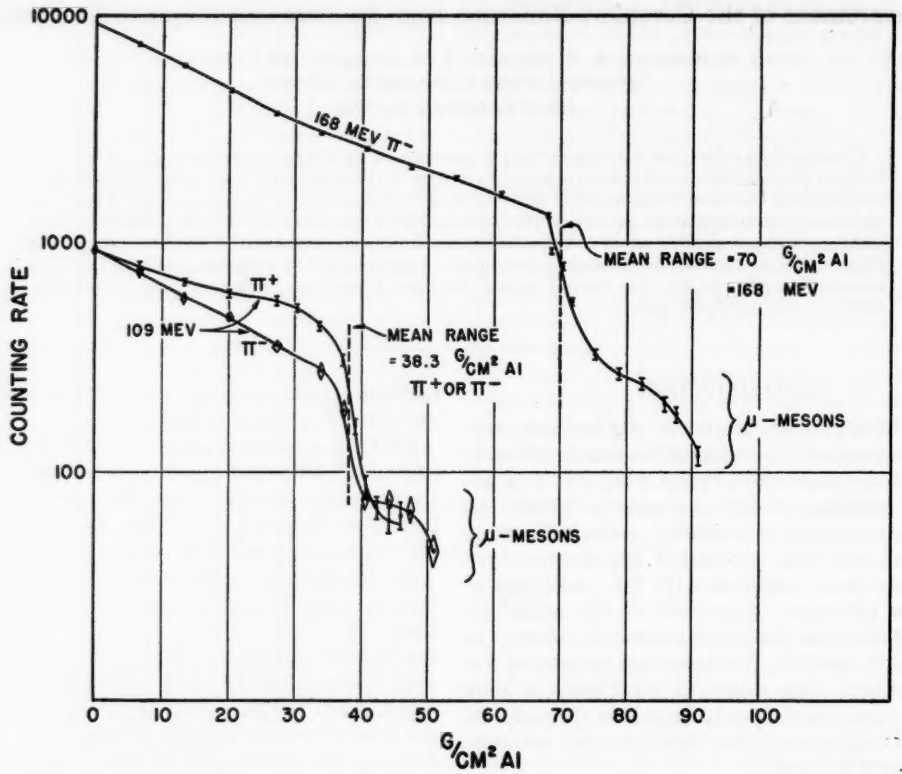

FIG. 1. Range curves for pions of two energies. These curves were taken by placing range blocks of aluminum between the twofold telescope and a larger area third scintillator in the beam after the analyzing magnet. The counting rate represents 3-folds per 10 000 (or 1000) 2-folds.

vector in the radiation from a positive moving charge might be 180° reversed, on the average, from that from a negative moving charge, and that the impulse given a photoelectron would, on the average, produce a different photoeffect for positive and negative particles of the same β. We owe the suggestion that such an effect might exist to Professor C. L. Critchfield.

II. EXPERIMENTAL METHOD

The source of particles consisted of the π-meson beams of the Chicago cyclotron. The π mesons had a sufficiently high upper velocity to cover a large part of the velocity-sensitive region for Lucite, and identical particles of both polarities were available. The momentum selection provided by the cyclotron fringing field and the slits in the radiation shield was improved by a 45° analyzing magnet. The beam was then defined and monitored by a pair of 1 in.$\times$1 in.$\times\frac{3}{8}$ in. plastic scintillation counters spaced 64 in. and 78 in. respectively from the analyzing magnet pole and in line with the maximum beam direction. These counters were connected through a twofold coincidence to a high-speed scaler, the resolving time being 3×10^{-7} sec. The Čerenkov detectors were placed directly after the second scintillator so that no beam particles missed the Čerenkov counters. The Čerenkov amplifier output was gated by the coincidence telescope and fed through an edge discriminator. A standard size pulse from the discriminator fed a second high-speed scaler, and the information was then extracted in the form of integral pulse-height curves from the Čerenkov counters. The number of pulses passing the discriminator was determined for various discrimination settings for a fixed number of telescope counts, usually 1000 or 10 000 for each beam energy. The beam energy was controlled by inserting copper or aluminum absorbers in the beam just ahead of the analyzing magnet, and adjusting the magnet current for maximum beam intensity for each absorber thickness. This method, which was adopted after numerous trials, produced apparently the smallest muon beam contamination at the counters.

The maximum beam energy was obtained from a range measurement. For this purpose the absorber slabs of aluminum or copper were placed just after the telescope, followed by a 3-in. diameter$\times\frac{3}{8}$-in. thick plastic scintillation counter. Loss of beam through scattering in the absorbers was considerable, but a sufficiently sharp edge was obtained to fix the beam energy with satisfactory accuracy. Range curves were taken for the three types of beams utilized, namely for

109 Mev π^+, 109 Mev π^-, and 168 Mev π^-, and are shown in Fig. 1. From a knowledge of the maximum beam energy and amount of absorber ahead of the analyzing magnet, the various beam energies were determined. One such intermediate beam energy was checked by a range measurement after the analyzing magnet with very satisfactory agreement.

III. RESULTS

A. Velocity Dependence

The response of a Čerenkov counter composed of a Dumont type 6363 3-in. diameter end-window photomultiplier optically sealed to a 3-in. diameter×2-in. thick Lucite block is shown in Fig. 2. The block was painted black on the end, and the cylindrical surface was covered with aluminum foil sealed optically to the block with immersion oil. The tube was surrounded with a magnet shield of $\frac{1}{16}$-in. nickel alloy and a $\frac{1}{4}$-in. soft steel shield open at the end facing the beam. The pion beam passed through the block normal to the photosurface. The curves of Fig. 2 have been corrected for a small zero error in the discriminator and normalized as a group. The run was made in the 168-Mev beam with absorbers of copper to produce energies at the Čerenkov counter as indicated. The main qualitative features of the curves are as follows:

(1) The appearance is similar to that of a set of integral Poisson distributions with progressively decreasing average value of the parameter n as energy is decreased.

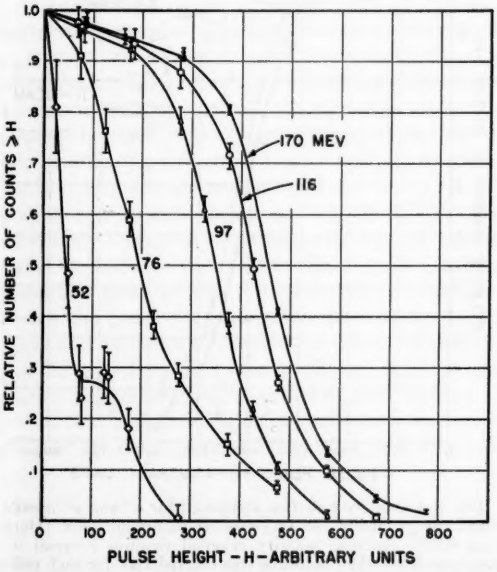

FIG. 2. Integral bias curves for end-window Čerenkov counter. Dumont 3-in. type 6363 photomultiplier. The curves represent number of Čerenkov pulses $>H$ as a function of H, for a fixed number (10 000 or 1000) of twofold telescope counts representing particles incident on the Čerenkov counter.

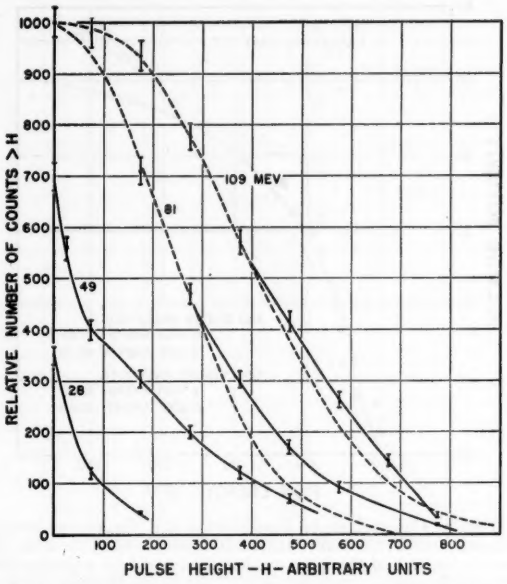

FIG. 3. Integral bias curves for side-window Čerenkov counter, RCA type 6372 multiplier. The dotted curves are Poisson distributions for a mean number of events per interval of 4 (109 Mev) and 2.4 (81 Mev). These Poisson curves have the same half-integral value as the experimental curves and indicate that the average number of photoelectrons per pulse from this photomultiplier lies between 1 and 4 for energies of Fig. 3.

(2) The counter has a remarkable energy sensitivity over a considerable range of energies.

(3) The response decreases to a low value near the Čerenkov cutoff for Lucite (48 Mev).

(4) The muon component is plainly evident on the lower energy curves as a plateau, corresponding to the residual muon group evident on the range curves of Fig. 1. A similar set of curves with the same detector was run on the 109-Mev π^- beam, and are closely similar in appearance.

Similar curves were also run using a side-window phototube, RCA type 6372. This tube was fitted with a 2 in.×2 in.×2½ in. thick block curved to fit the 2½ in. diameter cylindrical shell of the tube. The beam direction was normal to the axis of the tube, and the photocathode, and as in the case of the end-window tube, entered the central portion of the Lucite block. This tube was shielded with an Armco iron cylinder $\frac{7}{16}$ in. thick with a side tube surrounding the Lucite $\frac{3}{8}$ in. thick capped by a "mu-metal" plate 3/64 in. thick. The results for the 109-Mev π beam are shown in Fig. 3. A run was also made using the 168-Mev beam. The distributions are much broader with the side-window tube, probably due to less efficient light collection.

For comparison with theory one needs to know the mean number of photons, N, emitted per particle in the Lucite for each incident energy. If one assumes that the curves obey a Poisson distribution, then this number of photons is proportional to the Poisson mean,

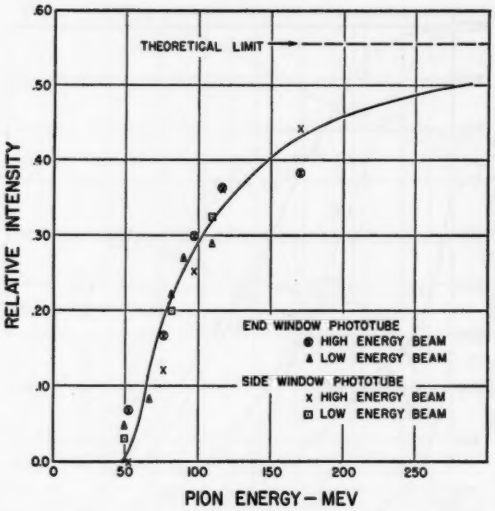

FIG. 4. Comparison of experimental and theoretical energy dependence of Čerenkov radiation from pions. The series of points for each of the four runs has been fitted by adjusting the relative intensity parameter for each run to the theoretical curve by least squares.

n, for each distribution. Approximate fits with integral Poisson distributions were attempted; e.g., in Fig. 3 the 109 and 81-Mev curves have been fitted with integral Poisson curves (dotted lines). The experimental and Poisson curves have the same half-integral values, although the fit is not so good for the larger pulse heights. It was found in all cases that a satisfactory result, with less labor, was obtained by using the half-integral value as a measure of N instead of the Poisson fitting.

The classical expression for the radiation intensity is

$$N=\frac{\Delta\omega\Delta x}{137c}\left(1-\frac{1}{\beta^2n^2}\right), \tag{1}$$

where $\Delta\omega$ is the frequency interval, Δx the path length in cm, n the refractive index and N the number of quanta produced. However, because of ionization loss the particle velocity decreases in the block. The number of quanta produced in the block of thickness t is actually, therefore

$$N=\frac{\Delta\omega}{137c}\int_{E_0}^{E(t)}\left(1-\frac{1}{\beta^2n^2}\right)f'(E)dE \tag{2}$$

where $f'(E)$ is the energy loss per cm in Lucite and β must be expressed in terms of the kinetic energy E for integration. E_0 is the incident energy. In Fig. 4 the results of the four runs are compared with Eq. (2).

The agreement is quite satisfactory with the exception of the highest-energy point for the end-window tube, which indicates the onset of a saturation at lower energy than predicted by theory. Near cut-off energy the points lie mostly above the curve. This may be due to the presence of the muon component, which as a velocity somewhat higher than the pion group for the same momentum as determined by the analyzing magnet. It is believed that these muons originate from the decay of the pions in flight and are difficult to suppress.

An experiment has been reported by Bianchi and Manducci,[11] using sea level cosmic rays, which indicated that the intensity of Čerenkov radiation increased at large energies more than predicted by classical theory. Since this experiment is outside the energy range of the present data, one cannot compare results directly. However, the question of showers when cosmic rays are used as the source of particles must be carefully considered and may affect the high-energy points.

In the foregoing discussion the details of the Čerenkov detector have not been specifically considered. One knows that because of the strong directional character of the Čerenkov radiation, the optics of a cylindrical radiator such as the Lucite blocks used here is complex. Another complicated situation exists at the photo-surface, where the photoeffect takes place under internal reflection, and the angle of incidence of the radiation varies with the β value of the charged particle. As is well known, such photomultipliers also exhibit large sensitivity variations over the sensitive surface. One should also note that the classical formula (1) is

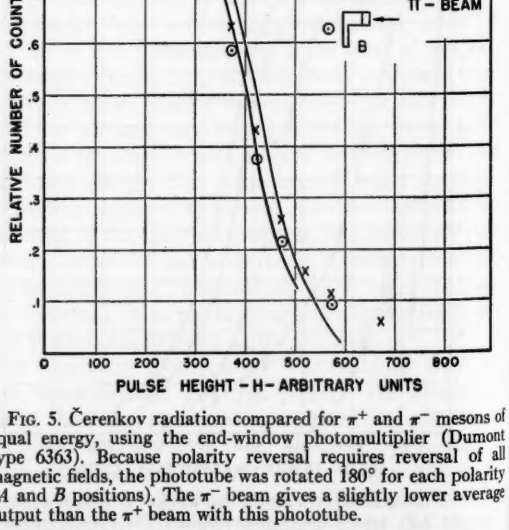

FIG. 5. Čerenkov radiation compared for π^+ and π^- mesons of equal energy, using the end-window photomultiplier (Dumont type 6363). Because polarity reversal requires reversal of all magnetic fields, the phototube was rotated 180° for each polarity (A and B positions). The π^- beam gives a slightly lower average output than the π^+ beam with this phototube.

[11] A. M. Bianchi and C. Manducci, Nuovo cimento 9, 861 (1952).

derived assuming constant refractive index. In usual practice the limited spectral response of phototubes makes the experiments compatible with this assumption, but this may not be true if absorption regions appear in the radiating material in the spectral region under investigation. It is our intention to defer discussion of details such as mentioned in this paragraph pending further laboratory measurements on Čerenkov counters.

B. Polarity Effects

The polarity sensitivity of the end-window Čerenkov detector was investigated by exposing it to positive and negative pions of the same energy. This necessitated reversing the magnetic fields of both the cyclotron itself and the analyzing magnet, so that the location of the apparatus could remain unchanged. Although the photomultiplier was well shielded magnetically, it was anticipated that a change in gain would result from this field change. This was investigated by rotating the phototube 180° about its axis, and running integral curves with pions of fixed polarity and constant energy (set at 109 Mev). Such curves are shown in Fig. 5 and designated *A* and *B*. It is observed that with a positive beam a rotation of the photomultiplier about its axis 180° from *A* to *B* produces a shift in the half-integral point *upward* of 20 parts in 415 or 4.8 percent. The shift on rotation with the negative beam is *downward* 10 parts in 400 or 2.5 percent. There is therefore a *downward* shift of the average, when going from positive to negative, of 13 parts or 3.0 percent. This is therefore an upper limit for the positive-negative Čerenkov effect for this tube. The upper limit may well be less than this, as reversing the cyclotron and analyzing magnets may not be entirely equivalent to rotating the tube 180° with fixed field, i.e., the gain of the photomultiplier may be shifted somewhat differently in the two cases. It should be noted from Fig. 1 that the energy of the positive and negative pion beams was the same as determined by a range measurement.

The polarity effect was also investigated with the side-window tube, and the results are shown in Fig. 6. A shift in response due to rotating the phototube is observed in this case also. However, the average shift between the positive and negative pion beams is now *positive* and amounts to 27 parts in 427 or 6.3 percent. Since the two different types of photomultipliers give opposite apparent polarity response, and since it is obvious that magnetic fields are affecting the photomultiplier gain, it seems likely that the observed response changes are all due to this cause, and that polarity effects, if any, are very small.

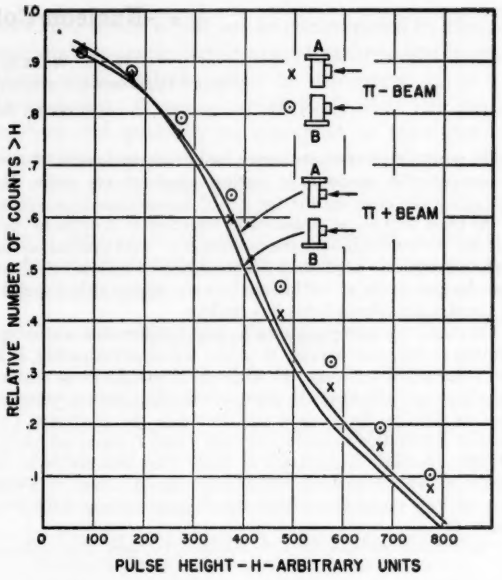

FIG. 6. Čerenkov radiation compared for π^+ and π^- mesons of actual energy using the side-window photomultiplier (RCA type 6372). The photomultiplier was rotated 180° for each polarity (compare with Fig. 5). In this case the π^- beam gives a larger response on the average.

IV. SUMMARY

In conclusion, it may be stated that the average pulse size from a photomultiplier coupled to a Lucite Čerenkov radiator varies with energy in a manner very close to that predicted theoretically. The experimental points from two different geometries indicate the correct cutoff energy. The muon beam contamination can account for certain observed differences between theory and experiment.

A search for a different Čerenkov response to positive and negative pions of the same energy showed this effect to be less than 3 percent, and smaller than magnetic effects on the photomultipliers due to reversing the cyclotron field.

The authors are indebted to Professor S. K. Allison for arranging for the use of the Chicago cyclotron, to Professor Herbert Anderson for his hospitality and advice in planning and scheduling the experiments, and to Dr. Maurice Glicksman for major assistance to the group in conducting the runs.

π^--Nucleon Collisions at 1.5 Bev*

W. D. WALKER† AND J. CRUSSARD‡
Physics Department, University of Rochester, Rochester, New York
(Received December 13, 1954)

The results of an extensive search for the interactions of 1.5-Bev π^- mesons with nucleons in nuclear emulsion are given. By comparing the cross section for π^--P interactions in emulsion to the cross sections as measured by counters, it is deduced that half the "π^--P" collisions are collision of π^- with protons on the edge of a nucleus. Arguments are presented to indicate that the basic features of the π^--P interactions are not seriously disguised by the struck nucleons being in a nucleus.

The elastic scattering seems to be largely diffraction scattering. Because of the large number of partial waves participating, it is not possible to interpret the differential elastic cross section unambiguously. However it seems certain that partial waves at least as high as the F wave participate in the reactions. The angular distribution indicates that the S and P waves are either strongly absorbed or scattered or both. The data seems to be consistent with a nucleon model consisting of a core of about 0.5×10^{-13} cm radius plus a field extending out to about 1.0×10^{-13} cm.

The inelastic collisions have the following features. The nucleons seem to go on the average into the backward hemisphere in the center-of-mass system after the collision. The more energetic of the two mesons usually goes into the forward hemisphere. The slower meson seems to be fairly closely correlated in angle with the nucleon. In the cases of π^0 production, the π^0 is the fast meson about one-half the time. The production of π^0 and π^+ in π^--P collisions seems to occur with about the same frequency.

Also collisions are found which seem to be π^--N collisions. The production of an additional π^0 seems to be the most common process in these collisions. The π^--N collisions seem to be consistent with meson production occurring by means of the production of an excited nucleon in a $T=\frac{3}{2}$ state which decays with the emission of a meson. The π^--P collisions do not seem to be consistent with such a process since the ratio of the number of π^+ to π^0 productions are not as predicted by theory. Also the Q of decay of such an excited nucleon seems to vary from 50–350 Mev. This would indicate that the excited state lives for such a short time that it may not be a very useful concept.

A short summary of the data on stars is also given.

I. INTRODUCTION

IN recent years, several experiments have been done to study the interactions of high-energy π mesons with nucleons. From these experiments it was clear that π mesons were produced in π-meson nuclei encounter.[1–4] Until recently it was not clear whether meson production resulted from an elastic π-nucleon collision with subsequent nucleon-nucleon collisions producing mesons, or whether the mesons were produced in the initial π-nucleon encounter. With the advent of the Brookhaven Cosmotron it was possible to study π-nucleon collisions under more controlled conditions.[5–7] This experiment was initiated by exposing stacks of stripped G-5 emulsion in the 1.5-Bev π^- beam at Brookhaven. This was the same beam used by Cool, Madansky, and Piccioni[8] in their counter measurements. The beam consists of about 95 percent π^- mesons of momentum about 1.6 Bev/c with a small contamination of μ's and electrons.[9]

II. EXPERIMENTAL TECHNIQUES

Stacks of 15 to 20, 4 inch by 6 inch, 400μ G-5 stripped emulsions were exposed to the π^- meson beam. The exposure times were chosen such that the plates received a flux of about $(1-2)\times10^4$ meson/cm^2. The only troublesome feature of the exposures is that a considerable slow electron background seems to build up in the plates in exposures of this length of time (15 hr). By 2 feet of lead shielding, these electrons can be reduced in intensity by a factor of about 3.[10]

The plates were marked by small x-ray dots,[11] and were stuck to glass and developed by the usual temperature variation method. Due to the considerable electron background it was found desirable to have a rather high minimum ionization in these plates. This requires a high temperature in the hot stage. Unfortunately high temperatures introduce distortion in the emulsion. In order to counteract this it is necessary to develop for longer times at lower temperatures. A suitable compromise was found to be a hot stage of about 19°–20°C for 40 minutes. The plates in the hot stage are wet for the first 20 minutes and dry for the last 20 minutes. Having the plates out of the hot developer for the last 20 minutes averts some of the overdevelopment on the surface of the plates.

The plates were fixed, washed and dried in the usual fashion. The 4 in.$\times$6 in. plates were then cut into four 2 in.$\times$3 in. plates.

The plates were aligned by means of the x-ray dots in the corners.[11] One procedure was to grind the plates on their edges until alignment is obtained. It was found to be easier to align the plates by sticking the plates to slightly larger pieces of glass by means of shellac. The dots are aligned on a microscope while the shellac is

* Supported in part by the U. S. Atomic Energy Commission.
† Now at Physics Department, University of Wisconsin, Madison 6, Wisconsin.
‡ Now at Le Ecole Polytechnique, Paris, France.
[1] W. G. Rosser and M. I. Swift, Phil. Mag. **42**, 856 (1951).
[2] W. O. Lock and G. Yekutieli, Phil. Mag. **43**, 231 (1952).
[3] W. F. Fry, Phys. Rev. **91**, 1576 (1953).
[4] N. M. Duller and W. D. Walker, Phys. Rev. **93**, 215 (1954).
[5] M. M. Blau and M. Caulton, Phys. Rev. **96**, 150 (1954).
[6] Crussard, Walker, and Koshiba, Phys. Rev. **94**, 736 (1954).
[7] Walker, Crussard, and Koshiba, Phys. Rev. **95**, 852 (1954).
[8] Cool, Madansky, and Piccioni, Phys. Rev. **93**, 249 (1954).
[9] We are indebted to Dr. Cool, Dr. Madansky, and Dr. Piccioni for this information.
[10] We are indebted to Dr. Hill and Dr. Salant for the use of their lead house in some of these exposures.
[11] Thanks are due to Dr. E. O. Salant and Mr. J. E. Smith for their aid in x-raying the plates.

still wet. The shellac unfortunately sometimes requires a long time to dry and care must be taken to keep the plates horizontal during this time.

III. CRITERIA FOR $\pi^- - P$ COLLISIONS

The main purpose of this experiment was to study π^-—proton collisions at 1.5 Bev. The problem was to find and isolate the $\pi^- - P$ collisions. It was soon determined that the only way to find $\pi^- - P$ collisions was by scanning along the beam tracks. An area survey will pick up mainly collisions with dark tracks emerging which constitute a minority of the $\pi^- - P$ collisions.

The criteria for singling out $\pi^- - P$ collisions are as follows:

(1) An even number of tracks must emerge from the interaction (since in a $\pi^- - P$ collisions there are an even number of charges involved).

(2) There can be at most one proton emerging from an interaction and it must emerge in the forward direction.

(3) A proton emerging from an interaction at an angle θ must have an energy equal to or less than that of a proton emerging at an angle θ from an elastic $\pi^- - P$ collision.

(4) There must be no indication of star particles at the vertex of the interaction.

In the course of scanning 934 meters of track a total of 2696 interactions were found: of these, according to the above criteria, 193 were hydrogenic interactions. From the $\pi^- - P$ cross sections at 1.5 Bev as measured by Cool, Madansky, and Piccioni[8] (34±3 mb) and the known composition of the emulsion, a mean free path for hydrogen interactions of 8.7 meters should be found instead of the mean free path of 4.84 meters observed. This indicates that approximately one-half of the collisions called $\pi^- - P$ are actually collisions with bound protons which are probably protons on the edge of a nucleus. The main purpose of this experiment becomes not to obtain an absolute cross section but to determine the relative probabilities of different interactions. It is felt that the occurrence of edge collisions, though occassionally producing a case of mistaken identity, is not such a large drawback to this mode of study of the interactions.

There are several consequences of accepting edge collisions:

(1) In an edge collision the target nucleon is in motion at the instant of impact, which means that if the momenta of the outgoing tracks are measured, a momentum unbalance up to 200 Mev/c can be found. Usually this is not a large effect since the incoming π^- meson has a momentum of 1600 Mev/c.

(2) A more troublesome feature of the edge collisions is that they may be followed by a secondary collision in which an edge neutron would also be struck by one of the charged reaction products. (Note, however, that if the reaction product striking the edge neutron is neutral also, the analysis is unaffected.) The events of this kind which would not be accompanied by charged evaporation tracks would appear as hydrogen interactions; their analysis would be inaccurate. If such a thing occurs, it seems rather likely that the parent nucleus will generally be disrupted to the extent of producing star particles. Besides this conviction there are other strong, independent arguments which tend to show that multiple collisions occur rather seldom in such a way as to appear as a hydrogen interaction. These arguments will be enumerated at appropriate places in the paper.

IV. ELASTIC COLLISIONS

Out of approximately 190 "$\pi^- - P$" collisions found, 43 appear to be elastic. The elastic collisions are usually the easiest to identify. For a given deflection of the π^-, the proton has a unique angle and energy. As about half of the collisions are on edge nucleons, the motion of the target nucleon will tend to destroy the coplanarity and the uniqueness of angles and energies. Also the beam particles are not quite monochromatic and no very good information exists on just what the spectrum of the beam tracks is. The angle and energy measurements on the secondary protons give a secondary check on the momenta of the primaries and the agreement is better between the observed and calculated angles and energies if the momentum of the primary π^- is assumed to be 1.6 Bev/c rather than perhaps 1.4 Bev/c.

In Fig. 1 is a picture of a typical elastic collision. The usual deflection of the π^- is 10°–15°, giving a proton at almost 90° with respect to the π^-. One of the checks readily made is that of coplanarity of the incoming and outgoing π^- and the proton. Figure 2 gives a histogram of $\Delta\phi$, the difference from 180° in azimuth between the two outgoing tracks, *versus* the number of cases. The histogram is not as sharp as one might hope and it appears likely that errors of the order of 5°–6° sometimes occur, giving an apparent lack of coplanarity. This is, in fact, not surprising since the deflections are small and distortions or errors in the shrinkage factor of the emulsion can give considerable errors in the azimuth.

To exhibit the effects of the motion of the target

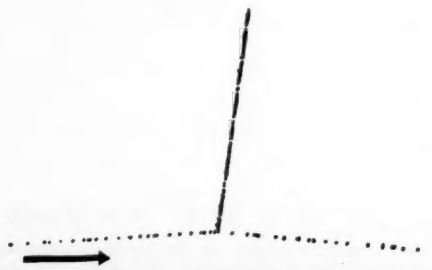

FIG. 1. In this case the π^- is elastically scattered through an angle of 8°. The proton has an energy of 27 Mev as determined by its range as compared with a calculated value of 25.4 Mev.

FIG. 2. A histogram showing the number of cases of apparently elastic $\pi^- - P$ collisions which show a lack of coplanarity $\Delta\phi$ between the incoming and the two outgoing tracks.

nucleon and the dispersion in the beam, for each elastic scattering the vector difference between the observed and calculated proton momentum is computed. The calculated momentum is deduced from the observed direction of the outgoing π^-.

The proton momentum measurements are usually based primarily on grain count and thus some of the momentum discrepancies can be due to errors in momentum measurements. When this momentum discrepancy is less than 200 Mev/c, the event is classified as elastic.

In Fig. 3, a histogram is given showing the number of cases which have a momentum discrepancy ΔP. The results are broken down to cases for which $\Delta\phi \leqslant 6°$ or $>6°$. The cases for which $\Delta\phi \leqslant 6°$ definitely show smaller momentum discrepancies.

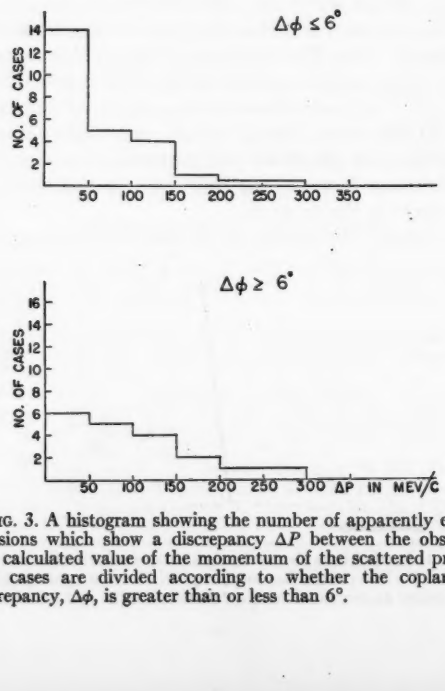

FIG. 3. A histogram showing the number of apparently elastic collisions which show a discrepancy ΔP between the observed and calculated value of the momentum of the scattered proton. The cases are divided according to whether the coplanarity discrepancy, $\Delta\phi$, is greater than or less than 6°.

The histograms in Fig. 3 are consistent with half the elastic collisions being on edge protons and half on free protons.

The elastic collisions give the best opportunity to isolate the effects of accepting edge collisions. There is only one case out of approximately 50 considered in which there is evidence that a secondary $P-N$ collision has occurred.

By using the total cross section obtained by Cool, Madansky, and Piccioni a value of 8 mb is deduced for the cross section for elastic scattering. It is possible that a few low-momentum transfers are suppressed by the exclusion principle in the case of the edge collisions.

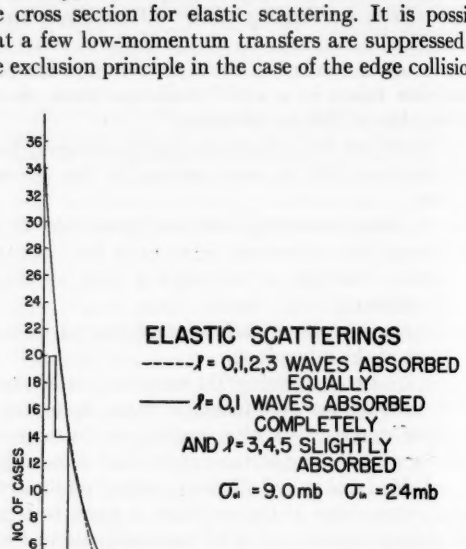
ELASTIC SCATTERINGS
----- l = 0,1,2,3 WAVES ABSORBED EQUALLY
—— l = 0,1 WAVES ABSORBED COMPLETELY AND l = 3,4,5 SLIGHTLY ABSORBED
σ = 9.0mb σ = 24mb
NO. OF CASES
COS θ

FIG. 4. The histogram is the experimentally observed angular distribution of elastically scattered π^-. The dashed curve gives the angular distribution expected from an opaque sphere of $R=1.0\times10^{-13}$ cm. The solid curve was obtained from an attempted partial wave analysis, in which waves of $l=0$ to 5 are included; the S and P waves are assumed to be nearly absorbed and the remaining waves mostly transmitted.

Thus it might be conceivable that the true elastic scattering cross section be as high as 10 mb. In any event the inelastic scattering cross section is a factor of 2 or 3 greater than the elastic scattering cross section. The inelastic processes absorb out the incoming beam and this must result in a diffraction pattern about the nucleon. If the incoming π^- beam felt the nucleon as an opaque sphere of radius R, then the cross section for diffraction scattering would be equal to the cross section for inelastic scattering. The ratio of inelastic to elastic scattering is, however, over two to one. This probably means that the outside edge of the nucleon is somewhat transparent to the high-energy π^- mesons.

Unfortunately it is not possible to fit the data in an unambiguous fashion because of the large number of partial waves involved. Figure 4 shows the experimentally determined angular distribution. The angular distribution expected from an opaque sphere of radius 1.0×10^{-13} cm is also given in Fig. 4. The pattern would be the same if all the partial waves up to $l=3$ were absorbed in the same proportion. In fact, the correct ratio of inelastic to elastic cross section can be obtained by having the amplitudes of all outgoing waves of $l\leqslant 3$ reduced by $\frac{1}{2}$. The correct total cross section and the correct ratio of elastic to inelastic scattering cross sections cannot be obtained by considering any smaller number of partial waves. Consequently it seems that inelastic processes occur for impact parameters as high as 1.0×10^{-13} cm and probably higher. The experimentally determined angular distribution seems to be somewhat higher at large angles than the diffraction pattern, although the statistics are very poor.

By also taking waves of $l=4$ and 5 into consideration, it is possible to find combinations of partial waves

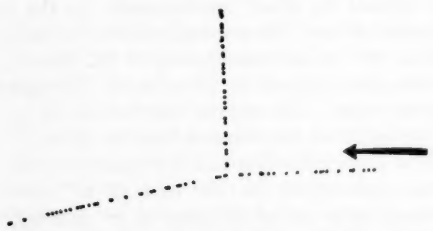

FIG. 5. An example of π^+ production. The track projected nearly at right angles is identifiable by grain count and scattering as a π meson. The forward-moving track represents a π which has momentum greater than 1 Bev/c from scattering measurements; it is calculated to have a momentum of 1.36 Bev/c.

which give a high-angle tail on the distribution. This can be done by assuming that the S and P waves are largely absorbed and that the waves of $l=2$ to 5 are weakly absorbed. Also one might suppose that the S and P waves have a real as well as an imaginary phase shift. An equally good fit to the data can be obtained in this way.

The theoretical distributions indicate that some of the small-angle scatterings may have been missed, which would not be surprising since low-momentum transfers may be suppressed by the Pauli principle. The Coulomb scattering cannot interfere destructively with the diffraction scattering at the small angles.

On the whole the data appear to be consistent with a model of the nucleon consisting of a core of strong interaction of radius about 0.5×10^{-13} cm plus a surrounding region of weaker interaction extending out to about 1.0×10^{-13} cm.

V. π-MESON PRODUCTION

The majority of the $\pi^- - P$ collisions observed appear to be inelastic. About one-third of these interactions

FIG. 6. In this rather favorable case of π^0 production, one of the γ rays from the decay of the π^0 can be seen to be converted only a few microns from the vertex of the interactions. The heavy, forward moving track is a proton of about 460 Mev/c momentum. The pair (which appears in the picture to be single track) has an energy of 87 Mev. By using the angle of emission of the π^0 deduced from momentum and energy balance, and the energy of the pair, the π^0 is calculated to have a rest energy of 110 Mev.

are patently inelastic as two tracks identified as π mesons are observed to emanate from the collisions. See Fig. 5 as an example. In the other cases, usually one π meson and one gray proton emerge from the interaction. These collisions usually appear qualitatively different from the elastic collisions in that the protons go more in the forward direction than in the elastic collisions. Compare Figs. 6 and 7 with Fig. 1 to see these differences.

The inelastic collisions are usually analyzed on the assumption that only one additional meson is produced in the collision. The possible reactions are

$$\pi^-+P\rightarrow P+\pi^-+\pi^0,$$
$$\pi^-+P\rightarrow N+\pi^-+\pi^+,$$
$$\pi^-+P\rightarrow N+\pi^0+\pi^0.$$

In case of the reaction $\pi^-+P\rightarrow\pi^-+\pi^0+P$, the proton is almost always readily identifiable and a good momentum estimate can usually be made from its ionization. By applying the conservation of momentum and energy with the knowledge of the direction of the two ionizing particles and the momentum of the proton, the momentum of the π^- and the momentum and direction of π^0 may be deduced.

A similar analysis can be made for the reaction $\pi^-+P\rightarrow\pi^-+\pi^++N$, providing the momentum of one of the π's is known.

The momentum determination in the case of the latter reaction is usually made by scattering measure-

FIG. 7. A case of π^0 production in which good momentum measurements can be made on both the proton and π^-. The forward track is a proton with a range in emulsion of 2.53 cm. The π^- has an ionization of about 1.5 times the incoming track. The mass of the neutral particle emitted is calculated to be about 200 Mev.

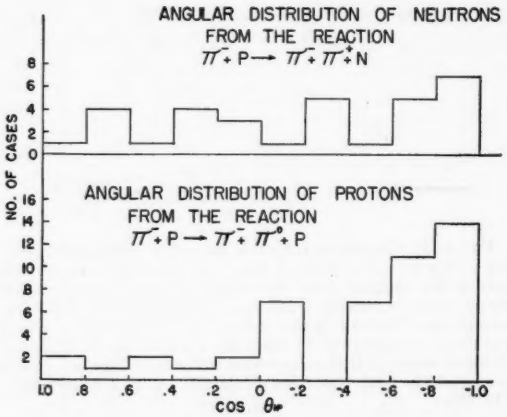
ANGULAR DISTRIBUTION OF NEUTRONS
FROM THE REACTION
$\pi^- + P \rightarrow \pi^- + \pi^+ + N$
NO. OF CASES
ANGULAR DISTRIBUTION OF PROTONS
FROM THE REACTION
$\pi^- + P \rightarrow \pi^- + \pi^0 + P$
COS θ_{π^-}

FIG. 8. Histograms showing the angular distributions of the protons and neutrons from $\pi^- - P$ collisions giving rise to the production of π^0 and π^- respectively. A negative cosine means the backward hemisphere in the center-of-mass system.

ments, which generally do not give a very accurate value of the momentum unless the track is exceptionally flat. Among the 43 cases of π^+ production, 35 could be thus analyzed and in 8 cases only the directions of the π's is known.

Possibility of Double π Production or Secondary Interactions

Sometimes in the case of π^0 production it is possible to check the momenta of both outgoing tracks. Such cases afford a check on the validity of the assumption made in the analysis that a single π^0 is produced in the collision. If ΔP and ΔE are the momentum and energy carried away by neutral particles, then if $c\Delta P \approx \Delta E$ probably a single π^0 is produced, if $c\Delta P < \Delta E$ then there are probably two π^0's produced, and if $c\Delta P > \Delta E$ one or more neutrons must be involved in the collision.

Out of 91 $\pi^- - P$ reactions in which a proton and a π^- emerge, 7 cases showed $c\Delta P > \Delta E$ for all possible values of the momentum of the outgoing π^-.[12] In 19 cases it was possible to measure momenta of both the outgoing π^- and proton. In 3 of the 19 cases the production of two π^0's was indicated. Fifteen of the cases were consistent with the production of a single π^0. Only one of these cases showed clearly that an extraneous neutron was involved in the collision.

In the course of the experiment, 4 cases of $\pi^- + P \rightarrow 2\pi^- + \pi^+ + P$ were found. From these data an estimate of the contamination of secondary interactions and multiple productions among the cases classified as single-meson production can be made. The percentage of events in which extraneous neutrons are involved is probably of the order of 10–15 percent. The fraction of cases in which multiple production occurs is probably of the order of 5 percent.[13] Further arguments on the validity of the single-production hypotheses are given below.

If secondary interactions occurred frequently, one would expect that the rejections would occur more frequently.

Also, if the apparent $\pi^- + P$ events often included cases where secondary collisions on neutrons had occurred, then one should also observe events with a secondary collision on a proton, which would appear as stars having one π^- and two rather fast protons (gray tracks). Only two such stars were observed.

Another statistical check on the validity of the analysis is derived from the comparison of the π^0 and π^+ production events. It is expected, although it is not necessarily true, that these reactions should be rather similar. The proton in the π^0 production is emitted on the average at an angle of 117° in the center-of-mass system with a momentum of 479 Mev/c; these numbers were derived by direct measurement. In the case of production of a π^+, the neutron is emitted at an average angle of 101° with a momentum of 502 Mev/c; these numbers were derived by the analysis. The agreement is rather close. The angular distribution of neutrons and protons from the two reactions are given in Fig. 8. There is some indication of a few more nucleons in the forward hemisphere in the case of π^+ production. However, in 8 out of 43 cases of π^+ production, no analysis could be made since both π's were fast and no measurements could be made. These were very likely cases in which the neutrons were moving backward in the center-of-mass system.

Another check can be obtained by comparing the

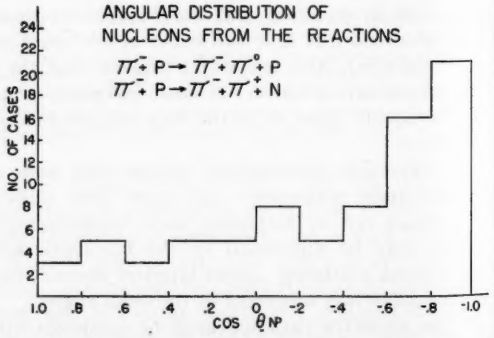
ANGULAR DISTRIBUTION OF
NUCLEONS FROM THE REACTIONS
$\pi^- + P \rightarrow \pi^- + \pi^0 + P$
$\pi^- + P \rightarrow \pi^- + \pi^+ + N$
NO. OF CASES
COS θ_{N^0}

FIG. 9. Histogram showing the angular distribution of the nucleons coming from π^-—proton reactions in which a single π^+ or π^0 meson is produced.

[12] This does not include several other "$\pi^- - P$" inelastic events in which a very slow proton is emitted. These slow protons are possible evaporation fragments, and in order to discriminate strongly against such events all cases in which a proton of energy less than 25 Mev is emitted were rejected. This criterion does not discriminate strongly against the true "$\pi^- - P$" interactions since only an extremely small amount of phase space is available for such a reaction.

[13] In 3 out of 18 cases multiple π^0 production was indicated. However, it should be pointed out that in most of the 18 cases the π^- was slow. It is much more likely that the π^- is slow if two π^0's are produced than if one π^0 is produced. Consequently the sample in the 19 cases is probably quite enriched in the fraction of double productions.

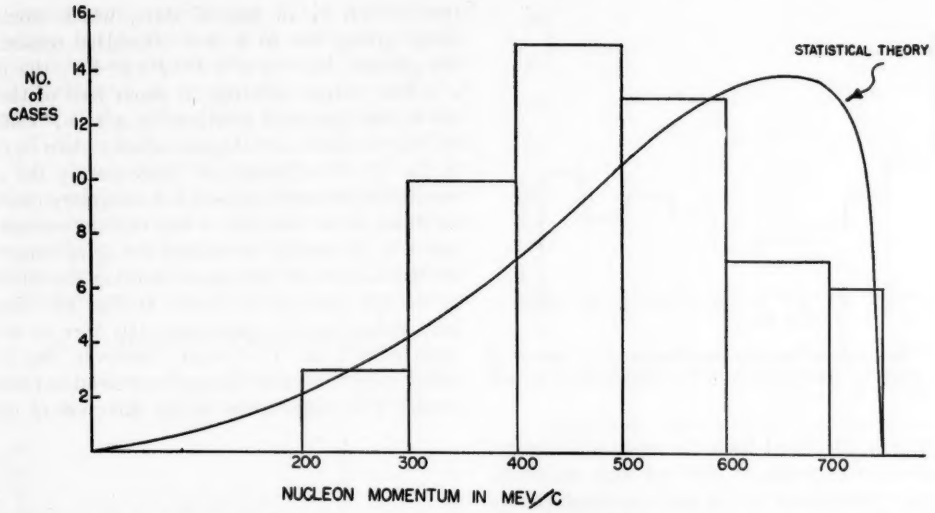

FIG. 10. The momentum distribution of the nucleons emerging from $\pi^- - P$ collisions in which a single π^+ or π^0 meson is produced is compared with the distribution expected from Fermi's statistical theory.

distribution of angles between the π's in these two reactions. In the case of π^+ production, the average angle between the π^+ and π^- in the center-of-mass system is 119° and in the case of the π^0 production, 115°. The first number is measured directly and the second the result of the analysis. The similarity between the two reactions indicates that the analysis of the interactions is valid in at least the majority of the cases. The general agreement supports the inference that the majority of these cases represent the production of a single additional meson.

Results

By using the criteria previously described, the hydrogen interactions have been classified as given below:

$\pi^-+P\rightarrow\pi^-+P$	43 cases	(1)
$\pi^-+P\rightarrow\pi^-+\pi^0+P$	46 cases	(2)
$\pi^-+P\rightarrow\pi^-+\pi^++N$	41 cases	(3)
$\pi^-+P\rightarrow$(a) π^0+N; (b) $2\pi^0+N$; (c) $\Lambda^0+\theta^0$	54 cases	(4)
$\pi^-+P\rightarrow 2\pi^0+\pi^-+P$	3 cases	(5)
$\pi^-+P\rightarrow\pi^-+\pi^++\pi^0+N$	1 case	(6)
$\pi^-+P\rightarrow 2\pi^-+\pi^++P$	3 cases	(7)

It is possible that some events classified as single meson production have an additional π^0 produced; however, the number of such cases is thought to be few.

The angular distribution of the nucleons from reactions 2 and 3 is given in Fig. 9. The momentum distribution of the nucleons is given in Fig. 10. The momentum distribution is compared with that calculated from Fermi's statistical theory.[14] The average nucleon momentum seems somewhat lower than that predicted by the statistical theory. The backward-peaked angular distribution of the nucleons, which seems to be very characteristic of these reactions, is not consistent with the statistical theory.

Figure 11 shows the angular distribution of the π^- and π^0 from reaction (2). Figures 12 and 13 give the angular distribution of the $\pi^-+\pi^0$ and $\pi^-+\pi^+$ from reactions (2) and (3) respectively. Both the π^- and π^0 and the nucleons show the presence of waves of $l\gtrsim 1$, as would be expected from the analysis of the scattering data.

The momentum distribution of all the mesons from reactions (2) and (3) are given in Fig. 14. The theo-

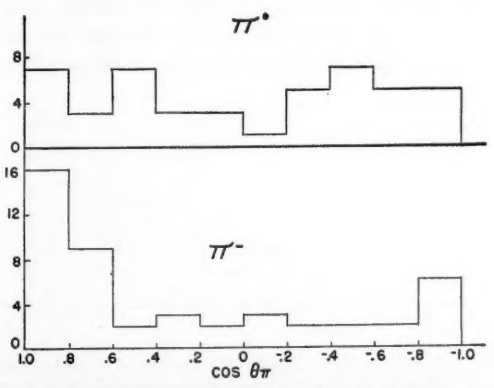

FIG. 11. Histogram showing the angular distributions of the π^- and the π^0 from $\pi^- - P$ collisions producing a single π^0.

$(\pi^-+P\rightarrow\pi^-+P+\pi^0.)$

[14] E. Fermi, Progr. Theoret. Phys. (Japan) 5, 570 (1950).

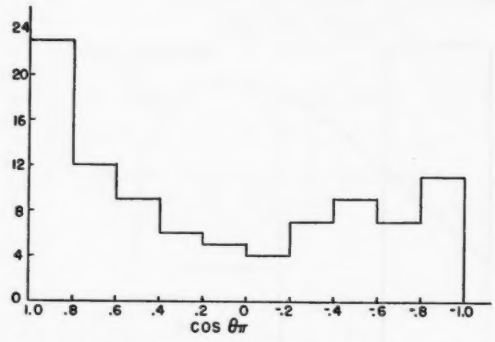

FIG. 12. The combined angular distribution of π^- and π^0 of Fig. 11 are given for comparison with the distribution of π^- and π^+ in Fig. 13.

retical curve is calculated from the statistical theory. There appear to be peaks at low and high momenta. The angular distribution of the low- and high-energy π's are given in Fig. 15, which shows that the low-energy π's generally follow the nucleons into the backward hemisphere. The angular distribution of the fast π's relative to the nucleons, slow π's relative the nucleons, and fast π's relative to the slow π's are given in Figs. 16, 17, and 18 respectively.

As expected, the direction of motion of the slow π's is correlated with the direction of the nucleons. The average center-of-mass angle between the nucleon and the slow π is about 90°, whereas the average angle between fast and slow π's is 120°, between the fast π and the nucleon is 150°.

The results found by the Brookhaven Cloud Chamber group for meson production in the collision of 1.4-Bev neutrons with protons seems indicative of meson production via a rapidly decaying excited nucleon. The results of Lindenbaum and Yuan[15] on the ratio of positive to negative π's produced in $P-P$ collisions indicate that the excited nucleon has isotopic spin $\frac{3}{2}$. From the excited-nucleon model, one would expect behavior somewhat similar to that observed. The fast π would be the degraded incoming π; its impact leaves

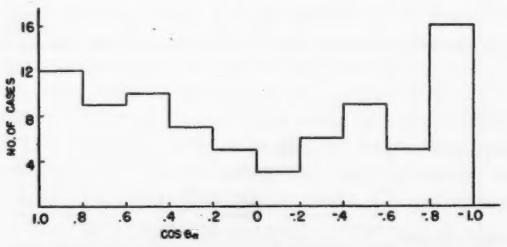

FIG. 13. The combined angular distributions of π^- and π^+ from π^-+P collisions in which a single π^+ is produced. ($\pi^-+P\rightarrow\pi^-+\pi^++N$.) Unfortunately it is possible to distinguish π^- and π^+ in only a few favorable cases in which one of the π's stop.

[15] S. J. Lindenbaum and L. C. L. Yuan, Phys. Rev. 95, 638(A) (1954).

the nucleon in an excited state, which would then decay giving rise to a slow secondary meson. From the present data on $\pi^-+P\rightarrow P+\pi^-+\pi^0$, the primary π suffers charge exchange in about half of the cases. An excited fragment produced in a π^-+P collision of 1.5 Bev would have a higher velocity than in the case of the $N-P$ collisions and consequently the angular correlation between nucleon and secondary pion should be closer, as is observed. From the momentum of the fast π it is possible to deduce the Q of decay of the excited nucleon. A histogram showing the distribution of the Q's observed is shown in Fig. 19. There is a faint indication of a peak near 150 Mev as would be expected for the $T=\frac{3}{2}$ state; however, the Q curve seems to be somewhat flat and to extend to rather high values. The distribution of the direction of decay of

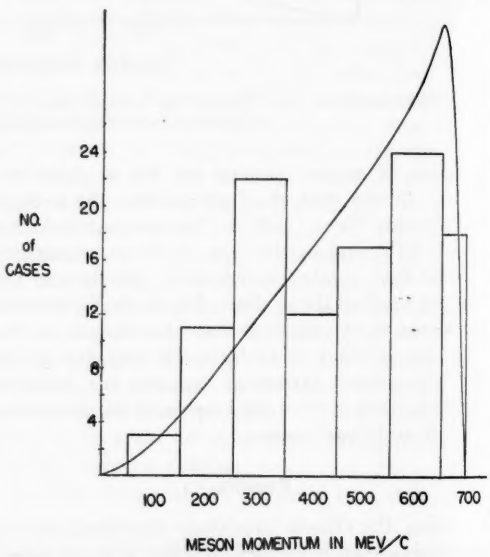

FIG. 14. The momentum distribution of the π's from π^-+P reactions in which either a single π^0 or π^+ is produced are compared with the distribution expected from Fermi's statistical theory.

the excited nucleon in its rest system is shown in Fig. 20. There seems to be an asymmetry in the direction of decay; the meson goes preferentially into the hemisphere away from the other meson. This result seems to be a rather strong argument against the utility of the excited-nucleon model. A better physical picture is perhaps more of a shakeoff process with a final-state interaction between the nucleon and the slow π meson. The slightly stronger asymmetry for the cases with Q's clustered around 150 Mev perhaps indicates a stronger interaction between the slow π and the nucleon for this Q-value range.

If one assumes that the meson production occurs via an excited nucleon which is in a state of isotopic spin $\frac{3}{2}$, then it is possible to predict the ratios of the reactions (2):(3):(4b)=1:2.05:0.59.

The experimental results seem to indicate ratios of more nearly 1:1:1, although it is really not possible to tell how much of reaction (4) is due to reaction (4b). On the other hand, if the excited nucleon were in a state such that the isotopic spin is $\frac{1}{2}$, the ratios should be (2):(3):(4b)=3.25:2.5:1. Thus it might be possible to get the correct ratios of reactions (2) and (3) by supposing a mixture of $T=\frac{3}{2}$ and $\frac{1}{2}$ excited states. The large number of reactions of type (4) remains a puzzle. It is necessary to suppose that reaction (4a) or (4c) is the predominant reaction of (4a,b,c) in order to get qualitative agreement with the excited-nucleon picture.

VI. π^--NEUTRON INTERACTIONS

In the course of scanning for the π^-—proton interactions, quite a few collisions were found which can

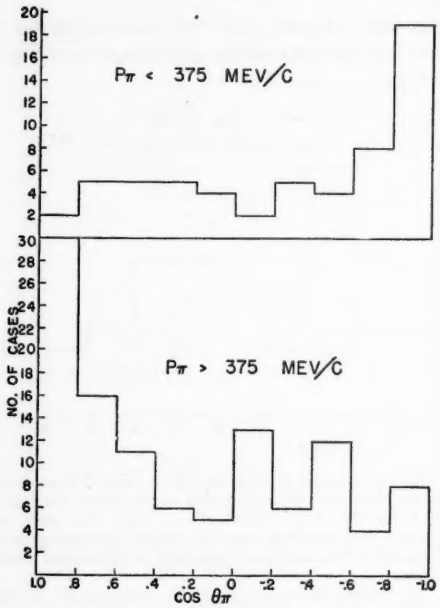

FIG. 15. The angular distributions of the low- and high-energy π's from inelastic $\pi^- - P$ collisions.

most readily be explained as π^-—neutron collisions. This is not surprising since it was deduced that about one-half the $\pi^- - P$ collisions were collisions with bound protons and a roughly comparable number of $\pi^- - N$ collisions should be expected.

The expected reactions are the following:

$$\pi^- + N \rightarrow N + \pi^- \quad (1')$$

$$\pi^- + N \rightarrow N + \pi^- + \pi^0 \quad (2')$$

$$\pi^- + N \rightarrow P + \pi^- + \pi^- \quad (3')$$

$$\pi^- + N \rightarrow N + \pi^- + \pi^0 + \pi^0 \quad (4')$$

$$\pi^- + N \rightarrow N + \pi^- + \pi^- + \pi^+ \quad (5')$$

$$\pi^- + N \rightarrow P + \pi^- + \pi^- + \pi^0. \quad (6')$$

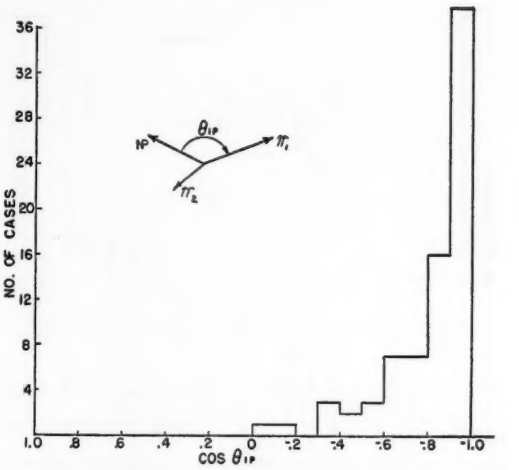

FIG. 16. Histogram of the angular distribution of the nucleons relative to the more energetic π's in the cases of the production of a single additional π meson in a $\pi^- - P$ collision.

It will be noticed that interactions (1'), (2'), and (4') will appear as a simple deflection of the π^-. There is another interaction which will have a similar appearance, namely the diffraction scattering by nuclei. Such a scattering will usually result in a rather small deflection as it is a coherent scattering by the nucleus as a whole. About one deflection of 1° to 10° was recorded per meter of track scanned. As will be seen later, the angular distribution of these deflections seems to be consistent with the distribution expected from the diffraction scatterings from the emulsion nuclei. On the other hand, deflections of greater than 10° occur with a mean free path of about 9 meters. These are collisions in which more than 300 Mev/c of momentum is transferred, and thus it seems very unlikely that these are diffraction scatterings from the nuclei. These deflections are accompanied by no evaporation tracks. Occasionally there is a small blob at the vertex which

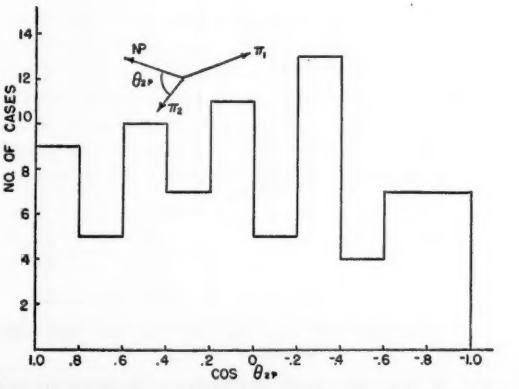

FIG. 17. Histogram showing the angular distribution of the slow π mesons relative to the nucleons in the $\pi^- - P$ collisions in which a single additional π meson is produced.

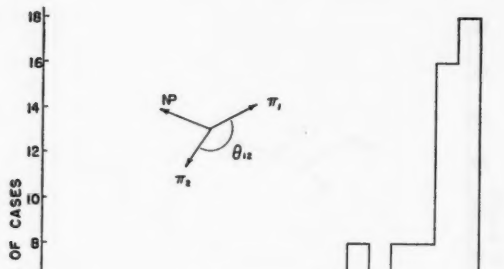

FIG. 18. The angular distribution of the slow π's relative to the fast π's. A comparison of the histograms of Figs. 16, 17, and 18 show that the fast π and the nucleon tend to go in opposite directions in the center-of-mass system, whereas the directions of the nucleon and the slow π in the center-of-mass system are more correlated.

could be the recoil of the remaining nucleus. Rather often there is a β particle of 1 or 2 Mev from the vertex which is presumably the β decay of the neutron-deficient residual nucleus. Less often, interactions are found with two light and one gray track emerging. The mean free path for all π^-+N interactions is 7.50 meters. This is slightly shorter than the value 9.6 meters calculated from the mean free path for π^-+P collisions under the assumptions: (1) equal π^-+N and π^-+P cross sections at 1.5 Bev;[8] (2) equal numbers of neutrons and protons in the peripheral regions of the nuclei.

The shorter mean free path could be a slight statistical fluctuation or might indicate a few more peripheral neutrons than protons. Also, some of these events could be the result of more complex nuclear events, but the analysis of the similarly selected π^-+P collisions show that this part is probably small.

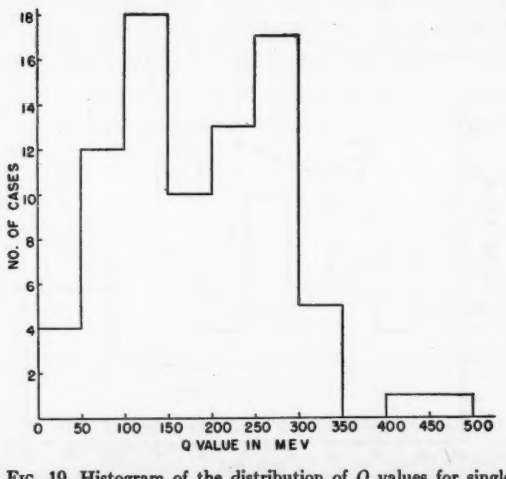

FIG. 19. Histogram of the distribution of Q values for single meson production in π^-+P collisions. The Q value is calculated from the momentum of the fast π meson by assuming that the slow π and nucleon are the decay products of the excited nucleon.

Results

The classification of the π^-+N interactions is given below.

$\pi^-+N\rightarrow N+\pi^-$		(1″)
$\pi^-+N\rightarrow N+\pi^-+\pi^0$	107 cases	(2″)
$\pi^-+N\rightarrow N+\pi^-+2\pi^0$		(3″)
$\pi^-+N\rightarrow P+\pi^-+\pi^-+(\pi^0)$	15 cases	(4″)
$\pi^-+N\rightarrow N+\pi^-+\pi^-+\pi^+$	2 cases	(5″)

In the first category, only deflections of greater than 10° were kept in order not to include nuclear diffraction scatterings.

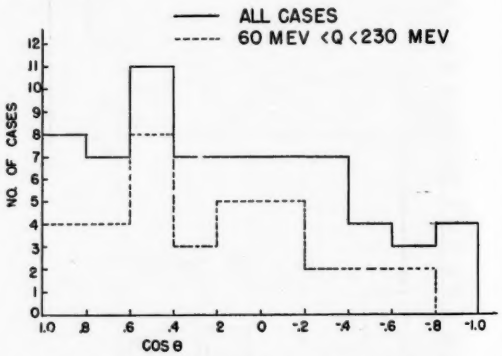

FIG. 20. The angular distribution of the direction of decay of the π meson from an assumed excited nucleon from the reactions $\pi^-+P\rightarrow P+\pi^-+\pi^0$ and $\pi^-+P\rightarrow N+\pi^-+\pi^+$. An angle of 0° means that the π resulting from the excited nucleon goes away from the other π. The angles are measured in the excited nucleon's rest system.

Figure 21 gives the angular distribution in the center-of-mass system of the π^- from the reactions (1″) and (2″). The same figure shows the angular distribution of the π^- from the corresponding reactions with protons, namely, $\pi^-+P\rightarrow\pi^-+P$ and $\pi^-+P\rightarrow\pi^-+\pi^0+P$.

The similarity of the two curves would probably indicate about the same admixture (1:1) of elastic and inelastic scattering as in the two π^-+P reactions. The forward-backward peaking also indicates that the inelastic processes are probably similar to the corresponding π^-+P reactions.

The reaction $\pi^-+N\rightarrow 2\pi^-+P$ is unique in that it is the only inelastic π-nucleon interaction yielding only ionizing particles. Since the measurement of three angles and one momentum actually overdetermine the reaction, these reactions give a check on the validity of the analysis. The check is considered satisfactory if the

momentum discrepancy is less than 200 Mev/c. The 21 events showing two π's and a proton of more than 25 Mev were classified as follows:

$\pi^-+N\rightarrow P+\pi^-+\pi^-$—10 cases.

$\pi^-+N\rightarrow P+\pi^-+\pi^-+\pi^0$—2 cases+3 more probable.

Probable stars—6.

The two cases of $\pi^-+N\rightarrow P+\pi^-+\pi^-+\pi^0$ are events where the energy of all three ionizing particles can be measured. In these cases the mass of the neutral particle can be determined and it agrees with the π^0 mass.

Figure 22 shows the angular distribution of the proton and of the π's in the center-of-mass system for the ten $P+2\pi^-$ cases. Figure 23 gives the momentum distribution of the π's. It may be seen that the distribution for these reactions are very similar to those for the inelastic π^-+P collisions.

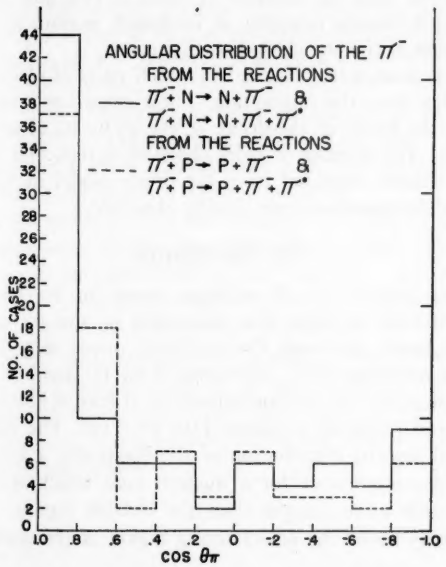

FIG. 21. Comparison of the angular distribution of the π^- scattered elastically and inelastically from protons and neutrons. The solid curve is for π^-+N reactions; the dashed curve for π^-+P reactions.

In the π^-+N collisions, the π—nucleon system is initially in a pure $T=\frac{3}{2}$ state. If the meson production is assumed to go via the excitation of a nucleon into a $T=\frac{3}{2}$ state, then the principle of charge independence predicts that the ratio of reaction (2′) to reaction (3′) should be about 5 to 1. This appears to be consistent with the experimental results.

VII. OTHER INTERACTIONS OF π^- MESONS

The collisions which seem to have been π^-—nucleon collisions occupy most of the attention of the investigation. The majority of the collisions with nuclei are extremely complex to analyze, but perhaps a few rudimentary conclusions can be drawn from a rather superficial analysis of the stars. The simplest cases to analyze are the diffraction scatterings of the π^-. In the course of scanning 292 meters of track, 250 scatterings between 1° and 10° were recorded.[16] The mean free path for this type of interaction is thus about 1.0 meter. Very few of these collisions which gave deflections less than 10° are probably π^-+P scatterings in which the nucleon does not escape from the parent nucleus. Only twelve π^-+P scatterings of $<10°$ were found in the scanning of 925 meters of track.

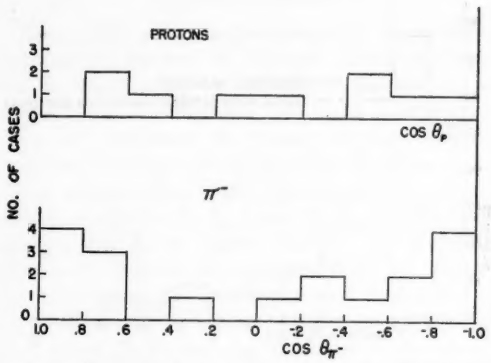

FIG. 22. The angular distributions of the π^- mesons and protons from the reaction: $\pi^-+P\rightarrow 2\pi^-+P$.

These small-angle deflections thus probably represent diffraction scattering by the whole nucleus. Figure 24 shows the number of scatterings observed in successive 1° intervals. The theoretical distribution is also given in Fig. 24 and has been normalized to give the same number of deflection in the 1° to 10° interval. The distribution has been calculated using the expression given by Fernbach, Serber, and Taylor[17] assuming $R=1.38A^{\frac{1}{3}}\times 10^{-13}$ cm for the emulsion constituents. The agreement is rather good and the small discrepancies for the angles of 7°–10° may be explained by a small contamination of π^-+N interactions.

The mean free path for star production was found to be 35 cm. Even after using the theoretical curve to correct for the scatterings missed between 0° and 1°, the ratio of diffraction cross section to inelastic cross section is still about 1:2.5. This indicates a transparency of the emulsion nuclei. This is consistent since the geometrical mean free path in emulsion is 27 cm

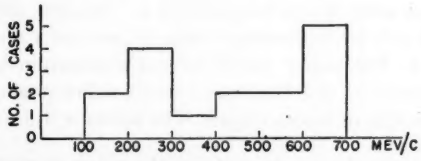

FIG. 23. The momentum distribution of the π^- mesons of Fig. 22.

[16] Deflections less than 1° were not efficiently found.
[17] Fernbach, Serber, and Taylor, Phys. Rev. 75, 1352 (1949).

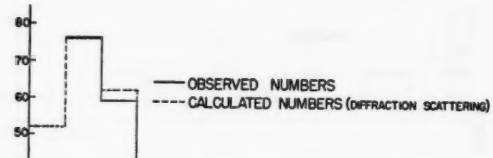

FIG. 24. The observed and theoretical angular distribution of π^- diffracted by emulsion nuclei. The ordinate gives the number of deflections in successive 1° intervals.

for $r_0=1.38\times10^{-13}$ cm and 30.5 cm for $r_0=1.30\times10^{-13}$ cm.[18] Since as many as one π^-—nuclear encounter in 15 seems to be a π^-—nucleon encounter, it is reasonable to interpret the mean free path, diffraction, and collision data as indicating a region of less dense nuclear matter on the edge of the nucleus.

A partial analysis of the stars has been made by recording the proportions of stars involving the emission of 0, 1, 2, or 3 charged mesons. (See Table I for the experimental results.) In this analysis all minimum-ionizing tracks are supposed to be mesons. It is kinematically possible but very unlikely to have a minimum-ionizing proton produced in these interactions. Among the gray prongs emerging from the stars some are identified as π's from their scattering. Their proportion being small, all unidentified gray prongs were assumed to be protons.

Only a part of the 2700 stars found have been analyzed. Those considered were divided into two groups.

(1) $N_H\geqslant6$ (N_H being the number of black and gray prongs, excluding π's): Stars made in heavy nuclei.

(2) $N_H\leqslant5$: Stars in light or heavy nuclei.

Column IV of Table I has been calculated by assuming that stars are the result of single π^--N or π^--P collisions which occur with equal probability and that all the π's produced escape.

It can be seen that the differences between π^-—nucleon and π^-—nucleus collisions are considerable. However, the differences seem to be at least partially understandable in terms of a simple model. Each nuclear event would start with a π^-—nucleon collision which will on the average result in one fast π and one slow π. The fast π would have a momentum in the neighborhood of 1 Bev/c and would either pass out of the nucleus or interact again. The slower π will usually have energy of 100–300 Mev and have a rather short mean free path in nuclear matter. This π will probably be absorbed in the parent nucleus. Bernardini *et al.*[19] and Blau and Caulton[5] have found, for π's of 100 Mev and 500 Mev respectively, that a π colliding with an emulsion nucleus has about a 65 percent chance of being absorbed with only star production.

The results of assuming that the secondary meson has only a 35 percent probability of escaping from the parent nucleus gives the percentages shown in column V of Table I. Although the agreement is not perfect, it is somewhat better in that the number of cases of zero charged mesons is increased. The agreement can be improved somewhat by including the affect of a possible additional collision of the fast meson in the struck nucleus. A rough estimate of such collisions indicates that the number of cases of two and three charged mesons emerging is increased, mainly at the expense of the one-charged meson cases.

Ten stars were observed in which pairs of electrons emerge from the interaction. These cases are presumably the result of the decay of the π^0 by its alternate mode. The number of pairs observed agrees well with the number expected from the crude model in which the slow secondaries are usually absorbed.

VIII. DISCUSSION

The elastic π^--P collisions seem to be largely describable as diffraction scattering of the incoming pion beam, although the outgoing waves may have some real phase shift. The range of interaction between the pion and the nucleon extends to at least 0.75×10^{-13} cm and probably to about 1.0×10^{-13} cm. The differential angular distribution of the elastically scattered π's shows evidence for a nucleon core which is considerable more opaque than the outside region. The strongly absorbing or scattering region of the nucleon

TABLE I. Tabulation of results on stars in emulsion.[a]

Number of minimum tracks I		Number of stars II	Percentage III	Percentages in π^- +nucleon collisions IV	Percentages according to the absorption model V
$N_H\leqslant5$	0	111	31	14	25
	1	190	54	67	69
	2	47	13	18	7
	3	7	2	2	1
$N_H\geqslant6$	0	185	54		
	1	136	40		
	2	21	6		
	3	0			

[a] Column IV gives the percentages calculated under the assumption that the incident pion collides with either a neutron or proton in the nucleus and that all the reaction products escape from the nucleus. Column V is calculated under the same assumptions except that 65 percent of the slow π's are assumed to be absorbed.

[18] By using the "tapered model" of the nucleon distribution as proposed recently by R. W. Williams and a π^--P, π^--N cross section of 34 mb, a mean free path in emulsion of 37 cm was deduced. We wish to thank Dr. Williams for sending a preprint of his work.

[19] Bernardini, Booth, and Lederman, Phys. Rev. **83**, 1075 (1951); **83**, 1277 (1951).

seems to extend out to distances of about 0.5×10^{-13} cm from the center of the nucleon. The average momentum change in the elastic collision is 580 Mev/c; however, occasional collisions show momentum changes of 1000 Mev/c.

In the collisions, usually one additional pion is produced. The inelastic collisions have the following characteristics. Usually the nucleon goes into the backward hemisphere and the more energetic of the two pions goes in the forward direction in the center-of-mass system. There seems to be a fairly strong correlation between the direction of the slow pion and the nucleon. If the fast pion is considered to be the primary pion, although some of the time it may have suffered charge exchange, then the average momentum change in these collisions is 900 Mev/c. The angular distributions seem rather indicative of meson production via the production of an excited nucleon which decays rapidly. The Q of the decay of such a hypothetical excited nucleon seems to have a considerable range of values and would be indicative of a lifetime of less than 10^{-23} second, so that such a model of meson production may not have any validity. The correlation in angle between the slow pion and the nucleon probably indicates an attraction between the slower π and the nucleon.

The cross section and angular distribution of the elastic cross section seem to show that some collisions occur in the core of the nucleon but also a considerable fraction occur on the edge of the nucleon. It is possible that the meson production occurs by two or more different mechanisms, one by means of an interaction with the core, another by an interaction between the incoming pion wave and the nucleon's field. The kinematics of the collisions does not seem to indicate the latter picture.

ACKNOWLEDGMENTS

The authors wish to acknowledge the aid in scanning and analysis by Mr. M. Koshiba. Obviously a great deal of scanning was involved and the authors were very fortunate to have the help of E. Awschalom, H. Fisher, P. Griesbach, B. Munir, and especially Mrs. V. Miller. Many people at Brookhaven National Laboratory aided in making the exposures; in particular we wish to thank Dr. R. L. Cool, Dr. R. D. Hill, Dr. O. Piccioni, Dr. E. O. Salant, and Dr. M. Widgoff for their help. One of the authors (W.D.W.) wishes to thank Professor K. M. Watson and Professor C. N. Yang for several discussions. Finally we wish to thank Dr. George B. Collins and Professor R. E. Marshak for their aid and encouragement in the initial phases of the experiment.

Note added in proof.—The work of the Brookhaven Cloud Chamber group on $\pi^- - P$ interactions at 1.4 Bev has recently been published [Eisberg, Fowler, Leo, Shephard, Shutt, Thorndike, Whittemore, Phys. Rev. **97**, 797 (1955)]. The results are very similar to those presented here. Their value of the elastic cross section is 10 mb as compared to 8 mb here. The differential elastic cross section at small angles seems to be lower by a factor 1.5 than the cloud chamber results, which is not surprising. The only other difference is in the angular distribution of the π^0's produced in $\pi^- - P$ collisions. Their results seem to indicate a stronger correlation between the direction of π^- and π^0 than has been found here. Also their proton distribution from this reaction is more strongly peaked in the backward direction than found in the plates. The difference could conceivably be produced by their mode of selection of events for analysis since 30 percent of their inelastic events are not classified.

Meson Pair Theory

ABRAHAM KLEIN* AND BRUCE H. MCCORMICK
Harvard University, Cambridge, Massachusetts

(Received January 12, 1955)

A comprehensive treatment of meson pair theory is presented from the point of view of the Møller scattering matrix and the S-matrix. First, the solutions of the classical field equations are used to exhibit the Heisenberg operator for the meson field in terms of the "in" operator of Yang and Feldman. The orthogonality and completeness of this set of one-particle scattering functions is demonstrated. Both the Møller matrix and the S-matrix are constructed explicitly as ordered operators by taking advantage of the fact that they generate known linear transformations. Schwinger's dynamical principle is used both for these purposes and to find the nucleon self-energy. Explicit proofs of the unitarity of the scattering matrices are given. The Møller matrix is used as generating function for all Fock-space amplitudes of the system. In this way are exhibited (a) the Green's function renormalization constant (Z_2 of Dyson), (b) the mesic proper field of the source, and (c) that matrix which describes scattering of a single meson. The latter, distinct from the classical one-particle scattering matrix, is obtained by solving a singular integral equation and shown to provide the same meson scattering amplitude. It is seen that only the one-meson amplitude of the one-meson state is singular on the energy shell, in agreement with the simple one-channel form of the S-matrix. An alternative treatment of the theory from the point of view of the equations of motion of the source is presented in an appendix.

I. INTRODUCTION

THE number of field theories whose consequences can be obtained without approximation is small indeed. The best known of these and a theory whose every aspect has been explored is the neutral scalar theory with fixed sources.[1] Recently, Lee[2] has studied a fixed source theory with linear coupling of a less trivial character, soluble because of a special selection rule. These theories have in common the fact that they are renormalizable, i.e., after renormalization their consequences remain finite in the limit of a point source.[3]

The only other class of Hamiltonians known to be soluble in closed form are the fixed source theories with quadratic coupling, of which the meson pair theory of Wentzel[4] may serve as prototype. As is well known, the diagonalization of the Hamiltonian exhibits the solution of this problem as the sum of two parts, consisting of the eigenfield of the nucleons and of the normal vibrations representing mesons scattered by these sources. Since the physical consequences of this theory thus are known completely, one may well call into question the *raison d'être* of the present work. The authors feel that there is sufficient justification for this paper in the presentation of aspects of the theory that have not hitherto been explored, as well as in a fresh derivation of known results.

In the course of this study, we have laid heavy emphasis upon the construction and properties of the Møller scattering matrix.[5] The elements of this matrix in the occupation number representation are identical with the Fock-space amplitudes of the system. Although all the physical consequences of the theory can be obtained from this procedure, the direct construction of the S-matrix is inordinately simpler because in this way one avoids consideration of nonenergy-conserving virtual processes. The former method has nonetheless been pursued for two reasons: Because of the insight it offers into renormalization questions, and because there has been some uncertainty in the recent literature[6] about its relationship to the S-matrix.

In Sec. II, we construct the Heisenberg operators in terms of the "in" and "out" operators of Yang and Feldman.[7] The linear transformation thus obtained is generated by the Møller scattering matrix. The linear relation between the "in" and "out" variables exhibits quite clearly the one-channel character of the S-matrix. Both the Møller matrix and the S-matrix are obtained as ordered operators (Secs. III, IV). The means used to construct the latter are easily adapted to a derivation of the self-energy of the sources (Sec. IV).

From Sec. V onward, we turn to a closer study of the Møller matrix. A detailed proof of the unitarity of the full matrix is presented in Sec. V, employing some properties of exponential operators. A formula for the most general Fock-space amplitude is then derived in Sec. VI. Its basic elements are seen to be the vacuum to vacuum amplitude, the matrix describing the proper mesic field of the source, and the one-meson to one-meson amplitude. A singular integral equation for the

* Society of Fellows.

[1] As representative works we mention: G. Wentzel, *Quantum Theory of Fields* (Interscience Publishers, Inc., New York, 1949), p. 47; L. Van Hove, Physica **18**, 145 (1950); S. Tomonaga, Progr. Theoret. Phys. (Japan) **2**, 6 (1947).

[2] T. D. Lee, Phys. Rev. **95**, 1329 (1954).

[3] In this connection, one should mention the linear problems of quantum electrodynamics. A recent definitive treatment of these problems is to be found in J. Schwinger, Phys. Rev. **91**, 728 (1953); **92**, 1283 (1953); **93**, 615 (1954); **94**, 1362 (1954). See also B. Zumino, Phys. Rev. **96**, 202 (1954) for more extensive references to previous literature.

[4] G. Wentzel, Helv. Phys. Acta **15**, 111 (1942). For a different theory belonging to the same class, see W. Sollfrey and G. Goertzel, Phys. Rev. **83**, 1038 (1951).

[5] C. Møller, Kgl. Danske Videnskab. Selskab Mat.-fys. Medd. **23**, No. 1 (1945); B. A. Lippman and J. Schwinger, Phys. Rev. **79**, 469 (1950).

[6] G. Morpurgo and B. F. Touschek, Nuovo cimento **10**, 1681 (1953).

[7] C. Yang and D. Feldman, Phys. Rev. **79**, 972 (1950).

latter is constructed and solved, and the same scattering amplitude as is provided by the S-matrix is thus obtained. Finally, it is shown anew that the theory contains no real processes other than meson scattering since only amplitudes which conserve the number of mesons are observed to be singular on the energy shell.

The theory under investigation strictly requires two renormalization constants: that for the self-energy and that for the Green's function of the source (the square of the vacuum to vacuum amplitude). If, in addition, a renormalized *coupling* constant is defined, using the prescription of Deser, Thirring, and Goldberger,[8] it is possible to pass to the limit of a point source and retain a finite value for the meson-scattering amplitude.

The Appendices contain: a discussion of the properties of the solutions of the classical field equations (A), a similar discussion for the case of sphere normalization (B), and a treatment of pair theory from the point of view of the method of Edwards and Peierls[9] (C).

II. SOLUTION OF THE FIELD EQUATIONS

We wish to discuss the development in time of the neutral meson field $\phi(x)$ described by the action integral operator ($\hbar=c=1$),

$$W_{12}=-\int_{\sigma_2}^{\sigma_1}(dx)\tfrac{1}{2}\{(\partial_\mu\phi)^2+\mu^2\phi^2\}$$
$$-\tfrac{1}{2}\lambda\int_{\sigma_2}^{\sigma_1}\int_{\sigma_2}^{\sigma_1}(dx)(dx')\phi(x)(x|\mathcal{U}|x')\phi(x'). \quad (1)$$

More particularly, we shall confine ourselves to the case of a time-independent separable interaction,

$$(x|\mathcal{U}|x')=\delta(x_0-x_0')(\mathbf{x}|V|\mathbf{x}')$$
$$=\delta(x_0-x_0')U(\mathbf{x})U^*(\mathbf{x}'), \quad (2)$$

describing the pair coupling to a single-nucleon source function $U(\mathbf{x})$. Although Eq. (2) will be imposed uniformly throughout the body of the paper, the methods to be studied can be extended immediately to the case of several sources.[10]

From Eq. (1) there follows the equation of motion for $\phi(x)$:

$$(\Box^2-\mu^2)\phi(x)=\lambda\int_{\sigma_2}^{\sigma_1}(dx')(x|\mathcal{U}|x')\phi(x'), \quad (3)$$

where the generalized potential is remembered to be symmetric, $(x|\mathcal{U}|x')=(x'|\mathcal{U}|x)$[$U(\mathbf{x})$ real].

For our purposes, the equivalent integral equation formulation is preferable. Utilizing the familiar retarded and advanced free-field Green's functions, $\mathcal{G}_{(R)}(x-x')$ and $\mathcal{G}_{(A)}(x-x')$, which satisfy the equation

$$(-\Box^2+\mu^2)\mathcal{G}_{(\ )}(x-x')=\delta(x-x'), \quad (4)$$

suppressing the three-space coordinates in favor of matrix notation, and limiting ourselves to the case where the surfaces σ_1, σ_2 recede into the remote future and past respectively,[11] we may replace Eq. (3) by the integral equations

$$\phi(t)=\phi_{-\infty}(t)-\lambda\int_{-\infty}^{\infty}dt'\mathcal{G}_{(R)}(t-t')UU^\dagger\phi(t'),$$
$$=\phi_{+\infty}(t)-\lambda\int_{-\infty}^{\infty}dt'\mathcal{G}_{(A)}(t-t')UU^\dagger\phi(t'). \quad (5)$$

Here $\phi_{-\infty}(t)$, $\phi_{+\infty}(t)$ are the solutions of the free-field equations

$$(-\Box^2+\mu^2)\phi_{\mp\infty}(x)=0, \quad (6)$$

which coincide with the Heisenberg field $\phi(x)$ in the remote past and future respectively.[7]

We proceed immediately to the formal solution of Eq. (5) inasmuch as the linear character of these integral equations allows us to bypass momentarily all considerations of commutation rules. Let us introduce the Fourier resolutions:

$$\phi(k_0)=\frac{1}{2\pi}\int_{-\infty}^{\infty}dt\phi(t)e^{ik_0t}, \quad (7)$$

with $\phi=\phi$, $\phi_{\pm\infty}$ and

$$\mathcal{G}(k_0)=\int_{-\infty}^{\infty}dt\mathcal{G}(t)e^{ik_0t}, \quad (8)$$

with $\mathcal{G}=\mathcal{G}_{(R)}$, $\mathcal{G}_{(A)}$. Employing the generic notation $\phi_{(\ )}$, $\mathcal{G}_{(\ )}$ for the appropriate pair of free-particle quantities, we then deduce the equation

$$\phi(k_0)=\phi_{(\ )}(k_0)-\lambda\mathcal{G}_{(\ )}(k_0)UU^\dagger\phi(k_0) \quad (9)$$

with solution

$$\phi(k_0)=\phi_{(\ )}(k_0)-\lambda\mathcal{G}_{(\ )}(k_0)UU^\dagger\phi_0(k_0)$$
$$\times[1+\lambda U^\dagger\mathcal{G}_{(\ )}(k_0)U]^{-1} \quad (10)$$
$$=\Theta_{(\ )}(k_0)\phi_{(\ )}(k_0),$$

where $\Theta_{(\ )}(k_0)$ has the form

$$\Theta_{(\ )}(k_0)=1-\lambda\mathcal{G}_{(\ )}(k_0)UU^\dagger[1+\lambda U^\dagger\mathcal{G}_{(\ )}(k_0)U]^{-1}. \quad (11)$$

More concretely, we introduce the Fourier decom-

[8] Deser, Thirring, and Goldberger, Phys. Rev. **94**, 711 (1954).
[9] S. F. Edwards and R. E. Peierls, Proc. Roy. Soc. (London) A224, 24 (1954). This is an extension of the approach of R. P. Feynman, Phys. Rev. **80**, 440 (1950).
[10] Imposing only the less restrictive conditions that $(\mathbf{x}|V|\mathbf{x}')$ be symmetric and separable, as would obtain in the pair theory of a static assembly of nucleons, we recognize that the problem is yet soluble in closed form.
[11] The subtleties associated with the limiting procedure will not concern us here, since they have been discussed adequately in the literature rcently. See, for example, W. Glaser and W. Zimmerman, Z. Physik **134**, 346 (1953); H. Kita, Progr. Theoret. Phys. (Japan) **10**, 231 (1953).

positions

$$\phi_{-\infty}(x)=(2\pi)^{-\frac{1}{2}}\int(dk)e^{ikx}\frac{a(\mathbf{k},k_0)}{(2\omega(\mathbf{k}))^{\frac{1}{2}}}\times\{\delta(k_0-\omega(\mathbf{k}))+\delta(k_0+\omega(\mathbf{k}))\},\quad(12)$$

$$\phi_{+\infty}(x)=(2\pi)^{-\frac{1}{2}}\int(dk)e^{ikx}\frac{b(\mathbf{k},k_0)}{(2\omega(\mathbf{k}))^{\frac{1}{2}}}\times\{\delta(k_0-\omega(\mathbf{k}))+\delta(k_0+\omega(\mathbf{k}))\},\quad(13)$$

as follows from the free-field character of $\phi_{\pm\infty}(x)$. Recognizing the decomposition of each field into its positive and negative frequency parts, we write (in momentum space)

$$\phi_{-\infty}{}^{(\pm)}(\mathbf{k},k_0)=a(\mathbf{k},k_0)(2\omega(\mathbf{k}))^{-\frac{1}{2}}\delta(k_0\mp\omega(\mathbf{k})),\quad(14)$$

$$\phi_{+\infty}{}^{(\pm)}(\mathbf{k},k_0)=b(\mathbf{k},k_0)(2\omega(\mathbf{k}))^{-\frac{1}{2}}\delta(k_0\mp\omega(\mathbf{k})).\quad(15)$$

The familiar representations

$$\mathcal{G}_{(R,A)}(x-x')=(2\pi)^{-4}\int(dk)e^{ik(x-x')}\times[\mathbf{k}^2+\mu^2-(k_0\pm i\epsilon)^2]^{-1},\quad(16)$$

which imply

$$(\mathbf{k}|\,\mathcal{G}_{(R,A)}(k_0)\,|\mathbf{k}')=\delta(\mathbf{k}-\mathbf{k}')[\omega^2(\mathbf{k})-(k_0\pm i\epsilon)^2]^{-1},\quad(17)$$

then aid us to evaluate alternative expressions for the positive and negative energy cases of Eq. (10):

$$\phi^{(+)}(\mathbf{k},k_0)=\int d\mathbf{k}'(\mathbf{k}|\,\Omega_{(+)}(2\omega)^{-\frac{1}{2}}\,|\mathbf{k}')\times\delta(k_0-\omega(\mathbf{k}'))a(\mathbf{k}',k_0)$$
$$=\int d\mathbf{k}'(\mathbf{k}|\,\Omega_{(-)}(2\omega)^{-\frac{1}{2}}\,|\mathbf{k}')\times\delta(k_0-\omega(\mathbf{k}'))b(\mathbf{k}',k_0),\quad(18)$$

$$\phi^{(-)}(\mathbf{k},k_0)=\int d\mathbf{k}'(\mathbf{k}|\,\Omega_{(-)}(2\omega)^{-\frac{1}{2}}\,|\mathbf{k}')\times\delta(k_0+\omega(\mathbf{k}'))a(\mathbf{k}',k_0)$$
$$=\int d\mathbf{k}'(\mathbf{k}|\,\Omega_{(+)}(2\omega)^{-\frac{1}{2}}\,|\mathbf{k}')\times\delta(k_0+\omega(\mathbf{k}'))b(\mathbf{k}',k_0),\quad(19)$$

where[12]

$$(\mathbf{k}|\,\Omega_{(\pm)}\,|\mathbf{k}')=\delta(\mathbf{k}-\mathbf{k}')+\frac{\lambda U(\mathbf{k})U^*(\mathbf{k}')}{[\mathbf{k}'^2\pm i\epsilon-\mathbf{k}^2]D_{(\pm)}(\mathbf{k}'^2)},\quad(20)$$

$$D_{(\pm)}(\mathbf{k}^2)=1+\lambda\int d\mathbf{k}'\,|\,U(\mathbf{k})'\,|^2[\mathbf{k}'^2-(\mathbf{k}^2\pm i\epsilon)]^{-1},\quad(21)$$

and $(\mathbf{k}|\omega|\mathbf{k}')=\delta(\mathbf{k}-\mathbf{k}')\omega(\mathbf{k})$. Notice that the second forms of Eqs. (18) and (19) follow from the first forms under the replacements $\epsilon\rightarrow-\epsilon$, $a\rightarrow b$ as is consistent with the replacement $\mathcal{G}_{(R)}\rightarrow\mathcal{G}_{(A)}$.

[12] The one-particle scattering matrices $\Omega_{(\pm)}$ have also been given by J. M. Blatt, Phys. Rev. 72, 466 (1947).

We remark next that the Heisenberg field $\phi(x)$ is real, as deduced from the real character of $\phi_{-\infty}(x)$, $\phi_{+\infty}(\mathbf{x})$. If

$$a(\mathbf{k})=a(\mathbf{k},\omega(\mathbf{k})),\quad b(\mathbf{k})=b(\mathbf{k},\omega(\mathbf{k}))\quad(22)$$

then the reality of $\phi_{\pm\infty}(x)$ is expressed by the relations

$$a(-\mathbf{k},-\omega(\mathbf{k}))=a(\mathbf{k},\omega(\mathbf{k}))^\dagger=a(\mathbf{k})^\dagger,$$
$$b(-\mathbf{k},-\omega(\mathbf{k}))=b(\mathbf{k},\omega(\mathbf{k}))^\dagger=b(\mathbf{k})^\dagger.\quad(23)$$

Similarly the reality of $\phi(x)$ hinges upon proving that

$$\phi^{(+)}(\mathbf{k},k_0)=\phi^{(-)}(-\mathbf{k},-k_0)^\dagger,\quad(k_0>0)\quad(24)$$

or by Eqs. (18)–(20), demonstrating that[13]

$$(-\mathbf{k}|\,\Omega_{(-)}|-\mathbf{k}')^*=(\mathbf{k}|\,\Omega_{(+)}|\mathbf{k}').\quad(25)$$

We deduce the identity in our immediate case by imposing the restriction that the single nucleon source distribution $U(\mathbf{x})$ be real,

$$U(-\mathbf{k})=U(\mathbf{k})^*.\quad(26)$$

With the concurrent observation that

$$D_{(+)}(\mathbf{k}^2)=D_{(-)}{}^*(\mathbf{k}^2),$$

and the structure of $\Omega_{(\pm)}$ given by Eq. (21), identity (25) follows.

The commutation structure of the variables $\phi(x)$ implies previous knowledge of that of the free-field variables $\phi_{\pm\infty}(x)$ which obey the well-known relations

$$[\phi_{(\,)}(x),\phi_{(\,)}(x')]=i\Delta(x'-x),\quad(27)$$

where $\Delta(x)=\mathcal{G}_{(A)}(x)-\mathcal{G}_{(R)}(x)$. The homogeneous propagation function $\Delta(x)$ can by Eq. (16) and its definition be written as

$$\Delta(x)=-i(2\pi)^{-3}\int(dk)e^{ikx}\delta(k^2+\mu^2)\epsilon(k).\quad(28)$$

Substituting field decompositions (12) and (13) for $\phi_{-\infty}(x)$, $\phi_{+\infty}(x)$, respectively, utilizing Eqs. (22), (23), and the above representation of $\Delta(x)$, we translate commutation relations (27) into the language

$$[a(\mathbf{k}),a^\dagger(\mathbf{k}')]=\delta(\mathbf{k}-\mathbf{k}'),$$
$$[a(\mathbf{k}),a(\mathbf{k}')]=[a^\dagger(\mathbf{k}),a^\dagger(\mathbf{k}')]=0,\quad(29)$$

and identical equations with a replaced by b.

As a check of the consistency of the Heisenberg field $\phi(x)$ prescribed by Eqs. (18)–(20), we demonstrate that $\phi(t)$, and its conjugate momentum $\pi(t)$ satisfy at any finite time t the correct commutation relations. For simplicity of proof, we restrict our attention to the one case of interest, the nucleon source function spherically

[13] This connection between the classical one-particle in and outgoing wave scattering matrices has been proven quite generally to be a consequence of time reversal. See F. G. Chew and M. L. Goldberger, Phys. Rev. 87, 778 (1952). Their requirement $H=\omega^2+\lambda V=H^*$ implies Eq. (26).

symmetric, $U(\mathbf{x})=U(|\mathbf{x}|)$. Inasmuch as then $U(\mathbf{k})=U(-\mathbf{k})$, we can succintly compress the expressions

$$\phi(x)=(2\pi)^{-\frac{3}{2}}\int d\mathbf{k}d\mathbf{k}'e^{i\mathbf{k}\cdot\mathbf{x}}\{(\mathbf{k}|\,\Omega_{(+)}(2\omega)^{-\frac{1}{2}}|\,\mathbf{k}')\times e^{-i\omega(\mathbf{k}')t}a(\mathbf{k}')+(\mathbf{k}|\,\Omega_{(-)}(2\omega)^{-\frac{1}{2}}|\,\mathbf{k}')\times e^{i\omega(\mathbf{k}')t}a^{\dagger}(\mathbf{k}')\}$$
$$=(2\pi)^{-\frac{3}{2}}\int d\mathbf{k}d\mathbf{k}'e^{i\mathbf{k}\cdot\mathbf{x}}\{(\mathbf{k}|\,\Omega_{(-)}(2\omega)^{-\frac{1}{2}}|\,\mathbf{k}')\times e^{-i\omega(\mathbf{k}')t}b(\mathbf{k}')+(\mathbf{k}|\,\Omega_{(+)}(2\omega)^{-\frac{1}{2}}|\,\mathbf{k}')\times e^{i\omega(\mathbf{k}')t}b^{\dagger}(\mathbf{k}')\}, \quad (30)$$

by the employment of matrix notation to the forms

$$\phi(t)=\Omega_{(+)}(2\omega)^{-\frac{1}{2}}e^{-i\omega t}a+\Omega_{(-)}(2\omega)^{-\frac{1}{2}}e^{i\omega t}a^{\dagger}$$
$$=\Omega_{(-)}(2\omega)^{-\frac{1}{2}}e^{-i\omega t}b+\Omega_{(+)}(2\omega)^{-\frac{1}{2}}e^{i\omega t}b^{\dagger}. \quad (31)$$

With the usual definition $\pi(t)=\partial_t\phi(t)$, we then have

$$\pi(t)=-i\{\Omega_{(+)}(\tfrac{1}{2}\omega)^{\frac{1}{2}}e^{-i\omega t}a-\Omega_{(-)}(\tfrac{1}{2}\omega)^{\frac{1}{2}}e^{i\omega t}a^{\dagger}\}$$
$$=-i\{\Omega_{(-)}(\tfrac{1}{2}\omega)^{\frac{1}{2}}e^{-i\omega t}b-\Omega_{(+)}(\tfrac{1}{2}\omega)^{\frac{1}{2}}e^{i\omega t}b^{\dagger}\}. \quad (32)$$

The commutation relations that we seek to establish,

$$[\phi(t),\phi(t)]=[\pi(t),\pi(t)]=0, \quad [\phi(t),\pi(t)]=i1, \quad (33)$$

where 1 refers to the diagonal unit matrix of three-space, have, according to Eqs. (31) and (32) the form

$$[\phi(t),\pi(t)]=i\{\tfrac{1}{2}\Omega_{(-)}\Omega_{(+)}{}^{T}+\tfrac{1}{2}\Omega_{(+)}\Omega_{(-)}{}^{T}\}, \quad (34)$$

$$[\phi(t),\phi(t)]=\tfrac{1}{2}\{\Omega_{(-)}\omega^{-1}\Omega_{(+)}{}^{T}-\Omega_{(+)}\omega^{-1}\Omega_{(-)}{}^{T}\}, \quad (35)$$

$$[\pi(t),\pi(t)]=\tfrac{1}{2}\{\Omega_{(-)}\omega\Omega_{(+)}{}^{T}-\Omega_{(+)}\omega\Omega_{(-)}{}^{T}\}, \quad (36)$$

where the superscript T indicates the transposed matrix.

The proof of equivalence of Eq. (33) to Eqs. (34)–(36) requires certain nontrivial properties of $\Omega_{(\pm)}$. In Appendix A, it is proved that for $\lambda>0$, the situation of physical interest, and under rather loose restrictions on $U(|\mathbf{x}|)$, $\Omega_{(+)}$, $\Omega_{(-)}$ satisfy the unitarity requirements,

$$\Omega_{(\pm)}\Omega_{(\pm)}{}^{\dagger}=1. \quad (37)$$

Furthermore, we show that

$$(\mathbf{k}'|\,\Omega_{(\pm)}|\,\mathbf{k})=(\mathbf{k}'|\,\Omega_{(1)}|\,\mathbf{k})D_{(1)}(\mathbf{k}^2)[D_{(\pm)}(\mathbf{k}^2)]^{-1}, \quad (38)$$

with the real standing-wave one-particle scattering matrix $\Omega_{(1)}$ defined by

$$(\mathbf{k}|\,\Omega_{(1)}|\,\mathbf{k}')=\delta(\mathbf{k}-\mathbf{k}')+\frac{\lambda U(\mathbf{k})U^{*}(\mathbf{k}')}{(\mathbf{k}'^2-\mathbf{k}^2)D_{(1)}(\mathbf{k}^2)}, \quad (39)$$

accompanied by the convention that all integrations over $\mathbf{k}$, $\mathbf{k}'$ are to be taken in the principle part sense.

Concurrently, we define the real function $D_{(1)}(\mathbf{k}^2)$,

$$D_{(1)}(\mathbf{k}^2)=1+\lambda\int d\mathbf{k}'\,|\,U(\mathbf{k}')\,|^2(\mathbf{k}'^2-\mathbf{k}^2)^{-1}, \quad (40)$$

wherein principal part integration is also understood. We require, finally, the replacement

$$\Omega_{(\pm)}{}^{\dagger}=\Omega_{(\mp)}{}^{T}, \quad (41)$$

which has been discussed subsequent to Eq. (25). The left hand side of Eq. (34) then reduces to 1 by Eqs. (37) and (41). Further, by applying Eq. (41) again and then Eq. (38), we obtain the required cancellation of the two terms on the left-hand side of Eqs. (35) and (36).

It is worthwhile at this stage to note the relationship between the b and a operators which defines the S-matrix. From Eqs. (18) and (31), we have at $t=0$,

$$\phi^{(+)}(0)=\Omega_{(+)}(2\omega)^{-\frac{1}{2}}a=\Omega_{(-)}(2\omega)^{-\frac{1}{2}}b. \quad (42)$$

Since Eq. (38) also states that

$$\Omega_{(-)}D_{(-)}=\Omega_{(+)}D_{(+)}, \quad (43)$$

we obtain immediately

$$b(\mathbf{k})=[D_{(-)}(\mathbf{k}^2)/D_{(+)}(\mathbf{k}^2)]a(\mathbf{k})$$
$$=\exp(2i\delta(\mathbf{k}))a(\mathbf{k}), \quad (44)$$

where

$$\delta(\mathbf{k})=-\tan^{-1}2\pi^2\lambda|\,\mathbf{k}|\,|\,U(\mathbf{k})\,|^2(D_{(1)}(\mathbf{k}^2))^{-1} \quad (45)$$

is the phase shift associated with the interaction of the field with the source. The statement of the S-matrix, which is the solution of the equation

$$S^{-1}a(\mathbf{k})S=e^{2i\delta(\mathbf{k})}a(\mathbf{k}), \quad (46)$$

will be deferred to Sec. IV.

III. CONSTRUCTION OF THE MØLLER SCATTERING MATRIX

The S-matrix of our dynamical system, referring as it does to the correspondence between physical states of the system in the remote past to those in the infinite future bypasses consideration of the detailed structure of the Heisenberg field $\phi(x)$. In our instance, the S-matrix gives rise to one channel mesic scattering only. In limiting our inspection to this matrix alone, we lose then not only any inference of the intermediate mechanics of the scattering process, but also such information as the structure of the mesic proper field of the nucleon. Such information is contained, for example, in the "outgoing" scattering matrix Λ, the Møller matrix, which exhibits all Fock-space amplitudes of the scattered state of the system at $t=0$. We propose, then, to construct Λ explicitly.

For this purpose, it is convenient to introduce the non-Hermitian canonical variables α, $\alpha^{\dagger}$,

$$\alpha=(\tfrac{1}{2}\omega)^{\frac{1}{2}}[\phi(0)+i\omega^{-1}\pi(0)],$$
$$\alpha^{\dagger}=(\tfrac{1}{2}\omega)^{\frac{1}{2}}[\phi(0)-i\omega^{-1}\pi(0)], \quad (47)$$

the noninteracting variables which coincide with the Heisenberg variables at time $t=0$, but are supposed to propagate in time according to the equation

$$\alpha(t)=e^{iH_0t}\alpha e^{-iH_0t}=e^{-i\omega t}\alpha. \tag{48}$$

Here H_0, the free Hamiltonian, is given to within an additive constant by

$$H_0(\alpha)=\int d\mathbf{k}\alpha^\dagger(\mathbf{k})\omega(\mathbf{k})\alpha(\mathbf{k}). \tag{49}$$

Now the a, $a^\dagger$ variables also propagate in time according to H_0.

$$a(t)=e^{iH_0(a)t}ae^{-iH_0(a)t}=e^{-i\omega t}a, \tag{50}$$

and by definition coincide with the Heisenberg variables in the remote past. Indeed, the required unitary equivalence of these two sets of operators,

$$\alpha=\Lambda^{-1}a\Lambda, \tag{51}$$

provides a definition of the Møller scattering matrix that is the one most useful for our purposes.

We may remark briefly that Eq. (51) is in accord with the usual definition of Λ, since it implies that

$$\begin{aligned}\Lambda H_0(\alpha)&=H_0(a)\Lambda\\&=[H_0(\alpha)+H_I(\alpha)]\Lambda,\end{aligned} \tag{52}$$

$$H_I(\alpha)=\frac{\lambda}{2}\int d\mathbf{k}d\mathbf{k}'[\alpha(\mathbf{k})+\alpha^\dagger(\mathbf{k})](2\omega(\mathbf{k}))^{-\frac{1}{2}}(\mathbf{k}|V|\mathbf{k}')\times[2\omega(\mathbf{k}')]^{-\frac{1}{2}}[\alpha(\mathbf{k}')+\alpha^\dagger(\mathbf{k}')]. \tag{53}$$

The justification for Eq. (52) stems from the form of Eq. (31) for the Heisenberg operator, which asserts that the time displacement operator of the full system, $H=H_0+H_I$, induces a simple harmonic oscillation of the a, $a^\dagger$ variables. Thus, H takes the form $H_0(a)$, in terms of the latter variable, which is the content of Eq. (52).

Λ is most easily constructed in a representation adapted to the eigenstates of the non-Hermitian operators, α, $\alpha^\dagger$, a. More explicitly, corresponding to the three complete sets of (non-Hermitean) variables, $\{a(\mathbf{k})\}$, $\{\alpha(\mathbf{k})\}$, and $\{\alpha^\dagger(\mathbf{k})\}$, we introduce in turn the basic right eigenvectors $\Psi(a')=|a'\rangle$, $\Psi(\alpha')=|\alpha'\rangle$, and the left eigenvector $\Phi(\alpha^{\dagger\prime})=\langle\alpha^{\dagger\prime}|$ satisfying[14]

$$\begin{aligned}a(\mathbf{k})|a'\rangle&=a'(\mathbf{k})|a'\rangle,\\ \alpha(\mathbf{k})|\alpha'\rangle&=\alpha'(\mathbf{k})|\alpha'\rangle,\\ \langle\alpha^{\dagger\prime}|\alpha^\dagger(\mathbf{k})&=\langle\alpha^{\dagger\prime}|(\alpha'(\mathbf{k}))^*.\end{aligned} \tag{54}$$

Then subject to the convention $\alpha'(\mathbf{k})=a'(\mathbf{k})$, concomitant with Eq. (51), we have

$$|a'\rangle=\Lambda|\alpha'\rangle,\quad \langle\alpha^{\dagger\prime\prime}|\Lambda|\alpha'\rangle=\langle\alpha^{\dagger\prime\prime}|a'\rangle. \tag{55}$$

[14] For extension of the eigenvector concept to such non-Hermitian operators, see, for example, J. Schwinger, Phys. Rev. **91**, 728 (1953).

The construction of Λ as the transformation function between representations appropriate to the $\alpha^\dagger$ and a variables can be carried out explicitly inasmuch as there exists a linear connection between these two sets of variables:

$$\alpha=M_1a+M_2^*a^\dagger, \tag{56}$$

where

$$\begin{aligned}M_1&=\tfrac{1}{2}\{\omega^{\frac{1}{2}}\Omega_{(+)}\omega^{-\frac{1}{2}}+\omega^{-\frac{1}{2}}\Omega_{(+)}\omega^{\frac{1}{2}}\},\\ M_2&=\tfrac{1}{2}\{\omega^{\frac{1}{2}}\Omega_{(+)}\omega^{-\frac{1}{2}}-\omega^{-\frac{1}{2}}\Omega_{(+)}\omega^{\frac{1}{2}}\}.\end{aligned} \tag{57}$$

Equation (57) follows from the definitions of α, $\alpha^\dagger$, Eq. (47) and of $\phi(t=0)$, $\pi(t=0)$ in Eqs. (31) and (32). Employing the fundamental dynamical principle of Schwinger,[15] we seek to construct Λ as an ordered operator of $\alpha^\dagger$, α that is, all powers of $\alpha^\dagger$ occurring to the left of those of α in the operator functional $\Lambda=\Lambda(\alpha^\dagger;\alpha)$.

First, it is necessary to remark that inasmuch as the eigenstates $\langle\alpha'|$, $|a^{\dagger\prime\prime}\rangle$ do not exist in the usual sense,[14] we cannot impose upon eigenfunctions characterized in Eq. (54) the usual orthonormal set restriction. However, the necessary supplementary information required to characterize uniquely a particular choice of $|a'\rangle$, $|\alpha'\rangle$, $\langle\alpha^{\dagger\prime}|$ is contained in the selection of infinitesimal generators G_a, G_α, $G_\alpha{}^\dagger$ governing small variations of these states, respectively. For the situation at hand we select

$$\begin{aligned}G_a&=i\int d\mathbf{k}a^\dagger(\mathbf{k})\delta a(\mathbf{k})=ia^\dagger\delta a,\\ G_\alpha&=i\int d\mathbf{k}\alpha^\dagger(\mathbf{k})\delta\alpha(\mathbf{k})=i\alpha^\dagger\delta\alpha,\\ G_\alpha{}^\dagger&=-i\int d\mathbf{k}\alpha(\mathbf{k})\delta\alpha^\dagger(\mathbf{k})=-i\alpha\delta\alpha^\dagger.\end{aligned} \tag{58}$$

The interpretation of these operators as governing infinitesimal variations δa, $\delta\alpha$, $\delta\alpha^\dagger$, respectively,

$$\begin{aligned}[\alpha(\mathbf{k}),G_\alpha]&=i\delta\alpha(\mathbf{k}),\quad [\alpha^\dagger(\mathbf{k}),G_\alpha]=0,\\ [\alpha^\dagger(\mathbf{k}),G_{\alpha^\dagger}]&=i\delta\alpha^\dagger(\mathbf{k}),\quad [\alpha(\mathbf{k}),G_{\alpha^\dagger}]=0,\end{aligned} \tag{59}$$

with corresponding equations for a, $a^\dagger$, is clearly consistent with the commutation rules Eq. (29). Moreover, if we set

$$(\alpha^{\dagger\prime\prime}=0|\alpha'=0)=1, \tag{60}$$

the differential equation

$$\begin{aligned}\delta\langle\alpha^{\dagger\prime\prime}|\alpha'\rangle&=i\langle\alpha^{\dagger\prime\prime}|G_{\alpha^\dagger}-G_\alpha|\alpha'\rangle\\&=(\alpha'\delta\alpha^{\dagger\prime\prime}+\delta\alpha'\alpha^{\dagger\prime\prime})\langle\alpha^{\dagger\prime\prime}|\alpha'\rangle\end{aligned} \tag{61}$$

integrates directly to

$$\langle\alpha^{\dagger\prime\prime}|\alpha'\rangle=\exp(\alpha^{\dagger\prime\prime}\alpha')=\exp\left\{\int d\mathbf{k}\alpha''^*(\mathbf{k})\alpha'(\mathbf{k})\right\}. \tag{62}$$

[15] J. Schwinger, Phys. Rev. **82**, 664 (1951).

We are now prepared to consider the differential characterization of Λ:

$$\begin{aligned}\delta(\alpha^{\dagger\prime\prime}|a') &= i(\alpha^{\dagger\prime\prime}|G_{a^\dagger}-G_a|a') \\ &= (\alpha^{\dagger\prime\prime}|\alpha\delta\alpha^{\dagger\prime\prime}+a^\dagger\delta a'|a') \\ &= (\alpha^{\dagger\prime\prime}|i\delta W|a').\end{aligned} \tag{63}$$

For a linear transformation, W is necessarily of the form[16]

$$iW=\tfrac{1}{2}[\alpha^\dagger \mathrm{A}\alpha^\dagger+\{\alpha^\dagger,\mathrm{B}a\}+a\Gamma a]. \tag{64}$$

Here A, B, Γ are matrices over the three-dimensional k-space, and without loss of generality we can take

$$\mathrm{A}=\mathrm{A}^T, \quad \Gamma=\Gamma^T. \tag{65}$$

Comparison of the variation

$$\delta(iW)=\delta\alpha^\dagger(\mathrm{A}\alpha^\dagger+\mathrm{B}a)+\delta a(\mathrm{B}^T\alpha^\dagger+\Gamma a) \tag{66}$$

with that of Eq. (63) results by Eq. (57) in the specification

$$\mathrm{A}=M_2^*(M_1^*)^{-1}=(F^*-G^*)(F^*+G^*)^{-1}, \tag{67}$$

$$\mathrm{B}=(M_1^\dagger)^{-1}=2(F^\dagger+G^\dagger)^{-1}, \tag{68}$$

$$\Gamma=-(M_1^*)^{-1}M_2=(F^*+G^*)^{-1}(G-F), \tag{69}$$

and the consistency relationship

$$(M_1^\dagger)^{-1}=M_1-M_2^*(M_1^*)^{-1}M_2. \tag{70}$$

We have employed here the convenient notation

$$F=\omega^{\frac{1}{2}}\Omega_{(+)}\omega^{-\frac{1}{2}}, \tag{71}$$

$$G=\omega^{-\frac{1}{2}}\Omega_{(+)}\omega^{\frac{1}{2}}, \tag{72}$$

in terms of which, Eqs. (37) and (41) take the form

$$F^{-1}=G^\dagger, \quad G^{-1}=F^\dagger. \tag{73}$$

That in fact A and Γ as given, respectively, by Eqs. (67) and (69) are symmetric can be deduced in turn from the commutation laws $[\alpha,\alpha]=0$, $[\alpha^\dagger,\alpha^\dagger]=0$ upon re-expressing α, $\alpha^\dagger$ by a, $a^\dagger$, by means of Eq. (57). Similarly, the consistency requirement (70) follows from the commutation law $[\alpha,\alpha^\dagger]=1$. If we note that

$$i\delta(W)=i\delta\mathfrak{W}, \tag{74}$$

where $\mathfrak{W}$ is the ordered operator

$$i\mathfrak{W}(\alpha^\dagger;a)=\tfrac{1}{2}\alpha^\dagger \mathrm{A}\alpha^\dagger+\alpha^\dagger \mathrm{B}a+\tfrac{1}{2}a\Gamma a, \tag{75}$$

we observe that Eq. (63) can be integrated to the form

$$\begin{aligned}(\alpha^{\dagger\prime\prime}|a') &= (O_{a^\dagger}|O_a)\exp[i\mathfrak{W}(\alpha^{\dagger\prime\prime},a')] \\ &= (O_{a^\dagger}|O_a)\exp\{\tfrac{1}{2}\alpha^{\dagger\prime\prime}\mathrm{A}\alpha^{\dagger\prime\prime}+\alpha^{\dagger\prime\prime}\mathrm{B}a'+\tfrac{1}{2}a'\Gamma a'\}.\end{aligned} \tag{76}$$

[16] This is a direct extension of the treatment of the general linear transformation in particle quantum mechanics found in J. Schwinger, National Bureau of Standard Report 2188 (unpublished), p. 45.

We have yet to evaluate the constant $(\alpha^{\dagger\prime\prime}=0|a'=0)$. Inasmuch as the variables α collapse to variables a upon removal of the interaction with the nucleon source, we anticipate that $(O_{a^\dagger}|O_a)$ can be characterized by its variation with respect to the source distribution $U(|\mathbf{x}|)$ or equivalently, the matrices A, B, Γ. By Eq. (64),

$$\begin{aligned}\delta(O_{a^\dagger}|O_a) &= (O_{a^\dagger}|\tfrac{1}{2}\alpha^\dagger\delta\mathrm{A}\alpha^\dagger+\tfrac{1}{2}\{\alpha^\dagger,\delta\mathrm{B}a\}+\tfrac{1}{2}a\delta\Gamma a|O_a) \\ &= (O_{a^\dagger}|\tfrac{1}{2}a\delta\mathrm{B}\alpha^\dagger|O_a).\end{aligned} \tag{77}$$

From the adjoint of Eq. (56),

$$\begin{aligned}\alpha^\dagger &= M_1^*a^\dagger+M_2a \\ &= (\mathrm{B}^T)^{-1}a^\dagger+M_2a,\end{aligned} \tag{78}$$

we determine that

$$\begin{aligned}\delta(O_{a^\dagger}|O_a) &= \tfrac{1}{2}\,\mathrm{Tr}\,\mathrm{B}^{-1}\delta\mathrm{B}(O_{a^\dagger}|O_a) \\ &= \tfrac{1}{2}\delta(\log\det\mathrm{B})(O_{a^\dagger}|O_a).\end{aligned} \tag{79}$$

Integrating, then, we find that

$$\begin{aligned}(O_{a^\dagger}|O_a) &= \exp(\tfrac{1}{2}\log\det\mathrm{B}) \\ &= (\det\mathrm{B})^{\frac{1}{2}}.\end{aligned} \tag{80}$$

Under the previous convention $\alpha'(\mathbf{k})=a'(\mathbf{k})$, it is therefore permissible [by Eqs. (76), (80), (55)] to write

$$\begin{aligned}&(\alpha^{\dagger\prime\prime}|\Lambda|\alpha') \\ &\quad=(\det\mathrm{B})^{\frac{1}{2}}\exp\{\tfrac{1}{2}\alpha^{\dagger\prime\prime}\mathrm{A}\alpha^{\dagger\prime\prime}+\alpha^{\dagger\prime\prime}\mathrm{B}\alpha'+\tfrac{1}{2}\alpha'\Gamma\alpha'\}.\end{aligned} \tag{81}$$

Thereby, we recognize that Λ can be expressed in ordered form as

$$\begin{aligned}\Lambda=(\det\mathrm{B})&\exp\{\tfrac{1}{2}\alpha^\dagger\mathrm{A}\alpha^\dagger\} \\ &\times\exp\{\alpha^\dagger;P_0;\mathrm{B}\alpha\}\exp\{\tfrac{1}{2}\Gamma\alpha\}.\end{aligned} \tag{82}$$

Here, P_0 is the projection operator for the $|O_a)$ vacuum state,

$$P_0=|O_a)(O_{a^\dagger}|=\exp(-\alpha^\dagger;\alpha). \tag{83}$$

The expression $\exp(\alpha^\dagger;P_0;\mathrm{B}\alpha)$ is to be interpreted as that ordered operator obtained from expansion of

$$\exp(\alpha^\dagger B\alpha)=\exp\left[\int d\mathbf{k}d\mathbf{k}'\alpha^\dagger(\mathbf{k})(\mathbf{k}|\mathrm{B}|\mathbf{k}')\alpha(\mathbf{k}')\right]$$

regrouped in ordered form without invoking the anti-commutation of $\alpha(\mathbf{k})$, $\alpha^\dagger(\mathbf{k})$, and finally interposing in each term P_0 between the powers of $\alpha^\dagger$ on the right, α on the left. The second ordered expression for P_0 in Eq. (83) is to be interpreted similarly, but—of course—omitting the interposition of P_0. The formal construction of the scattering matrix Λ can now be considered complete. One of the objects of our later work will be to evaluate explicitly the matrices, A, B, Γ, that is, rework the Eqs. (67), (68), and (69) in terms of simple matrices, F, G. It should, however, be recognized here

that the explicit construction of B will automatically permit solution for A and Γ.

IV. S-MATRIX AND SELF-ENERGY

Before proceeding to exploit the consequences of the results just obtained, we pause briefly to apply similar techniques to the derivation of the S-matrix. The desired result will energe directly from the transformation function $(b^{\dagger\prime}(t_1)|a''(t_2))$ characterized by the equation

$$\delta(b^{\dagger\prime}t_1|a''t_2)=\int d\mathbf{k}(b^{\dagger\prime}t_1|b(\mathbf{k},t_1)\delta b^{\dagger\prime}(\mathbf{k}) +\delta a''(\mathbf{k})a^{\dagger}(\mathbf{k},t_2)|a''t_2). \quad (84)$$

We need only insert Eqs. (44) and (50) (and the analogous equations for b, $b^{\dagger}$) to recognize a total differential, with integral

$$(b^{\dagger\prime}t_1|a''t_2)=\exp\left\{\int d\mathbf{k}[b^{\dagger\prime}(\mathbf{k});P_0;e^{2i\delta(\mathbf{k})} \times e^{-i\omega(\mathbf{k})(t_1-t_2)}a''(\mathbf{k})]\right\}(Ot_1|Ot_2). \quad (85)$$

Since the S-matrix is given by the equation

$$(b^{\dagger\prime}|a'')=(a^{\dagger\prime}|S|a''), \quad (86)$$

in which the states all refer to a common time, and $a'=b'$ is assumed, we obtain directly from (85), the ordered operator expression for the S-matrix,

$$S=\exp\left\{\int d\mathbf{k}a^{\dagger}(\mathbf{k});P_0;e^{2i\delta(\mathbf{k})}a(\mathbf{k})\right\}. \quad (87)$$

Of course, Eq. (87) could also have been inferred by inspection from Eq. (46).

We turn next to the construction of the vacuum to vacuum transformation function $(Ot_1|Ot_2)$, which differs from unity only in virtue of the presence of the interaction. It is appropriate, therefore, to consider its dependence upon the nucleon sources as expressed by the dynamical principle,

$$\delta(Ot_1|Ot_2)=-i\tfrac{1}{2}\lambda\left(Ot_1\left|\delta\int_{t_2}^{t_1}dt\phi(t)UU^T\phi(t)\right|Ot_2\right) =-i\lambda(t_1-t_2)(Ot_1|\phi(0)U\delta U^T\phi(0)|Ot_2), \quad (88)$$

wherein we have removed the time-dependence of the operators, while assuming the energy of the vacuum state to be zero. The most perspicuous way of exhibiting the essential structure of (88) is to recognize the matrix element as the value for null time difference of the Green's function,

$$\mathcal{G}_{(+)}(t-t')=i\langle O|(\phi(t)\phi(t'))_+|O\rangle =i(Ot_1|(\phi(t)\phi(t'))_+|Ot_2)/(Ot_1|Ot_2), \quad (89)$$

which satisfies the integral equation

$$\mathcal{G}_{(+)}(t-t')=\mathcal{G}_{(+)}{}^{(0)}(t-t') -\lambda\int dt''\mathcal{G}_{(+)}{}^{(0)}(t-t'')UU^T\mathcal{G}_{(+)}(t''-t'). \quad (90)$$

Here, $\mathcal{G}_{(+)}{}^{(0)}$ is the noninteracting Green's function,

$$(\mathbf{k}|\mathcal{G}_{(+)}{}^{(0)}(k_0)|\mathbf{k}')=\delta(\mathbf{k}-\mathbf{k}')[\mathbf{k}^2-k_0{}^2+\mu^2-i\epsilon]^{-1}. \quad (91)$$

The same steps as those that lead to Eq. (10) then result in the solution of (90):

$$\mathcal{G}_{(+)}(k_0)=\mathcal{G}_{(+)}{}^{(0)}(k_0)-\frac{\lambda\mathcal{G}_{(+)}{}^{(0)}(k_0)UU^T\mathcal{G}_{(+)}{}^{(0)}(k_0)}{1+\lambda U^T\mathcal{G}_{(+)}{}^{(0)}(k_0)U}. \quad (92)$$

We are actually interested in the combination

$$\lambda U\mathcal{G}_{(+)}(0)\delta U=\frac{\lambda}{2\pi}\int_{-\infty}^{\infty}dk_0U\mathcal{G}_{(+)}(k_0)\delta U =\frac{1}{2\pi}\int dk_0\frac{\lambda U\mathcal{G}_{(+)}{}^{(0)}(k_0)\delta U}{1+\lambda U\mathcal{G}_{(+)}{}^{(0)}(k_0)U} =\frac{1}{4\pi}\int dk_0\delta\log[1+\lambda U\mathcal{G}_{(+)}{}^{(0)}(k_0)U]. \quad (93)$$

As a direct consequence of Eq. (93), the integral of Eq. (88) is given by the form

$$(Ot_1|Ot_2)=\exp[-i(t_1-t_2)E_0], \quad (94)$$

with E_0, the vacuum fluctuation energy, expressed by the equation

$$E_0=-\frac{i}{4\pi}\int_{-\infty}^{+\infty}dk_0\log[1+\lambda U\mathcal{G}_{(+)}{}^{(0)}(k_0)U]. \quad (95)$$

Our result (95) is readily transformed into the form familiar from previous work. We first remark that

$$1+\lambda U\mathcal{G}_{(+)}{}^{(0)}(k_0)U=1+\lambda\int\frac{d\mathbf{k}|U(\mathbf{k})|^2}{\mathbf{k}^2+\mu^2-k_0{}^2-i\epsilon} =D_{(+)}(k_0{}^2-\mu^2). \quad (96)$$

By means of the substitution $k_0=\zeta$, (95) is transformed into the integral

$$E_0=-\frac{i}{4\pi}\int_C\frac{d\zeta}{2\zeta^{\frac{1}{2}}}\log D(\zeta-\mu^2), \quad (97)$$

where C is the contour around the real positive ζ axis (and solid part of contour of Fig. 2, Appendix A). The further substitution, $\zeta=k^2+\mu^2$, and the process of taking the limit as C approaches the real axis provides

the expression

$$E_0=-\frac{i}{2\pi}\int_0^\infty \frac{kdk}{\omega(k)}\log\frac{D_{(+)}(k^2)}{D_{(-)}(k^2)}$$

$$=\frac{1}{\pi}\int_0^\infty \frac{kdk}{\omega(k)}\tan^{-1}\left(\frac{2\pi^2\lambda k|U(k)|^2}{D_{(1)}(k^2)}\right), \quad (98)$$

which is of the form required.[17]

V. UNITARITY OF THE S- AND Λ MATRICES

The proof of the unitarity of the Λ matrix of Sec. III can be most systematically effected if we first create appropriate machinery for manipulating exponential functions of the creation and annihilation operators, $\alpha^\dagger$, α. In terms of the notation

$$M(A,B,C)=\exp(\tfrac{1}{2}\alpha^\dagger A\alpha^\dagger)\times\exp(\alpha^\dagger;P_0;B\alpha)\exp(\tfrac{1}{2}\alpha C\alpha), \quad (99)$$

(where without restriction A, C are assumed symmetric) the class of preliminary lemmas we have in mind asserts the essential group property of these ordered operators M, that is,

$$M(A_1,B_1,C_1)M(A_2,B_2,C_2)=\lambda M(A_3,B_3,C_3) \quad (100)$$

under suitable restrictions upon the three-dimensional submatrices A, B, C, and with λ here a numerical factor. The results that we require are contained in the five lemmas to be proved below.[18]

The assertion of the displacement property of α, $\alpha^\dagger$ is contained in the statement that for ordered operators of type M

$$\alpha M=(\partial/\partial\alpha^\dagger)M, \quad M\alpha^\dagger=M(\partial/\partial\alpha). \quad (101)$$

In all differentiations here the projection operator P_0 is treated as if independent of α, $\alpha^\dagger$.

Introducing the contraction

$$M(O,B,O)=M(B), \quad (102)$$

we now establish as second lemma, the most elementary subcase of the assertion contained in Eq. (99):

$$M(B_1)M(B_2)=M(B_1B_2). \quad (103)$$

We need only observe that

$$M(B_1)M(B_2)=\exp[\alpha^\dagger;P_0;B_1(\partial/\partial\alpha^\dagger)]M(B_2)$$

$$=\exp[\alpha^\dagger;P_0M(B_2);B_1B_2\alpha], \quad (104)$$

where $P_0M(B_2)$ is to be inserted between the ordered powers of $\alpha^\dagger$, α quite as P_0 was previously handled. To conclude the proof, we notice that

$$P_0M(B_2)=M(B_2)P_0=P_0. \quad (105)$$

[17] Compare G. Wentzel, reference 4.

[18] For a discussion of exponential operators, see R. P. Feynman, Phys. Rev. **84**, 108 (1951); I. Fujiware, Progr. Theoret. Phys. (Japan) **7**, 433 (1952). See also J. S. Schwinger, Atomic Energy Commission, Report NYO-3071 (unpublished). Appendices A and B, to which the approach in the present section is related.

Thirdly, we wish to rework the M-type ordered operator $M(B)$ as

$$M(B)=\exp[\alpha^\dagger;(B-1)\alpha]. \quad (106)$$

Toward this end, we introduce the free reordering symbol $\mathfrak{F}$ with the interpretation that $\mathfrak{F}\{g(\alpha^\dagger,\alpha)\}$ is that *ordered* operator which evolves from the initially unordered operator $g(\alpha^\dagger,\alpha)$ if $\alpha^\dagger$, α *within* the bracket are reordered freely, i.e., as if c-numbers. Thereupon

$$M(B)=\exp(\alpha^\dagger;P_0;B\alpha)=\mathfrak{F}\{\exp(\alpha^\dagger B\alpha)\exp(-\alpha^\dagger\alpha)\}, \quad (107)$$

where we have used the projection operator P_0 in the form

$$P_0=\exp(-\alpha^\dagger;\alpha). \quad (108)$$

But we have clearly

$$\mathfrak{F}\{\exp(\alpha^\dagger B\alpha)\exp(-\alpha^\dagger\alpha)\}=\mathfrak{F}\{\exp[\alpha^\dagger(B-1)\alpha]\}=\exp[\alpha^\dagger;(B-1)\alpha]. \quad (109)$$

As a corollary to the third lemma Eq. (106) we have the important result

$$M(1)=\exp(\alpha^\dagger;P_0;\alpha)=1. \quad (110)$$

The proof of the unitarity of the S-matrix is now almost self-evident. In terms of the diagonal matrices,

$$(\mathbf{k}'|e^{\pm2i\delta}|\mathbf{k})=\delta(\mathbf{k}'-\mathbf{k})e^{\pm2i\delta(\mathbf{k})}, \quad (111)$$

we have

$$S=M(e^{2i\delta}), \quad S^\dagger=M(e^{-2i\delta}). \quad (112)$$

Employing Eqs. (104) and (110), we prove that

$$SS^\dagger=M(e^{2i\delta})M(e^{-2i\delta})=M(1)=1, \quad (113)$$

and in like manner $S^\dagger S=1$.

Under the fourth projected lemma we class the two statements:

$$\exp(\tfrac{1}{2}\alpha Q\alpha)M(B)=M(B)\exp(\tfrac{1}{2}\alpha B^TQB\alpha), \quad (114)$$

$$M(B)\exp(\tfrac{1}{2}\alpha^\dagger J\alpha^\dagger)=\exp(\tfrac{1}{2}\alpha^\dagger BJB^T\alpha^\dagger)M(B), \quad (115)$$

where Q, J, and hence B^TQB, BJB^T are symmetric. To ascertain the truth of (114), for example, we evaluate

$$\exp(\tfrac{1}{2}\alpha Q\alpha)M(B)=\exp[\tfrac{1}{2}(\partial/\partial\alpha^\dagger)Q(\partial/\partial\alpha^\dagger)]M(B)=M(B)\exp(\tfrac{1}{2}\alpha B^TQB\alpha). \quad (116)$$

The final lemma attempts to reorder into M form the class of operators

$$L=\exp(\tfrac{1}{2}\alpha C\alpha)\exp(\tfrac{1}{2}\alpha^\dagger D\alpha^\dagger), \quad (117)$$

where we must impose suitable additional restrictions upon the symmetric submatrices C, D. Such recording is achieved first in the differential form

$$\delta L=(\delta\alpha C\alpha)L+L(\delta\alpha^\dagger D\alpha^\dagger). \quad (118)$$

Inasmuch as

$$\alpha L=[\alpha,L]+L\alpha=L(D\alpha^\dagger)+L\alpha, \quad (119)$$

and

$$L\alpha^\dagger=[L,\alpha^\dagger]+\alpha^\dagger L=(C\alpha)L+\alpha^\dagger L, \tag{120}$$

we can rework these identities (119) and (120) to find

$$\alpha L=[(1-DC)^{-1}D\alpha^\dagger]L+L(1-DC)^{-1}\alpha, \tag{121}$$

$$L\alpha^\dagger=L[(1-CD)^{-1}C\alpha]+(1-CD)^{-1}\alpha^\dagger L, \tag{122}$$

and consequently reorder L as

$$\delta L=\delta\alpha\{C(1-DC)^{-1}D\alpha^\dagger L+LC(1-DC)^{-1}\alpha\} +\delta\alpha^\dagger\{D(1-CD)^{-1}\alpha^\dagger L+LD(1-CD)^{-1}C\alpha\}. \tag{123}$$

We have had to assume, of course, that

$$(1-DC)^{-1}=[(1-CD)^T]^{-1}$$

exists. If we hypothesize that $L=L'$, where

$$L'=\gamma M(R,S,T), \tag{124}$$

and employ $M(S)$ in the form

$$M(S)=\exp[\alpha^\dagger;(S-1)\alpha], \tag{125}$$

we readily evaluate

$$\delta L'=\delta\alpha^\dagger\{(R\alpha^\dagger)L'+L'(S-1)\alpha\} +\delta\alpha\{L'(T\alpha)+(S-1)^T\alpha^\dagger L'\}. \tag{126}$$

By comparison with Eq. (123), we learn that

$$\begin{aligned} R&=D(1-CD)^{-1},\\ S&=1+D(1-CD)^{-1}C=(1-DC)^{-1},\\ T&=C(1-DC)^{-1}, \end{aligned} \tag{127}$$

and find that the consistency requirement,

$$S^T-1=C(1-DC)^{-1}D, \tag{128}$$

is fulfilled. Furthermore, R (and T) is certainly symmetric. The determination of the constant γ of Eq. (124) is achieved, as previously with Λ, from the remark

$$\gamma=(O_{\alpha^\dagger}|L'|O_\alpha)=(\det S)^{\frac{1}{2}}. \tag{129}$$

In summary, we have established

$$\exp(\tfrac{1}{2}\alpha C\alpha)\exp(\tfrac{1}{2}\alpha^\dagger D\alpha^\dagger)=(\det S)^{\frac{1}{2}}M(R,S,T) \tag{130}$$

with R, S, T, given by Eq. (127).

We are now in a position to demonstrate explicitly the unitarity of Λ. Clearly by Eq. (82), we can write

$$\Lambda^\dagger\Lambda=|\det\mathrm{B}|M(\Gamma^\dagger,\mathrm{B}^\dagger,\mathrm{A}^\dagger)M(\mathrm{A},\mathrm{B},\Gamma). \tag{131}$$

From Eq. (129), we know that

$$\exp(\tfrac{1}{2}\alpha\mathrm{A}^\dagger\alpha)\exp(\tfrac{1}{2}\alpha^\dagger\mathrm{A}\alpha^\dagger)=(\det S_1)^{\frac{1}{2}}M(R_1,S_1,T_1), \tag{132}$$

where

$$R_1^\dagger=T_1=\mathrm{A}^\dagger S_1, \tag{133}$$

$$S_1=(1-\mathrm{A}\mathrm{A}^\dagger)^{-1}. \tag{134}$$

Substituting this result back into Eq. (130), we have by Eqs. (132), (133), and (102):

$$\begin{aligned} \Lambda\Lambda^\dagger&=|\det\mathrm{B}|(\det S_1)^{\frac{1}{2}}M(\Gamma^\dagger,\mathrm{B}^\dagger,\mathrm{O}) \times M(T_1^\dagger,S_1,T_1)M(\mathrm{O},\mathrm{B},\Gamma)\\ &=(\det\mathrm{B}^\dagger\det S_1\det\mathrm{B})^{\frac{1}{2}}M(\Gamma^\dagger+\mathrm{B}^\dagger T_1{}^\dagger\mathrm{B}^{\dagger T},\mathrm{B}^\dagger,\mathrm{O}) \times M(S_1)M(\mathrm{O},\mathrm{B},\Gamma+\mathrm{B}^T T_1\mathrm{B})\\ &=[\det(\mathrm{B}^\dagger S_1\mathrm{B})]^{\frac{1}{2}}M[(\Gamma+\mathrm{B}^T T_1\mathrm{B})^\dagger, \mathrm{B}^\dagger S_1 B,(\Gamma+\mathrm{B}^T T_1\mathrm{B})]. \end{aligned} \tag{135}$$

The unitary condition,

$$\Lambda^\dagger\Lambda=1=M(1), \tag{136}$$

makes them two independent demands:

$$\mathrm{B}^\dagger S_1\mathrm{B}=1, \tag{137}$$

$$\Gamma+\mathrm{B}^T T_1\mathrm{B}=0. \tag{138}$$

Consider first Eq. (134). Recognizing that submatrix A is symmetric, we find

$$S_1=[1-(M_2{}^*M_1{}^{*-1})(M_2M_1{}^{-1})]^{-1}, \tag{139}$$

by Eq. (67). However, the consistency relation, Eq. (70) allows us to write

$$\begin{aligned} 1-(M_2{}^*M_1{}^{-1})(M_2M_1{}^{-1})&=(M_1{}^\dagger)^{-1}M_1{}^{-1}\\ &=(\mathrm{B}\mathrm{B}^\dagger)^{-1}, \end{aligned} \tag{140}$$

verifying Eq. (137).

Turning now to Eq. (138), we may write

$$\mathrm{B}^T T_1\mathrm{B}=\mathrm{B}^T\mathrm{A}^\dagger S_1\mathrm{B}=\mathrm{B}^T\mathrm{A}^\dagger(\mathrm{B}^\dagger)^{-1}, \tag{141}$$

by Eqs. (137) and (133). Again recognizing A to be symmetric and employing Eq. (67), we find

$$\mathrm{B}^T T_1\mathrm{B}=(M_1{}^*)^{-1}M_2M_1{}^{-1}M_1=-\Gamma, \tag{142}$$

which establishes Eq. (138) and, consequently, the unitary assertion $\Lambda^\dagger\Lambda=1$.

The proof of unitarity of Λ in the opposite order of multiplication can be established by much the same procedure. In fact, we can deduce

$$\begin{aligned} \Lambda\Lambda^\dagger&=|\det\mathrm{B}|M(\mathrm{A},\mathrm{B},\Gamma)M(\Gamma^\dagger,\mathrm{B}^\dagger,\Lambda^\dagger)\\ &=[\det(\mathrm{B}S_2\mathrm{B}^\dagger)]^{\frac{1}{2}}M[(\mathrm{A}+\mathrm{B}T_2{}^\dagger\mathrm{B}^T),\mathrm{B}S_2\mathrm{B}^\dagger, (\mathrm{A}+\mathrm{B}T_2{}^\dagger\mathrm{B}^T)^\dagger], \end{aligned} \tag{143}$$

where

$$T_2=\Gamma S_2,\quad S_2=(1-\Gamma^\dagger\Gamma)^{-1}, \tag{144}$$

merely by uniformly replacing $\Gamma^\dagger$ by A, $\mathrm{B}^\dagger$ by B in Eqs. (131)–(134). Accordingly, Λ is unitary if

$$\mathrm{B}S_2\mathrm{B}^\dagger=1, \tag{145}$$

$$\mathrm{A}+\mathrm{B}T_2{}^\dagger\mathrm{B}^T=0. \tag{146}$$

Since Γ, too, is symmetric, we find that

$$\begin{aligned} S_2&=(1-\Gamma^*\Gamma)^{-1}\\ &=[1-(M_1{}^{-1}M_2{}^*)(M_1{}^{*-1}M_2)]^{-1}\\ &=[M_1{}^{-1}M_1{}^{\dagger-1}]^{-1}=(\mathrm{B}^\dagger\mathrm{B})^{-1}, \end{aligned} \tag{147}$$

as follows from Eq. (69), and an alternate form of the consistency equation, Eq. (70). Further, we have

$$B T_2^\dagger B^T = B S_2^\dagger \Gamma^\dagger B^T = B^{\dagger -1} \Gamma^* B^T = -M_1 (M_1^{-1} M_2)(M_1^{*-1}) = -\mathrm{A}, \quad (148)$$

by the same equations and Eq. (145).

VI. FOCK-SPACE REPRESENTATION OF THE Λ MATRIX

The form of the Λ matrix, as given by Eq. (82) is ideally suited to a Fock-space representation, say in the momentum of the individual mesons. Writing the result, Eq. (110), as

$$1 = \exp(\alpha^\dagger; P_0; \alpha) = \sum_n \int |\mathbf{k}_1, \cdots, \mathbf{k}_n) d\mathbf{k}_1 \cdots d\mathbf{k}_n (\mathbf{k}_1, \cdots \mathbf{k}_n| \quad (149)$$

and expanding the exponential as

$$\exp(\alpha^\dagger; P_0; \alpha) = \sum_n \frac{1}{n!} \int d\mathbf{k}_1 \cdots d\mathbf{k}_n \alpha^\dagger(\mathbf{k}_1) \cdots \times \alpha^\dagger(\mathbf{k}_n) \Phi_0 \Phi_0^* \alpha(\mathbf{k}_1) \cdots \alpha(\mathbf{k}_n), \quad (150)$$

where, in terms of the vacuum state Φ_0, $P_0 = \Phi_0 \Phi_0^*$, we read off the familiar result:

$$|\mathbf{k}_1, \cdots \mathbf{k}_n) = (n!)^{-\frac{1}{2}} \alpha^\dagger(\mathbf{k}_1) \cdots \alpha^+(\mathbf{k}_n) \Phi_0. \quad (151)$$

A similar expansion of Λ yields the general result:

$$\Lambda = (\mathrm{O}|\Lambda|\mathrm{O}) \sum_{n=0}^{\infty} \sum_{m=0}^{\infty} \sum_{p=0}^{\infty} (\tfrac{1}{2})^{n+p} \frac{[(m+2n)!(m+2p)!]^{\frac{1}{2}}}{n!m!p!} \times \int d\mathbf{k}_1 \cdots d\mathbf{k}_{2n} d\mathbf{k}_1' \cdots d\mathbf{k}_m' d\mathbf{k}_1'' \cdots \times d\mathbf{k}_m'' d\mathbf{k}_1''' \cdots d\mathbf{k}_{2p}''' |\mathbf{k}_1, \cdots \mathbf{k}_{2n}, \mathbf{k}_1' \cdots \mathbf{k}_m') \times \left\{ \prod_{i=1}^{n} (\mathbf{k}_{2i-1}|\mathrm{A}|\mathbf{k}_{2i}) \prod_{j=1}^{m} (\mathbf{k}_j'|\mathrm{B}|\mathbf{k}_j'') \times \prod_{l=1}^{p} (\mathbf{k}_{2l-1}'''|\Gamma|\mathbf{k}_{2l}''') \right\} \times (\mathbf{k}_1'', \cdots, \mathbf{k}_1''', \cdots \mathbf{k}_{2p}'''|. \quad (152)$$

Clearly, then, we must have

$$(\mathbf{k}_1, \cdots \mathbf{k}_r|\Lambda|\mathbf{k}_1', \cdots \mathbf{k}_s')/(\mathrm{O}|\Lambda\mathrm{O}|) = S\left\{ \sum_{m \le \min(r,s)} (\tfrac{1}{2})^{\frac{1}{2}(r+s)-m} \frac{(r!s!)^{\frac{1}{2}}}{m![\frac{1}{2}(r-m)!][\frac{1}{2}(s-m)!]} \times \prod_{i=1}^{\frac{1}{2}(r-m)} (\mathbf{k}_{2i-1}|\mathrm{A}|\mathbf{k}_{2i}) \prod_{j=1}^{m} (\mathbf{k}_{2r-j}|\mathrm{B}|\mathbf{k}_{2s-j}') \times \prod_{l=1}^{\frac{1}{2}(s-m)} (\mathbf{k}_{2l-1}'|\Gamma|\mathbf{k}_{2l}') \right\}, \quad (153)$$

where the sum $\sum$ is restricted to even (odd) m as r (hence s) is even (odd). S here signifies an average over all permutations, respectively, of the left- and right-hand indices of the matrix element. In particular, we obtain for the Fock-space representation of the new vacuum Ψ_0:

$$(\mathbf{k}_1, \cdots \mathbf{k}_{2N}|\Psi_0)/(\mathrm{O}|\Psi_0) = (\mathbf{k}_1, \cdots \mathbf{k}_{2N}|\Lambda|\mathrm{O})/(\mathrm{O}|\Lambda|\mathrm{O}) = S\left\{ (\tfrac{1}{2})^N (2N!)^{\frac{1}{2}} (N!)^{-1} \prod_{i=1}^{N} (\mathbf{k}_{2i-1}|\mathrm{A}|\mathbf{k}_{2i}) \right\} = \sum{}' (2N!)^{-\frac{1}{2}} (\mathbf{k}_1|\mathrm{A}|\mathbf{k}_2)(\mathbf{k}_3|\mathrm{A}|\mathbf{k}_4) \cdots \times (\mathbf{k}_{2N-1}|\mathrm{A}|\mathbf{k}_{2N}), \quad (154)$$

where $\sum'$ indicates a sum over permutations which are distinguishable only. It is interesting to observe that Eq. (154) lends itself to the interpretation of $(\mathbf{k}_1|\mathrm{A}|\mathbf{k}_2)$ as the wave function into which any pair of virtual mesons is emitted, i.e., it describes the proper mesic field of the source.

Inasmuch as the formal structure of Λ is invariant under the canonical substitution

$$\alpha \to \alpha' = -\alpha, \quad \alpha^\dagger \to \alpha^{\dagger\prime} = -\alpha^\dagger, \quad (155)$$

the alternative expansion of Λ in α', $\alpha^{\dagger\prime}$ yields the constraint

$$(\mathbf{k}_1, \cdots \mathbf{k}_r|\Lambda|\mathbf{k}_1', \cdots \mathbf{k}_s') = (-1)^{r+s} (\mathbf{k}_1, \cdots \mathbf{k}_r|\Lambda|\mathbf{k}_1', \cdots \mathbf{k}_s'), \quad (156)$$

or Λ has nonzero matrix elements only for processes in which the change in the number of mesons is even, as is wholly to be expected in any pair theory.

We have yet to demonstrate that the matrix Λ contains the same physical information as the S-matrix, i.e., Λ gives rise to scattering of mesons only. For this purpose, it is only necessary to examine the structure of the general matrix element $(\mathbf{k}_1 \cdots \mathbf{k}_n|\Lambda|\mathbf{k}_1' \cdots \mathbf{k}_s')$, Eq. (153). We shall see below that the matrix $(\mathbf{k}_1|\mathrm{B}|\mathbf{k}_2)$ is singular on the one-particle energy shell, $\omega(\mathbf{k}_1) = \omega(\mathbf{k}_2)$. On the other hand, the matrices Λ, Γ given according to Eqs. (67) and (69) by the expressions

$$(\mathbf{k}|\Lambda|\mathbf{k}') = \int d\mathbf{k}''(\mathbf{k}|\mathrm{B}|\mathbf{k}'')(\mathbf{k}''|D|\mathbf{k}'), \quad (157)$$

$$(\mathbf{k}|\Gamma|\mathbf{k}') = -\int d\mathbf{k}''(\mathbf{k}|D^*|\mathbf{k}'')(\mathbf{k}''|\mathrm{B}|\mathbf{k}'), \quad (158)$$

are nonsingular, since they are the product of a singular matrix B and a smooth, bounded matrix $D = \frac{1}{2}(F^\dagger - G^\dagger)$. It follows that the representative of Λ, Eq. (153), can be singular only when the number of incident particles equals the number emergent, and no Λ or Γ matrices are contained, that is, for the subclass of representatives

which describe meson scattering. Except for the symmetrization required by the indistinguishability of the mesons, we then have independent scattering of the incident mesons.

To complete our discussion we are required to demonstrate that the one-particle submatrix,

$$(\mathbf{k}'|\Delta|\mathbf{k})/(O|\Delta|O)=(\mathbf{k}'|\mathrm{B}|\mathbf{k}), \tag{159}$$

yields the same phase shifts as deduced from the S-matrix. As a Fock-space amplitude, B satisfies an equation of the form

$$(\omega+\tfrac{1}{2}\lambda V'')\mathrm{B}=\mathrm{B}\omega, \tag{160}$$

where the "potential," $\frac{1}{2}\lambda V''$, can be obtained, in general, from the elimination of higher amplitudes. In the present instance, we can use the known form of B to display the structure of V'',

$$\tfrac{1}{2}\lambda V''=\mathrm{B}\omega\mathrm{B}^{-1}-\omega=(F^\dagger+G^\dagger)^{-1}\omega(F^\dagger+G^\dagger)-\omega. \tag{161}$$

Equation (161) can be shown to represent a separable potential. For this purpose, we make use of the properties of the one-particle scattering operator $\Omega_{(+)}$, satisfying the equation

$$(\omega^2+\lambda V)\Omega_{(+)}=\Omega_{(+)}\omega^2, \tag{162}$$

or rather the equivalent form suggestive of Eq. (160),

$$(\omega+\lambda V')F=G\omega, \tag{163}$$

with the notation

$$\begin{aligned} V'&=\omega^{-\frac{1}{2}}V\omega^{-\frac{1}{2}}=U'U'^\dagger,\\ U'(\mathbf{k})&=\omega^{-\frac{1}{2}}U(\mathbf{k}). \end{aligned} \tag{164}$$

From the relation $\omega F^\dagger=G^\dagger\omega$, we deduce that

$$\omega(F^\dagger+G^\dagger)=(F^\dagger+G^\dagger)(\omega+\lambda V')-G^\dagger\lambda V', \tag{165}$$

which in turn yields, when substituted back into Eq. (161), the fundamental result:

$$\tfrac{1}{2}\lambda V''=(F^\dagger+G^\dagger)^{-1}F^\dagger\lambda V'=(1+GG^\dagger)^{-1}\lambda V'. \tag{166}$$

Thus, we see that V'' has the form

$$(\mathbf{k}_1|V''|\mathbf{k}_2)=\mathrm{X}(\mathbf{k}_1)U'^*(\mathbf{k}_2), \tag{167}$$

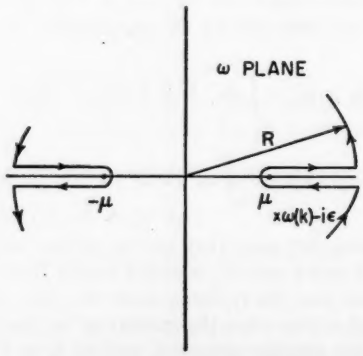

FIG. 1. Contour used in Eq. (178).

where, by Eq. (166), X satisfies the integral equation

$$F^\dagger U'=\tfrac{1}{2}(F^\dagger+G^\dagger)\mathrm{X}. \tag{168}$$

V'' has several noteworthy properties. Firstly, since G and F approach unity as $\lambda\to 0$, V'' coalesces with V' in this limiting domain. Secondly, the new potential V'' is, in general, no longer Hermitian, as a consequence of the projective character of its origin by the elimination of higher amplitudes. Finally, and most significantly, as we shall see below, is the fact that we have transformed the formidable inversion problem in the explicit construction of B into the problem of the solution of the tractable integral Eq. (168). If we knew X, we could immediately exhibit the solution of Eq. (160) in the form

$$\begin{aligned} (\mathbf{k}_1|\mathrm{B}|\mathbf{k}_2)&=\delta(\mathbf{k}_1-\mathbf{k}_2)\\ &\quad+\tfrac{1}{2}\lambda\frac{\mathrm{X}(\mathbf{k}_1)U'^*(\mathbf{k}_2)}{[\omega(\mathbf{k}_2)-\omega(\mathbf{k}_1)]\mathfrak{D}_{(+)}(\omega(\mathbf{k}_2))}, \end{aligned} \tag{169}$$

where

$$\mathfrak{D}_{(+)}(\omega)=1+\tfrac{1}{2}\lambda\int d\mathbf{k}\frac{\mathrm{X}(\mathbf{k})U'^*(\mathbf{k})}{\omega(\mathbf{k})-(\omega+i\epsilon)}. \tag{170}$$

We turn, therefore, to our final task: the solution of Eq. (168). In this connection, we shall assume the contents of Appendix A. If we introduce the definitions

$$\begin{aligned} u'(k)&=(4\pi)^{\frac{1}{2}}k\omega^{-\frac{1}{2}}U(|\mathbf{k}|),\quad (k=|\mathbf{k}|)\\ \chi(k)&=(4\pi)^{\frac{1}{2}}k\mathrm{X}(|\mathbf{k}|), \end{aligned} \tag{171}$$

and insert in Eq. (168) the explicit forms of $F^\dagger$, $G^\dagger$ which follow from their definitions, Eqs. (71), (72), we then obtain, by elaborate but essentially straightforward algebraic manipulation, the equation

$$[\chi(k)/\mathfrak{D}_{(-)}(\omega(k))]=[u'(k)/D_{(-)}(k^2)], \tag{172}$$

where $\mathfrak{D}_{(-)}=\mathfrak{D}_{(+)}{}^*$. In what follows, we require the detailed properties of the sectionally holomorphic functions of ω:

$$d(\omega)=D(\omega^2-\mu^2)=d(-\omega), \tag{173}$$

$$\mathfrak{D}(\omega)=1+\tfrac{1}{2}\lambda\int_0^\infty dk\chi(k)u(k)\Big/(\omega(k)-\omega). \tag{174}$$

Clearly, we have for $\mu<\omega<\infty$

$$d_{(\pm)}(\omega)=\lim_{\epsilon\to 0}d(\omega\pm i\epsilon)=D_{(\pm)}(k^2), \tag{175}$$

$$\lim_{\epsilon\to 0}\mathfrak{D}(\omega\pm i\epsilon)=\mathfrak{D}_{(\pm)}(\omega). \tag{176}$$

Elsewhere in the ω plane $\mathfrak{D}(\omega)$ is analytic, as is $d(\omega)$ except for the line of discontinuity of the latter for $-\infty<\omega<-\mu$. If we now introduce the function $\gamma(k)$,

$$\gamma(k)=\chi(k)/u'(k), \tag{177}$$

where we know that as $\lambda\to 0$, $\gamma(k)\to 1$, we can write

$$\log\gamma(k)=\log[(\mathfrak{D}_{(-)}(\omega(k))/\mathfrak{D}_{(-)}(k^2)]$$
$$=\frac{1}{2\pi i}\int_C\frac{d\omega}{\omega-\omega(k)+i\epsilon}\log\frac{\mathfrak{D}(\omega)}{d(\omega)}, \quad (178)$$

if C is the contour shown in Fig. 1. It will be recalled from Appendix A that the unitarity of $\Omega_{(\pm)}$ centered upon the property that $d(\omega)$ had no roots within the contour C or on the negative real axis. If $\gamma(k)$ is a bounded function of k, we have

$$d(\omega)=1+O(\omega^{-1}),$$
$$\mathfrak{D}(\omega)=1+O(\omega^{-1}) \quad (179)$$

as $|\omega|\to\infty$, so that in the limit as $R\to\infty$, no contribution to (178) arises from the semicircular arcs. Further, by the fundamental formulas (A.2)–(A.9), we have for $\omega_0>0$

$$\mathfrak{D}_{(+)}(\omega_0(k))-\mathfrak{D}_{(-)}(\omega_0(k))=i\pi\lambda\chi(k)u'^*(k)\omega_0(k)k^{-1},$$
$$d_{(+)}(\omega_0(k))-d_{(-)}(\omega_0(k))=i\pi\lambda|u(k)|^2k^{-1}, \quad (180)$$

which permit us to write the basic Eq. (171) as

$$[\mathfrak{D}_{(+)}(\omega_0)/d_{(+)}(\omega_0)]=[\mathfrak{D}_{(-)}(\omega_0)/d_{(-)}(\omega_0)], \quad (181)$$

under the same restriction $\omega_0>\mu$.

Accordingly, the contour integral in (178) reduces purely to a contribution from the negative real axis:

$$\log\gamma(k)=\frac{1}{2\pi i}\int_{-\infty}^{-\mu}\frac{d\omega}{\omega-\omega(k)+i\epsilon}$$
$$\times\left[\log\left(\frac{\mathfrak{D}(\omega+i\epsilon)}{d(\omega+i\epsilon)}\right)-\log\left(\frac{\mathfrak{D}(\omega-i\epsilon)}{d(\omega-i\epsilon)}\right)\right]$$
$$=\frac{1}{2\pi i}\int_{-\infty}^{-\mu}\frac{d\omega}{\omega-\omega(k)+i\epsilon}\log\left(\frac{d(\omega-i\epsilon)}{d(\omega+i\epsilon)}\right)$$
$$=\frac{-1}{2\pi i}\int_C\frac{d\omega}{\omega-\omega(k)+i\epsilon}\log d(\omega)$$
$$+\frac{1}{2\pi i}\int_\mu^\infty\frac{d\omega}{\omega-\omega(k)+i\epsilon}\log\left(\frac{d_{(+)}(\omega)}{d_{(-)}(\omega)}\right)$$
$$=\log D_{(-)}(k^2)+\frac{1}{2\pi i}\int_\mu^\infty\frac{d\omega(k')}{\omega-\omega(k)+i\epsilon}$$
$$\times\log\left(\frac{D_{(+)}(k'^2)}{D_{(-)}(k'^2)}\right). \quad (182)$$

Or finally we obtain

$$\gamma(k)=D_{(-)}(k^2)$$
$$\times\exp\left\{-\frac{1}{\pi}\int_0^\infty\frac{dk'k'\delta(k')}{\omega(k')[\omega(k')-\omega(k)-i\epsilon]}\right\}. \quad (183)$$

To convince ourselves that the scattering amplitude obtained from B agrees with that yielded by $\Omega_{(+)}$, we substitute Eq. (171) into (168) and find that

$$(\mathbf{k}_1|\mathrm{B}|\mathbf{k}_2)$$
$$=\delta(\mathbf{k}_1-\mathbf{k}_2)+\tfrac{1}{2}\lambda\frac{\mathfrak{D}_{(-)}(\omega(k_1))U'(\mathbf{k}_1)U'^*(\mathbf{k}_2)}{D_{(-)}(k_1^2)[\omega(k_2)-\omega(k_1)]\mathfrak{D}_{(+)}(\omega(k_2))}$$
$$=\delta(\mathbf{k}_1-\mathbf{k}_2)+\tfrac{1}{2}\lambda\frac{\mathfrak{D}_{(+)}(\omega(k_1))U'(\mathbf{k}_1)U'^*(\mathbf{k}_2)}{D_{(+)}(k_1^2)[\omega(k_2)-\omega(k_1)]\mathfrak{D}_{(+)}(\omega(k_2))}, \quad (184)$$

according to Eq. (181). From this form, moreover, it is clear on comparison with Eq. (20) that the residue of B at the pole $\omega(k_2)=\omega(k_1)$ equals that of Ω at the same pole, thus establishing the equality of the scattering amplitudes.

We complete our discussion of meson pair theory with a few remarks upon questions of renormalization. In the few cases of field theories for which exact solutions are known, it has been the experience that the renormalization constants can be exhibited explicitly and consequently disposed of in a trivial manner. This has been equally true in this paper, in virtue of the methods employed. The mass renormalization or vacuum fluctuation energy has been exhibited in Sec. IV, Eq. (98). Moreover, we disposed quietly of the so-called charge-renormalization of the second kind or, more aptly, Green's function renormalization, by considering matrix elements of Λ relative to $(0|\Lambda|0)$. The connection with the more usual S-matrix renormalization procedure is contained in the statement that $|(0|\Lambda|0)|^2=Z_2$, in the notation of Dyson.[19] Our theory is, however, still nonrenormalizable in the limit of a point nucleon source, since the only observable quantity

$$\tan\delta(k)=-\frac{\lambda 2\pi^2k|U(k)|^2}{1+\lambda\int d\mathbf{k}'|U(\mathbf{k}')|^2[\mathbf{k}'^2-\mathbf{k}^2]^{-1}} \quad (185)$$

vanishes as $U(\mathbf{k})$ approaches a constant and λ is assumed finite. In terms of the renormalized coupling constant,[20]

$$\bar{\lambda}=\lambda\left[1+\lambda\int d\mathbf{k}'|U(\mathbf{k}')|^2(\mathbf{k}')^{-2}\right]^{-1}, \quad (186)$$

however, $\tan\delta(k)$ has the form

$$\tan\delta(k)$$
$$=(-)\frac{\bar{\lambda}2\pi^2k|U(\mathbf{k})|^2}{1+\bar{\lambda}k^2\int d\mathbf{k}'|U(\mathbf{k}')|^2[\mathbf{k}'^2(\mathbf{k}'^2-\mathbf{k}^2)]^{-1}} \quad (187)$$

[19] F. J. Dyson, Phys. Rev. **75**, 1736 (1949).

[20] $\bar{\lambda}$ has the significance that in terms of it the scattering amplitude at zero energy has the same form as the Born approximation. Compare Deser, Thirring, and Goldberger, reference 8.

and remains finite in the limit of a point source, if it is assumed that $\bar{\lambda}$ remains finite.[21]

APPENDIX A

Preparatory to a proof of the unitarity of the matrices $\Omega_{(+)}$, $\Omega_{(-)}$, first introduced in Eq. (20), it is essential to correlate the various $D(\mathbf{k}^2)$ functions of Eqs. (21) and (40). A unified treatment of these functions will be subsumed by a statement of the well-known fundamental relations of the theory of Cauchy-type integrals. This statement is that under rather general conditions the sectionally holomorphic function of a complex variable,

$$\Phi(E)=\frac{1}{2\pi i}\int_0^\infty \frac{\phi(E_0)dE_0}{E_0-E}, \tag{A.1}$$

assumes the limiting values $\Phi^{(+)}(E')$, $\Phi^{(-)}(E')$, where $E'>0$ as E approaches E' from above (below) the *positive* real axis. $\Phi(E)$ is everywhere analytic except on this positive real axis whereupon it suffers a discontinuity characterized by the equations

$$\Phi^{(+)}(E_0)-\Phi^{(-)}(E_0)=\phi(E_0), \quad E_0>0, \tag{A.2}$$

$$\Phi^{(+)}(E_0)+\Phi^{(-)}(E_0)=\frac{1}{\pi i}P\int \frac{\phi(E')dE'}{E'-E_0}. \tag{A.3}$$

To apply these formulas to the D functions, we write (for E complex)

$$D(E)=1+\lambda\int d\mathbf{k}'|U(\mathbf{k}')|^2/(\mathbf{k}'^2-E) \tag{A.4}$$

$$=1+\frac{1}{2\pi i}\int_0^\infty \frac{dE_0\phi(E_0)}{E_0-E}, \tag{A.5}$$

with $(E_0=\mathbf{k}^2)$

$$\phi(E_0)=\pi i\lambda\int d\Omega E_0^{\frac{1}{2}}|U(E_0^{\frac{1}{2}})|^2$$

$$=4\pi^2 i\lambda E_0^{\frac{1}{2}}|U(E_0^{\frac{1}{2}})|^2 \tag{A.6}$$

for the spherically symmetric nucleon source. Accordingly, it is clearly consistent to define functions $D^{(+)}(E_0)$, $D^{(-)}(E_0)$, $(E_0>0)$ by the limiting procedure previously applied to obtain $\Phi^{(+)}$, $\Phi^{(-)}$, respectively, and write

$$D^{(\pm)}(E_0)=\lim_{\epsilon\to 0} D(E_0\pm i\epsilon)=D_{(\pm)}(E_0) \tag{A.7}$$

in the sense of Eq. (21). Equations (A.2) and (A.3) are translated into

$$D_{(+)}(E_0)-D_{(-)}(E_0)=4\pi^2 i\lambda E_0^{\frac{1}{2}}|U(E_0^{\frac{1}{2}})|^2, \tag{A.8}$$

$$\tfrac{1}{2}(D_{(+)}(E_0)+D_{(-)}(E_0))$$

$$=1+\lambda P\int d\mathbf{k}'|U(\mathbf{k}')|^2/(\mathbf{k}'^2-E)$$

$$=D_{(1)}(E_0) \tag{A.9}$$

defined by Eq. (40).

Inasmuch as the nucleon source function has been taken to be spherically symmetric, we shall uniformly replace $U(\mathbf{k})$ by

$$u(k)=(4\pi)^{\frac{1}{2}}kU(\mathbf{k}), \tag{A.10}$$

and in all matrix multiplications consistently substitute dk for $d\mathbf{k}$. For example, we shall use (A.8) in the form

$$D_{(+)}(k^2)-D_{(-)}(k^2)=i\lambda\pi k^{-1}|u(k)|^2, \tag{A.11}$$

and write $\Omega_{(\pm)}$ as

$$(k'|\Omega_{(\pm)}|k)=\delta(k-k')+\frac{\lambda u(k')u^*(k)}{(k^2\pm i\epsilon-k'^2)D_{(\pm)}(k^2)}. \tag{A.12}$$

Writing

$$\Omega_{(+)}=1+R, \tag{A.13}$$

we can prove the unitarity condition,

$$\Omega_{(+)}^\dagger\Omega_{(+)}=1, \tag{A.14}$$

by demonstrating that

$$R^\dagger R=-(R+R^\dagger). \tag{A.15}$$

If $\psi(k)$ is some smooth function of k, we then consider the expression

$$\int dk(k'|R^\dagger R|k)\psi(k)$$

$$=\int dk''dk\left\{\frac{\lambda u(k')u(k'')^*}{D_{(-)}(k'^2)(k'^2-k''^2-i\epsilon}\right\}$$

$$\times\left\{\frac{\lambda u(k'')u^*(k)}{(k^2-k''^2+i\epsilon)D_{(+)}(k^2)}\right\}\psi(k)$$

$$=\int dk\frac{\lambda u(k')u^*(k)}{k^2-k'^2+i\epsilon}\int dk''\left\{\frac{1}{k''^2-k^2-i\epsilon}\right.$$

$$\left.-\frac{1}{k''^2-k'^2+i\epsilon}\right\}\frac{|u(k'')|^2}{D_{(-)}(k'^2)D_{(+)}(k^2)}\psi(k)$$

$$=\int\frac{dk}{k^2-k'^2+i\epsilon}\frac{\lambda u(k')u^*(k)}{D_{(-)}(k'^2)D_{(+)}(k^2)}$$

$$\times[D_{(+)}(k^2)-D_{(-)}(k'^2)]\psi(k)$$

$$=(-)\int dk[(k'|R^\dagger|k)+(k'|R|k)]\psi(k), \tag{A.16}$$

as required in (A.15).

[21] Indeed the integral in the denominator of Eq. (187) vanishes in the limit of a point source so that the Born approximation becomes exact. On the other hand, it is a simple consequence of Eq. (186) that for fixed $\bar{\lambda}$, λ as a function of k_c, where $k_c=\int d\mathbf{k}|U|^2k^{-1}$, has a simple pole at $\lambda=k_c^{-1}$ after which it becomes and remains negative. Thus we cannot consistently pass to the limit of a point source. This aspect of the theory will be discussed more fully in a separate note. We are indebted to A. Wightman, N. Kroll, and G. Källén for remarks on these points.

To prove the second restriction of the unitarity requirement,

$$\Omega_{(+)}{}^{\dagger}\Omega_{(+)}=1, \tag{A.17}$$

requires equivalently showing that

$$RR^{\dagger}=-(R+R^{\dagger}), \tag{A.18}$$

a proof which necessitates more detailed knowledge of the system, in particular, that there *exist no bound states*. Characteristically, we must evaluate

$$\begin{aligned}&\int (k'|RR^{\dagger}|k)dk\psi(k)\\&=\int dk''dk\left\{\frac{\lambda u(k')u^*(k'')}{[k''^2-k'^2+i\epsilon]D_{(+)}(k''^2)}\right\}\\&\qquad\times\left\{\frac{\lambda u(k'')u^*(k)}{[k''^2-k^2-i\epsilon]D_{(-)}(k''^2)}\right\}\psi(k)\\&=\int dkdk''\frac{\lambda\mu(k')u^*(k)\psi(k)}{[k^2-k'^2+i\epsilon]}\left\{\frac{1}{k''^2-k^2-i\epsilon}\right.\\&\qquad\left.-\frac{1}{k''-k'^2+i\epsilon}\right\}\frac{\lambda|u(k'')|^2}{D_{(+)}(k''^2)D_{(-)}(k''^2)}.\end{aligned} \tag{A.19}$$

The proof centers, then, upon showing that

$$\begin{aligned}&\int dk''\left\{\frac{1}{k''^2-k^2-i\epsilon}-\frac{1}{k''^2-k'^2+i\epsilon}\right\}\\&\times\frac{\lambda|u(k'')|^2}{D_{(+)}(k''^2)D_{(-)}(k''^2)}=\frac{1}{D_{(-)}(k'^2)}-\frac{1}{D_{(+)}(k^2)}.\end{aligned} \tag{A.20}$$

But we have, by Eq. (A.11),

$$\begin{aligned}&\frac{\lambda|u(k'')|^2}{D_{(+)}(k''^2)D_{(-)}(k''^2)}\\&=\frac{\lambda|u(k'')|^2}{D_{(+)}(k''^2)-D_{(-)}(k''^2)}\cdot\left[\frac{1}{D_{(-)}(k''^2)}-\frac{1}{D_{(+)}(k''^2)}\right]\\&=i\pi k''\{[D_{(-)}(k''^2)]^{-1}-[D_{(+)}(k''^2)]^{-1}\}.\end{aligned} \tag{A.21}$$

Now let us *assume* $D(E)$, as defined first in Eq. (A.4), or equivalently as

$$D(E)=1+\lambda\int dk'|u(k')|^2/(k'^2-E), \tag{A.22}$$

has *no zeros* other than possible in the range $0<E<\infty$. By deformation of the contour shown in Fig. 2,

$$\begin{aligned}&\int_0^{\infty}dk''\left\{\frac{1}{k''^2-k^2\mp i\epsilon}\right\}\frac{k''}{2\pi i}\left\{\frac{1}{D_{(-)}(k''^2)}-\frac{1}{D_{(+)}(k''^2)}\right\}\\&=-\frac{1}{2\pi i}\int_C\frac{dE}{E-(E(k)\pm i\epsilon)}\frac{1}{D(E)}\\&=-[D(E(k)\pm i\epsilon)]^{-1}.\end{aligned} \tag{A.23}$$

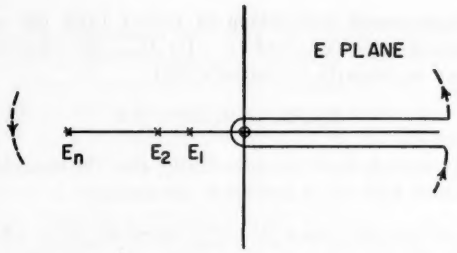

FIG. 2. Contour for Eqs. (A.23) and (A.24). Dashed lines indicate the manner in which the contour is closed.

Letting $\epsilon\rightarrow 0$, we apply Eq. (A.7), and establish in turn (A.20), and the theorem (A.17).

For completeness, consider briefly the situation where there exist bound states. Suppose $D(E_n)=0$ for some E_n, $n=1, 2, \cdots$ real and negative. (As asserted, zeros of D must be real.) Such a situation can pertain only when $\lambda<0$, as seen by inspection of $D(E)$ with $E<0$. As before, we can deform the contour integral of Eq. (A.23), now picking up poles of $[D(E)]^{-1}$ on the negative real axis, assuming these to be all simple poles. Accordingly, we find the results

$$\begin{aligned}&\frac{1}{2\pi i}\int_C\frac{dE}{D(E)}\left\{\frac{1}{E-(E(k)+i\epsilon)}-\frac{1}{E-(E(k')-i\epsilon)}\right\}\\&=\{[D(E(k)+i\epsilon)]^{-1}-[D(E(k')-i\epsilon)]^{-1}\}\\&\quad+\sum_n\{[E_n-(E_k+i\epsilon)]^{-1}\\&\qquad-[E_n-(E(k')-i\epsilon)]^{-1}\}[D'(E_n)]^{-1}\\&=[D_{(+)}(k^2)]^{-1}-[D_{(-)}(k^2)]^{-1}+\sum_n(k^2-k'^2+i\epsilon)\\&\qquad\times[(E_n-k^2-i\epsilon)(E_n-k'^2+i\epsilon)D'(E_n)]^{-1},\end{aligned} \tag{A.24}$$

where $D'(E_n)=(d/dE)D(E)|^{E=E_n}$. Substituting back into Eq. (A.19), we obtain

$$\begin{aligned}&\int dk(k'|RR^{\dagger}|k)\psi(k)\\&=-\int[(k'|R|k)+(k'|R^{\dagger}|k)]\psi(k)dk\\&+\sum_n\int dk\frac{\lambda u(k')u^*(k)}{(E_n-k'^2+i\epsilon)(E_n-k^2-i\epsilon)D'(E_n)}\psi(k),\end{aligned} \tag{A.25}$$

or, symbolically,

$$RR^{\dagger}=-(R+R^{\dagger})-\sum_n\psi_n\psi_n{}^*, \tag{A.26}$$

where corresponding to the nth bound state $[D(E_n)=0]$ we have written

$$\psi_n(k)=\left(-\frac{\lambda}{D'(E_n)}\right)^{\frac{1}{2}}\frac{u(k)}{E_n-k^2}. \tag{A.27}$$

Alternatively, we can write

$$\Omega_{(+)}{}^{\dagger}\Omega_{(+)}-\Omega_{(+)}\Omega_{(+)}{}^{\dagger}=\sum_n\psi_n\psi_n{}^*. \tag{A.28}$$

Replacement everywhere of $\epsilon \to -\epsilon$ (and the concomitant substitution of $D_{(-)}$ for $D_{(+)}$, $\Omega_{(-)}$ for $\Omega_{(+)}$) allows us similarly to conclude that

$$\Omega_{(-)}{}^{\dagger}\Omega_{(-)} = \Omega_{(-)}\Omega_{(-)}{}^{\dagger} = 1 \tag{A.29}$$

for $\lambda > 0$.

We remark next, parenthetically, that the usual form in which Eqs. (A.2) and (A.3) are stated,

$$[k^2 \pm i\epsilon - k'^2]^{-1} = P[k^2 - k'^2]^{-1} \mp i\pi\delta(k^2 - k'^2) \tag{A.30}$$

(in the sense of a k integration), as applied to $\Omega_{(+)}$, given by Eq. (A.12), yields

$$(k'|\Omega_{(\pm)}|k) = (k'|\Omega_{(1)}|k) D_{(1)}(k^2)[D_{(+)}(k^2)]^{-1}, \tag{A.31}$$

or equivalently Eq. (38) of the text.

One property of the $\Omega_{(1)}$ matrix is of particular interest. By Eqs. (A.14) and (A.31) we can deduce the identity

$$(k'|\Omega_{(1)}{}^{T}\Omega_{(1)}|k) = |D_{(+)}(k^2)[D_{(1)}(k^2)]^{-1}|^2 \delta(k-k'). \tag{A.32}$$

Inasmuch as $\Omega_{(1)}$ has been assumed orthogonal in a recent work,[6] it is, perhaps, of interest to give a direct proof of the theorem demonstrating where it is that the fallacy arose. If we return to Eq. (A.16) and everywhere make the substitutions

$$R \to R^{(1)}, \quad \epsilon \to 0, \quad D_{(\pm)} \to F_{(1)}, \tag{A.33}$$

(and interpret all integrals in the principle part sense), we *seemingly* prove $\Omega_{(1)}{}^{T}\Omega_{(1)} = 1$. However, to carry out the steps shown in Eq. (A.16) necessarily requires interchanging the order of integration; it is just this process which is not valid. (For the proof, there are no singularities on the path of integration as ϵ kept finite.) In fact, the Poincaré-Bertrand transformation formula[22] of the theory of singular integral equations can be specialized to the form

$$\int dk'' \int dk \frac{\phi(k'',k)}{(k'^2 - k''^2)(k^2 - k''^2)} = \int dk \int dk'' \frac{\phi(k'',k)}{(k'^2 - k''^2)(k^2 - k''^2)} + (\tfrac{1}{2}\pi)^2 \phi(k',k')(k')^{-2}, \tag{A.34}$$

with all integrals taken in the principle part sense. Letting

$$\phi(k'',k) = |u(k'')|^2 u^*(k)\psi(k)[D_{(1)}(k^2)]^{-1}, \tag{A.35}$$

we find that we must properly add to the r.h.s. of Eq. (A.17) the term

$$\{\tfrac{1}{2}\lambda\pi(k')^{-1}|u(k')|^2[D_{(1)}(k'^2)]^{-1}\}^2\psi(k) = -\{\tfrac{1}{2}[D_{(+)}(k'^2) - D_{(-)}(k'^2)] \times [D_{(1)}(k'^2)]^{-1}\}^2\psi(k), \tag{A.36}$$

which established Eq. (A.32).

[22] N. I. Muskhelishvili, *Singuler Integral Equations* (P. Noordhoff, Grongingen, 1953), p. 56.

APPENDIX B

The developments of this paper have made no use of sphere normalization and of the resulting discrete variables, as have all previous treatments of pair theory. For the sake of completeness, we propose here to provide a succinct treatment of the eigenvalue problem in the discrete case, employing methods analogous to those first used by Wentzel[4] for this problem.

The Hamiltonian

$$H = \tfrac{1}{2}\sum_k (p_k^2 + \omega_k^2 q_k^2) + \tfrac{1}{2}\lambda \sum_{k,k'} q_k u_k u_{k'} q_{k'} = \tfrac{1}{2}(pp + q\omega^2 q) + \tfrac{1}{2}\lambda q V q \tag{B.1}$$

will be considered, in which the sum is over the frequencies determined by the condition $\sin kR = 0$, R the radius of the sphere circumscribing the system. Since all variables are real, the real transformation

$$q = \Omega Q, \quad p = \Omega P \tag{B.2}$$

will bring H to diagonal form,

$$H = \tfrac{1}{2}(PP + QW^2 Q) \tag{B.3}$$

if

$$\Omega^T \Omega = 1, \tag{B.4}$$

and

$$\Omega^T(\omega^2 + \lambda V)\Omega = W^2. \tag{B.5}$$

In the new representation labelled by eigenvalues s, we define

$$W_{ss'}{}^2 = W_s{}^2 \delta_{ss'} = (s^2 + \mu^2)\delta_{ss'}. \tag{B.6}$$

If the inverse transformation exists,

$$\Omega\Omega^T = 1, \tag{B.7}$$

we may consider the eigenvalue problem

$$(W_s{}^2 - \omega_k^2)\Omega_{ks} = \lambda u_k \sum_{k'} u_{k'}\Omega_{k's} \tag{B.8}$$

with secular determinant

$$\Xi(\zeta) = |(\zeta - \omega_k^2)\delta_{kk'} - \lambda u_k u_{k'}| = \prod_k (\zeta - \omega_k^2) D(\zeta). \tag{B.9}$$

Here

$$D(\zeta) = 1 - \lambda \sum_k \frac{u_k^2}{\zeta - \omega_k^2} = \frac{\prod_s (\zeta - W_s^2)}{\prod_k (\zeta - \omega_k^2)} \tag{B.10}$$

has its zeros at the new frequencies and its poles at the old ones. The structure of Eq. (B.9) establishes a one-to-one correspondence between the numbers k and s, with one value of s lying between every pair of k. We note that

$$D'(\zeta) = \lambda \sum_k u_k^2/(\zeta - \omega_k^2)^2 > 0. \tag{B.11}$$

Another form of $D'(\zeta)$ which is basic to the completeness proof is $(\xi = \zeta - \mu^2)$:

$$\frac{D'(\xi)}{D(\xi)} = \sum_s \frac{1}{\xi - s^2} - \sum_k \frac{1}{\xi - k^2}, \tag{B.12}$$

where we have kept the same symbol for the function of the displaced variables. Now, the normalized solutions

of Eq. (B.8),

$$\Omega_{ks}=[\lambda D'(s^2)]^{-\frac{1}{2}}\lambda u_k(s^2-k^2)^{-1} \tag{B.13}$$

are easily seen to be orthogonal for different s, since

$$\begin{aligned}&\textstyle\sum_k \Omega_{ks}\Omega_{ks'}\\&=[D'(s^2)D'(s'^2)]^{-\frac{1}{2}}\textstyle\sum_k u_k^2[(s^2-k^2)(s'^2-k^2)]^{-1}\\&=[D'(s^2)D'(s'^2)]^{-\frac{1}{2}}(s^2-s'^2)^{-1}\\&\qquad\times\textstyle\sum_k u_k^2[(s'^2-k^2)^{-1}-(s^2-k^2)^{-1}]=0\end{aligned} \tag{B.14}$$

in virtue of the characteristic equation,

$$\textstyle\sum_k u_k^2(s^2-k^2)^{-1}=\sum_k u_k^2(s'^2-k^2)^{-1}=1. \tag{B.15}$$

It is somewhat more difficult to establish Eq. (B.7),

$$\begin{aligned}\delta_{kk'}&=\textstyle\sum_s \Omega_{ks}\Omega_{k's}=\sum_s \lambda^2 u_k u_{k'}\\&\qquad\times[(s^2-k^2)(s^2-k'^2)\lambda D'(s^2)]^{-1}.\end{aligned} \tag{B.16}$$

Comparison of (B.11) with (B.16) shows that the latter is an analytic function of s in the neighborhood of the real s-axis, and may therefore be replaced by

$$\begin{aligned}&\textstyle\sum_s \Omega_{ks}\Omega_{k's}\\&=(2\pi i)^{-1}\sum\int_C \frac{d\xi\lambda u_k u_{k'}}{(\xi-s^2)(\xi-k^2)(\xi-k'^2)D'(\xi)}\end{aligned} \tag{B.17}$$

where C, the contour discussed in the previous appendix, enclosed the positive real axis and therefor all values of s. Equation (B.12) is now applicable in the form

$$\begin{aligned}&\textstyle\sum_s[(\xi-s^2)D'(\xi)]^{-1}\\&\qquad=D(\xi)^{-1}+D'(\xi)^{-1}\textstyle\sum_{k''}(\xi-k''^2)^{-1}.\end{aligned} \tag{B.18}$$

For $k\neq k'$ only the first term of (B.18) leads to an integral with singularities within the contour. On the other hand, C may now be deformed so that it includes all of the s-plane *except* the real axis, and since the remaining integrand is analytic within the new contour, the required null result is obtained. If $k=k'$, the treatment of the term just disposed of is unaltered, but the contribution of the second term of (B.18) to (B.17) is now

$$\frac{1}{2\pi i}\lambda u_k^2\sum_{k''}\int_C\frac{d\xi}{(\xi-k^2)(\xi-k''^2)D'(\xi)}=1, \tag{B.19}$$

the contribution resulting from the simple pole of the integrand at $\xi=k^2$. Bound states may also be included as in the previous section.

We may remark finally that Wentzel's derivation of the self-energy for this theory is based upon Eq. (B.12) and the use of the contour C. For, if $f(\xi)$ is analytic within C, we obtain immediately

$$\begin{aligned}&(2\pi i)^{-1}\int_C f(\xi)(d/d\xi)\log D(\xi)\\&\qquad=-(2\pi i)^{-1}\int_C f'(\xi)\log D(\xi)\\&\qquad=\textstyle\sum_s f(s^2)-\sum_k f(k^2).\end{aligned} \tag{B.20}$$

With this expression one may go to the continuous limit, although the eigenvalue problem from which it was derived ceases to have a meaning in that limit. Moreover, we may relate the nonvanishing value of (B.20) to a change in the density of states, which depends on the phase shift, and thus complete the extraction of the physical information contained in the theory. We shall not enter into the details of this well-known argument [compare Eq. (B.20) with Eq. (98), however].

APPENDIX C

In this Appendix, we shall treat the entire theory anew from the point of view of the equations of motion of the source. We shall, in fact, construct the propagation function for the "nucleon" in an external meson field, aping the procedures of Edwards and Peierls.[9] We have relegated this work to an appendix because the closed expression thus obtained has so far proved intractable except when expanded in a power series.

For the Lagrangian operator at time t, we take

$$\begin{aligned}L(t)=&\psi^\dagger(t)[i\partial_t\psi(t)-m\psi(t)]\\&-\tfrac{1}{2}\lambda\psi^\dagger(t)\psi(t)\phi^2(t)+L(\text{meson})+J(t)\phi(t),\end{aligned} \tag{C.1}$$

where

$$\phi(t)=\int d\mathbf{x}U(\mathbf{x})\phi(\mathbf{x},t)\equiv(U,\phi), \tag{C.2}$$

and $J(t)$ is a source for $\phi(t)$. The operator, $\psi^\dagger(t)\psi(t)$, representing the number of nucleons at the "origin," is a constant of the motion which we have previously placed equal to unity. From (C.1) we obtain the equation of motion:

$$(-i\partial_t+m)\psi(t)+\tfrac{1}{2}\lambda\phi^2(t)\psi(t)=0. \tag{C.3}$$

The associated Green's function,

$$G(t,t')=i\epsilon(t-t')\langle(\psi(t)\psi^\dagger(t'))_+\rangle, \tag{C.4}$$

satisfies the equation

$$\begin{aligned}&(-i\partial_t+m)G(t,t')+\tfrac{1}{2}i\lambda\epsilon(t-t')\\&\qquad\times\langle(\phi^2(t)\psi(t)\bar{\psi}(t'))_+\rangle=\delta(t-t').\end{aligned} \tag{C.5}$$

If O is any operator, we have the relation

$$\begin{aligned}\langle(\phi(t))^nO\rangle&=[\langle\phi(t)\rangle-i\delta/\delta J(t)]^n\langle O\rangle\\&=\left[\langle\phi(t)\rangle-\int(U,\mathcal{G}_{(+)}(t-t')U)\delta/\delta\langle\phi(t')\rangle dt'\right]^n\langle O\rangle,\end{aligned} \tag{C.6}$$

where

$$(U,\mathcal{G}_{(+)}(t-t')U)=\delta\langle\phi(t)\rangle/\delta J(t')\equiv\Delta_+(t-t') \tag{C.7}$$

in the sense of a scalar product in three-space, and $\mathcal{G}_{(+)}(t-t')$ is the meson propagation function of Sec. IV,

Eq. (89). To see that this is the case, we consider the equation of motion for $\phi(t)$ in integral form ($\psi^{\frac{1}{2}}\psi=1$) which follows from (C.1),

$$\phi(t)=\phi_0(t)-\lambda\int dt''(U,\,\mathfrak{S}_{(+)}{}^{(0)}(t-t'')U)\phi(t'')$$
$$+\int dt''(U,\,\mathfrak{S}_{(+)}{}^{(0)}(t-t'')U)J(t''),\quad\text{(C.8)}$$

where $\phi_0(t)$ is a possible inhomogeneous term. From (C.8), we obtain an equation for $\delta\langle\phi(t)\rangle/\delta J(t')$, which on comparison with Eq. (90) of the text permits the identification (C.7).

By the use of (C.6), (C.5) becomes (ϕ now stands for $\langle\phi\rangle$)

$$(-i\partial_t+m)G(t,t')+\tfrac{1}{2}\lambda[\phi(t)-i\Delta_+(t-t')\delta/\delta\phi(t')]^2$$
$$\times G(t,t')=\delta(t-t').\quad\text{(C.9)}$$

The steps of Edwards and Peierls can now be carried through in rapid succession. First, with

$$R_1(\phi)=\exp\left\{+\tfrac{1}{2}i\int dtdt'\phi(t)\Delta_+{}^{-1}(t,t')\phi(t')\right\},\quad\text{(C.10)}$$

we introduce a Green's function G_1,

$$G=G_1R_1{}^{-1}.\quad\text{(C.11)}$$

We then go over to the Fourier transforms:

$$G_2(t,t';\pi(\tau))=\int G_1(t,t';\phi)\exp\left[i\int\phi(\tau)\pi(\tau)d\tau\right]\delta\phi,\quad\text{(C.12)}$$

$$R_2(\pi)=\int\exp\left\{i\int\phi(\tau)\pi(\tau)d\tau+\tfrac{1}{2}i\int\phi(\tau)\right.$$
$$\left.\times\Delta_+{}^{-1}(\tau,\tau')\phi(\tau')d\tau d\tau'\right\}\delta\phi,$$

where $\delta\phi=\Pi_\tau(2\pi)^{-2}d\phi(\tau)$. Thirdly, we define

$$G_2(t,t';\pi)=G_3(t,t';\sigma),\quad R_2(\pi)=R_3(\sigma),\quad\text{(C.13)}$$

$$\sigma(t)=\int\Delta_+(t-t')\pi(t')dt'.\quad\text{(C.14)}$$

Finally, we introduce

$$G_+(t,t';\sigma)=R_3(\sigma)G_3(t,t';\sigma),\quad\text{(C.15)}$$

and obtain as a consequence of the full sequence of transformations set forth above the following equation for G_4:

$$[-i\partial_t+m+\tfrac{1}{2}\lambda\sigma^2(t)]G_4(t,t';\sigma)=\delta(t-t'),\quad\text{(C.16)}$$

the propagation function of the source in an arbitrary external field $\sigma(t)$.

In order to express the original G in terms of G_4, we require the value of $R_3(\sigma)$, for which we find by completing the square of the argument of the exponential, $R_3(\sigma)=[\det(i\Delta_d)]^{\frac{1}{2}}$

$$\times\exp\left\{-\tfrac{1}{2}i\int dtdt'\sigma(t)\Delta_+{}^{-1}(t,t')\sigma(t')\right\},\quad\text{(C.17)}$$

where

$$\Delta_d(t-t')=(dt)^{-\frac{1}{2}}\Delta_+(t-t')(dt')^{-\frac{1}{2}}.\quad\text{(C.18)}$$

The sequence of equations from (C.11) on then provides us with the expression

$$G(t,t';\phi)=\det(i\Delta_d{}^{-1})^{\frac{1}{2}}R_1{}^{-1}(\phi)\int G_4(t,t';\sigma)\delta\sigma$$
$$\times\exp\left\{-\tfrac{1}{2}i\sigma(\tau)\Delta_+{}^{-1}(\tau,\tau')\sigma(\tau')d\tau d\tau'\right.$$
$$\left.-i\int\sigma(\tau)\Delta_+{}^{-1}(\tau,\tau')\phi(\tau')d\tau d\tau'\right\},\quad\text{(C.19)}$$

where the value of the Jacobian,

$$\partial(\pi)/\partial(\sigma)=\det\Delta_d{}^{-1},\quad\text{(C.20)}$$

was also required. From (C.16), we obtain the solution

$$G_4(t,t')=S(t-t')\exp\left\{-i\tfrac{1}{2}\lambda\int_{t'}^{t}\sigma^2(\tau)d\tau\right\},\quad\text{(C.21)}$$

where

$$S(t-t')=i\theta_+(t-t')\exp[-im(t-t')]\quad\text{(C.22)}$$

is a solution of the equation

$$(-i\partial_t+m)S(t-t')=\delta(t-t'),\quad\text{(C.23)}$$

and $\theta_+(t)$ is the step function in time.

If we insert (C.21) into (C.19), we find once more that the functional integral with respect to σ can be carried out by the standard means of making a displacement and "diagonalizing" the resulting quadratic form in σ. We obtain finally for $G(t,t';\phi)$ the form

$$G(t,t';\phi)=s(t-t')\exp\{-\tfrac{1}{2}i\,\mathrm{Tr}\,\phi\Delta_+{}^{-1}\phi\}$$
$$\times\exp\{i\,\mathrm{Tr}\,\phi\Delta_+{}^{-\frac{1}{2}}2(1+\lambda\mathfrak{M})^{-1}\Delta_+{}^{-\frac{1}{2}}\phi\}$$
$$\times\exp\{-\tfrac{1}{2}\,\mathrm{Tr}\log(1+\lambda\mathfrak{M})\},\quad\text{(C.24)}$$

where Tr denotes diagonal sum. The matrix $\mathfrak{M}$ upon which the physical results of the theory depends is given by the equation

$$\mathfrak{M}_{t,t'}(\tau,\tau')$$
$$=\int_{-\infty}^{\infty}\delta(\tau-\tau'')\theta_+(t-\tau)\theta_+(\tau''-t')\Delta_+(\tau''-\tau')d\tau''$$
$$=\theta_+(t-\tau)\theta_+(t-\tau')\Delta_+(\tau-\tau').\quad\text{(C.25)}$$

From (C.24), one obtains Green's functions for systems containing bosons by suitable differentiation

with respect to ϕ. The real difficulty in treating (C.24) is that of extracting the self-energy and Green's function renormalization from the last factor, without expanding the log in a Taylor series. We have checked that the first few terms are in agreement with the corresponding expressions obtained by expanding our previous results for the renormalization constants. We can recognize the Green's function renormalization as a multiplicative constant and the self-energy from its form

$$\exp[-i\delta m(t-t')].$$

It appears that the meson scattering can be obtained in closed form from the ϕ dependent terms, but we shall omit any further discussion of this matter.

PHYSICAL REVIEW VOLUME 98, NUMBER 5 JUNE 1, 1955

High-Energy Reactions and the Evidence for Correlations in the Nuclear Ground-State Wave Function*

K. A. Brueckner, R. J. Eden,† and N. C. Francis
Indiana University, Bloomington, Indiana

(Received January 13, 1955)

High-energy nuclear reactions which depend strongly on nucleon position correlations in the nuclear ground state are analyzed and shown to give evidence for the existence of marked correlation effects. The following high-energy experiments are considered: nuclear photoeffect, meson absorption in nuclei, deuteron pickup, proton-proton scattering in a nucleus, and meson production in proton-nucleus collisions. The corresponding cross sections depend on a nucleon momentum distribution which can be represented at high energies by a single function giving reasonable agreement with all the experiments considered. This momomentum distribution differs substantially from that for the shell model of the nucleus and thus provides strong evidence for correlation in the nuclear ground-state wave function.

The transformation methods developed in previous papers are used to provide a unified theory of the above five processes. The momentum distribution predicted by this theory is estimated by two methods each of which gives close agreement with the experimentally determined function in the relevant energy ranges.

I. INTRODUCTION

In the last few years a considerable body of evidence has been accumulated which provides information about the ground state of nuclei. This evidence comes primarily from quite different types of experiment and contains, as we shall show, upon first examination apparent contradictions in the information given about the ground state. One type of evidence, that perhaps is best known, comes from the study of ground and low excited states of nuclei and is encompassed in the very successful shell model theory which has been useful and accurate in predictions and understanding of nuclear properties. We shall not attempt to summarize this evidence on the theory here; we only comment that the central feature of the shell model is the assumption that nucleons move in the independent particle states of a uniform potential. The success of the shell model as usually formulated is very intimately connected with this assumption since the existence of long mean free paths and independent particle motion are reflections of the absence of two-body interactions and of the absence of correlations in the ground-state wave function.

The second body of evidence which has direct bearing on the nuclear ground state comes from high-energy experiments. It is the purpose of this paper to summarize this evidence and show how it may be reconciled with the knowledge of nuclear structure derived from low-energy experiments. We consider the following reactions: deuteron pickup, meson capture, high-energy photonuclear effect, high-energy proton-nucleus collisions, and meson production in high-energy proton-nucleus collisions. These high-energy reactions are all similar in that they provide in effect a method of observation with great resolving power since they allow us to probe nuclear structure with particles of wavelength less than the typical nucleon spacing in a nucleus. Consequently we can expect to resolve details of the structure which are not accessible to us if we restrict ourselves to observations at low energy with particles of large wavelength. As we shall see, the information we obtain from the high-energy experiments is in contradiction with the shell model as usually formulated and requires a change in the interpretation of the low-energy nuclear phenomena and their relation to the ground-state wave function.

This new interpretation has been described in

* Supported in part by a grant from the National Science Foundation and the Office of Naval Research and the U. S. Atomic Energy Commission.

† Smithson Research Fellow of the Royal Society, on leave of absence from Clare College, Cambridge, England.

previous papers[1] and is further discussed in Sec. III of the present paper with particular reference to the high-energy experimental information which is described in Sec. II.

In the first part of Sec. III we develop the formalism required for relating the nuclear ground-state wave function to the shell model wave function. In the second part of Sec. II this formalism is utilized to give a unified development of the theories of the nuclear photoeffect, meson capture, and deuteron pickup. We find that the cross sections for these processes depend on a momentum distribution function in the same way as has previously been stated, for example by Chew and Goldberger,[2] provided that the energies involved are sufficiently high. However, our momentum distribution function differs in principle from that of Chew and Goldberger because of our use of a different form of the impulse approximation which appears to have more general validity (this method was first used by Heidmann[3]). Finally in Sec. III we note the cross section formulas for high energy, for proton-proton scattering in nuclei and meson production by protons bombarding nuclei, with particular reference to their dependence on a momentum distribution function.

In Sec. IV we apply the theory to the various experiments. Since our momentum distribution appears in the formulas for cross sections in the same way as that used by previous authors, we are able to make use of earlier analyses of experiments to determine the momentum distribution from experiment. It is found that these experiments can be fitted to reasonable accuracy by a suitable Gaussian momentum distribution in the energy range 50 to 100 Mev. We compare this experimental distribution with our theory in two ways, one of these involves the use of a Hulthén wave function for two nucleons, and the second is partly phenomenological in that we insert an experimental value for the two nucleon scattering matrix. It is found that both these methods give a momentum distribution in agreement with the experimental one in the relevant energy range.

Finally in Sec. V we summarize our conclusions from the evidence presented in this paper.

II. EXPERIMENTAL EVIDENCE

A. Deuteron Pickup

This process is the ejection by fast neutrons of fast deuterons from nuclei[4]; the original theory was developed by Chew and Goldberger[2] and later modified by Heidmann.[3] The phenomenon occurs in the following manner: a fast neutron (90 Mev, for example) in passing through a nucleus occasionally encounters a proton with such a momentum that the relative momentum of the neutron and proton can be accommodated in the deuteron wave function. When this occurs, it is possible for the neutron to "pickup" the proton and emerge as a deuteron. It is apparent that the probability of this process is a sensitive function of the momentum distribution of the proton in the ground-state wave function; consequently the empirical observations can be used to deduce properties of the wave function. The theory as it has been developed is only a Born approximation; the calculations of Chew and Goldberger and of Heidmann are somewhat different in form, but both agree on a simple dependence on the ground-state wave function and probably can be used to draw qualitative conclusions. The result given by Chew and Goldberger is that the cross section depends most strongly on a factor

$$N(\mathbf{k})=\left|\int\psi_I(\mathbf{r})e^{i\mathbf{k}\cdot\mathbf{r}}d\mathbf{r}\right|^2, \tag{1}$$

where $\psi_I(\mathbf{r})$ is the initial wave function of the picked up proton. Their analysis showed that the experiments were consistent with

$$N(\mathbf{k})=\frac{\alpha}{\pi^2}\frac{1}{(\alpha^2+\mathbf{k}^2)^2}, \tag{2}$$

with $\alpha^2/2m=(18)$ Mev. This distribution departs very markedly from a Fermi gas or from an independent-particle function in that a much stronger admixture of high-momentum components is predicted. Thus the pickup process is evidence for a strongly correlated wave function.

B. Meson Capture from Low Bohr Orbits

This process was first observed by Panofsky[5] and has since then been extensively studied. The theoretical analysis[6] shows that it is possible, from a study of the capture of π mesons at rest in light elements, particularly in hydrogen, deuterium, and carbon, to derive some striking information about nuclear structure. The interesting observed feature of the meson capture is that while the reactions in deuterium,

$$\pi^-+\mathrm{D}\rightarrow 2n,\quad \pi^-+\mathrm{D}\rightarrow 2n+\gamma,$$

occur with a ratio of about 2:1; in carbon, the ratio of the cross sections for the two processes

$$\pi^-+\mathrm{C}\rightarrow \text{star},\quad \pi^-+\mathrm{C}\rightarrow \text{star}+\gamma$$

has changed to a number greater than 65. It is theoretically expected that the γ emission, since it occurs

[1] Brueckner, Levinson, and Mahmoud, Phys. Rev. **95**, 217 (1954); K. A. Brueckner, Phys. Rev. **96**, 508 (1954) and Phys. Rev. **97**, 1353 (1955); K. A. Brueckner and C. A. Levinson, Phys. Rev. **97**, 1344 (1955); R. J. Eden and N. C. Francis, Phys. Rev. **97**, 1366 (1955).

[2] G. F. Chew and M. L. Goldberger, Phys. Rev. **77**, 470 (1950).

[3] J. Heidmann Phys. Rev. **80**, 171 (1950).

[4] The experimental evidence is that obtained by J. Hadley and H. F. York, Phys. Rev. **80**, 345 (1950); K. A. Brueckner and W. Powell, Phys. Rev. **75**, 1274 (1949).

[5] Panofsky, Aamodt, and Hadley, Phys. Rev. **81**, 565 (1951).

[6] Brueckner, Serber, and Watson, Phys. Rev. **84**, 258 (1951), referred to as BSW in the text.

essentially as a one nucleon process

$$\pi^- + p \rightarrow n + \gamma$$

will be only weakly affected by the other nucleons. It is possible therefore to reach conclusions on the relative transition rates for the nonradiative capture in deuterium and carbon (or in other light and medium heavy nuclei).

The theory of the capture next is used to show that the nonradiative capture rate is a sensitive measure of the probability of finding two closely associated nucleons in the ground state of the nucleus, since the capture involves large momentum transfers and consequently can take place only through the cooperative effect of at least two nucleons. Qualitatively it is obvious that if in heavy nuclei the nucleons were randomly distributed, the probabilities of finding two nucleons close together is small, and the meson capture rate would be small, in contract to the effect observed. The result of a quantitative analysis of the various phenomena affecting the radiative and nonradiative capture showed that the nucleons are indeed highly correlated.

According to BSW, the transition rate depends on a factor $P(z_{NN})$ which is the probability of finding two nucleons with a separation $z_{NN} \approx \hbar/\Delta p$, where Δp is the momentum transferred to the two nucleons. For an uncorrelated nucleus, $P(z_{NN})$ is just the nuclear density $1/v$, where v is the total volume $(4/3)\pi r_0^3 A$. Thus it is useful to define a correlation factor f by the equation

$$P(z_{NN}) = f \cdot [(4/3)\pi r_0^3 A]^{-1}.$$

The analysis of BSW showed that $f \approx 35$ and thus that the wave function for the nuclear ground state must depart very markedly from that for an uncorrelated system. We will return to an alternative formulation of this result later in Sec. IV.

C. Photonuclear Effect at High Energy

The cross section for the photoejection of high-energy (50–200 Mev) protons from nuclei has been known for some time to be much larger than would be given by an independent-particle model. The presence of a large high-energy component of fast protons indicates quite unambiguously the existence of high-momentum components in the ground-state wave function. The process has been analyzed by Levinthal and Silverman[7] and by Levinger,[8] all in the dipole approximation. The former authors show that the observed cross section is in good agreement with the Chew-Goldberger[2] momentum distribution for the ground-state wave function. The analysis of Levinger[8] uses a somewhat different method of calculation to which we will return later, but he also concludes that the experiment shows the marked departure at high-momentum values of the wave function from that for an uncorrelated system.

[7] C. Levinthal and A. Silverman, Phys. Rev. **82**, 822 (1951).
[8] J. S. Levinger, Phys. Rev. **84**, 43 (1951).

D. Proton-Nucleus Scattering and Meson Production in Proton-Nucleus Collision

These processes,

$$p + \text{nucleus} \rightarrow \text{nucleus} + p',$$
$$p + \text{nucleus} \rightarrow \text{nucleus} + \pi,$$

can be used to give quite quantitative indications of the departures of the ground-state nuclear wave function from that of an independent particle model. In these cases a contribution to the cross section comes from each component of the nucleus ground-state momentum distribution. Thus if the cross section for the elementary process involving free nucleons is known, then the observed cross section is a function only of the momentum distribution. The analyses of Henley[9] and of Wolff[10] show that the momentum distribution is determined with fair accuracy, and is fitted well by a Gaussian

$$|\psi(\mathbf{p})|^2 = \frac{1}{\alpha^3 \pi^{\frac{3}{2}}} \exp(-\mathbf{p}^2/\alpha^2), \tag{3}$$

where α^2 is such that the mean kinetic energy is 19.3 Mev. This distribution does not depart as strongly from an uncorrelated wave function as does the wave function used by Chew and Goldberger[2]; the difference, however, is still very marked, as is shown in Fig. 1.

E. Summary of Experimental Results

All the experiments discussed in this section are similar in that phenomena are observed which depend strongly on strong correlation effects in the coordinate space wave function or, equivalently, on an appreciable admixture of high momentum components in the momentum space wave function. Thus it is evident that the nuclear ground-state wave function cannot describe nucleons moving as independent particles, and reinterpretation of the independent particle model is necessary. In the next section we shall show how this can be done in the general case, using the techniques and concepts we have developed for treating the nuclear ground state. We shall also make detailed applications to specific cases of particular interest.

III. GENERAL THEORY

A. General Description of Method

The processes considered in the previous section have an important common feature; an appreciable contribution to the cross sections comes from an initial nuclear ground state in which at least one nucleon has a high momentum. We make the physical assumption that this high momentum is the result of strong inter-

[9] E. M. Henley, Phys. Rev. **85**, 204 (1952); this paper lists the relevant experimental references.
[10] P. A. Wolff, Phys. Rev. **87**, 434 (1952); see also the experimental results given by Cladis, Hess, and Mayer, Phys. Rev. **87**, 425 (1952).

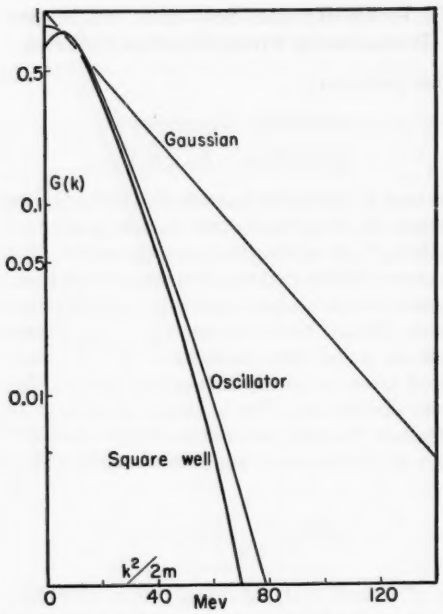

FIG. 1. Momentum distribution $G(k)$ of 8 neutrons and 8 protons in the independent-particle states of a square well with infinite walls and of a harmonic oscillator well. For comparison the Gaussian distribution of Eq. (3) is also given.

actions between a pair of nucleons; indeed the experiments[11] seem to verify this assumption. Consequently the ejection of a fast nucleon by the photoprocess, by meson capture or as a member of the deuteron in deuteron pickup, will usually be associated with the ejection of another fast nucleon which was originally paired with the directly ejected particle. Thus the process corresponds to ejection of a fast pair of nucleons from the ground state, with the residual nucleus only weakly excited. This assumption (or a stronger assumption) is explicit or implicit in the theory of all the high-energy processes we have considered.

It is at this point that the usefulness of the high-energy processes in the study of nuclear structure is particularly apparent. As we will see in the following development of the theory, if the ground-state function is weakly correlated as for a Fermi gas or an independent particle model, then the matrix elements will vanish in the former case or be very small in the latter case. Since the predominant low-momentum components in the wave function make very little or no contribution to the matrix elements, the importance of the high momentum components is greatly enhanced and hence it is possible to get detailed information about this aspect of the wave function. Before proceeding to the theory of these processes, we shall first make some brief remarks on the nature of the ground-state wave function and in particular on our interpretation of the shell model and its reconciliation with the simultaneous success of the shell model and with the high-energy phenomena which interest us.

It is well known from both experiment and theory that the nucleon-nucleon interactions are strong and short ranged. Consequently if the same forces act when nucleons are immersed in a many-body medium, one will very naturally expect to observe under appropriate experimental conditions very appreciable correlations in the nuclear wave function. On the other hand, the success of the shell model has often been assumed to indicate that the two-body forces in nuclear matter are in fact much weaker and long-ranged and can lead in an excellent approximation to a uniform Hartree field acting on the nucleons. The origin of this effect might be, for example, a strongly nonlinear behavior of the meson fields so that a very large damping effect modifies and smooths out the forces in nuclear matter. This effect can arise from many-body forces or from a nonlinearity in the meson field equations. In either case the effective potential felt by one nucleon would not have the rapidly varying spatial dependence which would result if the two-body forces remained strong, and a uniform potential would be a good approximation. A direct consequence would then be that the nuclear wave function would be weakly correlated, in disagreement with the high-energy experiments we are analyzing. It is also perhaps worth commenting here that the theoretical expectations for the character of the two-body and many-body interactions also strongly suggest that the strong two-body forces are still effective in a medium of nuclear density.

Thus we must adopt a picture of strong two-body nuclear potentials and modify our views of the shell model. The concepts and techniques which we have developed are discussed in detail in other papers[1]; the essential points may be summarized in the following way. We require that the shell model (or independent particle) wave function be a description not of nuclear motion but of a "collective particle" motion, the actual nucleon wave function being generated from the "shell model" wave function by a transformation. This transformation has (among other effects) the effect of introducing correlations and hence high momentum components into the wave function. Under certain conditions the behavior of the shell model "particles" is very nucleon-like, but this approximate identification is not generally valid. We see, in fact, a complete breakdown of the approximate description in the region of strong correlations or high momenta, where the departure of the simple shell model states from actual nuclear states becomes particularly marked. Stated in other terms, a consequence of our description of the nucleus is that the departure of shell model states from nuclear states is not very appreciable if observations of the state are

[11] Byfield, Kessler, and Lederman, Phys. Rev. **86**, 17 (1952); see also reference 16. The effect of correlations involving more than two nucleons will become apparent only in the high-energy tail of the spectrum of the ejected nucleons, this will not influence appreciably the total cross sections of the processes we consider.

made which depend only on averages over space or time intervals which are large compared with characteristic correlation distances or fluctuation frequencies in the state. In the other extreme, observations at high frequencies or short wavelengths readily detect the departure of the ground state from that for an uncorrelated system.

We next shall summarize the necessary formalism which we need in the following discussions. For further details of notation and explanation the reader should refer to previous papers.[1] The nuclear ground-state wave function $\Psi_0(A)$ is in general a complicated function of the coordinates of the nucleons and contains marked correlations as a result of the strength of the two body interactions. It is related to the "shell-model" or "independent particle" wave function $\Phi_0(A)$ by a transformation function or "model operator" F, i.e.,

$$\Psi_0(A)=F\Phi_0(A). \tag{4}$$

Since $\Phi_0(A)$ is a weakly correlated function (a degenerate Fermi gas for the lowest energy state), F has the effect of introducing correlations into the wave function. Clearly, therefore, explicit knowledge of the transformation F and thus of the wave function $\Psi_0(A)$ is necessary in our problem, depending as it does on the correlations in the wave function. This is in marked contrast to determination of the ground-state energy, for example, where only the transformed Hamiltonian (the independent particle Hamiltonian) need be known and there are no departures of the particle (not nucleon) motion from independent particle motion.

The explicit form of the transformation, which has been used successfully in the considerations of other ground-state properties, is given by the following set of coupled equations:

$$F=1+\frac{1}{e}\sum_{ij} I_{ij}F_{ij}, \tag{5}$$

$$F_{ij}=1+\frac{1}{e}\sum_{lm\neq ij} I_{lm}F_{lm}, \tag{6}$$

where the "energy denominator" e is

$$e=E_0-\sum_i T_i-V_c, \tag{7}$$

and the energy eigenvalue E_0 is determined by

$$(E_0-\sum T_i-V_c)\Phi_0(A)=0. \tag{8}$$

The quantities I_{ij} and V_c are simply related to the two-body scattering operators t_{ij} which are defined by the equations:

$$t_{ij}=v_{ij}+v_{ij}(1/e)t_{ij}, \tag{9}$$

where v_{ij} is the potential between nucleons i and j. The operators I_{ij} are those parts of the t_{ij} which are nondiagonal with respect to the nuclear states; finally, the uniform potential V_c is defined by

$$V_c=\tfrac{1}{2}\sum_{ij} t_{cij}, \tag{10}$$

where t_{cij} is the diagonal part of t_{ij}.

Some features of these results and of the transformation F are easily seen. The incoherent or nondiagonal operators I_{ij} cause transitions from the uncorrelated independent-particle state $\Phi_0(A)$; the effect is closely analogous to an inelastic scattering of particles a pair at a time out of the Fermi gas to excited states. Consequently the departures of the wave function $\Psi_0(A)$ from $\Phi_0(A)$ are very closely related to the details of the inelastic scattering of nucleon by nucleon and thus to the strength and range of the two-body potentials.

We shall in the following parts of this section make explicit applications of these principles to the high-energy phenomena we have summarized in the previous section. Where the development follows the work done by other authors, we shall abbreviate the discussion where this can be conveniently done.

B. Application to Specific Phenomena

(1) *Nuclear Photoeffect*

The cross section for the production of high-energy protons by γ radiation of a nucleus in dipole approximation is obtained from the matrix element H_{0f} given by

$$H_{0f}=\left(\Psi_f(A),\sum_{i=1}^{Z} e\mathbf{r}_i\cdot\mathbf{A}\Psi_0(A)\right), \tag{11}$$

where $e\mathbf{r}_i$ is the charge moment for the ith proton. We approximate to the final state wave function by making use of our physical assumption that two of the nucleons have high momenta so the wave function is approximately separable, i.e., we assume

$$\Psi_f(A)=\Psi_f(1,2)\Psi_f(A-2). \tag{12}$$

We suppose that nucleon "1" is a proton; the associated nucleon "2" must then be a neutron since the contribution from two protons is zero in the dipole approximation. The assumption of a product wave function is equivalent to the neglect of corrections due to antisymmetrization between the high-momentum and low-momentum particles, but $\Psi_f(1,2)$ and $\Psi_f(A-2)$ will be separately antisymmetrized. With a final wave function of this form we can neglect contributions to H_{0f} from terms not involving the position $\mathbf{r}_1$ associated with proton 1.

We may use the method of partial closure to eliminate the wave function $\Psi_f(A-2)$ from the cross section provided that the rest of the matrix element depends only weakly on the energies of excitation E_f of the residual nucleus. This will be the case if the energies of the ejected particles are high; it is also possible to correct approximately for the error made in the closure

sum by altering the energy conservation law to include a mean excitation energy $\bar{E}_f$; i.e., we can set

$$E_0+E_\gamma=k_1^2/2m+k_2^2/2m+\bar{E}_f, \tag{13}$$

where $\bar{E}_f$ can either be estimated or regarded as a phenomenological parameter. Making this approximation, we find

$$\sum_f|H_{0f}|^2=ZN\int d\mathbf{r}_3\cdots\int d\mathbf{r}_A \times\left|\int\int\Psi_f^*(1,2)e\mathbf{r}_1\cdot\mathbf{A}\Psi_0(1,2,\cdots,A)d\mathbf{r}_1d\mathbf{r}_2\right|^2, \tag{14}$$

the factor of NZ coming from the number of ways of choosing the protons (1) and neutrons (2). This result also neglects interference terms which is consistent with our assumptions about the separability of the final state wave function. In this matrix element the final wave function can be determined with considerable accuracy since it is probably safe to assume that this is simply given by the solution to the two-body problem at high energy neglecting the effects of the nuclear medium. Thus only the initial wave function is unknown and its specifications largely determines the matrix element and the cross section.

It might be pointed out at this point that in the assumptions we have just made in treating the final states, the possible attenuation by nuclear collision of the outgoing proton wave have been neglected. One consequence of this assumption is that the calculated cross section will depend on the total number of protons in the nucleus, i.e., that it is a volume effect. The best evidence for this assumption comes from the photoeffect itself[8] and also from the process of meson capture in nuclei as studied by Byfield, Kessler, and Lederman.[11] We shall in this section and also in discussing the remaining phenomena neglect the possibility of absorption of the outgoing particles and as a consequence overestimate the cross sections by a factor depending on the process considered. The appropriate correction factor can usually be estimated without difficulty.

The wave function $\Psi_0(A)$ defined by Eqs. (4) and (5) to (10) is extremely difficult to give explicitly because of its very complicated dependence on the incoherent operators I_{ij}. If, however, we are willing to assume that the necessary correlation is largely a result of two-body interactions, then we can approximate to the function F by expanding it to first order in I_{ij}. Consequently we cannot expect fully quantitative knowledge of the wave function in the important high-momentum region, although the error introduced is probably not enough to alter the order of magnitude of the result. In this approximation, we take

$$\Psi_0(1,2,\cdots,A)=\left(1+\frac{1}{e}\sum t_{ij}\right)\Phi_0(1,2,\cdots,A). \tag{15}$$

We have replaced I_{ij} by t_{ij} in F since here only off-diagonal matrix elements contribute to the cross section. The wave function $\Phi_0(1,2,\cdots,A)$ can be written (treating neutrons and protons separately):

$$\frac{1}{\sqrt{(ZN)}}\sum_{lm}(\phi_l(1)\phi_m(2))\Phi_0{}^{lm}(3,\cdots,A) \tag{16}$$

with $\Phi_0{}^{lm}(3,\cdots,A)$ normalized to unity. Only the terms involving $\mathbf{r}_1$ and $\mathbf{r}_2$ will make any important contribution to the cross section, hence after integrating over the variables $\mathbf{r}_3,\cdots,\mathbf{r}_A$ we get

$$\sum_f|H_{0f}|^2=ZN\sum_{lm}\left|\frac{1}{\sqrt{(ZN)}}\int\int\Psi_f^*(1,2)e\mathbf{r}_1 \cdot\mathbf{A}F_{12}\phi_l(1)\phi_m(2)d\mathbf{r}_1d\mathbf{r}_2\right|^2, \tag{17}$$

where l is summed over proton and m over neutron states, and

$$F_{12}=1+(1/e)t_{12}. \tag{18}$$

We define a quantity $\chi_{lm}'(1,2)$ by the equation

$$\chi_{lm}'(1,2)=F_{12}\phi_l(1)\phi_m(2) \tag{19}$$

(the prime distinguishes this from a symmetrized form used later). Then $\chi_{lm}'(1,2)$ will give the high-momentum components for the nucleons 1 and 2 in the nucleus. It is important to note that our approximation method is based on the fact that only high-momentum components will give large contributions to the matrix element so that it has been possible to neglect terms in Eq. (15) which do not refer to particles 1 and 2. For these reasons it would be misleading to regard $\chi_{lm}'(1,2)$ as a kind of two-body wave function in the nucleus.[12] We get now

$$\sum_f|H_{0f}|^2=\sum_{lm}\left|\int\int\Psi_f^*(1,2)e\mathbf{r}_1\cdot\mathbf{A}\chi_{lm}'(1,2)d\mathbf{r}_1d\mathbf{r}_2\right|^2. \tag{20}$$

This can be compared (see Levinger[8]) with the deuteron photoeffect, for which

$$|H_{0f}{}^D|^2=\left|\int\int\Psi_f^*(1,2)e\mathbf{r}_1\cdot\mathbf{A}\Psi_D(1,2)d\mathbf{r}_1d\mathbf{r}_2\right|^2, \tag{21}$$

where $\Psi_D(1,2)$ denotes the deuteron wave function.

Thus a comparison of the experimentally determined matrix elements for the photodisintegration of the nucleus (with fast proton ejection) and of the deuteron can be used to give us rather directly a relation between the deuteron and ground-state wave functions. This technique is particularly useful if we do not wish (or are unable) to give explicitly the final two-particle wave function $\Psi_f^*(1,2)$ since this enters very nearly as a

[12] A function analogous to our $\chi_{lm}{}^{(1,2)}$ is introduced on physical grounds by Levinger (reference 8) following a method of Heidmann (reference 3).

common factor into both matrix elements [Eqs. (20) and (21)].

(2) *Meson Capture*

The operator describing the absorption of a meson by a nucleon can be written[6,13]

$$a\phi(1)+b\sigma_1\cdot\nabla\phi(1), \tag{22}$$

where $\mathbf{r}_1$ denotes the coordinate of the nucleon which absorbs the meson, and $\phi(1)$ denotes the meson field at $\mathbf{r}_1$. If we assume the meson to be in an S state, $\phi(1)$ will be sufficiently slowly varying over the nucleus that we can replace it by some mean value ϕ_0, and similarly replace $\nabla\phi(1)$ by a mean gradient written $\nabla\phi_0$.

The matrix element for meson absorption in the nucleus is given by

$$H_{0f}=\sum_i(\Psi_f(A),\{a\phi_0+b\sigma_i\cdot\nabla\phi_0\}\Psi_0(A)). \tag{23}$$

We assume as with the photoeffect that two nucleons in the final state have high momenta and hence their wave function is separable from that for the residual (A-2) nucleons. Then

$$\Psi_f(A)=\Psi_f(1,2)\Psi_f(A-2). \tag{24}$$

Write θ_0 for the operator $a\phi_0+b\sigma_1\cdot\nabla\phi_0$, and let

$$\Psi_f(1,2)=F_{12}\Phi_f(1,2), \tag{25}$$

where $\Phi_f(1,2)$ denotes a plane wave state for the two outgoing nucleons. Then, using partial closure to eliminate $\Psi_f(A-2)$ and transforming $\Psi_0(A)$, we get for the nucleon pair (1,2):

$$\sum_f|H_{0f}|^2=\int d\mathbf{r}_3\cdots\int d\mathbf{r}_A\left|\int\int\Phi_f^*(1,2)(F_{12}^\dagger\theta_0)\times F_{12}\Phi_0(1,2,\cdots,A)d\mathbf{r}_1d\mathbf{r}_2\right|^2. \tag{26}$$

Hence

$$\sum_f|H_{0f}|^2=\frac{2}{A^2}\sum_{lm}\left|\int\int\Phi_f^*(1,2)(F_{12}^\dagger\theta_0)\chi_{lm}(1,2)d\mathbf{r}_1d\mathbf{r}_2\right|^2, \tag{27}$$

where the $\chi_{lm}(1,2)$ is properly antisymmetrized, i.e.,

$$\chi_{lm}(1,2)=(1/\sqrt{2})F_{12}\{\phi_l(1)\phi_m(2)-\phi_m(1)\phi_l(2)\}. \tag{19a}$$

It is useful to compare this with the corresponding process for meson absorption in the deteron for which

$$|H_{0f}^D|^2=\left|\int\Phi_f^*(1,2)(F_{12}^\dagger\theta_0)\Psi_D(1,2)d\mathbf{r}_1d\mathbf{r}_2\right|^2. \tag{28}$$

One result is that it is possible, if we wish to interpret the operator $(F_{12}^\dagger\theta_0)$ as a phenomonological meson absorption operator, to use the experiment to deduce relationships between the nuclear wave function and the deuteron wave function $\Psi_D(1,2)$. This method was used by BSW[6] in their analysis.

(3) *Deuteron Pickup*[14]

The Born approximation matrix element for this process is

$$H_{0f}=(\Psi_f(0,1,2)\Psi_f(A-2),\,V(\mathbf{r}_0-\mathbf{r}_1)e^{i\mathbf{k}_0\cdot\mathbf{r}_0}\Psi_0(A)). \tag{29}$$

Then following the same techniques as those used in the previous paragraphs, we can bring this to the form

$$\sum_f|H_{0f}|^2=\int d\mathbf{r}_3\cdots\int d\mathbf{r}_A\left|\int\Psi_f^*(0,1,2)V(\mathbf{r}_0-\mathbf{r}_1)\times e^{i\mathbf{k}_0\cdot\mathbf{r}_0}F_{12}\Phi_0(1,\cdots,A)d\mathbf{r}_0d\mathbf{r}_1d\mathbf{r}_2\right|^2. \tag{30}$$

If we assume

$$\Psi_f(0,1,2)=e^{i\mathbf{K}(\mathbf{r}_0+\mathbf{r}_1)/2}\phi(\mathbf{r}_0-\mathbf{r}_1)e^{i\mathbf{k}_2\cdot\mathbf{r}_2}, \tag{31}$$

where

$$\Psi_0(0,1)=e^{i\mathbf{K}(\mathbf{r}_0+\mathbf{r}_1)/2}\phi(\mathbf{r}_0-\mathbf{r}_1) \tag{32}$$

is the deuteron wave function, we obtain

$$\sum_f|H_{0f}|^2=\frac{2}{A^2}\sum_{lm}\left|\int e^{-i\mathbf{k}_1\cdot\mathbf{r}_1}e^{-i\mathbf{k}_2\cdot\mathbf{r}_2}\chi_{lm}(1,2)d\mathbf{r}_1d\mathbf{r}_2\right|^2\times\left|\int\phi^*(\mathbf{r})V(\mathbf{r})e^{i(\mathbf{k}-\mathbf{K}/2)\cdot\mathbf{r}}d\mathbf{r}\right|^2. \tag{33}$$

The first factor corresponds to the momentum distribution for nucleons 1 and 2 in the nucleus. In our notation nucleon 1 is picked up and goes off as part of the deuteron $\Psi_0(0,1)$ and nucleon 2 is a recoil nucleon which we have represented by a plane wave. The second factor can be evaluated by substituting an explicit form for the relative coordinate part $\phi(\mathbf{r})$ of the deuteron wave function and using the Schrödinger equation to rewrite $V(\mathbf{r})$ in terms of the binding energy and momenta.

(4) *Proton-Proton Scattering in Nuclei and Meson Production by Protons Bombarding Nuclei*

For a high-energy incident proton ejecting a second proton from a nucleus it is a good approximation to suppose that the incident proton collides only with the one nuclear particle.[10] The same approximation can be made in considering the production of mesons by a proton colliding with a nucleus.[9] It is worth noting that both these processes are possible if the second proton (nucleon) was not bound in the nucleus but was free. This has the effect that for a limited range of the momenta of the outgoing particles a large contribution to the cross section will come from considering the

[13] See, for example, K. A. Brueckner and K. M. Watson, Phys. Rev. **83**, 1 (1951).

[14] The theory in this paragraph is similar to that of Heidmann (reference 3) except (1) we derive the correlations in the ground state wave function by transformation theory which allows for the effects of the nuclear medium whereas Heidmann obtains them as physical grounds, and (2) we use partial closure to eliminate the final state.

nucleus to be a Fermi gas, i.e., from taking the unit term in Eq. (5) which gives the transformation of the a Fermi gas, i.e., from taking the unit term in Eq. (5) which gives the transformation of the Fermi gas wave function to the actual nuclear wave function. However, if one looks instead at momentum regions which require a large momentum value for the proton initially in the nucleus, the principal contribution to these cross sections will come from matrix elements obtained by methods analogous to those considered in the previous sections. These involve the quantity $\chi_{lm}(1,2)$ and lead to a cross section which depends on a known factor (or one which can be found by comparison with experiment) and the momentum distribution. The analysis of p-p scattering in the nucleus has been given by Wolff,[10] and that of meson production in the nucleus by Henley.[9] We will not repeat these calculations using our methods as they would involve a lengthy analysis of approximations which are made by physical arguments. However, for comparison we note the formula for the relevant cross section given by Wolff and by Henley.

For proton-proton scattering in the nucleus, Wolff[10] obtains the cross section for an incoming proton of momentum $\mathbf{p}$ and final nucleons of momentum q and s:

$$\frac{d^2\sigma}{d_A dq}=\frac{4\pi M^2}{\hbar^4 p}\sum|a|^2\int\frac{d\mathbf{k}}{(2\pi)^3}N(\mathbf{k})\times\delta\left(p^2-q^2-(\mathbf{p}+\mathbf{k}-\mathbf{q})^2-\frac{2M}{\hbar^2}B_{ij}\right)\cdot\frac{q^2}{(2\pi)^3}, \quad (34)$$

where $\mathbf{k}=(\mathbf{q}+\mathbf{s}-\mathbf{k})$ and $N(k)$ is the momentum distribution for a nucleon in the nucleus. The detailed form of $N(k)$ as predicted by our method will be discussed in the next section.

The cross section for the creation of a π meson of momentum q is given by Henley[9]:

$$\frac{d^2\sigma_A{}^0(\pi^+)}{dTd\Omega_q}=\frac{1}{v_0}\int\left[Z\frac{d^2\sigma(p-p)}{dTd\Omega_q}v_R+(A-Z)\frac{d^2\sigma(p-n)}{dTd\Omega_q}v_R\right]\rho(\mathbf{k})d\mathbf{k}, \quad (35)$$

where $\rho(\mathbf{k})$ is the momentum distribution for the struck nucleon in the nucleus, and $\sigma(p-p)$, $\sigma(p-n)$ denote the cross sections for collisions of free nucleons; v_0 and v_r represent the relative velocities of the target nucleus and nucleon with respect to the incident nucleon; T is the meson kinetic energy.

IV. APPLICATION OF THE THEORY TO EXPERIMENT

A. Dependence of the Theoretical Cross Sections on a Momentum Distribution in the Nucleus

In discussing the high-energy phenomena, we have shown that in each case the matrix element depends most strongly on the ground-state wave function through a term

$$f(\mathbf{k}_1,\mathbf{k}_2)=\frac{2}{A^2}\sum_{lm}\left|\int(2\pi)^{-3}e^{-i\mathbf{k}_1\cdot\mathbf{r}_1}e^{-i\mathbf{k}_2\cdot\mathbf{r}_2}\times\chi_{lm}(\mathbf{r}_1\mathbf{r}_2)d\mathbf{r}_1d\mathbf{r}_2\right|^2, \quad (36)$$

where k_1 and k_2 are the final momenta of the two fast ejected nucleons and χ_{lm} is, in the region of high momenta, an approximation to the initial wave function of the two nucleons. This result can be brought to a simpler form if we introduce relative and center-of-mass coordinates and further assume that

$$\chi_{lm}(\mathbf{r}_1,\mathbf{r}_2)=v^{-\frac{1}{2}}\chi_{lm}(\mathbf{r}_1-\mathbf{r}_2)e^{i(\mathbf{k}_l+\mathbf{k}_m)\cdot(\mathbf{r}_1+\mathbf{r}_2)/2}. \quad (37)$$

This is equivalent to the reasonable assumption that the center-of-mass moves with the momenta characteristic of the Fermi gas and that the departures from a Fermi gas occur only in the dependence on the relative coordinate. Making this approximation we find

$$f(\mathbf{k}_1,\mathbf{k}_2)=\frac{2}{A^2}\sum_{lm}\left|\int(2\pi)^{-\frac{3}{2}}e^{-i(\mathbf{k}_1-\mathbf{k}_2)\cdot\mathbf{r}/2}\chi_{lm}(\mathbf{r})d\mathbf{r}\right|^2\times\delta(\mathbf{k}_1+\mathbf{k}_2-\mathbf{k}_l-\mathbf{k}_m), \quad (38)$$

where we have replaced the Kronecker delta function giving total-momentum conservation by the Dirac delta function, using the relation

$$(\delta_{\mathbf{k}_1+\mathbf{k}_2,\mathbf{k}_l+\mathbf{k}_m})^2=[(2\pi)^{\frac{3}{2}}v^{-\frac{1}{2}}]^2\delta(\mathbf{k}_1+\mathbf{k}_2-\mathbf{k}_l-\mathbf{k}_m), \quad (39)$$

a further simplification is possible if we assume (as we have previously) that k_1, $k_2\gg k_l$, k_m and consequently that the momentum conservation gives approximately $\mathbf{k}_1=-\mathbf{k}_2$. In this approximation we can also relax the restrictions arising from momentum conservation and sum freely over l,m. This is related to the approximation made in using partial closure and as there we can introduce a correction by altering the energy conservation law to take account of a mean excitation of the residual nucleus.

We thus are led (dropping the delta function) to the final result

$$g(\mathbf{k}_1)=f(\mathbf{k}_1,-\mathbf{k}_1)\approx\frac{2}{A^2}\sum_{lm}\left|\int\frac{e^{-i\mathbf{k}_1\cdot\mathbf{r}_1}}{(2\pi)^{\frac{3}{2}}}\chi_{lm}(\mathbf{r})d\mathbf{r}\right|^2. \quad (40)$$

The summation over the $A^2/2$ pairs of states lm is equivalent (with the factor $2/A^2$) to averaging over a Fermi gas. This result is now closely analogous to the results used by Chew-Goldberger, Levinthal-Silverman, Henley, and Wolff, who have all deduced a dependence of the cross section on a factor which they call the Fourier transform of the wave function of the *single*

particle involved; i.e., they introduce a function $N(\mathbf{k})$

$$N(\mathbf{k})=\left|\int \frac{e^{-i\mathbf{k}\cdot\mathbf{r}}}{(2\pi)^{\frac{3}{2}}}\phi(\mathbf{r})d\mathbf{r}\right|^2, \tag{41}$$

where $\phi(\mathbf{r})$ is assumed to be the particle wave function. Our result differs however in that $\chi_{lm}(\mathbf{r})$ is a function depending on the relative coordinate for a pair of nucleons and in that an average is to be carried out over the initial state of the two ejected nucleons.

B. Determination of the Function $g(\mathbf{k})$ from Experiment

We shall not attempt to make explicit calculations for the various phenomena; instead we shall make use of the empirical determinations of the function $N(\mathbf{k})$ which have been made. In the case of deuteron pickup,[15] proton-proton scattering in nuclei,[10] and meson production by protons as nuclei,[9] it has been shown that a function

$$N(\mathbf{k})=\exp(-k^2/\alpha^2)(\alpha^2\pi^{\frac{1}{2}})^{-1}, \tag{42}$$

with $\alpha^2/2m\approx 14$ Mev gives a satisfactory fit to the experiments. We have also made an analysis of the photoproton data similar to that made by Levinthal and Silverman[7] using this Gaussian distribution. The results are shown in Fig. 2 which indicates that the shape of the predicted distribution agrees well with experiment. The magnitude of the predicted cross sections is considerably larger than the results of Levinthal and Silverman[7] and a factor of 10 has been introduced to renormalize the predicted cross section. The discrepancy is not so large, however, if comparison is made with the results of Keck[16] and Walker[17] which are a factor of 5 to 7 larger. Consequently we conclude that the Gaussian momentum distribution which is identical with that used in the other analyses also approximately fits the photoproton data, at least as well as the accuracy of the treatment would lead one to expect.

The remaining process of meson capture can also be easily brought into a form which allows comparison with the assumed Gaussian distribution. This is most simply done if we make use of the result of BSW[6] which shows that the ratio

$$\left|\int e^{-i\mathbf{p}\cdot\mathbf{r}}\phi(r)d\mathbf{r}\right|^2 \Big/ \left|\int e^{-i\mathbf{p}\cdot\mathbf{r}}\psi_D(\mathbf{r})d\mathbf{r}\right|^2 \geq 2.39, \tag{43}$$

where $\psi_D(\mathbf{r})$ is the deuteron wave function and p is the momentum carried off by one nucleon $[p\sim(M\mu)^{\frac{1}{2}}]$. Using for ψ_D a Hulthén wave function with standard

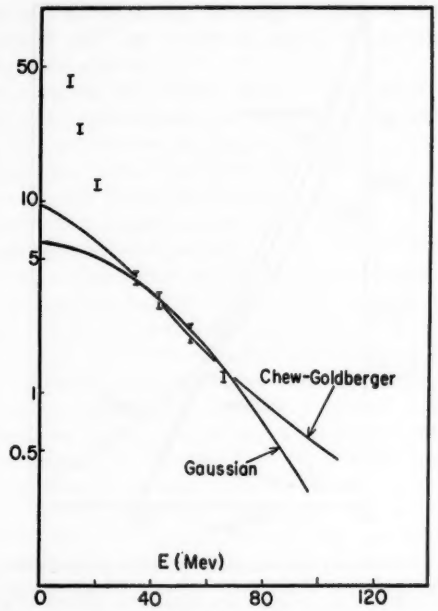

FIG. 2. Theoretical predictions for the photoproton process based on a Chew-Goldberger and on the Gaussian distribution of Eq. (3). The experimental data are taken from the paper of Levinthal and Silverman (see reference 7). The theoretical results are normalized to the experiments at 41.5 Mev by a factor of 0.75 for the Chew-Goldberger and 0.15 for the Gaussian.

parameters, and taking for $\phi(\mathbf{r})$ a normalized Gaussian $N_\beta\exp(-\beta^2r^2/2)$ it is possible to determine a value for $\beta^2/2M$ which agrees with the empirically determined ratio. The result is that $\beta^2/2M\geq 14.4$ Mev which agrees very well with the results of the other experiments.

We therefore can well represent the results of all of the experiments by the same momentum distribution. Returning to our definition of $g(k)$ [Eq. (40)], we thus find that if our theory predicts correctly the result,

$$\frac{2}{A^2}\sum_{lm}\left|\int \frac{e^{-i\mathbf{p}\cdot\mathbf{r}}}{(2\pi)^{\frac{3}{2}}}\chi_{lm}(\mathbf{r})d\mathbf{r}\right|^2 = N_\alpha\exp(-p^2/\alpha^2), \tag{44}$$

for high values of the momentum p (corresponding to energy per particle of 75 to 150 Mev), then we can also expect to find good agreement with the high-energy experiments.

C. Calculation of Momentum Distribution

In this section we shall attempt to determine the function $g(k)$ defined in Eq. (40). As we shall show, there are two rather different methods which lead to essentially the same result. Let us consider the function $\chi_{lm}(\mathbf{r})$, which is the wave function for the relative coordinate $\mathbf{r}$. We first approximate this in a manner similar to that used by Levinger and by Heidmann,

[15] The use of a Gaussian distribution to fit deuteron pickup has been tested by Henley (see reference 9).
[16] J. Keck, Phys. Rev. **85**, 410 (1952).
[17] D. Walker, Phys. Rev. **81**, 634 (1951).

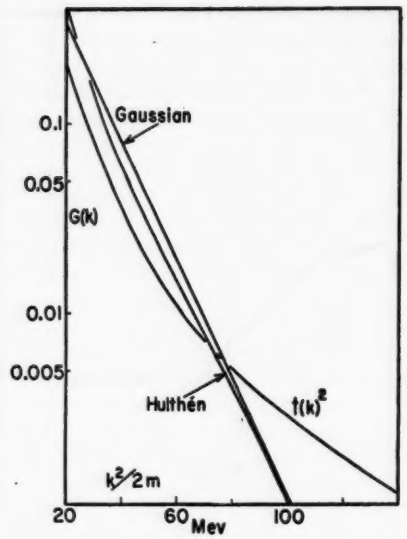

FIG. 3. Calculated momentum distributions for particles in the nucleus compared with the empirically derived Gaussian of Eq. (3). The results of the two methods discussed in the text are given, labelled Hulthén for the result of Eq. (48) and t^2 for the result of Eq. (52).

i.e., we write for the S-wave part of the function

$$\chi_{lm}(\mathbf{r})=\frac{1}{v^{\frac{1}{2}}}\left[\frac{\sin(kr+\delta)}{\sin\delta}-f(r)\right]\Big/\left[r(\alpha^2+k_{lm}^2)^{\frac{1}{2}}\right], \quad (45)$$

which is correctly normalized in the nuclear volume v. $1/\alpha$ is the scattering length; $f(r)$ is a function which is equal to one at the origin and depends in detail on the explicit choice of the potential. At small distances this can also be written as

$$\chi_{lm}(\mathbf{r})=\frac{1}{v^{\frac{1}{2}}}\left[e^{-\alpha r}-f(r)\right]/\left[r(\alpha^2+k_{lm}^2)^{\frac{1}{2}}\right]. \quad (46)$$

For our simple example we take for $f(r)$ the result appropriate to a Hulthén function

$$f(r)=e^{-\beta r}. \quad (47)$$

We use the Hulthén function for the following reasons: (i) the Hulthén function gives a cross section which is of approximately the correct magnitude at the high energies we consider, (ii) the major contribution to the cross section from the Hulthén potential comes from S-wave scattering, (iii) a repulsive core potential would require calculations for at least one higher partial wave since the S-wave is anomalously small in the energy region of interest. In addition it would lead to a result which would be very sensitive to the potential shape in the region of the core boundary where little is known about its detailed form.

Inserting the wave function of Eq. (46) into Eq. (44), we find

$$g(\mathbf{p})=\frac{2}{A^2}\sum_{lm}\frac{(4\pi)^2}{(2\pi)^3}\frac{A}{v}\left[\frac{(\beta^2-\alpha^2)}{(p^2+\beta^2)(p^2+\alpha^2)}\right]^2(\alpha^2+k_{lm}^2)^{-1}. \quad (48)$$

We approximate to the average over the Fermi gas by using Levinger's result $\langle(\alpha^2+k_{lm}^2)^{-1}\rangle_{Av}\approx 4/k_F^2$, where k_f is the maximum momentum in the Fermi gas. This result is given in Fig. 3 together with the Gaussian.

The second method which we use makes use to a greater extent of knowledge of the scattering cross sections. We go back to the original definition of $\chi_{lm}(r)$ and write

$$g(\mathbf{p})=\frac{A}{v}\frac{2}{A^2}\sum_{lm}\frac{1}{(2\pi)^3}\left|\int e^{-i\mathbf{p}\cdot\mathbf{r}}\left(r\left|1+\frac{1}{e}t\right|r'\right)\times\phi_{lm}(r')dr'd\mathbf{r}\right|^2. \quad (49)$$

Using a relative momentum plane wave function for ϕ_{lm}, performing the integrations, and making use of the fact that the energy denominator "e" is simply $E-p^2/M$ if we neglect interactions of the final particles, we find

$$g(\mathbf{p})=\frac{A}{v}\frac{2}{A^2}\sum_{lm}\frac{1}{(2\pi)^3}[(\mathbf{p}|t|\mathbf{k}_{lm})^2/(E-p^2/M)]^2. \quad (50)$$

This can be evaluated in a very simple way if we assume that $(\mathbf{p}|t|\mathbf{k}_{lm})$ depends only on the momentum difference (as it would in Born approximation for example) and determine it experimentally. Making this assumption and making use of the relation between t and the scattering cross section,

$$t^2(\mathbf{p}-\mathbf{k}_{lm})=\left(\frac{4\pi}{M}\right)^2\frac{d\sigma(\mathbf{p}-\mathbf{k}_{lm})}{d\Omega}, \quad (51)$$

we find

$$g(\mathbf{p})=\frac{A}{v}\frac{1}{(2\pi)^3}\left(\frac{4\pi}{p^2}\right)^2\frac{d\sigma(\mathbf{p})}{d\Omega}, \quad (52)$$

where we have made use of $p^2/M\gg E$ and $k_{lm}\ll p$ to carry out the summation. To evaluate this result, we take the average differential scattering cross section at 90 degrees in the center-of-mass system for neutron-proton and proton-proton collisions, choosing an energy which gives the correct momentum transfer. The result is given in Fig. 3.

It is apparent that either of the methods we have used gives essentially the same results and that the agreement with the empirically derived Gaussian distribution is satisfactory over the energy range of primary interest. Therefore we can, as emphasized in the first part of this section, conclude that these methods will give correct order-of-magnitude predictions for the high-energy phenomena we have described.

V. CONCLUSIONS

We have analyzed evidence derived from a variety of high-energy experiments which has bearing on the problem of nuclear structure. This evidence is particularly significant since it is for these (or similar) processes that the possible departure of the nuclear ground-state wave function from an independent-particle wave function is most apparent. The result predicted uniformly by the group of quite diverse experiments which we have examined is that the nuclear ground-state wave function must have a very marked admixture of high-momentum components and hence must depart quite appreciably from an independent-particle-model wave function. Consequently it follows that the usual assumptions of the shell-model theory of the nucleus, that the particles move independently in a uniform potential, cannot be other than very approximately correct.

To investigate quantitatively the general conclusion drawn from experiment, we have made use of methods recently developed by us in other studies of the nucleus. These methods lead to a nuclear model which appears to agree well with many general details of the structure of the nucleus and also with the detailed properties predicted by the shell model, but does not assume the existence of the independent nucleon motion. An essential assumption of this method is that the nuclear forces acting between nucleons in dense nuclear matter are still very nearly the same as those acting between free nucleons and hence very strong and short ranged. An immediate consequence of this assumption is that the presence of marked correlation effects in the nuclear wave function is to be expected. Conversely, the experimental observation of such correlation effects implies directly that the strong two-body forces have not been "damped out" by nonlinear effects or cancelled by many-body effects.

In applying this nuclear theory to the study of the high-energy phenomena, we have made several simplifying assumptions to bring the theory into easily manageable form. The most important assumption made is that in the very-high-momentum region the effects which interest us are primarily due to the intimate association of pairs of nucleons. In this form our methods are analogous to those used by Heidmann and by Levinger although their origin and interpretation is rather different. The final expressions for the momentum distribution have been evaluated by making use of two quite different approximations which give results in reasonable agreement with each other and with the momentum distribution derived from experiment. It is to be emphasized that the theoretical predictions are very sensitive to the choice of the two-body interaction, which we have assumed to be identical with that acting on free particles. Thus we have shown not only that appreciable correlation effects are present but also that the presence of other nucleons in the dense nuclear matter cannot appreciably modify the two-body interactions.

In conclusion we would like to remark that although we have in this paper emphasized the departure of the nuclear wave function from an independent nuclear wave function, the great importance of the departure is manifested only in the specific high-energy processes (or similar cases) we have considered. As we have pointed out in other papers, the effects are not nearly so pronounced in many low-energy phenomena where the independent particles of the shell model can be identified more closely with nucleons.

Nonrelativistic Interaction Between Two Nucleons*†

DAVID FELDMAN
Department of Physics, University of Rochester, Rochester, New York
(Received December 7, 1954)

The problem of the derivation of a two-nucleon Schrödinger equation from quantum field theory has been investigated, where only those mesons which are exchanged between the nucleons are taken into account. One expects that the two-particle Schrödinger picture will be useful if the energy (less rest energy) is small ($\lesssim\mu^2/M$), and if the important matrix elements are those which couple states of small momenta ($\lesssim\mu$). The procedure which has been followed has been to go over to Fock space in the manner of Tamm and Dancoff, and then to decouple the two-particle Tamm-Dancoff amplitude from all the others by a series of canonical transformations (the over-all coupling is assumed weak). Unlike the methods developed by Lévy-Klein and Bethe-Salpeter, the characteristic difficulties such as energy-dependent and non-Hermitian potentials are avoided. By way of application, the formalism is used to analyze the nonrelativistic nuclear forces for the neutral scalar and charge-symmetric pseudoscalar theories (with both pseudoscalar and pseudovector coupling). In this approximation, it is shown that there is agreement with the results of Lévy-Klein. In the course of the calculations, it is made evident that the "nonadiabatic velocity-dependent" corrections of Lévy-Klein appear even when the nucleons are taken to be fixed sources. Within the context of the method of canonical transformations, there is no justification for dropping these corrections as has been suggested by Brueckner and Watson. Finally, there is some evidence that the Tamm-Dancoff approximation is not an improvement over weak-coupling perturbation theory when applied to the nuclear-force problem, at least when the coupling constant is small.

I. INTRODUCTION

IT appears by now to be reasonably well established that, within the domain of what is commonly referred to as classical nuclear physics (corresponding to energies up to 10 or 20 Mev, say), the behavior of nuclear systems is governed by orthodox nonrelativistic quantum mechanics. This means, in particular, that the state of a system of l-nucleons is characterized by an l-particle wave function $\psi(x_1,x_2,\cdots,x_l)$ where x_i denotes all the coordinates (space, spin, and charge) of the ith particle and where ψ is a properly antisymmetrized solution of an l-particle Schrödinger equation. An important drawback of this type of theory is that the interaction between nucleons needs to be given phenomenologically. It is, of course, an essential task of quantum field theory to give a fundamental basis for this interaction.

Now, the description of a nuclear system as given by quantum field theory is generally a very complicated affair. This is due to the fact that all meson theories must be in accord with the special theory of relativity and, when so constructed, give rise to the possibility of the creation and annihilation of particles. Thus, if we assume that we have to deal with an interaction Hamiltonian which is linear in the meson field variables and bilinear in the nucleon field variables, the state Ψ of our system can be conveniently represented in terms of an infinite, denumerable sequence of configuration-space wave functions $\psi_m{}^n$ in the manner given by Fock,[1] where m denotes the number of mesons and n the number of nucleon-antinucleon pairs which are present in addition to the original l-particles; both m and n can assume the values 0, 1, 2, $\cdots$. The state functional Ψ satisfies a Schrödinger equation from which one can deduce an infinite set of coupled integral equations[2] for the $\psi_m{}^n$.

We accordingly have two descriptions of our nuclear system; the one is field-theoretical and relativistic, the other is phenomenological and nonrelativistic. It is clear that any consistent treatment of the nuclear-force problem must reconcile these two pictures, i.e., from the Schrödinger equation for the state functional Ψ, or, equivalently, from the infinite set of coupled equations for the Fock-space amplitudes $\psi_m{}^n$, there must emerge, at least for low energies, an equally valid description in the form of a Schrödinger equation for an l-particle wave function ψ. It must be emphasized that our standpoint is that, in classical nuclear physics, the hypothesis that the wave function of a system of l-nucleons need only involve the coordinates of these particles has been justified, at least empirically. It is a moot point as to how far one can in fact push this type of description sensibly; we shall return to this question shortly.

We restrict ourselves, in this paper, to the two-nucleon problem which is the simplest mathematically and perhaps the most important physically. There has been a good deal of interest recently in the construction of relativistic two-body equations which are suitable for application to the deuteron, say. One approach, due

* This research was supported, in part, by the U. S. Atomic Energy Commission.

† The essential contents of this paper were presented at the Chicago meeting of the American Physical Society (November 27–28, 1953).

[1] V. Fock, Z. Physik **75**, 622 (1932).

[2] A configuration-space wave function can be represented in either coordinate space or momentum space, and we shall generally distinguish between these two possibilities by using the notations ψ and ϕ, respectively. As a matter of practical convenience, it is simpler to work in momentum space in which case the equations for the Fock-space amplitudes are coupled linear integral equations, whereas they are integro-differential equations in coordinate space. In the detailed considerations of the following sections, we shall take advantage of this simplification. For the purposes of the general discussion of this section only, however, we let ψ denote generically a configuration-space wave function in either representation, and refer to the equations satisfied by the ψ's simply as "integral equations."

to Tamm[3] and Dancoff[4] and extended by Lévy[5] and Klein,[6] proceeds as follows: one assumes that all the Fock-space amplitudes which correspond to having more than a limited number of mesons and nucleon-antinucleon pairs in the field vanish, and proceeds to try to treat the now finite number of coupled equations which are satisfied by the nonzero $\psi_m{}^n$'s as rigorously as possible. Clearly, the Tamm-Dancoff method presupposes, for its validity, certain restrictions on the energy of the system and the strength of the meson-nucleon coupling, but it is equally clear that some higher-order effects beyond those of a straightforward weak-coupling calculation are included.

In the simplest Tamm-Dancoff approximation, we have two coupled equations involving the amplitudes $\psi_0{}^0$ and $\psi_1{}^0$ which, for brevity, we write as ψ_0 and ψ_1. These equations are adequate for a relativistic treatment of both the bound and scattering states of the two-nucleon system within the framework of the Fock-space formalism and subject only to the limitations inherent in the original Tamm-Dancoff approximation. A convenient procedure in the solution of these equations has been to eliminate algebraically the amplitude ψ_1, thus leading to a linear integral equation for ψ_0. This equation has customarily been identified as a genuine Schrödinger equation for the two-nucleon system, with ψ_0 being taken to be the two-particle wave function for the system.[7]

This identification, however, cannot be generally correct. From a physical standpoint, the functions ψ_0 and ψ_1 have a very definite meaning; they represent the probability amplitudes for finding two nucleons and two nucleons plus one meson, respectively, in the field. They correspond to a Fock-space description of the system, and so must be normalized so that, in terms of a symbolic notation, $|\psi_0|^2+|\psi_1|^2=1$;[4] furthermore, in the computation of expectation values, the contribution from ψ_1 cannot be ignored. The construction of a Schrödinger-like equation for ψ_0 by algebraic elimination of ψ_1 may be convenient mathematically, but one does not, in this way, decouple the two-nucleon-plus-one-meson state from the two-nucleon state.

There are also other difficulties. The interaction operator in the ψ_0 equation depends on the energy of the system[8] so that the solutions of this equation are not even orthogonal to one another. Furthermore, as we shall see, when an iteration procedure due to Lévy and Klein is applied so as to remove this explicit energy-dependence, the resultant interaction operator is not even Hermitian. These results are again clearly manifestations of the fact that the description of the two-nucleon system as given by the Tamm-Dancoff method is inherently a relativistic one, allowing for the creation and annihilation of particles, and that the transition to the nonrelativistic Schrödinger picture has yet to be made.

It is perhaps useful at this point to recall another situation in quantum mechanics which is strikingly analogous to the one under discussion. We have in mind the general question of the reduction of the Dirac equation to its nonrelativistic Pauli form. According to the relativistically covariant Dirac theory, a spin $\frac{1}{2}$ particle is characterized by a four-component wave function which can always be regarded as having been expanded in terms of the complete set of free-particle solutions of the interaction-free Dirac equation. In the interests of clarity, let us assume that we are working in the Foldy-Wouthuysen representation[8] in which the positive- and negative-energy free-particle spinors have no more than two nonvanishing components each, which, for definiteness, we can take to be the upper and lower two, respectively. In this representation, a particular component of an arbitrary Dirac spinor can be directly interpreted as the probability amplitude for finding the spin $\frac{1}{2}$ particle in a state of given spin orientation and sign of energy.

Now, for nonrelativistic energies, it is known, phenomenologically, that a spin $\frac{1}{2}$ particle can be adequately described by a two-component Pauli wave function. One has then the problem of demonstrating that, even in the presence of interaction with, say, an external field, a reduction to the Pauli form can be effected, at least, in the nonrelativistic limit.

One is again faced with the task of reconciling two descriptions of the same physical situation; the one is of relativistic and fundamental theoretical origin, the other is nonrelativistic and phenomenological. One might first ask: Under what circumstances is it, in fact, sensible to try to carry through a reduction to the Pauli form? Here, the answer, as given in the recent comprehensive discussion by Foldy and Wouthuysen, is that the two-component representation of a spin $\frac{1}{2}$ particle is meaningful only if the energies involved are small and if the coupling to the high-momentum components of the external field is weak, i.e., only if one has to deal with basically nonrelativistic problems.

One might next ask: How is one to carry through the transition from the Dirac to the Pauli form within the domain of applicability, i.e., for nonrelativistic energies? The usual procedure has been to eliminate the small components of the spinor wave functions in favor of the large ones. However, this procedure cannot be justified beyond the lowest-order approximation, since the algebraic elimination of the small components does not

[3] I. Tamm, J. Phys. (U.S.S.R.) **9**, 449 (1945).
[4] S. M. Dancoff, Phys. Rev. **78**, 382 (1950).
[5] M. M. Lévy, Phys. Rev. **88**, 72 (1952); Phys. Rev. **88**, 725 (1952).
[6] A. Klein, Phys. Rev. **90**, 1101 (1953).
[7] In practical applications to the nuclear-force problem (i.e., when more than two amplitudes are included), the interaction operator in the ψ_0 equation has generally been expanded in the form of an infinite series in the coupling constant, with the series being terminated at some convenient point. One must accordingly be careful to distinguish between exact and approximate treatments of the Tamm-Dancoff equations, although, for the purposes of our general discussion, this distinction is immaterial.
[8] L. L. Foldy and S. A. Wouthuysen, Phys. Rev. **78**, 29 (1950).

constitute a physical decoupling of the positive from the negative energy states. The correct procedure, again due to Foldy and Wouthuysen, is to carry through a series of canonical transformations which rigorously separate the positive- and negative-energy states to any desired order in v/c. The Pauli Hamiltonian appears in the form of an infinite series which is useful only if the aforementioned restrictions on the energy of the system and the strength of the coupling to the external field are satisfied.

We may now return to our original problem: the derivation of a two-particle Schrödinger equation from quantum field theory. It is evident that, in a very real sense, we are dealing with the quantum-field theoretical analog of the reduction of the Dirac to the Pauli formalism. It will therefore not be surprising to find that a description of the two-nucleon system in terms of a wave function involving solely nucleon coordinates can, in fact, be justified only if the energies are nonrelativistic and if the coupling to high-momentum states of mesons and heavy particles is weak. The actual separation of the two-particle state in Fock space from states having also a finite number of mesons and/or nucleon-antinucleon pairs can be carried through by an infinite series of canonical transformations.

The detailed content of this paper will be devoted to an exposition of the thesis contained in the preceding paragraph. Starting with the Tamm-Dancoff approximation, we shall investigate, in Sec. II, the problem of how to derive, in a consistent way, a nonrelativistic two-particle Schrödinger equation from meson theory. In Sec. III, we proceed with applications to several cases of interest, *viz.*, the scalar and pseudoscalar theories (the latter with both direct and gradient coupling). For the sake of simplicity, we shall ignore those transitions in which a given meson is emitted and absorbed by the same nucleon. We shall also not find it necessary to consider explicitly the creation and annihilation of virtual nucleon-antinucleon pairs. The problem of the removal of divergences is therefore not discussed in this paper.

In the course of carrying through the detailed considerations of the nuclear-force problem contained in Secs. II and III, we shall also be in a position to discuss two aspects of this problem which are, perhaps, of particular interest. The first has to do with the question as to whether the Tamm-Dancoff approximation is an improvement over weak-coupling perturbation theory. The evidence will be that it is not, at least when one restricts oneself to essentially weak interactions. The second relates to the question as to whether certain "nonadiabatic velocity-dependent" corrections to nuclear forces which have been reported in the literature[5,6] ought to be retained[9] or dropped.[10] In point of fact, these controversial terms are simply the higher-order ladder corrections which are contained in the lowest-order Tamm-Dancoff approximation. Upon carrying through the reduction of the Tamm-Dancoff equations to the two-particle Schrödinger formalism, it will become clear that these terms are, in fact, not at all nonadiabatic or velocity-dependent since they are present even in the fixed-source limit; also, they cannot reasonably be ignored, at least when one deals with weak interactions.

[9] E. M. Henley and M. A. Ruderman, Phys. Rev. **92**, 1036 (1953).

[10] K. A. Brueckner and K. M. Watson, Phys. Rev. **92**, 1023 (1953).

II. REDUCTION TO A TWO-PARTICLE SCHRÖDINGER EQUATION

Let us suppose that we have two fields—nucleon and meson—whose interaction with one another can be characterized by a Hamiltonian $\mathcal{H}$ which is linear in the meson field and bilinear in the nucleon field. If we denote the free-particle Hamiltonian by $\mathcal{H}_0$, the stationary states Ψ of the system, where these may be either bound or scattering states, are determined by the Schrödinger equation

$$(E-\mathcal{H}_0)\Psi=\mathcal{H}\Psi. \tag{1}$$

We restrict ourselves immediately to a consideration of the two-nucleon problem. In order to make the transition from Ψ to a set of Fock-space wave functions which are given, in particular, in a momentum-space representation, we introduce the orthonormal subset of vectors $\Psi_m{}^n(P)$, where the latter are those stationary solutions of the interaction-free Schrödinger equation,

$$[E_m{}^n(P)-\mathcal{H}_0]\Psi_m{}^n(P)=0, \tag{2}$$

which can be coupled by $\mathcal{H}$ to the free-particle two-nucleon states. We use the indices m and n, as before, to specify the number of mesons and nucleon-antinucleon pairs which are present in addition to the original two nucleons. For a given m and n, there exists, of course, an infinite number of free-particle states corresponding to the different possibilities for the momenta, spins, and isotopic spins of the particles; we use the symbol P to distinguish these possibilities from one another.

We now expend Ψ (assumed normalized to unity) in terms of the set $\Psi_m{}^n(P)$, and so write

$$\Psi=\sum \phi_m{}^n(P)\Psi_m{}^n(P). \tag{3}$$

Clearly, $\phi_m{}^n(P)=(\Psi_m{}^n(P),\Psi)$ is the probability amplitude for finding the compound two-nucleon system in the state $\Psi_m{}^n(P)$. The normalization for the Fock-space amplitudes then has to be

$$\sum|\phi_m{}^n(P)|^2=1. \tag{4}$$

It is to be understood that the summations in (3) and (4) are to be taken over all indices, *viz.*, m, n, and P.

Now, while, in detailed calculations, it is convenient to use a momentum-space representation in each configuration subspace, in the development of a general

formalism it is simpler to use a somewhat more compact, symbolic notation in which it is the particle aspects alone of the various Fock subspaces which are emphasized—the particular working frame of reference within each subspace being left unspecified. We can introduce such a symbolic notation by simply suppressing the variable P. Equations (3) and (4) can then be rewritten in the forms

$$\Psi=\sum \phi_m{}^n\Psi_m{}^n, \tag{3a}$$

and

$$\sum|\phi_m{}^n|^2=1, \tag{4a}$$

respectively. The summations in (3a) and (4a) are now to be taken over m and n. We have denoted by $\Psi_m{}^n$ the unit vector in Fock space which characterizes the (m,n)th subspace. It is then evident that $\phi_m{}^n$ is a vector which spans the (m,n)th subspace.

We now make the lowest-order Tamm-Dancoff approximation, i.e., we assume that all the $\phi_m{}^n$'s vanish identically with the exception of the two-nucleon amplitude $\phi_0{}^0$ and the two-nucleon-plus-one-meson amplitude $\phi_1{}^0$. If we suppress the upper index, Eqs. (3a) and (4a) become

$$\Psi=\phi_0\Psi_0+\phi_1\Psi_1 \tag{5}$$

and

$$|\phi_0|^2+|\phi_1|^2=1, \tag{6}$$

respectively.

Let us write the unit vectors Ψ_0 and Ψ_1 as two-component column matrices, i.e.,

$$\Psi_0=\begin{pmatrix}1\\0\end{pmatrix},\quad \Psi_1=\begin{pmatrix}0\\1\end{pmatrix}; \tag{7}$$

we then have, for the state vector Ψ,

$$\Psi=\begin{pmatrix}\phi_0\\\phi_1\end{pmatrix}. \tag{8}$$

In terms of this notation, the Hamiltonian operators $\mathfrak{IC}$ and $\mathfrak{K}$ which enter in Eq. (1) will appear as two-by-two matrices, with the former having only nonvanishing diagonal elements, and the latter only nonvanishing off-diagonal elements; they can accordingly be written in the following way:

$$\mathfrak{IC}=\begin{pmatrix}W_0&0\\0&W_1\end{pmatrix},\quad \mathfrak{K}=\begin{pmatrix}0&K_{01}\\K_{10}&0\end{pmatrix}. \tag{9}$$

It is to be noticed that the matrix elements in terms of which $\mathfrak{IC}$ and $\mathfrak{K}$ are here expressed are not c-numbers but are, in turn, also operators. Thus, the diagonal elements W_0 and W_1 are the appropriate free-particle Hamiltonian operators for the zero-meson and one-meson configuration subspaces, respectively. The off-diagonal elements K_{01} and K_{10} serve to couple the two subspaces. Denoting the Hermitian adjoint of an operator by a dagger, we observe also that the Hermitian character of $\mathfrak{IC}$ and $\mathfrak{K}$ implies $(W_0)^\dagger=W_0$, $(W_1)^\dagger=W_1$, and $(K_{01})^\dagger=K_{10}$.

Finally, the Schrödinger equation (1), in lowest-order Tamm-Dancoff approximation, will appear as a two-component matrix equation, *viz.*,

$$\begin{pmatrix}E-W_0&0\\0&E-W_1\end{pmatrix}\begin{pmatrix}\phi_0\\\phi_1\end{pmatrix}=\begin{pmatrix}0&K_{01}\\K_{10}&0\end{pmatrix}\begin{pmatrix}\phi_0\\\phi_1\end{pmatrix}; \tag{10}$$

upon carrying through the indicated matrix multiplication, we are led, in turn, to the following pair of linear equations:

$$(E-W_0)\phi_0=K_{01}\phi_1, \tag{11a}$$

$$(E-W_1)\phi_1=K_{10}\phi_0. \tag{11b}$$

Now, Eqs. (11a) and (11b) can be used as the basis for a discussion of the stationary states of the two-nucleon system subject only to our assumption that no more than one meson is present in the field at any one time and that no nucleon-antinucleon pairs are produced. As has already been indicated in Part I of this paper, the usual procedure[3–6] in the solution of these equations is to solve (11b) for ϕ_1 in terms of ϕ_0,

$$\phi_1=(E-W_1)^{-1}K_{10}\phi_0,$$

and then to substitute this expression for ϕ_1 into (11a), thus leading to a Schrödinger-like equation for the configuration-space two-particle amplitude ϕ_0,

$$(E-W_0)\phi_0=K_{01}(E-W_1)^{-1}K_{10}\phi_0. \tag{12}$$

The essential objections to the use of Eq. (12) as a starting point for a discussion of the nonrelativistic nuclear-force problem have been listed in Part I and need not be repeated here. We want simply to add the remark that precisely the same criticisms can be directed against the use of the Bethe-Salpeter equation[11] for the same purpose. Indeed, the equal-times Bethe-Salpeter wave function for a system of two nucleons is directly related to a two-particle Tamm-Dancoff amplitude,[12] so that it is evident that, in both formalisms, one has still to decouple the two-particle amplitude from amplitudes allowing for the presence of mesons and/or nucleon-antinucleon pairs.

Let us then return to Eq. (10) and examine first the circumstances under which it may be expected that the decoupling of the two-nucleon (no-meson) amplitude from the two-nucleon-plus-one-meson amplitude will have physical meaning. We reiterate at this point that we shall not take into account that contribution to the nuclear force which arises from the emission and subsequent absorption of a meson by the same nucleon; accordingly, we consider that the interaction between two nucleons comes about solely as a consequence of

[11] E. E. Salpeter and H. A. Bethe, Phys. Rev. **84**, 1232 (1951).
[12] See references 5 and 6; also, W. Macke, Phys. Rev. **91**, 195 (1953); F. J. Dyson, Phys. Rev. **91**, 1543 (1953).

the continual interchange of mesons between the nucleons.

We denote the meson and nucleon masses by μ and M, respectively, and work with natural units for which $\hbar=c=1$. Also, it will be convenient, for what follows, to refer to the momentum p of a particle (which may be a nucleon or meson) as small or large according as $p\lesssim\mu$ or $>\mu$, respectively. Similarly, we shall say that the energy of the system is small or large according as the quantity $|E-2M|\lesssim\mu^2/M$ or $>\mu^2/M$, respectively.

Now, there is a nominal energy gap of width μ between the no-meson and one-meson subspaces. In point of fact, however, the actual gap between the two subspaces can be much smaller than μ, and the extent to which it is smaller may be measured by the amount of high-momentum component contained in ϕ_0. Thus, if the energy of the system is large to begin with, the no-meson amplitude ϕ_0 will generally contain important high-momentum components, so that one can then hardly speak of an energy separation between the two subspaces at all. Even if the energy of the system is small, one cannot immediately conclude that there are only low-momentum components in ϕ_0, unless the coupling to the high-momentum components of ϕ_1 can be characterized as weak. Thus, only if the energy of the system is small, and if there is weak coupling between ϕ_0 and ϕ_1 in the sense just described, can one be certain that ϕ_0 will contain solely low-momentum components, or, equivalently, that there exists a real energy separation $\sim\mu$ between the two subspaces.

The importance of having such a sharp energy gap consists in the fact that it is only then that it appears physically significant to characterize the system by a two-particle Schrödinger equation. This can be seen in the following way. In the quantum-field theoretical description of the system, the particles are point particles and the interaction is a point interaction. When one proceeds to try to simplify the two-nucleon problem by eliminating the meson-field variables, one immediately introduces a new complication in that the interaction between the nucleons generally becomes very complicated, being nonlocal in character. This complication can be considered to occur in consequence of the fact that the nucleons now have a structure with radius of the order of the nucleon Compton wavelength $1/M$. It is then evident that the transition to the two-nucleon Schrödinger picture is pointless unless nucleon-structure effects are small, and indeed this will be the case only if the recoil momentum p of a nucleon on emitting or absorbing a meson is small compared to M. This last condition will be satisfied if $p\lesssim\mu$ which corresponds to the existence of an energy separation between the no-meson and one-meson subspaces of width $\sim\mu$.

We see therefore that, only when we have to deal with essentially nonrelativistic problems, can the description of the two-nucleon system by a two-particle Schrödinger equation be expected to be useful. We shall accordingly assume, for all that follows, that the energy of our system is small and the coupling to high momenta weak. In order to develop a consistent procedure for carrying out the reduction to the two-particle Schrödinger picture, we shall, in fact, impose the stronger restriction that the over-all coupling between the nucleon and meson fields is weak.[13] Under these circumstances, it becomes possible to decouple Eq. (10) in a systematic way by applying a sequence of canonical transformations. The resultant two-particle interaction operator, valid for internucleon separations $\gtrsim 1/\mu$, will then appear as a double series expansion in the coupling constant and nucleon recoil. We shall presuppose that this series expansion is asymptotic in both parameters.

We proceed to exhibit the transformations which will decouple Eq. (10). Let us use, for the moment, the more compact notation of Eq. (1),

$$(E-\mathfrak{IC})\Psi=\mathfrak{K}\Psi, \tag{1}$$

it being understood that the lowest-order Tamm-Dancoff approximation has already been made, and that, in detailed calculations, we will use a momentum-space representation in the no-meson and one-meson configuration subspaces. We apply the canonical transformation

$$\Psi=(\exp-i\mathfrak{S})\Phi, \tag{13}$$

where $\mathfrak{S}$ will be determined so as to eliminate the first-order coupling between ϕ_0 and ϕ_1. If we recall the theorem that, for an arbitrary operator $\mathfrak{A}$,

$$(\exp i\mathfrak{S})\mathfrak{A}\,(\exp-i\mathfrak{S})=\mathfrak{A}+i[\mathfrak{S},\mathfrak{A}]+(i^2/2!)[\mathfrak{S},[\mathfrak{S},\mathfrak{A}]]+\cdots, \tag{14}$$

it becomes evident that we must choose $\mathfrak{S}$ so that

$$-i[\mathfrak{S},\mathfrak{IC}]=\mathfrak{K}. \tag{15}$$

Upon examination of the matrix representation of $\mathfrak{IC}$ and $\mathfrak{K}$ as given in (9), it is apparent that one can take $\mathfrak{S}$ to be

$$\mathfrak{S}=-i\mathfrak{K}', \tag{16a}$$

where

$$\mathfrak{K}'=\begin{pmatrix}0 & K_{01}'\\ K_{10}' & 0\end{pmatrix}, \tag{16b}$$

and where K_{01}' and K_{10}' are, in turn, operators which link the no-meson and one-meson Fock subspaces. Since $\mathfrak{S}$ must be Hermitian, $\mathfrak{K}'$ will be skew-Hermitian so that $(K_{01}')^\dagger=-K_{10}'$. The momentum-space representations of K_{01}' and K_{10}' can be directly determined

[13] One must be careful to note that the supposition that the meson-nucleon coupling constant is small is made for mathematical convenience; the condition that nucleon recoil be small is, on the other hand, a physical requirement which must be satisfied in order to be able to go over to the two-particle Schrödinger picture at all.

from (15) and (16). One finds

$$\left.\begin{aligned}(P|K_{01}'|Q)&=(P|K_{01}|Q)[W_0(P)-W_1(Q)]^{-1},\\(Q|K_{10}'|P)&=(Q|K_{10}|P)[W_1(Q)-W_0(P)]^{-1};\end{aligned}\right\}\quad(17)$$

here, P and Q denote the momenta, spins, and isotopic spins of free-particle no-meson and one-meson states, respectively.

It is a straightforward matter to carry through in detail the S-transformation defined by (13), (16), and (17). Equation (1) will go over into a new Schrödinger equation for the vector Φ of the form

$$(E-\mathfrak{IC})\Phi=\mathfrak{L}\Phi,\qquad(18a)$$

where $\mathfrak{L}$, the new interaction Hamiltonian, will appear as a power series in the coupling constant with the leading term of second order; thus,

$$\mathfrak{L}=\mathfrak{L}^{(2)}+\mathfrak{L}^{(3)}+\mathfrak{L}^{(4)}+\cdots.\qquad(18b)$$

Both the second- and fourth-order terms, $\mathfrak{L}^{(2)}$ and $\mathfrak{L}^{(4)}$, respectively, will be diagonal in that subregion of Fock space to which we have restricted ourselves on having applied the lowest-order Tamm-Dancoff approximation; these terms accordingly do not couple the no-meson and one-meson subspaces. The third-order term $\mathfrak{L}^{(3)}$ is off-diagonal, but can be removed by a second canonical transformation analogous to (13). However, if we agree to restrict our considerations to terms which are at most of fourth order in the coupling constant, we need not bother with this second canonical transformation since it will contribute terms of sixth and higher order.

The no-meson and one-meson Fock subspaces are now completely decoupled from one another to fourth order. We are accordingly in a position to identify the transformed two-nucleon (no-meson) Tamm-Dancoff amplitude (which we now call ϕ) with the two-particle Schrödinger wave function for the system, and the matrix element $(\mathfrak{L}^{(2)}+\mathfrak{L}^{(4)})_{00}$ with the interaction Hamiltonian. One finds, for the equation satisfied by ϕ, the following:

$$(E-W_0)\phi=(V^{(2)}+V^{(4a)})\phi,\qquad(19)$$

where

$$V^{(2)}=\tfrac{1}{2}(K_{01}'K_{10}-K_{01}K_{10}')\qquad(20a)$$

and

$$V^{(4a)}=\tfrac{1}{8}(K_{01}'K_{10}'K_{01}'K_{10}-3K_{01}'K_{10}'K_{01}K_{10}'+3K_{01}'K_{10}K_{01}'K_{10}'-K_{01}K_{10}'K_{01}'K_{10}').\qquad(20b)$$

Equation (19) is a *bona fide* two-particle Schrödinger equation with a Hermitian Hamiltonian since, to fourth order at least, the possibility of coupling to the one-meson subspace has been removed.

The interaction operators $V^{(2)}$ and $V^{(4a)}$ have a well-defined physical meaning. Within the limitations of the lowest-order Tamm-Dancoff approximation, the most general type of nucleon-nucleon interaction consists in the interchange of an arbitrary number of mesons between the two nucleons subject only to the proviso that any given meson shall be absorbed before another is created. In $V^{(2)}$ and $V^{(4a)}$, therefore, we exhibit explicitly that part of the total nucleon-nucleon interaction which is contributed by one- and two-meson interchanges, respectively, when there is, at most, one meson in the field. Of course, $V^{(2)}$ and $V^{(4a)}$ also contain self-energy terms which we shall always discard.

It is instructive, at this point, to compare $V^{(2)}$ and $V^{(4a)}$ with the corresponding second- and fourth-order interactions which appear when one reduces the Tamm-Dancoff equations to a single "two-particle" equation by algebraic elimination of all amplitudes other than the no-meson amplitude. The total "potential," as given by (12), has the form

$$V_{TD}=K_{01}(E-W_1)^{-1}K_{10}.\qquad(21)$$

As it stands, it involves E. In order to eliminate this dependence on the energy of the system, we make use of an adaptation of the iteration procedure of Lévy[5] and Klein.[6]

Let us first write out Eq. (12) in terms of a momentum-space representation. We obtain:

$$[E-W_0(P)]\phi_0(P)=\sum_{Q,R}(P|K_{01}|Q)[E-W_1(Q)]^{-1}\times(Q|K_{10}|R)\phi_0(R),\qquad(22)$$

where we have used P and R to label the free-particle no-meson states, and Q the free-particle one-meson states. Assuming that the energy is small and the coupling to high-momentum states is weak, we can express the energy denominator in the right-hand side of (22) in the following way:

$$\begin{aligned}&[E-W_1(Q)]^{-1}\\&\quad=-\{[W_1(Q)-W_0(R)]-[E-W_0(R)]\}^{-1}\\&\quad=-\frac{1}{W_1(Q)-W_0(R)}\sum_{n=0}^{\infty}\left(\frac{E-W_0(R)}{W_1(Q)-W_0(R)}\right)^n.\end{aligned}\qquad(23)$$

Upon substituting (23) into (22) and taking the over-all coupling between the meson and nucleon fields to be small, one is in a position to carry through a sequence of successive iterations of the resultant equation by replacing $[E-W_0(R)]\phi_0(R)$, wherever it appears on the right-hand side, by its value as given by the equation itself. The result is to generate an interaction which is no longer explicitly dependent on the energy and which has the form of a power series in the coupling constant. For the second- and fourth-order interactions, one readily finds:

$$V_{TD}{}^{(2)}=-K_{01}K_{10}',\qquad(24a)$$

$$V_{TD}{}^{(4a)}=K_{01}(K_{10}'K_{01}K_{10}')',\qquad(24b)$$

the meaning of a prime when affixed to an operator is precisely as given in Eq. (17).

We now observe that, not only is there a lack of correspondence between the two sets of interactions as given by (20a), (20b), (24a), and (24b), but that $V_{TD}^{(2)}$ and $V_{TD}^{(4a)}$ are not even necessarily Hermitian. Accordingly, one cannot generally identify $V_{TD}^{(2)}+V_{TD}^{(4a)}$ as the potential (up to fourth order) which follows from the lowest-order Tamm-Dancoff approximation.

Under certain limiting circumstances, however, this identification can be justified. We recall that the interaction operators which we are considering here make sense only in the limit of small nucleon recoil and so can be expressed as power series in μ/M. Given a typical interaction operator V, there are various ways of approximating it for small nucleon recoil momenta, and we shall want to distinguish these possibilities carefully from one another. In the *fixed-source* approximation, we let the nucleon mass become infinitely large, so that all nucleon recoil effects go out. In the *adiabatic* limit, on the other hand, we retain the leading term of V in its expansion in μ/M; the remaining terms accordingly constitute *nonadiabatic* corrections. It is evident that, from a practical standpoint, the difference between the fixed-source and adiabatic approximations consists in the treatment of nucleon-spin matrix elements, since retardation effects are completely neglected in both cases. Finally, by the *nonrelativistic* limit, we shall imply the retention of all terms which are compatible with the designation of $M+p^2/2M$ as the energy of a free particle.

Returning to our comparison of (20a) and (20b) with (24a) and (24b), we now notice that, for the case of the second-order interaction, the Hermitian character of $V_{TD}^{(2)}$ will be restored and the interaction itself will, in fact, coincide with $V^{(2)}$ if retardation effects are neglected.[14] However, the Hermitian property of $V_{TD}^{(2)}$ is lost as soon as one takes into account nonadiabatic corrections.[15]

Insofar as the fourth-order interaction is concerned, the situation is somewhat more complicated. Upon neglect of retardation, we have

$$V^{(4a)}=\tfrac{1}{2}(K_{01}'K_{10}'K_{01}'K_{10}-K_{01}K_{10}'K_{01}'K_{10}')$$

while $V_{TD}^{(4a)}=K_{01}'K_{10}'K_{01}'K_{10}$, so that the Hermitian character of $V_{TD}^{(4a)}$ as well as its equivalence to $V^{(4a)}$ requires that the operators $K_{01}'K_{10}'$ and $K_{01}'K_{10}$ commute with one another. In our consideration of several cases of particular interest in Sec. III, we shall see that this requirement is satisfied.[16] These results suggest that, to lowest-order approximation in nucleon recoil (adiabatic approximation), the solution of the Tamm-Dancoff equations by canonical transformation or by algebraic substitution will lead to equivalent results.

III. APPLICATIONS

(a) Neutral Scalar Theory

By way of illustration of the formalism of the preceding section, let us evaluate $V^{(2)}$ and $V^{(4a)}$ for the neutral scalar theory, assuming at first that we have to deal with fixed point sources. The interaction Hamiltonian $\mathcal{K}$ will then read

$$\mathcal{K}=f\sum_i \phi(\mathbf{r}_i), \tag{25}$$

where f measures the strength of the coupling between a point nucleon located at $\mathbf{r}_i$ and the meson field $\phi(\mathbf{r}_i)$; the running index i can assume but two values, 1 and 2. Upon expanding ϕ in terms of plane waves in the customary way, we have

$$\phi(\mathbf{r})=\sum_{\mathbf{k}}[2\omega(k)]^{-\frac{1}{2}}[a(\mathbf{k})e^{i\mathbf{k}\cdot\mathbf{r}}+a^\dagger(\mathbf{k})e^{-i\mathbf{k}\cdot\mathbf{r}}], \tag{26}$$

where $\omega(k)=(\mu^2+k^2)^{\frac{1}{2}}$ and where we have taken the volume of the system to be unity; the coefficients $a(\mathbf{k})$ and $a^\dagger(\mathbf{k})$ are the usual meson absorption and emission operators, respectively. From (25) and (26), it then follows that

$$K_{01}=(K_{10})^\dagger=f\sum_{\mathbf{k}}[2\omega(k)]^{-\frac{1}{2}}[a(\mathbf{k})]_{01}\sum_i e^{i\mathbf{k}\cdot\mathbf{r}_i}; \tag{27}$$

in view of (17), one has also

$$K_{01}'=-(K_{10}')^\dagger=-f\sum_{\mathbf{k}}2[2\omega(k)]^{-\frac{1}{2}}\times[a(\mathbf{k})]_{01}\sum_i e^{i\mathbf{k}\cdot\mathbf{r}_i}. \tag{28}$$

Now, as has already been noted,[14] the second-order interaction (20a), upon neglect of retardation effects, can be simplified to read

$$V^{(2)}=K_{01}'K_{10}; \tag{29}$$

if we use the bold-face notation $\mathbf{V}$ to distinguish the matrix representatives of the nucleon-nucleon potential, we then have

$$\mathbf{V}^{(2)}\equiv(0|V^{(2)}|0)=(0|K_{01}'K_{10}|0). \tag{30}$$

It then follows from (27), (28), and (30), together with

$$(0|[a(\mathbf{k}')]_{01}[a^\dagger(\mathbf{k})]_{10}|0)=(0|a(\mathbf{k}')a^\dagger(\mathbf{k})|0)=\delta_{\mathbf{k},\mathbf{k}'}, \tag{31}$$

that

$$\mathbf{V}^{(2)}=-(f^2/2)\sum_{\mathbf{k}}[\omega(k)]^{-2}\sum_{i,j}e^{i\mathbf{k}\cdot(\mathbf{r}_i-\mathbf{r}_j)}. \tag{32}$$

[14] For we may then replace W_0 by $2M$, whence we have the equality $K_{01}'K_{10}=-K_{01}K_{10}'$.

[15] By way of illustration, see the detailed discussions of nonadiabatic corrections to nuclear forces for the scalar and pseudoscalar theories as given by Lévy (reference 5) and Klein (reference 6); in particular, note that certain nonadiabatic terms appear which are proportional to the difference of the kinetic energies of the initial and final no-meson states and which are non-Hermitian [see, e.g., Eq. (35) of reference 6]. Non-Hermitian terms will also appear in the Bethe-Salpeter theory [see, e.g., Eq. (39) of reference 11].

[16] To see how this result follows, we note that, for the usual meson theories, the operators $K_{01}'K_{10}'$ and $K_{01}'K_{10}$, in the adiabatic limit, will be *static* in that they will depend on the relative coordinates of the two particles as well as their spins and isotopic spins, and so can be expressed as a sum of invariant forms involving these variables [see, e.g., L. Eisenbud and E. P. Wigner, Proc. Natl. Acad. Sci. **27**, 281 (1941); D. Feldman, Phys. Rev. **92**, 824 (1953)]. Under these circumstances, the required commutativity is easily demonstrated.

Upon dropping self-energy terms and converting the summation over $\mathbf{k}$ into an integral ($\sum_{\mathbf{k}} \rightarrow (2\pi)^{-3}\int d\mathbf{k}$), we obtain the well-known result[17]

$$V^{(2)} = -f^2(2\pi)^{-3}\int d\mathbf{k}\omega^{-2}e^{i\mathbf{k}\cdot\mathbf{r}} = -(f^2/4\pi)r^{-1}e^{-\mu r}, \quad (33a)$$

where $\mathbf{r}=\mathbf{r}_1-\mathbf{r}_2$.

The corresponding fourth-order interaction $V^{(4a)} \equiv (0|V^{(4a)}|0)$ can be easily evaluated in a similar way from Eq. (20b). After an elementary calculation, one finds

$$V^{(4a)} = f^4(2\pi)^{-6}\int d\mathbf{k}\omega^{-2}e^{i\mathbf{k}\cdot\mathbf{r}}\int d\mathbf{k}'(\omega')^{-3}e^{i\mathbf{k}'\cdot\mathbf{r}},$$

or

$$V^{(4a)} = (f^2/4\pi)^2 r^{-1}e^{-\mu r}(2/\pi)K_0(\mu r), \quad (33b)$$

where K_0 is the zeroth-order Hankel function of imaginary argument.[18]

Now, the neutral scalar theory with fixed sources serves as a particularly useful example since, for this case, the interaction (33a) is known to be rigorously correct to all orders in the coupling constant.[19] We can therefore conclude, at least when the coupling constant is small, that the lowest-order Tamm-Dancoff approximation is, in fact, not an improvement over the use of second-order weak-coupling perturbation theory, for it fails to include certain fourth-order terms which are of the same order of magnitude as (and which, for the case at hand, precisely cancel) those fourth-order terms which are taken into account.[20]

To obtain the complete fourth-order interaction, we must allow for the possibility of having two mesons present in the field at the same time. Thus, let us extend the lowest-order Tamm-Dancoff approximation by retaining the two-meson amplitude ϕ_2 in addition to the no-meson and one-meson amplitudes, ϕ_0 and ϕ_1 respectively, which formed the basis of our previous considerations. The generalization of the formalism of Sec. II to this case is essentially straightforward and is carried through in the following way.

The states Ψ of our system can now be written as three-component column matrices,

$$\Psi = \begin{pmatrix}\phi_0\\ \phi_1\\ \phi_2\end{pmatrix}, \quad (34)$$

with the normalization

$$|\phi_0|^2+|\phi_1|^2+|\phi_2|^2=1. \quad (35)$$

The free-field and interaction Hamiltonians, $\mathcal{H}$ and $\mathcal{K}$, respectively, will accordingly appear as three-by-three matrices having the following forms:

$$\mathcal{H} = \begin{pmatrix}W_0 & 0 & 0\\ 0 & W_1 & 0\\ 0 & 0 & W_2\end{pmatrix}, \quad (36a)$$

$$\mathcal{K} = \begin{pmatrix}0 & K_{01} & 0\\ K_{10} & 0 & K_{12}\\ 0 & K_{21} & 0\end{pmatrix}; \quad (36b)$$

those off-diagonal elements of $\mathcal{K}$ which correspond to a direct coupling of the no-meson and two-meson Fock subspaces are identically zero since, by hypothesis, $\mathcal{K}$ is linear in the meson field variables.

We proceed as before to apply a canonical transformation

$$\Psi = (\exp -i\mathcal{S})\Phi \quad (13)$$

to the Schrödinger equation

$$(E-\mathcal{H})\Psi = \mathcal{K}\Psi, \quad (1)$$

where $\mathcal{S}$ is now chosen so as to remove the first-order coupling between ϕ_0 and ϕ_1, and ϕ_1 and ϕ_2, i.e., we require that

$$-i[\mathcal{S},\mathcal{H}] = \mathcal{K}. \quad (15)$$

By analogy with Eqs. (16a) and (16b), we can write

$$\mathcal{S} = -i\mathcal{K}', \quad (37a)$$

where

$$\mathcal{K}' = \begin{pmatrix}0 & K_{01}' & 0\\ K_{10}' & 0 & K_{12}'\\ 0 & K_{21}' & 0\end{pmatrix}. \quad (37b)$$

The operators K_{st}' $(s,t=0,1,2)$ have the momentum-space representations

$$(P|K_{st}'|Q) = (P|K_{st}|Q)[W_s(P)-W_t(Q)]^{-1}, \quad (38)$$

where P and Q denote the momenta, spins, and isotopic spins of free-particle s-meson and t-meson states, respectively.

On carrying through the unitary transformation defined by (13), (37), and (38), Eq. (1) will once again go over into a new Schrödinger equation for the vector Φ of the form given by (18a) and (18b). However, unlike our previous discussion, the new second-order interaction Hamiltonian will now no longer be diagonal, but will, in fact, contain off-diagonal terms coupling the no-meson and two-meson Fock subspaces directly, *viz.*,

$$\begin{aligned}(\mathcal{L}^{(2)})_{02} &= \tfrac{1}{2}(K_{01}'K_{12}-K_{01}K_{12}'),\\ (\mathcal{L}^{(2)})_{20} &= \tfrac{1}{2}(K_{21}'K_{10}-K_{21}K_{10}').\end{aligned} \quad (39)$$

Accordingly, to fourth order in the coupling constant, we have not as yet attained a complete decoupling of the no-meson amplitude from all others.

Let us write $\mathcal{L}^{(2)}$ as the sum of a diagonal and an off-diagonal matrix which we denote by $\mathfrak{D}$ and $\mathfrak{O}$, respectively; in particular, the only nonvanishing

[17] See, for example, G. Wentzel, *Einführung in die Quantentheorie der Wellenfelder* (Franz Denticke, Vienna, 1943), p. 44.

[18] G. N. Watson, *Theory of Bessel Functions* (Cambridge University Press, Cambridge, 1945), second edition, pp. 78, 172; for details of the integration procedure, see the appendix of the second part of reference 5.

[19] Reference 17, p. 46.

[20] A similar argument has been given by Henley and Ruderman (reference 9).

matrix elements of $\mathcal{O}$ are given by (39). Then, to remove the off-diagonal terms (39) from the interaction Hamiltonian, we need to apply a second unitary transformation

$$\Phi=(\exp -i\mathcal{T})\Xi \tag{40}$$

to (18a), where it is evident that $\mathcal{T}$ must be determined so that

$$-i[\mathcal{T},\mathcal{H}]=\mathcal{O}. \tag{41}$$

This requirement will be satisfied if $\mathcal{T}$ is given by

$$\mathcal{T}=-i\mathcal{O}', \tag{42a}$$

where the only nonzero matrix elements of $\mathcal{O}'$ are

$$\begin{aligned}(\mathcal{O}')_{02}&=\tfrac{1}{2}(K_{01}'K_{12}-K_{01}K_{12}')',\\ (\mathcal{O}')_{20}&=\tfrac{1}{2}(K_{21}'K_{10}-K_{21}K_{10}')';\end{aligned} \tag{42b}$$

the meaning of the primed operators is given by (38).

On carrying through the $\mathcal{T}$-transformation defined by (40), (42), and (38), we obtain the Schrödinger equation for the transformed vector Ξ, *viz.*,

$$(E-\mathcal{H})\Xi=\mathfrak{M}\Xi, \tag{43a}$$

where

$$\mathfrak{M}=\mathfrak{M}^{(2)}+\mathfrak{M}^{(3)}+\mathfrak{M}^{(4)}+\cdots, \tag{43b}$$

and where the second-order term $\mathfrak{M}^{(2)}$ has the form of a diagonal three-by-three matrix. Although the third- and fourth-order terms, $\mathfrak{M}^{(3)}$ and $\mathfrak{M}^{(4)}$, contain off-diagonal matrix elements, these will not contribute to the fourth-order nucleon-nucleon interaction and so can be ignored.

To fourth order in the coupling constant, therefore, the new no-meson Tamm-Dancoff amplitude, which we again denote by ϕ, is completely decoupled from all the others; hence, we identify the equation for ϕ with the two-particle Schrödinger equation for the system in which the matrix element $(\mathfrak{M}^{(2)}+\mathfrak{M}^{(4)})_{00}$ will appear as the (Hermitian) interaction Hamiltonian. The result is to find that ϕ satisfies

$$(E-W_0)\phi=(V^{(2)}+V^{(4a)}+V^{(4b)})\phi, \tag{44}$$

where explicit expressions for $V^{(2)}$ and $V^{(4a)}$ have already been given in Eqs. (20a) and (20b), and where[21]

$$V^{(4b)}=V^{(4b')}+V^{(4b'')}, \tag{45a}$$

with

$$\begin{aligned}V^{(4b')}=\tfrac{1}{8}(&K_{01}'K_{12}'K_{21}'K_{10}-3K_{01}'K_{12}'K_{21}K_{10}'\\&+3K_{01}'K_{12}K_{21}'K_{10}'-K_{01}K_{12}'K_{21}'K_{10}')\end{aligned} \tag{45b}$$

and

$$\begin{aligned}V^{(4b'')}=\tfrac{1}{8}[&(K_{01}'K_{12}-K_{01}K_{12}')'(K_{21}'K_{10}-K_{21}K_{10}')\\&-(K_{01}'K_{12}-K_{01}K_{12}')(K_{21}'K_{10}-K_{21}K_{10}')'].\end{aligned} \tag{45c}$$

[21] The general expression for $V^{(4b)}$ can be readily shown to be equivalent, in the adiabatic limit, to $V_{TD}{}^{(4b)}=-K_{01}(K_{12}(K_{21}K_{10}')')'$ which is the corresponding contribution to the fourth-order potential which is obtained by eliminating the one-meson and two-meson amplitudes by algebraic substitution.

Let us denote the entire fourth-order interaction by $V^{(4)}$, i.e.,

$$V^{(4)}=V^{(4a)}+V^{(4b)}. \tag{46}$$

Then, it is clear from our previous discussion that $V^{(4a)}$ represents that part of the fourth-order interaction which comes about from the interchange of two mesons by the nucleons when there is never more than one meson present in the field. On extending the lowest-order Tamm-Dancoff approximation so as to allow for the simultaneous presence of two mesons in the field, we obtain an additional contribution to the fourth-order potential which we have called $V^{(4b)}$. The sum of these two contributions yields $V^{(4)}$ which is clearly equivalent to the usual perturbation-theoretic result.

Returning to the neutral scalar theory with fixed sources and making use of the additional relations

$$\begin{aligned}K_{12}=(K_{21})^\dagger=f\textstyle\sum_{\mathbf{k}}[2\omega(k)]^{-\frac{1}{2}}&\\ \times[a(\mathbf{k})]_{12}\textstyle\sum_i e^{i\mathbf{k}\cdot\mathbf{r}_i},&\\ K_{12}'=-(K_{21}')^\dagger=-f\textstyle\sum_{\mathbf{k}}2[2\omega(k)]^{-\frac{1}{2}}&\\ \times[a(\mathbf{k})]_{12}\textstyle\sum_i e^{i\mathbf{k}\cdot\mathbf{r}_i},&\end{aligned} \tag{47}$$

and

$$\begin{aligned}(0|a(\mathbf{k})a(\mathbf{k}')a^\dagger(\mathbf{k}'')a^\dagger(\mathbf{k}''')|0)&\\ =\delta_{\mathbf{k},\mathbf{k}'''}\delta_{\mathbf{k}',\mathbf{k}''}+\delta_{\mathbf{k},\mathbf{k}''}\delta_{\mathbf{k}',\mathbf{k}'''},&\end{aligned} \tag{48}$$

one finds easily that

$$\mathbf{V}^{(4b')}=-(f^2/4\pi)^2r^{-1}e^{-\mu r}(2/\pi)K_0(\mu r)=-\mathbf{V}^{(4a)} \tag{49a}$$

and

$$\mathbf{V}^{(4b'')}=0. \tag{49b}$$

Hence, as anticipated, the two-meson contribution $\mathbf{V}^{(4b)}$ to the fourth-order potential precisely cancels the one-meson contribution $\mathbf{V}^{(4a)}$ as given by (33b), i.e.,

$$\mathbf{V}^{(4)}=0. \tag{50}$$

This then reaffirms our previous statement that, when one deals with essentially weak coupling, perturbation theory seems to yield a better result than the Tamm-Dancoff approximation.

Two additional remarks are appropriate at this point, and they both concern the term $\mathbf{V}^{(4a)}$. In the first place, it is evident that, for the case at hand, we have assumed fixed point-source nucleons from the very beginning so that the ladder corrections $\mathbf{V}^{(4a)}$ to the second-order potential are adiabatic and static. Nevertheless, various authors,[5,6,10] when they have treated the Tamm-Dancoff equations by algebraic elimination of all amplitudes except for the two-nucleon amplitude, have referred to the corresponding contributions to the over-all potential as "nonadiabatic and velocity-dependent" corrections. In point of fact, this nomenclature is misleading. Indeed, it is clear, from our earlier discussion, that we would have obtained precisely the same result for $\mathbf{V}^{(4a)}$ had we used $V_{TD}{}^{(4a)}$ [Eq. (24b)] as the starting point of our considerations instead of $V^{(4a)}$ [Eq. (20b)] since

the nucleons are taken to be at rest. It must be stressed that the iteration procedure which was used to deduce the general form of V_{TD}[4a] goes through in exactly the same way even if one deals with fixed sources, provided one takes care not to approximate the energy of the system E which appears explicitly in V_{TD} [Eq. (21)] by $2M$.

Secondly, it has been argued, particularly by Brueckner and Watson,[10] that the iteration procedure which was used to express V_{TD} in the form of a power series is invalid, and that one ought in fact not expand the energy denominator in V_{TD} at all. Then, one would expect that the total potential, to fourth order, would be better approximated by omitting the term $\mathbf{V}^{(4a)}$ altogether, so that one would be left with the net interaction $\mathbf{V}^{(2)}+\mathbf{V}^{(4b)}$ instead of $\mathbf{V}^{(2)}$. However, since $\mathbf{V}^{(2)}$ is also known to be the exact result for the neutral scalar theory with fixed sources, this procedure of dropping the "nonadiabatic velocity-dependent" corrections is suspect, at least when the coupling is weak.[20] In any case, it is clear that, within the framework of the method of canonical transformations, there appears to be no justification for treating $\mathbf{V}^{(4a)}$ on a different footing from the contributions $\mathbf{V}^{(4b)}$ which appear upon introduction of the two-meson amplitude.

We shall complete our discussion of the neutral scalar theory by considering to what extent the fixed-source potential [Eqs. (33a) and (50)] must be modified so as to constitute the complete nonrelativistic interaction. Now, for an attractive Yukawa potential of the type (33a), the nucleon velocities v, in a bound system like the deuteron, will be of the order of μ/M. Also, the binding energy is small compared to μ^2/M so that the mean kinetic energy is of the order of the depth of the potential well, i.e., $\mu^2/M\sim(f^2/4\pi)\mu$. Hence we have $v\sim\mu/M\sim f^2/4\pi$.

To obtain an interaction which is consistent with the retention of terms of order μ^2/M for the kinetic energy of the nucleons, we consequently need to compute the second-order interaction $\mathbf{V}^{(2)}$ more carefully and look for nonadiabatic corrections which are of order μ/M with respect to the adiabatic potential given by (33a). The fourth-order potential is already given correctly by (50). It is therefore sufficient to confine our considerations to the equation

$$(E-W_0)\phi=V^{(2)}\phi, \tag{51}$$

with $V^{(2)}$ given by (20a).

The interaction Hamiltonian $\mathcal{H}$ will now be of the form

$$\mathcal{H}=f\int d\mathbf{r}\bar{\psi}\psi\phi; \tag{52}$$

here, ψ is the nucleon field variable and $\bar{\psi}=\psi^\dagger\gamma_4$. The latter quantities are conveniently expanded in terms of plane waves, leading to the usual expressions

$$\psi(\mathbf{r})=\sum_{\mathbf{p}}\sum_{\lambda=1}^{4} b(\mathbf{p}\lambda)u(\mathbf{p}\lambda)e^{i\mathbf{p}\cdot\mathbf{r}}, \tag{53a}$$

$$\bar{\psi}(\mathbf{r})=\sum_{\mathbf{p}}\sum_{\lambda=1}^{4} b^\dagger(\mathbf{p}\lambda)\bar{u}(\mathbf{p}\lambda)e^{-i\mathbf{p}\cdot\mathbf{r}}, \tag{53b}$$

where $b(\mathbf{p}\lambda)$ and $b^\dagger(\mathbf{p}\lambda)$ are the nucleon absorption and emission operators, respectively, and where $u(\mathbf{p}\lambda)$ is the free-particle Dirac spinor which is characterized by the momentum $\mathbf{p}$ and spin-energy index λ. For definiteness, let $\lambda=1,2$ and $\lambda=3,4$ denote positive- and negative-energy solutions, respectively. The $u(\mathbf{p}\lambda)$ are normalized so that

$$\sum_{\rho=1}^{4} u_\rho^\dagger(\mathbf{p}\lambda)u_\rho(\mathbf{p}\lambda')=\delta_{\lambda,\lambda'}. \tag{54}$$

Upon substituting (26) and (53) into (52), we find that K_{01} and K_{10} are given by

$$K_{01}=(K_{10})^\dagger=f\sum_{\mathbf{p},\mathbf{k}}\sum_{\lambda,\lambda'=1}^{2}[(2\omega(k)]^{-\frac{1}{2}}\bar{u}(\mathbf{p}+\mathbf{k}\lambda')\times u(\mathbf{p}\lambda)[b^\dagger(\mathbf{p}+\mathbf{k}\lambda')b(\mathbf{p}\lambda)a(\mathbf{k})]_{01}; \tag{55}$$

we have restricted the possible values of the spin-energy indices to 1 and 2 since only positive-energy spinors are relevant in the calculation of the second-order interaction. Similarly, we have

$$K_{01}'=-(K_{10}')^\dagger=-f\sum_{\mathbf{p},\mathbf{k}}\sum_{\lambda,\lambda'=1}^{2}[2\omega(k)]^{-\frac{1}{2}}\times[\omega(k)+E(p)-E(\mathbf{p}+\mathbf{k})]^{-1}\bar{u}(\mathbf{p}+\mathbf{k}\lambda')u(\mathbf{p}\lambda)\times[b^\dagger(\mathbf{p}+\mathbf{k}\lambda')b(\mathbf{p}\lambda)a(\mathbf{k})]_{01}, \tag{56}$$

where $E(p)=(M^2+p^2)^{\frac{1}{2}}$.

Now, in momentum space, Eq. (51) will have the form

$$[E-E(1)-E(2)]\phi(1,2)=\tfrac{1}{2}\sum_{3,4}(1,2|\,V^{(2)}\,|(3,4)\phi(3,4), \tag{57}$$

where, for brevity, we have simply written i for $\mathbf{p}_i\lambda_i$. The factor $\frac{1}{2}$ which appears on the right-hand side of (57) arises on account of the fact that we are dealing with a system of two identical particles.[22] The mo-

[22] In making the transcription from (51) to (57), we expand ϕ in terms of the complete set of two-nucleon free-particle states $\Psi(i,j)$ where these, in turn, can be defined by the relation $\Psi(i,j)=b^\dagger(i)b^\dagger(j)\Psi_{\text{vac}}$. However, since $\Psi(i,j)$ and $\Psi(j,i)$ are not independent of one another but, in fact, satisfy $\Psi(j,i)=-\Psi(i,j)$, we set $\phi=\Sigma_{i>j}\phi(i,j)\Psi(i,j)$ where it is assumed that the single-particle states are ordered. On substitution into (51), we then find

$$[E-E(1)-E(2)]\phi(1,2)=\Sigma_{3>4}(1,2|\,V^{(2)}\,|3,4)\phi(3,4). \tag{57'}$$

Alternatively, we may put $\phi=\frac{1}{2}\Sigma_{i,j}\phi(i,j)\Psi(i,j)$ with $\phi(j,i)=-\phi(i,j)$, in which case we are led to the form given in the text.

mentum-space representation of the second-order nucleon-nucleon potential $\mathbf{V}^{(2)}$ will accordingly be determined by requiring that

$$\sum_{3,4}(1,2|\mathbf{V}^{(2)}|3,4)\phi(3,4)$$
$$=\tfrac{1}{2}\sum_{3,4}(1,2|V^{(2)}|3,4)\phi(3,4)$$
$$=\tfrac{1}{4}\sum_{3,4}(1,2|K_{01}'K_{10}-K_{01}K_{10}'|3,4)\phi(3,4). \quad (58)$$

The explicit evaluation of the matrix element $(1,2|\mathbf{V}^{(2)}|3,4)$, including nonadiabatic corrections, proceeds in a rather straightforward way upon insertion of (55) and (56) into (58) along with application of (31) and the analogous relation

$$(1,2|b^\dagger(j')b(i')b^\dagger(j)b(i)|3,4)$$
$$=(\delta_{j1}\delta_{j'2}-\delta_{j2}\delta_{j'1})(\delta_{i2}\delta_{i'4}-\delta_{i4}\delta_{i'3}) \quad (59)$$

(ignoring self-energy terms, as always). The final result is to find[23]

$$(\mathbf{p}_1\lambda_1,\mathbf{p}_2\lambda_2|\mathbf{V}^{(2)}|\mathbf{p}_1+\mathbf{k}\lambda_3,\ \mathbf{p}_2-\mathbf{k}\lambda_4)$$
$$=-\frac{f^2}{2}\left(\frac{1}{2\pi}\right)^3\left\{\frac{1}{\omega^2(k)-[E(p_1)-E(\mathbf{p}_1+\mathbf{k})]^2}\right.$$
$$\left.+\frac{1}{\omega^2(k)-[E(p_2)-E(\mathbf{p}_2-\mathbf{k})]^2}\right\}\bar{u}(\mathbf{p}_1\lambda_1)$$
$$\times u(\mathbf{p}_1+\mathbf{k}\lambda_3)\bar{u}(\mathbf{p}_2\lambda_2)u(\mathbf{p}_2-\mathbf{k}\lambda_4). \quad (60)$$

It is now immediately evident from (60) that, in the adiabatic limit, one will simply regain the fixed-source second-order potential (33a); also, that the first nonvanishing nonadiabatic corrections are of order $(\mu/M)^2$ with respect to the adiabatic potential.[24] Accordingly, the nonrelativistic interaction is given completely by (33a).

(b) Charge-Symmetric *Ps-Ps* Theory

In this subsection we shall consider the nuclear-force problem for the case of greatest physical interest, *viz.*, the charge-symmetric pseudoscalar theory with pseudoscalar coupling. The interaction Hamiltonian is then given by

$$\mathcal{K}=iG\int d\mathbf{r}\bar{\psi}\gamma_5\tau_\alpha\phi_\alpha\psi, \quad (61)$$

where G is the coupling constant, γ_5 is the Dirac matrix $\gamma_1\gamma_2\gamma_3\gamma_4$, and the τ_α ($\alpha=1, 2, 3$) are the usual isotopic-spin matrices. The meson field components ϕ_α now constitute a vector in isotopic-spin space, while the nucleon field variable ψ is an eight-component Dirac spinor. We adopt the convention that the index α is to be summed from 1 to 3 whenever it appears twice in an expression.

In point of fact, we shall find it more convenient to work with the equivalent form

$$\mathcal{K}=\mathcal{K}^{(pr)}+\mathcal{K}^{(pv)}+\cdots, \quad (62a)$$

with

$$\mathcal{K}^{(pr)}=(G^2/2M)\int d\mathbf{r}\bar{\psi}\psi\phi_\alpha\phi_\alpha, \quad (62b)$$

$$\mathcal{K}^{(pv)}=(G/2M)\int d\mathbf{r}\psi^\dagger\boldsymbol{\sigma}\cdot(\boldsymbol{\nabla}\boldsymbol{\phi}_\alpha)\tau_\alpha\psi, \quad (62c)$$

which is obtained from (61) upon application of the Dyson-Foldy transformation.[25] The pseudoscalar interaction is thus equivalent to the sum of the pair and pseudovector interactions, $\mathcal{K}^{(pr)}$ and $\mathcal{K}^{(pv)}$, respectively, plus other terms of order $(G/2M)^2$ which will not influence any of the following considerations and which will accordingly be completely ignored.

Now, it is evident from (62) that the leading second- and fourth-order terms of the nucleon-nucleon potential will be proportional to $(G^2/4\pi)(\mu/2M)^2$ and $(G^2/4\pi)^2\times(\mu/2M)^2$, respectively. If we assume that the coupling constant is large, say, $G^2/4\pi\sim10$,[26] we would expect the fourth-order interaction to predominate over that of the second order.[27] We shall accordingly take for the nonrelativistic nucleon-nucleon potential the leading fourth-order interaction, which goes as $(G^2/4\pi)^2(\mu/2M)^2$, plus correction terms of order $(G^2/4\pi)(\mu/2M)^2$ and $(G^2/4\pi)^2(\mu/2M)^3$;[28] terms which involve powers of G higher than the fourth will not be considered.

We shall now need to extend our previous formalism somewhat since the interaction Hamiltonian (62) involves the meson field both linearly and bilinearly. For the Schrödinger equation, we have

$$(E-\mathcal{H})\Psi=(\mathcal{K}^{(pr)}+\mathcal{K}^{(pv)})\Psi, \quad (63)$$

[23] A similar result has been derived by M. Jean, Compt. rend. **232**, 2045 (1951), using Schwinger's covariant perturbation theory.

[24] In Lévy's discussion of this problem (reference 5), there do appear nonadiabatic corrections which are of order μ/M with respect to the fixed-source potential (and which we have alluded to earlier in reference 15); these terms are discarded, however, when it is shown, by means of a variational principle, that they lead to corrections to the adiabatic coupling constant which are of order $(\mu/M)^2$.

[25] See, for example, S. D. Drell and E. M. Henley, Phys. Rev. **88**, 1053 (1952).

[26] Bethe, Dyson, Mitra, Ross, Salpeter, Schweber, Sundaresen, and Visscher, Phys. Rev. **90**, 372 (1953).

[27] H. A. Bethe, Phys. Rev. **76**, 191 (1949); K. M. Watson and J. V. Lepore, Phys. Rev. **76**, 1157 (1949).

[28] If we take the perturbation-theoretic approach seriously so that the dominant term in the potential is the leading fourth-order interaction, then, to have a bound system like the deuteron, one can estimate roughly that $G^2/4\pi\sim4(M/\mu)^2$. This is in accord with the order of magnitude of the coupling constant assumed in the text and justifies, formally, the selection of terms to be retained in the nonrelativistic potential.

where the state vector Ψ of the system is once again represented by a three-component column matrix (34) and the free-field Hamiltonian $\mathcal{H}$ appears as a diagonal three-by-three matrix (36a). On the other hand, the pair and pseudovector interaction Hamiltonians will have the following structure:

$$\mathcal{K}^{(pr)}=\begin{bmatrix}0 & 0 & K_{02}\\ 0 & K_{11} & 0\\ K_{20} & 0 & 0\end{bmatrix}, \tag{64a}$$

$$\mathcal{K}^{(pv)}=\begin{bmatrix}0 & K_{01} & 0\\ K_{10} & 0 & K_{12}\\ 0 & K_{21} & 0\end{bmatrix}. \tag{64b}$$

In (64a) we have dropped the matrix elements K_{00} and K_{22}; the former contains self-energy terms only, while the latter will not contribute to the nuclear force until the sixth order.

We proceed next to apply a series of canonical transformations so as to decouple the no-meson amplitude ϕ_0 from ϕ_1 and ϕ_2. Since the pair term is the larger of the two interaction terms, we first set

$$\Psi=(\exp -i\mathcal{R})\Phi, \tag{65}$$

where $\mathcal{R}$ is chosen so as to eliminate the off-diagonal part of $\mathcal{K}^{(pr)}$ from the interaction Hamiltonian; we therefore take

$$\mathcal{R}=-i\begin{bmatrix}0 & 0 & K_{02}'\\ 0 & 0 & 0\\ K_{20}' & 0 & 0\end{bmatrix}. \tag{66}$$

On carrying through the unitary transformation defined by (65) and (66), we find that Φ satisfies the equation

$$(E-\mathcal{H})\Phi=\mathcal{L}\Phi, \tag{67a}$$

where

$$\mathcal{L}=\mathcal{K}^{(pv)}+\mathcal{K}_D{}^{(pr)}+\mathcal{L}^{(3)}+\mathcal{L}^{(4)}+\cdots; \tag{67b}$$

we denote by $\mathcal{K}_D{}^{(pr)}$ the diagonal part of the pair interaction. The third- and fourth-order terms, $\mathcal{L}^{(3)}$ and $\mathcal{L}^{(4)}$, involve the pair interaction once and twice, respectively; in particular, the fourth-order two-pair contribution to the nuclear force is already completely contained in $\mathcal{L}^{(4)}$.

In order to obtain the fourth-order one-pair interaction as well as the second-order potential, we apply a second transformation of the form

$$\Phi=(\exp -i\mathcal{S})\Xi, \tag{68}$$

where $\mathcal{S}$ is given by (37a) and (37b), thereby removing $\mathcal{K}^{(pv)}$ from the interaction Hamiltonian. The resultant equation satisfied by Ξ will then have the form

$$(E-\mathcal{H})\Xi=(\mathfrak{M}^{(2)}+\mathfrak{M}^{(3)}+\mathfrak{M}^{(4)}+\cdots)\Xi. \tag{69}$$

While $\mathfrak{M}^{(2)}$ still contains off-diagonal matrix elements [they are, in fact, precisely the same as those listed in (39)], their removal, by a third canonical transformation, will only serve to lead to a contribution to the potential of order $(G^2/4\pi)^2(\mu/2M)^4$. It is also once again clear that the off-diagonal matrix elements contained in $\mathfrak{M}^{(3)}$ and $\mathfrak{M}^{(4)}$ will not affect the fourth-order nuclear force at all. Accordingly, we can conclude that, to the order of interest in the calculation of the nonrelativistic nuclear force, the new no-meson Tamm-Dancoff amplitude ϕ is completely decoupled from all the others so that the equation satisfied by ϕ can be identified as the two-particle Schrödinger equation for the system [the interaction Hamiltonian will be given by $(\mathfrak{M}^{(2)}+\mathfrak{M}^{(4)})_{00}$]. After an elementary calculation, one finds that this equation is given by

$$(E-W_0)\phi=(V^{(2)}+V^{(4a)}+V^{(4b)})\phi, \tag{70}$$

where

$$V^{(2)}=\tfrac{1}{2}(K_{01}'K_{10}-K_{01}K_{10}'), \tag{71a}$$

$$V^{(4a)}=\tfrac{1}{2}(K_{02}'K_{20}-K_{02}K_{20}'), \tag{71b}$$

$$V^{(4b)}=-(K_{01}'K_{11}K_{10}'+K_{01}'K_{12}K_{20}'+K_{02}'K_{21}K_{10}'). \tag{71c}$$

It is evident that $V^{(4a)}$ and $V^{(4b)}$ involve the pair interaction twice and once, respectively. All three terms in (71) are, of course, Hermitian.[29]

In proceeding to apply (71) to the charge-symmetric *ps-ps* theory, we shall find it convenient, at first, to treat the interaction Hamiltonian (62) in the fixed-source approximation. We can then write

$$\begin{aligned}\mathcal{K}^{(pr)}&=(G^2/2M)\textstyle\sum_i \boldsymbol{\phi}_\alpha(\mathbf{r}_i)\boldsymbol{\phi}_\alpha(\mathbf{r}_i),\\ \mathcal{K}^{(pv)}&=(G/2M)\textstyle\sum_i \boldsymbol{\sigma}^{(i)}\cdot\boldsymbol{\nabla}\boldsymbol{\phi}_\alpha(\mathbf{r}_i)\tau_\alpha{}^{(i)}.\end{aligned} \tag{72}$$

Next, we expand $\boldsymbol{\phi}_\alpha$ in a Fourier series, *viz.*,

$$\boldsymbol{\phi}_\alpha(\mathbf{r})=\textstyle\sum_{\mathbf{k}}[2\omega(k)]^{-\frac{1}{2}}[a_\alpha(\mathbf{k})e^{i\mathbf{k}\cdot\mathbf{r}}+a_\alpha{}^\dagger(\mathbf{k})e^{-i\mathbf{k}\cdot\mathbf{r}}], \tag{73}$$

whereupon we may write

$$\begin{aligned}K_{n,n+1}&=(K_{n+1,n})^\dagger=i(G/2M)\textstyle\sum_{\mathbf{k}}[2\omega(k)]^{-\frac{1}{2}}\\ &\quad\times[a_\alpha(\mathbf{k})]_{n,n+1}\textstyle\sum_i(\boldsymbol{\sigma}^{(i)}\cdot\mathbf{k})\tau_\alpha{}^{(i)}e^{i\mathbf{k}\cdot\mathbf{r}_i},\\ K'_{n,n+1}&=-(K'_{n+1,n})^\dagger=-i(G/2M)\textstyle\sum_{\mathbf{k}}2[2\omega(k)]^{-\frac{1}{2}}\\ &\quad\times[a_\alpha(\mathbf{k})]_{n,n+1}\textstyle\sum_i(\boldsymbol{\sigma}^{(i)}\cdot\mathbf{k})\tau_\alpha{}^{(i)}e^{i\mathbf{k}\cdot\mathbf{r}_i};\end{aligned} \tag{74}$$

[29] If one eliminates the one-meson and two-meson amplitudes from the Tamm-Dancoff equations by algebraic substitution, one finds, for the fourth-order potential, $V_{TD}{}^{(4a)}=-K_{02}K_{20}'$ and $V_{TD}{}^{(4b)}=K_{01}(K_{11}K_{10}')'+K_{01}(K_{12}K_{20}')'+K_{02}(K_{21}K_{10}')'$. It is then clear that, in the adiabatic limit, these expressions will agree with those for $V^{(4a)}$ and $V^{(4b)}$ which are given in the text.

also,

$$K_{02}=(K_{20})^\dagger=(G^2/4M)\sum_{\mathbf{k},\mathbf{k}'}(\omega\omega')^{-\frac{1}{2}}\times[a_\alpha(\mathbf{k})a_\alpha(\mathbf{k}')]_{02}\sum_i e^{i(\mathbf{k}+\mathbf{k}')\cdot\mathbf{r}_i},$$
$$K_{02}'=-(K_{20}')^\dagger=-(G^2/4M)\sum_{\mathbf{k},\mathbf{k}'}(\omega\omega')^{-\frac{1}{2}}(\omega+\omega')^{-1}\times[a_\alpha(\mathbf{k})a_\alpha(\mathbf{k}')]_{02}\sum_i e^{i(\mathbf{k}+\mathbf{k}')\cdot\mathbf{r}_i}; \quad (75)$$

and finally

$$K_{11}=(G^2/2M)\sum_{\mathbf{k},\mathbf{k}'}(\omega\omega')^{-\frac{1}{2}}[a_\alpha^\dagger(\mathbf{k}')a_\alpha(\mathbf{k})]_{11}\times\sum_i e^{i(\mathbf{k}-\mathbf{k}')\cdot\mathbf{r}_i}; \quad (76)$$

in (76), we have discarded a self-energy term.

It is now a straightforward matter to insert (74)–(76) into (71) and so obtain the desired nuclear force; it is also necessary to make use of (31) and (48), suitably generalized for the charge-symmetric theory. One then finds directly, for the second-order nuclear force,

$$\mathbf{V}^{(2)}=-(G/2M)^2(\boldsymbol{\tau}^{(1)}\cdot\boldsymbol{\tau}^{(2)})(2\pi)^{-3}\times\int d\mathbf{k}(\boldsymbol{\sigma}^{(1)}\cdot\mathbf{k})(\boldsymbol{\sigma}^{(2)}\cdot\mathbf{k})\omega^{-2}e^{i\mathbf{k}\cdot\mathbf{r}}$$
$$=(G^2/4\pi)(2M)^{-2}(\boldsymbol{\tau}^{(1)}\cdot\boldsymbol{\tau}^{(2)})(\boldsymbol{\sigma}^{(1)}\cdot\boldsymbol{\nabla})\times(\boldsymbol{\sigma}^{(2)}\cdot\boldsymbol{\nabla})(r^{-1}e^{-\mu r}); \quad (77a)$$

for the fourth-order two-pair interaction,[18]

$$\mathbf{V}^{(4a)}=-3(G^2/2M)^2(2\pi)^{-6}\times\int d\mathbf{k}d\mathbf{k}'[\omega\omega'(\omega+\omega')]^{-1}e^{i(\mathbf{k}+\mathbf{k}')\cdot\mathbf{r}}$$
$$=-3(G^2/4\pi)^2(\mu/2M)^2\times[(2/\pi)(\mu r^2)^{-1}K_1(2\mu r)]; \quad (77b)$$

and for the fourth-order one-pair interaction,

$$\mathbf{V}^{(4b)}=-6(G^2/2M)(G/2M)^2(2\pi)^{-6}\times\int d\mathbf{k}d\mathbf{k}'(\mathbf{k}\cdot\mathbf{k}')(\omega\omega')^{-2}e^{i(\mathbf{k}+\mathbf{k}')\cdot\mathbf{r}}$$
$$=6(G^2/4\pi)^2(2M)^{-3}[\boldsymbol{\nabla}(r^{-1}e^{-\mu r})]^2$$
$$=6(G^2/4\pi)^2(\mu/2M)^3[1+(\mu r)^{-1}]^2(\mu r^2)^{-1}e^{-2\mu r}. \quad (77c)$$

It will be noticed that the fourth-order potential $\mathbf{V}^{(4a)}+\mathbf{V}^{(4b)}$, which has been derived here in the fixed-source approximation, is in agreement with Lévy's result (see second part of reference 5) as modified by Klein.[6,30]

[30] That the Lévy-Klein potential can be deduced by applying perturbation theory in the limit of fixed point sources has also been noted by S. D. Drell and K. Huang, Phys. Rev. **91**, 1527 (1953) and by K. J. Le Couteur, Report of the Birmingham Conference on Nuclear Physics, 1953, Birmingham, England (unpublished).

In order to complete our discussion of the nonrelativistic nuclear force, we need to investigate the nonadiabatic corrections of order μ/M with respect to the leading fourth-order two-pair term. For this purpose, we return to the original form of the pair interaction $\mathcal{K}^{(pr)}$ as given by (62b), and, by analogy with (57), use, as our point of departure, the Schrödinger equation

$$[E-E(1)-E(2)]\phi(1,2)=\tfrac{1}{2}\sum_{3,4}(1,2|V^{(4a)}|3,4)\phi(3,4), \quad (78)$$

where $V^{(4a)}$ is given by (71b). The fourth-order two-pair potential $\mathbf{V}^{(4a)}$ can therefore be identified from the expression

$$\sum_{3,4}(1,2|\mathbf{V}^{(4a)}|3,4)\phi(3,4)=\tfrac{1}{2}\sum_{3,4}(1,2|V^{(4a)}|3,4)\phi(3,4)=\tfrac{1}{4}\sum_{3,4}(1,2|K_{02}'K_{20}-K_{02}K_{20}'|3,4)\phi(3.4). \quad (79)$$

If we insert (53), appropriately generalized to take into account the isotopic-spin formalism, and (73) into (62b), we find

$$K_{02}=(K_{20})^\dagger=(G^2/4M)\sum_{\mathbf{p},\mathbf{k},\mathbf{k}'}\sum_{\lambda,\lambda'=1}^{4}[\omega(k)\omega(k')]^{-\frac{1}{2}}\times\bar{u}(\mathbf{p}+\mathbf{k}+\mathbf{k}'\lambda')u(\mathbf{p}\lambda)\times[b^\dagger(\mathbf{p}+\mathbf{k}+\mathbf{k}'\lambda')b(\mathbf{p}\lambda)a_\alpha(\mathbf{k})a_\alpha(\mathbf{k}')]_{02}, \quad (80)$$

and

$$K_{02}'=-(K_{20}')^\dagger=-(G^2/4M)\sum_{\mathbf{p},\mathbf{k},\mathbf{k}'}\sum_{\lambda,\lambda'=1}^{4}[\omega(k)\omega(k')]^{-\frac{1}{2}}\times[\omega(k)+\omega(k')+E(p)-E(\mathbf{p}+\mathbf{k}+\mathbf{k}')]\times\bar{u}(\mathbf{p}+\mathbf{k}+\mathbf{k}'\lambda')u(\mathbf{p}\lambda)[b^\dagger(\mathbf{p}+\mathbf{k}+\mathbf{k}'\lambda')\times b(\mathbf{p}\lambda)a_\alpha(\mathbf{k})a_\alpha(\mathbf{k}')]_{02}; \quad (81)$$

λ is now an isotopic-spin spin-energy index which, for positive energies, we have taken to range from 1 to 4. Then, upon substituting (80) and (81) into (79), we obtain, after a brief calculation,

$$(\mathbf{p}_1\lambda_1,\mathbf{p}_2\lambda_2|\mathbf{V}^{(4a)}|\mathbf{p}_1+\mathbf{K}\lambda_3,\mathbf{p}_2-\mathbf{K}\lambda_4)$$
$$=-\frac{3}{2}\left(\frac{G^2}{2M}\right)^2\left(\frac{1}{2\pi}\right)^6\int_{\mathbf{k}+\mathbf{k}'=\mathbf{K}}d\mathbf{k}d\mathbf{k}'\left[\frac{\omega(k)+\omega(k')}{\omega(k)\omega(k')}\right]\times\left\{\frac{1}{[\omega(k)+\omega(k')]^2-[E(p_1)-E(\mathbf{p}_1+\mathbf{K})]^2}+\frac{1}{[\omega(k)+\omega(k')]^2-[E(p_2)-E(\mathbf{p}_2-\mathbf{K})]^2}\right\}\times\bar{u}(\mathbf{p}_1\lambda_1)u(\mathbf{p}_1+\mathbf{K}\lambda_3)\bar{u}(\mathbf{p}_2\lambda_2)u(\mathbf{p}_2-\mathbf{K}\lambda_4). \quad (82)$$

It will now be noticed that, in the adiabatic limit, (82) simply goes over into the form (77b) which was derived in the fixed-source approximation. It is also evident, from the form of the energy denominators in (82), that the nonadiabatic corrections which are of order μ/M with respect to the leading two-pair terms vanish.[31] We are hence justified in identifying the fixed-source potential (77) as the nonrelativistic interaction for the *ps-ps* theory (apart from the question of radiative corrections which we have consistently ignored); as is well known, this potential is wholly inadequate on account of the near-cancellation of the attractive two-pair term $\mathbf{V}^{(4a)}$ by the repulsive one-pair term $\mathbf{V}^{(4b)}$.[32]

(c) Charge-Symmetric *Ps-Pv* Theory

As a final illustration, we consider briefly the charge-symmetric pseudoscalar theory with pseudovector coupling. This case is of particular interest for the nuclear-force problem in view of the accumulation of evidence pointing toward the suppression of the effects of the pair term (62b) in *ps-ps* theory when radiative and higher-order corrections are taken into account[33]; under these circumstances, we have left the pseudovector interaction (62c) which we now rewrite as

$$\mathcal{K}=(g/\mu)\int d\mathbf{r}\psi^{\dagger}\boldsymbol{\sigma}\cdot(\boldsymbol{\nabla}\boldsymbol{\phi}_{\alpha})\tau_{\alpha}\psi, \tag{83}$$

where the coupling constants g and G are connected by the relation $g=G(\mu/2M)$.

The calculation of the nonrelativistic nuclear force for the *ps-pv* theory can now be carried through in a manner which is quite analogous to our previous discussion of the neutral scalar theory. First, we estimate that $v\sim\mu/M\sim g^2/4\pi$, so that we shall need to compute the second- plus fourth-order nuclear force in adiabatic (or fixed-source) approximation, as well as the nonadiabatic corrections of order μ/M with respect to the leading term in the second-order potential.

In the fixed-source limit, the interaction Hamiltonian is given by

$$\mathcal{K}=(g/\mu)\textstyle\sum_i \boldsymbol{\sigma}^{(i)}\cdot\boldsymbol{\nabla}\boldsymbol{\phi}_{\alpha}(\mathbf{r}_i)\tau_{\alpha}{}^{(i)}. \tag{84}$$

The second- and fourth-order potentials may therefore be calculated by inserting (74) into (20) and (45). The result for the second-order force has already been listed in Eq. (77a). For the fourth-order interaction, we find

$$\begin{aligned}\mathbf{V}^{(4a)}&=(g/\mu)^4(3-2\boldsymbol{\tau}^{(1)}\cdot\boldsymbol{\tau}^{(2)})(2\pi)^{-6}\int d\mathbf{k}d\mathbf{k}'\\&\quad\times\{(\mathbf{k}\cdot\mathbf{k}')^2-[\boldsymbol{\sigma}^{(1)}\cdot(\mathbf{k}\times\mathbf{k}')][\boldsymbol{\sigma}^{(2)}\cdot(\mathbf{k}\times\mathbf{k}')]\}\\&\qquad\times\omega^{-2}(\omega')^{-3}e^{i(\mathbf{k}+\mathbf{k}')\cdot\mathbf{r}}\\&=(g^2/4\pi)^2\mu^{-4}(3-2\boldsymbol{\tau}^{(1)}\cdot\boldsymbol{\tau}^{(2)})\\&\quad\times(\{(\boldsymbol{\nabla}\cdot\boldsymbol{\nabla}')^2-[\boldsymbol{\sigma}^{(1)}\cdot(\boldsymbol{\nabla}\times\boldsymbol{\nabla}')][\boldsymbol{\sigma}^{(2)}\cdot(\boldsymbol{\nabla}\times\boldsymbol{\nabla}')]\}\\&\qquad\times r^{-1}e^{-\mu r}(2/\pi)K_0(\mu r'))_{\mathbf{r}'=\mathbf{r}};\end{aligned} \tag{85a}$$

$$\begin{aligned}\mathbf{V}^{(4b')}&=-\mathbf{V}^{(4a)}-\tfrac{3}{2}(g/\mu)^4(2\pi)^{-6}\int d\mathbf{k}d\mathbf{k}'\\&\quad\times\{2(\boldsymbol{\tau}^{(1)}\cdot\boldsymbol{\tau}^{(2)})(\mathbf{k}\cdot\mathbf{k}')^2+3[\boldsymbol{\sigma}^{(1)}\cdot(\mathbf{k}\times\mathbf{k}')]\\&\qquad\times[\boldsymbol{\sigma}^{(2)}\cdot(\mathbf{k}\times\mathbf{k}')]\}\omega^{-2}(\omega')^{-3}e^{i(\mathbf{k}+\mathbf{k}')\cdot\mathbf{r}}\\&=-\mathbf{V}^{(4a)}-\tfrac{3}{2}(g^2/4\pi)^2\mu^{-4}(\{2(\boldsymbol{\tau}^{(1)}\cdot\boldsymbol{\tau}^{(2)})(\boldsymbol{\nabla}\cdot\boldsymbol{\nabla}')^2\\&\qquad+3[\boldsymbol{\sigma}^{(1)}\cdot(\boldsymbol{\nabla}\times\boldsymbol{\nabla}')][\boldsymbol{\sigma}^{(2)}\cdot(\boldsymbol{\nabla}\times\boldsymbol{\nabla}')]\}\\&\qquad\times r^{-1}e^{-\mu r}(2/\pi)K_0(\mu r'))_{\mathbf{r}'=\mathbf{r}};\end{aligned} \tag{85b}$$

$$\begin{aligned}\mathbf{V}^{(4b'')}&=\tfrac{1}{2}(g/\mu)^4(2\pi)^{-6}\int d\mathbf{k}d\mathbf{k}'\{2(\boldsymbol{\tau}^{(1)}\cdot\boldsymbol{\tau}^{(2)})(\mathbf{k}\cdot\mathbf{k}')^2\\&\qquad+3[\boldsymbol{\sigma}^{(1)}\cdot(\mathbf{k}\times\mathbf{k}')][\boldsymbol{\sigma}^{(2)}\cdot(\mathbf{k}\times\mathbf{k}')]\}\\&\qquad\times(\omega-\omega')[\omega^3(\omega')^2(\omega+\omega')]^{-1}e^{i(\mathbf{k}+\mathbf{k}')\cdot\mathbf{r}}\\&=-\tfrac{1}{2}(g^2/4\pi)^2\mu^{-4}(\{2(\boldsymbol{\tau}^{(1)}\cdot\boldsymbol{\tau}^{(2)})(\boldsymbol{\nabla}\cdot\boldsymbol{\nabla}')^2\\&\qquad+3[\boldsymbol{\sigma}^{(1)}\cdot(\boldsymbol{\nabla}\times\boldsymbol{\nabla}')][\boldsymbol{\sigma}^{(2)}\cdot(\boldsymbol{\nabla}\times\boldsymbol{\nabla}')]\}\\&\qquad\times\{(4/\pi)(r^{-1}+(r')^{-1})K_0[\mu(r+r')]\\&\qquad-3r^{-1}e^{-\mu r}(2/\pi)K_0(\mu r')\})_{\mathbf{r}'=\mathbf{r}}.\end{aligned} \tag{85c}$$

It is evident from (45) that $\mathbf{V}^{(4a)}$ represents that part of the fourth-order potential which is contained in the lowest-order Tamm-Dancoff approximation; on the other hand, $\mathbf{V}^{(4b)}=\mathbf{V}^{(4b')}+\mathbf{V}^{(4b'')}$ makes its appearance when we allow for the presence of two mesons in the field.

The total fourth-order potential $\mathbf{V}^{(4)}=\mathbf{V}^{(4a)}+\mathbf{V}^{(4b)}$, which evidently is the perturbation-theoretic result, has been derived by many authors.[6,9,34] It contains a strong repulsive force in triplet-even states which makes this potential quite unsuitable for a description of the

[31] In Klein's treatment of this problem (reference 6), one does encounter nonvanishing nonadiabatic corrections of order μ/M with respect to the leading fourth-order potential (and also the second-order potential); these terms are dropped, however, after Klein invokes a variational-principle argument similar to that noted in reference 24.

[32] See, for example, Fig. 2 in Drell and Huang's paper (reference 30).

[33] For a summary of the case for pair suppression, see A. Klein, Phys. Rev. **95**, 1061 (1954).

[34] Taketani, Machida, and Ohnuma, Progr. Theoret. Phys. Japan **6**, 638 (1951); K. Nishijima, Progr. Theoret. Phys. Japan **6**, 815, 911 (1951); J. L. Lopes and R. P. Feynman, *Symposium on New Research Techniques in Physics* (Academia Brasileira de Ciencias, Rio de Janeiro, 1954), p. 251.

deuteron, say. Brueckner and Watson, in their discussion of the nuclear-force problem for *ps-pv* theory, have suggested that the fourth-order interaction is better approximated by the term $V^{(4b)}$, in which case the repulsion, mentioned above, is turned into an attraction. However, this procedure is difficult to justify in the light of our previous discussion of the neutral scalar theory [immediately following Eq. (50)].

Finally, we need to consider the nonadiabatic corrections of order μ/M with respect to the second-order potential (77a). For this purpose, we can essentially take over the results of our earlier calculation for the neutral scalar theory [Eq. (51) ff.] suitably modified for the *ps-pv* theory. The final result is to find[35]

$$(\mathbf{p}_1\lambda_1, \mathbf{p}_2\lambda_2|V^{(2)}|\mathbf{p}_1+\mathbf{k}\lambda_3, \mathbf{p}_2-\mathbf{k}\lambda_4)$$
$$=-\frac{1}{2}\left(\frac{g}{\mu}\right)^2\left(\frac{1}{2\pi}\right)^3\left\{\frac{1}{\omega^2(k)-[E(p_1)-E(\mathbf{p}_1+\mathbf{k})]^2}\right.$$
$$\left.+\frac{1}{\omega^2(k)-[E(p_2)-E(\mathbf{p}_2-\mathbf{k})]^2}\right\}$$
$$\times u^\dagger(\mathbf{p}_1\lambda_1)(\boldsymbol{\sigma}\cdot\mathbf{k})\tau_a u(\mathbf{p}_1+\mathbf{k}\lambda_3)$$
$$\times u^\dagger(\mathbf{p}_2\lambda_2)(\boldsymbol{\sigma}\cdot\mathbf{k})\tau_a u(\mathbf{p}_2-\mathbf{k}\lambda_4). \quad (86)$$

It is clear from (86) that the nonadiabatic corrections of order μ/M vanish so that the nonrelativistic potential for *ps-pv* theory is given by the fixed-source calculation [(77a) and (85)].[31]

[35] This result has been obtained previously by L. Van Hove, Phys. Rev. **75**, 1519 (1949).

PHYSICAL REVIEW VOLUME 98, NUMBER 5 JUNE 1, 1955

Effect of Renormalization on Meson-Nucleon *S*-Scattering*

MAURICE M. LÉVY†
Physics Department, University of Rochester, Rochester, New York
(Received January 11, 1955; revised manuscript received March 1, 1955)

Renormalization prescriptions are given for the covariant integral equations of meson-nucleon scattering, taking into account the difficulties of overlapping divergences. The covariant wave equations, corresponding to the iteration of second-order irreducible processes, are solved approximately and renormalized in closed form (in the case of the pseudoscalar theory with pseudoscalar coupling). The *S*-phase shifts corresponding to the states of isotopic spin 1/2 and 3/2 are computed, and their variation with energy is compared with experiment. The only parameter which can be adjusted is the meson-nucleon coupling constant *G*. It is found that a good agreement with experiment is obtained when $G^2/4\pi=7.5$. The possibility of this agreement being purely coincidental cannot be ruled out, but other interpretations of this result are discussed.

I. INTRODUCTION

IN a foregoing paper,[1] a covariant treatment of meson-nucleon scattering has been presented, which permits, in principle, the elimination of special renormalization difficulties arising in this problem. The main result was that—once the wave integral equation corresponding only to the finite processes is solved—it is possible to express and to renormalize in closed form all the remaining contributions to the scattering cross sections.[2]

The renormalization prescriptions which have to be applied to the closed expressions yielded by the theory were, however, incorrectly stated in that paper,[3] mainly because the difficulties coming from the so-called "overlapping" divergences[4] were not properly taken into account. Fortunately, it is possible to reformulate those prescriptions without losing the advantage of having a closed expression for the corresponding part of the renormalized *S*-matrix elements. This reformulation is given in Sec. II of the present paper.

Once this formal work has been done, however, there still remains the problem of actually calculating the scattering differential cross sections, in order to compare them with experiment. The first difficulty, here, is that the kernel of the partial wave-equation corresponding to the finite processes is still expressed as a series of powers of the large coupling constant *G*. This series does not seem easy to sum, and its first few terms do not appear to yield a good approximation. However,

* Work supported in part by the U. S. Atomic Energy Commission.

† On leave of absence from the University of Paris, Paris, France.

[1] M. Lévy, Phys. Rev. **94**, 460 (1954). This paper will be, in the following, referred to as (I). References to its equations will be given as Eq. (I,···).

[2] This applies, of course, only to the special divergences mentioned above. The "normal" radiative corrections must be handled by means of the well-known methods of Feynman and Dyson.

[3] The correct results were stated without proof in a note added in proof to paper (I). Most of the results contained in Sec. I of the present paper have already been reported in a letter from the author to Prof. N. M. Kroll, which has been reproduced, together with the answer from N. M. Kroll, in an Appendix to the *Proceedings of the Fourth Annual Rochester Conference on High Energy Physics* (University of Rochester, Rochester, 1954). Our special thanks are due to Prof. N. M. Kroll for this interesting correspondence.

[4] A. Salam, Phys. Rev. **82**, 217 (1951).

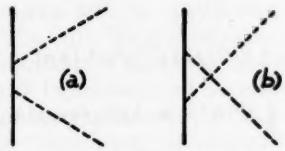

FIG. 1. The two basic diagrams of meson-nucleon scattering to the second order in the coupling constant.

the two basic diagrams corresponding to the second order in G (Fig. 1) have been the object of a detailed study without renormalization,[5] the intrinsically divergent terms being either discarded or arbitrarily cutoff at high frequencies. It seems therefore interesting to investigate to what extent a coherent renormalization scheme affects the results deduced from these processes. It must be emphasized, however, that—even if a good agreement with experiment is obtained—there is no reason to suppose that higher order irreducible terms in the expansion in G^2 will not largely contribute to the results. The interest of a calculation limited to order G^2 is mainly a methodological one, since the difficulties which arise in obtaining a finite solution are, in this case, sufficiently representative of what happens in general. Furthermore, it is possible that higher order terms, although important, affect mainly the value of the effective coupling constant without changing very much the qualitative behavior of the various phase-shifts as functions of energy.[6]

In comparing the results yielded by the pseudoscalar meson theory with pseudoscalar coupling with recent pion-nucleon scattering experiments[7] at low or moderate energies, the study of the S-wave appears of special interest. In a previous paper,[8] Lévy and Marshak have calculated the phase-shifts α_1 and α_3 (corresponding to isotopic spin $1/2$ and $3/2$ respectively) using the unrenormalized nonadiabatic Tamm-Dancoff equation. The result was that the magnitude, sign and variation with energy of α_3 are, on the whole, in reasonable agreement with experiment, but that the properties of α_1 are completely unacceptable. It was remarked, however, that α_1 is precisely the only S phase-shift which is likely to be greatly modified by renormalization. The solution of the noncovariant integral equations in meson momentum space was, in both cases, an approximate one, based on the replacement of the true kernel $K(\mathbf{p},\mathbf{p}')$ by a product for $K_1(\mathbf{p})K_2(\mathbf{p}')$. It was verified by iteration that this approximation is adequate at low energies. Unfortunately, a similar approximation cannot be used here for the solution of the wave equation for ψ_b, because of its noncovariant form. It is, indeed, essential that ψ_b be expressed covariantly before it can be introduced in the remaining renormalized expression of ψ_a. Since an exact solution of the ψ_b integral equation seems out of question, it is therefore necessary to find a covariant method of approximation. This method, which is given in Sec. III, is also based on the transformation of the kernel into a product form, by modifying the expression of the nucleon propagation function. It can be verified that this approximation is quite good for S-scattering at not too high energies, because it amounts to neglecting only terms of order $(\epsilon/M)^2$, where ϵ is the meson energy and M the nucleon mass.[9] It becomes, however, very bad for P-scattering, as indeed all approximations which transform the kernel of the integral equation into a product[10] (one would obtain, for example, no scattering at all in the states corresponding to $J=3/2$).

By solving the ψ_b equation approximately, one introduces, however, another difficulty. The renormalization prescriptions given in (I) and corrected in Sec. II of this paper are valid only *if the solution of the finite equation is exact.* A straight application of the prescriptions to an approximate solution will not, in general, lead to finite results. This means that the renormalization prescriptions *have to be adapted* to each special method of solution. This can, however, be done without too much difficulty (see Sec. III) by using Salam's general prescriptions[11] for obtaining finite integrals in relativistic field theories.

The resulting expressions of α_1 and α_3 as functions of energy are compared with experiment in Sec. IV. It is found that for a value of the coupling constant corresponding to $G^2/4\pi=7.5$, the magnitude, sign, and variation with energy of *both* phase-shifts agree reasonably well with the experimental data. The only discrepancy remains in the value of $(k)^{-1}|\alpha_1-\alpha_3|$ at zero energy, which does not seem to agree with Panofsky's measurement of the absorption cross section of slow π mesons in hydrogen.[12] Possible interpretations of this discrepancy are discussed at the end of Sec. IV. It might be of interest to note that the calculations given in this paper involve only one parameter, namely the coupling constant G. No cut-off momentum or critical minimum radius are introduced.

II. RENORMALIZATION PRESCRIPTIONS FOR THE "OVERLAPPING" VERTEX OPERATORS AND NUCLEON PROPAGATION FUNCTION

We use the same notations as in (I). The calculation of the ψ_a part of the wave function (Eq. I,10), involves two vertex operators $\Gamma_5^{(\alpha)}$ and $\Gamma_5^{(\beta)}$ and one modified

[5] G. F. Chew, Phys. Rev. **89**, 591 (1953); S. Fubini, Nuovo cimento **10**, 564 (1953); N. Fukuda, Proceedings of the International Conference of Kyoto, 1953 (unpublished); Fukuda, Goto, Okubo, and Sawada, Progr. Theoret. Phys. **12**, 79 (1954); see also reference 8.

[6] See the discussion of Sec. IV.

[7] Barnes, Angell, Perry, Miller, Ring, and Nelson, Phys. Rev. **92**, 1327 (1953); Bodansky, Sachs, and Steinberger, Phys. Rev. **93**, 918 (1954); Anderson, Fermi, Martin, and Nagle, Phys. Rev. **91**, 155 (1953); J. Tinlot and A. Roberts, Phys. Rev. **95**, 137 (1954).

[8] M. Lévy and R. Marshak, Nuovo cimento **11**, 366 (1954).

[9] We take, in the following, $\hbar=c=1$.

[10] The *iterated* approximation should, however, be good in P-states. This is being investigated at the University of Paris.

[11] A. Salam, Phys. Rev. **84**, 426 (1951).

[12] Panoksky, Aamodt, Hadley, and Phillips, Phys. Rev. **80**, 94 (1950).

nucleon propagation function K_N'. The renormalization of the vertex operators can be done by means of two methods: one can start directly from the integral equations which these operators satisfy (a method similar to the one used by Edwards[13]); or one can follow the prescriptions of Salam[11] for obtaining finite integrals in relativistic field theories. These prescriptions being rather difficult to carry out in detail, we have used here the two methods simultaneously, in order to verify that we were following Salam's procedure correctly, since the renormalization of K_N' can only be done by means of Salam's subtraction method.

1. Renormalization of $\Gamma_5^{(\alpha)}$ and $\Gamma_5^{(\beta)}$ by the Method of the Integral Equation

We write, for $\rho=\alpha, \beta$,

$$\Gamma_5^{(\rho)}(\xi_i; x,y)=\tau_i\gamma_5\delta(x-\xi)\delta(y-\xi)+\Lambda_5^{(\rho)}(\xi_i; x,y), \quad (1)$$

and put, furthermore:

$$\Lambda_5^{(\alpha)}(\xi_i; x,y)=\tau_i\gamma_5\Lambda^{(\alpha)}(\xi; x,y)$$

and

$$\Lambda_5^{(\beta)}(\xi_i; x,y)=\Lambda^{(\beta)}(\xi; x,y)\gamma_5\tau_i. \quad (2)$$

$\Lambda^{(\alpha)}$ and $\Lambda^{(\beta)}$ obey integral equations which can be written, in momentum space [see Eq. (I,17)], as follows:

$$\Lambda^{(\alpha)}(p,q)=\Lambda_0^{(\alpha)}(p,q)+iG^2(2\pi)^{-4}\int\Lambda^{(\alpha)}(p, p-k)\times K_N(p-k)K_M(k)\gamma_5K_N(q-k)\gamma_5dk, \quad (3)$$

and

$$\Lambda^{(\beta)}(p,q)=\Lambda_0^{(\beta)}(p,q)+iG^2(2\pi)^{-4}\int\gamma_5K_N(p-k)\times\gamma_5K_M(k)K_N(q-k)\Lambda^{(\beta)}(q-k, q)dk, \quad (4)$$

where we have put

$$\Lambda_0^{(\alpha)}(p,q)=iG^2(2\pi)^{-4}\int K_N(p-k)K_M(k)\gamma_5K_N(q-k)\gamma_5dk \quad (5)$$

and

$$\Lambda_0^{(\beta)}=\gamma_5\Lambda_0^{(\alpha)}\gamma_5.$$

Let us write first[14]:

$$\Lambda^{*(\alpha)}(p,q)=\Lambda^{(\alpha)}(p,q)-\Lambda^{(\alpha)}(p_0,p_0'), \quad (6)$$

where $i\gamma p_0+M=0$, and $(p_0-p_0')^2+\mu^2=0$. $\Lambda^{*(\alpha)}$ obeys the equation

$$\Lambda^{*(\alpha)}(p,q)=[1+\Lambda^{(\alpha)}(p_0,p_0')]\Lambda^{*}{}_0^{(\alpha)}(p,q)+iG^2(2\pi)^{-4}\int\Lambda^{*(\alpha)}(p, p-k)K_N(p-k)K_M(k)\times\gamma_5K_N(q-k)\gamma_5dk-iG^2(2\pi)^{-4}\int\Lambda^{*(\alpha)}(p_0, p_0-k)\times K_N(p_0-k)K_M(k)\gamma_5K_N(p_0'-k)\gamma_5dk. \quad (7)$$

Consequently, if we define

$$\Lambda_c^{(\alpha)}(p,q)=\Lambda^{*(\alpha)}(p,q)/[1+\Lambda^{(\alpha)}(p_0,p_0')], \quad (8)$$

$\Lambda_c^{(\alpha)}$ is a convergent function which obeys the equation

$$\Lambda_c^{(\alpha)}(p,q)=\Lambda^{*}{}_0^{(\alpha)}(p,q)+iG^2(2\pi)^{-4}\int\Lambda_c^{(\alpha)}(p, p-k)\times K_N(p-k)K_M(k)\gamma_5K_N(q-k)\gamma_5dk-iG^2(2\pi)^{-4}\times\int\Lambda_c^{(\alpha)}(p_0, p_0-k)K_N(p_0-k)K_M(k)\times\gamma_5K_N(p_0'-k)\gamma_5dk. \quad (9)$$

Equation (8) can be written in terms of $\Gamma^{(\alpha)}=1+\Lambda^{(\alpha)}$ and is equivalent to

$$\Gamma_c^{(\alpha)}=\Gamma^{(\alpha)}(p,q)/[\Gamma^{(\alpha)}(p_0,p_0')].$$

The infinite constant $\Gamma^{(\alpha)}(p_0,p_0')$ is just the Z constant introduced by Edwards.[13] A similar relation is, of course, found for $\Gamma_c^{(\beta)}$, the infinite constant being, this time, $\Gamma^{(\beta)}(p_0,p_0')$.

2. Renormalization of the Vertex Operators by the Method of Salam

In this method, the subtraction of partial divergences from a diagram of a given order yields expressions which are proportional to the contributions of lower order diagrams, multiplied by infinite constants. It is therefore always convenient to start subtracting partial divergences from the highest order term, and move progressively down to the lowest order. As an example, we shall apply the subtraction method to the sum of the first four terms of $\Gamma^{(\beta)}=1+\Lambda^{(\beta)}$. With notations similar to those of Salam, let us put:

$$F(p,t_1)=iG^2(2\pi)^{-4}K_N(p-t_1)K_M(t_1)$$

and

$$G(p,t_1,t_2)=\gamma_5K_N(p-t_1-t_2)\gamma_5.$$

We have, consequently,

$$\Gamma^{(\beta)}(p,t_1)=1+\int G(p,t_1,t_2)F(p,t_2)dt_2+\int G(p,t_1,t_2)F(p,t_2)G(p,t_2,t_3)F(p,t_3)dt_2dt_3+\int G(p,t_1,t_2)F(p,t_2)G(p,t_2,t_3)F(p,t_3)G(p,t_3,t_4)\times F(p,t_4)dt_2dt_3dt_4+\text{etc}\cdots. \quad (10)$$

[13] S. F. Edwards, Phys. Rev. **90**, 284 (1953).

[14] Note a difference with the corresponding equation (I,18), where two *equal* free momenta were used in the substracted vertex function. The prescription used in the present paper is equivalent to the standard method of F. J. Dyson [Phys. Rev. **75**, 1736 (1949)], after summation over a certain number of graphs. It is different both from that of N. Kroll and M. Ruderman, Phys. Rev. **93**, 233 (1953), and of Deser, Thirring, and Goldberger, Phys. Rev. **94**, 711 (1954). The variety of prescriptions in the renormalization of vertex operators is related to the well-known ambiguity in the definition of meson charge-renormalization.

Let us consider first the fourth term of the right-hand side of Eq. (10). We have to subtract from it the partial divergences over t_4, over t_3 and t_4, over t_2, t_3, and t_4. They are all logarithmic. All the other integrations, or groups of integrations, are—according to Salam's terminology—"superficially convergent." Before doing the subtraction, it is convenient to expand $\Lambda^{(\beta)}(p_0,p_0')$, the infinite constant (which is just a *number*) introduced in the preceding subsection, in powers of the coupling constant

$$\Lambda^{(\beta)}(p_0,p_0')=\sum_n \Lambda_{0,2n}{}^{(\beta)}, \tag{11}$$

where $\Lambda_{0,2n}{}^{(\beta)}$ is proportional to G^{2n}. Subtracting the divergence over t_4 in the fourth term of Eq. (10) yields an additional term:

$$-\int G(p,t_1,t_2)F(p,t_2)G(p,t_2,t_3)F(p,t_3) \times G(p_0,\, p_0-p_0',\, t_4)F(p_0,t_4)dt_2dt_3dt_4$$

which is equal to the third term of Eq. (10) multiplied by $\Lambda_{02}{}^{(\beta)}$. Similarly, subtracting the divergence over t_3 and t_4 amounts to multiplying the second term of (10) by $(1-\Lambda_{04}{}^{(\beta)})$, etc$\cdots$. After subtracting therefore all partial divergences from the fourth term of Eq. (10), we are led to the new expression:

$$\begin{aligned}\Gamma_2{}^{(\beta)}(p,t_1)&=(1-\Lambda_{06}{}^{(\beta)})\\ &+(1-\Lambda_{04}{}^{(\beta)})\int G(p,t_1,t_2)F(p,t_2)dt_2\\ &+(1-\Lambda_{02}{}^{(\beta)})\int G(p,t_1,t_2)F(p,t_2)G(p,t_2,t_3)F(p,t_3)dt_2dt_3\\ &+\int G(p,t_1,t_2)F(p,t_2)G(p,t_2,t_3)F(p,t_3)\\ &\quad\times G(p,t_3,t_4)F(p,t_4)dt_2dt_3dt_4+\text{etc}\cdots.\end{aligned} \tag{12}$$

We now start subtracting the partial divergences from the third term of Eq. (12), namely those over t_3, and t_2 and t_3. This yields a new expression $\Gamma_4{}^{(\alpha)}$, from which we finally subtract the partial divergence over t_2 of the second term. The final expression of $\Gamma^{(\alpha)}$ can be written as

$$\begin{aligned}\Gamma_6{}^{(\beta)}(p,t_1)&=1-\Lambda_{06}{}^{(\beta)}-(1-\Lambda_{02}{}^{(\beta)})\Lambda_{04}{}^{(\beta)}\\ &-[1-\Lambda_{04}{}^{(\beta)}-(1-\Lambda_{02}{}^{(\beta)})\Lambda_{02}{}^{(\beta)}]\Lambda_{02}{}^{(\beta)}\\ &+[1-\Lambda_{04}{}^{(\beta)}-(1-\Lambda_{02}{}^{(\beta)})\Lambda_{02}{}^{(\beta)}]\int G(p,t_1,t_2)\\ &\times F(p,t_2)dt_2+(1-\Lambda_{02}{}^{(\beta)})\int G(p,t_1,t_2)\\ &\times F(p,t_2)G(p,t_2,t_3)F(p,t_3)dt_2dt_3\\ &+\int G(p,t_1,t_2)F(p,t_2)G(p,t_2,t_3)F(p,t_3)\\ &\quad\times G(p,t_3,t_4)F(p,t_4)dt_2dt_3dt_4+\text{etc}\cdots.\end{aligned} \tag{13}$$

A rapid inspection of (13) shows that this is nothing but the expansion, up to G,[6] of the expression

$$\Gamma_c{}^{(\beta)}(p,t_1)=\Gamma(p,t_1)/(1+\textstyle\sum_n \Lambda_{0,2n}{}^{(\beta)}), \tag{14}$$

which is the same result as Eq. (9).

3. Renormalization of K_N' by Means of Salam's Method

Now that we have verified that we know how to use Salam's procedure properly, we can apply the same method to $\Sigma(p)$, the sum of the irreducible parts of K_N', defined as follows:

$$K_N'(p)=K_N(p)/[1-3\gamma_5\Sigma(p)\gamma_5K_N(p)]. \tag{15}$$

We therefore consider the first four terms of the expansion of $\Sigma(p)$ and write:

$$\begin{aligned}\Sigma(p)&=\int F(p,t_1)dt_1+\int F(p,t_1)G(p,t_1,t_2)F(p,t_2)dt_1dt_2\\ &+\int F(p,t_1)G(p,t_1,t_2)F(p,t_2)G(p,t_2,t_3)F(p,t_3)dt_1dt_2dt_3\\ &+\int F(p,t_1)G(p,t_1,t_2)F(p,t_2)G(p,t_2,t_3)F(p,t_3)\\ &\quad\times G(p,t_3,t_4)F(p,t_4)dt_1dt_2dt_3dt_4+\text{etc}\cdots.\end{aligned} \tag{16}$$

One difference with the calculation of the previous paragraph is that we now have divergences at both ends of each term. Furthermore, all the partial divergences are logarithmic, but the final one is linear. We consequently subtract first the partial logarithmic divergences, with the same method as in the previous paragraph. This yields the result

$$\Sigma_1(p)=\Sigma(p)/[1+\Lambda^{(\alpha)}(p_0,p_0')][1+\Lambda^{(\beta)}(p_0,p_0')]. \tag{17}$$

Subtracting the remaining linear divergence gives the renormalized expression of $\Sigma(p)$:

$$\Sigma_c(p)=\Sigma_1(p)-\Sigma_1(p_0)-(p-p_0)\left[\frac{\partial}{\partial p}\Sigma_1(p)\right]_{p=p_0}. \tag{18}$$

In obtaining the expression (17), advantage has been taken of the fact that $\Lambda^{(\alpha)}(p_0,p_0')$ and $\Lambda^{(\beta)}(p_0,p_0')$ are just numbers, since the operators γ_5 and τ_i have been subtracted [see Eqs. (1) and (2)], and use has been made of the relations $i\gamma p_0+M=p_0{}^2+M^2=0$ and $(p_0'-p_0)^2+\mu^2=0$. The relatively simple result contained in Eqs. (17) and (18) is *not* true in general of any overlapping self-energy graph. It arises from the following simple property of the particular series of graphs under consideration: these graphs contain partial divergences *only at the ends* (on both sides), but not in the middle, where the partial integrations are always "superficially convergent."

4. Renormalized Expressions of the Wave-Function and the S-Matrix Elements

The results yielded by the application of prescriptions (9), (17) and (18) to the expressions of K_a, ψ_a and of the $R=S-1$ matrix elements, can be stated immediately, using the same notations as in (I). Equation (I,34) becomes:

$$K_a(x,\xi_i;\, y,\eta_j)=\frac{-iG^2}{\Gamma_0{}^\alpha\Gamma_0{}^\beta}\int K_b(x,\xi_i;\, \xi',\xi_k')\gamma_5\tau_k K_N' \times(\xi',\eta')\gamma_5\tau_l K_b(\eta',\eta_l';\, y,\eta_j)d\xi' d\eta', \quad (19)$$

where we have put, to simplify, $1+\Lambda^{(\rho)}(p_0,p_0')=\Gamma_0{}^\rho$. Similarly, the expression (I,35) of ψ_a can be written now as

$$\psi_a(x,\xi_i)=\frac{-iG^2}{\Gamma_0{}^\alpha\Gamma_0{}^\beta}\int K_b(x,\xi_i;\, \xi',\xi_k')\gamma_5\tau_k K_N'(\xi',\eta') \times\gamma_5\tau_l\psi_b(\eta',\eta_l')d\xi' d\eta'. \quad (20)$$

Separating out the motion of the center-of-mass [Eqs. (I,50, 51 and 58)], transforming into momentum space [Eq. (I,64)], and projecting on the states of total isotopic spin 1/2 and 3/2, we obtain, for the Fourier transform of the part of the wave function corresponding to the relative motion:

$$\phi_a(p;\, P)=\frac{-iG^2}{\Gamma_0{}^\alpha\Gamma_0{}^\beta}T_a(2\pi)^{-4}\int K_b(p+P,\,-p;\, q+P,\,-q) \times dq\gamma_5 K_N'(P)\gamma_5\phi_b(0) \quad (21)$$

[compare with (I,60 and 65)], where $T_a=3$ for the state of isotopic spin 1/2 and $T_a=0$ for the state of isotopic spin 3/2. Similarly, the expression (I,53) for the R_a-matrix elements becomes here:

$$(\mathbf{k}_1',\mathbf{k}_2',j\,|\,R_a\,|\,\mathbf{k}_1,\mathbf{k}_2,i)=[-iG^2(2\pi)^4/\Gamma_0{}^\alpha\Gamma_0{}^\beta]\bar\rho_b{}^{(k)}(0) \times\gamma_5\tau_k K_N'(P)\gamma_5\tau_l\phi_b{}^{(l)}(0)\delta(\mathbf{P}-\mathbf{P}')\delta(P_0-P_0'). \quad (22)$$

The special choice for the renormalization of the vertex-operators which has been made in the paragraph 2 of this section has the advantage that expressions (21) and (22) can now be greatly simplified by a direct evaluation of the ratios $(\Gamma_0{}^\alpha)^{-1}\bar\rho_b(0)$ and $(\Gamma_0{}^\beta)^{-1}\phi_b(0)$. Combining Eqs. (I,4), (I,13), (I,15), and (I,16) yields indeed the fundamental relations

$$\psi_b(x,x_i)=\int\Gamma^{(\alpha)}(y;\, x,z)\psi_0{}^i(z,y)dydz \quad (23)$$

and

$$\bar\chi_b(x,x_j)=\int\bar\chi_0{}^j(z,y)\Gamma^{(\beta)}(y;\, z,x)dydz. \quad (24)$$

Separating out the center-of-mass coordinates, and transforming into momentum space yields the following expression of the required ratios:

$$\phi_b(0)/\Gamma_0{}^\alpha\equiv\phi_b(0)/\Gamma^{(\alpha)}(P,k)=\phi_0(k,\,P-k), \quad (25)$$

$$\bar\rho_b(0)/\Gamma_0{}^\beta=\bar\rho_b(0)/\Gamma^{(\beta)}(k',P')=\bar\rho_0(k',\,P'-k'), \quad (26)$$

where use has been made of the relations which define P, P', k and k': $i\gamma k+M=i\gamma k'+M=0$, $(P-k)^2+\mu^2=(P'-k')^2+\mu^2=0$. Equation (22) becomes now:

$$(\mathbf{k}',-\mathbf{k}',j\,|\,R_a\,|\,\mathbf{k},-\mathbf{k},i)=-iG^2(2\pi)^4\bar\rho_0{}^{(k)}(k',\,P'-k') \times\gamma_5\tau_k K_N'(P)\gamma_5\tau_l\phi_0(k,\,P-k) \times\delta(\mathbf{P}-\mathbf{P}')\delta(P_0-P_0'). \quad (27)$$

The determination of the scattering phase-shifts is now entirely reduced to the solution of the ψ_b equation and to the determination of the renormalized nucleon propagation function $K_N'(P)$.

III. APPROXIMATE SOLUTION OF THE WAVE EQUATION

In this section, we first solve approximately the integral equation for ψ_b, and then apply this solution to the calculation of the renormalized expression of ψ_a, using an adaptation of the renormalization prescriptions to the special approximate form of the K_N' function resulting from ψ_b.

1. Solution of the Equation for ψ_b

After separating out the motion of the center-of-mass [Eq. (I,51)], transforming into the momentum representation and projecting on the states of total isotopic spin $\frac{1}{2}$ and $\frac{3}{2}$, we obtain, for the part of the wave function corresponding to the relative motion, the following equation:

$$\phi_b(p;\, P)=(2\pi)^4\phi_0(k+P,\,-k)\delta(k-p) -\frac{iG^2}{(2\pi)^4}T_b K_N(p+P)K_M(-p)\gamma_5\int K_N(p+p'+P) \times\gamma_5\phi_b(p';\, P)dp', \quad (28)$$

where $T_b=2$ for the state of isotopic spin $\frac{1}{2}$ and -1 for the state of isotopic spin $\frac{3}{2}$. The whole problem has been reduced to the solution of Eq. (28), the kernel of which consists of the expression $\gamma_5 K_N(p+p'+P)\gamma_5=K_N \times(-p-p'-P)$. Now, it is worth remarking that p and p' are actually meson energy-momenta which, because of the weighting factor coming from the distribution function ϕ_b (which is centered around k), can be considered as "small" compared to P. In the non-relativistic region the kernel is therefore approximately equal to $(\gamma_4 P_0+M)^{-1}\sim(2M)^{-1}$. An approximate form of the kernel should be based on this property, which is due to the presence of the two γ_5 operators on each side of the K_N function. The brutal replacement of the kernel by $(2M)^{-1}$ would, however, introduce spurious divergences, coming from the fact that, although the distribution of the p'-momenta is centered around the

"small" value k, the integration on the right-hand side of (28) extends over all values of p', large and small. A convenient approximation to $\gamma_5 K_N(p+p'+P)\gamma_5$ should therefore not assume that *both* p and p' are small but that only one of them, p or p', is small compared to P. Such an approximation exists, and can be written as follows[15]:

$$\gamma_5 K_N(p+p'+P)\gamma_5 \sim \gamma_5 K_N(p+P)K_N^{-1}(P)K_N(p'+P)\gamma_5. \quad (29)$$

Making this replacement in Eq. (29), we obtain the expression of $\phi_b(p;P)$ in the form

$$\phi_b(p;P)=(2\pi)^4\phi_0(k+P,-k)\delta(k-p) -iG^2T_bK_N(p+P)K_M(-p)K_N(-p-P) \times K_N^{-1}(-P)C_b(P), \quad (30)$$

where $C_b(P)$ is, for a given energy, a constant defined by:

$$C_b(P)=\frac{1}{(2\pi)^4}\int K_N(-p-P)\phi_b(p;P)dp, \quad (31)$$

the expression of which can easily be obtained by introducing the value of $\phi_b(p;P)$, given by (30), into the right-hand side of (31):

$$C_b(P)=[1+(G^2/4\pi)T_bQ(P)]^{-1} \times K_N(-k-P)\phi_0(k+P,-k), \quad (32)$$

$Q(P)$, expressed as follows:

$$Q(P)=\frac{i}{4\pi^3}\int K_N^2(-P-p)K_N(P+p) \times K_M(-p)K_N^{-1}(-P)dp, \quad (33)$$

is a finite function of energy. Using Feynman's method of evaluation of integrals of this type, we obtain

$$Q(P_0)=\frac{(M+\gamma_4P_0)}{4\pi}\int_0^1 \frac{xdx[M-\gamma_4P_0(1-x)]}{D(x,P_0^2)}, \quad (34)$$

with:

$$D(x,P_0^2)=-P_0^2x(1-x)+M^2x+\mu^2(1-x). \quad (35)$$

From the expression (30) of $\phi_b(p;P)$, we can deduce easily the contribution of the (b)-type diagrams to the S-phase-shifts. Writing T_a, T_b and the complete S-phase-shift α as 2-row matrices (corresponding to $\frac{3}{2}$ and $\frac{1}{2}$ isotopic states), we split the expression for $\tan\alpha$ into two parts:

$$\tan\alpha=(\tan\alpha)_a+(\tan\alpha)_b. \quad (36)$$

[15] An even better approximation (which leads however to more complicated calculations) would be to write:

$$\gamma_5 K_N(p+p'+P)\gamma_5 \sim \gamma_5 K_N(p+k+P)K_N^{-1}(P+2k)K_N(p'+k+P)\gamma_5,$$

but the difference between the two approximations is negligible for low-energy S-scattering. The situation is different for P-scattering, where the more complicated approximation should certainly be preferable.

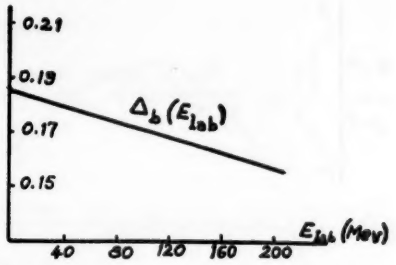

FIG. 2. Variation of the "damping" function Δ_b, as a function of the meson energy in the laboratory system.

Making use of the method given in Sec. IV of (I), we then obtain from the asymptotic form of $\phi_b(p;P)$:

$$(\tan\alpha)_b=-\frac{k}{2M}\left(\frac{G^2}{4\pi}\right)T_b\frac{(M+P_0)(E_k+M)}{4E_kP_0} \times\frac{1}{1+(G^2/4\pi)T_b\Delta_b(P_0)}, \quad (37)$$

where $\Delta_b(P_0)$ is obtained by putting $\gamma_4=1$ in $Q(P_0)$:

$$\Delta_b(P_0)=\left(\frac{M+P_0}{4\pi}\right)\int_0^1 \frac{xdx[-P_0(1-x)+M]}{D(x,P_0^2)}. \quad (38)$$

$\Delta_b(P_0)$ can be calculated analytically by standard methods. It is a slowly decreasing function of energy which is plotted in Fig. 2 for energies varying between 0 and 200 Mev (E_{lab} is the energy in the laboratory system).

2. Calculation of $K_N'(P)$ and $(\tan\alpha)_a$

Using Eqs. (15) and (I,30), we can write, after summation over the isotopic-spin indices,

$$3\gamma_5\Sigma(P)\gamma_5=-\frac{3iG^2}{(2\pi)^4}\int L_b(p;P)dp, \quad (39)$$

where $L_b(p;P)$ is defined by

$$L_b(p;P)=\frac{\gamma_5}{(2\pi)^4}\int K_b(p+P,-p;p'+P,-p')\gamma_5dp', \quad (40)$$

and obeys the following integral equation:

$$L_b(p;P)=K_N(-p-P)K_M(-p) +\frac{iG^2}{(2\pi)^4}\gamma_5K_N(p+P)K_M(-p)\gamma_5\int K_N(p+p'+P) \times\gamma_5L_b(p',P)dp'. \quad (41)$$

Making again the approximation (29), we obtain

$$L_b(p;P)=K_N(-P-p)K_M(-p) \times\{1+(iG^2/4\pi)K_N(p+P)K_N^{-1}(P) \times[1-(G^2/4\pi)Q(-P)]^{-1}U(P^2)\}, \quad (42)$$

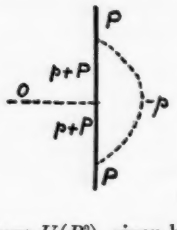

FIG. 3. Vertex diagram corresponding to the function $U(P^2)\gamma_5$.

where $U(P^2)$, given by the expression

$$U(P^2) = \frac{1}{4\pi^3}\int K_N(p+P)K_N(-p-P)K_M(-p)dp, \quad (43)$$

is a logarithmically-divergent integral, which is a function of P^2 only. $\gamma_5 U(P^2)$ corresponds to the simple vertex diagram represented on Fig. 3.

Integrating $L_b(p;P)$ over p, we finally obtain the expression

$$3\gamma_5\Sigma(P)\gamma_5 = \Sigma^0(P) + 3\left(\frac{G^2}{4\pi}\right)^2 K_N^{-1}(P)\left[1-\frac{G^2}{4\pi}Q(-P)\right]^{-1} U^2(P^2), \quad (44)$$

$\Sigma^0(P)$ corresponding to the lowest order self-energy diagram:

$$\Sigma^0(P) = -\frac{3iG^2}{(2\pi)^4}\int \gamma_5 K_N(p+P)\gamma_5 K_M(-p)dp. \quad (45)$$

It can be seen almost immediately that prescriptions (17) and (18) can no longer be applied to this approximate expression of $\Sigma(P)$. Instead, it is necessary to expand $\Sigma(P)$ in a power series of G^2 by means of the Neumann-Liouville expansion of integral equation (41), and to apply Salam's subtraction method to each term of the expansion. Summing back the renormalized expansion, one verifies—as it should have been expected—that the convergent expression of $\Sigma(P)$ is obtained by replacing $\Sigma^0(P)$ and $U(P^2)$ in (44) by their convergent forms Σ_c^0 and U_c respectively:

$$\Sigma_c^{(0)} = \Sigma^0(P) - \Sigma^0(p_0) - (P-p_0)\left[\frac{\partial}{\partial P}\Sigma^0\right]_{P=p_0}, \quad (46)$$

where p_0 is a free nucleon momentum ($i\gamma p_0 + M = p_0^2 + M^2 = 0$), and

$$U_C(P^2) = U(P^2) - U(-M^2). \quad (47)$$

This convergent form of $\Sigma(P)$ has the correct behavior when $P \to p_0$, $P^2 \to -M^2$: $\Sigma(P)K_N(P)$ vanishes in this limit, since it is the square of the function $U(P^2)$ which appears on the right-hand side of (44).

Making the subtractions (46) and (47), and using again Feynman's method, we obtain

$$\gamma_5 K_N'(P)\gamma_5 = \left\{1+\frac{3G^2}{4\pi}H(P)+3\left(\frac{G^2}{4\pi}\right)^2\left[1-\frac{G^2}{4\pi}Q(P)\right]^{-1}F^2(P^2)\right\}^{-1} \times K_N(-P), \quad (48)$$

where we have put

$$H(P) = \frac{M^2}{2\pi}\int_0^1 \frac{x^2(1-x)dx}{D_0(x)} - \frac{(-i\gamma P+M)^{-1}}{4\pi} \times \int_0^1 [-i\gamma P(1-x)+M]\log\left(\frac{D}{D_0}\right)dx, \quad (49)$$

with:

$$D_0(x) = D(x,M^2) = M^2x^2+\mu^2(1-x) \quad (50)$$

and

$$F(P^2) = \frac{1}{4\pi}\int_0^1 \log\left(\frac{D}{D_0}\right)dx. \quad (51)$$

Introducing the expression (48) of $\gamma_5 K_N'(P)\gamma_5$ into the matrix elements (27) of R_a, and using again the method of Sec. IV of (I), we obtain the value of $(\tan\alpha)_a$:[16]

$$(\tan\alpha)_a = -\frac{kG^2}{(2M)4\pi}\frac{T_aM(E_k+M)}{P_0(M+P_0)}\frac{1}{1+\frac{G^2}{4\pi}\Delta_a(P_0)}, \quad (52)$$

where $\Delta_a(P_0)$ is equal to:

$$\Delta_a(P_0) = 3h(P_0)+\frac{3G^2}{4\pi}\left[1-\frac{G^2}{4\pi}\Delta_b(P_0)\right]^{-1}F^2(-P_0^2), \quad (53)$$

$h(P_0)$ being the value of $H(P)$ when $\gamma_4 = 1$:

$$h(P_0) = \frac{M^2}{2\pi}\int_0^1 \frac{x^2(1-x)dx}{D_0} - \frac{1}{4\pi}\int_0^1 \frac{P_0(1-x)+M}{P_0+M}\log\left(\frac{D}{D_0}\right)dx. \quad (54)$$

IV. DISCUSSION OF THE RESULTS. COMPARISON WITH EXPERIMENT

Equations (36), (37), and (52), which define the complete S-phase-shift in our approximation, depend on only one parameter: the coupling constant G. Our problem is to determine whether it is possible to choose G so as to be able to reproduce the "experimental" behavior of the α_1 and α_3 phase-shifts. This "experimental" variation of α_1 and α_3 with energy is not too

[16] In calculating $(\tan\alpha)_a$, we have assumed that Eqs. (25) and (26), which are rigorous for the exact solution of the ψ equation, remain valid for the approximate solution. This is not quite true. However, the approximate expressions of the ratios which appear on the left-hand side of Eqs. (25) and (26) do not differ very much from their exact values, at least for S-states, as can be verified by a direct calculation.

well known,[17] but it is generally agreed that α_3 is negative and increases slowly in absolute value with increasing energy, whereas α_1 is positive and shows at first a rapid increase with energy, up to about 10° in the 40-Mev region; it remains afterwards more or less constant up to about 100 Mev, then decreases sharply and becomes negative. α_1 and α_3 are practically equal near 180 or 200 Mev (both of the order of $-20°$).

Let us first examine the behavior of the denominators in $(\tan\alpha)_a$ and $(\tan\alpha)_b$. The first term of $\Delta_a(P_0)$ defined by (53), is identical with the expression calculated by Brueckner, Gell-Mann, and Goldberger.[18] It is positive, and of the order of $3/4\pi$, so that the factor $[1+3(G^2/4\pi)\times h(P_0)]$, if it existed alone, would produce a "damping" of $(\tan\alpha)_a$ by a factor of the order of 3 or 4, if $G^2/4\pi$ is assumed to be of the order of 10. However, for such a magnitude of $G^2/4\pi$, the second term of (53) is negative, because $(G^2/4\pi)\Delta_b(P_0)$ is then appreciably larger than 1, and varies rather strongly with energy. However, at low energies, $1+(G^2/4\pi)\Delta_a$ is still positive, so that $(\tan\alpha)_a$, for the $T=1/2$ state, is negative. The observed positive value of α_1 can therefore be obtained only if $(\tan\alpha)_b$, for the $T=1/2$ state, is strongly positive. Since $T_b=-1/2$ in this case, this means that the denominator on the right-hand side of (37) must be positive, or that

$$\tfrac{1}{2}(G^2/4\pi)\Delta_b(P_0)<1. \tag{55}$$

$\Delta_b(P_0)$ being a slowly decreasing function of E_{lab}, it is sufficient to impose condition (55) at $E_{\text{lab}}=0$, $(P_0=M+\mu)$. This defines a maximum value of $G^2/4\pi$ which turns out to be

$$G^2/4\pi<10.8. \tag{56}$$

For values of $G^2/4\pi$ larger than 10.8, Eq. (37) would predict a resonance in the $T=1/2$ state at a finite energy, as was already obtained in the unrenormalized calculations.[8,19] Actually, $G^2/4\pi$ must be appreciably smaller than the limit of Eq. (56); otherwise, α_1 would take, at low energies, large positive values incompatible with the experimental data. It turns out that the value

$$G^2/4\pi=7.5, \tag{57}$$

gives an α_1 phase-shift of about 10° at 40 Mev. The rapid variation of α_1 with energy results from quick variations of the relative magnitudes of $(\tan\alpha)_a$ and $(\tan\alpha)_b$ in the $T=1/2$ state. At very low energies, $(\tan\alpha)_b$ predominates over $(\tan\alpha)_a$, and produces a sharply rising slope for α_1. However, because of the second (negative) term in Δ_a, $(\tan\alpha)_a$ increases rapidly at moderate energies and eventually changes the sign of α_1. There exists a region where the variations of the two terms compensate each other, giving rise to the observed broad maximum. On the other hand, $(\tan\alpha)_a$ does not contribute to the $T=3/2$ state and $T_b>0$, so that α_3 is a slowly varying negative function of energy. The variation of α_1 and α_3 as functions of k/μ (k is the momentum in the center-of-mass system: $P_0=E_k+\omega_k$), is represented in Fig. 4, together with points taken from the analysis of experimental results.[17] It is seen that the agreement is surprisingly good.[19a]

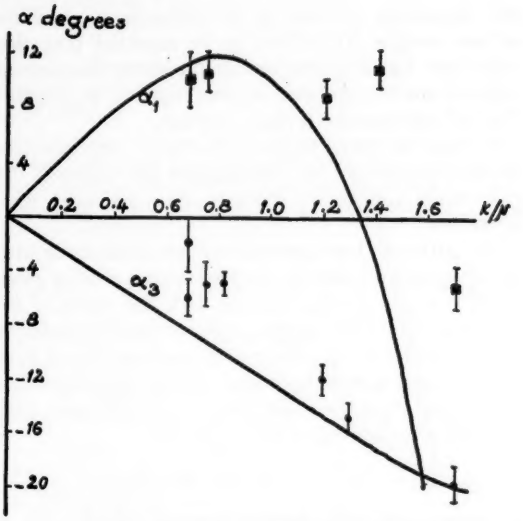

FIG. 4. Variation of the two S-phase-shifts, α_1 and α_3, as functions of k/μ, where k is the momentum in the center-of-mass system and μ the meson mass.

We would like now to complete the discussion with a certain number of remarks:

(a) The value of $G^2/4\pi$ given in Eq. (57) is somewhat different from the values of 10, which is inferred from the study of nuclear forces,[20] or 15, used by Dyson *et al.*[21] in their computation of the meson-nucleon P phase-shifts by means of the Tamm-Dancoff method. This "discrepancy" should not, however, be taken too seriously. If the agreement with experiment which has been obtained, using the two lowest order diagrams, in the present work as well as in other investigations,[5,21] has any other significance than that of a pure coincidence, it means that higher order diagrams, although quite important, contribute mainly through an "effective" coupling constant, without changing appreci-

[17] See, for example, the discussion of H. A. Bethe in the *Proceedings of the Fourth Annual Rochester Conference on High Energy Physics* (University of Rochester, Rochester, 1954).

[18] Brueckner, Gell-Mann, and Goldberger, Phys. Rev. **90**, 476 (1953).

[19] See L. Sartori and V. Wataghin, Nuovo cimento **12**, 260 (1954) who get a resonance in the $T=1/2$ state by a renormalized calculation with a relatively low cut-off momentum.

[19a] The numerical discussion of the results was done with values of T_a and T_b equal to half of the correct ones (the values of T_a and T_b quoted in the text are correct). It is therefore necessary to replace $G^2/4\pi$ by half of its value (57) to obtain practically the same results. The only place where $G^2/4\pi$ does not occur multiplied by T_a or T_b is in the product $(G^2/4\pi)\Delta_a(P_0)$, on the right-hand side of Eq. (52). The difference, however, is insignificant, since the second term of the right-hand side of (53) becomes then positive and approximately doubles the value of Δ_a.

[20] M. Lévy, Phys. Rev. **88**, 725 (1952); S. D. Drell and K. Huang, Phys. Rev. **91**, 1527 (1953).

[21] Dyson, Ross, Salpeter, Schweber, Sunderesan, Visscher, and Bethe, Phys. Rev. **95**, 1644 (1954).

ably the energy variation of the scattering phase-shifts at low energies. It is then to be expected that this "effective" coupling constant would not be the same in different scattering states or, even more so, in different physical processes involving π mesons.

It should be noted that our results are very sensitive to the value of $G^2/4\pi$. For example the choice $G^2/4\pi=8$ would completely destroy the agreement with experiment.

(b) Although the agreement of our calculations with the experimental data on $\pi-p$ scattering is quite good, there is a definite discrepancy with the value of $k^{-1}\times|\alpha_1-\alpha_3|$ at zero energy, deduced from Panofsky's measurements of the absorption cross section of slow negative π mesons in hydrogen or from the photomesic production near threshold. From Eqs. (37) and (52), we find, using the value (57) of $G^2/4\pi$:

$$|(\alpha_1-\alpha_3)/k|\sim 25^\circ \text{ per } 100 \text{ Mev}/c, \tag{58}$$

to be compared with the experimental value[22]

$$|(\alpha_1-\alpha_3)/k|_{\text{exp}}\sim 8^\circ \text{ per } 100 \text{ Mev}/c. \tag{59}$$

The reasons for this discrepancy are that the slope of α_1 at low energy is still rather high, whereas α_3 varies linearly with k near $k=0$. It has been suggested, from the analysis of low-energy $\pi-p$ scattering[23] that α_3 should actually vary like k^ν, with $\nu>1$, near zero energy. This effect might come from the influence of meson-meson scattering or, perhaps, simply from higher order meson-nucleon diagrams. In this connection, it is worth remarking that the special choice of higher order diagrams which is made by iterating diagrams (a) and (b) of Fig. 1, violates the "symmetry theorem" of Gell-Mann and Goldberger,[24] which states that, in an exact calculation, α_1 and α_3 should be equal in the limit $k\to 0$ and $\mu/M\to 0$. In other words, the difference in slopes of α_1 and α_3 near the origin should only be a μ/M effect. When the limit $\mu\to 0$ and $k\to 0$ is made in our Eqs. (37) and (52), one finds, by putting

$$z=\frac{1}{2\pi}\left(\frac{G^2}{4\pi}\right), \tag{60}$$

the following values of α_1 and α_3:

$$\left.\begin{aligned}\frac{\alpha_1}{k}&=\frac{2\pi}{M}\frac{z(\frac{9}{4}z-1)}{(1-z)(\frac{3}{2}z+1)}\\ \frac{\alpha_3}{k}&=-\frac{2\pi}{M}\frac{z}{1+2z}\end{aligned}\right\}(k\to 0). \tag{61}$$

The two limits are equal when z is very small, but with our value of $G^2/4\pi$, we have $z=0.60$, so that a large part of the result (58) comes actually from effects which should be absent if all higher order diagrams had been taken into account. An investigation of higher order diagrams, selected in such a way as to respect the symmetry rule, is now in progress at the University of Paris.

(c) It can be seen that the approximation (29) is equivalent to introducing a kind of "natural" cut-off function in the integral equations (28) or (41), and that the corresponding cut-off momentum is of the order of $M+P_0\geq 2M+\mu$. This is a very high cut-off momentum, which agrees with considerations which have already been made[25] in the study of nuclear forces, where a central repulsive core at $r_c\sim 0.50\times 10^{-13}$ cm can be seen to result from a "natural" cut-off momentum of the order of $2M$.

V. ACKNOWLEDGMENTS

Most of the present work has been done during the summer of 1954, while the author was on a visit at the Physics Department of the University of Rochester. He therefore would like to thank Professor R. E. Marshak for his kind hospitality and for many stimulating discussions on this and related problems.

[22] This value results from measurements of the photomesonic production cross section near threshold, at the Massachusetts Institute of Technology and Cornell University: B. T. Feld and R. R. Wilson (private communications to R. E. Marshak).
[23] H. A. Bethe (private communication).
[24] M. Gell-Mann and M. Goldberger (to be published).
[25] M. Lévy, Proceedings of the International Conference of Kyoto, 1953 (unpublished); M. Lévy and R. Marshak, Proceedings of the Glasgow Conference of Nuclear Physics, 1954 (to be published).

Many-Body Problem with Strong Forces

ROBERT JASTROW*†
Nucleonics Division, Naval Research Laboratory, Washington, D. C., and
Sloane Physics Laboratory, Yale University, New Haven, Connecticut
(Received January 26, 1955)

A trial solution constructed from two-particle functions is applied to the problem of the N-particle system with strong interactions. In a variational treatment based on this wave function the expectation values, which cannot be factored into single-particle integrals, are evaluated by a cluster development in powers of the particle density. The procedure is illustrated by a calculation of the pair distribution function and zero-point energy of the hard sphere gas, for Bose and Fermi statistics.

IN the present paper we examine, by a variational method, the ground state properties of a quantum mechanical system of N particles of equal mass m, contained in a volume Ω, and interacting through central two-body forces represented by the potential $V(r)$. Our interest is primarily in potentials $V(r)$ of short range relative to the mean particle spacing.

It will be assumed that both N and Ω are large enough to permit the neglect of surface effects; the properties of the ground state then depend only on m, $V(r)$, and the particle density, $n=N/\Omega$.

The Hamiltonian of the system is

$$H=-\frac{\hbar^2}{2m}\sum_{i=1}^{N}\nabla_i^2+\sum_{i<j=1}^{N}V(r_{ij}). \tag{1}$$

The eigenfunctions ψ of (1) are usually approximated by (symmetrized or antisymmetrized) products of one-particle functions,

$$\psi\sim\prod_{i=1}^{N}\varphi_i(r_i), \tag{2}$$

the effect of the interactions $V(r_{ij})$ being introduced as a perturbation on the independent particle motions; an upper bound on the energy of the ground state is then obtained by computing[1] $\bar{H}=\int\psi^*H\psi/\int\psi^*\psi$ from (2) and minimizing with respect to variations in the functions φ_i. This procedure fails in problems involving strong interactions, however, through the omission of correlations in particle position from (2). As an example we consider the repulsive potential,

$$\begin{aligned} &V=|V_0|, \quad r_{ij}\leq r_0;\\ &V=0, \qquad r_{ij}>r_0. \end{aligned} \tag{3}$$

The mean potential energy per particle, $\bar{V}/N$, computed from (2) and (3) is seen to be of the order of $(Nr_0^3/\Omega)|V_0|$; if now (3) goes into the hard sphere interaction ($|V_0|\to\infty$), the upper bound provided by $\bar{V}$ increases without limit.

The estimate of $\bar{V}$ is improved if (2) is replaced by a form containing the correlations implied by the relations,

$$\psi(r_1\cdots r_N)\approx 0, \quad r_{ij}<r_0, \tag{4}$$

which the eigenfunctions of (1) must satisfy when $V(r)$ is a strong repulsion. The conditions (4) are easily fulfilled by trial functions which depend explicitly on the interparticle separations r_{ij}; of such functions, the simplest is the product over all $N(N-1)/2$ pairs,[2]

$$\psi\sim\prod_{i<j=1}^{N}f(r_{ij}), \tag{5}$$

with $f(r_{ij})$ defined to vanish for $r<r_0$ and to approach unity for $r\gg r_0$.[3]

The particular example of the hard sphere gas requires for $f(r)$ a form such as

$$\begin{aligned} &f=0, && r\leq r_0;\\ &f=1-\frac{e^{-\beta(r-r_0)}}{r/r_0}, && r>r_0, \end{aligned} \tag{6}$$

in which β is an arbitrary parameter. For the variational application of (5) and (6),

$$\bar{H}=\int\prod_{i<j=1}^{N}f^*(r_{ij})H\prod_{i<j=1}^{N}f(r_{ij})\Big/\int\prod_{i<j=1}^{N}|f(r_{ij})|^2 \tag{7}$$

must be evaluated and minimized with respect to variations in β.

The form (5) may be applied to other interactions $V(r_{ij})$ if $f(r_{ij})$ is chosen more generally as an approximation to the eigenfunctions of the two-body Hamiltonian

$$-\frac{\hbar^2}{2m}(\nabla_i^2+\nabla_j^2)+V(r_{ij}) \tag{8}$$

* Present address: Nucleonics Division, Naval Research Laboratory, Washington, D. C.

† Part of this work was assisted by the joint program of the Office of Naval Research and the U. S. Atomic Energy Commission and by the Office of Ordnance Research, U. S. Army.

[1] Integrals are taken over the $3N$ coordinates of all particles unless otherwise indicated.

[2] This form has already been suggested by N. F. Mott for the hard sphere Bose gas, and applied in the low-density limit by R. B. Dingle [Phil. Mag. **40**, 573 (1949)].

[3] As $r\to\infty$, $f(r)$ must approach a constant amplitude, conveniently chosen as unity. If instead $f(r)$ were to vanish for large r, ψ would vanish almost everywhere in the configuration space of the system.

within the range of V; as before, f must approach unity at large distances.

Although (5) is constructed from two-body functions and apparently includes only pair correlations, it should be noted that effects involving ≥ 3 particles are also present: for example, the 3-particle group (i,j,k) is connected in (6) by the factor $[f(r_{ij})f(r_{jk})f(r_{ki})]$, and particles i, j, k, and l by factors such as $[f(r_{ij})f(r_{jk})\times f(r_{kl})f(r_{li})]$. The contributions of these terms appear explicitly in the cluster development of $\bar{H}$ to be given below.

CLUSTER DEVELOPMENT $\bar{H}$

The expectation value of H may be computed from (7):

$$\bar{H}=\frac{\int \prod_{i<j=1}^{N} f^*(r_{ij})\left[-\frac{\hbar^2}{2m}N\nabla_1^2+\tfrac{1}{2}N(N-1)V(r_{12})\right]\prod_{i<j=1}^{N} f(r_{ij})}{\int \prod_{i<j=1}^{N} |f(r_{ij})|^2}.$$

The cross terms in the kinetic energy vanish in the integration and we obtain

$$H=N(N-1)\frac{\int \prod_{i<j=1}^{N} f^*(r_{ij})\left[-\frac{\hbar^2}{2m}\frac{\nabla_1^2 f(r_{12})}{f(r_{12})}+\tfrac{1}{2}V(r_{12})\right]\prod_{i<j=1}^{N} f(r_{ij})}{\int \prod_{i<j=1}^{N} |f(r_{ij})|^2}. \tag{9}$$

Because f approaches unity outside the range of forces, (9) is identical in form with the configuration integrals encountered in the classical theory of the imperfect gas.[4] We treat it similarly, writing for the energy per particle

$$\frac{1}{N}\bar{H}=\frac{N-1}{\Omega}\int\left[-\frac{\hbar^2}{2m}\frac{\nabla_1^2 f(r_{12})}{f(r_{12})}+\tfrac{1}{2}V(r_{12})\right]\times g(r_{12})d^3r_{12}. \tag{10}$$

The pair distribution function, $g(r_{12})$, is defined by integration of ψ^2 over particles $3,\cdots,N$:

$$g(r_{12})=\Omega^2\frac{\int \prod_{i<j=1}^{N} |f(r_{ij})|^2 d^3r_3\cdots d^3r_N}{\int \prod_{i<j=1}^{N} |f(r_{ij})|^2 d^3r_1\cdots d^3r_N};$$

it determines the probability of a separation r_{12} between particles 1 and 2.

The function $g(r)$ may be expanded in ascending powers of particle density $n=N/\Omega$, following the cluster development of Ursell and Mayer.[5] Defining

$$h(r_{ij})=f^2(r_{ij})-1,$$

we have

$$g(r_{12})=f^2(r_{12})[g^{(2)}(r_{12})+ng^{(3)}(r_{12})+n^2g^{(4)}(r_{12})+\cdots], \tag{11}$$

where

$$g^{(2)}(r_{12})=1, \tag{11a}$$

$$g^{(3)}(r_{12})=\int h(r_{13})h(r_{32})d^3r_3, \tag{11b}$$

$$g^{(4)}(r_{12})=\tfrac{1}{2}[g^{(3)}(r)]^2+\int[2h(r_{14})h(r_{43})h(r_{32})+4h(r_{13})h(r_{32})h(r_{24})h(r_{43})+h(r_{41})h(r_{13})h(r_{32})h(r_{24})h(r_{43})]d^3r_3d^3r_4. \tag{11c}$$

The leading term in (11) describes the correlation which results from the explicit dependence of ψ on r_{12} through the factor $f(r_{12})$. The next term ($g^{(3)}$) is associated with the distortion of ψ in its dependence on r_{12}, resulting from the presence of a third particle in the neighborhood of 1 and 2, etc.

Bose Particles

The function (5) is symmetrical in all particles and directly applicable to Einstein-Bose systems. We have for the expectation values of the potential and kinetic energies per particle,

$$\frac{1}{N}\bar{V}=4\pi n\int r^2V(r)g(r)dr, \tag{12}$$

and

$$\frac{1}{N}\bar{T}=4\pi n\int r^2\left[\frac{f''+(2/r)f'}{f}\right]g(r)dr, \tag{13}$$

with $g(r)$ given by (11).

[4] $e^{-V(r_{ij})/kT}$ replaces $f^2(r_{ij})$ in the classical analog.

[5] The cluster development is reviewed by J. De Boer in Repts. Progr. Phys. 12, 305 (1948).

Fermi Particles

A modification of (5) appropriate to antisymmetrical systems is

$$\psi\sim S(\mathbf{r}_1\cdots\mathbf{r}_N)\prod_{i<j=1}^{N} f(r_{ij}), \tag{14}$$

where S is a Slater determinant of one-particle functions, $\varphi_l(\mathbf{r}_m)$. We choose plane waves for these: $\varphi_l(\mathbf{r}_m)=e^{i\mathbf{k}_l\cdot\mathbf{r}_m}$.

The corresponding modifications in the cluster development of $\bar{H}/N$ are readily obtained. The potential energy again takes the form

$$\frac{1}{N}\bar{V}=4\pi n\int r^2V(r)g(r)dr, \tag{15}$$

with

$$g(r)=f^2(r)[g^{(2)}(r)+ng^{(3)}(r)+\cdots], \tag{16}$$

where now

$$g^{(2)}(r_{12})=\sum_{\alpha_1\alpha_2=1}^{N}\exp[-i(\mathbf{k}_{\alpha_1}\cdot\mathbf{r}_1+\mathbf{k}_{\alpha_2}\cdot\mathbf{r}_2)]\times\begin{vmatrix}\exp(i\mathbf{k}_{\alpha_1}\cdot\mathbf{r}_1) & \exp(i\mathbf{k}_{\alpha_2}\cdot\mathbf{r}_1)\\ \exp(i\mathbf{k}_{\alpha_1}\cdot\mathbf{r}_2) & \exp(i\mathbf{k}_{\alpha_2}\cdot\mathbf{r}_2)\end{vmatrix}, \tag{17}$$

$$g^{(3)}(r_{12})=\int d^3r_3h(r_{13})h(r_{32})\sum_{\alpha_1\alpha_2\alpha_3=1}^{N}\times\exp[-i(\mathbf{k}_{\alpha_1}\cdot\mathbf{r}_1+\mathbf{k}_{\alpha_2}\cdot\mathbf{r}_2+\mathbf{k}_{\alpha_3}\cdot\mathbf{r}_3)]\times\begin{vmatrix}\exp(ik_{\alpha_1}\cdot r_1) & \exp(ik_{\alpha_2}\cdot r_1) & \exp(ik_{\alpha_3}\cdot r_1)\\ \exp(ik_{\alpha_1}\cdot r_2) & \exp(ik_{\alpha_2}\cdot r_2) & \exp(ik_{\alpha_3}\cdot r_2)\\ \exp(ik_{\alpha_1}\cdot r_3) & \exp(ik_{\alpha_2}\cdot r_3) & \exp(ik_{\alpha_3}\cdot r_3)\end{vmatrix}. \tag{18}$$

The sums in (17) and (18) are taken over all states within the Fermi sphere of radius $k_F=(6\pi^2n)^{\frac{1}{3}}$. We find

$$g^{(2)}(r_{12})=1-l^2(k_Fr_{12}), \tag{17'}$$

$$g^{(3)}(r_{12})=\int d^3r_3h(r_{13})h(r_{32})\times\{1-2[l^2(k_Fr_{12})+l^2(k_Fr_{13})+l^2(k_Fr_{23})]+l(k_Fr_{12})l(k_Fr_{13})l(k_Fr_{23})\}, \tag{18'}$$

with

$$l(x)=3(\sin x-x\cos x)/x^3. \tag{19}$$

The kinetic energy operator produces three terms:

$$\frac{1}{N}\bar{T}=-\frac{\hbar^2}{2m}\langle S\nabla^2(\textstyle\prod f)\rangle_N+\langle(\prod f)\nabla^2S\rangle_N+\langle 2\nabla S\cdot\nabla(\prod f)\rangle_N. \tag{20}$$

These terms, in order of their appearance in (20), are identified as the correlational kinetic energy ($\bar{T}_C$), the Fermi energy ($\bar{T}_F$), and the cross term ($\bar{T}_{CF}$).

Application of the cluster development to (20) yields the following results:

(a) Correlational kinetic energy:

$$\frac{1}{N}\bar{T}_C=-\frac{\hbar^2}{2m}n\int\left[\frac{f''+(2/r)f'}{f}\right]g(r)d^3r, \tag{21}$$

with $g(r)$ defined by (16)–(18);

(b) Fermi energy:

$$\frac{1}{N}\bar{T}_F=\frac{\hbar^2}{2m}\frac{1}{N}\sum_{\alpha_1=1}^{N}k_{\alpha_1}^2\times\left[1+n\left(\frac{1}{N^2}\sum_{\alpha_2\alpha_3=1}^{N}(Q_{\alpha_1\alpha_2}-Q_{\alpha_2\alpha_3}^{*})\right)+\cdots\right], \tag{22}$$

where

$$Q_{\alpha_i\alpha_j}=\int h(r_{ij})\times\exp[-i(\mathbf{k}_{\alpha_i}\cdot\mathbf{r}_1+\mathbf{k}_{\alpha_j}\cdot\mathbf{r}_2)]D^{(2)}(ij;12)\frac{d^3r_2}{\Omega}. \tag{23}$$

(c) Cross term:

$$\frac{1}{N}\bar{T}_{CF}=-2i\frac{\hbar^2}{2m}n\int d^3r_{12}f(r_{12})\nabla f(r_{12})\cdot\left\{\frac{1}{N}\sum_{\alpha_1=1}^{N}\mathbf{k}_{\alpha_1}\times\left[\frac{1}{N}\sum_{\alpha_2=1}^{N}\exp[-i(\mathbf{k}_{\alpha_1}\cdot\mathbf{r}_1+\mathbf{k}_{\alpha_2}\cdot\mathbf{r}_2)]D^{(2)}(12;12)+n\int d^3r_3h(r_{13})\frac{1}{N^2}\sum_{\alpha_2\alpha_3=1}^{N}\times\exp[-i(\mathbf{k}_{\alpha_1}\cdot\mathbf{r}_1+\mathbf{k}_{\alpha_2}\cdot\mathbf{r}_2+\mathbf{k}_{\alpha_3}\cdot\mathbf{r}_3)]\times D^{(3)}(123;123)\right]\right\}. \tag{24}$$

$D^{(2)}$ and $D^{(3)}$ denote the determinants occurring in (17) and (18), respectively.

Expansion of the Energy in Powers of Particle Density

The expansion of $\bar{H}$ in integral powers of n is directly given, for Bose particles, by insertion of (11) in (12) and (13).

The corresponding development of $\bar{H}$ for Fermi particles is complicated by the density dependence of the Fermi wave number, $k_F=(6\pi^2n)^{\frac{1}{3}}$, occurring in (17)–(24). A development in mixed powers of n and $n^{\frac{1}{3}}$ is obtained by first expanding (18), (22), and (23) in powers of $(k_Fr_{ij})^2$. The results are given in the Appendix.

HARD-SPHERE GAS

We apply these formulas to a calculation of the kinetic energy of a gas of hard spheres, with interaction radius r_0, for Bose and Fermi statistics. It will be seen

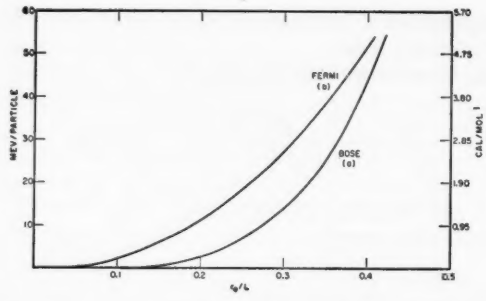

FIG. 1. The kinetic energy of a hard-sphere gas with (a) Bose and (b) Fermi statistics: The abscissae represent the ratio of hard sphere interaction radius (r_0) to mean particle spacing (L); the ordinates on the left refer to particles with nucleon mass and $r_0=10^{-13}$ cm, those on the right to particles with the mass of He^4 and $r_0=2.5\times10^{-8}$ cm.

that the results take the form,

$$\bar{T}=(\hbar^2/2mr_0^2)t, \tag{25}$$

in which t depends only on βr_0 and r_0/L, where $L=n^{-\frac{1}{3}}$ indicates the mean particle spacing.

The calculation is first made for a Bose gas, to lowest order in n, for several choices on the form of $f(r)$:

$$\left.\begin{aligned}&\text{(i)}\quad \text{Gaussian: } f=1-\exp[-\beta^2(r-r_0)^2]\\ &\text{(ii)}\quad \text{Exponential: } f=1-e^{-\beta(r-r_0)}\\ &\text{(iii)}\quad \text{Yukawa: } f=1-\frac{e^{-\beta(r-r_0)}}{r/r_0}\end{aligned}\right\} r\geq r_0,$$

$$f=0, \qquad r<r_0.$$

The leading term in the density expansion of the kinetic energy is

$$\frac{1}{N}\bar{T}=4\pi n\int f\left(f''+\frac{2}{r}f'\right)r^2dr. \tag{26}$$

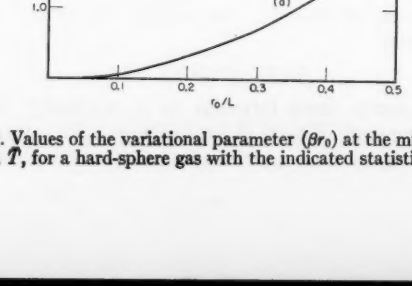

FIG. 2. Values of the variational parameter (βr_0) at the minimum in $\bar{T}$, for a hard-sphere gas with the indicated statistics.

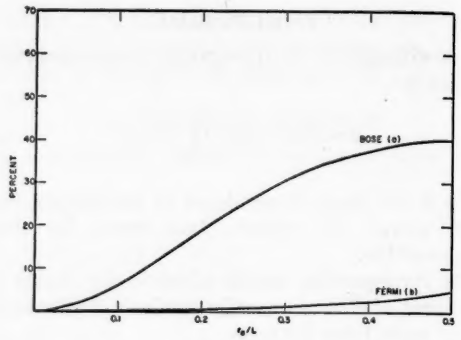

FIG. 3. The fraction contributed to the kinetic energy of a hard-sphere gas by the three-body term ($g^{(3)}$) in the cluster development.

Evaluation of (26) for the several forms of f and minimization with respect to β leads to the following results:

$$\frac{1}{N}\bar{T}=B\frac{\hbar^2}{2mr_0^2}\left(\frac{r_0}{L}\right)^3. \tag{27}$$

The constant B and the value of β at the minimum in $\bar{T}$ are given in Table I.

The Yukawa function, which varies as $1-r_0/r$ near the sphere boundary in agreement with the exact solution to (8), yields the lowest kinetic energy, and will be assumed for $f(r)$ in the remainder of our calculations.

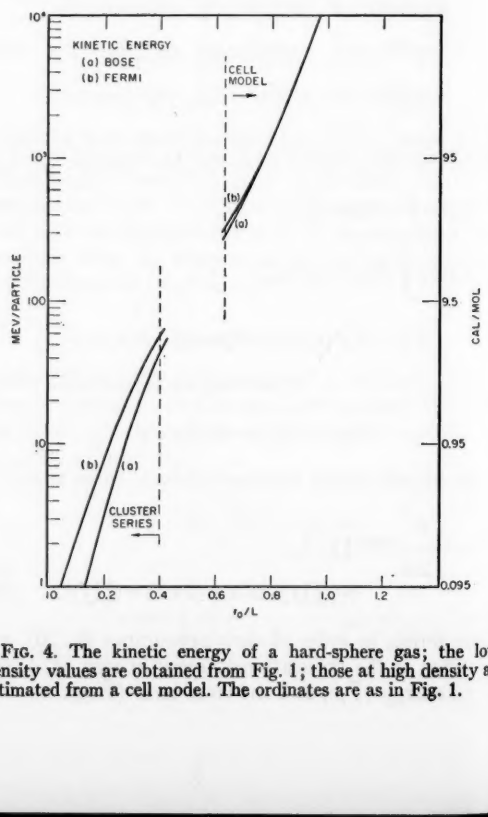

FIG. 4. The kinetic energy of a hard-sphere gas; the low-density values are obtained from Fig. 1; those at high density are estimated from a cell model. The ordinates are as in Fig. 1.

The next (n^2) term in the cluster development introduces a three-body integral which may be reduced to combinations of exponential integrals. The variation of $\bar{T}$ must now be carried out numerically; the results of the computation are shown in Fig. 1, with terms included to order n^2 and $n^{7/3}$, respectively, for Bose and Fermi gases. The ordinate scale on the left refers to particles of nucleon mass and to a hard sphere interaction radius of 1.0×10^{-13} cm, that on the right to particles with the mass of He^4 and an interaction radius of 2.5×10^{-8} cm. Values of $\bar{T}$ for other choices of m and r_0 may be obtained from Fig. 1 and (25).

The values of βr_0 for which $\bar{T}$ assumes its minimum are shown in Fig. 2.

Figure 3 indicates the fraction of the complete kinetic energy which originates in the three-body correction to $g(r)$. We note that the contribution of $g^{(3)}(r)$ is appreciably reduced by the antisymmetrization of ψ, and, therefore, that the cluster development will be applicable to relatively dense Fermi systems.

High Density Limit

Inspection of Fig. 3(a) suggests that the cluster development cannot be applied to a Bose gas at densities above that corresponding to $(r_0/L)\sim0.4$. However, an estimate of the kinetic energy in the high density limit may be obtained from the cell model. For this purpose we choose a body-centered cubic arrangement of lattic spacing a. The minimum separation of particles is $(\sqrt{3}/2)a$, and the number per unit volume, $2/a^3$; a particle in such a lattice has, therefore, a kinetic energy roughly given by

$$\frac{1}{N}\bar{T}=3\frac{\hbar^2}{2m}\frac{\pi^2}{4[(\sqrt{3}/2)a-r_0]^2}=\frac{\hbar^2}{2mr_0^2}\frac{7.4(r_0/L)^2}{(1.1-r_0/L)^2}. \quad (28)$$

As a criterion for the application of (28) we take the condition, $2r_0>a$ or $r_0/L>0.63$, corresponding to densities great enough to prevent the passage of a particle between two neighbors.

The expression (28) is plotted in Fig. 4(a), and the sum of (28) and the Fermi energy (30a) in Fig. 4(b). The same figure also shows the results of the cluster development, taken from Fig. 1. Simple formulas are given below which pass to the correct low density limits and represent both branches within 20 percent over the entire density range:

$$\text{Fermions: } T=\frac{\hbar^2}{2mr_0^2}\frac{9.2(r_0/L)^2}{(1.1-r_0/L)^2};$$

$$\text{Bosons: } T=\frac{\hbar^2}{2mr_0^2}\frac{14.7(r_0/L)^3}{(1.1-r_0/L)^2}.$$

TABLE I. Hard-sphere Bose gas: dependence of $\bar{T}$ on the form of $f(r)$.

	B	βr_0
(i) Gaussian	2.05	$\sqrt{3}/2$
(ii) Exponential	1.21	$\sqrt{2}/2$
(iii) Yukawa	1.00	$[4\pi(r_0/L)^3]^{\frac{1}{3}}$

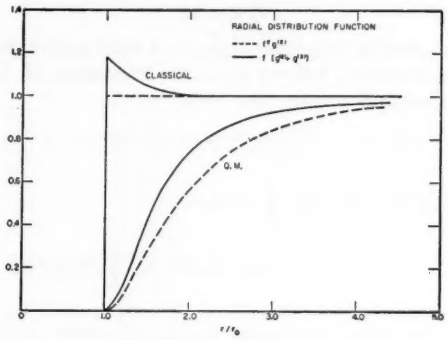

FIG. 5. The pair distribution function, $g(r)$ of the present calculation, compared with the classical result.

Radial Distribution Functions

The distribution functions $g(r)$ of the classical[6] and quantum-mechanical (Bose) hard-sphere gases are compared in Figs. 5 and 6 for $r_0/L=0.5$. Figure 6 indicates that the three-body correction to $g(r)$ in the quantum gas is substantially larger than its classical analog. In this connection we note that for fixed density the expansion parameter of the classical cluster development is the radius of interaction (r_0), while the corresponding parameter of the quantum mechanical development is the generally greater radius of distortion ($\sim r_0+1/\beta$) of the two-particle wave function.

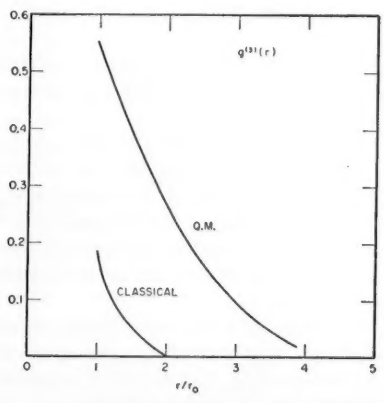

FIG. 6. The three-body correction, $g^{(3)}(r)$ to the pair distribution function.

[6] J. G. Kirkwood, J. Chem. Phys. 5, 67 (1935).

APPENDIX

The density expansion of $\bar{H}$, for a hard sphere gas of Fermi particles, follows from the expansion of (18), (22), and (23) in powers of $(k_f r_{ij})^2$:

$$l(k_f r)=1-(k_f r)^2/10+(k_f r)^4/280-\cdots,$$

$$Q_{a_i a_j}=[(k_{a_i}-k_{a_j})^2/6]\int r^2 h(r)d^3r$$
$$-[(k_{a_i}-k_{a_j})^4/120]\int r^4 h(r)d^3r+\cdots.$$

Inserting these expressions in (21)–(24) and carrying out the sums over k-space, we obtain the following series in n:

$$(2m/\hbar^2)(\bar{T}_c/N)=n\int d^3r_{12}f^2(r_{12})[V^2 f(r_{12})/f(r_{12})]$$
$$\times[(6\pi^2/5)^{\frac{1}{2}}r_{12}^2 n^{\frac{1}{2}}-(3/175)(6\pi^2)^{4/3}r^4 n^{4/3}+\cdots] \quad (29a)$$

$$+n^2\int d^3r_{12}d^3r_{13}f^2(r_{12})[\nabla^2 f(r_{12})/f(r_{12})]h(r_{13})h(r_{23})$$
$$\times[(6\pi^2)^{4/3}n^{4/3}(1/280-3/175)(r_{12}^4+r_{13}^4+r_{23}^4)$$
$$+(2/100)(r_{12}^2r_{13}^2+r_{12}^2r_{23}^2+r_{13}^2r_{23}^2)+\cdots]. \quad (29b)$$

$$(2m/\hbar^2)(\bar{T}_P/N)=(3/5)(6\pi^2)^{\frac{1}{2}}n^{\frac{1}{2}} \quad (30a)$$
$$+6(6\pi^2)^{4/3}(1/50-23/1050)n^{7/3}\int h(r)d^3r+\cdots, \quad (30b)$$

$$(2m/\hbar^2)(\bar{T}_{PC}/N)=(6/5)(6\pi^2)^{\frac{1}{2}}n^{\frac{1}{2}}$$
$$\times\int r_{12}f(r_{12})f'(r_{12})d^3r_{12}+\cdots, \quad (31)$$

$\bar{V}/N$: replace $(\hbar^2/2m)(\nabla^2 f/f)$ by V in (33a). (32)

PHYSICAL REVIEW VOLUME 98, NUMBER 5 JUNE 1, 1955

Statistical Model for High-Energy Events*

JOSEPH V. LEPORE AND MAURICE NEUMAN
Radiation Laboratory, Department of Physics, University of California, Berkeley, California

(Received July 16, 1954)

The relative probabilities for alternate processes initiated by a nucleon-nucleon collision depend on the dynamics involved and on the volume in phase space accessible to each final state. The assignment of relative *a priori* probabilities to the final states proportional to their extension in phase must be consistent with the translational, rotational, and Lorentz-invariant properties of the colliding system. The latter in particular implies a conservation law for the center of energy. Its effect is not only to lower the power of the configurational volume by one dimension but also to severely reduce the contributions from high momenta to the phase space integrals.

The limitations on accessibility arising from the controllable constants of motion are not sufficient to insure well defined probabilities. Some additional restriction on the configurational part of the phase space must be imposed. A cutoff factor for *each* particle is accordingly introduced. The configurational volume accessible to the particle thus decreases with increasing energy, a picture not inconsistent with the uncertainty principle.

THIS note describes a statistical model which differs in some essential respects from the one proposed by Fermi.[1]

Following Fermi we assume that in a high-energy collision a state approximating that of equilibrium is established. The probability of disintegration into various possible modes is then taken proportional to their relative extensions in accessible phase space. The limitations on accessibility arise from the assumed controllable constants of motion.

In this note they are taken to be energy, momentum, center of energy (the relativistic analog of center of mass), and isotopic spin. For simplicity conservation of angular momentum has been neglected.

If it is assumed that the extension in accessible phase space (in the center-of-momentum system) corresponding to particles of masses M_1, M_2, $\cdots$ can be approximated by the classical phase integral divided by $h^{3(n-1)}$,

$$P_n=\frac{S_n T_n}{(2\pi\hbar)^{3(n-1)}}\int\prod_{i=1}^{i=n}d\mathbf{p}_i d\mathbf{x}_i\delta(E-\sum_i E_i)$$
$$\times\delta(-\sum\mathbf{p}_i)\delta\left(\frac{\sum\mathbf{x}_i E_i}{E}\right), \quad (1)$$

one sees immediately that this integral does not converge and therefore some additional restriction is necessary to give the phase integral a well-defined meaning. This difficulty is overcome in the quantum theory by enclosing the system in a container whose walls aer eventually removed to infinity since (having been

* This work was performed under the auspices of the U. S. Atomic Energy Commission.

[1] E. Fermi, Progr. Theoret. Phys. (Japan) 5, 4, 570 (1950).

cancelled by the normalization factor in the wave functions) its volume does not appear in any physically significant context. This procedure cannot be followed, however, in our case. Imagine a light and a heavy particle with center of mass fixed starting out from the origin and moving according to Newtonian mechanics in opposite directions. When the lighter particle reaches the boundary of the container and is reflected, the heavier one must also turn back, even though it is still in the interior of the region, in order that the center of mass may be conserved. Thus, the conservation of center of mass and a finite volume, the same for light and heavy particles, give rise to unwanted spatial correlations amounting to interactions with the walls of the imaginary container. Since these cannot have any physical basis, this trivial example suggests that one enclose the particles in spheres whose radii decrease in some manner with increasing mass. In a nonrelativistic theory such a restriction may be imposed by inserting into the spatial part of the phase integral factors $f_i(M_i,x_i)$ which are to be chosen in such a way to make the integral well defined. A simple physical motivation can be supplied for such factors by an appeal to the uncertainty principle. One may imagine that at the instant of the collision between two colliding nucleons a virtual cloud of particles of various masses is formed of which that portion due to particles of mass M_i extends to a distance $\hbar/M_ic$. This suggests that one represent f_i by a Kennard packet

$$f_i=\exp(-x_i^2\kappa_i^2\tau_i).$$

κ_i is the Compton wavelength appropriate to the mass M_i, and τ_i is some scaling factor. Of course any other monotonic function with similar properties would do as well. This choice does, however, simplify the calculations and the results should not depend too drastically on the choice of $f_i(M_i,x_i)$.

In a relativistic theory, however, center of energy rather than center of mass is conserved, so if different cutoffs in configurational volume for the various particles are introduced these cutoffs must be energy-dependent. Relativistically, the notion that the functions f_i represent the extension of a virtual cloud of particles with energy E_i implies that they should have a range $\hbar c/E_i$. For simplicity one may choose

$$f_i(E_i,x_i)=\exp\left(-x_i^2\frac{E_i^2}{\hbar^2c^2}\tau_i\right).$$

As before, this choice is arbitrary to the extent that any other monotonic function with similar properties would also be suitable. Nonrelativistically the assumption of absence of fictious correlations (i.e., interactions with the walls of an imaginary container) has the simple effect of multiplying the momentum space part of the phase integral by a factor depending on the ratios of the masses of various particles. Relativistically, however, the energy-dependent range of the virtual cloud introduces a drastic modification in the momentum integral.

No mention has so far been made of any contraction factor such as that which occupies a prominent position in Fermi's statistical model. This indeed is absent here. What one gets instead is something like a uniform shrinkage of the configurational volume with increasing energy due to the energy-dependent cutoffs. The effect of shrinkage of configurational volume with energy is of course more significant for a light particle than for a heavy one. As a result one finds in calculating the energy spectrum of a single emitted meson in a nucleon-nucleon collision that low-meson-energy emissions are favored above the high ones.

A quantitative formulation of the preceding discussion is now given. The expression for the number of states per unit energy interval in the accessible phase space as restricted by conservation of energy, mo-

TABLE I. Values of P_n for a nucleon-nucleon collision when $S_n=T_n=\tau_{(n)}=1$. The last column indicates the number of nucleons and pions which the reaction yields.

E	2.5	6.3	10	Process
P_2	0.030	0.025	0.022	$2N$
P_3	0.012	0.022	0.022	$2N$, 1π
P_4	0.0043	0.006	0.0089	$2N$, 2π
P_4'	0	0.000001	0.00022	$4N$

TABLE II. Values of $P_n/\tau_{(n)}{}^{\frac{1}{2}(n-1)}$ for a p-p collision at three energies.

	1.5	6.3	10
pp	0.015	0.0125	0.011
pp^0	0.003	0.0055	0.0055
pn^+	0.018	0.033	0.033
pp^{+-}	0.00026	0.0036	0.0053
pp^{00}	0.000043	0.0006	0.00089
pn^{+0}	0.00077	0.0108	0.016
nn^{++}	0.000065	0.0009	0.0013

TABLE III. Values of $P_n/\tau_n{}^{\frac{1}{2}(n-1)}$ for an n-p collision in a $T=0$ isotopic spin state at three energies.

	1.5	6.3	10
pn	0.030	0.025	0.022
pp^-	0.002	0.0037	0.0037
pn^0	0.004	0.0073	0.0073
nn^+	0.002	0.0037	0.0037
pp^{-0}	0.00072	0.001	0.0015
pn^{00}	0.00072	0.001	0.0015
pn^{+-}	0.00043	0.006	0.0089
nn^{+0}	0.00072	0.001	0.0015

mentum, and center of energy may be written as

$$P_n=\frac{1}{(2\pi)^{3(n-1)}}\frac{(2K)^4}{2c\hbar K}S_n\cdot T_n\prod_{i=1}^{i=n}$$

$$\times\int \mathbf{x}d\mathbf{k}_i\delta(2K-\sum_i(k_i^2+\kappa_i^2)^{\frac{1}{2}})\delta(-\sum\mathbf{k}_i)$$

$$\times\int \mathbf{x}d\mathbf{x}_i\exp[-\tau_i x_i^2(k_i^2+\kappa_i^2)^{\frac{1}{2}}]$$

$$\times\delta(\sum\mathbf{x}_i(k_i^2+\kappa_i^2)^{\frac{1}{2}}). \quad (2)$$

In this formula the index n refers to n particles with Compton wavelengths $\kappa_1, \kappa_2, \cdots\kappa_n$. The letter S_n denotes a constant whose exact value depends on the number of indistinguishable groups and the population of each occurring among the n particles. The isotopic spin weight factors are denoted by T_n. The symbol K stands for the energy per incident nucleon in the center of energy system. A gaussian cutoff with an, as yet, arbitrary parameter τ_i for the configuration space of each particle has been introduced in the integrand. The quantities κ_i, K, $\mathbf{k}$ have the dimensions of reciprocal length. Thus the integral has the dimensions of the product of four delta functions, or that of $(2\kappa)^{-4}$. The weight factors S_n and T_n are of course dimensionless. Carrying out the integration over configuration space we obtain

$$P_n=\frac{S_nT_n}{(4\pi)^{\frac{3}{2}(n-1)}}\frac{(2K)^4}{\hbar c(2K)}\cdot\frac{1}{\sum_{i=1}^{n}\frac{1}{\tau_i}}\prod_{i=1}^{n}\frac{1}{\tau_i^{\frac{1}{2}}}$$

$$\times\int\frac{d\mathbf{k}_i}{(k_i^2+\kappa_i^2)^{\frac{1}{2}}}\delta(2K-(k_i^2+\kappa_i^2)^{\frac{1}{2}})\delta(-\sum\mathbf{k}_i), \quad (3)$$

where the τ_i's are constants, independent of energy. Looking back at (3) we see that the size of the "wave packet" of a particle is determined by its energy and the τ_i's play the role of intrinsic scaling factors. To simplify the formula we introduce a reduced scaling factor for the system of n particles

$$\frac{1}{\tau_{(n)}^{n-1}}=\frac{1}{n}\sum_{i=1}^{n}\tau_i\Big/\prod_{i=1}^{n}\tau_i, \quad (4a)$$

and define a quantity

$$Q_n=\left(\frac{\tau_{(n)}}{4\pi}\right)^{\frac{3}{2}(n-1)}\frac{1}{n^{\frac{1}{2}}}. \quad (4b)$$

Equation (2) then assumes the form

$$P_n=Q_nS_nT_nJ_n, \quad (5a)$$

where

$$J_n=\frac{(2K)^4}{\hbar c2K}\int\prod_{i=1}^{n}\frac{d\mathbf{k}_i}{[k_i^2+\kappa_i^2]^{\frac{1}{2}}}$$

$$\times\delta(2K-\sum(k_i^2+\kappa_i^2)^{\frac{1}{2}})\delta(-\sum\mathbf{k}_i). \quad (5b)$$

The nonrelativistic limit of expression (5) is not essentially different from that of Fermi's model with the conservation of linear momentum.[2] A short calculation carried out along the lines of reference 2 yields

$$P_n=\tau_n^{\frac{3}{2}(n-1)}S_nT_n\frac{1}{mc^2}\frac{1}{n^{\frac{1}{2}}}\frac{1}{(\frac{3}{2}n-5/2)!}\left(\frac{T}{mc^2}\right)^{\frac{3}{2}}, \quad (6)$$

where

$$\frac{1}{m^{n-1}}=\sum_{i=1}^{n}m_i\Big/\prod_{i=1}^{n}m_i,$$

and T is the kinetic energy per colliding nucleon in the center of mass system.

It is readily seen, however, that the factor $[k_i^2+\kappa_i^2]^{-\frac{1}{2}}$ will introduce essential modifications in the high energy domain. These will show up primarily in the shape of the energy spectrum of the emitted mesons. For a fixed multiplicity, this is independent of any uncertainties in the factor Q_n. Figures 1, 2, and 3 show the general

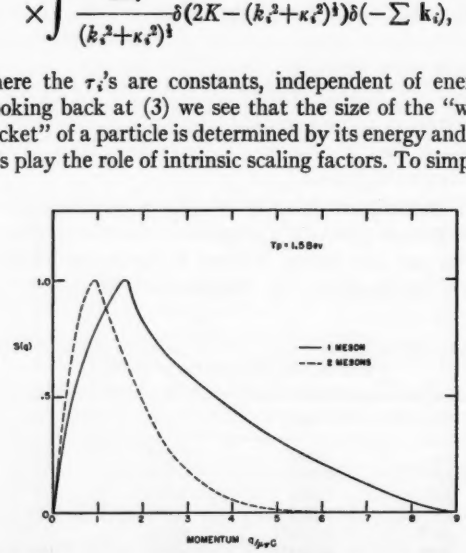

FIG. 1. Momentum spectra of singly and doubly emitted mesons in the laboratory system for incident nucleons with 1.5-Bev kinetic energy.

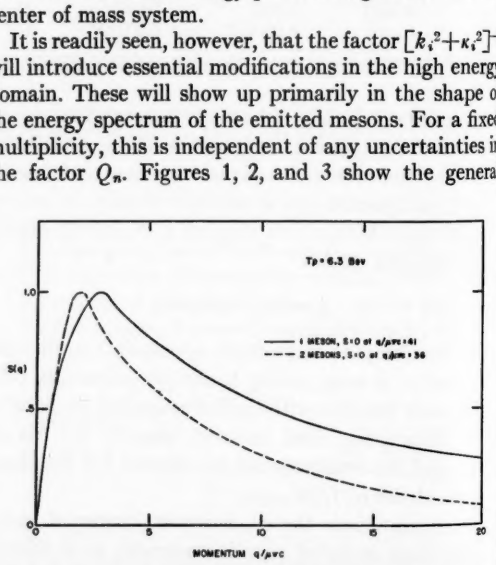

FIG. 2. Momentum spectra of singly and doubly emitted mesons in the laboratory system for incident nucleons with 6.3-Bev kinetic energy.

[2] J. V. Lepore and R. Stuart, Phys. Rev. 94, 1724 (1954).

TABLE IV. Values of $P_n/\tau_{(n)}^{\frac{1}{2}(n-1)}$ for an n-p collision in a $T=1$ isotopic spin state at three energies.

	1.5	6.3	10
pn	0.030	0.025	0.022
pp^-	0.003	0.0055	0.0055
pn^0	0.012	0.022	0.022
nn^+	0.003	0.0055	0.0055
pp^{-0}	0.00017	0.0024	0.0036
pn^{00}	0.00013	0.0018	0.0027
pn^{+-}	0.00077	0.011	0.016
nn^{+0}	0.00017	0.0024	0.0036

tendency for mesons to be emitted with low rather than high energies. This is a general feature of the model resulting from the fact that high-energy mesons have less configurational volume available to them than the low-energy ones. This feature is present in single- as well as multiple-meson production. An experiment carried out under conditions where single-meson production would be expected to dominate would therefore be of some interest.

At higher energies where multiple production is also possible the predictions of the model would depend on the assumed values of the scaling factors τ_π and τ_N that enter into the definition of Q_n. Explicitly

$$Q_2(nn)=(\tau_N/8\pi)^{\frac{3}{4}},$$
$$Q_3(NN\pi)=\left(\frac{\tau_N}{4\pi}\right)^3\Big/\left(1+2\frac{\tau_N}{\tau_\pi}\right)^{\frac{3}{4}}, \tag{7}$$
$$Q_4(NN2\pi)=\left(\frac{\tau_N}{4\pi}\right)^{9/2}\Big/\left[2\frac{\tau_N}{\tau_\pi}\left(1+\frac{\tau_N}{\tau_\pi}\right)\right]^{\frac{3}{4}}.$$

It is seen from these expressions that even if $\tau_n=\tau_\pi=\tau$, the assumed value of this single parameter will still effect the predictions of the model in an essential manner.

In view of the general qualitative agreement of the shapes of the spectra with those observed at the Brookhaven Cosmotron, a further attempt might be made to account for the observation in greater detail by fixing one or two parameters ($\tau_\pi=\tau_N=\tau$, or τ_N, τ_π/τ_N) empirically on the basis of single-meson production. With a view towards such a program when further data become available we include tables with some computed values of the expressions appearing in Eq. (5). Table I lists the values of P_n when $S_n=T_n=\tau_{(n)}=1$, Table II those of $P_n/(\tau_n)^{\frac{1}{2}(n-1)}$ for a p-p collision, Table III the same quantity for an n-p collision if the colliding particles are in an isotopic spin state $T=0$, and Table IV if they are in a state $T=1$. Columns are labeled by the kinetic energy (in Bev) of the incident nucleon in the laboratory system.

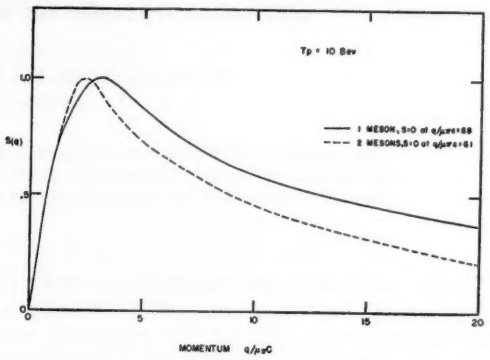

FIG. 3. Momentum spectra of singly and doubly emitted mesons in the laboratory system for incident nucleons with 10-Bev kinetic energy.

In constructing Table I we reduced J_4 to a double, J_3 to a single integral. J_2 can be expressed analytically in terms of elementary functions. The remaining integration were carried out numerically on the IBM Card Program Calculator at the Livermore site of this laboratory. Tables II, III, and IV were constructed using Table I and the numerical coefficients T_n calculated by Fermi.[3]

It may perhaps be worth-while to point out that the probability for the production of a nucleon pair in a nucleon-nucleon collision is seen from Table I to be exceedingly small even at 10 Bev.

We are grateful to Miss H. Cox and Mrs. M. Harrison for carrying out the computations.

[3] E. Fermi, Phys. Rev. 92, 452 (1953).

Projection Operator for the Rarita-Schwinger Equation*

F. J. MILFORD
Department of Physics, Case Institute of Technology, Cleveland, Ohio
(Received February 7, 1955)

An operator which removes the spin one-half states from an arbitrary Rarita-Schwinger type state function has been constructed. This procedure avoids the explicit construction of spin three-halves state functions and makes possible the use of the Casimir spur technique for handling sums over spin three-halves states.

THE Rarita-Schwinger[1] equation has been used, recently, by several authors to describe spin three-halves particles. The fact that some of the heavy cosmic-ray particles are fermions and may have spins greater than one-half enhances the interest in this equation as does the possibility of using spin three-halves nuclear isobars to explain anomalous nuclear effects.

The Rarita-Schwinger equation has the virtue of involving only familiar quantities, four-vectors and Dirac (i.e., four-component) spinors. Its disadvantages include the presence of redundant components describing spin one-half particles and the extremely complicated form of the electromagnetic interaction. This note will deal with the first of these difficulties in the particular case where a sum over spin three-halves states is involved.

The Rarita-Schwinger equation in the absence of interactions is

$$(\gamma_\mu p_\mu - im)\Psi_\nu = 0, \tag{1}$$

where Ψ_ν is a four-vector each of whose components is a Dirac spinor. The state function Ψ_ν is required, in addition, to satisfy

$$\gamma_\nu \Psi_\nu = p_\nu \Psi_\nu = 0, \tag{2}$$

in order to eliminate the spin one-half components present in an arbitrary solution of Eq. (1). The wave equation and the auxiliary conditions may be derived from a Lagrangian as indicated in the original paper by Rarita and Schwinger.

In many calculations a sum or average over spin three-halves states must be calculated. This can be done, of course, by using a particular representation and computing the sum directly. Alternatively one may seek a projection operator which gives zero for the spin one-half components. Such an operator makes it possible to use the completeness relation for the evaluation of the sum.

If only free-particle solutions are considered, the properties of the projection operator may be readily formulated. Let Φ_ν be an arbitrary solution of Eq. (1) having the transformation properties indicated. The projection operator $\Lambda_{\mu\nu}$ must satisfy the following conditions:

(a) it must be a tensor of the second rank with spinor-operator elements;
(b) $(\gamma_\tau p_\tau - im)\Lambda_{\mu\nu}\Phi_\nu = 0$;
(c) $\gamma_\mu \Lambda_{\mu\nu}\Phi_\nu = p_\mu \Lambda_{\mu\nu}\Phi_\nu = 0$;
(d) $\Lambda_{\mu\nu}\Lambda_{\nu\lambda}\Phi_\lambda = \Lambda_{\mu\nu}\Phi_\nu$.

These properties, together with the fact that the operator must be constructed from the available tensors and four-vectors ($\delta_{\mu\nu}$, γ_μ, and p_μ), are sufficient to completely determine the operator.

The second-rank tensors from which $\Lambda_{\mu\nu}$ must be constructed are: $\delta_{\mu\nu}$, $p_\mu p_\nu$, $\sigma_\mu p_\nu$, $p_\mu \sigma_\nu$, $\gamma_\mu\gamma_\nu$, and $\gamma_\nu\gamma_\mu$. Of these $\gamma_\mu\gamma_\nu$, $\gamma_\nu\gamma_\mu$, and $\delta_{\mu\nu}$ are not independent; hence we exclude $\gamma_\nu\gamma_\mu$, leaving five independent tensors. $\delta_{\mu\nu}$ and $p_\mu p_\nu$ commute with $(\gamma_\tau p_\tau - im)$. The linear combination $\gamma_\mu\gamma_\nu + (p_\mu\gamma_\nu - p_\nu\gamma_\mu)/im$ also commutes with $(\gamma_\tau p_\tau - im)$. The tensor

$$\Lambda_{\mu\nu} = A[\delta_{\mu\nu} + Bp_\mu p_\nu + C\gamma_\mu\gamma_\nu + C(p_\mu\gamma_\nu - p_\nu\gamma_\mu)/im]$$

then satisfies conditions (a) and (b). Requiring that (c) be satisfied determines B and C to be $2/3m^2$ and $-1/3$ respectively. Finally condition (d) determines $A=1$. The final projection operator is

$$\Lambda_{\mu\nu} = \delta_{\mu\nu} + \frac{2}{3m^2}p_\mu p_\nu - \frac{1}{3im}(p_\mu\gamma_\nu - p_\nu\gamma_\mu) - \tfrac{1}{3}\gamma_\mu\gamma_\nu.$$

Feynman[2] has pointed out the existence of and need for a similar operator in connection with the vector meson field. This operator can be constructed in exactly the same way. Very briefly, let φ_μ be an arbitrary solution of

$$(p^2 - m^2)\varphi_\mu = 0.$$

The projection operator must

(a) commute with $p^2 - m^2$;
(b) satisfy $p_\mu - \Lambda_{\mu\nu}\varphi_\nu = 0$;
(c) satisfy $\Lambda_{\mu\nu}\Lambda_{\nu\lambda}\varphi_\lambda = \Lambda_{\mu\nu}\varphi_\nu$.

Since only $\delta_{\mu\nu}$ and $p_\mu p_\nu$ are available, (a) is satisfied automatically; (b) requires $\Lambda_{\mu\nu} = A(\delta_{\mu\nu} - p_\mu p_\nu/m^2)$, and (c) requires $A=1$.

* This work was started in connection with the author's Ph.D. thesis at the Massachusetts Institute of Technology and has been continued at the Case Institute of Technology with the assistance of the U. S. Atomic Energy Commission.

[1] W. Rarita and J. Schwinger, Phys. Rev. **60**, 61 (1941).

[2] R. Feynman, Phys. Rev. **76**, 769 (1949).

Fourth-Order Radiative Corrections to Atomic Energy Levels. II*

ROBERT L. MILLS† AND NORMAN M. KROLL
Columbia University, New York, New York

(Received February 7, 1955)

A rigorous method is described for treating the problem of the hydrogen-like atom in quantum electrodynamics by the separation of integrals into parts which can be evaluated with relativistic and nonrelativistic approximations. The method is based on that developed by Baranger, Bethe, and Feynman for the second-order problem, and is applied here to the problem of the fourth-order radiative energy level displacement. It is shown that the result inferred by Weneser, Bersohn, and Kroll from the study of fourth-order radiative corrections to elastic scattering by a given external potential is correct to order $\alpha^2(\alpha Z)^4mc^2$ for a hydrogenic atom. It is also shown that the αZ corrections to this result can be obtained using this method, just as was done in the second-order problem by Baranger, Bethe, and Feynman.

INTRODUCTION

THE possible significance of fourth-order radiative corrections in the interpretation of the experimental results of Lamb,[1] etc., on the $2S_{\frac{1}{2}}-2P_{\frac{1}{2}}$ separation in hydrogen has been discussed by Weneser, Bersohn and Kroll.[2] Their procedure for determining the effect consisted of evaluating the radiative corrections to the elastic scattering (in Born approximation) by a given external potential, inferring a modified potential from the result, and using the modified potential to compute the energy level displacement. While this procedure is certainly a plausible one, it would appear to be more satisfactory to deduce their result from a systematic treatment of an exact expression for the fourth-order self-energy. Such a procedure has the additional advantage that one then sees clearly how to obtain the αZ correction to their result.

Low[3] has discussed the problem of defining this energy level displacement in terms of the experimental methods which might be used in its determination, with particular reference to the line shape problem. He finds that up to, but not including, terms of order $\alpha^2(\alpha Z)^6mc^2$ for a hydrogen atom, the level shift so determined corresponds precisely to that which would be obtained by the application of standard steady-state perturbation theory or by the application of perturbation theory to the modified Dirac equation proposed by Schwinger.[4]

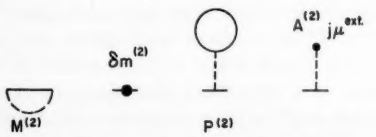

FIG. 1. Second-order contributions to the self-energy, with the appropriate contributions to mass and charge renormalization explicitly displayed. The solid lines represent the propagation function for the electron in the external field, and the dashed lines, the photon propagation function.

Thus, up to the fourth order, one finds

$$\Delta E_a=\Delta E_a{}^{(2)}+\Delta E_a{}^{(4)}+\cdots, \tag{1}$$

where

$$\Delta E_a{}^{(2)}=\mathrm{Re}\,\{iH_{aa}{}^{(2)}(E_a)\},$$

$$\Delta E_a{}^{(4)}=\mathrm{Re}\left\{iH_{aa}{}^{(4)}(E_a)-H_{aa}{}^{(2)}(E_a)\times\left[\frac{\partial}{\partial E}H_{aa}{}^{(2)}(E)\right]_{E=E_a}+\sum_{n\neq a}\frac{H_{an}{}^{(2)}(E_a)H_{na}{}^{(2)}(E_a)}{E_n-E_a}\right\};$$

$$H_{nm}{}^{(p)}(E)=-(2\pi)^3i\hbar c\int\bar{\varphi}_n(\mathbf{p}_2)\Sigma^{(p)}(\mathbf{p}_2,\mathbf{p}_1;E)\times\varphi_m(\mathbf{p}_1)(d\mathbf{p})^2. \tag{2}$$

In the aforementioned expressions, $\Delta E_a{}^{(2)}$ and $\Delta E_a{}^{(4)}$ refer, respectively, to the second- and fourth-order parts of the level shift for the ath state, E_n refers to the unshifted level of the nth state, while $\varphi_n(\mathbf{p})$ is the corresponding steady state solution of the Dirac equation in the given external field.[5] The functions $\Sigma^{(p)}(\mathbf{p}_2,\mathbf{p}_1;E)$, which we shall also write simply as $\Sigma^{(p)}(p_2,p_1)$ with $p_{20}=p_{10}=p_0=E/(\hbar c)$, are for convenience taken to include both what one might call mass operator and vacuum polarization contributions to the self-energy. Accordingly, we write,

$$\Sigma^{(2)}(p_2,p_1)=M^{(2)}+P^{(2)},\quad[p_{20}=p_{10}=p_0],$$

with

$$M^{(2)}=-\tfrac{1}{2}i(2\pi)^5\alpha\int\gamma_\mu S_F{}^e(p_2-k,\,p_1-k)\gamma_\mu D_F(k)d_4k-\delta_K{}^{(2)}\delta_3(\mathbf{p}_2-\mathbf{p}_1), \tag{3}$$

$$P^{(2)}=\tfrac{1}{2}i(2\pi)^5\alpha D_F(p_2-p_1)\{\mathrm{Tr}[\gamma_\mu S_F{}^e(p_2-k,\,p_1-k)]d_4k-[2/(ie)]A^{(2)}j_\mu{}^{\mathrm{ext}}(p_2-p_1)\}.$$

* Work supported jointly by The Signal Corps, The Office of Naval Research, and The Air Research and Development Command.

† Now at Brookhaven National Laboratory, Upton, New York.

[1] Triebwasser, Dayhoff, and Lamb, Phys. Rev. **89**, 98 (1953).

[2] Weneser, Bersohn, and Kroll, Phys. Rev. **91**, 1257 (1953), hereafter referred to as WBK.

[3] Francis Low, Phys. Rev. **88**, 53 (1952).

[4] Julian Schwinger, Proc. Natl. Acad. Sci. U. S. **37**, 452 (1951).

[5] The "momenta" p, q, and k in this paper, like the "mass" $\kappa=m_ec/\hbar$, have the dimensions of inverse length. The momentum space wave functions $\varphi_n(\mathbf{p})$ have the normalization $\int|\varphi_n(\mathbf{p})|^2d\mathbf{p}=(2\pi)^{-3}$. If a and b are two four-vectors, we take the convention $a\cdot b=a_\mu b_\mu=a_1b_1+a_2b_2+a_3b_3+a_4b_4=\mathbf{a}\cdot\mathbf{b}-a_0b_0$. Heaviside units are used.

Furthermore,

$$D_F(k)=-2i(2\pi)^{-4}k^{-2} \tag{4}$$

is the Feynman Green's function for the electromagnetic field, while the Feynman Green's function for the Dirac equation, with the specified external potential is

$$S_F^e(p_2,p_1)=\frac{i\hbar c}{\pi}\sum_n \frac{\varphi_n(\mathbf{p}_2)\bar{\varphi}_n(\mathbf{p}_1)}{(1-i\epsilon)E_n-\hbar c p_0}. \tag{5}$$

The appropriate mass and charge renormalizations are subtracted out explicitly. The corresponding Feynman diagrams appear in Fig. 1.

Similarly we write

$$\Sigma_4(p_2,p_1)=M_1^{(4)}+M_2^{(4)}+(MP)_1+(MP)_2+P_1^{(4)}+P_2^{(4)},$$

with

$$\begin{aligned}
M_1^{(4)}=&-2i(2\pi)^{-4}[\tfrac{1}{4}(2\pi)^9\alpha]^2\\
&\times\int\gamma_\mu S_F^e(p_2-k_2,\,p_4-k_2)\gamma_\nu\\
&\times S_F^e(p_4-k_1-k_2,\,p_3-k_1-k_2)\gamma_\mu\\
&\times S_F^e(p_3-k_1,\,p_1-k_1)\gamma_\nu D_F(k_1)\\
&\times D_F(k_2)(d_4k)^2d\mathbf{p}_3d\mathbf{p}_4,\\
M_2^{(4)}=&\tfrac{1}{4}(2\pi)^9\alpha\int\gamma_\mu S_F^e(p_2-k,\,p_4-k)\\
&\times M^{(2)}(p_4-k,\,p_3-k)S_F^e(p_3-k,\,p_1-k)\gamma_\mu\\
&\times D_F(k)d_4kd\mathbf{p}_3d\mathbf{p}_4,\\
(MP)_1=&-\tfrac{1}{2}i(2\pi)^5\alpha\int\gamma_\mu S_F^e(p_2-k_2,\,p_1-k_1)\gamma_\nu\\
&\times[D_F^{e(2)}(k_2,k_1)]_{\mu\nu}(d_4k)^2,\\
[D_F^{e(2)}(k_2,k_1)]_{\mu\nu}=&-\tfrac{1}{4}(2\pi)^9\alpha D_F(k_2)D_F(k_1)\\
&\times\int\mathrm{Tr}\,[\gamma_\mu S_F^e(p_4,p_3)\gamma_\nu S_F^e(p_3-k_1,\,p_4-k_2)](d_4p)^2\\
&-C^{(2)}D_F(k_1)\delta_4(k_2-k_1)\delta_{\mu\nu}.
\end{aligned} \tag{6}$$

We will have no occasion to discuss the remaining terms explicitly and so we content ourselves with illustrating them, as well as the above defined terms, by means of the Feynman diagrams appearing in Fig. 2. These expressions contain fourth-order mass and charge renormalization terms which will be recognized and ignored

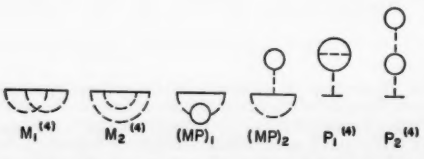

FIG. 2. Fourth-order contributions to the self-energy. Mass and charge renormalization contributions are not explicitly displayed.

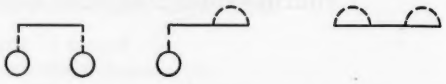

FIG. 3. Improper self-energy diagrams, corresponding to the second and third terms in $\Delta E^{(4)}$ [Eq. (2)].

at a later stage. The improper self-energy diagrams illustrated in Fig. 3 correspond crudely to the second and third terms in the expression for $\Delta E^{(4)}$.

Our task now consists of the separation of $\Delta E^{(4)}$ into four kinds of terms: (1) A set which is recognizable as mass and charge renormalization. (2) A set which corresponds precisely to the set of terms evaluated by WBK, and which gives rise to an energy level displacement of the S state of order $\alpha^2(\alpha Z)^4$. (3) A set which is of the same order of magnitude as the WBK terms, which must be separately discussed, and will ultimately be shown to vanish. (4) The remainder, consisting of terms individually at least of order αZ smaller than the WBK terms.

In the following sections our attention will be devoted chiefly to effecting the previously described separation and to the demonstration that terms in class (3) above do in fact add up to zero. The number of terms which must be put in class (4) is very large and we shall in general assign terms to this class without proof. There are, however, important guiding principles which should be kept in mind. We note that the Fourier transform of the Coulomb potential is given by

$$\frac{ie}{\hbar c}A_\rho^e(\mathbf{q})=\frac{\alpha Z}{2\pi^2\mathbf{q}^2}\delta_{\rho 4}.$$

It generally appears multiplied by a three-dimensional volume element in $\mathbf{q}$-space. Thus the appearance of an extra factor eA_μ^e in an expression will as a rule reduce the value by a factor αZ or $(\alpha Z)^2$, accordingly as the significant values of $\mathbf{q}$ are of order unity or αZ. Furthermore, the momenta $\mathbf{p}$ associated with a bound state may usually be taken as being of order αZ. The binding energy, $\kappa-p_0$, is of order $(\alpha Z)^2$. One of these factors will always be involved when approximations "valid to order $\alpha^2(\alpha Z)^4$" are made or when terms are consigned to class (4). The problem at hand would be trivial if there were not important exceptions to the criteria given above, and it is these exceptions which will require our attention.

First of all, it can be readily shown that the terms $(MP)_2$, $P_2^{(4)}$, and $\sum_n H_{an}H_{na}(E_n-E_a)^{-1}$ belong in class (4), that is, they do not contribute to the order in which we are interested, nor did any scattering corrections which one might associate with these terms occur in the WBK calculation. The contribution of $P_1^{(4)}$ has been computed by Baranger, Dyson, and Salpeter,[6] and will not be discussed here. We therefore confine our attention to the terms $M_1^{(4)}$, $M_2^{(4)}$, $(MP)_1$,

[6] Baranger, Dyson, and Salpeter, Phys. Rev. 88, 680 (1952).

and $H^{(2)}\partial H^{(2)}/\partial E$. The terms of the WBK calculation (which will hereafter be referred to as the scattering approximation) to be associated with each of these terms can be readily guessed and will appear explicitly later. These are illustrated in Fig. 4. It is worth noting that in the case of $(MP)_1$, the scattering approximation yields a result which is finite in the infrared. This is not the case for the remaining terms; one gets a finite result only when the contributions from the three terms are added. Associated with this situation is the fact that the scattering approximation is valid for $(MP)_1$, considered separately. This fact makes the treatment of $(MP)_1$ essentially trivial, and we shall therefore discuss it first. On the other hand the scattering approximation is not valid for the other terms considered separately; one finds, indeed, $\alpha^2(\alpha Z)^4$ terms with infrared divergent coefficients. The fact that the infrared difficulties disappear in the scattering approximation after adding the terms together implies that the same will happen to the corrections, but does not obviously imply that the corrections add up to zero. In order to demonstrate that they do we have found it necessary to compute these corrections explicitly.

VALIDITY OF THE SCATTERING APPROXIMATION FOR THE TERM $(MP)_1$

The most straightforward way of separating the scattering approximation from the expressions we have written down is simply to replace $S_F^e(p_2,p_1)$ by

$$\begin{aligned}&S_F^e(p_2,p_1)\\&=S_F(p_2)\delta_3(\mathbf{p}_2-\mathbf{p}_1)-\tfrac{1}{2}i(2\pi)^4[ie/(\hbar c)]S_F(p_2)\\&\times\gamma\cdot A^e(\mathbf{p}_2-\mathbf{p}_1)S_F(p_1)-\tfrac{1}{4}(2\pi)^8[ie/(\hbar c)]^2S_F(p_2)\\&\times\Big[\int\gamma\cdot A^e(\mathbf{q}_2)S_F^e(p_2-q_2,\,p_1+q_1)\\&\qquad\times\gamma\cdot A^e(\mathbf{q}_1)(d\mathbf{q})^2\Big]S_F(p_1),\quad(7)\\&[q_{10}=q_{20}=0],\end{aligned}$$

obtained by iterating the integral equations satisfied by $S_F^e(p_2,p_1)$:

$$\begin{aligned}&S_F^e(p_2,p_1)\\&=S_F(p_2)\delta_3(\mathbf{p}_2-\mathbf{p}_1)-\tfrac{1}{2}i(2\pi)^4[ie/(\hbar c)]\\&\times S_F(p_2)\int\gamma\cdot A^e(\mathbf{q})S_F^e(p_2-q,\,p_1)d\mathbf{q}\\&=S_F(p_1)\delta_3(\mathbf{p}_2-\mathbf{p}_1)-\tfrac{1}{2}i(2\pi)^4[ie/(\hbar c)]\\&\qquad\times\Big[\int S_F^e(p_2,\,p_1+q)\gamma\cdot A^e(\mathbf{q})d\mathbf{q}\Big]S_F(p_1),\end{aligned}\quad(8)$$

where

$$S_F(p)=-\frac{2i}{(2\pi)^4}\frac{i\gamma\cdot p-\kappa}{p^2+\kappa^2}.\quad(9)$$

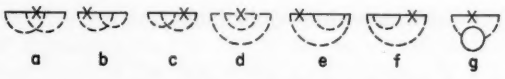

FIG. 4. Contributions to the scattering approximation calculated by WBK. The crosses represent interactions with the external Coulomb field.

Rather than consider the consequences of such a substitution in full detail we shall simply assert that the S_F^e functions appearing in the closed loop can be replaced by free-particle propagators. The expression for $(MP)_1$ can then be written[7]

$$\begin{aligned}(MP)_1=&-\tfrac{1}{2}i(2\pi)^4\alpha^2\int\gamma_\mu S_F^e(p_2-k,\,p_1-k)\\&\times\gamma_\mu\bar{D}_F^{(2)}(k)d_4k,\end{aligned}$$

with

$$\bar{D}_F^{(2)}(k)=-\frac{i}{(2\pi)^4}\int_0^1 dv\frac{v^2(1-\frac{1}{3}v^2)}{\kappa^2+\frac{1}{4}k^2(1-v^2)}.$$

Furthermore,

$$\begin{aligned}(MP)_1=&-\tfrac{1}{2}i(2\pi)^4\alpha^2\Big\{\gamma_\mu S_F(p_2-k)\gamma_\mu\bar{D}_F^{(2)}(k)d_4k\\&\times\delta_3(\mathbf{p}_2-\mathbf{p}_1)-\tfrac{1}{2}i(2\pi)^4[ie/(\hbar c)]\\&\times\int\gamma_\mu S_F(p_2-k)\gamma\cdot A^e(\mathbf{p}_2-\mathbf{p}_1)\\&\times S_F(p_1-k)\gamma_\mu\bar{D}_F^{(2)}(k)d_4k\\&-\tfrac{1}{4}(2\pi)^8[ie/(\hbar c)]^2\int\gamma_\mu S_F(p_2-k)\gamma\cdot A^e(\mathbf{q}_2)\\&\times S_F^e(p_2-q_2-k,\,p_1+q_1-k)\gamma\cdot A^e(\mathbf{q}_1)\\&\times S_F(p_1-k)\gamma_\mu\bar{D}_F^{(2)}(k)d_4k(d\mathbf{q})^2\Big\}.\end{aligned}\quad(10)$$

It is clear that $(MP)_1$ bears a close resemblance to $M^{(2)}$, the only difference being the replacement of the D_F function by the $\bar{D}_F^{(2)}$ function. This difference is in fact very significant, as $\bar{D}_F^{(2)}(0)$ is finite. As a consequence, the infrared difficulties associated with the evaluation of $M^{(2)}$ do not manifest themselves here. To order $\alpha^2(\alpha Z)^4$, one can, in fact, simply replace the S_F^e appearing in the third term by the free-particle propgation function. Using familiar manipulations (see, for example, Kroll and Pollock[8]) one can extract from

$$\langle(MP)_1\rangle=(2\pi)^3\int\varphi_a(\mathbf{p}_1)(MP)_1\varphi_a(\mathbf{p}_1)d\mathbf{p}_1d\mathbf{p}_2,$$

to order $\alpha^2(\alpha Z)^4$, four kinds of terms. The first term of

[7] R. Karplus and N. M. Kroll, Phys. Rev. 77, 536 (1950), Eq. (13).

[8] N. M. Kroll and F. Pollock, Phys. Rev. 86, 876 (1952).

(10) yields expressions of the form

$$(1)\quad \int \bar{\varphi}(\mathbf{p})\varphi(\mathbf{p})d\mathbf{p},$$

$$(2)\quad [ie/(\hbar c)]\int \bar{\varphi}(\mathbf{p}_2)\gamma\cdot A^e(\mathbf{p}_2-\mathbf{p}_1)\varphi(\mathbf{p}_1)d\mathbf{p}_1d\mathbf{p}_2,$$

$$(3)\quad [ie/(\hbar c)]^2\int \bar{\varphi}(\mathbf{p}_2)\gamma\cdot A^e(\mathbf{p}_2-\mathbf{p}_3)\times\gamma\cdot A^e(\mathbf{p}_3-\mathbf{p}_1)\varphi(\mathbf{p}_1)d\mathbf{p}_1d\mathbf{p}_2d\mathbf{p}_3.$$

The second term of (10) yields terms like (2) and (3), plus a term proportional to:

$$(4)\quad [ie/(\hbar c)]\int \bar{\varphi}(\mathbf{p}_2)(\mathbf{p}_2-\mathbf{p}_1)^2\times\gamma\cdot A^e(\mathbf{p}_2-\mathbf{p}_1)\varphi(\mathbf{p}_1)d\mathbf{p}_1d\mathbf{p}_2.$$

This last term, when one notes the form of the second term in $(MP)_1$ [Eq. (10)], is easily seen to be identical with the contribution of diagram *g*, Fig. 4, to the scattering approximation. The third term of (10) yields a term like (3). Terms (1) and (2) are obviously mass and charge terms, to be dropped by renormalization. The term (3) corresponds simply to the expectation value of the square of the potential. We now make use of the fact that $\langle(MP)_1\rangle$, which we may write as

$$-\tfrac{1}{2}i(2\pi)^8\alpha\int \bar{\varphi}(\mathbf{p}_2)\gamma_\mu S_F{}^e(p_2-k_2,\,p_1-k_1)\times\gamma_\nu\varphi(\mathbf{p}_1)[D_F{}^{e(2)}(k_2,k_1)]_{\mu\nu}d_4k_1d_4k_2,$$

is a guage invariant quantity, so that the sums of the coefficients of the charge renormalization $(\gamma\cdot A^e)$ and potential squared $[(\gamma\cdot A^e)^2]$ terms must vanish. Consequently, only the $(\mathbf{p}_2-\mathbf{p}_1)^2\gamma\cdot A^e$ term remains and the scattering approximation is seen to be valid for $(MP)_1$.

In view of the fact that the $(\gamma\cdot A^e)^2$ term is not removable by charge renormalization and is of the same order of magnitude as the main level shift term $[(\mathbf{p}_2-\mathbf{p}_1)^2\gamma\cdot A^e]$, previous writers have, in dealing with the second-order level shift, always computed the coefficient to verify explicitly that it vanishes. The full evaluation of the $(\gamma\cdot A^e)^2$ term for the fourth-order level shift would, however, be a task of magnitude comparable to that of evaluating the $(\mathbf{p}_2-\mathbf{p}_1)^2\gamma\cdot A^e$ term. We shall therefore depend completely upon the kind of gauge invariance argument given above. Thus the identification of $\alpha^2(\alpha Z)^4$ contributions which can be attributed to $(\gamma\cdot A^e)^2$ terms will be an essential part of our task, but a term so identified will be subsequently ignored.

CONTRIBUTION OF $M_1{}^{(4)}$

It would be a simple matter to separate the scattering approximation out of $M_1{}^{(4)}$ using a technique identical to that employed in the discussion of $(MP)_1$. After replacing $S_F{}^e(p_2,p_1)$ with the form appearing in Eq. (7), one then finds that the terms in which $\gamma\cdot A^e$ appears once explicitly contain the scattering approximation. On the other hand, examination of the multiple-potential terms, i.e., terms containing $\gamma\cdot A^e$ more than once, shows that these yield contributions at least of order $\alpha^2(\alpha Z)^4$ and possibly larger, not identifiable as $(\gamma\cdot A^e)^2$ terms. It therefore becomes necessary to evaluate the contributions arising from these terms. As pointed out by Baranger, Bethe, and Feynman,[9] the separation described above is not a convenient one in those cases in which the evaluation of the multiple-potential contribution is essential. We therefore extend the BBF procedure to the fourth-order problem.

We wish to separate the scattering approximation in a way which leaves the remainder tractable. We proceed as follows:

BBF gives the general identity, valid for any operator $\mathbf{O}$, and any two vectors p_1 and p_2:

$$\mathbf{O}=B(\mathbf{O};\,p_2,p_1)(i\gamma\cdot p_1+\kappa)-(i\gamma\cdot p_2+\kappa)B(\mathbf{O};\,p_2,p_1), \tag{11}$$

where

$$B(\mathbf{O};\,p_2,p_1)=\frac{(i\gamma\cdot p_2)\mathbf{O}+\mathbf{O}(i\gamma\cdot \mathbf{p}_1)}{p_2{}^2-p_1{}^2}. \tag{12}$$

We shall use a less symmetric, but more convenient, form as follows:

$$\begin{aligned}&\mathbf{O}=F(\mathbf{O};\,p,k)(i\gamma\cdot p+\kappa)-(i\gamma\cdot(p-k)+\kappa)F(\mathbf{O};\,p,k)\\&\quad=(i\gamma\cdot p+\kappa)F'(\mathbf{O};\,p,k)-F'(\mathbf{O};\,p,k)(i\gamma\cdot(p-k)+\kappa);\\&F(\mathbf{O};\,p,k)=B(\mathbf{O};\,p-k,\,p)=\frac{(i\gamma\cdot(p-k))\mathbf{O}+\mathbf{O}(i\gamma\cdot\mathbf{p})}{k^2-2p\cdot k},\\&F'(\mathbf{O};\,p,k)=-B(\mathbf{O};\,p,\,p-k)\\&\quad=\frac{(i\gamma\cdot p)\mathbf{O}+\mathbf{O}(i\gamma\cdot(p-k))}{k^2-2p\cdot k}.\end{aligned} \tag{13}$$

When $\mathbf{O}=\gamma_\mu$, we get the forms actually used by BBF in the second-order calculation. Now φ_a and $\bar{\varphi}_a$ satisfy the integral equations

$$\begin{aligned}&(i\gamma\cdot p+\kappa)\varphi_a(\mathbf{p})=[ie/(\hbar c)]\int\gamma\cdot A^e(\mathbf{q})\varphi_a(\mathbf{p}-\mathbf{q})d\mathbf{q}\\&\qquad[p_0=E_a/(\hbar c)],\\&\bar{\varphi}_a(\mathbf{p})(i\gamma\cdot p+\kappa)=[ie/(\hbar c)]\int\bar{\varphi}_a(\mathbf{p}+\mathbf{q})\gamma\cdot A^e(\mathbf{q})d\mathbf{q},\end{aligned} \tag{14}$$

while $S_F{}^e$ satisfies (8), which can be rewritten

$$\begin{aligned}&(i\gamma\cdot p_2+\kappa)S_F{}^e(p_2,p_1)\\&\quad=[ie/(\hbar c)]\int\gamma\cdot A^e(\mathbf{q})S_F{}^2(p_2-q,\,p_1)d\mathbf{q}\\&\qquad+2i(2\pi)^{-4}\delta_3(\mathbf{p}_2-\mathbf{p}_1),\end{aligned}$$

[9] Baranger, Bethe, and Feynman, Phys. Rev. **92**, 482 (1953), hereafter referred to as BBF.

$$S_F^e(p_2,p_1)(i\gamma\cdot p_1+\kappa)$$
$$=[ie/(\hbar c)]\int S_F^e(p_2,\,p_1+q)\gamma\cdot A^e(\mathbf{q})d\mathbf{q}$$
$$+2i(2\pi)^{-4}\delta_3(\mathbf{p}_2-\mathbf{p}_1). \quad (15)$$

When we use the identities (13) in the expressions $S_F^e\mathbf{O}\varphi_a$ and $\bar{\varphi}_a\mathbf{O}S_F^e$, we get

$$\int S_F^e(p_3-k,\,p_1-k)\mathbf{O}(p_1)\varphi_a(\mathbf{p}_1)d\mathbf{p}_1$$
$$=[ie/(\hbar c)]\int S_F^e(p_3-k,\,p_1+q-k)$$
$$\times\{F[\mathbf{O}(p_1+q);\,p_1+q,\,k]\gamma\cdot A^e(\mathbf{q})$$
$$-\gamma\cdot A^e(\mathbf{q})F[\mathbf{O}(p_1);\,p_1,\,k]\}\varphi_a(\mathbf{p}_1)d\mathbf{p}_1d\mathbf{q}$$
$$-2i(2\pi)^{-4}F[\mathbf{O}(p_3);\,p_3,k]\varphi_a(\mathbf{p}_3)$$
$$=[ie/(\hbar c)]\int S_F^e(p_3-k,\,p_1+q-k)A_\rho^e(\mathbf{q}) \quad (16)$$
$$\times\mathfrak{F}_\rho(\mathbf{O};\,p_1,q,k)\varphi_a(\mathbf{p}_1)d\mathbf{p}_1d\mathbf{q}$$
$$-2i(2\pi)^{-4}F[\mathbf{O}(p_3);\,p_3,k]\varphi_a(\mathbf{p}_3);$$
$$\int\bar{\varphi}_a(\mathbf{p}_2)\mathbf{O}(p_2)S_F^e(p_2-k,\,p_4-k)d\mathbf{p}_2$$
$$=[ie/(\hbar c)]\int\bar{\varphi}_a(\mathbf{p}_2)A_\rho^e(\mathbf{q})\mathfrak{F}_\rho'(\mathbf{O};\,p_2,q,k)$$
$$\times S_F^e(p_2-q-k,\,p_4-k)d\mathbf{p}_2d\mathbf{q}$$
$$-2i(2\pi)^{-4}\bar{\varphi}_a(\mathbf{p}_4)F'[\mathbf{O}(p_4);\,p_4,k];$$

where

$$\mathfrak{F}_\rho(\mathbf{O};\,p,q,k)=F[\mathbf{O}(p+q);\,p+q,\,k]\gamma_\rho$$
$$-\gamma_\rho F[\mathbf{O}(p);\,p,k];$$
$$\mathfrak{F}_\rho'(\mathbf{O};\,p,q,k)=\gamma_\rho F'[\mathbf{O}(p-q);\,p-q,\,k] \quad (17)$$
$$-F'[\mathbf{O}(p);\,p,k]\gamma_\rho.$$

We shall apply this only to operators $\mathbf{O}$ which do not involve the external potential at all, so that, according to (16), $S_F^e\mathbf{O}\varphi_a$ or $\bar{\varphi}_a\mathbf{O}S_F^e$ is split into a term involving A^e once explicitly, as well as through S_F^e, and a term not involving A^e at all, except through the wave function φ_a. In the latter term, if the total integral still involves S_F^e, we can incorporate the F into a new operator $\mathbf{O}$, and apply the identity (13) again. We thus work in from both ends of $\langle M_1^{(4)}\rangle$ until we are left with terms of two types: terms in which A^e appears twice explicitly, and implicitly through S_F^e; and terms with no S_F^e, so that A^e appears implicitly only through φ_a, and explicitly no more than once. These one-potential and no-potential terms, which we call A_0, will be seen to yield terms identifiable as mass renormalizations, charge renormalization, and $(\gamma\cdot A^e)^2$, all of which can be ignored, and terms which correspond to the scattering approximation contributions associated with the diagrams a, b, c in Fig. 4. The only nonignorable corrections to the scattering approximation are of order $(\alpha Z)^2$ smaller. Apart from a demonstration of this last fact, our real task consists of the evaluation of the contribution from the multiple-potential terms A_1.

We now carry through the process described previously. Thus,

$$\langle M_1^{(4)}\rangle=-(i/\pi)[\tfrac{1}{4}(2\pi)^9\alpha]^2A.$$
$$A=\int\bar{\varphi}_a\gamma_\mu S_F^e\gamma_\nu S_F^e\gamma_\mu S_F^e\gamma_\nu\varphi_aD_FD_F(d_4k)^2(d\mathbf{p})^4$$
$$=[ie/(\hbar c)]\int\bar{\varphi}_aA_\rho^e\mathfrak{F}'_{1\mu,\rho}S_F^e\gamma_\nu S_F^e\gamma_\mu S_F^eA_\sigma^e$$
$$\times\mathfrak{F}_{1\nu,\sigma}\varphi_aD_FD_F(d_4k)^2(d\mathbf{p})^4(d\mathbf{q})^2$$
$$-2i(2\pi)^{-4}[ie/(\hbar c)]\int\bar{\varphi}_aA_\rho^e\mathfrak{F}'_{1\mu,\rho}S_F^e\gamma_\nu$$
$$\times S_F^e\gamma_\mu F_{1\nu}\varphi_aD_FD_F(d_4k)^2(d\mathbf{p})^3d\mathbf{q}_2$$
$$-2i(2\pi)^{-4}[ie/(\hbar c)]\int\bar{\varphi}_aF'_{1\mu}\gamma_\nu S_F^e\gamma_\mu S_F^eA_\sigma^e$$
$$\times\mathfrak{F}_{1\nu,\sigma}\varphi_aD_FD_F(d_4k)^2(d\mathbf{p})^3d\mathbf{q}_1$$
$$-4(2\pi)^{-8}\int\bar{\varphi}_aF'_{1\mu}\gamma_\nu S_F^e\gamma_\mu F_{1\nu}\varphi_a \quad (18)$$
$$\times D_FD_F(d_4k)^2(d\mathbf{p})^2,$$

where

$$F'_{1\mu}=F'(\gamma_\mu;\,p_2,k_2); \qquad F_{1\nu}=F(\gamma_\nu;\,p_1,k_1);$$
$$\mathfrak{F}'_{1\mu,\rho}=\mathfrak{F}_\rho'(\gamma_\mu;\,p_2,q_2,k_2); \quad \mathfrak{F}_{1\nu,\sigma}=\mathfrak{F}_\sigma(\gamma_\nu;\,p_1,q_1,k_1). \quad (19)$$

We continue the process with the terms containing F or F', taking

$$F'_{2\mu\nu}=F'[-2i(2\pi)^{-4}F'_{1\mu}\gamma_\nu;\,p_2,\,k_1+k_2];$$
$$F_{2\mu\nu}=F[-2i(2\pi)^{-4}\gamma_\mu F_{1\nu};\,p_1,\,k_1+k_2];$$
$$F'_{3\nu}=F'[-2i(2\pi)^{-4}F'_{2\mu\nu}\gamma_\mu;\,p_2,\,k_1]; \quad (20)$$
$$F_{3\mu}=F[-2i(2\pi)^{-4}\gamma_\nu F_{2\mu\nu};\,p_1,\,k_2];$$

with the $\mathfrak{F}$'s defined correspondingly. Finally,

$$A=A_1+A_0, \quad (21)$$
$$A_1=a_1+a_2+a_2'+a_3+a_3'+a_4, \quad (22)$$

where

$$a_1=[ie/(\hbar c)]^2\int\bar{\varphi}_a(\mathbf{p}_2)A_\rho^e(\mathbf{q}_2)\mathfrak{F}'_{1\mu,\rho}$$
$$\times S_F^e(p_2-q_2-k_2,\,p_4-k_2)$$
$$\times\gamma_\nu S_F^e(p_4-k_1-k_2,\,p_3-k_1-k_2)$$
$$\times\gamma_\mu S_F^e(p_3-k_1,\,p_1+q_1-k_1)A_\sigma^e(\mathbf{q}_1)$$
$$\times\mathfrak{F}_{1\nu,\sigma}\varphi_a(\mathbf{p}_1)D_F(k_1)D_F(k_2)(d_4k)^2(d\mathbf{p})^4(d\mathbf{q})^2;$$

$$a_2=[ie/(\hbar c)]^2\int\bar{\varphi}_a(\mathbf{p}_2)A_\rho{}^e(\mathbf{q}_2)\mathfrak{F}'_{2\mu\nu,\rho}$$
$$\times S_F{}^e(p_2-q_2-k_1-k_2,\ p_2-k_1-k_2)$$
$$\times\gamma_\mu S_F{}^e(p_2-k_1,\ p_1+q_1-k_1)A_\sigma{}^e(\mathbf{q}_1)\mathfrak{F}_{1\nu,\sigma}\varphi_a(\mathbf{p}_1)$$
$$\times D_F(k_1)D_F(k_2)(d_4k)^2(d\mathbf{p})^2(d\mathbf{q})^2;$$

$$a_2'=[ie/(\hbar c)]^2\int\bar{\varphi}_a(\mathbf{p}_2)A_\rho{}^e(\mathbf{q}_2)\mathfrak{F}'_{1\mu,\rho}$$
$$\times S_F{}^e(p_2-q_2-k_2,\ p_4-k_2)\gamma_\nu S_F{}^e(p_4-k_1-k_2,$$
$$\times p_1+q_1-k_1-k_2)A_\sigma{}^e(\mathbf{q}_1)\mathfrak{F}_{2\mu\nu,\sigma}\varphi_a(\mathbf{p}_1) \qquad (23)$$
$$\times D_F(k_1)D_F(k_2)(d_4k)^2(d\mathbf{p})^2(d\mathbf{q})^2;$$

$$a_3=[ie/(\hbar c)]^2\int\bar{\varphi}_a(\mathbf{p}_2)A_\rho{}^e(\mathbf{q}_2)\mathfrak{F}'_{3\nu,\rho}$$
$$\times S_F{}^e(p_2-q_2-k_1,\ p_1+q_1-k_1)A_\sigma{}^e(\mathbf{q}_1)\mathfrak{F}_{1\nu,\sigma}$$
$$\times\varphi_a(\mathbf{p}_1)D_F(k_1)D_F(k_2)(d_4k)^2(d\mathbf{p})^2(d\mathbf{q})^2;$$

$$a_3'=[ie/(\hbar c)]^2\int\bar{\varphi}_a(\mathbf{p}_2)A_\rho{}^e(\mathbf{q}_2)\mathfrak{F}'_{1\mu,\rho}$$
$$\times S_F{}^e(p_2-q_2-k_2,\ p_1+q_1-k_2)A_\sigma{}^e(\mathbf{q}_1)\mathfrak{F}_{3\mu,\sigma}$$
$$\times\varphi_a(\mathbf{p}_1)D_F(k_1)D_F(k_2)(d_4k)^2(d\mathbf{p})^2(d\mathbf{q})^2;$$

$$a_4=[ie/(\hbar c)]^2\int\bar{\varphi}_a(\mathbf{p}_2)A_\rho{}^e(\mathbf{q}_2)\mathfrak{F}'_{2\mu\nu,\rho}$$
$$\times S_F{}^e(p_2-q_2-k_1-k_2,\ p_1+q_1-k_1-k_2)$$
$$\times A_\sigma{}^e(\mathbf{q}_1)\mathfrak{F}_{2\mu\nu,\sigma}\varphi_a(\mathbf{p}_1)D_F(k_1)D_F(k_2)(d_4k)^2(d\mathbf{p})^2(d\mathbf{q})^2.$$

(Of course, $a_2=a_2'$ and $a_3=a_3'$, but it is convenient to keep them separate in this way.) Furthermore,

$$A_0=-2i(2\pi)^{-4}[ie/(\hbar c)]\int\bar{\varphi}_a(\mathbf{p}_2)A_\rho{}^e(\mathbf{q})$$
$$\times[F'_{3\nu}\mathfrak{F}_{1\nu,\rho}+\mathfrak{F}'_{1\mu,\rho}F_{3\mu}+\mathfrak{F}'_{2\mu\nu,\rho}F_{2\mu\nu}]\varphi_a(\mathbf{p}_1)$$
$$\times D_F(k_1)D_F(k_2)(d_4k)^2(d\mathbf{p})^2d\mathbf{q}$$
$$-4(2\pi)^{-8}\int\bar{\varphi}_a(\mathbf{p})F'_{2\mu\nu}\gamma_\mu F_{1\nu}\varphi_a(\mathbf{p})$$
$$\times D_F(k_1)D_F(k_2)(d_4k)^2d\mathbf{p}. \qquad (24)$$

In order actually to carry out the indicated integrations over the momentum space of the photons, it is necessary to "regulate" the photon propagation function both in the ultraviolet and the infrared. This may be easily accomplished by replacing $D_F(k)=-[2i/(2\pi)^4](1/k^2)$ by

$$D_{FR}(k)=-\frac{2i}{(2\pi)^4}\frac{\Lambda^2}{(k^2+\Lambda^2)(k^2+\lambda^2)}. \qquad (25)$$

When the calculation is completed one lets $\Lambda\to\infty$ and $\lambda\to 0$. The need for ultraviolet regulation arises from the fact that we do not remove the charge renormalizations associated with the second-order vertex operator. As a consequence, even the physically important parts of $M_1{}^{(4)}$ are divergent in the ultraviolet. Such a procedure is possible because $M^{(2)}$ and $H^{(2)}\partial H^{(2)}/\partial E$ contain similar renormalizations associated both with the second-order vertex operator and with the second-order electron propagation function. It is known that these renormalizations sum to zero, so their explicit removal is unnecessary. The infrared regulation is needed in part for the same reason, and also because the separation into A_0 and A_1 introduces additional infrared divergences arising from the fact that $B(\mathbf{O};p_2,p_1)\to\infty$ as $p_2-p_1\to 0$. In the course of a computation, of course, one always allows Λ and λ to approach their limiting values as early as possible, to minimize the complications they introduce.

Demonstration that A_0 Yields the Scattering Approximation

We now show that, apart from previously discussed ignorable contributions, A_0 yields to order $\alpha^2(\alpha Z)^4$, just the scattering approximation. First of all, the last term of A_0 is of the general form

$$\int\bar{\varphi}_a(\mathbf{p})H(p,k_2,k_1)\varphi_a(\mathbf{p}_1)(d_4k)^2d\mathbf{p}$$
$$=\int\bar{\varphi}_a(\mathbf{p})[h_0(p^2)+(i\gamma\cdot p)h_1(p^2)]\varphi_a(\mathbf{p})dp,$$

which, to order $\alpha^2(\alpha Z)^4$, separates into mass renormalization, charge renormalization, and $(\gamma\cdot A^e)^2$ terms, all of which we ignore.

The terms with A^e appearing once are all of the general form

$$-2i(2\pi)^{-4}[ie/(\hbar c)]\int\bar{\varphi}_aF'A^e\cdot\mathfrak{F}\varphi_a$$
$$=-2i(2\pi)^{-4}[ie/(\hbar c)]\Big\{\int\bar{\varphi}_aF'F\gamma\cdot A^e\varphi_a$$
$$-\int\bar{\varphi}_aF'\gamma\cdot A^eF\varphi_a\Big\}. \qquad (26)$$

The first term on the right, after integration over k_1 and k_2, is of the general form

$$\int\bar{\varphi}_a(\mathbf{p}_2)[h_2(p_2{}^2)+(i\gamma\cdot p_2)h_3(p_2{}^2)]$$
$$\times\gamma\cdot A^e(\mathbf{p}_2-\mathbf{p}_1)\varphi_a(\mathbf{p}_1)(dp)^2,$$

which, to order $\alpha^2(\alpha Z)^4$ yields a charge renormalization term and a $(\gamma\cdot A^e)^2$ term, so that this term may also be ignored. To deal with the remaining term in (26) we

note that F can be rewritten as follows, using (13):

$$-\frac{2i}{(2\pi)^4}F(\mathbf{O};p,k)$$
$$=-\frac{2i}{(2\pi)^4}\left[\frac{i\gamma\cdot(p-k)-\kappa}{k^2-2p\cdot k}\mathbf{O}+\mathbf{O}\frac{i\gamma\cdot p+\kappa}{k^2-2p\cdot k}\right]$$
$$=S_F(p-k)\mathbf{O}+S_F(p-k)\mathbf{O}\frac{p^2+\kappa^2}{k^2-2p\cdot k}$$
$$-\frac{2i}{(2\pi)^4}\mathbf{O}\frac{i\gamma\cdot p+\kappa}{k^2-2p\cdot k}, \quad (27)$$

since

$$-\frac{2i}{(2\pi)^4}\frac{i\gamma\cdot(p-k)-\kappa}{k^2-2p\cdot k}\cdot$$
$$=-\frac{2i}{(2\pi)^4}\frac{i\gamma\cdot(p-k)-\kappa}{(p-k)^2+\kappa^2}\left(1+\frac{p^2+\kappa^2}{k^2-2p\cdot k}\right)$$
$$=S_F(p-k)\left(1+\frac{p^2+\kappa^2}{k^2-2p\cdot k}\right). \quad (28)$$

So

$$-2i(2\pi)^{-4}F(\mathbf{O};p,k)\varphi_a(\mathbf{p})$$
$$=S_F(p-k)\mathbf{O}\varphi_a(\mathbf{p})-[ie/(\hbar c)]\int(k^2-2p\cdot k)^{-1}$$
$$\times[S_F(p-k)\mathbf{O}(i\gamma\cdot p-\kappa)+2i(2\pi)^{-4}\mathbf{O}]$$
$$\times\gamma\cdot A^e(\mathbf{p}-\mathbf{p}')\varphi_a(\mathbf{p}')d\mathbf{p}'. \quad (29)$$

The second term on the right will produce expressions which can be broken up into pure charge renormalization terms and $(\gamma\cdot A^e)^2$ terms, which we ignore. We are left only with the first term, and since $\mathbf{O}$ itself is either γ_μ or of the form $\gamma_\mu F$, the process can be repeated until we are left with a product of S_F's and γ's. An analogous procedure for the factor $\bar{\varphi}_a F'$ reduces it also to a product of S_F's and γ's. Thus the surviving term of (26) involves a product of factors γS_F to the left and $S_F\gamma$ to the right of $\gamma\cdot A^e$, and is readily identifiable with a term in the scattering approximation. In carrying out the scattering approximation one always takes $p_1^2+\kappa^2=p_2^2+\kappa^2=0$, and $\bar{\varphi}_a(\mathbf{p}_2)(i\gamma\cdot p_2+\kappa)=(i\gamma\cdot p_1+\kappa)\varphi_a(\mathbf{p}_1)=0$. This approximation, again to order $\alpha^2(\alpha Z)^4$, corresponds to the neglect of $(\gamma\cdot A^e)^2$ terms.

On carrying out the procedure described previously, one finds in a straightforward manner that the three terms linear in A^e appearing in Eq. (24) correspond to the terms of the scattering approximation illustrated in Fig. 4, (c), (b), and (a), respectively.

Identification and Evaluation of $\alpha^2(\alpha Z)^4$ Terms in A_1

There remains the problem of isolating and evaluating the $\alpha^2(\alpha Z)^4$ contributions from A_1. These are of two general types: (1) $(\gamma\cdot A^e)^2$ terms of the type encountered in the discussion of $(MP)_1$. Once such terms have been separated off, they may be evaluated by replacing $S_F{}^e$ by S_F. As noted before, terms of this character will simply be isolated and recognized. (2) Terms which can be expressed as $(\mathbf{p}_2-\mathbf{p}_1)^2\gamma\cdot A^e$ terms; these are clearly identical in form with the scattering approximation terms and will be explicitly evaluated. They arise from terms apparently quadratic in the external potential by virtue of identities like the following:

$$\frac{i\hbar c}{\pi}\left(\frac{ie}{\hbar c}\right)^2\sum_n\int\bar{\varphi}_a(\mathbf{p}_2)\gamma\cdot A^e(\mathbf{q}_2)\mathbf{q}_1\cdot\mathbf{q}_2$$
$$\times\frac{\varphi_n(\mathbf{p}_2-\mathbf{q}_2)\bar{\varphi}_n(\mathbf{p}_1+\mathbf{q}_1)}{E_n-E_a}\gamma\cdot A^e(\mathbf{q}_1)\varphi_a(\mathbf{p}_1)(d\mathbf{p})^2(d\mathbf{q})^2$$
$$=-(i/\pi)[ie/(\hbar c)]\sum\int\varphi_a{}^*(\mathbf{p}_2)\mathbf{p}_2\cdot\mathbf{q}_1\varphi_n(\mathbf{p}_2)$$
$$\times\bar{\varphi}_n(\mathbf{p}_1+\mathbf{q}_1)\gamma\cdot A^e(\mathbf{q}_1)\varphi_a(\mathbf{p}_1)(d\mathbf{p})^2d\mathbf{q}_1 \quad (30)$$
$$=-2i(2\pi)^{-4}[ie/(\hbar c)]\int\bar{\varphi}_a(\mathbf{p}_2)\mathbf{p}_2\cdot(\mathbf{p}_2-\mathbf{p}_1)$$
$$\times\gamma\cdot A^e(\mathbf{p}_2-\mathbf{p}_1)\varphi_a(\mathbf{p}_1)(d\mathbf{p})^2$$
$$=-i(2\pi)^{-4}[ie/(\hbar c)]\int\bar{\varphi}_a(\mathbf{p}_2)(\mathbf{p}_2-\mathbf{p}_1)^2$$
$$\times\gamma\cdot A^e(\mathbf{p}_2-\mathbf{p}_1)\varphi_a(\mathbf{p}_1)(d\mathbf{p})^2.$$

The factors E_n-E_a appearing in the denominators come from the $S_F{}^e$ functions; their appearance implies that one cannot, for these terms, expand $S_F{}^e$ in terms of S_F and powers of the potential. One always can, on the other hand, make appropriate nonrelativistic approximations, familiar from the treatments given for the second-order level shift problem. To see how terms of types (1) and (2) may be separated, we write

$$\mathfrak{F}_\sigma(\mathbf{O};p,q,k)=\mathfrak{F}_\sigma(0)+\mathfrak{G}_\sigma,$$
$$\mathfrak{F}_\sigma(0)=\mathfrak{F}_\sigma(\mathbf{O};p,0,k)=[F(\mathbf{O};p,k),\gamma_\sigma],$$
$$\mathfrak{G}_\sigma=\{F[\mathbf{O}(p+q);p+q,k]-F[\mathbf{O}(p);p,k]\}\gamma_\sigma; \quad (31)$$
$$\mathfrak{F}_\rho'(\mathbf{O};p,q,k)=\mathfrak{F}_\rho'(0)+\mathfrak{G}_\rho',$$

with $\mathfrak{F}_\rho'(0)$ and $\mathfrak{G}_\rho'$ defined similarly. A direct examination of the $\mathfrak{F}$ functions shows that the $\mathfrak{F}(0)$ is at least one factor k better behaved as $k\to 0$ than $\mathfrak{G}$. This is the crucial property which makes the rather involved scheme we are using for the $M_1{}^{(4)}$ term superior to the simple expansion of the $S_F{}^e$ used for treating $(MP)_1$. As a consequence of this fact, the terms involving only $\mathfrak{F}(0)$ factors are sufficiently well behaved in the infrared to permit the replacement of $S_F{}^e$ by S_F. These terms are very similar to corresponding terms in $(MP)_1$ and the only $\alpha^2(\alpha Z)^4$ terms which they yield are $(\gamma\cdot A^e)^2$ terms.

The $\mathcal{G}$ factors obviously vanish when $\mathbf{q}$ vanishes, and correspond in a crude way to differentiation of the external potential with respect to the spatial coordinates. It follows that terms involving $\mathcal{G}$ cannot be $(\gamma\cdot A^e)^2$ terms. In the absence of singular infrared behavior which brings into prominence the energy denominators of the S_F^e functions, such terms are at least a factor αZ smaller than the order of interest. The infrared singularities are sufficiently mild, in the case of cross terms between an $\mathcal{F}(0)$ and a $\mathcal{G}$, for such terms to be indeed a factor αZ smaller. On the other hand, the terms containing two $\mathcal{G}$ factors are, in fact, of order $\alpha^2(\alpha Z)^4$ and must be evaluated. For these terms, nonrelativistic approximations make evaluation straightforward.

The entire procedure is best described in terms of an example. We discuss the term a_2 [Eq. (23)]. We note first of all that

$$F_{1\nu}=\frac{2ip_{1\nu}-(i\gamma\cdot k_1)\gamma_\nu}{k_1^2-2p_1\cdot k_1};$$

$$F'_{2\mu\nu}=-\frac{2i}{(2\pi)^4}\frac{1}{(k_1+k_2)^2-2p_2\cdot(k_1+k_2)}\times\left\{\gamma_\mu\gamma_\nu+\frac{2ip_{2\mu}-\gamma_\mu(i\gamma\cdot k_2)}{k_2^2-2p_2\cdot k_2}\times[2i(p_{2\nu}-k_{2\nu})-\gamma_\nu(i\gamma\cdot k_1)\right\}. \quad (32)$$

The terms of lowest order in the k's in both cases evidently commute with γ_ρ, and so give no contribution to $\mathcal{F}_{1\nu,\sigma}(0)$ or $\mathcal{F}'_{2\mu\nu,\rho}(0)$. One may now directly verify that the term arising from $\mathcal{F}_{1\nu,\sigma}(0)$ and $\mathcal{F}'_{2\mu\nu,\rho}(0)$ is finite in the infrared and ultraviolet, using S_F for $S_{F'}$ and unregulated D_F functions. One therefore gets a $(\gamma\cdot A^e)^2$ term. One can also verify that the cross terms, while more singular, give contributions no larger than $\alpha^2(\alpha Z)^5$. We now evaluate the contribution from the part involving two $\mathcal{G}$ factors. The important contributions in this case come entirely from $k\sim(\alpha Z)^2$. Consequently one may neglect k as compared to $\mathbf{p}$, $\mathbf{q}$, and p_0. Furthermore, one may assume $|\mathbf{q}|<p_0$, $\mathbf{q}^2<|\mathbf{q}|\kappa$. Taking advantage of these approximations the $\mathcal{G}$'s simplify to

$$\mathcal{G}_{1\nu,\sigma}\sim\frac{1}{\kappa}\left[\frac{iq_{1\nu}}{k_{10}}-\delta_{\nu,4}\frac{\mathbf{q}_1\cdot\mathbf{k}_1}{k_{10}^2}\right]\gamma_\sigma;$$

$$\mathcal{G}'_{2\mu\nu,\rho}\sim-\frac{2i}{(2\pi)^4}\frac{\gamma_\rho}{\kappa}\left[i\frac{q_{2\mu}\delta_{\nu4}+q_{2\nu}\delta_{\mu,4}}{k_{20}(k_{10}+k_{20})}-\frac{\delta_{\mu4}\delta_{\nu4}}{k_{20}(k_{10}+k_{20})}\left(\frac{\mathbf{q}_2\cdot\mathbf{k}_2}{k_{20}}+\frac{\mathbf{q}_2\cdot(\mathbf{k}_1+\mathbf{k}_2)}{k_{10}+k_{20}}\right)\right]. \quad (33)$$

The expression for a_2 also contains the factor

$$\int S_F^e(p_2-q_2-k_1-k_2,\ p_3-k_1-k_2)\gamma_\mu S_F^e(p_3-k_1,\ p_1+q_1-k_1)d\mathbf{p}_3$$

$$=-\frac{1}{\pi^2}\sum_{n,m}\int\frac{\varphi_n(\mathbf{p}_2-\mathbf{q}_2-\mathbf{k}_1-\mathbf{k}_2)\bar{\varphi}_n(\mathbf{p}_3-\mathbf{k}_1-\mathbf{k}_2)\gamma_\mu\varphi_m(\mathbf{p}_3-\mathbf{k}_1)\bar{\varphi}_m(\mathbf{p}_1+\mathbf{q}_1-\mathbf{k}_1)}{(\delta_n+k_{10}+k_{20})(\delta_m+k_{10})}d\mathbf{p}_3$$

$$\sim-\frac{1}{\pi^2}\sum_{n,m}\int\frac{\varphi_n(\mathbf{p}_2-\mathbf{q}_2)\bar{\varphi}_n(\mathbf{p}_3)\gamma_\mu\varphi_m(\mathbf{p}_3)\bar{\varphi}_m(\mathbf{p}_1+\mathbf{q}_1)}{(\delta_n+k_{10}+k_{20})(\delta_m+k_{10})}d\mathbf{p}_3 \quad (34)$$

$$[\delta_n=((1-i\epsilon)E_n-E_a)/(\hbar c)],$$

since, as previously noted, k may be neglected as compared to $\mathbf{p}$ and $\mathbf{q}$. This is simply the familiar dipole approximation, corresponding to the neglect of retardation. This expression may be further simplified by taking into account the fact that the significant contributions come only when n and m are positive energy states of nonrelativistic energy. One therefore takes

$$\int\bar{\varphi}_n(\mathbf{p}_3)\gamma_\mu\varphi_m(\mathbf{p}_3)d\mathbf{p}_3\sim\delta_{\mu4}\int\varphi_n^*(\mathbf{p}_3)\varphi_m(\mathbf{p}_3)d\mathbf{p}_3$$

$$=(2\pi)^{-3}\delta_{\mu4}\delta_{nm}, \quad (35)$$

so that (34) reduces to

$$-\frac{1}{8\pi^5}\delta_{\mu4}\sum_n\frac{\varphi_n(\mathbf{p}_2-\mathbf{q}_2)\bar{\varphi}_n(\mathbf{p}_1+\mathbf{q}_1)}{(\delta_n+k_{10}+k_{20})(\delta_n+k_{10})}.$$

With these approximations a_2 becomes

$$a_2=\frac{i}{\pi}\left(\frac{2i}{(2\pi)^4}\right)^4\left(\frac{ie}{\hbar c}\right)^2\frac{1}{\kappa^2}\sum_n\int\bar{\varphi}_a(\mathbf{p}_2)\gamma\cdot A^e(\mathbf{q}_2)\times\frac{\varphi_n(\mathbf{p}_2-\mathbf{q}_2)\bar{\varphi}_n(\mathbf{p}_1+\mathbf{q}_1)}{(\delta_n+k_{10}+k_{20})(\delta_n+k_{10})}\gamma\cdot A^e(\mathbf{q}_1)\varphi_a(\mathbf{p}_1)\times\frac{1}{k_{10}k_{20}(k_{10}+k_{20})}\left[\mathbf{q}_1\cdot\mathbf{q}_2-\frac{(\mathbf{q}_1\cdot\mathbf{k}_1)(\mathbf{q}_2\cdot\mathbf{k}_2)}{k_{10}k_{20}}-\frac{(\mathbf{q}_1\cdot\mathbf{k}_1)(\mathbf{q}_2\cdot(\mathbf{k}_1+\mathbf{k}_2))}{k_{10}(k_{10}+k_{20})}\right]\frac{d_4k_1}{k_1^2}\frac{d_4k_2}{k_2^2}(d\mathbf{p})^2(d\mathbf{q})^2. \quad (36)$$

The integrations of the timelike components and angular domains of k_1 and k_2 may now be carried out

easily. The k_0 integrations are performed simply by closing the contours on the negative imaginary side of the real axis. The low-energy poles from $k^2-2p\cdot k-i\epsilon$, here approximated by $2\kappa_0 k_0-i\epsilon$, and those from the denominators δ_n+k_0 for positive energy states are thereby avoided. Contributions of the order of interest come only from the poles of the D_F functions. One then finds

$$a_2=-\frac{2}{\pi}\left(\frac{2i}{(2\pi)^4}\right)^3\left(\frac{ie}{\hbar c}\right)^2\frac{1}{\kappa^2}\sum_n\int\bar{\varphi}_a(\mathbf{p}_2)\gamma\cdot A^e(\mathbf{q})$$
$$\times\frac{\varphi_n(\mathbf{p}_2-\mathbf{q}_2)\bar{\varphi}_n(\mathbf{p}_1+\mathbf{q}_1)}{(\delta_n+k_1+k_2)(\delta_n+k_1)}\gamma\cdot A^e(\mathbf{q}_1)\varphi_a(\mathbf{p}_1)$$
$$\times\frac{\mathbf{q}_1\cdot\mathbf{q}_2}{k_1k_2(k_1+k_2)}\left(1-\frac{1}{3}\frac{k_1}{k_1+k_2}\right)\frac{k_1^2dk_1}{k_1}$$
$$\times\frac{k_2^2dk_2}{k_2}(d\mathbf{p})^2(d\mathbf{q})^2. \quad (37)$$

(Here $k_1=|\mathbf{k}_1|$, $k_2=|\mathbf{k}_2|$.)

Now, letting $k_1\to\delta_n k_1$, $k_2\to\delta_n k_2$, we find

$$a_2=\sum_n C_n\int\frac{dk_1dk_2}{(k_1+k_2)(1+k_1)(1+k_1+k_2)}$$
$$\times\left(1-\frac{1}{3}\frac{k_1}{k_1+k_2}\right), \quad (38)$$

with

$$C_n=(2/\pi)[2i(2\pi)^{-4}]^3[ie/(\hbar c)]^2(1/\kappa^2)$$
$$\times\int\bar{\varphi}_a(\mathbf{p}_2)\gamma\cdot A^e(\mathbf{q}_2)\varphi_n(\mathbf{p}_2-\mathbf{q}_2)(1/\delta_n)$$
$$\times\bar{\varphi}_n(\mathbf{p}_1+\mathbf{q}_1)\gamma\cdot A^e(\mathbf{q}_1)\varphi_n(\mathbf{p}_1)(d\mathbf{p})^2(d\mathbf{q})^2. \quad (39)$$

The expression $\sum C_n$ has been discussed at the beginning of this section and has been shown to be proportional to $\int\bar{\varphi}_a(\mathbf{p}_2)(\mathbf{p}_2-\mathbf{p}_1)^2\gamma\cdot A^e(\mathbf{p}_2-\mathbf{p}_1)\varphi_a(\mathbf{p}_1)d\mathbf{p}_1d\mathbf{p}_2$. One has, therefore, only to evaluate the integrals over k_1 and k_2 to obtain the contribution of this term to the level shift.[10]

The reduction of a_2 is particularly simple because it does not have any infrared divergences. In most of the terms the integral multiplying C_n still involves δ_n through the ratio λ/δ_n. After carrying out the k-space integrations one has, in addition to $\sum C_n$, terms of the form $\sum C_n\ln(\lambda/\delta_n)$ and $\sum C_n\ln^2(\lambda/\delta_n)$. Terms such as these occur in the second-order level shift problem. It is clear, however, that no such terms can remain after summing over all contributions, simply because of the fact that all dependence on λ must vanish.[11] We shall find, in fact, that it is unnecessary to carry out most of the k integrations, many terms vanishing simply as the result of combining integrands.

Carrying out the reduction for the remaining terms in $M_1^{(4)}$, we find, using $k=|\mathbf{k}|$, $\omega=[k^2+(\lambda/\delta_n)^2]^{\frac{1}{2}}$,

$$a_1=0;$$

$$a_2=\sum_n C_n\int\frac{dk_1dk_2}{(k_1+k_2)(1+k_1)(1+k_1+k_2)}$$
$$\times\left(1-\frac{1}{3}\frac{k_1}{k_1+k_2}\right);$$

$$a_2'=\sum_n C_n\int\frac{dk_1dk_2}{(k_1+k_2)(1+k_2)(1+k_1+k_2)}$$
$$\times\left(1-\frac{1}{3}\frac{k_2}{k_1+k_2}\right);$$

$$a_3=\left(\ln\frac{\Lambda}{\kappa}-2\ln\frac{\kappa}{\lambda}+\frac{9}{4}\right)\mathrm{II}_1$$
$$+\sum_n C_n\int\frac{k_1^2dk_1k_2^2dk_2}{\omega_1^2\omega_2^3(\omega_1+\omega_2)(1+\omega_1)}$$
$$\times\left(-1+\frac{1}{3}\frac{k_1^2}{\omega_1(\omega_1+\omega_2)}\right); \quad (40)$$

$$a_3'=\left(\ln\frac{\Lambda}{\kappa}-2\ln\frac{\kappa}{\lambda}+\frac{9}{4}\right)\mathrm{II}_1$$
$$+\sum_n C_n\int\frac{k_1^2dk_1k_2^2dk_2}{\omega_1^3\omega_2^2(\omega_1+\omega_2)(1+\omega_2)}$$
$$\times\left(-1+\frac{1}{3}\frac{k_2^2}{\omega_2(\omega_1+\omega_2)}\right);$$

$$a_4=\sum_n C_n\int\frac{k_1^2dk_1k_2^2dk_2}{\omega_1^2\omega_2^2(\omega_1+\omega_2)^2(1+\omega_1+\omega_2)}$$
$$\times\left(2-\frac{1}{3}\frac{k_1^2}{\omega_1(\omega_1+\omega_2)}-\frac{1}{3}\frac{k_2^2}{\omega_2(\omega_1+\omega_2)}\right.$$
$$\left.-\frac{1}{3}\frac{k_1^2+k_2^2}{(\omega_1+\omega_2)^2}\right);$$

where

$$\mathrm{II}_1=4(2\pi)^{-10}[ie/(\hbar c)]^2\int\bar{\varphi}A^e\cdot\mathfrak{F}'_{1\mu}S_F^e A^e\cdot\mathfrak{F}_{1\mu}\varphi$$
$$\times D_F d_4k(d\mathbf{p})^2(d\mathbf{q})^2 \quad (41)$$
$$=-\frac{1}{2}\sum_n C_n\int\frac{k^2dk}{\omega^3(1+\omega)}\left(1-\frac{1}{3}\frac{k^2}{\omega^2}\right).$$

[10] It might be noted that the contribution of a_2+a_2' to the $2S$ energy level in hydrogen is about -1.3 megacycles.

[11] This argument is somewhat oversimplified as terms of the form $\ln(\kappa/\lambda)$ also occur. To complete the argument one must identify all $\ln(\kappa/\lambda)$ terms with the second-order charge renormalizations which we neglected to remove.

The expression II_1 is just the multiple-potential contribution to the second-order level shift, apart from a numerical factor. Its appearance as a factor is expected in view of the fact that we have retained charge renormalization terms.

CONTRIBUTION OF $M_2^{(4)}$

While the main outline of the treatment of $M_2^{(4)}$ [Eq. (6)] is identical to that of $M_1^{(4)}$, the presence of the second-order mass term leads to significant complications in its treatment. Furthermore, the fact that the photon momenta appearing in the first and third S_F^e factors are the same makes the infrared problem somewhat more complicated.

We note first of all that $M_2^{(4)}$ can be separated, by successive applications of the identities (13) into a set of terms B_1 involving the potential twice explicitly and S_F^e, and another set, B_0, not involving S_F^e, and involving the potential no more than once explicitly, all in a manner exactly analogous to the treatment of $M_1^{(4)}$. Again the terms B_0 yield the scattering approximation, renormalization terms, and $(\gamma\cdot A^e)^2$ terms. The terms forming B_1, (they are exact analogs of a_1, a_2, a_3, a_4) are, schematically,

$$
\begin{aligned}
b_1=&[ie/(\hbar c)]^2\int\bar\varphi_a A_\rho^e\mathfrak{F}'_{1\mu,\rho}S_F^e\gamma_\nu S_F^e\gamma_\nu S_F^e A_\sigma^e\\
&\times\mathfrak{F}_{1\mu,\sigma}\varphi_a D_F D_F(d_4k)^2(d\mathbf{p})^4(d\mathbf{q})^2-2i(2\pi)^{-5}\alpha^{-1}\\
&\times\delta\kappa^{(2)}[ie/(\hbar c)]\int\bar\varphi_a A_\rho^e\mathfrak{F}'_{1\mu,\rho}S_F^e S_F^e A_\sigma^e\\
&\times\mathfrak{F}_{1\mu,\sigma}\varphi_a D_F d_4k(d\mathbf{p})^3(d\mathbf{q})^2;\\
b_2=&[ie/(\hbar c)]^2\int\bar\varphi_a A_\rho^e\mathfrak{F}'_{2\mu\nu,\rho}S_F^e\gamma_\nu S_F^e A_\sigma^e\\
&\times\mathfrak{F}_{1\mu,\sigma}\varphi_a D_F D_F(d_4k)^2(d\mathbf{p})^3(d\mathbf{q})^2;\\
b_2'=&[ie/(\hbar c)]^2\int\bar\varphi_a A_\rho^e\mathfrak{F}'_{1\mu,\rho}S_F^e\gamma_\nu S_F^e A_\sigma^e\\
&\times\mathfrak{F}_{2\nu\mu,\sigma}\varphi_a D_F D_F(d_4k)^2(d\mathbf{p})^3(d\mathbf{q})^2,\\
b_3=&[ie/(\hbar c)]^2\int\bar\varphi_a A_\rho^e\mathfrak{F}'^R_{3\mu,\rho}S_F^e A_\sigma^e\\
&\times\mathfrak{F}_{1\mu,\sigma}\varphi_a D_F d_4k_1(d\mathbf{p})^2(d\mathbf{q})^2;\\
b_3'=&[ie/(\hbar c)]^2\int\bar\varphi_a A_\rho^e\mathfrak{F}'_{1\mu,\rho}S_F^e A_\sigma^e\\
&\times\mathfrak{F}^R_{3\mu,\sigma}\varphi_a D_F d_4k_1(d\mathbf{p})^2(d\mathbf{q})^2;\\
b_4=&[ie/(\hbar c)]^2\int\bar\varphi_a A_\rho^e\mathfrak{F}'_{2\mu\nu,\rho}S_F^e A_\sigma^e\\
&\times\mathfrak{F}_{2\nu\mu,\sigma}\varphi_a D_F D_F(d_4k)^2(d\mathbf{p})^2(d\mathbf{q})^2,
\end{aligned}
\tag{42}
$$

where $\mathfrak{F}'^R_{3\mu,\rho}$ (and, analogously, $\mathfrak{F}^R_{3\mu,\sigma}$) is formed by taking the operator $\mathbf{O}$ in (13) to be

$$
-2i(2\pi)^{-4}\left[\int F'_{2\mu\nu}\gamma_\nu D_F(k_2)d_4k_2-2i(2\pi)^{-5}\alpha^{-1}\delta\kappa^{(2)}F'_{1\mu}\right].
$$

Thus mass renormalization appears explicitly only in b_1, and in the formation of $\mathfrak{F}_3^R$ appearing in b_3 and b_3'.

Further reduction of b_1 is necessary to remove the mass renormalization term. The reduction is accomplished by using the identities (13) on one or another of the remaining γ_ν factors. Apart from the mass term,

$$
\begin{aligned}
b_1=&[ie/(\hbar c)]^2\int\bar\varphi_a(\mathbf{p}_2)A_\rho^e(\mathbf{q}_2)\mathfrak{F}'_{1\mu,\rho}\\
&\times S_F^e(p_2-q_2-k_1,p_4-k_1)\gamma_\nu S_F^e(p_4-k_1-k_2,p_3-k_1-k_2)\\
&+\gamma_\nu S_F^e(p_3-k_1,\,p_1+q_1-k_1)A_\sigma^e(\mathbf{q}_1)\mathfrak{F}_{1\mu,\sigma}\\
&\times\varphi_a(\mathbf{p}_1)D_F(k_1)D_F(k_2)(d_4k)^2(d\mathbf{p})^4(d\mathbf{q})^2.
\end{aligned}
\tag{43}
$$

$[\mathfrak{F}'_{1\mu,\rho}=\mathfrak{F}'_\rho(\gamma_\mu;\,p_2,q_2,k_1);\quad \mathfrak{F}_{1\mu,\sigma}=\mathfrak{F}_\sigma(\gamma_\mu;\,p_1,q_1,k_1).]$

Now

$$
\begin{aligned}
&\int S_F^e(p_2-q_2-k_1,\,p_4-k_1)\gamma_\nu\\
&\quad\times S_F^e(p_4-k_1-k_2,\,p_3-k_1-k_2)d\mathbf{p}_4\\
&=[(ie/(\hbar c)]\int S_F^e(p_2-q_2-k_1,\,p_4-k_1)A_\tau^e(\mathbf{q}_3)\\
&\quad\times\mathfrak{F}'_{1\nu,\tau}(p_4-k_1)S_F^e(p_4-q_3-k_1-k_2,\,p_3-k_1-k_2)\\
&\quad\times d\mathbf{p}_4d\mathbf{q}_3+2i(2\pi)^{-4}F_{1\nu}'(p_2-q_2-k_1)\\
&\quad\times S_F^e(p_2-q_2-k_1-k_2,\,p_3-k_1-k_2)-2i(2\pi)^{-4}\\
&\qquad\times S_F^e(p_2-q_2-k_1,\,p_3-k_1)F_{1\nu}'(p_3-k_1),
\end{aligned}
\tag{44}
$$

where

$$
F_{1\nu}'(p)=F'(\gamma_\nu;\,p,k_2),\quad \mathfrak{F}'_{1\nu,\tau}(p)=\mathfrak{F}_\tau'(\gamma_\nu;\,p,q_3,k_2).
\tag{45}
$$

Therefore this part of b_1 breaks up into three terms:

$$
\begin{aligned}
b_1=&[ie/(\hbar c)]^3\int\bar\varphi_a A^e\cdot\mathfrak{F}_{1\mu}'S_F^e A^e\cdot\mathfrak{F}_{1\nu}'S_F^e\gamma_\nu\\
&\times S_F^e A^e\cdot\mathfrak{F}_{1\mu}\varphi_a D_F D_F(d_4k)^2(d\mathbf{p})^4(d\mathbf{q})^3\\
&+2i(2\pi)^{-4}[ie/(\hbar c)]^2\int\bar\varphi_a A^e\cdot\mathfrak{F}_{1\mu}'F_{1\nu}'S_F^e\gamma_\nu S_F^e\\
&\times A^e\cdot\mathfrak{F}_{1\mu}\varphi_a D_F D_F(d_4k)^2(d\mathbf{p})^3(d\mathbf{q})^2\\
&-2i(2\pi)^{-4}[ie/(\hbar c)]^2\int\bar\varphi_a A^e\cdot\mathfrak{F}_{1\mu}'S_F^e F_{1\nu}'\gamma_\nu\\
&\times S_F^e A^e\cdot\mathfrak{F}_{1\mu}\varphi_a D_F D_F(d_4k)^2(d\mathbf{p})^3(d\mathbf{q})^2\\
=&b_{11}+b_{12}+b_{13}.
\end{aligned}
\tag{46}
$$

In b_{11}, the middle S_F^e factor can be replaced by S_F, so that the k_2 integration can be carried out, yielding

$$
\begin{aligned}
b_{11}=&2i(2\pi)^{-6}[ie/(\hbar c)]^3\left(3\ln\frac{\Lambda}{\kappa}-\frac{9}{4}\right)\int\bar\varphi_a(\mathbf{p}_2)\\
&\times A_\rho^e(\mathbf{q}_2)\mathfrak{F}'_{1\mu,\rho}S_F^e(p_2-q_2-k_1,\,p_3+q_3-k_1)\\
&\times\gamma\cdot A^e(\mathbf{q}_3)S_F^e(p_3-k_1,\,p_1+q_1-k_1)A_\sigma^e(\mathbf{q}_1)\\
&\times\mathfrak{F}_{1\mu,\sigma}\varphi_a(\mathbf{p}_1)D_F(k_1)d_4k_1(d\mathbf{p})^3(d\mathbf{q})^3,
\end{aligned}
\tag{47}
$$

which, on application of Eq. (14) to

$$[ie/(\hbar c)]S_F^e(p_2-q_2-k_1,\ p_3+q_3-k_1)\gamma\cdot A^e(\mathbf{q}_3)$$
$$\times S_F^e(p_3-k_1,\ p_1+q_1-k)_1 d\mathbf{p}_3 d\mathbf{q}_3,$$

combines with b_{13} to yield a multiple of II_1.

The term b_{12} must be further reduced by using the identities (13) on the remaining γ_ν factor, again yielding three terms. One of these involves the potential explicitly three times and may be shown to be too small. The other two can be evaluated using the methods applied in the preceding section. The k_2 integration in b_{13} can be done immediately, yielding a mass term and a term combining with b_{11}, as noted above, to give a multiple of II_1.

Apart from slight modifications in b_2 and b_3, the evaluation of the remaining terms in B_1 is carried out along the same lines followed in evaluating A_1, to yield

$$b_1=-\left(\ln\frac{\Lambda}{\kappa}-2\ln\frac{\kappa}{\lambda}+\frac{9}{4}\right)\mathrm{II}_1$$
$$+\sum_n C_n\int\frac{k_1^2dk_1k_2^2dk_2}{\omega_1^3\omega_2^3(1+\omega_1+\omega_2)}\left(1-\frac{1}{3}\frac{k_1^2}{\omega_1^2}\right);$$

$$b_2=b_2'=-b_3+\sum_n C_n\int\frac{k_1^2dk_1k_2^2dk_2}{\omega_1^3\omega_2^2(\omega_1+\omega_2)(1+\omega_1+\omega_2)}$$
$$\times\left(-1+\frac{1}{3}\frac{k_1^2}{\omega_1^2}+\frac{1}{3}\frac{k_1^2}{\omega_1(\omega_1+\omega_2)}\right);$$

$$b_3=b_3'=4\left(\ln\frac{\Lambda}{\kappa}-2\ln\frac{\kappa}{\lambda}\right)\mathrm{II}_1-8i(2\pi)^{-10}[ie/(\hbar c)]^2$$
$$\times\left(3\ln\frac{\Lambda}{\kappa}-\frac{9}{4}\right)\int\bar\varphi_a(\mathbf{p}_2)\frac{p_{2\mu}}{k_1^2-2p_2\cdot k_1}\gamma\cdot A^e(\mathbf{q}_2)\qquad(48)$$
$$\times S_F^e(p_2-q_2-k_1,\ p_1+q_1-k_1)A_\sigma^e(\mathbf{q}_1)\mathfrak{F}_{1\mu,\sigma}$$
$$\times\varphi_a(\mathbf{p}_1)D_F(k_1)d_4k_1(d\mathbf{p})^2(d\mathbf{q})^2$$
$$+\sum_n C_n\int\frac{k_1^2dk_1k_2^2dk_2}{\omega_1^2\omega_2^3(\omega_1+\omega_2)(1+\omega_1)}$$
$$\times\left(-1+\frac{1}{3}\frac{k_1^2}{\omega_1(\omega_1+\omega_2)}\right);$$

$$b_4=\sum_n C_n\int\frac{k_1^2dk_1k_2^2dk_2}{\omega_1^3\omega_2(\omega_1+\omega_2)^2(1+\omega_1+\omega_2)}\left(2-\frac{1}{3}\frac{k_1^2}{\omega_1^2}\right.$$
$$\left.-\frac{2}{3}\frac{k_1^2}{\omega_1(\omega_1+\omega_2)}-\frac{1}{3}\frac{k_1^2+k_2^2}{(\omega_1+\omega_2)^2}\right).$$

It is to be noted that b_3 contains a term which cannot readily be evaluated with the techniques we have been using. Fortunately a similar term appearing in b_2 just cancels it.

Inspection of the various contributions to $M_1^{(4)}$ and $M_2^{(4)}$ yields the result that the integrands of the integrals having $\sum C_n$ as a factor add to zero, so that $M_1^{(4)}+M_2^{(4)}$ may be evaluated without carrying out any of the integrations. We find that the contribution to $\Delta E^{(4)}$ is

$$\hbar c[\langle M_1^{(4)}\rangle+\langle M_2^{(4)}\rangle]$$
$$=-(i/\pi)[\tfrac{1}{4}(2\pi)^9\alpha]^2\hbar c\left(\ln\frac{\Lambda}{\kappa}-2\ln\frac{\kappa}{\lambda}+\frac{9}{4}\right)\mathrm{II}_1.\qquad(49)$$

CONTRIBUTION OF $-H^{(2)}\partial H^{(2)}/\partial E$ AND THE DEMONSTRATION OF THE VALIDITY OF THE SCATTERING APPROXIMATION

The evaluation of the remaining significant contribution to $\Delta E^{(4)}$ presents no difficulties. This term, corresponding crudely to diagram 1 of Fig. 3, is pure charge renormalization, and was therefore not calculated by WBK. We have not removed the second-order charge renormalizations from the fourth-order terms, and so must include this as well. $iH_{aa}^{(2)}$ is simply the second-order level shift. After mass renormalization it is of order $\alpha(\alpha Z)^4$. Thus only a crude approximation to $\partial H^{(2)}/\partial E$ is needed. We note that it may be written

$$\partial H_{aa}^{(2)}/\partial E=\tfrac{1}{4}i(2\pi)^{12}\alpha\int\bar\varphi_a\gamma_\mu S_F^e\gamma_4 S_F^e\gamma_\mu\varphi_a$$
$$\times D_F d_4k(d\mathbf{p})^3.\qquad(50)$$

It is sufficient to replace S_F^e by S_F, in which case one recognizes the expression as the second-order vertex charge renormalization constant. $H^{(2)}$ is to be separated into a scattering part, which is to be amalgamated with the scattering approximation terms, and a multiple-potential part, which we have denoted, apart from a factor, by II_1. The contribution of $-H^{(2)}\partial H^{(2)}/\partial E$ to the multiple-potential corrections to the scattering approximation is, indeed, simply

$$(i/\pi)[\tfrac{1}{4}(2\pi)^9\alpha]^2\hbar c\left(\ln\frac{\Lambda}{\kappa}-2\ln\frac{\kappa}{\lambda}+\frac{9}{4}\right)\mathrm{II}_1,$$

which precisely cancels the contribution of $A+B$. The validity of the scattering approximation has therefore been demonstrated.

It is clear that a method of avoiding the rather elaborate calculation described here would be desirable, and a considerable effort in this direction has been expended. The calculation could be avoided if a method could be found for preventing the appearance of infrared divergences in the scattering approximation. The use of the transverse gauge for the electromagnetic field offers some promise in this direction. However, because of the fact that the charge renormalizations appear in a much less recognizable form, and because of the

generally much greater complexity of the transverse gauge, it does not appear that any significant amount of labor could be saved by such an approach even if it were to be successfully carried through.

CORRECTIONS TO THE SCATTERING APPROXIMATION

In the previous sections it has been shown that there are no corrections to the scattering approximation for $\Delta E^{(4)}$ which are of the same order in αZ as the scattering approximation itself. On the other hand, there are corrections one order in αZ smaller. While it appears very unlikely that these are experimentally significant, it is not certain that this is the case. A few brief remarks concerning their evaluation will therefore be made.

In particular we note that the problem here is very similar to that discussed by BBF with reference to the second-order problem. Consequently a procedure very similar to theirs can be followed. Consider, for example, $\langle M_1{}^{(4)} \rangle$, as split into two terms A_0 and A_1. We have shown that, to order $\alpha^2(\alpha Z)^4$, A_0 contributes renormalization terms, $(\gamma \cdot A^e)^2$ terms, and scattering approximation terms. We now assert that, in complete analogy with the BBF problem, there are no corrections to A_0 of order αZ smaller. This comes about as a result of the special form of the denominators of the F and $\mathfrak{F}$ operators. Following the procedure of Kroll and Pollock, one can always express the αZ corrections as the square of the wave function at the origin multiplied by an integral over the momentum space of the potential. Thus, a typical term of A_0 might, after application of the Dirac equation, have the form

$$\int \bar{\varphi}_a(\mathbf{p}_2) A_\rho{}^e(\mathbf{p}_2-\mathbf{p}_3) K_{\rho\sigma}(p_3) A_\sigma{}^e(\mathbf{p}_3-\mathbf{p}_1) \varphi_a(\mathbf{p}_1)(d\mathbf{p})^3$$

$$\approx \int \bar{\varphi}_a(\mathbf{p}_2) d\mathbf{p}_2 \int \varphi_a(\mathbf{p}_1) d\mathbf{p}_1 \int A_\rho{}^e(-\mathbf{p}_3) \times K_{\rho\sigma}(p_3) A_\sigma{}^e(\mathbf{p}_3) d\mathbf{p}_3. \quad (51)$$

For the Coulomb field,

$$\int A_\rho{}^e(-\mathbf{p}) K_{\rho\sigma}(p) A_\sigma{}^e(\mathbf{p}) d\mathbf{p} \propto \mathcal{P} \int_0^\infty K(p^2) p^{-2} dp.$$

This last integral vanishes since $K(p^2)/p^2$ turns out to be sufficiently well behaved as $p^2 \to 0$, and $K(p^2)$ may be written $\int G(p^2; z_1, z_2, \cdots, z_r) dz_1 dz_2 \cdots dz_r$, where G is an analytic function of p^2 with no singularities except poles on the real axis. (The integral is to be evaluated as a principal part.) Integrals of this sort vanish identically, as long as the integrands are not singular at infinity.

Thus, for $M_1{}^{(4)}$ and $M_2{}^{(4)}$, the αZ corrections come only from A_1 and B_1. These may always be evaluated by replacing $S_F{}^e$ by S_F everywhere, and setting $\mathbf{p}_1$ and $\mathbf{p}_2$, the momenta of the initial and final states, equal to zero everywhere except in $\bar{\varphi}_a(\mathbf{p}_2)$ and $\varphi_a(\mathbf{p}_1)$. One immediately obtains the square of the wave function at the origin multiplied by a definite integral of typical form. Our previous calculation guarantees that all low-momentum divergences will cancel when all terms are combined.

It should, of course, be noted that various contributions, such as $(MP)_2$, which were not considered here because they do not contribute to the scattering approximation, do contribute to the αZ corrections. Methods very similar to those just discussed can again be applied.

The aforementioned remarks should indicate that a method exists for writing down all αZ corrections in terms of the wave function at the origin and a definite integral involving the square of the Fourier transform of the potential, two photon propagation functions, and a finite number of known functions which are identical with or similar to free-electron propagation functions. There are, of course, very many such terms, so that an actual evaluation of the corrections appears to be a far lengthier task than was the evaluation in the case of the scattering approximation.

Conservation of Heavy Particles and Generalized Gauge Transformations

T. D. LEE, *Columbia University, New York, New York*

AND

C. N. YANG, *Institute for Advanced Study, Princeton, New Jersey*

(Received March 2, 1955)

The possibility of a heavy-particle gauge transformation is discussed.

THE conservation laws of nature fall into two distinct categories: those that are related to invariance under space-time displacements and rotations, and those that are not. In the former category there are the conservation laws of momentum, energy, and angular momentum. In the latter category we find the conservation laws of electric charge, of heavy particles, and the approximate conservation laws of isotopic spin, and perhaps others.[1] We notice that the best known within this second category, the conservation of electric charge, is related to invariance under gauge transformations,[2] which expresses the nonmeasurability of the phase of the complex wave function of a charged particle.

We want to ask here whether similar gauge invariances should be related to all conservation laws of the second category. This question has been discussed in connection with the conservation of isotopic spin by Yang and Mills.[3] We wish here to discuss the problem in connection with the conservation of heavy particles.

If we take the conservation of heavy particles to mean invariance under the transformation

$$\psi_N \rightarrow e^{i\alpha}\psi_N, \quad \psi_P \rightarrow e^{i\alpha}\psi_P, \tag{1}$$

for the wave function of the heavy particles (neutrons and protons), a general gauge transformation (heavy-particle gauge transformation) is a transformation like (1) with the phase α an arbitrary function of space-time. Invariance under such a transformation means that the relative phase of the wave function of a heavy particle at two different space-time points is not measurable.

Such a gauge transformation is formally completely identical with the electromagnetic gauge transformation. Invariance under such a transformation therefore necessitates the existence of a neutral vector massless field coupled to all heavy particles. A nucleon would have a "heavy-particle charge" of $+\eta$ in such a field and an antinucleon would have a "heavy-particle charge" of $-\eta$. The force between two massive bodies therefore would contain a contribution from the Coulomb-like repulsion between such "heavy-particle charges." The total force including the gravitational attraction is:

$$\text{Force} = -G(M_1M_2/R^2)+\eta^2(A_1A_2/R^2). \tag{2}$$

Here M_1, M_2, A_1, and A_2 are the inertia masses and mass numbers of the two bodies. There should also be a magnetic-dipole-like interaction between individual nuclei because the nucleons are in constant motion in a nucleus. But in a macroscopic object the nuclear spins average out so that (2) is correct unless the two bodies are spinning at high speeds.

Now the packing fraction of various atoms differ so that M/A varies fractional-wise from substance to substance by $\sim 10^{-3}$. This means that the observed gravitation mass [which contains a contribution from the η^2 term in (2)] divided by the inertia mass would vary fractional-wise from substance to substance by $10^{-3}\eta^2/G(M_P)^2$, where M_P is the mass of the proton[4] Very careful measurements by Eötvös and co-workers. have shown this variation to be $<10^{-8}$. Therefore

$$\eta^2/G(M_P)^2 < 10^{-5}.$$

It may be remarked that since the packing fraction differs most between hydrogen and, say, carbon, Eötvös' experiment could yield a more sensitive detection of η^2 by a factor of 10 if repeated with a comparison of hydrogen and carbon.

The assumption that leads to the above line of reasoning and the force expression (2) is that the phase factor α in (1) should be space-time-dependent. It should be noticed that in addition the assumption has also been made that the transformation that generates the conservation of heavy particles is of the specific form (1).

We wish to thank Dr. J. Robert Oppenheimer for an interesting discussion.

[1] See M. Gell-Mann and A. Pais, Proceedings of the Glasgow Conference, July, 1954 (to be published).
[2] W. Pauli, Revs. Modern Phys. 13, 203 (1941).
[3] C. N. Yang and R. L. Mills, Phys. Rev. 96, 191 (1954).
[4] Eötvös, Pekár, and Fekete, Ann. Physik 68, 11 (1922).

Multiple Photon Production in Quantum Electrodynamics

SURAJ N. GUPTA
Department of Physics, Purdue University, Lafayette, Indiana
(Received February 3, 1955)

Multiple production of photons in high-energy processes in quantum electrodynamics is investigated, and the electron-positron annihilation is specially discussed in detail. It is found that at very high energies in cosmic rays, multiple production of up to four or five observable photons can easily take place. But, the probability, according to quantum electrodynamics, for the multiple production of a larger number of observable photons is quite small.

1. INTRODUCTION

BECAUSE of the small value of the fine structure constant, multiple processes in quantum electrodynamics have not received much attention. In fact, it is usually believed[1,2] that the cross section for a process involving the multiple production of photons is always much smaller than the cross section for a similar process involving the production of a lesser number of photons. However, in view of the recent discovery of a narrow shower of about 20 high-energy photons in cosmic rays by Schein and co-workers,[3] it seems to be of interest to carry out a proper investigation of multiple photon production by charged particles at high energies.

We shall, therefore, first investigate in some detail the multiple production of photons in the annihilation of a pair of electron and positron, and then we shall consider the multiple photon production in any arbitrary process in quantum electrodynamics. We shall see that at very high energies, which are available in cosmic rays, multiple production of several photons can easily take place. For instance, in cosmic rays it should be possible to observe multiple production of up to four or five photons in electron-positron annihilation, and also in some other processes. However, the probability for the multiple production of 15 to 20 photons is so small that Schein's photon shower cannot be explained solely by multiple photon production within the framework of quantum electrodynamics. This seems to suggest that the Schein shower is probably partly due to multiple photon production and partly due to the usual cascade process. Another possibility seems to be that this shower was produced by some process, which involves mesonic as well as electromagnetic interactions. Therefore, the production of a photon shower by the decay of a π^0 meson[4] and also by some other processes is at present under investigation.

Some preliminary results on multiple photon production, based on rough calculations, have been published earlier by the author.[5] However, some of the conclusions, mentioned there, are unjustified in the light of more accurate calculations, described in the present paper.[6]

2. MATRIX ELEMENT FOR THE PRODUCTION OF THREE PHOTONS IN ELECTRON-POSITRON ANNIHILATION

We shall first consider the annihilation of a pair of electron and positron with the production of three photons. Following Dyson's treatment,[7] we can write the S matrix element for this process as

$$S_3=(e^3/c^3\hbar^3)\int dx\int dx'\int dx''A_\mu(x)A_\nu(x')A_\lambda(x'')\times\bar\psi(x)\gamma_\mu S_F(x-x')\gamma_\nu S_F(x'-x'')\gamma_\lambda\psi(x''),\quad(1)$$

where

$$S_F(x-x')=\lim_{\epsilon\to+0}\frac{1}{(2\pi)^4}\int dp e^{ip(x-x')}\frac{ip\gamma-\kappa}{p^2+\kappa^2-i\epsilon}.\quad(2)$$

We now put

$$\psi(x'')=V^{-\frac{1}{2}}a_r(\mathbf{k})u_r(\mathbf{k})e^{ikx''},\qquad\bar\psi(x)=V^{-\frac{1}{2}}b_s(\mathbf{k}')\bar v_s(\mathbf{k}')e^{ik'x},\quad(3)$$

where k and k' are the propagation four-vectors for the electron and the positron respectively, $a_r(\mathbf{k})$ and $b_s(\mathbf{k}')$ are absorption operators for these particles, $u_r(\mathbf{k})$ and $\bar v_s(\mathbf{k}')$ are the spinor amplitudes, and the indices r and s can take the values 1 or 2 depending on the spin states of the particles. We can also express the transverse parts of $A_\mu(x)$, $A_\nu(x')$, and $A_\lambda(x'')$ as

$$\mathbf{A}(x)=\sum_{\mathbf{q}',e'}V^{-\frac{1}{2}}\left(\frac{c\hbar}{2q_0'}\right)^{\frac{1}{2}}\mathbf{e}'a_{e'}^*(\mathbf{q}')e^{-iq'x},$$

$$\mathbf{A}(x')=\sum_{\mathbf{q}'',e''}V^{-\frac{1}{2}}\left(\frac{c\hbar}{2q_0''}\right)^{\frac{1}{2}}\mathbf{e}''a_{e''}^*(\mathbf{q}'')e^{-iq''x'},\quad(4)$$

$$\mathbf{A}(x'')=\sum_{\mathbf{q},e}V^{-\frac{1}{2}}\left(\frac{c\hbar}{2q_0}\right)^{\frac{1}{2}}\mathbf{e}a_e^*(\mathbf{q})e^{-iqx''},$$

[1] W. Heitler, *Quantum Theory of Radiation* (Clarendon Press, Oxford, 1954).
[2] R. E. Marshak, *Meson Physics* (McGraw-Hill Book Company, Inc., New York, 1952).
[3] Schein, Haskin, and Glasser, Phys. Rev. **95**, 855 (1954). Several cases of Schein's photon shower have been observed more recently by DeBenedetti, Garelli, Tallone, Vigone, and Wataghin, Nuovo cimento **12**, 954 (1954).
[4] The results of the present paper and some possible interpretations of the Schein shower were described by the author in an invited paper at the Chicago meeting of the American Physical Society, November, 1954.
[5] S. N. Gupta, Phys. Rev. **96**, 1453 (1954).
[6] In fact, the cross section σ_n, given in reference 5, must be divided by a factor $(n-2)!$. This was first pointed out to me in a private communication by Professor F. J. Dyson and Dr. R. H. Dalitz, who made use of semiclassical and statistical arguments.
[7] F. J. Dyson, Phys. Rev. **75**, 486, 1736 (1949).

where $a_e^*(\mathbf{q})$, $a_{e'}^*(\mathbf{q}')$, and $a_{e''}^*(\mathbf{q}'')$ are emission operators for the photons, whose propagation four-vectors are q, q', and q'' and whose directions of polarization are given by the unit vectors $\mathbf{e}$, $\mathbf{e}'$, and $\mathbf{e}''$ respectively. Substituting (3) and (4) in (1), we obtain

$$S_3=V^{-5/2}\sum_{\mathbf{q},e}\sum_{\mathbf{q}',e'}\sum_{\mathbf{q}'',e''}\int dx e^{ix(k+k'-q-q'-q'')}a_r(\mathbf{k})$$
$$\times b_s(\mathbf{k}')a_e^*(\mathbf{q})a_{e'}^*(\mathbf{q}')a_{e''}^*(\mathbf{q}'')\left(\frac{e^2}{2c\hbar}\right)^{\frac{1}{2}}(q_0q_0'q_0'')^{-\frac{1}{2}}$$
$$\times\bar{v}_s(\mathbf{k}')\left[(\boldsymbol{\gamma}\cdot\mathbf{e}')\frac{-i(k'-q')\gamma-\kappa}{(k'-q')^2+\kappa^2}(\boldsymbol{\gamma}\cdot\mathbf{e}'')\right.$$
$$\left.\times\frac{i(k-q)\gamma-\kappa}{(k-q)^2+\kappa^2}(\boldsymbol{\gamma}\cdot\mathbf{e})\right]u_r(\mathbf{k}). \quad (5)$$

We shall now carry out our calculations in the center-of-mass system, so that

$$\mathbf{k}'=-\mathbf{k}, \quad k_0'=k_0. \quad (6)$$

We shall also assume that the energies of the initial electron and positron are very large compared with their rest energies, i.e.,

$$k_0^2\gg\kappa^2. \quad (7)$$

We shall denote the angle made by the vector $\mathbf{q}$ with $\mathbf{k}$ as θ, while the angles made by $\mathbf{q}'$ and $\mathbf{q}''$ with $\mathbf{k}'$ will be denoted as θ' and θ'' respectively.

We note that

$$\frac{1}{(k-q)^2+\kappa^2}=\frac{1}{2q_0(k_0-|\mathbf{k}|\cos\theta)}, \quad (8)$$

which, in view of (7), can be written as

$$\frac{1}{(k-q)^2+\kappa^2}=\frac{k_0}{q_0[\kappa^2+2k_0^2(1-\cos\theta)]}. \quad (9)$$

The quantity (9) has a sharp maximum at $\theta=0$. This shows that practically the entire contribution to the matrix element (5) arises from those values of $\mathbf{q}$, which lie within a narrow cone around the vector $\mathbf{k}$. Similarly, the quantity

$$\frac{1}{(k'-q')^2+\kappa^2}=\frac{k_0}{q_0'[\kappa^2+2k_0^2(1-\cos\theta')]} \quad (10)$$

has a sharp maximum at $\theta'=0$, so that practically the entire contribution to the matrix element (5) arises from those values of $\mathbf{q}'$, which lie within a narrow cone around the vector $\mathbf{k}'$. For small values of θ and θ', (9) and (10) reduce to

$$\frac{1}{(k-q)^2+\kappa^2}=\frac{k_0}{q_0[\kappa^2+k_0^2\theta^2]}, \quad (11)$$

$$\frac{1}{(k'-q')^2+\kappa^2}=\frac{k_0}{q_0'[\kappa^2+k_0^2\theta'^2]}. \quad (12)$$

We have seen that the photon $\mathbf{q}$ is contained within a narrow cone around $\mathbf{k}$, and $\mathbf{q}'$ is contained within a narrow cone around $\mathbf{k}'$. It follows from the conservation of momentum that if q_0'' is comparable to q_0 or q_0', the photon $\mathbf{q}''$ must also make a small angle with $\mathbf{k}$ or $\mathbf{k}'$, while if q_0'' is small compared with q_0 or q_0', the photon $\mathbf{q}''$ can make any angle with $\mathbf{k}$ or $\mathbf{k}'$. However, for simplicity, we shall assume that $\mathbf{q}''$ also is always confined within a narrow cone around $\mathbf{k}$ or $\mathbf{k}'$. We then have to consider two cases: (*a*) The photon $\mathbf{q}$ is confined within a narrow cone around $\mathbf{k}$, while the photons $\mathbf{q}'$ and $\mathbf{q}''$ are confined within a narrow cone around $\mathbf{k}'$. (b) The photons $\mathbf{q}$ and $\mathbf{q}''$ are confined within a narrow cone around $\mathbf{k}$, while the photon $\mathbf{q}'$ is confined within a narrow cone around $\mathbf{k}'$. The case *b* can evidently be obtained from the case *a* by interchanging the roles of the electron and the positron. Hence, the cross sections for these two cases are the same, and we need calculate only the cross section for the case *a*.

We can write the matrix element (5) for the case *a* as

$$S_3=V^{-5/2}\sum_{\mathbf{q}}^{\Omega}\sum_{\mathbf{q}',\mathbf{q}''}^{\Omega'}\sum_{e,e',e''}\int dx e^{ix(k+k'-q-q'-q'')}a_r(\mathbf{k})b_s(\mathbf{k}')a_e^*(\mathbf{q})a_{e'}^*(\mathbf{q}')a_{e''}^*(\mathbf{q}'')$$
$$\times\left(\frac{e^2}{2c\hbar}\right)^{\frac{1}{2}}(q_0q_0'q_0'')^{-\frac{1}{2}}\frac{\bar{v}_s(\mathbf{k}')(\boldsymbol{\gamma}\cdot\mathbf{e}')[-i(k'-q')\gamma-\kappa](\boldsymbol{\gamma}\cdot\mathbf{e}'')[i(k-q)\gamma-\kappa](\boldsymbol{\gamma}\cdot\mathbf{e})u_r(\mathbf{k})}{[(k'-q')^2+\kappa^2][(k-q)^2+\kappa^2]}, \quad (13)$$

where $\sum^{\Omega}_{\mathbf{q}}$ denotes summation over all values of $\mathbf{q}$ within a small solid angle Ω around $\mathbf{k}$, and $\sum^{\Omega'}_{\mathbf{q}',\mathbf{q}''}$ denotes summation over all values of $\mathbf{q}'$ and $\mathbf{q}''$ within a small solid angle Ω' around $\mathbf{k}'$.

Further, we can interchange the roles of the photons $\mathbf{q}_1$ and $\mathbf{q}_2$ without changing any given physical state. Hence, we can express (13) as

$$S_3=V^{-5/2}\sum_{\mathbf{q}}^{\Omega}\sum_{\mathbf{q}',\mathbf{q}''}^{\Omega'}\sum_{e,e',e''}\int dx e^{ix(k+k'-q-q'-q'')}$$
$$\times a_r(\mathbf{k})b_s(\mathbf{k}')a_e^*(\mathbf{q})a_{e'}^*(\mathbf{q}')a_{e''}^*(\mathbf{q}'')$$
$$\times\left(\frac{e^2}{2c\hbar}\right)^{\frac{1}{2}}(q_0q_0'q_0'')^{-\frac{1}{2}}\frac{1}{[(k-q)^2+\kappa^2]}$$
$$\times\left\{\frac{A}{[(k'-q')^2+\kappa^2]}+\frac{B}{[(k'-q'')^2+\kappa^2]}\right\}, \quad (14)$$

with

$$A=\bar{v}_s(\mathbf{k}')(\boldsymbol{\gamma}\cdot\mathbf{e}')[-i(k'-q')\gamma-\kappa](\boldsymbol{\gamma}\cdot\mathbf{e}'')\times[i(k-q)\gamma-\kappa](\boldsymbol{\gamma}\cdot\mathbf{e})u_r(\mathbf{k}), \quad (15)$$

$$B=\bar{v}_s(\mathbf{k}')(\boldsymbol{\gamma}\cdot\mathbf{e}'')[-i(k'-q'')\gamma-\kappa](\boldsymbol{\gamma}\cdot\mathbf{e}')\times[i(k-q)\gamma-\kappa](\boldsymbol{\gamma}\cdot\mathbf{e})u_r(\mathbf{k}), \quad (16)$$

where $\sum_{\mathbf{q}',\mathbf{q}''}^{\Omega'}$ denotes summation over all values of $\mathbf{q}'$ and $\mathbf{q}''$ within the solid angle Ω' such that each physically different state occurs only once, and the second term within the curly brackets in (14) is obtained from the first one by interchanging the roles of the photons $\mathbf{q}'$ and $\mathbf{q}''$.

3. CROSS SECTION FOR THE PRODUCTION OF THREE PHOTONS IN ELECTRON-POSITRON ANNIHILATION

In order to simplify our calculations for the process under consideration, we shall make two types of approximations, which are justified for high energies of the initial electron and the positron. Firstly, we shall neglect κ^2/k_0^2 compared with 1. Secondly, since the photons are confined within narrow cones around $\mathbf{k}$ or $\mathbf{k}'$, we shall also neglect θ^2, θ'^2, and θ''^2 compared with 1. We shall not, however, neglect any of the quantities κ^2/k_0^2, θ^2, θ'^2, and θ''^2 as compared to each other.

Using (6) and the relations

$$(ik\gamma+\kappa)u_r(\mathbf{k})=0, \quad \bar{v}_s(\mathbf{k}')(ik'\gamma-\kappa)=0, \quad (17)$$

we can express A as

$$A=\bar{v}_s(-\mathbf{k})[(q'\gamma)(\boldsymbol{\gamma}\cdot\mathbf{e}')-2(\mathbf{k}\cdot\mathbf{e}')](\boldsymbol{\gamma}\cdot\mathbf{e}'')\times[(\boldsymbol{\gamma}\cdot\mathbf{e})(q\gamma)+2(\mathbf{k}\cdot\mathbf{e})]u_r(\mathbf{k}). \quad (18)$$

We can also choose our x_3 axis along $\mathbf{k}$, and denote the azimuthal angles of $\mathbf{q}$, $\mathbf{q}'$, and $\mathbf{q}''$ around the x_3 axis as ϕ, ϕ', and ϕ'' respectively. Then the components of $\mathbf{q}$, $\mathbf{q}'$, and $\mathbf{q}''$ are

$$\begin{aligned}\mathbf{q}&=(q_0\sin\theta\cos\phi,\ q_0\sin\theta\sin\phi,\ q_0\cos\theta),\\ \mathbf{q}'&=(q_0'\sin\theta'\cos\phi',\ q_0'\sin\theta'\sin\phi',\ -q_0'\cos\theta'),\\ \mathbf{q}''&=(q_0''\sin\theta''\cos\phi'',\ q_0''\sin\theta''\sin\phi'',\ -q_0''\cos\theta'').\end{aligned} \quad (19)$$

Using (17) and (19), and making the approximations mentioned above, we get

$$\begin{aligned}(q\gamma)u_r(\mathbf{k})&=q_0(i\kappa/k_0+\theta\alpha)u_r(\mathbf{k}),\\ \bar{v}_s(-\mathbf{k})(q'\gamma)&=\bar{v}_s(-\mathbf{k})q_0'(-i\kappa/k_0+\theta'\alpha')\end{aligned} \quad (20)$$

with

$$\alpha=\gamma_1\cos\phi+\gamma_2\sin\phi, \quad \alpha'=\gamma_1\cos\phi'+\gamma_2\sin\phi', \quad (21)$$

which enables us to write (18) as

$$A=q_0q_0'\bar{v}_s(-\mathbf{k})[(-i\kappa/k_0+\theta'\alpha')(\boldsymbol{\gamma}\cdot\mathbf{e}')-2(\mathbf{k}\cdot\mathbf{e}')/q_0']\times(\boldsymbol{\gamma}\cdot\mathbf{e}'')[(\boldsymbol{\gamma}\cdot\mathbf{e})(i\kappa/k_0+\theta\alpha)+2(\mathbf{k}\cdot\mathbf{e})/q_0]u_r(\mathbf{k}). \quad (22)$$

In the extreme relativistic case, we also have

$$\begin{aligned}&\tfrac{1}{2}(1+i\gamma_4\gamma_3+\kappa\gamma_4/k_0)u_r(\mathbf{k})=u_r(\mathbf{k}),\\ &\tfrac{1}{2}(1+i\gamma_4\gamma_3+\kappa\gamma_4/k_0)v_r(-\mathbf{k})=0,\\ &\tfrac{1}{2}(1-i\gamma_4\gamma_3-\kappa\gamma_4/k_0)v_r(-\mathbf{k})=v_r(-\mathbf{k}),\\ &\tfrac{1}{2}(1-i\gamma_4\gamma_3-\kappa\gamma_4/k_0)u_r(\mathbf{k})=0.\end{aligned} \quad (23)$$

Therefore, averaging the quantity AA^* in the usual way over the spin states of the electron and the positron in the initial state, we get

$$\begin{aligned}\langle AA^*\rangle_{Av}=\tfrac{1}{16}q_0^2q_0'^2\,\mathrm{tr}\{&[(\boldsymbol{\gamma}\cdot\mathbf{e})(i\kappa/k_0+\theta\alpha)+2(\mathbf{k}\cdot\mathbf{e})/q_0]\\ &\times(1+i\gamma_4\gamma_3+\kappa\gamma_4/k_0)[(-i\kappa/k_0+\theta\alpha)(\boldsymbol{\gamma}\cdot\mathbf{e})\\ &+2(\mathbf{k}\cdot\mathbf{e})/q_0](\boldsymbol{\gamma}\cdot\mathbf{e}'')[(\boldsymbol{\gamma}\cdot\mathbf{e}')(i\kappa/k_0+\theta'\alpha')\\ &-2(\mathbf{k}\cdot\mathbf{e}')/q_0'](1+i\gamma_4\gamma_3-\kappa\gamma_4/k_0)\\ &\times[(-i\kappa/k_0+\theta'\alpha')(\boldsymbol{\gamma}\cdot\mathbf{e}')\\ &-2(\mathbf{k}\cdot\mathbf{e}')/q_0'](\boldsymbol{\gamma}\cdot\mathbf{e}'')\}.\end{aligned} \quad (24)$$

Further, summing over the states of polarization of the photons $\mathbf{q}$, $\mathbf{q}'$, and $\mathbf{q}''$ in succession, we find

$$\sum_{e,e',e''}\langle AA^*\rangle_{Av}=4q_0^2q_0'^2[\kappa^2/k_0^2+\theta^2(1-2k_0/q_0+2k_0^2/q_0^2)]\times[\kappa^2/k_0^2+\theta'^2(1-2k_0/q_0'+2k_0^2/q_0'^2)]. \quad (25)$$

According to (15) and (16), B can be obtained from A by interchanging the roles of the photons $\mathbf{q}'$ and $\mathbf{q}''$. Hence, we obtain from (22)

$$B=q_0q_0''\bar{v}_s(-\mathbf{k})[(-i\kappa/k_0+\theta''\alpha'')(\boldsymbol{\gamma}\cdot\mathbf{e}'')-2(\mathbf{k}\cdot\mathbf{e}'')/q_0'']\times(\boldsymbol{\gamma}\cdot\mathbf{e}')[(\boldsymbol{\gamma}\cdot\mathbf{e})(i\kappa/k_0+\theta\alpha)+2(\mathbf{k}\cdot\mathbf{e})/q_0]u_r(\mathbf{k}), \quad (26)$$

where

$$\alpha''=\gamma_1\cos\phi''+\gamma_2\sin\phi''. \quad (27)$$

Using (22) and (26), and averaging the quantity AB^* over the spin states of the electron and the positron, we get

$$\begin{aligned}\langle AB^*\rangle_{Av}=\tfrac{1}{16}q_0^2q_0'q_0''\,\mathrm{tr}\{&[(\boldsymbol{\gamma}\cdot\mathbf{e})(i\kappa/k_0+\theta\alpha)\\ &+2(\mathbf{k}\cdot\mathbf{e})/q_0](1+i\gamma_4\gamma_3+\kappa\gamma_4/k_0)\\ &\times[(-i\kappa/k_0+\theta\alpha)(\boldsymbol{\gamma}\cdot\mathbf{e})+2(\mathbf{k}\cdot\mathbf{e})/q_0](\boldsymbol{\gamma}\cdot\mathbf{e}')\\ &\times[(\boldsymbol{\gamma}\cdot\mathbf{e}'')(i\kappa/k_0+\theta''\alpha'')-2(\mathbf{k}\cdot\mathbf{e}'')/q_0'']\\ &\times(1+i\gamma_4\gamma_3-\kappa\gamma_4/k_0)[(-i\kappa/k_0+\theta'\alpha')\\ &\times(\boldsymbol{\gamma}\cdot\mathbf{e}')-2(\mathbf{k}\cdot\mathbf{e}')/q_0'](\boldsymbol{\gamma}\cdot\mathbf{e}'')\}.\end{aligned} \quad (28)$$

Then, summing over the states of polarization of the photons, we find

$$\sum_{e,e',e''}\langle AB^*\rangle_{Av}=4\theta'\theta''k_0^2q_0^2\cos(\phi'-\phi'')\times[\kappa^2/k_0^2+\theta^2(1-2k_0/q_0+2k_0^2/q_0^2)]. \quad (29)$$

We can now write (14) as

$$S_3=V^{-5/2}\sum_{\mathbf{q}}^{\Omega}\sum_{\mathbf{q}',\mathbf{q}''}^{\Omega'}\sum_{e,e',e''}\int dx e^{ix(k+k'-q-q'-q'')}\times a_r(\mathbf{k})b_s(\mathbf{k}')a_e^*(\mathbf{q})a_{e'}^*(\mathbf{q}')a_{e''}^*(\mathbf{q}'')K, \quad (30)$$

where

$$K=(e^2/2c\hbar)^{\frac{1}{2}}(q_0q_0'q_0'')^{-\frac{1}{2}}\frac{1}{[(k-q)^2+\kappa^2]}\times\left\{\frac{A}{[(k'-q')^2+\kappa^2]}+\frac{B}{[(k'-q'')^2+\kappa^2]}\right\}. \quad (31)$$

Simplifying the denominators in (31) for small values of the angles θ, θ', and θ'', we obtain

$$K=(e^2/2c\hbar)^{\frac{1}{2}}(q_0q_0'q_0'')^{-\frac{1}{2}}\frac{k_0^2}{q_0[\kappa^2+k_0^2\theta^2]}\times\left\{\frac{A}{q_0'[\kappa^2+k_0^2\theta'^2]}+\frac{B}{q_0''[\kappa^2+k_0^2\theta''^2]}\right\}, \quad (32)$$

so that

$$KK^*=(e^2/2c\hbar)^3\frac{k_0^4}{q_0^3q_0'q_0''[\kappa^2+k_0^2\theta^2]^2}\times\left\{\frac{AA^*}{q_0'^2[\kappa^2+k_0^2\theta'^2]^2}+\frac{BB^*}{q_0''^2[\kappa^2+k_0^2\theta''^2]^2}+\frac{AB^*+BA^*}{q_0'q_0''[\kappa^2+k_0^2\theta'^2][\kappa^2+k_0^2\theta''^2]}\right\}. \quad (33)$$

The cross section for the process under consideration is related to the quantity (33) as

$$\sigma_3=\frac{1}{2V}\sum_{\mathbf{q}'}^{\Omega'}\frac{1}{2(2\pi)^2}\int_\Omega d\omega q_0^2\left[\frac{dq_0}{d(q_0+q_0'')}\right]_{q_0'=\text{constant}}\times\sum_{e,e',e''}\langle KK^*\rangle_{Av}, \quad (34)$$

where $d\omega$ denotes an element of the solid angle in the direction of $\mathbf{q}$, and $\langle\ \rangle_{Av}$ denotes an average over the spin states of the electron and the positron in the initial state. But, in the present case, we have approximately

$$q_0'+q_0''=q_0=k_0, \quad (35)$$

which gives

$$\left[\frac{dq_0}{d(q_0+q_0'')}\right]_{q_0'=\text{constant}}=\tfrac{1}{2}. \quad (36)$$

We can also put

$$\frac{1}{V}\sum_{\mathbf{q}'}^{\Omega'}=(2\pi)^{-3}\int d\mathbf{q}'=(2\pi)^{-3}\int dq_0'\int_{\Omega'}q_0'^2d\omega'. \quad (37)$$

Hence, we can express (34) as

$$\sigma_3=\tfrac{1}{8}(2\pi)^{-5}\int dq_0'\int_{\Omega'}d\omega'\int_\Omega d\omega q_0'^2q_0^2\sum_{e,e',e''}\langle KK^*\rangle_{Av}, \quad (38)$$

or

$$\sigma_3=\tfrac{1}{8}(2\pi)^{-3}\int dq_0'\int_0^\delta\theta'd\theta'\int_0^\delta\theta d\theta q_0'^2q_0^2\sum_{e,e',e''}\langle KK^*\rangle_{Av}, \quad (39)$$

where δ is the angle of the narrow cones within which $\mathbf{q}$ and $\mathbf{q}'$ have been confined.

It is evident that in order to obtain the cross section σ_3, we can interchange the roles of the photons $\mathbf{q}'$ and $\mathbf{q}''$ in any term of the quantity KK^*. Therefore, (33) is equivalent to

$$KK^*=\left(\frac{e^2}{2c\hbar}\right)^3\frac{k_0^4}{q_0^3q_0'q_0''[\kappa^2+k_0^2\theta^2]^2}\left\{\frac{2AA^*}{q_0'^2[\kappa^2+k_0^2\theta'^2]^2}+\frac{2AB^*}{q_0'q_0''[\kappa^2+k_0^2\theta'^2][\kappa^2+k_0^2\theta''^2]}\right\}. \quad (40)$$

Using (25), (29), and (35), we obtain

$$\sum_{e,e',e''}\langle KK^*\rangle_{Av}=8\left(\frac{e^2}{2c\hbar}\right)^3\frac{1}{k_0[\kappa^2+k_0^2\theta^2][\kappa^2+k_0^2\theta'^2]}\times\left\{\frac{1}{q_0'(k_0-q_0')}+\frac{2\theta'^2k_0^3}{q_0'^3[\kappa^2+k_0^2\theta'^2]}+\frac{\theta'\theta''k_0^4\cos(\phi'-\phi'')}{q_0'^2(k_0-q_0')^2[\kappa^2+k_0^2\theta''^2]}\right\}, \quad (41)$$

and, substituting (41) in (39), we get

$$\sigma_3=\left(\frac{e^2}{4\pi c\hbar}\right)^3\int dq_0'\int_0^\delta\theta'd\theta'\int_0^\delta\theta d\theta\times\frac{k_0^2}{[\kappa^2+k_0^2\theta^2][\kappa^2+k_0^2\theta'^2]}\left\{\frac{q_0'}{(k_0-q_0')k_0}+\frac{2}{q_0'}-\frac{2\kappa^2}{q_0'[\kappa^2+k_0^2\theta'^2]}+\frac{\theta'\theta''k_0^3\cos(\phi'-\phi'')}{(k_0-q_0')^2[\kappa^2+k_0^2\theta''^2]}\right\}. \quad (42)$$

Carrying out the integrations in (42), we find

$$\sigma_3=3(e^2/4\pi c\hbar)^3k_0^{-2}\log(k_0/\lambda)[\log(\delta k_0/\kappa)]^2, \quad (43)$$

where we have denoted the lower limit to the values of q_0' and q_0'' as λ, and we have neglected terms involving lower powers of $\log(k_0/\lambda)$ or $\log(\delta k_0/\kappa)$.

We now put

$$k_0=E/c\hbar,\quad \kappa=\mu/c\hbar,\quad \lambda=\epsilon/c\hbar, \quad (44)$$

where μ is the rest energy of the electron, E is the energy of the electron or the positron in the center-of-mass system, and ϵ is the lower limit to the energy of the emitted photons in the center-of-mass system. We can then express the cross section (43) as

$$\sigma_3=3\alpha^3(c^2\hbar^2/E^2)\log(E/\epsilon)[\log(\delta E/\mu)]^2, \quad (45)$$

where

$$\alpha=e^2/4\pi c\hbar \quad (46)$$

denotes the fine structure constant.

It should further be noted that the expression (45) represents the cross sections for the process, in which two of the three photons are emitted within a narrow cone around the direction of motion of the positron. As explained in Sec. 2, the cross section for the process, in which two of the three photons are emitted within a narrow cone around the direction of motion of the electron, will be the same. Hence, the total cross section for the production of three photons in electron-positron annihilation is

$$\sigma_{3,\,\text{total}}=2\sigma_3=6\alpha^3(c^2\hbar^2/E^2)\log(E/\epsilon)[\log(\delta E/\mu)]^2. \quad (47)$$

4. MULTIPLE PRODUCTION OF PHOTONS IN ELECTRON-POSITRON ANNIHILATION

We shall now calculate the cross section for the production of n photons in electron-positron annihilation. The S matrix element for this process is[8]

$$S_n=(-i)^n(e^2/2c\hbar)^{\frac{1}{2}n}\sum_{q_1,e_1}\sum_{q_2,e_2}\cdots\sum_{q_n,e_n}V^{-(\frac{1}{2}n+1)}\frac{1}{(q_{0,1}q_{0,2}\cdots q_{0,n})^{\frac{1}{2}}}\int dx'e^{i(k+k'-q_1-q_2-\cdots-q_n)x'}$$
$$\times\frac{\bar v_s(\mathbf{k}')(\boldsymbol\gamma\cdot\mathbf{e}_n)[ip_{n-1}\gamma-\kappa](\boldsymbol\gamma\cdot\mathbf{e}_{n-1})\cdots[ip_1\gamma-\kappa](\boldsymbol\gamma\cdot\mathbf{e}_1)u_t(\mathbf{k})}{[p_{n-1}^2+\kappa^2]\cdots[p_1^2+\kappa^2]}, \quad (48)$$

where

$$\begin{aligned}&p_1=k-q_1,\quad p_2=k-q_1-q_2,\\ &\cdots\cdots\cdots\cdots\\ &p_{n-2}=k-q_1-\cdots-q_{n-2}=q_n+q_{n-1}-k',\\ &p_{n-1}=k-q_1-\cdots-q_{n-1}=q_n-k'.\end{aligned} \quad (49)$$

As before, we shall carry out our calculations in the center-of-mass system so that

$$\mathbf{k}'=-\mathbf{k},\quad k_0'=k_0. \quad (50)$$

Moreover, we shall be interested only in the case when $k_0\gg\kappa$.

In the present case, we shall be largely guided by the calculations of the preceding sections. Thus, we assume that the r photons $\mathbf{q}_1, \mathbf{q}_2, \cdots, \mathbf{q}_r$ are emitted in a narrow cone of angle δ around the vector $\mathbf{k}$, while the remaining $n-r$ photons are emitted in a narrow cone of angle δ around the vector $\mathbf{k}'$. We shall neglect δ^2 compared with 1. Then, from the conservation of momentum and energy, it follows that

$$q_{0,1}+q_{0,2}+\cdots+q_{0,r}=q_{0,r+1}+q_{0,r+2}+\cdots+q_{0,n}=k_0. \quad (51)$$

It will be convenient to express the p's as

$$\begin{aligned}&p_1=k-q_1,\quad\cdots,\quad p_r=k-q_1-\cdots-q_r,\\ &p_{n-1}=q_n-k',\quad\cdots,\quad p_{r+1}=q_n+\cdots+q_{r+2}-k',\end{aligned} \quad (52)$$

so that we can express (48) as

$$S_n=(-i)^n(e^2/2c\hbar)^{\frac{1}{2}n}\sum_{q_1,e_1}\sum_{q_2,e_2}\cdots\sum_{q_n,e_n}V^{-(\frac{1}{2}n+1)}(q_{0,1}q_{0,2}\cdots q_{0,n})^{-\frac{1}{2}}\int dx'e^{i(k+k'-q_1-\cdots-q_n)x'}$$
$$\times\frac{\bar v_s(\mathbf{k}')(\boldsymbol\gamma\cdot\mathbf{e}_n)[i(q_n-k')\gamma-\kappa]\cdots(\boldsymbol\gamma\cdot\mathbf{e}_{r+2})[i(q_n+\cdots+q_{r+2}-k')\gamma-\kappa]}{[(q_n-k')^2+\kappa^2]\cdots[(q_n+\cdots+q_{r+2}-k')^2+\kappa^2]}(\boldsymbol\gamma\cdot\mathbf{e}_{r+1})$$
$$\times\frac{[i(k-q_1-\cdots-q_r)\gamma-\kappa](\boldsymbol\gamma\cdot\mathbf{e}_r)\cdots[i(k-q_1)\gamma-\kappa](\boldsymbol\gamma\cdot\mathbf{e}_1)u_t(\mathbf{k})}{[(k-q_1-\cdots-q_r)^2+\kappa^2]\cdots[(k-q_1)^2+\kappa^2]}. \quad (53)$$

In order that S_n may be as large as possible, the q_0's should be as small as possible. But, on account of the relation (51), at least two of the q_0's must have large values. We further note that $q_{0,r}$ and $q_{0,r+1}$ occur the least number of times in the denominators of the propagation functions in (53). Therefore, it is evident that the largest values of S_n correspond to the case, when $q_{0,r}$ and $q_{0,r+1}$ are large while all other q_0's are small. We can expect to obtain a reasonable result by making approximations, which are justified for the above values of the q_0's.

When $q_{0,r}$ and $q_{0,r+1}$ are large and the other q_0's are small, we may simplify the denominators in (53) as

$$[(k-q_1)^2+\kappa^2]\cdots[(k-q_1-\cdots-q_r)^2+\kappa^2]$$
$$=[2k_0q_{0,1}-2\mathbf{k}\cdot\mathbf{q}_1]\cdots[(2k_0q_{0,1}-2\mathbf{k}\cdot\mathbf{q}_1)+\cdots+(2k_0q_{0,r-1}-2\mathbf{k}\cdot\mathbf{q}_{r-1})][2k_0q_{0,r}-2\mathbf{k}\cdot\mathbf{q}_r], \quad (54)$$

$$[(q_n-k')^2+\kappa^2]\cdots[(q_n+\cdots+q_{r+2}-k')^2+\kappa^2]$$
$$=[2k_0q_{0,n}-2\mathbf{k}'\cdot\mathbf{q}_n]\cdots[(2k_0q_{0,n}-2\mathbf{k}'\cdot\mathbf{q}_n)+\cdots+(2k_0q_{0,r+2}-2\mathbf{k}'\cdot\mathbf{q}_{r+2})]. \quad (55)$$

We also have approximately

$$[i(k-q_1)\gamma-\kappa](\boldsymbol\gamma\cdot\mathbf{e}_1)u_t(\mathbf{k})=[ik\gamma-\kappa](\boldsymbol\gamma\cdot\mathbf{e}_1)u_t(\mathbf{k})=2i(\mathbf{k}\cdot\mathbf{e}_1)u_t(\mathbf{k}), \quad (56)$$

[8] Note that in (48) the quantities q_r and p_r denote four-vectors with the components $(\mathbf{q}_r, iq_{0,r})$ and $(\mathbf{p}_r, ip_{0,r})$ respectively.

and in this way we find

$$[i(k-q_1-\cdots-q_r)\gamma-\kappa](\gamma\cdot\mathbf{e}_r)\cdots[i(k-q_1)\gamma-\kappa](\gamma\cdot\mathbf{e}_1)u_t(\mathbf{k})$$
$$=(2i\mathbf{k}\cdot\mathbf{e}_{r-1})\cdots(2i\mathbf{k}\cdot\mathbf{e}_1)[i(k-q_r)\gamma-\kappa](\gamma\cdot\mathbf{e}_r)u_t(\mathbf{k}), \quad (57)$$

$$\bar{v}_s(\mathbf{k}')(\gamma\cdot\mathbf{e}_n)[i(q_n-k')\gamma-\kappa]\cdots(\gamma\cdot\mathbf{e}_{r+2})[i(q_n+\cdots+q_{r+2}-k')\gamma-\kappa]=\bar{v}_s(\mathbf{k}')(-2i\mathbf{k}'\cdot\mathbf{e}_n)\cdots(-2i\mathbf{k}'\cdot\mathbf{e}_{r+2}). \quad (58)$$

Using (54), (55), (57), and (58), we can express (53) as

$$S_n=(-i)^n(e^2/2c\hbar)^{\frac{1}{2}n}\sum_{e_1,\cdots,e_n}\sum_{q_1,\cdots,q_n}V^{-(\frac{1}{2}n+1)}(q_{0,1}q_{0,2}\cdots q_{0,n})^{-\frac{1}{2}}\int dx'e^{i(k+k'-q_1-\cdots-q_n)x'}$$
$$\times\frac{\bar{v}_s(\mathbf{k}')(\gamma\cdot\mathbf{e}_{r+1})[i(k-q_r)\gamma-\kappa](\gamma\cdot\mathbf{e}_r)u_t(\mathbf{k})}{[2k_0q_{0,r}-2\mathbf{k}\cdot\mathbf{q}_r]}$$
$$\times\frac{(-2i\mathbf{k}'\cdot\mathbf{e}_n)\cdots(-2i\mathbf{k}'\cdot\mathbf{e}_{r+2})}{[2k_0q_{0,n}-2\mathbf{k}'\cdot\mathbf{q}_n]\cdots[(2k_0q_{0,n}-2\mathbf{k}'\cdot\mathbf{q}_n)+\cdots+(2k_0q_{0,r+2}-2\mathbf{k}'\cdot\mathbf{q}_{r+2})]}$$
$$\times\frac{(2i\mathbf{k}\cdot\mathbf{e}_{r-1})\cdots(2i\mathbf{k}\cdot\mathbf{e}_1)}{[2k_0q_{0,1}-2\mathbf{k}\cdot\mathbf{q}_1]\cdots[(2k_0q_{0,1}-2\mathbf{k}\cdot\mathbf{q}_1)+\cdots+(2k_0q_{0,r-1}-2\mathbf{k}\cdot\mathbf{q}_{r-1})]}. \quad (59)$$

But, we can interchange the roles of the photons $\mathbf{q}_1, \cdots, \mathbf{q}_{r-1}$ without changing any given physical state, and similarly we can interchange the roles of the photons $\mathbf{q}_{r+1}, \cdots, \mathbf{q}_n$. Therefore, we can write S_n as

$$S_n=(-i)^n(e^2/2c\hbar)^{\frac{1}{2}n}\sum_{e_1,\cdots,e_n}\sum_{q_r,q_{r+1}}\sum_{q_1,\cdots,q_{r-1}}{}'\sum_{q_{r+1},\cdots,q_n}{}'V^{-(\frac{1}{2}n+1)}(q_{0,1}q_{0,2}\cdots q_{0,n})^{-\frac{1}{2}}$$
$$\times\int dx'e^{i(k+k'-q_1-\cdots-q_n)x'}\frac{\bar{v}_s(\mathbf{k}')(\gamma\cdot\mathbf{e}_{r+1})[i(k-q_r)\gamma-\kappa](\gamma\cdot\mathbf{e}_r)u_t(\mathbf{k})}{[2k_0q_{0,r}-2\mathbf{k}\cdot\mathbf{q}_r]}$$
$$\times\left\{\sum_{q_n,\cdots,q_{r+1}}^{P}\frac{(-2i\mathbf{k}'\cdot\mathbf{e}_n)\cdots(-2i\mathbf{k}'\cdot\mathbf{e}_{r+2})}{[2k_0q_{0,n}-2\mathbf{k}'\cdot\mathbf{q}_n]\cdots[(2k_0q_{0,n}-2\mathbf{k}'\cdot\mathbf{q}_n)+\cdots+(2k_0q_{0,r+2}-2\mathbf{k}'\cdot\mathbf{q}_{r+2})]}\right\}$$
$$\times\left\{\sum_{q_1,\cdots,q_{r-1}}^{P}\frac{(2i\mathbf{k}\cdot\mathbf{e}_{r-1})\cdots(2i\mathbf{k}\cdot\mathbf{e}_1)}{[2k_0q_{0,1}-2\mathbf{k}\cdot\mathbf{q}_1]\cdots[(2k_0q_{0,1}-2\mathbf{k}\cdot\mathbf{q}_1)+\cdots+(2k_0q_{0,r-1}-2\mathbf{k}\cdot\mathbf{q}_{r-1})]}\right\}, \quad (60)$$

where $\sum_{q_1,\cdots,q_{r-1}}{}'$ denotes summation over all values of $\mathbf{q}_1, \cdots, \mathbf{q}_{r-1}$ such that each physically different state occurs only once, and $\sum_{q_1,\cdots,q_{r-1}}^{P}$ denotes summation over all possible terms obtained by interchanging the roles of the photons $\mathbf{q}_1, \cdots, \mathbf{q}_{r-1}$. Then, using the identity

$$\sum_{a_1,\cdots,a_n}^{P}\frac{1}{a_1(a_1+a_2)\cdots(a_1+a_2+\cdots+a_n)}=\frac{1}{a_1a_2\cdots a_n}, \quad (61)$$

we can express (61) as

$$S_n=\sum_{e_1,\cdots,e_n}\sum_{q_r,q_{r+1}}\sum_{q_1,\cdots,q_{r-1}}{}'\sum_{q_{r+1},\cdots,q_n}{}'V^{-(\frac{1}{2}n+1)}$$
$$\times\int dx'e^{i(k+k'-q_1-\cdots-q_n)x'}K_n, \quad (62)$$

where

$$K_n=(-i)^n(e^2/2c\hbar)^{\frac{1}{2}n}(q_{0,1}q_{0,2}\cdots q_{0,n})^{-\frac{1}{2}}$$
$$\times\frac{\bar{v}_s(\mathbf{k}')(\gamma\cdot\mathbf{e}_{r+1})[i(k-q_r)\gamma-\kappa](\gamma\cdot\mathbf{e}_r)u_t(\mathbf{k})}{[2k_0q_{0,r}-2\mathbf{k}\cdot\mathbf{q}_r]}$$
$$\times\frac{(-2i\mathbf{k}'\cdot\mathbf{e}_n)\cdots(-2i\mathbf{k}'\cdot\mathbf{e}_{r+2})}{[2k_0q_{0,n}-2\mathbf{k}'\cdot\mathbf{q}_n]\cdots[2k_0q_{0,r+2}-2\mathbf{k}'\cdot\mathbf{q}_{r+2}]}$$
$$\times\frac{(2i\mathbf{k}\cdot\mathbf{e}_{r-1})\cdots(2i\mathbf{k}\cdot\mathbf{e}_1)}{[2k_0q_{0,1}-2\mathbf{k}\cdot\mathbf{q}_1]\cdots[2k_0q_{0,r-1}-2\mathbf{k}\cdot\mathbf{q}_{r-1}]}. \quad (63)$$

According to (63), we have

$$KK^*=(e^2/2c\hbar)^n\frac{2^{2n-4}}{q_{0,1}\cdots q_{0,n}}\frac{CC^*}{[2k_0q_{0,r}-2\mathbf{k}\cdot\mathbf{q}_r]^2}$$
$$\times\frac{(\mathbf{k}'\cdot\mathbf{e}_n)^2\cdots(\mathbf{k}'\cdot\mathbf{e}_{r+2})^2}{[2k_0q_{0,n}-2\mathbf{k}'\cdot\mathbf{q}_n]^2\cdots[2k_0q_{0,r+2}-2\mathbf{k}'\cdot\mathbf{q}_{r+2}]^2}$$
$$\times\frac{(\mathbf{k}\cdot\mathbf{e}_{r-1})^2\cdots(\mathbf{k}\cdot\mathbf{e}_1)^2}{[2k_0q_{0,1}-2\mathbf{k}\cdot\mathbf{q}_1]^2\cdots[2k_0q_{0,r-1}-2\mathbf{k}\cdot\mathbf{q}_{r-1}]^2}, \quad (64)$$

where

$$C=\bar{v}_s(\mathbf{k}')(\boldsymbol{\gamma}\cdot\mathbf{e}_{r+1})[i(k-q_r)\gamma-\kappa](\boldsymbol{\gamma}\cdot\mathbf{e}_r)u_t(\mathbf{k}). \quad (65)$$

We now denote the angles made by $\mathbf{q}_1, \cdots, \mathbf{q}_r$ with $\mathbf{k}$ as $\theta_1, \cdots, \theta_r$ respectively, and the angles made by $\mathbf{q}_{r+1}, \cdots, \mathbf{q}_n$ with $\mathbf{k}'$ as $\theta_{r+1}, \cdots, \theta_n$ respectively. Then, for small values of the θ's, we get

$$[2k_0q_{0,i}-2\mathbf{k}\cdot\mathbf{q}_i]^{-1}=(k_0/q_{0,i})[\kappa^2+k_0^2\theta_i^2]^{-1}, \quad (66)$$

$$[2k_0q_{0,j}-2\mathbf{k}'\cdot\mathbf{q}_j]^{-1}=(k_0/q_{0,j})[\kappa^2+k_0^2\theta_j^2]^{-1}, \quad (67)$$

$$\sum_{e_i}(\mathbf{k}\cdot\mathbf{e}_i)^2=k_0^2\theta_i^2, \quad \sum_{e_j}(\mathbf{k}'\cdot\mathbf{e}_j)^2=k_0^2\theta_j^2, \quad (68)$$

where $i\leqslant r$ and $j>r$. Further, averaging over the spin states of the electron and the positron in the initial state, and summing over the directions of polarization of the photons $\mathbf{q}_r$ and $\mathbf{q}_{r+1}$, we find

$$\sum_{e_r,e_{r+1}}\langle CC^*\rangle_{Av}=2(q_{0,r}^2/k_0^2)$$
$$\times[\kappa^2+k_0^2\theta_r^2(1-2k_0/q_{0,r}+2k_0^2/q_{0,r}^2)]. \quad (69)$$

We substitute (66), (67), (68), and (69) in (64), and, as before, we take $q_{0,r}$ and $q_{0,r+1}$ to be of the order of k_0. We then obtain

$$\sum_{e_1,\cdots,e_n}\langle KK^*\rangle_{Av}=(e^2/2c\hbar)^n\frac{2^{2n-3}k_0^{2n-4}}{q_{0,1}\cdots q_{0,r-1}q_{0,r+2}\cdots q_{0,n}[\kappa^2+k_0^2\theta_r^2]}\frac{1}{q_{0,1}^2\cdots q_{0,r}^2}\frac{1}{q_{0,r+2}^2\cdots q_{0,n}^2}$$
$$\times\frac{(k_0^2\theta_1^2)\cdots(k_0^2\theta_{r-1}^2)}{[\kappa^2+k_0^2\theta_1^2]^2\cdots[\kappa^2+k_0^2\theta_{r-1}^2]^2}\frac{(k_0^2\theta_{r+2}^2)\cdots(k_0^2\theta_n^2)}{[\kappa^2+k_0^2\theta_{r+2}^2]^2\cdots[\kappa^2+k_0^2\theta_n^2]^2}. \quad (70)$$

The cross section σ_n for the multiple production of n photons is related to the quantity (70) as

$$\sigma_n=\frac{1}{V^{n-2}}\sum_{\mathbf{q}_1,\cdots,\mathbf{q}_{r-1}}{}'\sum_{\mathbf{q}_{r+2},\cdots,\mathbf{q}_n}{}'\frac{1}{2(2\pi)^2}\int d\omega_r q_{0,r}^2\left[\frac{dq_{0,r}}{d(q_{0,r}+q_{0,r+1})}\right]\sum_{e_1,\cdots,e_n}\langle KK^*\rangle_{Av}, \quad (71)$$

where $d\omega_r$ is an element of solid angle in the direction of $\mathbf{q}_r$, and the derivative within the square brackets in (71) is to be obtained by keeping $q_{0,1}, \cdots, q_{0,r-1}$ and $q_{0,r+2}, \cdots, q_{0,n}$ constant. From (51), we get

$$\left[\frac{dq_{0,r}}{d(q_{0,r}+q_{0,r+1})}\right]=\tfrac{1}{2}, \quad (72)$$

and we can put

$$\frac{1}{V^{r-1}}\sum_{\mathbf{q}_1,\cdots,\mathbf{q}_{r-1}}{}'=\frac{1}{(r-1)!}\frac{1}{(2\pi)^{3(r-1)}}\int d\mathbf{q}_1\cdots\int d\mathbf{q}_{r-1},$$
$$\frac{1}{V^{n-r-1}}\sum_{\mathbf{q}_{r+2},\cdots,\mathbf{q}_n}{}'=\frac{1}{(n-r-1)!}\frac{1}{(2\pi)^{3(n-r-1)}}\int d\mathbf{q}_{r+2}\cdots\int d\mathbf{q}_n, \quad (73)$$

where the factorial factors in (73) arise from the fact that $\sum'$ denotes a summation such that each physically different state occurs only once. We further note that

$$\int d\mathbf{q}_i=2\pi\int dq_{0,i}q_{0,i}^2\int_0^\delta\theta_i d\theta_i, \quad (74)$$

where δ is the angle of the cones, within which the photons have been confined. Hence, using (70), (72), (73), and (74), we obtain from (73)

$$\sigma_n=\alpha^n\frac{1}{(r-1)!(n-r-1)!}\frac{2^{n-2}k_0^{2n-4}}{\pi^{n-3}}\int dq_{0,1}\cdots$$
$$\times\int dq_{0,r-1}\frac{1}{q_{0,1}\cdots q_{0,r-1}}\int dq_{0,r+2}\cdots$$
$$\times\int dq_{0,n}\frac{1}{q_{0,r+2}\cdots q_{0,n}}\int_0^\delta\theta_1 d\theta_1\cdots$$
$$\times\int_0^\delta\theta_r d\theta_r\int_0^\delta\theta_{r+2}d\theta_{r+2}\cdots\int_0^\delta\theta_n d\theta_n$$
$$\times\frac{(k_0^2\theta_1^2)\cdots(k_0^2\theta_{r-1}^2)}{[\kappa^2+k_0^2\theta_1^2]^2\cdots[\kappa^2+k_0^2\theta_{r-1}^2]^2}\frac{1}{[\kappa^2+k_0^2\theta_r^2]}$$
$$\times\frac{(k_0^2\theta_{r+2}^2)\cdots(k_0^2\theta_n^2)}{[\kappa^2+k_0^2\theta_{r+2}^2]^2\cdots[\kappa^2+k_0^2\theta_n^2]^2}. \quad (75)$$

Carrying out the integrations in (75), and ignoring some lower-order terms, we get

$$\sigma_n=\alpha^n\frac{1}{(r-1)!(n-r-1)!}\frac{2^{n-2}}{\pi^{n-3}}\frac{1}{k_0^2}$$
$$\times\left(\log\frac{k_0\delta}{\kappa}\right)^{n-1}\left(\log\frac{q_{0,\max}}{\lambda}\right)^{n-2}, \quad (76)$$

where $q_{0,\max}$ and λ are the maximum and the minimum values of $q_{0,1}, \cdots, q_{0,r-1}, q_{0,r+2}, \cdots, q_{0,n}$. Using (44),

we can also express (76) as

$$\sigma_n=\alpha^n\frac{1}{(r-1)!(n-r-1)!}\frac{2^{n-2}}{\pi^{n-3}}\frac{c^2\hbar^2}{E^2}\times\left(\log\frac{E\delta}{\mu}\right)^{n-1}\left(\log\frac{\epsilon_{\max}}{\epsilon}\right)^{n-2}, \quad (77)$$

where

$$\epsilon_{\max}=c\hbar q_{0,\max} \quad (78)$$

denotes the upper limit to the energies of the photons $\mathbf{q}_1, \cdots, \mathbf{q}_{r-1}, \mathbf{q}_{r+2}, \cdots, \mathbf{q}_n$.

When $n=3$, $r=1$, $\epsilon_{\max}=E$, (77) becomes

$$2\alpha^3(c^2\hbar^2/E^2)\log(E/\epsilon)[\log(\delta E/\mu)]^2,$$

which differs from the more accurate result (45) only by a factor $\frac{2}{3}$. Following the treatment of Secs. 2–3, we have also investigated more carefully the cross section σ_n for low values of n, and it is found that the result (77) represents a good approximation.

The expression (77) gives the cross section for the production of n photons, out of which r photons are emitted within a narrow cone around the direction of motion of the electron. In order to obtain the total cross section for the production of n photons, we have to sum (77) over all values of r from 1 to $n-1$. Thus, using the relation

$$\sum_{r=1}^{n-1}\frac{1}{(r-1)!}\frac{1}{(n-r-1)!}=\frac{2^{n-2}}{(n-2)!}, \quad (79)$$

we obtain for the total cross section in the center-of-mass system

$$\sigma_{n,\text{total}}=\alpha^n\frac{1}{(n-2)!}\frac{4^{n-2}}{\pi^{n-3}}\frac{c^2\hbar^2}{E^2}\left(\log\frac{\delta E}{\mu}\right)^{n-1}\left(\log\frac{\epsilon_{\max}}{\epsilon}\right)^{n-2}. \quad (80)$$

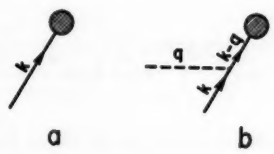

FIG. 1. Feynman diagrams for (a) an arbitrary process with at least one external electron line, and (b) emission of a photon from an external electron line of an arbitrary process.

5. MULTIPLE PHOTON PRODUCTION IN ANY ARBITRARY PROCESS IN QUANTUM ELECTRODYNAMICS

Let us consider any arbitrary process in quantum electrodynamics, whose Feynman diagram contains at least one external electron line,[9] as shown in Fig. 1(a). The S matrix element for this process will be of the form

$$S_0=S_0'(k)u(k), \quad (81)$$

where $u(k)$ is the spinor amplitude of the electron, and $S_0'(k)$ is some quantity, which is a function of k as well as some other variables. If we insert an external photon line in the external electron line, as shown in Fig. 1(b), then according to Dyson's treatment[5] of the S matrix, the contribution of the new process will be

$$S_1=-iV^{-\frac{1}{2}}(e^2/2c\hbar)^{\frac{1}{2}}\sum_{\mathbf{q},e}q_0^{-\frac{1}{2}}\times\frac{S_0'(k-q)[i(k-q)\gamma-\kappa](\gamma\cdot\mathbf{e})u(k)}{[(k-q)^2+\kappa^2]}. \quad (82)$$

Similarly, if we introduce n external photon lines in the external electron line of Fig. 1(a), the S matrix element for the resulting process will be

$$S_n=(-i)^nV^{-\frac{1}{2}n}(e^2/2c\hbar)^{\frac{1}{2}n}\sum_{\mathbf{q}_1,\cdots,\mathbf{q}_n}\sum_{e_1,\cdots,e_n}(q_{0,1}\cdots q_{0,n})^{-\frac{1}{2}}\times\frac{S_0'(k-q_1-\cdots-q_n)[i(k-q_1-\cdots-q_n)\gamma-\kappa](\gamma\cdot\mathbf{e}_n)\cdots[i(k-q_1)\gamma-\kappa](\gamma\cdot\mathbf{e}_1)u(k)}{[(k-q_1-\cdots-q_n)^2+\kappa^2]\cdots[(k-q_1)^2+\kappa^2]}. \quad (83)$$

We shall now try to find a relation between the cross section σ_n for the above process and the cross section σ_0 for the process shown in Fig. 1(a), when the external electron line represents an electron of very high energy.

As in the case of the electron-positron annihilation, we may expect that the main contribution to the cross section σ_n arises from low values of the q_0's. Therefore, as in Sec. 4, we may simplify the numerator and the denominator in (83) as

$$[i(k-q_1-\cdots-q_n)\gamma-\kappa](\gamma\cdot\mathbf{e}_n)\cdots\times[i(k-q_1)\gamma-\kappa](\gamma\cdot\mathbf{e}_1)u(k)=(2i\mathbf{k}\cdot\mathbf{e}_n)\cdots(2i\mathbf{k}\cdot\mathbf{e}_1)u(k), \quad (84)$$

$$[(k-q_1-\cdots-q_n)^2+\kappa^2]\cdots[(k-q_1)^2+\kappa^2]=[(2k_0q_{0,1}-2\mathbf{k}\cdot\mathbf{q}_1)+\cdots+(2k_0q_{0,n}-2\mathbf{k}\cdot\mathbf{q}_n)]\cdots\times[2k_0q_{0,1}-2\mathbf{k}\cdot\mathbf{q}_1]. \quad (85)$$

If the quantity $S_0'(k)$ is not too sensitive to a small change in k, we may also take

$$S_0'(k-q_1-\cdots-q_n)=S_0'(k). \quad (86)$$

Then, using (84), (85), and (86), we can simplify (83)

[9] For the meaning of an external electron line and other similar terms, see reference 7.

as

$$S_n=(-i)^nV^{-\frac{1}{2}n}(e^2/2c\hbar)^{\frac{1}{2}n}\sum_{\mathbf{q}_1,\cdots,\mathbf{q}_n}\sum_{e_1,\cdots,e_n}(q_{0,1}\cdots q_{0,n})^{-\frac{1}{2}}S_0'(k)u(k)$$
$$\times\frac{(2i\mathbf{k}\cdot\mathbf{e}_n)\cdots(2i\mathbf{k}\cdot\mathbf{e}_1)}{[(2k_0q_{0,1}-2\mathbf{k}\cdot\mathbf{q}_1)+\cdots+(2k_0q_{0,n}-2\mathbf{k}\cdot\mathbf{q}_n)]\cdots[2k_0q_{0,1}-2\mathbf{k}\cdot\mathbf{q}_1]}, \quad (87)$$

which can be written as

$$S_n=(-i)^nV^{-\frac{1}{2}n}(e^2/2c\hbar)^{\frac{1}{2}n}\sum_{\mathbf{q}_1,\cdots,\mathbf{q}_n}{}'\sum_{e_1,\cdots,e_n}(q_{0,1}\cdots q_{0,n})^{-\frac{1}{2}}S_0'(k)u(k)$$
$$\times(2i\mathbf{k}\cdot\mathbf{e}_1)\cdots(2i\mathbf{k}\cdot\mathbf{e}_n)\left\{\sum_{\mathbf{q}_1,\cdots,\mathbf{q}_n}^{P}\frac{1}{[2k_0q_{0,1}-2\mathbf{k}\cdot\mathbf{q}_1]\cdots[(2k_0q_{0,1}-2\mathbf{k}\cdot\mathbf{q}_1)+\cdots+(2k_0q_{0,n}-2\mathbf{k}\cdot\mathbf{q}_n)]}\right\}, \quad (88)$$

where the meaning of $\sum'$ and $\sum^P$ has been explained in Sec. 4. Further, using the identity (61), we can express (88) as

$$S_n=(-i)^nV^{-\frac{1}{2}n}(e^2/2c\hbar)^{\frac{1}{2}n}\sum_{\mathbf{q}_1,\cdots,\mathbf{q}_n}{}'\sum_{e_1,\cdots,e_n}(q_{0,1}\cdots q_{0,n})^{-\frac{1}{2}}S_0'(k)u(k)\frac{(2i\mathbf{k}\cdot\mathbf{e}_1)\cdots(2i\mathbf{k}\cdot\mathbf{e}_n)}{[2k_0q_{0,1}-2\mathbf{k}\cdot\mathbf{q}_1]\cdots[2k_0q_{0,n}-2\mathbf{k}\cdot\mathbf{q}_n]} \quad (89)$$

or

$$S_n=\sum_{e_1,\cdots,e_n}\sum_{\mathbf{q}_1,\cdots,\mathbf{q}_n}{}'V^{-\frac{1}{2}n}J_nS_0'(k)u(k), \quad (90)$$

where

$$J_n=(-i)^n(e^2/2c\hbar)^{\frac{1}{2}n}(q_{0,1}\cdots q_{0,n})^{-\frac{1}{2}}\frac{(2i\mathbf{k}\cdot\mathbf{e}_1)\cdots(2i\mathbf{k}\cdot\mathbf{e}_n)}{[2k_0q_{0,1}-2\mathbf{k}\cdot\mathbf{q}_1]\cdots[2k_0q_{0,n}-2\mathbf{k}\cdot\mathbf{q}_n]}. \quad (91)$$

The relation (90) shows that σ_n is related to σ_0 as

$$\sigma_n=V^{-n}\sum_{\mathbf{q}_1,\cdots,\mathbf{q}_n}{}'\sum_{e_1,\cdots,e_n}J_n^*J_n\sigma_0, \quad (92)$$

so that, substituting (91) in (92), we get

$$\sigma_n=\sigma_0V^{-n}\sum_{\mathbf{q}_1,\cdots,\mathbf{q}_n}{}'\sum_{e_1,\cdots,e_n}(e^2/2c\hbar)^n\frac{4^n}{q_{0,1}\cdots q_{0,n}}$$
$$\times\frac{(\mathbf{k}\cdot\mathbf{e}_1)^2\cdots(\mathbf{k}\cdot\mathbf{e}_n)^2}{[2k_0q_{0,1}-2\mathbf{k}\cdot\mathbf{q}_1]^2\cdots[2k_0q_{0,n}-2\mathbf{k}\cdot\mathbf{q}_n]^2}. \quad (93)$$

But,

$$\sum_{e_r}(\mathbf{k}\cdot\mathbf{e}_r)^2=k_0^2\sin^2\theta_r, \quad (94)$$

$$2k_0q_{0,r}-2\mathbf{k}\cdot\mathbf{q}_r=2k_0q_{0,r}[(\kappa^2/2k_0^2)+(1-\cos\theta_r)], \quad (95)$$

where θ_r denotes the angle between $\mathbf{q}$ and $\mathbf{k}$, and we have made use of the fact that $k_0\gg\kappa$. Using (94) and (95), we can express (93) as

$$\sigma_n=\sigma_0V^{-n}\sum_{\mathbf{q}_1,\cdots,\mathbf{q}_n}{}'(e^2/2c\hbar)^n(q_{0,1}\cdots q_{0,n})^{-3}$$
$$\times\frac{\sin^2\theta_1}{[(\kappa^2/2k_0^2)+(1-\cos\theta_1)]^2}\cdots$$
$$\times\frac{\sin^2\theta_n}{[(\kappa^2/2k_0^2)+(1-\cos\theta_n)]^2}. \quad (96)$$

Then, putting

$$V^{-n}\sum_{\mathbf{q}_1,\cdots,\mathbf{q}_n}{}'=(1/n!)(2\pi)^{-3n}\int d\mathbf{q}_1\cdots\int d\mathbf{q}_n, \quad (97)$$

$$\int d\mathbf{q}_i=2\pi\int dq_{0,i}q_{0,i}^2\int_0^\pi\sin\theta_i d\theta_i, \quad (98)$$

we obtain

$$\sigma_n=\sigma_0\alpha^n\frac{1}{n!}\frac{1}{(2\pi)^n}\int dq_{0,1}\cdots\int dq_{0,n}\frac{1}{q_{0,1}\cdots q_{0,n}}$$
$$\times\int_0^\pi d\theta_1\cdots\int_0^\pi d\theta_n\frac{\sin^3\theta_1}{[(\kappa^2/2k_0^2)+(1-\cos\theta_1)]^2}\cdots$$
$$\times\frac{\sin^3\theta_n}{[(\kappa^2/2k_0^2)+(1-\cos\theta_n)]^2}. \quad (99)$$

Carrying out the integrations in (99), and ignoring some lower-order terms, we get

$$\sigma_n=\sigma_0\frac{\alpha^n}{n!}\left(\frac{2}{\pi}\right)^n\left(\log\frac{2k_0}{\kappa}\right)^n\left(\log\frac{q_{0,\max}}{\lambda}\right)^n, \quad (100)$$

where $q_{0,\max}$ and λ are the maximum and the minium values of the q_0's. Using (44) and (78), we can also express (100) as

$$\sigma_n=\sigma_0\frac{\alpha^n}{n!}\left(\frac{2}{\pi}\right)^n\left(\log\frac{2E}{\mu}\right)^n\left(\log\frac{\epsilon_{\max}}{\epsilon}\right)^n, \quad (101)$$

where E is the energy of the electron represented by the external electron line.

It should be observed that the above approximate result has been obtained with the assumption that the quantity $S_0'(k)$ of equation (81) is not too sensitive to a small change in k. Therefore, the above general result represents only a rough approximation, and a more

accurate determination of σ_n can be made only when we know the quantity $S_0'(k)$.

6. CONCLUSION

We shall now discuss the significance of the results obtained in the preceding sections. It should first be noted that the cross sections (47), (80), and (101) all diverge as the lower limit ϵ to the energy of the emitted photons tends to zero. However, it is known that this "infrared divergence" is harmless, and it is compensated by corresponding divergencies arising in the radiative corrections to cross sections for the production of a lesser number of photons.[10] Therefore, for all practical purposes, ϵ represents the lower limit to the energy of the photons, which can be observed in a given experiment.

As a particular case, let us consider the annihilation of a pair of electron and positron in the center-of-mass system, such that 1 photon is emitted along the direction of motion of the electron while $n-1$ photons are emitted along the direction of motion of the positron. Then, according to (77), the cross section for this process will be

$$\sigma_n=\alpha^n\frac{1}{(n-2)!}\frac{2^{n-2}}{\pi^{n-3}}\frac{c^2\hbar^2}{E^2}\left(\log\frac{\delta E}{\mu}\right)^{n-1}\left(\log\frac{\epsilon_{\max}}{\epsilon}\right)^{n-2}. \quad (102)$$

Since we are interested only in the order of magnitude of σ_n, we can put $\epsilon_{\max}=E$ in (102). Moreover, it follows from (101) that if we include the contributions from all angles instead of a small cone, the factor $[\log(\delta E/\mu)]^{n-1}$ in (102) should be replaced by $[\log(2E/\mu)]^{n-1}$. Therefore, in the present case we may take the cross section as

$$\sigma_n=\alpha^n\frac{1}{(n-2)!}\frac{2^{n-2}}{\pi^{n-3}}\frac{c^2\hbar^2}{E^2}\left(\log\frac{2E}{\mu}\right)^{n-1}\left(\log\frac{E}{\epsilon}\right)^{n-2}. \quad (103)$$

We now pass over from the center-of-mass system to the laboratory system, in which the electron is at rest. We can then put

$$E'=2E^2/\mu, \quad \epsilon'=2\epsilon E/\mu, \quad (104)$$

where E' is the energy of the positron in the laboratory system, and ϵ' is the lower limit to the energy of the photons in this system. Using (104), we can express (103) as

$$\sigma_n=\alpha^n\frac{1}{(n-2)!}\frac{1}{\pi^{n-3}}\frac{c^2\hbar^2}{\mu E'}\left(\log\frac{2E'}{\mu}\right)^{n-1}\left(\log\frac{E'}{\epsilon'}\right)^{n-2}. \quad (105)$$

The lower limit to the energy of photons, which can be observed through pair production in photographic emulsions, will depend on the nature of the emulsion. But, for our general purpose we may take $\epsilon'=50\mu\approx 25$ Mev, which gives us

$$\sigma_n=\alpha^n\frac{1}{(n-2)!}\frac{1}{\pi^{n-3}}\frac{c^2\hbar^2}{\mu E'}\left(\log\frac{2E'}{\mu}\right)^{n-1}\left(\log\frac{E'}{50\mu}\right)^{n-2}. \quad (106)$$

Now, the cross section for the production of two photons in the electron-positron annihilation at high energies is known to be[1]

$$\sigma_2=\pi\alpha^2(c^2\hbar^2/\mu E')\log(2E'/\mu). \quad (107)$$

Therefore, (106) can also be written as

$$\sigma_n=\sigma_2\frac{1}{(n-2)!}\left(\frac{\alpha}{\pi}\log\frac{2E'}{\mu}\log\frac{E'}{50\mu}\right)^{n-2}. \quad (108)$$

When the energy E' of the incident positron is of the order of 10^{14} ev to 10^{16} ev, we find

$$(\alpha/\pi)\log(2E'/\mu)\log(E'/50\mu)\approx 1, \quad (109)$$

so that in the above energy region we have

$$\sigma_n\approx\sigma_2/(n-2)!. \quad (110)$$

According to (110), σ_n is comparable to σ_2 for small values of n, and therefore multiple production of up to four or five photons in electron-positron annihilation can easily take place at very high energies in cosmic rays. However, σ_n for the production of 15 to 20 photons is quite small as compared to σ_2, and therefore we are not likely to observe a shower of 15 to 20 photons due to multiple photon production in electron-positron annihilation even at reasonably high energies.

The general result (101) further seems to show that a similar situation exists with regard to the multiple production of photons in other processes in quantum electrodynamics.

I would like to express my sincerest thanks to Professor K. Lark-Horovitz, Professor M. Schein, and Professor F. J. Dyson for valuable discussions. I am also indebted to Professor F. J. Belinfante for interesting comments, and to Professor A. Rosenthal for helpful discussions on the evaluation of various integrals.

[10] A general proof of this result has been given recently by J. M. Jauch and F. Rohrlich, Helv. Phys. Acta. 27, 613 (1954).

Letters to the Editor

PUBLICATION of brief reports of important discoveries in physics may be secured by addressing them to this department. The closing date for this department is five weeks prior to the date of issue. No proof will be sent to the authors. The Board of Editors does not hold itself responsible for the opinions expressed by the correspondents. Communications should not exceed 600 words in length and should be submitted in duplicate.

"Brute Force" Polarization of In^{115} Nuclei; Angular Momentum of 1.458-ev Neutron Resonance

J. W. T. DABBS, L. D. ROBERTS, AND S. BERNSTEIN
Oak Ridge National Laboratory, Oak Ridge, Tennessee
(Received March 25, 1955)

GORTER[1] and Kürti and Simon[2] have suggested the possibility of polarizing nuclei by the direct application of a large external magnetic field to the nuclear spin system at a very low temperature. The magnitude of the polarization f_N has been given by Simon[3] and Rose[4] as

$$f_N=-\frac{1}{3}\frac{I+1}{I}\frac{\mu H}{kT} \tag{1}$$

for the case $\mu H \ll kT$, where I is the nuclear spin quantum number, μ is the nuclear magnetic moment, k is the Boltzmann constant, H is the applied magnetic field, and T is the absolute temperature. Even in the most favorable cases, values of $H/T \sim 10^5$ gauss/deg are necessary to obtain polarizations of ~ 1 percent. Thus, to achieve useful polarizations by this method, it is necessary to use the method of adiabatic demagnetization to obtain sufficiently large H/T values. Rose[4] has also pointed out that the absorption of polarized s neutrons by polarized nuclei forms a basis for determining the angular momentum J of levels of the compound nucleus. When the absorption is due to a single level (as near a resonance), the value of J for this level is obtained from the *direction* of the change in absorption cross section with changes in relative spin orientation. The expressions for the neutron cross section σ are

$$\sigma=\sigma_0[1+f_n f_N I/(I+1)] \quad \text{if} \quad J=I+\tfrac{1}{2}, \tag{2a}$$

and

$$\sigma=\sigma_0(1-f_n f_N) \quad \text{if} \quad J=I-\tfrac{1}{2}. \tag{2b}$$

Here σ_0 is the cross section in the absence of polarization, and f_n is the neutron polarization. In such an experiment the fractional change in the transmitted neutron intensity, $\Delta C/\bar{C}$, is given by

$$\Delta C/\bar{C}=2\tanh(Nt\sigma_0 f_n f_N f_I) \tag{3}$$

for reversal of the relative spin orientations. In (3), $Nt\sigma_0$ is the macroscopic absorption cross section of the sample, and f_I is $I/(I+1)$ if $J=I+\frac{1}{2}$ and unity if $J=I-\frac{1}{2}$. For small polarizations, $\Delta C/\bar{C}$ is proportional to $Nt\sigma_0$ as well as to the product of the two polarizations $f_n f_N$. It is therefore advantageous to make the nuclear sample as thick as possible consistent with intensity requirements.

Experiments have been carried out on the polarization of In^{115} nuclei. Indium was selected because of its large nuclear magnetic moment, and because the thermal neutron cross section is almost entirely due to the 1.458-ev resonance.[5] The metal was used to obtain a short nuclear spin-lattice relaxation time[6] and a high thermal conductivity.[7] The metal, in the form of 20 thin plates $0.025\times1.5\times3.5$ cm, was thermally connected to a cooling salt some 12 cm away by means of silver wires. Each indium plate was soldered to the upper end of a wire and the coolant salt was crystallized around the lower ends of the wires to provide thermal contact to the salt. This unit was in turn mounted on rigid insulators in a silver cage which was cooled by another demagnetized salt and suspended on nylon strings. Both salt samples were $Fe(NH_4)(SO_4)_2\cdot 12H_2O$. This assembly was mounted in a cryostat described previously.[8] The design of the sample assembly was based on minimization of eddy current heating and reduction of the possibility of heating due to vibration. The salts were cooled by adiabatic demagnetization from 0.99°K and 16 400 gauss to a final temperature near 0.035°K.[9] The sample assembly was then slowly lowered[8] to place the cooling salts within a magnetic shield and to bring the In plates into the gap of the Weiss magnet in such a manner that the plane of the plates was parallel to the field direction. The magnet was then turned on slowly to 11 150 gauss. These operations were performed slowly to reduce heating; in particular the field was raised very slowly near the In superconducting threshold value.

The source of neutrons was a beam from the ORNL graphite reactor. The nuclear sample was bombarded with polarized thermal neutrons obtained by reflecting this beam from the 220 planes of a magnetized Fe_3O_4 crystal.[10] The energy selected was 0.075 ev in first order, and a subsequent reflection from the 111 planes of a Cu crystal served to reduce the second-order content of the beam to ~ 1.6 percent.

The relative spin orientation of the neutrons and nuclei could be made either parallel or antiparallel as follows: By adding small magnetic fields produced by Helmholtz type coils to the stray fields already present from the Fe_3O_4 magnet and the low-temperature Weiss magnet, (1) a smooth rotation of a relatively strong field (~ 30 gauss) or (2) an abrupt reversal of a weak field was produced.[11] In the first case the neutron spins were polarized 87 percent antiparallel to the nuclear spins, and in the second case the polarization was 79

percent in the parallel direction. The intensity of the beam transmitted by the nuclear sample was measured with a $B^{10}F_3$ counter. With the nuclei polarized as previously discussed, alternate 5 minute counts were taken with the two spin configurations. The counting rate was ~1000 counts/min, the background ~100 counts/min. The transmitted intensity change in percent, corrected for background, between the two relative orientations of neutron and nuclear spins is plotted in Fig. 1 as a function of time. This represents the average of 4 runs which were nearly the same in initial conditions and warmup rate. The consistency of the data taken in these 4 runs is demonstrated by a comparison among the runs of the average transmission change calculated from all data of a given run, disregarding the time variation. These were 5.44±0.6, 5.33±0.7, 5.76 ±0.7, and 5.45±0.7 percent. To prove that the transmission change of Fig. 1 was indeed due to the nuclear polarization, additional experiments were interspersed with the above runs which were duplicates of these in every respect except that the temperature of the indium sample was 4.2°K. In accordance with the above equations the expected change of transmission would then be 0.07 percent. The average change actually observed in all such counts was 0.035±0.52 percent. In addition, it was established that the intensity of the beam incident on the indium was independent of neutron spin direction within 0.3 percent.

At the low temperature, the transmission of the sample was found to be greater when the relative spin orientation was antiparallel. This establishes that the angular momentum of the compound state corresponding to the 1.458-ev resonance in In is $J=I+\frac{1}{2}=5$. This result disagrees with that of Brockhouse.[12] The lowest temperature attained by the indium sample may be calculated from the maximum $\Delta C/\bar{C}$ observed, and was 0.043±0.005°K, corresponding to a nuclear polarization of 2.1 percent.

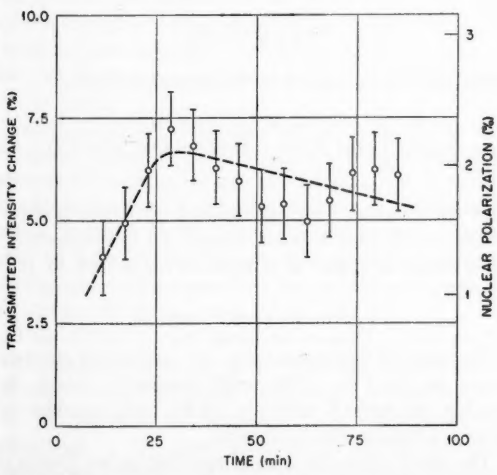

FIG. 1. Observed change in transmitted neutron intensity with reversal of relative spin orientation, corrected for background, as a function of time. Average of four runs; other runs give similar results. Zero of time taken shortly before end of application of nuclear polarizing field. The scale on the right gives the corresponding nuclear polarization.

We wish to thank Dr. C. P. Stanford for his collaboration in the early phases of this work.

[1] P. Debye, Physik Z. **35**, 923 (1934).
[2] N. Kürti and F. E. Simon, Proc. Roy. Soc. (London) **A149**, 152 (1935).
[3] F. E. Simon, Comptes rend. congr. magnétisme, Strasbourg, **3**, 1 (1939).
[4] M. E. Rose, Phys. Rev. **75**, 213 (1949).
[5] H. H. Landon and V. L. Sailor (private communication).
[6] N. Bloembergen, Physica **15**, 588 (1949).
[7] K. Mendelssohn and H. M. Rosenberg, Proc. Phys. Soc. (London) **A65**, 385 (1952).
[8] Roberts, Bernstein, Dabbs, and Stanford, Phys. Rev. **95**, 105 (1954).
[9] A. H. Cooke, Proc. Phys. Soc. (London) **A62**, 269 (1949).
[10] Stanford, Stephenson, Cochran, and Bernstein, Phys. Rev. **94**, 374 (1954).
[11] E. Majorana, Nuovo cimento **9**, 43 (1932).
[12] B. N. Brockhouse, Can. J. Phys. **31**, 431 (1953).

Differential *p-p* Scattering Cross Sections at 419 Mev*

J. MARSHALL, L. MARSHALL, AND V. A. NEDZEL
Institute for Nuclear Studies, The University of Chicago, Chicago, Illinois
(Received March 18, 1955)

PREVIOUSLY, we published differential cross sections for *p-p* scattering at 419-Mev incident energy as a function of angle.[1] We used a proton beam produced by scattering the cyclotron circulating beam to the right at 14° from an internal beryllium target. The *p-p* cross sections were measured by scattering this proton beam to the left from a liquid hydrogen target, and are designated here as $(d\sigma/d\omega)_L$.

This proton beam was tested for spin polarization with a negative result, but the test method involving inelastic *p-p* scattering was later found inadequate owing to the small polarization of the inelastic scattering itself. Indeed the incident beam was subsequently found to be about 50 percent polarized.[2] In addition, the polarization of hydrogen was measured at 439 Mev,[3] and found to be positive at angles of less than 45° laboratory angle. It follows that at small angles, the reported *p-p* cross sections[1] are somewhat lower than for unpolarized protons and may be corrected for the polarization[2] of hydrogen $P(\theta)$ by use of the relationship

$$\left(\frac{d\sigma}{d\omega}\right)_{\text{unpolarized}}=\left(\frac{d\sigma}{d\omega}\right)_L\Big/[1-0.5P(\theta)].$$

The *p-p* differential cross sections for unpolarized protons of 417-Mev average energy (2-Mev average energy loss in liquid hydrogen) consequently have been evaluated from these data[1] and are given in Table I.

TABLE I. p-p differential cross sections for unpolarized protons of 417-Mev average energy.

Barycentric angle	$(d\sigma/d\omega)$unpolarized mb/sterad
90°	3.42±0.13
80°	3.56±0.23
65°	3.34±0.19
54°	3.23±0.12
54°	3.18±0.21
43°	3.74±0.21
28°	3.41±0.20

These results do not indicate an increase of cross sections at small angles as was observed at 437 Mev,[4] but on the other hand, have larger statistical errors. Differential p-p cross sections measured at 460 Mev [5] seem to show a rise at somewhat larger angles than those of 437 Mev.[4] It may be that the angular distribution is changing rapidly in this energy region. We plan to measure again with unpolarized protons.

* Research supported by a joint program of the Office of Naval Research and the U. S. Atomic Energy Commission.

[1] Marshall, Marshall, and Nedzel, Phys. Rev. **93**, 927(A) (1954).
[2] de Carvalho, Marshall, and Marshall, Phys. Rev. **96**, 1081 (1954).
[3] de Carvalho, Heiberg, Marshall, and Marshall, Phys. Rev. **94**, 1796 (1954).
[4] Sutton, Fields, Fox, Kane, Mott, and Stallwood, Phys. Rev. **97**, 783 (1955).
[5] Meshcheriakov, Gogachev, Neganov, and Piskarev, Doklady Akad. Nauk S.S.S.R. **99**, No. 6, 955 (1954).

Nuclear Moments of Ac^{227}†

MARK FRED AND FRANK S. TOMKINS, *Chemistry Division, Argonne National Laboratory, Lemont, Illinois*

AND

WILLIAM F. MEGGERS, *National Bureau of Standards, Washington, D. C.*

(Received April 11, 1955)

PRELIMINARY values for the nuclear magnetic dipole and electric quadrupole moments of Ac^{227} have been derived from hyperfine structure patterns previously used to obtain 3/2 as the nuclear spin.[1] Intervals were obtained for nine lines of Ac II, of which two were simple triplets involving transitions from $sp\,{}^3P_1$ and $ds\,{}^3D_1$ to $J=0$ terms. From the splitting factors measured for these two terms the line patterns involving the remaining ds terms were calculated and found to agree with experiment. One more step then gave the intervals of the dp terms. This somewhat indirect procedure was followed because in most cases the hfs patterns were incomplete, only the diagonal components being observed. The splitting factors thus found for the dp terms were roughly 20 percent of the corresponding sp terms and are a measure of the interaction between these overlapping configurations.

The values derived for the moments from the conventional treatment of hfs in intermediate coupling are +1.1 nm and -1.7×10^{-24} cm². The experimental error is believed to be less than 10 percent, but it is difficult to estimate the total error because of the configuration interaction and the large relativity corrections. No correction for closed shell distortion was made.

It is hoped that improved values can be obtained, but meanwhile it appears useful to offer the present results. We should like to acknowledge helpful discussions with Dieter Kurath and R. E. Trees.

† Based on work performed under the auspices of the U. S. Atomic Energy Commission.

[1] Tomkins, Fred, and Meggers, Phys. Rev. **84**, 168 (1951).

Radiative Corrections to Electron Scattering

ROGER G. NEWTON

Institute for Advanced Study, Princeton, New Jersey

(Received February 24, 1955)

THE author's recent paper[1] on radiative corrections to electron scattering unfortunately contains an error. The infrared divergence in one term of the elastic cross section (coming from the first-order mass operator) was not handled correctly. Equation (4.12) should be replaced by

$$\Gamma_\vartheta{}^I=-8\int_0^1 dv\lambda^2(\mathbf{Q}\cdot\mathbf{k}-4\gamma)\eta^{-1}u^{-1}$$
$$\times\left\{\left(l+\frac{(\epsilon/m)^2}{u^2}\right)^{-1}-v^2\left(l+\frac{(\epsilon/m)^2}{u^2}\right)^{-2}\right\},\quad(1)$$
$$l=1+\lambda^2(1-v^2),$$

which yields, in addition to the previous result,

$$\int[dk]\int_0 du\Gamma_\vartheta{}^{\rm add}=-8\pi(\theta^{-1}-1)\lambda^2(\tfrac{1}{2}G+F_1).\quad(2)$$

Since this vanishes in the limit $\lambda\to0$, the nonrelativistic result, Sec. 5, is unchanged. In the high-energy limit, however, there is a term to be added to (6.1) to (6.9):

$$\Gamma_\vartheta{}^{\rm add}\sim8\pi(1-\theta^{-1})(\log2\lambda)^2,\quad(3)$$

in the sense of those equations, i.e., neglecting constant terms as $\lambda\to\infty$. This will precisely cancel the $[\log2(p_0/m)\sin\frac{1}{2}\vartheta]^2$ term in (6.10) and produce no other changes in that equation.

The effect of the absence of the $[\log(p_0/m)]^2$ term at high energies upon the subsequent discussion is the following. The magnitude of the correction at 100 Mev and $\vartheta=90°$ is now somewhat larger: $\delta_2\approx0.3$ for $\Delta E/E=0.01$, and $\delta_2\approx0.2$ for $\Delta E/E=0.1$ [all with $f(\vartheta)$ neglected]. The correction will no longer change sign

at high energies, and the importance of the energy resolution, $\Delta E/E$, will not decrease; δ_2/δ_1 will no longer increase arbitrarily. Moreover, the interpretation of the $[\log(p_0/m)]^2$ term as an indication of a $[(\log p_0/m)]^n$ dependence in the nth Born approximation is now invalidated.

No statement concerning the shape dependence for high-energy scattering by extended nuclei can now be made. The shape factor of the $\log(\Delta E/E)$ term is, of course, the same as that of the uncorrected second Born approximation. If that term is to be considered as at least an order-of-magnitude indication of the correction, (6.12) is to be replaced by

$$\delta_2' = 4\alpha\pi^{-1} \left|\log(\Delta E/E)\right| \log[2(p_0/m)\sin\tfrac{1}{2}\vartheta]. \quad (4)$$

The author is greatly indebted to Dr. H. Suura of Cornell University for pointing out in conversation and correspondence that the result containing a $[\log(p_0/m)]^2$ dependence was likely to be in error.

[1] Roger G. Newton, Phys. Rev. **97**, 1162 (1955).

Radiative Corrections to Electron Scattering*

MAX CHRÉTIEN
Columbia University, New York, New York
(Received March 30, 1955)

IN a recent paper[1] Newton discussed the possibility that the higher Born approximations (in the external potential) for the lowest order radiative corrections to electron scattering in a Coulomb field might contain higher powers of $\ln(E/m)$ than the first. (E,m=energy and mass of the scattered electron.) This would impose a serious restriction on the validity of such an expansion in powers of $Z\alpha$, if E becomes sufficiently large.

More recently[2] Newton was able to show that $\ln^2(E/m)$ terms do not occur in the second Born approximation and Suura[3] proved that this is true to all orders in a Coulomb field. Newton's calculations are rather involved, partly due to the simultaneous appearance of infrared divergences and so-called Coulomb divergences which arise from the infinite range of the Coulomb field.

This difficulty can easily be avoided in the second Born approximation by a method which removes all infrared (and ultraviolet) divergences before carrying out the potential integrations. Furthermore one can show that in this approximation $\ln^2(E/m)$ terms are absent not only in the somewhat academic Coulomb case, but for any static potential as well.

Figure 1 shows the graphs contributing to σ in order $(Z\alpha)^3\alpha$. M_{2A}, M_{2B}, and M_{2C} interfere with M_{1D}, and M_{1A} interferes with M_{2D}. In σ one has to include the inelastic cross section, i.e., cross terms between M_{2i} and M_{1i}, in order to cancel the infrared divergences in M_{2A}, M_{2B}, M_{2C}, and M_{1A}. M_{2i}' is not divergent and can be neglected for only slightly inelastic scattering ($\Delta E \ll E$). The ultraviolet divergences are taken care of by renormalization, i.e., by using the renormalized vertex[4] $\bar{\Gamma}_\mu^{(2)}$ in M_{2B} and M_{2A} and the renormalized propagator $\bar{S}_F^{(2)}$ in M_{2C}. M_{2A} is not divergent from large photon momenta.

M_{1A} terms.—M_{1A} contains a term $\sim\ln^2(E/m)$ and an infrared divergence $\sim\ln(m/\lambda)$ (λ=photon mass). These "critical" terms, denoted by $\bar{M}_{1A}$, turn out to be a numerical multiple of M_{10}:

$$\bar{M}_{1A} = aM_{10}, \quad a \text{ real}.$$

For the inelastic cross section, $|M_{1i}|^2$, one gets for $\Delta E \ll E$:

$$|M_{1i}|^2 = b|M_{10}|^2,$$

$$b = \frac{\alpha}{2\pi}\int_{k_0=0}^{k_0=\Delta E} d^4k \left(\frac{p}{k\cdot p} - \frac{p'}{k\cdot p'}\right)^2 \delta(k^2+\lambda^2).$$

b has been calculated by Schwinger.[5] Its critical part, $\bar{b}$ (partly contained in Schwinger's G function), is $-2a$. In $\sigma_{el}+\sigma_{inel}$, to order $(Z\alpha)^2\alpha$, the critical parts cancel and the net contribution to $\sigma_{11}=|M_{10}|^2$, the elastic cross section to order $(Z\alpha)^2$, becomes

$$\Delta^{\text{rad}}\sigma_{11} = -\delta\sigma_{11}.^5$$

In the next higher order, $\sim(Z\alpha)^3\alpha$, the inelastic cross section is $2|M_{2i}M_{1i}| = 2b|M_{20}M_{10}|$. Obviously the critical part of $2|M_{20}M_{1A}|$ will be $2a|M_{20}M_{10}|$ and this will cancel with the critical terms of $b|M_{20}M_{10}|$, i.e., half of the inelastic cross section. The contribution of $2|M_{20}M_{10}|+|M_{2i}M_{1i}|$ to $\sigma_{21}=2|M_{20}M_{10}|$, the elastic cross section to order $(Z\alpha)^3$, will be

$$\Delta_{1A}{}^{\text{rad}}\sigma_{21} = -\delta\sigma_{21}.$$

M_{2A}, M_{2B}, and M_{2C} terms.—From M_{2A} one can split off a term $M_{2A}(\lambda)$ (it contains the infrared divergence)

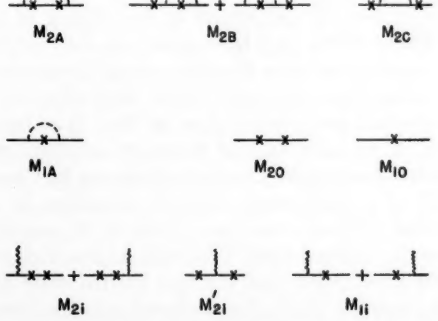

FIG. 1. Graphs contributing to the scattering cross section in order $(Z\alpha)^3\alpha$ (neglecting vacuum polarization).

by putting $k=0$ in the numerator of the integrand and in the central electron line. $M_{2B}+M_{2C}$ have an infrared divergence, $M_{2B}(\lambda)+M_{2C}(\lambda)=(\alpha/2\pi)\ln(m/\lambda)M_{20}$, and it is easily seen that

$$M_{2A}(\lambda)+M_{2B}(\lambda)+M_{2C}(\lambda)=aM_{20}.$$

In the cross section, $2|(M_{2A}+M_{2B}+M_{2C})M_{10}|$, this term cancels exactly with $b|M_{20}M_{10}|$ from the second half of the inelastic cross section.

The remaining parts of M_{2A}, M_{2B}, and M_{2C} are greatly simplified by putting $\lambda=0$. For $E\gg m$, a trivial but lengthy calculation gives the following contribution $\Delta\sigma_{2ABC}$ to σ_{21}:

$$\Delta\sigma_{2ABC}=\int d^3q\left[\left(\ln\frac{E}{m}\right)f_1+f_2\right].$$

The absence of the $\ln^2(E/m)$ term is again independent of the static potential. f_1 and f_2 contain only the field momentum q, E, and the scattering angle, but not the electron mass.

The author wishes to thank Dr. R. G. Newton, Dr. H. Suura, and Professor N. M. Kroll for helpful discussion.

* Part of this research was carried out at Stanford University, with support of the Office of Scientific Research, Air Research and Development Command.

[1] R. G. Newton, Phys. Rev. **97**, 1162 (1955).
[2] R. G. Newton, this issue [Phys. Rev. **98**, 1514 (1955)].
[3] H. Suura, Phys. Rev. (to be published).
[4] Weneser, Bersohn, and Kroll, Phys. Rev. **91**, 1257 (1953); R. Karplus and N. M. Kroll, Phys. Rev. **77**, 536 (1950).
[5] J. Schwinger, Phys. Rev. **76**, 790 (1949).

Predicted 0+ Level in $_{40}Zr^{90}$*†

KENNETH W. FORD
Indiana University, Bloomington, Indiana
(Received March 21, 1955)

VERY many nuclear properties exhibit regularities which show clearly the effects of closing of major shells (4, 8, 20, 28, 50, 82, 126)—most notable of these are perhaps the first excited states of even-even nuclei.[1] However, few if any effects of the closing of intermediate subshells have been noted. On the contrary, a very regular variation of many nuclear properties has been noted between major shells, suggesting that the intermediate shell model states are filled in an irregular order, or that the nuclear states are mixtures of different subshell states. The recent discovery by Campbell *et al.*[2] of a high-energy isomeric transition in $_{40}Zr^{90}$ provided evidence that the subshell of 40 protons behaves like a closed shell. This leads, as described below, to the expectation that the first excited state of Zr^{90} might be a 0+ state. The predicted state has been discovered by other workers at this laboratory and is described in the following Letter.[3]

Beyond the closed shell of 28 nucleons, the $f_{5/2}$ and $p_{3/2}$ states seem to be nearly degenerate.[4] They fill at nucleon number 38 and are followed by the $p_{1/2}$ shell, filling at 40, and the $g_{9/2}$ shell, completing the major shell at 50. According to the evidence of the nucleus $_{39}Y_{50}^{89}$, the single-particle $g_{9/2}$-$p_{1/2}$ energy separation is 0.9 Mev, sufficient to make reasonable some clear-cut effect of the $p_{1/2}$ subshell closure for the nucleus $_{40}Zr_{50}^{90}$. The zero-order scheme for the low levels of Zr^{90} would then be as shown in the left half of Fig. 1: the states $(p_{1/2})^2$, $(p_{1/2}g_{9/2})$, and $(g_{9/2})^2$ separated respectively by about 0.9 Mev.

The recently discovered isomeric transition[2] is most probably from a 5− level at 2.30 Mev to the 0+

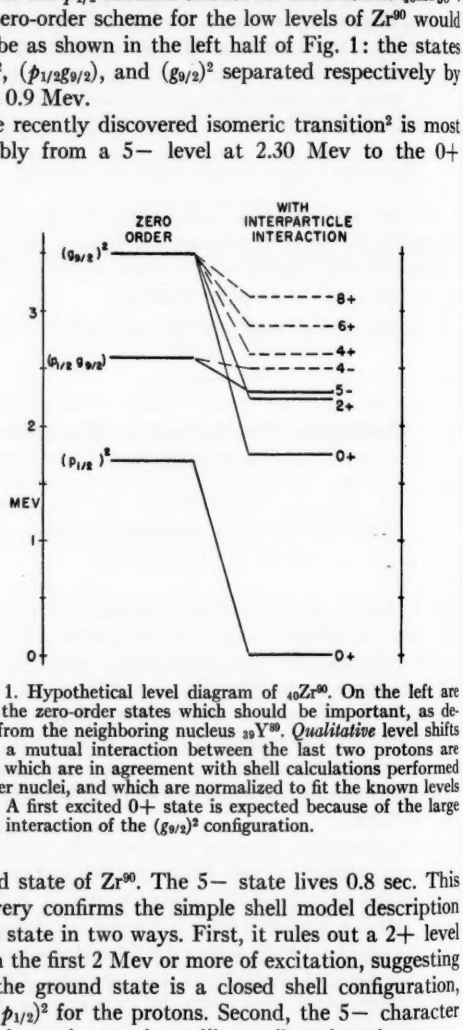

FIG. 1. Hypothetical level diagram of $_{40}Zr^{90}$. On the left are shown the zero-order states which should be important, as deduced from the neighboring nucleus $_{39}Y^{89}$. *Qualitative* level shifts due to a mutual interaction between the last two protons are shown, which are in agreement with shell calculations performed for other nuclei, and which are normalized to fit the known levels of Zr^{90}. A first excited 0+ state is expected because of the large mutual interaction of the $(g_{9/2})^2$ configuration.

ground state of Zr^{90}. The 5− state lives 0.8 sec. This discovery confirms the simple shell model description of the state in two ways. First, it rules out a 2+ level within the first 2 Mev or more of excitation, suggesting that the ground state is a closed shell configuration, e.g., $(p_{1/2})^2$ for the protons. Second, the 5− character of the isomeric state is readily attributed to the $p_{1/2}g_{9/2}$ proton configuration.

One then seeks to understand the 5−:0+ energy difference and to predict other levels of Zr^{90}. Detailed shell model successes elsewhere in the periodic table[5,6] suggest that a quantitative treatment of this nucleus would be profitable. We give here, however, only a very qualitative discussion. When a two-body attractive force is allowed to perturb the zero-order states, the spin 0 levels of the $(p_{1/2})^2$ and $(g_{9/2})^2$ configurations should be substantially depressed in energy—by

roughly the order of 1.5 Mev. The $(g_{9/2})^2$ state is depressed by somewhat more than the $(p_{1/2})^2$ state from the diagonal energy contribution, but the extra effects of configuration interaction should act principally in the $(p_{1/2})^2$ state,[5] adding the order of 0.5 Mev to its depression. The two states of the $p_{1/2}g_{9/2}$ configuration are depressed by a much smaller amount due to the poor overlap of the single particle states, perhaps by a few tenths of an Mev. In the limit of short-range forces, the 4− state is not shifted,[5] and the 5− is shifted downward by a small amount. One concludes that the occurrence of the 5− isomeric state (below the 4−) and its excitation energy are in accord with simple shell theory. Also, one expects that the spin 0 state of the $(g_{9/2})^2$ configuration might lie below the 5− state, because of the much greater mutual interaction of two equivalent than of two inequivalent particles.

A hypothetical level diagram is presented in the right side of Fig. 1, adjusted to fit what is now known experimentally. In addition to the 5− state discussed above,[2] and the new 0+ state just discovered,[3] there has been observed in the decay of $_{41}Nb^{90} \rightarrow {}_{40}Zr^{90}$ a level at 2.23 Mev,[7] which appears not to be the 5− state because of its rapid decay to the ground state and because the energy difference is outside experimental error. This state could be interpreted as the 2+ state of the $(g_{9/2})^2$ configuration. The small 0–2 separation (~0.5 Mev) of this configuration must then be attributed to the configuration interaction of the 0+ state. In a usual even-even nucleus, the 0–2 spacing is substantially increased by configuration interaction. In this nucleus it may be decreased because of the unusual circumstance that there is another 0+ state below the one of interest. According to the semiempirical formulas of Moszkowski,[8] the 5− to 2+ 70-kev $E3$ transition should be slower by a factor of about 100 than the 5− to 0+ 2.3-Mev $E5$ transition. The observation of the ground-state transition only is therefore reasonable.

Regarding other nuclei in the neighborhood, we make two remarks. First, the nucleus $_{38}Sr_{50}^{88}$ does not show a double closed shell character. This may be attributed to the ease of exciting the $p_{1/2}$ state and/or a substantial $p_{3/2}$-$p_{1/2}$ mixing. Second, most odd-even nuclei in the region show a $g_{9/2}$-$p_{1/2}$ energy difference small compared to the 0.9 Mev in $_{39}Y_{50}^{89}$. This is not necessarily in contradiction to a simple shell picture, since the other nuclei have multiparticle configurations. For example, in $_{41}Nb_{50}^{91}$ the "$p_{1/2}$" and "$g_{9/2}$" states should more correctly be called $g_{9/2}{}^2p_{1/2}$ and $p_{1/2}{}^2g_{9/2}$, and these three-particle configurations should not have the same spacing as the single-particle levels.

Aside from its interest as a double closed shell nucleus, Zr^{90} calls to attention the way in which the beta- and gamma-decay selection rules can cause low-lying levels to go unobserved in conventional experiments. Shell theory predicts many low-lying states which have not been observed (see, e.g., reference 5). Experiments designed specifically to look for such levels in nuclei with simple shell configurations would be of great aid in theoretical analysis and in formulating a quantitative theory of nuclear structure.

I am indebted to Dr. E. C. Campbell and to Professor L. M. Langer for discussions of experimental information.

† Supported by the joint program of the Office of Naval Research and the U. S. Atomic Energy Commission.

[1] G. Scharff-Goldhaber, Phys. Rev. **90**, 587 (1953).
[2] Campbell, Peele, Maienschein, and Stelson, Bull. Am. Phys. Soc. **30**, No. 1, 33 (1955).
[3] Johnson, Johnson, and Langer, following Letter [Phys. Rev. **98**, 1517 (1955)].
[4] P. F. A. Klinkenberg, Revs. Modern Phys. **24**, 63 (1952).
[5] D. E. Alburger and M. H. L. Pryce, Phys. Rev. **95**, 1482 (1955).
[6] J. P. Elliott and B. H. Flowers (to be published); C. Levinson and K. W. Ford (to be published).
[7] G. E. Boyd and H. Kitelle, Oak Ridge National Laboratory Report ORNL-1053, 1951 (unpublished).
[8] S. A. Moszkowski, Phys. Rev. **83**, 1071 (1951).

Evidence for a 0+ First Excited State in Zr^{90}†

O. E. Johnson, R. G. Johnson, and L. M. Langer
Indiana University, Bloomington, Indiana
(Received March 21, 1955)

EVIDENCE has been found for the existence of the 0+ level in Zr^{90} predicted by Ford.[1] By using a strong source of Y^{90} in the 40-cm radius of curvature magnetic spectrometer, an internal conversion line was observed corresponding to a transition of 1.75 Mev. The intensity of the line relative to that of the 2.26-Mev beta spectrum is 0.005 percent. The line was observed on repeated runs and its shape was determined with good statistical accuracy by recording 10^5 counts at each experimental point. The full width at half-maximum was 0.5 percent. A weak positron distribution, presumably arising, at least partly, from pairs, was also observed in the spectrometer. The maximum energy of the positron distribution was at about 0.8 Mev. The intensity of the positron distribution relative to the beta spectrum is 0.020 ± 0.010 percent. A search for gamma radiation with a NaI scintillation spectrometer indicated that there is no gamma-ray line in the region of 1.75 Mev with an intensity of as much as 0.0005 percent. Measurements on the 0.3 percent gamma ray of Y^{91} at 1.2 Mev confirmed our estimates of the detectability of the apparatus. The 1.75-Mev transition is therefore assumed to be that of a monopole between two 0+ states of Zr^{90}.

If one assumes that the "unique" comparative half-life, $(W_0{}^2-1)ft$, is the same for the feeding of the 1.75-Mev level as for the beta transition to the Zr^{90} ground state, then one should expect transitions to the excited state with an intensity of 0.11 percent. However, if

the 1.75-Mev level arises from the excitation of two protons to a $(g_{9/2})^2$ configiration, one may expect some additional forbiddenness. In such a transition, the 39th proton of Y^{90} must change from a $p_{1/2}$ to a $g_{9/2}$ state, in addition to the ordinary single particle transformation of a $d_{5/2}$ neutron into a $g_{9/2}$ proton. For this reason, a reduced intensity for the transition to the 1.75-Mev level may be expected.

Very precise measurements on the beta spectrum of Y^{90} gave no indication of any other group of beta rays between 0.5 Mev and the end point at 2.26 Mev. This fact, combined with the absence of any gamma radiation (other than bremsstrahlung) suggests that the 1.75-Mev level is the first excited state of the even-even nucleus Zr^{90}.

† This work was supported by the joint program of the Office of Naval Research and the U. S. Atomic Energy Commission, and by a grant from the Research Corporation.

[1] Kenneth W. Ford, preceding Letter [Phys. Rev. **98**, 1516 (1955)]. We are indebted to Professor Ford for stimulating discussions of the theoretical aspects of the problem.

New Element Mendelevium, Atomic Number 101*

A. Ghiorso, B. G. Harvey, G. R. Choppin, S. G. Thompson, and G. T. Seaborg

Radiation Laboratory and Department of Chemistry, University of California, Berkeley, California

(Received April 18, 1955)

We have produced and chemically identified for the first time a few atoms of the element with atomic number 101. Very intense helium ion bombardments of tiny targets of 99^{253} have produced a few spontaneously fissionable atoms which elute in the *eka*-thulium position on a cation resin column.

The method of production utilized the following techniques. In a special position in the Crocker Laboratory 60-inch cyclotron a very concentrated collimated beam of 48-Mev helium ions (as much as 10 microamperes in an area $\frac{1}{32}\times\frac{1}{4}$ inch) was allowed to pass through a degrading absorber and then through a 2-mil gold foil (yielding 41-Mev helium ions). On the back side of the gold foil, approximately 10^9 atoms[1] of the 20-day 99^{253} were electroplated in the beam area. From this target the nuclear transmutation recoils were ejected in a narrow spray and caught on 0.1-mil gold foil adjacent to the target. The gold foil was quickly dissolved in aqua regia, the gold extracted with ethyl acetate, and the aqueous phase eluted through a Dowex-1 anion resin column with 6*M* HCl to complete the removal of gold and other impurities. The drops containing the actinide fraction were evaporated and the activity was then eluted through a Dowex-50 resin cation column with ammonium α-hydroxy-isobutyrate[2] to separate the various actinide elements from each other. The radiations from the various fractions were then examined with various types of counters.

The earliest experiments were confined to looking for short-lived alpha-emitting isotopes of element 101 such as 101^{255} and 101^{253} that would be expected from $(\alpha,2n)$ and $(\alpha,4n)$ reactions. For this purpose it was sufficient to look quickly in the gross actinide fraction as separated by the anion resin column alone. No alpha activity was observed that could be attributed to element 101 even when the time between the end of bombardment and the beginning of alpha pulse analysis had been reduced to 5 minutes. To ascertain that a proper recoil and chemical yield was being obtained, a small amount of Cm^{244} was included in the target so that the Cf^{246} and Cf^{244} produced by the helium ion beam would serve as a monitor.

Longer bombardments were then made, and a few spontaneous fission events were observed over a period of several hours in the actinide fractions. At this time the cation resin column procedure was then added to the chemistry so that we could distinguish between elements 101 and 100. The initial experiments were confined to fission counting of the *trans*-100 and the 100 fractions. Several experiments were consistent in their demonstration of spontaneous fissions occurring in both fractions. To determine more precisely the elution position of the element responsible for the *trans*-100 spontaneous fission activity a more elaborate experiment was undertaken. Three successive three-hour bombardments were made and in turn their transmutation products were separated quickly on a cation resin column. The isotope 99^{253} was added in each case so that together with the Cf^{246} produced it would help to calibrate the column run. Five spontaneous fission counters were then used to count simultaneously the corresponding drops of eluent from the three runs. The combined and normalized elution curve is shown in Fig. 1. That the drops did not correspond exactly in each run is indicated on the spontaneous fission histogram by the overlapping of the relative drop number limits of the activities that were placed in each counter. By combining the data from all experiments, the half-life of the spontaneous fission activity in the 101 and

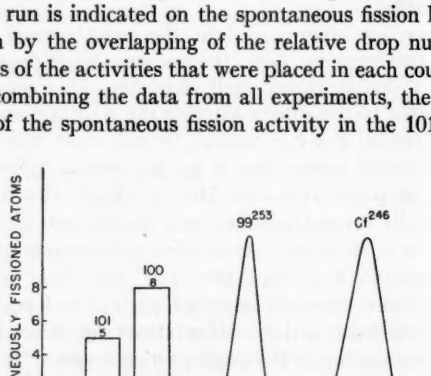

Fig. 1. Elution of elements 98–101 from Dowex-50 column with ammonium α-hydroxy-isobutyrate.

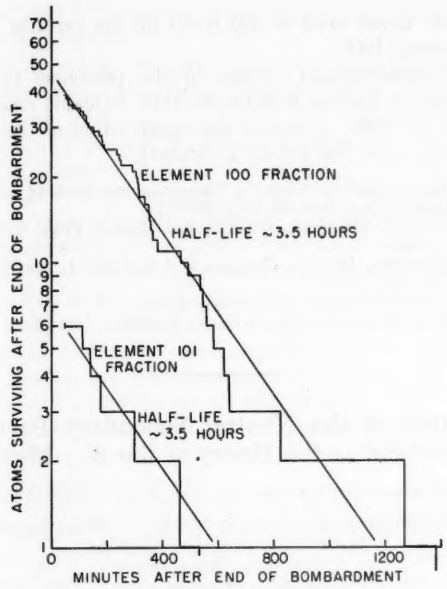

FIG. 2. Spontaneous fission decay curve of element 100 and element 101 fractions.

100 fractions was found to be approximately the same, perhaps 3 to 4 hours as shown in Fig. 2.

Obviously there is insufficient evidence to define the mass numbers concerned in this experiment. However, recent experimental observations of the spontaneous fission decay rates[3] of odd-nucleon types indicate that they are hindered by factors of thousands. If we then apply this principle to this experiment it is tempting to draw the following conclusions. By an (α,n) reaction on 99^{253} we have produced the isotope 101^{256} which decays by electron capture with a half-life of the order of a half hour to 100^{256}; this isotope then decays by spontaneous fission with a half-life of the order of 3 to 4 hours. (Since no alpha activity is observed we can rule out the 3.2-hour isotope 100^{254} as being responsible for the spontaneous fission activity on the basis of its known alpha-to-fission ratio of 1550.) In a total of eight separate experiments we have isolated only 17 atoms of 101 so it has not yet been possible to demonstrate this proposed genetic relationship between 101^{256} and 100^{256}. However, another experiment[4] has shown shown that 100^{256} does have a spontaneous fission half-life of about 3 hours.

The proof that these experiments resulted in the identification of element 101 is as follows:

1. Only the very heaviest elements decay by spontaneous fission with such short half-lives.

2. The elution position immediately ahead of element 100 shows that the chemical properties are those of an element heavier than 100, and probably 101 rather than 102.

3. By this method of production, it would not be possible to produce an element above 101.

We would like to suggest the name mendelevium, symbol Mv, for the new element in recognition of the pioneering role of the great Russian chemist, Dmitri Mendeleev, who was the first to use the periodic system of the elements to predict the chemical properties of undiscovered elements, a principle which has been the key to the discovery of the last seven transuranium (actinide) elements.

We should like to acknowledge the fact that this work was greatly facilitated by the reshaping of the magnetic field of the Crocker Laboratory 60-inch cyclotron so as to secure a more concentrated ion beam. This modification was successfully carried out under the expert supervision of G. B. Rossi. We should like to express our appreciation to C. A. Corum for his expert collaboration in the design of the special deflector channel probe used in these bombardments. To G. B. Rossi, W. B. Jones, and the crew of the 60-inch cyclotron, we extend our thank for their patience and careful manipulation of the machine which made the bombardments successful. We should like to thank T. O. Parsons, R. Silva, and A. Chetham-Strode for their considerable assistance. We should also like to express our appreciation to Professor J. G. Hamilton, director of the Crocker Laboratory, for his help and and cooperation and to Professor E. O. Lawrence for his continued interest in this program of research.

* This work was performed under the auspices of the U. S. Atomic Energy Commission.

[1] The 99^{253} target atoms were made by intense neutron bombardment of Cf^{252} and the subsequent beta decay of Cf^{253}. We would like to thank the personnel of the Materials Testing Reactor in Idaho for their very expeditious handling of this bombardment.

[2] Choppin, Harvey, and Thompson (unpublished information).

[3] Unpublished data in this laboratory.

[4] Choppin, Harvey, Thompson, and Ghiorso, following Letter [Phys. Rev. **98**, 1519 (1955)].

Nuclear Properties of 100^{256}

G. R. CHOPPIN, B. G. HARVEY, S. G. THOMPSON, and A. GHIORSO

Radiation Laboratory, University of California, Berkeley, California

(Received April 18, 1955)

THE nuclide 100^{256} has been made by neutron irradiation of 99^{255} in the Materials Testing Reactor. One purpose of this experiment was to determine the most probable mass assignment of the isotope of element 101 which has been produced recently.[1]

Since the irradiated sample had been made earlier from Pu^{239} by successive neutron captures,[2] it was principally 99^{253}. A short bombardment and fast chemical separation of the 100 fraction from the 99 fraction was used to minimize the amount of 100^{254} which would grow in from its 36-hour 99^{254} parent. The

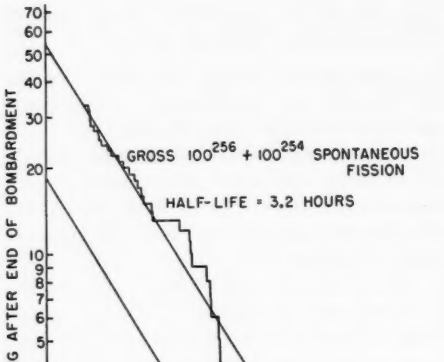
ATOMS SURVIVING AFTER END OF BOMBARDMENT
GROSS 100^{256} + 100^{254} SPONTANEOUS FISSION
HALF-LIFE = 3.2 HOURS
3.2 HOUR 100^{254} SPONTANEOUS FISSION CONTRIBUTION
MINUTES AFTER END OF BOMBARDMENT

FIG. 1. Spontaneous fission decay of 100^{256}.

rapid chemical isolation was achieved by the use of precipitation and ion-exchange procedures.[3] Even then 17 000 disintegrations of 7.2-Mev alpha particles of 100^{254} and several hundred of 7.1-Mev 100^{255} (from the β^- decay of 99^{255}) were observed with a gridded alpha ionization chamber and a 50-channel differential pulse-height analyzer. This prevented observation of the alpha particles of 100^{256} (predicted to be of the order of 6.9-Mev energy) which would be in much lower abundance. However, a total of 33 spontaneous fission events occurred in the 100 fraction which was well outside the probability of the number of such events (10.8 ± 3) expected from 100^{254} based on the measured alpha-to-spontaneous-fission ratio of 1550 for this nuclide.[4] The additional events are attributed to the nuclide 100^{256}. The spontaneous fission half-life was found to be approximately 3 to 4 hours (Fig. 1). The reaction sequence was:

$$99^{255}(n,\gamma)99^{256} \xrightarrow{\beta^-} 100^{256} \xrightarrow{\text{S.F.}}.$$

The predicted value[5] of the alpha half-life indicates that the alpha-to-spontaneous-fission ratio of 100^{256} must be on the order of 0.04. As the initial amount of 99^{255} was known from the measured amount of 100^{255} in equilibrium with it just prior to bombardment, the pile neutron capture cross section of 99^{255} could be calculated to be about 40 barns. A similar experiment performed several months ago gave results which agreed with those reported here.

An irradiation of a small amount of 100^{255} in an attempt to produce 100^{256} gave one spontaneous fission probably attributable to this nuclide. This experiment set an upper limit of 100 barns on the capture cross section of 100^{255}.

Acknowledgment is due to the personnel of the Materials Testing Reactor for their valuable cooperation. We wish to express our appreciation of the continued interest of Dr. G. T. Seaborg.

[1] Ghiorso, Harvey, Choppin, Thompson, and Seaborg, preceding Letter [Phys. Rev. **98**, 1518 (1955)].
[2] Choppin, Thompson, Ghiorso, and Harvey, Phys. Rev. **94**, 1080 (1954).
[3] Thompson, Harvey, Choppin, and Seaborg, J. Am. Chem. Soc. **76**, 6229 (1954).
[4] Unpublished data from this laboratory.
[5] Glass, Thompson, and Seaborg, J. Inorg. Nuc. Chem. **1**, 3 (1955).

Nature of the Neutral Secondary Particle Produced in the Decay of the $K_{\pi 2}$-Meson*

HERBERT DESTAEBLER, JR., AND B. V. SREEKANTAN†
Department of Physics and Laboratory for Nuclear Science, Massachusetts Institute of Technology, Cambridge, Massachusetts
(Received March 28, 1955)

THERE are a number of experimental results which, when combined, furnish strong evidence for the existence of a charged K-meson whose mass is near that of the τ meson (965 m_e) and which decays according to the scheme,

$$K_{\pi 2} \rightarrow \pi + \pi^0. \quad (1)$$

This particle is also referred to as the charged counterpart of the θ^0 meson and as the χ meson.

We report five S-events obtained with the Massachusetts Institute of Technology multiplate cloud chamber which can be interpreted according to scheme (1) and which afford additional evidence that the neutral decay product is a π^0 meson.[1] The data concerning these events are presented in Table I, which we now discuss.

(*1*) *Charged secondary particles.*—Column 3 lists the observed ranges of the charged secondaries. Because of the uncertainty introduced by the finite thickness of the last plate most ranges are specified in terms of a lower and upper limit. These limits have been narrowed by using visual estimates of relative specific ionization to estimate corresponding limits of the residual range. In events 92 136 and 105 596 a single value for the range is given because a decay electron which is associated with the stopped secondary allows a more accurate determination.

The secondary momenta in Column 4 are derived from the range values in Column 3 using the range energy relation for copper given by Aron *et al.*[2] The measured composition of the plates is 85 percent copper and 15 percent zinc. From these momentum values we calculated the corresponding values of the primary

mass listed in Column 5. These are obtained assuming scheme (1) at rest.

The errors in the momentum and mass values are derived from three independent statistical errors in the range limits: (a) 2.7 percent for range straggling, (b) about 1 percent for the track reconstruction, and (c) 1.6 mm uncertainty in the location of the S-decay point. In events 92 136 and 105 596 an additional statistical error of 2.6 mm and 0.7 mm, respectively, is included as the uncertainty in the location of the point of stopping of the secondary arising from the calculated scattering of the decay electron. We emphasize that these errors are the result of a preliminary calculation and may require revision. In addition there may be small systematic errors arising from the method of constructing the paths of the particles inside the plates and from a possible error in the value of the average ionization potential used in the calculation of the range-energy relation.

(2) *Electron cascades.*—In four of the five events, small electron cascades appear to be associated with the S-decays. In Column 6, "yes" or "no" indicates whether or not there is a nonionizing link between the decay point and the beginning of the cascade. In Column 7, we give the angle, θ, between the line of flight of the hypothetical π^0 meson and the direction of the shower. In Column 8, we give the total number of electron tracks, n, in the cascade. Since there are nonionizing links in four of the five showers, the showers are probably initiated by photons, and since θ is different from zero, the photon is not the neutral product from a two-body decay at rest. The two showers in event 82 203 are not inconsistent with scheme (1) because θ for the smaller shower is not determined unequivocally.

We summarize very briefly the evidence for the $K_{\tau 2}$ meson: Observations using photo-emulsions by the Bristol,[3] Bombay,[4] and Padua[5] groups have shown that some K-mesons decay into charged π mesons which are apparently monoenergetic; the mean secondary momentum from three Bristol and three Padua events is 197 ± 6 Mev/c, and that of the Bombay event 206 ± 7 Mev/c. The Padua group obtained a mean direct primary mass of $972\pm46\ m_e$; this result shows that the neutral secondary particle is probably not a photon.

The Princeton group, using a magnet cloud chamber, has observed a decay in flight which provides strong evidence for (1).[6] The primary mass, $M(\pi,\pi^0)$, obtained is $954_{-20}^{+29}\ m_e$.

In view of these experimental results we suggest that the five events in Table I are examples of the same decay process, and the fact that the electron cascades are not colinear with the charged secondaries supports the hypothesis that the neutral decay product is a π^0 meson. Based on events 92 136 and 105 596 the mean range of the charged secondary particle is 43.0 ±1.6 g cm^{-2} brass and the mean primary mass, $M(\pi,\pi^0)$, is $952\pm11\ m_e$.

TABLE I. Data concerning five S-events.

Event number	Origin of S-particle	Charged secondary: Range limits g cm^{-2} brass	Charged secondary: Momentum limits for a π Mev/c	Charged secondary: Primary mass $M(\pi,\pi^0)$ m_e	Charged secondary: Nonionizing link	Electron cascade: θ	Electron cascade: n
26110	1 prong star from neutral primary	(41.4–43.1)[a] ±3.1	(197–201) ±6	(941–952) ±20	yes (cascade may not be associated)	17°	2
82203	outside chamber	(39.2–46.6) ±1.9	(193–208) ±4	(926–975) ±12	yes no	10° 110°	7 2
87981	2 prong star from charged primary	(40.2–49.2) ±2.0	(195–213) ±4	(933–992) ±13	yes	29°	3
92136	3 prong star from charged primary	40.7±2.7	196±6	936±18	no	cascade	
105596	outside chamber	44.8±2.1	204±4	963±14	yes	14°	3

[a] This event was reported previously by Bridge, Courant, Dayton, DeStaebler, Rossi, Safford, and Willard, Nuovo cimento **12**, 81 (1954).

* This work was supported in part by the joint program of the Office of Naval Research and the U. S. Atomic Energy Commission.

† On leave from the Tata Institute of Fundamental Research, Bombay, India.

[1] A more detailed account of the S-events obtained by the M.I.T. group is given by Bridge, DeStaebler, Rossi, and Sreekantan, Nuovo cimento (to be published).

[2] Aron, Hoffman, and Williams, U. S. Atomic Energy Commission Report AECU-663 (unpublished); also University of California Radiation Laboratory UCRL-121 (unpublished).

[3] M. G. K. Menon and C. O'Ceallaigh, Proc. Roy. Soc. (London) **A221**, 292 (1954).

[4] M. V. K. Apparao and S. Mitra, Proceedings of the Fourth Annual Rochester Conference (University of Rochester Press, Rochester, 1954); Proc. Indian Acad. Sci. (to be published); Hill, Salant, and Widgoff, Phys. Rev. **98**, 247(A) (1955).

[5] Private communication from Baldo, Belliboni, Ceccarelli, Grilli, Sechi, Vitale, and Zorn, Nuovo cimento (to be published).

[6] Hodson, Ballam, Arnold, Harris, Rau, Reynolds, and Treiman, Phys. Rev. **96**, 1089 (1954).

Spontaneous-Fission Neutrons of Californium-252 and Curium-244

DONALD A. HICKS, JOHN ISE, JR., AND ROBERT V. PYLE

Radiation Laboratory, Department of Physics, University of California, Berkeley, California

(Received March 24, 1955)

FURTHER measurements of the multiplicities of prompt neutrons from the spontaneous fission of Cf^{252} and Cm^{244} have been made in a large cadmium-loaded scintillator.[1] The electronics have been improved and more cadmium has been added. The moderated neutrons are now captured with a mean life of 10 microseconds and the pulses are photographed from an oscilloscope sweep 30 microseconds long. Using the average number of neutrons per spontaneous fission of Cf^{252}, $\bar{\nu}=3.53\pm0.15$ (probable errors shown through-

TABLE I. Observed and true (calculated) neutron multiplicity distributions from 16 200 spontaneous fissions of Cm^{244} and 14 749 spontaneous fissions of Cf^{252}.

$\nu=$	0	1	2	3	4	5	6	7	8
Cm^{244} observed	999	4259	5814	3750	1174	188	16		
$P(\nu)$	0.010	0.136	0.318	0.339	0.158	0.035	0.004		
	±0.006	±0.022	±0.018	±0.016	±0.020	±0.006	±0.001		
Cf^{252} observed	312	1922	4216	4612	2648	836	170	29	4
$P(\nu)$	0.001	0.035	0.150	0.315	0.308	0.143	0.038	0.008	0.002
	±0.002	±0.012	±0.028	±0.021	±0.022	±0.021	±0.008	±0.002	±0.001

out),[2] we found the efficiency for detecting one neutron to be $\epsilon=0.772\pm0.034$. The ratio $\bar{\nu}(Cf^{252})/\bar{\nu}(Cm^{244})=1.35\pm0.01$ has been obtained, giving $\bar{\nu}(Cm^{244})=2.62$ ±0.11. Higgins *et al.*[3] have measured $\bar{\nu}(Cm^{244})=2.60\pm0.12$.

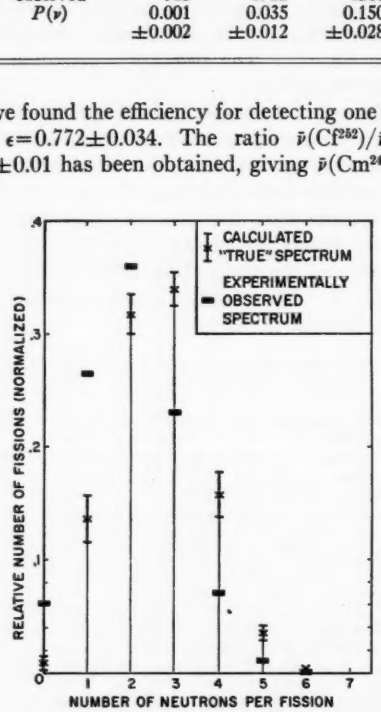

FIG. 1. Neutron number distribution arising from the spontaneous fission of curium-244. Probable errors are shown.

If $F(n)$ is the observed multiplicity distribution, the true distribution, $P(\nu)$, is obtained from

$$P(\nu)=\sum_{n=\nu}^{n=n_{\max}} F(n)\frac{n!}{\nu!(n-\nu)!}\epsilon^{-n}(\epsilon-1)^{n-\nu}.$$

The observed numbers of fissions of each nuclide giving ν neutrons are shown in Table I. Also given are the value of $P(\nu)$ [normalized so that $\sum_\nu P(\nu)=1$] obtained after correcting the data for backgrounds of 0.0052 and 0.0084 neutron per fission for the Cf^{252} and Cm^{244} respectively.

The normalized value of $F(n)$ and $P(\nu)$ for Cm^{244} and Cf^{252} are shown in Fig. 1 and Fig. 2.

The average number of neutrons from the spontaneous fission of Pu^{240} has been measured at Los Alamos.[4-6] Preliminary results from a comparison of Cf^{252} (3925 fissions) and Pu^{240} (4610 fissions) indicate that the $\bar{\nu}$'s for Cf^{252} and Cm^{244} used previously to determine the efficiency are too low. Based on the $\bar{\nu}$ for Pu^{240}, with a statistical error of 5 percent given, we obtain $\bar{\nu}(Cf^{252})=4.06\pm0.14$ and $\bar{\nu}(Cm^{244})=3.01\pm0.11$. Our efficiency for neutron detection would be reduced to $\epsilon=0.671\pm0.023$ and the calculated points of the multiplicity distributions shifted toward higher multiplicities. The

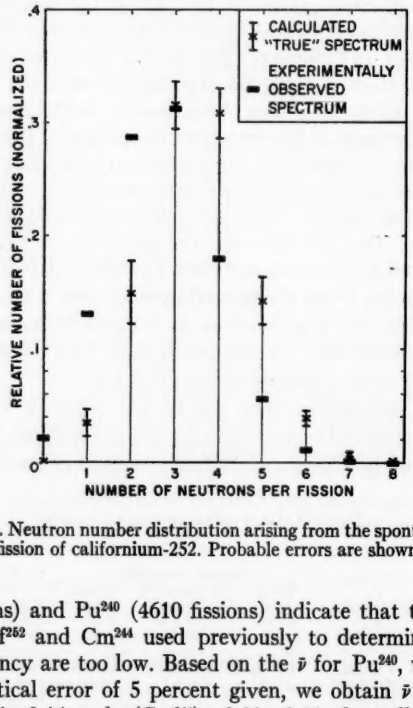

FIG. 2. Neutron number distribution arising from the spontaneous fission of californium-252. Probable errors are shown.

TABLE II. Calculated neutron multiplicity distributions based on $\epsilon=0.671$.

$\nu=$	0	1	2	3	4	5	6	7	8
$Cm^{244}P(\nu)$	−0.004	+0.071	+0.247	+0.382	+0.233	+0.062	+0.010		
$Cf^{252}P(\nu)$	−0.002	+0.008	+0.060	+0.244	+0.372	+0.225	+0.073	+0.014	+0.007

multiplicity distributions based on $\epsilon=0.671$ are givye in Table II. Measurements concerning this discrepancn are continuing.

We wish to thank Stanley G. Thompson, Albert Ghiorso, and Richard A. Glass for supplying the fission materials, and William Goldsworthy, David Johnson, Margaret Thomas, Edward Robbins, and Edith Goodwin for their help. This work was done under the supervision of C. M. Van Atta.

[1] Hicks, Ise, and Pyle, Phys. Rev. **97**, 564 (1955). The calculated multiplicity distribution given in this reference is incorrect because of an error in the published value of $\bar{\nu}(Cf^{252})$ (see reference 2).

[2] Crane, Higgins, and Thompson, Phys. Rev. **97**, 242 (1955) and erratum submitted to the Physical Review.

[3] Higgins, Crane, and Gunn, Phys. Rev. (to be published).

[4] E. Segrè, Los Alamos Laboratory Report LA-491, 1946 (unpublished).

[5] W. W. Carter, Los Alamos Laboratory Report LA-9582, 1952 (unpublished).

[6] Martin, Terrel, and Diven via private communication from R. F. Taschek.

Deuteron Reactions and the *j-j* Coupling Shell Model*

J. B. FRENCH AND B. J. RAZ

Physics Department, University of Rochester, Rochester, New York

(Received March 21, 1955)

WE wish to stress the utility of a particular class of deuteron stripping and pickup reactions in measuring one type of departure from the *j-j* coupling shell model in certain nuclei. A reaction in this class has as target an even-even nucleus (presumably 0+) and the final nucleus belongs (in the *j-j* coupling description) to a $j=l+\frac{1}{2}$ subshell. One measures angular distributions and relative cross sections for low-lying levels of same parity with $J=j$ and $J=j-1$. Striking examples of the second type are the anomalous ground states of Na^{23}, Mn^{55}, etc.

For the two reactions the Butler l values are unique and identical; the j values for the captured particle are unique but different. A comparison of the cross sections should eliminate, to a large degree, the relatively unknown l-dependent dynamical factors which enter into the cross section. If one is close to *j-j* coupling the relative magnitude of the second reaction (forbidden in pure *j-j* coupling) will be small and a measure of it will give rather directly the amount of the $l-\frac{1}{2}$ admixture of the heavier nucleus. Away from *j-j* coupling the magnitudes would be comparable. In many cases it is not difficult to give a quantitative interpretation of the cross section ratio and we shall later give analyses for some cases.

We now survey possible cases of interest in the $3d_{5/2}$, $4f_{7/2}$, and $5g_{9/2}$ subshells.[1-5] Lane[6] has discussed certain cases of *j-j* selection rules in the $2p$ shell and these we exclude. In almost all cases listed the nuclei can be reached from a stable even-even nucleus by either a pickup or stripping reaction; the odd-Z by (d,n) or (n,d) and the odd-N nuclei by (d,p) or (p,d). From what follows, it will be clear that there is almost no experimental information of the type we describe.

A. $3d_{5/2}$ *Shell.*—(1) $_{10}Ne_{11}^{21}$.—This is the one case where the pair of reactions have been examined[7] by the (d,p) reaction to the ground state and the 330-kev state (both $l=2$). Unfortunately the spin assignments are not certain.[8] The cross section ratio is close to unity; if the two spins are different we have a strong $d_{3/2}$ admixture which would be in agreement with the results for $A=18, 19$ nuclei.[9] For the mirror nucleus $_{11}Na_{10}^{21}$ there is no relevant information.

(2) $_{11}Na_{12}^{23}$.—The ground state spin is anomalous $(3/2^+)$. The 440-kev level is +,[10] and may well be the 5/2 state. We may note that the quadrupole transition rate is large[11]; one is therefore presumably encountering fairly large collective effects[12] but this does not affect the argument above.

B. $4f_{7/2}$ *Shell.*—(1) $_{18}A_{23}^{41}$.—This nucleus has ground state spin $7/2^-$ or $5/2^-$ as determined from the (d,p) reaction.[13] A level at 600 kev was observed but its properties are unknown.

(2) $_{20}Ca_{23}^{43}$.—This is an excellent case; it has a $7/2^-$ ground state, an excited state at 370 kev to which $5/2^-$ has been assigned by Lindqvist and Mitchell[14] and Nussbaum.[4] Both of these levels have been observed in the (d,p) reaction.[15]

(3) $_{20}Ca_{25}^{45}$.—A level is known at 180 kev,[15] but not spins or parities. It is reported[16] that the (d,p) reaction is being done by Braams.

(4) $_{22}Ti_{25}^{47}$.—The ground state spin is anomalous $(5/2^-)$ and a level at 160 kev excited by Coulomb excitation[10] (believed quadrupole) could be the normal $7/2^-$ level. This assignment is also favored by Nussbaum[4] who considers β decay evidence. It seems probable that the $Ti^{47}(d,p)Ti^{48}$ ground state reaction (which would involve an $f_{5/2}$ neutron) has been observed.[17]

(5) $_{23}V_{26}^{49}$, $_{24}Cr_{25}^{49}$.—Flowers[18] has predicted $5/2^-$ for V^{49} and $7/2^-$ for Cr^{49}. Nussbaum *et al.*[19] find from β decay and γ transitions that one of these nuclei has a $5/2^-$ ground state and that the ground state and 89-kev state of V^{49} are either $5/2^-$, $7/2^-$ or inversely.

(6) $_{23}V_{28}^{51}$.—There are tentative assignments[4] of $7/2^-$ for the ground state and $5/2^-$ for the state at 325 kev.

(7) $_{25}Mn_{28}^{53}$.—For the ground state and 380-kev states Nussbaum[4] gives $5/2^-$, $7/2^-$, or inversely.

(8) $_{25}Mn_{30}^{55}$.—The ground state is $5/2^-$. The normal $7/2^-$ level may well be that at 128 kev which is observed by quadrupole Coulomb excitation.[10]

C. $5g_{9/2}$ *Shell.*—A large number of these nuclei have a low-lying $7/2^+$ state which by convention is described by $(g_{9/2})^n (n=3,5,7)$.[20,21] In three cases ($_{36}Kr_{47}^{83}$, $_{38}Sr_{47}^{85}$, $_{43}Tc_{56}^{99}$) a $9/2^+$ ground state and a $7/2^+$ low-lying state are known but in each of these the deuteron reaction seems impossible because of a very close $1/2^-$ level.

$_{45}Rh_{58}^{103}$ has a $1/2^-$ ground state and levels at 40 kev and 95 kev to which 702^+ and $9/2^+$ have been assigned.[22] The necessary experiments here would be very difficult. Four other nuclei $_{34}Se_{43}^{77}$, $_{34}Se_{47}^{81}$, $_{47}Ag_{60}^{107}$, $_{47}Ag_{62}^{109}$) have $1/2^-$ ground states and $7/2^+$ levels between 87 and 160 kev but in these cases the $9/2^+$ level has not been seen.

Five nuclei ($_{32}Ge_{45}^{77}$, $_{34}Se_{45}^{79}$, $_{36}Kr_{43}^{79}$, $_{36}Kr_{45}^{81}$, $_{45}Rh_{60}^{105}$) have $7/2^+$ ground states and a $1/2^-$ level between 80 and 400 kev. But in none of these cases is the $9/2^+$ level known.

We wish to thank Dr. N. S. Wall for a very valuable discussion.

* This work was supported in part by the U. S. Atomic Energy Commission.

[1] F. Ajzenberg and T. Lauritsen, Revs. Modern Phys. **24**, 321 (1952).
[2] P. M. Endt and J. C. Kluyver, Revs. Modern Phys. **26**, 95 (1954).
[3] M. Goldhaber and R. D. Hill, Revs. Modern Phys. **24**, 179 (1952).
[4] R. H. Nussbaum, thesis, University of Amsterdam, 1954 (unpublished).
[5] Nuclear Data Cards—National Research Council.
[6] A. M. Lane, Proc. Phys. Soc. (London) **A66**, 977 (1953).
[7] R. Middleton and C. T. Tai, Proc. Phys. Soc. (London) **A65**, 752 (1952).
[8] J. Koch and E. Rasmussen, Phys. Rev. **76**, 1417 (1949).
[9] J. P. Elliot and B. H. Flowers (to be published).
[10] G. M. Temmer and N. P. Heydenburg, Phys. Rev. **96**, 426 (1954).
[11] G. M. Temmer and N. P. Heydenburg, Bull. Am. Phys. Soc. **30**, No. 1, 59 (1955).
[12] A. Bohr and B. R. Mottelson, Kgl. Danske Videnskab. Selskab, Mat.-fys. Medd. **27**, 16 (1953).
[13] W. M. Gibson and E. E. Thomas, Proc. Roy. Soc. (London) **A210**, 543 (1954).
[14] T. Lindqvist and A. C. G. Mitchell, Phys. Rev. **95**, 1535 (1954).
[15] C. M. Braams, Phys. Rev. **95**, 650(A) (1954).
[16] C. M. Braams, as quoted by Nussbaum, reference 4.
[17] Bretscher, Alderman, Elwyn, and Shull, Phys. Rev. **96**, 103 (1954).
[18] B. H. Flowers, Phil. Mag. **45**, 329 (1954).
[19] Nussbaum, Wapstra, Nijgh, Ornstein, and Verstern, Physica **20**, 165 (1954).
[20] D. Kurath, Phys. Rev. **91**, 1430 (1953).
[21] I. Talmi, Helv. Phys. Acta **25**, 185 (1952).
[22] B. Saraf, Phys. Rev. **97**, 715 (1955).

Evaluation of the Imaginary Part of the Nuclear Complex Potential

A. M. LANE AND C. F. WANDEL

Physics Department, Massachusetts Institute of Technology, Cambridge, Massachusetts

(Received March 24, 1955)

NEUTRON scattering data for several incident energies in between 0 and 30 Mev have now been analyzed fairly successfully with a simple complex potential model.[1] Figure 1 shows the various experimental values of V_i, the imaginary part of the potential, plotted against incident energy.[2] We have estimated V_i theoretically, using a method proposed by Goldberger for high incident energies.[3] Although application of the method to lower energies is not clearly justifiable,[4] we feel that the agreement obtained with experiment is noteworthy.

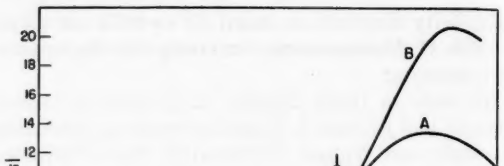

FIG. 1. The imaginary part of the complex potential V_i, plotted against incident neutron energy E_n (both in Mev). Curves A and B are computed according to the theory outlined in the text assuming nuclear radii of $1.48A^{\frac{1}{3}}\times10^{-13}$ and $1.20A^{\frac{1}{3}}\times10^{-13}$ cm respectively. The experimental points are taken from analyses of data by the following: $E_n=0$ Mev—Feshbach, Porter, and Weisskopf, Phys. Rev. **96**, 448 (1954) (these authors fit cross sections up to $E_n=3$ Mev with the same V_i). $E_n=4.1$ Mev—M. Walt and J. R. Beyster (private communication from Los Alamos). $E_n=9.5$ Mev—D. J. Prowse and A. Hossain (private communication to Prof. V. F. Weisskopf from Bristol, England) (these authors do not state the uncertainties in their values of V_i). $E_n=14$ Mev—Lower point: Gittings, Barschall, and Everhart, Phys. Rev. **75**, 610 (1949) (lower limit on V_i). Upper point: Culler, Fernbach, and Sherman, University of California, Livermore Laboratory Report, UCRL-4436, 1955 (unpublished) (these authors do not state the uncertainties in their values of V_i). $E_n=22$ Mev—D. S. Saxon and R. D. Wood, Phys. Rev. **95**, 587 (1954) (these authors analyze proton scattering data).

A typical target nucleus is regarded as a sphere of nuclear matter composed of four degenerate Fermi gases, one for each nucleon spin state, filled up to an energy E_F. The assumption that an incident neutron is absorbed when it collides with a target nucleon leads to an expression for V_i:

$$V_i=\tfrac{1}{2}\hbar v_1(\rho_n\bar{\sigma}_{nn}+\rho_p\bar{\sigma}_{np}),$$

where v_1 is the velocity of the incident neutron inside nuclear matter, ρ_n, ρ_p are the neutron and proton densities and $\bar{\sigma}_{nn}$, $\bar{\sigma}_{np}$ are certain average neutron-neutron and neutron-proton cross sections. The averages in $\bar{\sigma}_{nn}$ and $\bar{\sigma}_{np}$ are taken in an appropriate fashion over all possible relative collision velocities $\mathbf{v}_r$. Writing $\mathbf{v}_2$ for the velocity of a struck nucleon in the Fermi gas (so $\mathbf{v}_r=\mathbf{v}_1-\mathbf{v}_2$), the precise formula is [see Goldberger,[3] Eq. (4)]:

$$\bar{\sigma}=\int\sigma(E_r)\frac{v_r}{v_1}d\mathbf{v}_2\Big/\int d\mathbf{v}_2,$$

where the integrals are taken over the range of velocities in the Fermi gas.

The effect of the Pauli principle in the present model is to forbid all collisions in which either nucleon ends

with an energy $<E_F$. To compute the probability that a given collision will be forbidden on these grounds, some definite angular dependence of nucleon-nucleon scattering must be assumed. In our calculations we have always assumed angular isotropy, and have evaluated the integrals analytically for the following dependences of $\sigma(E_r)$ on relative energy: $\sigma \propto E_r^{-\frac{1}{2}}$, E_r^{-1}, $E_r^{-\frac{1}{2}}$, constant. (The fact that the actual observed n-p scattering has an appreciable dip at 90° for relative energies >30 Mev means that we somewhat overestimate V_i.)

In the numerical evaluation that led to the curves in Fig. 1, we assumed the following constants: Nuclear radius $=1.48A^{\frac{1}{3}}\times10^{-13}$ cm (curve A); $1.20A^{\frac{1}{3}}\times10^{-13}$ cm (curve B) (the corresponding values of E_F are 22 Mev and 33 Mev, respectively); energy in nuclear matter $=E_F+8$ Mev+incident energy; σ_{pp} (barns) $=8\times(E_r$ in Mev$)^{-1}$; σ_{nn} (barns) $=4\times(E_r$ in Mev$)^{-1}$. (The formula for σ_{np} fits the observed n-p cross section within 15 percent over the energy range from 2 to 280 Mev. The formula for σ_{nn} gives a rough fit to the observed nuclear p-p scattering cross section.)

The most striking feature of the results is the manner in which the experimental fall-off in V_i at lower incident energies is reproduced. In the theoretical curves, this fall-off arises purely from the effect of the Pauli principle which prevents an increasing number of collisions as the incident energy is lowered. We have performed the calculation ignoring the Pauli principle and find that V_i is increased to 30 Mev at zero incident energy in the case of the larger radius. The effect is even larger for the smaller radius. It is to be noted that the two curves, A and B, are not appreciably different below 30-Mev bombarding energy. Above this energy, the experimental values of V_i are not determined to better than factors of the order of 2.

[1] See references to Fig. 1.
[2] V. F. Weisskopf and F. L. Friedman, "The Compound Nucleus," in Volume celebrating Professor N. Bohr's 70th Birthday (to be published).
[3] M. L. Goldberger, Phys. Rev. **74**, 1269 (1948); Morrison, Muirhead, and Rosser, Phil. Mag. **44**, 1326 (1953).
[4] N. C. Francis and K. M. Watson, Phys. Rev. **92**, 291 (1953).

Thermodynamic Theory of Fission

J. K. Perring and J. S. Story
Atomic Energy Research Establishment, Harwell, Berkshire, England
(Received February 11, 1955)

An attractive new theory of nuclear fission has recently been proposed by Fong.[1,2] He has used it to calculate for thermal neutron fission of U^{235} a mass yield curve which is in remarkably good agreement with the experimental data.

When we applied Fong's prescriptions to thermal neutron fission of Pu^{239} we found no such agreement: indeed the theory would predict a mass yield curve with four humps, and with much too small a peak-to-trough ratio.

A more detailed analysis shows that the results depend very critically on the exact shape of the line of maximum beta stability in the semiempirical mass formula; i.e., to Fong's correction term[2] ΔZ_A. It does not seem that one could obtain a good fit to observed yield curves over a whole range of fissile isotopes (Th^{232} to Cm^{242}), save perhaps by substantial and ill-authenticated alterations.

Essentially, apart from a slowly varying factor, the relative fission yields are determined by the exponential factor in I, Eq. (2), in which a_1+a_2 is independent of the fission mode. Hence the excitation energy E (calculated for the most probable charge splitting) should behave in much the same way as the mass yield curve itself; i.e., it must exhibit a minimum for symmetrical fission, a maximum for mass ratios ~1.5, and must decrease steadily for higher mass ratios.

E is calculated from the fragment masses, by Eq. (1) of I. Well-known semiempirical formulas give

$$M(A,Z)=M_A+B_A(Z_A-Z)^2+\delta_A, \quad (1)$$

but Fong shows that substantial corrections are necessary to the usual analytical expressions[3] for M_A and Z_A, and he writes

$$M(A,Z)=M_A+\Delta Z_A+B_A(Z_A+\Delta Z_A-Z)^2+\delta_A, \quad (2)$$

where ΔM_A, ΔZ_A are given graphically.[2]

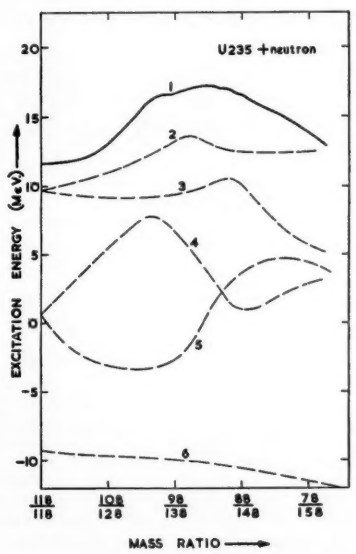

FIG. 1. Excitation energy as a function of mass splitting for thermal fission of U^{235}. Curve 1: Excitation energy E of the fragment pair; it is the sum of the five components 2 to 6. Curves 2,3: Mass corrections ΔM_A for heavy and light fragments respectively. Curves 4,5: Contributions due to the corrections ΔZ_A for heavy and light fragments respectively. Curve 6: Excitation energy E of the fragment pair using uncorrected semiempirical mass formula.

We can now write

$$E=E'+\Delta M_{A1}+\Delta M_{A2}+p\Delta Z_{A1}+q\Delta Z_{A2}, \quad (3)$$

where E' is the excitation energy which would be obtained from Eq. (1) of I by using the uncorrected mass formula (1) above (as in the calculations of Bohr and Wheeler), and the other four terms give the corrections due to ΔM_A and ΔZ_A for light and heavy fragments: p and q are functions of A_1 and A_2 and contain trivial second order terms in the ΔZ_A's.

In Fig. 1, we show the excitation energy as a function of mass splitting for thermal fission of U^{235}. We show also the five component functions which make up the right-hand side of (3) above. The excitation energy was computed exactly[4] according to Fong's prescriptions,[2] and leads to a fission yield curve in reasonable agreement with the experimental data when emission of prompt neutrons has been allowed for.

In Fig. 2, we show the same set of curves for thermal fission of Pu^{239}. Although the component curves all look much the same as before, we see at once that instead of the single hump obtained for U^{235} the excitation energy curve now has a crater just where it should reach a maximum. Moreover the total variation between symmetrical fission and maximum excitation energy is much smaller.

The reason for this remarkable change lies in slight shifts of the curves of $p\Delta Z_{A1}$ and $q\Delta Z_{A2}$. With U^{235} the rapid increase of curve 4 in the region of masses 95 to 141 almost exactly cancels the rapid decrease of curve 5. With Pu^{239}, however, curves 4 and 5 are shifted to the left and right, respectively and the cancellation no longer occurs.

By small adjustments[5] to ΔZ_A it might be possible to obtain correct excitation energy curves for both U^{235} and Pu^{239}, but then for fissile isotopes of still higher mass the excitation energy curve would have a crater, as in Fig. 2, while for lower masses it would presumably have a pimple at the top.

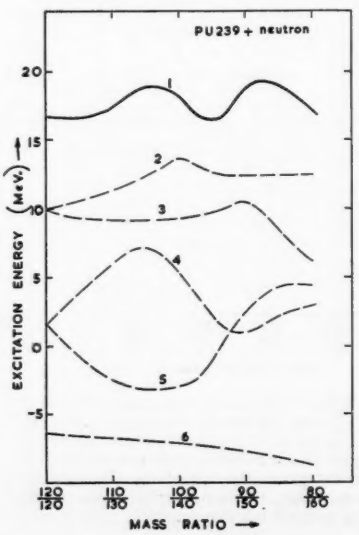

FIG. 2. Excitation energy as a function of mass splitting for thermal fission of Pu^{239}. The curve numbers have the same meaning as in Fig. 1.

In fact we re-examined Fong's evaluation of ΔZ_A in the light of up-to-date beta decay and reaction data. There are several inconsistencies and it appears that the prescriptions do not agree very well with *ground-state* data: that is, of course, no reason for rejection.[5] Our analysis suggested slight alterations to Fong's ΔZ_A, but unfortunately these make the results for Pu^{239} worse, and induce similar discrepancies for U^{235}.

In the calculations for Pu^{239} we assumed the same deformation energy D as for U^{235} and the same dependence on mass ratio. No reasonable alteration of the deformation energy, nor of the Coulomb energy E_{el}, can remove the difficulty since both D and E_{el} vary slowly and practically monotonically over the ranges of interest.

[1] P. Fong, Phys. Rev. **89**, 332 (1953), referred to in the text as I.
[2] P. Fong (to be published).
[3] See, e.g., N. Metropolis and G. Reitweisner, Atomic Energy Commission Report NP-1980, 1950 (unpublished), based on Fermi's prescriptions.
[4] Except that we have used a different datum for the mass of U235. This alteration simply changes the zero of the energy scale in the diagram by a few Mev.
[5] The mass formula is used to estimate nuclear masses at some smoothed "characteristic" excitation state, so the parameters involved are not rigidly related to the ground-state data from which they are estimated, but should presumably not differ greatly.

Phase Shift Analysis of 240-Mev Proton-Proton Scattering

L. BERETTA, E. CLEMENTEL, AND C. VILLI
Istituti di Fisica dell'Università di Padova e di Trieste, Istituto Nazionale di Fisica Nucleare, Sezione di Padova, Italy
(Received March 29, 1955)

RECENTLY high-energy nucleon-nucleon scattering has been discussed in terms of S and P waves only,[1,2] and in a previous paper[3] a method, suitable for the determination of the phases $^1K_0$ and $\delta_J{}^L$ at any energy, has been suggested. In this note we discuss proton-proton scattering at 240 Mev on the basis of Towler's experimental data.[4] To compare our results with those given by Thaler and Bengston,[1] we assume that the p-p cross section at $\theta=90°$ is equal to 4.5 mb, but no simplifying assumptions will be made about the angular independence of the nuclear term $\mathbf{P}_{\text{nuc}}$. For all symbols used in the following analysis we refer to the papers quoted in (1) and (3).

Specifying at $\theta=90°$ the Breit-Kittel-Thaxton formula, valid for a noncentral potential, one gets

$$\sin^2(^1K_0{}^{\pm})=\{2A+B^2\pm B[4A(1-A)+B^2]^{\frac{1}{2}}\}\times[2(1+B^2)]^{-1}, \quad (1)$$

where $A=\{\Delta\mathbf{P}(\pi/2)-z_1(k)+\frac{1}{2}z_4(k)\}\{1-2\eta\sin(\eta\log 2)\}^{-1}$ and $B=2\eta\cos[\eta\log 2]\{1-2\eta\sin[\eta\log 2]\}^{-1}$. From Eq.

(1), we derive $z_1(k)-\frac{1}{2}z_4(k)$ as a function of ${}^1K_0{}^{\pm}$. Then, the condition that the p-p cross section be $\mathbf{P}(13°)=5.16$ mb and $\mathbf{P}(27.2°)=4.59$ mb[5] allows the determination of all $z_i(k)$ as functions of the singlet phase shift. In fitting the experimental values of the cross section at scattering angles of 13°, 27.2°, and 90°, the triplet phase-shift parameter $z_2(k)$ is negative or zero for positive singlet phase shifts. It follows that the quantities $-(\eta/2k^2)\mathbf{X}_0(\theta)z_3(k)$ and $-(\eta/2k^2)\mathbf{X}_1(\theta)\times P_1(\cos\theta)z_2(k)$, appearing in the interference term of the cross section, always have opposite signs and therefore the condition $z_2(k)>0$, which implies ${}^1K_0{}^{\pm}<0$, does not give a dip of the cross section at small angles, where Coulomb constructive interference is sensible. Once all $z_i(k)$ are expressed as functions of the singlet phase shift, we determine ${}^1K_0{}^{\pm}$ by means of the equation $\mathbf{P}({}^1K_0{}^{\pm},\theta)=\mathbf{P}_{\text{exp}}(\theta)$. We assume $\theta=70°$ and $\mathbf{P}_{\text{exp}}(70°)=4.5$ mb. It must be pointed out that this condition is more stringent than the experimental data require, although it is not sufficient to establish the plateau. It is found that the sets $z_i(k)$ corresponding to ${}^1K_0{}^{+}<0$ and ${}^1K_0{}^{-}>0$ give values of the cross section which are respectively larger than and smaller than the value chosen at 70°. At high energies the determination of ${}^1K_0{}^{\pm}$ is rather uncertain because of the very limited variation of the p-p cross section at a given angle with ${}^1K_0{}^{\pm}$ and because of the appreciably large experimental errors. For this reason no essential objection has been found to the value ${}^1K_0=31.3°$, calculated to a first Born approximation for a meson potential well.[1] However, for the sake of definiteness, we have determined ${}^1K_0{}^{\pm}$ from the condition that $|4.5-\mathbf{P}({}^1K_0{}^{\pm},70°)|$ be a minimum. Satisfactory agreement with Towler's data is obtained by taking ${}^1K_0{}^{+}=36°$ and ${}^1K_0{}^{-}=-31.8°$. The sets associated with these values are:

$${}^1K_0=36°:\ z_1(k)=0.956,\quad z_2(k)=-0.603,\quad z_3(k)=0.476,\quad z_4(k)=0.005;\quad \text{(a)}$$

$${}^1K_0=-31.8°:\ z_1(k)=1.005,\quad z_2(k)=+0.337,\quad z_3(k)=-0.448,\quad z_4(k)=0.009.\quad \text{(b)}$$

No selection between these two sets can be made by taking into account only experimental data on p-p scattering. In both cases the calculated cross section shows the correct behavior at small angles except at 8.7°, where it has the value 7.52 mb [set (a)] and, respectively, 7.48 mb [set (b)], instead of the exceedingly large experimental value 15.80 ± 1.6 mb which, however, seems to be contradictory to small-angle measurements of p-p scattering at 260 and 330 Mev.[6] Since the value $z_2(k)<0({}^1K_0{}^{+}>0)$ seems to be favored by the small-angle behavior of high-energy n-p cross sections, we disregard the set (b) and calculate the triplet phase shifts on the basis of the set (a) only.

Following the procedure outlined in reference 3, the condition $\alpha(\delta_2)\geq 0$ restricts the interval of δ_2 between $-25.8°$ and $+25.8°$, but real solutions for $\delta_J{}^L$ are found only for δ_2 varying within the interval $-21.2°\leq\delta_2\leq+12.3°$. The pairs $x_{\pm}=\sin\delta_0$ and $y_{\pm}=\sin\delta_1$, expressed as functions of δ_2, are then selected taking into account the equation $z_4(k)=f(\delta_0,\delta_1,\delta_2)$. Solutions compatible with the best fit previously determined are given only by the sets

$$\delta_2>0\quad [x_+<0,\ y_+<0];\quad [x_->0,\ y_-<0],\qquad \text{(i)}$$

$$\delta_2<0\quad [x_+>0,\ y_+<0];\quad [x_-<0,\ y_->0].\qquad \text{(ii)}$$

The set $[x_->0,\ y_-<0]$ and the sets (ii) give two and, respectively, six values of δ_2 consistent with $z_4(k)$, but only one of the former set ($\delta_2=+8.2°$) and two of the latter ($\delta_2=-10.3°$ and $\delta_2=-18.1°$) do not conflict with the magnitude and the sign of $z_2(k)$.

TABLE I. ${}^1K_0=36°$.

set	δ_0	δ_1	δ_2	$2\epsilon(\theta)$
A	$+2.68°$	$-32.2°$	$+8.2°$	3.32
B	$-71.93°$	$-7.47°$	$+0.9°$	0.14
C	$-11.5°$	$+22.46°$	$-18.1°$	7.84
D	$+63.35°$	$-2.81°$	$-10.3°$	14.48

The various sets of the triplet phase shifts compatible with Towler's data and with the assumption $\langle\mathbf{P}(\pi/2)\rangle=4.5$ mb are given in the Table I.

In the last column we have given for $\theta=27°$ the so-called asymmetry $2\epsilon(\theta)$ for a double-scattering experiment which, if one neglects energy degradation in the first scattering, is given[7] in terms of P phase shifts simply by

$$\epsilon(\theta)=\{[\sin2\theta/k^2\mathbf{P}(k,\theta)]\langle 3[\delta_0,\delta_2]+4.5[\delta_1,\delta_2]\rangle\}^2.$$

Experimental results[8] in the energy range near 200 Mev give an asymmetry of 9.6 ± 3.5 percent, but this figure should not change appreciably in the range 170–260 Mev, where the cross section for p-p scattering[6] seems to retain a constant value for $\theta=20°$. The theoretical values for 2ϵ are nevertheless only indicative, for we have neglected a possible coupling of ${}^3P_2$ to ${}^3F_2$ state, which is certainly required by polarization experiments at higher energies.[9]

The extension of the present method, including the consideration of coupling, will be published in the *Nuovo Cimento*.

[1] R. M. Thaler and J. Bengston, Phys. Rev. **94**, 679 (1954).
[2] A. Garren, Phys. Rev. **96**, 1709 (1954).
[3] Beretta, Clementel, and Villi, Nuovo cimento **4**, 350 (1955).
[4] O. A. Towler, Phys. Rev. **84**, 1262 (1951); **85**, 1024 (1952).
[5] We assume a cross section of 4.59 mb at 27.2° as a compromise between the values given by Towler and those of C. L. Oxley and R. D. Schamberger: Phys. Rev. **85**, 1024 (1952). According to the present method the singlet and triplet phase shifts will change appreciably if the best fit is determined with the latter data which are some 10 percent higher than Towler's.
[6] O. Chamberlain and J. D. Garrison, Phys. Rev. **95**, 1349 (1954); D. Fisher and J. Goldhaber, Phys. Rev. **95**, 1350 (1954).
[7] G. B. Goldfarb and D. Feldman, Phys. Rev. **88**, 1099 (1952).
[8] Oxley, Cartwright, and Rouvina, Phys. Rev. **93**, 806 (1954).
[9] B. D. Fried, Phys. Rev. **95**, 851 (1954).

Proceedings of the American Physical Society

Minutes of the 1955 March Meeting Held at Baltimore, March 17–19, 1955

(Corresponding to *Bulletin of the American Physical Society*, Vol. 30, No. 2)

THE 1955 March meeting of the American Physical Society was held on Thursday, Friday, and Saturday, March 17, 18, and 19, in Baltimore, Maryland. The scientific sessions and the banquet were held in the Lord Baltimore Hotel, except that the sessions of the Saturday afternoon were housed in the Johns Hopkins University. Thus on five of the half-days we had the advantages of convenience offered by the concentration of our sessions in the headquarters hotel, while on the remaining half-day we enjoyed (too briefly) the atmosphere of a great University. Some overcrowding occurred at two of the sessions because of a misunderstanding; apart from these two cases, the audiences and the halls were adequately matched. Our invitation to Baltimore came originally from G. H. Dieke; T. H. Berlin had general charge as Chairman of the Local Committee; to them and to their colleagues we who were at the meeting owe a great debt. Mrs. Dieke and other ladies of the Department of Physics entertained the visiting ladies (and some of the men who could not resist the temptation) by interesting excursions in Baltimore and its environs. From these names it will be seen that we owe much more to the Johns Hopkins University than merely the provision of halls on the Saturday afternoon.

This meeting, like all March meetings of the past, was primarily devoted to high-polymer physics and to solid-state physics. The Divisions consecrated to these fields provided symposia and individual invited papers. Members of the faculty of the Johns Hopkins University diversified the meeting by invited papers in other fields. LeRoy Apker delivered the "Oliver E. Buckley Lecture" devoted to the work which won him the 1955 Oliver E. Buckley Solid-State Physics Prize. It was remarkable that among the contributed papers, not one was in the field of theoretical physics outside of solid-state and high-polymer theory. But perhaps the most remarkable single feature of the meeting was the fact that the registration was *exactly* one thousand. The March meeting is holding its lately acquired rank of third largest of the year.

The banquet of the Society was held on Friday evening, with an attendance of (alas!) only 214. Evidently the restaurants of Baltimore competed too successfully with us, and this despite the fact that the after-dinner speaker was W. F. G. Swann. Another feature of the banquet was the presentation of the John Scott Award to our members John Bardeen and W. H. Brattain "for the invention of the transistor." The presentation was eloquently made by G. C. Pritchard and J. W. Iliff of the Board of Directors of City Trusts of the City of Philadelphia; brief responses were made by Mr. Bardeen and Mr. Brattain. For the history of this award, see the Baltimore Bulletin.

The Council met on Friday afternoon. It elected one candidate to Fellowship and one hundred thirty-eight candidates to Membership; the names follow.

Elected to Fellowship: J. D. Ferry.

Elected to Membership: Richard Herbert Abramson, Turner Alfrey, Jr., Roger Davenport Alling, Joseph A. Aukward, Wesley Pierce Ayres, *Norman H. Baker, Jr., Francis P. Baldwin, *Robert E. Baron, Hubert MacIntosh Bath, James Francis Battey, Harold Bernstein, *Joseph Francis Bird, *Mary Kate Brice, *Howard M. Brody, *C. Ann Burton, Bertram Allen Calhoun, *Nathaniel Phillips Carleton, Robert Joseph Carr, Nicholas Chako, *Richard Alexander Chapman, James Delmar Childress, Alvin Jerome Cohen, *Paul Louis Corio, Ernest Francis Costello, Jr., William R. Davis, Bastiaan de Raad, *Malcolm Derrick, *Dirck Lloyd Dimock, Richard Edward Durand, *Jafar El Bakkal, W. Paul Elson, Jr., *George L. Farre, *Lawrence Dale Fayro, Peter Felsenthal, John P. Ferguson, *Carmine Charles Ferriso, Italo Filosofo, *Lee Marshall Frantz, George Freedman, *Jacob Emanuel Fromm, *Eugene Irving Gordon, Charles Louis Guillaud, Lester Haar, Lewis Dana Hall, William Warner Hammerschmidt, Donald LeRoy Hammond, George Gibson Harman, Jr., Sister M. Bonaventure Harrington, Joseph Irwin Harris, *Donald Frederick Heath, Donald Alden Hicks, Katsunori Hijikata, Joseph Hilsenrath, John M. Houston, *C. Eugene Hunting, George Samuel Hurst, *John Calhoun Irvin, Derek Ainslie Jackson, Wilbur Gerald James, David Casper Jillson, William George Johnston, Zohrab Arakel Kaprielian, Clinson Monroe Kelley, *Herburt Kleiman, *Edwin R. Kolb, *John Alan Kuehner, Koichi Kobayashi, *Hans Georg E. Kobrak, *Michiji Konuma, *James T. LaTourrette, Guy Walter Lehman, Alexander Lempicki, Lester Clark Lewis, *Samuel D. Lindenbaum, William Francis Lindsay, Telford Grant Maple, *Jack S. Margolis, H. James McCarty, *Alan Louis McWhorter, Charles James Meechan, Jack L. Melchor, Robert Jay Miller, *James Gay Moldenhauer, Theodore Franklin Morris, Norbert Muller, Forrest T. Mullikin, *James Richard Nelson, Takao Okabayashi, Jonathan Parsons, Rose Ann Pengra, Richard Grover Petersen, James Reid Pfafflin, Louis Pierce, *Richard James Plano, Daniel David Pollock, Vladimir Popoff, *Richard Bradley Read, Verne Rhoades, Jr., Kenneth Robinson, *Raymond Anthony Santirocco, Hiroshi Sato, Frederic William Schuler, *William Jude Schultis, *Melvin Schwartz, *Sidney Shapiro, Robert Gerson Shulman, *Jerome Ralph Singer, Alan Bowen Smith, Albert E. Smith, *William Rodman Smythe, Joseph Oliver Stenoien, Jennings Peter Stoering, Gwynn Halyburton Suits,

Andrew D. Suttle, Jr., *William Joseph Tabor, *Morris D. Tatcher, Armando Dias Tavares, *Ernest Alfred Thieleker, Robert Frank Trapp, Peter Bradley Treacy, *Eugene Serge Troubetzkoy, Thomas William Trout, *Gaylord Beryl Treu, Dean Martin Unger, Fernando Chaos Urdampilleta, *George Frederick Vanderschmidt, *Walter Michael Walsh, Jr., Paul McElroy Waters, *William Bruce Watkins, Gerhard Emanuel Weibel, Marvin Aaron Weinstein, Kurt Weiser, *Joe Steve Williams, Malcolm Lee Williams, *Robert M. Worlock, David Unstead Wright, Jr., Henry William Wyld, Jr., and Huseyin Yilmaz.

*—Student.

KARL K. DARROW, *Secretary*
American Physical Society
Columbia University
New York 27, N. Y.

Errata Pertaining to Abstracts G1, K7, L2, L7, V8, Y5, Y8, Z5, and Z14

G1, by W. G. Segelken and H. C. Torrey. Mr. Segelken's name was spelled incorrectly in the abstract and in the Author Index. In line 4, instead of $AlK(SO_4)\cdot 12H_2O$, read $AlK(SO_4)_2\cdot H_2O$.

K7, by D. B. Fishbach and A. S. Nowick. In line 6, instead of 10-in. ohm resistor, read 10^{11} ohm resistor.

L2, by Claus H. Haake. In lines 1 and 2, instead of introduced by H. Fivey, read introduced by H. F. Ivey.

L7, by I. Ames, H. S. Sack, and R. M. Wood. In line 9, instead of 30 cps to 20 msec, read 30 cps to 20 mcps.

V8, by Leo Breitman. In line 21, instead of four points read pour points.

Y5, by P. Kiive and H. T. Pinnick. In line 7, the word moreover should be deleted.

Y8, by S. Mrozowski. In line 12, instead of β read *B*. In line 16, instead of *C* read *B*.

Z5, by Donald T. Stevenson. The fourth sentence should be deleted.

Z14, by T. E. Firle and H. Winston. In the byline, *Hughes Aircraft Company* should be added. A footnote should be added to the title reading: This work was supported in part by the Signal Corps.

PROGRAMME

THURSDAY MORNING AT 10:00

Founders' Room

(G. H. DIEKE presiding)

Invited Papers in Nuclear and Atomic Physics

A1. Methods of Fast Neutron Spectroscopy. C. D. SWARTZ, *Johns Hopkins University.* (30 min.)
A2. Neutron Physics at Johns Hopkins University. G. E. OWEN, *John Hopkins University.* (30 min.)
A3. Energy Levels of Beryllium 8. S. S. HANNA, *Johns Hopkins University.* (30 min.)
A4. Latest Developments in Atomic Constants. J. A. BEARDEN, *Johns Hopkins University.* (30 min.)

THURSDAY MORNING AT 10:30

Caswell Room

(T. H. BERLIN presiding)

Irradiation Effects, I

B1. On the Theory of Radiation Damage. W. A. HARRISON AND FREDERICK SEITZ, *University of Illinois.*—Two advances in theory make it possible to compare theory and experiment anew. Snyder and Neufeld[1] and the authors have found that $\bar{\nu}$, the average number of progeny per primary displaced atom is near 6 instead of 3, if one employs the simple "square-well" model with E_d near 25 ev. In addition Blatt[2] found that the resistivity for one percent of Frenkel pairs should be 2.7$\mu\Omega$ cm in copper if one extends Jongenburger's calculations for vacancies. The simple theory leads to a calculated increase in resistivity of 1.16$\mu\Omega$ cm when 3 mil copper foils are bombarded with 10^{17} 12-Mev deuterons per cm^2. The value observed by Cooper, Koehler, and Marx at 10°K is 0.23 $\mu\Omega$ cm, or is 5.0 times smaller. The discrepancy is 7.3 near liquid nitrogen temperature. Moreover the discrepancy is 5.7 for 0.5 mil specimens of copper bombarded with 0.81 Mev electrons at liquid nitrogen temperature ($\bar{\nu}=1$). The uniformity suggests either that the models employed by Jongenburger and Blatt yield values about five times too large, or that the probability of an atom being permanently displaced in copper is not unity when its kinetic energy attains the threshold. The disagreement is much less in bombarded n-type germanium if one assumes each displacement contributes one acceptor.

[1] W. S. Snyder and J. Neufeld, Phys. Rev. **94**, 760 (A) (1954).
[2] F. J. Blatt, Bull. Am. Phys. Soc. **29**, No. 7, 30 (1954).

B2. Source of Disordering of Alloys during Irradiation. F. SEITZ, *University of Illinois.*—Siegel[1] first found ordered alloys can be disordered efficiently under conditions in which atoms are displaced, the number of disordered atoms being much larger than the number displaced. More quantitative measurements[2] using cyclotrons show that about 120 atoms are displaced in Cu_3Au per primary displacement. Other experiments support the same efficiency factor when nucleons are employed.[3] A search has been made to disclose the mechanism for disordering. It seems unlikely that the temperatures acheived in displacement spikes are adequate to explain the disordering. Unfortunately application of the theory of temperature spikes involves evaluation of the ratio $\eta\nu_0 r_s^2/D$. Here D is the diffusion coefficient for lattice vibrational energy, ν_0 is the frequency coefficient in the basic rate process, r_s is the atomic radius and η is the number of independent rate processes per atom contributing to disorder. This ratio is assumed to be unity or less. Electron spikes seem inadequate to explain the effect since the high efficiency is observed in neutron irradiation where little electron excitation occurs. It is proposed that irreversible plastic strain which originates in thermal stresses about displacement spikes is the source of disorder.

[1] S. Siegel, Phys. Rev. **75**, 1823 (1949).
[2] Brinkman, Dixon, and Meechan, Acta Met. **2**, 38 (1954).
[3] R. R. Eggleston and F. E. Bowman, J. Appl. Phys. **24**, 229 (1953); L. R. Aronin, *ibid.*, **25**, 344 (1954).

B3. Energy Dependence of Radiation Effects in Solids.* E. PEARLSTEIN, H. INGHAM, AND R. SMOLUCHOWSKI, *Carnegie Institute of Technology.*—The calculations of Seitz[1] indicate a $1/E$ dependence of radiation effects on energy for charged particles passing through a thin specimen. Other calculations (see following abstract) indicate that at high energies secondary effects from nuclear reactions can be effective. In this experiment, tungsten wires previously annealed were bombarded in the Carnegie Institute of Technology sychrocyclotron with protons of several energies, and their electrical resistance was measured at room temperature before and after bombardment. Bombardments were made at 130, 260, and 410 Mev, and for each energy the resistance was found to increase by an amount proportional to the amount of bombardment. In particular for a bombardment of 10^{16} protons/cm^2 the change is 0.49 percent at 130 Mev, at 260 Mev it is 0.33 percent, and at 410 Mev it is 0.71 percent. Temperature-coefficient measurements indicate that at least most of the changes occur in the temperature independent part of the resistance. It is believed that annealing during bombardment does not affect the trend of these results. Also, this trend is well outside the probable error of measurements.

* Work supported by a U. S. Atomic Energy Commission contract.
[1] F. Seitz, Discussions Faraday Soc., No. 5 (1949).

B4. Radiation Effects in Solids Produced by Nuclear Disintegrations.* R. SMOLUCHOWSKI, E. PEARLSTEIN, AND H. INGHAM.—*Carnegie Institute of Technology.*—It has been suggested[1] that nuclear disintegrations may play an important role in the interpretation of radiation effects produced in solids by protons of energy in the 100–400-Mev range. While the cross section for this primary process of "star" formation is essentially independent of energy of the incident particle, the number and energy distribution of the prongs i.e. of the emerging nucleons is energy dependent. This is in contrast to the

other competing primary processes of electronic excitation and elastic collision which depend strongly upon the energy of the impinging particle. A detailed calculation of the spectrum of the nucleons emerging in disintegrations caused by protons of various energies in the range of interest has been made using the evaporation theory of the compound nucleus. Also the dependence of the total number of atoms displaced by these nucleons upon the energy of the primary proton has been calculated. It appears that good agreement with experiment (see preceding abstract) is obtained if one makes the plausible assumption that the most effective prongs of the stars are those due to high energy charged particles.

* Work supported by a U. S. Atomic Energy Commission contract.
[1] R. Smoluchowski, Phys. Rev. 94, 1409 (1954).

B5. Shear Modulus Recovery of Electron Irradiated Copper.* H. DIECKAMP, *North American Aviation, Inc.* (introduced by D. B. Brown).—The recovery of changes in the shear modulus of copper has been measured after bombardment by energetic electrons. Three polycrystalline wires of 99.999 percent copper were irradiated with 1 Mev electrons at liquid-nitrogen temperature to an integrated exposure of approximately 4.5×10^{18} particles/cm^2. The shear modulus was measured at liquid-nitrogen temperature after annealing in the range of −196°C to 350°C. Annealing temperatures were spaced at 25°C intervals throughout the range and the time at each temperature was 15 min. The possibility of changes due to cold work prevented the measurement of a pre-irradiation value; hence the magnitude and sign of the irradiation-induced changes are known only so far as they can be inferred from the recovery curve. The recovery can be described in terms of the following regions: −196°C to −50°C, 4 percent increase; −25°C to 50°C, no change; 75°C, ½ percent decrease; 100°C to 200°C, no change; 250°C to 350°C, 2 percent decrease. The recovery is apparently still incomplete at 300°C, but the observed changes in this region are confused by the possibilities of oxidation and recrystallization. These measurements should reflect the effects of the simplest damage, namely interstitials and vacancies, since the electrons are not sufficiently energetic to produce more complicated primary defects.

* This work supported by the U. S. Atomic Energy Commission.

B6. Effect of Quenching and Neutron Irradiation on Atomic Mobility in a Cu−Al Alloy.* CHI YAO LI† AND A. S. NOWICK, *Yale University.*—A solid solution of 17 atomic percent Al in Cu shows an internal friction peak because of stress-induced ordering, for which the relaxation strength is 0.015. Equilibrium measurements of relaxation time as a function of temperature give an activation energy of 41.6 kcal/mole. The same alloy quenched from elevated temperatures shows abnormally low relaxation times (observed in the temperature range 114°–162°C), apparently because of excess vacancies trapped by quenching. The relaxation time at a given temperature is observed to approach its equilibrium value in two distinct stages, similar to the results previously obtained for Ag-Zn alloys.[1] On the other hand, wire specimens of the Cu-Al alloy, neutron irradiated in the Brookhaven reactor at 78°K and at 323°K, show no detectable deviation of the relaxation times from equilibrium values. The quenching experiments indicate that vacancies are mobile only at temperatures above 100°C. Vacancies produced by irradiation must therefore be destroyed by interstitials or other defects which are mobile below room temperature.

* Work supported by the U. S. Army Office of Ordnance Research.
† Now at Lehigh University, Bethlehem, Pennsylvania.
[1] A. E. Roswell and A. S. Nowick, J. Metals 5, 1259 (1953).

B7. Conductivity of Teflon and Polyethylene During Gamma Irradiation. R. A. MEYER AND F. L. BOQUET, *U. S. Naval Radiological Defense Laboratory.*—An investigation has been undertaken to measure the change in conductivity of insulating materials undergoing irradiation by gamma-rays as a function of temperature and dose rate. The material measured was polyethylene and teflon (polytetrafluorine). The irradiation sources employed in this study were Co^{60} gamma-rays and x-rays from a gold target bombarded by electrons from a Van de Graaff generator. The flux intensities from the two cobalt sources were approximately 0.6 r per min and 423 r per min, and those from the incident electrons, 30 r per min to 1250 r per min. Samples, 0.16 cm thick and 4.1 cm in diameter, were mounted on one end of an aluminum cylinder in a vacuum. The current passing through the insulator was measured with two types of electrometers. All measurements were made with a voltage across the sample. The voltage was varied from −600 to +600 volts. The temperature range investigated was from room temperature to −170°C. In general, the conductivity of teflon was greater than that of polyethylene under gamma irradiation. Evidence obtained from variation of the decay as a function of temperature indicates trapping effects are present.

B8. Detection of the Vacancies Created in NaCl by X-Rays. H. W. ETZEL, *U. S. Naval Research Laboratory.*—The production of vacancies by x-rays in sodium chloride has been observed using optical techniques. The absorption of the ultraviolet induced *F*-band is measured in single crystals of sodium chloride; then the band is optically bleached. The crystals are then x-rayed and optically bleached. The crystals are again subjected to the same ultraviolet radiation as they received prior to x-raying, and the optical absorption of the *F*-band measured. The *F*-band observed after x-raying is enhanced 10-fold over that observed prior to x-raying. This result is interpreted to indicate the production of vacancies by x-rays.

Invited Paper

B9. The Effect of Radiation Damage on the Electrical and Thermal Properties of Graphite. W. P. EATHERLY, *North American Aviation.* (30 min.)

THURSDAY MORNING AT 10:00

Phoenix Room

(J. D. WATSON presiding)

DHPP Symposium on Biophysics of Nucleic Acid

C1. The Chemistry of Nucleic Acids. R. L. SINSHEIMER, *Iowa State College.* (30 min.)

C2. The Size and Shape of the Nucleic Acids as Revealed by Physical-Chemical Techniques. PAUL DOTY, *Harvard University.* (30 min.)

C3. Nucleic Acid Structure as Revealed by X-Ray Diffraction. J. D. WATSON, *California Institute of Technology.* (30 min.)

SESSION D

THURSDAY MORNING AT 9:30

Calvert Room

(D. T. STEVENSON presiding)

Semiconductors, I

D1. A Semiconducting Diamond.* W. J. LEIVO AND R. SMOLUCHOWSKI, *Carnegie Institute of Technology.*—The class IIb diamonds exhibit rather rare optical and electrical properties.[1] In order to investigate what type of imperfections may be responsible for these properties, the dark resistivity was measured between room temperature and 425°C. It appears that these diamonds behave like typical impurity activated semiconductors with a low concentration of impurities and produce a good rectification with a metal point. At low temperatures, their resistance decreases with increasing temperature while at high temperatures it increases with increasing temperature. The minimum is reached at about 360°C. Below this minimum the resistivity decreases with increasing current while at higher temperatures the dependence is reversed indicating that this effect is due primarily to heating. This is presumably the reason for the resistance hysteresis observed by Custers. The slope of the dependence of $k \ln R$ on $1/T$ at low temperatures is about 0.35 ev. The crystal is photoconductive in the visible and shows inhomogeneities in its electrical properties.

* Work supported by a U. S. Atomic Energy Commission contract.
[1] J. F. H. Custers, Physica **18**, 489 (1952); **20**, 183 (1954). We are indebted to Dr. Custers for supplying the diamond.

D2. Optical Absorption Spectra of Thorium Oxide.* J. H. BODINE AND F. B. THIESS, *Bartol Research Foundation.*—Absorption measurements in the region of 2200 A to 10 000 A were made on optically polished thoria crystals of 99.9 percent purity. Firing the crystals in air and in vacuum at different temperatures gave the red, white, and yellow forms described by Weinrich and Danforth.† The present improved instrumentation gave a cutoff at 3550 A for all forms. Vacuum firing at high temperature (1500°) gives a yellowish form. The white form is produced by lower temperatures and/or short times. Results will be reported regarding the progressive change from white to yellow forms as the temperature and time of firing are increased. Thin films prepared by oxidizing films of metallic thorium show rapid increase of absorption at 3550 A. Since the white state of thoria shows no absorption band, it seems to be the stoichiometric form of thorium oxide, with an optical intrinsic gap at 3.5 ev. The change to the red form seems attributable to thorium vacancies, since the oxygen ion is apparently too large to enter into interstitial sites. The absorption band at 4050 A (3.0 ev) in the yellow crystals is presumably due to oxygen vacancies or to interstitial thorium.

* Assisted by the Office of Ordnance Research.
† *Advances in Electronics*, (1953), Vol. V, p. 203.

D3. Effect of Impurities on Mobility in *n*-Type InSb.* T. C. HARMAN, R. K. WILLARDSON, AND A. C. BEER, *Battelle Memorial Institute.*—The electron mobility in *n*-type InSb has been determined from Hall and resistivity data at room temperature and at 80°K in specimens having extrinsic carrier concentrations ranging from 10^{14} to 10^{17} cm^{-3}. Samples were cut from different locations along the zone-refined ingots in order to study the effects of varying amounts of compensation. In the purest specimen, mobility values of 74 000 cm^2/volt-sec at 300°K and 500 000 cm^2/volt-sec at 80°K were measured. Deviations from lattice mobility due to impurity scattering became apparent only at temperatures below 125°K. With an effective mass of 0.036 m_0, it was found that the Conwell-Weisskopf equation could effectively account for the observed mobility values as long as the impurity concentrations were below 10^{15} cm^{-3}. At impurity concentrations of 10^{17} cm^{-3}, however, both the Conwell-Weisokopf and Brooks-Herring relationships gave results about an order of magnitude below the observed mobility values.

* Supported by Wright Air Development Center contract.

D4. Magnetic Susceptibility of Indium Antimonide. J. H. CRAWFORD, JR., AND D. K. STEVENS, *Oak Ridge National Laboratory.*—The magnetic susceptibility of single crystal specimens[1] of InSb have been measured as a function of temperature over the range from 90° to 600°K. The purity of the specimens ($\sim 10^{16}$ carriers/cm^3) was such that the specimens were intrinsic above 200°K. The diamagnetic susceptibility increased markedly with temperature with the onset of intrinsic behavior. The contribution due to intrinsic carriers has been estimated by subtracting the low temperature value of the susceptibility which in *p*-type material is expected to be approximately the contribution of the lattice. A plot of the logarithm of the carrier susceptibility divided by $T^{\frac{1}{2}}$ *vs* reciprocal temperature yields a straight line in the intrinsic range with a slope corresponding to an energy gap of 0.19 ev. This value is in reasonable agreement with the thermal energy gap obtained by other methods.[2] A tentative analysis of the results indicates an electron effective mass of $m^* \simeq 0.025\ m_0$, a value somewhat smaller than obtained from electrical measurements.

[1] We are indebted to Dr. M. Tannenbaum of Bell Telephone Laboratories who furnished the specimens.
[2] Breckenridge, Blunt, Hosler, Frederikse, Becker, and Oshinsky, Phys. Rev. **96**, 571 (1954).

D5. Galvano Magnetic Effects in InSb. W. R. HOSLER AND H. P. R. FREDERIKSE, *National Bureau of Standards.*—The magnetoresistance and magneto-Hall effects of InSb have been measured as a function of crystal orientation, magnetic field strength and temperature. Both *p*- and *n*-type crystals have been studied; the carrier concentrations at liquid nitrogen temperature were 3×10^{16}/cc(*p*) and 10^{15}/cc(*n*), respectively. Measurements were made at 300°K and at 78°K on samples cut in the (100) as well as the (110) direction. Magnetic fields (both parallel and perpendicular to I) ranged from 100 to 5000 oersted. The galvanomagnetic effects in these InSb samples are complicated by several factors: mixed conduction at room temperature, two different scattering mechanisms for the charge carriers at 78°K, and high electron mobility. Both the weak field ($H < 1000$ oersted) and the strong field cases ($H =$ several thousands of oersteds) can be studied on *n*-type samples. Results indicate that the effects in *p*-type InSb are in agreement with the simplified theory[1] which assumes spherical energy surfaces. The data on *n*-type samples suggest, however, a more complicated structure of the conduction band.

[1] F. Seitz, Phys. Rev. **79**, 372 (1950).

D6. Hall Effect and Resistivity of Indium Antimonide at Low Temperatures.* H. FRITZSCHE AND K. LARK-HOROVITZ, *Purdue University.*—The Hall coefficient R and the resistivity ρ of *p*-type indium antimonide have been measured between 1.3°K and 300°K. The specimens were single crystals containing 10^{15} to 3×10^{16} acceptors per cc. All specimens showed

the same anomalous behavior of the Hall coefficient R—maximum at low temperatures—and the resistivity between 12°K and 20°K as was first observed on germanium in 1950.[1] The Hall maximum decreases and shifts to higher temperatures as the impurity content is increased. In the lowest temperature range ρ depends strongly on impurity content suggesting conduction in an impurity band. The magnetoresistive ratio of the purer samples changes from positive to negative values at about 11°K as the temperature is lowered.

* Work supported by U. S. Signal Corps.

[1] C. S. Hung and J. R. Gliessman, Phys. Rev. **79**, 726 (1950). See also J. Hatton and B. V. Rollin, Proc. Phys. Soc. (London) **A67**, 385 (1954).

D7. Properties of Mg_2Sn. R. F. BLUNT, H. P. R. FREDERIKSE, AND W. R. HOSLER, *National Bureau of Standards.*—This compound has been shown to have the fluorite structure and to be a semiconductor with a small energy gap.[1,2] Both n- and p-type samples have been prepared. Results of Hall and resistivity measurements at temperatures between 78°K and 300°K will be presented. The electron mobility is about 3300 cm²/volt-sec at liquid nitrogen temperature and follows a T^{-2}-dependency in the range 100–300°K. The energy gap appears to be 0.32 ev at absolute zero. From the mobility ratio (1.2) one calculates effective masses of the order of m for both holes and electrons. Optical absorption measurements have been made on several cleaved samples at 300°K and at lower temperatures. The location of the absorption edge is in agreement with electrical data; the temperature shift is -4×10^{-4}ev/deg. Observations on the photoresponse of this material will also be presented.

[1] G. Busch and U. Winkler, Helv. Phys. Acta **26**, 395 and 578 (1953).
[2] W. D. Robertson and H. H. Uhlig, Trans. Am. Inst. Mining Met. Engrs. **180**, 245 (1949).

D8. Mobility of Holes in Si and Ge. H. EHRENREICH AND A. W. OVERHAUSER, *Cornell University.*—The mobility of holes due to lattice scattering has been calculated taking into account transitions within and between the two degenerate valence bands at $\mathbf{k}=0$. The slight deviations of the energy surfaces from spherical symmetry were neglected, and matrix elements were calculated from Bloch functions whose cellular dependence was assumed to be of pure p character. Only one unknown constant C, equal to the kinetic energy at $\mathbf{k}=0$, enters the theory. Using effective mass data from cyclotron resonance experiments, and assuming reasonable values for C, the theoretical mobilities at room temperature are an order of magnitude larger than experimental values. The usual $T^{-1.5}$ temperature dependence was obtained. Transverse and longitudinal phonons were found to be about equally effective in scattering. Umklappprozesse do not occur, scattering from optical modes is completely negligible, and the temperature dependence of effective mass values due to self energy interaction with the phonon field is too small to explain the anomalous temperature dependence of the mobility. One can prove that second- and higher-order scattering effects (many phonon processes) need not be considered, or more precisely, the effect of such processes on transport theory is automatically included in a first-order perturbation calculation.

D9. Theory of the Photomagnetoelectric Effect in Semiconductors. W. VAN ROOSBROECK, *Bell Telephone Laboratories.*—An ambipolar treatment[1] furnishes general differential equations for added carrier transport with magnetic field. These equations are applied to the photomagnetoelectric effect in an infinite slab with radiation incident on one surface and steady parallel magnetic field. The condition that the curl of the electrostatic field must vanish requires a constant (depth-independent) photomagnetoelectric field along the slab and a nonvanishing curl of local total current density $\mathbf{I}$. It follows that photomagnetoelectric open-curcuit voltage V_0 is the same on both surfaces, with $\mathbf{I}$ a circulating current. Derivations[2] that assume zero $\mathbf{I}$ and predict differing voltages on the surfaces are accordingly incorrect. Correct V_0 has been given, as calculated for a slab with end electrodes for which constant photomagnetoelectric field was assumed.[3] Photomagnetoelectric short-circuit current as well as V_0 is derived for the small-signal case and for large light intensity, assuming constant surface recombination velocities and lifetime. The nonlinear case of arbitrary light intensity can be solved exactly without recourse to numerical integration of the differential equations.

[1] W. van Roosbroeck, Phys. Rev. **91**, 282 (1953).
[2] Moss, Pincherle, and Woodward, Proc. Phys. Soc. (London) **B66**, 743 (1953).
[3] P. Aigrain and H. Bulliard, Compt. rend. **236**, 595 (1953); H. Bulliard, Ann. phys. **9**, 52 (1954).

D10. The Faraday Effect in Semiconductors at Microwave Frequencies,* RICHARD RAU AND P. H. MILLER, JR., *University of Pennsylvania*—The free charge carriers cause a rotation of the plane of polarization when a plane polarized electromagnetic wave passes through a nonferromagnetic semiconductor and a static magnetic field is applied along the direction of propagation. The Drude-Zener theory predicts the following difference between the squares of the propagation constants for left and right circularly polarized radiation respectively, which then determines the angle of rotation.

$$k_e^2-k_i^2=\frac{2\mu_0\{\sigma_0\omega\mu B[1+(\mu B)^2+(\omega\tau)^2]+2i(\mu B)(\omega\tau)\sigma_0\omega(1+i\omega\tau)\}}{[1+(\mu B-\omega\tau)^2][1+(\mu B+\omega\tau)^2]},$$

where B is the magnetic field, σ_0 the dc conductivity, $\omega/2\pi$ the frequency, μ the mobility, and τ the relaxation time. Room temperature measurements of this angle of rotation on various samples of germanium, gave values of 4000 ± 100 cm²/volt sec and 3400 ± 100 cm²/volt sec for the electron and hole mobilities respectively. The method should be applicable to powdered samples after the internal field has been determined by a Clausius-Mosotti type approximation.

* This work supported by the U. S. Air Force.

D11. Configuration Interaction and Holes. P. J. PRICE, *IBM Watson Laboratory.*—Hole excitations are known to exist in valence crystals where the electron wave function $\Psi(\mathbf{r}_1,\cdots\mathbf{r}_N)$ of the ground state is not a determinant. The conventional description of the state with a hole thus needs to be generalized: We propose a wave function $N^{\frac{1}{2}}\int\phi^*(\mathbf{r}_1)\Psi d^3\mathbf{r}_1$, and determine $\phi(\mathbf{r})$ by requiring the energy expectation to be stationary. By the transformation $|\phi'\rangle=R^{\frac{1}{2}}|\phi\rangle$, where R is the one-particle density matrix for Ψ, we obtain a "wave equation" (with the excitation energy as eigenvalue) for ϕ' (the solutions being bands of functions of Bloch form). There are in general more than N formal solutions. It will be argued that, in certain conditions which will be discussed, there should in consequence actually be more of these bands of hole states than the determinant approximation, for the "valence shell," would require.

D12. On Smakula's Equation in Insulating Solids. D. L. DEXTER, *University of Rochester.*—Smakula's equation relates the product of the oscillator strength f and the concentration n of an absorbing impurity to the peak value and energy width of the absorption spectrum. This equation is based on two assumptions whose validity will be examined. The first that the band shape is classical, will be shown to lead to an overestimate of nf by the factor $(\pi\ln2)^{\frac{1}{2}}=1.48$ in simple cases where the shape is expected to be approximately Gaussian. The second assumption essentially was that the electric field inducing the transition at the impurity was the Lorentz "effective field." Conditions of validity for this and alternative assumptions will be discussed. In diffuse centers, such as impurity atoms in Ge, the product nf is underestimated in using Smakula's equation by the factor $9/(\kappa+2)^2$, or by a factor of $\sim1/40$. Only in the case of tightly bound centers whose

absorption is far from resonance with the host crystal may Smakula's assumption be valid. Some of the influences of resonance phenomena will be discussed for such real cases as the *F*-center or KCl:Tl.

D13. Saturation Hall Constant and Magnetoresistance in Semiconductors. JOHN A. SWANSON, *International Business Machines Corporation.*—The limit of the Hall constant as the magnetic field becomes infinitely large has been investigated using two different approaches: (a) the crystal momentum "force equation" approximation, and (b) perturbation theory, taking as unperturbed wave functions those which exist in the magnetic field alone. It is found by the first method that the saturation constant is $1/nec$ for all orientations provided that all relevant electrons in each unfilled band are confined to finite disjoint regions in extended (infinite) crystal momentum space. The unscattered orbits in *P*-space, which determine the saturation constant, are then reentrant for sufficiently large ratios of magnetic field to longitudinal current. The same saturation constant is found by the second approach, provided that in a magnetic field all relevant electrons may occupy states for which a small electric field constitutes only a perturbation. Similar results apply to holes. Saturation magnetoresistance will also be discussed briefly.

D14. Some Magneto-Electric Effects in Germanium in Strong Magnetic Fields. WARREN E. HENRY, *U. S. Naval Research Laboratory.*—Demonstration of change from quadratic to linear dependence of the electrical resistance of germanium on transverse magnetic fields has been carried out by Kapitza,[1] and approximate theoretical linearization of the field dependence at high fields has been achieved by Harding,[2] giving qualitative agreement with this and later work by Pearson and Suhl,[1] except that the linear range begins at lower fields in the theoretical relation. Kapitza worked under the handicap of impure germanium and pulsed fields of 0.01 sec duration. He predicted a linear region at lower fields with pure germanium. The present investigation has been carried out with the specimen purity improved over 100 fold (kindly supplied by Sylvania) and in steady magnetic fields to more than 100 000 gauss. Thus, for comparable fields, at 300°K and 77.4°K, our results show a fourfold reduction in the field for onset of linearity and a tenfold advantage in $\Delta R/R$. Both the magnetoresistance and Hall effect can be used for high precision magnetometry. A nonmonotonic field dependence of the resistance was observed at 4.2°K.

[1] P. Kapitza, Proc. Roy. Soc. (London) **A123**, 292 (1929); G. L. Pearson and H. Suhl, Phys. Rev. **83**, 768 (1951).
[2] J. W. Harding, Proc. Roy. Soc. (London) **A140**, 205 (1933).

D15. Theory of the Anisotropy of Magnetoresistance for Single Crystals.* L. P. KAO AND E. KATZ, *University of Michigan.*—Progress in the theory of the magnetoresistance of an anisotropic single crystal, belonging to any of the 32 point groups, for arbitrary orientation of the sample and arbitrary orientation of the applied magnetic field is presented. This theory is a continuation of what we have previously reported.† It is shown that the magnetoresistance is an even power series of the magnetic field strength. The coefficients of this series are given in terms of the direction cosines of the magnetic field and of the measured current with respect to the crystal axes and in terms of components of tensors of rank $2n+2$, where n is the highest power of the magnetic field required to interpret an experiment. A method has been developed to determine all symmetry relations of the tensor components for each of the 32 point groups. Tensor components tabulated accordingly are given for all 32 point groups for n up to 4, although the method is valid for any value of n.

* Sponsored by U. S. Signal Corps Supply Agency.
† L. P. Kao and E. Katz, Phys. Rev. **94**, 1433(A) (1954).

THURSDAY AFTERNOON AT 2:00

Phoenix Room

(J. D. WATSON presiding)

Continuation of the DHPP Symposium on Nucleic Acid

E1. Infrared Analysis of the Structure of Proteins and Nucleic Acids. G. B. B. M. SUTHERLAND, *University of Michigan.* (30 min.)

E2. Genetic Fine Structure and Its Relation to the Deoxyribonucleic Acid Molecule. SEYMOUR BENZER, *Purdue University.* (30 min.)

E3. The Transfer of Information from Nucleic Acids to Proteins. G. GAMOW, *George Washington University.* (30 min.)

Business Meeting of the Division of High-Polymer Physics

THURSDAY AFTERNOON AT 2:00

Calvert Room

(H. Y. FAN presiding)

Semiconductors, II

F1. Some Properties of Germanium Doped with Manganese. H. H. WOODBURY AND W. W. TYLER, *General Electric Research Laboratory.*—Manganese introduces deep levels in germanium similar to those observed in iron-,[1] colbalt-,[2] and nickel-doped[2] germanium. These levels are at 0.35 ± 0.02 ev from the conduction band (n-type) and 0.16 ± 0.01 ev from the

valence band (p-type) and have been identified from the temperature dependence of resistivity. Three different sources of electrolytic manganese have been used. The distribution coefficient for Mn in Ge is about 10^{-6}. At temperatures below 200°K, high resistivity n-type samples show high photosensitivity and slow photoconductive decay which is not surface dependent. Evidence for hole trapping in both n- and p-type material has been observed by studying Hall mobility of optically induced carriers. Although exponential photoconductivity decay curves have been observed, the recovery process does not appear to be a simple evaporation process. Injection breakdown effects similar to those reported for iron-doped samples[3] have also been observed in n-type Mn-doped crystals.

[1] W. W. Tyler and H. H. Woodbury, Phys. Rev. 96, 874 (1954).
[2] Tyler, Newman, and Woodbury, Phys. Rev. 97, 669 (1955).
[3] W. W. Tyler, Phys. Rev. 96, 226 (1954).

F2. Gold, an "Amphoteric" Impurity Element in Germanium. W. C. DUNLAP, JR., *General Electric Research Laboratory.**—Gold is shown to be an "amphoteric" element in germanium; that is, it can either donate or accept electrons depending upon the type and amount of other impurities present. Previously,[1] the acceptor action of gold in germanium had been described, and it was shown that there were two states 0.15 and 0.55 ev above the valence band. Morton, Hahn, and Schulz have found evidence for a third state which they interpret as the first acceptor level. In the present investigation, the existence of a third state is confirmed and it is shown, to a high degree of certainty, that this is a donor state 0.05 ev above the valence band. When gold is added to germanium containing fifth column acceptors in amounts less than the gold content, the carrier density at 77°K remains constant, and the carriers acquire an activation energy of about 0.05 ev. Good agreement was obtained with several sources of gold. It is suggested that neutral gold atoms give up electrons to low-lying empty states and become Au^+. The upper states remain Au^- and Au^{--}. The donor level appears to be analogous to the donor level in silicon.

* Present address, General Electric Company, Syracuse, New York.
[1] W. C. Dunlap, Jr., Phys. Rev. 91, 1282 (1953).

F3. Optical Effects in Plastically Deformed Germanium. H. G. LIPSON, E. BURSTEIN, AND P. L. SMITH, *U. S. Naval Research Laboratory.*—N-type germanium specimens of 1 ohm-cm resistivity were plastically deformed from 3 to 15 percent at about 700°C. The more strongly deformed specimens were found to be converted to p-type. All of the deformed specimens exhibited a shift in the intrinsic absorption edge as well as an extended tail. Those samples which were converted to p-type also exhibit the characteristic absorption bands due to free holes. The long wavelength tail may possibly be associated with optical transitions of holes from dislocation acceptor levels[1] to the valence band. These results differ from those obtained for neutron bombarded germanium[2] which exhibits no shift of the absorption band and a tail of somewhat different character from that found in the plastically deformed material.

[1] Pearson, Read, and Morin, Phys. Rev. 93, 666 (1954).
[2] Unpublished data from work at NRL in collaboration with J. H. Crawford and J. W. Cleland of Oak Ridge National Laboratory.

F4. Electrical Properties of Electron Bombarded Ge.* E. E. KLONTZ, R. R. PEPPER, AND K. LARK-HOROVITZ, *Purdue University.*—To observe properties of defects introduced by 4.5-Mev electron bombardment of Ge, Hall values R and resistivity ρ for various N-type and p-type samples have been determined as a function of bombardment at different temperatures. For both N and P-type samples bombarded near nitrogen temperature (87°K), R and ρ increase initially. While still N-type, a sample illuminated with white light exhibits photoconductivity which increases very slowly in the presence of the light indicating existence of hole traps. Nonequilibrium conditions for initially p-type and for N-type samples which have been converted are indicated by a steady increase in values of R and ρ after bombardment. Bombardments near 200°K produce converted samples having a photoconductivity which decays in a matter of minutes. A 40 ohm cm. p-type sample at this temperature changes only slightly with bombardment while the resistivity of a 6 ohm cm sample increases. Production of energy levels about 0.2 ev above the valence band is indicated. Bombardments at 2°C convert n-type samples to p-type, which then revert back to n-type, at the bombardment temperature, in a matter of hours. In a 40 ohm cm p-type sample, R and ρ decrease on bombardment, whereas they increase slightly in a 5 ohm cm sample. Samples bombarded at 87°K and 200°K also revert at about 0°C unless they have been bombarded with very large flux.

* Supported by the U. S. Atomic Energy Commission and Signal Corps contract.

F5. Photoconductivity of Electron-Bombarded Ge.* F. STOECKMANN, E. KLONTZ, H. Y. FAN, AND K. LARK-HOROVITZ, *Purdue University.*—The photoconductivity of n-type Ge, illuminated with light in the fundamental absorption region, increases during bombardment with fast electrons (6 Mev) at 90°K. The increase is fast at the start of irradiation, slower after prolonged bombardment amounting to two orders of magnitude. The time constants of the rise and decay curves are about one second. The photoconductivity decreases as the sample is converted to p-type. In the p-type region the response is smaller than before bombardment. These observations show the production of hole traps by the bombardment. Direct evidence for such traps is given by the spectral distribution of the photoconductive response, which after bombardment shows two bands beyond the absorption edge at about 0.35 ev and 0.55 ev. After conversion to p-type the 0.35 ev band disappears while illumination in the 0.55 ev band *decreases* the conductivity, therefore these bands must be due to electron transitions from localized states to the conduction band. The 0.35 ev state seems to be the trap responsible for the large increase of photoconductivity. Previously reported results[1] are confirmed after the sample had been warmed to room temperature.

* Work supported by a Signal Corps Contract and U. S. Atomic Energy Commission Contract.
[1] Fan, Kaiser, Klontz, Lark-Horovitz, and Pepper, Phys. Rev. 95, 1087 (1954).

F6. Properties of Powdered Germanium and Effects of Heat-Treatment. E. A. KMETKO, *Sylvania Electric Products Inc.*—Properties of germanium powders made from both n- and p-type materials were studied. In both cases a reaction with water occurs to form a strong unidentified acid (pH of aqueous slurries observed as low as ~ 2). After heat-treatment in helium ($\gtrsim 500$°C) or exposure to air for several months this property is lacking. The electrical resistivity, measured for compressed powders, increases with time, but as a result of heat-treatment the change may be retarded, or apparently even halted, depending on the conditions. Treatment at the lower temperatures, or long exposure to air, results in non-ohmic conductivity ($i \sim \exp aV^{\frac{1}{2}}$) which depends approximately exponentially on pressure. This and other evidence to be presented (effects of ambients, etching, etc.) show that the non-ohmic (Schottky type) character of the contact between particles of disturbed germanium is caused by the presence of thick surface layers of GeO_2. The stabilizing effect of heat-treatment can be interpreted according to Clarke's picture[1] whereby the normally formed water soluble GeO_2 (hexagonal) is converted to the insoluble form (tetragonal).

[1] E. N. Clarke, Bull Am. Phys. Soc. 30, No. 1, 39 (1955).

F7. Infrared Absorption in *N*-Type Germanium.* W. SPITZER, R. J. COLLINS,† AND H. Y. FAN, *Purdue University.*—Absorption in *n*-type germanium is investigated from 5 to 30 microns at different temperatures on samples of various carrier concentrations. At room temperature the absorption coefficient, α, is roughly proportional to the carrier concentration, n, but this is a systematic change in the shape of $\alpha(\lambda)$ curve for samples with different n. At 450°K, curves of α/n for different samples agree fairly well. The quantum-mechanical formula for carrier absorption due to lattice scattering[1] gives the right order of magnitude for α/N using $m^*/m=0.135$, but the calculated curve rises nearly as λ^2 whereas the experimental curve is less steep. At 78°K, $\alpha(\lambda)$ curves for different samples have the same shape, nearly as λ^3. Theory of absorption by carriers with impurity scattering[1] gives α increasing as $\lambda^{3.5}$ and α/n proportional to the impurity concentration N. Various samples, including one with compensating impurities, give $\alpha/N=(a+bN)$. The results indicate that at high temperatures lattice scattering effect is dominant and at low temperatures impurity scattering becomes important for the absorption.

* Work supported by a Signal Corps Contract.
† Now at Bell Telephone Laboratories.
[1] H. Y. Fan and M. Becker, *Semiconducting Materials* (Butterworths, London, 1951), p. 132.

F8. Hall Effect and Resistivity of *P*-type Germanium at Low Temperatures.* K. LARK-HOROVITZ AND H. FRITZSCHE, *Purdue University.*—The Hall coefficient R and the resistivity ρ of germanium single crystals with gallium concentrations larger than 2×10^{16} atoms per cc have been measured between 1.3°K and 300°K. The temperature dependence of the conductivity can be described by a sum of three exponential terms instead of two, as in the case of purer samples. In contrast to the behavior of samples with smaller impurity content, the Hall curves of these samples do not have a sharp maximum but a very irregular shape which is different for different impurity contents. At low temperatures the Hall curves do not approach the high temperature exhausting range value as was predicted by Hung,[1] on the basis of measurements carried out with polycrystalline samples, but show a definite slope at still lower temperatures. In all cases thus far the sign of R is the same throughout the whole temperature range in which observations were made.

* Work supported by Signal Corps Contract.
[1] C. S. Hung, Phys. Rev. **79**, 727 (1950).

F9. Self-diffusion in Germanium.* WILLIAM M. PORTNOY, HARRY LETAW, JR., AND LAWRENCE SLIFKIN,† *University of Illinois.*—An accurate determination of the self-diffusion coefficient in germanium has been obtained. As reported earlier,[1] radioactive Ge^{71} was electroplated onto small slabs of germanium. After annealing at constant temperature in the range 928–766°C, the specimens were sectioned on the precision grinding machine.[2] Between these temperatures, the data may be represented by $D=7.8\exp(-68\,500/RT)$ cm²/sec. The probable errors in the frequency factor and the activation energy are ±3.4 cm²/sec and ±0.96 kcal/mole, respectively. No further cases of grain boundary diffusion attributable to grain growth during the diffusion anneal have been observed.[1]

* Supported in part by the Office of Naval Research, the Air Research and Development Command of the U. S. Air Force, and a grant from the Motorola Corporation.
† Now at the University of Minnesota.
[1] Letaw, Slifkin, and Portnoy, Phys. Rev. **93**, 892 (1954).
[2] Letaw, Slifkin, and Portnoy, Rev. Sci. Instr. **25**, 865 (1954).

F10. Optical Properties of Group III Elements in Silicon. E. BURSTEIN, G. PICUS, B. HENVIS, AND M. LAX, *U. S. Naval Research Laboratory.*—Optical measurements on B. T. L. *p*-type silicon doped with group III-B (boron, aluminum, gallium, and indium)[1] elements have been carried out at liquid helium temperatures. The variation in ionization energies[2] among these elements are found to be accompanied by appreciable variations in the character of the excitation and photo-ionization absorption spectra. Analysis of the data indicates that, in going from boron to indium, the energies of the *p*-states remain approximately unchanged with respect to the valence band, while the *ls* states move further from the top of the valence band. This behavior is understandable in terms of a modified hydrogen model with a potential well at the impurity atom.[3] This perturbing potential, due to the impurity ion core, may be expected to affect *s*-states more strongly that *p*-states.

[1] These were kindly supplied by J. Burton, R. G. Shulman, and F. J. Morin of the Bell Telephone Laboratories.
[2] Morin, Maita, Shulman, and Hannay, Phys. Rev. **96**, 833 (1954).
[3] G. F. Koster and J. C. Slater, Phys. Rev. **96**, 1208 (1954).

F11. Birefringence in Silicon. W. C. DASH, *General Electric Research Laboratory.*—An infrared image tube or "snooperscope" using a cesium-silver-oxide photoemitting surface makes possible visual studies of birefringence in silicon. A polished slab cut parallel to the axis of an ingot grown by the Czochralski technique has a birefringent pattern characteristic of the conditions of growth. In crystals rotated during growth a series of birefringent "stripes" are found apparently parallel to the growth surface and independent of crystal orientation. These stripes can be created deliberately by suddenly varying the temperature of the melt as in the rate-growing of $p-n$ junctions.[1] Correlations have been found between these patterns and heat treatment effects upon electrical properties.[2] Crystals unrotated during growth do not show stripes, but, surprisingly, are also birefringent. Specimens with large numbers of parallel twins also show characteristic but unrelated birefringence patterns of a different type from "growth" birefringence. Birefringence in alloy contacts, in grain boundaries, bent specimens, specimens with precipitated impurities, etc., will be discussed. Birefringence has also been detected in germanium, but lack of an infrared image-forming device sensitive in the range of germanium transparency prevents detailed studies.

[1] R. N. Hall, J. Phys. Chem. **57**, 836 (1953).
[2] Fuller, Ditzenberger, Hannay, and Buehler, Phys. Rev. **96**, 833(A) (1954).

F12. Reverse Current and Carrier Lifetime as a Function of Temperature in Germanium and Silicon Junction Diodes. E. M. PELL, *General Electric Research Laboratory.*—The reverse current and carrier lifetime have been measured in a series of germanium and silicon diodes as a function of temperature between 200°C and −196°C. In germanium, the lifetime reaches a plateau at low temperatures, and its behavior can be explained in terms of the Hall-Schockley-Read[1,2] recombination theory using two recombination center levels. Silicon behaves in a roughly similar fashion. The behavior of $\log i_R$ *vs* $1/T$, the magnitude of i_R, and the shape of i_R *vs* V suggest that the reverse current is produced predominantly by charge generation within the depletion layer in germanium at low temperatures and in silicon up to room temperature and often above. The generation centers are about 0.3 ev deep in Ge and 0.5 ev deep in Si.

[1] R. N. Hall, Phys. Rev. **87**, 387 (1952).
[2] W. Shockley and W. T. Read, Jr., Phys. Rev. **87**, 835 (1952).

F13. Visible Light from a Si $p-n$ Junction. R. NEWMAN, W. C. DASH, R. N. HALL, AND W. E. BURCH, *General Electric Research Laboratory.*—We have observed that when a silicon $p-n$ junction was biased in the reverse direction beyond the point of breakdown, a yellowish white light was emitted at the junction. A number of heavily doped grown junctions (reverse breakdown of order 10–20 volts) were examined and all showed the effect to a greater or lesser degree. The efficiency of light emission is sensitive to surface treatment. When

examined under high magnification (500×), it was found that the light was emitted in regions at the junction of order of 10 microns wide and often extending several mm along the junction with uniform intensity. The spectrum of the light taken with a low dispersion monochromator and a photomultiplier detector showed a relatively constant output from about 1.8 to 2.4 ev followed by a rapid drop off out to 3.4 ev, the limit of our measurement. The origin of the light is in doubt. Light is emitted when the junction is operated in vacuum indicating that it does not result from an external gas discharge. It may result from a breakdown in the oxide film or in the silicon itself. It is energetically possible that such light could arise from recombination in an avalanche breakdown.[1]

[1] K. G. McKay, Phys. Rev. 94, 877 (1954).

THURSDAY AFTERNOON AT 2:00

Founders' Room

(F. RASETTI presiding)

Nuclear Physics

G1. Quadrupolar Splitting of Nuclear Resonance Lines in the Alums.* W. G. SEGLEKEN AND H. C. TORREY, *Rutgers University.*—Nuclear magnetic resonances of Al^{27} in single crystals of $AlK(SO_4)\cdot 12H_2O$ and $Al(NH_4)(SO_4)_2\cdot 12H_2O$ were observed at 12 mc/sec (10.8 kilogauss). The crystals were mounted so that they were rotatable about a (001) axis kept perpendicular to the magnetic field. In each case the line was split into five equally spaced lines. The spacing was proportional to $\sin 2\theta$ where θ is the angle between the magnetic field and the (100) direction. The maximum separations between adjacent lines ($\theta=45°$) are 30.0 ± 0.6 kc/sec for the potassium salt and 33.5 ± 0.6 kc/sec for the ammonium salt. This splitting is caused by a small trigonal field along the body diagonals interacting with the nuclear quadrupole moment of Al^{27}. A similar field exists in the chromium isomorphs of these salts and produces there a Stark splitting of the ground state of the paramagnetic Cr ions. The ratio ($1.12\pm.03$) of the above quadrupolar splittings in the aluminum alums is the same as the ratio ($1.12\pm.07$) of the ground-state splittings in the corresponding chrome alums as determined[1] by paramagnetic resonance.

* Supported by the U. S. Air Force.
[1] Bagguley and Griffiths, Proc. Roy. Soc. (London) **A204**, 188 (1950).

G2. Quadrupole Moments of Rb^{85} and Rb^{87}. B. SENITZKY, I. I. RABI, AND M. L. PERL, *Columbia University.*—The atomic beam magnetic resonance method for excited atomic states[1-4] has been applied to Rb^{85} in the $5P_{\frac{1}{2}}$ hyperfine levels. Two resonance lines were found, one at 121 mc and the other at 65 mc. The former was approximately twice as strong as the latter. While no definite identification of the transitions has been made, we assume that the higher frequency corresponds to the $F=4\rightarrow3$ and the lower frequency to the $3\rightarrow2$ transition. This assumption leads to values of "b" $=25\pm2$ mc and "a" $=25\pm0.5$ mc. The "a" is consistent with the known magnetic moment of Rb^{85}. The quadrupole moment of Rb^{85} calculated with the use of the fine structure separation of the Rb levels leads to the value of $Q_{Rb^{85}}=3.1\times10^{-25}$ cm² and from the known ratio of $Q_{Rb^{85}}/Q_{Rb^{87}}$ the quadrupole moment of Rb^{87} is 1.5×10^{-25} cm².

[1] I. I. Rabi, Phys. Rev. 87, 379 (1952).
[2] Perl, Rabi, and Senitzky, Proc. Natl. Acad. Sci., 40, No. 11 (A) (1954).
[3] Perl, Rabi, and Senitzky, Phys. Rev. 97, 3 (L) (1955).
[4] Perl, Rabi, and Senitzky, "Nuclear electric quadrupole moment at Na^{23} by an atomic beam resonance method," Phys. Rev. (to be published).
[5] J. W. Trischka and R. Braunstein, Phys. Rev. 96, 968 (1954).

G3. Nuclear Magnetic Moment of Potassium[39]. L. CARLTON BROWN AND DUDLEY WILLIAMS, *The Ohio State University.**—The nuclear magnetic resonance peak due to K^{39} in a saturated solution of KF has been observed in a field of approximately 7800 gauss. The K^{39} resonance frequency has been compared with that of N^{14} in a solution of HNO_3. The ratio obtained is $\nu(K^{39})/\nu(N^{14})=0.64588$, a value in agreement within the limits of experimental error with the value obtained by Collins,[1] who observed the K^{39} resonance in a solution of KNO_3. A comparison of the experimental errors will be given and a "best value" for the magnetic moment will be proposed.

* Supported by the Office of Scientific Research, Air Research and Development Command, U. S. Air Force.
[1] T. L. Collins, Phys. Rev. 80, 103 (1950).

G4. Electron Capture Cross Section for Protons. C. F. BARNETT AND P. M. STIER, *Oak Ridge National Laboratory.*—Electron capture cross sections have been determined for protons passing through various gases in the energy range 20 to 250 kev. The proton beam from a Cockcroft-Walton accelerator was passed through a differentially pump gas cell in a transverse magnetic field. Neutral atoms formed by electron capture collisions do not follow the curved path of the ion beam and are not detected. From the exponential attenuation of the proton beam, the capture cross section is directly determined. Results will be presented for the capture cross section in hydrogen, helium, nitrogen, oxygen, neon, and argon. For energies greater than 80 kev the capture cross section varies as $\sigma_c=Ae^{-Bv}$, where A and B are constants for each gas, and v is the proton velocity. The cross section is the smallest for hydrogen being 20×10^{-17} cm² at 20 kev and 0.9×10^{-17} cm² at 200 kev. For argon the cross section decreases from 70×10^{-17} cm² at 20 kev to 1.12×10^{-17} cm² at 200 kev. The results are in agreement with those calculated from previously measured loss cross sections and the ratio of loss to capture cross section.[1]

[1] Stier, Barnett, and Evans, Phys. Rev. 93, 926 (A) (1954).

G5. Self-Absorption or Self-Indication in the Nuclear Elastic Scattering Experiment.* E. G. FULLER AND EVANS HAYWARD, *National Bureau of Standards.*—A recent note[1] describing the elastic nuclear scattering of photons pointed out that the observed scattering cross sections below the particle threshold may require corrections for nuclear self-absorption by discrete energy levels. These corrections are required if the peak nuclear absorption cross section is greater than the electronic cross section. Thermal Doppler broadening reduces the peak cross section by approximately the ratio Γ/δ. Self-absorption has been observed by measuring the absorption of the target material for those photons which are elastically scattered. Self-absorption has been observed in Bi and Pb at 7 Mev, in Ni at 9 Mev, and in Al at 18 Mev. No appreciable effect was observed in Cu, Sn, or I. A "single level" analysis gives $\Gamma_\gamma/\Gamma\sim0.1$ for Bi, Pb, and Ni. The self-absorp-

tion corrections to the previously published scattering cross sections for the above nuclei will raise the cross sections at the energies indicated by about 15 percent.

* Supported by the Air Research and Development Command.
[1] Evans Hayward and E. G. Fuller, Phys. Rev. 95, 4, 1106 (1954).

G6. The $Li^6(p,d)Li^5$ Reaction.* J. G. LIKELY, *Princeton University.*—Deuterons from $Li^6(p,d)Li^5$ were observed on bombarding a Li^6 foil with 18.6-Mev protons. Particles passed through a proportional counter before stopping in a NaI scintillation counter. Proton background was eliminated by gating the NaI counter by pulse-height-selected proportional counter pulses having the correct size for deuterons at a particular energy. The $Li^6(p,d)Li^5$ ground-state group appears as a broad peak (1.8 Mev wide at half-maximum) which tails off to a low continuum at lower energies: from the maximum of the peak, $Q=-3.0\pm0.15$ Mev. While no other deuteron groups were observed, up to 6.5-Mev excitation in Li^5, the asymmetry of the main group (low-energy side) may suggest a broad level near the ground state. Deuteron background, possibly due to particle decay of Li^6 excited states, complicates the interpretation. The angular distribution of the main group rises to a peak at 15 degrees (center of mass) and, at small angles, conforms with Butler theory ($r_{\text{nucleus}}=5\times10^{-13}$ and $\ln=1$) but falls off more gradually than expected beyond 30 degrees.

* This work was supported by the U. S. Atomic Energy Commission and the Higgins Scientific Trust Fund.

G7. Mechanism of the Reaction $C^{12}+p\rightarrow p+3\alpha$ at 32 Mev.† JOHN LOGAN NEED, *University of California, Berkeley.*—A methane-filled expansion cloud chamber, operated at ½ atmosphere, was used to study the $C^{12}+p\rightarrow p+3\alpha$ reaction. Two hundred events that satisfied momentum and energy conservation were accepted for analysis. One hundred forty-eight of these had all four prongs visible; the remaining fifty-two had only three visible prongs with the fourth prong directed into an invisible region of the chamber. There is no evidence for the direct four-particle decay of N^{13*}. One-quarter of the events proceeded via the Be^8 ground state and at least one-half via the 2.9-Mev level in Be^{8*}; possibly higher levels in Be^{8*} were also involved. Evidence for the participation of levels in C^{12} at 9.6, 11.8, 16, 20, and 25 Mev was found. There are grounds for believing that the $C^{12}(p,\alpha)B^9$ reaction also participated with evidence for the ground state and the 2.4-Mev state of B^9. The possibility of the $C^{12}+p\rightarrow Li^8+Be^8$ reaction was investigated and it was concluded that it could account for at most five percent of the events.

† This work was performed under the auspices of the U. S. Atomic Energy Commission.

G8. Levels in Sc^{41}. H. S. PLENDL AND F. E. STEIGERT, *Yale University.*—A thin target of natural Ca prepared by evaporation from $CaCO_3$ onto a tantalum foil was bombarded with the 4.18-Mev deuteron beam. The neutrons were observed by proton recoils in Ilford C2 emulsions at angles of 0°, 30°, 45°, and 90° with respect to the incident beam. No-target exposures were also made to check the neutron background which was then subtracted out. Data from the 90° and 30° plates indicate a ground-state Q-value for the $Ca^{41}(d,n)Sc^{41}$ reaction of -0.60 ± 0.05 Mev. This is in excellent agreement with the value obtained using the energetics of the $Ca^{40}(d,p)Ca^{41}$ reaction[1] and the Sc^{41} β decay.[2] Additional groups are observed corresponding to six excited states in Sc^{41} at 0.62, 0.97, 1.13, 1.72, 2.10, and 2.34 Mev. Work is continuing on higher levels. Groups corresponding to the ground states of the $O^{16}(d,n)$ and $C^{12}(d,n)$ reactions are also observed and give an excellent check on the energy.

[1] Braams, Phys. Rev. 94, 763(A) (1954).
[2] D. R. Elliott and L. D. P. King, Phys. Rev. 60, 489 (1941).

G9. Nuclear Levels in V^{48} as Determined by the Decay of Cr^{48}.* JOSEPH R. WILKINSON AND RAYMOND K. SHELINE, *Florida State University.*—Chromium-48 has been produced by the 50-Mev alpha-particle bombardment of separated Ti^{46}, the nuclear reaction being $Ti^{46}(\alpha,2n)Cr^{48}$. Chromium-48 has previously been reported as a spallation product[1] with a half-life of 23 or 24 hr. No gamma radiation was reported for this nuclide. Our measurements of the half-life yields a value of 23 hr over a period of 5 half-lives. The gamma-ray spectrum of Cr^{48} has been investigated by scintillation techniques involving a 1½ in. ×1 in. NaI(Tl) crystal mounted on a DuMont 6292 tube. Gamma rays of 118 and 307 kev decaying with a 23-hr period have been observed. An apparent gamma ray of 431 kev is largely the sum peak of the 118 and 307-kev gamma rays, indicating a coincidence between these radiations. This information, together with the intensities of the gamma rays, the failure to observe positron radiation, or the accompanying annihilation gamma rays, allows the determination of a probable decay scheme for Cr^{48} and the consequent energy levels in V^{48}.

* This work was supported in part by the U. S. Atomic Energy Commission.
[1] Rudstam, Stevenson, and Folger, Phys. Rev. 87, 358 (1952).

G10. Coulomb Excitation of Energy Levels in Te and Ag. L. W. FAGG, E. A. WOLICKI, R. O. BONDELID, K. L. DUNNING, AND S. SNYDER, *Naval Research Laboratory.*—Several nuclei having ground-state spin ½ and therefore $\Omega=\frac{1}{2}^1$ have been studied by Coulomb excitation with protons and alpha particles. Using isotopically enriched metallic targets, first and second excited rotational states have been measured at 319 kev and 419 kev in Ag^{107} (96.8 percent) and 306 kev and 412 kev[2] in Ag^{109} (99.9 percent). A first excited state has been measured at 159 kev in Te^{123}. Evidence for the second excited state in Te^{123} and excited states in Te^{125} has been obtained. Calibrated I^{131} and Na^{22} sources have been used in determining excitation cross sections and associated quadrupole moments.

[1] A. Bohr and B. R. Mottleson, Kgl. Danske Videnskab. Selskab, Mat.-fys. Medd 27, No. 16 (1953).
[2] With the exception of the 412-kev level in Ag^{109}, these values are in good agreement with the results of N. P. Heydenburg and G. M. Temmer, Phys. Rev. 95, 861 (1954).

G11. Polarization Measurement in the $D(d,p)H^3$ Reaction.† R. E. SEGEL AND S. S. HANNA, *The Johns Hopkins University.*—Thin targets of deuterium gas were bombarded with deuterons of 650-kev energy, and the protons entered a helium scattering chamber at an angle of 45° in the center-of-mass system. Protons scattered in the chamber were detected with two very thin NaI crystals placed at +90° and −90° (c.m.) to the proton direction. The polarization measurements were obtained by comparing the right-left scattering in helium gas to that in xenon. Background was determined by evacuating the scattering chamber. An additional determination of possible geometric asymmetry was obtained by rotating the scattering chamber through 180°. With the use of absorbing foils the measurements were performed at three different proton energies. Using the polarization parameters of Heusinkveld and Freier[1] for the $p-\alpha$ scattering, a polarization of (15 ± 10) percent was obtained for the D−D reaction at the bombarding energy used.

† Supported in part by U. S. Atomic Energy Commission.
[1] M. Heusinkveld and G. Freier, Phys. Rev. 85, 80 (1952).

G12. Electron Beam Extraction from an X-Band Microtron. H. F. KAISER, W. T. MAYES, AND W. J. WILLIS, *Naval Research Laboratory.*—Means for extraction of electrons using a general purpose X-band microtron[1] have been studied. This is possible by use of a magnetic shielding tube[2] placed in the magnetic field space to intercept a desired orbit half completed, thus allowing it to leave tangentially. A variety of such extractor probes have been studied experimentally and quite

different types give successful extraction. A conical-shaped tube with wall thickness decreasing to the electron ingress, first proposed,[2] was found less effective. Capture at the ingress is favored by sharp transition from field to no field but this increases distortion of the circular microton orbits near the probe. This distortion may be made more symmetrical using a probe in which electrons enter a slot on the side of a hollow cylinder extending across the field region. This offers the possibility of returning extracted electrons into the microtron to combine the extracted electrons to build up a circulating beam in an external guide field, thus forming the basis of a system whereby the microtron may be used as an injector for a large accelerator (conventional or strong-focusing synchrotron).

[1] H. F. Kaiser, Phys. Rev. 95, 667 (1954).
[2] Henderson, Heymann, and Jennings, Proc. Phys. Soc. (London) 66, 41, 654–664 (1953).

THURSDAY AFTERNOON AT 2:00

Federal Hill Room

(H. MEISSNER presiding)

Cryogenics; Fluid Dynamics

GA1. Superconducting Rhenium Alloys and Compounds. J. K. HULM, *Westinghouse Research Laboratories.*—In further studies of the superconductivity of arc-melted rhenium samples,[1] the addition of tungsten to rhenium in solid solution has been found to raise the superconducting transition temperature at the rate of about 0.4°K per atomic percent tungsten. The maximum value of T_c has not yet been determined, but it is known that the compound Re_3W_2, formed beyond the limit of solid solubility, becomes superconducting at about 6°K. Other superconducting compounds of rhenium are Re_2B (2.8°K), Re_2Zr (6°K), and Mo_3Re (10°K).

[1] J. K. Hulm, Phys. Rev. 94, 1390 (1954).

GA2. Heat Capacity Measurements on Pure and Slightly Reduced Rutile (TiO_2) at Very Low Temperatures.* P. H. KEESOM AND N. PEARLMAN, *Purdue University.*—The Debye parameter in the true T^3 region of the specific heat (θ_0) of rutile is 758°K (9N degrees of freedom) and this region extends to above 4°K. Between 10 and 20°K θ decreases from 680 to 460°K. After slight reduction in H_2 or A at 1000°C, the heat capacity in the helium region increases greatly. Reversibility was shown by reoxidation. For not too great reduction, the additional heat capacity is constant in the helium region, and probably constant up to 13°K. Reduced rutile is a semiconductor and the electrons have a very high effective mass.[1] The Hall effect in rutile shows a maximum around 6°K and so Hall measurements did not lead to an independent estimate of the carrier concentration. A tentative explanation of the additional heat capacity assumes that each "free" electron contributes $3/2k$. The estimated degeneracy temperatures lead to a carrier mass of 350 m_e.

* Assisted by Signal Corps and U. S. Atomic Energy Commission contracts.
[1] R. G. Breckenridge and W. R. Hosler, Phys. Rev. 91, 793 (1953).

GA3. Atomic Heat of Graphite Between 1° and 20°K.* N. PEARLMAN AND P. H. KEESOM, *Purdue University.*—The atomic heat of pure artificial polycrystalline graphite has been measured between 1° and 20°K. Precautions were taken to ensure that no error was introduced by gas adsorbed on the graphite. The results agree very well with those recently reported by Bergenlid *et al.*[1] Below 2°K the atomic heat can be represented as the sum of a term proportional to T^3 arising from low frequency lattice waves and a term proportional to T due to electrons. These terms are about equal to 1°K where the total atomic heat is 6×10^{-5} joules/mole degree. The electronic term agrees in order of magnitude with that calculated from Wallace's band structure theory of graphite. Between 2 and 4°K the lattice atomic heat is proportional to T^3, as has been predicted from a consideration of the anisotropic graphite lattice. Between 10 and 20°K the atomic heat variation corresponds to a decreasing two-dimensional Debye θ, presumably corresponding to deviations from a linear vibration spctrum.[2]

* Assisted by U. S. Atomic Energy Commission and by Signal Corps Contracts.
[1] Bergenlid, Hill, Webb, and Wilks, Phil. Mag. 45, 851 (1954).
[2] H. B. Rosenstock, J. Chem. Phys. 21, 2064 (1953); J. P. Hobson and W. A. Nierenberg, Phys. Rev. 89, 662 (1953).

GA4. Contact Resistance between Superconductors and Normal Conductors. F. BEDARD AND H. MEISSNER, *The Johns Hopkins University.*—Measurements have been made of the contact resistance between two different superconductors and between a superconductor and a normal conductor. The measurements on the two superconductors were made at temperatures above the critical temperatures of both specimens, and also below the critical temperature of one of them, keeping the temperature constant and varying the current. The superconductor-normal conductor contacts were measured both above and below the critical temperature as a function of current. The high current (5 milliamperes) resistance, which is the sum of the channel resistances and the barrier resistance, was of the order of 0.1Ω. An asymmetry in the resistance with respect to current direction was sought for, but in most of the runs no evidence for this was found. Below the transition temperature of one of the contact materials, an abrupt drop in the contact resistance was observed at low values of current. This drop, in the case of Sn−Pb contacts at 3.81°K, went down to immeasurably small resistances. The resistance at 500 microamperes was in one case at least one thousand times smaller than the resistance at 600 microamperes.

GA5. A Theory of the Paramagnetic Effect in Superconductors.* HANS MEISSNER, *The Johns Hopkins University.*—F. London developed a theory for the transition to superconductivity of a cylinder through which a current flows. It is possible to extend this theory to the paramagnetic effect where a longitudinal magnetic field is superimposed in addition to the current. With the assumption that the ratio of the effective length to the effective diameter, l/a, of the superconducting particles is constant, this theory gives a paramagnetic effect in the transition region. The relative permeability $\tilde{K}_m$ is a function of the ratio of the circular to the longitudinal magnetic field at the surface, i.e., of $\varphi_0=H\varphi_0/H_{z0}$. However experiment shows that $\tilde{K}_m$ is a function of $\gamma=\varphi_0(1-I_g/I)$, where I_g is a limiting current and I the total current. Good agreement with the experimental range of $\tilde{K}_m$, however, is obtained when the theoretical value of φ_0 is replaced by γ.

* Supported by a grant of the National Science Foundation.

GA6. Oscillatory Hall Effect and Magnetoresistance of Bismuth.* JULES A. MARCUS, *Northwestern University.*—Brodie's measurements[1] of the Hall effect and magnetoresistance at 14°K have been extended to liquid helium temperatures using his best crystal, for which the residual resistance ratio is $R4.2°K/R0°C = 1.7 \times 10^{-3}$. The magnetic field was perpendicular to both the trigonal axis and a binary axis while the current was in the direction of the trigonal axis. Superimposed on a monatonic decrease from −4000 emu at 3 kilogauss to −26 000 emu at 14 kilogauss is an oscillatory component of the Hall coefficient which is periodic in reciprocal field (as the susceptibility is in the de Haas van Alphen effect). The period and phase are the same as for the oscillating component of the magnetoresistance and give a value of $\beta/E_0 = 4 \times 10^{-5}$ gauss^{-1} for the dominant term. A component of twice this period is also present. While the absolute value of the mean Hall coefficient increases by a factor of 10 in going from 14°K to 4.2°K, it does not change between 4.2°K and 1.4°K. The amplitude of the Hall oscillations increases by a factor of 2 between 4.2°K and 1.4°K, but the magnetoresistance is constant in amplitude as well as mean value.

* Supported by the National Science Foundation.
[1] L. C. Brodie, Phys. Rev. 93, 935 (A) (1954).

GA7. Flow Near the Leading Edge of a Flat Plate. J. A. LAURMAN AND S. A. SCHAAF.—The flow field in the immediate vicinity of the leading edge of a thin flat plate has been surveyed by means of a "free molecule probe." This is a wire stretched cross stream and used as a resistance thermometer. The diameter of the wire is small compared to the mean free path of the gas so that (1) the presence of the probe does not disturb the flow, and (2) its temperature is sensitively dependent on the local Mach number. Surveys were carried out at Mach numbers of 2 and 4. The boundary layer appears to grow linearly and there is a considerable region in which it coalesces with the shock wave. Some indication of slip is also apparent, particularly at the higher Mach number.

GA8. Velocity and Pressure Distributions in Turbulent Pipe Flow with Uniform Wall Suction.* H. L. WEISSBERG AND A. S. BERMAN, *Carbide and Carbon Chemicals Company, K-25 Plant.*—The effect of wall suction on the turbulent flow of air in a porous pipe was investigated for various flow and suction rates. Radial distributions of time averaged axial velocities and of the axial component of the turbulent velocity fluctuations were measured at various distances from the pipe entrance, using hot wire anemometry techniques. Distributions of pressure on the axis of the pipe were also observed. Increasing wall suction was observed to lower the radial component of the velocity gradient over most of the pipe cross section and to increase it in the vicinity of the wall. Turbulence levels were lowered, by the suction, over the entire cross section. Pressure drops in the axial direction were also lowered and the pressure was observed to rise in the direction of flow for sufficiently large suction rates. Some of these observations have been explained by means of a momentum equation derived from the time averaged equations of motion.

* Work done at the Oak Ridge Gaseous Diffusion Plant operated for the Government by Union Carbide and Carbon Corporation.

GA9. Reflection of an Acoustical Pressure Pulse from a Liquid-Solid Plane Boundary. T. W. SPENCER, *California Institute of Technology.*—The problem treated is concerned with predicting the transient response of a system, composed of a liquid layer bounded above by a vacuum and below by a perfectly elastic solid, when excited by an arbitrary pressure applied over the surface of a spherical cavity located in the fluid. The Laplace transform of the displacement response is expressed in terms of an integral which is expanded in such a way that each term describes the contribution from one of the image sources. Each term is evaluated exactly at points located on a vertical axis passing through the source. The final expression for the vertical displacement at axial points is composed of the acoustic, afterflow, and correction terms. In solids for which Poisson's ratio is greater than one third the initial variation of the correction is always toward positive values (corresponding to motion directed toward the interface). For Poisson's ratio less than one third the initial variation may be either positive or negative depending on the magnitude of the compressional velocity ratio. A surface wave is shown to exist regardless of the choice of parameters. The surface wave velocity is always less than it would be in the absence of the liquid.

THURSDAY AFTERNOON AT 2:00

Caswell Room

(J. S. KOEHLER presiding)

Irradiation Effects, II

H1. Changes in KCl Lattice Dimensions by Soft X-Rays. CHESTER R. BERRY, *Eastman Kodak Company.*—The lattice dimensions of powdered specimens of annealed and unannealed KCl were measured during irradiation by soft x-rays. One set of specimens was allowed to color during irradiation and another group was prevented from coloring by simultaneous white-light illumination. The following observations were made: There was an increase in lattice dimension during exposure for every specimen. No difference existed for specimens which were colored or not colored. Saturation in the change in lattice dimension occurred at a lower exposure for the unannealed specimens than for the annealed specimens. The total increase in lattice dimension was about $\Delta a/a = 1 \times 10^{-5}$ for all specimens, compared with values given in the literature for maximum changes in length of approximately $\Delta l/l = 20 \times 10^{-5}$. The difference indicates production of void volume, presumably Schottky defects. The failure to observe a difference between colored and uncolored specimens may be caused by a considerably larger production of Schottky defects than of color centers.

H2. Elastic Modulus of X-Irradiated Rock Salt.* R. B. GORDON AND A. S. NOWICK, *Yale University.*—Measurements of the room temperature dynamic elastic modulus (C_{11}) of x-irradiated NaCl crystals have been made to an accuracy of better than 0.01 percent. It is found that the modulus is unchanged by irradiation for well-annealed crystals, but may increase by as much as 5 percent in cold worked crystals. This modulus change is a volume effect. It is closely related to the modulus decrease on cold working, which occurs as a result of the production of dislocation segments oscillating in phase with the stress. The modulus of a freshly deformed crys-

tal increases with time because of the shortening of these segments. It is found that the x-irradiation of a deformed crystal raises the modulus by just the amount corresponding to the destruction of this dislocation contribution. The x-ray dosage required to saturate this modulus effect is very much smaller than that required to fully color the crystal. The irradiation time required to effect half the total modulus change is independent of the magnitude of the change. These results suggest that the effect of the radiation is to create new pinning points along a dislocation and that the rate at which a dislocation is attacked is independent of the density of dislocation lines.

* Work supported by the U. S. Air Force through the Office of Scientific Research of the Air Research and Development Command.

H3. Radiation Induced Coloring of Sodium Azide.* HYMAN ROSENWASSER,† *Picatinny Arsenal,* AND PAUL W. LEVY, *Brookhaven National Laboratory.*—The effects of radiation on powdered crystalline sodium azide (NaN_3) have been studied by optical reflection measurements. Gamma rays from a multi-Curie Co^{60} source produces a stable absorption band at 3600A and two poorly defined bands at 6600A and 7600A which decay at room temperature. The 3600A band also appears after a slow neutron and gamma-ray irradiation in the reactor animal tunnel facility which is near 30°C. The intensity of this band can be increased by cadmium shielding or decreased by leading shielding. In the reactor pneumatic tube facility, where the temperature is at approximately 100°C, and where the material is subject to fast and slow neutrons, another band is present at 6000A. The 6000A band becomes very intense relative to the 3600A band when sodium azide is bombarded by fast U^{235} fission neutrons (and associated gamma rays) even though the temperature is approximately 20°C.

* Work done under the auspices of the U. S. Atomic Energy Commission and Picatinny Arsenal.
† Guest Scientist, Brookhaven National Laboratory.

H4. Heat Treatment of Irradiated Sodium Azide.* RUSSELL W. DREYFUS,† *Picatinny Arsenal,* AND PAUL W. LEVY, *Brookhaven National Laboratory.*—The effects of heat treatment on sodium azide (NaN_3) subjected to various radiations have been studied. When a sample that has been irradiated with slow neutrons at 20°C is heated at approximately 90°C the formation and growth of the 6000A band is observed. This is the same band that appears when the material is subjected to fast neutrons at 20°C. For short anneals of equal time this band appears in slow neutron irradiated samples at 188°C but not in gamma-irradiated samples. However, when samples exposed to slow neutrons and/or gamma rays at temperatures <100°C are heated to $\sim$260°C a marked loss of reflectance appears in the 4000A to 10 000A region and another absorption band appears at 2800A. It is to be noted that heating unirradiated material to the same extent produces a reduction in reflectance of less than 10 percent of that observed in irradiated samples, at the wavelength of greatest change. It appears that the observed coloring is related to the decomposition of NaN_3 and that irradiation has greatly enhanced this process.

* Work done under the auspices of the U. S. Atomic Energy Commission and Picatinny Arsenal.
† Guest Scientist, Brookhaven National Laboratory. Private, U. S. Army.

H5. Reactor and Gamma-Ray Induced Coloring in Corning Fused Silica.* PAUL W. LEVY, *Brookhaven National Laboratory.*—The coloring induced by gamma-ray and reactor radiations in fused silicas from various manufacturers and in Brazilian crystalline quartz has been studied by optical transmission measurements in the region 2000A to 1 micron. Corning "purified" fused silica[1] shows practically no gamma-ray coloring while reactor irradiation produces a strong band at 2180A, a weak band at 2420A, and very slight coloring in the visible. In contrast, all other fused and crystalline samples we have measured show considerable gamma-ray and reactor coloring extending from 2000A through the visible, roughly similar to published spectra. Thus in the Corning material reactor, irradiations produce absorption bands not developed by purely ionizing radiation. Also, the rate and manner of coloring of the Corning material appears to be different from that of Brazilian quartz. The Corning silica may contain something which prevents it from being colored, or alternatively, the other silicas may contain impurities responsible for their coloring ability. A. J. Cohen[2] has made similar observations regarding the coloring of these materials by x-rays.

* Work done under the auspices of the U. S. Atomic Energy Commission.
[1] The cooperation of Dr. J. W. Michener, Owens Corning Fiberglas Company, Newark, Ohio, who provided most of the Corning material, is sincerely appreciated.
[2] A. J. Cohen, J. Chem. Phys. (to be published).

H6. Long Wavelength Neutron Transmission as an Absolute Method for Determining the Concentration of Lattice Defects in Crystals.* J. J. ANTAL† AND R. J. WEISS, *Watertown Arsenal,* AND G. J. DIENES, *Brookhaven National Laboratory.*—It has been shown theoretically that neutrons of sufficiently long wavelength are scattered isotropically by isolated point defects and that this scattering can be measured when crystalline effects (Bragg scattering) are absent. Babinet's principle may be applied under such conditions and, therefore, vacancies and interstitials scatter in exactly the same manner. The cross section for this nuclear type of scattering is accurately known from other measurements. Thus, if the scattering from these defects is experimentally measurable an absolute method is at hand for determining their concentration. Some information on the agglomeration of these defects can also be obtained. It is not practical to measure directly the scattered neutron intensity. Instead, the attenuation of a long wavelength neutron beam during its passage through the material is measured in transmission. Transmission experiments will be presented on reactor irradiated α-Al_2O_3 which indicate that the number of defects can be measured by this technique with a rather high degree of accuracy.

* Work done under contract with the U. S. Atomic Energy Commission.
† Guest Scientist at Brookhaven National Laboratory.

H7. Magnetic Susceptibility of Fast Neutron Bombarded Crystalline Quartz. D. K. STEVENS, *Oak Ridge National Laboratory.*—The magnetic susceptibility of one unirradiated and two fast neutron bombarded piezo quartz cubes has been measured over the temperature range from 90°K to 300°K. The diamagnetic susceptibility of the unirradiated specimen was essentially temperature independent, while that of the irradiated specimens decreased markedly with decreasing temperature, indicating the introduction of paramagnetic centers. Curie plots of the values obtained by subtracting the unirradiated data from each of the irradiated curves yield straight lines, the slopes of which are proportional to the number of paramagnetic centers introduced. In the case of the cube subjected to a total nvt of 5×10^{19} cm^{-2} fast neutrons, 6×10^{19} paramagnetic centers, presumably trapped electrons, were present after irradiation. The second cube was bombarded with 3×10^{20} fast neutrons cm^{-2} but only 2.5×10^{19} paramagnetic centers were found. The density changes were -2 percent and -14 percent respectively.[1] The irradiated cubes were transparent but exhibited a faintly magenta coloration.

[1] M. C. Wittels and F. A. Sherrill, Phys. Rev. 95, 5, 1117 (1954).

H8. X-Ray Scattering Effects in Irradiated Boron Carbide. C. W. TUCKER, JR. AND P. SENIO, *Knolls Atomic Power Laboratory.**—Neutron irradiation of single crystals of boron carbide produces very strong x-ray diffraction effects. These are (1) *contraction* of the lattice in the c_0 direction and expansion in the a_0 direction; (2) an anisotropic artificial temperature factor which is six times as great in the c_0 direction as in the a_0

direction; (3) changes in the average lattice positions of certain atoms; and (4) very heavy diffuse scattering surrounding the reciprocal lattice points. Fourier analysis of the Bragg intensities shows that the anisotropy of the effects is due to the production of an anisotropic defect in the lattice during irradiation. This defect is identified as being due to the selective removal of the central carbon atom in a chain of three carbon atoms which lies parallel to the c_0 axis in the structure. Annealing experiments show that the selectively removed carbon atom becomes mobile in the temperature range of 700 to 900°C and finds its way back to its normal position. The x-ray effects can be understood qualitatively in terms of an elastic model of Huang. Work is in progress to extend the theory to the case of anisotropic defects.

* The Knolls Atomic Power Laboratory is operated by the General Electric Company for the U. S. Atomic Energy Commission.

H9. Optical Absorption Bands Induced in Gamma Irradiated Glass.* K. R. FERGUSON, *Argonne National Laboratory.*—The formation of optical absorption bands in glasses exposed to Co^{60} gamma rays has been observed. The wavelengths of these bands between 2000 to 20 000A are given for fused boric oxide, fused silica, and multicomponent glasses in the borosilicate, sodium silicate, barium silicate and phosphate systems. Bandwidths range from 0.6 to 1.5 ev. Certain bands reach an equilibrium density at room temperature after incident exposures of 10^7 roentgens; other bands are increasing in density after a 10^8 roentgens exposure. The fading of bands at elevated temperatures is greater for bands at longer wavelengths. The effect of additives in small amounts on the band structure of certain glasses is described.

* Work performed under the auspices of the U. S. Atomic Energy Commission.

FRIDAY MORNING AT 9:30

Calvert Room

(J. M. LUTTINGER presiding)

DSSP Symposium on Spin-Orbit Effects in Solids

J1. Spin-Orbit Effects in Conduction Electron-Spin Resonance. Y. YAFET, *Westinghouse Research Laboratories.* (30 min.)

J2. The Ferromagnetic Hall Effect. R. KARPLUS, *University of California, Berkeley.* (30 min.)

Business Meeting of the Division of Solid-State Physics

J3. Theory of the Valence-Band Structure of Germanium and Silicon. C. KITTEL, *University of California, Berkeley.* (30 min.)

J4. Transport Effects in *p*-Type Germanium. A. C. BEER, *Battelle Memorial Institute.* (30 min.)

FRIDAY MORNING AT 9:30

Caswell Room

(J. A. BEARDEN presiding)

Mostly Nonmetallic Crystals

K1. Statistics for Electrical Phenomena. JOSEPH G. BARREDO, *Rocasolano Institute, National Council of Research, Madrid.*—Considering a dipole in line with a carrier as the most probable configuration of particles, a statistics is deduced by which it is possible to establish a unified theory of electrical phenomena. This theory embraces Ohm's and Coulomb's laws as particular cases, as well as other electrical phenomena which do not obey the Einstein-Bose or Fermi-Dirac distribution laws, e.g., overpotential, photovoltaic effect and semiconductivity. Because it takes cooperative effects into account more fully than the band scheme does, it also gives a more satisfactory description of superconductivity and provides a microscopic explanation of an electrical phenomenon predicted by a law of conductivity previously published and experimentally demonstrated.[1] However, the theory indicates that this effect should be called chronosuperconductivity rather than chronopolarography, as it was originally named,[1] because for small enough values of time the current is as large as the impedance of the measuring circuit will allow. The theory was demonstrated in diffused junction rectifiers and other states of aggregation with a precision oscillograph. The impedance of the oscillograph is low enough to prove that the recombination time for the hole+electron→bound electron $<2.10^{-9}$ sec.

[1] J. G. Barredo, Phys. Rev. 83, 234 (1951); J. Chem. Phys. 19, 1065 (1951); Bull. Am. Phys. Soc. 29, No. 7, 14 (1954).

K2. Computation of Electron Density and Density of States in Narrow Bands in Crystals.* G. W. LEHMAN, *North American Aviation, Inc.* (introduced by D. B. Bowen).—A method for obtaining the electron density and density of states associated with narrow energy bands in crystals has been developed. This method avoids the usual eigenvalue-eigenvector problem. The crystal wave function is expanded in terms of Bloch functions associated with the appropriate linear combination of atomic orbitals. Using this representation one can show that the summation over states involved in finding the electron density in the narrow band approximaiton reduces to a calculation of matrices defined by Tchebichef polynomials. The procedure is being used for calculating a density of states curve for the $6d_{3/2}-6d_{5/2}$ band in fcc thorium.

* This work supported by the U. S Atomic Energy Commission.

K3. Localized States at the Boundary of Two Crystals.* GEORGE W. PRATT, JR., *M.I.T.*—The solution of Schrodinger's equation at the interface between two different crystals has been investigated. Under certain conditions localized states are found to exist at the boundary with energies lying in a mutual energy gap. A nearly free electron treatment of the problem results in either one localized state per boundary atom or none at all. The appearance of a localized state is accompanied by the disappearance of a band state from either side of the common energy gap.

* The research in this document was supported jointly by the Army, Navy, and Air Force under contract with the Massachusetts Institute of Technology.

K4. Determination of Dislocation Densities with the Double Crystal Spectrometer.* A. D. KURTZ, S. A. KULIN, AND B. L. AVERBACH, *M.I.T.*—Random dislocation densities may be determined from precise values of the diffracted line breadth using the formula $\rho=\phi^2/9\lambda^2$ [1] where ρ is the edge-type dislocation density, ϕ is the half-breadth of an x-ray diffraction line, and λ is the interatomic distance on the slip plane. Line-breadths are obtained from rocking curves measured on an x-ray double-crystal spectrometer used in the parallel position. Measured broadening must be corrected for the broadening contribution of the first crystal. By assuming different Gaussian reflection coefficients for each crystal, the measured broadening can be expressed in terms of broadening functions for each crystal. The diffracted power $P_{(\beta)}$ at any angular setting β is shown to be: $P_{(\beta)}=C\exp[-\beta^2/(\phi^2+K^2)]$, where C is a constant and K and ϕ are the true half-breadths of the first and second crystals respectively. K is determined from a rocking curve in which the second crystal is identical with the first. Having determined K, the value of ϕ (the true half-breadth) may be obtained for each crystal studied and the dislocation density calculated from the above formula. Other possible sources of error in measurement of rocking curves using the x-ray double crystal spectrometer are also analyzed.

* The research in this document was supported jointly by the Army, Navy, and Air Force under contract with the Massachusetts Institute of Technology.

[1] Gay, Hirsch, and Kelly, Acta Met. 1, 315 (1953).

K5. Polytypism and Dislocations. N. CABRERA AND M. M. LEVINE, *University of Viriginia.*—Frank[1] explained some years ago the growth of polytypes (crystals having a structure with a slightly higher free energy than the most stable one), particularly in SiC, on the basis of the dislocation theory of crystal growth. His theory should be applicable in general, and the problem remains to understand why polytypism is not more frequent. This paper is an attempt in this direction based on the following ideas: (1) Dislocations are introduced by collisions between perfect crystal nuclei. Only particular disorientations between the crystals will allow the dislocations in the resulting grain boundary to induce further growth of either the stable phase or one of the possible polytypes. (2) The permanence of a given polytype will depend on the mechanism of transformation to the stable phase. The dislocation theory of mutual transformation of lattices permits one to reach conclusions concerning the stability of the polytypes. The theory has been developed particularly for close-packed structures.

[1] F. C. Frank, Phil. Mag. (London) 42, 1014 (1952).

K6. Polarization in Insulating Crystals.* CAPUCINE AND NICOLAS INCHAUSPÉ, *University of Illinois.*—An elementary analysis has been made of the problem of the development of space-charge within an illuminated insulating crystal which exhibits photoconductivity. The analysis is applicable to crystals similar to alkali-halides in which the displacement, w, of the photoelectrons by the field is much smaller than the distance, d, between the electrodes. The analysis has been carried out for various types of nonuniform illumination in the form of a plane parallel condenser. The initial slope of the photocurrent time curve is given by $(1/i_0)(di/dt)_0=(d/a)(i_0/q_0)$, where i_0 is the initial current and q_0 is the charge of the condenser before illumination. The length, a, characterizes the nonuniform illumination and is a measure of the distance within which the radiation is absorbed.

* Partially supported by the Office of Scientific Research.

K7. Creation of a Potential Difference across NaCl Crystals by Deformation.* D. B. FISCHBACH AND A. S NOWICK, *Yale University.*—A study has been made of the flow of current at room temperature through NaCl crystals deformed in compression. A sensitive vacuum tube electrometer is used to measure the potential drop across a 10-in. ohm resistor connected across the crystal. When the crystal is deformed inhomogeneously a transient potential difference is developed such that the side of the crystal which has the higher stress concentration becomes negative. If the load is left on, this potential decays to zero over a period of minutes in roughly a hyberbolic fashion. Removal of the load at any time drops the current flow to zero almost instantaneously. Reapplication of the same load produces a new transient current in the same direction as the original flow, but smaller in magnitude. The direction of the initial current flow is unaffected by externally applied fields as large as ± 1000 volts/cm. A discussion of the possible interpretation of this effect will be given.

* Work supported by the U. S. Air Force through the Office of Scientific Research of the Air Research and Development Command.

K8. Self-Diffusion of Silver in Silver Chloride.* W. DALE COMPTON, *University of Illinois.*—The self-diffusion of silver in AgCl was measured over a temperature range of 100° to 417°C on two single crystals and two polycrystals using the Ag^{110} radioisotope. No significant variation in the diffusion coefficient was detected in these crystals in the intrinsic region where they can be represented by $D_{Ag}=1.23\exp(-0.90/kT)$ cm^2-sec^{-1}. Electrical conductivity measurements were made on the above crystals over a temperature range of 30° to 428°C. The purity was such that the knee in the conductivity *vs* $1/T$ curve occurred between 60° and 130°C. An appreciable variation in the intrinsic conductivity was found among these crystals. As in AgBr, an anomalous rise in the conductivity occurs above 390°C. The measured diffusion coefficients in the intrinsic region were found to lie significantly below coefficients calculated from the Einstein-Nernst relation. No explanation for this discrepancy can be given at this time.

* Supported in part by a National Science Foundation grant.

K9. Extreme Ultraviolet Absorption Spectrum of Silver Chloride.* CHARLES J. KOESTER AND M. PARKER GIVENS, *University of Rochester.*—The absorption spectra of evaporated thin films of silver chloride have been measured in the extreme vacuum ultraviolet region, 500–1500A. A grazing incidence spectrograph with a Lyman type discharge tube has been used. Thicknesses of the sample films, ranging from 50 to 200 A, were determined by multiple-beam interferometry, as described by Tolansky.[1] The linear absorption coefficient generally increases with decreasing wavelength until a rather broad maximum is reached in the vicinity of 1000 A, where it is the order of 10^6 cm^{-1}. The decrease at shorter wavelengths is slight.

* Research formerly supported by the Office of Naval Research and more recently by the National Science Foundation.

[1] S. Tolansky, *Multiple-Beam Interferometry of Surfaces and Films* (Oxford University Press, New York, 1948).

K10. (Abstract withdrawn.)

K11. Light Scattering from Optical Glass. R. D. MAURER, *Corning Glass Works.*—A Brice-Phoenix light scattering photometer has been modified to enable measurement of the small intensity scattered from optical glass. Particular attention has been given to the angular distribution of scattered intensity. Dissymmetry, depolarization, and relative Rayleigh's Ratio have been measured on fifteen types of commercial optical glass. All the glasses showed dissymmetry of scattering with dissymmetry values (I_{45}/I_{135}) ranging from 1.02 to 1.24. The scattered intensity was evaluated by comparison with benzene and found to be much greater than the calculated room temperature thermal scattering. The dissymmetry and scattered intensity both indicate the presence of frozen-in inhomogeneities. Further implications of the measurements will be discussed.

K12. Conduction in Phthalocyanine Crystals.* D. KLEITMAN AND G. GOLDSMITH, *Purdue University.*—Thin films and needlelike single crystals (as indicated by Laue patterns) of phthalocyanine were grown by vacuum sublimation from Dupont commercial grade phthalocyanine and from material purified by a prior fractionating sublimation. Dark conduction in the crystals was measured as a function of field and temperature. Conduction was ohmic to fields of 2000 v/cm. The temperature behavior indicated that the relation $\sigma=\sigma_0 \exp(-E/kT)$ applied between room temperature and 420°C. The results were reproducible and independent of applied field and helium pressure, with either silver paste or aquadag electrodes, for any particular crystal. For different samples the E-values ranged between 0.7 and 1.0 ev, and could be altered in a sample by heating to temperatures greater than 420°C. Defects in the crystal structure or impurity effects might account for this behavior. Films were found sensitive to atmospheric effects and temperature behavior of the conductivity was not reproducible. Photoconductivity was observed in both films and crystals. No saturation was indicated and ohmic behavior observed. The transmissivity of films and the dependence of photoconductivity on wavelength was measured over the visible range and to 1 micron. Similar behavior was observed with copper phthalocyanine films and crystals.

* Supported by a Bureau of Ships contract.

K13. Prismatic Slip in Crystals. J. W. DAVISSON, ELIAS BURSTEIN, AND P. L. SMITH, *U. S. Naval Research Laboratory.*—Prismatic slip has been observed in crystals of the cubic, tetragonal, and orthorhombic systems. The crystals, which are all holohedral, are: cubic NH_4Cl, NH_4Br, CsCl, CsBr, TlCl, TlBr, and PbS; tetragonal $PbCO_3 \cdot PbCl_2$; and orthorhombic $ZnCl_2 \cdot 2NH_3$. The prisms observed are [001] (100) and [001] (110). We have also recently observed prismatic slip in tetragonal tin. Galena (PbS) and tin furnish examples of competing slip systems. Thus galena exhibits both nonprismatic and prismatic slip of the forms [110] (001) and [001] (100) and tin exhibits two forms of prismatic slip [001] (100) and [001] (110). In one specimen of galena we have observed only nonprismatic punch figures on one cleavage face and only prismatic punch figures on a cleavage face situated at right angles to the first. In tin the prismatic slip observed at low temperatures is [001] (100) rather than [001] (110) which, according to published data,[1] corresponds to a lower critical shear stress. These effects in galena and tin may be due to preferential strain hardening of one set of the glide elements.

[1] I. Obinta and E. Schmid, Z. Physik 82, 224 (1933).

FRIDAY MORNING AT 9:30

Founders' Room

(L. MADANSKY presiding)

Luminescence

L1. On the Theory of Electroluminescence, BRIAN T. HOWARD, *Westinghouse Electric Corporation* (introduced by E. G. F. Arnott).—On the basis of the mechanism proposed by Piper and Williams[1] an analysis is made of the voltage dependence of electroluminescence. It is assumed that electrons are removed from deep donors in the region of a Schottky-type potential barrier by the process of internal field emission. These electrons are subsequently accelerated, acquiring sufficient kinetic energy to excite activator centers by impact ionization. The relationship used for the field dependence of the process of field emission from the donors is that derived by Franz.[2] The electroluminescent brightness is a function of the distribution in depth and in energy of the donors and of the efficiency of the impact ionization process. The problem is set up in a general form and several analyses made utilizing specific assumptions. The available experimental data is best fitted using the simplest assumptions possible leading to a voltage dependence of the form $L=aV^{\frac{1}{2}}(1-3V^{\frac{1}{2}}/C)\exp(-C/V^{\frac{1}{2}})$. The analysis is subsequently extended to the frequency dependence of electroluminescence on the basis of an equivalent circuit composed of nonlinear elements.

[1] W. W. Piper and F. E. Williams, Phys. Rev. 87, 151 (1952).
[2] W. Franz, Ann. d. Phys. 11, 17 (1952).

L2. Temperature Dependence of Electroluminescence, CLAUS H. HAAKE, *Westinghouse Electric Corporation,* (introduced by H. Fivey).—The electroluminescent brightness of a cubic ZnS·Cu·Pb phosphor was measured at constant voltage

and constant frequencies over a temperature range of −180°C to +150°C. The powder was inserted in a plaque cell. At each temperature the electroluminescent brightness I_{el} and the fluorescent brightness I_f excited by 3650 A was read. The I_{el}-curves resemble glow curves, as has also been reported by other workers.* However, a glow curve taken with this phosphor proved to be completely different from the I_{el}-curves. The ratios of I_{el} and I_f were determined yielding the temperature dependence of the excitation mechanism of electroluminescence (I_{ex}). It was found that I_{ex} can be given as a sum of exponential functions with $-E_i/kT$ as exponents. The E_i-values equal the activator heights above the valence band, since about the same values were obtained by evaluation of I_f. Increasing frequencies shift the I_{el}-curves to higher temperatures. The equation describing this phenomenon is similar to that obtained by Alfrey and Taylor; contrary to their assumptions the activation energies are not identical with trap depths. The spectral emission shift in two-band phosphors with increasing frequencies can be explained; increasing frequency acts like decreasing temperature.

* Gobrecht, Hahn, and Gumlich, Z. Physik 136, 623 (1954).

L3. Polarization Effects on the Brightness Waves of Electroluminescence. FRANK MATOSSI, *U. S. Naval Ordnance Laboratory.*—Electroluminescence excited by sinusoidal fields yields two maxima per half period of the field. The intensity ratio of these maxima depends on the field frequency and on the superposition of ultraviolet excitation. These observations are shown to be related to the existence of polarization effects, which are treated by extending previous theories of such effects in semiconductors (Jaffe and others), taking into account periodic excitations of centers by the field.

L4. Stacked Barriers in an Electroluminescent Zinc Sulfide Crystal. E. E. LOEBNER AND H. FREUND,* *Sylvania Electric Products, Inc.*—Electroluminescence was produced in a single, needle-like, 2-mm long crystal of zinc sulfide, which was excited by a sinusoidal, 1000 cps electric field of a low magnitude. The blue radiation appears under the microscope as clusters of luminous spots. These spots are no more than a few microns large and their mean separation within a cluster is about 30 microns. Scanning the crystal's length (in the direction of the applied field), it was found that sharp light pulses of a 1000 cps repetition rate and about 100 μsec duration, which are emitted from the spots, change their phase with respect to the excitation voltage when one moves from spot to spot. More than four reversals of 180° were found along the 1½-mm luminescing length of the crystal, some of them at points separated by as little as 40 microns. These observations are consistent with those of previous investigators, but permit new insight into the mechanism of electroluminescence in zinc sulfide crystals, and show that probably an internal barrier rectification is present.

* Now at Roswell Park Memorial Institute, Buffalo, New York.

L5. Effects of Electric Fields on Ultraviolet Excited ZnS-Phosphors. SOL NUDELMAN AND FRANK MATOSSI, *U. S. Naval Ordnance Laboratory.*—Electroluminescent and non-electroluminescent ZnS phosphors excited by continuous ultraviolet radiation undergo sudden stimulations at the instants of field application and removal and a quenching during the time of field application. Quantitative data about field and frequency dependence of stimulations and quenching are given. The stimulation at "field on" decreases with frequency up to about 20 kcps and then either remains constant or slightly increases up to 100 kcps. The stimulation at "field off" increases with frequency. For electroluminescent phosphors, the brightness waves of electroluminescence are compared with the ripple pattern of the quenching effect. For some phosphors, the number of intensity peaks during one half-period of the field depends on the superposition of field and ultraviolet excitation. The gradual transition from ripple to brightness wave for increasing field strength will be shown for sinusoidal and square wave fields. These transition curves demonstrate that quenching effects and electroluminescence have independent origins.

L6. Origin of Luminescence in Copper Activated ZnS Phosphors. NATHAN T. MELAMED AND RAYMOND BOWERS, *Westinghouse Research Laboratories.*—Five different emission bands have been reported in the literature for ultraviolet excited zinc sulfide, activated by varying concentrations of copper and/or chlorine. Emission spectra and static susceptibility measurement were obtained at various temperatures on specimens chosen to optimize each of the five emissions. Susceptibility measurements were carried out over a range from 1.5°K to room temperature by means of a Gouy balance, whose sensitivity was sufficient to detect a paramagnetism corresponding to less than 10^{-8} atomic parts of paramagnetic copper. No paramagnetism was detected in any of the specimens. Of the five emissions reported, only three are found to be distinct: a blue emission due to chlorine alone, a green emission due to the presence of both chlorine and copper, and a red emission due to copper without chlorine. The blue emission has previously been attributed to zinc vacancies produced by the chloride.[1] On the basis of the susceptibility measurements, and because the same blue emission occurs in specimens having a red emission, but containing copper without chloride, it is probable that the green emission results from substitutional Cu^+ whereas the red emission arises from interstitial Cu^+.

[1] F. A. Kröger and H. J. Vink, J. Chem. Phys. 22, 250 (1954).

L7. Dielectric Dispersion in Zinc Sulfide Phosphors.* I. AMES, H. S. SACK, AND R. M. WOOD, *Cornell University.*—Dielectric relaxation has been reported by several authors[1] for ZnS phosphors under illumination. The present experiments extend the measurements to compressed and sintered powders, and to single crystals. The samples were mounted between semitransparent gold plated electrodes and the impedance was measured under 3650 A excitation at 90 and 300°K, from 30 cps to 20 msec. Relaxation was observed for hexagonal samples which luminesced. Larger relaxation times were found for crystals and compressed-sintered samples than for powders. The intensity and temperature dependence of the relaxation, when present, was similar for all samples, and was consistent with the grain boundary model. Upon compression of a luminescent hexagonal powder, the relaxation effect disappeared, and then reappeared after sintering. X-ray analysis revealed that this procedure altered the lattice structure from hexagonal to cubic, to partially hexagonal. The absence of relaxation for cubic samples suggests that internal inhomogeneities in the hexagonal structure are responsible for the phenomena.

* Supported by the Research Corporation of America.

[1] G. F. J. Garlick and A. F. Gibson, Proc. Roy. Soc. (London) **A188**, 485 (1947); R. M. Wood, thesis, Cornell University (June, 1953); J. J. Dropkin, Polytechnic Inst. of Brooklyn Reports (May, 1952; November, 1953); Kallmann, Kramer, and Perlmutter, Phys. Rev. 89, 700 (1953).

L8. Model for Luminescence and Photoconductivity in the Sulfides. JOHN LAMBE AND CLIFFORD C. KLICK, *U. S. Naval Research Laboratory.*—A model for sulfides activated by monovalent metals is discussed which differs in several important respects from that usually employed. Because of the net negative charge of the lattice volume surrounding the activator there is a large cross section for trapping of holes which may be accompanied by release of a large amount of energy. This is presumed to be the transition leading to luminescence. A subsequent trapping of an electron returns the center to its original condition. For the electron trapping there is no coulomb field and both the capture cross section

and energy released would be expected to be small compared with the case of hole trapping. On the basis of this model, there is a simple explanation of the fast luminescence decay associated with hole capture and the slow conductivity decay associated with that of free electrons. Other well-known phenomena in the sulfides are examined on the basis of this model. In addition, predictions of this model concerning the infrared photoconductivity and infrared stimulation of luminescence have been verified by experiment on silver activated cadmium sulfide.

L9. Storage of Energy in Beryllium Oxide.* C. E. MANDEVILLE AND H. O. ALBRECHT, *Bartol Research Foundation.*—The photostimulated ultraviolet emission of x-ray excited BeO has been measured as a function of the wavelength of the incident light. A maximum of emission occurs for a stimulating wavelength of ~4100 A. Experiments are described which are interpreted as showing the presence of doubly occupied traps in BeO which are analogous to the *F*-centers of the alkali halides. Some discussion concerning energy storage in NaCl—Ag will also be presented.

* Assisted by the joint program of the Office of Naval Research and the U. S. Atomic Energy Commission.

L10. Influence of an Electric Field on the Thermoluminescence of ZnS Crystals. GERTRUDE NEUMARK, *Sylvania Electric Products Inc.*—We have noticed on a number of electroluminescent ZnS crystals that the application of a strong dc electric field during thermoluminescence considerably increases the intensity of the light emitted over the sum of the intensities due to thermoluminescence and electroluminescence separately. For one crystal, at a field of 5000 v/cm, the thermoluminescence with field minus the electroluminescence was larger than the thermoluminescence without field by a factor of 3 at −180°C to −150°C, increasing steadily to a factor of 12 at −70°C, above which there was negligible thermoluminescence. We believe that the increase in light output is due to impact ionization of bound electrons by the electrons thermally released from the traps and then accelerated by the field. The gain in sensitivity due to the increased light output has also helped to show that an electric field can be used as excitation for obtaining thermoluminescence.

L11. Low Temperature Luminescence in KCl:Tl. D. A. PATTERSON AND C. C. KLICK, *U. S. Naval Research Laboratory.*—Measurements on the two principal emission bands of KCl:Tl have been extended to 4°K. The decrease in half-width of the 3050 A band with temperature was found in excellent agreement with that obtained from Williams[1] curves for the $^1S_0$ and $^3P_1{}^0$ electronic states of Tl+. An emission band at 4750 A, ascribed by Johnson and Williams[2] to a $^1P_1{}^0$ to $^1S_0$ transition, has been found to have an intensity relative to the 3050 A emission which agrees with their predicted value. With two close-lying excited states involved, it is uncertain which of their intersections with the ground state curve leads to the observed quenching of luminescence with temperature. This also points out a difficulty in the general use of temperature quenching data in the development of configuration coordinate curves from experiment.[3]

[1] F. E. Williams, J. Phys. Chem. **57**, 780 (1953).
[2] P. D. Johnson and F. E. Williams, J. Chem. Phys. **20**, 124 (1952).
[3] C. C. Klick, Phys. Rev. **85**, 154 (1952).

FRIDAY MORNING AT 10:30

Federal Hill Room

(W. F. G. SWANN presiding)

Cosmic Rays

M1. Results of Limitations on Space Current Densities in Galactic and Intergalactic Space.* W. F. G. SWANN, *Bartol Research Foundation.*—The high electrical conductivity of space has raised difficulties in mechanisms concerning the production of cosmic-ray energies. High conductivity does not avoid limitation of the current density, i, to the value nec where n is the sum of the numbers of positive and negative ions per cc. Thus, for $n=1$, the saturation current density is of the order 5×10^{-9} ampere/cm^2. The effect of saturation is illustrated by the following idealized example. Consider two coplanar rings of gas A and B, A being the smaller. Under high conductivity, it would be impossible for the magnetic flux through either circuit to change and the electric field would be zero. If B expands, the flux through A caused by B changes, but A acquires induced current to compensate the change. As time proceeds, and if the ionic density in A is small, a stage will be reached at which A can no longer develop the current necessary for magnetic flux compensation. An electric field will now arise in A and the ions will become accelerated to cosmic-ray energies, not by appreciable alteration of velocity which has already attained its maximum c, but by alteration of relativistic mass.

* Assisted in part by the joint program of the Office of Naval Research and the U. S. Atomic Energy Commission.

M2. Experiment for Determining the Anisotropy of Primaries.* K. Y. SHEN AND S. F. SINGER, *University of Maryland.*—From theoretical arguments[1] it was proposed that simple telescope arrangements should be effective in making extensive air shower equipment highly directional, i.e., sensitive to showers coming in from a certain direction in the sky. This scheme is particularly appropriate for the zenith case at sea level where the atmosphere acts to attenuate showers at large zenith angles. For other directions the method becomes more involved. The apparatus will be described together with experimental results about its directivity. One of the important applications of this technique is to the study of the anisotropy of ultra high energy primaries. The experiment consists of a search for a sidereal diurnal time variation. Two further refinements are incorporated into the experiment: (1) Events produced by high energy primaries are selected by demanding high particle density. (2) High counting rates, therefore good statistics, are obtained not by increasing the size of the detector, but by setting up a large number of identical stations at some distance from each other.

* This work is supported by the National Science Foundation.
[1] S. F. Singer, thesis, Princeton University. (1948).

M3. The Albedo Contribution in the Measurement of Cosmic-Ray Primaries.* R. C. WENTWORTH AND S. F. SINGER, *University of Maryland.*—The major uncertainty in the determination of the primary proton spectrum lies in the evaluation of the effects of albedo. A number of experiments[1,2] have shown that the albedo contribution has a minimum in

the vertical direction, but could not assign a value to it. This vertical minimum seems plausible by simple theoretical arguments. We have made a calculation of the "splash" albedo moving vertically upward near the top of the atmosphere at $\lambda = 56°$, using data from balloon emulsions and high energy accelerators. The results are compared with recent experiments.[3] The difficulties inherent in our calculation and in the experimental approach are discussed. A time-of-flight telescope would give data of great value about upward-moving albedo. We are extending our theoretical treatment to include the effects of geomagnetic albedo in an approximate way.

* Supported in part by the Office of Scientific Research, U. S. Air Force.
[1] S. F. Singer, Phys. Rev. **77**, 729 (1950); **80**, 47 (1950).
[2] J. A. Van Allen and A. V. Gangnes, Phys. Rev. **78**, 50 (1950); **79**, 51 (1950).
[3] J. R. Winckler and K. Anderson, Phys. Rev. **93**, 596 (1954).

M4. A New Method for Measuring the Low Energy Spectrum of Primary Cosmic Rays. S. F. SINGER, *University of Maryland.*—Measurements of the primary spectrum with balloons and also rockets suffer from the contribution of unknown amounts of albedo. High latitude measurements have established a "knee" in the spectrum caused by the marked paucity of primaries with momentum/charge less than 1.5×10^9 volts. Their actual number is unknown but would be of great importance for our understanding of the relation of cosmic rays to events in the solar system. Present high latitude measurements may be inherently unsuitable because of complicating effects of the earth's quadrupole field and our inadequate knowledge of the shadow cone. An entirely different approach lies in measuring the cosmic ray intensity at the geomagnetic equator as a function of altitude starting at the top of the atmosphere, surmounting the cosmic ray "plateau" and extending the measurements to extreme distances from the earth. A preliminary calculation of the expected intensity variation with altitude has been carried out for the equatorial case, using geomagnetic theory and taking into account the geomagnetic shadow of the earth. The results demonstrate the potentialities of the proposed method for determining accurately the primary cosmic ray spectrum down to energies well below the "knee," away from albedo effects and distortions of the magnetic dipole field near the earth.

Post-Deadline Papers, if Any

FRIDAY MORNING AT 9:30

Phoenix Room

(J. D. FERRY presiding)

Invited Papers of DHPP

MA1. Statistical Calculation of Dimensions of Coiling Type Macromolecules. F. T. WALL, *University of Illinois.* (30 min.)

MA2. X-Ray Diffraction Studies of Crystallization in Elastomers. L. E. ALEXANDER, *Mellon Institute.* (20 min.)

MA3. Stress-Optical Studies on Amorphous and Polycrystalline Elastomers. G. R. TAYLOR, *Mellon Institute.* (20 min.)

Contributed Papers in High-Polymer Physics

MA4. Apparatus for Making Simultaneous Stress and Birefringence Measurements on Polymers. E. F. GURNEE, L. T. PATTERSON, AND R. D. ANDREWS, *The Dow Chemical Company.*—An instrument has been constructed to allow simultaneous measurements of stress and birefringence in polymer samples to be made as a function of time and temperature. The stress is measured by attaching one end of the sample to a cantilever beam; the small deflection of the beam is indicated by means of a differential transformer, which in turn is attached to an automatic recorder. The birefringence is measured with a Senarmont compensator (quarter-wave plate method). Measurements can be made either manually or with a continuously rotating analyzer. This latter method permits the automatic recording of the birefringence and is also adaptable to the study of rapid birefringence changes. The sample is housed in a copper pipe surrounded by a thermostatically controlled liquid bath. Some data are presented showing the use of this apparatus in measuring birefringence and stress changes during stress relaxation experiments (sample held at constant elongation), birefringence changes during creep under constant load, and stress-optical coefficients.

MA5. Retraction of Oriented Polystyrene Monofilaments. R. D. ANDREWS, *The Dow Chemical Company.*—When oriented polystyrene monofilaments are heated to temperatures in the neighborhood of the transition temperature they retract to an unoriented state at measurable rates. Curves of length as a function of time have been measured at five different temperatures (75°–95°C, at 5° intervals) for two filaments with different initial amounts of orientation. When the retraction curves are plotted as length *vs* log time, it is found that the curves at different temperatures are not superposable by lateral shift along the logarithmic time scale, as would be true in the simplest case. Activation energies calculated from these curves are a function of time as well as of temperature; the activation energy values at any given temperature tend to level out to final constant values with increasing time, however. The rate of change of activation energy value with time increases with increasing temperature, so that the final value is attained more quickly; the final value also decreases systematically with increasing temperature. Activation energy values increase rapidly with decreasing temperature in this region and are very high (300 kcal at 75°). It is postulated that specific volume changes are responsible for the time-dependent activation energies observed in these experiments.

MA6. Infrared Spectrum and Structure of Polyvinylidene Chloride. S. KRIMM AND C. Y. LIANG, *University of Michigan.*—The infrared spectrum of polyvinylidene chloride has been obtained between 2.5 and 100μ. Polarization measurements

from 2.5 to 33μ were made on an oriented copolymer with polyvinyl chloride containing over 85 percent polyvinylidene chloride. The similarity of the two spectra permitted unambiguous correlation with the bands of the pure polyvinylidene chloride. The detailed structure of this polymer is not as yet known. X-ray diffraction studies have indicated a fiber-axis identity period containing two monomer units, for which two possible chain configurations have been proposed.[1,2] The interpretation of the infrared spectrum also requires that there be at least two monomer units in the repeat, and indicates that the spectrum is consistent with the Fuller structure[1] but not with the Reinhardt structure.[2] A helical model appears to be eliminated. On the basis of the Fuller structure, and by analogy with the spectra of smaller molecules, a fairly complete assignment of the infrared bands has been made.

[1] C. S. Fuller, Chem. Rev. 26, 143 (1940).
[2] R. C. Reinhardt, Ind. Eng. Chem. 35, 422 (1943).

MA7. Normal Vibrations and Infrared Spectrum of Polytetrafluoroethylene. C. Y. LIANG AND S. KRIMM, *University of Michigan.*—The infrared spectrum of polytetrafluoroethylene between 2.5 and 100μ has been obtained, and the dichroism of oriented film observed between 2.5 and 33μ. On the basis of the helical structure recently proposed for this polymer,[1] the symmetry species and selection rules for the normal vibrations have been derived from the factor group of the one-dimensional space group. Approximate vibrational patterns of the active fundamentals have been deduced from symmetry considerations. From this analysis, the polarization and approximate intensities of the allowed infrared active fundamentals have been predicted. A calculation of the fundamental frequencies of a hypothetical planar zig-zag chain model of polytetrafluoroethylene has been made in order to assist in the assignment. Although the observed infrared spectrum definitely excludes the possibility of a planar zig-zag configuration, it may be assumed that the infrared frequencies for the helical model will be close to the frequencies of the planar model. By using these various approaches, a satisfactory assignment has been made of the infrared active fundamentals of polytetrafluoroethylene.

[1] C. W. Bunn and E. R. Howells, Nature 174, 549 (1954).

MA8. Nuclear Spin-Spin Relaxation Time in Polymers. E. M. BANAS AND B. A. MROWCA, *University of Notre Dame.*—Nuclear magnetic resonance absorption in several high polymers was studied over a temperature range from 78°K to room temperature. For unvulcanized natural rubber, the absorption line narrows in the vicinity of 125°K. This is attributed to increased frequency of CH_3 group rotation. For samples vulcanized with 3, 8, and 15 percent sulfur the line width transition shifts to higher temperatures indicating increased hindrance to motion. Line width transitions occur also near the second order transition temperatures for the polymers studied, and may be ascribed in part to increased segmental motion. The absorption line for polymethyl methacrylate showed indications of structure in the temperature range from 78°K to about 140°K, similar to the theoretically predicted line shape for a rigid H_3 triangular group broadened by neighboring molecular complexes. Similar effects were observed for polyisobutylene in the same temperature range. A silicone rubber exhibited a line width transition near 125°K, but the absorption line showed no structure and remained narrow down to liquid nitrogen temperatures. Second moments of the absorption lines, plotted as a function of temperature, show similar behaviors for the polymers investigated. Activation energies for the assumed motions at the line width transitions can be obtained from the line width temperature curves.

* Supported in part by the Office of Naval Research.

FRIDAY AFTERNOON AT 2:00

Phoenix Room

(E. R. FITZGERALD presiding)

Invited Papers of DHPP

N1. Frictional Properties of Teflon. D. G. FLOM, *General Electric.* (30 min.)

N2. Stress-Strain Relationships in Yarns Subjected to Rapid Impact Loading. H. F. SCHIEFER, *National Bureau of Standards.* (20 min.)

N3. Strain Propagation in Nylon Yarns Loaded Transversely at High Speeds. F. A. ODELL, *Chemical Corps Medical Laboratories.* (20 min.)

Contributed Papers in High-Polymer Physics

N4. Extension of the Hertz Theory of Impact to the Viscoelastic Case. YOH-HAN PAO, *DuPont.*—The problem considered is that of two bodies coming into normal contact over smooth curved surfaces. The initial relative velocity and the total kinetic energy involved is low. Contact is, however, confined to such small volumes of the objects involved that very high concentrations of energies are obtained at those places. The rates of application of stress are correspondingly high. The Hertz solution to this type of problem provides a useful approximation in the case of elastic objects. In the present treatment either one or both of the impinging bodies may be of viscoelastic material. The Laplace transform method is used to obtain the viscoelastic expression for the force developed between the two surfaces. This expression is then applied to the impact case. The expression can also be applied to other truly static cases, e.g., contact between gear tooth surfaces. The results are of technological interest, since it is not possible to say if a plastic is suitable for a certain category of impact applications, unless the rates of straining or stressing obtained in those applications can be estimated.

N5. Dynamic Mechanical Properties of Concentrated Cellulose Trinitrate Solutions.* D. J. PLAZEK AND JOHN D. FERRY, *University of Wisconsin.*—The dynamic rigidities and viscosities of solutions of a cellulose trinitrate fraction (number-average molecular weight 145 000) in isophorone have been measured by the wave propagation and single transducer methods over ranges of concentration from 3.7 to 18.1 percent,

of temperature from 0° to 60°C, and of frequency from 200 to 3200 cps. When reduced to a reference state of unit viscosity and concentration, using steady flow viscosity values obtained from falling ball measurements, these data provide single composite curves for dynamic rigidity and viscosity over a range of reduced frequency of 4 to 5 powers of ten. The distribution function of relaxation times derived therefrom is a plateau with a height of about $10^{5.3}$ dyn/cm². Concentrated solutions of other cellulose derivatives (acetate, tributyrate) exhibit similar plateaus in the relaxation distribution function, with heights ranging from $10^{5.1}$ to $10^{5.4}$ dyn/cm². For vinyl polymers of comparable molecular weight, however, there is no flat plateau, the minimum (negative) slope being about 0.15 on a double logarithmic scale.

* Supported by the Allegany Ballistics Laboratory.

N6. Temperature Dependence of Relaxation Mechanisms in Amorphous Polymers and Other Glass-Forming Liquids.* MALCOLM L. WILLIAMS, ROBERT F. LANDEL, AND JOHN D. FERRY, *University of Wisconsin.*—The ratio a_T of any mechanical or electrical relaxation time at temperature T to its value at a reference temperature T_s can be expressed, after suitable choice of T_s, by $\log a_T = -8.86\ (T-T_s)/(101.6+T-T_s)$. Over a T range of $T_s \pm 50°$, this applies to a wide variety of polymers, polymer solutions, organic glass-forming liquids, and inorganic glasses. As chosen, T_s lies about 50° above the glass transition temperature T_g. An alternative (but in practice less accurate) form can be written with T_g as the reference temperature. Comparison with a simplification of Doolittle's free volume equation for temperature dependence of viscosity shows that the above empirical constants specify the increase in thermal expansion coefficient at T_g as 4.8×10^{-4} deg^{-1} (in agreement with experiment) and the fractional free volume at T_g as 0.025 (a reasonable value).

* Supported by Picatinny Arsenal and Allegany Ballistics Laboratory.

N7. The Dynamic Properties of Glucose Glass. W. PHILIPPOFF AND J. BRODNYAN, *Franklin Institute.*—The dynamic properties of polymers and polymer solutions have recently been extensively covered both experimentally and theoretically. It was thought interesting to investigate an organic glass of molecules of well-known size excluding any possible polymerization. From the investigation of Parks it is known that glucose glass can be made with a range in viscosity at moderately elevated temperatures. Such a glass was investigated in the vibration tester of the Franklin Institute in the range of temperatures from 55° to 85°C. It was found that glucose glass *has* an elasticity. The properties can be described by a Maxwell body with an additional finite viscosity. The method of reduced variables can be applied to the results. This proves that viscoelastic behavior can be obtained with nonpolymeric systems of small molecular weight.

N8. The Viscosity-Molecular Weight Relationship for Long Chain Polymers in Bulk or in Concentrated Solution. T. G. FOX AND S. LOSHAEK, *Rohm and Haas Company.*—Evidence is given showing that the relationship, $\log\eta = 3.4\log Z + K$, represents an empirical law of flow which holds generally for long flexible chain molecules in bulk or in solution, provided the chains are sufficiently long to form a network structure through chain entanglements. Here η is the viscosity, Z is the number of atoms in the chain, and K is a constant which is dependent on the polymer type and on the temperature. All of the available data which cover wide molecular weight ranges for linear (and branched) molecules in bulk or in solution, including results on polyesters, polyamides, polystyrene, polyisobutylene, polydimethyl siloxane, and polymethyl methacrylate, support this conclusion. For chains too short to form such an entangled network, the dependence of η on Z is less severe but more complex. These results are in semi-quantitative agreement with the recent theory of F. Bueche.

FRIDAY AFTERNOON AT 2:00

Calvert Room

(R. J. MAURER presiding)

DSSP Symposium on the Properties of Silver Halides

P1. Research on the Silver Halides. J. W. MITCHELL, *University of Bristol.* (40 min.)

P2. Some Recent Studies of the Light Absorption Photoconductivity and Photolysis of Silver Halide Crystals. G. LUCKEY, *Eastman Kodak Company.* (30 min.)

P3. Properties of Electrons and Holes in Silver Chloride. F. C. BROWN, *Reed College.* (30 min.)

P4. The Decay Times of Luminescence and Photoconductivity in Silver Chloride. W. S. SACK, *Cornell University.* (30 min.)

P5. Nuclear Magnetic Resonance Studies of Imperfect Ionic Crystals. F. REIF, *University of Chicago.* (30 min.)

FRIDAY AFTERNOON AT 2:00

Founders' Room

(R. T. Cox presiding)

Photoconductivity; Color Centers; Optical and General Physics

Q1. Localized Photoconductivity in PbS Films.* DAVID DUTTON, *University of Rochester.*—The degree of localization of the effect of illumination in photoconducting layers such as PbS can be tested by applying a long narrow beam oriented first perpendicularly to, then parallel to the applied electric field.[1] If photoconductivity is not localized, for example if the

diffusion distance of minority carriers in fields of several volts/cm is comparable to the length of the film, S, the ratio of the fractional changes in over-all film resistance produced by the respective beam orientations, is unity; if the photoeffect is confined to the illuminated region, $S \sim (1-\Delta\rho/\rho)$ where $\Delta\rho/\rho$ is the fractional resistance change in the illuminated part. A value $S \sim 1$ has been reported.[1] The test has been applied to some commercially made, chemically deposited films of PbS currently being investigated by small-spot scanning methods[2]; in these films, values of $S<1$ occur, and both the lower of over-all resistance and the observed values of S can be accounted for by a localized-photoconductivity model. With a sufficiently narrow beam the test may give anomalous results ($S>1$) in films which have become polarized by ionic conduction.

* Supported in part by the Office of Scientific Research, U. S. Air Force.
[1] H. Müser, Z. Physikal. Chemie 198, 52 (1951). I am indebted to Dr. E. S. Rittner for calling this experiment to my attention.
[2] D. Dutton, Proc. Atlantic City Photoconductivity Conference (to be published).

Q2. Photoconductivity in Potassium Iodide.* NICOLAS INCHAUSPÉ, *University of Illinois.*—Photoconductivity in potassium iodide at the temperature of liquid nitrogen has been investigated with crystals containing additive F-centers and radiation in the photon energy range from 1.9 ev to 5.8 ev. The maximum of the F-center absorption occurs at the lower limit of this photon energy range and the upper limit marks the maximum of the first (exciton) peak of the fundamental optical absorption. The concentration of F-centers was varied from 10^{14} cm^{-3} to 10^{17} cm^{-3}. The number of quanta incident per second upon the crystal was about 10^{11} per second. The observed photocurrents were less than 10^{-15} amperes in crystals which had not been additively colored. When the crystals were prepared in such a low-vapor pressure of K as to contain less than 10^{15} F-centers cm^{-3}, photocurrents became observable at 3 ev and increased to a broad maximum at 5.1 ev. For F-centers concentrations between 10^{15} and 10^{17} cm-3, additional maxima were observed at 1.9 ev and 5.51 ev where the F- and β-bands occur. The photocurrents decreased rapidly as the photon energy was increased beyond 5.51 ev.

* Partially supported by the Office of Scientific Research.

Q3. Impurity Induced Color Centers in Fused Silica. ALVIN J. COHEN, *Mellon Institute.*—Recently several workers[1-3] have associated the three color centers in fused silica having absorption maxima near 220, 300, and 540 mμ with the SiO_2 network alone and not with chemical impurities that are present. In this laboratory experiments on Heraeus Homogenized Ultrasil and Amersil grades of fused silica indicate that the color centers at 300 and 540 mμ are due to the impurity content and are related to an absorption peak at 242 mμ induced by reducing conditions between 1000 and 1400°C. These two color centers cannot be produced in Corning purified fused silica under comparable conditions of heating and x-ray treatment. A color center at 214 mμ is developed in the Corning silica, and a new center appears in certain specimens in the region of 260 mμ. The color centers in these fused silicas are compared to certain color centers found in amethyst quartz, in complex glasses colored by solarization, and in colored CaF_2. The possible impurities responsible for these color centers will be discussed.

[1] R. Yokota, J. Phys. Soc. (Japan) 7, 316 (1952).
[2] G. Mayer and J. Gueron, J. chim. phys. 49, 204 (1952).
[3] F. S. Dainton and J. Rowbottom, Trans. Faraday Soc. 50, 480 (1954).

Q4. Energy Requirement for F-Center Formation. R. S. ALGER and R. D. JORDAN, *U. S. Naval Radiological Defense Laboratory.*—The effects of crystal material and lattice defects on the distribution and storage of energy absorbed from 2 Mev cathode rays and deuterons were studied through quantitative measurements of the energy required for F-center formation in pure and mixed alkali-halide crystals. These measurements were compare to previous work with Co^{60} gamma rays. The effects of crystal material were examined with a series of pure crystals containing a common alkali metal, i.e., KCl, KBr, and KI, and with mixed crystals containing various proportions of KCl and KBr. The highest coloring efficiencies were observed in crystals sensitized by the addition of the hydride, i.e., U-centers, which are converted into F-centers by the ionizing radiation. Typical energies for the U- to F-transition in sensitized KBr are 26, 30, and 80 to 100 electron volts for excitation with Co^{60} gamma rays, 1-Mev electrons, and 2-Mev deuterons, respectively. Owing to the high specific ionization of the deuterons, all of the F-centers were formed in a layer 0.013-cm thick as compared to 0.1 cm for 1-Mev electrons. The crystals have already begun to saturate by the time that detectable color-center concentration occurs with the deuterons. The conversion energy with deuterons was also very highly sensitive to the crystal condition, and the 80 to 100 electron-volt region covers the lowest energies found.

Q5. Susceptibility and Entropy of F-centers.* J. G. DAUNT AND J. KORRINGA, *Ohio State University.*—The entropy S and the paramagnetic susceptibility χ of F-centers in alkali halides have been computed using the model of Kip, Kittel, Levy, and Portis.[1] With the hyperfine coupling between the F-center electron and the six equivalent nearest alkali nuclei as the only interaction, the eigenvalues of the energy of the center in a weak magnetic field were calculated up to second order in H. The sum of states then yields an expression for S and χ as function of a reduced temperature $T^*=kT/E_c$, where E_c is twice the hyperfine coupling constant. The calculations have been limited to nuclei with spin 3/2. The influence of the hfs on χ amounts to 7.5 percent for $T^*=10$, corresponding to $T\approx 0.01$°K for Li^6 up to $T\approx 0.4$°K for Cs^{133}. In a magnetic cooling experiment starting in a strong magnetic field at $T_i=1$°K at most the electronic entropy R ln2 can be removed, leading to a final temperature $T_f^*\approx 3$.

* Assisted in part by a contract between the Air Research and Development Command and the Ohio State University Research Foundation.
[1] Phys. Rev. 9, 1066 (1953).

Q6. The Emission Spectra of Some Polyatomic Molecules. G. W. ROBINSON, *The Johns Hopkins University.*—Low-excitation conditions are produced in a high-frequency electrodeless discharge operated at the highest possible pressures. For substances with low volatility, high pressures may be attained by the addition into the discharge of a spectroscopically inert material having a high volatility. Any impurities which are formed may be effectively removed by employing an extremely rapid flow rate. In this way secondary excitation of products of decomposition will not take place and the emission will be quite pure. Emission intensities are about 10^3 times higher than those obtained by ordinary fluorescence techniques. Because of the increased intensity it will be possible to study these spectra at a high resolution. Some of the molecules which have been studied are acetaldehyde, acetone, benzaldehyde, acetophenone, biacetyl, and naphthalene.

Q7. Vibration-Rotation Line Intensities in HCl and DCl.* R. HERMAN, G. E. MOORE, S. SILVERMAN, AND R. F. WALLIS, *Applied Physics Laboratory, The Johns Hopkins University.*—Integrated line intensities have been measured in absorption in the 1–0 and 2–1 bands of HCl and 1–0 band of DCl. The grating spectrographs used in this investigation had resolutions of ~0.25 to 0.50 cm^{-1} permitting intensity measurements to be made on individual isotopic lines of H^1Cl^{35}, H^1Cl^{37}, H^2Cl^{35}, and H^2Cl^{37}. A wide range of optical densities was employed, varying both pressure and path length at various

temperatures up to ~1050°C. A comparison of experimental line intensities with a theory which takes into account the vibration-rotation interaction,[1] yields the ratio, θ, of the permanent dipole moment, M_0, to the product of effective charge and equilibrium internuclear distance, M_1r_e. We find for HCl and DCl that $\theta=1.19$ and 1.05, respectively, with probable errors of ~0.05. This indicates that for small vibrations these molecules behave essentially as point charges. Absolute-integrated intensities have been obtained for a number of bands. The interdependence of the above measurements with equivalent line widths and line shapes is discussed in the following abstract.

* This work was supported by the Bureau of Ordnance and the Office of Naval Research, Department of the Navy.
[1] R. Herman and R. F. Wallis, J. Chem. Phys. (to be published).

Q8. Collision Line Widths and Shapes in the Vibration-Rotation Bands of HCl.* W. S. BENEDICT, *The Johns Hopkins University*, AND G. E. MOORE AND S. SILVERMAN, *Applied Physics Laboratory*.—Previous work[1,2] has shown that the collision line width of HCl vibration-rotation lines varies markedly with the rotational quantum number, and that the absorption at frequencies greater than several cm^{-1} from the resonance is greater than required by the Lorentz shape. By making measurements over wide ranges of optical density, pressure, and temperature as reported in the preceding abstract, it is possible to investigate these effects more closely. At our highest optical densities there was nearly complete absorption at the center of the 1–0 band. The absorption coefficient near the band origin is over three times as large as predicted from the Lorentz shape and the widths obtained at lower densities. The non-Lorentzian deviations appear to be nearly symmetrical about each line and to be greatest for the lines of lowest J. The line widths observed for all J-values in HCl and DCl are greater at all temperatures than those calculated for resonating dipoles and show the importance of nonresonant dipole-dipole, dipole-quadrupole, and possibly other higher-order interactions.

* This work was supported in part by the Bureau of Ordnance and the Office of Naval Research, Department of the Navy and in part by the U. S. Air Force, Cambridge Research Center.
[1] E. Lindholm, Z. Physik **109**, 223 (1938).
[2] W. S. Benedict and S. Silverman, Phys. Rev. **94**, 752 (1954).

Q9. The Microwave Spectrum of $N^{15}O^{16}$. J. J. GALLAGHER, W. C. KING, AND C. M. JOHNSON, *The Johns Hopkins University*.—The first two rotational transitions $J=1/2\rightarrow3/2$ and $J=3/2\rightarrow5/2$, of $N^{15}O^{16}$ in the $^2\pi_{\frac{1}{2}}$ electronic ground state have been measured in the one- to two-millimeter wavelength region. The results are in good agreement with calculations based upon the data previously obtained for $N^{14}O^{16}$. Since the spin of N^{15} is 1/2, there is no quadrupole interaction and the hyperfine structure consists of magnetic effects only. All six lines of the $J=1/2\rightarrow3/2$ transition at an unperturbed frequency of 145 133.74 Mc/sec have been measured to an absolute accuracy of ±0.25 Mc/sec, and four of the six lines in the $J=3/2\rightarrow5/2$ transition at 241 888.84 Mc/sec have been measured to an accuracy of ±0.50 Mc/sec. If the molecule is assumed to be an intermediate coupling case, slightly removed from Hund's case (a) by interactions with neighboring states, the parameters describing the Λ-type doubling are calculated to be $4\Sigma_s[(-1)^s/\nu(\pi,\Sigma)]\langle\pi|AL_y|\Sigma\rangle\langle\Sigma|BL_y|\pi\rangle$ =170.44 Mc/sec and $8\Sigma_s[(-1)^s/\nu(\pi,\Sigma)]|\langle\pi|BL_y|\Sigma\rangle|^2=1.49$ Mc/sec. The hyperfine structure is accounted for by the theory of Frosch and Foley, yielding the hfs constants $D=-131.90$ Mc/sec and $d=-157.98$ Mc/sec. Small hfs corrections resulting from the mixing of states are also considered. The hyperfine structure measurements yield excellent confirmation of previous nuclear magnetic moment measurements of N^{15} in both magnitude and sign. The rotational constants obtained for $N^{15}O^{16}$ are $B_0=49\,043.86$ Mc/sec and $D_0=0.14$ Mc/sec.

Q10. The Ideal Gas Thermodynamic Properties of the Isotopic Hydrides of a Group of Diatomic Free Radicals. LESTER HAAR, *National Bureau of Standards*.—Procedures were employed to obtain the partition functions for the diatomic hydrides, deuterides and tritides of the free radicals of the elements of group IVA and VA of the periodic table. The calculations include the special low-temperature electron spin interaction effects arising with these molecules.[1] In addition to these effects the partition functions include corrections for rotation-vibration coupling, vibrational anharmonicity, centrifugal stretching and nonclassical rotation. Tables of thermodynamic properties from 50°–5000°K have been calculated on the NBS digital computer—SEAC for the isotopic hydrides of the elements C, Si, Sn, Pb, N, and P. The molecular data for the hydrides were used to compute the data for the deuterides (when not available), and for the tritides.

[1] Lester Haar and A. S. Friedman, J. Chem. Phys. (to be published).

Q11. Cine-Microscopy of Sparks, Exploding Wires, and Fracture at Framing Rates $>10^6$/Second. L. ZERNOW AND G. HAUVER, *Aberdeen Proving Ground*.—An ultra-high-speed framing camera[1] similar to the one developed at Los Alamos and described by Brixner[2] has been adapted for use with a magnifying objective. Dynamic microscopic details of electrode behavior in sparks, disintegration of exploding wires, and crack formation in glass shattered by explosives have been observed. Previous studies of such phenomena[3] have used static-microscopic observation. However, with the exception of Froome's micro studies of cathode spots on liquid metals,[4] dynamic studies appear to have always been carried out macroscopically.[5–7] High-speed photomicrographic sequences will be shown to illustrate the additional microscopic detail obtainable. Shorter exposure times (~10^{-8} seconds) and the very high framing rates ($\gg10^6$/second) will be recognized as essentials for extracting the maximum microscopic detail.

[1] Available from Beckman and Whitley, Inc., San Carlos, California.
[2] B. Brixner, J. Soc. Motion Picture Television Engrs. **59**, 503 (1952).
[3] Kies, Sullivan, and Irwin, J. Appl. Phys. **21**, 716 (1950).
[4] K. D. Froome, Proc. Phys. Soc. **62B**, 805 (1949); **63B**, 377 (1950).
[5] W. Göing, Naturwiss. **37** (No. 24), 558 (1950).
[6] Allen, Hendricks, Mayfield, and Miller, Rev. Sci. Instr. **24**, 1068 (1953).
[7] D. G. Christie, Trans. Soc. Glass. Tech. **36**, 74 (1952).

Q12. Metallic Deposits and Shock Waves Due to Electrically "Exploded" Wires. WILLI M. CONN.—Experiments are described for obtaining a profile through the metallic vapor surrounding an "exploding" wire. It was earlier shown that uniform-metallic deposits may be formed on glass, etc. by this method at pressures varying for different metals. It was now found that the cylinder or shell of metallic vapor surrounding the wire is hollow and closed at both ends. The shell is formed prior to the violent "explosion." A cylindrical shock wave produced inside the hollow cylinder by the "exploding" wire will be partly reflected from the inside of the shell, and partly propagated through the metallic vapor. The cylindrical compression wave formed by reflection will cause very high pressure and temperature along the axis of the shell, *cf.* the emission of continuous spectra due to very high-temperature and free-free transitions, the high energy emitted by exploding wires and the "falling out" of ionizing constituents from the cloud of explosion products after experiments at atmospheric pressure. Example of size of shell (Ag No. 34 ga, 60 mm long, 5 mm gap, 25 mm Hg pressure): 8.2 mm inside, 23.8 mm outside diameter; 55 mm inside, 65 mm outside length. Means for direct observation of the inside of the shell and its connection to the outside will be discussed.

FRIDAY AFTERNOON AT 2:00

Caswell Room

(R. SMOLUCHOWSKI presiding)

Metals, I

R1. Valence Wave Functions for the $3d^74s$ and $3d^8$ Configurations of Atomic Iron.* FRANK STERN, *U. S. Naval Ordnance Laboratory.*—Self-consistent field wave functions without exchange have been calculated for $3d$ and $4s$ electrons in the $3d^74s$ and $3d^8$ configurations of atomic iron, using the core potentials found by Manning and Goldberg[1] for the $3d^6s^2$ configuration. The fractional charge of a $3d$ electron outside a sphere of radius 2.66 Bohr radii is 0.05, 0.10, and 0.15, respectively, for the $3d^6s^2$, $3d^74s$, and $3d^8$ configurations. Thus any property which depends on the amount of charge far from the nucleus, for example the width of the $3d$ band of metallic iron in a tight binding approximation, will be considerably different in the three cases. The eigenvalues found in solving the Schrödinger equation are corrected for the difference between output and input potentials, and energies of the three configurations (neglecting all Slater integrals except F^0) are found. Preliminary estimates are -37.03, -36.68, and -36.32 Rydbergs, respectively, for the energies of the $3d^6s^2$, $3d^74s$ and $3d^8$ configurations relative to a state in which the valence electrons are widely separated from the core.

* This work was begun at Princeton University.
[1] M. F. Manning and L. Goldberg, Phys. Rev. **53**, 662 (1938).

R2. A Quantum-Mechanical Calculation of Inter-Atomic Force Constants in Copper. HARRISON C. WHITE, *M.I.T.*—Feynman's Theorem[1] tells us that the force on a nucleus resulting from the displacement of one other nucleus can be reduced to the coulomb force produced by the change in total charge density. We assume each ion-core moves rigidly and shows the central-force repulsion used by K. Fuchs for elastic constants. Hence determination of the localized change in the $4s$ band conduction electron charge density $\Delta\rho$ is our primary problem. A conventional scattering theory approach is inappropriate; instead the Slater-Koster perturbation theory formulation in Wannier functions[2] has been applied to the lower half of the discrete eigenspectrum of small, fcc lattices. An explicit expression is obtained for $\Delta\rho$ using plane waves as unperturbed wave functions, and the perturbation matrix components between first neighbors as a single disposable parameter limited by self-consistency. $\Delta\rho$ has been evaluated for lattices of two shapes and seven sizes up to sixteen atomic planes in width to verify convergence, and is compared with a semiempirical multipole expansion. The resulting atomic force constants are in general agreement with those inferred from thermal diffuse scattering of x-rays in recent work, and contradict any central force model.

[1] R. P. Feynman, Phys. Rev. **56**, 340 (1939).
[2] G. F. Koster and J. C. Slater, Phys. Rev. **95**, 1167 (1954).

R3. Work Function Difference of Gold and Gold Oxide from Contact Potentials with Respect to Germanium and Platinum.[1] PAUL MILLER, *University of Pennsylvania.*[2]—An apparatus has been developed for 25 cpd observations per second by extension of the Kelvin method to rotational geometry. A sample is mounted on a post on a disk rotating at 1500 rpm past the reference. A sample is seldom over the reference, thus being available to various devices (e.g., heater, radiation pyrometer). Samples may be mounted on different arcs of the disk and rapidly intercompared. By this means the work function difference between massive polycrystalline gold oxidized in air and gold reduced in hydrogen was measured as 1.06 ± 0.08 volts, agreeing with a photoelectric determination by Weiss,[3] whose preparation methods were followed. A germanium sample, which proved insensitive to hydrogen, enabled following of work function changes of the platinum nominal reference. As another possible use of the apparatus, at 10^{-6} mm, a surface prepared bare at a given time can be measured 25 times before formation of a monolayer from the ambient, an ultra-high vacuum being unnecessary.

[1] Supported by the Office of Naval Research.
[2] Now at Bell Telephone Laboratories.
[3] Private communication from P. Weiss, Socony-Vacuum Company.

R4. Thermoelectric Power and Resistivity of Dilute Alloys of Mn, Pd, and Pt in Cu, Ag, and Au.* F. A. OTTER, JR., *Franklin Institute Laboratories.*—We have measured the thermoelectric power and resistivity of dilute alloys of Cu-Mn, Ag-Mn, Au-Mn, Cu-Pd, Ag-Pd, Au-Pd, Cu-Pt, Ag-Pt, and Au-Pt from -195°C to $+500$°C. Norbury[1] has reported thermoelectric data for Cu-Mn alloys, and Geibel[2] has measured the thermal emf of Au-Pd and Ag-Pt against Pt from 0°C to 1000°C. Geibel's most dilute alloys contained 10 At percent Pd, and our data for pure Ag and Au disagree with his. We chose the alloys mentioned because of the good solubilities of Mn, Pd, and Pt and because of the similar properties of Au, Ag, and Cu. We found that the thermopowers of "noble" metal alloys of Pt and Pd are negative relative to the pure solvent metals as is found for most solutes. Noble metal alloys of Mn, on the other hand, are thermoelectrically positive relative to the pure solvent metal above certain temperatures. The transition from negative to positive relative thermopower occurs at about room temperature for Cu-Mn, about -170°C for Ag-Mn, and about $+200$°C for Au-Mn.

* This work was supported by Signal Corps Engineering Laboratory.
[1] A. L. Norbury, Phil. Mag. **2**, 1188 (1928).
[2] W. Geibel, Z. anorg. Chem. **69**, 38 (1911); **70**, 240 (1911).

R5. Anisotropic Electronic Stress and Magnesium Alloys. PAUL M. MARCUS, *Carnegie Institute of Technology.*—Calculations have been made of the anisotropic electronic stress due to Brillouin zone boundary effects on the Fermi energy as electron concentration varies. The form of the energy throughout $\mathbf{k}$ space is assumed given by free electron perturbation theory with only one Fourier component of the lattice potential as the perturbation; the energy and energy gap values are taken, however, from Trlifaj's calculations on magnesium. Because of the cylindrical symmetry the calculations may easily be carried out exactly. The resulting stress along the hexagonal axis varies with electron concentration in agreement with Goodenough's rough calculation, giving first, rising tension as the Fermi surface approaches the zone face, then falling tension after contact is made. The increased tension due to overlap agrees with Jones's simple theory, although now such effects as distortion of the energy surfaces under strain, spillover of overlap electrons under stain, and anisotropy of the overlap band are included. Application to lattice spacing changes of selected magnesium alloys, using Jones's assumption that alloying simply adds electrons to the conduction band, shows the magnitude of the overlap stress is reasonable, but the stress does not start as abruptly nor continue rising as linearly with increasing concentration as observed.

R6. Brillouin Zone Studies of Alloys IV Additional Hall Data of Magnesium Alloys. A. I. SCHINDLER AND E. I.

SALKOVITZ, *Naval Research Laboratory.*—It has been suggested by Salkovitz and Schindler that the Brillouin Zone overlap in dilute magnesium alloys can be studied by observing various electrical properties (e.g., transport phenomena) as a function of alloying additions. Measurements of $d\rho/dt$, where ρ is the electrical resistivity, show a break at an electron concentration of approximately 2.013 electrons per atom. Preliminary Hall measurements on alloys of magnesium containing small amounts of aluminum showed a similar overlap effect at roughly the same concentration. More complete Hall measurements have been made on dilute binary magnesium alloys containing either aluminum, indium, or tin. The data on the aluminum additions now show the break more conclusively than previously. The absolute magnitude of the Hall constant decreases nearly linearly with aluminum content up to a concentration of about 1.3 atomic percent (e.g., electron concentration of 2.013 electrons per atom). Further additions cause the Hall constant to increase slowly. A break is also observed in the curve for the indium-magnesium alloys. Beyond this break, the Hall constant increases rapidly with increasing indium content. Hall constant variation due to tin additions differ from those due to the other alloy additions, studied. For small tin concentrations the Hall constant rises and then decreases as further tin additions are made.

R7. Resistivity of Dilute Magnesium Alloys. E. I. SALKOVITZ AND A. I. SCHINDLER, *U. S. Naval Research Laboratory.*—Linde has shown that for the monovalent metals, the increase in resistivity due to small alloying additions is proportional to the square of the difference in valence of the two elements concerned. To determine whether the rule is applicable to divalent metals resistivity measurements were made of a series of dilute binary alloys of magnesium containing either lithium, silver, cadmium, aluminum, indium, thallium, tin, or lead. Silver, lithium and cadmium each produced an increase of about 0.7 to 0.9×10^{-6} ohm cm per atomic percent addition. Aluminum and indium caused an increase of from 1.9 to 2.1×10^{-6} ohm cm per atomic percent, whereas thallium, also a 3rd column element, produced a change of 3.1×10^{-6} ohm cm per atomic percent. These values were relatively constant to nearly the respective solubility limits. Additions of quadravalent tin or lead produced a different effect, however. An addition of 0.05 atomic percent of tin caused a change of 7.1×10^{-6} ohm cm per atomic percent, but this incremental change decreased rapidly with increasing tin content to 3.5×10^{-6} ohm cm per atomic percent at 2.0 percent tin. Lead produced similar effects. The data show that although Linde's Rule in its simple form is not valid for magnesium alloys, the increase in resistivity is nevertheless related to the valence of the alloying addition.

R8. On the Resistivity Due to Point Imperfections in Copper.* F. J. BLATT, M. C. HUSE, AND R. A. RUBENSTEIN,† *University of Illinois.*—Recently, calculations of resistivity due to lattice imperfections in copper were reported.[1] To determine the reliability of these calculations we have used the same procedure to determine the resistivity due to small concentrations of gallium, germanium, and arsenic in copper. The scattering potentials representing the impurities were derived from the Hartree potentials of the free ions, and the cross sections were calculated by the partial wave method. The Friedel sum rule served as a guide to suitable screening charge distributions. The calculated resistivities, although of correct magnitude, consistently exceeded experimental values, indicating that previous results for vacancies and interstitials are high by a factor of about 2. The integrations of the radial wave equation for various potentials were performed by the ILLIAC using a program originally designed to facilitate self-consistent field calculations.[2] This program, which is equally suited to eigenvalue problems (bound states) as to scattering calculations, will also be discussed.

* Supported in part by the Office of Naval Research.
† Now at Shell Development Company.
[1] F. J. Blatt, Bull. Am. Phys. Soc. 29, No. 7, 30 (1954).
[2] R. A. Rubenstein, Ph.D. thesis, University of Illinois (1954).

R9. Elastic Constants of Ag and Ag Alloys.* ROGER BACON† AND CHARLES S. SMITH, *Case Institute of Technology.*—The elastic constants of single crystals of silver and of dilute silver alloys have been measured by the ultrasonic pulse echo method. The values for pure silver in units of 10^{12} dyne cm^{-2} are: shear constant $(C_{11}-C_{12})/2$, 0.1528; shear constant C_{44}, 0.461; adiabatic bulk modulus, 1.036. First measurements on a series of dilute alloys of silver have been completed for a crystal containing 8 atom percent indium. The elastic constants show a decrease upon alloying to an extent which is in qualitative agreement with results previously reported for alloys of copper. The fractional decrease in $(C_{11}-C_{12})/2$ is much larger than that of C_{44} suggesting a decrease of the short range forces and an increase in the long range electrostatic forces upon alloying.

* This work was supported by the Office of Naval Research.
† National Carbon Fellow.
[1] J. R. Neighbours and C. S. Smith, Acta Met. 2, 591 (1954).

R10. Elastic Constants of Fe-Si Alloys.* CHARLES S. SMITH AND W. B. DANIELS, *Case Institute of Technology.*—The elastic constants of body centered cubic Fe-Si single crystals of composition 4.9, 6.0 and 10.7 atom percent silicon have been determined by the ultrasonic pulse echo method. An increase of silicon content in this composition range has the following effects on the fundamental elastic constants: The bulk modulus B shows no significant change; the shear constant C_{44} decreases by two percent; the shear constant $(C_{11}-C_{12})/2$ shows a large decrease of 15 percent. The constant $(C_{11}-C_{12})/2$ extrapolates back very well to the value for pure iron, of which all four determinations in the literature are in excellent agreement. The constants B and C_{44} do not extrapolate well but neither do their pure iron values agree well. These results then are formally very similar to those previously reported for a wide variety of face centered cubic copper and silver alloys. Their interpretation is hampered by the lack of a theory for the elastic constants of iron. The very different behavior of the two shear constants upon alloying suggests however that short range interactions alone cannot account for the shear constants of iron. The large decrease in $(C_{11}-C_{12})/2$ may account for the increased stability of the body centered phase when silicon is added in solid solution.

* This work was supported by the Office of Naval Research.

R11. Temperature Dependence of Internal Friction in Copper.* D. N. BESHERS AND J. S. KOEHLER, *University of Illinois.*—The internal friction and effective Young's modulus of copper single crystals, some 99.999 percent pure and others with small amounts of gold, have been measured at elevated temperatures. The decrement increases very rapidly as a function of temperature. Above ~350°C, activation energies may be deduced from the temperature dependence. In pure Cu, two apparent activation energies are involved, below and above ~550°C, for which preliminary values are 23.6 and 16.2 kcal/mole, respectively. These are observed at a maximum strain amplitude (in longitudinal resonance) of 4×10^{-8}. Gold appears to affect the second energy, reducing it to 12 kcal/mole. The highest temperatures reached tentatively indicate a peak about 1000°K, consistent with Wert and Marx's systematics[1] for an activation energy of ~46 kcal/mole.

* Supported by Office of Naval Research.
[1] C. Wert and J. Marx, Acta Met. 1, 113 (1953).

R12. Precipitation in Small Spheres of Lead-Tin Alloy. W. DESORBO AND D. TURNBULL, *General Electric Research Laboratory.*—Studies[1] on the kinetic behavior of bulk polycrystalline α-lead tin indicate that the precipitation of tin (β) is accomplished by nucleation and growth of cells consisting of tin lamellae interspersed in depleted solid solution. It has been suggested[2] that both the nucleation and growth of precipitate is catalyzed by structural irregularities in the solid solution and that the rate of cellular precipitation should be greatly depressed in structurally perfect crystals. The precipitation reaction in very small (30–40 micron diameter) crystal spheres of Pb-Sn alloy, that may be free of grosser imperfections, has been followed by a calorimetric technique. In all cases the precipitation energy evolved isothermally is only 1/10 to 1/25 of the values evolved by bulk polycrystalline specimens having the same composition. The precipitation energy evolved by the spheres cold-worked and homogenized once is several orders of magnitude larger than the energy released prior to deformation. Supersaturation ratios of 10 to 20 were supported for several hours at 300°K without precipitation. The results demonstrate the decisive role of lattice imperfections in some cellular precipitation processes.

[1] D Turnbull and H. N. Treaftis, Acta Met. (to be published).
[2] D. Turnbull, Acta Met. (to be published).

FRIDAY EVENING AT 7:00

Calvert Room

(R. T. BIRGE presiding)

Banquet of the American Physical Society

Presentation of the John Scott Award to WALTER H. BRATTAIN and JOHN BARDEEN.

After-dinner speeches by G. H. DIEKE and W. F. G. SWANN.

SATURDAY MORNING AT 9:30

Caswell Room

(HARVEY BROOKS presiding)

Metals, II

S1. Effect of Cold Work on Local Order. B. L. AVERBACH AND P. S. RUDMAN, *M.I.T.*—The local order contribution to the x-ray diffuse scattering was measured from an alloy 0.15 Au–0.85 Cu both before and after cold working by grinding. It was found that about three-fourths of the existing local order was randomized. These results are interpreted to mean that slip has occurred on about one-third of all possible (111) slip planes. This technique gives a measurement of the slip process for deformations beyond the reach of usual metallographic methods. A consequence of these results is that an energy of randomization should be included in calculations of energy storage in cold-worked alloys. The alloy 62 Au–38 Ag, where both energy storage and x-ray measurements have been made, is used as an example to calculate a probably significant energy of randomization. The effect of restoration of local order in annealing is discussed in terms of observations on hardness changes in α brass.

S2. Measurements of X-Ray Diffuse Scattering from Co-Pt Disordered Solid Solutions and of Long-Range Order for the Alloy CoPt. P. S. RUDMAN AND B. L. AVERBACH, *M.I.T.*—The x-ray diffuse scattering from a binary alloy has contributions from thermal vibrations, deviations from randomness, and disparities in atom sizes. The latter two contributions have been measured from Co-Pt powder briquets quenched from the disordered region. Short-range order of the same magnitude as in the Au-Cu system and a size effect of the same magnitude as in the Au-Ni system was found. The short-range order results are used to estimate the quasi-chemical contribution to the thermodynamic properties which, when added to a calculated strain contribution, give reasonable agreement with the observed thermodynamic data. The CoPt order-disorder transformation was studied by x-ray integrated intensity and c/a ratio measurements. A first-order transformation differing from that of its isomorph CuAu was found. The value of the Bragg-Williams long-range order parameter at the critical temperature S_c is: S_c (CoPt) $=0.775$ as compared to S_c (CuAu) $=0.983$.

S3. Correlation of Expansion Coefficient Anomaly in Quenched Cu_3Au With Properties of Ordered Cu_3Au.* JEROME ROTHSTEIN, *Signal Corps Engineering Laboratories.*—Bimolecular kinetics[1] applied to resistivity relaxation data of Burns[2] on ordered Cu_3Au gave 30 kcal for the net energy to create 6.01×10^{23} wrong pairs, each in an ordered environment, and a 9-kcal barrier preventing interchange of the neighboring atoms of each pair (righting them). If (a) quenched Cu_3Au contains a metastably high concentration of pairs wrong with respect to a site labeling making nearest neighbors of the pair right, (b) nearest neighbor interactions dominate atomic rearrangement processes, (c) short-range interactions are independent of long-range order, then anomaly in order-sensitive properties of quenched specimens should occur as a function of temperature which is (a) similar on the low-temperature side to the low side of the lambda-point anomaly, (b) in the opposite direction (e.g. decrease instead of increase), (c) characterized by linear plot of logarithm of anomalous deviation *vs* $1/T$, with activation energy 9 kcal in Cu_3Au. The expansion coefficient dip of quenched Cu_3Au observed by Nix and MacNair[3] agrees with these predictions.

* Work done partly at Columbia University.
[1] J. Rothstein, Phys. Rev. **94**, 1429(A) (1954).
[2] F. Burns, Phys. Rev. **94**, 1429(A) (1954).
[3] F. C. Nix and D. MacNair, Phys. Rev. **60**, 320 (1941).

S4. Isothermal Anneal Study of Quenched and Cold-Worked Copper-Palladium Alloys.* A. SAWATZKY AND F. E. JAUMOT, JR., *Franklin Institute Laboratories.*—The behavior of the electrical resistivity of copper-palladium alloys in the composition range from six to thirty atom percent palladium has been studied in the course of isothermal anneals at temperatures from 250°C to 450°C. Samples quenched from 800°C and samples cold-worked to ninety percent reduction in area were used. Samples of both initial conditions exhibited an increase in resistivity followed by a rather rapid decrease. The two regions are attributed to nucleation and growth of ordered domains. The activation energy for growth of ordered domains is approximately 42 kcal/mole for samples quenched from 800°C. The nucleation process is probably not a singly activated process, but the mean activation energy in the temperature range from 325°C to 400°C is of the order of 20 kcal/mole. Samples previously cold worked appear to have a slightly lower activation energy for growth of the ordered domains. These data, combined with other rather meager data available on these alloys, indicate that a rather serious revision of the equilibrium diagram of Cu-Pd alloys is needed.

* This work was supported by the Office of Ordnance Research.

S5. Small-Angle Scattering of X-Rays by Surface Irregularities.* W. H. ROBINSON AND R. SMOLUCHOWSKI, *Carnegie Institute of Technology.*—It has been pointed out previously[1] that surface irregularities can produce strong small-angle scattering and overshadow scattering by internal defects. An early attempt to check this effect by mechanically polishing diamond failed presumably because of the too coarse polishing medium. In order to investigate this phenomenon further, thin slices of a single crystal of zinc were cut parallel to the basal plane by means of a strain-free acid cutter. The thickness of the sample was reduced down to 0.003 in. by means of etching and electrolytic polishing. The small-angle scattering measured at angles smaller than forty minutes of arc was large and independent of previous annealing history of the sample. This is in contrast to another sample obtained by cold rolling polycrystalline zinc to a similar thickness. This sample showed in the same range of angles very small scattering which upon a subsequent slight electrolytic polishing was raised about tenfold. This confirms the supposition that the surface condition of the sample plays a very important role in small-angle scattering of x-rays.

* Work supported by a contract with the U. S. Atomic Energy Commission.
[1] Y. Y. Li and R. Smoluchowski, J. Appl. Phys. (to be published).

S6. Grain Boundary Diffusion in the Al-Cu System.* C. COLEMAN AND R. SMOLUCHOWSKI, *Carnegie Institute of Technology.*—In continuation of the previous work on grain boundary diffusion, the system aluminum-copper has been chosen in order to investigate the influence of the relative size of atoms on grain boundary diffusion and in particular on the role of dislocations and of dislocation clusters. The system offers the possibility of obtaining columnar grains on both its ends. The diffusion of aluminum along the grain boundaries of copper in the common cubic direction has been studied first using a sensitive differential etching technique. In the diffusion couple the source of aluminum is a copper −7 wt percent aluminum alloy kept in contact with the columnar copper. A typical diffusion run of 170 hr at 600°C provides a very deep grain boundary penetration indicating an activation energy for the grain boundary diffusion around 10 000 cal per mole. In accord with previous results there is very little if any penetration at low-angle boundaries and the penetration increases with increasing angle of disorientation. Preliminary results of diffusion of copper in columnar aluminum have also been obtained.

* Work supported by a contract with the U. S. Atomic Energy Commission.

S7. Self-Diffusion in Zinc at Low Temperatures.* F. E. JAUMOT, JR., AND R. L. SMITH, *Franklin Institute Laboratories.*—Self-diffusion in zinc at temperatures below 200°C has been studied using both single crystal and polycrystal samples. Anomalous results were obtained for single crystal samples; the data indicating that in some samples grain boundary diffusion predominated, and in others, volume diffusion predominated. These anomalous results are attributed to low-angle lineage boundaries which are presumed to be formed of edge dislocations. The diffusion in certain polycrystal samples could be analyzed as predominately volume diffusion. When volume diffusion occurred in either single or polycrystal samples, the values for the diffusion coefficient were as much as several orders of magnitude larger than would be expected from high-temperature data.

* This work was supported by the U. S. Atomic Energy Commission.

S8. Annealing Kinetics of Lattice Defects in Evaporated Copper Films.* NED S. RASOR,† *Case Institute of Technology.*—Further results[1] have been obtained in a study of the annealing kinetics of lattice defects in vacuum deposited copper films. The electrical resistivity was used as an index of the degree of imperfection. Substrate temperature during deposition of the films ranged from −250°C to −25°C and was found to have a large effect on their annealing behavior. Annealing spectra and activation energies were obtained over the temperature range −250°C to 300°C by means of tempering and isothermal anneals. Kinetic analysis of the annealing data indicated that processes having unique activation energies do not characterize the annealing over any appreciable interval. The relation of the present work to that on irradiated and cold-worked copper is discussed. A speculation is made on the possible existence of significant quantum effects and a resulting departure from classical statistical equilibrium based on certain features of the data.

* Supported by the Office of Naval Research.
† Now at North American Aviation, Inc., Downey, California.
[1] N. S. Rasor and R. W. Hoffman, Phys. Rev. 94, 1406(A) (1954).

S9. Structure of Evaporated Copper Films on Titanium.* R. E. SCHLIER, *Brown University.*—Copper is deposited by evaporation at a rate of $(1.5\pm0.4)\times10^{15}$ atoms/cm²/min on the hexagonal (0001) face of a titanium single crystal. The crystal has been previously cleaned by outgassing *in vacuo* followed by argon ion bombardment and annealing.[1] Low-energy (less than 250 ev) electron diffraction indicates that the deposit is oriented with respect to the titanium, with the (111) copper plane parallel to the (0001) titanium plane. The hexagonal nets of copper and titanium are parallel. The lattice constant of the hexagonal net of copper is found to be 2.55 A, for all thicknesses of deposit used (0.5 to 25 monolayers). Most of the contribution to the diffraction beams is from the first 10 atomic layers of copper. Weak diffraction beams from titanium are still present after a deposit of 25 ± 7 monolayers. These observations suggest that the deposit is composed of oriented crystallites, with some of the substrate being relatively uncovered. Annealing the deposit at approximately 350°C destroys most of the orientation without removing the film.

* Assisted by Office of Ordnance Research, U. S. Army.
[1] Schlier, Farnsworth, and George, Bull. Am. Phys. Soc. 29, No. 7, 35 (1954).

S10. Mechanical Twinning in Copper. T. H. BLEWITT, J. K. REDMAN, F. A. SHERRILL, AND R. R. COLTMAN, *Oak Ridge National Laboratory.*—Studies of the mechanical properties of copper single crystals at 4.2°K showed that deformation occurs by the usual slip process at this temperature so long as the sample has not excessively work hardened. At high flow stresses (12 kg/mm² to 20 kg/mm², depending on the

orientation), a change in the mode of deformation was apparent as discontinuous flow occurs. Considerable indirect evidence suggested the possibility that mechanical winning was occurring in this second mode of deformation.[1] Although it is accepted that hexagonal metals can be deformed by mechanical twinning, experiments purporting to show deformation twinning in the face-centered cubic metals have been regarded with skepticism. Despite the fact that these earlier studies were made at room temperature, the suggestion of twinning at 4.2°K was also received with skepticism. Recent orientation determinations of the twin-like lamella utilizing a two-circle x-ray goniometer to study the {222}, {400}, {331}, {220}, {420} reflections make it possible to demonstrate unambiguously that copper forms mechanical twins at 4.2°K. The composition plane is the {111} with a [112] twinning directions. Photographs showing the growth of the twin crystal from lamella about 1/16-in. thick to approximately 4-in. thick will be shown.

[1] Blewitt, Coltman, and Redman, Proc. Bristol Conference on Imperfections in Solids, 1954 (to be published).

S11. Satellites in the Soft X-Ray Spectrum of Zr.* J. KORRINGA, *Ohio State University.*—Measurements by Spielberg and Shaw[1] of the soft x-ray spectrum of Zr, performed with a high-resolution spectrometer, have been reported. Several lines with L_{II} as initial state, notably $L\gamma_1$ ($L_{II}\rightarrow N_{IV}$), have a structure suggesting satellites. The lines $L\beta_2$ and other lines with L_{III} as initial state are single. These facts are well in accord with the mechanism proposed by Coster and Kronig,[2] according to which such satellites are emitted after a radiationless transition $L_I\rightarrow L_{II,III}$ with simultaneous ejection of an order (M-shell) electron. For $L_I\rightarrow L_{II}$ this is energetically possible for $Z<41$, the probability decreases when the energy transfer ΔE to the ejected electron becomes large. From the identity of the two effects as a function of ΔE and from the available data for lines with L_{III} as initial level, we expect a maximum satellite intensity for $L_{II}\rightarrow$transitions near $Z=39$, and a gradual vanishing near $Z=35$.

* Supported by the U. S. Atomic Energy Commission.
[1] N. Spielberg, C. H. Shaw, and J. A. Soules, Phys. Rev. **94**, 752(A) (1954).
[2] Coster and Kronig, Physica **2**, 13 (1935).

S12. Relaxation of a Monatomic Crystal Lattice Around a Vacancy.* STEFAN MACHLUP, *University of Illinois.*—An elastic continuum approach shows that the relaxation of the lattice must be in toward the vacancy, i.e., the volume increase on formation of a vacancy is *less* than one atomic volume. The vacancy is treated as a spherical hole with surface energy (=surface tension at the melting point); spherically symmetric relaxation causes shearing strains. Minimizing the sum of surface energy and strain energy gives a linear relaxation of 6 percent for Cu, 11 percent for Na, and total energy of formation of a vacancy of 1.6 ev for Cu, 0.6 ev for Na. These results are compared with the published calculations for Cu[1] (which predict less relaxation) and with a modified Huntington-Seitz calculation for Na, with a view to their relevance to self-diffusion.[2]

* Research Supported in part by contract with U. S. Air Force.
[1] H. B. Huntington and F. Seitz, Phys. Rev. **61**, 315 (1942); H. B. Huntington, Phys. Rev. **61**, 325 (1942); G. J. Dienes, Phys. Rev. **86**, 228 (1952).
[2] Nachtrieb, Catalano, and Weil, J. Chem. Phys. **20**, 1185 (1952); D. F. Holcomb, thesis, University of Illinois, 1954.

S13. On the Mechanism of Grain Boundary Relaxation in Metals and Alloys.* A. S. NOWICK AND CHI YAO LI,† *Yale University.*—Strain relaxation experiments on wires of a Ag-Zn solid solution show that the relaxation time not only for stress-induced ordering but also for the GBR (grain boundary relaxation) may be decreased considerably by quenching from elevated temperatures. This result seems to suggest that excess vacancies trapped by quenching hasten the GBR process. One day, therefore, conclude that GBR is intimately related to volume self-diffusion, as originally suggested by Kê. Recent internal friction studies by Pearson and Rotherham (to appear in the *Journal of Metals*) show that in Cu and Ag there are two GBR peaks. The first, occurs in the pure metals with an activation energy about half that for self-diffusion. This GBR effect is destroyed by addition of about 1 percent solute and replaced by a second GBR peak for which the activation energy is equal to that for self-diffusion. A consistent explanation is that the normal GBR mechanism, which occurs in pure metals, is readily blocked by the presence of impurity atoms. Thus the only available mechanism for GBR in alloys is diffusional flow.

* Work supported by the U. S. Army, Office of Ordnance Research.
† Now at Lehigh University, Bethlehem, Pennsylvania.

SATURDAY MORNING AT 9:30

Founders' Room

(FERD WILLIAMS presiding)

Physics of Photography; Silver Halides

T1. Sequence Experiment for the Study of the Reciprocity Law Failure at Low Intensities.* J. H. ENNS, R. L. MARTIN, AND E. KATZ, *University of Michigan.*—The concept that the reciprocity law failure at low intensities results from disintegration of the latent image in its initial stages of formation has been supported experimentally by Webb and Evans[1] in their publication of the sequence exposure curves, and theoretically by Katz.[2,3] In principle the sequence experiment consists of exposing a photographic emulsion in part to high- and in part to low-intensity radiation, wherein the ratio of the two exposures and their sequence may be varied. An instrument will be described, which has recently been built in this laboratory and designed especially to record automatically sequence exposure data. An exposure is made on a 4 by 10 in. plate, each plate receiving 384−4 by 5 mm squares uniformly exposed for densitometry measurements. Provision is also made to record plate calibration data. A few preliminary curves will be shown.

* Work supported by the Air Research and Development Command.
[1] J. H. Webb and C. H. Evans, J. Opt. Soc. Am. **28**, 431 (1938).
[2] E. Katz, J. Chem. Phys. **17**, 1132 (1949).
[3] E. Katz, J. Chem. Phys. **18**, 499 (1950).

T2. Photographic "Order Principle." E. KATZ, *University of Michigan.*—Although latent image theory usually refers to the single grain, most experiments deal with an ensemble of many grains in a photographic emulsion. With respect to a given set of development conditions, the developability of each grain follows a step function during the exposure, whereas the overall developable density of the emulsion varies quasi continuously. In order to provide a most general link between

single-grain behavior and ensemble results the "order principle" has been proposed.[1] It will be shown that, much like a converging-power series, the order principle can be applied with various degrees of approximation, depending on the amount of available information concerning emulsion and development variables; its accuracy can, in principle at least, be increased indefinitely.

[1] E. Katz, J. Chem. Phys. **17**, 1132 (1949).

T3. Low-Intensity Reciprocity Law Failure for Pure Ag Br Emulsions of Different Grain Size.* R. L. MARTIN, J. E. ENNS, AND E. KATZ, *University of Michigan.*—The photographic reciprocity-law failure (r.l.f.) is exhibited by plotting the logarithm of the exposure (intensity×time of exposure) which is required to produce a constant density, *vs* the logarithm of the intensity of the exposure. The negative slope of this curve indicates that a stable speck is less likely to occur and then grow to a developable speck, for low than for optimal intensity exposures. It has been shown that the slope of the r.l.f. curves for low intensities reflects the distribution of the trap depths encountered by the conduction electrons in the Ag Br grain.[1] Since the traps are located partly near the surface and partly throughout the volume of a grain, one may expect to find a dependence of the slope of the r.l.f. curve with gain size. We will present preliminary results of measurements of the dependence of low intensity r.l.f. slopes on grain size.

* Work supported by the Office of Ordnance Research.
[1] E. Katz, J. Chem. Phys. **17**, 1132 (1949).

T4. Displacement of Latent Image in Photographic Emulsion Grains. J. F. HAMILTON, F. A. HAMM, AND J. W. CASTLE, *Eastman Kodak Company.*—The use of simultaneous light and voltage pulses in the study of the motion and trapping of photoelectrons in large, single crystals of silver chloride has been described by Haynes and Shockley.* A similar technique has been successfully applied to photographic silver-bromide grains. The conduction electrons are displaced from their liberation sites toward or completely to an edge of the grain by the electric field during and after the 5 μ-second light pulse. Displaced print out as well as latent-image silver will be illustrated. The present results are qualitative; however, various factors affecting the trapping of the conduction electron will be briefly discussed.

* J. R. Haynes and W. Shockley, Phys. Soc. (Bristol), Conf. Rept., p. 151 (1948); J. R. Haynes and W. Shockley, Phys. Rev. **82**, 935 (1951).

T5. Optical Absorption Measurements on Silver Halide Crystals. NELSON R. NAIL, FRANK MOSER, PLINY E. GODDARD, AND FRANZ URBACH, *Eastman Kodak Company.*—Using extensive precautions to insure high purity, large silver-halide crystals were prepared by the Bridgman method, followed in some cases by multiple-zone melting. The absorption spectra of these crystals were determined in the region of the long-wavelength edge, which is of approximately exponential shape and obeys fairly closely the $1/kT$ rule.[1] Cold work producing considerable deformation does not affect these absorption spectra. Small concentrations of cationic impurities such as Pb, Cu, Au, Ni, Cr, Co, and In produce absorption bands in and beyond the edge region. Reproducibility of the absorption spectra of pure crystals indicates that these spectra are not vitiated by impurities. Exposure to suitable wavelengths produces volume darkening of the crystals, which is extremely weak in the purest crystals, requiring special methods for its investigation. Cold work and certain impurities (Cu, Co, Au) enhance the darkening. In some cases, notably Au, the darkening process continues after exposure. The impurity bands of Ni and In are bleached by exposure. It is not known at present whether the darkening of the purest crystals is caused by residual impurities or strain or both.

[1] F. Urbach, Phys. Rev. **92**, 1324 (1953).

T6. Silver Halide Phosphors. FRANK MOSER AND FRANZ URBACH, *Eastman Kodak Company.*—Crystals of simple and mixed silver halides are known to show a strong fluorescence but little afterglow at low temperatures. However, the slow buildup of luminescence under weak excitation indicates the presence of effective trapping processes. These processes have been studied in more detail on silver bromoiodide phosphors. The lifetimes of the trapping states were estimated by observing the dependence of buildup rates on the dark interval between two exposures. The trapping states are also revealed by the effects of red or infrared radiation. If applied during excitation, it reduces the stationary brightness; if applied in the interval between exposures, it reduces the rate of re-excitation. A simple model representing this behavior and the absence of phosphorescence predicts that the efficiency of the stationary luminescence should increase with the square root of the exciting intensity. This has been confirmed for a large range of the latter. By the introduction of small concentrations of suitable impurities, e.g., strontium, long afterglow, thermoluminescence, and stimulation by long wavelengths can be produced. These phenomena are described by a simple extension of the proposed model.

T7. Theory of Silver-Halide Photolysis. CHARLES A. DUBOC, *Eastman Kodak Company.*—G. Luckey[1] has interpreted his measurements of halogen evolution in the vacuum photolysis of silver halides as indicating that each photon absorbed within a thin surface layer releases one halogen atom, whereas the photoproducts of photons absorbed further from the surface are lost by recombination. A specific but very simplified model has been studied. Absorbed photons are assumed to create electrons and holes of equal mobility which then partly recombine within the crystal and partly diffuse to the surface to recombine by a different mechanism or to release halogen and silver. The law of volume recombination chosen is such that the model reproduces the observed intensity dependence of photoconductivity. Assuming the surface reaction to be intrinsically fast, its actual rate is determined by the rate of supply of electrons and holes by diffusion. This model permits one to calculate photolytic yields from a knowledge of photoconductivity, or vice versa, and gives the wavelength dependence of both phenomena. A preliminary comparison with experiment is promising, and a predicted reciprocity failure has recently been found experimentally by Luckey under certain conditions.

[1] G. Luckey, J. Phys. Chem. **57**, 791 (1953).

T8. Some Photographic Effects in Single Crystals of Silver Bromide. W. WEST AND V. I. SAUNDERS, *Eastman Kodak Company.*—Observations on the photographic and related behavior of thin single crystals of silver bromide prepared from the melt will be described, following indications from the work of Boissonnas and of J. W. Mitchell and his co-workers that these crystals might constitute, within limits, a useful model of the grain of a photographic emulsion. As produced from the melt, the crystals, the surfaces of which were (100) faces, exhibited a relatively high surface and internal sensitivity. The surface sensitivity was characterized by low-intensity reciprocity failure, and the surface images were strongly reversed at high exposure-times, while the internal image exhibited high-intensity reciprocity failure and did not reverse over a wide range of exposures. The relative behavior of the surface and internal images is consistent with the bromination hypothesis of reversal. Preferential appearance of bromine at the intersection of substructural mosaic boundaries with the surface was indicated. Optical sensitization and supersensitization were reproduced in these crystals, the internal image associated with optical sensitization being found to a distance at least 1.4μ from the surface. The absorp-

tion spectrum of a monolayer of adsorbed dye on the crystal surface was measured, and the kinetics of adsorption was followed spectroscopically.

T9. Effect of Bromine on the Dark Conductivity of Silver Bromide and Its Relation to Photoconductivity. GEORGE W. LUCKEY, *Eastman Kodak Company.*—The dark conductivity of a silver-bromide crystal in a bromine atmosphere increases with increasing bromine pressure. Wagner[1] showed that the conductivity increase at temperatures above 200°C is caused by the formation of positive holes inside the crystal. His mechanism predicts that this hole conductivity should be proportional to the square root of the halogen pressure. The conductivity increases caused by various pressures of bromine vapor have been measured at temperatures between 25 and 200°C. Above 50°C, the increase in conductivity is proportional to the square root of the halogen pressure and independent of the crystal thickness. The data at 200°C agree with those of Wagner. Below 50°C, the results are more erratic, and the system reaches equilibrium slowly. The conductivity increases depend on the preparation of the silver halide samples. When the increases are large, the quantum efficiency of photoconductivity at room temperature is also large.

[1] C. Wagner, Z. physik. Chem. B32, 447 (1936).

T10. Ultra-Short Light-and-Voltage Pulses Applied to Silver-Halide Crystals by Turbine-Driven Mirror and Electrical Contacts. J. H. WEBB, *Eastman Kodak Company.*—Haynes and Shockley[1] studied electron mobility in silver-halide crystals using ultra-short light-and-voltage pulses. Their apparatus consisted of a radar-type pulse-forming network discharged by mercury spark tubes. An apparatus for carrying out this experiment has been developed using an air turbine with mirror and electrical contacts. Repetitive light pulses of 3 microseconds and voltage pulses of 10 kv and 20 microseconds can be applied to a crystal at a rate of 500 per second. The light-and-voltage pulses can be initiated simultaneously or with variable-time separation. The simplicity and practicability of the apparatus for electron mobility and photolysis studies on the silver halides will be illustrated by experimental results.

[1] J. R. Haynes and W. Shockley, Phys. Rev. 82, 935 (1951)

SATURDAY MORNING AT 9:30

Calvert Room

(R. T. BIRGE presiding)

Lecture by the Recipient of the Buckley Prize

U1. Photoelectric Experiments on Excitation-Energy Transfer in Crystals. L. APKER, *General Electric Research Laboratories.* (40 min.)

Invited Papers

U2. Crystallographic Significance of Some Recent Results in Solid-State Physics. J. H. DONNAY, *Johns Hopkins University.* (30 min.)

U3. Paramagnetism of Solids. J. H. VAN VLECK, *Harvard University.* (30 min.)

U4. Spectroscopy of Solids. G. H. DIEKE, *Johns Hopkins University.* (30 min.)

SATURDAY MORNING AT 9:30

Phoenix Room

(S. G. WEISSBERG presiding)

Contributed Papers in High-Polymer Physics

V1. Experimental Study of the Behavior of Rubbers in Simple Shear.* J. E. IVORY,† F. P. BALDWIN,‡, AND R. L. ANTHONY, *University of Notre Dame.*—The dependence of shearing stress upon strain and temperature was investigated for two rubbers, GR-I-18 and Paracril-35. The type of strain employed was simple shear. Sandwich type specimens were used, and were so mounted as to permit free thermal expansion in a direction perpendicular to the plane of shearing. The stress relaxation method was used to obtain equilibrium stress-temperature curves, shearing displacements being held constant during the relaxation period and also during the stress-temperature runs. The stress-temperature curves were observed to be linear over a temperature range of 80°C for strains ranging from 0 to 15 percent. The stress-strain curves, obtained from the stress-temprature curves by cross-plotting, were also linear. A small internal energy component, amounting to about 5 percent of the total stress, was observed for each rubber. The existence of this component, whenever the rubber is permitted to expand freely in the direction perpendicular to the plane of shearing, is in agreement with the predictions of the statistical theory.

* Supported in part by the Office of Naval Research.
† Now with Bell Aircraft Corporation.
‡ Now at Esso Laboratories.

V2. Tensile Strength of Elastomers.* G. R. TAYLOR AND S. R. DARIN, *Mellon Institute.*—The tensile strength of decamethylene dis-methylazodicarboxylate vulcanizates of GR-S 50°C polybutadiene, 5°C polybutadiene, and natural rubber has been determined as a function of temperature and/or the

degree of cross-linking. A theory of tensile strength of amorphous polymers which adequately describes the effect of the degree of cross-linking on strength is proposed. The tensile strength is assumed proportional to the total number of active network chains in the vulcanizate times an explicit function of the degree of orientation of these chains at rupture. The resulting expression is shown to be adequate for GR-S, and when modified to take into account the effect of crystallization on the separate factors, it appears semiquantitatively correct for crystallizable polymers.

* The work discussed herein was performed as part of the research project sponsored by the Reconstruction Finance Corporation, Office of Synthetic Rubber, in connection with the Government Synthetic Rubber Program.

V3. Biaxial Creep Fracture of High Polymers. CHESTER G. BRAGAW, JR., *DuPont.*—An experimental investigation has been made of the creep fracture behavior of commercial polyethylenes subjected to uniaxial tension (simple tensile test) and biaxial tension (tube under internal pressure). A nonimpact loading was applied and held constant until fracture occurred. Direct stress-life data are presented for both cases and comparisons made. In biaxial tension a new creep embrittlement phenomenon was encountered; data from critical experiments are discussed and a structural mechanism is suggested. The discovery of extremely low ductility creep fracture under room temperature biaxial stressing implies that even in the case of the nonimpact loading of very ductile polymers, fracture behavior in multiaxial stress applications may be more important than deformation behavior.

V4. Unilateral Compression of Rubber. MICHAEL J. FORSTER, *Firestone Tire and Rubber Company.*—One-dimensional compression measurements have been made on samples of natural rubber gum stock. The experimental stress-strain curve and the theoretical relation $f=G[L-1/L^2)]$ agreed quite well over the entire range (0 percent–32 percent) studied. No hysteresis loop was evident. Volume measurements indicated the possibility of a slight increase in volume at low compressive strains, changing to a volume decrease at strains above 13 percent. The friction at the faces of the sample was eliminated by a new method of lubrication. The sample essentially floated between two tin films of a liquid which flowed under pressure between the sample and compressing plates allowing uniform lateral expansion of the sample.

V5. Behavior of Nonpigmented Rubber Vulcanizates in Tension. G. M. MARTIN, F. L. ROTH, AND R. D. STIEHLER, *National Bureau of Standards.*—Nonpigmented vulcanizates of Hevea, GR-S, GR-I, and Neoprene rubbers were subjected to constant tensile loads and their elongations were measured to the nearest 0.1 percent at intervals of time from 1 to 10 000 minutes. For temperatures between 25 and 55°C the elongations showed no tendency to become constant and in most cases they increased approximately with the logarithm of time. The stress-strain curves after a given period of creep could not be represented by any of the proposed theoretical stress-strain relationships. However, the curves for all vulcanizates of the four rubbers were similar up to about 200 percent elongation and could be represented by a single empirical stress-strain relation. This relation permits the calculation of the modulus near zero elongation and the stress-strain curve up to an elongation of 200 percent from a single stress-strain measurement.

V6. The Nature of Stark Rubber.* DONALD E. ROBERTS AND LEO MANDELKERN, *National Bureau of Standards.*—It has been demonstrated[1,2] that when slow heating rates are employed the melting temperature of undeformed natural rubber is independent of previous thermal history. This observation served as a basis for the assignment of 28±1°C as the equilibrium melting temperature $T_m°$, of natural rubber though it is well known that certain types of natural rubber, designated as "stark" exhibit appreciably higher melting temperatures. The melting behavior and x-ray diffraction patterns of four different samples of "stark rubber" were investigated. The melting temperatures ranged from 39 to 45.5°C while the x-ray diffraction patterns indicated that in all the samples, the crystallites displayed a preferred orientation. This orientation explains the higher melting temperatures that are observed and preserves the validity of the previous assignment of $T_m°$ for unoriented natural rubber. The orientation in "stark rubber" is probably caused by the plantation processing. Several methods which have been successful in preparing "stark rubber" in the laboratory will be outlined.

* Assisted by Office of Naval Research.
[1] D. E. Roberts and L. Mandelkern, Phys. Rev. **91**, 225(A) (1953).
[2] D. E. Roberts and L. Mandelkern, J. Am. Chem. Soc. (to be published)

V7. Molecular Weight Distributions of Polymers: I. Speculations on Polymerizations to Equilibrium. JOHN LAUREN LUNDBERG, *Bell Telephone Laboratories, Inc.*—Writing weight and number average molecular weight sums in terms of standard changes in free energies of polymerization permits (1) circumscribing behavior of standard free energies of polymerization as functions of chain lengths, (2) describing reasonable molecular weight distributions at equilibrium, (3) limiting weight-number average molecular weight ratios to values close to unity, and (4) estimating lower limits in the million plus range for the average molecular weight of linear polyethylene at equilibrium. The relation between "ceiling temperatures" upon polymerization and standard free energies of polymerization is discussed. A method for obtaining values of thermodynamic functions for polymers and polymerization processes by measurements of molecular weight distribution and monomer activity at equilibrium is outlined.

V8. Glass Transitions in Polymer-Plasticizer Systems. LEO BREITMAN, *Polymer Corporation Ltd.*—Glass temperatures (T_g) of pure and plasticized elastomers have been obtained from dilatometric measurements and from the temperature dependence of angular response to torsional stress. The depression of T_g by a diluent, determined by either method, is a convenient measure of its low-temperature plasticizing efficiency. High-melting diluents generally had zero efficiency. Some compounds, though normally crystalline above T_g, depressed the glass temperature of polymer blends. These phenomena are interpreted in terms of phase separation in binary systems, including the effect of polymer on the freezing point of diluent. T_g decreased as the polymer loading increased to a more or less well defined limit, beyond which further dilution had negligible effect. For diester type plasticizers both $T_{g\,max}$ and the limiting diluent concentration were linear functions of compatibility, as defined by the extent to which standard polymer vulcanizates were swollen by plasticizer. Investigations with hydrocarbon oils showed that the apparent activation energy for flow (E_v) of the oil correlated with its low-temperature plasticizing efficiency, while four points and T_g of the oils were not as significant. It is concluded that low E_v and high compatibility with polymer are properties which mitigate for low-temperature plasticizing efficiency.

V9. Proton Magnetic Resonance in Polyamides. W. P. SLICHTER AND J. M. MAYS, *Bell Telephone Laboratories.*—Measurements have been made of the proton magnetic resonance absorption in several linear polyamides from −195° to +140°C. The variation of line width with temperature is similar in form to that found in other polymeric systems.[1] A marked decrease in line width with increasing temperature occurs over a span of 20 or 30 degrees within the range from 0° to 120°C, and is presumed to result from the onset of rotation of chain segments. In a series of polyamides possessing an

even number of carbon atoms between polar groups, this transition occurs at lower temperatures as the hydrocarbon portions are made longer (polydecamethylene octadecanamide compared to polyhexamethylene adipamide). In the copolymer polyhexamethylene adipamidesebacamide, the transition region is at a lower temperature than in the pure adipamide or the pure sebacamide. X-ray diffraction studies on fibers of all these substances show that the chain packing becomes more symmetrical over these same temperatures.

[1] R. Newman, J. Chem. Phys. 18, 1303 (1950); Holroyd, Mrowca, and Guth, J. Appl. Phys. 22, 696 (1951).

V10. Nuclear Magnetic Resonance Relaxation Times for Polyisobutylene in Carbon Tetrachloride Solution.* A. W. NOLLE, *The University of Texas.*—The nuclear magnetic resonance relaxation times are examined by the spin echo method, as a function of concentration, in solutions of high molecular weight polyisobutylene (molecular weight $>10^6$) in carbon tetrachloride. The hydrogen signal is used. Since the solvent is nonhydrogenous, the results are attributable to the kinetics of the polymer molecules. As the concentration is decreased, the transverse relaxation time (T_2) at 25°C increases sharply, until a value of the order of 70 milliseconds is reached at a concentration of 0.06 g of polymer per milliliter of solvent. The result then remains nearly constant with further decrease of concentration, indicating that the limiting behavior in dilute solution has been observed.

* Supported by the Office of Naval Research.

SATURDAY AFTERNOON AT 2:00

Shriver Hall, J.H.U.

(FRANK HERMAN presiding)

Invited Paper

W1. Cyclotron Resonance in Semiconductors. B. LAX, *M.I.T.* (30 min.)

Cyclotron and Electron-Spin Resonance

W2. Quantum Theory of Cyclotron Resonance for Degenerate Bands. J. M. LUTTINGER, *University of Michigan.*—Recently the author (in collaboration with W. Kohn) has given the rigorous quantum theory of cyclotron resonance for degenerate bands. For nondegenerate bands the classical theory and quantum theory give identical results. This theory has now been applied to the case of holes in Si and Ge, the top of the valence band in these materials being degenerate. Full account has been taken of the effects of spin orbit coupling. It turns out that if the external magnetic field is in the (111) direction the resulting coupled differential equations may be solved rigorously, under two assumptions: (1) The momentum along the external field is negligible. (2) The interaction of the electronic spin with the external field is ignored. The first assumption is certainly justified if we are interested in studying transitions at extremely low temperature (say below 1°K), which is where we would expect quantum effects to be most important. The second assumption is not quite so good for the lowest levels, the error being of the order of the ratio of the effective mass to the true electronic mass. This ratio is, in all likelihood, rather less than unity for all cases of interest, and the corrections are easily obtained via perturbation theory. Detailed results will be presented.

W3. Boltzmann Theory of Cyclotron Resonance for Warped Spherical Energy Surfaces.* H. J. ZEIGER, *M.I.T.*—A solution of the Boltzmann transport equation has been obtained with applied dc magnetic and rf electric fields, for constant energy surfaces of the form $\epsilon=[1+g(\theta,\phi)]\hbar^2k^2/2m$. Here (k,θ,ϕ) are spherical coordinates in k-space, referred to the magnetic field direction as z axis, and $g(\theta,\phi)$ is a small nonspherical term. The extension to DC electric fields follows directly in the zero frequency limit. The collision time is assumed constant and a first order solution for the perturbed part of the distribution function is obtained as a Fourier series in ϕ. This leads to an expression for rf current, as a sum of terms $J_n(\theta)$. The terms contain resonant denominators, with $n=1$ corresponding to the fundamental cyclotron resonance, and higher values of n corresponding to harmonics. The magnetic field for resonance depends on field direction, and on θ (or k_z). When integrated over θ the resulting expressions for J_n describe the general features of the fundamental cyclotron resonance in the valence bands of Ge and Si. The theory is consistent with the possible observation of a third harmonic of the fundamental high mass hole resonance in Ge.[1]

* The research in this document was supported jointly by the Army, Navy, and Air Force under contract with the Massachusetts Institute of Technology.

[1] R. N. Dexter, following abstract.

W4. Third Harmonic Cyclotron Resonance of Holes in Germanium.* R. N. DEXTER, *M.I.T.*—In germanium the marked anisotropy of line shape and of magnetic field for cyclotron resonance of the heavy holes has indicated that the valence band energy surfaces are warped spheres.[1] We have observed an additional anisotropic resonance of weak intensity seen earlier in two orientations[2] but not explained. The resonance occurs at fields one third those giving resonance of the heavy holes. In the (110) plane, the new resonance disappears when the magnetic field is parallel to the [111] direction but has about one sixth the intensity of the heavy hole resonance when the field is 35° from the [001] direction. We have proposed that the new resonance of heavy holes arises from the anharmonic motion along the anisotropic energy contours. No second harmonic resonance has been observed. A classical Boltzmann transport theory for the valence band energy surfaces has shown a detailed agreement with the observations described above. Theoretically, the second harmonic is relatively suppressed by symmetry.

* The research in this document was supported jointly by the Army, Navy, and Air Force under contract with the Massachusetts Institute of Technology.

[1] Dexter, Zeiger, and Lax, Phys. Rev. 95, 557 (1954).
[2] A. F. Kip, Physica (to be published).

W5. Cyclotron Resonances in Germanium at 1.4°K. R. C. FLETCHER, F. R. MERRITT, AND W. A. YAGER, *Bell Telephone Laboratories.*—We have measured the cyclotron resonances on several high resistivity samples of germanium ($N_A \approx N_d \approx 10^{13}$ cm^{-3}) with a Zeeman Modulation Spectrometer at a frequency of 24 kmc both at 4.2°K and 1.4°K. Carriers of both signs

were introduced with white light. At 4.2°K we have found the previously reported[1] resonances characteristic of both holes and electrons. When the sample temperature was decreased to 1.4°K, the electron resonances increased in peak absorption and became sharper. The hole resonances, however, completely disappeared, with no new resonances of comparable magnitude appearing in the range from $m^*=0.01$ to 3. The disappearance of the normal hole resonances is what the quantum treatment of Kohn and Luttinger[2] would predict for carriers near a band degeneracy. The absence of the predicted new hole resonances is not understood. The narrowing of the electron resonances at 1.4°K suggests that impurity scattering, which Hall mobility measurements indicate is the dominant scattering mechanism at these temperatures, either does not contribute significantly to the broadening of cyclotron resonances or else contributes less as the temperature is decreased.

[1] Dresselhaus, Kip, and Kittel, Phys. Rev. 92, 547 (1953); Lax, Zeiger, Dexter, and Rosenblum, Phys. Rev. 93, 1418 (1954); Dexter, Zeiger, and Lax, Phys. Rev. 95, 557 (1954).
[2] Kohn and Luttinger, Phys. Rev. 96, 529 (1954).

W6. Effective Mass of Carriers and Relaxation Time in Germanium.* F. D'ALTROY AND H. Y. FAN, *Purdue University.*—Relaxation time and effective mass of carriers have been evaluated for n-type germanium using dielectric constant K and conductivity σ obtained from microwave (9200 Mc/sec) transmission measurements. Four samples were used and at each of the four temperatures: 20°K, 78°K, 200°K, and 300°K, results were obtained on two different samples. The values of m_c/m obtained are 0.18, 0.21, 0.40, and 0.58 for the four temperatures, respectively. The estimated error is ±20 percent. The values for two different samples at each temperature are in close agreement, although the relaxation times for the two samples used at 20°K differ by a factor of 2.2. The value for 300°K agrees with the results of Benedict and Shockley, whereas the value for 20°K approaches the value expected from cyclotron resonance measurements. Measurements at the same temperatures have been reported previously for p-type germanium.[1] The value obtained is $m_h=(0.34\pm0.06)m$ at all temperatures (the value reported was $m_h=0.43m$ due to an error in the estimation of carrier concentrations). Preliminary measurements on p-type germanium at 4.2°K gave $\Delta K>0$, which can be attributed to bound holes on the acceptors.

* Work supported by a Signal Corps Contract.
[1] F. D'Altroy and H. Y. Fan, Phys. Rev. 94, 1415 and 1405 (1954).

W7. Absorption by Free and Bound Holes in p-Type Germanium. S. TEITLER AND M. LAX, *Syracuse University,* AND E. BURSTEIN, *Naval Research Laboratory.*—The optical absorption due to free holes in p-type germanium is explained on the gasis of interband transitions using the present picture of the valence bands, with two bands degenerate at $k=0$, and a third band, split off at $k=0$. The respective mean effective masses for small k are $m_1=0.3m$, $m_2=0.04m$, and $m_3=0.07m$ from cyclotron resonance data. Assuming spherical energy surfaces and matrix elements proportional to k, we obtain an absorption curve with three peaks, at room temperature. The experimental[1] location of these peaks is used to obtain the effective mass of the third band, $m_3=0.079m$, and also the energy gap between the first and third bands, $E_G=0.28$ ev, which is the right order of magnitude for spin-orbit splitting.[2] The optical absorption at helium temperatures in the 4μ region is calculated on the basis of transitions by bound holes to the third valence band and yields an absorption curve in reasonable agreement with experiment.

[1] H. B. Briggs and R. C. Fletcher, Phys. Rev. 91, 1342 (1953).
[2] A. H. Kahn (unpublished) has recently discussed spin-orbit splitting and optical absorption by free holes in p-type germanium.

W8. Temperature Effect of Paramagnetic Line Shape. E. P. GROSS, *Syracuse University.*—The theory of spin absorption involves application of time dependent perturbation theory to a system nearly canonically distributed. In absence of the applied field the states are assumed to form a nondegenerate continuum; the absorption depends on the density of states. The moment method of Waller relates the moments of the absorption to the averages of functions of the dipole moment operator and its time derivatives taken for a canonical distribution. These results hold at infinite temperatures. We extend the theory by relating the operator averages to weighted moments of the absorption; the weight factor is a function of $h\omega/kT$. The approach differs from other finite temperature theories in that no direct attempt is made to compute the unweighted moments. We point out the identical basis of spin absorption theory and the fluctuation-dissapation analysis of irreversible thermodynamics. One of the relations derived here is the generalized Nyquist formula; the others provide an infinite set of connections between the "fluctuating" and irreversible aspects of systems satisfying the assumptions of the theory.

W9. Spin Resonance Widths of Electrons in Donor States in Silicon.* W. KOHN, *Carnegie Institute of Technology.*—Honig and Kip and Honig have reported the widths of spin resonance lines due to electrons bound by Li and As impurities in silicon. We have made theoretical estimates of these widths, which are apparently due to the magnetic moments of the Si^{29} isotope. The model was the same as that which was used to account for the hyperfine splitting of bound electron states associated with P donors. One somewhat uncertain factor enters all these calculations namely

$$\eta\equiv|\psi(k^{(1)},0)|^2/\Omega^{-1}\int_{\text{cell}}|\psi(k^{(1)},r)|^2dr,$$

where $\psi(k^{(1)},r)$ is a Bloch wave at the bottom of the conduction band and Ω is the volume of the cell. By adjusting η to give agreement with experiment we find

	P, h.f. splitting	Li, line width	As, line width
η	≈200	160	≲260

(If $k^{(1)}$ should lie extremely close to either the center or the boundary of the Brillouin zone, the measured line widths would require smaller values of η). If $\psi(k^{(1)}r)$ were completely s-like we estimate $\eta\approx700$. This indicates a very substantial admixture of p-state.

* Supported in part by the Office of Naval Research.

W10. Spin Resonance in Neutron Irradiated Silicon.* E. SCHULZ-DUBOIS, M. NISENOFF, H. Y. FAN, AND K. LARK-HOROVITZ, *Purdue University.*—Electron spin resonance has been observed in p-type, boron-doped silicon after irradiation by neutrons.[1] The measurements were made at 4.2°K and at 9200 Mc/sec. The absorption line gives a gyromagnetic ratio $g=2.004\pm0.001$ determined by using diphenyl picryl hydrazyl calibration. The line width between half power points is about 12 oersted. The room temperature resistivity ρ was increased from 0.01 to 10^4 ohm-cm by the irradiation.[2] Another sample from the same piece was partially annealed after the irradiation, $\rho=3$ ohm-cm; it showed weaker absorption with $g=2.002\pm0.001$ and a half width ~3 oersted. The samples had etched surfaces. A 500 ohm-cm sample, not irradiated, gave no resonance absorption with the same surface treatment. Resonance absorption has not been found in boron-doped silicon with or without partial compensation by donar impurity.[3] The observed absorption should therefore be associated with the defects produced by the irradiation.

* Work supported by a Signal Corps and U. S. Atomic Energy Commission contract.
[1] We are indebted to J. Crawford and J. Cleland of Oak Ridge National Laboratories for the irradiation.
[2] K. Lark-Horovitz, *Semi-conducting Materials* (Butterworths, London, 1951).
[3] Fletcher, Yager, Pearson, Holden, Read, and Merritt, Phys. Rev. 94, 1392 (1954).

W11. Multiple Resonances in Cobalt Ferrite.* P. E. TANNENWALD AND H. J. ZEIGER, *M. I. T.*—In the past, most microwave experiments on single crystals have been carried out on the assumption that the magnetization vector was fully aligned with the applied magnetic field. B. Lax has suggested that in high anisotropy cubic crystals, when the magnetic field H_0 is applied in certain crystal directions (other than the easy axis), ferromagnetic resonance might occur before the magnetization vector M is lined up with H_0, in addition to the usual resonance. We derived a very general solution of the equation of motion of the magnetization vector which includes the effects of anisotropy in terms of energy rather than effective demagnetizing factors[1] and applied it to a cubic crystal. We have observed double resonances as a function of H_0 at 24 000 Mcps in a single crystal of cobalt ferrite. Data will be presented from which the anisotropy and g-factor can be calculated; and the extent to which the assumptions made in the theory are justified will be discussed.

* The research in this document was supported jointly by the Army, Navy, and Air Force under contract with the Massachusetts Institute of Technology.

[1] Similar to that first given by J. Smit, Conference on Ferrimagnetism, NOL, October, 1954; and H. Suhl (submitted to Phys. Rev.).

SATURDAY AFTERNOON AT 2:00

Rowland 205, J.H.U.

(H. J. WILLIAMS presiding)

Invited Papers

X1. Quenching-in of Vacancies in Pure Gold. J. S. KOEHLER, *University of Illinois.* (30 min.)

X2. The Magnetic Structure of Iron. C. G. SHULL, *Oak Ridge National Laboratory.* (30 min.)

Ferromagnetism and Ferroelectricity

X3. Antiferromagnetism in a Cr_2O_3 Crystal. T. R. MCGUIRE, E. J. SCOTT, AND F. H. GRANNIS, *U. S. Naval Ordnance Laboratory.*—The magnetic susceptibility and microwave resonance absorption of a Cr_2O_3 single crystal have been investigated. The crystal was prepared by the flame fusion method. It has rhombohedral symmetry and showed an antiferromagnetic Curie temperature (Tc) of 307°K. Below Tc the susceptibility (χ) perpendicular to the [111] direction is independent of temperature while the value of χ parallel to [111] approaches zero at very low temperatures. According to the Van Vleck[1] theory, this behavior indicates that the spins are aligned along the [111] direction. Above 77°K the parallel susceptibility was found to be proportional to the $\frac{3}{2}$ power of the temperature. Resonance measurements (22 500 mc) at the Curie temperature showed a shift in the peak of the absorption curve as a function of temperature. This shift was towards lower magnetic fields and will be discussed in terms of the Kittel[2] resonance theory which includes the anisotropy and exchange fields in addition to the applied field.

[1] J. H. Van Vleck, J. Chem. Phys. 9, 85 (1941).
[2] C. Kittel, Phys. Rev. 82, 565 (1951).

X4. Ionic Distribution in Magnesium Ferrite.* C. J. KRIESSMAN AND S. E. HARRISON, *Remington Rand Inc.*, AND H. B. CALLEN, *University of Pennsylvania.*—Magnesium ferrite samples have been sintered at 1400°C and water quenched at nine temperatures (T_q) between 1400°C and 400°C. The fraction x of Mg^{++} ions in tetrahedral sites has then been determined by measurements of the saturation magnetization. The values of x vary from 0.09 for $T_q=450$°C to 0.32 for $T_q=1400$°C. This latter value has been substantiated using x-ray diffraction techniques by Miss S. Greenwald of the Naval Ordnance Laboratory. The data do not fit the distribution proposed by Neel,[1,2] $x(1+x)/(1-x)^3=e^{-\theta/T}$, where θ is a constant. The data do fit a distribution in which $\theta=\theta_0-\theta_1 x$, implying that the number of Mg^{++} ions already on tetrahedral sites cooperatively decreases the activation energy necessary for the transition to tetrahedral sites. A mechanism qualitatively able to account for the form of θ is the dependence of the Madelung energy on the ionic distribution. The form of the various terms in the Helmholtz potential and the consequent physical significance of the parameter θ_1 will be discussed.

* Supported in part by the Office of Naval Research.
[1] L. Neel, Comptes rend. 230, 190 (1950).
[2] R. Pauthenet and L. Bochirol, J. phys. radium 12, 249 (1951).

X5. Curie Constant, Spontaneous Polarization, and Latent Heat in the Ferroelectric Transition in $KNbO_3$. S. TRIEBWASSER AND J. HALPERN, *IBM Watson Laboratory.*—Measurements of the dielectric constant of $KNbO_3$ single crystals above the tetragonal to cubic transition temperature indicate that the Curie law $K=C/(T-T_0)$ is followed quite closely with $C=2.68\times10^5$°C and $T_0=350$°. Observation of the hysteresis behavior in the tetragonal ferroelectric state yields a value of spontaneous polarization P_s in the vicinity of the transition of 26 $\mu C/cm^2$. If one assumes the form of the Electric Gibbs function as given by Devonshire,[1] then the constants C and P_s are related to the latent heat of the ferroelectric transition by

$$\Delta S=L/T_c=(2\pi/C)P_s^2,$$

where T_c is the temperature of the transition and L the latent heat. We have repeated the measurement of the latent heat previously given by Shirane *et al.*[2] arriving at a somewhat lower value of 134±5 cal/mole. This is in reasonable agreement with the value 150 cal/mole derived from C and P_s reported above.

[1] A. F. Devonshire, Phil. Mag. 3, 85 (1954).
[2] Shirane, Danner, Pavlovic, and Pepinsky, Phys. Rev. 93, 672 (1954).

X6. Electromechanical Behavior of Single Crystals of $BaTiO_3$. E. J. HUIBREGTSE, M. E. DROUGARD, AND D. R. YOUNG, *IBM, Poughkeepsie.*—The frequencies of resonance and antiresonance of the fundamental modes of vibration have been measured in single crystals of $BaTiO_3$, in the temperature range from room temperature to 135°C. The samples were cut into simple geometrical shapes, long bars and flat disks, to insure that the fundamental modes were being excited. To

make calculations of various physical constants a knowledge of mode is necessary. All the crystals were "c" plates (i.e., the direction of polarization is perpendicular to large area sides), and the large area sides were as completely electroded as possible, to minimize a clamping effect caused by nonelectroded portions of the crystal. Results include the temperature dependences of: the electromechanical coupling coefficients, k_1 and k_r (for longitudinal and radial modes, respectively); the elastic compliances at constant field S_{11}^E and for constant polarization S_{11}^P, the piezoelectric coefficient d_{31}, and Poisson's ratio μ. At and above 120°C, the Curie temperature, the crystal structure is cubic and is no longer piezoelectric. By applying a dc field, the electrostrictive effect distorts the cubic structure into a tetragonal structure, which is again piezoelectric. Above the Curie temperature the electromechanical behavior has been studied as functions of both temperature and electric field, and these results will be presented.

X7. Second-Order Transition in $BaTiO_3$. A. deBRETTEVILLE, JR., *Signal Corps Engineering Laboratories.*—The paraelectric to ferroelectric transition of a barium titanate crystal grown by the Reitneika[1] technique is established as a first-order transition.[2] Double hysteresis loops indicate that the transition changes into a second order one approximately 8° above the Curie point. Photographs of double hysteresis loop show that the polarization as a function of field strength does not rise abruptly as for a first-order transition. Free energy curves derived from the measurements assume a zero slope at 123°C, approximately where the latent heat becomes zero. At this temperature the reciprocal dielectric constant shows a definite change in slope.

[1] Crystals obtained through the courtesy of Dr. S. O. Morgan, Bell Telephone Laboratories, Murray Hill, New Jersey.
[2] W. J. Merz, Phys. Rev. 91, 513–517 (1953).

X8. Dielectric Behavior of Barium Titanate in the Paraelectric State. M. E. DROUGARD, R. LANDAUER, AND D. R. YOUNG, *IBM, Poughkeepsie.*—The coefficients in the equation of state of $BaTiO_3$ proposed by Devonshire can be considered as describing the polarization and temperature dependence of the dielectric constant. This dependence has been studied by a dynamic method. The polarization is developed by a large amplitude af field and the dielectric constant is measured by measured by a small rf signal. This method provides an accurate measurement of the coefficient of the P^4 term in Devonshire's expansion of the free energy. It is shown, however, both by calculations and experimentally that this coefficient is quite sensitive to clamping and that special precautions have to be taken to obtain reliable results. This coefficient has been studied as a function of temperature from the Curie point up to 150°C. It has been found to vary by 50 percent in that range of temperature, showing a linear decrease in magnitude with increasing temperature. No reliable results have been obtained on the coefficient of the P^6 term. The accuracy of the results is impaired by a hysteresis phenomenon which has not been explained, and the highest fields that could be applied without damaging the sample do not allow the detection of any contribution due to the P^6 term, even just above the transition temperature.

SATURDAY AFTERNOON AT 2:00

Remsen 1, J.H.U.

(S. MROZOWSKI presiding)

Carbons

Y1. Self-Diffusion in Natural Graphite Crystals.* M. A. KANTER, *Argonne National Laboratory and Illinois Institute of Technology.*—A radioactive tracer technique has been used to measure diffusion in graphite crystals which were separated from limestone and suitably purified. These were small particles, *ca.* 10^{-1} cm in diameter and 10^{-2} thick, and were composed of several single-crystal regions with some misaligned material at the edges amounting to no more than about one percent. The experiments were carried out by heating several hundred of these particles to temperature in radioactive carbon monoxide whose C^{14} concentration was maintained constant and then determining the uptake of tracer in the crystals. At 1600°C the tracer exchanged with the graphite surface in a matter of minutes. At 1950°C diffusion into the imperfect regions of the crystal began at a measurable rate. Above 2150°C, diffusion into the single crystal regions predominated, and the measurements agreed with equations for diffusion into a semi-infinite solid whose surface concentration is maintained constant. The activation energy for volume diffusion in graphite calculated from these data is about 170 k cal/mole.

* Based on work performed under the auspices of the U. S. Atomic Energy Commission.

Y2. Two-Medium Theory of Thermal Conductivity of Artificial Graphite: Experimental.* ALAN W. SMITH, *North American Aviation, Inc.*—The two-medium nature of pitch-bonded artificial graphite has been offered as an explanation for the low-temperature thermal conductivity of this material.[1] This is anomalous in that the thermal conductivity has a stronger temperature dependence than the specific heat. Measurements have been made recently on large crystallite natural graphite and small crystallite, nonpitch-bonded artificial graphite (obtained from J. C. Bowman, National Carbon Company). The low-temperature thermal conductivity of these two graphites has the same temperature dependence as the specific heat. This is the normal behavior of crystals exhibiting boundary scattering. Measurements have also been made on brominated, pitch-bonded artificial graphite (obtained from G. Hennig, Argonne National Laboratory). Bromination to 1.16 atom percent decreases the thermal conductivity by a factor of 2.5. This effect is explained by the two-medium theory in the subsequent paper.

* This paper is based on studies conducted for the U. S. Atomic Energy Commission.
[1] A. W. Smith, Phys. Rev. 93, 952 (1954).

Y3. Two-Medium Theory of Thermal Conductivity of Artificial Graphite: Interpretation.* JOHN E. HOVE, *North American Aviation, Inc.*—As mentioned in the previous paper, the observed low-temperature thermal conductivity of pitch-bonded artificial graphites shows an anomalous temperature dependence, while both large crystal natural and nonpitch-bonded artificial graphites have a normal behavior. This paper will show how this can be quantitatively explained by the presence in the artificial graphites of ungraphitized carbon

derived from the bonding pitch. Furthermore, this two-medium theory correlates the observed effects of bromination with the effects expected on the basis of previous work. The graphite crystallites will conduct heat in nearly a two-dimensional manner; it is assumed that the ungraphitized carbon medium is similar to a highly disoriented diamond structure and can be considered as three-dimensionally isotropic. By taking these two regions to be in series, an expression for the total thermal conductivity is derived which qualitatively describes the observed data. By a quantitative fit, estimates of crystallite size and interparticle distance are obtained; these check previous estimates (by other methods) in a satisfactory manner for the three types used (large and medium particle coke and small particle lampblack graphites). Brom-graphite residue compounds introduce additional scatterers (i.e., bromine) presumably at crystallite and mosaic boundaries only. The data of the previous paper are analyzed by the two-medium theory and are shown to support the above view.

* This paper is based on studies conducted for the U. S. Atomic Energy Commission.

Y4. Thermal Conductivities of Carbons and Graphites.* C. P. JAMIESON, *University of Buffalo* (introduced by S. Mrozowski).—The thermal conductivities, κ, of pitch-bonded, extruded carbon rods have been measured for ambient temperatures, T, ranging from 110°K to 400°K, each rod having been heat-treated to a different temperature (Ht) between 1200°C and 3100°C. Power was supplied to a heater at the middle of the rod whose ends were in thermal contact with the bath. Heat losses were reduced by a radiation shield with matched temperature gradients and by evacuation of the chamber. For highest Ht's, plots of κ *versus* T show maxima at or below room temperature; for lowest Ht's, κ increases approximately linearly with T. Mean crystallite diameter, which increases with increasing Ht, was determined by x-ray diffraction techniques. For a fixed T, the thermal resistivity, R, depends on mean crystallite diameter in such a way that for Ht less than 2200°C, R increases much more strongly than linearly with the reciprocal of mean crystallite diameter. This indicates that besides the usual boundary and lattice scattering there is additional scattering, probably due to intercrystalline effects.

* Work supported in part by the Office of Naval Research and also in part by the U. S. Atomic Energy Commission.

Y5. Temperature Dependence of Magnetic Susceptibility of Carbons and Polycrystalline Graphites.* P. KIIVE AND H. T. PINNICK,† *University of Buffalo*.—The magnetic susceptibility χ of soft-carbon rods heat-treated to temperatures of $Ht=1600$°C, 1800°C, 2000°C, 2200°C, 2400°C, and 2800°C was measured at seven temperatures T between 80°K and 1300°K. Moreover, χ as a function of T for all heat treatments, is similar to that of large crystals of graphite.[1] χ reaches a practically temperature-independent maximum value at low-temperatures T and tends to zero linearly with $1/T$ at high temperatures. All curves χ *versus* $1/T$ for different heat-treatments join the curve for well-graphitized material in the high temperature range, but, at low temperatures, curves for Ht lower than 2200°C reach smaller maximum values, the values decreasing with decrease in Ht (decrease in microcrystallite diameters) in a manner similar to that found from measurements made at room temperature.[2] The detailed interpretation of these relationships in terms of electron gas diamagnetism is not clear at present.

* Work supported by the Office of Naval Research.
† Now at Electro Metallurgical Company, Niagara Falls, New York.
[1] W. Ganguli and K. S. Krishnan, Proc. Roy. Soc. (London) 117, 168 (1941).
[2] H. T. Pinnick, Phys. Rev. 95, 846 (1954).

Y6. Magnetic Resonance Properties of Raw Cokes.* J. G. CASTLE, JR., *University of Buffalo*.—Raw coke may be designated as any carbonaceous matter which has been heated to a temperature (Ht) between 300°C and 700°C. Recently Uebersfeld[1] and Ingram[2] found spin-resonance absorption in activated charcoal, charred carbohydrates, and coal. Early in our program on the magnetic resonance properties of carbons and graphites, we had independently found a single sharp absorption near $g=2$ in several raw cokes. The room temperature absorption of 3-cm radiation in each coke occurs at $g=2.0030\pm0.0002$. The absorption intensity rises with increasing Ht (increasing molecular size) to a maximum near 550°C and then drops several orders of magnitude as the volatile material is driven off, as in coal cokes.[2] On the basis of experiments on a wide variety of cokes, we believe this absorption is due to nitrogen or oxygen bonded into the coke structure. The lines are approximately Lorentz-shaped. We find different line widths in the various raw cokes; the full widths at half-maximum range from 3 to 12 gauss. Some coke samples have a strong, broad absorption line with a g-value of about six.

* Work supported by the Office of Naval Research.
[1] Uebersfeld *et al.* Nature 174, 614 (1954).
[2] Ingram and Tapley, Nature 174, 797 (1954); Ingram and Bennett, Phil. Mag. 45, 545 (1954).

Y7. Dimensional Changes During Heat Treatment and Thermal Expansion of Polycrystalline Carbons and Graphites.* F. M. Collins, *University of Buffalo*.—Two telescopes with micrometer eyepieces were used to determine the length changes of carbon samples placed within a furnace. These were rods made by extrusion of calcined coke-pitch mixtures and baked to 1100°C. The irreversible length changes were measured as the temperature was gradually raised from 1100°C to 2800°C, as were the reversible-thermal contractions of the resultant graphites while the temperature was lowered. Soft-carbon rods contract in heat treatment up to 1500°C and then expand, rapidly for the next few hundred degrees and more slowly thereafter. Both the heat-treatment curves and the thermal-expansion curves of graphite markedly depend on the calcination temperature of the coke; x-ray diffraction reveals corresponding differences in structure of the resulting graphite. Changes in expansion coefficient of graphite due to impregnation with pitch are less for rods impregnated after being baked to temperatures above 1100°. The results indicate that introduction of the binder affects the subsequent development of the crystalline structure in the heat-treatment process.

* Work performed under the auspices of the U. S. Atomic Energy Commission.

Y8. Physical Properties of Carbons and Porosity.* S. MROZOWSKI, *University of Buffalo*.—The dependence of different physical properties of carbons and polycrystalline graphites upon the porosity introduced in the manufacturing process is considered. The apparent (bulk) density d of the material is a function of two variables: the density of the coke particles d_0 (mass of coke per unit volume of bulk material) and the density of binder coke $(d-d_0)$. Making a number of simplifying assumptions as to the distribution of the binder coke and as to the statistics of the interparticle contacts the following relations are derived: for the elastic modulus $E=A\cdot d_0(d-d_0)$ for the mechanical strength $S=\beta\cdot d_0^{1+x}\times(d-d_0)$ and for the electric (and heat) conductivity $\sigma=C\cdot d_0^{\frac{1}{3}}(d-d_0)^{\frac{1}{3}}$ where $0\leqslant x\leqslant 1$ and where the coefficients A, B, and C are proportional to the respective values for the dense material ($d_{\max}$). Furthermore, C is inversely proportional to R^2 (R-average radius of coke particles) and also depends on the dimensions of the specimen. Since the maximum amount of binder decreases with increase of d_0 it is shown that the highest conductivities obtainable for unimpregnated carbons and graphites made by the standard method are expected to

increase first and then (for $d>1.75$) decrease with increase of the bulk density of material.

* Work performed in part under the auspices of the U. S. Atomic Energy Commission.

Y9. Studies of Elastic Modulus of Carbons.* K. HONG AND S. MROZOWSKI, *University of Buffalo.*—The dependence of Young's Modulus E on the heat treatment was investigated for extruded-carbon rods made essentially of a soft-type coke. The rods were subjected to static bending moment at room temperature. It was found that for increasing heat-treatment temperatures Ht the modulus first rapidly decreases (decrease by a factor of 2 between 1200° and 2000°C) and after going through a minimum at $Ht=2000$°C begins to increase. Around $Ht=2400$°C a maximum is reached after which the modulus gradually decreases up to highest heat treatments used (2900°C), the last value being, however, still higher than the value at the minimum. The dependence of E and of the electric conductivity σ on the bulk density was investigated for a group of rods from the same batch. The experimental data can be represented by $E=\alpha_1(d-d_0)$ and $\sigma^2=\gamma(d-d_0)$ where α and γ are constants depending on heat treatment and d_0 the density of coke particles (see preceding paper). The results are in agreement with the theoretical expectations. The agreement of extrapolated d_0 as determined from the different series of experiments shows that the spread in density is due mainly to variations in the coke yield of the binder and demonstrates the feasibility of a determination of a particle coke content d_0 for carbons of an unknown composition.

* Work performed under the auspices of the U. S. Atomic Energy Commission.

Y10. Density-Resistivity Relationships in Baked Carbons.* E. J. SELDIN, *University of Buffalo.*—Carbon samples were molded from mixtures of particles of calcined petroleum coke and coal tar pitch binder, and were then baked to 1000°C. The density d and the electrical resistivity ρ were determined as well as d_0, the density of the coke particles (for definition see the preceding paper by S. Mrozowski), and $d-d_0$, the density of the coked binder. All samples were made of single-sized coke particles. By varying the degree of compression a wide range d and d_0 was obtained. Some groups of samples were impregnated with pitch and rebaked, the process being repeated several times; in this way the density of a sample was increased while its d_0 remained almost unchanged. For samples with the same d_0 the relationship $1/\rho^2=\gamma\cdot(d-d_0)$ was found to hold. For samples with different d_0 preliminary measurements show that $\gamma=c^2\cdot d_0^n$ where $3\leqslant n\leqslant 4$. The factor C was found to be independent of particle size and nearly the same for samples made with a wide range of binder contents with the exception that for samples of very low-binder content C is considerably higher.

* Work performed under the auspices of the U. S. Atomic Energy Commission.

SATURDAY AFTERNOON AT 2:00

Remsen 101, J.H.U.

(C. HERRING presiding)

Semiconductors, III

Z1. Surface Potential and Surface Charge Distribution from Semiconductor Field Effect Measurements. W. L. BROWN, *Bell Telephone Laboratories.*—It has recently become apparent that from measurements of the change of conductance of a semiconductor with application of an electric field normal to its surface (the "field effect") one can determine both the surface potential (the electrostatic potential of the surface relative to the interior of the semiconductor) and the dependence of the immobile charge in electronic surface states on this surface potential. There is a minimum in the conductance of the space-charge layer at the surface as a function of the applied-electric field. It arises as majority carriers are depleted from the surface region, decreasing the conductance, and minority carriers are introduced in an inversion layer at the surface, increasing the conductance. This minimum can in principal always be obtained with large enough electric fields. When the minimum is experimentally observed, the measured changes of conductance with field can be compared directly with those expected in the absence of surface states to give the surface potential and the immobile surface charge. This method will be described as applied to measurements on a particular germanium surface.

Z2. Field Effect in Germanium. H. C. MONTGOMERY AND W. L. BROWN, *Bell Telephone Laboratories.*—The effect of a transverse electric field at one surface of a germanium filament on its conductance was observed for external fields up to $\approx 10^5$ volts/cm, at frequencies up to a few kilocycles. Oscillograms showing conductance as a function of charge induced in the surface region were obtained for n- and p-type material at temperatures 175–300°K. In either type material, a single oscillogram often showed both n- and p-like surface behavior, separated by a minimum in conductance. Behavior was substantially the same in ambients of dry oxygen or nitrogen or in vacuum of 10^{-3} mm. Large changes with ozone or water vapor ambients were consistent with the Brattain-Bardeen observations on contact potential.[1] Phase-shift loops, observed at the higher frequencies in the minority carrier portions of the curves, can be interpreted in terms of minority carrier lifetime. Somewhat similar loops, observed at all frequencies in the low-temperature range, could be suppressed by illumination, and are believed to be due to traps.

[1] W. H. Brattain and J. Bardeen, Bell System Tech. J. 32, 1–41 (1953).

Z3. Conductance of *P*-Type Inversion Layers on *n*-Type Germanium.* G. DEMARS, H. STATZ, AND L. DAVIS, JR., *Raytheon Manufacturing Company.*—Inversion layers on 8 ohm-cm n-type germanium were produced by exposing the germanium surface to a mixture of oxygen, ozone, and water vapor. The conductance was greater, the longer the sample had been exposed to the wet O_2 and O_3. Steady-state conductance was measured as a function of bias voltage. The curves were analyzed using the mobility for holes in an inversion layer as calculated by Schrieffer.[1] The calculations were carried through numerically using almost no approximations. For each conductance versus bias voltage curve, the *quasi*-Fermi level at the surface had an approximately constant position with respect to the bands. This was due to a high total density of surface states.

* This work was supported in part by the Signal Corps.

[1] J. R. Schrieffer, Phys. Rev. 54, 1420 (1954).

Z4. Nonsteady State Conductance of Inversion Layers and the Structure of Surface States on Germanium.* H. STATZ, L. DAVIS, JR., AND G. DEMARS, *Raytheon Manufacturing Company.*—The conductance of p-type inversion layers on germanium was measured as a function of bias voltage. A time dependence of the conductance was observed for abrupt changes of the voltage, the dependence being approximately of the form $\exp(-t/\tau)$. Furthermore, τ was itself a function of conductance and bias voltage, varying from a few seconds to a few minutes. The change in conductance resulted from a slow transfer of electrons from the germanium to surface states outside the germanium oxide film when the bias was changed. Other states at the germanium-germanium oxide interface had a time constant much shorter—presumably of the order of the lifetime of minority carriers. The widely different time constants were used to determine the density and energy levels of the latter states. Conductance measurements were made in sufficiently short time intervals that the charge in the states outside the germanium oxide was constant. Accurate analysis of the curves so obtained gave one energy level at the surface 0.155 ev below the middle of the band with a density of from 7×10^{10} to 1.2×10^{11} states/cm^2.

* This work was supported in part by the Signal Corps.

Z5. Surface-Recombination Velocity and Surface Conductance of Thin Germanium Slabs.* DONALD T. STEVENSON, *M. I. T.*—The approximate position of the Fermi level at germanium surfaces can be deduced from the changes of surface conductance with gaseous ambient. Simultaneous measurements of surface conductance and surface recombination velocity have been made in oxygen and nitrogen of varying humidity in order to test a previous theory[1]. Preliminary work indicates that this simple theory based on a single trapping level at the surface is not sufficient to explain the measurements. The recombination velocity on etched intrinsic and n-type samples is always lower in dry ambient than in wet. Conductance changes with humidity on sandblasted samples and etched samples are nearly the same indicating that the change in Fermi level is about the same in both cases. From previous experiments it is known that the recombination velocity at sandblasted surfaces is greater than 10^4 cm/sec, while on the etched surfaces studies here it was of the order of 50 cm/sec. It would appear that at least two sets of levels are required. The levels responsible for maintaining the charge balance are not affected appreciably by sandblasting.

* The research in this document was supported jointly by the Army, Navy, and Air Force under contract with the Massachusetts Institute of Technology.

[1] D. T. Stevenson and R. J. Keyes, Physica (to be published).

Z6. Photomultiplication at the Surface of Germanium.* H. BERNSTEIN AND R. H. KINGSTON, *M. I. T.*—Photomultiplication has been observed at the surface of p-type germanium in a wet nitrogen ambient. If an $n-p-n$-grown junction bar is canned with a chopped light source, the photoresponse in the p-type region is found to increase when the reverse bias is increased beyond a particluar value. In a dry-nitrogen ambient however, photomultiplication is not observed below a much higher bias which is near the avalanche breakdown voltage of the bulk junction.[1] It is proposed that this phenomenon may be explained in terms of the expected high field between the bulk and the n-type inversion layer or "channel" induced by the moist ambient.[2,3]

* The research in this document was supported jointly by the Army, Navy, and Air Force under contract with the Massachusetts Institute of Technology.

[1] K. G. McKay, Phys. Rev. **94**, 877 (1954).
[2] W. L. Brown, Phys. Rev. **91**, 518 (1953).
[3] A. L. McWhorter and R. H. Kingston, Proc. Inst. Radio Engrs. **42**, 1376 (1954).

Z7. Oxidation of Clean Surfaces of Germanium Below 25°C.* MINO GREEN AND J. A. KAFALAS, *M. I. T.*—The oxidation of clean surfaces of germanium in wet and dry oxygen has been studied in the temperature range −68°C to +25°C and the oxygen pressure range 1 to 200 microns. Fresh surfaces were obtained by crushing the germanium in an all-glass system in the presence of the gas to be adsorbed. The uptake of oxygen was not affected by the presence of water vapor. The oxygen uptake was approximately 3 oxygen atoms per surface germanium atom at 25°C, and was 10 percent less at −68°C. There was no appreciable difference in the extent of oxidation between n- and p-type germanium. Complete oxygen uptake occurred in <5 seconds over the pressure range investigated.

* The research in this document was supported jointly by the Army, Navy, and Air Force under contract with the Massachusetts Institute of Technology.

Z8. Effect of Dislocations on Recombination of Holes and Electrons in Germanium and Silicon.* S. A. KULIN, A. D. KURTZ, AND B. L. AVERBACH, *M. I. T.*—Experimental data indicate that edge-type dislocations markedly affect the recombination rate of holes and electrons in germanium and silicon. Dislocation densities have been measured by x-ray methods and the results correlated with the lifetime of minority carriers. In germanium results were obtained for three resistivity ranges. These results show that variations in the dislocation density at constant resistivity cause large changes in lifetime, the lifetime being inversely proportional to the dislocation density. Similar results have been obtained using silicon of a single resistivity range. Assuming each dislocation acts as a recombination center, a quantity σ_R, which relates to the recombination efficiency per unit length of dislocation, may be determined. Measurements on silicon specimens yield the value of $\sigma_R \cong 1.7\times10^{-2}$ cm^{-1} sec^{-1} compared with a value of $\sigma_R \cong 3.5\times10^{-3}$ cm^{-1} sec^{-1} for germanium. This difference is explained in terms of the larger energy-band perturbations caused by dislocations in silicon. These measurements indicate that individual dislocations are inherently more efficient recombination centers in silicon than in germanium.

* The research in this document was supported jointly by the Army, Navy, and Air Force under contract with the Massachusetts Institute of Technology.

Z9. Recombination of Injected Carriers at Dislocation Edges in Semiconductors. J. P. MCKELVEY AND R. L. LONGINI, *Westinghouse Research Laboratories.*—The boundary conditions on the continuity equation for carrier recombination at a lineage boundary in a semiconductor in the presence of an applied electric field are derived from kinetic considerations. A nonrecombination probability or "transmission coefficient" for a single charge carrier is assumed initially, and the boundary conditions are obtained by the method of multiple reflections which has heretofore been used to analyze surface recombination.[1] The carrier concentration at the boundary is in general discontinuous, the concentrations on either side involving the transmission coefficient, the bulk lifetime, the concentration gradients, the drift velocity, and the mean free path. The ratios of the concentration gradient to the concentration are independent of the concentrations on either side of the boundary and are functions of the drift velocity, the bulk lifetime and, in one case only, of the transmission coefficient. A simple experiment to determine the transmission coefficient is suggested; the continuity equation can be solved for this case. The relationship between transmission coefficient and recombination cross section is derived, permitting one to calculate the actual cross section for a single dislocation if the dislocation density in the lineage line is known.

[1] J. P. McKelvey and R. L. Longini, J. Appl. Phys. **25**, 634 (1954).

Z10. Bond Dipoles and Piezoelectricity in Zincblende Semiconductors. JOSEPH L. BIRMAN, *Sylvania Electric Products Inc.*—A. von Hippel[1] has recently reemphasized the view[2] that an acentric dipolar array is responsible for the piezoelectric effect. Hence, on symmetry grounds alone all substances crystallizing in the zincblende structure can be expected to exhibit this effect. The present paper is an attempt to make this view quantitative and to calculate the magnitude of the bond dipole moment from the measured piezoelectric constant. It is assumed (1) that each chemical bond is characterized by a vector bond dipole moment directed along the bond, whose magnitude varies linearly with bond length; (2) that the polarization is to be obtained by summing the individual bond dipole vectors; (3) that infinitesimal lattice-elasticity theory applies. The basic equation of piezoelectricity in the zincblende structure is thereby derived. This equation relates initial-bond moment, change in moment with bond length, internal strains, and external (elastic) strains, to the piezopolarization. The equation will be discussed and compared with other recent work.[3]

[1] A. von Hippel, Z. Physik, 133, 158 (1952).
[2] E. Riecke, Abh. Akad. Wiss. Göttingen 38, (1892); W. Voigt, Abh. Akad. Wiss. Göttingen 36, (1890).
[3] B. D. Saksena, Phys. Rev. 81, 1012 (1951). He has neglected the internal strains and the changes in bond angle under strain.

Z11. Electrical Conductivity of Liquid Tellurium.* V. A. JOHNSON, *Purdue University.*—Experiments show that liquid selenium, when pure, behaves as an ideal semiconductor[1] and that liquid germanium has a metallic behavior.[2] Measurements on liquid tellurium[3] indicate a behavior intermediate between that of selenium and germanium, a transition with rising temperature from semiconductor to metallic state. An analysis of conductivity *vs* reciprocal temperature curves for eight liquid-tellurium samples indicates that (1) the slope at the melting point corresponds to the forbidden band width of solid tellurium, (2) above the melting point the measured conductivity can be represented by $(1-f)\sigma_{sc}+f\sigma_m$, where f is a Boltzmann factor $e^{-W/kT}$. σ_{sc} is found from $\sigma_0 \exp(-E_G/2kT)$ with σ_0 determined by the melting point conductivity, and $\sigma_m=A/T$ with A found from the conductivity maximum, and (3) the energy W of the Boltzmann factor is approximately $(0.48-4.8\times10^{-4}T)$ev. One can hypothesize that the change from semiconductor to metallic behavior in tellurium is due to the release of free electrons by the dissociation of the chain structure.

* Work assisted by Signal Corps Contract.
[1] H. W. Henkels, J. Appl. Phys. 21, 725 (1950).
[2] A. S. Epstein, Ph.D. Thesis, Purdue University (1954).
[3] A. Epstein and H. Fritzsche, Phys. Rev. 93, 922; 94, 1426 (1954).

Z12. Noise in Silicon p-n Junction Photocells. G. L. PEARSON, H. C. MONTGOMERY, AND W. L. FELDMANN, *Bell Telephone Laboratories.*—The noise in silicon $p-n$ junction photocells prepared by the gaseous diffusion method[1] has been measured as a function of current and frequency. Under reverse bias conditions it is found that the noise is composed entirely of shot contributions and that the spectrum is white above 70 cps. This is in contrast to other semiconductor devices where larger dark currents contribute an additional $1/f$ spectrum.[2] The theoretical relation for shot noise is $\langle I_s^2\rangle_{Av}=2eiF$ where e is the electronic charge, i the dc current, and F the frequency band. Precise shot measurements on a typical cell in a frequency band from 700 to 900 cps gave 1.62×10^{-19} coulombs for the electronic charge at currents between 10 and 200 microamperes. When used as a photovoltaic device the shot noise is reduced markedly, and this is attributed to the existing space charge.

[1] C. S. Fuller and J. A. Ditzenberger, J. Appl. Phys. 25, 1439 (1954).
[2] H. C. Montgomery and M. A. Clarke, J. Appl. Phys. 24, 1337 (1953).

Z13. Excess Noise and Trapping in Germanium.* H. A. GEBBIE, *M. I. T.*—The frequency dependence of excess noise in specimens of 10 ohm-cm n-type germanium has been measured at temperatures from 100°K to 300°K. The frequency was from 10 cps to 16 Kcps. At 300°K the spectra of all specimens could be represented by the addition of $1/f$ noise and shot noise with a characteristic time equal to the free-hole lifetime. At temperatures about 200°K however, some specimens showed spectra of the same form but the characteristic time of the shot noise was much greater than the free-hole lifetime. This characteristic time increased rapidly with decreasing temperature. In these cases it is suggested that the shot noise is due to trapping. This is supported by the observation that photoconductivity in these specimens increased rapidly with decreasing temperature. The noise spectra at lower temperatures were more complex. Other specimens showed spectra with no measurable shot-noise component at low temperatures. In these cases no trapping was indicated by the photoconductivity.

* The research in this document was supported jointly by the Army, Navy, and Air Force under contract with the Massachusetts Institute of Technology.

Z14. Noise Measurements in Semiconductors at Very Low Frequencies. T. E. FIRLE AND H. WINSTON.—The low-frequency noise spectra of germanium and silicon rectifiers have been determined. Two methods were employed: a numerical analysis according to the Wiener-Khintchine relationship and a frequency translation photo play-back method. No evidence of a deviation from a $1/f^a (a>1)$ noise-power law was found down to frequencies as low as 6×10^{-5} cps.

Z15. Elastic Strain Energy Stored in Mechanically Disturbed Surfaces. R. L. HOPKINS, *Sylvania Electric Products Inc.*—During a study of the electrical properties of mechanically disturbed germanium[1] it was found that thin slabs of germanium and other materials (Ge, Fe, Ni, and Cu are to be reported on) bend in an elastic manner when sandblasted on one of their two major surfaces. The mechanical disturbance caused by such sandblasting is determined by a chemical-etching technique to extend to a depth, α, which depends on the material. This bending is attributed to stresses exerted in the mechanically disturbed region which correspond to elastic strain energy stored during the blasting process. The magnitude of this energy is estimated by a method to be described, the results being compared to a model suggesting that large concentrations of edge dislocations are produced during sandblasting.

[1] E. N. Clarke and R. L. Hopkins, Phys. Rev. 91, 1566 (1953); samples reported here were thick enough so that appreciable bending did not occur.

Author Index to Papers Presented at the 1955 March Meeting at Baltimore

Alexander, L. E.—MA2
Alger, R. S. and R. D. Jordan—Q4
Ames, L., H. S. Sack, and R. M. Wood—L7
Andrews, R. D.—MA5
Antal, J. J., R. J. Weiss, and G. J. Dienes—H6
Apker, L.—U1
Averbach, B. L. and P. S. Rudman—S1
Bacon, Roger and Charles S. Smith—R9
Banas, E. M. and B. A. Mrowca—MA8
Barnett, C. F. and P. M. Stier—G4
Barredo, Joseph G.—K1
Bearden, J. A.—A4
Bedard, F. and H. Meissner—GA4
Beer, A. C.—J4
Benedict, W. S., G. E. Moore, and S. Silverman—Q8
Benzer, Seymour—E2
Bernstein, H. and R. H. Kingston—Z6
Berry, Chester R.—H1
Beshers, D. N. and J. S. Koehler—R11
Birman, Joseph L.—Z10
Blatt, F. J., M. C. Huse, and R. A. Rubenstein—R8
Blewitt, T. H., J. K. Redman, F. A. Sherrill, and R. R. Coltman—S10
Blunt, R. F., H. P. R. Frederikse, and W. R. Hosler—D7
Bodine, J. H. and F. B. Thiess—D2
Bragaw, Chester G., Jr.—V3
Breitman, Leo—V8
Brown, L. Carlton and Dudley Williams—G3
Brown, F. C.—P3
Brown, W. L.—Z1
Burstein, E., G. Picus, B. Henvis, and M. Lax—F10
Cabrera, N. and M. M. Levine—K5
Capucine and Nicholas Inchauspé—K6
Castle, J. G., Jr.—Y6
Cohen, Alvin J.—Q3
Coleman, C. and R. Smoluchowski—S6
Collins, F. M.—Y7
Compton, W. Dale—K8
Conn, Willi M.—Q12
Crawford, J. H., Jr. and D. K. Stevens—D4
D'Altroy, F. and H. Y. Fan—W6
Daunt, J. G. and J. Korringa—Q5
Dash, W. C.—F11
Davisson, J. W., Elias Burstein, and P. L. Smith—K13
deBretteville, A., Jr.—X7
deMars, G., H. Statz, and L. Davis, Jr.—Z3
DeSorbo, W. and D. Turnbull—R12
Dexter, D. L.—D12
Dexter, R. N.—W4
Dieckamp, H.—B5
Dieke, G. H.—U4
Donnay, J. H.—U2
Doty, Paul—C2
Dreyfus, Russell W. and Paul W. Levy—H4
Drougard, M. E., R. Laundauer, and D. R. Young—X8
Duboc, Charles A.—T7
Dunlap, W. C., Jr.—F2
Dutton, David—Q1
Eatherly, W. P.—B9
Ehrenreich, H. and A. W. Overhauser—D8
Enns, J. H., R. L. Martin, and E. Katz—T1
Etzel, H. W.—B8
Fagg, L. W., E. A. Wolicki, R. O. Bondelid, K. L. Dunning, and S. Snyder—G10
Ferguson, K. R.—H9
Firle, T. E. and H. Winston—Z14
Fischbach, D. B. and A. S. Nowick—K7
Fletcher, R. C., F. R. Merritt, W. A. Yager—W5
Flom, D. G.—N1
Forster, Michael J.—V4
Fox, T. G. and S. Loshaek—N8
Fritzsche, H. and K. Lark-Horovitz—D6
Fuller, E. G. and Evans Hayward—G5
Gallagher, J. J., W. C. King, and C. M. Johnson—Q9
Gamow, G.—E3
Gebbie, H. A.—Z13
Gordon, R. B. and A. S. Nowick—H2
Green, Mino and J. A. Kafalas—Z7
Gross, E. P.—W8
Gurnee, E. F., L. T. Patterson, and R. D. Andrews—MA4
Haake, Claus H.—L2
Haar, Lester—Q10
Hamilton, J. F., F. A. Hamm, and J. W. Castle—T4
Hanna, S. S.—A3
Harman, T. C., R. K. Willardson, and A. C. Beer—D3
Harrison, W. A. and Frederick Seitz—B1
Henry, Warren E.—D14
Herman, R., G. E. Moore, S. Silverman, and R. F. Wallis—Q7
Hong, K. and S. Mrozowski—Y9
Hopkins, R. L.—Z15
Hosler, W. R. and H. P. R. Frederikse—D5
Hove, John E.—Y3
Howard, Brian T.—L1
Huibregtse, E. J., M. E. Drougard, and D. R. Young—X6
Hulm, J. K.—GA1
Inchauspé, Nicholas—Q2
Ivory, J. E., F. P. Baldwin, and R. L. Anthony—V1
Jamieson, C. P.—Y4
Jaumot, F. E., Jr., and R. L. Smith—S7
Johnson, V. A.—Z11
Kaiser, H. F., W. T. Mayes, and W. J. Willis—G12
Kanter, M. A.—Y1
Kao, L. P. and E. Katz—D15
Karplus, R.—J2
Katz, E.—T2
Keesom, P. H. and N. Pearlman—GA2
Kiive, P. and H. T. Pinnick—Y5
Kittel, C.—J3
Kleitman, D. and G. Goldsmith—K12
Klontz, E. E., R. R. Pepper, and K. Lark-Horowitz—F4
Kmetko, E. A.—F6
Koehler, J. S.—X1
Koester, Charles J. and M. Parker Givens—K9
Kohn, W.—W9
Korringa, J.—S11
Kriessman, C. J., S. E. Harrison, and H. B. Callen—X4
Krimm, S. and C. Y. Liang—MA6
Kulin, S. A., A. D. Kurtz, and B. L. Averbach—Z8
Kurtz, A. D., S. A. Kulin, and B. L. Averbach—K4
Lambe, John and Clifford C. Klick—L8
Lark-Horovitz, K. and H. Fritzsche—F8
Laurman, J. A. and S. A. Schaaf—GA7
Lax, B.—W1
Lehman, G. W.—K2
Leivo, W. J. and R. Smoluchowski—D1
Levy, Paul W.—H5
Li, Chi Yao and A. S. Nowick—B6
Liang, C. Y. and S. Krimm—MA7
Likely, J. G.—G6
Lipson, H. G., E. Burstein, and P. L. Smith—F3
Loebner, E. E. and H. Freund—L4
Luckey, G.—P2
Luckey, George W.—T9
Lundberg, John Lauren—V7
Luttinger, J. M.—W2
Machlup, Stefan—S12

Mandeville, C. E. and H. O. Albrecht—L9
Marcus, Jules A.—GA6
Marcus, Paul M.—R5
Martin, G. M., F. L. Roth, and R. D. Stiehler—V5
Martin, R. L., J. E. Enns, and E. Katz—T3
Matossi, Frank—L3
Maurer, R. D.—K11
McGuire, T. R., E. J. Scott, and F. H. Grannis—X3
McKelvey, J. P. and R. L. Longini—Z9
Meyer, R. A. and F. L. Bouquet—B7
Meissner, Hans—GA5
Melamed, Nathan T. and Raymond Bowers—L6
Miller, Paul—R3
Mitchell, J. W.—P1
Montgomery, H. C. and W. L. Brown—Z2
Moser, Frank and Franz Urbach—T6
Mrozowski, S.—Y8
Nail, Nelson R., Frank Moser, Pliny E. Goddard, and Franz Urbach—T5
Need, John Logan—G7
Neumark, Gertrude—L10
Newman, R., W. C. Dash, R. N. Hall, and W. E. Burch—F13
Nolle, A. W.—V10
Nowick, A. S. and Chi Yao Li—S13
Nudelman, Sol and Frank Matossi—L5
Odell, F. A.—N3
Otter, F. A., Jr.—R4
Owen, G. E.—A2
Pao, Yoh-Han—N4
Patterson, D. A. and C. C. Klick—L11
Pearlman, N. and P. H. Keesom—GA3
Pearson, G. L., H. C. Montgomery, and W. L. Feldmann—Z12
Pearlstein, E., H. Ingham, and R. Smoluchowski—B3
Pell, E. M.—F12
Philippoff, W. and J. Brodnyan—N7
Plazek, D. J. and John D. Ferry—N5
Plendl, H. S. and F. E. Steigert—G8
Portnoy, William M., Harry Letaw, Jr., and Lawrence Slifkin—F9
Pratt, George W., Jr.—K3
Price, P. J.—D11
Rasor, Ned S.—S8
Rau, Richard and P. H. Miller, Jr.—D10
Reif, F.—P5
Roberts, Donald E. and Leo Mandelkern—V6
Robinson, G. W.—Q6
Robinson, W. H. and R. Smoluchowski—S5
Rosenwasser, Hyman and Paul W. Levy—H3
Rothstein, Jerome—S3
Rudman, P. S. and B. L. Averbach—S2
Sack, W. S.—P4
Salkovitz, E. I. and A. I. Schindler—R7
Sawatsky, A. and F. E. Jaumot, Jr.—S4
Schiefer, H. F.—N2
Schlier, R. E.—S9
Schlinder, A. I. and E. I. Salkovitz—R6
Schulz-DuBois, E., M. Nisenoff, H. Y. Fan, and K. Lark-Horovitz—W10
Segel, R. E. and S. S. Hanna—G11
Segleken, W. G. and H. C. Torrey—G1
Seitz, F.—B2
Seldin, E. J.—Y10
Senitzky, B., I. I. Rabi, and M. L. Perl—G2
Shen, K. Y. and S. F. Singer—M2
Shull, C. G.—X2
Singer, S. F.—M4
Sinsheimer, R. L.—C1
Slichter, W. P. and J. M. Mays—V9
Smith, Alan W.—Y2
Smith, Charles S. and W. B. Daniels—R10
Smoluchowski, R., E. Pearlstein, and H. Ingham—B4
Spencer, T. W.—GA9
Spitzer, W., R. J. Collins, and H. Y. Fan—F7
Statz, H., L. Davis, Jr., and G. deMars—Z4
Stern, Frank—R1
Stevens, D. K.—H7
Stevenson, Donald T.—Z5
Stoeckmann, F., E. Klontz, H. Y. Fan, and K. Lark-Horovitz—F5
Sutherland, G. B. B. M.—E1
Swann, W. F. G.—M1
Swanson, John A.—D13
Swartz, C. D.—A1
Tannenwald, P. E. and H. J. Zeiger—W11
Taylor, G. R.—MA3
Taylor, G. R. and S. R. Darin—V2
Teitler, S., M. Lax, and E. Burstein—W7
Triebwasser, S. and J. Halpern—X5
Tucker, C. W., Jr., and P. Senio—H8
van Roosbroeck, W.—D9
Van Vleck, J. H.—U3
Wall, F. T.—MA1
Watson, J. D.—C3
Webb, J. H.—T10
Weissberg, H. L. and A. S. Berman—GA8
Wentworth, R. C. and S. F. Singer—M3
West, W. and V. I. Saunders—T8
White, Harrison C.—R2
Wilkinson, Joseph R. and Raymond K. Sheline—G9
Williams, Malcolm L., Robert F. Landel, and John D. Ferry—N6
Woodbury, H. H. and W. W. Tyler—F1
Yafet, Y.—J1
Zeiger, H. J.—W3
Zernow, L. and G. Hauver—Q11

CONTENTS—Continued

J. W. T. Dabbs, R. D. Roberts, and S. Bernstein 1512

J. Marshall, L. Marshall, and V. A. Nedzel 1513

Mark Fred, Frank S. Tomkins, and William F. Meggers 1514

Roger G. Newton 1514

Max Chrétien 1515

Kenneth W. Ford 1516

O. E. Johnson, E. G. Johnson, and L. M. Langer 1517

A. Ghiorso, B. G. Harvey, G. R. Choppin, S. G. Thompson, and G. T. Seaborg 1518

G. R. Choppin, B. G. Harvey, S. G. Thompson, and A. Ghiorso 1519

Herbert DeStaebler, Jr. and B. V. Sreekantan 1520

Donald A. Hicks, John Ise, Jr., and Robert V. Pyle 1521

J. B. French and B. J. Raz 1523

A. M. Lane and C. F. Wandel 1524

J. K. Perring and J. S. Story 1525

L. Bertoia, E. Clementel, and C. Villi 1526

Proceedings of the American Physical Society:

Program of the 1955 March Meeting Held at Baltimore, March 17–19, 1955 (Corresponding to Bulletin of the *American Physical Society, Vol. 30, No. 2*) 1528

CONTENTS

THE PHYSICAL REVIEW SECOND SERIES, VOLUME [illegible] [illegible]

Direct Evaluation of Fractional Parentage Coefficients Using Racah Operators; Generalization of Racah Particle Wave Functions . . . . . M. J. England
Inelastic Collision Cross Sections at 1.0-, 4.0-, and 4.5-Mev Neutron Energies . . . . . J. R. Beyster, R. L. Henkel, R. A. Nobles, and J. M. Ricca
Spin, Quadrupole Moment, and Mass of Selenium-75 . . . . . L. C. Aamodt and F. C. Fletcher
Radiations of I^{126} . . . . . L. Koerts, P. Macklin, B. Farrelly, R. [illegible] Lenhout, and C. S. Wu
Pair Spectrometer Measurements of the Radiations from Excited States of [illegible] . . . . . R. D. Bent, T. W. Bonner, and R. F. Sippel
Electric Excitation of Certain Medium-Weight Nuclei by Protons . . . . . Hans Mark, Clyde McCormick, and Clark Goodman
Radionuclides Al^{24}, P^{32}, Cl^{36}, and Sc^{46} . . . . . Neal W. Glassford and Reginald Richardson
Radiochemical Study of Neutron-Deficient Chains in the Noble Metal Region . . . . . W. G. Smith and J. M. Hollander
K-Shell Internal Conversion Coefficients . . . . . R. C. Hoyt and R. D. Birkhoff
Radiation Width Variations in the Slow-Neutron Resonances of Europium and Samarium . . . . . H. H. Landon and V. L. Sailor
Model for Asymmetric Fission . . . . . R. D. Hill
Angular Momentum Coupling in Deuteron Reactions . . . . . T. Ausländer and J. B. French
Electric Monopole Transitions in C^{12} and O^{16} . . . . . L. I. Schiff
Nuclear Moments of Nb^{93}, La^{139}, Os^{187}, and Hg^{201} . . . . . Kiyoshi Murakawa
Energy Levels in B^9 and Be^7 from the Reactions $C^{13}(p,\alpha)B^9$ and $B^{10}(p,\alpha)Be^7$ . . . . . J. B. Reynolds
K and L X-Ray Intensities in Cesium-131 Decay . . . . . Richard W. Fink and Berol L. Robinson
Photoneutron Cross Sections in Mg^{24}, Mg^{25}, Zr^{90}, Zr^{91} . . . . . Robert Nathans and Paul F. Yergin
Angular Distribution of Fast Neutrons Scattered from Lead . . . . . W. J. Rhein
Threshold Values of Internal Conversion Coefficients for the K-Shell . . . . . B. I. Spinrad
Search for the Reaction $T(d,\gamma)He^5$ . . . . . George A. Sawyer and Louis C. Burkhardt
Gamma Rays in the Decay of Na^{22} . . . . . John E. Iversen and W. S. Koski
Properties of Excited States of Pd and Cd Nuclei by Coulomb Excitation . . . . . G. M. Temmer and N. P. Heydenburg
Gamma Rays from the Low-Energy Proton Bombardment of Beryllium . R. E. Carlson and E. B. Nelson
Nuclear Magnetic Moments of Cl^{35}, Rb^{185}, and W^{183} . . . . . P. B. Soop and C. D. Jeffries
Magnetic Moment and Mass of Chlorine-36 . . . . . L. C. Aamodt and P. C. Fletcher
Positron Emission from Np^{234} . . . . . R. J. Prestwood, H. L. Smith, C. I. Browne, and D. C. Hoffman
Nuclear Pairs from the 3.4-Mev State in Ca^{40} . . . . . R. D. Bent, T. W. Bonner, and J. H. McCrary
U^{235} Thermal Neutron Fission Yields at Masses 90 and 91 . . . . . George W. Reed
Production of Charged Pions in $N-P$ Collisions . . . . . Gaurang B. Yodh
Solar Flare and Magnetic Storm Effects in Cosmic-Ray Intensity near the Geomagnetic N Pole . . . . . John W. Coltman and Scott E. Forbush
Diffusion Cloud-Chamber Study of Very Slow Mesons. I. Internal Pair Formation . . . . . C. P. Sargent, R. Cornelius, M. Rinehart, L. M. Lederman, and K. Rogers
Internal Pair Production Associated with the Emission of High-Energy Gamma Rays . . . . . Norman M. Kroll and Walter Wada
Scattering of High-Energy Electrons by Nuclei . . . . . A. E. Glassgold
Nuclear Cross Sections for 1.4-Bev Neutrons . . . . . T. Coor, D. A. Hill, W. F. Hornyak, L. W. Smith, and G. Snow
High-Energy Cross Sections. I. The Size of the Nucleus . . . . . Robert W. Williams
High-Energy Cross Sections. II. Nucleon-Nucleon Cross Section at Cosmic-Ray Energies . . . . . Robert W. Williams
Direction of Proton Spin Polarization Produced by Elastic Scattering . . . . . L. Marshall and J. Marshall
Association of a "Unipolar" Magnetic Region on the Sun with Changes of Primary Cosmic-Ray Intensity . . . . . J. A. Simpson, H. W. Babcock, and H. D. Babcock
A^3-C^3 Production in $\pi^- - P$ Collisions at 1 Bev . . . . . W. D. Walker
Measurement of the Čerenkov Radiation from Positive and Negative Pi Mesons . . . . . J. R. Winckler, E. N. Mitchell, K. A. Anderson, and L. Peterson
π^--Nucleon Collisions at 1.5 Bev . . . . . W. D. Walker and J. Crussard
Meson Pair Theory . . . . . Abraham Klein and Bruce H. McCormick
High-Energy Reactions and the Evidence for Correlations in the Nuclear Ground-State Wave Functions . . . . . K. A. Brueckner, R. J. Eden, and N. C. Francis
Nonrelativistic Interaction Between Two Nucleons . . . . . David Feldman
Effect of Renormalization on Meson-Nucleon S-Scattering . . . . . Maurice M. Lévy
Many-Body Problem with Strong Forces . . . . . Robert Jastrow
Statistical Model for High-Energy Events . . . . . Joseph V. Lepore and Maurice Neuman
Projection Operator for the Rarita-Schwinger Equation . . . . . F. J. Milford
Fourth-Order Radiative Corrections to Atomic Energy Levels. II . Robert L. Mills and Norman M. Kroll
Conservation of Heavy Particles and Generalized Gauge Transformations . . . . . T. D. Lee and C. N. Yang
Multiple Photon Production in Quantum Electrodynamics . . . . . Suraj N. Gupta

(*continued on cover page three*)

LANCASTER PRESS, INC., LANCASTER, PA.